

Complexity

Computational Methods for Modeling, Simulating, and Optimizing Complex Systems

Lead Guest Editor: Raúl Baños

Guest Editors: Frédéric Magoulès and Francisco G. Montoya





**Computational Methods for Modeling,
Simulating, and Optimizing Complex Systems**

Complexity

**Computational Methods for Modeling,
Simulating, and Optimizing Complex
Systems**

Lead Guest Editor: Raúl Baños


Guest Editors: Frédéric Magoulès and Francisco G.
Montoya



Copyright © 2020 Hindawi Limited. All rights reserved.

This is a special issue published in "Complexity." All articles are open access articles distributed under the Creative Commons Attribution License, which permits unrestricted use, distribution, and reproduction in any medium, provided the original work is properly cited.

Chief Editor

Hiroki Sayama , USA

Associate Editors

Albert Diaz-Guilera , Spain
Carlos Gershenson , Mexico
Sergio Gómez , Spain
Sing Kiong Nguang , New Zealand
Yongping Pan , Singapore
Dimitrios Stamovlasis , Greece
Christos Volos , Greece
Yong Xu , China
Xinggang Yan , United Kingdom



Academic Editors

Andrew Adamatzky, United Kingdom
Marcus Aguiar , Brazil
Tarek Ahmed-Ali, France
Maia Angelova , Australia
David Arroyo, Spain
Tomaso Aste , United Kingdom
Shonak Bansal , India
George Bassel, United Kingdom
Mohamed Boutayeb, France
Dirk Brockmann, Germany
Seth Bullock, United Kingdom
Diyi Chen , China
Alan Dorin , Australia
Guilherme Ferraz de Arruda , Italy
Harish Garg , India
Sarangapani Jagannathan , USA
Mahdi Jalili, Australia
Jeffrey H. Johnson, United Kingdom
Jurgen Kurths, Germany
C. H. Lai , Singapore
Fredrik Liljeros, Sweden
Naoki Masuda, USA
Jose F. Mendes , Portugal
Christopher P. Monterola, Philippines
Marcin Mrugalski , Poland
Vincenzo Nicosia, United Kingdom
Nicola Perra , United Kingdom
Andrea Rapisarda, Italy
Céline Rozenblat, Switzerland
M. San Miguel, Spain
Enzo Pasquale Scilingo , Italy
Ana Teixeira de Melo, Portugal



Shahadat Uddin , Australia
Jose C. Valverde , Spain
Massimiliano Zanin , Spain

Contents





Extension of Optimal Homotopy Asymptotic Method with Use of Daftardar–Jeffery Polynomials to Coupled Nonlinear-Korteweg-De-Vries System

Rashid Nawaz , Zawar Hussain, Abraiz Khattak, and Adam Khan 
Research Article (6 pages), Article ID 6952709, Volume 2020 (2020)





Evolutionary Hyperheuristics for Location-Routing Problem with Simultaneous Pickup and Delivery

Yanwei Zhao , Longlong Leng , Jingling Zhang, Chunmiao Zhang, and Wanliang Wang
Research Article (24 pages), Article ID 9291434, Volume 2020 (2020)


A Methodology for Classifying Search Operators as Intensification or Diversification Heuristics

Jorge A. Soria-Alcaraz , Gabriela Ochoa, Andres Espinal , Marco A. Sotelo-Figueroa , Manuel Ornelas-Rodriguez, and Horacio Rostro-Gonzalez 
Research Article (10 pages), Article ID 2871835, Volume 2020 (2020)




A Fault Diagnosis Method for Power Transmission Networks Based on Spiking Neural P Systems with Self-Updating Rules considering Biological Apoptosis Mechanism

Wei Liu, Tao Wang , Tianlei Zang , Zhu Huang, Jun Wang, Tao Huang , Xiaoguang Wei , and Chuan Li
Research Article (18 pages), Article ID 2462647, Volume 2020 (2020)




Optimizing Transmit Sequence and Instrumental Variables Receiver for Dual-Function Complexity System

Yu Yao , Junhui Zhao, and Lenan Wu
Research Article (13 pages), Article ID 4134851, Volume 2020 (2020)

A Hybrid Grey Prediction Model for Small Oscillation Sequence Based on Information Decomposition

Meng Zhou , Bo Zeng , and Wenhao Zhou 
Research Article (13 pages), Article ID 5071267, Volume 2020 (2020)




Self-Organized Criticality on Twitter: Phenomenological Theory and Empirical Investigation Based on Data Analysis Results

Andrey Dmitriev , Victor Dmitriev , and Stepan Balybin 
Research Article (16 pages), Article ID 8750643, Volume 2019 (2019)






Modeling a Simulation for Sociotechnical Resilience

Fredy Tantri and Sulfikar Amir 
Research Article (11 pages), Article ID 7950629, Volume 2019 (2019)



Ship Steering Control Based on Quantum Neural Network

Wei Guan , Haotian Zhou, Zuoqing Su , Xianku Zhang , and Chao Zhao
Research Article (10 pages), Article ID 3821048, Volume 2019 (2019)





CC²: Defending Hybrid Worm on Mobile Networks with Two-Dimensional Circulation Control

Hailu Yang , Deyun Chen , Guanglu Sun , Xiaoyu Ding , and Yu Xin 
Research Article (19 pages), Article ID 9057531, Volume 2019 (2019)

An Optimal Composition Strategy for Knowledge Service Component Based on Flexible Tracking Particle Swarm Algorithm

Yan-chao Yin , Fu-zhao Chen, Wei-zhi Liao , and Cui-yin Liu
Research Article (14 pages), Article ID 8545364, Volume 2019 (2019)

Computing the Mean-Variance-Sustainability Nondominated Surface by ev-MOGA

A. Garcia-Bernabeu , J. V. Salcedo , A. Hilario , D. Pla-Santamaria , and Juan M. Herrero
Research Article (12 pages), Article ID 6095712, Volume 2019 (2019)

Traffic Model and On-Ramp Metering Strategy under Foggy Weather Conditions Using T-S Fuzzy Systems

Changle Sun and Hongyan Gao 
Research Article (12 pages), Article ID 5125724, Volume 2019 (2019)



Dynamic Game and Coordination Strategy of Multichannel Supply Chain Based on Brand Competition

Junhai Ma , Fang Zhang , and Binshuo Bao 
Research Article (26 pages), Article ID 4802360, Volume 2019 (2019)


Dynamically Dimensioned Search Grey Wolf Optimizer Based on Positional Interaction Information

Fu Yan , Jianzhong Xu , and Kumchol Yun 
Research Article (36 pages), Article ID 7189653, Volume 2019 (2019)

Simulation Modeling of a Pharmaceutical Tablet Manufacturing Process via Wet Granulation

Zhengsong Wang , Zhen Pan, Dakuo He , Jiahui Shi, Shouxin Sun, and Yue Hou
Research Article (16 pages), Article ID 3659309, Volume 2019 (2019)



A Novel Model with GA Evolving FWNN for Effluent Quality and Biogas Production Forecast in a Full-Scale Anaerobic Wastewater Treatment Process

Zehua Huang, Renren Wu, XiaoHui Yi, Hongbin Liu, Jiannan Cai, Guoqiang Niu, Mingzhi Huang , and Guangguo Ying
Research Article (13 pages), Article ID 2468189, Volume 2019 (2019)


Path Optimization of Mobile Sink Node in Wireless Sensor Network Water Monitoring System

Fan Chao, Zhiqin He, Aiping Pang , Hongbo Zhou, and Junjie Ge
Research Article (10 pages), Article ID 5781620, Volume 2019 (2019)

Research on Dynamic Game Model and Application of China's Imported Soybean Price in the Context of China-US Economic and Trade Friction



Yi Wang , Hui Wang, and Shubing Guo 
Research Article (13 pages), Article ID 6048186, Volume 2019 (2019)

Study on the User Density Identification via Improved Whale Optimization Algorithm in Device-to-Device Communication

Yao Zhang , Zhongliang Deng, and Aihua Hu
Research Article (9 pages), Article ID 8147289, Volume 2019 (2019)


Contents

The Evolution of Collective Strategies in SMEs' Innovation: A Tripartite Game Analysis and Application

Lixia Liu , Yuanshi Huang, and Xueli Zhan 

Research Article (15 pages), Article ID 9326489, Volume 2019 (2019)

A New Decision Method for Public Opinion Crisis with the Intervention of Risk Perception of the Public

Zhiying Wang , Xiaodi Liu , and Shitao Zhang

Research Article (14 pages), Article ID 9527218, Volume 2019 (2019)

Research Article

Extension of Optimal Homotopy Asymptotic Method with Use of Daftardar–Jeffery Polynomials to Coupled Nonlinear-Korteweg-De-Vries System

Rashid Nawaz ¹, Zawar Hussain,¹ Abraiz Khattak,² and Adam Khan ^{3,4}

¹Department of Mathematics, Abdul Wali Khan University, Mardan, KP, Pakistan

²Department of Electrical Power Engineering, U.S.-Pakistan Center for Advanced Studies in Energy (USPCAS-E), National University of Sciences and Technology, Islamabad (44000), Pakistan

³Department for Management of Science and Technology Development, Ton Duc Thang University, Ho Chi Minh City, Vietnam

⁴Faculty of Electrical & Electronics Engineering, Ton Duc Thang University, Ho Chi Minh City, Vietnam

Correspondence should be addressed to Adam Khan; adamkhan@tdtu.edu.vn

Received 25 July 2019; Revised 3 November 2019; Accepted 28 November 2019; Published 9 March 2020

Guest Editor: Raúl Baños

Copyright © 2020 Rashid Nawaz et al. This is an open access article distributed under the Creative Commons Attribution License, which permits unrestricted use, distribution, and reproduction in any medium, provided the original work is properly cited.

In this paper, Daftardar–Jeffery Polynomials are introduced in the Optimal Homotopy Asymptotic Method for solution of a coupled system of nonlinear partial differential equations. The coupled nonlinear KdV system is taken as test example. The results obtained by the proposed method are compared with the multistage Optimal Homotopy Asymptotic Method. The results show the efficiency and consistency of the proposed method over the Optimal Homotopy Asymptotic Method. In addition, accuracy of the proposed method can be improved by taking higher order approximations.

1. Introduction

Differential equations play a vital role in engineering and applied sciences. The nonlinear coupled Partial Differential Equations (PDEs) have a variety of applications in physics, acoustics, optics, elasticity, hydrodynamics, aerodynamics, electromagnetism, chemical kinetics, economics, computer science, and financial mathematics. The exact solutions of nonlinear PDEs cannot be found easily. Different approaches have been adopted by researchers for the approximate solutions of these equations. The well-known approaches are Runge–Kutta method (R-K) [1, 2], Shooting method (SM) [3, 4], Finite Difference Method (FDM) [5–7], Finite Element Method (FEM) [8, 9], Collocation Method [10–13], and Homotopy Analysis Method (HAM) [14, 15]. Recently, Marinca et al. introduced the Optimal Homotopy Asymptotic Method (OHAM) for the solution of nonlinear

problems [16–18] which made the perturbation methods independent of the hypothesis of small parameters and huge computational work. They used more flexible function called the auxiliary function which controls the convergence of the proposed method. To improve the accuracy and to ensure the faster convergence, one can use an increased number of convergence control parameters in the first order of approximation. A more general formulation, which emphasizes the above features, was presented in [19, 20]. Later on, Ali et al. introduced a new method based on adaptation of the Optimal Homotopy Asymptotic Method (OHAM) with Daftardar–Jeffery polynomials, called OHAM-DJ, to solve nonlinear problems [21, 22]. Shah et al. applied OHAM-DJ for the solution of linear and nonlinear Klein–Gordon equations [23]. Our main goal in this work is to extend the applications of OHAM-DJ to a coupled nonlinear KdV system.

The coupled nonlinear KdV system has the following form:

$$\begin{aligned} \frac{\partial \zeta(\eta, t)}{\partial t} - 0.5 \frac{\partial^3 \zeta(\eta, t)}{\partial \eta^3} + 3\zeta(\eta, t) \frac{\partial \zeta(\eta, t)}{\partial \eta} \\ - 3 \frac{\partial}{\partial \eta} \zeta(\eta, t) w(\eta, t) = 0, \\ \frac{\partial \xi(\eta, t)}{\partial t} + \frac{\partial^3 \xi(\eta, t)}{\partial \eta^3} - 3\zeta(\eta, t) \frac{\partial \xi(\eta, t)}{\partial \eta} = 0, \\ \frac{\partial w(\eta, t)}{\partial t} + \frac{\partial^3 w(\eta, t)}{\partial \eta^3} - 3\zeta(\eta, t) \frac{\partial w(\eta, t)}{\partial \eta} = 0. \end{aligned} \quad (1)$$

2. Basic Idea of OHAM-DJ

Consider the nonlinear differential equation:

$$L(\zeta(\eta, t)) + N(\zeta(\eta, t)) + g(\eta, t) = 0, \quad \eta \in \Omega, \quad B\left(\zeta, \frac{\partial \zeta}{\partial t}\right) = 0. \quad (2)$$

In equation (2), L is a linear operator, N is a nonlinear operator, ζ is an unknown function, g is a known function, and B is a boundary operator. According to OHAM-DJ, the optimal homotopy $H(\varphi(\eta, t; s)): \Omega \times [0, 1] \rightarrow R$ satisfies the following equation:

$$(1-s)[L(\varphi(\eta, t; s)) + g(\eta, t)] = H(s)[L(\varphi(\eta, t; s)) + N(\varphi(\eta, t; s)) + g(\eta, t)]. \quad (3)$$

In equation (3), $s \in [0, 1]$ is an embedding parameter, $H(s)$ is a nonzero auxiliary function for $s \neq 0$, and its value is zero for $s = 0$. The unknown function $\zeta(\eta, t; s)$ starts from $\zeta(\eta, t; 0) = \zeta_0(\eta, t)$ to $\zeta(\eta, t; 1) = \zeta(\eta, t)$ as s approaches from 0 to 1.

The auxiliary function $H(s)$ is chosen in the form:

$$H(s) = \sum_{i=1}^{\infty} s^i C_i. \quad (4)$$

Here, C_1, C_2, C_3, \dots are constants. Next, we use the Taylor series to expand the function $\varphi(\eta, t; s)$ about s :

$$\varphi(\eta, t; s) = \zeta_0(\eta, t) + \sum_{j=1}^{\infty} \zeta_j(\eta, t; C_i) s^j. \quad (5)$$

The nonlinear function $N(\zeta(\eta, t; s))$ is decomposed as

$$\begin{aligned} N(\zeta(\eta, t; s)) = N(\zeta_0(\eta, t)) + s[N(\zeta_0(\eta, t) + \zeta_1(\eta, t)) \\ - N(\zeta_0(\eta, t))] + s^2[N(\zeta_0(\eta, t) + \zeta_1(\eta, t) \\ + \zeta_2(\eta, t)) - N(\zeta_0(\eta, t) + \zeta_1(\eta, t))] + \dots \end{aligned} \quad (6)$$

The expressions on the right-hand side of (6) are the DJ polynomials given as follows:

$$\begin{aligned} N(\zeta_0(\eta, t)), [N(\zeta_0(\eta, t) + \zeta_1(\eta, t)) - N(\zeta_0(\eta, t))], \\ [N(\zeta_0(\eta, t) + \zeta_1(\eta, t) + \zeta_2(\eta, t)) - N(\zeta_0(\eta, t) + \zeta_1(\eta, t))]. \end{aligned} \quad (7)$$

In fact, the above polynomials are the terms of Taylor's series of the nonlinear term. The convergence of these polynomials was determined by Bhalekar and Daftardar-Gejji [24]. For simplification we expressed the polynomials as

$$N_0 = N(\zeta_0(\eta, t)), \quad (8)$$

$$N_m = N\left(\sum_{i=0}^m \zeta_i(\eta, t)\right) - N\left(\sum_{i=0}^{m-1} \zeta_i(\eta, t)\right). \quad (9)$$

Now, we can also express

$$N(\zeta(\eta, t; s)) = N_0 + \sum_{k=1}^{\infty} s^k N_k. \quad (10)$$

Substituting equations (8)–(10) in equation (3) and comparing the like terms of s , we get the different order problems given as follows.

The zero-th order problem is

$$\begin{aligned} N(\zeta_0(\eta, t)) + g(\eta, t) = 0, \\ B\left(\zeta_0, \frac{\partial \zeta_0}{\partial t}\right) = 0. \end{aligned} \quad (11)$$

The first-order problem is

$$\begin{aligned} L(\zeta_1(\eta, t)) = C_1 N_0(\zeta_0(\eta, t)), \\ B\left(\zeta_1, \frac{\partial \zeta_1}{\partial t}\right) = 0. \end{aligned} \quad (12)$$

The second-order problem is

$$\begin{aligned} L(\zeta_2(\eta, t)) - L(\zeta_1(\eta, t)) = C_2 N_0(\zeta_0(\eta, t)) + C_1 [L(\zeta_1(\eta, t)) \\ + N_1(\zeta_0(\eta, t), \zeta_1(\eta, t))], \\ B\left(\zeta_2, \frac{\partial \zeta_2}{\partial t}\right) = 0. \end{aligned} \quad (13)$$

The general governing equation for $\zeta_j(\eta, t)$ is given by using

$$\begin{aligned} L(\zeta_j(\eta, t)) - L(\zeta_{j-1}(\eta, t)) = C_j N_0(\zeta_0(\eta, t)) \\ + \sum_{i=1}^{j-1} C_i [L(\zeta_{j-i}(\eta, t)) \\ + N_{j-i}(\zeta_0(\eta, t), \zeta_1(\eta, t), \\ \dots, \zeta_{j-i}(\eta, t))], \\ B\left(\zeta_j, \frac{\partial \zeta_j}{\partial t}\right) = 0, \quad j = 2, 3, \dots \end{aligned} \quad (14)$$

The solution of higher order problems can be easily estimated; however, the second-order solution gives encouraging results.

For $s = 1$, equation (5) reduces to

$$\tilde{\zeta}(\eta, t; C_i) = \zeta_0(\eta, t) + \sum_{j \geq 1} \zeta_j(\eta, t; C_i). \quad (15)$$

Replacing equation (15) into equation (2), we get the residual as

$$\mathfrak{R}(\eta, t; C_i) = L(\tilde{\zeta}(\eta, t; C_i)) + N(\tilde{\zeta}(\eta, t; C_i)) + g(\eta, t). \quad (16)$$

If $\mathfrak{R}(\eta, t; C_i) = 0$, then we get the exact solution. Different methods can be used to estimate the values of constants $C_1, C_2, C_3, \dots, C_j$; but the method of least square is the most common method. In the method of least square, we minimize the errors by taking the square of the residuals over the given domain to get the following functional:

$$\mathfrak{F}(C_i) = \int_0^t \int_{\Omega} \mathfrak{R}^2(\eta, t; C_i) d\eta dt. \quad (17)$$

Differentiating J with respect to $C_1, C_2, C_3, \dots, C_j$, we get the following system of equations containing $C_1, C_2, C_3, \dots, C_j$:

$$\frac{\partial \mathfrak{F}}{\partial C_1} = \frac{\partial \mathfrak{F}}{\partial C_2} = \dots = \frac{\partial \mathfrak{F}}{\partial C_j} = 0. \quad (18)$$

Solving the above system, we get the values of $C_1, C_2, C_3, \dots, C_j$. Replacing the values of $C_1, C_2, C_3, \dots, C_j$ in equation (14), we get the approximate solution.

The method of least squares is a powerful technique and has been used in many other methods such as Optimal Homotopy Perturbation Method (OHPM) and Optimal Auxiliary Functions Method (OAFM) for calculating the optimum values of arbitrary constants [25, 26].

3. Implementation of OHAM-DJ to a Coupled System of Nonlinear KdV Equations

Problem 1. Consider system (1) with initial conditions [27]:

$$\begin{aligned} \zeta(\eta, 0) &= \frac{1}{3}(\omega - 8l^2) + 4l^2 \tanh^2(l\eta), \\ \xi(\eta, 0) &= \frac{-4l^2(3l^2C_0 - 2\omega C_2 + 4l^2C_2)}{3C_2^2} + \frac{4l^2}{C_2} \tanh^2(l\eta), \\ w(\eta, 0) &= C_0 + C_2 \tanh^2(l\eta). \end{aligned} \quad (19)$$

Exact solution of equation (1) is

$$\begin{aligned} \zeta(\eta, t) &= \frac{1}{3}(\omega - 8l^2) + 4l^2 \tanh^2(l(\eta + \omega t)), \\ \xi(\eta, t) &= \frac{-4l^2(3l^2C_0 - 2\omega C_2 + 4l^2C_2)}{3C_2^2} + \frac{4l^2}{C_2} \tanh^2((\eta + \omega t)), \\ w(\eta, t) &= C_0 + C_2 \tanh^2(l(\eta + \omega t)), \end{aligned} \quad (20)$$

where $t = 1, \omega = 1.5, l = 0.1, C_0 = 1.5$, and $C_2 = 0.1$ are different parameters. Applying the proposed method, we have the following.

The zero-th order problem is

$$\begin{aligned} \frac{\partial \zeta_0(\eta, t)}{\partial t} &= 0, \\ \zeta_0(\eta, 0) &= \frac{1}{3}(\omega - 8l^2) + 4l^2 \tanh^2(l\eta), \\ \frac{\partial \xi_0(\eta, t)}{\partial t} &= 0, \\ \xi_0(\eta, 0) &= \frac{-4l^2(3l^2C_0 - 2\omega C_2 + 4l^2C_2)}{3C_2^2} + \frac{4l^2}{C_2} \tanh^2(l\eta), \\ \frac{\partial w_0(\eta, t)}{\partial t} &= 0, \\ w_0(\eta, 0) &= C_0 + C_2 \tanh^2(l\eta). \end{aligned} \quad (21)$$

Its solution is

$$\begin{aligned} \zeta_0(\eta, t) &= 0.04000000000000001(11.833333333333333 \\ &\quad + 1. \tanh^2(0.1\eta)), \\ \xi_0(\eta, t) &= 0.40000000000000001(0.8366666666666666 \\ &\quad + 1. \tanh^2(0.1\eta)), \\ w_0(\eta, t) &= 0.1(15. + 1. \tanh^2(0.1\eta)). \end{aligned} \quad (22)$$

The first-order problem is

$$\begin{aligned} \frac{\partial \xi_0(\eta, t)}{\partial \eta} - 3C_1 \xi_0(\eta, t) \frac{\partial w_0(\eta, t)}{\partial \eta} + 0.5C_1 \frac{\partial^3 \zeta_0(\eta, t)}{\partial \eta^3} &= 0, \zeta_1(\eta, 0) = 0, \\ -\frac{\partial \xi_0(\eta, t)}{\partial t} - C_3 \frac{\partial \xi_0(\eta, t)}{\partial t} + \frac{\partial \xi_1(\eta, t)}{\partial t} + 3C_3 \zeta_0(\eta, t) \frac{\partial \xi_0(\eta, t)}{\partial \eta} \\ - C_3 \frac{\partial^3 \xi_0(\eta, t)}{\partial \eta^3} &= 0, \xi_1(\eta, 0) = 0. \\ -\frac{\partial w_0(\eta, t)}{\partial \tau} - C_5 \frac{\partial w_0(\eta, t)}{\partial t} + 3C_5 \zeta_0(\eta, t) \frac{\partial w_0(\eta, t)}{\partial t} + \frac{\partial w_1(\eta, t)}{\partial t} \\ - C_5 \frac{\partial^3 w_0(\eta, t)}{\partial \eta^3} &= 0, w_1(\eta, 0) = 0. \end{aligned} \quad (23)$$

TABLE 1: Absolute errors obtained by first-order OHAM-DJ and comparison is made with MOHAM of $\zeta(\eta, t)$ at $t = 1, \omega = 1.5, l = 0.1, C_0 = 1.5$, and $C_2 = 0.1$.

	$t = 0.1$		$t = 0.01$	
η	MOHAM [27]	OHAM-DJ	MOHAM [27]	OHAM-DJ
0	8.8667×10^{-4}	8.99865×10^{-6}	8.99865×10^{-6}	8.99999×10^{-8}
20	7.128×10^{-4}	1.1948×10^{-4}	8.06039×10^{-5}	1.20499×10^{-5}
40	1.38951×10^{-5}	2.35856×10^{-6}	1.58421×10^{-6}	2.38×10^{-7}
60	2.54789×10^{-7}	4.32582×10^{-8}	2.90535×10^{-8}	4.3652×10^{-9}
80	4.66673×10^{-9}	7.92321×10^{-10}	5.32147×10^{-10}	7.99535×10^{-11}
100	8.54742×10^{-11}	1.45118×10^{-11}	9.74665×10^{-12}	1.46427×10^{-12}

TABLE 2: Absolute errors obtained by first order OHAM-DJ and comparison is made with MOHAM of $\xi(\eta, t)$ at $t = 1, \omega = 1.5, l = 0.1, C_0 = 1.5$, and $C_2 = 0.1$.

	$t = 0.1$		$t = 0.01$	
η	MOHAM [27]	OHAM-DJ	MOHAM [27]	OHAM-DJ
0	8.8667×10^{-3}	8.99865×10^{-5}	8.99865×10^{-5}	8.99999×10^{-7}
20	7.128×10^{-3}	7.7428×10^{-4}	8.06039×10^{-4}	7.84417×10^{-5}
40	1.38951×10^{-4}	1.50524×10^{-5}	1.58421×10^{-5}	1.52668×10^{-6}
60	2.54789×10^{-6}	2.75994×10^{-7}	2.90535×10^{-7}	2.79932×10^{-8}
80	4.66673×10^{-8}	5.05511×10^{-9}	5.32146×10^{-9}	5.12724×10^{-10}
100	8.54741×10^{-10}	9.25876×10^{-11}	9.7466×10^{-11}	9.39082×10^{-12}

TABLE 3: Absolute errors obtained by first order OHAM-DJ and comparison is made with MOHAM of $w(\eta, t)$ at $t = 1, \omega = 1.5, l = 0.1, C_0 = 1.5$, and $C_2 = 0.1$.

	$t = 0.1$		$t = 0.01$	
η	MOHAM [27]	OHAM-DJ	MOHAM [27]	OHAM-DJ
0	2.2166×10^{-3}	2.2495×10^{-5}	2.2496×10^{-5}	2.5×10^{-7}
20	1.782×10^{-3}	1.93585×10^{-4}	2.0151×10^{-4}	1.9611×10^{-5}
40	3.4737×10^{-5}	3.76347×10^{-6}	3.9605×10^{-6}	3.8170×10^{-7}
60	6.3697×10^{-7}	6.9005×10^{-8}	7.2633×10^{-8}	6.9989×10^{-9}
80	1.1666×10^{-8}	1.2639×10^{-9}	1.3303×10^{-9}	1.2819×10^{-10}
100	2.1368×10^{-10}	2.3149×10^{-11}	2.4366×10^{-11}	23479×10^{-12}

Solution of the first-order problem is given as

$$\begin{aligned}
 \zeta_1(\eta, t, C_1) &= 0.000320000000000000013t(473.249999999999999999C_1 \operatorname{sech}^2(0.1\eta) \tanh(0.1\eta) + 1.C_1 \operatorname{sech}^4(0.1\eta) \tanh(0.1\eta) \\
 &\quad + 102.49999999999999999999999C_1 \operatorname{sech}^2(0.1\eta) \tanh^3(0.1\eta)), \\
 \xi_1(\eta, t, C_3) &= -0.0064000000000000002t(1.C_3 \operatorname{sech}^4(0.1\eta) \tanh(0.1\eta) - 0.5C_3 \operatorname{sech}^2(0.1\eta) \tanh^3(0.1\eta)), \\
 w_1(\eta, t, C_5) &= -0.00160000000000000005t(1.C_5 \operatorname{sech}^4(0.1\eta) \tanh(0.1\eta) - 0.5C_5 \operatorname{sech}^2(0.1\eta) \tanh^3(0.1\eta)).
 \end{aligned} \tag{24}$$

Adding equations (22) and (24), we get first-order approximate solution by OHAM-DJ as

$$\begin{aligned}
 \tilde{\zeta}(\eta, t) &= \zeta_0(\eta, t) + \zeta_1(\eta, t, C_1), \\
 \tilde{\xi}(\eta, t) &= \xi_0(\eta, t) + \xi_1(\eta, t, C_3), \\
 \tilde{w}(\eta, t) &= w_0(\eta, t) + w_1(\eta, t, C_5).
 \end{aligned} \tag{25}$$

The values of convergence control constants are calculated using the method of least squares whose values are given as follows:

$$\begin{aligned}
 C_1 &= -0.03137136500930365, \\
 C_3 &= 1.8490804836636396, \\
 C_5 &= 1.8456318876033717.
 \end{aligned} \tag{26}$$

4. Results and Discussion

OHAM-DJ has been extended for the solution of coupled system of KdV equations. Tables 1–3 show the comparison of absolute errors of first-order approximate solutions

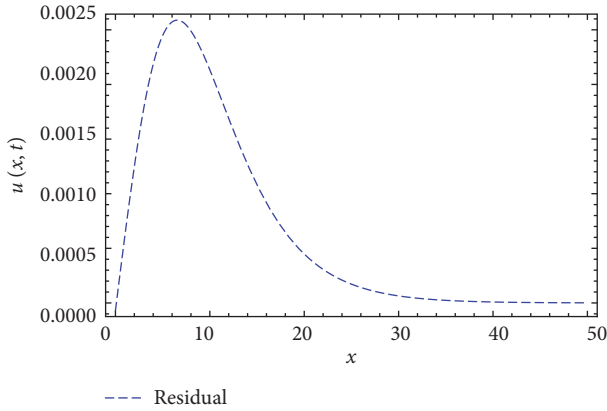


FIGURE 1: Residual of $\zeta(\eta, t)$ by OHAM-DJ at $t = 0.1$.

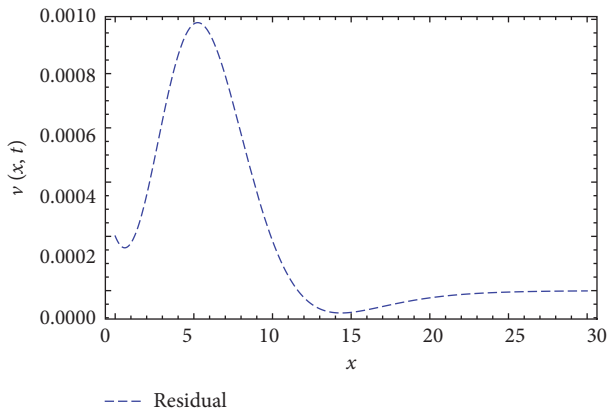


FIGURE 2: Residual of $\xi(\eta, t)$ by OHAM-DJ at $t = 0.1$.

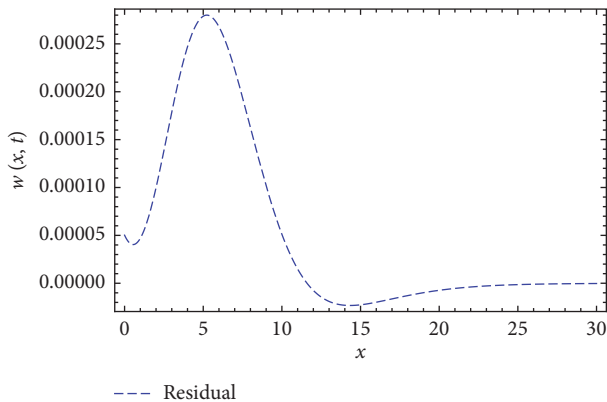


FIGURE 3: Residual of $w(\eta, t)$ by OHAM-DJ at $t = 0.1$.

$\zeta(\eta, t)$, $\xi(\eta, t)$, and $w(\eta, t)$ by OHAM-DJ with MOHAM. Figures 1–3 show the residual graphs for $\zeta(\eta, t)$, $\xi(\eta, t)$, and $w(\eta, t)$ at $t = 0.1$. It is worth pointing out that OHAM-DJ grants fast convergence solutions than OHAM.

5. Conclusions

OHAM-DJ has been successfully applied for the solution of a coupled nonlinear KdV system. The proposed method

contains an adaptable auxiliary function that is used to control the convergence of the solution and grants alteration inside the convergence region wherever it is required. This strategy is free from small parameter assumption and does not need any initial guess. The proposed method does not use discretization, and the convergence is controlled by self-assertive constants. Results revealed that OHAM-DJ is very consistent in comparison with MOHAM. The proposed method is an essential analytical method and well-organized in finding the solutions for an extensive class of coupled systems of PDEs. The accuracy of the proposed method can be further improved by taking higher order approximations. Extension of OHAM-DJ to the coupled nonlinear Korteweg-de-Vries system is more accurate and as a result, it will be more appealing for researchers to apply this method to the coupled system of partial differential equations arising in different fields of engineering sciences.

Data Availability

All the data and meta-data concerning the findings of the manuscript are given in the manuscript.

Conflicts of Interest

The authors declared that they have no conflicts of interest.

Authors' Contributions

Zawar Hussain carried out the simulations. Rashid Nawaz linguistically edited and sequenced the paper. Abraiz Khattak made the corrections in the paper, and Adam Khan drafted the paper.

References

- [1] J. C. Butcher, *The Numerical Analysis of Ordinary Differential Equations: Runge-Kutta and General Linear Methods*, Wiley-Interscience, Hoboken, NJ, USA, 1987.
- [2] E. Hairer, M. Roche, and C. Lubich, *The Numerical Solution of Differential-Algebraic Systems by Runge-Kutta Methods*, Springer, Berlin, Germany, 1989.
- [3] S. N. Ha, "A nonlinear shooting method for two-point boundary value problems," *Computers & Mathematics with Applications*, vol. 42, no. 10-11, pp. 1411–1420, 2001.
- [4] M. R. Osborne, "On shooting methods for boundary value problems," *Journal of Mathematical Analysis and Applications*, vol. 27, no. 2, pp. 417–433, 1969.
- [5] V. Thomée, "From finite differences to finite elements a short history of numerical analysis of partial differential equations," *Journal of Computational and Applied Mathematics*, vol. 128, no. 1-2, pp. 1–54, 2001.
- [6] Q. Fang, T. Tsuchiya, and T. Yamamoto, "Finite difference, finite element and finite volume methods applied to two-point boundary value problems," *Journal of Computational and Applied Mathematics*, vol. 139, no. 1, pp. 9–19, 2002.
- [7] M. Dehghan, "Weighted finite difference techniques for the one-dimensional advection-diffusion equation," *Applied Mathematics and Computation*, vol. 147, no. 2, pp. 307–319, 2004.

- [8] F. Ihlenburg and I. Babuška, "Finite element solution of the Helmholtz equation with high wave number," *Computers & Mathematics with Applications*, vol. 30, no. 9, pp. 9–37, 1995.
- [9] Y. W. Hwon and H. Bank, *The Finite Element Method Using MATLAB*, CRC Press, New York, NY, USA, 1996.
- [10] H.-Y. Hu and Z.-C. Li, "Collocation methods for Poisson's equation," *Computer Methods in Applied Mechanics and Engineering*, vol. 195, no. 33–36, pp. 4139–4160, 2006.
- [11] M. Uddin, S. Haq, and S. Siraj-ul-Islam, "Numerical solution of complex modified Korteweg–de Vries equation by mesh-free collocation method," *Computers & Mathematics with Applications*, vol. 58, no. 3, pp. 566–578, 2009.
- [12] R. Alt and J. Vignes, "Validation of results of collocation methods for ODEs with the CADNA library," *Applied Numerical Mathematics*, vol. 21, no. 2, pp. 119–139, 1996.
- [13] J. Goh, A. A. Majid, and A. I. Ismail, "Cubic B-spline collocation method for one-dimensional heat and advection-diffusion equations," *Journal of Applied Mathematics*, vol. 2012, Article ID 4587018, 8 pages, 2012.
- [14] S. J. Liao, *The proposed homotopy analysis technique for the solution of nonlinear problems*, Ph.D. thesis, Shanghai Jiao Tong University, Shanghai, China, 1992.
- [15] S. J. Liao, "A kind of linearity-invariance under homotopy and some simple applications of it in mechanics," Technical Report 520, Institute of Ship Building, University of Hamburg, Hamburg, Germany, 1992.
- [16] V. Marinca and N. Herişanu, "Application of optimal homotopy asymptotic method for solving nonlinear equations arising in heat transfer," *International Communications in Heat and Mass Transfer*, vol. 35, no. 6, pp. 710–715, 2008.
- [17] V. Marinca, N. Herişanu, C. Bota, and B. Marinca, "An optimal homotopy asymptotic method applied to steady flow of a fourth-grade fluid past a porous plate," *Applied Mathematics Letters*, vol. 22, no. 2, pp. 245–251, 2009.
- [18] N. Herisanu, V. Marinca, T. Dordea, and G. Madescu, "A new analytical approach to nonlinear vibration of an electric machine," *Romanian Academy Series A—Mathematics Physics Technical Sciences Information Science*, vol. 9, pp. 229–236, 2008.
- [19] V. Marinca and N. Herişanu, "On the flow of a Walters-type B' viscoelastic fluid in a vertical channel with porous wall," *International Journal of Heat and Mass Transfer*, vol. 79, pp. 146–165, 2014.
- [20] N. Herisanu, V. Marinca, and G. Madescu, "Nonlinear dynamics of a wind turbine permanent magnet generator system in different wind Profile conditions," *AIP Conference Proceedings*, vol. 1863, 2017.
- [21] J. Ali, S. Shah, S. Islam, and H. Khan, "Application of optimal homotopy asymptotic method with daftardar-jeffery polynomials to non-linear differential equations," *World Applied Sciences Journal*, vol. 28, pp. 1456–1462, 2013.
- [22] M. Abdou and A. Elgarayhi, "On optimal homotopy asymptotic method of quantum Zakharov-Kuznetsov equation in ion acoustic waves," *Walailak Journal of Science and Technology*, vol. 13, no. 9, 2015.
- [23] Z. Shah, R. Nawaz, S. Shah, S. I. A. Shah, and M. Shah, "Use of the daftardar-jeffery polynomials in optimal homotopy asymptotic method for the solution of linear and nonlinear klein-gordon equations," *Journal of Applied Environmental and Biological Sciences*, vol. 6, pp. 71–81, 2016.
- [24] S. Bhalekar and V. Daftardar-Gejji, "Convergence of the new iterative method," *International Journal of Differential Equations*, vol. 2011, Article ID 989065, 10 pages, 2011.
- [25] F. Ghani, C. L. Ali, M. M. Rashidi, and T. Hajjari, "Application of modified optimal homotopy perturbation method to higher order boundary value problems in a finite domain," *Hacettepe Journal of Mathematics and Statistics*, vol. 5, no. 45, pp. 1049–1060, 2016.
- [26] N. Herisanu, V. Marinca, G. Madescu, and F. Dragan, "Dynamic response of a permanent magnet synchronous generator to a wind gust," *Energies*, vol. 12, no. 5, p. 915, 2019.
- [27] M. Fizza, H. Ullah, S. Islam, Q. Shah, F. I. Chohan, and M. B. Mamat, "Modifications of the multistep optimal homotopy asymptotic method to some nonlinear KdV-equations," *Journal of Pure and Applied Mathematics*, vol. 11, no. 2, pp. 537–552, 2018.

Research Article

Evolutionary Hyperheuristics for Location-Routing Problem with Simultaneous Pickup and Delivery

Yanwei Zhao ¹, Longlong Leng ¹, Jingling Zhang,¹ Chunmiao Zhang,¹
and Wanliang Wang²

¹Key Laboratory of Special Equipment Manufacturing and Advanced Processing Technology, Ministry of Education, Zhejiang University of Technology, Hangzhou 310023, China

²College of Computer Science, Zhejiang University of Technology, Hangzhou 310023, China

Correspondence should be addressed to Yanwei Zhao; ywz@zjut.edu.cn

Received 14 June 2019; Revised 11 January 2020; Accepted 3 February 2020; Published 28 February 2020

Guest Editor: Francisco G. Montoya

Copyright © 2020 Yanwei Zhao et al. This is an open access article distributed under the Creative Commons Attribution License, which permits unrestricted use, distribution, and reproduction in any medium, provided the original work is properly cited.

This paper presents an evolution-based hyperheuristic (EHH) for addressing the capacitated location-routing problem (CLRP) and one of its more practicable variants, namely, CLRP with simultaneous pickup and delivery (CLRPSPD), which are significant and NP-hard model in the complex logistics system. The proposed approaches manage a pool of low-level heuristics (LLH), implementing a set of simple, cheap, and knowledge-poor operators such as “shift” and “swap” to guide the search. Quantum (QS), ant (AS), and particle-inspired (PS) high-level learning strategies (HLH) are developed as evolutionary selection strategies (ESs) to improve the performance of the hyperheuristic framework. Meanwhile, random permutation (RP), tabu search (TS), and fitness rate rank-based multiarmed bandit (FRR-MAB) are also introduced as baselines for comparisons. We evaluated pairings of nine different selection strategies and four acceptance mechanisms and monitored the performance of the first four outstanding pairs in 36 pairs by solving three sets of benchmark instances from the literature. Experimental results show that the proposed approaches outperform most fine-tuned bespoke state-of-the-art approaches in the literature, and PS-AM and AS-AM perform better when compared to the rest of the pairs in terms of obtaining a good trade-off of solution quality and computing time.

1. Introduction

As one of the complex systems, logistics network design brings plenty of benefits in terms of economy, society, and environment. Recent years have witnessed great success in applying various tools for optimizing and managing complex logistics system to drive profit and service quality of freight transport [1]. One of such tools is location-routing problem (LRP) [2], integrating two types of decisions: facility location problem and vehicle routing problem (VRP) [3]. Among various extensions to the basic LRP, CLRP and CLRPSPD have been proposed in order to represent different features of practical problems in the complex logistics systems. Meanwhile, an effective solution method should be developed for providing competitive solutions for benchmark instances within reasonable computing time for both CLRP and CLRPSPD. Hence, this paper presents a novel approach to solve both problems.

Both CLRP and CLRPSPD are NP-hard, and they are more complicated and time-consuming to solve, especially CLRPSPD. Therefore, it is unlikely to achieve the proven optimality for large instances within reasonable computing time [4]. Our previous work [2] applied a novel framework of hyperheuristic to solve CLRPSPD using tabu search, FRR-MAB, and combination of both as selection strategies and five acceptance criteria. However, the main difference between this paper and our previous work can be obtained: (1) the high-level strategies were inspired from evolutionary algorithms instead of the above strategies; (2) four basic acceptance criteria were developed in this paper which were not used by our previous work; (3) this paper aims at solving the benchmark instances of the CLRP and CLRPSPD, but our previous work only tackled the latter; (4) the pool of operators in our previous work was classified under the premise of nature of operators which was given in advance, but in this paper, the nature of operators was unknown.

Moreover, the difference between this paper and Ref. [4] can be drawn that our paper focuses on a different solution method for both CLRP and CLRPSPD, namely, hyperheuristic approach. Therefore, the main contributions are as follows:

- (i) Aiming at solving two basic models in complex logistics system, we explore a generality-oriented and emerging heuristic for solving both subjects in complex logistics network, namely, evolutionary hyperheuristic-based iterated local search.
- (ii) Inspired from the process of metaheuristics, several ESs are developed for implementing an online learning strategy for adaptively selecting promising sequence of LLHs to attempt to realize the global search, that is, QS, AS, and PS. Other most recent and relevant nonevolutionary selection strategies (RP, TS, and FRR-MAB) [5–7] are also chosen as the baseline for comparison.
- (iii) Four basic acceptance criteria are used to pair up with ES and non-ES to examine their performance, that is, All Moves (AM), Naïve Acceptance (NA), Great Deluge (GD), and Simulated Annealing (SA).

The remainder of this study is organized as follows. Section 2 provides a brief review about the approaches for problem domains and hyperheuristic over recent decades. In Section 3, the three-index MIP formulation for CLRPSPD is defined. The proposed evolution-based selection strategies are described in Section 4, and evaluation and discussion are presented in Section 5. Finally, conclusions are given in Section 6.

2. Literature Review

Two types of reviews are concerned in this section: one for problem domains (CLRP/LRPSPD) and one for approaches (i.e., hyperheuristic and HH). The former mainly focuses on effective approaches for solving CLRP and CLRPSPD, while the latter reviews recent technologies in developing HH and applications of HH in real world.

2.1. Location-Routing Problem. In the complex logistics, CLRPSPD is a more practical variant version of CLRP by considering reverse logistics, that is, goods need to be picked up from clients when vehicles deliver goods to clients. Firstly, we review some recent approaches for CLRP, and then recent state of CLRPSPD is investigated.

As the main component in CLRP, VRP has been studied for decades. In the last years, several researchers have devoted to the development of VRP. Ant colony algorithm was applied to solve network intensive vehicle service [8]. Multiple population-based genetic algorithm was utilized to solve train-set circulation plan problem [9]. A hybrid tabu search algorithm was developed for a real-world problem [10], that is, open VRP considering fuel consumption. Meanwhile, several approaches were developed for solving a variant of VRP [11], namely, VRP with time windows.

However, the above papers did not analyse the effects of depots on the logistics networks.

Among the variants of LRP, the CLRP has recently emerged as one of the most addressed, initiated in Ref. [12], applied in many practical applications, such as, glass recycling [13], food distribution [14], obnoxious waste [15], disaster relief [16], and so on. Several surveys on CLRP are provided in Refs. [17–21]. The above surveys proposed classification schemes in aspects of either structural characteristics or solution approaches and also summarized variants and extensions of CLRP, but summary on the best approaches for solving CLRP was not provided.

Considering the tailored solution methods of solving the CLRP, several exact methods have been devoted to solving CLRP, such as, branch-and-cut-and-price [22], branch-and-cut [23, 24], and dynamic programming [25], which are the most effective exact methods in tackling CLRP. However, no one is able to achieve proven optimality to large-scale instances within reasonable CPU time. The most effective heuristics have been suggested to tackle large instances and mentioned hereafter.

A two-phase metaheuristic method with TS architecture was proposed by decomposing CLRP into two subproblems [26]. An iterative two-phase approach was applied in Ref. [27]. In their algorithm, clients were clustered into supercustomers, then the Lagrangian relaxation method was used in the location phase, and granular TS (GTS) constraints were suggested to improve the routes in the second phase. A clustering analysis was presented to generate the routes data, and then depot location is solved with the collapsed routes [28]. In the method proposed in Ref. [29], a neural network combining with a self-organizing map and TS was applied to solve single-depot LRP. An iterative heuristic was presented for LRP on the plane by iteratively processing feedback information of two decision problems [30].

More recently, a hybridized GRASP was developed [31], and an evolutionary local search (ELS) procedure was used to search within two solution spaces. SA heuristic based on three random neighbourhoods was studied [32]. An adaptive large neighbourhood search heuristic by combining hierarchical structure and several operators was developed [33]. Two-phase hybrid heuristic was presented by constructing two phases: construction phase and improvement phase [34]. The method was developed using a hierarchical ant colony structure in multiple ant colony optimization algorithm [35]. GTS with a variable neighbourhood search algorithm was for solving CLRP [36]. A unique genetic algorithm was proposed for CLRP [37], using local search procedures in the mutation phase without changing the standard GA framework. Besides, the aforementioned exact and heuristic approaches have been applied successfully to CLRP by many researchers, and most require efficient constructive methods for obtaining the initial population.

Little attention has been received in developing the CLRPSPD. This subject was first addressed in Ref. [38]. In their paper, an exact algorithm named branch-and-cut method combined SA (BC-SA) was studied. Next year, the same authors developed two types of formulas for CLRPSPD: node- and flow-based formulas [39].

Multistart SA was proposed to incorporate multistart hill climbing strategies into SA framework [40]. Two-echelon CLRPSPD has been addressed to tackle the instances with less than 50 clients [41]. However, no instances with more than 100 clients have been solved to prove optimality by the above four approaches. The SA employing three local neighbourhood search mechanisms was developed to solve few instances with more than 100 clients [4]. The aforementioned methods have devoted to the development of CLRPSPD and achieved significant success in obtaining high solution quality at the expense of significantly high computing times. Our previous work [2] could outperform the above papers in terms of computing times and solution quality by developing a general framework of hyperheuristics using iterated local search procedures.

2.2. Hyperheuristic. Conclusion derived from the aforementioned approaches for CLRP and CLRPSPD can be drawn that different search operators are involved in those methods, e.g., hill climbers, mutation heuristics, and crossovers, which may be effective in finding global optima. However, it is hard for them to obtain trade-off between exploration (exploring new solutions) and exploitation (exploiting better solutions) rooting in that no corresponding strategies are suggested to efficiently evaluate and manage those operators at right time, showing poor performance concerning computing times. Moreover, existing search-based approaches are generally domain-dependent, resulting in a hard task for tester without a deep knowledge in domain. The ideal of hyperheuristic was defined as “heuristics to choose heuristics” [5, 42]. Posteriorly, an extensive version was developed as a methodology and classified into two types: heuristic selection and heuristic generation (heuristics to generate heuristics) [43]. This paper focuses on the former based on single-point-search method, and brief description and review is provided hereafter.

In the framework of selection HH, two levels are concerned: HLH and LLH. The HLH manipulates the space consisting of a fixed pool of LLHs which directly modify the space of solutions [44]. Two main categories can be considered in HLH: selection strategies and acceptance criteria [45]. The role of heuristic selection mechanism is to intelligently construct effective sequences of heuristics from the pool of LLHs, while acceptance criterion aims at deciding whether to accept or reject new solution after applying the chosen LLH [46]. By analysing the source of feedback information, three modules can be considered: online, offline, and no-learning. Choice function [5, 47], reinforcement learning [48], TS [2, 6, 49–52], and FRR-MAB [2, 53–57] are examples for online selection strategies, and simple random, random descent, RP, etc., are viewed as no-learning methods. Several metaheuristic-based strategies for designing hyperheuristics have been proposed in the literature: ant colony-, particle-, and quantum-inspired hyperheuristic. Characteristics of most evolutionary hyperheuristics in the literature are presented in Table 1, where for each

EHH category, application domain, source of publication, main feature, and publishing year are provided. As far as acceptance criterion is concerned, two types are involved: determinate and nondeterminate methods. The former determinately accepts the resultant result, such as all moves, only improving, improving, and equal while NA, SA, GD, and Monte Carlo are instanced as the non-determinate methods for accepting the new solutions.

With the popularity of hyperheuristic, it has been widely applied in practice, such as 2D regular and irregular packing problems [73], nurse rostering [74], vehicle routing problem [54], construction levelling problem [52], software project scheduling problem [56], t -ways test suite generation [6, 75], deriving products for variability test of feature models [55], fast machine reassignment [76], and timetabling [77–81]. We refer interested readers to these papers [43, 82, 83] for extensive review on hyperheuristic.

To the best of our knowledge, evolutionary hyperheuristics have not been used thus far to address the basic models of complex logistics network, i.e., CLRP and CLRPSPD.

3. Mathematical Formulation

CLRPSPD is a more practical variant of CLRP considering the reverse logistics in which the pickup and delivery take place at the same time for each client [4]. The CLRPSPD and CLRP are defined on a complete directed graph $G = (V, E)$, where $V = J \cup I$ is a set of nodes in which J and I represent the potential depot and client nodes, respectively, and $E = \{(i, j) : i, j \in V, i \neq j\} \setminus \{(i, j) : i, j \in J\}$ is the set of arcs. Each arc $(i, j) \in E$ has a nonnegative distance c_{ij} . Each client $i \in I$ has a positive delivery demand q_i and pickup demand p_i (only for the CLRPSPD). A storage capacity w_j and a fixed opening cost f_j are associated with each potential depot $j \in J$. The index set of vehicle types is denoted by K consisting of homogeneous vehicles with capacity Q . The objective is to determine the optimal plan of the set of depots and routes to minimize the total costs consisting of opened depot, vehicle, and travel costs.

Two types of MIP formulations for CLRPSPD are defined in Refs. [38, 39]: node- and flow-based formulations, whose distinction depends on the definition of additional variables in the graph: nodes or arcs, and similarity of the above two is built on two-index concept. In this paper, three-index flow-based MIP formulation is defined for CLRPSPD. Before describing this formulation, some assumptions should be considered:

- (i) Each route is served by one vehicle, and each client is served only once.
- (ii) Each vehicle must return to the departure depot at the end of the route.
- (iii) Goods of each client are delivered and picked up at the same location, and the goods are delivered to each client before being picked up.
- (iv) The total vehicle load at any arc must not exceed the vehicle capacity.

TABLE 1: Ant-, particle-, and quantum-based hyperheuristics.

Evolutionary type	Application domain	Publication	Main feature
Ant-based HH	Scheduling	[60]	Population/paired
	Project presentation scheduling	[61]	Population/paired
	2D bin packing	[62]	Population/paired
	Travelling tournament	[63]	Population/paired
	P -median	[64]	Population/paired
	WDM networks	[65]	Population & single-point/paired
	WDM networks	[66]	Population/paired
	Dynamic environment	[67]	Single-point/paired
	Travelling salesman	[68]	Population/paired
Flow shop scheduling	[69]	Population/single	
Particle-based HH	Academic scheduling	[70]	Population/multi-heuristics
	Examinations scheduling	[71]	Population/multi-heuristics
	Project scheduling	[72]	Population/multi-heuristics
	Grid resource scheduling	[73]	Population/single-heuristic
Quantum-based HH	Energy-aware scheduling	[74]	Population/single-heuristic

(v) The total delivery and pickup demands of clients served by each depot cannot exceed the depot capacity.

$$\sum_{j \in I} x_{ijk} + \sum_{j \in I} x_{jgk} \leq 1, \forall i, g \in J, \forall k \in K, i \neq g, \quad (8)$$

Decision variables:

$$x_{ijk} = \begin{cases} 1, & \text{if arc } (i, j) \text{ is operated by vehicle } k \\ 0, & \text{otherwise} \end{cases}$$

$$z_{ij} = \begin{cases} 1, & \text{if client } i \text{ is served by depot } j \\ 0, & \text{otherwise} \end{cases}$$

$$y_i = \begin{cases} 1, & \text{if depot } i \text{ is selected to operate} \\ 0, & \text{otherwise} \end{cases}$$

Additional variables:

U_{ijk} : the dynamic load of each arc (i, j) operated by vehicle k .

Based on the aforementioned assumptions and notations, the proposed flow-based formulation [2] is as follows:

$$\min \text{Fitness} = \sum_{j \in J} f_j y_j + \sum_{i \in J} \sum_{j \in I} \sum_{k \in K} f_k x_{ijk} + \sum_{i \in V} \sum_{j \in V} \sum_{k \in K} c_{ij} x_{ijk}, \quad (1)$$

subject to

$$\sum_{i \in V} \sum_{k \in K} x_{ijk} = 1, \forall j \in I, \quad (2)$$

$$\sum_{i \in J} \sum_{j \in J} x_{ijk} = 0, \forall k \in K, \quad (3)$$

$$\sum_{i \in V} x_{ijk} = \sum_{i \in V} x_{jik}, \forall j \in V, \forall k \in K, \quad (4)$$

$$\sum_{i \in J} \sum_{j \in I} x_{ijk} \leq 1, \forall k \in K, \quad (5)$$

$$\sum_{i \in S} \sum_{j \in S} x_{ijk} \leq |S| - 1, \forall k \in K, \quad (6)$$

$$\sum_{j \in J} z_{ij} = 1, \forall i \in I, \quad (7)$$

$$\sum_{i \in I} z_{ij} \geq y_j, \forall j \in J, \quad (9)$$

$$z_{ij} \leq y_j, \forall i \in I, \forall j \in J, \quad (10)$$

$$\sum_{j \in I} \sum_{k \in K} x_{ijk} \geq y_i, \forall i \in J, \quad (11)$$

$$\sum_{j \in I} x_{ijk} \leq y_i, \forall i \in J, \forall k \in K, \quad (12)$$

$$x_{ijk} + z_{ig} + \sum_{m \in J, g \neq m} z_{jm} \leq 2, \forall i, j \in I, \forall k \in K, \forall g \in J, \quad (13)$$

$$\max \left\{ \sum_{i \in I} z_{ij} \times q_i, \sum_{i \in I} z_{ij} \times p_i \right\} \leq w_j \times y_j, \forall j \in J, \quad (14)$$

$$\sum_{i \in J} \sum_{j \in I} U_{ijk} = \sum_{i \in V} \sum_{j \in I} x_{ijk} \times q_j, \forall k \in K, \quad (15)$$

$$\sum_{i \in I} \sum_{j \in J} U_{ijk} = \sum_{i \in V} \sum_{j \in J} x_{ijk} \times p_j, \forall k \in K, \quad (16)$$

$$\sum_{k \in K} \sum_{i \in V} U_{ijk} - q_j = \sum_{k \in K} \sum_{i \in V} U_{jik} - p_j, \forall j \in I, \quad (17)$$

$$0 \leq U_{ijk} \leq Q \times x_{ijk}, \forall i, j \in V, \forall k \in K. \quad (18)$$

In this three-index flow-based MIP formulation, objective function (1) represents the fitness value *Fitness* consisting of the total costs composed of fixed lease cost of depots and vehicles and travelling cost of edges; constraint (2) guarantees that each client is served only once; constraint (3) eliminates routes between depots; constraint (4) ensures

that entering and leaving edge to each node is equal; constraint (5) requires that only one route is assigned to one vehicle and the vehicle only departs from one depot; sub-circuits in each route are forbidden by constraint (6); constraint (7) eliminates the situation that one client is served by plural different depots; constraint (8) specifies that plural different depots must not exist in the same route; constraints (9) and (10) enforce that clients are assigned to the selected depots and each depot to open must serve at least one client; each vehicle is assigned to the chosen depots and each selected depot must have at least one vehicle, which is ensured by constraints (11) and (12); constraint (13) ensures two consecutive clients of each route are served by the same depot; constraint (14) forbids that total delivery and pickup demands of clients must not exceed the depot's capacity; constraint (15) guarantees that the total delivery demands of all clients served by each depot should equal to depot's total delivery load; constraint (16) requires that the total pickup demands of all clients served by each depot should equal to depot's total pickup load; equation (17) expresses the proper movement of load delivery and/or pickup; constraint (18) makes sure that the total load of each arc of vehicles must not exceed vehicle's capacity.

4. Proposed Approach

In the following sections, we introduce HH by describing the adopted solution representation, effective constructive heuristic, low-level heuristics for domains, nine selection strategies, and four acceptance criteria for high-level heuristic.

4.1. Solution Representation. The solution representation plays an important role in improving the performance of an algorithm for the CLRPSPD, which should include all routes and the chosen depot of each route. Therefore, a string of cells are used to represent a complete solution which determines the assigned clients to each vehicle, the depots to be selected, and the sequence of clients to be visited by a specific vehicle starting and ending at the same depot. The solution representation in this paper applies a simple and efficient encoding [2], which is a complete set of vehicle routes, that is, $R = \{r_1, r_2, \dots, r_K\}$ with inserting the chosen depot at two ends of each route. Meanwhile, we also store the attributes of each route in the second subcell of each route. It is worth noting that our chromosome representation can meet the constraints (2)–(18) for avoiding restoring the feasibility of solutions and allowing fast evaluation of its fitness value without the need for decoding.

4.2. Initial Solution. The initialization method is an improved greedy heuristic (inspired from the approach in Ref. [4]), named here as regret- k greedy heuristic (RKGH), proposed by our previous work [2]. After implementing greedy heuristic [4], configuration of depots ($m \geq 2$) has been determined. Let $x_{ik} \in \{1, 2, \dots, m\}$ be a variable that indicates the depot for client i that has the k^{th} lowest cost, that is, $c(i, x_{ik}) \leq c(i, x_{ik'})$. Using this notation, we can define a regret-

k value $\Delta c^k(i)$ as $\Delta c^k(i) = c(i, x_{ik}) - c(i, x_{i1})$. In other words, the regret- k value is the difference in the cost for client placed in the first best depot and its k^{th} best depot. The RKGH chooses to assign the client i that maximizes

$$\max \left\{ \alpha \times \sum_{j \in k} \Delta c^j(i) \right\}. \quad (19)$$

The multiplier α depends the remaining capacity of each depot, $\alpha = 1$ representing that client i is served by this depot without violating the capacitated constraints; otherwise, α is set to 0. In this paper, the value of k is also set to 2, namely, R2GH is applied.

4.3. Hyperlevel Heuristics. In this paper, we use different pairings of operators' vector and acceptance criterion. There are 36 possible pairings of nine operators' vectors and four acceptance criteria. Several strategies are involved: RP, TS, FRR-MAB, QS, AS, and PS, and three variants are also developed. The strategies implementing QS, PS, AS, and their variants can be categorised as ES. Four acceptance criteria are provided in this paper: AM, NA, GD, and SA. The brief descriptions are presented in the following sections.

4.3.1. Operator Selection Vector Design. Operator selection strategies in the literature generally assign a probability to each operator and use a roulette wheel or tournament-like process to select the LLHs according to them [54], named as operator selection vector. The selection vector consists of an array of operators, each with a probability of selection. In this paper, selection vector is designed by assigning a probability to each LLH, and the initial selection vector of LLHs has an equal probability of selection.

- (1) RP: the initial vector is not changed during the run, and all LLHs have an equal selection probability regardless of performance, also called as fixed selector [84], so the random one is chosen as a baseline for comparison with others.
- (2) TS: tabu list is used to prohibit LLHs with recently poor performance from being applied too soon. The LLHs belonging to be tabu (i.e., the selection probability is 0) are released (i.e., the selection probability is initial value) whenever other LLHs make a change in objective function, which is slightly different from the aspiration criterion [51].
- (3) FRR-MAB [7]: FRR-MAB was proposed to adaptively select appropriate LLH based on its recent performance storing in slide windows implementing FIFO mechanism. Two successive stages are discussed: credit assignment and selection mechanism. The former offers the method to measure the impact on the quality in search process caused by the application of recent LLHs, while the latter selects one LLH with maximizing received credit values for generating new solution. For applying selection vector, the reward value of each LLH is normalized as selection probability. The other version based on

FRR-MAB is combined with TS (viewed as FMT) proposed by our previous work [2], absorbing the rapid response capability of TS to exclude LLHs with poor performance.

- (4) QS: a heuristics search space with ξ LLHs in QS is defined as

$$H = (h_1, h_2, L, h_\xi) = \begin{bmatrix} \beta_1 & \beta_2 & L & \beta_\xi \\ \alpha_1 & \alpha_2 & L & \alpha_\xi \end{bmatrix}, \quad (20)$$

where $h_i = [\beta_i \ \alpha_i]$ represents h_i Q-bit and $|\beta_i|^2$ and $|\alpha_i|^2$ give the probability that h_i selects and disuses state, respectively, and guarantee $|\alpha_i|^2 + |\beta_i|^2 = 1$. A learning strategy based on Q-gate is utilized to update selection probability $|\beta_i|^2$ of h_i based on real-time performance.

$$\begin{bmatrix} \alpha_i^{t+1} \\ \beta_i^{t+1} \end{bmatrix} = \begin{bmatrix} \cos(\theta_i^t) & -\sin(\theta_i^t) \\ \sin(\theta_i^t) & \cos(\theta_i^t) \end{bmatrix} \times \begin{bmatrix} \alpha_i^t \\ \beta_i^t \end{bmatrix}, \quad (21)$$

$$\Delta\theta^t = \Delta\theta_0 \times \left(1 - k \frac{t}{t_{\max}}\right), \quad (22)$$

$$\theta_i^t = \frac{(f(\pi^t) - f(\pi_{\text{best}}^t)) \times \alpha_i^t \times \beta_i^t \times (x_i^t - bx_i^t)}{|f(\pi^t) - f(\pi_{\text{best}}^t)| \times |\alpha_i^t \times \beta_i^t|} \times \Delta\theta^t, \quad (23)$$

where $[\alpha_i^t \ \beta_i^t]$ is the Q-bit of h_i during t^{th} iteration and θ_i^t is the rotation angle of each Q-bit; $\Delta\theta^t$ is rotation angle in t^{th} iteration; k is uniformly distributed within $[0 \ 1]$; t_{\max} is the maximum iteration; π^t and π_{best}^t are, respectively, sequence of current selected LLHs and selected LLHs in obtaining the best solution; x_i^t and bx_i^t are the state of h_i of current and global sequence of selected LLHs; $\pi^t = [4 \ 6 \ 7 \ 1]$ represents the current sequence of LLHs; and x^t can be illustrated as $x^t = [1 \ 0 \ 0 \ 1 \ 0 \ 1 \ 1]$ if $\xi = 7$. The other version based on QS is combined with TS (named as QS2), absorbing the rapid response capability of TS to exclude LLHs with poor performance.

- (5) AS: inspired from application of ant colony optimization (ACO) in travelling salesman problem (TSP) and 0/1 knapsack problem, two versions of AS are developed into adaptively making decisions on selecting favourable sequence of LLHs. The first variant (paired-AS, AS2) highlights the joint performance of pairs of LLHs by determining next LLH (one at a time) based on probabilities proportional to the pheromone levels of each heuristic pair shown in equation (24); in this version, pheromone laying criterion [59] is modified for laying the pheromone for pairs which reach an improvement to the previous function, that is, if an ant performs heuristics h_x , h_y , and h_z and h_y leads to a nonimproving

solution and h_z provides a better solution, pheromone will be laid on edge x - z and neither x - y nor y - z , while the latter (single-AS, AS) emphasizes individual performance of each LLH by viewing the performance information of individual LLH as its pheromone trail [67]. Possible sequence of LLHs is selected by normalizing pheromone trail as selection probabilities.

$$p_{ij}^{t+1} = \frac{\tau_{ij}^{t+1}}{\sum_{j \in \xi, j \neq i} \tau_{ij}^{t+1}}, \quad (24)$$

$$\tau_{ij}^{t+1} = \begin{cases} \rho \cdot \tau_{ij}^t + \frac{FIR_j}{\eta_{ij}}, & \text{if ant } k \text{ selects } (i, j), \\ \rho \cdot \tau_{ij}^t, & \text{otherwise,} \end{cases} \quad (25)$$

where τ_{ij}^t ($\xi \times \xi$) and p_{ij}^t ($\xi \times \xi$) define, respectively, the pheromone trail and selection probability of i - j edge in t^{th} iteration; $0 < \rho \leq 1$ represents the evaporation rate for pheromone; FIR_j is fitness improvement rate compared to previous solutions [7, 55]; and η_{ij} ($\xi \times \xi$) is the visibility information illustrating heuristic information. The above equation (25) is used to update pheromone trail with $\eta_{ij} = T_i + T_j$ (T_i indicates the running time of h_i), while equation (25) can be modified for AS with $\eta_j = T_j$ by ignoring the previous h_i .

- (6) PS: PS has been nominated as HLH strategies to measure effectiveness of their order placement and selection mechanism. Each particle is a vector of ξ numbers representing the selection probabilities of LLHs obtained by normalizing the position (using the original formulations) of this particle. The particles impose the order that the LLHs are applied to solution domain. Each particle is evaluated using performance indicator FIR.

$$p_i^t = \frac{X_i(t)}{\sum_{i \in \xi} X_i(t)}. \quad (26)$$

Among the last seven selection strategies, probabilities of selecting LLHs are utilized to order LLHs, with the maximum utility score/weight being placed in the front of the list. The chosen LLHs are then applied in sequence following this order. However, the sequence of selected LLHs are randomly permuted to modify the current solution for RP and TS.

4.3.2. Acceptance Criteria Design. After recent application of the LLHs, the obtained solution is considered for accepting as incumbent solution into next iteration. If the new solution is at least as good as the previous solution it will replace, and then it is automatically accepted as current solution regardless of the nature of an acceptance mechanism; otherwise, acceptance criterion is utilized to whether discard the

new solution or not [65, 84]. The following four acceptance criteria are proposed to pair up with the above selection strategies, aiming at pointing out which pairs perform better than others.

- (1) AM [5]: the current result is replaced by all new results with probability value at 1.
- (2) NA [84]: the current result is replaced by no-improving results with probability value at 0.5.
- (3) GD [50, 84]: a no-improving result is accepted if it is better than a dynamically changing threshold value which depends on the current and historical fitness information. For determining the range of accepting a child solution, a threshold value is applied, which decreases with the increase in iteration.

$$S_{threshold}^t = \left(1 + 0.5 \times \left(1 - \frac{t}{t_{max}} \right) \right) \times G_{best}(t), \quad (27)$$

where t and t_{max} indicate the current steps and the maximum iteration and $G_{best}(t)$ represents the global best solution objective value found so far.

- (4) SA [65]: new solutions are accepted as the current solutions if the probability criterion is met, that is, improving results are accepted with probability value at 1 while no-improving results are accepted if a uniform value within $[0, 1]$ is less the critical value. The probability of accepting a no-improving solution in SA is calculated for making a decision on whether accepting it or not [65]:

$$p^t = e^{-(\Delta f / \Delta F^t (1 - (t) / (t_{max})))}, \quad (28)$$

where Δf is the difference in the quality between the new solution and current solution and ΔF^t represents the expected range for maximum solution quality change, $\Delta F^t = G_{best}(t) - G_{best}(0)$.

4.4. Low-Level Heuristics. The pool of LLHs can be viewed as a “black box” which are used to perturb the incumbent solution by either intensifying or diversifying the search in the search region, which is used in Ref. [2]. They normally are a set of simple, cheap, and knowledge-poor LLHs [5]. The module of this paper is composed of 13 LLHs h_1, h_2, \dots, h_{13} across two pools of heuristics: mutational heuristic (MH) and local search/hill climber (HC), which are identified by the role in improving or worsening the solution. The first six LLHs are implemented to explore new region: 2-opt, or-opt, shift, interchange, add, and Shaw. Others are utilized to exploit better solutions: relocation, 2-opt, 3-opt, relocate, and 1-interchange algorithm, which apply intra and inter-route moves.

The detailed information of $h_1 \sim h_4$ can be obtained from Ref. [54], which are simple and basic mutational heuristics. The h_5 heuristic diversifies the open depots by opening a new one and randomly assigning between 1 and 2/3 of the routes to it [37]. As to the last diversified LLH h_6 [85], it is a method named as destroy-and-repair operator proposed to remove

related clients, i.e., clients that are geographically close to each other and reinserted into best positions. In our paper, basic greedy heuristic [86] is suggested to reinsert removal clients back into routes. The disturbed solutions are accepted as long as the above acceptance criteria and the vehicle capacity at each arc and depots capacity are obeyed.

The relocation h_7 is developed to reselect the appropriate depots for determined routes. Each route is collapsed into a cluster and the smallest insertion costs can be calculated as the distance of the depots in the original routes. The depots with the larger number of clusters take priority to open. And then other unassigned clusters (from large to small order) sharing same closest depot will be arranged to its closest depot, unless the assigned depots’ capacity and cost are not satisfied. The 2-opt [87] inside the routes is equivalent to the well-known 2-opt move (h_8) [88], whereas the other version of 2-opt implemented between different routes is identified (h_9). Due to reduced CPU time, the intral-3-opt (h_{10}) [89] is only considered. The relocate heuristic [90] reinserts a single client in another position inside the incumbent route (h_{11}) or in another route (h_{12}). The 1-interchange [91] heuristic swaps each position of client from one route with each client in another route if not sharing the same depot (h_{13}). If improvements are found and depot capacity and vehicle load at each arc are met, the above moves are implemented, allowing them to improve incumbent solutions.

The MHs often perform simple random moves to perturb the incumbent solution without guaranteeing competitive results. Although insufficient for achieving competitive results, they are useful for providing randomization and helpful for navigating out of local optima. However, HCs play a key role in quickly obtaining much better solutions at each step. Moreover, it might be desirable to apply HCs after application of any MH and to apply MHs if it is hard for HCs to provide promising solutions. Considering the above features, the proposed nine selection strategies are utilized to adaptively manage the HCs, inspired from the mechanism on management of local search heuristics [5, 54] and the method for automatically classifying according to the performance proposed in Ref. [57]. The probability for selecting any one MH as guider for getting rid of local optimality is set to 1 if and only if no HC can provide an improvement to previous objective value; otherwise, the probability value is set to 0. Hence, Figure 1 is the framework of hyperheuristics applied in this paper.

Moreover, a stopping mechanism is defined by evaluation limits with maximum number of fitness evaluation (α_{max}), aiming at providing fair comparison.

5. Computational Evaluation

In this paper, we explore the performance of a set of hyperheuristics in solving CLRP and CLRPSPD. The experiments consist of four parts. In the first part, an overall picture related to the selection strategies and acceptance alternatives is provided to rank the performance of 36 pairs and determine first four outstanding pairs for the following experiments. Then, the efficiency and features are analysed for the chosen pairs by implementing on the three sets of

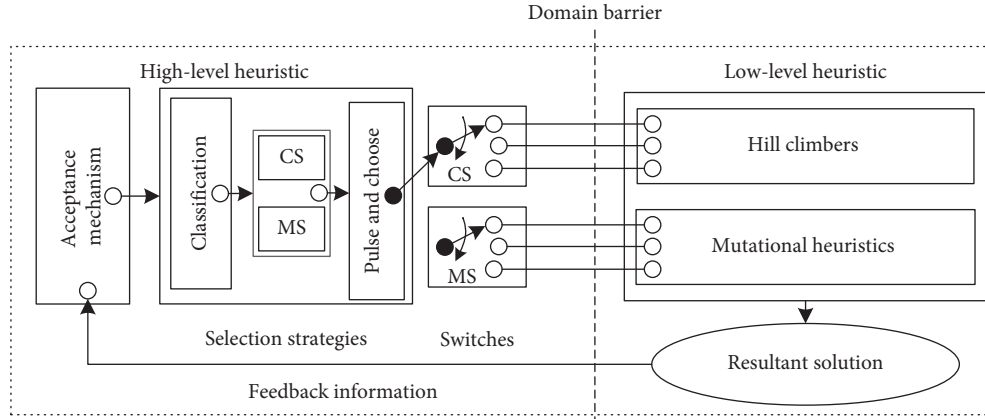


FIGURE 1: Framework of hyperheuristic approach.

TABLE 2: Configuration for each selection strategy.

Strategies	Parameters	Values	Common parameters
FRR-MAB	Scaling factor C	0.5 [7]	Initial probability $p = 0.5$ Population size $S_{LLH} = 1$ (single-point search)
	Sliding windows size W	25 [56]	
QS/QS2	Initial rotation angle, $\Delta\theta_0$	0.02π	Population size $S_{HLH} = 1$ (only one individual) Maximum fitness evaluation α_{\max} (Eq. 29)
	Initial probability amplitudes α, β	0.7071 [74]	
AS/AS2	Initial pheromone, τ_{ij}/τ_i	0	Maximum iteration $t_{\max} = 10^6$
	Initial visibility, η_{ij}/η_i	0	
	Evaporation rate, ρ	0.2 [69]	
PS	Learning factors, c_1, c_2	2 [72]	
	Inertia weight, w	1 [72]	

CLRP benchmark instances. In the third part, we explore the performance of selected pairs in solving CLRPSPD benchmark sets. Finally, the performance of selected pairs is tested against recent and effective tailored approaches in the literature.

5.1. Experimental Design. The presented HH approach with 36 pairs is coded in Matlab 8.6 and runs on a desktop computer with Intel Core (TM) i7-6700K (4.00 GHz) and 8 GB RAM, under Windows 10; it is embedded in the CLOR tool, available by emailing to us.

As far as calibration is considered, two types of parameters are concerned: specific selection strategy parameters and common hyperheuristic parameters. The former relates to the setting of selection strategies, while the latter accounts for the common parameters between LLHs and HLH, and they are summarized in Table 2.

Some of the specified parameters follow defaults suggested in the literature, and others were determined by conducting an initial experiment with various settings aiming at obtaining relative better results within reasonable CPU time. As to common hyperheuristic parameters, initial selection probability p is set to 0.5 for each LLH in line with the initial probability amplitudes of QS; tabu list size l_t is set to 7 which is the number of HCs; as single-point-based search hyperheuristic framework is investigated in this paper, the sizes of population used in the LLH and HLH are set at 1. For fairly comparing the running time of each pair,

the maximum number of fitness evaluation for each instance is provided, which was different from the method in Ref. [2] (i.e., the maximum iterations without improving solution), depending directly on the number of clients, depots, and vehicles:

$$\alpha_{\max} = a \times (m + n + K)^2. \quad (29)$$

Aiming at obtaining a good trade-off between solution quality and computing time, the multiplier a is taking on the value 5 for all instances in this paper.

5.2. Benchmark Instances. Three sets of CLRP benchmark instances were adopted to evaluate the efficiency and features of each pair for hyperheuristic. These sets are provided in Refs. [26–28]. One separation approach is used to generate the datasets of CLRPSPD from the above CLRP benchmarks, instanced as W type in Ref. [92] with setting 0.8 for β .

The first benchmark instances [28] contain 19 cases. The number of clients ranges from 12 to 318, and the number of depots m varies between 2 and 15, and the fixed vehicle cost f_v is not given. In the randomly generated set [27], the number of clients ranges from 20 to 200, the number of depots m is 5 and 10, and vehicle capacity Q is $\{70, 150\}$ and $f_v = 1000$. The benchmark instances [26] are also randomly generated which contain 36 cases with $n \in \{100, 150, 200\}$, $m \in \{10, 20\}$, $Q = 150$, and $f_v = 10$. And the clients' demand of this benchmark ranges from 1 to 20. The above three

benchmark sets are available at http://sweet.ua.pt/sbarreto/or_http://prodhonc.free.fr/homepage.

Euclidean distances are applied in all datasets. In Prins et al. benchmark set for CLRPSPD, the obtained distances are multiplied by 100 (rounded up to the next integer in CLRP) and the total costs are rounded up to the next integer, which is different from the sets obtained in Refs. [4, 38]. The working cost of vehicle for each instance with less than 100 clients in the first set increases to 20, namely, $f_v = 20$.

5.3. Results

5.3.1. Experiment on 36 Pairs. The first set of experiment is performed to compare the performance of 36 pairs of hyperheuristics aiming at determining the first four outstanding pairs for the following experiments. Nine CLRP instances in Barreto set with the number of clients ranging from 50 to 318 were used to test performance of each pair, implementing fifty runs on each instance. The maximum number of fitness evaluation is set to 10000. Aiming at comparing and scoring for all pairs, formula (1) scoring system was adopted, which was used to rank the approaches by CHESC (Cross-domain Heuristic Search Challenge) before 2010 (<http://www.asap.cs.nott.ac.uk/external/chesc2011/>). The top eight approaches are given a score of 10, 8, 6, 5, 4, 3, 2, and 1 point for each problem from the best to the worst, successively [65]. The rest of the methods receive a score of 0. In this paper, the score of 10 points is assigned to the pairs which can exploit the best known solution (BKS), and the scores for the rest of pairs are similar to formula (1) scoring system. Therefore, 90 is the maximum overall score a pair can get.

Experiment results are shown in Table 3, where the overall scores of the best four pairs, nine selection strategies, and four acceptance criteria are provided. As can be seen from the results, HH performing AS-AM is the best clear winner, and PS-AM, QS2-SA, and TS-SA also outperform other pairs. The hyperheuristic using AS, FRR-MAB-TS, TS, and RP as selection components performs better than others regardless of the acceptance component, and several interesting conclusions can be drawn from the overall scores that (1) TS could promote better performance for selection strategies by excluding the LLHs with poor performance, when compared with the performance of selection strategies without TS, reaching an average improvement about score 25 point; (2) the performance of AS using 0/1 knapsack problem outperforms AS2 applying TSP, in other words, compared to the one laying ant pheromone trails at routes, the mechanism laying ant pheromone trails on vertices (i.e., LLHs) have a greater chance of success in guiding ants to select the promising sequence of LLHs; (3) PS-AM and QS2-SA ranks the second/third place in overall scores of pairings, even if the performance of PS/QS2 is barely satisfactory. From the last four scores of acceptance component regardless of the selection component, AM and SA rank, respectively, the first and second with a score 529 and 518, while the other two receive a score of 473 and 429, respectively.

TABLE 3: The overall formula (1) scores for the top four pairs and strategies.

Pairs	Overall score
AS-AM	73
PS-AM	67
QS2-SA	66
TS-SA	65
RP	222
TS	229
FRR-MAB	204
FMT	233
QS	176
QS2	215
AS	242
AS2	212
PS	216
AM	529
NA	473
GD	429
SA	518

Figure 2 shows the box plot for the scores of nine selection strategies and four acceptance criteria. In the box plot, the minimum and maximum values obtained (excluding the outliers), the lower and upper quartiles, and median are shown.

From such analysis and answering the first experiments, we identify AS-AM as the best pair considering most cases and scores, and additional PS-AM, QS2-SA, and TS-SA are also selected to conduct the following experiments.

5.3.2. Experiment on CLRP. The first four outstanding pairs were tested performing fifty runs on each instance, from which best found solution, gaps to BKS, and computing time are shown, providing the insufficient page space. Results for three CLRP benchmark instances are shown in Tables 4–6. The first column of each table is the name of each instances, followed by BKS, and results concerning four pairs which contain best found results (Best), gap (in percentage) to the BKS, and average computing time in seconds (CPU). Average and median values for gaps and CPU are displayed in the last two rows.

For the first three pairs (Table 4), the BKSs of instances with less than 150 clients are exploited with average gap at -0.04% for TS-SA, -0.07% for QS2-SA, and -0.05% for AS-AM. Only one BKS cannot be found by the last pair with highest gap at 0.06% and average value at -0.04% . Concerning the median values of gaps to BKS, they take on the value 0. Computing times are on average less than 29, 25, 27, and 17 s, and median values are lower than 6 s even if the largest instances exist. Two new BKS are found by four pairs, obtaining an improvement of over 0.5% for Perl83-318 \times 4 by PS-AM and over 0.7% for Perl83-318 \times 4-2 by QS2-SA.

In the second benchmark (Table 5), at least 16 BKS can be found by the four pairs, with difference in finding the Best of 50-5-2b. Four new BKSs in this set are obtained, respectively, reaching an improvement of over 0.3% for 200-10-1b by TS-SA and PS-AM and 0.1% for 200-10-2b and

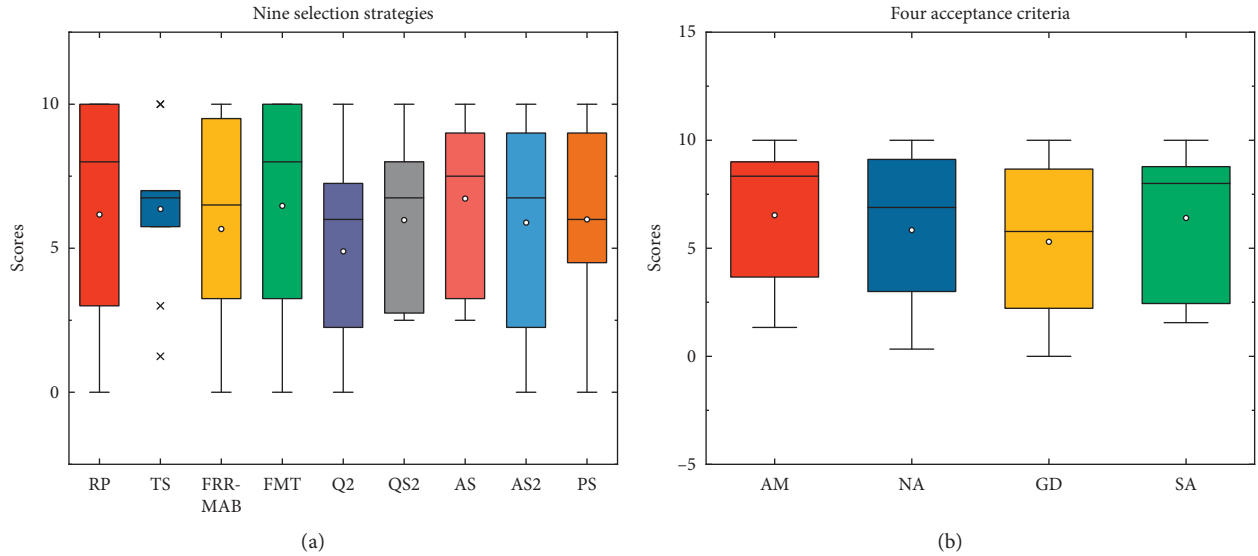


FIGURE 2: Box plots of scores for a statistical comparison of (a) selection strategies and (b) acceptance criteria.

TABLE 4: Results for the CLRP instances in Barreto set.

Set	BKS	TS-SA			QS2-SA			AS-AM			PS-AM		
		Best	Gap	CPU	Best	Gap	CPU	Best	Gap	CPU	Best	Gap	CPU
P12-2	204.0	204.0	0.00	0.1	204.0	0.00	0.1	204.0	0.00	0.1	204.0	0.00	0.1
G21-5	424.9	424.9	0.00	0.4	424.9	0.00	0.4	424.9	0.00	0.4	424.9	0.00	0.3
G22-5	585.1	585.1	0.00	0.3	585.1	0.00	0.4	585.1	0.00	0.3	585.1	0.00	0.3
M27-5	3062.0	3062.0	0.00	0.6	3062.0	0.00	0.6	3062.0	0.00	0.5	3062.0	0.00	0.5
G29-5	512.1	512.1	0.00	0.6	512.1	0.00	0.6	512.1	0.00	0.5	512.1	0.00	0.5
G32-5	562.2	562.2	0.00	0.7	562.2	0.00	0.7	562.2	0.00	0.6	562.2	0.00	0.6
G32-5-2	504.3	504.3	0.00	0.6	504.3	0.00	0.7	504.3	0.00	0.6	504.3	0.00	0.5
G36-5	460.4	460.4	0.00	0.9	460.4	0.00	0.9	460.4	0.00	0.8	460.4	0.00	0.7
C50-5	565.6	565.6	0.00	2.0	565.6	0.00	2.2	565.6	0.00	1.8	565.6	0.00	1.6
P55-15	1112.1	1112.1	0.00	4.2	1112.1	0.00	5.2	1112.1	0.00	4.6	1112.8	0.06	4.2
C75-10	844.4	844.4	0.00	7.9	844.4	0.00	7.9	844.4	0.00	7.0	844.4	0.00	6.3
P85-7	1622.5	1622.5	0.00	9.6	1622.5	0.00	9.7	1622.5	0.00	8.6	1622.5	0.00	7.7
D88-8	355.8	355.8	0.00	7.0	355.8	0.00	6.3	355.8	0.00	6.5	355.8	0.00	5.9
C100-10	833.4	833.4	0.00	11.4	833.4	0.00	12.3	833.4	0.00	10.6	833.4	0.00	8.3
O117-14	12290.3	12290.3	0.00	18.3	12290.3	0.00	18.4	12290.3	0.00	16.4	12290.3	0.00	14.6
M134-8	5709.0	5709.0	0.00	32.7	5709.0	0.00	33.0	5709.0	0.00	29.9	5709.0	0.00	24.1
D150-10	43919.9	43919.9	0.00	42.7	43919.9	0.00	45.0	43919.9	0.00	38.3	43919.9	0.00	33.1
P318-4	7249.3 ^a	<u>4484.2</u>	-0.50	156.4	<u>4145.9</u>	-0.56	110.0	<u>3966.0</u>	-0.59	126.8	<u>3991.1</u>	-0.58	78.8
P318-4-2	13070.0 ^b	<u>10866.5</u>	-0.33	243.4	<u>8293.0</u>	-0.72	213.0	<u>10269.4</u>	-0.42	260.6	<u>10905.1</u>	-0.33	125.3
AV	68099.3	67837.8	-0.04	28.4	67684.6	-0.07	24.6	67779.1	-0.05	27.1	67813.9	-0.04	16.5
MD			0.00	4.2		0.00	5.2		0.00	4.6		0.00	4.2

Bold numbers are the best known solutions. Italic numbers are the minimum value among four obtained solutions. Underscore numbers are the obtained values less than the best known solutions. ^aResults minus 550000. ^bResults minus 650000.

200-10-3b by TS-SA. Concerning gaps of Best, average values are, respectively, 0.06% for TS-SA and 0.07% for other pairs, and the highest gaps are less than 0.8% for four pairs. Median values equal to 0 for all pairs. Average and median values for CPU are, respectively, 50.8 and 14.9 s for TS-SA, 47.7 and 15.3 s for QS2-SA, 41 and 13.1 s for AS-AM, and 33.6 and 12.6 s for PA-AM.

For the Tuzun and Burke benchmark (Table 6), TS-SA and PS-AM tie for first place in the number of new BKS found with 13 new BKSs, and QS2-SA tails the winner to

take the second place by exploiting 12 new BKSs and AS-AM is in the last place. Concerning the number of solution less than or equal to BKS, TS-SA, PS-AM, and QS2-SA, respectively, rank the first, second, and third with 29, 28, and 27 solutions less than or equal to BKS, and AS-AM ranks the last place with 26 solutions less than or equal to BKS. What surprised us is that the number of new BKS accounts for over 30%, except for AS-AM with 27.8% of 36 instances in this benchmark. Concerning gaps of Best, average values are, respectively, -0.01% for TS-SA, 0.01% for QS2-SA and PS-

TABLE 5: Results for the CLRP instances in Prins set.

Set	BKS	TS-SA			QS2-SA			AS-AM			PS-AM		
		Best	Gap	CPU	Best	Gap	CPU	Best	Gap	CPU	Best	Gap	CPU
20-5-1	54793	54793	0.00	0.5	54793	0.00	0.5	54793	0.00	0.5	54793	0.00	0.5
20-5-1b	39104	39104	0.00	0.3	39104	0.00	0.3	39104	0.00	0.2	39104	0.00	0.2
20-5-2	48908	48908	0.00	0.5	48908	0.00	0.6	48908	0.00	0.4	48908	0.00	0.4
20-5-2b	37542	37542	0.00	0.3	37542	0.00	0.3	37542	0.00	0.3	37542	0.00	0.2
50-5-1	90111	90111	0.00	3.9	90111	0.00	4.1	90111	0.00	2.9	90111	0.00	2.6
50-5-1b	63242	63242	0.00	1.8	63242	0.00	2.0	63242	0.00	1.9	63242	0.00	1.7
50-5-2	88298	88298	0.00	4.2	88298	0.00	4.3	88298	0.00	3.6	88298	0.00	3.4
50-5-2b	67308	67373	0.10	2.1	67308	0.00	2.1	67449	0.21	1.7	67308	0.00	1.5
50-5-2bis	84055	84055	0.00	3.5	84055	0.00	3.7	84055	0.00	3.1	84055	0.00	2.9
50-5-2bbis	51822	51822	0.00	2.4	51822	0.00	2.5	51822	0.00	2.1	51822	0.00	2.0
50-5-3	86203	86203	0.00	3.9	86203	0.00	4.3	86203	0.00	3.4	86203	0.00	3.1
50-5-3b	61830	61830	0.00	1.9	61830	0.00	1.9	61830	0.00	1.6	61830	0.00	1.6
100-5-1	274814	276096	0.47	28.9	276144	0.48	30.9	275601	0.29	25.8	275598	0.29	22.6
100-5-1b	213615	213654	0.02	14.1	213654	0.02	13.5	213671	0.03	12.2	213654	0.02	10.9
100-5-2	193671	193671	0.00	35.1	193671	0.00	34.4	193671	0.00	26.6	193671	0.00	26.0
100-5-2b	157095	157129	0.02	14.1	157144	0.03	15.2	157110	0.01	13.8	157129	0.02	12.3
100-5-3	200079	200079	0.00	34.3	200079	0.00	34.5	200079	0.00	25.7	200079	0.00	26.8
100-5-3b	152441	152441	0.00	13.8	152441	0.00	13.0	152441	0.00	12.3	152441	0.00	11.3
100-10-1	287695	<u>287688</u>	0.00	31.7	<u>287688</u>	0.00	32.8	<u>287688</u>	0.00	27.4	<u>287688</u>	0.00	25.4
100-10-1b	230989	<u>231608</u>	0.27	17.6	231833	0.37	16.7	231833	0.37	11.1	232222	0.53	13.8
100-10-2	243590	243590	0.00	28.6	243590	0.00	29.2	243590	0.00	24.4	243590	0.00	22.0
100-10-2b	203988	203988	0.00	15.7	203988	0.00	17.4	203988	0.00	15.5	203988	0.00	14.1
100-10-3	250882	252890	0.80	33.8	252890	0.80	33.2	252751	0.74	27.9	252890	0.80	27.2
100-10-3b	204317	<u>204567</u>	0.12	15.8	<u>204567</u>	0.12	15.4	<u>204567</u>	0.12	13.8	<u>204567</u>	0.12	12.9
200-10-1	475294	<u>475770</u>	0.10	268.1	476166	0.18	263.8	476002	0.15	219.6	476722	0.30	190.0
200-10-1b	377043	<u>375820</u>	-0.32	135.0	<u>376313</u>	-0.19	121.4	<u>376662</u>	-0.10	96.7	<u>375836</u>	-0.32	91.0
200-10-2	449006	<u>449037</u>	0.01	250.9	449142	0.03	236.7	449332	0.07	210.4	449110	0.02	132.4
200-10-2b	374280	<u>373882</u>	-0.11	153.0	<u>373973</u>	-0.08	151.1	<u>374039</u>	-0.06	125.8	<u>374093</u>	-0.05	110.6
200-10-3	469433	<u>470780</u>	0.29	247.8	471043	0.34	223.1	471043	0.34	208.2	471073	0.35	124.8
200-10-3b	362653	<u>362276</u>	-0.10	161.2	<u>362349</u>	-0.08	122.0	<u>362596</u>	-0.02	110.0	<u>362640</u>	0.00	113.1
AV	196470	196608	0.06	50.8	196663	0.07	47.7	196667	0.07	41.0	196674	0.07	33.6
MD		196875	0.00	14.9		0.00	15.3		0.00	13.1		0.00	12.6

Bold numbers are the best known solutions. Italic numbers are the minimum value among four obtained solutions. Underscore numbers are the obtained values less than the best known solutions.

AM, and 0.03% for SA-AM, and median values are 0 for all pairs. Computing times are on average 77.6, 74.5, 59.6, and 52.5 s, and median values are 62.6, 64.4, 53.8, and 50.3 s.

We conduct statistical analysis for obtained results of three CLRP benchmark sets in Tables 4–6 through Table 7 based on multiple pairwise comparisons with 95% confidence level (i.e., $\alpha=0.05$), namely, Friedman tests. In the Friedman test, the null hypothesis (H_0) is only rejected if the Friedman statistic (χ^2) is greater than the critical value, looking up in χ^2 table through sample size and confidence level, and post hoc test based on Wilcoxon Rank-Sum should be carried out to detect the significant difference among samples, when needed; otherwise, the null hypothesis (H_0) is accepted indicating that no significant difference is concerned among four pairs. In Table 7, Friedman statistics (χ^2) take the values 3.923 for Barreto et al., 6.750 for Prins et al., and 6.201 for Tuzun and Burke, which are, respectively, lower than 10.117, 18.493, and 23.269, indicating that there is no significant difference among performance of four pairs.

5.3.3. *Experiment on CLRPSPD.* The CLRPSPD benchmark instances, which were first converted in Refs. [2, 38], were also used to evaluate the features of the best four pairs. However, this paper only considered the W type of the above sets for the CLRPSPD. The main reason is that the sets of X , Y , and Z types show the same characteristics with the original sets of CLRP, and it is most difficult to obtain BKSs for the instances using W type separation approach. All BKSs were obtained from Ref. [1]. Results for the three CLRPSPD benchmark instances are shown in Tables 8–10. The first column of each table is the name of each instances, followed by the best known solution (BKS), data concerning the first four best pairs which contain best results (Best), gap (in percentage) to the BKS, and average computing time in seconds (CPU). Average (AV) and median values (MD) for gaps or gap and CPU are displayed in the last two rows.

For the Barreto benchmark set, computing times are on average lower than 35, 30, 29, and 18 s and median values are 3.9, 4, 3.4, and 3.1 s, respectively. Concerning gaps of Best,

TABLE 6: Results for the CLRP instances in Tuzun and Burke.

Set	BKS	TS-SA			QS2-SA			AS-AM			PS-AM		
		Best	Gap	CPU	Best	Gap	CPU	Best	Gap	CPU	Best	Gap	CPU
P1	1467.68	1467.68	0.00	15.2	1467.68	0.00	15.4	1467.68	0.00	13.0	1467.68	0.00	11.6
P2	1449.20	<i>1448.37</i>	-0.06	20.4	1449.20	0.00	20.1	1449.20	0.00	17.6	<i>1448.37</i>	-0.06	14.7
P3	1394.80	1394.80	0.00	15.1	1394.80	0.00	16.4	1394.93	0.01	14.2	1394.80	0.00	12.3
P4	1432.29	1432.29	0.00	20.7	1432.29	0.00	20.9	1432.29	0.00	17.6	1432.29	0.00	15.4
P5	1167.16	1167.16	0.00	14.5	1167.16	0.00	15.7	1167.16	0.00	13.2	1167.16	0.00	12.0
P6	1102.24	1102.24	0.00	19.0	1102.24	0.00	18.8	1102.24	0.00	16.2	1102.24	0.00	14.5
P7	791.66	791.66	0.00	15.6	791.66	0.00	15.8	791.66	0.00	13.4	791.66	0.00	12.6
P8	728.30	728.30	0.00	17.8	728.30	0.00	17.6	728.30	0.00	15.4	728.30	0.00	12.9
P9	1238.24	<i>1238.49</i>	0.02	16.6	<i>1238.49</i>	0.02	15.9	<i>1238.49</i>	0.02	14.6	<i>1238.49</i>	0.02	13.6
P10	1245.31	1245.31	0.00	23.9	1245.42	0.01	27.6	1245.31	0.00	18.1	1245.31	0.00	15.5
P11	902.26	902.26	0.00	15.3	902.26	0.00	15.4	902.26	0.00	12.9	902.26	0.00	11.9
P12	1018.29	1018.29	0.00	17.9	1018.29	0.00	18.2	1018.29	0.00	15.6	1018.29	0.00	12.7
P13	1866.75	1895.83	1.56	61.8	1895.83	1.56	63.1	<i>1892.17</i>	1.36	53.6	1895.83	1.56	52.9
P14	1823.20	<i>1820.12</i>	-0.17	62.1	<i>1822.69</i>	-0.03	61.3	<i>1822.15</i>	-0.06	53.8	<i>1822.69</i>	-0.03	42.1
P15	1964.30	<i>1965.12</i>	0.04	57.0	<i>1965.12</i>	0.04	57.9	<i>1965.12</i>	0.04	48.9	<i>1965.12</i>	0.04	42.6
P16	1792.80	<i>1792.77</i>	-0.00	70.9	<i>1792.77</i>	-0.00	69.9	<i>1792.77</i>	-0.00	66.9	<i>1792.77</i>	-0.00	55.3
P17	1443.33	<i>1443.32</i>	-0.00	58.6	<i>1443.32</i>	-0.00	64.5	<i>1443.32</i>	-0.00	53.7	<i>1443.32</i>	-0.00	51.3
P18	1434.60	<i>1434.82</i>	0.02	63.0	<i>1433.16</i>	-0.10	64.1	<i>1433.49</i>	-0.08	53.2	<i>1431.24</i>	-0.23	46.6
P19	1204.42	1204.42	0.00	63.5	1204.42	0.00	64.6	1204.42	0.00	57.1	1204.42	0.00	61.7
P20	930.99	<i>927.63</i>	-0.36	64.3	931.28	0.03	65.6	931.28	0.03	54.3	<i>929.26</i>	-0.19	43.8
P21	1694.18	1694.18	0.00	71.3	1694.18	0.00	64.2	1694.18	0.00	55.3	1694.18	0.00	52.1
P22	1392.01	1392.01	0.00	61.6	1392.18	0.01	64.6	1392.01	0.00	53.1	1392.01	0.00	49.3
P23	1198.20	<i>1197.95</i>	-0.02	57.5	<i>1197.95</i>	-0.02	57.2	<i>1197.95</i>	-0.02	48.3	<i>1197.95</i>	-0.02	40.8
P24	1151.80	1151.80	0.00	72.1	1151.80	0.00	73.1	1151.80	0.00	61.2	1151.80	0.00	52.9
P25	2243.40	<i>2237.73</i>	-0.25	136.6	<i>2240.37</i>	-0.14	131.1	2244.64	0.06	91.2	2244.79	0.06	84.9
P26	2138.40	<i>2139.67</i>	0.06	137.9	<i>2139.67</i>	0.06	130.1	2144.49	0.28	102.5	2141.09	0.13	73.2
P27	2209.30	<i>2204.93</i>	-0.20	178.8	<i>2208.48</i>	-0.04	151.4	2209.36	0.00	110.0	<i>2207.69</i>	-0.07	96.1
P28	2222.90	<i>2226.50</i>	0.16	160.4	<i>2223.61</i>	0.03	150.3	<i>2228.27</i>	0.24	113.2	<i>2221.59</i>	-0.06	110.4
P29	2073.70	<i>2074.86</i>	0.06	137.7	<i>2079.96</i>	0.30	130.6	<i>2076.16</i>	0.12	100.4	<i>2077.01</i>	0.16	88.9
P30	1692.17	<i>1685.65</i>	-0.39	135.8	<i>1685.65</i>	-0.39	129.5	<i>1687.38</i>	-0.28	102.6	<i>1685.78</i>	-0.38	80.6
P31	1453.18	<i>1449.96</i>	-0.22	175.1	<i>1449.46</i>	-0.26	153.4	<i>1450.90</i>	-0.16	114.8	<i>1453.89</i>	0.05	100.4
P32	1082.46	1082.46	0.00	167.3	1082.46	0.00	152.6	1082.46	0.00	108.5	1082.46	0.00	111.2
P33	1954.70	<i>1949.29</i>	-0.28	126.3	<i>1950.60</i>	-0.21	127.8	<i>1947.84</i>	-0.35	112.6	<i>1949.38</i>	-0.27	78.6
P34	1918.93	<i>1916.18</i>	-0.14	137.4	<i>1911.73</i>	-0.38	129.6	<i>1917.98</i>	-0.05	91.7	<i>1912.61</i>	-0.33	82.5
P35	1762.00	<i>1760.60</i>	-0.08	155.6	<i>1761.22</i>	-0.04	161.1	<i>1760.04</i>	-0.11	117.3	<i>1760.63</i>	-0.08	113.3
P36	1390.87	1390.87	0.00	167.3	1390.87	0.00	148.2	1390.87	0.00	111.1	1390.94	0.01	117.5
AV	1499.33	1499.32	-0.01	77.6	1499.63	0.01	74.5	1499.97	0.03	59.6	1499.59	0.01	52.5
MD		1439.07	0.00	62.6		0.00	64.4		0.00	53.8		0.00	50.3

Bold numbers are the best known solutions. Italic numbers are the minimum value among four obtained solutions. Underscore numbers are the obtained values less than the best known solutions.

TABLE 7: Friedman's test results for CLRP benchmark instances ($\alpha=0.05$).

Benchmark	Mean ranks for four pairs				n	Test statistics			Conclusion
	TS-SA	QS2-SA	AS-AM	PS-AM		χ^2	df	p	
Barreto set	2.58	2.42	2.37	2.63	19	3.923	3	0.270	$\chi^2 < \text{critical value, accept } H_0$
Prins set	2.18	2.58	2.60	2.63	30	6.750	3	0.080	
Tuzun and Burke	2.19	2.61	2.65	2.54	36	6.201	3	0.102	

average values are, respectively, 0, 0.03%, 0.01%, and 0.03%, and median values equal to 0. New BKSs for instance with 318 clients are found with an improvement of 0.11% to previous BKS by AS-AM and PS-AM. Gaps to BKS are very low for all instances with highest gaps lower than 0.08% for

the first pair, 0.25% for the second and third pairs, and 0.42% for the last one.

Looking at Table 9, computing times are on average less than 65, 60, 50, and 40 s, respectively, and median values are, respectively, 17.6, 18.3, 16.2, and 13.8 s. Concerning gaps to

TABLE 8: Results for the CLRPSD instances in Barreto set.

Instance	BKS	TS-SA			QS2-SA			AS-AM			PS-AM		
		Best	Gap	CPU	Best	Gap	CPU	Best	Gap	CPU	Best	Gap	CPU
P12-2	243.98	243.98	0.00	0.1	243.98	0.00	0.1	243.98	0.00	0.1	243.98	0.00	0.1
G21-5	528.42	528.42	0.00	0.4	528.42	0.00	0.5	528.42	0.00	0.3	528.42	0.00	0.3
G22-5	653.8	653.80	0.00	0.3	653.80	0.00	0.4	653.80	0.00	0.3	653.80	0.00	0.2
M27-5	3142.02	3142.02	0.00	0.6	3142.02	0.00	0.7	3142.02	0.00	0.5	3142.02	0.00	0.5
G29-5	592.1	592.10	0.00	0.6	592.10	0.00	0.6	592.10	0.00	0.4	592.10	0.00	0.4
G32-5	696.38	696.38	0.00	0.9	696.38	0.00	1.0	696.38	0.00	0.8	696.38	0.00	0.7
G32-5-2	595.27	595.27	0.00	0.7	595.27	0.00	0.8	595.27	0.00	0.6	595.27	0.00	0.6
G36-5	540.37	540.37	0.00	0.9	540.37	0.00	1.0	540.37	0.00	0.7	540.37	0.00	0.7
C50-5	708.37	708.37	0.00	1.9	708.37	0.00	2.0	708.37	0.00	1.5	708.37	0.00	1.4
P55-15	1327.06	1327.06	0.00	3.9	1327.06	0.00	4.0	1327.06	0.00	3.4	1327.06	0.00	3.1
C75-10	1132.8	1132.80	0.00	8.4	1135.61	0.25	8.6	1135.61	0.25	7.2	1137.59	0.42	6.1
P85-7	1855.55	1855.55	0.00	12.2	1855.55	0.00	12.4	1855.55	0.00	10.3	1855.55	0.00	6.3
D88-8	497.6	497.98	0.08	7.1	497.98	0.08	7.4	497.60	0.00	6.4	497.98	0.08	5.8
C100-10	1011.53	1011.53	0.00	13.7	1013.12	0.16	14.0	1011.53	0.00	11.4	1011.53	0.00	10.6
O117-14	12350.2	12350.20	0.00	17.4	12350.20	0.00	17.2	12350.20	0.00	15.3	12350.20	0.00	13.3
M134-8	5913.51	5913.51	0.00	28.5	5922.38	0.15	29.8	5913.51	0.00	24.8	5922.38	0.15	21.2
D150-10	44955.31	44955.31	0.00	46.6	44955.31	0.00	42.2	44960.92	0.01	37.2	44955.31	0.00	35.7
P318-4	4650.09 ^a	4650.85 ^a	0.00	199.7	4650.85 ^a	0.00	144.9	4650.85 ^a	0.00	151.3	4650.85 ^a	0.00	105.0
P318-4-2	6435.73 ^b	6435.73^b	0.00	310.7	6435.73^b	0.00	268.2	5633.50^b	-0.11	259.9	5633.50^b	-0.11	114.6
AV	72362.55	70938.49	0.00	34.5	70939.18	0.03	29.3	70896.69	0.01	28.0	70896.98	0.03	17.2
MD			0.00	3.9		0.00	4.00		0.00	3.4		0.00	3.1

Bold numbers are the best known solutions. Underscore and italic numbers are the obtained values less than the best known solutions. ^aResults minus 560000. ^bResults minus 700000.

TABLE 9: Results for the CLRPSD instances in Prins set.

Instance	BKS	TS-SA			QS2-SA			AS-AM			PS-AM		
		Best	Gap	CPU	Best	Gap	CPU	Best	Gap	CPU	Best	Gap	CPU
20-5-1	56350	56350	0.00	0.5	56350	0.00	0.5	56350	0.00	0.3	56350	0.00	0.3
20-5-1b	40678	40678	0.00	0.3	40678	0.00	0.3	40678	0.00	0.2	40678	0.00	0.2
20-5-2	49712	49712	0.00	0.5	49712	0.00	0.6	49712	0.00	0.3	49712	0.00	0.3
20-5-2b	38357	38357	0.00	0.3	38357	0.00	0.3	38357	0.00	0.2	38357	0.00	0.2
50-5-1	100240	100240	0.00	4.0	100240	0.00	4.1	100240	0.00	3.4	100240	0.00	3.1
50-5-1b	68993	68993	0.00	1.8	68993	0.00	2.3	68993	0.00	2.1	68993	0.00	1.8
50-5-2	94280	94280	0.00	5.1	94280	0.00	5.2	94280	0.00	4.4	94280	0.00	3.1
50-5-2b	69123	69123	0.00	2.7	69123	0.00	2.7	69123	0.00	2.2	69123	0.00	2.0
50-5-2bis	86349	86349	0.00	4.0	86349	0.00	4.0	86349	0.00	3.5	86349	0.00	3.3
50-5-2bbis	52356	52356	0.00	2.8	52356	0.00	2.6	52356	0.00	2.3	52356	0.00	2.1
50-5-3	90419	90419	0.00	4.9	<u>89737</u>	-0.75	4.7	90419	0.00	3.4	90419	0.00	3.8
50-5-3b	62178	62178	0.00	2.0	62178	0.00	2.1	62178	0.00	1.7	62178	0.00	1.6
100-5-1	290168	290280	0.04	43.5	290280	0.04	46.6	290401	0.08	38.7	290505	0.12	34.1
100-5-1b	219199	223968	2.18	18.9	223966	2.17	18.6	223968	2.18	16.9	223966	2.17	18.0
100-5-2	206049	206170	0.06	32.9	206078	0.01	36.7	206170	0.06	30.2	206308	0.13	29.8
100-5-2b	162077	162083	0.00	15.1	162077	0.00	15.7	162077	0.00	13.4	162077	0.00	12.1
100-5-3	209142	209142	0.00	43.2	209142	0.00	41.5	209142	0.00	34.5	209142	0.00	30.6
100-5-3b	156971	157027	0.04	16.2	157027	0.04	15.9	157027	0.04	14.4	157027	0.04	12.2
100-10-1	326093	326093	0.00	40.5	326093	0.00	40.8	326093	0.00	35.1	326093	0.00	30.8
100-10-1b	272889	272889	0.00	21.8	272889	0.00	21.6	272889	0.00	18.5	272889	0.00	14.1
100-10-2	253074	253609	0.21	39.4	253096	0.01	40.5	253640	0.22	34.1	253074	0.00	29.6
100-10-2b	208941	208941	0.00	20.9	208944	0.00	21.8	208941	0.00	18.9	208941	0.00	16.5
100-10-3	268137	268451	0.12	41.3	268416	0.10	39.0	268531	0.15	35.7	268349	0.08	32.6
100-10-3b	214828	214828	0.00	16.0	214828	0.00	17.9	214828	0.00	15.5	214828	0.00	13.5
200-10-1	529512	<u>498257</u>	-5.90	334.6	<u>498451</u>	-5.87	306.0	<u>499084</u>	-5.75	233.5	<u>498066</u>	-5.94	187.8
200-10-1b	393699	<u>384277</u>	-2.39	195.2	393924	0.06	170.2	<u>385287</u>	-2.14	155.7	<u>385737</u>	-2.02	135.7
200-10-2	463637	463968	0.07	316.4	463913	0.06	282.1	464111	0.10	249.2	464031	0.08	178.3
200-10-2b	380670	380924	0.07	206.4	380833	0.04	173.4	381031	0.09	138.5	<u>380611</u>	-0.02	117.0
200-10-3	485379	485882	0.10	307.9	485946	0.12	304.5	486009	0.13	240.8	486134	0.16	162.3
200-10-3b	369201	369938	0.20	183.3	370303	0.30	171.8	370213	0.27	131.5	370412	0.33	101.6
AV		206192	-0.17	64.1	206485	-0.12	59.8	206283	-0.15	49.3	206241	-0.16	39.3
MD			0.00	17.6		0.00	18.3		0.00	16.2		0.00	13.8

Bold numbers are the minimum value among four obtained solutions. Underscore and italic numbers are the obtained values less than the best known solutions.

TABLE 10: Results for the CLRPSPD instances in Tuzun and Burke.

Case	BKS	TS-SA			QS2-SA			AS-AM			PS-AM		
		Best	Gap	CPU	Best	Gap	CPU	Best	Gap	CPU	Best	Gap	CPU
P1	1504.45	1504.45	0.00	18.8	1504.45	0.00	19.5	1504.45	0.00	16.5	1504.86	0.03	14.2
P2	1474.33	1474.33	0.00	19.5	1474.33	0.00	18.8	1474.33	0.00	17.2	1474.33	0.00	14.4
P3	1414.35	1414.46	0.01	17.6	1415.13	0.06	17.5	1414.35	0.00	15.4	1414.35	0.00	13.2
P4	1477.49	1481.50	0.27	20.3	1484.29	0.46	19.5	1477.49	0.00	18.2	1477.49	0.00	15.1
P5	1230	1233.69	0.30	18.9	1233.24	0.26	18.6	<u>1227.89</u>	-0.17	16.5	1233.54	0.29	14.7
P6	1123.72	1123.72	0.00	17.9	1123.72	0.00	19.2	1123.72	0.00	16.6	1123.72	0.00	12.2
P7	812.42	812.42	0.00	18.8	812.42	0.00	22.0	812.42	0.00	16.3	812.42	0.00	15.0
P8	752.66	<u>751.89</u>	-0.10	24.0	754.15	0.20	23.3	<u>752.41</u>	-0.03	19.0	759.21	0.87	11.6
P9	1273.3	1273.30	0.00	18.8	1273.30	0.00	19.2	1273.30	0.00	15.8	1273.30	0.00	14.5
P10	1265.1	1265.10	0.00	22.5	<u>1265.02</u>	-0.01	22.8	1266.20	0.09	20.0	1265.10	0.00	17.4
P11	911.52	911.52	0.00	20.3	911.52	0.00	18.4	911.52	0.00	16.8	911.52	0.00	15.4
P12	1033.38	<u>1031.94</u>	-0.14	23.5	1033.38	0.00	22.6	<u>1033.27</u>	-0.01	20.2	1033.38	0.00	18.1
P13	1943.41	1947.92	0.23	59.1	1946.58	0.16	58.5	1949.76	0.33	49.9	1947.98	0.24	41.9
P14	1848.69	1848.69	0.00	66.1	1856.10	0.40	67.4	1859.17	0.57	58.4	1862.25	0.73	46.4
P15	2011.29	2011.32	0.00	67.7	2011.39	0.00	71.3	2016.29	0.25	58.5	2012.29	0.05	49.1
P16	1856.03	1861.73	0.31	63.5	1859.97	0.21	69.8	1862.65	0.36	59.4	1859.32	0.18	47.5
P17	1479.77	1484.97	0.35	69.3	1490.83	0.75	69.3	1483.73	0.27	58.7	1491.36	0.78	48.9
P18	1452.49	1453.05	0.04	67.1	1453.58	0.08	68.4	<u>1452.28</u>	-0.01	58.6	1452.73	0.02	47.8
P19	1228.49	<u>1228.11</u>	-0.03	60.6	1228.52	0.00	61.3	1228.49	0.00	53.9	1228.69	0.02	47.5
P20	949.82	949.82	0.00	68.3	951.62	0.19	68.7	950.06	0.03	58.9	949.82	0.00	45.7
P21	1732.81	1736.52	0.21	60.9	1736.45	0.21	61.9	1737.80	0.29	53.2	1735.63	0.16	42.9
P22	1426.41	1426.45	0.00	76.6	1426.66	0.02	77.4	1427.57	0.08	64.6	<u>1425.37</u>	-0.07	57.6
P23	1238.78	<u>1229.69</u>	-0.73	70.0	<u>1226.08</u>	-1.03	69.6	<u>1229.69</u>	-0.73	59.0	<u>1229.69</u>	-0.73	49.4
P24	1166.8	1166.80	0.00	64.0	1166.80	0.00	66.3	1166.80	0.00	57.0	1166.80	0.00	51.4
P25	2338.89	2343.12	0.18	153.2	2339.54	0.03	146.9	2343.64	0.20	102.4	2351.63	0.54	76.7
P26	2224.86	2226.41	0.07	177.6	2240.00	0.68	173.0	2238.67	0.62	122.9	2228.80	0.18	115.1
P27	2293.85	2298.34	0.20	175.9	2298.04	0.18	178.3	2297.87	0.18	115.3	2302.65	0.38	112.1
P28	2292.91	2303.17	0.45	154.4	2303.63	0.47	147.1	2301.04	0.35	107.2	2307.62	0.64	95.8
P29	2159.62	2163.17	0.16	160.2	<u>2158.57</u>	-0.05	159.8	2159.83	0.01	110.2	2169.93	0.48	89.4
P30	1727.67	1731.95	0.25	175.1	1733.80	0.35	172.7	1729.77	0.12	132.2	1729.04	0.08	103.6
P31	1483.34	1486.36	0.20	172.0	1484.89	0.10	171.2	1484.87	0.10	116.8	1486.35	0.20	114.3
P32	1101.65	1102.31	0.06	149.0	1102.29	0.06	138.4	1103.93	0.21	96.7	1102.44	0.07	100.5
P33	2001.36	2002.82	0.07	154.9	2003.39	0.10	147.4	2002.79	0.07	129.5	2003.16	0.09	75.5
P34	1973.43	1975.63	0.11	164.1	1977.83	0.22	165.5	1981.09	0.39	115.5	1982.10	0.44	107.9
P35	1801.82	1810.44	0.48	177.9	1825.68	1.32	164.5	1826.61	1.38	130.4	1822.02	1.12	148.1
P36	1418.8	1425.63	0.48	151.5	1423.96	0.36	140.0	1422.24	0.24	123.9	1432.10	0.94	101.2
Av.		1541.47	0.10	83.3	1542.53	0.16	82.1	1542.44	0.14	63.9	1543.42	0.21	55.3
MD.			0.05	66.6		0.09	68.6		0.08	58.6		0.08	47.7

Bold numbers are the minimum value among four obtained solutions. Underscore and italic numbers are the obtained values less than the best known solutions. The instances are represented by “PN,” where N represents the serial number.

BKs, average and median values are, respectively, -0.17% and 0 for TS-SA, -0.12% and 0 for QS2-SA, -0.15 and 0 for third pair, and -0.16 and 0 for the last pair. From the perspective of gaps to BKs, we verified the solutions achieved in Ref. [2]. Meanwhile, we obtained four improvements for four instances, i.e., 50-5-3 (QS2-SA), 200-10-1 (four pairs), 200-10-1b (four pairs except for QS2-SA), and 200-10-2b (PS-AM), one of them reaching an improvement of over 5.9% to previous BKs.

As shown in Table 10, the computing times are on average less than 84, 83, 64, and 56 s, and median values are 66.6, 68.6, 58.6, and 47.7 s, respectively. As far as gap to BKS is concerned, average/median values are 0.1/0.05%, 0.16/0.09%, 0.14/0.08%, and 0.21/0.08%, respectively. Meanwhile, new BKs of nine instances were obtained by our proposed algorithms, and the largest improvement was over 1% for P23 obtained by QS2-SA. The AS-AM outperformed others

obtaining five new BKs, followed by TS-SA and QS2-SA, and PS-AM performed the worst. However, the best-performing pairs was TS-SA in terms of average gap to BKs.

Statistical analysis is carried out for obtained results of three sets in Tables 8–10 through Table 11 based on Friedman test. In Table 11, Friedman statistics (χ^2) take the values 3.279 for Barreto et al., 4.621 for Prins et al., and 4.087 for Tuzun and Burke, which are, respectively, lower than 10.117, 18.493, and 23.269, indicating that there is no significant difference among the performance of four pairs. Therefore, we can strongly conclude that the proposed pairs could achieve high-quality solutions for the CLRPSPD benchmark instances.

Overall, among the four pairs, two types of discussion and conclusions are conducted: one for problem domains and one for hyperheuristic pairs. From perspective of both subjects, the amount of CPU time depends directly on the

TABLE 11: Friedman’s test results for CLRPSPD benchmark instances ($\alpha=0.05$).

Benchmark	Mean ranks for four pairs				n	Test statistics			Conclusion
	TS-SA	QS2-SA	AS-AM	PS-AM		χ^2	df	p	
Barreto set	2.39	2.68	2.37	2.55	19	3.279	3	0.351	$\chi^2 < \text{critical value, accept } H_0$
Prins set	2.42	2.33	2.77	2.48	30	4.621	3	0.202	
Tuzun and burke	2.25	2.51	2.44	2.79	36	4.087	3	0.252	

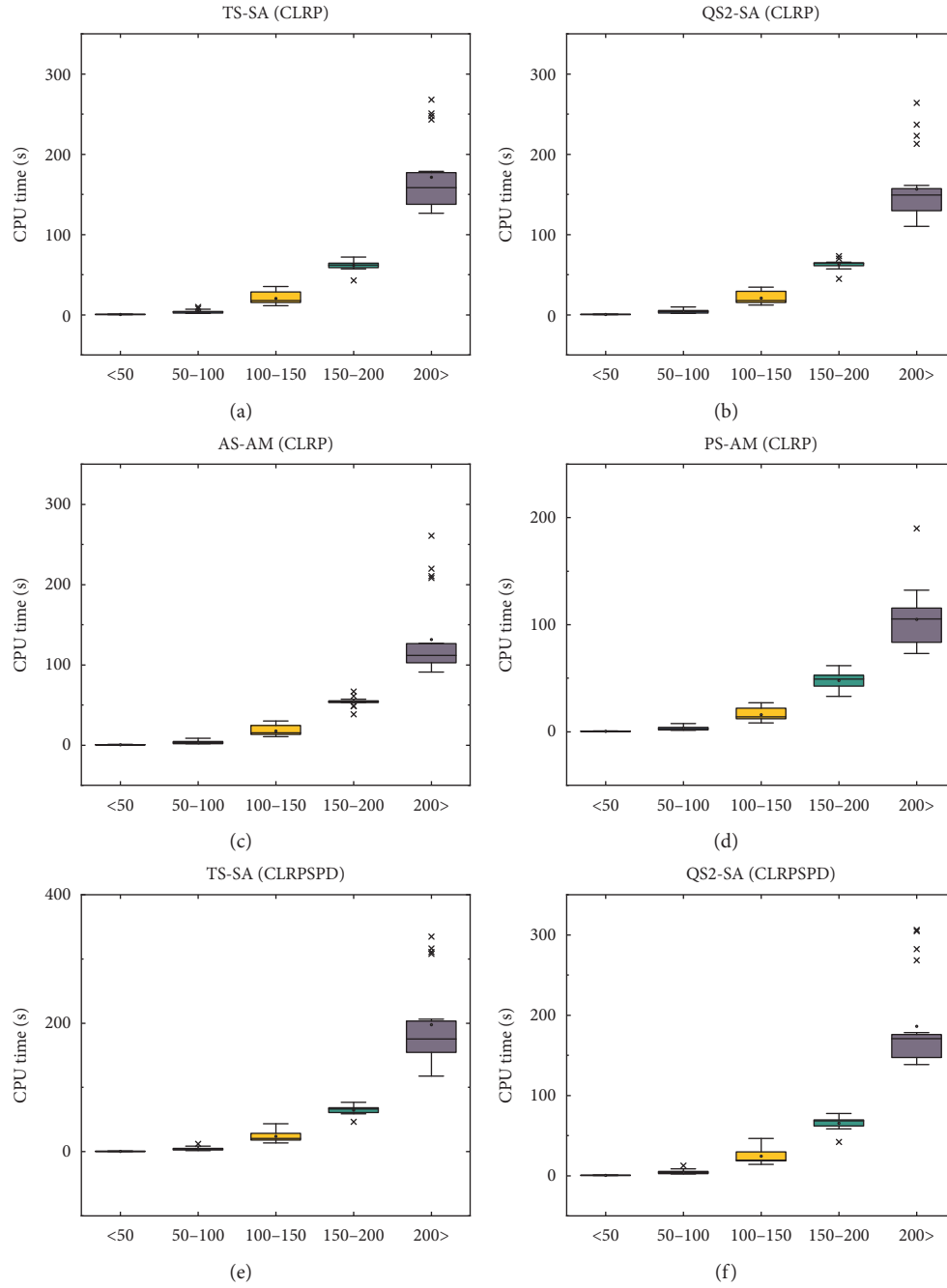


FIGURE 3: Continued.

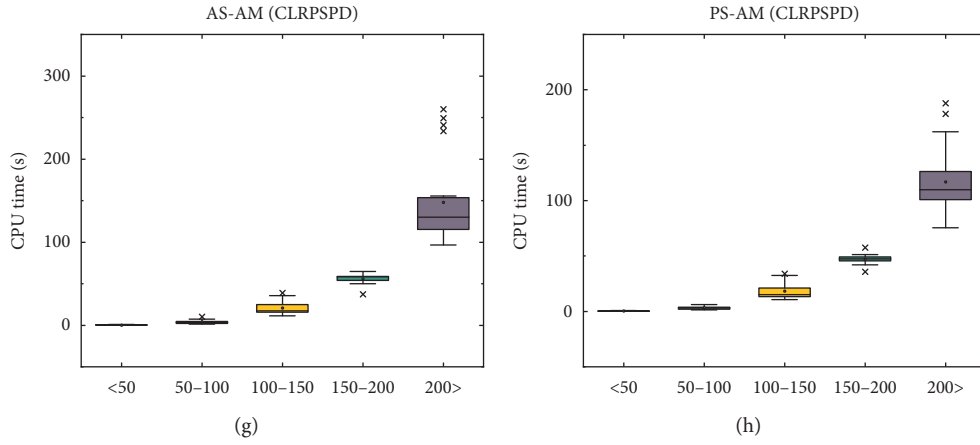


FIGURE 3: Box plots for relationship between computing time and number of clients.

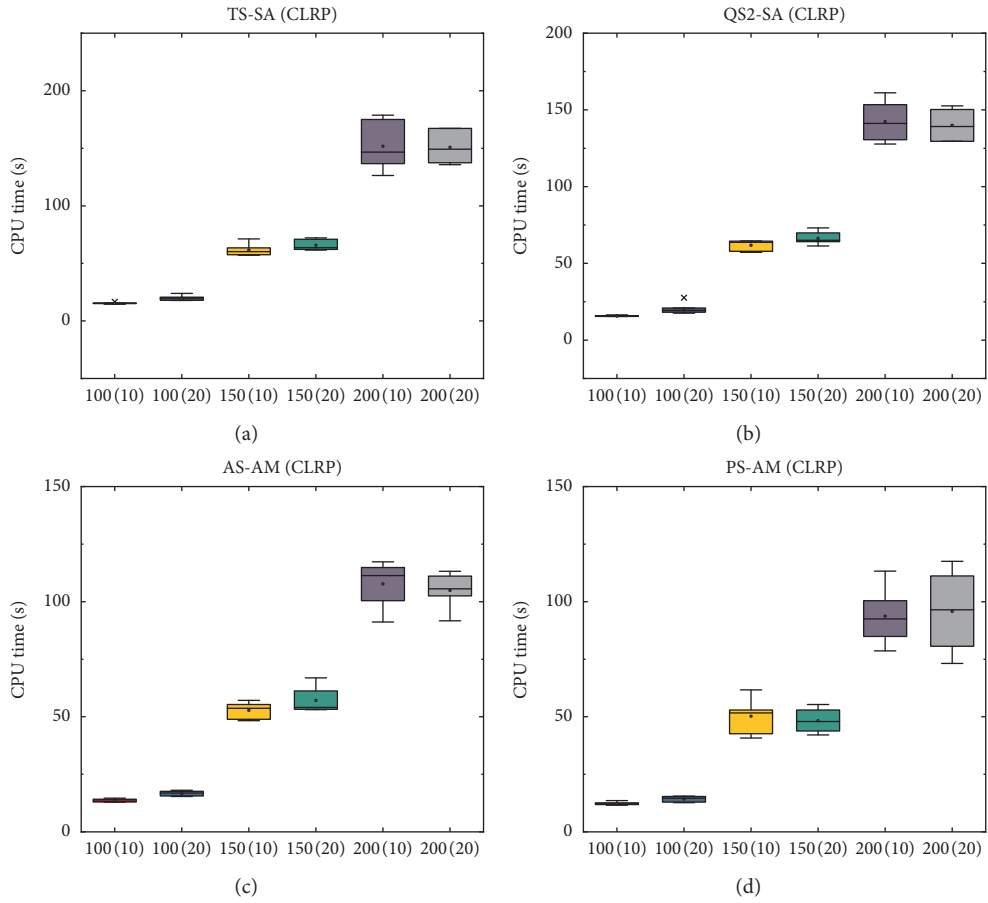


FIGURE 4: Continued.

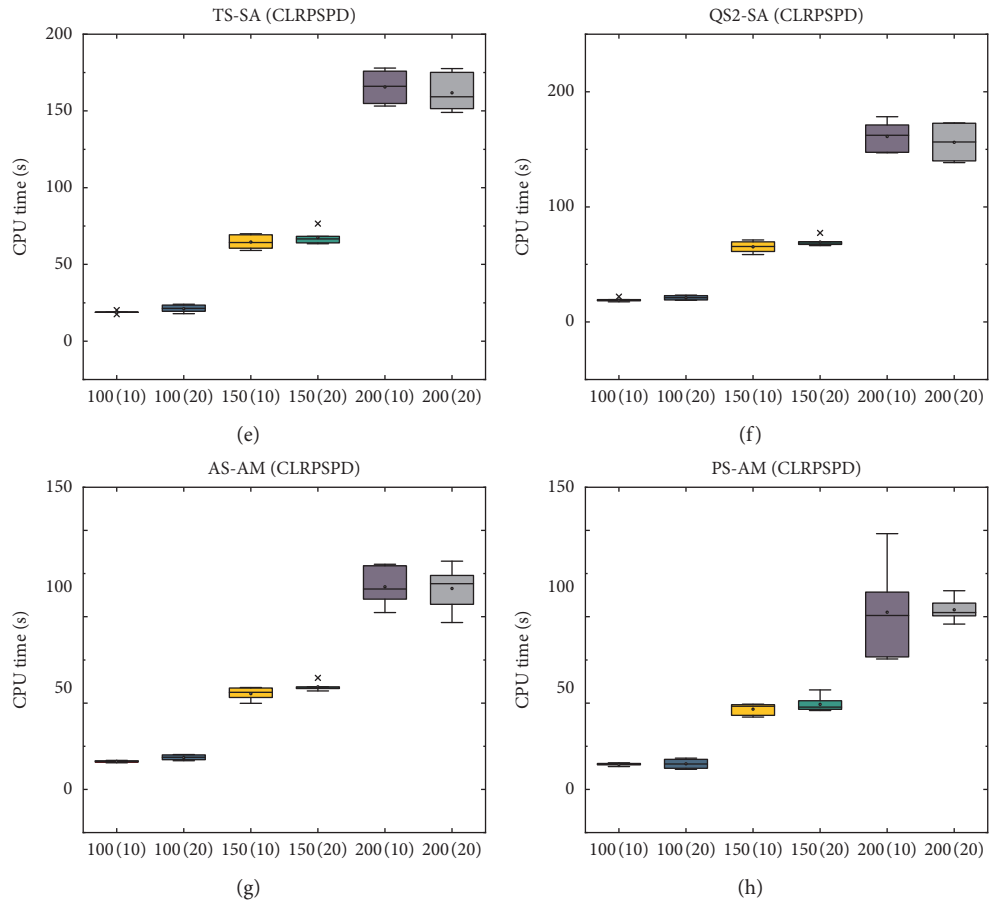


FIGURE 4: Box plots for relationship between computing time and number of depots.

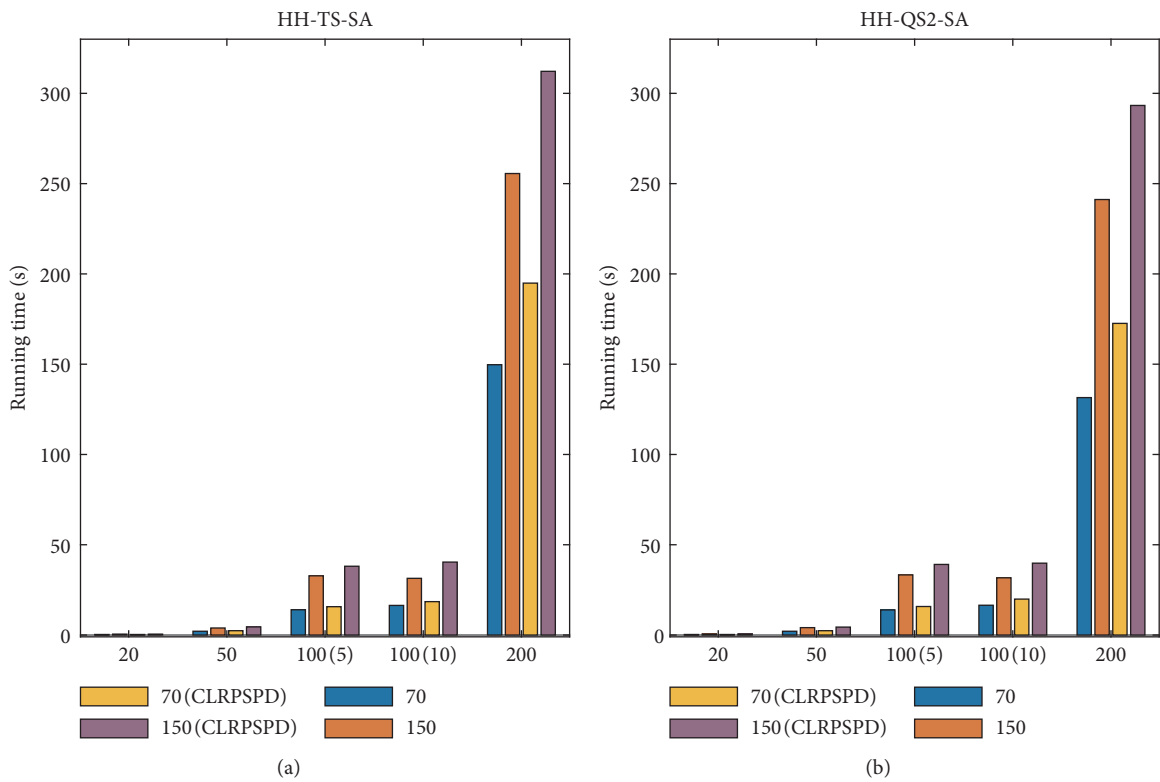


FIGURE 5: Continued.

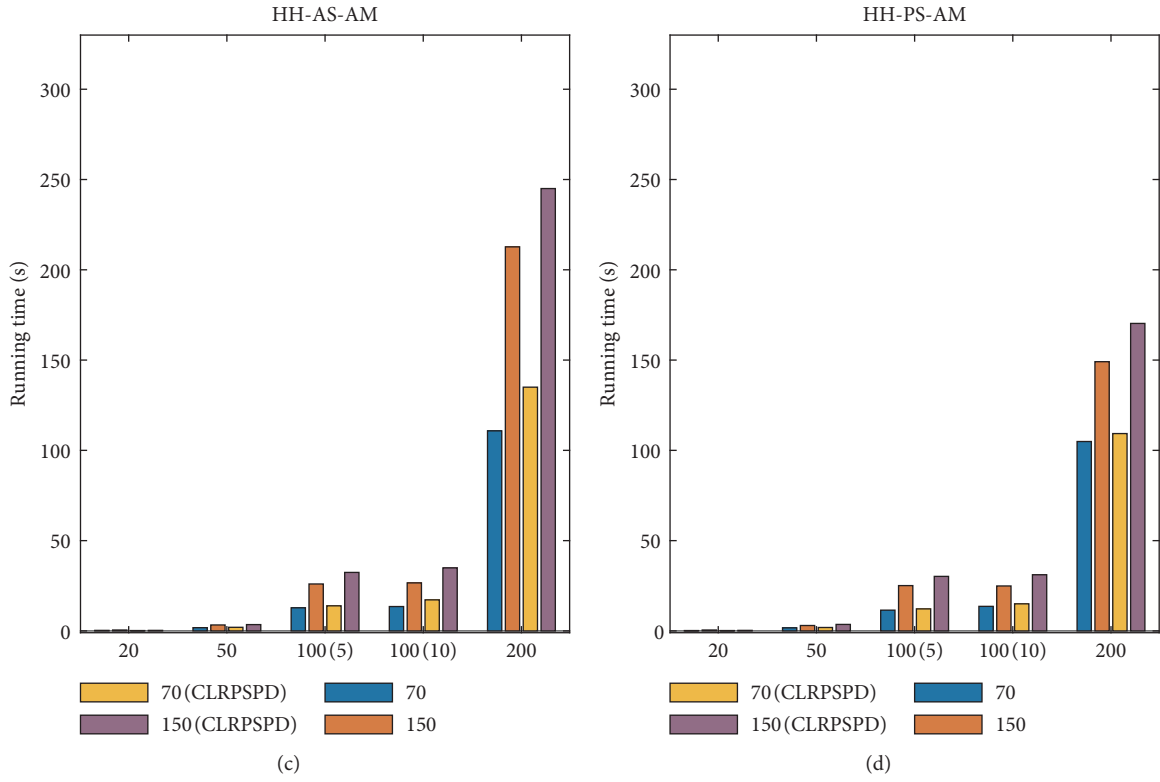


FIGURE 5: Histogram of computing times of different vehicle capacity.

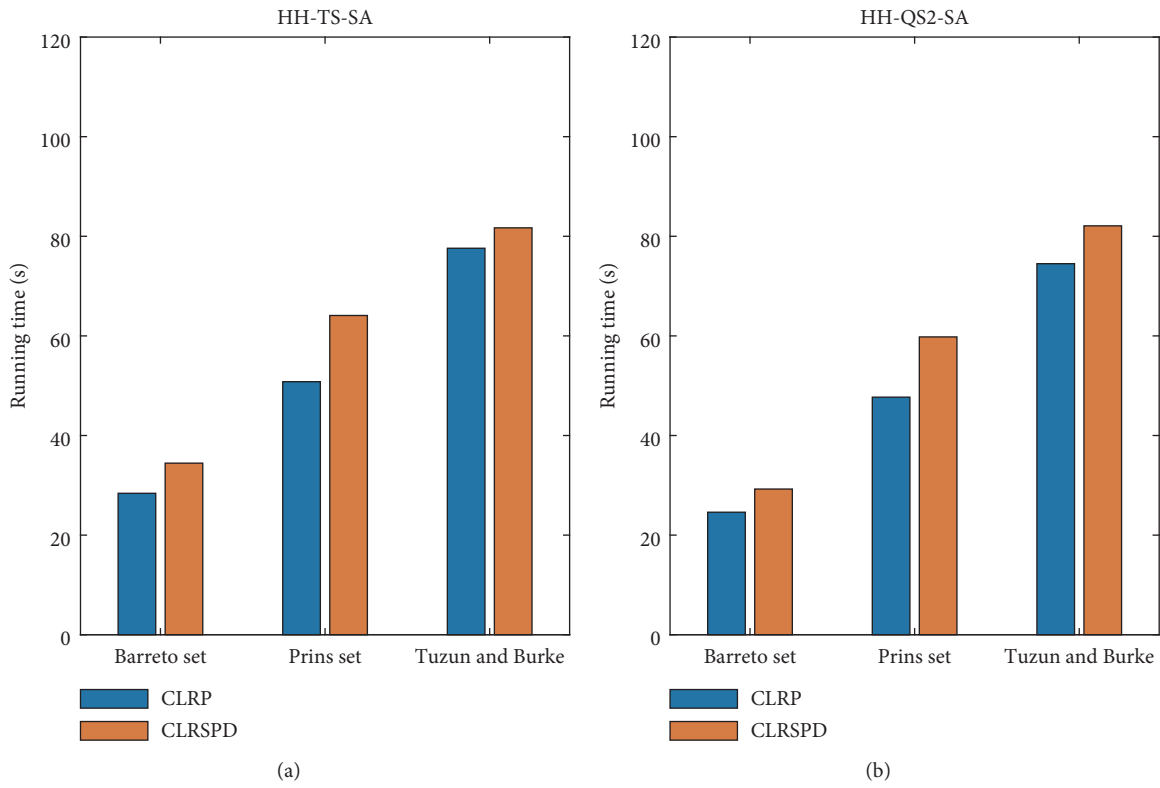


FIGURE 6: Continued.

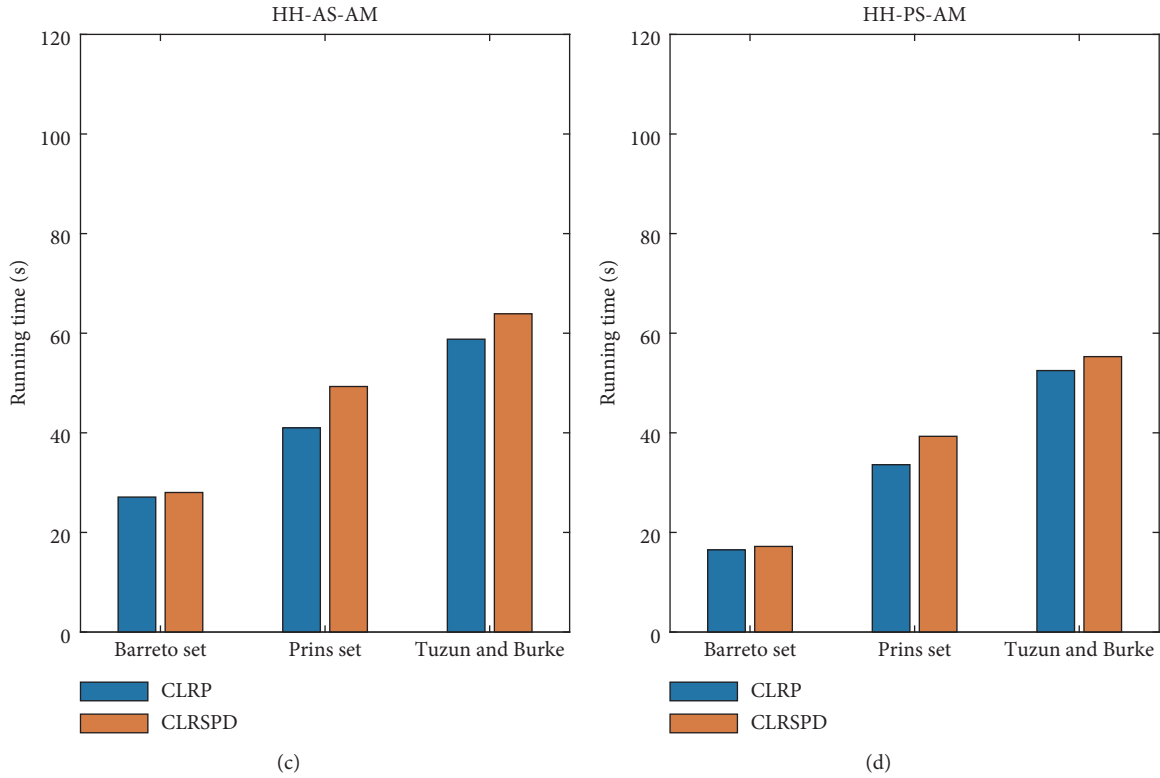


FIGURE 6: Histogram of computing times of both subjects.

number of clients (n), depots (m), and vehicle capacity (Q), and the relationship between running time and each of above factors is drawn in Figures 3 and 4 (excluding the outliers) and Figure 5. Several conclusions on running time are reached: (1) running time is affected by the number of clients in exponential way; (2) number of depots has slight impact on the running time, which may be resulted by few depots; (3) computing time increases with the decrease of the vehicle capacity in the form of polynomial; (4) the order of impact of the above factors effecting the running time is n , Q , and m . The first and third conclusions were also shared in Ref. [2]. Moreover, the time complexity and solution quality may depend in part on the complexity of the mathematical model. Figure 6 illustrates the impact of complexity of mathematical model on the running time. More specifically, the average computing time of tackling CLRSPD instances increases by 4.2–21.5% for Barreto set, 30.6–46.8% for Prins set, and 5.3–10.2% for Tuzun and Burke, respectively, compared with the average running times of tackling CLRP cases. Concerning solution quality and average standard deviation, the complexity of instances is the direct acting factor consisting of the number of clients, depots and vehicles, and the distribution of clients and depots. Furthermore, the complexity of approaches or pairs of selection strategies and acceptance criteria also significantly influence the running time, standard deviation, and solution quality. PS-AM seems to be among the fastest with declining 36, 33, and 20% average running time compared to others, and AS-AM and QS2-SA rank the second and third in aspects of average running time. In terms of solutions quality, there is

no significant difference among these four pairs concluded by the above Friedman tests, indicating that PS-AM and AS-AM outperform the others in obtaining a better trade-off solution quality and running time, but all pairs can obtain high solution quality within reasonable running time.

5.3.4. Comparison and Evaluation. To illustrate advantages of our proposed approaches for CLRP and CLRSPD, comparisons with the most recent and effective methods in the literature are carried out in Table 12, where average gaps (AG) of best found solutions to BKS and average running time of the proposed approaches for the CLRP are provided, and they are, respectively, GRASP+ELS [31], SALRP/SALRP+ [32], ALNS/ALNS+ [33], MACO [35], HGTS [34], GRASP+ILP [25], GVTNS [36], and HGA/HGA+ [37], and for the CLRSPD, the approaches were BC-SA [38], SA/SA* [4], and RP/TS/FRR-MAB/FMT [2].

Even though the time execution comparison can be unfair, depending on many factors (computer configuration, programming languages, the number of fitness evaluation, etc.), it is a significant performance indicator for judging the advantage of approaches. As shown in Table 12, our four pairs of hyperheuristic seem to be the fastest among the above methods. Furthermore, our approaches are the among best in aspects of solution quality on all CLRP and CLRSPD benchmark sets with very small gaps. In conclusion, we can strongly conclude that our hyperheuristics are able to outperform the most recent and effective methods in terms of either solution quality or computing time.

TABLE 12: Average solutions for CLRP and CLRPSPD benchmark sets.

Algorithm	Barreto set		Prins set		Tuzun and Burke	
	AG	CPU	AG	CPU	AG	CPU
<i>CLRP benchmark</i>						
GRASP + ELS	0.08 ^a	187.6 ^a	1.11	258.2	1.30	606.6
SALRP	0.48	464.1	0.46	422.4	1.49	826.4
SALRP+	0.08	NA	0.08	NA	0.53	NA
ALNS	0.16 ^a	177.2 ^a	0.44	451.1	0.43	829.6
ALNS+	0.06 ^a	1772.0 ^a	0.27	4221.0	0.18	8103.0
HGTS	0.78 ^a	105.2 ^a	0.57	176.4	1.14	392.3
MACO	0.17	191.7	0.40	191.3	1.23	201.9
GRASP + ILP	0.14 ^a	264.3 ^a	0.12	1163.0	0.17	2589.5
GVTNS	0.67 ^a	53.0 ^a	0.37	91.2	0.76	201.2
HGA	0.63	42.4	0.37	73.1	0.86	86.0
HGA+	0.00	429.6	0.32	199.1	0.70	363.6
TS-SA	-0.04	28.4	0.06	50.8	-0.01	77.6
QS2-SA	-0.07	24.6	0.07	47.7	0.01	74.5
AS-AM	-0.05	27.1	0.07	41.0	0.03	58.8
PS-AM	-0.04	16.5	0.07	33.6	0.01	52.5
<i>CLRPSPD benchmark</i>						
BC-SA	1.47 ^a	6604.1 ^a	NA	NA	NA	NA
SA	0.48	1460.1	NA	NA	NA	NA
SA*	0.21	NA	NA	NA	NA	NA
RP	0.08	32.2	0.07	60.2	0.21	83.4
TS	0.02	30.54	0.06	55.2	0.10	77.6
FRR-MAB	0.01	32.46	0.02	62.7	0.08	77.3
FMT	0.00	32.73	0.01	59.8	0.02	78.6
TS-SA	0.00	34.5	-0.17	64.1	0.10	83.3
QS2-SA	0.03	29.3	-0.12	59.8	0.16	82.1
AS-AM	0.01	28.0	-0.15	49.3	0.14	63.9
PS-AM	0.03	17.2	-0.16	39.3	0.21	55.3

^aConsidering only (the same) 13 out of the 19 instances.

6. Conclusion and Future Work

In this study, evolution-based hyperheuristics are proposed to tackle the CLRP and one of its variants, namely, CLRPSPD. Five evolutionary and four nonevolutionary selection strategies are developed as high-level selection strategies to pair up with four acceptance criteria to make a right decision on constructing effective sequences of LLHs at each step, guiding the proposed approaches to achieve the optimal values.

The first experiment was carried out to determine the top four pairs which can rightly reflect to performance information of each LLH and quickly respond to select the promising LLHs. Results show that (1) AM and SA as acceptance criteria performed better when compared to the rest two; (2) AS, FRR-MAB-TS, and TS as selection strategies performed better when compared to the rest of the selection strategies; (3) average performance of AS-AM, PS-AM, QS2-SA, and TS-SA as HLHs perform significantly better than the rest of the pairs. The first four outstanding pairs were picked out to implement the remaining two experiments. PS-AM and AS-AM outperform others in terms of obtaining a good trade-off between solution quality and computing time, and all four pairs can achieve solution of high quality within reasonable running time, providing several new BKSs accounted for over 30% in Tuzun and Burke CLRP set. A comparative analysis is also conducted with tailored

approaches in the published literature, and the results illustrate that the performance of our proposed approaches outperform the above methods in terms of both solution quality and computing time. As advocated in Ref. [93] for hyperheuristic, the proposed approaches have capability in exploiting good enough, soon enough, and cheap enough solutions.

The proposed hyperheuristic (36 pairs) has been already been implemented in a decision-support tool, and we refer the interested readers to consult us about the package. The next research content will focus on the adaptive selection of MHs and other selection strategies of hill climbers, e.g., choice function [5, 47], adaptive pursuit [94], and fair-share method [95]. For bringing CLRP/CLRPSPD closer to the reality, more practical constraints will also be taken into account in future works, such as time windows, dynamic demands, period delivery, and pickup.

Data Availability

The data used to support the findings of this study are available from the corresponding author upon request.

Conflicts of Interest

The authors declare that there are no conflicts of interest regarding the publication of this paper.

Acknowledgments

This work was partly supported by the National Natural Science Foundation of China (nos. 51875524 and 61873240) and National Natural Science Foundation of Zhejiang (no. Y19F030017).

References

- [1] N. Bhusiri, A. G. Qureshi, and E. Taniguchi, "The trade-off between fixed vehicle costs and time-dependent arrival penalties in a routing problem," *Transportation Research Part E: Logistics and Transportation Review*, vol. 62, pp. 1–22, 2014.
- [2] Y. Zhao, L. Leng, and C. Zhang, "A novel framework of hyperheuristic approach and its application in location-routing problem with simultaneous pickup and delivery," *Operational Research*, 2019.
- [3] L. Bouhafas, A. Hajjam, and A. Koukam, "A combination of simulated annealing and ant colony system for the capacitated location-routing problem," in *Proceedings of the 10th International Conference on Knowledge-Based and Intelligent Information and Engineering Systems*, vol. 4251, pp. 409–416, Bournemouth, UK, October 2006.
- [4] V. F. Yu and S.-Y. Lin, "Solving the location-routing problem with simultaneous pickup and delivery by simulated annealing," *International Journal of Production Research*, vol. 54, no. 2, pp. 526–549, 2016.
- [5] P. Cowling, G. Kendall, and E. Soubeiga, "A hyperheuristic approach to scheduling a sales summit," in *Proceedings of the Practice and Theory of Automated Timetabling III: Third International Conference*, vol. 2079, pp. 176–190, Constance, Germany, August 2001.
- [6] K. Z. Zamli, B. Y. Alkazemi, and G. Kendall, "A tabu search hyperheuristic strategy for t-way test suite generation," *Applied Soft Computing*, vol. 44, pp. 57–74, 2016.
- [7] K. Li, A. Fialho, S. Kwong, and Q. Zhang, "Adaptive operator selection with bandits for a multiobjective evolutionary algorithm based on decomposition," *IEEE Transactions on Evolutionary Computation*, vol. 18, no. 1, pp. 114–130, 2014.
- [8] S. P. Chen, J. Yang, Y. Li, and J. F. Yang, "Multiconstrained network intensive vehicle routing adaptive ant colony algorithm in the context of neural network analysis," *Complexity*, vol. 2017, Article ID 8594792, 9 pages, 2017.
- [9] Y. Zhou, L. S. Zhou, Y. Wang, Z. Yang, and J. Wu, "Application of multiple-population genetic algorithm in optimizing the train-set circulation plan problem," *Complexity*, vol. 2017, Article ID 3717654, 14 pages, 2017.
- [10] Y. Y. Niu, Z. H. Yang, P. Chen, and J. H. Xiao, "A hybrid tabu search algorithm for a real-world open vehicle routing problem involving fuel consumption constraints," *Complexity*, vol. 2018, Article ID 5754908, 12 pages, 2018.
- [11] R. Grosso, J. Muñuzuri, A. Escudero-Santana, and E. Barbadilla-Martín, "Mathematical formulation and comparison of solution approaches for the vehicle routing problem with access time windows," *Complexity*, vol. 2018, Article ID 4621694, 10 pages, 2018.
- [12] C. Watson-Gandy and P. Dohrn, "Depot location with van salesmen—a practical approach," *Omega*, vol. 1, no. 3, pp. 321–329, 1973.
- [13] F. Rahim and C. Sepil, "A location-routing problem in glass recycling," *Annals of Operations Research*, vol. 223, no. 1, pp. 329–353, 2014.
- [14] S. Solak, C. Scherrer, and A. Ghoniem, "The stop-and-drop problem in nonprofit food distribution networks," *Annals of Operations Research*, vol. 221, no. 1, pp. 407–426, 2014.
- [15] N. Asgari, M. Rajabi, M. Jamshidi, M. Khatami, and R. Z. Farahani, "A memetic algorithm for a multi-objective obnoxious waste location-routing problem: a case study," *Annals of Operations Research*, vol. 250, no. 2, pp. 279–308, 2017.
- [16] C. Burkart, P. C. Nolz, and W. J. Gutjahr, "Modelling beneficiaries' choice in disaster relief logistics," *Annals of Operations Research*, vol. 256, no. 1, pp. 41–61, 2017.
- [17] G. Nagy and S. Salhi, "Location-routing: issues, models and methods," *European Journal of Operational Research*, vol. 177, no. 2, pp. 649–672, 2007.
- [18] R. B. Lopes, C. Ferreora, B. S. Santo, and S. Barreto, "A taxonomical analysis, current methods and objectives on location-routing problems," *International Transactions in Operational Research*, vol. 20, no. 6, pp. 795–822, 2013.
- [19] C. Prodhon and C. Prins, "A survey of recent research on location-routing problems," *European Journal of Operational Research*, vol. 238, no. 1, pp. 1–17, 2014.
- [20] M. Drexler and M. Schneider, "A survey of variants and extensions of the location-routing problem," *European Journal of Operational Research*, vol. 241, no. 2, pp. 283–308, 2015.
- [21] J. W. Escobar, R. Linfati, and W. A. Jaimes, "The capacitated location routing problem: review of literature," *Facultad De Ingeniería*, vol. 24, no. 39, pp. 85–98, 2015.
- [22] R. Baldacci, A. Mingozzi, and R. Wolfler Calvo, "An exact method for the capacitated location-routing problem," *Operations Research*, vol. 59, no. 5, pp. 1284–1296, 2011.
- [23] J.-M. Belenguer, E. Benavent, C. Prins, C. Prodhon, and R. Wolfler Calvo, "A branch-and-cut method for the capacitated location-routing problem," *Computers & Operations Research*, vol. 38, no. 6, pp. 931–941, 2011.
- [24] C. Contardo, J.-F. Cordeau, and B. Gendron, "A computational comparison of flow formulations for the capacitated location-routing problem," *Discrete Optimization*, vol. 10, no. 4, pp. 263–295, 2013.
- [25] C. Contardo, J.-F. Cordeau, and B. Gendron, "An exact algorithm based on cut-and-column generation for the capacitated location-routing problem," *Informatics Journal on Computing*, vol. 26, no. 1, pp. 88–102, 2014.
- [26] D. Tuzun and L. I. Burke, "A two-phase tabu search approach to the location routing problem," *European Journal of Operational Research*, vol. 116, no. 1, pp. 87–99, 1999.
- [27] C. Prins, C. Prodhon, A. Ruiz, P. Soriano, and R. Wolfler Calvo, "Solving the capacitated location-routing problem by a cooperative lagrangean relaxation-granular tabu search heuristic," *Transportation Science*, vol. 41, no. 4, pp. 470–483, 2007.
- [28] S. Barreto, C. Ferreira, J. Paixão, and B. S. Santos, "Using clustering analysis in a capacitated location-routing problem," *European Journal of Operational Research*, vol. 179, no. 3, pp. 968–977, 2007.
- [29] M. Schwardt and K. Fischer, "Combined location-routing problems—a neural network approach," *Annals of Operations Research*, vol. 167, no. 1, pp. 253–269, 2009.
- [30] S. Salhi and G. Nagy, "Local improvement in planar facility location using vehicle routing," *Annals of Operations Research*, vol. 167, no. 1, pp. 287–296, 2009.
- [31] C. Duhamel, P. Lacomme, C. Prins, and C. Prodhon, "A GRASP × ELS approach for the capacitated location-routing problem," *Computers & Operations Research*, vol. 37, no. 11, pp. 1912–1923, 2010.





- [32] V. F. Yu, S.-W. Lin, W. Lee, and C.-J. Ting, "A simulated annealing heuristic for the capacitated location routing problem," *Computers & Industrial Engineering*, vol. 58, no. 2, pp. 288–299, 2010.
- [33] V. C. Hemmelmayr, J.-F. Cordeau, and T. G. Crainic, "An adaptive large neighborhood search heuristic for two-echelon vehicle routing problems arising in city logistics," *Computers & Operations Research*, vol. 39, no. 12, pp. 3215–3228, 2012.
- [34] J. W. Escobar, R. Linfati, and P. Toth, "A two-phase hybrid heuristic algorithm for the capacitated location-routing problem," *Computers & Operations Research*, vol. 40, no. 1, pp. 70–79, 2013.
- [35] C.-J. Ting and C.-H. Chen, "A multiple ant colony optimization algorithm for the capacitated location routing problem," *International Journal of Production Economics*, vol. 141, no. 1, pp. 34–44, 2013.
- [36] J. W. Escobar, R. Linfati, M. G. Baldoquin, and P. Toth, "A granular variable tabu neighborhood search for the capacitated location-routing problem," *Transportation Research Part B: Methodological*, vol. 67, no. 9, pp. 344–356, 2014.
- [37] R. B. Lopes, C. Ferreira, and B. S. Santos, "A simple and effective evolutionary algorithm for the capacitated location-routing problem," *Computers & Operations Research*, vol. 70, pp. 155–162, 2016.
- [38] I. Karaoglan, F. Altiparmak, I. Kara, and B. Dengiz, "A branch and cut algorithm for the location-routing problem with simultaneous pickup and delivery," *European Journal of Operational Research*, vol. 211, no. 2, pp. 318–332, 2011.
- [39] I. Karaoglan, F. Altiparmak, I. Kara, and B. Dengiz, "The location-routing problem with simultaneous pickup and delivery: formulations and a heuristic approach," *Omega*, vol. 40, no. 4, pp. 465–477, 2012.
- [40] V. F. Yu and S.-W. Lin, "Multi-start simulated annealing heuristic for the location routing problem with simultaneous pickup and delivery," *Applied Soft Computing*, vol. 24, pp. 284–290, 2014.
- [41] E. A. Demircan-Yildiz, I. Karaoglan, and F. Altiparmak, "Two echelon location routing problem with simultaneous pickup and delivery: mixed integer programming formulations and comparative analysis," in *Proceedings of the International Conference on Computational Logistics*, pp. 275–289, Lisbon, Portugal, September 2016.
- [42] J. Denzinger, M. Fuchs, M. Fuchs, and M. Fuchs, "High performance ATP systems by combining several AI methods," in *Proceedings of the International Joint Conference on Artificial Intelligence*, pp. 102–107, Nagoya, Japan, August 1997.
- [43] E. K. Burke, M. Gendreau, M. Hyde et al., "Hyper-heuristics: a survey of the state of the art," *Journal of the Operational Research Society*, vol. 64, no. 12, pp. 1695–1724, 2013.
- [44] M. Kalender, A. Kheiri, E. Ö.eir, and E. K. Burke, "A greedy gradient-simulated annealing selection hyper-heuristic," *Soft Computing*, vol. 17, no. 12, pp. 2279–2292, 2013.
- [45] E. Ö.bMe, B. Bilgin, and E. E. Korkmaz, "A comprehensive analysis of hyper-heuristics," *Intelligent Data Analysis*, vol. 12, no. 1, pp. 3–23, 2008.
- [46] N. R. Sabar, M. Ayob, G. Kendall, and R. Qu, "Automatic design of a hyper-heuristic framework with gene expression programming for combinatorial optimization problems," *IEEE Transactions on Evolutionary Computation*, vol. 19, no. 3, pp. 309–325, 2015.
- [47] J. H. Drake, E. Ö.ake, and E. K. Burke, "An improved choice function heuristic selection for cross domain heuristic search," in *Proceedings of the 12th International Conference on Parallel Problem Solving from Nature*, pp. 307–316, Taormina, Italy, September 2012.
- [48] A. Nareyek, "Choosing search heuristics by non-stationary reinforcement learning," in *Proceedings of the 4th Meta-heuristics International Conference*, vol. 86, pp. 523–544, Kyoto, Japan, August 2003.
- [49] L. Han and G. Kendall, "An investigation of a tabu assisted hyperheuristic genetic algorithm," in *Proceedings of the Congress on Evolutionary Computation (CEC)*, pp. 2230–2237, Canberra, Australia, December 2003.
- [50] G. Kendall and N. M. Hussin, "A tabu search hyperheuristic approach to the examination timetabling problem at the MARA University of Technology," in *Proceedings of the 5th International Conference on the Practice and Theory of Automated Timetabling*, vol. 3616, pp. 270–293, Pittsburgh, PA, USA, August 2004.
- [51] F. Glover and M. Rafael, "Tabu search," in *Metaheuristic Procedures for Training Neural Networks*, E. Alba and R. Marti, Eds., Springer, Boston, MA, USA, pp. 53–69, 2006.
- [52] G. K. Koulinas and K. P. Anagnostopoulos, "A new tabu search-based hyper-heuristic algorithm for solving construction leveling problems with limited resource availabilities," *Automation in Construction*, vol. 31, no. 3, pp. 169–175, 2013.
- [53] A. Fiahlo, L. D. Costa, M. Schoenauer, and M. Sebag, "Dynamic multi-armed bandits and extreme value-based rewards for adaptive operator selection in evolutionary algorithms," in *Proceedings of the 3rd Conference on Learning and Intelligent Optimization*, vol. 5851, pp. 176–190, Trento, Italy, January 2009.
- [54] J. D. Walker, G. Ochoa, M. Gendreau, and E. K. Burke, "Vehicle routing and adaptive iterated local search within the HyFlex hyper-heuristic framework," in *Proceedings of the International Conference on Learning & Intelligent Optimization*, pp. 265–276, Catania, Italy, January 2012.
- [55] A. Strickler, J. A. Prado Lima, S. R. Vergilio, and A. T. R. Pozo, "Deriving products for variability test of feature models with a hyper-heuristic approach," *Applied Soft Computing*, vol. 49, pp. 1232–1242, 2016.
- [56] X. Wu, P. Consoli, L. Minku, G. Ochoa, and X. Yao, "An evolutionary hyper-heuristic for the software project scheduling problem," in *Proceedings of the 14th International Conference on Parallel Problem Solving from Nature (PPSN)*, vol. 9921, pp. 37–47, Edinburgh, UK, September 2016.
- [57] L. L. Leng, Y. W. Zhao, Z. Wang, H. W. Wang, and J. L. Zhang, "Shared mechanism-based self-adaptive hyperheuristic for regional low-carbon location-routing problem with time windows," *Mathematical Problems in Engineering*, vol. 2018, Article ID 8987402, 21 pages, 2018.
- [58] E. K. Burke, G. Kendall, R. F. J. O'Brien, D. Redrup, and E. Soubeiga, "An ant algorithm hyperheuristic," in *Proceedings of the Fifth Meta-Heuristics International Conference (MIC 2003)*, Kyoto, Japan, 2003.
- [59] E. K. Burke, G. Kendall, D. L. Silva, R. F. J. O'Brien, and E. Soubeiga, "An ant algorithm hyper heuristic for the project presentation scheduling problem," in *Proceedings of the IEEE Congress on Evolutionary Computation*, pp. 2263–2270, Edinburgh, Scotland, September 2005.
- [60] A. Cuesta-Cañada, L. Garrido, and H. Terashima-Marín, "Building hyper-heuristics through ant colony optimization for the 2D bin packing problem," in *Proceedings of the 9th International Conference on Knowledge-Based Intelligent Information and Engineering Systems*, pp. 654–660, Melbourne, Australia, September 2005.

- [61] P. C. Chen, G. Kendall, and G. V. Berghe, "An ant based hyperheuristic for the travelling tournament problem," in *Proceedings of the IEEE Symposium on Computational Intelligence in Scheduling*, pp. 19–26, Honolulu, Hawaii, April 2007.
- [62] Z. Ren, H. Jiang, J. Xuan, and Z. Luo, "Ant based hyper heuristics with space reduction: a case study of the p-median problem," in *Proceedings of the 11th International Conference on Parallel Problem Solving from Nature*, pp. 546–555, Krakow, Poland, September 2010.
- [63] F. C. Ergin, A. Ş. Uyar, and A. Yayimli, "Investigation of hyper-heuristics for designing survivable virtual topologies in optical WDM networks," in *Proceedings of the Conference on EvoApplications*, pp. 1–10, Torino, Italy, April 2011.
- [64] F. C. Ergin, A. Yayimli, and A. S. Uyar, "Survivable cross-layer virtual topology design using a hyperheuristic approach," in *Proceedings of the 13th International Conference on Transparent Optical Networks*, pp. 1–4, Stockholm, Sweden, June 2011.
- [65] B. Kiraz, A. S. Etaner-Uyar, and E. Özcan, "An ant-based selection hyperheuristic for dynamic environments," in *Proceedings of the Applications of Evolutionary Computation 16th European Conference*, pp. 626–635, Málaga, Spain, April 2012.
- [66] Z. A. Aziz, "Ant colony hyper-heuristics for travelling salesman problem," in *Proceedings of the IEEE International Symposium on Robotics and Intelligent Sensors*, vol. 76, pp. 534–538, Langkawi, Malaysia, October 2015.
- [67] L. Chen, H. Zheng, D. Zhang, and D. Li, "An ant colony optimization-based hyperheuristic with genetic programming approach for a hybrid flow shop scheduling problem," in *Proceedings of the IEEE Congress on Evolutionary Computation*, pp. 814–821, Sendai, Japan, May 2015.
- [68] A. Ahmed, A. H. S. Bukhari, and I. A. Ismaili, "A comparative study on three hyperheuristic approaches for solving benchmark scheduling problems," *Sindh University Research Journal*, vol. 43, pp. 261–267, 2011.
- [69] A. Ahmed, M. Ali, and A. Sajid, "Particle swarm based hyperheuristic for tackling real world examinations scheduling problem," *Australian Journal of Basic & Applied Sciences*, vol. 5, no. 10, pp. 1406–1413, 2011.
- [70] G. Koulinas, L. Kotsikas, and K. Anagnostopoulos, "A particle swarm optimization based hyper-heuristic algorithm for the classic resource constrained project scheduling problem," *Information Sciences*, vol. 277, no. 2, pp. 680–693, 2014.
- [71] R. Aron, I. Chana, and A. Abraham, "A hyper-heuristic approach for resource provisioning-based scheduling in grid environment," *The Journal of Supercomputing*, vol. 71, no. 4, pp. 1427–1450, 2015.
- [72] S. Chen, Z. Li, B. Yang, and G. Rudolph, "Quantum-inspired hyper-heuristics for energy-aware scheduling on heterogeneous computing systems," *IEEE Transactions on Parallel and Distributed Systems*, vol. 27, no. 6, pp. 1796–1810, 2016.
- [73] H. Terashima-Marín, P. Ross, C. J. Fariás-Zárate, E. López-Camacho, and M. Valenzuela-Rendón, "Generalized hyper-heuristics for solving 2D regular and irregular packing problems," *Annals of Operations Research*, vol. 179, no. 1, pp. 369–392, 2010.
- [74] J. Blazewicz, E. K. Burke, G. Kendall, W. Mruczkiewicz, C. Oguz, and A. Swiercz, "A hyper-heuristic approach to sequencing by hybridization of DNA sequences," *Annals of Operations Research*, vol. 207, no. 1, pp. 27–41, 2013.
- [75] K. Z. Zamli, F. Din, G. Kendall, and B. S. Ahmed, "An experimental study of hyper-heuristic selection and acceptance mechanism for combinatorial t-way test suite generation," *Information Sciences*, vol. 399, pp. 121–153, 2017.
- [76] F. Buttelle, L. Alfandari, C. Coti et al., "Fast machine reassignment," *Annals of Operations Research*, vol. 242, no. 1, pp. 133–160, 2016.
- [77] E. K. Burke, G. Kendall, M. Mısı́r, and E. Özcan, "Monte Carlo hyper-heuristics for examination timetabling," *Annals of Operations Research*, vol. 196, no. 1, pp. 73–90, 2012.
- [78] S. Abdul-Rahman, E. K. Burke, A. Bargiela, B. McCollum, and E. Özcan, "A constructive approach to examination time-tabling based on adaptive decomposition and ordering," *Annals of Operations Research*, vol. 218, no. 1, pp. 3–21, 2014.
- [79] E. K. Burke, R. Qu, and A. Soghier, "Adaptive selection of heuristics for improving exam timetables," *Annals of Operations Research*, vol. 218, no. 1, pp. 129–145, 2014.
- [80] N. Pillay, "A review of hyper-heuristics for educational timetabling," *Annals of Operations Research*, vol. 239, no. 1, pp. 3–38, 2016.
- [81] A. Kheiri, E. Özcan, and A. J. Parkes, "A stochastic local search algorithm with adaptive acceptance for high-school timetabling," *Annals of Operations Research*, vol. 239, no. 1, pp. 135–151, 2016.
- [82] K. Chakhlevitch and P. Cowling, "Hyperheuristics: recent developments," *Studies in Computational Intelligence*, vol. 136, pp. 3–29, 2008.
- [83] E. K. Burke, M. Hyde, G. Kendall, G. Ochoa, and E. Özcan, "A classification of hyperheuristic approaches," in *Handbook of Metaheuristics*, M. Gendreau and J. Y. Potvin, Eds., pp. 449–468, Springer, Boston, MA, USA, 2010.
- [84] R. J. Marshall, M. Johnston, and M. Zhang, "Hyper-heuristic operator selection and acceptance criteria," in *Proceedings of the 15th European Conference on Evolutionary Computation in Combinatorial Optimization (EvoCOP)*, vol. 9026, pp. 99–113, 2015.
- [85] P. Shaw, "Using constraint programming and local search methods to solve vehicle routing problems," in *Proceedings of the International Conference on Principles and Practice of Constraint Programming*, pp. 417–431, Pisa, Italy, October 1998.
- [86] S. Ropke and D. Pisinger, "An adaptive large neighbourhood search heuristic for pickup and delivery with time windows," *Transportation Science*, vol. 40, no. 4, pp. 455–472, 2006.
- [87] C. Prins, C. Prodhon, and R. W. Calvo, "Solving the capacitated location-routing problem by a GRASP complemented by a learning process and a path relinking," *4OR*, vol. 4, no. 3, pp. 221–238, 2006.
- [88] S. Lin and B. W. Kernighan, "An effective heuristic algorithm for the traveling-salesman problem," *Operations Research*, vol. 21, no. 2, pp. 498–516, 1973.
- [89] S. Lin, "Computer solutions of the traveling salesman problem," *Bell System Technical Journal*, vol. 44, no. 10, pp. 2245–2269, 1965.
- [90] M. W. P. Savelsbergh, "The vehicle routing problem with time windows: minimizing route duration," *ORSA Journal on Computing*, vol. 4, no. 2, pp. 146–154, 1992.
- [91] I. H. Osman, "Metastrategy simulated annealing and tabu search algorithms for the vehicle routing problem," *Annals of Operations Research*, vol. 41, no. 4, 1993.
- [92] E. Angelelli and R. Mansini, "The vehicle routing problem with time windows and simultaneous pick-up and delivery," in *Quantitative Approaches to Distribution Logistics and Supply Chain Management*, A. Klose, M. G. Speranza, and L. N. Van-Wassenhove, Eds., Springer, Berlin, Heidelberg, Germany, pp. 249–267, 2002.

- [93] E. K. Burke, G. Kendall, and E. Soubeiga, "A tabu-search hyperheuristic for timetabling and rostering," *Journal of Heuristics*, vol. 9, no. 6, pp. 451–470, 2003.
- [94] D. Thierens, "An adaptive pursuit strategy for allocating operator probabilities," in *Proceedings of the Genetic & Evolutionary Computation Conference*, pp. 1539–1546, Washington, DC, USA, June 2005.
- [95] S. Adriaensen, T. Brys, and A. Nowe, "Fair-share ILS: a simple state-of-the-art iterated local search hyperheuristic," in *Proceedings of the 16th Genetic & Evolutionary Computation Conference*, pp. 1303–1310, Vancouver, BC, Canada, July 2014.

Research Article

A Methodology for Classifying Search Operators as Intensification or Diversification Heuristics

Jorge A. Soria-Alcaraz ¹, Gabriela Ochoa,² Andres Espinal ¹,
Marco A. Sotelo-Figueroa ¹, Manuel Ornelas-Rodriguez,³
and Horacio Rostro-Gonzalez ⁴

¹Department of Organizational Studies, University of Guanajuato, Guanajuato, Mexico

²University of Stirling, Stirling, UK

³Tecnológico Nacional De México, Instituto Tecnológico de León, Guanajuato, Mexico

⁴Department of Electronics Engineering, University de Guanajuato, Guanajuato 36885, Mexico

Correspondence should be addressed to Jorge A. Soria-Alcaraz; jorge.soria@ugto.mx

Received 11 June 2019; Revised 18 October 2019; Accepted 13 December 2019; Published 13 February 2020

Guest Editor: Francisco G. Montoya

Copyright © 2020 Jorge A. Soria-Alcaraz et al. This is an open access article distributed under the Creative Commons Attribution License, which permits unrestricted use, distribution, and reproduction in any medium, provided the original work is properly cited.

Selection hyper-heuristics are generic search tools that dynamically choose, from a given pool, the most promising operator (low-level heuristic) to apply at each iteration of the search process. The performance of these methods depends on the quality of the heuristic pool. Two types of heuristics can be part of the pool: diversification heuristics, which help to escape from local optima, and intensification heuristics, which effectively exploit promising regions in the vicinity of good solutions. An effective search strategy needs a balance between these two strategies. However, it is not straightforward to categorize an operator as intensification or diversification heuristic on complex domains. Therefore, we propose an automated methodology to do this classification. This brings methodological rigor to the configuration of an iterated local search hyper-heuristic featuring diversification and intensification stages. The methodology considers the empirical ranking of the heuristics based on an estimation of their capacity to either diversify or intensify the search. We incorporate the proposed approach into a state-of-the-art hyper-heuristic solving two domains: course timetabling and vehicle routing. Our results indicate improved performance, including new best-known solutions for the course timetabling problem.

1. Introduction

Hyper-heuristics are powerful tools for solving complex optimization problems [1–3]. The goal is to reduce the role of the human expert by means of more generally applicable search methodologies. Selection hyper-heuristics are high-level strategies that autonomously choose at run time the best-suited heuristic to apply at each step of the search process. A pool of heuristics to select from should be provided. There are, however, no clear guidelines in the literature about how to construct a potentially successful pool of heuristics [4]. It is well known that successful heuristic search methods should have a dynamic balance between *diversification* and *intensification* [5, 6]. Diversification refers to exploring new promising areas

of the search space, whereas intensification refers to focusing the search by exploiting the area nearby current good solutions. Move operators can thus be either predominantly diversifying or intensifying. However, for complex domains and solution representations, it is not straightforward to categorize a given operator as belonging to one of these two categories.

We consider an iterated local search hyper-heuristic for testing our proposed methodology. Iterated local search (Section 3.3) is a simple yet powerful search strategy [7]; it works by iteratively alternating between a diversification stage and an intensification stage. This algorithmic template makes it clear where to implement move operators of each category. Several variants of iterated local search hyper-heuristics have been proposed with good results [8, 9]. Soria-Alcaraz et al. [10]

proposed a methodology for determining the best subset of heuristics from a given pool, but they considered that all operators were intensification heuristics and the diversification stage contained a single fixed heuristic.

This article proposes an empirical methodology to classify a given operator as an intensification or diversification heuristic. The aim is to produce an effective operator pool in an iterated local search hyper-heuristic framework. The idea is to automatically divide the given complete set of operators into two groups: diversification and intensification. Then, these groups will be assigned to the respective stages of the hyper-heuristic framework. To the best of our knowledge, this is the first time such task is addressed in the literature. Our proposal is to have a preprocessing step where for a given problem domain, each heuristic in the pool is tested by means of a simple and fast probing technique, namely, a random walk with the given move operator. Based on this probing tool and statistical techniques, a set of measurements are collected indicating the effectiveness of each operator to either diversify or intensify the search.

The proposed methodology is tested within a state-of-the-art iterated local search hyper-heuristic [10] on two problem domains with different representations, namely, course timetabling and vehicle routing. Our results indicate improved performance, including new best-known solutions for the course timetabling problem.

The next section introduces relevant concepts and algorithms. The proposed methodology is described in Section 3, detailing the distance metrics, ranking criteria, and high-level search method used. Sections 4 and 5 report the empirical setup, results and analysis for two selected case studies, course timetabling, and vehicle routing, respectively. Finally, Section 6 summarizes our findings and gives suggestions for future work.

2. Background

2.1. Low-Level Heuristics. Heuristics are simple problem-solving techniques or “rules-of-thumb” that aim to produce good enough solutions in a reasonable time. This study considers perturbative heuristics also called move operators. Within a hyper-heuristic framework, these perturbative heuristics are called *low-level*, as they operate directly on the candidate solutions of the underlying optimization problem, leaving the higher-level decisions, such as which heuristic to apply next, to another mechanism. In this context, the low-level heuristics are below a *domain barrier* allowing a higher-level strategy to operate on a wide range of problems. Low-level heuristics are thus simpler procedures that perform changes in the incumbent solution and inform a higher-level mechanism about their performance. Within a hyper-heuristic framework, not all move operators have the same role, some operators are aimed at intensifying the search around the incumbent solution, while others at exploring new regions of the search space with potential better solutions.

2.2. Fitness Landscape Probing. Fitness landscapes constitute a widely used metaphor to describe the dynamics of search and optimization algorithms. Formally, a fitness landscape

[11] is a triplet (S, N, f) , where S is a set of potential solutions, i.e., a search space, $N: S \rightarrow 2^S$, a neighborhood structure, is a function that assigns to every $s \in S$ a set of neighbors $N(s)$, and $f: S \rightarrow R$ is a fitness function that can be pictured as the *height* of the corresponding solutions. When several move operators are considered (as is the case of hyper-heuristics), each of them will induce a different fitness landscape. A common technique to gather fitness landscape’s data is to conduct *random walks*. Formally, a random walk is a sequence of solutions (x_1, x_2, \dots, x_m) where $x_{i+1} \in N(x_i)$ with equiprobability on $N(x_i)$.

Algorithm 1 outlines the random-walk probing technique we used to quantify the behavior of operators. The stopping condition is based on a fixed number of objective function calls. In line 3, a given low-level heuristic (move operator) is used to modify the incumbent solution, and after the stopping condition is reached, a function named *metric* is applied to compute a distance metric between the initial solution and the final solution. The random-walk algorithm (Algorithm 1) is used to estimate the extent to which an operator changes the state of a solution. Several distance metrics (described in Section 3.1) are computed between the initial and the final solution of the walk and aggregated across several walks. The intuition is that the larger these measurements are, the more an operator is diversifying. These metrics are used both to rank the heuristics from the less to more diversifying and to identify, by means of post hoc statistical tests, if it is possible to separate the heuristics into two sets.

2.3. Hyper-Heuristics. Hyper-heuristics, initially conceptualized as *heuristics to choose heuristics* in [1], can be seen as methodologies that reduce the need for a human expert in designing effective solution schemes and, consequently, raise the level of generality at which search methodologies can operate. A recent definition considers a hyper-heuristic as “*automated methodologies for selecting or generating heuristics to solve computational search problems*” [3]. Two types of hyper-heuristics have been studied in the literature:

- (i) Heuristic selection: methodologies for choosing or selecting existing heuristics
- (ii) Heuristic generation: methodologies for generating new heuristics from given components

This study focuses on the first type, i.e., selection hyper-heuristics. Figure 1 illustrates the traditional framework for selective hyper-heuristics, with the *domain barrier* insulating the high-level search strategy from the underlying problem domain. The framework requires a pool of low-level heuristics from which the high-level strategy selects and applies to the incumbent solution. It is worth mentioning, however, that low-level heuristics usually encapsulate domain-specific information.

When a hyper-heuristic uses feedback from the search process to rank the performance of the pool of heuristics, it can be considered as a learning algorithm. According to the source of the feedback during learning, we can distinguish between *online* and *offline* learning hyper-heuristics [2].

Require: *metric*: $Solution \times Solution \rightarrow \mathbb{R}$, *InitialSolution*: a given solution to work with, h_i : Heuristic or operator.

- (1) $s \leftarrow InitialSolution$
- (2) **while** !*StopCriteria*() **do**
- (3) $s \leftarrow apply(h_i, s)$
- (4) **end while**
- (5) **return** *metric*(*initialSolution*, s)

ALGORITHM 1: Random-walk algorithm.

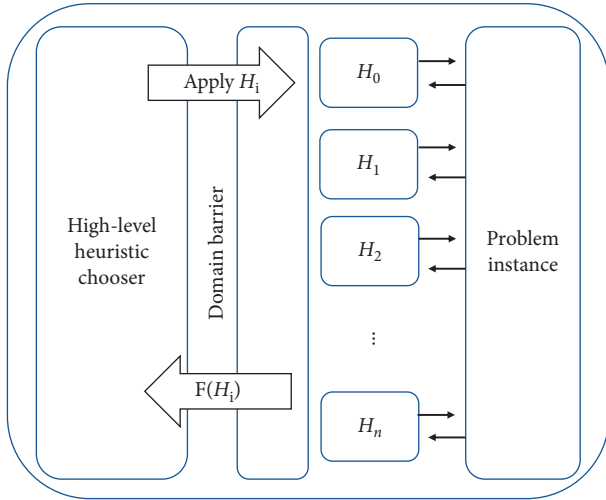


FIGURE 1: General framework of a selection hyper-heuristic based on [1].

Online learning or adaptation takes place on-the-fly when the algorithm is solving a problem instance, while offline learning requires a training process a priori of the execution of the hyper-heuristic. In this work, we use online learning through *adaptive operator selection*.

3. Methodology

Once a pool of low-level heuristics is selected for the problem domain under consideration, our approach studies the behavior of each heuristic separately. This is done by conducting several runs of the random-walk algorithm (Algorithm 1) with each operator from a fixed set of initial solutions generated uniformly at random. These runs produce a set of measurements that are used to rank operators from the less perturbative to most perturbative. The operators producing low distance measurements will be ranked top, while those producing high distance measurement will be ranked at the bottom. The top-ranked operators are categorized as intensification operators as they are the less perturbative.

Section 3.1 describes the distance metrics used to measure the behavior of heuristics. We considered two genotype-based metrics and one fitness-based metric. The genotype-based metrics measure the solution differences in representation space, while the fitness-based metric measures the solution difference in fitness value.

Once the measurements are taken, the operators are ranked using nonparametric ranking techniques. We use

three ranking statistical methods: Friedman, aligned Friedman, and Quade, detailed in Section 3.2, following the guidelines in [12]. Thereafter, we apply post hoc procedures in order to check for statistical significant differences between pairs of operator rankings. We identify those heuristics that do not show a statistical difference in their ranking. Thereafter, we separate heuristics into two groups: intensification heuristics and diversification heuristics. Finally, we execute the high-level iterated local search hyper-heuristic using the two groups of heuristics identified.

The sections below describe in more detail the components and steps of our proposed methodology.

3.1. Distance Metrics. We consider three distance metrics; the first two operate at the solution (genotype) level, while the last metric simply calculates the fitness (objective function) difference.

Hamming distance: it measures the number of substitutions required to change one string into the other [13]. Formally, it is a metric on \mathfrak{R}^n on two strings x_1, x_2, \dots, x_n and y_1, y_2, \dots, y_n of length n over a q -ary alphabet $0, 1, \dots, q-1$ described in the following equation:

$$|\{i: 1 \leq i \leq n, x_i \neq y_i\}|. \quad (1)$$

Lee distance: given two strings x_1, x_2, \dots, x_n and y_1, y_2, \dots, y_n of length n over a q -ary alphabet $0, 1, \dots, q-1$ of size $q \geq 2$ [14, 15]; this distance is defined as

$$\sum_{i=1}^n \min(|x_i - y_i|, q - |x_i - y_i|). \quad (2)$$

Fitness distance: it measures the difference in the fitness value between two given solutions using the absolute value operator. In our study, this metric evaluates how much the fitness of an initial solution is affected by a given heuristic. Equation (3) defines this metric. Given two strings $x = (x_1, x_2, \dots, x_n)$ and $y = (y_1, y_2, \dots, y_n)$ of length n over a q -ary alphabet $0, 1, \dots, q-1$,

$$|\text{Fit}(x) - \text{Fit}(y)|, \quad (3)$$

where $\text{Fit: String} \rightarrow \mathfrak{R}$. This function is domain-dependent and corresponds to a quality measurement of solutions, the objective of the optimization process.

We selected the two distance metrics at the solution level as they are well known in the study of meta-heuristics and offer a simple yet descriptive approach to measure the variation induced by the different operators. The Hamming distance measures the number of raw differences between two given solutions. For example, let us consider two integer-based strings, “5623” and “5827”; the Hamming distance between these strings is 2 since they differ in two locations. The Lee distance is more sophisticated since it reports not only how many differences are there between two given strings but also how large these differences are. Consider the same two strings, “5623” and “5827”; the Lee distance between them is 6 because $|6 - 8| + |3 - 7| = 2 + 4 = 6$. For binary strings, the Hamming and Lee distances produce the same values. In our study, solutions are represented as integer-based strings. The third metric gauges the solution differences in terms of quality or fitness, this is complementary to two genotype-based metrics.

The stopping condition in this phase is fixed to 200 function calls. On each test instance, the random-walk algorithm is run 500 times from different initial randomly generated solutions. This produces 500 distance values for each metric, and the average distance values are calculated. Finally, these average values are used to rank the heuristics from less to more perturbative in the next phase.

3.2. Ranking Heuristics with Nonparametric Statistics.

Once the distance metrics are gathered, we apply statistical tests in order to rank the heuristics. Parametric tests are sometimes used when contrasting the performance of stochastic algorithms. However, they assume independence, normality, and homoscedasticity of the data, which are not guaranteed in the case of low-level heuristics. In such cases, nonparametric statistics overcome this limitation. We used CONTROLTEST and MULTITEST [12] which are specially designed for nonparametric comparison among heuristic algorithms and considered the three tests proposed: Friedman, aligned Friedman, and Quade. The Friedman test uses mainly arithmetic mean, alignment Friedman uses a value of location computed as the average performance achieved by all heuristics in each problem, and Quade considers that some instances might be more difficult than others. All these tests consider ranks; therefore, the lower distance value will produce a higher rank. In our context, this means that heuristics with less perturbative behavior (i.e., intensification heuristics) will be ranking top.

We applied post hoc tests in order to determine if two operators are similar in terms of their perturbative behavior. A p value under 0.05 (0.95 confidence level) rejects this null hypothesis, indicating that the given pair of operators are significantly different in their perturbative behavior. Therefore, those operators are not grouped together. Operator pairs for which the p value is greater than 0.05 are classified in the same group. We applied the Holm procedure to adjust the p values. In our experiments, only two

well-defined groups were detected by the post hoc tests. We defined the group including the top-ranking heuristics as the intensification group and the other group as the diversification group.

3.3. Iterated Local Search Hyper-Heuristic. In order to test the performance of the previously defined intensification and diversification groups of heuristics, we follow the experimental setup in [10] with some adjustments detailed in this section. We also provide a description of the high-level strategy and adaptive operator selection mechanism used. The pool of heuristics is problem specific, and they will be described in the respective case study section.

3.3.1. High-Level Strategy. We utilize iterated local search (ILS) as the high-level strategy [8, 10, 16]. Iterated local search is a simple yet effective strategy, which works by iteratively alternating between an exploration move (diversification) and an exploitation move (intensification) from the perturbed solution [7]. With this search strategy, it is straightforward to identify where to apply the intensification and diversification heuristics groups.

Our implementation is outlined in Algorithm 2. Two independent adaptive operator selection steps are used: one in the local search phase (lines 2 and 5) using the intensification group of heuristics and another in the perturbation phase (line 4) using the diversification group. This implementation differs from our previous ILS hyper-heuristic [9, 10] in which adaptive operator selection is used on the two algorithm stages instead of only on the intensification stage. Line 6 must be set for maximization ($>$) or minimization ($<$) problems.

3.3.2. Adaptive Operator Selection. Adaptive operator selection [17, 18] allows high-level algorithms to autonomously select the next heuristic to apply to the incumbent solution. Two cooperating mechanisms are required: *selection rule*, which defines how to select the next operator or low-level heuristic from the pool according to their estimated qualities, and *credit assignment*, which defines how to estimate the operators’ quality based on the impact brought by their recent application. The mechanisms we implemented are described in detail:

Selection rule: we use dynamic multiarmed bandits (DMAB) [19] as the selection rule, where each operator is viewed as an arm. Let $l_{i,t}$ denote the number of times the i^{th} arm (heuristic) has been played and $\hat{r}_{i,t}$ the average reward it has received up to time t . At each time step t , from K alternative arms (heuristics), the algorithm selects the arm maximizing the quantity computed by the following expression:

$$\hat{r}_{j,t} + C \sqrt{\frac{2 * \log_{10}(\sum_{i=1}^K l_{i,t})}{l_{j,t}}}. \quad (4)$$

```

(1)  $s_0 = \text{GenerateInitialSolution}$ 
(2)  $s^* = \text{LocalSearch}(s_0)$ 
(3) while ! $\text{StopCriteria}()$  do
(4)    $s' = \text{perturbation}(s^*)$ 
(5)    $s^{*'} = \text{LocalSearch}(s')$ 
(6)   if  $f(s^{*'})$  better than  $f(s^*)$  then
(7)      $s^* = s^{*'}$ 
(8)   end if
(9) end while
(10) return  $s^*$ 

```

ALGORITHM 2: High-level strategy: iterated local search.

Factor C is used to balance the inner exploration and exploitation phases. The *DMAB* algorithm uses a *Page-Hinkley* statistical test, where two parameters are introduced: γ_{ph} , which controls the trade-off between false alarms and unnoticed changes, and δ , which enforces the robustness when dealing with slowly varying environments. Parameters C and γ_{ph} need to be tuned for every problem. We found in preliminary experiments that the values $C=10$ and $\gamma_{ph}=100$ obtain encouraging results consistently. For the parameter δ , we used the value suggested in [18] ($\delta=0.15$) for all our experiments.

Credit assignment: we use *extreme value* criteria for determining the operator's credit [17, 18]. When a heuristic op is selected and applied to the current solution by the selection rule, it is necessary to calculate an update in the reward value with the most recent behavior information of the last applied heuristic. Rewards are updated as follows depending on the ILS phase (diversification and intensification). For the *intensification phase*, the fitness of the new solution is computed and the change in fitness Δ_f is added to a FIFO list of size W . For the *diversification phase*, the Hamming distance between the new solution and the initial one is calculated and added to a FIFO list of size W . A separate list is kept for each operator for both phases. FIFO data structure is used to guarantee that only the latest observations in fitness improvement or Hamming distance are considered in operator selection computations for the last W iterations before being erased of credit assignment memory. We kept a list for each operator in order to identify which operator has achieved the best performance in the last W iterations.

Thereafter, the specific operator reward is updated to the maximal value in the list. Formally, let t be the current step and $\text{metric}(t)$ be the metric value (Δ_f or Hamming) estimated at time t for a given heuristic op and the expected reward \hat{r}_t for heuristic op is computed using the following equation:

$$\hat{r}_t = \text{argmax}[\text{metric}(t_i), i = 1, \dots, W]. \quad (5)$$

4. Course Timetabling Case Study

We first apply the proposed methodology to the course timetabling problem. This problem requires the assignment

of a fixed number of subjects into a number of time slots. The objective is to obtain a timetable minimizing the number of conflicts. Our formulation uses a generic modeling approach where solutions are represented as vectors of integer numbers of length equal to the number of events (courses) [9]. As test instances, we use the 24 instances from the *International timetabling competition (ITC) 2007 track 2* (postenrollment course timetabling) [20]. Many meta-heuristic [21, 22] and hyper-heuristic [9, 10] approaches have been proposed for solving variants of educational timetabling. Recent surveys have also been published [4, 23]. Here, we improve the performance of hyper-heuristics by incorporating our automated approach for categorizing low-level heuristics into intensification and diversification groups.

4.1. Low-Level Heuristics. Our implementation considers the following set of five low-level heuristics [10]. They range from a simple randomized exchange or swap neighborhoods to greedy and more informed procedures:

MLC (move to less conflict): it locates the variable producing the most conflicts and changes its value to that causing the minimum possible conflict

BSP (best single perturbation): it chooses a variable following a sequential order and changes its value to that producing the minimum conflict

WMLC (worst move to less conflict): it locates the variable and value that once modified cause the less conflict

MLS (move to less size): it changes the value of a given variable to that causing the event to move to the less occupied time slot

Two points: it selects uniformly at random two indexes in the integer string representation and modifies all variables between the indexes randomly

4.2. Ranking and Grouping of the Low-Level Heuristics. Table 1 shows the nonparametric ranking of the heuristics according to the genotypic and fitness distance metrics. The ranking indicates that closeness in genotypic space correlates with closeness in fitness space, a desirable property for heuristic search methods. Table 2 shows the adjusted p values of each pair of heuristics. The null hypothesis in this test establishes that between two heuristics (row and column), there is no significant difference in terms of perturbative behavior. A p value less than 0.05 (0.95 confidence level) means the null hypothesis is rejected. According to this criterion groups, {WMLC, MLC, BSP} and {MLS, TwoPoints} have a statistical difference. The top-ranking three heuristics {WMLC, MLC, BSP} are assigned to the intensification group, while the bottom two heuristics {MLS, TwoPoints} to the diversification group.

4.3. Hyper-Heuristic Performance Comparison. The selected groups of heuristics are then deployed within the iterated local search hyper-heuristic framework described in Section

TABLE 1: Ranking of the course timetabling heuristics.

Heuristic	Friedman	Aligned Friedman	Quade
Hamming distance			
WMLC	3.18	14.76	1.77
MLC	1.83	12.34	2.30
BSP	2.14	25.76	2.77
MLS	5.9	42.43	3.60
TwoPoints	7.95	51.9	4.2
Lee distance			
WMLC	2.15	11.38	1.47
BSP	1.25	12.724	2.17
MLC	3.37	28.12	2.47
MLS	6.31	47.21	3.12
TwoPoints	7.47	41.6	4.45
Fitness distance			
WMLC	1.56	11.76	1.12
MLC	2.95	15.33	1.77
BSP	3.66	27.92	2.14
MLS	6.72	36.42	2.77
TwoPoints	8.24	46.9	4.10

TABLE 2: Adjusted P values for every pair of heuristics in course timetabling domain.

	TwoPoints	MLS	BSP	MLC
Hamming distance				
WMLC	0.005	0.007	0.052	0.055
MLC	0.005	0.008	0.05	—
BSP	0.006	0.01	—	—
MLS	0.051	—	—	—
Lee distance				
WMLC	0.003	0.032	0.046	0.051
MLC	0.002	0.041	0.003	—
BSP	0.016	0.014	—	—
MLS	0.051	—	—	—
Fitness distance				
WMLC	0.001	0.017	0.048	0.045
MLC	0.002	0.035	0.05	—
BSP	0.003	0.035	—	—
MLS	0.051	—	—	—

3.3. Following the *ITC-2007* competition rules, each hyper-heuristic variant is run 10 times and the stopping condition corresponds to a time limit of about 10 minutes following the benchmark algorithm provided in the competition website (<http://www.cs.qub.ac.uk/itc2007/>). We compare our approach against the following methods:

Cambazard: the winner of the *ICT-2007* competition [24], a multistage local search algorithm considering several neighborhoods

Ceschia: a single-step meta-heuristic approach based on simulated annealing, with a neighborhood composed of moves that reschedule one event or swap two events [21]

AdapExAP: an adaptive iterated local search hyper-heuristics coupled with an adaptive mechanism based on the *adaptive pursuit* selection rule [9]

Goh: Iterative two-stage algorithm that uses tabu search and simulated annealing [25]

Nagata: a local search-based algorithm with a mechanism for adapting the size of search neighborhood [26]

HHADL: an iterated local search hyper-heuristic with Add-Delete list, which generates heuristics based on a fixed number of add and delete operations [27]

HHDMAb: an iterated local search with dynamic multiarm bandits, which selects from a pool of heuristics using an autonomous strategy [10]

The main difference between our proposal and other recent methodologies is the application of a categorization process to a predefined set of low-level heuristics. This categorization, detailed in Section 3, leads us to empirical construction of a reasonable good group of heuristics to use as intensification and diversification operators in a selection hyper-heuristic approach. Our selection hyper-heuristic has an empirically effective group of operators determined a priori of any exhaustive experimentation; this characteristic enhances the performance of our approach against other methodologies whose setting was made by the mere human expertise.

Table 3 shows comparative results of our proposed approach HH2DMAb against state-of-the-art solvers. The evaluation of the best-found solutions is shown, with the average and standard deviation results reported in brackets in the form (\bar{s}_σ) , when available. The best solutions are given in bold font.

Configurations designed by human experts are represented by the other entries in Table 3. Our approach offers an automated operator grouping and selection of the heuristics with no expert knowledge required. Results for instances 3 and 23 are new best-known solutions found by our approach. Consistently, our iterated local search hyper-heuristic with automatic selection of heuristic groups, HH2DMAb, presents lower average and standard deviation values than previous approaches. We argue that this improved performance is because of having additional heuristics at the diversification stage, which gives the algorithm more alternatives to escape from local optima. Figures 2 and 3 show the dynamic of selection probabilities for the intensification group (a) and diversification group (b) of heuristics during a HH2DMAb run on a selected instance (instance 2).

Figures 2 and 3 shows in X-axis the iterations of each run (1000x) and Y-axis shows the probability of selection of each heuristic (color line); the sum of selection probabilities for all heuristics is 1 at each iteration. In the intensification group, Figure 2, the heuristics WMLC and MLC are most frequently selected across the run than the third BSP heuristic and WMLC and MLC take dominance at different stages of the run. The diversification group dynamic, Figure 3, shows that the two heuristics are useful during the search, with heuristic MLS having prominence.

5. Vehicle Routing Case Study

In order to illustrate the generality of the proposed methodology, we considered a second case study, the vehicle

TABLE 3: Course timetabling problem. Comparison of our proposed approach HH2DMAB against state-of-the-art solvers. The evaluation of the best-found solutions are shown, with the average and standard deviation results reported in brackets in the form (\bar{s}_σ) , when available. The best solutions are given in bold font.

Instance	Cambazard	Ceschia	AdapExAP	HHADL	HHDMAAB	Goh	Nagata	HH2DMAB
1	571	59	650 (780.45 _{148.5})	630	630 (860.12 _{110.7})	307.6	81.7	630 (850.06 _{98.45})
2	993	0	470 (960.7 _{270.4})	450	380 (530.15 _{130.6})	63.4	48.0	365 (505.74 _{98.64})
3	164	148	290 (337 _{88.7})	300	137 (315.12 _{57.15})	199.4	155	135 (304.10 _{51.27})
4	310	25	600 (815 _{42.6})	602	475 (559.12 _{38.62})	328.8	254	452 (480.61 _{37.11})
5	5	0	35 (39.16 _{9.3})	6	0 (0 ₀)	2.7	0	0 (0 ₀)
6	0	0	20 (29.4 _{7.3})	0	0 (4.6 _{1.4})	33.2	0	0 (0 ₀)
7	6	0	30 (33.74 _{2.1})	0	0 (5.2 _{1.1})	18.0	3.6	0 (0 ₀)
8	0	0	0(0 ₀)	0	0 (0 ₀)	0.0	0.0	0 (0 ₀)
9	1560	0	630 (861.1 _{127.4})	640	602 (854.3 ₁₅₈)	100.7	58.9	595 (630.26 _{75.2})
10	2163	3	2349 (2458.2 _{185.2})	663	482 (615.12 _{72.14})	65.3	6.4	469 (630.57 _{70.46})
11	178	142	350 (405.7 _{57.3})	344	159 (355.12 _{49.12})	244.3	140.4	159 (303.82 _{34.55})
12	146	267	480 (506.4 _{27.4})	198	140 (278.43 _{25.9})	318.2	33	135 (230.63 _{22.46})
13	0	1	46 (77.37 _{49.2})	0	0 (15.2 _{12.7})	99.5	0	0 (3.27 _{1.2})
14	1	0	80 (108.3 _{33.5})	35	20 (25.12 _{17.4})	0.2	0	16 (23.58 _{12.55})
15	0	0	0 (5.75 _{9.4})	0	12 (44.16 _{16.0})	192.0	0	0 (2.04 _{1.2})
16	2	0	0 (2.22 _{4.1})	140	0 (73.76 _{33.4})	105.8	1.5	0 (50.14 _{18.66})
17	0	0	0(0 ₀)	0	0 (3 _{1.5})	0.8	0	0 (0 ₀)
18	0	0	20 (25.16 ₆)	0	0 (5.3 _{2.1})	12.5	0	0 (0 ₀)
19	1824	0	360 (404.51 _{39.1})	400	133 (214.6 _{33.6})	516.7	0	104 (188.2 _{25.44})
20	445	543	150 (177.12 _{37.1})	150	106 (311.07 _{31.5})	650.7	438	106 (230.11 _{15.41})
21	0	5	0 (3.78 _{5.7})	0	0 (2.5 _{2.3})	12.5	0	0 (1.87 _{1.11})
22	29	5	33 (45.71 _{12.7})	32	25 (54 _{18.5})	136.0	0	21 (37.22 _{9.55})
23	238	1292	1007 (1378.45 _{319.4})	238	267.4 (515.23 _{89.4})	504.4	777	233 (404.57 _{85.66})
24	21	0	0 (45.88 _{60.0})	640	76 (337.34 _{51.9})	192.6	0	77 (199.62 _{40.11})

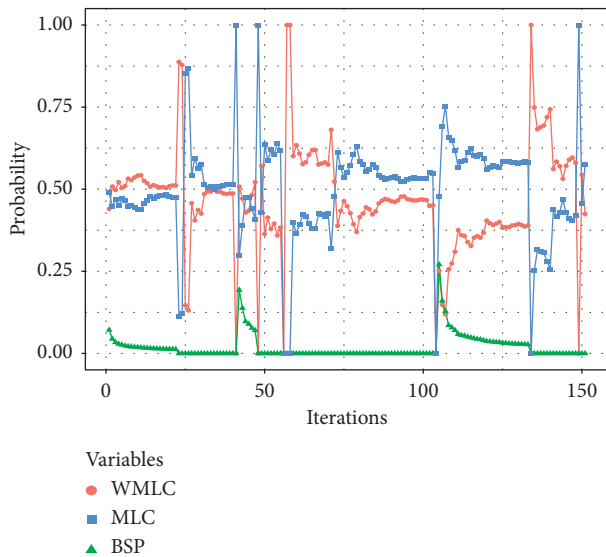


FIGURE 2: Intensification heuristics.

routing problem with time windows (VRPTW). In this problem, a set of customer demands must be addressed using as a few vehicles as possible. The time window constraint indicates that customer demands can only be served in a time window. The formulation and experimental setting follows the rules of the *Cross-Domain Heuristic Search Competition (CHeSC) 2011* [28]. CHeSC instances were taken from [29] and include 5 from the Solomon data set and 5 from the Gehring and Homberger data set.

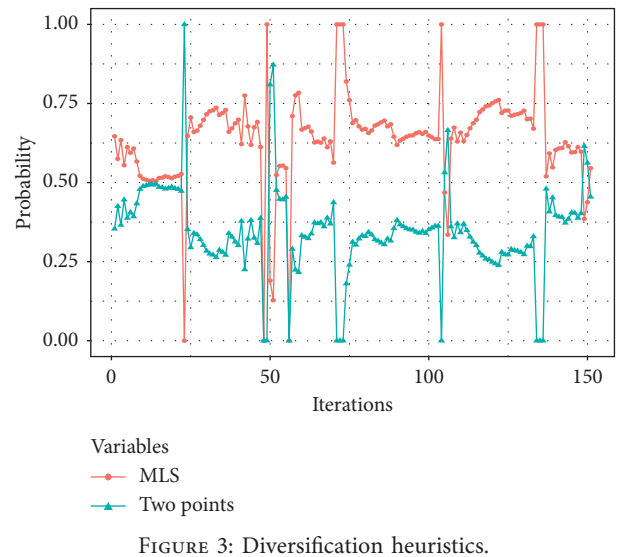


FIGURE 3: Diversification heuristics.

5.1. *Low-Level Heuristics.* Our implementation uses the following four heuristics:

TimeRR: it removes a number of locations based on time window proximity, reinserting into the best route possible

TwoOptStar: it takes the end sections of two routes and swaps them to create two new routes

locRR: it removes a number of locations based on location proximity, reinserting into the best route possible

ShiftMutate: it moves a single location from one route to another

5.2. Ranking and Grouping of the Low-Level Heuristics.

The experimental design resembles that of the previous case study. Each sampling procedure is executed 500 times, using 200 function calls for every instance-heuristic pair. The time expended in this phase was about 37 minutes using an i7 Intel Core, 8 Gb in Ram, Linux Operating System and JAVA Language. Table 4 shows the collected metric rankings.

As Table 4 indicates, heuristics locRR and TimeRR are the top two according to all metrics. This suggests they are more suitable as intensification heuristics. Heuristics TwoOpt* and Shift are the bottom two in the rank for all metrics. Table 5 shows the post hoc tests for heuristic pairs as the null hypothesis establishes that between two heuristics (row and column), there is no significant difference in terms of perturbative behavior. A p value less than 0.05 means the null hypothesis is rejected. According to this evidence, the groups {locRR, TimeRR} (intensification) and {TwoOpt*, Shift} (diversification) are defined.

5.3. Hyper-Heuristic Performance Comparison. The selected groups of heuristics are deployed within the iterated local search hyper-heuristic framework. In order to compare its performance, we consider the contestants in the *Cross-Domain Heuristic Search Competition (CHeSC) 2011* (<http://www.asap.cs.nott.ac.uk/external/chesc2011/results.html>). Following the competition rules, 31 runs are conducted, each lasting 600 CPU seconds according to the benchmark tool provided by the competition webpage. The algorithms are ranked according to their median performance and receive points according to a system inspired by formula (1) in [28]. The top eight performing algorithms receive 10, 8, 6, 5, 4, 3, 2, and 1 point, respectively. In case of ties, the points of the concerned positions are summed and equally shared.

According to this scoring system, our method HH2DMAB achieves 28 points (Table 6), which represents a tie in the 2nd position when compared against CHeSC contestants [30]. Moreover, HH2DMAB achieves better performance when compared with or previous state-of-the-art HHDMA B [10] hyper-heuristic, which obtained the 3rd position. Again, the evidence suggests that our current approach with more heuristics at the diversification stage allows the hyper-heuristic to achieve better results.

Our selection hyper-heuristic was enhanced by the application of *a priori* phase were the diversification and intensification operators were selected using the methodology detailed in Section 3. This allowed our approach to work with an empirically good-selected group of operators. Table 7 contrasts the best results obtained by HH2DMAB against the previous HHDMA B hyper-heuristic [10] and the best-known results for each instance. Consistently, HH2DMAB outperforms the previous HHDMA B and produces results that are close to the best-known solutions. This is a good result since the best-known solutions are achieved by problem-specific algorithms. Our approach, instead, is a more general methodology that usually requires only changing the set of low-level heuristics to address other problem domains. This

TABLE 4: Ranking of the vehicle routing heuristics.

Heuristic	Friedman	Aligned Friedman	Quade
Hamming distance			
locRR	2.33	13.12	2.10
TimeRR	1.62	16.24	2.40
TwoOpt*	2.74	22.14	3.66
Shift	3.14	29.89	4.50
Lee distance			
locRR	2.37	12.33	1.91
TimeRR	1.61	15.44	2.10
TwoOpt*	3.02	11.16	2.60
Shift	5.01	27.94	3.47
Fitness distance			
TimeRR	1.36	13.19	1.01
locRR	2.65	11.95	2.37
Shift	2.42	20.42	3.15
TwoOpt*	5.22	27.14	4.18

TABLE 5: Adjusted P values for every pair of heuristics in vehicle routing domain.

	Shift	TwoOpt*	TimeRR
Hamming distance			
locRR	0.0027	0.022	0.052
TimeRR	0.028	0.025	—
TwoOpt*	0.63	—	—
Lee distance			
locRR	0.017	0.020	0.061
TimeRR	0.021	0.007	—
TwoOpt*	0.077	—	—
Fitness distance			
locRR	0.031	0.016	0.057
TimeRR	0.024	0.020	—
TwoOpt*	0.075	—	—

TABLE 6: Comparison with CHeSC 2011 contestants.

Rank	Algorithm	Score
1	PHUNTER	33
2	HAEA	28
2	HH2DMAB	28
3	HHDMA B	25
4	KSATS-HH	23
5	ML	22
6	AdapHH	16
6	HAHA	16
8	EPH	12
9	AVEG-Nep	10
10	GISS	6
10	GenHive	6
10	VNS-TW	6
13	ISEA	5
13	XCJ	5
15	SA-ILS	5
16	ACO-HH	2
17	DynILS	1
18	NA-SLS	0
18	SelfSearch	0
18	Ant-Q	0
18	MCHH-S	0

TABLE 7: Comparison with best-known solutions as reported in SINTEF website.

Instance	HHDMAB		HH2DMAB		Best known	
RC207	4	1094.14	3	1075.67	3	1061.14
R101	19	1655.98	19	1650.95	19	1650.80
RC103	12	1395.01	11	1305.48	11	1261.67
R201	4	1275.30	4	1255.46	4	1252.37
R106	13	1296.86	12	1467.28	11	1424.73
C1-10-1	107	43956.7	102	426843.4	100	424478.9
RC2-10-1	22	31163.6	21	30291.5	20	30278.5
R1-10-1	101	55345.7	100	54075.4	100	53501.3
C1-10-8	113	49366.4	103	46133.9	92	44092.7
RC1-10-5	98	49154.5	94	46327.2	90	45564.8

evidence suggests that our algorithm setting was more efficient, producing competitive results against other methodologies configured only by human expertise.

6. Conclusions

We have proposed an empirical methodology to classify a set of operators into intensification and diversification heuristics, to be used within hyper-heuristic methods. Starting from a suitable set of low-level heuristics or search operators for a given domain, the proposed methodology probes their performance using fitness landscape and distance metrics and ranks the heuristics through non-parametric statistics instead of human expertise. This contributes to increasing the methodological rigor and automation for deploying hyper-heuristic approaches. Our methodology was tested within a state-of-the-art hyper-heuristic framework over two complex combinatorial optimization problems, namely, course timetabling and vehicle routing problem with time windows achieving new best-known solutions for ITC 2007 track 2 course timetabling instances and better results against previous studies in the case of CHESC vehicle routing instances. Our results indicate improved hyper-heuristic performance on both domains when our methodology is used to empirically identify a group of intensification and diversification operators. This suggests that well-designed hyper-heuristic methods are not only more general but can also be more effective than problem-specific meta-heuristics. In the future, we will investigate additional ranking methods and methodologies to automatically tune hyper-heuristic parameters. Finally, it is necessary to test this approach to other problem domains and heuristic pools.

Data Availability

The result data used to support the findings of this study are available from the corresponding author upon request.

Conflicts of Interest

The authors declare that there are no conflicts of interest regarding the publication of this paper.

Acknowledgments

The authors wish to thank the Consejo Nacional de Ciencia y Tecnología (CONACyT) for the support in the project Neurociencia Computacional: de la teoría al desarrollo de sistemas neuromórficos, N. 1961 and the University of Guanajuato. Special thanks to University of Stirling.

References

- [1] P. Cowling, G. Kendall, and E. Soubeiga, *A Hyperheuristic Approach to Scheduling a Sales Summit*, Springer, Berlin, Germany, 2001.
- [2] E. K. Burke, M. Hyde, G. Kendall, G. Ochoa, E. Özcan, and J. R. Woodward, *A Classification of Hyper-Heuristic Approaches*, Springer, Boston, MA, USA, 2010.
- [3] E. K. Burke, M. Gendreau, M. Hyde et al., “Hyper-heuristics: a survey of the state of the art,” *Journal of the Operational Research Society*, vol. 64, no. 12, pp. 1695–1724, 2013.
- [4] N. Pillay, “A review of hyper-heuristics for educational timetabling,” *Annals of Operations Research*, vol. 239, no. 1, pp. 3–38, 2016.
- [5] C. Blum and A. Roli, “Metaheuristics in combinatorial optimization,” *ACM Computing Surveys*, vol. 35, no. 3, pp. 268–308, 2003.
- [6] X. S. Yang, S. Deb, and S. Fong, “Metaheuristic algorithms: optimal balance of intensification and diversification,” *Applied Mathematics & Information Sciences*, vol. 8, no. 3, pp. 977–983, 2014.
- [7] H. R. Lourenço, O. C. Martin, and T. Stützle, *Iterated Local Search*, Springer, Boston, MA, USA, 2003.
- [8] G. Ochoa, J. Walker, M. Hyde, and T. Curtois, *Adaptive Evolutionary Algorithms and Extensions to the HyFlex Hyper-Heuristic Framework*, Springer, Berlin, Germany, 2012.
- [9] J. A. Soria-Alcaraz, G. Ochoa, J. Swan, M. Carpio, H. Puga, and E. K. Burke, “Effective learning hyper-heuristics for the course timetabling problem,” *European Journal of Operational Research*, vol. 238, no. 1, pp. 77–86, 2014.
- [10] J. A. Soria-Alcaraz, G. Ochoa, M. A. Sotelo-Figeroa, and E. K. Burke, “A methodology for determining an effective subset of heuristics in selection hyper-heuristics,” *European Journal of Operational Research*, vol. 260, no. 3, pp. 972–983, 2017.
- [11] P. F. Stadler, *Fitness Landscapes*, Springer, Berlin, Germany, 2002.
- [12] J. Derrac, S. García, D. Molina, and F. Herrera, “A practical tutorial on the use of nonparametric statistical tests as a methodology for comparing evolutionary and swarm intelligence algorithms,” *Swarm and Evolutionary Computation*, vol. 1, no. 1, pp. 3–18, 2011.
- [13] R. W. Hamming, “Error detecting and error correcting codes,” *Bell System Technical Journal*, vol. 29, no. 2, pp. 147–160, 1950.
- [14] C. Lee, “Some properties of nonbinary error-correcting codes,” *IEEE Transactions on Information Theory*, vol. 4, no. 2, pp. 77–82, 1958.
- [15] M. M. Deza and E. Deza, *Encyclopedia of Distances*, Springer, Berlin, Germany, 2009.
- [16] J. A. Soria Alcaraz, G. Ochoa, M. Carpio, and H. Puga, “Evolvability metrics in adaptive operator selection,” in *Proceedings of the 2014 Annual Conference on Genetic and Evolutionary Computation (GECCO)*, pp. 1327–1334, ACM, New York, NY, USA, 2014.

- [17] Á. Fialho, L. Da Costa, M. Schoenauer, and M. Sebag, “Analyzing bandit-based adaptive operator selection mechanisms,” *Annals of Mathematics and Artificial Intelligence*, vol. 60, no. 1-2, pp. 25–64, 2010.
- [18] Á. Fialho, L. Da Costa, M. Schoenauer, and M. Sebag, “Dynamic multi-armed bandits and extreme value-based rewards for adaptive operator selection in evolutionary algorithms,” *Lecture Notes in Computer Science*, vol. 3, pp. 176–190, 2009.
- [19] L. DaCosta, A. Fialho, M. Schoenauer, and M. Sebag, “Adaptive operator selection with dynamic multi-armed bandits,” in *Proceedings of the 10th Annual Conference on Genetic and Evolutionary Computation*, pp. 913–920, ACM, New York, NY, USA, 2008.
- [20] R. Lewis, B. Paechter, and B. McCollum, *Post Enrolment Based Course Timetabling: A Description of the Problem Model Used for Track Two of the Second International Timetabling Competition*, Cardiff Business School, Cardiff, Wales, 2007.
- [21] S. Ceschia, L. Di Gaspero, and A. Schaerf, “Design, engineering, and experimental analysis of a simulated annealing approach to the post-enrolment course timetabling problem,” *Computers & Operations Research*, vol. 39, no. 7, pp. 1615–1624, 2012.
- [22] R. Lewis and J. Thompson, “Analysing the effects of solution space connectivity with an effective metaheuristic for the course timetabling problem,” *European Journal of Operational Research*, vol. 240, no. 3, pp. 637–648, 2015.
- [23] H. Babaei, J. Karimpour, and A. Hadidi, “A survey of approaches for university course timetabling problem,” *Computers & Industrial Engineering*, vol. 86, pp. 43–59, 2015.
- [24] H. Cambazard, E. Hebrard, B. O’Sullivan, and A. Papadopoulos, “Local search and constraint programming for the post enrolment-based course timetabling problem,” *Annals of Operations Research*, vol. 194, no. 1, pp. 111–135, 2012.
- [25] S. L. Goh, G. Kendall, and N. R. Sabar, “Improved local search approaches to solve the post enrolment course timetabling problem,” *European Journal of Operational Research*, vol. 261, no. 1, pp. 17–29, 2017.
- [26] Y. Nagata, “Random partial neighborhood search for the post-enrollment course timetabling problem,” *Computers & Operations Research*, vol. 90, pp. 84–96, 2018.
- [27] J. A. Soria-Alcaraz, E. Özcan, J. Swan, G. Kendall, and M. Carpio, “Iterated local search using an add and delete hyper-heuristic for university course timetabling,” *Applied Soft Computing*, vol. 40, pp. 581–593, 2016.
- [28] G. Ochoa, M. Hyde, T. Curtois et al., *HyFlex: A Benchmark Framework for Cross-Domain Heuristic Search*, Springer, Berlin, Germany, 2012.
- [29] SINTEF, *Transportation Optimization Portal—Vehicle Routing Problem with Time Windows*, SINTEF, Trondheim, Norway, 2008.
- [30] F. Mascia and T. Stützle, *A Non-adaptive Stochastic Local Search Algorithm for the CHeSC 2011 Competition*, Springer, Berlin, Germany, 2012.

Research Article

A Fault Diagnosis Method for Power Transmission Networks Based on Spiking Neural P Systems with Self-Updating Rules considering Biological Apoptosis Mechanism

Wei Liu,^{1,2} Tao Wang ,^{1,2} Tianlei Zang ,^{3,4} Zhu Huang,^{1,2} Jun Wang,^{1,2} Tao Huang ,^{1,5} Xiaoguang Wei ,⁶ and Chuan Li⁷

¹School of Electrical Engineering and Electronic Information, Xihua University, Chengdu, China

²Key Laboratory of Fluid and Power Machinery, Ministry of Education, Xihua University, Chengdu, China

³College of Electrical Engineering, Sichuan University, Chengdu, China

⁴Key Laboratory of Network Assessment Technology, Institute of Information Engineering, Chinese Academy of Sciences, Beijing, China

⁵Department of Energy, Politecnico di Torino, Turin, Italy

⁶School of Electrical Engineering, Southwest Jiaotong University, Chengdu, China

⁷Shandong Electrical Engineering & Equipment Group Co., Ltd, Shandong, China

Correspondence should be addressed to Tao Wang; wangatao2005@163.com and Tianlei Zang; zangtianlei@126.com

Received 12 July 2019; Revised 2 November 2019; Accepted 24 December 2019; Published 21 January 2020

Guest Editor: Francisco G. Montoya

Copyright © 2020 Wei Liu et al. This is an open access article distributed under the Creative Commons Attribution License, which permits unrestricted use, distribution, and reproduction in any medium, provided the original work is properly cited.

Power transmission networks play an important role in smart grids. Fast and accurate faulty-equipment identification is critical for fault diagnosis of power systems; however, it is rather difficult due to uncertain and incomplete fault alarm messages in fault events. This paper proposes a new fault diagnosis method of transmission networks in the framework of membrane computing. We first propose a class of spiking neural P systems with self-updating rules (srSNPS) considering biological apoptosis mechanism and its self-updating matrix reasoning algorithm. The srSNPS, for the first time, effectively unitizes the attribute reduction ability of rough sets and the apoptosis mechanism of biological neurons in a P system, where the apoptosis algorithm for condition neurons is devised to delete redundant information in fault messages. This simplifies the complexity of the srSNPS model and allows us to deal with the uncertainty and incompleteness of fault information in an objective way without using historical statistics and expertise. Then, the srSNPS-based fault diagnosis method is proposed. It is composed of the transmission network partition, the SNPS model establishment, the pulse value correction and computing, and the protection device behavior evaluation, where the first two components can be finished before failures to save diagnosis time. Finally, case studies based on the IEEE 14- and IEEE 118-bus systems verify the effectiveness and superiority of the proposed method.

1. Introduction

Fast and accurate fault diagnosis is very important for power system restoration after a serious blackout [1, 2]. This first requires the identification of faulty equipment [3, 4]. To identify faulty equipment, dispatchers should first analyze the fault alarm messages received from the supervisory control and data acquisition (SCADA) system according to ancillary facilities and their operational experience. Fault

events in a power system can cause lots of fault alarm messages, and parts of them may be redundant ones which are not important with respect to the fault. Besides, protection devices may also fail leading to incomplete action information. All these cases can increase the uncertainty and incompleteness of fault alarm messages, making fault diagnosis more difficult [4–7]. Therefore, improving the fault information processing ability of fault diagnosis methods is significant for faulty equipment identification.

During the past three decades, several fault diagnosis approaches have been developed, such as expert systems (ESs) [8, 9], artificial neural networks (ANNs) [10–14], Bayesian networks (BNs) [15–18], Petri nets (PNs) [19–24], cause-effect networks (CENs) [2, 25], optimization methods (OMs) [26–30], fuzzy logic (FL) [2, 4, 10, 19–21, 23], rough sets (RSs) [31–35], and spiking neural P systems (SNPSs) [4, 36–38]. However, each above approach has its limitations which are in detail analyzed in [1, 2, 4–6]. In general, main shortcomings of these methods include (1) strong reliance on a large amount of historical data, such as BNs, PNs, ANNs, and SNPSs; (2) strong dependence on expert experience, such as ESs, BNs, PNs, and SNPSs; (3) poor interpretability of diagnosis results, such as ANNs, OMs, and CENs; (4) poor topological adaptability, such as ANNs, OMs, and BNs; (5) low fault tolerance, such as OMs and ANNs; and (6) cannot be used independently and need to be combined with other methods, such as the FL and RSs. Therefore, how to improve the above methods or put forward new ones is the main issue in the corresponding engineering domain.

Among these fault diagnosis methods, the SNPS is a novel bio-inspired distributed parallel computing model, which has powerful information processing and parallel computing ability (most models have been verified to be Turing equivalent [39, 40]). The SNPS has become a hot research topic in Membrane Computing [41] and Natural Computing. In recent years, it has been used to explore the new fault information processing mechanism and SNPS-based fault diagnosis methods with rich achievements. SNPSs are a special kind of neural-like P systems [42], inspired by the mechanism that biological neurons store, transmit, and exchange information by pulses (spikes) along axons from presynaptic neurons to postsynaptic neurons in a distributed and parallel manner [4, 43, 44]. Due to the similarity between the spike transmission among different neurons through synapses and the fault propagation in power systems, fault diagnosis models based on different variants of spiking neural P systems are proposed to reason fault events to find faulty equipment [4, 36–38, 45–49].

At present, SNPS-based fault diagnosis methods can be divided into two categories (according to the fault information processing way): fuzzy reasoning with real numbers (FRRN) [36–38, 45–48] and fuzzy reasoning with fuzzy numbers (FRFN) [4, 50–52]. The FRRN refers to process uncertain and incomplete fault alarm messages using probability numbers which correspond to historical statistics of action information of protection devices including protective relays (PRs) and circuit breakers (CBs). Therefore, the FRRN strongly depends on the historical data. However, with the increasing complexity of power systems, it is difficult to accurately obtain the historical statistics and update them in time. For the second kind of method, the FRFN is to deal with the uncertainty and incompleteness by fuzzy numbers. Wang et al. [4], for the first time, introduces trapezoidal fuzzy numbers, fault fuzzy production rules, and fault

confidence levels into the framework of SNPSs to propose a fault diagnosis method for power transmission networks, where neurons, spikes, firing rules, and firing conditions are redefined. Then, Tao et al., Yu et al., and Peng et al. [50–52] continue to explore and introduce triangular fuzzy numbers, interval valued fuzzy numbers, and intuitionistic fuzzy sets, respectively, to diagnose faults of transmission networks. However, for above-mentioned types of FRRN, the different kinds of fuzzy numbers are all obtained via expert experience. Therefore, the FRRN has high subjectivity, and its non-subjectivity is still a difficult problem to be solved. In addition, both the FRRN and the FRFN do not consider the preprocessing of fault alarm messages, that is, the fault alarm messages cannot be effectively utilized by deleting redundant information before modeling the SNPS-based diagnosis models. Therefore, when the scale and complexity [53–56] of a power system increase and the redundancy of fault information is high, the fault tolerance of SNPS-based methods will reduce rapidly. Therefore, more attention should be paid to how to effectively overcome the above shortcomings.

On the contrary, the rough set [57, 58] is a typical mathematical tool to deal with uncertain and imprecise information in an objective way. However, the rough set generally should be combined with other methods because it can only reason and calculate fault data itself weakly. To address the aforementioned issues, this paper first proposes a spiking neural P system with self-updating rules (srSNPS) considering biological apoptosis mechanism, which integrates the strong objectivity (i.e., no need of any priori or additional information [59]) and good uncertainty handling capacity of rough sets and excellent parallel information processing ability of SNPSs. Then, an srSNPS-based fault diagnosis method for transmission networks is further devised. The main contributions of this paper are described as follows:

- (1) To effectively deal with uncertain and incomplete fault information in an objectivity way, an srSNPS and its apoptosis algorithm (Algorithm 1) for condition neurons are proposed. This is the first time to availablely unify the attribute reduction function of rough sets and the apoptosis mechanism of biological neurons in the framework of membrane computing. This way makes the SNPSs handle the uncertainty and incompleteness without historical statistics and expert experience.
- (2) Besides, the self-updating matrix reasoning algorithm (Algorithm 2) and self-updating rules for input neurons are proposed. So, the srSNPS can effectively make comprehensive use of fault information including action information, start information, and overlimit signals of protection devices to improve its uncertainty and incomplete processing capacity based on a simple matrix reasoning process with a vivid graphical model-building way.

Input: t condition neurons, s decision-making neurons

- (1) Calculate $h(C)$ via (2) and let $L = C$
- (2) **while** ($j \leq t$)
- (3) Calculate $h(C - C_j)$ after the C_j dies via (2)
- (4) Calculate the importance degree $\text{Sig}(C_j)$ of the C_j via (1)
- (5) **if** $\text{Sig}(C_j) = 0$, **then**
- (6) $L = C - \{C_i\}$
- (7) **else**
- (8) $L = C$
- (9) **end if**
- (10) **end while**

Output: survival condition neuron set L

ALGORITHM 1: Apoptosis algorithm for condition neurons.

Input: $\theta_0, \delta_0, D_1, D_2, D_3, E, \mathbf{0}_1 = \{0, \dots, 0\}_p^T, \mathbf{0}_2 = \{0, \dots, 0\}_q^T$

- (1) Let $g = 0$
- (2) **if** input neurons satisfy with the firing conditions of self-updating rules, **then**
- (3) correct θ_g and the algorithm jumps to **Step 7**
- (4) **else**
- (5) the algorithm jumps to **Step 7** without pulse value correction
- (6) **end if**
- (7) **while** ($\theta_g \neq \mathbf{0}_1$ or $\delta_g \neq \mathbf{0}_2$)
- (8) **if** proposition neurons satisfy their firing conditions **then**
- (9) proposition neurons fire and compute δ_{g+1} via

$$\delta_{g+1} = (D_1^T \otimes \theta_g) + (D_2^T \cdot \theta_g) + (D_3^T \circ \theta_g)$$
- (10) **end if**
- (11) **if** rule neurons satisfy their firing conditions **then**
- (12) rule neurons fire and compute θ_{g+1} via

$$\theta_{g+1} = E^T \circ \delta_{g+1}$$
- (13) **end if**
- (14) $g = g + 1$
- (15) **end while**

Output: Pulse values of output neurons

ALGORITHM 2: Self-updating matrix reasoning algorithm.

- (3) Based on the proposed srSNPS and two algorithms, combined with the depth-first search algorithm (DSA), the weight network segmentation method (WNSM) and the protection device event tree (PDET), an srSNPS-based fault diagnosis method is proposed. This method has good diagnosis result interpretability while maintaining high-fault tolerance and a fast diagnosis speed under the uncertainty and incompleteness of fault alarm messages. In addition, it does not require historical statistics and expertise. These are not the case for previous SNPS-based methods (even for all the graphical reasoning diagnosis methods).

The remainder of this paper is organized as follows. Section 2 proposes the srSNPS and its algorithms. The srSNPS-based fault diagnosis method is proposed in Section 3. In Section 4, the proposed diagnosis method is applied to the IEEE 14- and 118-bus systems with the analysis of their effectiveness and superiority. Conclusions are finally drawn in Section 5.

2. Spiking Neural P Systems with Self-Updating Rules

This section first proposes the srSNPS and then presents its SMRA.

2.1. Spiking Neural P Systems with Self-Updating Rules

Definition 1. A spiking neural P system with self-updating rules (srSNPS) is a tuple:

$$\Pi = (O, M_e, \sigma_1, \dots, \sigma_m, \text{syn}, \text{in}, \text{out}), \quad (1)$$

where

- (1) $O = \{a\}$ is a singleton alphabet (a is called a spike, O is a set of spikes).
- (2) $M_e = (D_i, C_j)$ is called microenvironment, where
 - (a) $D_i = (\theta_{di/T}, T, f_i)$, $1 \leq i \leq s$, is the i -th decision-making neuron (DN) in M_e and represents

suspicious faulty equipment in the targeted power network, where

- (i) $\theta_{di/T}$ equals to 0 or 1 representing the pulse value of the i -th DN at time T . Note that $\theta_{di/T} = 1$ means the suspicious faulty equipment corresponding to D_i faults and vice versa.
 - (ii) T is the sequence time of spikes, and a DN produces a spike at each unit time. Thus, a pulse value sequence is formed and recorded in the DN after T unit time.
 - (iii) f_i is a forgetting rule of the i -th DN with the form $E/\{a^{\theta_{di/T}} \rightarrow \lambda; g = 0\}$, where g represents the reasoning step of the reasoning algorithm of the srSNPS, i.e., the self-updating matrix reasoning algorithm proposed in the next subsection. It means that if f_i is applied, then spikes in the D_i are emptied and the calculation process will be reinitialized (i.e., $g = 0$). The firing condition is $E = \{\theta'_{di/T} \neq \theta_{di/T}\}$, representing that the pulse value in D_i has changed.
- (b) $C_j = (\theta_{cj/T}, T, f_j, A_{rj})$, $1 \leq j \leq t$, is the j -th condition neuron (CN) in M_e and represents a protective relay or circuit breaker in the targeted power transmission network, where
- (i) $\theta_{cj/T}$ equals to 0 or 1 representing the pulse value of the j -th CN at time T . Note that $\theta_{cj/T} = 1$ means the protection device corresponding to C_j has acted and vice versa.
 - (ii) T is the sequence time of spikes, and a CN produces a spike at each unit time. Thus, a pulse value sequence is formed and recorded in the CN after T unit time.
 - (iii) f_j is a forgetting rule of the j -th CN with the form $E/\{a^{\theta_{cj/T}} \rightarrow \lambda; g = 0\}$. It means that if f_j is applied, then spikes in C_j are emptied and the calculation process will be reinitialized (i.e., $g = 0$). The firing condition is $E = \{\theta'_{cj/T} \neq \theta_{cj/T}\}$, representing that the pulse value in C_j has changed.
- (c) A_{rj} represents an apoptosis rule in M_e with the form $E/\{C_j\} \rightarrow \{\text{Algorithm 1}^{[L]}\}$, which means that if A_{rj} is applied, then C_j executes its apoptosis rule to determine whether it lives or dies. That is, CNs execute Algorithm 1 to output survival condition neuron (containing important information) set L . In the same time, CNs including redundant information die and will not participate in fault reasoning. The firing condition is $E = \{g = 0 \cap \text{sig}_j = 0\}$ indicating that the rule A_{rj} can be applied if and only if in the *initial configuration* [43] (that is, $g = 0$) with $\text{sig}_j = 0$ (please see Definition 2).
- (3) $\sigma_i = (\theta_i, r_i, e_i)$, $1 \leq i \leq p$, is the i -th proposition neuron (PN) corresponding to a protection device or

the equipment, $\sigma_j = (\delta_j, r_j)$, $1 \leq j \leq q$, is the j -th rule neuron (RN) corresponding to a fault production rule, and $p + q = m$, where

- (a) θ_i and δ_j are pulse values (equal to 0 or 1) in proposition neuron σ_i and rule neuron σ_j , respectively.
 - (b) r_i represents a firing rule of σ_i with the form $E/a^\theta \rightarrow a^\theta$, where $E = \{a\}$ is the firing condition, which means that once σ_i contains a spike, r_i can be applied. Then, σ_i will consume a spike with pulse value θ , produce a new spike with the same pulse value, and then transmit it to its postsynaptic neurons; r_j represents a firing rule of σ_j with the form $E/a^\delta \rightarrow a^\beta$, where $E = \{a\}$ is the firing condition, which means that once σ_j contains a spike, r_j can be applied. Then, σ_j will consume a spike with pulse value δ , produce a new spike with pulse value β (equals to 0 or 1), and then transmit it to its postsynaptic neurons.
 - (c) e_i represents a self-updating rule of the form $E/a^\theta \rightarrow a^{\bar{\theta}}$. The firing condition is $E = \{\varepsilon_i > 0\}$, which means that e_i can be applied if and only if the self-updating operator $\varepsilon_i > 0$. Then, σ_i will consume a spike with pulse value θ , produce a new spike with pulse value $\bar{\theta}$ (equals to 0 or 1, called the antispikes of θ), and then $\varepsilon_i = \varepsilon_i - 1$. Note that only input proposition neurons contain self-updating rules.
- (4) $\text{syn} \subseteq \{1, \dots, m\} \times \{1, \dots, m\}$ with $i \neq j$ for all $(i, j) \in \text{syn}$ for $1 \leq i, j \leq m$ is a directed synaptic connection between linked neurons.
- (5) in, out indicate the input neuron set and output neuron set, respectively.

Note that if a PN is an input neuron, then it corresponds to a protection device, i.e., a protective relay or a circuit breaker. In this case, the pulse value in σ_i represents the action information of its corresponding protection device, where $\theta_i = 1$ means that the device has acted, while $\theta_i = 0$ means it does not. If a PN is an output neuron, then it corresponds to suspicious faulty equipment. In this case, $\theta_i = 1$ indicates that the equipment is faulty, and $\theta_i = 0$ means it is not.

Definition 2. The importance degree of C_j ($1 \leq j \leq t$) is

$$\text{sig}(C_j) = I(C_j, D) = h(C - C_j) - h(C), \quad (2)$$

where $h(C - C_j)$ is the conditional information entropy (CIE) of the other condition neurons to decision-making neurons after C_j dies.

Definition 3. The CIE of a condition neuron C is

$$h(C) = - \sum_{i=1}^{|U/C|} p(X_i) \sum_{j=1}^{|U/D|} p(Y_j | X_i) \log p(Y_j | X_i), \quad (3)$$

where U is called the universe, D is a DN, $p(X_i)$ represents the probability of X_i on U , and $p(Y_j | X_i) = |Y_j \cap X_i|/|X_i|$

indicates the probability of the event Y_j under the occurrence event X_i .

Definition 4. M_e of neurons in an srSNPS is a knowledge base $K = (U, R)$, where R is a nonempty finite set of attributes. Set $X = \{X_1, X_2, \dots, X_n\}$ and $Y = \{Y_1, Y_2, \dots, Y_m\}$ as the partitions of P and Q on U , respectively. The probability distributions of P and Q on the σ algebra composed of subsets of U are

$$\begin{aligned} [X:p] &= \begin{bmatrix} X_1 & X_2 & \cdots & X_n \\ p(X_1) & p(X_2) & \cdots & p(X_n) \end{bmatrix}, \\ [Y:p] &= \begin{bmatrix} Y_1 & Y_2 & \cdots & Y_m \\ p(Y_1) & p(Y_2) & \cdots & p(Y_m) \end{bmatrix}, \end{aligned} \quad (4)$$

where $p(X_i) = |X_i|/|U|$, $i = 1, \dots, n$ and $p(Y_j) = |Y_j|/|U|$, $j = 1, \dots, m$.

Algorithm 1 used in the apoptosis rule is the apoptosis algorithm for condition neurons, described as follows. Its output is a survival condition neuron set L . The neurons in L will be connected according to the synaptic connection rule in Definition 5.

Definition 5. Synaptic connection rules in this study are (1) read the information sequences of DNs and survival CNs to form the minimum reduction decision table (MRDT); (2) create a fault production rule set (FPRS) for the MRDT; and (3) realize synaptic connection according to production rules in the FPRS. Note that only the living neurons (including DNs and survival CNs) can build synapses. The dead condition neurons are unable to establish any effective synapses.

To improve the intelligibility, a sketch map of neurons and the microenvironment are shown in Figure 1, and a diagram of evolutionary process of an srSNPS is shown in Figure 2, where the ODT represents the original decision table of a fault to be diagnosed. In an srSNPS, there are three types of rule neurons, i.e., *General*-, *And*-, and *Or*-rule neurons. All of them can represent fault production rules but with different processing methods of spikes, which will be described in detail in Section 2.2.

2.2. Self-Updating Matrix Reasoning Algorithm. To explain the SMRA, we first introduce its vectors, matrices, and operators as follows:

- (1) $\boldsymbol{\theta} = (\theta_1, \dots, \theta_p)^T$ is a pulse value vector of PNs, where θ_i ($1 \leq i \leq p$) represents the pulse value of i -th PN σ_i . If σ_i is an input neuron, then $\theta_i = 1$ means the protection device associated with σ_i has acted, and $\theta_i = 0$ means it has not acted. If σ_i is an output neuron, then $\theta_i = 1$ means the corresponding suspicious equipment is faulty, and $\theta_i = 0$ means it is not faulty.
- (2) $\boldsymbol{\delta} = (\delta_1, \dots, \delta_q)^T$ is a pulse value vector of RNs, where δ_j ($1 \leq j \leq q$) is the pulse value of the j -th RN.

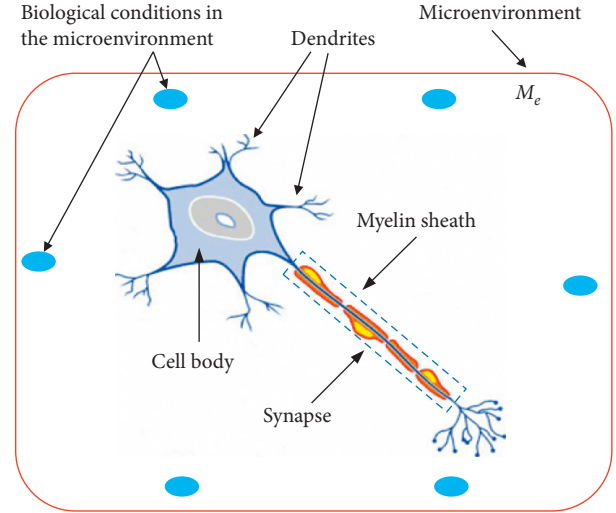


FIGURE 1: Sketch map of neurons and microenvironment.

- (3) $\boldsymbol{\varepsilon} = (\varepsilon_1, \dots, \varepsilon_l)^T$ ($1 \leq l \leq p$) is a self-updating operator vector of input neurons, where ε_i ($1 \leq i \leq l$) is the self-updating operator of the i -th input neuron.
- (4) $\mathbf{D}_1 = (d_{ij})_{p \times q}$ is a synaptic matrix, which represents the directed synaptic connection from PNs to *general* RNs. If there is a synapse from PN σ_i to *general* RN σ_j , then $d_{ij} = 1$; otherwise, $d_{ij} = 0$.
- (5) $\mathbf{D}_2 = (d_{ij})_{p \times q}$ is a synaptic matrix, which represents the directed synaptic connection from PNs to *And* RNs. If there is a synapse from PN σ_i to *And* RN σ_j , then $d_{ij} = 1$; otherwise, $d_{ij} = 0$.
- (6) $\mathbf{D}_3 = (d_{ij})_{p \times q}$ is a synaptic matrix, which represents the directed synaptic connection from PNs to *Or* RNs. If there is a synapse from PNs σ_i to *Or* RN σ_j , then $d_{ij} = 1$; otherwise, $d_{ij} = 0$.
- (7) $\mathbf{E} = (e_{ji})_{q \times p}$ is a synaptic matrix, which represents the directed synaptic connection from RNs to PNs. If there is a synapse from RN σ_j to PN σ_i , then $e_{ji} = 1$; otherwise, $e_{ji} = 0$.
- (8) $\mathbf{D}^T \otimes \boldsymbol{\theta} = (\bar{d}_1, \dots, \bar{d}_q)$, where $\bar{d}_j = d_{1j} \times \theta_1 + \dots + d_{sj} \times \theta_s$, $j = 1, \dots, q$.
- (9) $\mathbf{D}^T \cdot \boldsymbol{\theta} = (\bar{d}_1, \dots, \bar{d}_q)$, where $\bar{d}_j = \min(d_{1j} \times \theta_1, \dots, d_{sj} \times \theta_s)$, $j = 1, \dots, q$.
- (10) $\mathbf{D}^T \circ \boldsymbol{\theta} = (\bar{d}_1, \dots, \bar{d}_q)$, where $\bar{d}_j = \max(d_{1j} \times \theta_1, \dots, d_{sj} \times \theta_s)$, $j = 1, \dots, q$. Likewise, $\mathbf{E}^T \circ \boldsymbol{\theta} = (\bar{e}_1, \dots, \bar{e}_p)$, where $\bar{e}_i = \max(e_{1i} \times \theta_1, d_{2i} \times \theta_2, \dots, d_{qi} \times \theta_q)$, $i = 1, \dots, p$.

To parallelly reason and calculate fault alarm messages, we design the SMRA for srSNPSs as follows.

3. The Proposed Methodology

This section proposes a fault diagnosis method for power transmission networks based on the srSNPS, whose flow-chart is shown in Figure 3 and described as follows:

Step 1: transmission network partition.

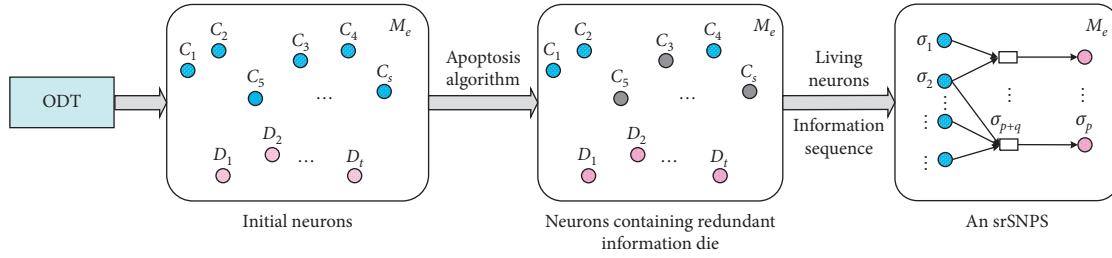


FIGURE 2: Diagram of evolutionary process of an srSNPS.

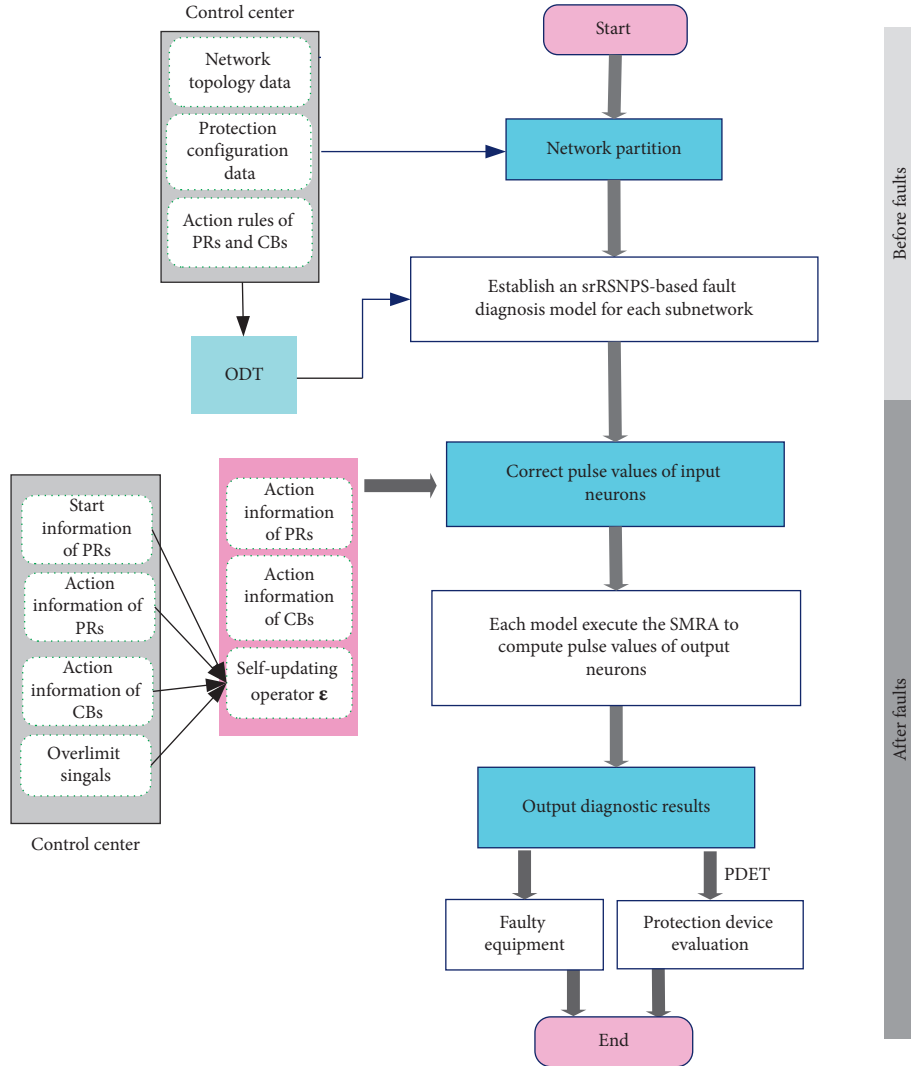


FIGURE 3: Flowchart of the proposed srSNPS-based fault diagnosis method.

- (a) *Generate the Depth-First Search Tree (DST)*. Employ the depth-first search algorithm [60, 61] to simplify the numbered transmission network to generate the corresponding DST, in which nodes represent buses.
- (b) *Divide the DST*. Use the weight network segmentation method [60, 61] to split the DST while ensuring that the computational burden of each

subnetwork after network partition is approximately the same.

Step 2: establish an srSNPS-based fault diagnosis model for each subnetwork. The subnetworks perform the following steps (a)–(d) in a parallel way:

- (a) *Select Living Neurons*. (i) Transport the ODT of the fault into the *microenvironment*, i.e., feed

conditional attributes of the ODT into CNs in M_e and decision-making attributes into DN neurons. (ii) CNs execute apoptosis rules (i.e., Algorithm 1) to select survival ones. The purpose of this step is to select out important fault alarm messages (i.e., the core attribute fault information) by deleting redundant ones.

- (b) *Establish MRDT*. Read the information sequences of DNs and survival CNs to form the MRDT.
- (c) Create the FPRS via the obtained MRDT.
- (d) *Realize Synaptic Connections to Build an srSNPS-Based Model for Each Subnetwork*. Establish synapses according to Definition 5. Note that each fault production rule corresponds to a rule neuron, while each antecedent or consequent proposition in a rule is associated with a proposition neuron. Now, the survival CNs mutate to input PNs and the DNs mutate to output PNs. The pulse values in the input PNs represent the core attribute fault information (corresponding to action information of PRs or CBs) in fault alarm messages.

Step 3: correct pulse values of input neurons. Integratedly utilize the start information and action information of protection devices based on the fault information matrix (please see Subsection 3.1) to get the self-updating operator vector of input neurons, i.e., ϵ . Then, each input neuron applies its self-updating rule to correct and update its pulse value. Accordingly, the wrong action information of protection devices is corrected because the pulse value of each input neuron represents the action information of a protective relay or a circuit breaker. The flowchart of this step is shown in Figure 4.

Step 4: compute pulse values of output neurons. Each subnetwork performs the SMRA (i.e., Algorithm 2) of its srSNPS-based fault diagnosis model in a parallel way to reasoning out the pulse values of output neurons.

Step 5: output diagnosis results. If and only if the pulse value of an output neuron is 1, its corresponding equipment is faulty.

Step 6: evaluate uncertain behaviors of protection devices. Search the protection device event tree (PDET, please see Subsection 3.2) to find the false or lost alarm messages of protection devices.

The purpose of Step 1 includes (a) simplify decision-making samples for srSNPS-based diagnosis models. The typical fault diagnosis methods based on rough sets establish the ODT of a fault event via the fault data of the entire transmission network, while our proposed method concurrently establishes the ODT for each subnetwork; (b) improve the topological adaptability of networks. When the topology of a transmission network changes, it just needs to modify the srSNPS-based diagnosis model of the corresponding subnetwork. Besides, Steps 1 and 2 are finished

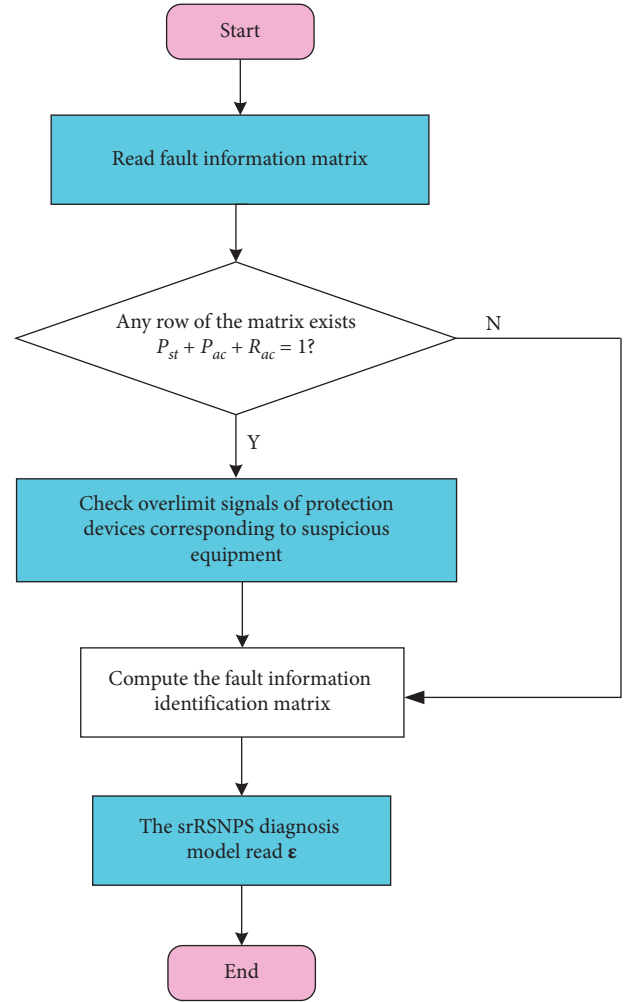


FIGURE 4: Flowchart of correction steps for action information.

before faults occur, and Steps 3–6 are executed immediately after failures. Thus, the proposed method can save some time.

3.1. Correct Pulse Values of Input Neurons in srSNPS-Based Diagnosis Models. Define the fault information matrix of a CB (labeled as A) as

$$M_A = \begin{bmatrix} P_{stA}^{(1)} & P_{acA}^{(1)} & R_{acA} \\ P_{stA}^{(2)} & P_{acA}^{(2)} & R_{acA} \\ P_{stA}^{(3)} & P_{acA}^{(3)} & R_{acA} \\ P_{stA}^{(4)} & P_{acA}^{(4)} & R_{acA} \end{bmatrix}, \quad (5)$$

where $P_{stA}^{(u)}$ is the start information of PRs, $P_{acA}^{(u)}$ is the action information of PRs, and $u = 1, 2, 3, 4$ represents the main protective, first backup protective, second backup protective, and bus protective relays associated with the CB, respectively; R_{acA} is the action information of the CB. Particularly, if there is no bus PR, $P_{stA}^{(4)} = P_{acA}^{(4)} = 0$.

Define the fault information identification matrix N_A as

$$N_A = \begin{bmatrix} P_{jA}^{(1)} & R_{jA} \\ P_{jA}^{(2)} & R_{jA} \\ P_{jA}^{(3)} & R_{jA} \\ P_{jA}^{(4)} & R_{jA} \end{bmatrix}, \quad (6)$$

where $P_{jA}^{(u)}$ ($P_{jA}^{(u)} = P_{stA}^{(u)} \oplus P_{acA}^{(u)}$, $u = 1, 2, 3, 4$) represents decision value of status for the corresponding PR and \oplus is the xor operation. When $P_{jA}^{(u)} = 1$, read overlmit signals of protection devices corresponding to the suspicious equipment.

$\boldsymbol{\varepsilon} = (\varepsilon_1, \dots, \varepsilon_l)^T$ is the self-updating operator vector of input neurons. Define ε_i ($1 \leq i \leq l$) as

$$\varepsilon_i = \begin{cases} \frac{0}{0}, & \bigcup_{z=1}^4 (P_{sti}^{(z)} + P_{aci}^{(z)}) = 0, \\ \frac{0}{(P_{ji}^{(3)} \oplus R_{ji}) \cup (P_{ji}^{(4)} \oplus R_{ji})}, & \bigcup_{z=1}^2 (P_{sti}^{(z)} + P_{aci}^{(z)}) = 0, \\ \frac{(P_{ji}^{(1)} \oplus R_{ji}) \cup (P_{ji}^{(2)} \oplus R_{ji})}{0}, & \bigcup_{z=3}^4 (P_{sti}^{(z)} + P_{aci}^{(z)}) = 0, \\ \frac{(P_{sti}^{(1)} \oplus R_{ji}) \cup (P_{ji}^{(2)} \oplus R_{ji})}{(P_{ji}^{(3)} \oplus R_{ji}) \cup (P_{ji}^{(4)} \oplus R_{ji})}, & \bigcup_{z=1}^4 (P_{sti}^{(z)} + P_{aci}^{(z)}) \neq 0, \end{cases} \quad (7)$$

where the symbol “—” is not the fraction line. The symbols above “—” indicate self-updating operators of lines where protective devices associated with input neurons are located, while the ones under “—” represent self-updating operators of buses.

3.2. Search the Protection Device Event Tree. According to start and action messages of PRs, action messages of CBs, and overlmit signals of faulty equipment, the PDET for a fault event is generated as shown in Figure 5, where P_{sti} and P_{aci} are the start and action information of the i -th PR, respectively, R_{aci} is the action information of the corresponding CB, and OL_i is the overlmit signal of the faulty equipment we have found; the start and action messages are represented by \ominus , the overlmit signals are indicated by \square , and the behaviors of protection devices are represented by \diamond ; the pink in above symbol represents the corresponding protection device has acted, while the gray color means it does not. When faulty equipment is got in Section 3-Step 5, then we search the PDET to evaluate uncertain behaviors of protection devices.

4. Case Study

The proposed method is applied to the IEEE 14-bus and IEEE 118-bus systems to demonstrate its effectiveness and superiority.

4.1. IEEE 14-Bus System. There are 14 buses, 20 lines, 40 circuit breakers, 40 line main protective relays, 40 line first

backup protective relays, 40 line second backup protective relays, and 14-bus protective relays.

4.1.1. Comparative Tests. Ten cases including uncertainty and incompleteness, such as maloperation and misinformation, are used to do the comparisons between the proposed method and three typical fault diagnosis methods, i.e., the cause-effect network (CEN) in [2], the fuzzy Petri net (FPN) in [18], and the fuzzy reasoning spiking neural P system (FRSNPS) in [36]. The reason choosing the three methods is that their performance over many other approaches has been demonstrated. The diagnosis results are shown in Table 1.

For cases 1 and 2, four methods can find the right faulty equipment. Therefore, they are all effective without uncertain or incomplete fault information. For case 3, only the proposed method and the FRSNPS are successful, while both CEN and FPN are failed. For cases 4–7, only our method can accurately diagnose the faults. Cases 8–10 are three extreme examples, i.e., all the action information of protective relays or circuit breakers are lost. The CEN, FPN, and FRSNPS are all failed for cases 8–10, while our method is successful for cases 8 and 9 and failed for the case 10. This is because the lost information in cases 8 and 9 is the redundant information in our method, and the one in case 10 is the core attribute information. Therefore, we can see that if the uncertainty and incompleteness occur in the redundant information, it has no effect on the diagnosis results of the proposed method. However, when it happens in the core attribute information, it will influence the results. Fortunately, due to the stability of the relay protection system, the case of complete loss of all core attribute information is very rare under normal operation of power systems. Therefore, Table 1 shows that the proposed method can obtain satisfying results in the situations with incomplete or uncertain alarm information for both single and multiple faults.

Besides, the computational complexities of the CEN, FPN, and FRSNPS are analyzed. Note that the computational complexities of the four methods are all in the linear order. Since the proposed method reduces redundant information by the apoptosis algorithm of condition neurons, the number of neurons used for establishing srSNPS-based fault diagnosis models is smaller than that of the CEN, FPN, and FRSNPS. The more the redundant information, the smaller the computational complexity of the proposed method. In a fault diagnosis problem, there is typically much redundant information. So, the upper limit of algorithm computational complexity for the proposed method is far less than that of the other three methods. Therefore, we can see that, although our method needs more information (such as start information and overlmit signals) to improve its diagnostic accuracy, the time complexity does not increase.

4.1.2. Disturbed Tests. To verify the fault-tolerant ability of our method, we take the disturbed test under different uncertain information ratios (UIRs). The test results are shown in Table 2.

Define the UIR as

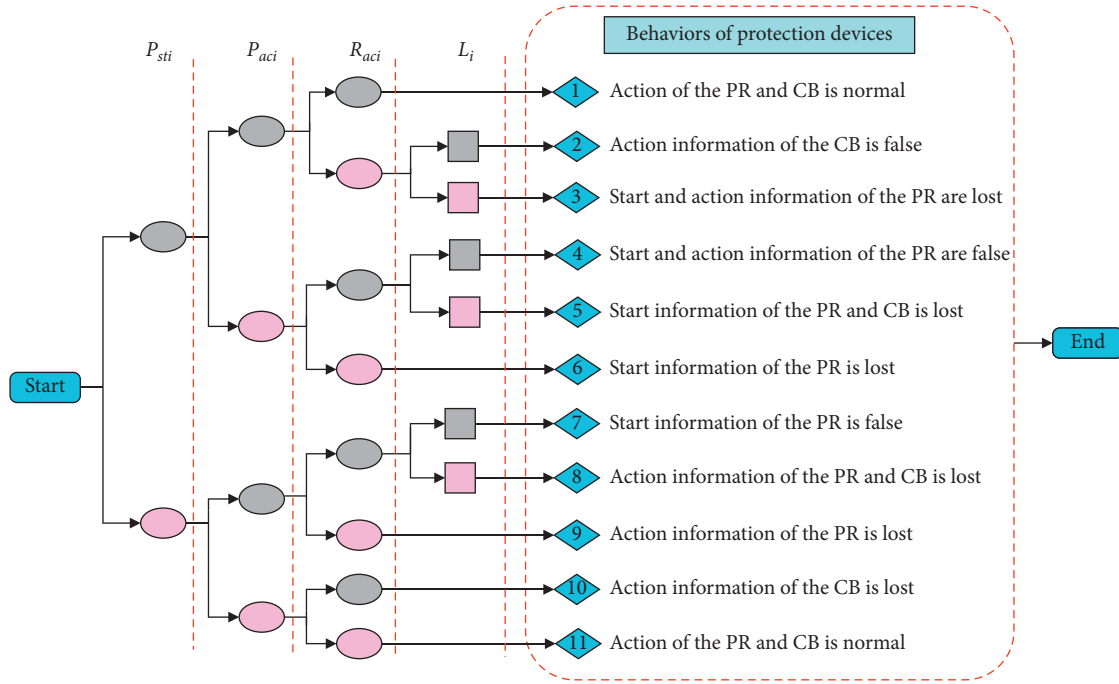


FIGURE 5: Protection device event tree.

TABLE 1: Comparisons of diagnosis results between the proposed method and three typical fault diagnosis methods for the 14-bus system.

Cases	Preset faults			The proposed method				
	Action information of protection devices		Faulty equipment	CEN [2]	FPN [18]	FRSNPS [36]	Diagnosis results	Information evaluation
	PRs	CBs						
1	MLR ₁₃₁₄ MLR ₁₄₁₃	CB ₁₃₁₄ CB ₁₄₁₃	L ₁₃₁₄	L ₁₃₁₄	L ₁₃₁₄	L ₁₃₁₄	L ₁₃₁₄	Correct action
2	MLR ₁₃₁₄ MLR ₁₄₁₃ SLR ₀₆₁₃ SLR ₁₂₁₃	CB ₁₂₁₃ CB ₀₆₁₃ CB ₁₄₁₃ CB ₁₃₁₄	L ₁₃₁₄ B ₁₃	L ₁₃₁₄ B ₁₃	L ₁₃₁₄ B ₁₃	L ₁₃₁₄ B ₁₃	L ₁₃₁₄ B ₁₃	Correct action
3	BR ₁₂ ML ₁₂₁₃ ML ₁₃₁₄	CB ₁₃₁₂ CB ₁₂₀₆	L ₁₂₁₃ B ₁₂	L ₁₂₁₃ B ₁₂	L ₁₂₁₃ B ₁₂	L ₁₂₁₃ B ₁₂	L ₁₂₁₃ B ₁₂	Lost information: CB ₁₂₁₃
4	BR ₁₃ MLR ₁₂₁₃	CB ₁₂₁₃ CB ₁₃₁₂	L ₁₂₁₃ B ₁₃	L ₁₂₁₃ B ₁₃	L ₁₂₁₃	L ₁₂₁₃ B ₁₃	L ₁₂₁₃ B ₁₃	Lost information: BLR ₁₃₁₂ , CB ₁₃₀₆ , CB ₁₃₁₄
5	MLR ₁₂₁₃ MLR ₁₃₁₂ SLR ₁₂₀₆	CB ₀₆₁₂	L ₁₂₁₃ B ₁₂	L ₁₂₁₃	L ₁₂₁₃	L ₁₂₁₃ B ₁₂	L ₁₂₁₃ B ₁₂	Lost information: CB ₁₃₁₂ , CB ₁₂₁₃ , SLR ₁₃₁₂
6	BR ₁₂ BR ₁₃ SLR ₁₃₁₂ SLR ₁₃₀₆	CB ₁₂₀₆ CB ₁₂₁₃ CB ₁₃₁₂ CB ₁₃₁₄ CB ₁₄₀₉ CB ₁₃₀₆	B ₁₂ L ₁₃₁₄	B ₁₂ B ₁₃ L ₁₃₁₄	B ₁₂ B ₁₃ L ₁₃₁₄	B ₁₂ B ₁₃ L ₁₃₁₄	B ₁₂ L ₁₃₁₄	False information: BR ₁₃ , CB ₁₃₁₂ , CB ₁₃₁₄ Lost information: SLR ₁₄₀₉
7	BR ₁₂ MLR ₁₃₁₄ MLR ₁₄₁₃	CB ₁₂₁₃ CB ₁₂₀₆ CB ₁₃₀₆ CB ₁₃₁₄ CB ₁₄₁₃	B ₁₂ B ₁₃ L ₁₃₁₄	B ₁₂ B ₁₃ L ₁₃₁₄	B ₁₂ B ₁₃ L ₁₃₁₄	B ₁₂ B ₁₃ L ₁₃₁₄	B ₁₂ B ₁₃ L ₁₃₁₄	Lost information: BR ₁₃ , CB ₁₃₁₂

TABLE 1: Continued.

Cases	Preset faults			The proposed method				
	Action information of protection devises		Faulty equipment	CEN [2]	FPN [18]	FRSNPS [36]	Diagnosis results	Information evaluation
	PRs	CBs						
8	—	CB ₁₃₁₂	B ₁₂	No fault	No fault	No fault	B₁₂	Lost information: SLR ₀₆₁₂ , SLR ₁₃₁₂ , CB ₀₆₁₂
9	BR ₁₃	—	B ₁₃	No fault	No fault	No fault	B₁₃	Lost information: CB ₁₂₀₆ , CB ₁₂₁₃
10	—	CB ₀₆₁₃	B ₁₃	No fault	No fault	No fault	No fault	Lost information: SLR ₁₂₁₃ , SLR ₀₆₁₃ , SLR ₁₄₁₃ , CB ₁₂₁₃ , CB ₁₄₁₃

TABLE 2: Diagnostic accuracy of the proposed method of IEEE 14-bus system for different κ .

κ (%)	Diagnostic accuracy		
	Uncertainty is in the RAI	Uncertainty is in the CAAI	Uncertainty is in the RAAI
1	0.9998216	0.9774273	0.9777241
3	0.9773322	0.9534217	0.9536811
5	0.9402314	0.9212946	0.9217332
7	0.9186726	0.8842735	0.8858784
9	0.8730823	0.8426232	0.8457151
10	0.8501379	0.8218934	0.8275321
20	0.7038297	0.6807239	0.6884047
30	0.6129324	0.5002955	0.5187934

$$\kappa = \frac{N_{\text{uncertain}}}{N_{\text{fault}}} \times 100\%, \quad (8)$$

where N_{fault} is the number of fault alarm messages from the SCADA system and $N_{\text{uncertain}}$ is the number of the uncertain fault messages which are caused by the refuse operation, unwanted operation, and information loss of protection devices (including PRs and CBs).

In Table 2, each diagnostic accuracy for different κ is got by computing the mean value under 1000 random tests. Note that the headers ‘‘Uncertainty is in the RAI’’ and ‘‘Uncertainty is in the CAAI’’ represent that uncertain fault alarm messages appear only in the redundant alarm information (RAI) and the core attribute alarm information (CAAI), respectively. Moreover, the ‘‘Uncertainty is in the RAAI’’ represents that uncertain fault alarm messages appear randomly both in RAI and CAAI, which is called random attribute alarm information (RAAI). Table 2 shows that when uncertain alarm messages contained in κ are all RAI, the diagnostic accuracy is the highest compared to the other two situations. This is because the RAI is deleted in Step 2 (a) and is not used in the fault diagnosis process. When there is too much RAI, it will interfere with the judgment of the CAAI which should be used in the diagnosis process. Therefore, when the uncertainty is in the RAI, the diagnostic accuracy is less than 100%, and it will decrease with the increasing UIRs of the RAI.

When the uncertain fault messages contained in κ are CAAI and RAAI, the diagnostic accuracy is also high because the start information and overlimit signals of protection devices will guarantee the diagnostic accuracy. Table 2 shows that the diagnostic accuracy of our proposed method is very high when κ is less than 5%, and the diagnosis results are still acceptable when κ is between 5% and 10%.

The diagnostic accuracy drops quickly when κ is more than 10%. Fortunately, this situation will not happen unless there are attacks [62, 63]. Therefore, we can get from Table 2 that the diagnostic accuracy of the proposed method is high for the three cases (uncertainty is in the RAI, CAAI, and RAAI, respectively) when κ is less than 5%, and the RAI has a smaller impact on fault diagnostic results.

4.1.3. Working Details of the Proposed Fault Diagnosis Method. This section takes the IEEE 14-bus system as an example to show how the proposed fault diagnosis method works.

(1) *Network Partition.* The system is first abstracted as a DST by the depth-first search algorithm, as shown in Figure 6(a). Then, the weight network segmentation method is employed to divide the DST, as shown in Figure 6(b). The relationship of subnetworks after division is shown in Figure 7. Note that the information on each line in Figure 7 will be used by its linked subnetworks. Finally, we get the network partition result, as shown in Figure 8.

(2) *Establish srSNPS-Based Models for Subnetworks.* Subnetwork S6 is considered to show how to establish an srSNPS-based fault diagnosis model for a subnetwork. The protection configuration of S6 is shown in Figure 9.

First, the ODT for S6 is established by using the protection configuration information and causality between PRs and CBs. Then, we obtain living neurons by executing Step 2 (a) in Section 3, where $L_C = \{\text{BR}_{13}, \text{BR}_{14}, \text{CB}_{1213}, \text{CB}_{1312}, \text{CB}_{1314}, \text{CB}_{1206}, \text{CB}_{0613}, \text{CB}_{0914}\}$, $L_D = \{\text{L}_{1213}, \text{L}_{1314}, \text{L}_{1206}, \text{L}_{1306}, \text{L}_{1409}, \text{B}_{12}, \text{B}_{13}, \text{B}_{14}\}$. Finally, the MRDT is obtained

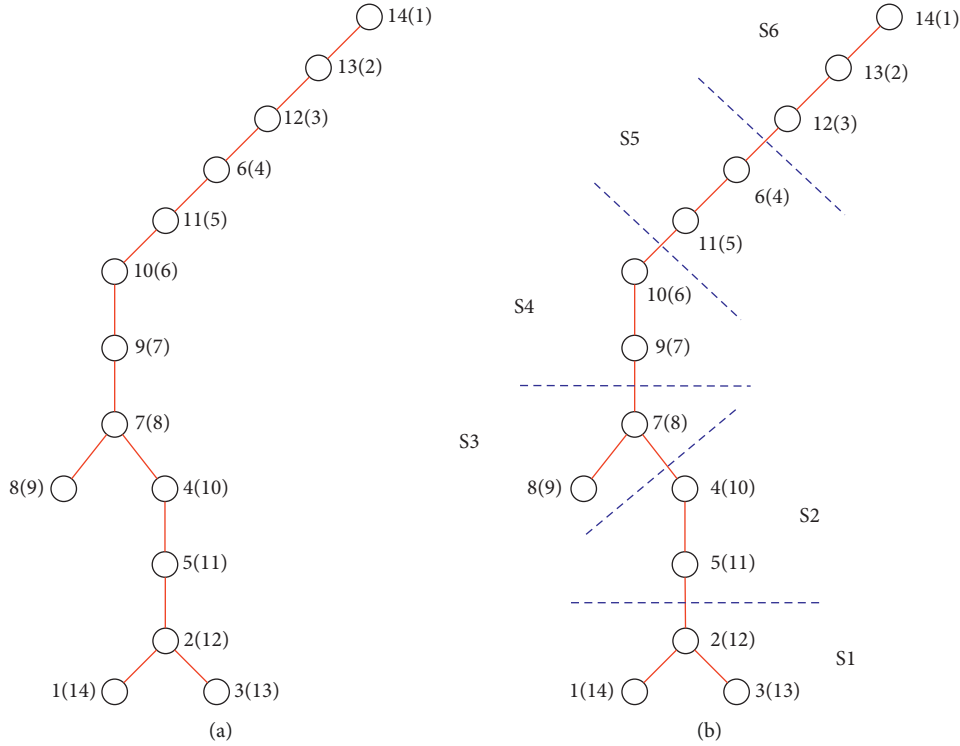


FIGURE 6: (a) The DST; (b) the segmentation result.

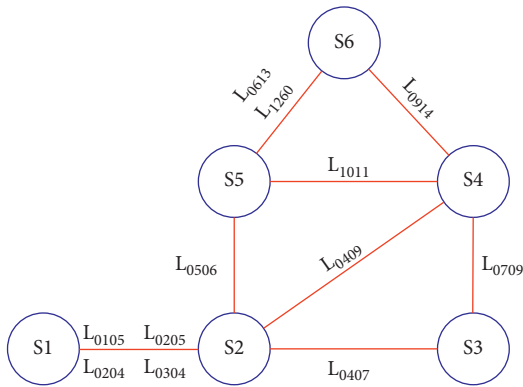


FIGURE 7: Relationship of the subnetworks.

(shown in Table 3) and accordingly the FPRS of S6 is created, as shown in Table 4.

The srSNPS-based diagnosis model for S6 is built, as shown in Figure 10, by connecting synapses based on the FPRS shown in Table 4 and the synaptic connection rule given in Definition 5.

(3) *Computational Process.* In this section, case 3 in Table 1 is considered as an example to show how an srSNPS-based model works.

Case 3. L_{1213} and B_{12} fault. Operated protective relays: MLR_{1213} , MLR_{1213} , and SLR_{0612} . Tripped CBs: CB_{1206} . Lost information: CB_{1312} and CB_{1213} . The fault alarm messages obtained from the SCADA system are shown in Table 5.

According to Table 5, we can get the fault information matrices of CB_{1213} , CB_{1312} , and CB_{1206} which are $M_{CB_{1213}}$,

$M_{CB_{1312}}$, and $M_{CB_{1206}}$, respectively. According to their fault information, the identification matrices $N_{CB_{1213}}$, $N_{CB_{1312}}$, and $N_{CB_{1206}}$ are obtained.

$$M_{CB_{1213}} = \begin{bmatrix} 1 & 1 & * \\ 0 & 0 & * \\ 0 & 0 & * \\ 0 & 0 & * \end{bmatrix},$$

$$M_{CB_{1206}} = \begin{bmatrix} 0 & 0 & 0 \\ 0 & 0 & 0 \\ 1 & 1 & 0 \\ 0 & 0 & 0 \end{bmatrix},$$

$$M_{CB_{1312}} = \begin{bmatrix} 1 & 1 & 0 \\ 0 & 0 & 0 \\ 0 & 0 & 0 \\ 0 & 0 & 0 \end{bmatrix},$$

$$N_{CB_{1213}} = \begin{bmatrix} 0 & 1 \\ 0 & 0 \\ 0 & 0 \\ 0 & 0 \end{bmatrix},$$

$$N_{CB_{1206}} = \begin{bmatrix} 0 & 0 \\ 0 & 0 \\ 0 & 1 \\ 0 & 0 \end{bmatrix},$$

$$N_{CB_{1312}} = \begin{bmatrix} 0 & 1 \\ 0 & 0 \\ 0 & 0 \\ 0 & 0 \end{bmatrix}.$$

(9)

TABLE 3: Minimum reduction decision table of S6.

BR ₁₃	BR ₁₄	CB ₁₂₁₃	CB ₁₃₁₂	CB ₁₃₁₄	CB ₁₂₀₆	CB ₀₆₁₃	CB ₀₉₁₄	F
0	0	1	1	0	0	0	0	L ₁₂₁₃
0	0	0	0	1	0	0	0	L ₁₃₁₄
0	0	0	0	0	1	0	0	L ₁₂₀₆
0	0	0	0	0	0	1	0	L ₁₃₀₆
0	0	0	0	0	0	0	1	L ₁₄₀₉
0	0	1	0	0	1	0	0	B ₁₂
0	0	1	0	0	0	0	0	B ₁₂
0	0	0	1	0	1	0	0	B ₁₂
0	0	0	1	0	0	0	0	B ₁₂
1	0	0	1	1	0	0	0	B ₁₃
1	0	1	0	1	0	0	0	B ₁₃
1	0	0	1	0	0	0	0	B ₁₃
1	0	0	1	1	0	1	0	B ₁₃
0	0	1	0	0	0	1	0	B ₁₃
0	1	0	0	0	0	0	0	B ₁₄
0	1	0	0	1	0	0	0	B ₁₄
0	1	0	0	0	0	0	1	B ₁₄
0	1	0	0	1	0	0	1	B ₁₄
0	0	0	0	1	0	0	1	B ₁₄

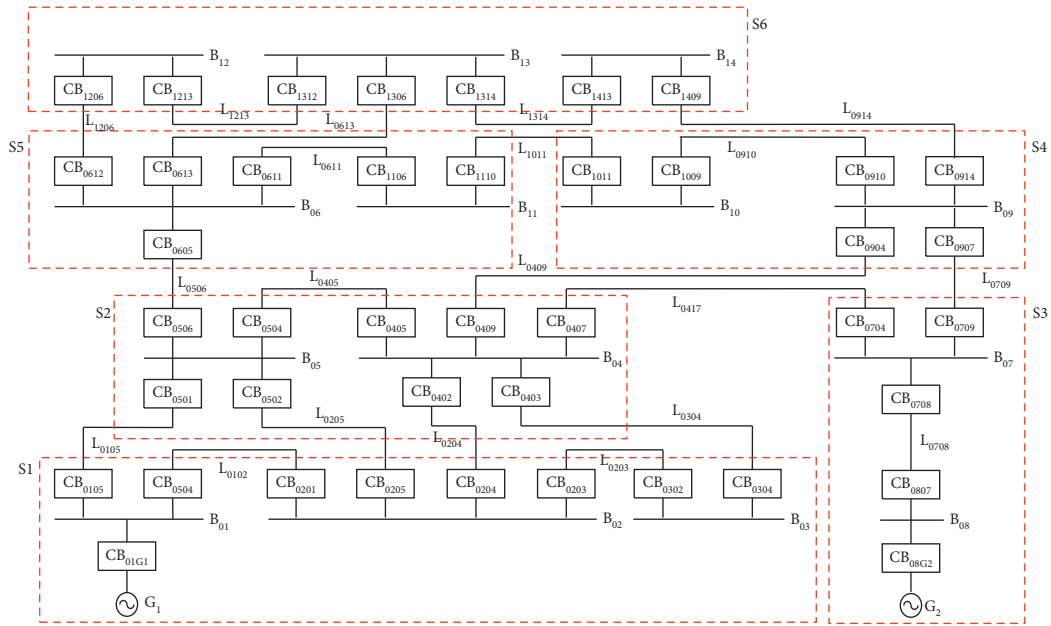


FIGURE 8: The partition result of the IEEE 14-bus system.

The self-updating vector of input neurons is

$$\boldsymbol{\varepsilon} = \begin{bmatrix} 1 & 1 & 0 & 0 & 0 & 0 & 0 & 0 \\ 0 & 0 & 0 & 0 & 0 & 1 & 0 & 0 \end{bmatrix}^T. \quad (10)$$

The pulse value vector of proposition neurons before correction is

$$\boldsymbol{\theta} = [\mathbf{O}]_{1 \times 15}^T. \quad (11)$$

The pulse value vector of proposition neurons after correction is

$$\boldsymbol{\theta} = [1 \ 1 \ \mathbf{O}_{1 \times 13}]^T. \quad (12)$$

When the SMRA stops, we get that

$$\boldsymbol{\theta} = [\mathbf{O}_{1 \times 8} \ 1 \ 0 \ 1 \ \mathbf{O}_{1 \times 4}]^T. \quad (13)$$

Now, both pulse values of output neurons σ_9 and σ_{11} are 1. Therefore, the equipment corresponding to them is faulty, i.e., L₁₂₁₃ and B₁₂ have failed.

Then, we search the PDET in Figure 5 for the fault event that “B₁₂ is faulty,” and the searching path is $P_{stMLR1213} = 1 \rightarrow P_{acMLR1213} = 1 \rightarrow R_{stCB1213} = * \rightarrow \langle 10 \rangle$, i.e., the action information of CB₁₂₁₃ is lost. The action information of protection devices of L₁₂₁₃ can be got in a similar way. Finally, we find that the action information of CB₁₂₀₆, CB₁₃₁₂, and CB₁₂₁₃ are lost. The computational work was performed in MATLAB running on a computer, and the

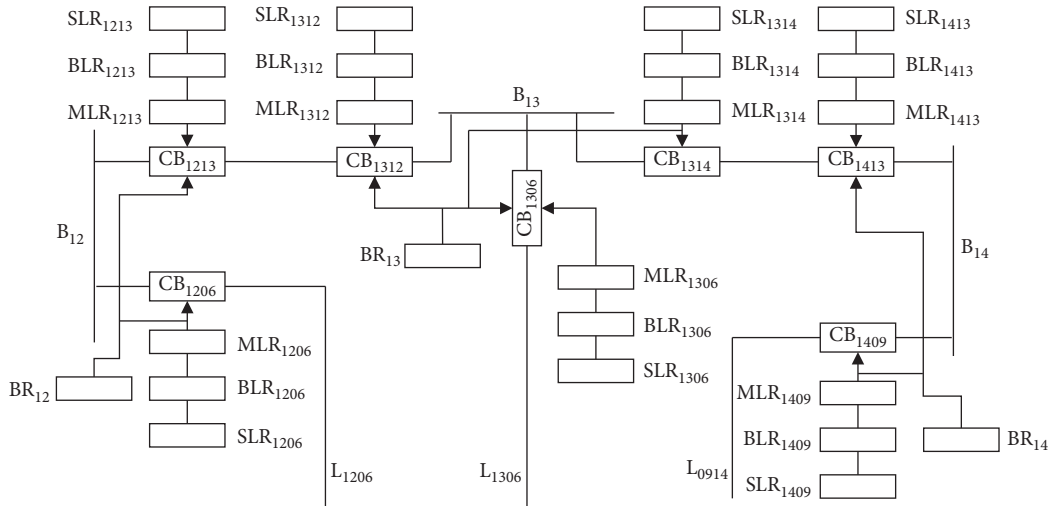


FIGURE 9: The protection configuration of S6.

TABLE 4: Fault production rule set of S6.

Number	Fault production rules
Rule 1	IF $CB_{1213} = 1$ AND $CB_{1312} = 1$ THEN L_{1213} faults
Rule 2	IF $CB_{1314} = 1$ THEN L_{1314} faults
Rule 3	IF $CB_{1206} = 1$ THEN L_{1206} faults
Rule 4	IF $CB_{0914} = 1$ THEN L_{1409} faults
Rule 5	IF $CB_{1213} = 1$ OR $CB_{1312} = 1$ THEN B_{12} faults
Rule 6	IF $CB_{1213} = 1$ AND $CB_{0613} = 1$ THEN B_{13} faults
Rule 7	IF $BR_{13} = 1$ THEN B_{13} faults
Rule 8	IF $CB_{0914} = 1$ OR $BR_{14} = 1$ THEN B_{14} faults

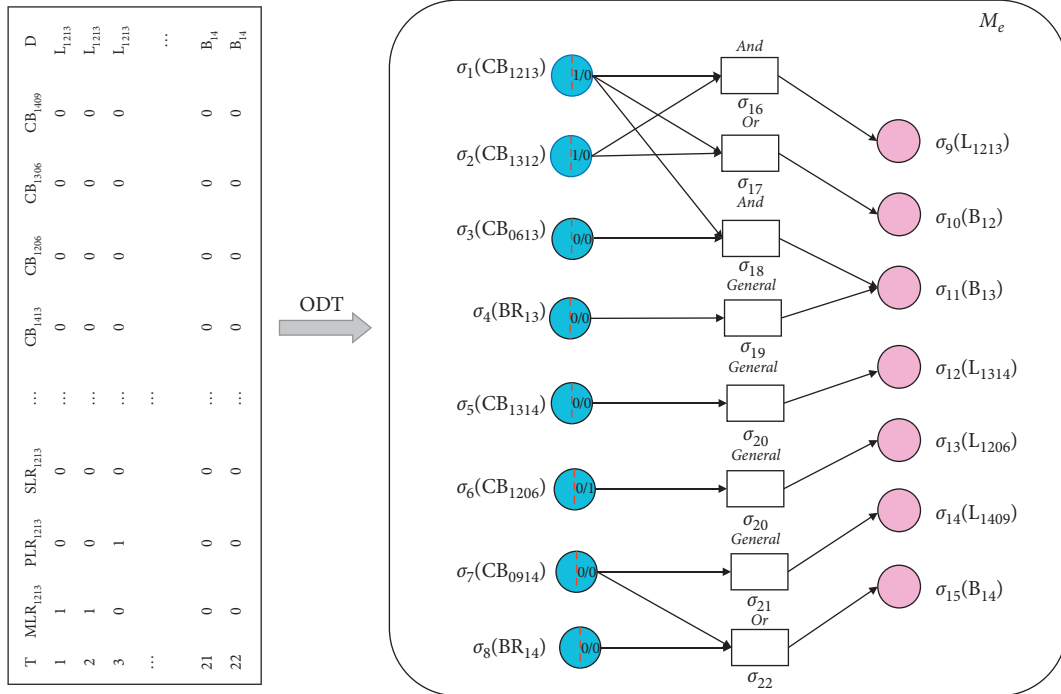


FIGURE 10: The srSNPS-based fault diagnosis model of S6.

TABLE 5: Start and action information of protective devices for case 4.

Startup information		Action information			
		PRs		CBs	
MLR ₁₂₁₃	1	MLR ₁₂₁₃	1		
BLR ₁₂₁₃	0	BLR ₁₂₁₃	0	CB ₁₂₁₃	*
SLR ₁₂₁₃	0	SLR ₁₂₁₃	0		
BR ₁₂	1	BR ₁₂	1		
MLR ₁₃₁₂	1	MLR ₁₃₁₂	1		
BLR ₁₃₁₂	0	BLR ₁₃₁₂	0	CB ₁₃₁₂	0
SLR ₁₃₁₂	0	SLR ₁₃₁₂	0		
BR ₁₃	0	BR ₁₃	0		
MLR ₁₂₀₆	0	MLR ₁₂₀₆	0	CB ₁₂₀₆	0
BLR ₁₂₀₆	0	BLR ₁₂₀₆	0		
SLR ₁₂₀₆	0	SLR ₁₂₀₆	0	CB ₀₆₁₂	1
BR ₁₂	1	BR ₁₂	1		

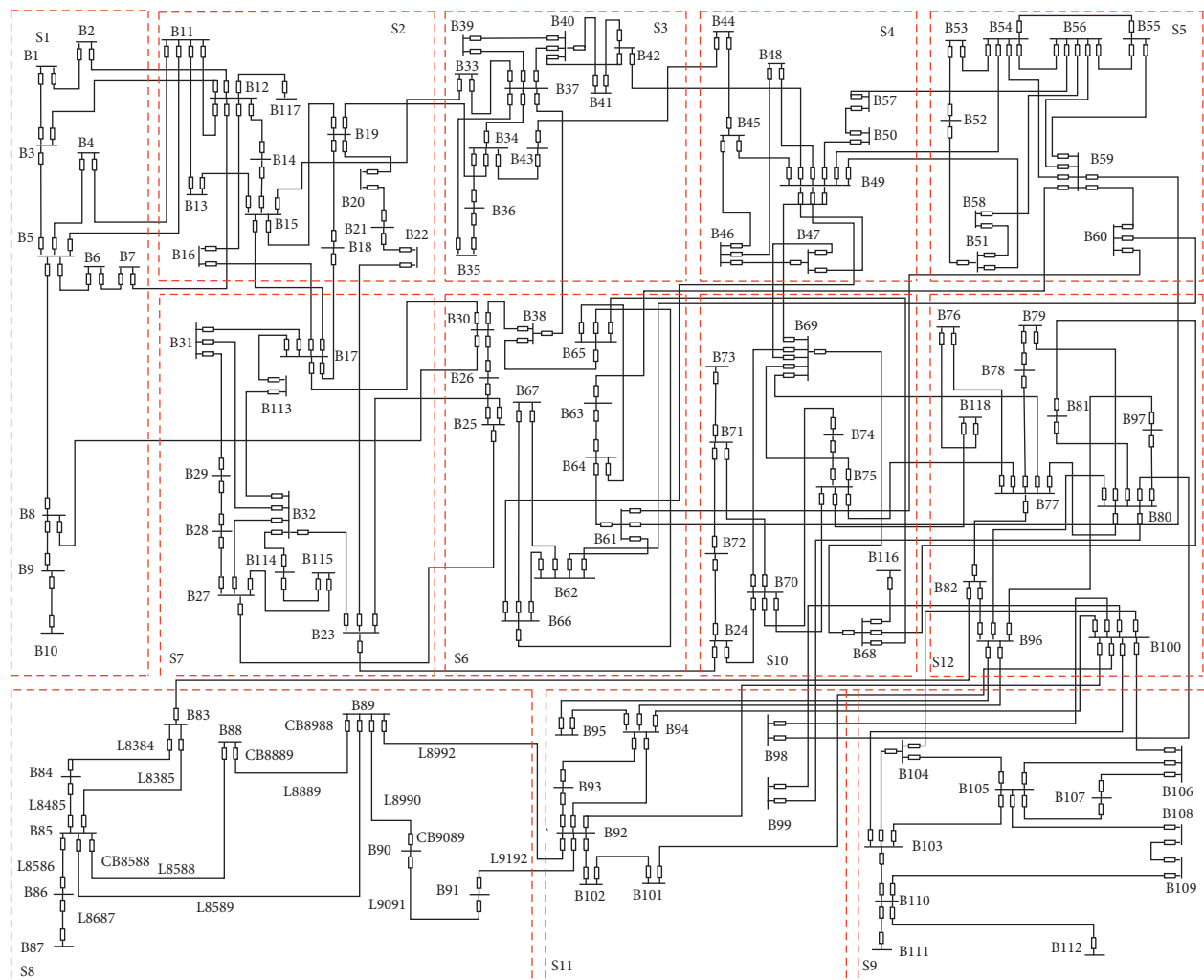


FIGURE 11: The partition result of the IEEE 118-bus system.

computing time is 0.001675 s. The computer was equipped with an Intel® Core™ i7-6700 @ 3.40 GHz CPU, 32.0 G RAM and 64 bit Windows 7 operating system.

4.2. *IEEE 118-Bus System.* The IEEE 118-bus system is complex, and it has 118 buses, 180 lines, 360 circuit breakers, 360

line main protective relays, 360 line first backup protective relays, 360 line second backup protective relays, and 236 bus protective relays. The system is divided into 12 subnetworks, as shown in Figure 11. For this system, ten typical cases are considered to do the comparison tests for the proposed method, CEN, FPN, and FRSNPS. The results are shown in Table 6.

TABLE 6: Comparisons of diagnosis results between the proposed method and three typical fault diagnosis methods for the 118-bus system.

Cases	Preset faults			The proposed method				
	Action information of protection devises PRs	CBs	Faulty equipment	CEN [2]	FPN [18]	FRSNPS [36]	Diagnosis results	Information evaluation
1	MLR ₈₃₈₄ , MLR ₈₄₈₃ , BR ₈₃	CB ₈₄₈₃ , CB ₈₃₈₅ , CB ₈₃₈₂	L ₈₃₈₄ B ₈₃	L ₈₃₈₄ B ₈₃	L ₈₃₈₄ B ₈₃	L ₈₃₈₄ B ₈₃	L ₈₃₈₄ B ₈₃	Lost information: CB ₈₃₈₄
2	BLR ₈₃₈₄ , BLR ₈₄₈₃ , BR ₈₃	CB ₈₄₈₃ , CB ₈₃₈₅ , CB ₈₃₈₂	L ₈₃₈₄ B ₈₃	L ₈₃₈₄ B ₈₃	B ₈₃	L ₈₃₈₄ B ₈₃	L ₈₃₈₄ B ₈₃	Lost information: CB ₈₃₈₄
3	BLR ₈₃₈₄ , BR ₈₃	CB ₈₃₈₄ , CB ₈₃₈₅ , CB ₈₃₈₂	L ₈₃₈₄ B ₈₃	B ₈₃	B ₈₃	B ₈₃	L ₈₃₈₄ B ₈₃	Lost information: BLR ₈₄₈₃ CB ₈₄₈₃
4	BR ₈₈ , BR ₈₉	CB ₈₈₈₅ , CB ₈₈₈₉ , CB ₈₉₈₈ , CB ₈₉₈₅	B ₈₈ B ₈₉	B ₈₈ B ₈₉	B ₈₈ B ₈₉	B ₈₈ B ₈₉	B ₈₈ B ₈₉	Lost information: CB ₈₉₉₀ , CB ₈₉₉₂
5	BR ₈₅	CB ₈₅₈₃ , CB ₈₅₈₉ , CB ₈₈₈₅ , CB ₈₈₈₉	B ₈₅ B ₈₈	B ₈₈	B ₈₈	B ₈₅ B ₈₈	B ₈₅ B ₈₈	Lost information: BR ₈₈ , CB ₈₅₈₄ , CB ₈₅₈₈ , CB ₈₅₆₄
6	BR ₈₈ , BR ₈₉ , BLR ₈₉₉₀ , SLR ₉₀₈₉	CB ₈₈₈₅ , CB ₈₉₉₂ , CB ₉₀₉₁	B ₈₈ B ₈₉ L ₈₉₉₀	B ₈₈	B ₈₈ L ₈₉₉₀	B ₈₈ L ₈₉₉₀	B ₈₈ B ₈₉ L ₈₉₉₀	Lost information: CB ₈₈₈₉ , CB ₈₉₈₈ , CB ₈₉₈₅ , CB ₈₉₉₀
7	—	CB ₈₈₈₅ , CB ₈₈₈₉ CB ₈₉₉₂ , CB ₉₀₉₁	B ₈₈ B ₈₉ B ₉₀	No fault	B ₈₈	B ₈₈	B ₈₈ B ₈₉ B ₉₀	Lost information: BR ₈₈ , BR ₈₉ , BR ₉₀ , CB ₈₉₈₈ , CB ₈₉₈₅ , CB ₈₉₉₀ , CB ₉₀₈₉
8	BR ₈₉ , SLR ₈₅₈₉	CB ₈₈₈₅ , CB ₈₉₉₂ , CB ₈₉₉₀ , CB ₈₅₈₉ , CB ₈₅₈₆ , CB ₉₀₈₉	B ₈₈ B ₈₉ B ₉₀ L ₈₅₈₉	No fault	No fault	B ₈₉	B ₈₈ B ₈₉ B ₉₀ L ₈₅₈₉	Lost information: BR ₈₈ , BR ₈₉ , MLR ₈₉₈₅ , CB ₈₈₈₉ , CB ₈₉₈₅ , CB ₈₉₈₈ , CB ₈₅₈₄ , CB ₈₅₈₃ , CB ₈₅₈₈ , CB ₉₀₉₁
9	—	CB ₈₈₈₅ , CB ₈₉₉₂ , CB ₈₉₉₀ , CB ₈₅₈₉ , CB ₈₅₈₆ , CB ₉₀₈₉	B ₈₈ B ₈₉ B ₉₀ L ₈₅₈₉	No fault	No fault	No fault	B ₈₈ B ₈₉ B ₉₀ L ₈₅₈₉	Lost information: BR ₈₈ , BR ₈₉ , BR ₉₀ , MLR ₈₉₈₅ , CB ₈₈₈₉ , CB ₈₉₈₅ , CB ₈₉₈₈ , CB ₈₅₈₄ , CB ₈₅₈₃ , CB ₈₅₈₈ , CB ₉₀₉₁
10	BR ₈₅ , BR ₈₉ , BLR ₈₉₈₅	CB ₈₅₈₃ , CB ₈₅₈₈ , CB ₈₅₈₄ , CB ₈₅₈₉ , CB ₈₅₈₆ , CB ₈₉₉₂ , CB ₈₉₈₅ , CB ₈₉₉₀	B ₈₅ B ₈₉ B ₉₀	B ₈₅ B ₈₉ B ₉₀ L ₈₅₈₉	B ₈₅ B ₈₉ B ₉₀ L ₈₅₈₉	B ₈₅ B ₈₉ B ₉₀ L ₈₅₈₉	B ₈₅ B ₈₉ B ₉₀	Lost information: BR ₉₀ , CB ₈₉₈₈ , CB ₈₉₈₄ , CB ₉₀₉₁ , CB ₈₅₈₈ False information: BLR ₈₅₈₉

In Table 6, cases 1–4 have faults with less information loss, while cases 5–10 have faults with serious information loss or many information errors. For cases 1 and 2, all the four methods can diagnose the right faulty equipment. For case 3, the FPN is failed, while the other three methods are successful. For case 4, only our method can diagnose the right faults and all the three other methods have missed diagnosis of faulty equipment. For case 5, CEN and FPN are failed, while the FRSNPS and the proposed method are successful. For case 6, the CEN, FPN, and FRSNPS have missed diagnosis, while the proposed method can diagnose all the right faults. When the

lost information increases, such as cases 7–9, the missed diagnosis of faulty equipment for the CEN, FPN, and FRSNPS becomes more serious, while the proposed method is still successful. Furthermore, for case 10, not only many fault alarm messages are lost but also the false information is involved. The results show that, for this case, our method is still valid, while all the other three methods misdiagnose the faults.

This is because that the redundant fault alarm information reduction ability of the apoptosis algorithm (Algorithm 1) and the false information correction ability of self-updating rules guarantee the high fault tolerance of the proposed

TABLE 7: Diagnostic accuracy of the proposed method of the IEEE 118-bus system for different κ .

κ (%)	Diagnostic accuracy		
	Uncertainty is in the RAI	Uncertainty is in the CAAI	Uncertainty is in the RAAI
1	0.9890323	0.9653048	0.9654454
3	0.9680938	0.9479018	0.9482381
5	0.9490233	0.9131209	0.9137391
7	0.9031862	0.8750283	0.8785287
9	0.8659286	0.8348030	0.8374533
10	0.8498392	0.8208349	0.8267387
20	0.6921393	0.6534890	0.6622308
30	0.5812309	0.4921039	0.5130250

method. Therefore, we can see from Table 6 that the proposed method can also obtain satisfying results for a complex system with fault information loss and information errors.

Besides, to further demonstrate the effectiveness and superiority of our proposed method, the IEEE 118-bus system is employed to do disturbed tests for different κ . The disturbed test method is the same as that of the IEEE 14-bus system, and test results are shown in Table 7. Table 7 shows that when uncertain alarm messages appear only in the RAI, the diagnostic accuracy is the highest. Besides, when the uncertain fault messages are contained in the CAAI and RAAI, the diagnostic accuracy is also high. Comparing the data in Tables 2 and 7, we find that, for the same case, the diagnostic accuracy of the IEEE 118-bus system is only 0.01 lower than that of the IEEE 14-bus system on average. Therefore, Table 7 shows that the proposed method is still feasible and effective with high diagnostic accuracy and fault tolerance for different kinds of faults for complex systems.

5. Conclusions

To reduce the error caused by historical statistic, expertise, and redundant fault information, this paper proposes a fault diagnosis method of power transmission lines based on an srSNPS, considering the biological apoptosis mechanism. The attribute reduction capacity of rough sets and the apoptosis mechanism of neurons are integrated in a system in the framework of membrane computing for the first time. The srSNPS can deal with uncertain and incomplete fault alarm messages without historical statistic and expert experience, while its apoptosis algorithm for CNs can delete the redundant fault information before modeling. This simplifies the problem complexity. Besides, the transmission network partition improves the topological adaptive ability. Case studies show that the proposed method has high diagnostic accuracy and fault tolerance with good diagnosis result interpretability and fast speed. Owing to the complexity of fault diagnosis for power systems, future work will focus on different applications, such as power plants, substations, distribution networks, integrated energy system, and cyber-physical power system considering network attacks.

Nomenclature

SCADA: Supervisory control and data acquisition

ES:	Expert system
ANN:	Artificial neural network
BN:	Bayesian network
PN:	Petri net
CEN:	Cause-effect network
OM:	Optimization method
FL:	Fuzzy logic
RS:	Rough set
SNPS:	Spiking neural P system
FRRN:	Fuzzy reasoning with real numbers
FRFN:	Fuzzy reasoning with fuzzy numbers
srSNPS:	Spiking neural P system with self-updating rules
SMRA:	Self-updating matrix reasoning algorithm
DSA:	Depth-first search algorithm
WNSM:	Weight network segmentation method
PDET:	Protection device event tree
DN:	Decision-making neuron
CN:	Condition neuron
PR:	Protective relay
CB:	Circuit breaker
PN:	Proposition neuron
RN:	Rule neuron
CIE:	Conditional information entropy
MRDT:	Minimum reduction decision table
FPRS:	Fault production rule set
ODT:	Original decision table
FPN:	Fuzzy Petri net
FRSNPS:	Fuzzy reasoning spiking neural P system
UIA:	Uncertain information ratio
RAI:	Redundant alarm information
CAAI:	Core attribute alarm information
RAAI:	Random attribute alarm information.

Data Availability

The data used to support the findings of this study are available from the corresponding author upon request.

Conflicts of Interest

All authors declare that they have no conflicts of interest.

Acknowledgments

This research was partially funded by grants from the National Natural Science Foundation of China (61703345), the

Key Fund Project of the Sichuan Provincial Education Department (18ZA0459), the Chunhui Project Foundation of the Education Department of China (Z201980), the Key Scientific Research Fund Project of Xihua University (Z17108), supported by the Open Research Subject of Key Laboratory of Fluid and Power Machinery (Xihua University), Ministry of Education (szjj2019-27), the Young Scholars Reserve Talents Support Project of Xihua University, and the Innovation Fund for Graduate Students of Xihua University (ycjj2019047).

References

- [1] Y. Zhu, L. Huo, and J. Lu, "Bayesian networks-based approach for power systems fault diagnosis," *IEEE Transactions on Power Delivery*, vol. 21, no. 2, pp. 473–477, 2018.
- [2] W.-H. Chen, "Online fault diagnosis for power transmission networks using fuzzy digraph models," *IEEE Transactions on Power Delivery*, vol. 27, no. 2, pp. 688–698, 2012.
- [3] S. Roostae, M. S. Thomas, and S. Mehfuz, "Experimental studies on impedance based fault location for long transmission lines," *Protection and Control of Modern Power Systems*, vol. 2, no. 1, pp. 169–177, 2017.
- [4] T. Wang, G. Zhang, J. Zhao, Z. He, J. Wang, and M. J. Perez-Jimenez, "Fault diagnosis of electric power systems based on fuzzy reasoning spiking neural P systems," *IEEE Transactions on Power Systems*, vol. 30, no. 3, pp. 1182–1194, 2015.
- [5] S. Wang and D. Zhao, "Research review and prospects for power grid fault diagnosis," *Automation of Electric Power System*, vol. 41, no. 19, pp. 164–175, 2017.
- [6] S. Lin, Z. He, and D. Zhao, "Review and development on fault diagnosis for power grid," *Power System Protection and Control*, vol. 38, no. 4, pp. 140–150, 2010.
- [7] Y. Cui, J. Shi, and Z. Wang, "Power system fault reasoning and diagnosis based on the improved temporal constraint network," *IEEE Transactions on Power Delivery*, vol. 31, no. 3, pp. 946–954, 2016.
- [8] Z. A. Vale and A. Machado e Moura, "An expert system with temporal reasoning for alarm processing in power system control centers," *IEEE Transactions on Power Systems*, vol. 8, no. 3, pp. 1307–1314, 1993.
- [9] D. Ma, Y. Liang, X. Zhao, R. Guan, and X. Shi, "Multi-BP expert system for fault diagnosis of powersystem," *Engineering Applications of Artificial Intelligence*, vol. 26, no. 3, pp. 937–944, 2013.
- [10] H.-J. Lee, D.-Y. Park, B.-S. Ahn, Y.-M. Park, J.-K. Park, and S. S. Venkata, "A fuzzy expert system for the integrated fault diagnosis," *IEEE Transactions on Power Delivery*, vol. 15, no. 2, pp. 833–838, 2000.
- [11] D. Thukaram, H. P. Khincha, and H. P. Vijaynarasimha, "Artificial neural network and support vector machine approach for locating faults in radial distribution systems," *IEEE Transactions on Power Delivery*, vol. 20, no. 2, pp. 710–721, 2005.
- [12] G. Rigatos, A. Piccolo, and P. Siano, "Neural network-based approach for early detection of cascading events in electric power systems," *IET Generation, Transmission & Distribution*, vol. 3, no. 7, pp. 650–665, 2009.
- [13] V. Miranda, A. R. G. Castro, and S. Lima, "Diagnosing faults in power transformers with autoassociative neural networks and mean shift," *IEEE Transactions on Power Delivery*, vol. 27, no. 3, pp. 1350–1357, 2012.
- [14] A. Flores Novelo, E. Quiles Cucarella, E. Garcia Moreno, and F. Morant Anglada, "Fault diagnosis of electric transmission lines using modular neural networks," *IEEE Latin America Transactions*, vol. 14, no. 8, pp. 3663–3668, 2016.
- [15] Z. Yongli, H. Limin, and L. Jinling, "Bayesian networks-based approach for power systems fault diagnosis," *IEEE Transactions on Power Delivery*, vol. 21, no. 2, pp. 634–639, 2006.
- [16] M. M. Mansour, M. A. A. Wahab, and W. M. Soliman, "Bayesian networks for fault diagnosis of a large power station and its transmission lines," *Electric Power Components and Systems*, vol. 40, no. 8, pp. 845–863, 2012.
- [17] B. Cai, L. Huang, and M. Xie, "Bayesian networks in fault diagnosis," *IEEE Transactions on Industrial Informatics*, vol. 13, no. 5, pp. 2227–2240, 2017.
- [18] B. Cai, Y. Liu, Q. Fan et al., "Multi-source information fusion based fault diagnosis of ground-source heat pump using Bayesian network," *Applied Energy*, vol. 114, pp. 1–9, 2014.
- [19] J. Sun, S.-Y. Qin, and Y. H. Song, "Fault diagnosis of electric power systems based on fuzzy Petri nets," *IEEE Transactions on Power Systems*, vol. 19, no. 4, pp. 2053–2059, 2004.
- [20] X. Luo and M. Kezunovic, "Implementing fuzzy reasoning Petri-net for fault section estimation," *IEEE Transactions on Power Delivery*, vol. 23, no. 2, pp. 676–685, 2008.
- [21] Y. Zhang, Y. Zhang, F. Wen et al., "A fuzzy Petri net based approach for fault diagnosis in power systems considering temporal constraints," *International Journal of Electrical Power & Energy Systems & Energy Systems*, vol. 78, pp. 215–224, 2016.
- [22] X. Tong, H. Xie, and M. Sun, "Power system fault diagnosis model based on layered Petri net considering temporal constraint checking," *Automation of Electric Power System*, vol. 37, no. 6, pp. 63–64, 2013.
- [23] X. Zhang, S. Yue, and X. Zha, "Method of power grid fault diagnosis using intuitionistic fuzzy Petri nets," *IET Generation, Transmission & Distribution*, vol. 12, no. 2, pp. 295–302, 2018.
- [24] Z. Jiang, Z. Li, N. Wu, and M. Zhou, "A Petri net approach to fault diagnosis and restoration for power transmission systems to avoid the output interruption of substations," *IEEE Systems Journal*, vol. 12, no. 3, pp. 2566–2576, 2018.
- [25] W.-H. Chen, S.-H. Tsai, and H.-I. Lin, "Fault section estimation for power networks using logic cause-effect models," *IEEE Transactions on Power Delivery*, vol. 26, no. 2, pp. 963–971, 2011.
- [26] F. Wen and Z. Han, "Fault section estimation in power systems using a genetic algorithm," *Electric Power Systems Research*, vol. 34, no. 3, pp. 165–172, 1995.
- [27] W. Guo, F. Wen, Z. Liao, L. Wei, and J. Xin, "An analytic model-based approach for power system alarm processing employing temporal constraint network," *IEEE Transactions on Power Delivery*, vol. 25, no. 4, pp. 2435–2447, 2010.
- [28] X. Lin, S. Ke, Z. Li, H. Weng, and X. Han, "A fault diagnosis method of power systems based on improved objective function and genetic algorithm-tabu search," *IEEE Transactions on Power Delivery*, vol. 25, no. 3, pp. 1268–1274, 2010.
- [29] Y. Zhang, C. Y. Chung, F. Wen, and J. Zhong, "An analytic model for fault diagnosis in power systems utilizing redundancy and temporal information of alarm messages," *IEEE Transactions on Power Systems*, vol. 31, no. 6, pp. 4877–4886, 2016.
- [30] T. Wang, S. Zeng, G. Zhang, M. J. Pérez-Jiménez, and J. Wang, "Fault section estimation of power systems with optimization spiking neural P systems," *Romanian Journal of Information Science and Technology*, vol. 18, no. 3, pp. 240–255, 2015.

- [31] J.-T. Peng, C. F. Chien, and T. L. B. Tseng, "Rough set theory for data mining for fault diagnosis on distribution feeder," *IEEE Proceedings—Generation, Transmission and Distribution*, vol. 151, no. 6, pp. 689–697, 2004.
- [32] Y. Zhang, Z. He, J. Zhao et al., "A power network fault diagnosis method based on rough set theory and naive Bayesian networks," *Power System Technology*, vol. 31, no. 1, pp. 37–43, 2007.
- [33] C.-L. Hor, P. A. Crossley, and S. J. Watson, "Building knowledge for substation-based decision support using rough sets," *IEEE Transactions on Power Delivery*, vol. 22, no. 3, pp. 1372–1379, 2007.
- [34] Q. Sun, C. Wang, Z. Wang, and X. Liu, "A fault diagnosis method of smart grid based on rough sets combined with genetic algorithm and tabu search," *Neural Computing and Applications*, vol. 23, no. 7-8, pp. 2023–2029, 2013.
- [35] R. Ghimire, C. Zhang, and K. R. Pattipati, "A rough set-theory-based fault-diagnosis method for an electric power-steering system," *IEEE/ASME Transactions on Mechatronics*, vol. 23, no. 5, pp. 2042–2053, 2018.
- [36] H. Peng, J. Wang, M. J. Pérez-Jiménez, H. Wang, J. Shao, and T. Wang, "Fuzzy reasoning spiking neural P system for fault diagnosis," *Information Sciences*, vol. 235, pp. 106–116, 2013.
- [37] G. Xiong, D. Shi, L. Zhu, and X. Duan, "A new approach to fault diagnosis of power systems using fuzzy reasoning spiking neural P systems," *Mathematical Problems in Engineering*, vol. 2013, no. 1, Article ID 815352, 13 pages, 2013.
- [38] M. Tu, J. Wang, H. Peng et al., "Application of adaptive fuzzy spiking neural P systems in fault diagnosis of power systems," *Chinese Journal of Electronics*, vol. 23, no. 1, pp. 87–92, 2014.
- [39] L. Pan, G. Păun, G. Zhang, and F. Neri, "Spiking neural P systems with communication on request," *International Journal of Neural Systems*, vol. 27, no. 8, p. 1750042, 2017.
- [40] T. Wu, A. Păun, Z. Zhang et al., "Spiking neural P systems with communication on request," *IEEE Transactions on Neural Networks and Learning Systems*, vol. 29, no. 8, pp. 3349–3360, 2018.
- [41] G. Păun, G. Rozenberg, and A. Salomaa, *The Oxford Handbook of Membrane Computing*, Oxford University Press, London, UK, 2009.
- [42] T. Wang, J. Wang, J. Ming et al., "Application of neural-like P systems with state values for power coordination of photovoltaic/battery microgrids," *IEEE Access*, vol. 6, pp. 46630–46642, 2018.
- [43] M. Ionescu, G. Păun, and T. Yokomori, "Spiking neural P systems," *Fundamenta Informaticae*, vol. 71, no. 2-3, pp. 279–308, 2006.
- [44] T. Wang, X. Wei, T. Huang et al., "Modeling fault propagation paths in power systems: a new framework based on event SNP systems with neurotransmitter concentration," *IEEE Access*, vol. 7, pp. 12798–12808, 2019.
- [45] J. Wang, J. M. Pérez-Jiménez, H. Peng, P. Shi, and M. Tu, "A fault diagnosis method of power systems based on an improved adaptive fuzzy spiking neural P systems and PSO algorithms," *Chinese Journal of Electronics*, vol. 25, no. 2, pp. 320–327, 2016.
- [46] T. Wang, G. Zhang, M. J. Pérez-Jiménez, and J. Cheng, "Weighted fuzzy reasoning spiking neural P systems: application to fault diagnosis in traction power supply systems of high-speed railways," *Journal of Computational and Theoretical Nanoscience*, vol. 12, no. 7, pp. 1103–1114, 2015.
- [47] Y. He, T. Wang, K. Huang et al., "Fault diagnosis of metro traction power systems using a modified fuzzy reasoning spiking neural P system," *Romanian Journal of Information Science and Technology*, vol. 18, no. 3, pp. 256–272, 2015.
- [48] K. Huang, T. Wang, Y. He, G. Zhang, and M. J. Pérez-Jiménez, "Temporal fuzzy reasoning spiking neural P systems with real numbers for power system fault diagnosis," *Journal of Computational and Theoretical Nanoscience*, vol. 13, no. 6, pp. 3804–3814, 2016.
- [49] T. Wang, G. Zhang, and M. J. Pérez-Jiménez, "Fuzzy membrane computing: theory and applications," *International Journal of Computers Communications & Control*, vol. 10, no. 6, pp. 144–175, 2015.
- [50] C. Tao, W. Yu, J. Wang, H. Peng, K. Chen, and J. Ming, "Fault diagnosis of power systems based on triangular fuzzy spiking neural P systems," *Bio-Inspired Computing—Theories and Applications*, vol. 618, pp. 385–398, 2017.
- [51] W. Yu, J. Wang, H. Peng et al., "Fault diagnosis of power systems using fuzzy reasoning spiking neural P systems with interval-valued fuzzy numbers," *Romanian Journal of Information Science and Technology*, vol. 1, no. 20, pp. 5–17, 2017.
- [52] H. Peng, J. Wang, J. Ming et al., "Fault diagnosis of power systems using intuitionistic fuzzy spiking neural P systems," *IEEE Transactions on Smart Grid*, vol. 9, no. 5, pp. 4777–4784, 2018.
- [53] T. Wang, X. Wei, T. Huang et al., "Cascading failures analysis considering extreme virus propagation of cyber-physical systems in smart grids," *Complexity*, vol. 2019, Article ID 7428458, 15 pages, 2019.
- [54] X. Wei, S. Gao, T. Huang, T. Wang, and W. Fan, "Identification of two vulnerability features: a new framework for electrical networks based on the load redistribution mechanism of complex networks," *Complexity*, vol. 2019, Article ID 3531209, 14 pages, 2019.
- [55] X. Wei, S. Gao, T. Huang, E. Bompard, R. Pi, and T. Wang, "Complex network-based cascading faults graph for the analysis of transmission network vulnerability," *IEEE Transactions on Industrial Informatics*, vol. 15, no. 3, pp. 1265–1276, 2019.
- [56] H. Rong, K. Yi, G. Zhang, J. Dong, P. Paul, and Z. Huang, "Automatic implementation of fuzzy reasoning spiking neural P systems for diagnosing faults in complex power systems," *Complexity*, vol. 2019, Article ID 2635714, 16 pages, 2019.
- [57] Z. Pawlak, "Rough sets and intelligent data analysis," *Information Sciences*, vol. 147, no. 1–4, pp. 1–12, 2002.
- [58] R. Jensen and Q. Shen, *Computational Intelligence and Feature Selection: Rough and Fuzzy Approaches*, Wiley-IEEE Press, Hoboken, NJ, USA, 2008.
- [59] H. Li, X. Zhou, and H. Bing, "Method to determine α in rough set model based on connection degree," *Journal of Systems Engineering and Electronics*, vol. 20, no. 1, pp. 98–105, 2009.
- [60] T. Bi, L. Jiao, Z. Yan et al., "Graph partitioning method for distributed fault section estimation system in power networks," *Automation of Electric Power System*, vol. 25, no. 16, pp. 16–21, 2001.
- [61] T. Bi, Y. Ni, C. M. Shen, and F. F. Wu, "Efficient multiway graph partitioning method for fault section estimation in large-scale power networks," *IEEE Proceedings—Generation, Transmission and Distribution*, vol. 149, no. 3, pp. 289–294, 2002.
- [62] W. Fan and Y. Liao, "Wide area measurements based fault detection and location method for transmission lines," *Protection and Control of Modern Power Systems*, vol. 4, no. 4, pp. 53–64, 2002.
- [63] A. Mohammadi, C. Yang, and Q. Chen, "Attack detection/Isolation via a secure multisensor fusion framework for cyberphysical systems," *Complexity*, vol. 2018, Article ID 1240149, 8 pages, 2018.

Research Article

Optimizing Transmit Sequence and Instrumental Variables Receiver for Dual-Function Complexity System

Yu Yao ¹, Junhui Zhao,¹ and Lenan Wu²

¹East China Jiaotong University, Nanchang, China

²Southeast University Nanjing, Nanchang, China

Correspondence should be addressed to Yu Yao; 1057604987@qq.com

Received 9 August 2019; Accepted 30 December 2019; Published 20 January 2020

Guest Editor: Francisco G. Montoya

Copyright © 2020 Yu Yao et al. This is an open access article distributed under the Creative Commons Attribution License, which permits unrestricted use, distribution, and reproduction in any medium, provided the original work is properly cited.

This correspondence deals with the joint cognitive design of transmit coded sequences and instrumental variables (IV) receive filter to enhance the performance of a dual-function radar-communication (DFRC) system in the presence of clutter disturbance. The IV receiver can reject clutter more efficiently than the match filter. The signal-to-clutter-and-noise ratio (SCNR) of the IV filter output is viewed as the performance index of the complexity system. We focus on phase only sequences, sharing both a continuous and a discrete phase code and develop optimization algorithms to achieve reasonable pairs of transmit coded sequences and IV receiver that fine approximate the behavior of the optimum SCNR. All iterations involve the solution of NP-hard quadratic fractional problems. The relaxation plus randomization technique is used to find an approximate solution. The complexity, corresponding to the operation of the proposed algorithms, depends on the number of acceptable iterations along with on and the complexity involved in all iterations. Simulation results are offered to evaluate the performance generated by the proposed scheme.

1. Introduction

Radar and wireless communication systems have always been researched independently. On the one hand, the radar system attempts to gain better target detection performance in the presence of noise interference. On the other hand, the aim of the wireless communication technique is to achieve the maximum information capacity over a noisy channel [1–3]. The works of [4–9] showed a possibility of employing the radar-communications integration concept to solve the lack of radio frequency (RF) spectrum. Efficient utilization of shared bandwidth between wireless communications and radar can be achieved by using dynamic frequency allocation. Ahmed et al. presented a joint radar-communication scheme to embed quadrature amplitude modulation (QAM-) based communication data in the radar pulses. In [10, 11], the authors developed a dual-function complexity system capable of performing radar and communication tasks. The complexity system performs both tasks by optimizing the power allocation of the diverse transmitters. The

proposed technique serves manifold communication receivers positioned in the vicinity of the complexity system. Numerous recent studies [12–14] considered that the developing concept of DFRC is secondary as the main radar task. Communication source embedding into the illumination of the radar system is realized using waveform diversity, sidelobe control, or time modulated array technique, which was studied in [13]. Hassanien et al. presented a signaling strategy for communication source embedding into the illumination of an FH-based MIMO radar system [15]. The main principle behind the signaling strategy is to embed phase modulation (PM)-based symbols by using phase rotating the FH pulses. The phase shift is implemented to each transmit FH pulse waveform of the radar system. The PM-based symbol embedding does not influence the function of the radar system, which uses the FH waveforms.

The performance of a radar system is prominently enhanced by sensibly optimizing receive filter and transmitted waveform. This optimization strategy generally copes with some problems containing the existence of signal-dependent

clutter along with signal-independent noise at the receiving end and radar signal constraint, such as similarity to a particular coded sequence. For a nonextended target hidden in the clutter interference environment, joint design of the transmission waveform and radar receiver to optimizing the signal-to-interference-and-noise ratio (SINR) were studied, considering a transmit power and a similarity constraints [16] on the transmission signal. The work of [17] developed a novel cognitive design method for the joint optimization of the phase-modulated (PM) pulse sequence and receive filter, representing a similarity between transmit waveform and a prearranged coded sequence. In [18], the authors developed novel approaches for maximizing the mean-square error of target feature estimation in the presence of clutter interference. For a nonmoving object, in [19], the authors used a frequency domain method to find an optimum energy spectral density (ESD) of the transmitted waveform and corresponding suitable receive filter and presented a synthesis technique to offer the time domain waveform. In [20], the authors considered a joint design problem to that of [19] subject to peak-to-average power ratio (PAR) and transmit power constraint. The work of [21] dealt with the joint design of constant-modulus transmit waveform and receive filter under a transmit power constraint. Some studies considered the joint optimization problem in signal-dependent and signal-independent disturbance scenarios (see, for example, [22–26]). In [24, 26], for a moving object, the unknown Doppler shift has been considered in the transmit waveform design. De Maio et al. discussed the problem of Doppler robust waveform optimization for signal-independent disturbance environment under similarity and transmit power constraint. In a signal-dependent interference environment, the work of [24] was generalized in [26] where the PAR and transmit power constraints are forced as well.

The usage of a matched filter can be considered as an ideal choice only when signal-dependent disturbance does not exist in the radar environment. The abovementioned problem can be tackled by utilizing an instrumental variables (IV) filter instead of the matched filter. The usage of the IV receive filter estimates in pulse compression radar has been distinctly presented many years ago (see, for example, [27, 28] and the references therein). The IV receiver can reject clutter more efficiently than the match filter. Furthermore, the radar waveform design related with the IV receive technique is a motivating research direction.

In this paper, we discuss the joint design problem of the probing coded sequence and IV filter for a DFRC system in the presence of signal-dependent interference, focusing on either continuous or discrete phase codes. Different from a transmit power constraint, we impose a similarity constraint to regulate several characteristics of the transmit waveform, for instance, variations in the waveform modulus and peak sidelobe level. The SCNR is considered as figure of merit. Thus, we present a reasonable coded sequence and IV receive filter, under a similarity constraint between the wanted coded sequence and a given waveform [29–31].

We develop constrained optimization techniques that consecutively enhance the SCNR. All iterations involve the

solution of NP-hard quadratic fractional problems. The relaxation plus randomization technique [30] is used to find an approximate solution. The complexity, corresponding to the operation of the proposed algorithms, depends on the number of acceptable iterations along with on and the complexity involved in all iterations. The performance of the proposed scheme is evaluated in signal-dependent interference surroundings, presenting that remarkable SCNR enhancements are achieved jointly designing the transmitted coded sequences and IV receive filter.

The organization of this paper is as follows. In Section 2, we describe the dual-function complexity system and the PM-based FH signal model. In Section 3, we introduce an IV filter for sensing receiver design. In Section 4, we formulate the constrained optimization problems for the joint design of the transmitted coded sequence and the IV filter. Moreover, we develop two successive optimization processes to produce a suitable coded sequence and IV receive filter to these problems. The simulation results demonstrating the proposed algorithms are presented in Section 5. Finally, our conclusions and directions for possible future work are drawn in Section 6.

1.1. Notation. Throughout this paper, the following notations will be used. We use boldface lowercase letters and boldface uppercase letters to denote vectors \mathbf{c} and matrices \mathbf{C} , respectively. The i th element of \mathbf{c} and the (i, k) th entry of \mathbf{C} are denoted by c_i and \mathbf{C}_{ik} , respectively. We use $(\cdot)^*$ to denote the conjugate operation, $(\cdot)^T$ to denote the transpose operation, $(\cdot)^H$ to denote the Hermitian operation, $E[\cdot]$ to denote statistical expectation, $\text{tr}(\cdot)$ to denote the trace of the square matrix argument, and $\mathbf{0}$ and \mathbf{I} to indicate the matrix with zero entries and the identity matrix, respectively. $\mathbf{A} \geq \mathbf{B}$ means that $\mathbf{A} - \mathbf{B}$ is an Hermitian positive semidefinite matrix. The set of real and complex numbers is denoted by \mathbb{R} and \mathbb{C} , respectively. The real parts of x is denoted by $\Re(x)$. The argument and the modulus of x are denoted by $\arg(x)$ and $|x|$, respectively. $\|\mathbf{x}\|$ is the Euclidean norm of the vector \mathbf{x} . $\|\mathbf{x}\|_\infty = \max_{k \in \{1, \dots, N\}} |x(k)|$ is the l_∞ norm of the vector \mathbf{x} . $|\cdot|$ denotes the determinant of a matrix. Finally, the letter $j = \sqrt{-1}$ indicates the imaginary unit.

2. Dual-Function System Configuration

We introduce the configuration for the DFRC system and the PM-based FH signal model [14]. The signal model is the special case of the quadrature amplitude modulation-(QAM-) based approach [6]. The key objective of the dual-function transmitter is to embed communication source toward the direction(s) of the communication receiver(s) as a subordinate mission without disturbing the primary mission, i.e., the radar function. We denote the FH waveform during one radar pulse as

$$\phi(t) = \sum_{q=1}^Q e^{j2\pi c_q \Delta f t} u(t - \Delta t). \quad (1)$$

In (1), $c_q, q = 1, \dots, Q$ describes the FH code and Q denotes the length of the FH code. Δf and Δt are the frequency

step and the hopping interval duration, respectively, and $u(t) = \begin{cases} 1, & 0 < t < \Delta t \\ 0, & \text{otherwise} \end{cases}$. Notice that the FH code can also be written as the multicarrier model [32]. The duration of a radar pulse can be given by $T_0 = Q\Delta t$. Consider that the FH code $c_q \in \{1, \dots, J\}$, where J describes a predefined value. Next, we discuss the PM-based information embedding strategy. Let $\{\Omega_q \in [0, 2\pi]\}$, $q = 1, \dots, Q$ be a set of Q phase symbols. Then, PM-based FH waveform can be defined as

$$s(t) = \sum_{q=1}^Q e^{j\Omega_q} e^{j2\pi c_q \Delta f t} u(t - \Delta t). \quad (2)$$

During a certain radar pulse, the PM-based FH transmit waveform is shown in Figure 1.

We consider that a phase symbol signifies B bits of binary sequence. During the i th radar pulse, the binary communication information that desires to be embedded is utilized to choose phase symbols $\Omega_q(i)$, $q = 1, \dots, Q$ from a preassigned constellation of $K = 2^B$ symbols. We consider the constellation is uniformly distributed between 0 and 2π , which can be expressed by $\mathbb{C}_{\text{PSK}} = \{0, (2\pi/K), \dots, ((K-1)2\pi/K)\}$. The PM-based FH waveform can be rewritten as

$$s(t, i) = \sum_{q=1}^Q e^{j\Omega_q(i)} e^{j2\pi c_q \Delta f t} u(t - \Delta t). \quad (3)$$

The term $\Omega_q(i) \in \mathbb{C}_{\text{PSK}}$. To simplify the discussion, we consider that a communication receiver is located at a known direction θ_c . Therefore, the received signal at the output of the communication receiver is expressed as

$$y(t, i) = \alpha_c s(t, i) + n(t, i), \quad (4)$$

where α_c describes the propagation channel coefficient. We assume that the coefficient α_c remain unchanged during the whole processing interval. $n(t, i)$ is the zero-mean white Gaussian noise with covariance δ_w^2 . At the communication receiver, it has full knowledge of the FH code c_q and the FH step Δf . Notice that we assume the communication receiver is the privacy breach for the radar system. Hassanien et al. stated similar assumption as well. Therefore, the received signals observed at the output of the communication receiver are match-filtered to the FH waveform yielding

$$\begin{aligned} r_q(i) &= \int_0^{\Delta t} y(t, i) e^{-j2\pi c_q \Delta f t} u(t - \Delta t) dt, \\ &= \alpha_c e^{-j\pi \sin \theta_c} e^{j\Omega_q(i)} + n_q(i). \end{aligned} \quad (5)$$

This implies that the communication receiver has the ability to undo $e^{-j\pi \sin \theta_c}$ before it estimates the symbol $\Omega_q(i)$. As a result, the embedded symbol $\Omega_q(i)$ can be restored from $r_q(i)$ at the output of the matched filter. It facilitates the receiver to update its direction with respect to the dual-function transmitter as well. The phase symbols that desire to be embedded can be estimated as

$$\hat{\Omega}_q(i) = \text{Angle}(r_q(i)) - \text{Angle}(\alpha_c) + 2\pi \sin \theta_c. \quad (6)$$

Once the phase shift keying (PSK) symbol has been estimated, then the receiver compares the estimates to the

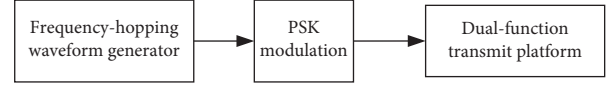


FIGURE 1: Illustrative diagram of a dual-function transmitter using FH waveform and PSK modulation.

preassigned constellation \mathbb{C}_{PSK} . It allows the receiver to determine the PM-based symbols and convert the symbols into the original binary data. Several papers proposed the PM-based DFRC system and corresponding waveform design approach (see [13] and references therein).

Since target detection is the main task of the proposed DFRC system, transmit waveform should be considered primarily based on the requirements of the radar function. Let $\mathbf{s} = [s(0), s(1), \dots, s(N-1)]^T \in \mathbb{C}^N$ be the FH-coded sequences. Let α_0 be a factor that is relative to the radar cross section (RCS) of the range bin of interest irradiated by the proposed DFRC system. Let $\{\alpha_i\}_{i=-N+1, n \neq 0}^{N-1}$ be the factors for the adjacent range bins or clutter patches. Notice that targets might exist at the adjacent range bins. $\forall i \in \{-(N-1), \dots, N-1\}$. \mathbf{J}_i denotes the $N \times N$ "shift" matrix that takes into account the fact that the clutter returning from adjacent range bins need different propagation times to reach the DFRC system receiver:

$$\mathbf{J}_i(l, m) = \begin{cases} 1, & \text{if } m - l = n \\ 0, & \text{if } m - l \neq n \end{cases}, \quad (l, m) \in \{1, \dots, N\}^2. \quad (7)$$

The target scattering signals that arrive at the receiving end of the proposed DFRC system are demodulated and analog-to-digital converted. Then, the received FH coded sequences can be denoted as

$$\mathbf{y} = \alpha_0 \mathbf{s} + \sum_{i=-N+1, n \neq 0}^{N-1} \alpha_i \mathbf{J}_i \mathbf{s} + \mathbf{n}, \quad (8)$$

where $\mathbf{y} = [y(0), y(1), \dots, y(N-1)]^T \in \mathbb{C}^N$. To simplify the analysis, we consider perfect synchronization between diverse dual-function complexity systems. The dual-function radar-communication operation is shown in Figure 2.

3. IV Receive Filter

The technique of IV can be utilized in sensing system recognition and array processing [33–36]. It is also used for sensing receiver filter design. Let an $N \times 1$ vector \mathbf{x} be the IV receive filter. Thus, the IV receive filter calculates

$$\mathbf{x}^T \mathbf{y} = \alpha_0 \mathbf{x}^T \mathbf{s} + \sum_{i=-N+1, n \neq 0}^{N-1} \alpha_i \mathbf{x}^T \mathbf{J}_i \mathbf{s}. \quad (9)$$

The signal-to-clutter ratio (SCR) at the output of the IV receive filter can be defined as

$$\text{SCR}_{\text{IV}} = \frac{|\alpha_0|^2 (\mathbf{x}^T \mathbf{s})^2}{\sum_{i=-N+1, n \neq 0}^{N-1} (\alpha_i \mathbf{x}^T \mathbf{J}_i \mathbf{s})^2} = \frac{|\alpha_0|^2 (\mathbf{x}^T \mathbf{s})^2}{\mathbf{x}^T \mathbf{R} \mathbf{x}}. \quad (10)$$

In (10), $\mathbf{R} = \sum_{i=-N+1, n \neq 0}^{N-1} |\alpha_i|^2 \mathbf{J}_i \mathbf{s} \mathbf{s}^T \mathbf{J}_i^T$. Generally, $|\mathbf{R}| \neq 0$ as presented in [37]. Let $\mathbf{R}^{1/2}$ be a symmetric square root of \mathbf{R} . Based on the Cauchy-Schwartz inequality

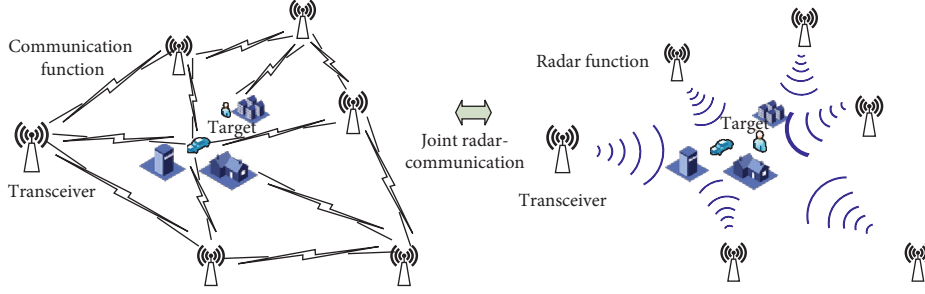


FIGURE 2: The joint communication-radar operation.

$(\mathbf{x}^T \mathbf{R}^{1/2} \mathbf{R}^{-1/2} \mathbf{s})^2 \leq (\mathbf{x}^T \mathbf{R} \mathbf{x}) (\mathbf{s}^T \mathbf{R}^{-1} \mathbf{s})$, we have $\text{SCR}_{\text{IV}}^{\circ} = \max \text{SCR}_{\text{IV}} = \mathbf{s}^T \mathbf{R}^{-1} \mathbf{s}$. The maximizing IV receive filter \mathbf{x} can be expressed by $\hat{\mathbf{x}} = \mathbf{R}^{-1} \mathbf{s}$. Clearly, we can obtain $\text{SCR}_{\text{MF}} = \text{SCR}_{\text{IV}}(\mathbf{x} = \hat{\mathbf{x}}) \leq \text{SCR}_{\text{IV}}^{\circ}$, and the equality holds if and only if \mathbf{R} is equivalent to \mathbf{I} .

The IV receive filter method is referred to as the mismatched filtering (MMF) method as well ([34, 36] and the references therein). An important phenomenon about the IV receive filter method is that $\text{SCR}_{\text{IV}}^{\circ}$ increases monotonically as the length of radar codes N increases [34]; precisely, $\text{SCR}_{\text{IV}}^{\circ}(\mathbf{s}) \leq \text{SCR}_{\text{IV}}^{\circ}(\mathbf{s}')$, where transmit waveform \mathbf{s}' denotes any coded sequence of length longer than N , which comprises \mathbf{s} among its codes. The phenomenon is exploited to increase the value of $\text{SCR}_{\text{IV}}^{\circ}$ prominently, without increasing complexity of the dual-function transmitter, by just adding zeros to coded sequence \mathbf{s} ; the IV receive filter method suggests selecting coded sequence \mathbf{s} as the solution to $\max_{\mathbf{s}} \mathbf{s}^T \mathbf{R}^{-1} \mathbf{s}$. Notice that, without solving $\max_{\mathbf{s}} \mathbf{s}^T \mathbf{R}^{-1} \mathbf{s}$, we utilize the IV receive filter instead of the matched filter to obtain a greater value of SCR for any \mathbf{s} . If the signal-independent disturbance is considered, equation (9) is rewritten as follows:

$$\mathbf{x}^T \mathbf{y} = \alpha_0 \mathbf{x}^T \mathbf{s} + 2 \sum_{i=1}^{N-1} \alpha_i \mathbf{x}^T \mathbf{J}_i \mathbf{s} + \mathbf{n}. \quad (11)$$

In (11), \mathbf{n} denotes the $N \times 1$ vector of the filtered signal-independent disturbance samples, which is assumed to be a zero-mean colored noise $E[\mathbf{n}] = 0$ and $E[\mathbf{n} \mathbf{n}^H] = \mathbf{W} > 0$. Hence, the SCR in (10) is revised to present the signal-to-clutter-and-noise ratio (SCNR) as follows:

$$\text{SCNR}_{\text{IV}} = f(\mathbf{x}, \mathbf{s}) = \frac{|\alpha_0|^2 (\mathbf{x}^T \mathbf{s})^2}{\mathbf{x}^T \mathbf{R} \mathbf{x} + \mathbf{x}^T \mathbf{W} \mathbf{x}}. \quad (12)$$

It is worth noting that the maximum value of (12) acquired by maximizing with regard to \mathbf{x} is larger than or equal to the SCNR value using a match filter [34].

4. Problem Formulations

We consider that the prior knowledge of signal-dependent and signal-independent disturbance is known on the transmitting terminal via cognitive approaches [38]. The SCNR in (12) is considered as the performance index of the proposed DFRC system [39]. Then, we intend to obtain a joint design of the transmitted waveform and the IV receive filter. As to the shape of the code, the focus is on both

continuous phase codes $|s(k)| = 1, k = 0, 1, \dots, N-1$ and discrete phase code $s(k) \in \{1, e^{j2\pi/M}, \dots, e^{j2\pi(M-1)/M}\}, k = 0, 1, \dots, N-1$. Along with the shape constraint, a similarity constraint is imposed on the coded sequence:

$$\|\mathbf{s} - \mathbf{s}_0\|^2 \leq \delta. \quad (13)$$

In (13), $\delta \geq 0$ denotes the size of the similarity region, and \mathbf{s}_0 signifies a specified coded sequence. By doing this, we can search for the good quality solution, which is similar to a given coded waveform \mathbf{s}_0 . The constrained optimization of SCNR led to a coded sequence with constant modulus variations, desired range resolution, and peak sidelobe levels. Assuming that the vector of observations \mathbf{y} is filtered through \mathbf{x} , the objective function $f(\mathbf{x}, \mathbf{s}) = (|\alpha_0|^2 (\mathbf{x}^T \mathbf{s})^2 / \mathbf{x}^T \mathbf{R} \mathbf{x} + \mathbf{x}^T \mathbf{W} \mathbf{x})$ is the SCNR at the output of the receive filter (obviously, we assume that $\mathbf{x} \neq 0$). Thus, we can formulate the joint design problem of the transmit coded sequence and the IV receive filter as the joint optimization problem:

$$\begin{aligned} \max_{\mathbf{s}, \mathbf{x}} \quad & \frac{|\alpha_0|^2 (\mathbf{x}^T \mathbf{s})^2}{\mathbf{x}^T \mathbf{R} \mathbf{x} + \mathbf{x}^T \mathbf{W} \mathbf{x}}, \\ \text{s.t.} \quad & |s(k)| = 1, \quad k = 0, 1, \dots, N-1, \\ & \|\mathbf{s} - \mathbf{s}_0\|^2 \leq \delta, \end{aligned} \quad (14)$$

for a continuous phase code and

$$\begin{aligned} \max_{\mathbf{s}, \mathbf{x}} \quad & \frac{|\alpha_0|^2 (\mathbf{x}^T \mathbf{s})^2}{\mathbf{x}^T \mathbf{R} \mathbf{x} + \mathbf{x}^T \mathbf{W} \mathbf{x}}, \\ \text{s.t.} \quad & s(k) \in \{1, e^{j2\pi/M}, \dots, e^{j2\pi(M-1)/M}\} \\ & k = 0, 1, \dots, N-1, \end{aligned} \quad (15)$$

$$k = 0, 1, \dots, N-1,$$

$$\|\mathbf{s} - \mathbf{s}_0\|^2 \leq \delta,$$

for a discrete phase code. The joint design problems (14) and (15) are nonconvex optimization problems because the objective function is a nonconvex function and the constraints $|s(k)| = 1, k = 0, 1, \dots, N-1$, and $s(k) \in \{1, e^{j2\pi/M}, \dots, e^{j2\pi(M-1)/M}\}, k = 0, 1, \dots, N-1$, define nonconvex sets. We develop sequential optimization processes, providing excellent approximate solutions for (14) and (15) with a polynomial time operational cost. The

fundamental way is to repeatedly enhance the SCNR in (12). Precisely, particularly for the IV receive filter $\mathbf{x}^{(n-1)}$ at the $(n-1)$ th iteration, we find a suitable coded sequence $\mathbf{s}^{(n)}$ at the n th iteration enhancing the SCNR with respect to $\mathbf{x}^{(n-1)}$ and $\mathbf{s}^{(n-1)}$ at the $(n-1)$ th iteration. When $\mathbf{s}^{(n)}$ is obtained, we update the sequence and find the IV receive filter $\mathbf{x}^{(n)}$ at n th iteration which enhances the SCNR with respect to $\mathbf{s}^{(n)}$ and $\mathbf{x}^{(n-1)}$ and so on. Otherwise stated, we use $\mathbf{x}^{(n)}$ and $\mathbf{s}^{(n)}$ as the initial point at the $(n+1)$ th iteration. To initiate the process, the initial filter $\mathbf{x}^{(0)}$ to a suitable coded sequence $\mathbf{s}^{(0)}$ is given. From the perspective of analysis, $\mathbf{x}^{(n)}$ denotes the optimum solution to an optimization problem, which can be expressed as

$$\max_{\mathbf{x}} \frac{|\alpha_0|^2 (\mathbf{x}^T \mathbf{s}^{(n)})^2}{\mathbf{x}^T \mathbf{R}^{(n)} \mathbf{x} + \mathbf{x}^T \mathbf{W} \mathbf{x}}. \quad (16)$$

In (16), $\mathbf{R}^{(n)} = 2 \sum_{i=1}^{N-1} |\alpha_i|^2 \mathbf{J}_i \mathbf{s}^{(n)} \mathbf{s}^{(n)T} \mathbf{J}_i^T$. According to literature [17], problem (16) is solvable. Then, for any feasible $\mathbf{s}^{(n)}$, we can obtain a closed form optimum solution $\mathbf{x}^{(n)}$. Precisely, an optimum solution to problem (14) can be written as follows:

$$\mathbf{x}^{(n)} = \frac{(\mathbf{R}^{(n)} + \delta_n^2 \mathbf{I})^{-1} \mathbf{s}^{(n)}}{\|(\mathbf{R}^{(n)} + \delta_n^2 \mathbf{I})^{-1/2} \mathbf{s}^{(n)}\|^2}, \quad (17)$$

from which the influence of phase coded sequence $\mathbf{s}^{(n)}$ on IV receive filter $\mathbf{x}^{(n)}$ is obvious. Moreover, phase coded sequence $\mathbf{s}^{(n)}$ can be expressed as

$$\mathbf{s}^{(n)} = \arg \max_{\mathbf{s} \in \{\mathbf{s}^{(n-1)}, \mathbf{s}^{(*)}\}} \frac{|\alpha_0|^2 (\mathbf{x}^{(n-1)T} \mathbf{s})^2}{\mathbf{x}^{(n-1)T} \mathbf{R} \mathbf{x}^{(n-1)} + \mathbf{x}^{(n-1)T} \mathbf{W} \mathbf{x}^{(n-1)}}. \quad (18)$$

In (18), $\mathbf{s}^{(*)}$ is a good solution of problem (19) if the focus is on (14) and a good solution of problem (19) if the focus is on (15), respectively, given by:

$$\begin{aligned} & \max_{\mathbf{s}} \frac{|\alpha_0|^2 (\mathbf{x}^{(n-1)T} \mathbf{s})^2}{\mathbf{x}^{(n-1)T} \mathbf{R} \mathbf{x}^{(n-1)} + \mathbf{x}^{(n-1)T} \mathbf{W} \mathbf{x}^{(n-1)}}, \\ & \text{s.t.} \quad |s(k)| = 1, \quad k = 0, 1, \dots, N-1, \\ & \quad \|\mathbf{s} - \mathbf{s}_0\|^2 \leq \delta, \\ & \max_{\mathbf{s}} \frac{|\alpha_0|^2 (\mathbf{x}^{(n-1)T} \mathbf{s})^2}{\mathbf{x}^{(n-1)T} \mathbf{R} \mathbf{x}^{(n-1)} + \mathbf{x}^{(n-1)T} \mathbf{W} \mathbf{x}^{(n-1)}}, \\ & \text{s.t.} \quad s(k) \in \{1, e^{j2\pi/M}, \dots, e^{j2\pi(M-1)/M}\}, \quad k = 0, 1, \dots, N-1, \\ & \quad \|\mathbf{s} - \mathbf{s}_0\|^2 \leq \delta. \end{aligned} \quad (19)$$

Based on [14], the sequential optimization technique has some properties presented in Proposition 1.

Proposition 1: Let $\{(\mathbf{s}^{(n)}, \mathbf{w}^{(n)})\}$ denote a sequence of points gained based on the sequential optimization technique, either for the continuous or the discrete phase code constraints; let $\text{SCNR}^{(n)}$ denote the value of SCNR with respect to the point $(\mathbf{s}^{(n)}, \mathbf{w}^{(n)})$ at the n th step. We obtain the following:

- (1) The sequence $\text{SCNR}^{(n)}$ is a monotonic increasing sequence and finally converges to an optimal value $\text{SCNR}^{(*)}$
- (2) Starting from the sequence $\{(\mathbf{s}^{(n)}, \mathbf{w}^{(n)})\}$, it is possible to construct another sequence $\{(\hat{\mathbf{s}}^{(n)}, \hat{\mathbf{w}}^{(n)})\}$ that converges to a feasible point $(\hat{\mathbf{s}}^{(*)}, \hat{\mathbf{w}}^{(*)})$ of problems (14) or (15), such that the SCNR evaluated in $(\hat{\mathbf{s}}^{(*)}, \hat{\mathbf{w}}^{(*)})$ is equal to $\text{SCNR}^{(*)}$

In practical terms, the sequential design process needs a situation to stop the iterations. We can find some methods to impose it, such as imposing an iteration gain constraint $|\text{SCNR}^{(n)} - \text{SCNR}^{(n-1)}| \leq \zeta$ or setting the maximum number of acceptable iterations or both use a two method, where ζ indicates the given threshold. In the following subsections, we are going to devote to the research of problems (19) and (20) in order to realize the sequential optimization processes.

4.1. Coded Sequence Design: Solution of (19). Based on [21], the SCNR in (12) can be expressed equivalently by $(|\alpha_0|^2 (\mathbf{s}^T \mathbf{x}^*)^2) / (\mathbf{s}^T \mathbf{R} \mathbf{x}^* + \mathbf{x}^T \mathbf{W} \mathbf{x})$. Then, a novel approach to obtain in polynomial time an approximate optimal solution to the NP-hard problem (19) is presented. We can equivalently reformulate problem (19) as follows:

$$\begin{aligned} & \max_{\mathbf{s}} \frac{|\alpha_0|^2 (\mathbf{s}^T \mathbf{x}^{(n-1)*})^2}{\mathbf{s}^T \mathbf{R} \mathbf{x}^{(n-1)} \mathbf{s}^* + \mathbf{x}^{(n-1)T} \mathbf{W} \mathbf{x}^{(n-1)}}, \\ & \text{s.t.} \quad |s(k)| = 1, \quad k = 0, 1, \dots, N-1, \end{aligned} \quad (20)$$

$$\|\mathbf{s} - \mathbf{s}_0\|^2 \leq \delta.$$

Observe that problem (20) is a nonconvex fractional quadratic problem [21]. Because $|s(k)| = |s_0(k)| = 1, k = 0, 1, \dots, N-1$, an equivalent expression of the similarity constraint $\max_{k \in [1, \dots, N]} |s(k) - s_0(k)| \leq \delta$ is expressed by $\Re[s^*(k) s_0(k)] \geq 1 - (\delta^2/2)$ for $k = 0, 1, \dots, N-1$, which can be equivalent to enforcing $\arg(s(k)) \in [\gamma_k, \gamma_k + \delta_c]$, where $\gamma_k = \arg(s_0(k)) - \arccos(1 - (\delta^2/2))$ and $\delta_c = 2 \arccos(1 - \delta^2/2)$ for $k = 0, 1, \dots, N-1$ [30]. Therefore, NP-hard problem (20) can be rewritten as

$$\begin{aligned} & \max_{\mathbf{s}} \frac{|\alpha_0|^2 (\mathbf{s}^T \mathbf{x}^{(n-1)*})^2}{\mathbf{s}^T \mathbf{R} \mathbf{x}^{(n-1)} \mathbf{s}^* + \mathbf{x}^{(n-1)T} \mathbf{W} \mathbf{x}^{(n-1)}}, \\ & \text{s.t.} \quad |s(k)| = 1, \quad k = 0, 1, \dots, N-1, \end{aligned}$$

$$\arg(s(k)) \in [\gamma_k, \gamma_k + \delta_c], \quad k = 0, 1, \dots, N-1.$$

(21)

Noting that (21) is generally an NP-hard problem, it is difficult to find optimal solutions for (21) with a polynomial time calculation burden. We present approximate optimization approaches and develop a semidefinite programming (SDP) relaxation and randomization technique that offers an expected feasible solution to (21). Let $\mathbf{Y} = \mathbf{x}^{(n-1)}\mathbf{x}^{(n-1)T}$ and $\mathbf{M} = \mathbf{R}(\mathbf{x}^{(n-1)})^* + (\delta_n^2/N)\|\mathbf{x}^{(n-1)}\|^2\mathbf{I}$. Therefore, the relaxed version of NP-hard problem (21), acquired ignoring the similarity constraint $\arg(s(k)) \in [\gamma_k, \gamma_k + \delta_c], k = 0, 1, \dots, N - 1$, can be expressed as

$$\begin{aligned} \max_{\mathbf{s}} \quad & \frac{|\alpha_0|^2 (\mathbf{s}^T \mathbf{x}^{(n-1)*})^2}{\mathbf{s}^T \mathbf{R} \mathbf{x}^{(n-1)} \mathbf{s}^* + \mathbf{x}^{(n-1)T} \mathbf{W} \mathbf{x}^{(n-1)}}, \\ \text{s.t.} \quad & |s(k)| = 1, \quad k = 0, 1, \dots, N - 1. \end{aligned} \quad (22)$$

The fractional quadratic problem (22) can be expressed equivalently as

$$\begin{aligned} \max_{\mathbf{x}, \mathbf{s}} \quad & \frac{\text{tr}(\mathbf{Y}\mathbf{S})}{\text{tr}(\mathbf{M}\mathbf{S})}, \\ \text{s.t.} \quad & |\mathbf{S}(k, k)| = 1, \quad k = 0, 1, \dots, N - 1, \\ & \mathbf{S} = \mathbf{s}\mathbf{s}^T. \end{aligned} \quad (23)$$

The SDP [40] of (23), acquired dropping the rank-one constraint $\mathbf{S} = \mathbf{s}\mathbf{s}^T$, can be denoted as

$$\begin{aligned} \max_{\mathbf{x}, \mathbf{s}} \quad & \frac{\text{tr}(\mathbf{Y}\mathbf{S})}{\text{tr}(\mathbf{M}\mathbf{S})}, \\ \text{s.t.} \quad & |\mathbf{S}(k, k)| = 1, \quad k = 0, 1, \dots, N - 1, \\ & \mathbf{S} > 0. \end{aligned} \quad (24)$$

According to literature [41], to find an optimal solution to (24), it is sufficient to solve the equivalent SDP problem:

$$\begin{aligned} \max_{\mathbf{x}, \mathbf{s}} \quad & \text{tr}(\mathbf{Y}\mathbf{S}), \\ \text{s.t.} \quad & \text{tr}(\mathbf{M}\mathbf{S}) = 1 \\ & \mathbf{S}(k, k) = u \\ & \mathbf{S} > 0. \end{aligned} \quad (25)$$

Let us observe that both (24) and (25) are solvable and have equivalent optimal solution; actually, if $(\hat{\mathbf{S}}, \hat{u})$ solves (25), then we can easily and clearly find out $\hat{\mathbf{S}}/\hat{u}$ is an optimal solution of (24); similarly, if $\hat{\mathbf{S}}$ solves (24), then $(\hat{\mathbf{S}}/\text{tr}(\mathbf{M}\hat{\mathbf{S}}), 1/\text{tr}(\mathbf{M}\hat{\mathbf{S}}))$ is an optimal solution of (25). Consequently, resorting to the scheme as presented in [30], we can find an expected feasible solution \mathbf{s}^* to (19) by using Algorithm 1 where the parameter L indicates the number of Randomizations.

The complexity, corresponding to the operation of Algorithm 1, is relative to the complexity required to solve a SDP problem $O(N^{3.5})$, whereas all randomizations involve $O(N^2)$ [21].

4.2. Coded Sequence Design: Solution of (20). At present, many sensing systems transmit phase coded sequences, where the phases are chosen from a finite alphabet. Consequently, we present a novel approach to obtain in polynomial time approximate optimal solutions to the NP-hard problem (20). We consider that $s_0(k) \in \{1, e^{j2\pi/M}, \dots, e^{j2\pi(M-1)/M}\}, k = 0, 1, \dots, N - 1$ where $M \geq 2$, if $M = 2$ and $\delta < 2$ and the optimal solution to (20) is the trivial one $\mathbf{s}^* = \mathbf{s}_0$. Thus, based on [21], (20) can be expressed equivalently as follows:

$$\begin{aligned} \max_{\mathbf{s}} \quad & \frac{|\alpha_0|^2 (\mathbf{s}^T \mathbf{x}^{(n-1)*})^2}{\mathbf{s}^T \mathbf{R} \mathbf{x}^{(n-1)} \mathbf{s}^* + \mathbf{x}^{(n-1)T} \mathbf{W} \mathbf{x}^{(n-1)}}, \\ \text{s.t.} \quad & s(k) \in \{1, e^{j2\pi/M}, \dots, e^{j2\pi(M-1)/M}\} \\ & k = 0, 1, \dots, N - 1, \\ & \|\mathbf{s} - \mathbf{s}_0\|_{\infty} \leq \delta. \end{aligned} \quad (26)$$

Let us observe that problem (26) is a nonconvex fractional quadratic problem as well. Since $\{s(k), s_0(k)\} \in \{1, e^{j2\pi/M}, \dots, e^{j2\pi(M-1)/M}\}^2, k = 0, 1, \dots, N - 1$, an equivalent expression of the similarity constraint $\max_{k \in \{1, \dots, N\}} |s(k) - s_0(k)| \leq \delta, k = 0, 1, \dots, N - 1$ is denoted by $\Re[s^*(k)s_0(k)] \geq 1 - (\delta^2/2)$ for $k = 0, 1, \dots, N - 1$, which in turn equals to imposing $s(k) \in \{e^{j2\pi(\beta_k/M)}, e^{j2\pi((\beta_k+1)/M)}, \dots, e^{j2\pi((\beta_k+\delta_d-1)/M)}\}$, where $\beta_k = \text{Marg}(s_0(k))/2\pi - \text{Marccos}(1 - \delta^2/2)/2\pi$ for $k = 0, 1, \dots, N - 1$ and $\delta_d = \begin{cases} 1 + 2\lceil(\arccos(1 - \delta^2/2)/2\pi)\rceil, & \delta \in [0, 2) \\ M, & \delta = 2 \end{cases}$. Therefore, NP-hard problem (26) can be rewritten as

$$\begin{aligned} \max_{\mathbf{s}} \quad & \frac{|\alpha_0|^2 (\mathbf{s}^T \mathbf{x}^{(n-1)*})^2}{\mathbf{s}^T \mathbf{R} \mathbf{x}^{(n-1)} \mathbf{s}^* + \mathbf{x}^{(n-1)T} \mathbf{W} \mathbf{x}^{(n-1)}}, \\ \text{s.t.} \quad & \arg(s(k)) \in \frac{2\pi}{M} [\beta_k, \beta_k + 1, \dots, \beta_k + \delta_d - 1] \\ & |s(k)| = 1, \quad k = 0, 1, \dots, N - 1. \end{aligned} \quad (27)$$

Notice that (21) is generally NP-hard problem as well, subsequently it is difficult to obtain polynomial time procedures for calculating optimal solutions to (21). We present approximate optimization approaches and develop a semidefinite programming (SDP) relaxation and randomization technique that offers an expected feasible solution to (27). Therefore, based on \mathbf{Y} and \mathbf{M} discussed above, making use of the similar relaxation technique as stated in (22)–(25) and resorting to the similar stages as presented in [30], we can obtain an expected feasible solution \mathbf{s}^* to (20) by using Algorithm 2.

Similar to Algorithm 1, the function of the L randomizations is to enhance the approximate capacity;

Input: The parameters $\mathbf{M}, \mathbf{Y}, L, \{\gamma_k\}, \delta_c$
Output: An approximation solution \mathbf{s}^* to Problem (19)
Step 1: Calculate the optimal solution (\mathbf{S}^*, u^*) of SDP Problem (25)
Step 2: Define $\hat{\mathbf{S}} = \mathbf{S}^*/u^*$
Step 3: Produce random vectors $(\xi)_i \in \mathbb{C}^N, i = 1, \dots, L$, from the normal distribution $N_{\mathbb{C}}(0, \mathbf{Z})$ where $\mathbf{Z} = \hat{\mathbf{S}} \odot \mathbf{z}_c \mathbf{z}_c^T$ and $\mathbf{z}_c = [e^{j\gamma_1}, \dots, e^{j\gamma_N}]^T$
Step 4: Let $(s(k))_i = y_c^*(k) \delta((\xi_k)_i), k = 1, \dots, N, i = 1, \dots, L$, where $\delta(x) = e^{(j \arg(x)/2\pi)\delta_c}, x \in \mathbb{C}$
Step 5: Calculate $t_i = (\mathbf{s}_i^T \mathbf{Y} \mathbf{s}_i / \mathbf{s}_i^T \mathbf{M} \mathbf{s}_i), i = 1, \dots, L$
Step 6: Choice the greatest value over $\{t_1, \dots, t_L\}$ say t_1 , **output** $\mathbf{s}^* = \mathbf{s}_1$

ALGORITHM 1: An approximation algorithm for the continuous phase code using the SDP relaxation technique.

Input: The parameters $\mathbf{M}, \mathbf{Y}, L, \{\beta_k\}, \delta_d, M$
Output: An approximation solution \mathbf{s}^* to Problem (20)
Step 1: Let (\mathbf{S}^*, u^*) be an optimum solution to SDP Problem (25)
Step 2: Define $\hat{\mathbf{S}} = \mathbf{S}^*/u^*$
Step 3: Produce random vectors $(\xi)_i \in \mathbb{C}^N, i = 1, \dots, L$, from the normal distribution $N_{\mathbb{C}}(0, \mathbf{W})$ where $\mathbf{W} = \hat{\mathbf{S}} \odot \mathbf{z}_d \mathbf{z}_d^T$ and $\mathbf{z}_d = [e^{j(2\pi/M)\beta_1}, \dots, e^{j(2\pi/M)\beta_N}]^T$
Step 4: Let $(s(k))_i = y_d^*(k) \delta((\xi_k)_i), k = 1, \dots, N, i = 1, \dots, L$, where $\mu(x) = \begin{cases} 1, & \text{if } \arg x \in [0, 2\pi(1/\delta_d)) \\ e^{j2\pi(1/M)}, & \text{if } \arg x \in [2\pi(1/\delta_d), 2\pi(2/\delta_d)) \\ \dots & \dots \\ e^{j2\pi((\delta_d-1)/M)}, & \text{if } \arg x \in [2\pi(\delta_d-1/\delta_d), 2\pi) \end{cases}$
Step 5: Calculate $t_i = (\mathbf{s}_i^T \mathbf{Y} \mathbf{s}_i / \mathbf{s}_i^T \mathbf{M} \mathbf{s}_i), i = 1, \dots, L$
Step 6: Choice the greatest value over $\{t_1, \dots, t_L\}$ say t_1 , **output** $\mathbf{s}^* = \mathbf{s}_1$

ALGORITHM 2: An approximation algorithm for the discrete phase code using the SDP relaxation technique.

furthermore, the overall complexity of Algorithm 2 is relative to the approximation solution of SDP relaxation $O(N^{3.5})$.

4.3. Coded Sequence-IV Receive Filter Design. We summarize the sequential optimization techniques for the coded sequence and the IV receive filter, separately, as Algorithm 3 for the continuous phase constraint and Algorithm 4 for the discrete phase constraint. To generate the iteration, an initial coded sequence $\mathbf{s}^{(0)}$, from which we can acquire the suitable IV receive filter $\mathbf{w}^{(0)}$, is necessary; a regular set is apparently $\mathbf{s}^{(0)} = \mathbf{s}_0$.

The complexity, corresponding to the operation of Algorithms 3 and 4, depends on the maximum number of acceptable iterations \hat{N} along with on and the computational complexity involved in all iterations. Specifically, the overall computational complexity is linear in regard to \hat{N} , while in all iterations, they contain the computation of the inverse of $\mathbf{R}^{(0)} + \delta_m^2 \mathbf{I}$ and the complexity effort of Algorithms 1 and 2, separately. The former is in the order of $O(N^3)$. The latter, for a reasonable number of randomizations, is relative to the complexity required to solve a SDP $O(N^{3.5})$ [21].

5. Performance Analysis

In this section, the capability provided by the constrained optimization techniques for the design of the coded sequence and the IV receiver is evaluated. Numerical results based on Monte Carlo simulations are offered to verify the effectiveness of the constrained optimization techniques. We

assume a DFRC system operating in the X-band with carrier frequency $f_c = 8.2$ GHz and bandwidth $B = 500$ MHz. The sampling frequency is $f_s = 10^9$ sample/sec. Furthermore, we assume the length of the coded sequence $N = 20$ and choose, as similarity coded sequence \mathbf{s}_0 , the N -dimensional generalized Barker codes and the M -quantized coded sequence for Algorithms 3 and 4, separately. Precisely, prearranging the coded sequence \mathbf{s} , we generate the M -quantized coded sequence \mathbf{s}^q , which is given by $s^q(k) = \bar{\mu}(s(k)), k = 1, \dots, N$, where $\bar{\mu}(x)$ is the nonlinearity, which is denoted as follows:

$$\bar{\mu}(x) = \begin{cases} 1, & \text{if } \arg x \in \left[0, 2\pi \frac{1}{M}\right), \\ e^{j2\pi(1/M)}, & \text{if } \arg x \in \left[2\pi \frac{1}{M}, 2\pi \frac{2}{M}\right), \\ \dots & \dots \\ e^{j2\pi((M-1)/M)}, & \text{if } \arg x \in \left[2\pi \frac{M-1}{M}, 2\pi\right). \end{cases} \quad (28)$$

In regard to the continuous phase code, the use of the similarity coded sequence is primarily owing to its auto-correlation properties. The explanation of the generalized Barker code has been presented in [21], which contains various length values. We consider that the randomizations in Algorithms 1 and 2 is $L = 150$. The exit condition in Algorithms 3 and 4 assumes $\xi = 10^{-5}$, viz.

Input: The parameters $\mathbf{s}_0, L, \delta, \xi, \delta_n^2$
Output: An approximate solution $(\mathbf{s}^*, \mathbf{x}^*)$ of Problem (14)
Step 1: Initialize $n = 0, \mathbf{s}^{(n)} = \mathbf{s}_0, \mathbf{x}^{(n)} = ((\mathbf{R}^{(0)} + \delta_n^2 \mathbf{I})^{-1} \mathbf{s}_0 / \|(\mathbf{R}^{(0)} + \delta_n^2 \mathbf{I})^{-1/2} \mathbf{s}_0\|^2)$, $\text{SCNR}^{(n)} = \text{SCNR}$
Step 2: **do**
Step 3: $n = n + 1$
Step 4: Let $\mathbf{Y} = \mathbf{x}^{(n-1)} \mathbf{x}^{(n-1)T}$; $\mathbf{M} = \mathbf{R}(\mathbf{x}^{(n-1)})^* + \delta_n^2 \|\mathbf{x}^{(n-1)}\|^2 \mathbf{I}$; Set $\{\gamma_k\}, \delta_c$
Step 5: Obtain an approximate optimal solution \mathbf{s}^* to (19) using Algorithm 1
Step 6: Calculate $\mathbf{s}^{(n)} = \arg \max_{\mathbf{s}} (|\alpha_0|^2 (\mathbf{x}^{(n-1)T} \mathbf{s})^2 / \mathbf{x}^{(n-1)T} \mathbf{R} \mathbf{x}^{(n-1)} + \mathbf{x}^{(n-1)T} \mathbf{W} \mathbf{x}^{(n-1)})$
Step 7: Construct $\mathbf{R}^{(n)} = \mathbf{R}(\mathbf{s}^{(n-1)}, \mathbf{s}^{(*)})$
Step 8: Calculate $\mathbf{x}^{(n)} = ((\mathbf{R}^{(n)} + \delta_n^2 \mathbf{I})^{-1} \mathbf{s}^{(n)} / \|(\mathbf{R}^{(n)} + \delta_n^2 \mathbf{I})^{-1/2} \mathbf{s}^{(n)}\|^2)$ and the SCNR value for $(\mathbf{s}^{(n)}, \mathbf{x}^{(n)})$
Step 9: Let $\text{SCNR}^{(n)} = \text{SCNR}$
Step 10: **until** $|\text{SCNR}^{(n)} - \text{SCNR}^{(n-1)}| \leq \varsigma$
Step 11: Obtain $\mathbf{s}^* = \mathbf{s}^{(n)}; \mathbf{x}^* = \mathbf{x}^{(n)}$

ALGORITHM 3: The sequential optimization Algorithm 3.

Input: The parameters $\mathbf{s}_0, L, \delta, \xi, \delta_n^2, M$
Output: An approximate solution $(\mathbf{s}^*, \mathbf{x}^*)$ of Problem (15)
Step 1: Initialize $n = 0, \mathbf{s}^{(n)} = \mathbf{s}_0, \mathbf{x}^{(n)} = ((\mathbf{R}^{(0)} + \delta_n^2 \mathbf{I})^{-1} \mathbf{s}_0 / \|(\mathbf{R}^{(0)} + \delta_n^2 \mathbf{I})^{-1/2} \mathbf{s}_0\|^2)$, $\text{SCNR}^{(n)} = \text{SCNR}$
Step 2: **do**
Step 3: $n = n + 1$
Step 4: Let $\mathbf{Y} = \mathbf{x}^{(n-1)} \mathbf{x}^{(n-1)T}$; $\mathbf{M} = \mathbf{R}(\mathbf{x}^{(n-1)})^* + \delta_n^2 \|\mathbf{x}^{(n-1)}\|^2 \mathbf{I}$; Set $\{\beta_k\}, \delta_d$
Step 5: Obtain an approximate optimal solution \mathbf{s}^* to (20) using Algorithm 2
Step 6: Calculate $\mathbf{s}^{(n)} = \arg \max_{\mathbf{s}} (|\alpha_0|^2 (\mathbf{x}^{(n-1)T} \mathbf{s})^2 / \mathbf{x}^{(n-1)T} \mathbf{R} \mathbf{x}^{(n-1)} + \mathbf{x}^{(n-1)T} \mathbf{W} \mathbf{x}^{(n-1)})$
Step 7: Construct $\mathbf{R}^{(n)} = \mathbf{R}(\mathbf{s}^{(n-1)}, \mathbf{s}^{(*)})$
Step 8: Calculate $\mathbf{x}^{(n)} = ((\mathbf{R}^{(n)} + \delta_n^2 \mathbf{I})^{-1} \mathbf{s}^{(n)} / \|(\mathbf{R}^{(n)} + \delta_n^2 \mathbf{I})^{-1/2} \mathbf{s}^{(n)}\|^2)$ and the SCNR value for $(\mathbf{s}^{(n)}, \mathbf{x}^{(n)})$
Step 9: Let $\text{SCNR}^{(n)} = \text{SCNR}$
Step 10: **until** $|\text{SCNR}^{(n)} - \text{SCNR}^{(n-1)}| \leq \varsigma$
Step 11: Obtain $\mathbf{s}^* = \mathbf{s}^{(n)}; \mathbf{x}^* = \mathbf{x}^{(n)}$

ALGORITHM 4: The sequential optimization Algorithm 4.

$|\text{SCNR}^{(n)} - \text{SCNR}^{(n-1)}| \leq 10^{-5}$. Furthermore, we assume the presence of a radar target with $|\alpha_T|^2 = 10$ dB. The performance evaluation is performed in terms of the achievable SCNR, with respect to the optimal coded sequence and IV filter, as well as the target detection probability. The convex optimization problems and SDP relaxation are solved via the MATLAB toolbox [42].

Figure 3 illustrates the value of the SCNR averaged over 250 independent repeated experiments of Algorithm 3 versus the number of acceptable iterations, for diverse values of the parameter $\delta = [0.1, 0.4, 1, 1.5, 1.7]$. In Figure 3, as the similarity constraint parameter δ increases, the maximum SCNR value enhances since the feasible set of the joint design scheme becomes greater and greater. In fact, for $\delta = 1.7$, performance gains generated by Algorithm 3 is 15 dB, as compared with 13 dB offered by the joint design approach as presented in [21], 11 dB by the cognition on transmitter only, and 10 dB by the cognition on receive filter only. Evidently, these are just theoretical results. In practical terms, the smaller value of the SCNR is observed because of various imprecisions in the obtainable observation.

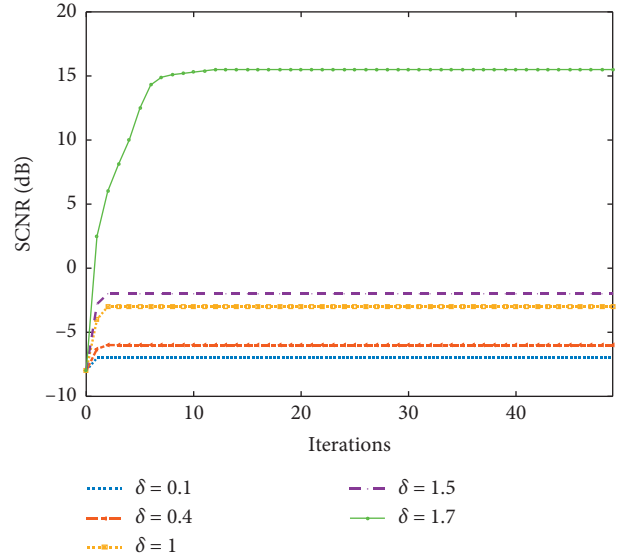


FIGURE 3: SCNR vs. number of iterations for continuous phase waveform.

Performance gains offered by Algorithm 3 converge after fifteen iterations, yielding 15 dB at $\delta = 1.7$ as compared with -2 dB at the beginning of the iteration. The performance gains of Algorithm 3 are improving as the number of iterations increases. However, there is an inappreciable amount of performance improvement after ten iterations.

Figure 4 demonstrates the value of the SCNR averaged over 250 independent repeated experiments of Algorithm 4 versus the number of acceptable iterations, for diverse values of $\delta = [0.1, 0.4, 1, 1.5, 1.7, 2]$ and the quantization levels $M = 16$. To discuss the results, we can use the similar explanations as in Figure 3. As can be seen from Figure 4, as the similarity constraint parameter δ increases, the bigger and bigger SCNR values are obtained through iterative operations, due to the enlargement of the feasible set of the joint optimization scheme. Indeed, for $\delta = 2$, performance gains generated by Algorithm 4 is 4 dB, as compared with 2 dB offered by the joint design approach as presented in [21], 1 dB by the cognition on transmitter only, and 0.5 dB by the cognition on receive filter only.

Figure 5 shows the attained average SCNR versus the number of acceptable iterations for $\delta = 2$ and several values of the number of quantization levels M ($M \in \{2, 4, 8, 16, 32\}$). We study the impacts of M on the optimized coded sequence for $\delta = 2$. As we can see from Figure 5, the result demonstrates that the greater the number of quantization levels is, the better the attained average SCNR will be until $M \geq 32$. That is to say, the better the cardinality of the alphabet, the larger the degrees of freedom obtainable in the selection of the PM-based FH codes. These results can be expected, and this is the saturation effect. The performance gains of the phase-quantized sequence offered by Algorithm 4 end up consistent with that produced by Algorithm 3.

We analyze detection performance of the optimal coded sequence and IV receive filter generated by Algorithm 3. The probability of target detection P_d versus SCNR, for some values of $\delta = [0.1, 0.5, 1, 1.5, 2, 2.5]$, is demonstrated in Figure 6. Figure 6 displays that greater the parameter δ leads to better detection performance. The result can be expected, since increasing the parameter δ results in less restriction on coded sequence and IV receive filter design, which amounts to increasing the size of the optimal solutions of the joint optimization problem.

Figure 7 describes the detection levels P_d versus SCNR, for $\delta = 1$ and the values of the number of randomizations $L \in \{1, 10, 20, 40\}$. We analyze the impact of L on P_d of the optimal coded sequence and IV receive filter offered by Algorithm 3. In Figure 7, P_d is importantly improved by enlarging the parameter L . The result is explicated through Algorithm 1, which finds the optimal coded sequence and IV receive filter assuring the excellent detection ability among all the L simulations. An indiscernible amount of capability enhancement is observed when $L \geq 10$. The detection ability is viewed acceptable. Consequently, we choose suitable value of L resulting in advisable enhancements in the detection levels.

In Figure 8, we analyze the similar performance stated in Figure 6 with regard to the detection levels P_d of the optimal

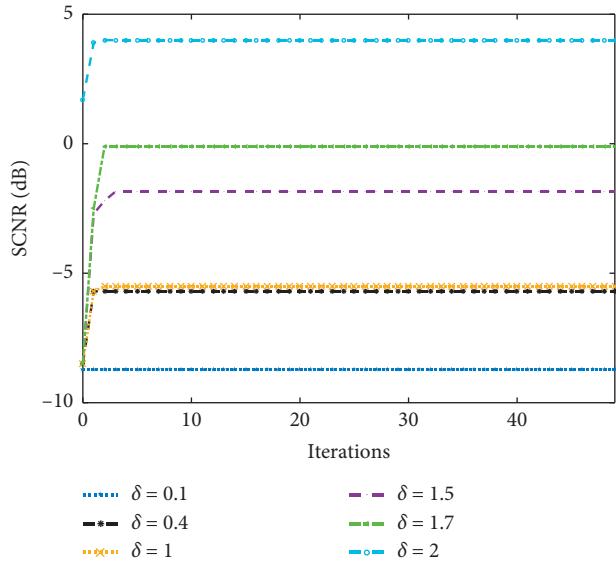


FIGURE 4: SCNR vs. number of iterations for phase quantized waveform.

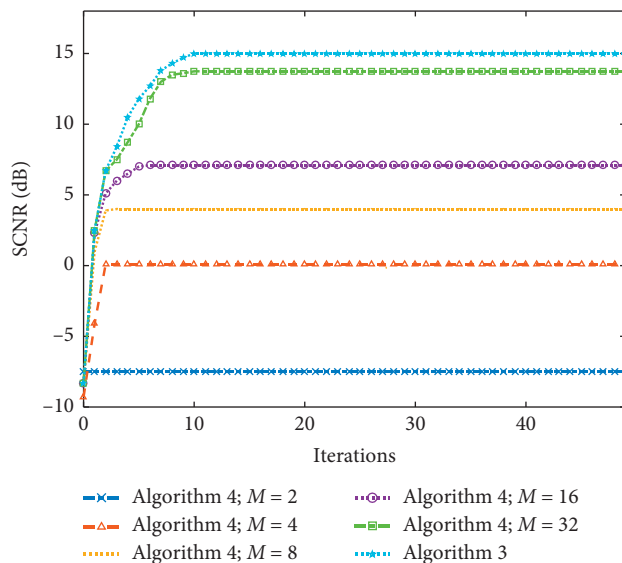


FIGURE 5: SCNR vs. number of iterations. Algorithm 4: phase quantized sequence. Algorithm 3: continuous phase sequence.

phase quantized sequence and IV receive filter provided by Algorithm 4. Figure 8 explains P_d of Algorithm 4 versus SCNR for some values of $\delta \in \{0.1, 0.5, 1, 1.5, 2, 2.5\}$ and quantization levels $M = 8$. Similar to Algorithm 3, as the value of δ becomes greater, P_d of the optimal phase-quantized sequence and IV receive filter provided by Algorithm 4 improved.

Figure 9 displays the performance of target detection P_d versus SCNR for $\delta = 1$ and several values of the number of quantization levels M ($M \in \{4, 8, 16, 32\}$). We analyze the performance of the optimal phase-quantized coded sequence and IV receive filter generated by Algorithm 4 and discuss the impact of the parameter M on the probability P_d . In Figure 9, this result demonstrates that the larger the

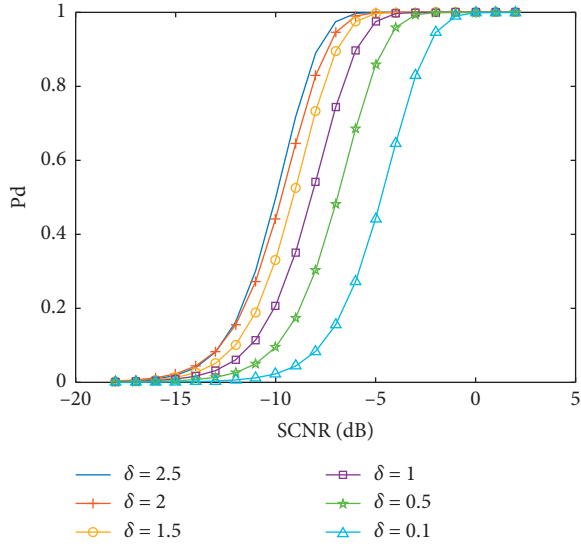


FIGURE 6: Detection probability vs. SCNR. Algorithm 3: continuous phase sequence.

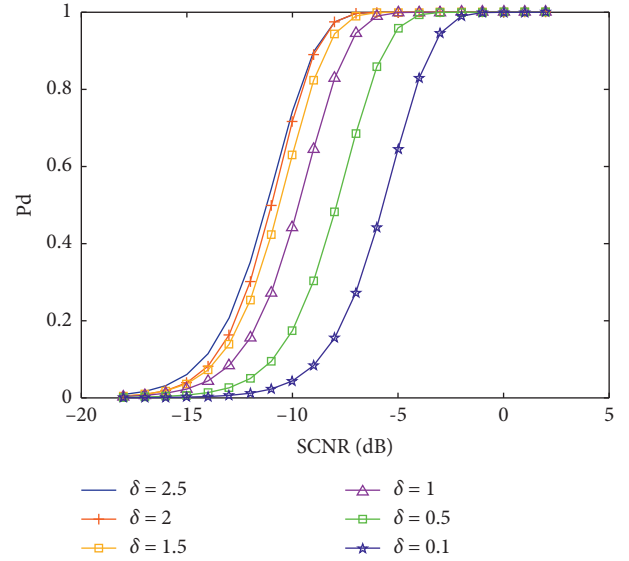


FIGURE 8: Detection probability versus SCNR. Algorithm 4: phase-quantized sequence.

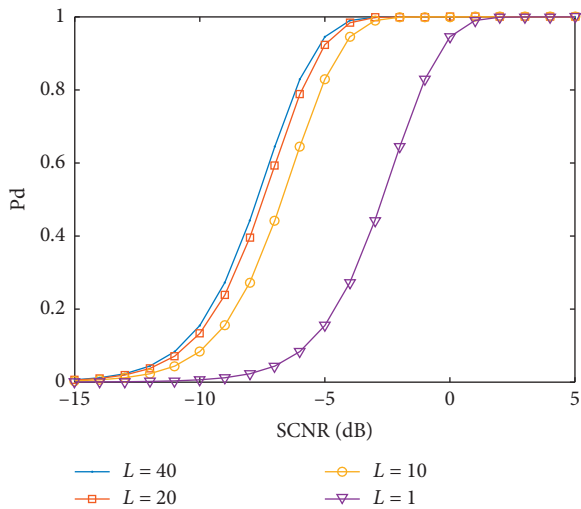


FIGURE 7: Detection probability versus SCNR. Algorithm 3 for same values of randomizations.

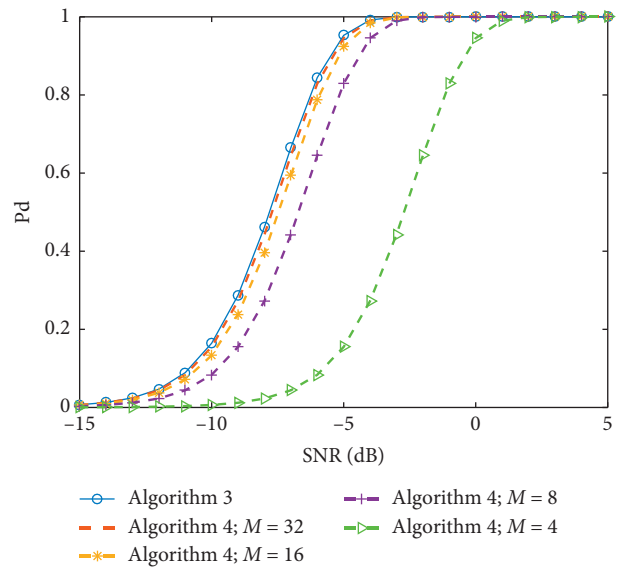


FIGURE 9: Detection probability versus SCNR. Algorithm 4: dashed curves. Algorithm 3: o-marked curve.

parameter M is, the improved the performance of target detection will be until $M \geq 8$. This conclusion is considered as the saturation effect. The performance of the optimal phase quantized coded sequence and IV receive filter generated by Algorithm 4 ends up consistent with that provided by Algorithm 3.

To implement the communication function, we assume that the FH step is $\Delta f = 10$ MHz, the length of the FH code is $Q = 20$, and the FH interval duration is $\Delta t = 0.1 \mu\text{s}$. We generate a 16 FH coded sequence. The parameter $J = 50$ is used. Therefore, the 320 FH code is generated randomly from the set $\{1, 2, \dots, J\}$, where $J = 50$.

In Figure 10, we compare the symbol error rate (SER) performance for the optimized waveform offered by Algorithm 3 with a random waveform using BPSK, QPSK, 16-PSK, and 256-PSK constellations. The data rates of the

abovementioned four types of signals are 1.2, 2.4, 4.8, and 9.6 Mbps, respectively. To investigate the SER performance, 14×10^7 random PM-based FH symbols have been generated. Figure 10 illustrates the SER performance versus SNR for BPSK, QPSK, 16-PSK, and 256-PSK constellation.

Figure 10 indicates that the SER performance of BPSK random waveform is enhanced by about 5 dB, 16 dB, and 33 dB as compared with QPSK, 16-PSK, and 256-PSK random waveform, respectively. Meanwhile, as we can see from Figure 10, for BPSK, QPSK, and 16-PSK, the SER performances of the optimized waveform offered by Algorithm 3 are as good as those of random waveform. However, for the 256-PSK, the SER performance of the optimized waveform is poor relatively. As the size of constellations

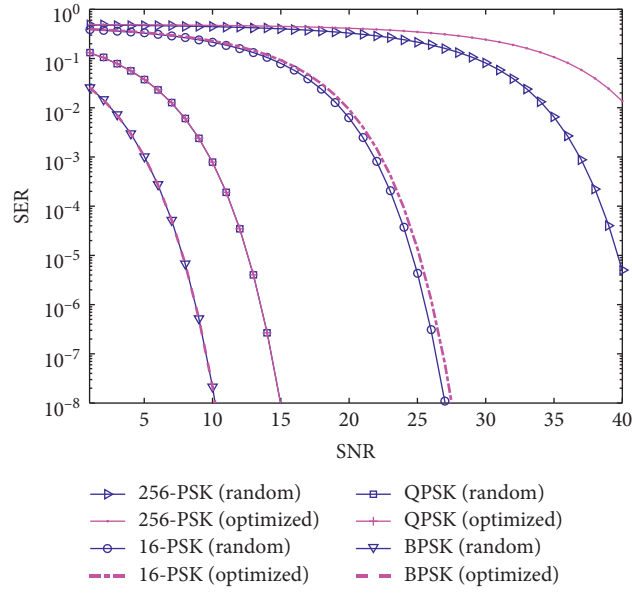


FIGURE 10: Comparative SER performance of BPSK, QPSK, 16-PSK, and 256-PSK.

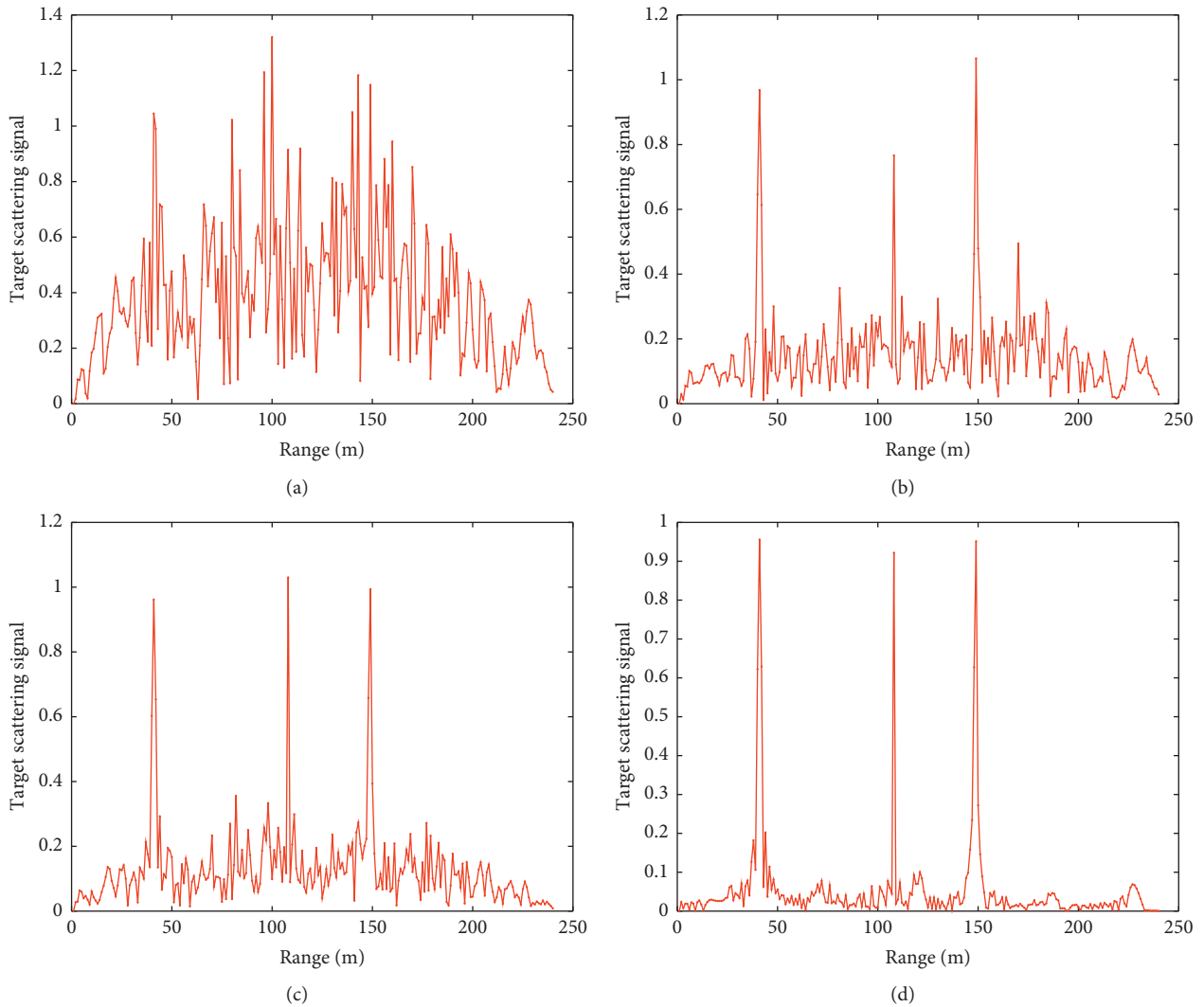


FIGURE 11: Target scattering signals profiles at (a) iteration 1, (b) iteration 5, (c) iteration 10, and (d) iteration 20, Algorithm 3.

increases, the cross correlation levels between the optimized waveform offered by Algorithm 3 becomes higher. As a result, to meet the more reasonable requirement mentioned above, we select suitable constellation size leading to a tradeoff between communication SER performance and data rate.

Transmit waveform design under a detection constraint is stated in some works [43, 44]. The problem of code optimization for target recognition in the presence of clutter interference is addressed. The purpose of the objective function is to optimize the Euclidean distance between the theoretical radar return from diverse target feature models. Moreover, the detection constraint involves that the attainable SCNR for all target feature models are greater than the given threshold.

Figure 11 indicates the detection variation of Algorithm 3 under the similarity constraint. We assume a radar scene, which has three targets. The target scattering signals derived from the radar scene is normalized and the dual-function complexity system intends to discriminate the scatterers by using a particular detection threshold.

With subsequent iterations of Algorithm 3, the detection performance of the multiple targets is enhanced. As can be seen from Figure 11, by suppressing noise, the dual-function complexity system could discriminate three scatterers effectively at the end of 20 iterations. The constrained joint optimization technique is superior to the waveform optimization scheme in [43]. By increasing the number of iterations, we can obtain more accurate estimates of the target responses, which are used to improve detection of the multiple targets.

6. Conclusions

In this paper, we developed the joint optimization design of cognitive radar waveform and IV receivers for the DFRC system. We presented a novel scheme trying to maximize the SCNR while accounting for a similarity constraint on the transmission phase code. At all iterations, the proposed processes involve the solution of both convex and NP-hard problems. In order to obtain an optimal solution, we turned to relaxation and randomization methods. The usefulness of the constrained optimization techniques was verified by offering simulation results. The capability of the proposed approaches in terms of achieved SCNR, detection levels, and detection variation of the coded sequence and IV filter pair was evaluated. In addition, pertaining to the discrete phase code, the influence of the quantization level on the radar capability was investigated. The complexity, corresponding to the operation of the proposed Algorithms, depends on the maximum number of acceptable iterations along with on and the computational complexity involved in all iterations. The dual-function complexity system could create an integrated platform for unmanned vehicle applications for which both situational awareness and construction of information links are important. Potential future study will focus on the joint design of the probing coded sequence and the corresponding IV filter bank optimizing the worst-case SCNR over the unknown number of lost return echo

samples (eclipsing conditions), under an energy constraint and a similarity constraint.

Data Availability

The MATLAB figure data used to support the findings of this study are included within the article.

Conflicts of Interest

The authors declare no conflicts of Interest.

Acknowledgments

This work was supported by the National Natural Science Foundation of China (61761019, 61861017, 61861018, and 61862024), the Natural Science Foundation of Jiangxi Province (Jiangxi Province natural Science Fund) (20181BAB211014 and 20181BAB211013), and the Foundation of Jiangxi Educational Committee of China (GJJ180352).

References

- [1] D. Ciuonzo, A. De Maio, G. Foglia, and M. Piezzo, "Intrapulse radar-embedded communications via multiobjective optimization," *IEEE Transactions on Aerospace and Electronic Systems*, vol. 51, no. 4, pp. 2960–2974, 2015.
- [2] A. R. Chiriyath, B. Paul, G. M. Jacyna, and D. W. Bliss, "Inner bounds on performance of radar and communications co-existence," *IEEE Transactions on Aerospace and Electronic Systems*, vol. 46, pp. 1185–1200, 2010.
- [3] Y. Yao, J. Zhao, and L. Wu, "Adaptive waveform design for MIMO radar-communication transceiver," *Sensors*, vol. 18, no. 6, p. 1957, 2018.
- [4] A. Hassaniien, M. G. Amin, Y. D. Zhang, and F. Ahmad, "Phase-modulation based dual-function radar-communications," *IET Radar, Sonar & Navigation*, vol. 10, no. 8, pp. 1411–1421, 2016.
- [5] Y. Yao and L. Wu, "Cognitive waveform design for radar-communication transceiver networks," *Journal of Advanced Transportation*, vol. 2018, pp. 1–11, 2018.
- [6] A. Ahmed, Y. D. Zhang, and Y. Gu, "Dual-function radar-communications using QAM-based sidelobe modulation," *Digital Signal Processing*, vol. 82, pp. 166–174, 2018.
- [7] D. W. Bliss, "Cooperative radar and communications signaling: the estimation and information theory odd couple," in *Proceedings of the IEEE Radar Conference*, pp. 50–55, Cincinnati, OH, USA, May 2014.
- [8] Z. Geng, H. Deng, and B. Himed, "Adaptive radar beamforming for interference mitigation in radar-wireless spectrum sharing," *IEEE Signal Processing Letters*, vol. 22, no. 4, pp. 484–488, 2015.
- [9] Z. Junhui, Y. Tao, G. Yi, W. Jiao, and F. Lei, "Power control algorithm of cognitive radio based on non-cooperative game theory," *China Communications*, vol. 10, no. 11, pp. 143–154, 2013.
- [10] A. Khawar, A. Abdelhadi, and C. Clancy, "Target detection performance of spectrum sharing MIMO radars," *IEEE Sensors Journal*, vol. 15, no. 9, pp. 4928–4940, 2015.
- [11] A. Ahmed, Y. D. Zhang, and B. Himed, "Distributed dual-function radar-communication MIMO system with optimized resource allocation," in *Proceedings of the IEEE Radar Conference*, Boston, MA, USA, April 2019.

- [12] A. Hassanien, M. G. Amin, Y. D. Zhang, and F. Ahmad, "Dual-function radar-communications: information embedding using sidelobe control and waveform diversity," *IEEE Transactions on Signal Processing*, vol. 64, no. 8, pp. 2168–2181, 2016.
- [13] A. Hassanien, M. G. Amin, Y. D. Zhang, and F. Ahmad, "Signaling strategies for dual-function radar communications: an overview," *IEEE Aerospace and Electronic Systems Magazine*, vol. 31, no. 10, pp. 36–45, 2016.
- [14] X. Wang, A. Hassanien, and M. G. Amin, "Dual-function MIMO radar communications system design via sparse array optimization," *IEEE Transactions on Aerospace and Electronic Systems*, vol. 55, no. 3, pp. 1213–1226, 2019.
- [15] A. Hassanien, B. Himed, and B. D. Rigling, "A dual-function MIMO radar-communications system using frequency-hopping waveforms," in *Proceedings of the 2017 IEEE Radar Conference (RadarConf)*, pp. 1721–1725, Philadelphia, PA, USA, May, 2017.
- [16] D. DeLong Jr. and E. Hofstetter, "The design of clutter-resistant radar waveforms with limited dynamic range," *IEEE Transactions on Information Theory*, vol. 15, no. 3, pp. 376–385, 1969.
- [17] A. Aubry, A. DeMaio, A. Farina, and M. Wicks, "Knowledge-aided (potentially cognitive) transmit signal and receive filter design in signal-dependent clutter," *IEEE Transactions on Aerospace and Electronic Systems*, vol. 49, no. 1, pp. 93–117, 2013.
- [18] P. Stoica, H. He, and J. Li, "Optimization of the receive filter and transmit sequence for active sensing," *IEEE Transactions on Signal Processing*, vol. 60, no. 4, pp. 1730–1740, 2011.
- [19] S. Kay, "Optimal signal design for detection of Gaussian point targets in stationary Gaussian clutter/reverberation," *IEEE Journal of Selected Topics in Signal Processing*, vol. 1, no. 1, pp. 31–41, 2007.
- [20] M. Soltanalian, B. Tang, J. Li, and P. Stoica, "Joint design of the receive filter and transmit sequence for active sensing," *IEEE Signal Processing Letters*, vol. 20, no. 5, pp. 423–426, 2013.
- [21] A. Aubry, M. Piezzo, A. De Maio, A. Farina, and M. Wicks, "Cognitive design of the receive filter and transmitted phase code in reverberating environment," *IET Radar, Sonar & Navigation*, vol. 6, no. 9, pp. 822–833, 2012.
- [22] X. Song, P. Willett, S. Zhou, and P. B. Luh, "The MIMO radar and jammer games," *IEEE Transactions on Signal Processing*, vol. 60, no. 2, pp. 687–699, 2012.
- [23] F. Gini, A. DeMaio, and L. Patton, *Waveform Design and Diversity for Advanced Radar Systems*, Institution of Engineering and Technology, London, UK, 2012.
- [24] A. De Maio, Y. Yongwei Huang, and M. Piezzo, "A Doppler robust max-min approach to radar code design," *IEEE Transactions on Signal Processing*, vol. 58, no. 9, pp. 4943–4947, 2010.
- [25] A. Aubry, A. De Maio, M. Piezzo, and A. Farina, "Radar waveform design in a spectrally crowded environment via nonconvex quadratic optimization," *IEEE Transactions on Aerospace and Electronic Systems*, vol. 50, no. 2, pp. 1138–1152, 2014.
- [26] A. De Maio, Y. Huang, M. Piezzo, S. Zhang, and A. Farina, "Design of optimized radar codes with a peak to average power ratio constraint," *IEEE Transactions on Signal Processing*, vol. 59, no. 6, pp. 2683–2697, 2011.
- [27] M. Ackroyd and F. Ghani, "Optimum mismatched filters for sidelobe suppression," *IEEE Transactions on Aerospace and Electronic Systems*, vol. AES-9, no. 2, pp. 214–218, 1973.
- [28] R. Sato and M. Shinriki, "Simple mismatched filter for binary pulse compression code with small PSL and small S/N loss," *IEEE Transactions on Aerospace and Electronic Systems*, vol. 39, no. 2, pp. 711–718, 2003.
- [29] J. Li, J. R. Guerci, and L. Xu, "Signal waveform's optimal-under-restriction design for active sensing," *IEEE Signal Processing Letters*, vol. 13, no. 9, pp. 565–568, 2006.
- [30] A. De Maio, S. De Nicola, Y. Yongwei Huang, Z. Q. Zhi-Quan Luo, and S. Shuzhong Zhang, "Design of phase codes for radar performance optimization with a similarity constraint," *IEEE Transactions on Signal Processing*, vol. 57, no. 2, pp. 610–621, 2009.
- [31] Y. Yao, J. Zhao, and L. Wu, "Frequency-hopping code design for target detection via optimization theory," *Journal of Optimization Theory and Applications*, vol. 10, pp. 1–26, 2019.
- [32] M. Bica and V. Koivunen, "Generalized multicarrier radar: models and performance," *IEEE Transactions on Signal Processing*, vol. 64, no. 17, pp. 4389–4402, 2016.
- [33] P. Stoica, J. Li, and M. Xue, "On binary probing signals and instrumental variables receivers for radar," *IEEE Transactions on Information Theory*, vol. 54, no. 8, pp. 3820–3825, 2008.
- [34] P. Stoica, J. Li, and M. Xue, "Transmit codes and receive filters for radar," *IEEE Signal Processing Magazine*, vol. 25, no. 6, pp. 94–109, 2008.
- [35] P. Stoica, M. Viberg, and B. Ottersten, "Instrumental variable approach to array processing in spatially correlated noise fields," *IEEE Transactions on Signal Processing*, vol. 42, no. 1, pp. 121–133, 1994.
- [36] P. Stoica, J. Li, and M. Xue, "Transmit codes and receive filters for pulse compression radar systems," *IEEE Signal Processing Magazine*, vol. 10, pp. 3649–3652, 2008.
- [37] J. Zhao, Q. Li, Y. Gong, and K. Zhang, "Computation off-loading and resource allocation for cloud assisted mobile edge computing in vehicular networks," *IEEE Transactions on Vehicular Technology*, vol. 68, no. 8, pp. 7944–7956, 2019.
- [38] A. Augusto, A. De Maio, and M. M. Naghsh, "Optimizing radar waveform and Doppler filter bank via generalized fractional programming," *IEEE Journal of Selected Topics in Signal Processing*, vol. 9, no. 8, pp. 1387–1399, 2015.
- [39] M. M. Naghsh, M. Soltanalian, P. Stoica, M. Modarres-Hashemi, A. De Maio, and A. Aubry, "A Doppler robust design of transmit sequence and receive filter in the presence of signal-dependent interference," *IEEE Transactions on Signal Processing*, vol. 62, no. 4, pp. 772–785, 2014.
- [40] A. Nemirovski, "Lectures on modern convex optimization," 2009, <http://www.isye.gatech.edu/faculty-staff/profile.php?entry=an63>.
- [41] A. De Maio, Y. Huang, D. P. Palomar, S. Zhang, and A. Farina, "Fractional QCQP with applications in ML steering direction estimation for radar detection," *IEEE Transactions on Signal Processing*, vol. 59, no. 1, pp. 172–185, 2011.
- [42] J. F. Sturm, "Using SeDuMi 1.02, a MATLAB toolbox for optimization over symmetric cones," *Optimization Methods and Software*, vol. 11, no. 1–4, pp. 625–653, 1999.
- [43] Y. Chen, Y. Nijssure, C. Yuen, Y. H. Chew, Z. Ding, and S. Boussakta, "Adaptive distributed MIMO radar waveform optimization based on mutual information," *IEEE Transactions on Aerospace and Electronic Systems*, vol. 49, no. 2, pp. 1374–1385, 2013.
- [44] S. Ni, J. Zhao, and Y. Gong, "Optimal pilot design in massive MIMO systems based on channel estimation," *IET Communications*, vol. 11, no. 7, pp. 975–984, 2016.

Research Article

A Hybrid Grey Prediction Model for Small Oscillation Sequence Based on Information Decomposition

Meng Zhou ¹, Bo Zeng ², and Wenhao Zhou ¹

¹National Research Base of Intelligent Manufacturing Service, Chongqing Technology and Business University, Chongqing, China

²College of Business Planning, Chongqing Technology and Business University, Chongqing, China

Correspondence should be addressed to Bo Zeng; bozeng@ctbu.edu.cn

Received 17 April 2019; Revised 8 July 2019; Accepted 11 August 2019; Published 16 January 2020

Guest Editor: Francisco G. Montoya

Copyright © 2020 Meng Zhou et al. This is an open access article distributed under the Creative Commons Attribution License, which permits unrestricted use, distribution, and reproduction in any medium, provided the original work is properly cited.

Grey prediction model has good performance in solving small data problem, and has been widely used in various research fields. However, when the data show oscillation characteristic, the effect of grey prediction model performs poor. To this end, a new method was proposed to solve the problem of modelling small data oscillation sequence with grey prediction model. Based on the idea of information decomposition, the new method employed grey prediction model to capture the trend characteristic of complex system, and ARMA model was applied to describe the random oscillation characteristic of the system. Crops disaster area in China was selected as a case study and the relevant historical eight-year data published by government department were substituted to the proposed model. The modelling results of the new model were compared with those of other traditional mainstream prediction models. The results showed that the new model had evidently superior performance. It indicated that the proposed model will contribute to solve small oscillation problems and have positive significance for improving the applicability of grey prediction model.

1. Introduction

Big data technology is a computational strategy and method for processing large data sets. It is based on large data and has gradually become a research hotspot in recent years. However, sometimes it is difficult to obtain large data. Due to technological capabilities or historical reasons, there are still many small data, such as unconventional energy production, short-term traffic flow, sulfur dioxide emissions, crops disaster area, and so on [1–4]. The above problems show that there are many grey systems in the real world, and the data of these grey systems are limited. Big data technology can not effectively describe the grey system from the small data.

Grey prediction model is a useful method to study uncertain systems with partly known information and partly unknown information [5, 6]. At present, there are mainly two kinds of sequences suitable for grey prediction model, one is monotone sequence [7–10], the other is a sequence with saturated “S” shape [11–13]. For other sequences, such as oscillation sequence or fluctuation sequence, the performance of grey prediction model is poor. However, the real world is complex. The monotonic sequence and the saturated S-shaped

sequence are only two special cases, and more sequences show oscillation characteristic [14–16]. Therefore, how to reasonably construct a grey prediction model to model with oscillation sequence has become a research trend.

Currently, grey prediction model has made some achievements in modelling with oscillation sequence. These studies are mainly manifested in the following three aspects: (a) increasing smoothness of oscillating sequences: the poor smoothness of the oscillation sequence is the main reason for the poor modelling accuracy of the oscillation sequence, so smoothing the oscillation sequence becomes a way to improve the modelling accuracy. At present, sequence smoothness is mainly improved by sequence transformation, such as smoothness operator and amplitude compression [17–20]; (b) modelling oscillation interval by envelope: from the perspective of scope, the oscillation sequence envelope is modelled. The envelope is modelled by grey prediction model, and the simulation and prediction of the oscillation sequence variation range are realized [21–23]; (c) improving the structure of grey prediction model by periodic operator: in order to adapt to periodic sequence, scholars have introduced periodic factor of triangular function and have established periodic grey

prediction model to match the periodic fluctuation of sequence and reduce modelling error [24, 25].

The above methods can improve the modelling ability of grey prediction model for oscillation sequence to a certain extent, but they still have some shortcomings. The sequence transformation method destroys the characteristics of the original sequence and can not make full use of the information transmitted by the sequence. The randomness of envelope design is too large and its generalization is weak. Grey periodic prediction model not only increases the complexity of the model structure, but also only works for periodic and regular fluctuation sequences. When the sequence has oscillation characteristic, the performance of grey periodic prediction model is poor.

The oscillation sequence is composed of different scales information, such as trend, randomness, periodicity, etc. It reflects the final result of the system under the influence of various uncertainties [26–28]. A single prediction method is suitable for modelling with a single time scale sequence. It can not simultaneously simulate and predict two or more time scale information of the oscillation sequence, which ultimately can not get intended effect.

However, preprocessing complex sequence into simpler mode, has often led to satisfactory predicting results. Empirical mode decomposition (EMD) algorithm is a multi-scale analysis method. It decomposes complex oscillation sequences into a set of sub-sequences, which contain the information of the original sequence in different time scales [29]. According to the characteristics of sub-sequences, appropriate models are selected to simulate and predict the corresponding sub-sequences. Integrating the simulated and predicted values of sub-sequences will obtain the simulated and predicted value of the original sequence.

Decomposed by EMD algorithm, the small sample oscillation sequence is usually decomposed into two sub-sequences. One part is short-time trend sub-sequence. The other is one or more random fluctuation sub-sequences. GM(1,1) model is the most classical model in grey prediction model, needs only a little data (not less than 4). It excavates the trend of system through grey generation processing, and then achieves the effect of simulating and prediction. Therefore, GM(1,1) has superior performance in modelling with small trend sub-sequence. Random fluctuation subsequence is usually modelled by ARMA model. Based on the above facts, we use GM(1,1) model and ARMA model to simulate and predict sub-sequences, respectively. According to the result of decomposition, there may be other kinds of sub-sequences, but trend and fluctuation subsequences are the most common cases. Therefore, we mainly study the general situation and specifically analyse the other situations.

In this paper, a hybrid grey model for predicting small oscillation sequence is proposed based on information decomposition. In order to verify the validity of the proposed model, we select the crops disaster area in China as the modelling object, which has small oscillation characteristics. Comparing the simulation accuracy of the new model with that of the traditional ARIMA and GM(1,1) models, the result shows that the new model is obviously superior to the traditional model, which proves the validity of the new model.

The remainder of this paper is organized as follows. In section 2, the principle of empirical mode decomposition is introduced. In Section 3, the EMD-ARMA-GM(1,1) prediction

model is proposed. In Section 4, modelling condition and testing method of model errors are studied. This is followed by comparisons of the proposed model with ARIMA and GM(1,1) model, and the proposed model is used to predict crops disaster area in China. Then, conclusions are drawn in Section 6.

A chart showing the structure of this paper is given as Figure 1.

2. Empirical Mode Decomposition Principle

Empirical mode decomposition (EMD) is a method of signal decomposition, which does not depend on prior data and completely relies on the intrinsic characteristic of the data itself. After EMD adaptively decomposed the original data according to its intrinsic characteristic, the obtained Intrinsic Mode Functions (IMFs) reflect the inherent characteristic of the data [30]. IMF satisfies the following two conditions at the same time: (i) in the whole data set, the number of extrema and the number of zero-crossings must either equal or differ at most by one; (ii) at any point, the mean value of the envelope defined by local maxima and the envelop defined by the local minima is zero [31]. The operation steps of the EMD algorithm for oscillation sequence $X(t)$ are as follows [32]:

Step 1. Recognize all the maximum points and minimum points in sequence $X(t)$, and use cubic spline interpolation function to fit all the maximum points to form the upper envelope, and then fit all the minimum points to form the lower envelope, which are marked as $E_{up}(t)$ and $E_{low}(t)$, respectively.

Step 2. In each time period t , the average of upper and lower envelopes of sequence $X(t)$ is denoted as $M_1(t)$, and is calculated as

$$M_1(t) = \frac{E_{up}(t) + E_{low}(t)}{2}. \quad (1)$$

Step 3. Minus the average envelope of sequence $X(t)$:

$$H_1(t) = X(t) - M_1(t). \quad (2)$$

If sequence $H_1(t)$ has negative local maxima and positive local minima, then $H_1(t)$ is regarded as a new original sequence $X(t)$. Repeat the above process until $H_1(t)$ satisfies the two conditions of IMF. It is denoted as $C_1(t)$, where $C_1(t) = H_1(t)$, which is called the first IMF component after decomposition of the original sequence $X(t)$.

Step 4. Sequence $C_1(t)$ is separated from the original sequence $X(t)$ and the residual component is obtained, which is denoted as $R_1(t)$, that is

$$R_1(t) = X(t) - C_1(t). \quad (3)$$

Step 5. The residual component $R_1(t)$ is regarded as a new original sequence, and the “filtering” process of Step 1 is repeated until the new IMF component can not be separated. At this time, the original sequence $X(t)$ is “filtered” by EMD algorithm to get N IMFs and one residual component, where

$$X(t) = \sum_{i=1}^N C_i(t) + R_N(t). \quad (4)$$

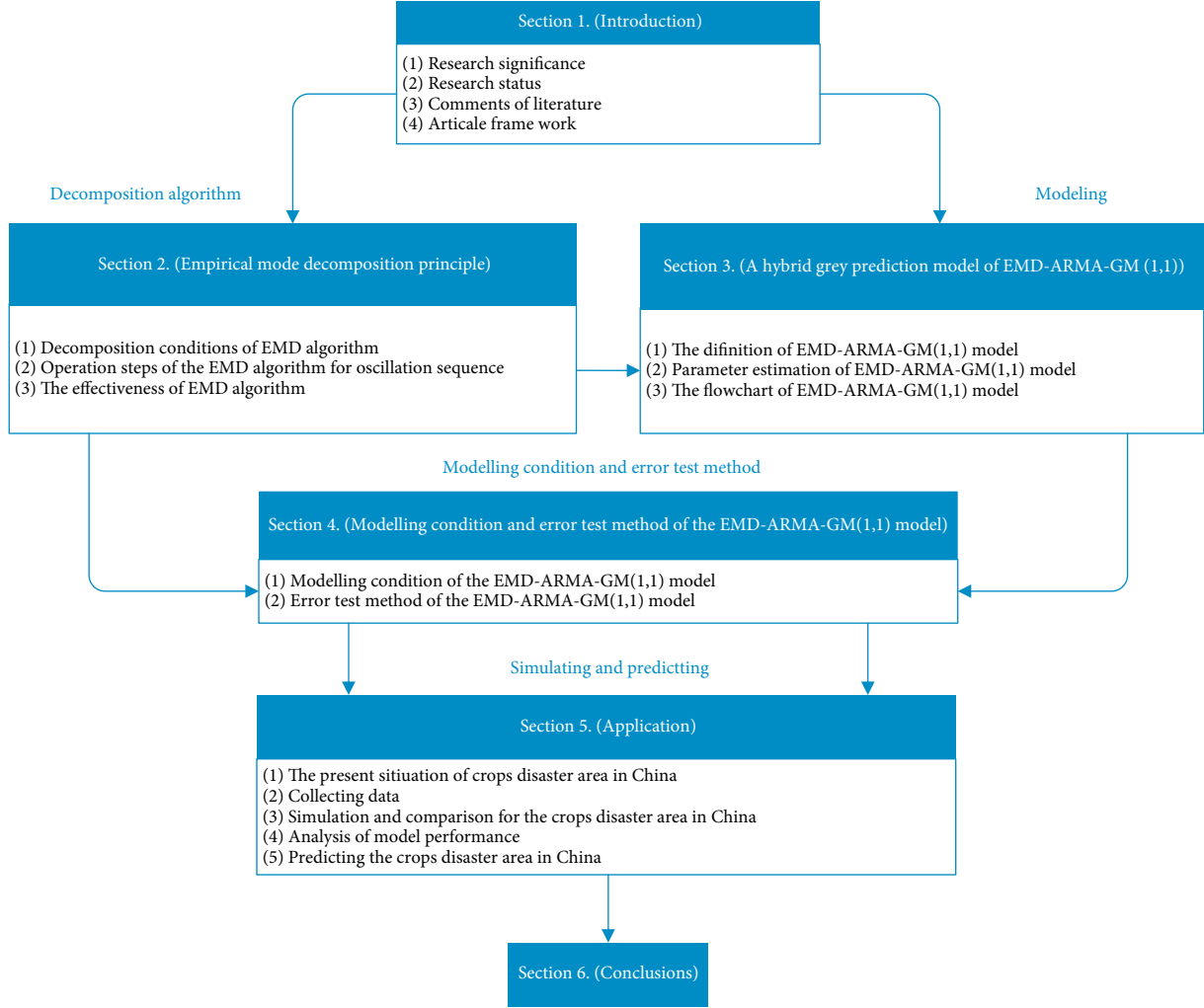


FIGURE 1: Structure of this paper.

An example of the empirical mode decomposition of an oscillating sequence is shown in Figure 2.

3. A Hybrid Grey Prediction Model of EMD-ARMA-GM(1,1)

Definition 1. Assume sequence $X = (x(1), x(2), \dots, x(n))$, $\forall k \in \{2, 3, \dots, t\}$, $\exists k' \in \{2, 3, \dots, t\}$, $x(k) - x(k-1) > 0$, $x(k') - x(k'-1) > 0$, X is called oscillation sequence.

Definition 2. Assume $C = (c(1), c(2), \dots, c(n))$ is an oscillation sequence and satisfies the following condition,

- $\forall t \in N$, $E(C^2) < \infty$;
- $\forall t \in N$, $E(C) = \mu$, μ is a constant;
- $\forall t, s \in N$, $Cov(c(t), c(s)) = \gamma_{t-s}$, γ_{t-s} is independence with t ,

then C is a stationary oscillation sequence.

Definition 3. Assume $X = (x(1), x(2), \dots, x(n))$ is an oscillation sequence,

$$C_i = (c_i(1), c_i(2), \dots, c_i(n)), \quad i = 1, 2, \dots, N, \quad (5)$$

$$R_N = (r_N^{(0)}(1), r_N^{(0)}(2), \dots, r_N^{(0)}(n)) \quad (6)$$

are IMFs and residual components of X decomposed by EMD algorithm, respectively. Then

$$\hat{c}_i(t) = \sum_{k=1}^p \phi_i(k)c_i(t-k) + a_t - \sum_{N=1}^q \theta_i(k)a_i(t-k), \quad a \sim N(0, \sigma^2) \quad (7)$$

is called ARMA (p, q) model. When $t = 2, 3, \dots, n$, $\hat{c}_i^{(0)}(t)$ is called the simulated data. When $t = n+1, n+2, \dots$, $\hat{c}_i^{(0)}(t)$ is called the predicted data.

In Equation (7), C_i is a stationary oscillation sequence; p is the ACF tail order of sequence C_i and q is the PACF tail order of C_i ; $\phi_i(1), \dots, \phi_i(p), \theta_i(1), \dots, \theta_i(q)$ are real parameters and be estimated by identification function ARMAX.

Definition 4. Assume sequence R_N is stated as
Definition 3. $R_N^{(1)} = (r_N^{(1)}(1), r_N^{(1)}(2), \dots, r_N^{(1)}(n))$ is accumulating generation sequence with one order of

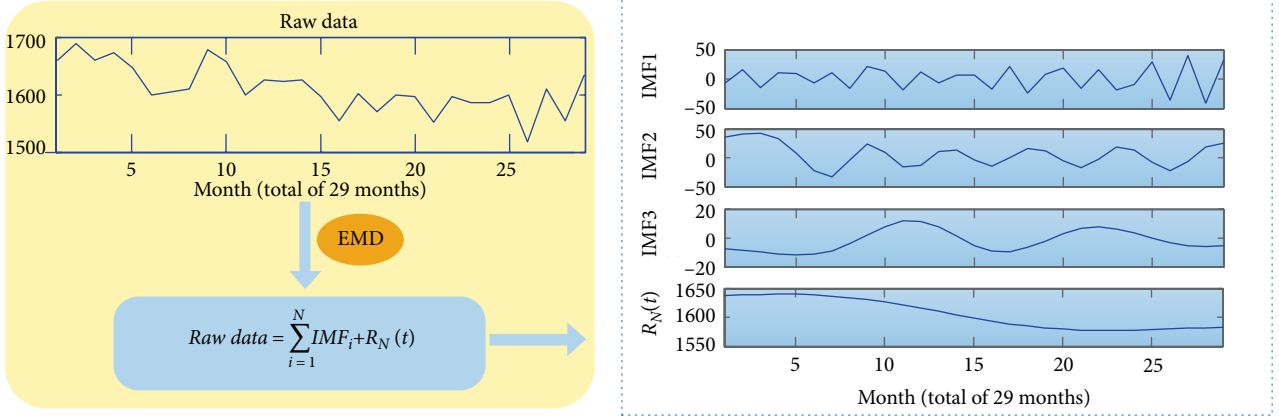


FIGURE 2: The effectiveness of EMD Algorithm.

$R_N, Z^{(1)} = (z_N^{(1)}(1), z_N^{(1)}(2), \dots, z_N^{(1)}(n))$ is mean sequence by consecutive neighbours of $R_N^{(1)}$, where

$$r_N^{(1)}(t) = \sum_{i=1}^t r_N^{(0)}(i), \quad t = 1, 2, \dots, n, \quad (8)$$

$$z_N^{(1)}(t) = 0.5 \times (r_N^{(1)}(t) + r_N^{(1)}(t-1)), \quad t = 1, 2, \dots, n. \quad (9)$$

Definition 5. Assume $R_N, R_N^{(1)}, Z^{(1)}$ are stated as Definition 3 and Definition 4. Then the following equation

$$r_N^{(0)}(t) + az_N^{(1)}(t) = b \quad (10)$$

is called GM (1,1) model, where a, b are real parameters.

Theorem 6. Assume that $P = [a, b]^T$ is parameter vector of Equation (10), where

$$Y = \begin{bmatrix} r_N^{(0)}(2) \\ r_N^{(0)}(3) \\ \vdots \\ r_N^{(0)}(n) \end{bmatrix}, \quad (11)$$

$$B = \begin{bmatrix} -z_N^{(1)}(2) & 1 \\ -z_N^{(1)}(3) & 1 \\ \vdots & \vdots \\ -z_N^{(1)}(n) & 1 \end{bmatrix},$$

then the parameters of GM(1,1) model are identified as $\hat{a} = (B^T B)^{-1} B^T Y$.

Proof. GM(1,1) model is rewritten as follows,

$$\begin{aligned} r_N^{(0)}(2) + az_N^{(1)}(2) &= b, \\ r_N^{(0)}(3) + az_N^{(1)}(3) &= b, \\ &\vdots \\ r_N^{(0)}(n) + az_N^{(1)}(n) &= b. \end{aligned} \quad (12)$$

Matrix form of GM(1,1) model is as follows,

$$\begin{bmatrix} r_N^{(0)}(2) \\ r_N^{(0)}(3) \\ \vdots \\ r_N^{(0)}(n) \end{bmatrix} = \begin{bmatrix} -z_N^{(1)}(2) & 1 \\ -z_N^{(1)}(3) & 1 \\ \vdots & \vdots \\ -z_N^{(1)}(n) & 1 \end{bmatrix} \begin{bmatrix} a \\ b \end{bmatrix}, \quad (13)$$

that is

$$Y = BP. \quad (14)$$

Among the above equations, Y and B are known and P is sequence of undetermined parameters. The number of known equations is one, and the variables are two. Moreover, when the equations are incompatible, there is no solution, but the least square solution can be obtained by the least square method (LSM).

Assume ε is error sequence as follows,

$$\varepsilon = Y - BP. \quad (15)$$

Let

$$S = \min \|Y - BP\|^2 = \min (Y - BP)^T (Y - BP), \quad (16)$$

that is

$$\begin{aligned} S &= \min \sum_{t=2}^n (r_N^{(0)}(t) - (b - az_N^{(1)}(t)))^2 \\ &= \min \left(\sum_{t=2}^n r_N^{(0)}(t)^2 + (n-1)b^2 + a^2 \sum_{t=2}^n z_N^{(1)}(t)^2 - 2b \sum_{t=2}^n r_N^{(0)}(t) \right. \\ &\quad \left. + 2a \sum_{t=2}^n z_N^{(1)}(t)r_N^{(0)}(t) - 2ab \sum_{t=2}^n z_N^{(1)}(t) \right). \end{aligned} \quad (17)$$

According to LSM, S can be minimised with respect to parameters a, b to obtain

$$\frac{\partial S}{\partial a} = 2a \sum_{t=2}^n z_N^{(1)}(t)^2 + 2 \sum_{t=2}^n z_N^{(1)}(t)r_N^{(0)}(t) - 2b \sum_{t=2}^n z_N^{(1)}(t) = 0, \quad (18)$$

$$\frac{\partial S}{\partial b} = 2(n-1)b - 2 \sum_{t=2}^n r_N^{(0)}(t) - 2a \sum_{t=2}^n z_N^{(1)}(t) = 0. \quad (19)$$

Parameters a, b can be obtained, as follows,

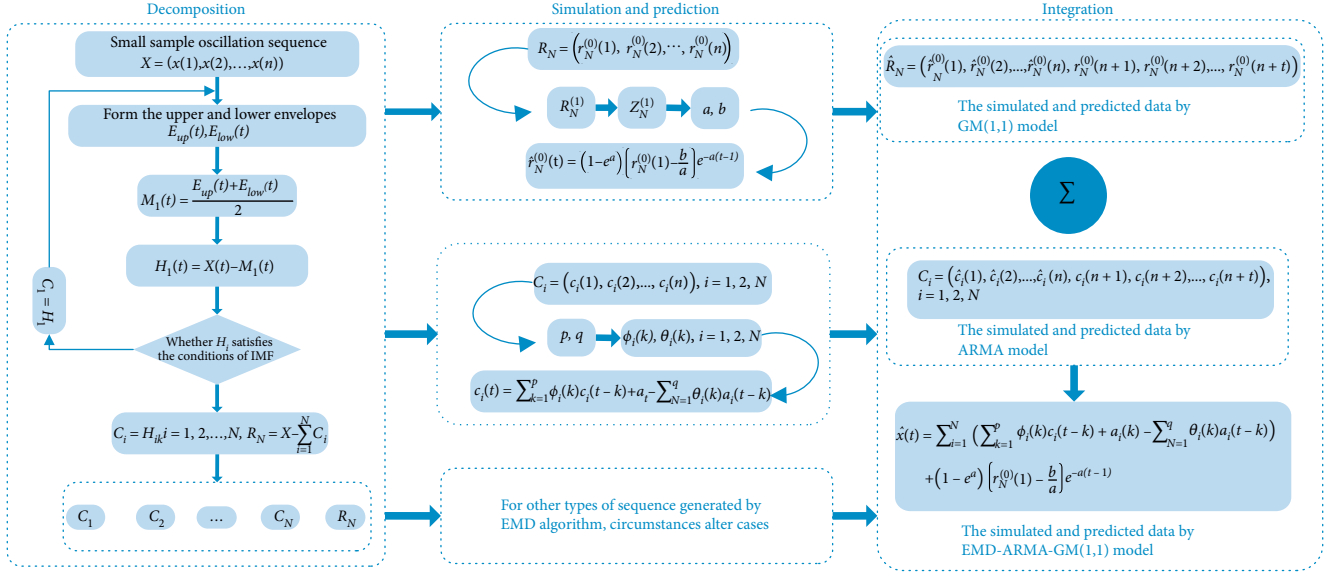


FIGURE 3: The flow chart of EMD-ARMA-GM(1,1) model.

TABLE 1: Data of crops disaster area in China from 2010 to 2017 (units: 1000 hectares).

Year	2010	2011	2012	2013	2014	2015	2016	2017
Crops disaster area	37425.9	32470.5	24962	31349.8	24890.7	21769.8	26220.7	18478.1

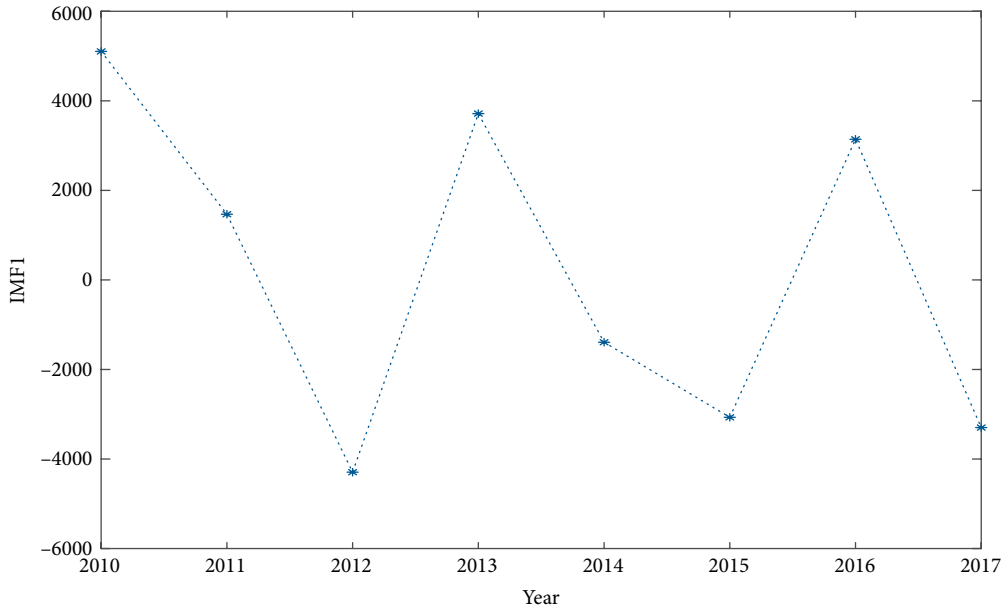
Data sources: <http://data.stats.gov.cn/easyquery.htm?cn=C01>.

FIGURE 4: The curve of IMF1.

$$a = \frac{\sum_{t=2}^n r_N^{(0)}(t) \sum_{t=2}^n z_N^{(1)}(t) - (n-1) \sum_{t=2}^n r_N^{(0)}(t) z_N^{(1)}(t)}{(n-1) \sum_{t=2}^n (z_N^{(1)}(t))^2 - \left(\sum_{t=2}^n z_N^{(1)}(t) \right)^2}, \quad (20)$$

$$b = \frac{\sum_{t=2}^n r_N^{(0)}(t) \sum_{t=2}^n (z_N^{(1)}(t))^2 - \sum_{t=2}^n z_N^{(1)}(t) \sum_{t=2}^n z_N^{(1)}(t) r_N^{(0)}(t)}{(n-1) \sum_{t=2}^n (z_N^{(1)}(t))^2 - \left(\sum_{t=2}^n z_N^{(1)}(t) \right)^2}. \quad (21)$$

Equations (20) and (21) are the expanded displays of parameter identification matrix. The proof is over. \square

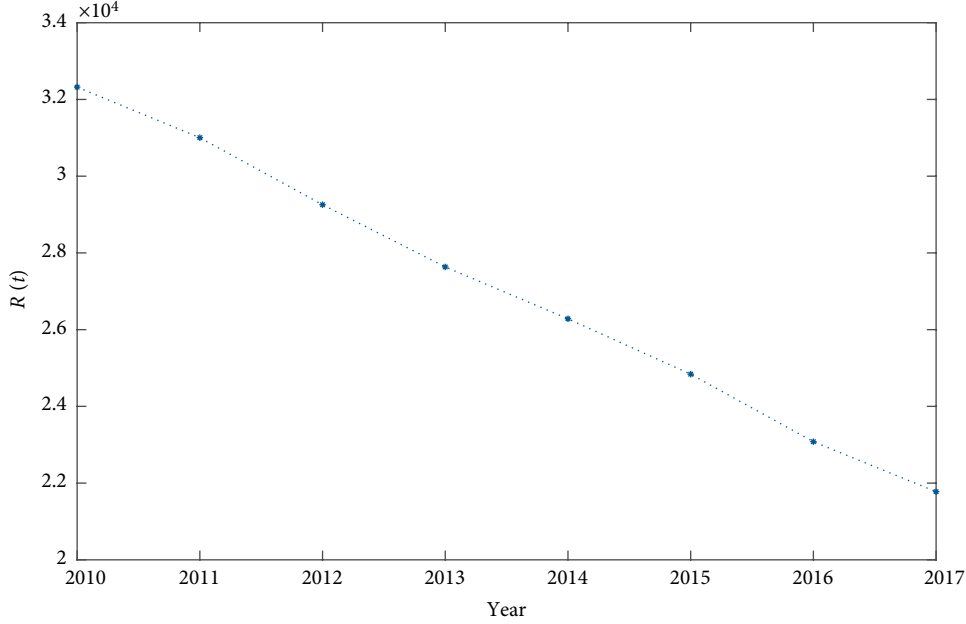
Definition 7. Assume sequence $R_N, R_N^{(1)}, Z_N^{(1)}$ and $\hat{a} = [a, b]^T$ are stated as Definition 4 and Theorem 1, then the following equation

$$\frac{dr^{(1)}}{dt} + ar^{(1)} = b \quad (22)$$

is named the whitening equation of GM(1,1) model.

The solution of the differential Equation (22) is as follows,

$$\hat{r}_N^{(0)}(t) = (1 - e^{-a}) \left(r_N^{(0)}(1) - \frac{b}{a} \right) e^{-a(t-1)}, \quad t = 1, 2, \dots, n. \quad (23)$$

FIGURE 5: The curve of $R(t)$.

Equation (23) is also called the time response function of the whitening differential equation. When $t = 2, 3, \dots, n$, $\hat{r}_N^{(0)}(t)$ is called the simulated data; When $t = n + 1, n + 2, \dots$, $\hat{r}_N^{(0)}(t)$ is called the predicted data.

Definition 8. Assume $\hat{c}_i(n)$, $\hat{r}_N^{(0)}(t)$ are stated as Definitions 3 and 7, then the following equation

$$\hat{x}(t) = \sum_{i=1}^N \left(\sum_{k=1}^p \phi_i(k) c_i(t-k)_{n-i} + a_i(k) - \sum_{k=1}^q \theta_i(k) a_i(t-k) \right) + (1 - e^a) \left(r_N^{(0)}(1) - \frac{b}{a} \right) e^{-a(t-1)} \quad (24)$$

is called EMD-ARMA-GM(1,1) model.

In the hybrid prediction model, EMD algorithm decomposes the original time series X into sequence C_i and sequence R_N to extract intrinsic characters of the complex system. sequence C_i is inputted into the ARMA model to describe the random changes and sequence R_N is substituted into GM(1,1) model to describe the trend. The value $\hat{x}(t)$ obtained by superposition $\hat{c}_i(n)$ and $\hat{r}_N^{(0)}(t)$ realizes the simulation or prediction of the original sequence. The flow of EMD-ARMA-GM(1,1) model is shown in Figure 3.

4. Modelling Condition and Error Checking Method for the EMD-ARMA-GM(1,1) Model

4.1. Modelling Condition of the EMD-ARMA-GM(1,1) Model. Each prediction model has a specific modelling condition and applicable rang. A model can be used for prediction only when the modelling condition is satisfied.

TABLE 2: The quasi-smooth condition of sequence $R(t)$.

Smoothness ratio	$\rho(3)$	$\rho(4)$	$\rho(5)$	$\rho(6)$	$\rho(7)$	$\rho(8)$
Value	0.462	0.298	0.218	0.169	0.134	0.112

TABLE 3: Parameter estimation of ARMA model.

Parameter of the ARMA model	p	q	ϕ_1	ϕ_2	θ_1
Estimated value	2	1	1.284	0.9363	0.9184

Definition 9. Assume that $T = (t(1), t(2), \dots, t(n))$, where $t(k) \geq 0$ for $k = 1, 2, \dots, n$, then the following is referred to as the smoothness ratio of sequence T :

$$\rho(k) = \frac{t(k)}{\sum_{i=1}^{k-1} t(i)}, \quad k = 2, 3, \dots, n. \quad (25)$$

The concept of smoothness ratio reflects the smoothness of a sequence. Obviously, the smoother the change of sequence T is, the smaller the smoothness ratio is.

Definition 10. If a sequence $T = (t(1), t(2), \dots, t(n))$, where $t(k) \geq 0$ for $k = 1, 2, \dots, n$ satisfies the following, then T is referred to as a quasi-smooth sequence:

- (1) $\rho(k+1)/\rho(k) < 1$, $k = 2, 3, \dots, n-1$,
- (2) $\rho(k) = [0, \varepsilon]$, $k = 3, 4, \dots, n$,
- (3) $\varepsilon < 0.5$.

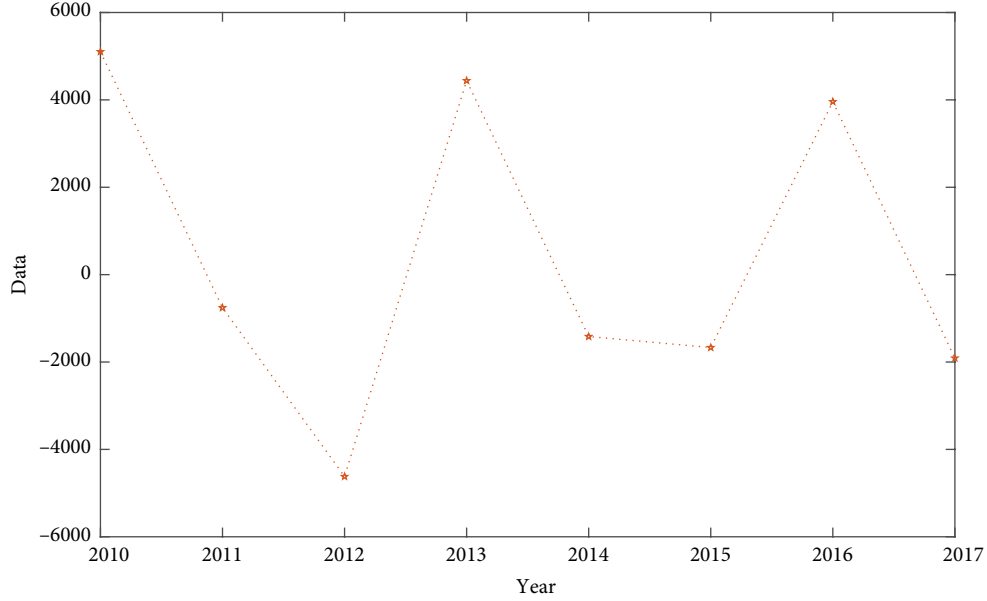


FIGURE 6: The simulated curve of IMF1.

The quasi-smooth condition of residual component is used to act as the criteria to test whether an oscillation sequence can be used to establish EMD-ARMA-GM(1,1) model.

4.2. Error Checking Method for the EMD-ARMA-GM(1,1) Model. A model's performance can be judged by testing, and only the model that pass test can be meaningfully employed to make predictions.

Definition 11. Assume that a raw sequence $T^{(0)}$ is

$$T^{(0)} = (t^{(0)}(1), t^{(0)}(2), \dots, t^{(0)}(n)). \quad (26)$$

EMD-ARMA-GM(1,1) model is employed to simulate sequence $T^{(0)}$, and its corresponding simulation sequence is as follows,

$$\hat{T}^{(0)} = (\hat{t}^{(0)}(1), \hat{t}^{(0)}(2), \dots, \hat{t}^{(0)}(n)). \quad (27)$$

The residual sequence of $\hat{T}^{(0)}$ is ε_T , as follows,

$$\varepsilon_T = (\varepsilon_T(1), \varepsilon_T(2), \dots, \varepsilon_T(n)), \quad (28)$$

where

$$\varepsilon_T(u) = |t^{(0)}(u) - \hat{t}^{(0)}(u)|, \quad u = 1, 2, \dots, n. \quad (29)$$

The relative simulation percentage error (RSPE) of the simulation sequence is

$$\Delta_T = (\Delta_T(1), \Delta_T(2), \dots, \Delta_T(n)), \quad (30)$$

where

$$\Delta_T(u) = \left| \frac{\varepsilon_T(u)}{t^{(0)}(u)} \times 100\% \right|, \quad u = 1, 2, \dots, n. \quad (31)$$

The mean relative simulation percentage error (MRSPE) of simulation sequence Δ_T is as follows:

TABLE 4: Parameter estimation of GM(1,1) model.

Parameter of the GM(1,1) model	a	b
Estimated value	0.058197	33854.68073

$$\bar{\Delta}_T = \frac{1}{n} \sum_{u=1}^n \Delta_T(u). \quad (32)$$

For given threshold value ξ in which the threshold is set according to the specific situation of the system, when $\bar{\Delta}_T < \xi$ holds true, the grey model is said to be error-satisfactory.

5. Application

China is a large agricultural country, but its special geographical location and climate environment lead to natural disasters frequently, which cause a large number of crops disasters every year. Large-scale crops disaster has seriously affected the national grain security, the basic status of agriculture and the sustainable development of rural economy. A scientific prediction of crops disaster areas can provide reasonable reference for arranging agricultural production subsidy and disaster relief subsidy, which has positive significance for promoting the sustainable development of agriculture and China's economy.

The crops disaster in China has a long history. To prevent and mitigate disasters, Chinese government proposes and implements many significant policies since 2010. These policies have effectively improved the situation of crops disaster and profoundly influenced the crops disaster area in China. The data of crops disaster area in China from 2010 to 2017 are a small oscillation sequence.

The data of crops disaster area in China from 2010 to 2017 are shown in Table 1.

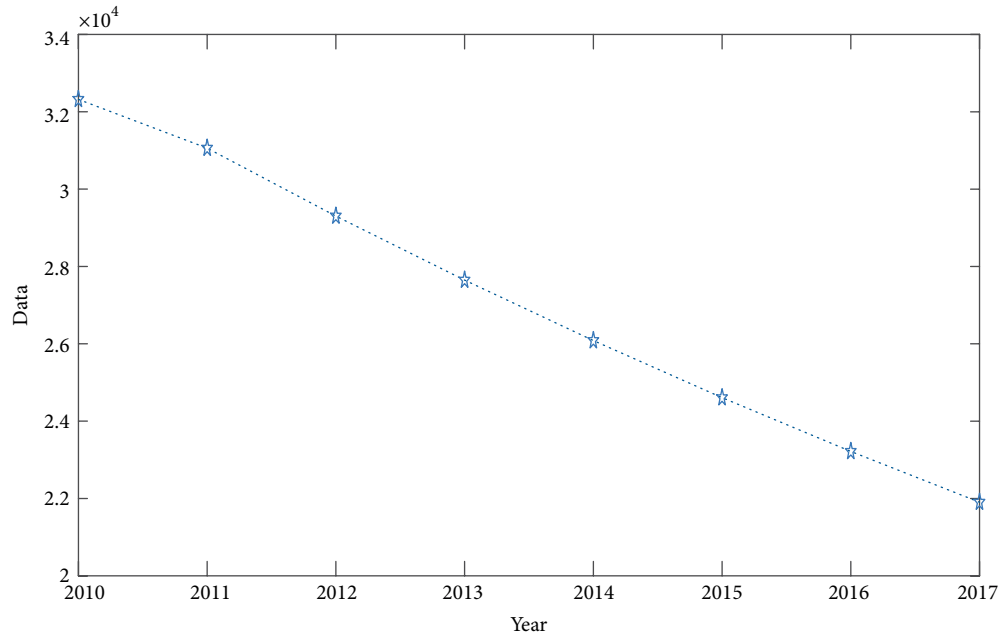


FIGURE 7: The simulated curve of $R(t)$.

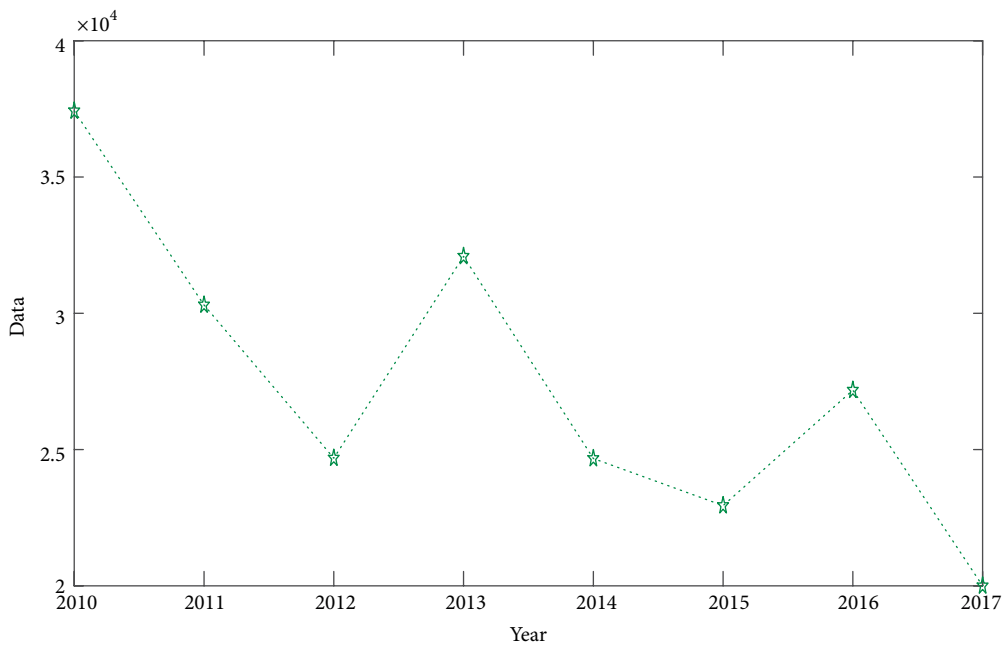


FIGURE 8: The simulated curve of crops disaster area in China.

5.1. *Data Decomposing.* EMD algorithm is applied to decompose the sequence of crops disaster area in China, and an IMF1 and a residual component $R(t)$ are obtained. The results are shown in Figures 4 and 5, respectively.

As can be seen from Figure 4, IMF1 is a curve of oscillations around the X -axis, showing linear and random characteristic of original sequence.

In Figure 5, $R(t)$ is a monotonic decreasing curve and shows the decreasing trend characteristic of the original sequence.

5.2. *Checking the Quasi-Smooth Condition before Modelling.* According to Definition 9, a sequence can be used to build the new model only when its residual component satisfies the quasi-smooth condition. Therefore, we check the quasi-smooth condition of sequence $R(t) = (32321.95, 31003.12, 29256.20, 27634.73, 26282.51, 24838.58, 23079.35, 21775.8)$ before building the new model to predict the crops disaster area.

From Definition 9, we can obtain the smoothness ratio of sequence $R(t)$ and the values of smoothness ratio are shown in

TABLE 5: EMD-ARMA-GM(1,1) model, ARIMA model and GM(1,1) model simulated values (units:1000 hectares).

Year	Raw data $x(t)$	EMD-GM(1,1)-ARMA		Model ARIMA		Model GM(1,1)	
		$\hat{x}(t)$	$\Delta_T(t)$	$\hat{x}(t)$	$\Delta_T(t)$	$\hat{x}(t)$	$\Delta_T(t)$
2010	37425.9	37425.9	—	38226.23	2.1384%	37425.9	—
2011	32470.5	30303.79	6.6729%	26364.23	18.8056%	31220.772	3.849%
2012	24962	24684.6	1.1113%	27976.36	12.0758%	29183.227	16.911%
2013	31349.8	32088.6	2.3566%	21655.3	30.9236%	27278.657	12.986%
2014	24890.7	24668.63	0.8922%	19212.75	22.8116%	25498.385	2.441%
2015	21769.8	22941.88	5.384%	18678.01	14.2022%	23834.297	9.483%
2016	26220.7	27177.18	3.6478%	20250.14	22.7704%	22278.812	15.033%
2017	18478.1	19995.16	8.21%	18478.1	—	20824.842	12.7%
MRSPE			4.0393%		17.6754%		10.4863%

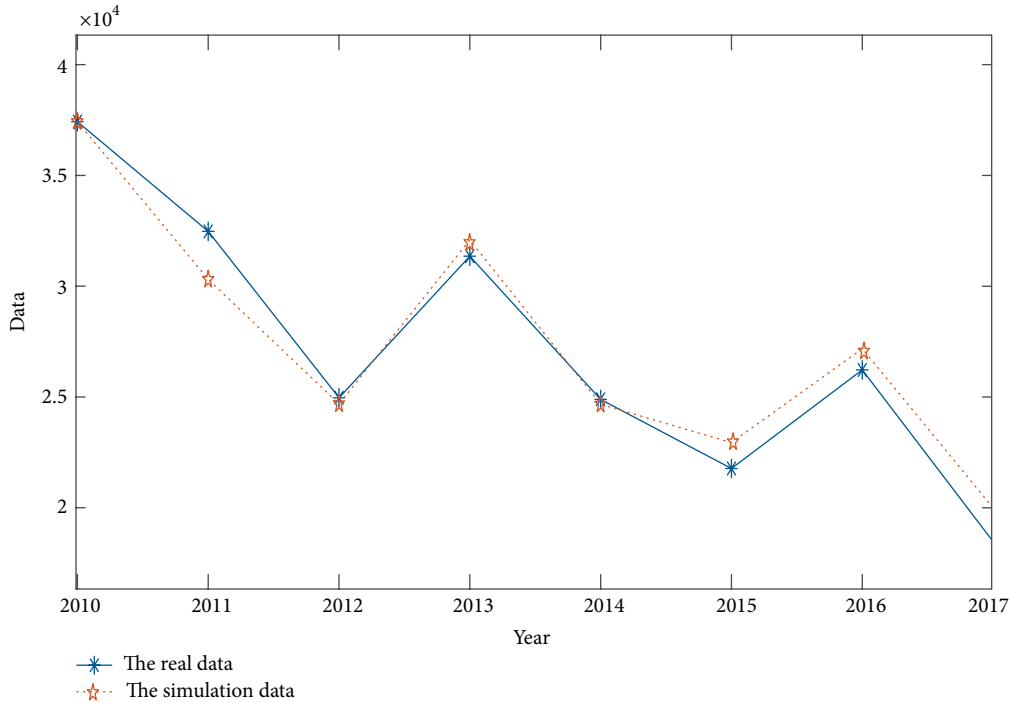


FIGURE 9: The simulated curve of the EMD-ARMA-GM(1,1) model.

Table 2. $\rho(8)/\rho(7) \approx 0.831513 < 1$, $\rho(6)/\rho(5) \approx 0.775513 < 1$, $\rho(5)/\rho(4) \approx 0.732441 < 1$ and $\rho(4)/\rho(3) \approx 0.646085 < 1$. Then, sequence of crops disaster area in China satisfies the quasi-smooth condition and can be used to build the new model. The modelling process is detailed in the next subsection.

5.3. Modelling. Firstly, IMF1 is introduced into ARMA (p, q) model. By increasing its order gradually, IMF1 is closer to the dependence of data. When fitting effect of the data is best, it stops and gets the value of p and q . Next, the parameter identification function ARMAX is used to estimate $\phi_1, \dots, \phi_p, \theta_1, \dots, \theta_q$. The optimal order and parameters are obtained as shown in Table 3.

As shown in Table 3, the proper value of p is 2 and q is 1. So we use ARMA(2, 1) model to simulate IMF1, and draw the simulated curve of this model based on IMF1, as shown in Figure 6.

Next, $R(t)$ is introduced into GM(1,1) and the parameters are estimated by least square method as shown in Table 4.

As provided in Table 4, We substitute the parameters into the whitening equation of GM(1,1) model, and get the simulated value of $R(t)$. The simulated curve of $R(t)$ is shown in Figure 7.

Finally, through integrating the simulated values of IMF1 and $R(t)$, we can get the simulated value of China's crops disaster area. The simulated curves of crops disaster area in China is shown in Figure 8.

5.4. Result and Analysis. To verify the performance of EMD-ARMA-GM(1,1) model, we compare the MRSPE of EMD-ARMA-GM(1,1) to that of traditional mainstream prediction models, including ARIMA model and GM(1,1) model. The simulated values $\hat{x}(t)$, $\Delta_r(t)$ and MRSPE of the three models are presented in Table 5.

As shown in Table 5, the proposed EMD-ARMA-GM(1,1) model has the lowest MRSPE among the three models and the MRSPE is 4.0393%; the MRSPEs of the other two models are

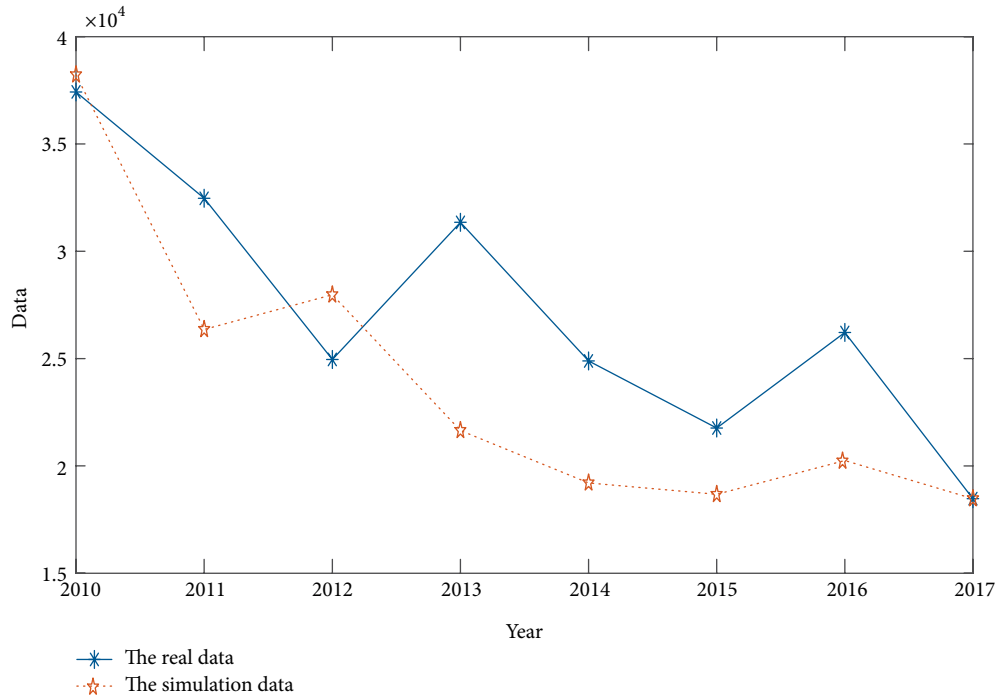


FIGURE 10: The simulated curve of the ARIMA model.

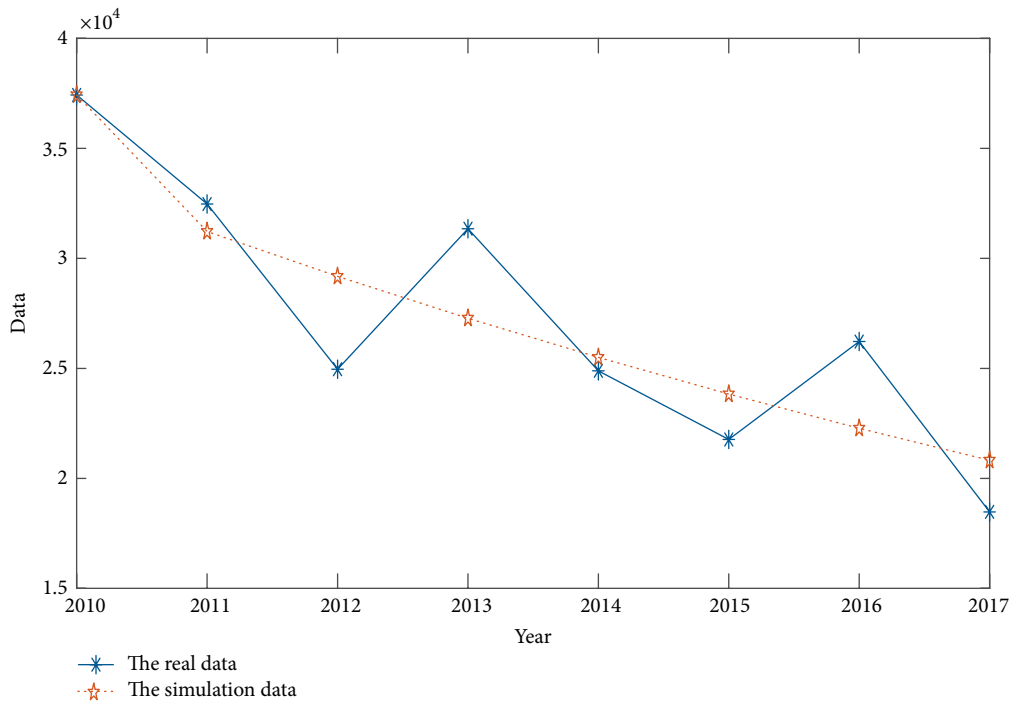


FIGURE 11: The simulated curve of the GM(1,1) model.

more than 10%. Comparatively, the performance of the GM(1,1) model is second to that of EMD-ARMA-GM(1,1) model because it does not consider the effect of random oscillation characteristic; the performance of the ARMA model is the worst among the three model because it does not consider the influence of trend characteristic. In order to clearly

illustrate the simulation effects of the three models for China's crops disaster area, we draw the simulated curves and errors of the three models based on the data in Table 5 in MATLAB as shown in Figures 9–12.

According to Figures 9–12, the performance of IEMD-ARMA-GM(1,1) model is best among the above three models.

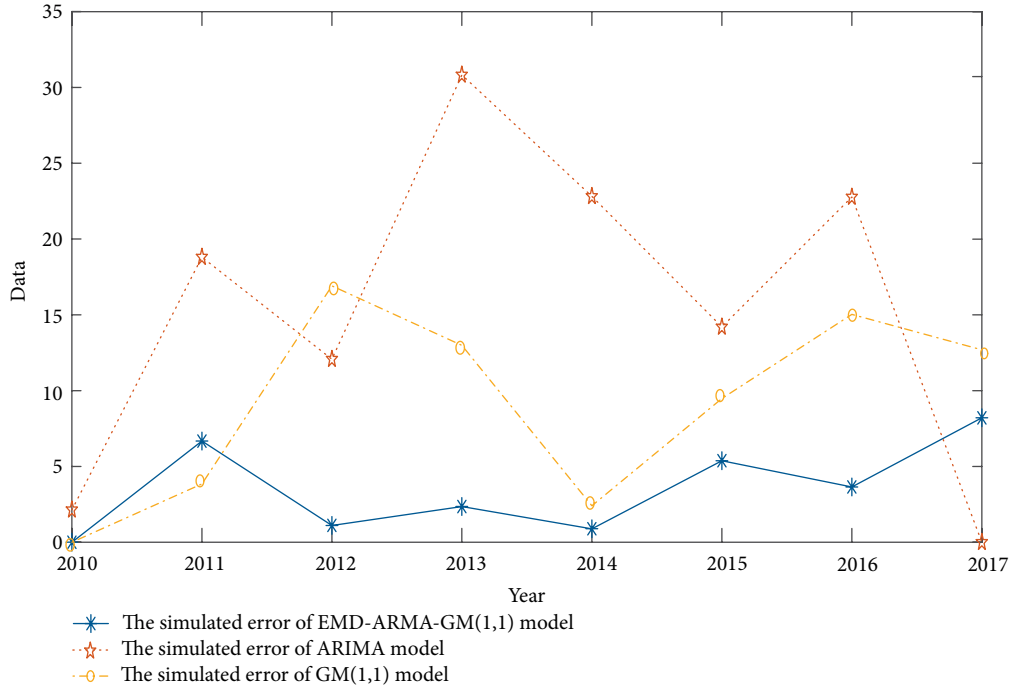


FIGURE 12: The simulated errors of EMD-ARMA-GM(1,1), ARIMA and GM(1,1).

TABLE 6: Prediction results of crops disaster area in China by EMD-ARMA-GM(1,1) model (units: 1000 hectares).

Year	2018	2019	2020	2021
Crops disaster area	20857.76	22335.99	14606.27	19633.39

Thus it is evident that the performance of EMD-ARMA-GM(1,1) model is better than that of traditional mainstream prediction models.

5.5. Prediction of Crops Disaster Area in China. The EMD-ARMA-GM(1,1) model is used to predict the crops disaster area in China from 2018 to 2021, and the results are shown in Table 6.

Table 6 shows that the overall trend of crops disaster area in China is decreasing in the next four years, but the crops disaster area is still very large. By 2021, it will reach 1963390 hectares. The large of crops disaster area may cause shortage of grain and inhibit rural economic. Therefore, in order to maintain the sustainable development of agriculture and national economy, the Chinese government needs to develop policies for production subsidies and disaster relief subsidies, and set aside sufficient funds to deal with the problems of crops failures caused by future natural disasters.

6. Conclusion

In this paper, the shortcomings of grey prediction model in modelling small oscillation sequence are analysed, and then we find out the reason why grey prediction model is

not effective in predicting oscillation sequence by analyzing the intrinsic characteristics of oscillation sequence: the system of oscillation sequence is complex, and the trend and random oscillation are often combined. Therefore, based on information decomposition and aiming at extracting the intrinsic characteristics of the sequence, a hybrid grey prediction model is established in this paper. The results of case analysis show that the proposed model considers the complexity of system information, effectively describes the operation behavior and rules of the system, and the effect is higher than that of a single classical prediction model.

The new grey hybrid prediction model provides a new idea and method for small oscillation sequence. However, when the size of oscillation sequence is big, the big data methods can be used to simulate and predict the oscillation sequence, such as neural network and support vector machine. At this time, the performance of the new hybrid grey prediction model needs to be compared with that of the big data method, and the simulation and prediction errors can be used to determine the performance of those methods, and then the superior one is selected for study the oscillation sequence.

In the following work, we will further consider the other characteristics of the sub-sequence generated by EMD algorithm, and establish suitable methods to study the oscillation sequence.

Data Availability

The China's crop disaster area data used to support the findings of this study are included within the article.

Conflicts of Interest

The authors declare that there are no conflicts of interest regarding the publication of this paper.

Acknowledgments

This work was supported by the National Natural Science Foundation of China (71771033).

References

- [1] H. M. Duan and X. P. Xiao, "A multimode dynamic short-term traffic flow grey prediction model of high-dimension tensors," *Complexity*, vol. 2019, Article ID 9162163, 18 pages, 2019.
- [2] M. Wei, D. L. Yang, and H. Huang, "Prediction of China's sulfur dioxide emissions by discrete grey model with fractional order generation operators," *Complexity*, vol. 2018, Article ID 8610679, 13 pages, 2018.
- [3] S. H. Mao, M. Y. Gao, J. H. Wen, and X. W. Nie, "Generalized admissible region of class ratio for fractional accumulated GM(1,1) model," *The Journal of Grey System*, vol. 26, no. 3, pp. 55–68, 2014.
- [4] B. Zeng and C. Li, "Forecasting the natural gas demand in China using a self-adapting intelligent grey model," *Energy*, vol. 112, no. 1, pp. 810–825, 2016.
- [5] X. Ma and Z. B. Liu, "The GMC (1, n) model with optimized parameters and its application," *The Journal of Grey System*, vol. 29, no. 4, pp. 122–138, 2017.
- [6] S. H. Mao and M. Y. Gao, "A novel fractional grey system model and its application," *Applied Mathematical Modelling*, vol. 40, no. 7–8, pp. 5063–5076, 2016.
- [7] B. Zeng and C. Li, "Improved multi-variable grey forecasting model with a dynamic background-value coefficient and its application," *Computers & Industrial Engineering*, vol. 118, pp. 278–290, 2018.
- [8] X. Ma, M. Xie, W. Q. Wu, and B. Zeng, "A novel fractional time delayed grey model with grey wolf optimizer and its applications in forecasting the natural gas and coal consumption in chongqing China," *Energy*, vol. 178, pp. 487–507, 2019.
- [9] B. Zeng, H. M. Duan, and Y. F. Zhou, "A new multivariable grey prediction model with structure compatibility," *Applied Mathematical Modelling*, vol. 75, pp. 385–397, 2019.
- [10] S. H. Mao, X. P. Xiao, M. Y. Gao, and X. Wang, "Nonlinear fractional order grey model of urban traffic flow short term prediction," *The Journal of Grey System*, vol. 30, no. 4, pp. 1–17, 2018.
- [11] J. Cui, H. Y. Ma, C. Q. Yuan, and S. Liu, "Novel grey verhulst model and its prediction accuracy," *The Journal of Grey System*, vol. 27, no. 2, pp. 122–138, 2017.
- [12] C. Puripat and S. Sarikavanij, "The comparison of grey system and the verhulst model for rainfall and water in dam prediction," *Advances in Meteorology*, vol. 2018, Article ID 7169130, 11 pages, 2018.
- [13] Z. X. Wang and Q. Li, "Modelling the nonlinear relationship between CO₂ emissions and economic growth using a PSO algorithm-based grey verhulst model," *Journal of Cleaner Production*, vol. 207, pp. 214–224, 2019.
- [14] D. Y. Chen and W. T. Han, "Prediction of multivariate chaotic time series via radial basis function neural network," *Complexity*, vol. 18, pp. 55–66, 2013.
- [15] J. Yang, J. F. Su, and L. J. Song, "Selection of manufacturing enterprise innovation design project based on consumer's green preferences," *Sustainability*, vol. 11, no. 5, p. 1375, 2019.
- [16] P. Jiang, X. Liu, J. Zhang, and X. Yuan, "A framework based on hidden markov model with adaptive weighting for microcystin forecasting and early-warning," *Decision Support Systems*, vol. 84, pp. 89–103, 2016.
- [17] X. Lu, J. Zhang, G. R. Wu, and X. Yuan, "On translation operator-based DGM(1,1) model and its properties," *The Journal of Grey System*, vol. 31, no. 1, pp. 13–22, 2019.
- [18] J. Zhang, X. Lu, M. F. Ran, and G. Han, "DGM model based on anti-cotangent function and its application," *The Journal of Grey System*, vol. 28, no. 3, pp. 63–74, 2016.
- [19] B. Zeng and S. F. Liu, "Prediction model of stochastic oscillation sequence based on amplitude compression," *Systems Engineering—Theory & Practical*, vol. 32, no. 11, pp. 2493–2497, 2012.
- [20] W. Y. Qian and Y. G. Dang, "GM(1,1) model based on oscillation sequences," *Systems Engineering—Theory & Practic*, vol. 29, no. 3, pp. 149–154, 2009.
- [21] A. Dejamkhooy, A. Dastfan, and A. Ahmadyfard, "Modelling and forecasting nonstationary voltage fluctuation based on grey system theory," *IEEE Transactions on Power Delivery*, vol. 32, no. 3, pp. 1212–1219, 2017.
- [22] X. Ma, W. Q. Wu, B. Zeng, Y. Wang, and X. Wu, "The conformable fractional grey system model," *ISA Transactions*, 2019.
- [23] F. M. Liu and W. C. Chuang, "A precaution diagnosis of financial distress via grey situation decision," *Journal of Grey System*, vol. 22, no. 3, pp. 395–403, 2010.
- [24] H. Zhou, J. J. Huang, Y. B. Yuan, and B. Tang, "Prediction of water consumption in hospitals based on a modified grey GM (0,1|sin) model of oscillation sequence: the example of Wuhan city," *Journal of Applied Mathematics*, vol. 2014, Article ID 521973, 7 pages, 2014.
- [25] J. L. Deng, "Undulating grey model (UGM) GM (1,1 tan(k-τ) p, sin(k-τ)p)," *The Journal of Grey System*, vol. 13, no. 3, pp. 201–205, 2001.
- [26] X. Du, Y. Wu, S. D. Gu, P. Sun, Y. Ji, and H.-M. Tai, "Power oscillation analysis and control of three-phase grid-connected voltage source converters under unbalanced grid faults," *IET Power Electronics*, vol. 9, no. 11, pp. 2162–2173, 2016.
- [27] X. F. Zhang and J. F. Su, "An integrated QFD and 2-tuple linguistic method for solution selection in crowdsourcing contests for innovative tasks," *Journal of Intelligent & Fuzzy Systems*, vol. 35, no. 6, pp. 6329–6342, 2018.
- [28] J. Z. Wang, P. Du, T. Niu, and W. Yang, "A novel hybrid system based on a new proposed algorithm-multi-objective whale optimization algorithm for wind speed forecasting," *Applied Energy*, vol. 208, pp. 344–360, 2017.
- [29] W. Ghezaiel, A. Ben Slimane, and E. Braiek Ben, "Nonlinear multi-scale decomposition by EMD for co-channel speaker identification," *Multimedia Tool and Applications*, vol. 76, no. 20, pp. 20973–20988, 2017.
- [30] F. T. Wang, G. Deng, C. X. Liu, W. Su, Q. Han, and H. Li, "A deep feature extraction method for bearing fault diagnosis based on empirical mode decomposition and kernel function," *Advances in Mechanical Engineering*, vol. 10, no. 9, pp. 1–12, 2018.

- [31] X. Tang, Z. F. Ma, X. X. Niu, and Y. X. Yang, "Robust audio watermarking algorithm based on empirical mode decomposition," *Chinese Journal of Electronics*, vol. 25, no. 6, pp. 1005–1010, 2016.
- [32] Y. Zhang, C. Zhang, J. Sun, and J. Guo, "Improved wind speed prediction using empirical mode decomposition," *Advances in Electrical and Computer Engineering*, vol. 18, no. 2, pp. 3–10, 2018.

Research Article

Self-Organized Criticality on Twitter: Phenomenological Theory and Empirical Investigation Based on Data Analysis Results

Andrey Dmitriev ¹, Victor Dmitriev ¹, and Stepan Balybin ²

¹School of Business Informatics, National Research University Higher School of Economics, Moscow, Russia

²Department of Physics, Lomonosov Moscow State University, Moscow, Russia

Correspondence should be addressed to Andrey Dmitriev; a.dmitriev@hse.ru

Received 16 August 2019; Revised 6 November 2019; Accepted 11 December 2019; Published 27 December 2019

Guest Editor: Raúl Baños

Copyright © 2019 Andrey Dmitriev et al. This is an open access article distributed under the Creative Commons Attribution License, which permits unrestricted use, distribution, and reproduction in any medium, provided the original work is properly cited.

Recently, there has been an increasing number of empirical evidence supporting the hypothesis that spread of avalanches of microposts on social networks, such as Twitter, is associated with some sociopolitical events. Typical examples of such events are political elections and protest movements. Inspired by this phenomenon, we built a phenomenological model that describes Twitter's self-organization in a critical state. An external manifestation of this condition is the spread of avalanches of microposts on the network. The model is based on a fractional three-parameter self-organization scheme with stochastic sources. It is shown that the adiabatic mode of self-organization in a critical state is determined by the intensive coordinated action of a relatively small number of network users. To identify the critical states of the network and to verify the model, we have proposed a spectrum of three scaling indicators of the observed time series of microposts.

1. Introduction

The general science development trend in the 20th century, which is also passed in the new century, is the gradual penetration of ideas and methods of physics in natural as well as traditional humanities. Since the 1970s, the methods of mathematical and then physical modeling have been increasingly used in such sciences as demography, sociology, economics, history, and political science. In all these sciences, the desire for an objective and, preferably, a quantitative description of various social and economic phenomena is increasing.

The development of quantitative models in sociology, political science, theory of transport flows, and other areas of society investigations is gradually moving relevant tasks from the humanities and engineering sciences to interdisciplinary applications of mathematics and physics. In the literature of recent years, the term sociophysics [1, 2] is assigned to all such areas. The main task of this new field of natural science is to search for objectively measurable and formalizable patterns that determine various social

processes. Sociophysics analyzes the structure and dynamics of all existing varieties of social systems, using ideas and methods borrowed from theoretical and experimental physics.

Some of the objects and phenomena studied by sociophysics are social networks (e.g., see the review [3] and references therein) and critical phenomena, such as phase transitions, observed in them (e.g., see the reviews [4, 5] and references therein). Dorogovtsev and co-authors state in their paper [4] that “Critical phenomena in networks include a wide range of issues: structural changes in networks, the emergence of critical—scale-free—network architectures, various percolation phenomena, epidemic thresholds, phase transitions in cooperative models defined on networks, critical points of diverse optimization problems, transitions in co-evolving couples—a cooperative model and its network substrate, transitions between different regimes in processes taking place on networks, and many others.” In the thermodynamics theory of irreversible processes, it is stated that significant structure reconstructions occur when the external parameter reaches a certain critical value (the

bifurcation point) and has the character of a kinetic phase transition [6]. The critical point is reached as a result of fine-tuning of the system external parameters. In a certain sense, such critical phenomena are not robust. The following types of self-organization of nonlinear systems can be identified that lead to nonrobust critical phenomena: self-organization during phase transitions, which are characterized by spatial-temporal scale invariance with a transition to the critical point, when the external parameter reaches its critical value; self-organization during geometric phase transitions, when the critical value of the cell filling probability is reached (for example, the percolation threshold); and self-organization of dissipative structures at the bifurcation point, in case when some external parameter (for example, the temperature gradient in the classical Benard problem) reaches its critical value.

At the end of the 1980s, Bak et al. [7, 8] found that there are complex systems with a large number of degrees of freedom that go into a critical mode as a result of the internal evolutionary trends of these systems. A critical state of such systems does not require fine-tuning of external control parameters and may occur spontaneously. Thus, the theory of self-organized criticality (SOC) was proposed. This is the theory claiming to be the universal theory, explaining the spontaneous occurrence of critical states in open nonequilibrium systems. A characteristic feature that qualitatively distinguishes SOC from other phenomena with a similar nature is the realization of a self-organized critical state in a wide range of external control parameters. For SOC, however, no special “parameter tuning” is required, and, in this sense, such critical phenomena are robust.

From the moment of the SOC model emergence, this model started to be applied to describe critical phenomena in systems regardless of their nature (e.g., see the review [9] and references therein). Not an exception is the application of the theory to the description of critical phenomena in social networks (e.g., see the works [10–13]).

The motivation of our investigation is the following. There is a number of studies (e.g., see the works [11, 13–20]), in which it is established that the observed flows of microposts generated by microblogging social networks (e.g., Twitter) are characterized by avalanche-like behavior. Time series of microposts depicting such streams are the time series with a power-law distribution of probabilities, with $1/f$ noise and long memory. As it will be shown in Section 2.2, these characteristics of the time series are key features of the social network in the SOC state. Despite this, there are no studies on the construction, analysis, and verification of physical models that explain the phenomenon of the emergence and spread of avalanche of microposts on Twitter. The construction, analysis, and verification of such a phenomenological model are the purpose of our research.

The presented work is structured as follows. Section 2.1 is devoted to the description of one of the scenarios of Twitter self-organizing transition in a critical state, determined by the specifics of the network functioning. Section 2.2 introduces the notion of a spectrum of indicators of self-organized network criticality, which is an identifier that allows

the SOC state of the network to be distinguished from a noncritical state, determined from the results of the analysis of the time series of microposts. Methods of mining and data analysis for identifying the state of the network, as well as the results of identifying network states from the observed data, are presented in Section 3. These data are used to verify the model presented in Section 4, which describes the conditions for Twitter self-organization transition to the critical state from its subcritical state. Section 5 presents the general conclusions from the study, as well as their discussion. Finally, Section 6 is devoted to a discussion of tasks that cannot be solved within the proposed model, and a brief description of the approaches to their solution.

2. Self-Organized Criticality on Twitter

This section presents a qualitative nonformalized description of the emergence mechanisms of a self-organized critical state on Twitter as a result of the coordinated action of strategically oriented network users. The range of indicators of self-organized criticality of a social network is defined as the identifier of the network functioning in the subcritical (SubC), the self-organized critical (SOC), and the supercritical (SupC) states.

2.1. Mechanisms of Self-Organized Criticality on Twitter.

The well-known physical model of self-organized criticality, Abelian sandpile model [21], provides one of the scenarios for the system to achieve a self-organized critical state in the robust case. A model with a pile of sand is metaphorical, and the real dynamics of such systems can be very diverse. We adapt this scenario to explain the emergence of the SOC state on Twitter, accompanied by the appearance of the avalanche of microposts on the network of various sizes: from small avalanches of the order of 10 microposts per second to large avalanches of about 1000 microposts per second or even more. The corresponding time series shows consistently measured numbers of microposts (avalanche sizes) at some time intervals.

We hypothesize that Twitter self-organization in a critical state results from the consistent behavior of a relatively small number of network users (S) when S reaches a critical state S_c . Further discussion is devoted to the substantiation of this assumption.

First of all, we introduce the concepts that will be needed for further discussion. Let \mathcal{N} be the total number of Twitter users who are interested in a particular topic, for example, “2016 United States Presidential Election.” Such users, who are united by an interest in a given topic, form a community on the network and, therefore, only these users can send microposts relevant to this topic. Let that S ($S \ll \mathcal{N}$) users of this community follow a certain strategy. For example, the goal of these users is to pump the network, i.e., to distribute as many microposts, related to a certain topic on the network, as possible. Call these users as strategically oriented users (SOUs). SOUs have a common goal, to achieve that they act in concert. Consolidation of users into a subcommunity of SOUs does not necessarily occur as a result of

a preliminary conspiracy, but also unconsciously. Examples of concerted action to achieve a common goal can be the promotion of a candidate in the political elections, as well as the coordination of actions of participants in protest movements and/or the involvement of citizens in protest movements. Recent protest movements have suggested that online social networks might play a key role in their organization, as adherents have a fast, many-to-many communication channel to help coordinate their mobilization [22]. The behavior of network users during natural disasters may be the result of their unconscious collusion. The remaining $\mathcal{N} - S$ users do not follow a single coherent strategy and, in this sense, are randomly oriented users (ROUs).

The rationale for dividing network users into two classes is the research results presented by Pramanik and co-authors in their paper [23]. They introduce two mention strategies: random mention and smart mention to model the mention preferences of the users. They proposed a model of the cascade formation in Twitter, incorporating both retweet and mention activities. Realizations of the model prove the elegance of smart mention strategy in boosting tweet popularity, especially in the low retweeting environment.

We use, in our opinion, the exhaustive classification of Twitter users presented in [24] to classify network users to one of the two classes. The classification consists of real users, which include personal users, professional users, and business users, and also digital actors, which include spam users, feed/news, and viral/marketing services. Of course, the assignment of one of these classes to SOUs or ROUs is conditional and is determined by the specifics of the topic, discussed by network users. However, in most cases, all digital actors who are using bots, professional users, and business users can be considered as SOUs. For example, the main goal of professional users and business users on the network is to involve as many users as possible, for example, personal users, in a discussion of a certain topic. Finally, personal users can be considered as ROUs. Indeed, such users create their Twitter profiles for entertainment, training, or to receive news, etc. This is the most numerous class of Twitter users.

Consider the features of the network users' interactions, which lead to the emergence of the SOC state on Twitter. To explain the mechanisms of the emergence of such state, it is appropriate to distinguish three consecutive network states: the SubC state, the SOC state, and the SupC state.

The SubC state is the chaotic network state, which is observed in a certain time interval or in subcritical time Δt_{SubC} (from 0 to t_c). A demonstration of the chaotic nature of this state is the chaotic (disordered) distribution of microposts avalanches on the network. The most common scenario for observation of this state corresponds to the presence of only ROUs ($S = 0$) on the network, who generates avalanches of microposts in terms of a certain topic. Such avalanches are not interconnected, and they are small in size and quickly fade out in time and space. This is due to the fact that ROUs do not behave in a consistent manner, do not pursue one goal, and do not pump the network with certain information, and, accordingly, it does

not lead to the formation of avalanches of microposts of all sizes. In such a network, self-organization in an ordered state, which is characterized by the existence of avalanches of microposts of all sizes, is impossible. ROUs are not characterized by cooperative (synchronous) behavior and, therefore, a spontaneous transition of the network from a chaotic to an ordered state, in which avalanches of microposts of all sizes distribute on the network, is not possible. We do not exclude that in the community of ROUs, connected exclusively by discussing a certain topic, there are local structures with a small number of hierarchical levels (user, his subscribers, subscribers of their subscribers, etc.). The avalanches follow a single tweet that is retweeted or similar tweets as they move across the network. But the avalanche of microposts distributed in such structure has relatively small size. Even the totality of such hierarchical structures will allow to generate only many avalanches of small sizes that are not interconnected.

Suppose that at each moment of time, one SOU ($S \neq 0$) goes on Twitter, wherein $S < S_c$. These users act in concert, trying to form the avalanches of microposts of all sizes relevant to a certain topic. Gradually, SOUs form hierarchical structures on the network. The cooperative behavior of these users gives them the opportunity to build hierarchical structures that are quite effective to generate avalanches of microposts of larger sizes. If SOUs are real users and most of them are influential persons of Twitter, then it is possible to form a hierarchical structure with a large number of levels (influential person #1, his subscribers, subscribers of their subscribers, etc.), which can generate avalanches of microposts of greater sizes. Even larger avalanches can be generated, if both ROUs, which are subscribers of subscribers on certain levels, and other influential persons (influential person #2, influential person #3, etc.) with their subscribers, including SOUs and ROUs, will be integrated in this structure. In some sense, ROUs are an active environment for increasing the size of the avalanches originally generated by SOUs.

It should be noted that the considered hierarchical structure is not the only structure through which it is possible to generate avalanches of microposts of larger sizes. Other possible mechanisms for generating criticality will be described in Conclusion. Nevertheless, the above-mentioned mechanism of the spread of microposts avalanches of all sizes, in our opinion, is the most justified. This is determined by the basic specifics of users' organization on Twitter: user (hierarchical level #1), his subscriber (hierarchical level #2), subscriber of his subscriber (hierarchical level #3), etc. Moreover, in [25], it was shown that the evolution of hierarchically subordinate complex networks reduces to anomalous diffusion in the ultrametric space of the hierarchical system. The stationary distribution over the levels of such a system is determined by a power law. Besides, Bakshy and co-authors state in their paper [26] "Unsurprisingly, we find that the largest cascades tend to be generated by users who have been influential in the past and who have a large number of followers." This study also provides a rationale for the existence of a hierarchical structure (influential person #1, his subscribers, subscribers

of their subscribers, etc.), as the most effective structure for the distribution of large avalanches of microposts. In the paper [27], a conceptual and practical model is proposed for the classification of topical networks on Twitter, based on their network-level structures. The existence of connection between hierarchical sequences of tweet-retweet-follow and cascades of retweets is discussed in [28].

If S does not reach its critical value S_c , then unrelated avalanches of microposts, although of larger sizes, are still forming on Twitter. The formed hierarchical system of SOUs and ROUs on the social network is still not able to form an avalanche of microposts of all sizes. SubC state is resistant to small external influences: adding one SOU on the network will not qualitatively change the network behavior.

At t_c moment of time, the number of SOUs reaches its critical value S_c , and the network goes into the SOC state. The SOC state is not resistant to small external influences: just one added SOU can cause an avalanche of microposts of any size. The behavior of avalanches of microposts distribution in a self-organized critical network is unpredictable based on the behavior of its individual users. In this case, the social network has the emergence property and in this sense is a complex system. Thus, the cause of the emergence of microposts avalanches of all sizes is the self-organized criticality of a certain network community, which users are united by interest in some topics. It should be noted that the network in the SubC state does not necessarily go to the SOC state. It is possible to relax the network until it reaches the SOC state. Relaxation may be caused by the decrease or the constancy of the SOUs number over time due to the loss of interest of SOUs in the topic discussed on the network.

Twitter self-organization in a critical state occurs when the number of microposts (η) relevant to a certain topic barely becomes nonzero ($+0$), i.e., corresponds to its separation from zero ($\eta = +0$). To ensure $\eta = +0$, one SOU is added in Twitter at each time interval Δt , corresponding to the relaxation time. The SOC state is robust in relation to possible changes on the social network. For example, if the nature of interactions between users changes, the social network temporarily deviates from the existing critical state, but after a while, it is restored in a slightly different form. The hierarchical network structure will change, but its dynamics will remain critical. Every time, when trying to divert Twitter from the SOC state, the social network invariably returns to this state.

The regular return to the SOC state for any deviations from it let us suggest that it is a special kind of stable equilibrium of the evolving network, which, according to Bak, is called a punctuated equilibrium [7, 8]. If the social network is in such an equilibrium, then significant changes in it can occur both with a strong external impact (for example, with the strong social network pumping by strategically oriented users) and as a result of gradual internal changes.

The ordered SupC state, observed if $S > S_c$, is resistant to small external influences: adding one SOU on the network will not qualitatively change the network behavior. In this state, characterized by a supercritical number of SOUs, the size of the avalanches of microposts continues to grow. If the

network does not pump by SOUs, then it relaxes, returning back to the SubC state.

2.2. Spectrum of Self-Organized Criticality Exponents. In Section 2.1, it was noted that the presence of avalanches of large microposts on the network is a characteristic feature of being Twitter in the SOC or the SupC state. Consequently, the results of a quantitative analysis of the avalanche sizes of microposts can be used as an identifier of the social network state.

To determine the network state, it is necessary to determine the size of avalanche microposts, which will allow the social network to be assigned to one of the critical states.

Considering that the theory of self-organized criticality is one of the foundations of the complexity theory (sometimes called the paradigm) [29], we will use the more general concept of complexity: a nonstrict definition of complexity at the level of external demonstrations of criticality of the system regardless of its internal structure. In this case, the complex system is the system, which is capable of generating extremal events: unexpected (unpredictable) and/or extraordinary events.

In the case of Twitter, we are talking about certain features of the observed time series of microposts (η_t), for example, the presence of sharply allocated values of the time series. Another feature is the existence of sharply increasing sequence of time series values up to a critical value corresponding to the distribution of the avalanche of microposts on the network.

The key features of the complexity of the social networks at the level of the time series generated by them are the power law for the probability distribution function (power-law PDF) of the time series of microposts, the power spectral density (PSD) of the time series, which is characterized by $1/f$ noise, and the power law for the autocorrelation function (power-law ACF), which is characterized by the presence of the long memory in the time series [30].

In the general case, the power-law PDFs can be considered as a statistical value of the scale invariance of the time series of microposts:

$$p(\eta) \propto \eta^{-\alpha}, \quad (1)$$

where $\alpha \in (1, 3)$. It should be noted that usually power-law PDFs are characterized by $\alpha \in (2, 3)$ [31]. We consider the most common case belonging to power-law PDF. Power laws with $\alpha \leq 1$ cannot be normalized and are usually not found in natural phenomena. Power-law PDF with a low value of α does not have a finite average η ($\eta \rightarrow \infty$ for $\alpha \leq 2$), but for $\alpha > 2$ the average is defined. The mean square $\eta^2 \rightarrow \infty$ for $\alpha \leq 3$, but η^2 has a well-defined value for $\alpha > 3$.

Power-law PDF (1) refers to distributions with heavy tails, for which, unlike compact distributions, the well-known 3σ rule (the possibility of neglecting the values of the number of microposts exceeding 3σ) is not satisfied. If the distribution (1) is fulfilled, then rare large events do not occur infrequently enough for their probability to be neglected. The possibility of gigantic, extraordinary events

appearing on Twitter indicates the network's tendency for disasters.

Another characteristic of the scale-invariant properties of the time series is $1/f$ noise, which is observed in the power form of PSD at low frequencies f :

$$S(f) \propto f^{-\beta}. \quad (2)$$

The β value in PSD (2) determines the color of the noise. For $1/f$ noise, $\beta \in (0.5, 1.5)$. The case of $\beta = 1$ is usually referred to as pink noise. $1/f$ noise is characteristic of all complex systems, regardless of their nature. If in the time series η_t there is $1/f$ noise, then for the social network there are no periodically repeated values of the number of microposts. This is due to the fact that, in the time series of microposts, it is impossible to distinguish one characteristic scale responsible for the appearance of large values of the number of microposts. The scale-invariant type of PSD demonstrates a strong nonlinearity of social network signals when it is impossible to isolate individual components in the spectrum and offer its physical interpretation. Thus, the dynamics of Twitter microposts, in which $1/f$ noise is observed, cannot be decomposed into separate components. Twitter, operating in a self-organized state, generates oscillations of microposts with PSD of the form (2).

The third universal feature of complexity associated with power laws (1) and (2) is the existence of the long memory in the time series of microposts. In simple systems, the time correlation function (for example, the autocorrelation function), which shows the extent of which the time series "remembers" its history, has the following form [30]:

$$\rho(\tau) \propto \exp\left(\frac{-\tau}{\tau_s}\right). \quad (3)$$

Complex systems are characterized by a power-law decrease in ACF as the time lag τ increases:

$$\rho(\tau) \propto \tau^{-\gamma}, \quad (4)$$

where $\gamma \in (0, 1)$.

The existence of power-law ACF for the time series of microposts means that the current number of microposts largely depends on the past number of microposts generated by Twitter, as well as the absence of characteristic times at which information about the previous appearance of microposts would be lost. In addition, dependence (4) determines a slow power decrease in the probability of a microposts flow at time t under the condition that the same flow appeared earlier at time t_0 ($t > t_0$).

It is fundamentally important that the existence of long temporal correlations states the fact of the emergence of Twitter. This fact determines the possibility of the emergence of the avalanche of microposts (extremal events) as a result of the coordinated behavior of strategically oriented network users. The mechanism of occurrence of emergent Twitter properties is described in detail in Section 2.1. If for the time series of microposts relevant to a certain topic, power laws (1), (2), and (4) are fulfilled, then the following important consequences are possible.

Firstly, the relevant Twitter segment, which includes SOUs and ROUs, distributing microposts relevant to a particular topic, is in the SOC state. Secondly, power laws describe large-scale invariance in the structure of time series of microposts generated by the self-organized critical social network. The approach to the study of scale invariance is considered in Section 3.2.

PDF, PSD, and ACF in the form of power laws make it possible to use the range of interval indicators α, β, γ as the indicator of the self-organized criticality (complexity) of the social network (Twitter). If the social network is in the SOC or the SupC states, then for such states the indicators of power laws take the values from the intervals (1, 3), (0.5, 1.5), (0, 1). Otherwise, Twitter is in the SubC state.

In conclusion of this section, we note that the proposed approach to identifying the network complexity is not based on a statistical analysis of its graph structure, but on a statistical and fractal analysis of time series generated by the network.

According to the definition of Dorogovtsev and co-authors [4], "complex networks are networks with more complex architectures than classical random graphs with their 'simple' Poissonian distributions of connections." These networks are networks with heavy-tailed distributions, in particular, with the power-law distributions. One of the complex networks classes are scale-free networks. The definition of the scale-free network at the level of its graph structure was proposed by Barabási and Albert more than 20 years ago [32]. The network is scale-free, if the distribution function of the vertices u by the number of edges k is determined by a power law:

$$u(k) \propto k^{-\alpha}, \quad (5)$$

where, as well as in (1), $\alpha \in (2, 3)$. But usually a network is considered as scale-free if $\alpha > 1$. For example, there are scale-free networks with $\alpha > 3$ [33].

It should be noted that Barabasi's preferential attachment is not the only one mechanism for scale-free networks to arise; there are several other mechanisms (e.g., see the works [32, 34, 35]). For further discussions, it is important that dependency (5) is satisfied regardless of the mechanism.

There are many studies that present an empirical justification of the feasibility of equation (5) for a large number of different types of social networks (e.g., see the works [36–38]). However, recent studies have appeared showing that not for all social networks, the power law (5) is statistically justified (e.g., see the works [39, 40]). It turned out that the identification of power laws of the distribution of vertices in natural or artificial systems is not so simple (e.g., see the works [39, 41, 42]). For example, it is not always possible to distinguish a power law from a lognormal one for samples of small size. A parabola corresponding to a lognormal law in logarithmic coordinates on a sufficiently small interval of values k looks like a straight line corresponding to a power law.

What is the advantage of our proposed approach?

First of all, there is no need to divide scale-free networks into several types depending on the value of the assessment of the indicator α and the level of significance with which this assessment was done, as proposed in [42]. Indeed, our approach involves the use of the three network complexity indicators α, β, γ . Using the spectrum of indicators of complexity α, β, γ as a network complexity identifier is only possible in the case of analysis of the time series generated by the network (realizations of some random process), but not when analyzing the data of the static network structure. Indeed, PSD and ACF are characteristics of signals, random processes, and time series.

Secondly, the use of the spectrum α, β, γ to identify network complexity has a rationale within the paradigm of the complexity, as one of the paradigms of nonlinear science, and, being its core, the theory of self-organized criticality. In the context of this theory, the network complexity is determined only by the values of the spectrum indicators and does not depend on the distribution type $u(k)$.

Third, the use of the spectrum α, β, γ allows us to identify the subcritical, the self-organized critical, and the supercritical states of the network operation.

Fourth, β and γ indicators can be independently estimated both as a static estimate of the slope ratio in a log-log scale and as a result of an estimation of the scaling indicator of time series of microposts, for example, using detrended fluctuation analysis (see Section 3.2).

3. Data Analysis, Results, and Discussion

This section provides a brief overview of using data mining techniques which are necessary for the formation of the time series of microposts and their statistical and fractal analysis, as well as the evaluation of Twitter complexity indicators and their interpretation.

3.1. Mining Twitter Time Series Data. The most suitable data source for mining of Twitter time series data that contain tweet ids (unique identifiers of tweets) regarding different events, such as political elections and natural disasters, is Harvard Dataverse. It contains the datasets of tweets ids on 12 different topics, and each dataset consists of more than 2 million unique tweet ids in the form of the 18-digit numbers (for example, 1128408193699340294) combined into one text file (.txt). Harvard Dataverse collected data using Social Feed Manager, which is the open source software that harvests social media data and web resources from Twitter. The reason why it is necessary to start to work with tweets ids, rather than tweets itself, is the fact that per Twitter's Developer Policy, tweet ids may be publicly shared for academic purposes, but tweets may not.

Nevertheless, in order to get Twitter time series, it is necessary to hydrate the obtained datasets of tweet ids. Hydrating is the process of loading JSON objects from tweets based on available tweet ids. It can be done using the

API-interface of Twitter, as well as using third-party applications. We did it with a Hydrator version 0.0.3 software. According to the obtained data, it is possible to build the interaction structure of users and time series of tweets (including retweets and other mentions).

We used the following relevant tweet ids time series events and themes for the formation and subsequent statistical and fractal analysis of the time series of microposts:

- (1) 2016 United States Presidential Election Tweet Ids [43]. The dataset contains the tweet ids of approximately 280 million tweets and retweets related to the 2016 United States Presidential Election. Tweets were collected between July 13, 2016, and November 10, 2016.
- (2) Women's March Tweet Ids [44]. The dataset consists of the tweet ids of 7,275,228 tweets and retweets related to the Women's March on January 21, 2017. Tweets were collected between December 19, 2016, and January 23, 2017.
- (3) End of Term 2016 US Government Twitter Archive [45]. The dataset consists of the tweet ids of 5,655,632 tweets and retweets, and the original tweets were made from approximately 3000 Twitter accounts, which are connected with the US government. Tweets were collected between October 21, 2016, and January 21, 2017.
- (4) Hurricanes Harvey and Irma Tweet Ids [46]. The dataset consists of the tweet ids of 35,596,281 tweets and retweets related to Hurricanes Irma and Harvey.
- (5) Immigration and Travel Ban Tweet Ids [47]. The dataset consists of the tweet ids of 16,875,766 tweets and retweets related to the immigration and travel ban that was announced by the Trump Administration in January 2017. Tweets were collected between January 30, 2017, and April 20, 2017.
- (6) Charlottesville Tweet Ids [48]. The dataset consists of the tweet ids of 7,665,497 tweets and retweets related to events in Charlottesville, Virginia, in August 2017.
- (7) Winter Olympics 2018 Tweet Ids [49]. The dataset consists of the tweet ids of 13,816,206 tweets and retweets related to the 2018 Winter Olympics held in Pyeongchang, South Korea. Tweets were collected between January 31, 2018, and February 27, 2018.
- (8) US Government Tweet Ids [50]. The dataset consists of the tweet ids of 9,673,959 tweets and retweets, and the original tweets were made from approximately 3400 US government accounts. These accounts are linked with the federal US government agencies. Tweets were collected between January 20, 2017, and July 20, 2018.
- (9) News Outlet Tweet Ids [51]. The dataset consists of the tweet ids of 39,695,156 tweets and retweets, and the original tweets were made from the Twitter

accounts of approximately 4500 news outlets; it means accounts of mass media that intended to disseminate news. Tweets were collected between August 4, 2016, and July 20, 2018.

- (10) 2018 US Congressional Election Tweet Ids [52]. The dataset consists of the tweet ids of 171,248,476 tweets and retweets related to the 2018 US Congressional Election. Tweets were collected between January 22, 2018, and January 3, 2019.
- (11) 115th US Congress Tweet Ids [53]. The dataset consists of the tweet ids of 2,041,399 tweets and retweets, and the original tweets were made from the Twitter accounts of members of the 115th US Congress. Tweets were collected between January 27, 2017, and January 2, 2019.
- (12) Ireland 8th Tweet Ids [54]. The dataset consists of the tweet ids of 2,279,396 tweets and retweets related to the referendum to repeal the 8th amendment to the Irish constitution on May 25, 2018. Tweets were collected between April 13, 2018, and June 4, 2018.

As a result, we got twelve equidistant (a step is 1 second) time series of microposts $\{\eta_i\}$ ($i = 1, 2, \dots, N$) of different lengths N , each of which is relevant to some topic (tweet Ids). Next, there is a description of the time series analysis methods $\{\eta_i\}$ (see Section 3.2), as well as the results of such analysis for each time series, obtained over its entire length N (see Section 3.3).

3.2. Statistical and Fractal Methods for Twitter Time Series Analysis. In the context of our study, the main purpose of analysis of the time series of microposts is to statistically confirm the statement that the range of empirical indicators of complexity α, β, γ takes values $(1, 3), (0.5, 1.5), (0, 1)$. Formally, we tested the statistical hypothesis of the significance of a simple linear regression:

$$\ln y_i = \delta_0 + \delta_1 \ln x_i + \varepsilon_i, \quad (6)$$

where $y_i \equiv p_i$, $x_i \equiv \eta_i$, $\delta_1 \equiv \alpha$ for PDF, $y_i \equiv S_i$, $x_i \equiv f_i$, $\delta_1 \equiv \beta$ for PSD, and $y_i \equiv \rho_i$, $x_i \equiv \tau_i$, $\delta_1 \equiv \gamma$ for ACF. This is a test of the null hypothesis $H_0: \delta_1 = 0$, with an alternative hypothesis $H_1: \delta_1 \neq 0$. As a measure of agreement with the null hypothesis, p value was used as an indicator of the minimum level of significance, in which H_0 being rejected. We used the ordinary least squares (OLS) method for estimating the parameters δ_0 and δ_1 .

The possibility of transition to simple linear regressions for statistical analysis of the time series is due to the scale invariance of the dependences (1), (2), and (4). On the one hand, such a transition will make it easier to obtain statistical estimates of the indicators α, β , and γ ; on the other hand, it will allow to establish a filter for separating power laws from other non-scale-invariant laws, for example, from normal, exponential, lognormal, and extended exponential laws for PDF.

The ACF for the observed time series $\{\eta_i\}$ represents the correlation of the values η_i and $\eta_{i+\tau}$ for different time lags τ

($\tau = 0, 1, 2, \dots, N$), i.e., correlations over different time scales τ . It is calculated based on formula $\rho(\tau) = \langle \Delta\eta_i \Delta\eta_{i+\tau} / \Delta\eta_i^2 \rangle$, where $\Delta\eta_i = \eta_i - \eta_{i-1}$ is an increment and $\langle \Delta\eta_i \Delta\eta_{i+\tau} \rangle$ and $\langle \Delta\eta_i^2 \rangle$ state the mean value for the data $\{\Delta\eta_i \Delta\eta_{i+\tau}\}$ and $\{\Delta\eta_i^2\}$, respectively. We applied standard spectral analysis techniques (Fourier transform) to calculate the PSD $S(f)$ of the time series $\{\eta_i\}$ as a function of the frequency f .

The traditional approach to the time series analysis relies on the measurement of PSD and ACF. However, only the implementation of Gaussian processes is exhaustively described by their second moments. Outside of such implementations, a complete statistical description requires an estimate of higher order moments. In addition, higher order moments do not always have such a clear physical meaning as ACF and PSD. Therefore, evaluations of a small number of values that can be given a certain meaning become important. These values include the fractal dimensions of the time series.

The fractal dimension is closely related to the scaling index s , which can be the Hurst exponent, estimated by the method of normalized range or fluctuation analysis (FA) [55], or the generalized Hurst exponent, estimated by the method of detrended fluctuation analysis (DFA) [56].

The DFA method is an efficient method for analysis of the time series characterized by the presence of the long memory or $1/f$ noise. The DFA method is a generalization of the FA method for analysis of the scale invariance of nonstationary time series.

The DFA method allows both to estimate the scaling indicator of the time series s and to obtain indirect estimates of β_s and γ_s indicators, calculated from the generalized scaling indicator s of the time series. In the first case, it is about the definition of s of scale-invariant (in the narrow sense) time series η_t , $t \in \mathbb{N}$, i.e., time series for which the equality of probability distributions (η_{at} and $a^s x_t$) takes place [57]; in the second case, it is about the existence of dependencies for the time series with power-law ACF and $1/f$ noise of the form [58]:

$$\begin{aligned} \gamma_s &= 2 - 2s, \\ \beta_s &= 2s - 1. \end{aligned} \quad (7)$$

The FA method does not always give correct estimates of the indicator s for the most time series [30]. Compared with the FA method, the DFA method gives more correct estimates in most cases [30], so we used this method to estimate s .

The DFA method is one of the algorithms based on the ideology of the transition from the original time series η_t , $t \in \mathbb{N}$ to the generalized model of one-dimensional random walks. In this algorithm, the data are first reduced to a null average with the subsequent construction of a random walk $x_k = \sum_{i=1}^k |\eta_i - \bar{\eta}|$. Next, the series x_k , $k \in \mathbb{N}$ is divided into nonintersecting segments of length a , within each of which the equation of a straight line is defined, approximating the sequence x_k . Found $x_k(a)$ approximation is treated as a local trend. Next, the mean square error of the linear approximation is calculated:

$$F(a) = \left[\left(\frac{1}{N} \right) \sum_{k=1}^N (x_k - x_k(a))^2 \right]^{0.5}, \quad (8)$$

and the corresponding calculations are made in a wide range of values a . It is believed that the dependence $F(a)$ often has the power form $F(a) \propto a^s$, and the presence of a linear segment in a log-log scale allows us to state that scaling exists.

Numerical values characterize different types of correlated dynamics of microposts, if $s \neq 0.5$ and uncorrelated behavior at $s = 0.5$. For example, the interval $0 < s < 0.5$ corresponds to anticorrelations (the alternation of large and small values in the time series of microposts); $0.5 < s < 1$ determines the correlated dynamics (large compared to the average values more often follow large values, and small values follow small ones). The special case $s = 1$ is observed for $1/f$ noise.

3.3. Data Analysis Results. Table 1 presents the OLS estimates of the spectrum complexity as a slope δ_1 of linearized dependencies (6) and DFA estimates of scaling indicators s , β_s , and γ_s , obtained using the dependencies (7). The corresponding p values are shown in brackets.

The symbol “–” denotes the absence of statistically significant DFA estimates for β_s and γ_s indicators (see equation (7)). This is due to the fact that there are no statistically significant linear dependencies of $\ln F(a) \propto s \ln a$ for the corresponding time series of microposts. Statistically significant values of the exponents are denoted in bold.

3.4. Results and Their Discussion. The most significant result in the context of our study is the existence of two classes of time series of microposts and tweet Ids corresponding to them.

The first class consists of time series for which $\alpha \in [1.23, 2.23]$, $\beta \in [1.05, 1.29]$, and $\gamma \in [0.12, 0.43]$. Indicators of the power laws of such time series belong to the spectrum of indicators of complexity (1, 3), (0.5, 1.5), (0, 1) and, consequently, Twitter, which generates such time series of microposts, is in the SOC state or the SupC state. The social network is capable of generating extreme events, which are avalanches of microposts of all sizes (regarding “sizes,” see Section 2.1) corresponding to the following tweet ids: “2016 United States Presidential Election,” “Women’s March,” “Hurricanes Harvey,” “Hurricanes Irma,” “Immigration and Travel Ban,” “Charlottesville,” “2018 US Congressional Election,” and “Ireland 8th.” In addition, the current number of microposts largely depends on the past number of microposts generated by Twitter. Indeed, for all the time series of this class indicator ACF, $\gamma \in (0, 1)$. It is noteworthy that all tweet ids relate either to protest movements or to political elections or to the population activities during natural disasters. PDF of such time series have infinite η^2 and infinite η for events related to political elections and finite η in all other cases. DFA estimates of β_s and γ_s give close values to the corresponding indicators β and γ , and the presence of statistically significant values of

the scaling exponent s determines the scale invariance of time series, which is one of the key features of the self-organized criticality of the social network. In addition, for all time series of the first class $s \cong 1$ and $\beta_s \cong 1$, which corresponds to the presence of pink noise and, accordingly, being Twitter in the SOC or the SupC states. The existence of a dependency (4) for the time series of microposts means that the current numbers of microposts largely depend on the past number of microposts generated by Twitter, as well as the absence of characteristic times at which information about previous occurrences of microposts would be lost.

The second class consists of time series for which $\alpha \in [3.24, 3.99]$, $\beta \in [0.19, 0.26]$, and $\gamma \in [5.24, 6.01]$; moreover, estimates of all indicators are not statistically significant: statistical hypothesis is accepted with previously considered p values shown in Table 1. Consequently, for these time series of microposts, at least the power laws (1) and (4) are not satisfied. This result is consistent with the results of the detrended fluctuation analysis, according to which there is no statistically significant estimate of the scaling exponent s ; therefore, these time series of microposts are not scale-invariant. Thus, Twitter, which generates these time series, is neither in the SOC state nor in the SupC state. Twitter users, that is, in such a state, are not coordinated. This leads to the generation of the time series, for which the spectrum is not performed. It may be the SubC state, but such a conclusion requires the determination of the explicit form of PDF and ACF dependencies, which is beyond the scope of our study. The only argument in favor of the assumption of Twitter being in the SubC state is the fact that indicator $\beta \in [0.19, 0.26]$ is close to the value corresponding to white noise ($\beta \cong 0$).

4. Three-Parameter Twitter Self-Organization Model

The results of the analysis of the time series of microposts presented in Section 3 are important not only for solving management problems and identifying the state of Twitter, but also as the basis for the development and verification of macroscopic models describing evolutionary processes on the social network. In the context of our study, the analysis of such time series is necessary for the verification of the model, describing the SOC state of Twitter. The construction and verification of such model is the purpose of the research presented in Section 4.

A sufficient verification of Twitter’s self-organized criticality model is that the indicators of the power laws (1), (2), and (4) of the theoretical and observable time series of microposts belong to the spectrum of complexity indicators (1, 3), (0.5, 1.5), (0, 1).

4.1. Generalized Three-Parameter Model. It is known (e.g., see the works [59–61]) that the concept of self-organization is a generalization of the physical concept of critical phenomena, such as phase transitions. Therefore, the phenomenological theory that we propose is a generalization of the theory of thermodynamic transformations for open

TABLE 1: Estimates of the values of the complexity spectrum indices for time series of microposts.

Tweet Ids	α	β	γ	β_s	γ_s	s
2016 United States Presidential Election	1.23 (0.0121)	1.29 (0.0182)	0.12 (0.0201)	0.92 (0.0036)	0.08 (0.0036)	1.04 (0.0036)
Women's March	2.11 (0.0234)	1.23 (0.0198)	0.42 (0.0211)	0.90 (0.0101)	0.10 (0.0101)	1.05 (0.0101)
End of Term 2016 US government	3.24 (0.6743)	0.24 (0.7235)	5.24 (0.6990)	—	—	0.45 (0.7699)
Hurricanes Harvey	2.12 (0.0312)	1.13 (0.0289)	0.34 (0.0320)	0.89 (0.0015)	0.11 (0.0015)	1.06 (0.0015)
Hurricanes Irma	2.23 (0.0234)	0.98 (0.0194)	0.18 (0.0209)	0.96 (0.0098)	0.04 (0.0098)	1.02 (0.0098)
Immigration and Travel Ban	2.18 (0.0401)	1.09 (0.0320)	0.21 (0.0128)	0.97 (0.0094)	0.03 (0.0094)	1.02 (0.0094)
Charlottesville	2.18 (0.0313)	1.21 (0.0287)	0.43 (0.0121)	0.90 (0.0101)	0.10 (0.0101)	1.05 (0.0101)
Winter Olympics 2018	3.59 (0.7239)	0.22 (0.6348)	5.64 (0.5341)	—	—	0.52 (0.8172)
US Government	3.28 (0.6361)	0.19 (0.7298)	6.01 (0.6399)	—	—	0.48 (0.7456)
News Outlet	3.36 (0.4275)	0.23 (0.3895)	5.50 (0.4458)	—	—	0.54 (0.6451)
2018 US Congressional Election	1.47 (0.0281)	1.05 (0.0398)	0.22 (0.0435)	0.95 (0.0099)	0.05 (0.0099)	1.03 (0.0099)
115th US Congress	3.99 (0.3189)	0.26 (0.4197)	5.24 (0.5618)	—	—	0.46 (0.9999)
Ireland 8 th	2.18 (0.0311)	1.18 (0.0270)	0.35 (0.0311)	0.97 (0.0129)	0.03 (0.0129)	1.02 (0.0129)

systems. Twitter self-organization is possible due to its openness, since there are incoming and outgoing network flows of its users constantly; its macroscopic nature, because it includes a large number of users; and its dissipation, because there are losses in the flows of microposts and associated information.

Based on the synergetic principle of subordination, it can be argued that Twitter's self-organization in a critical state is completely determined by the suppression of the behavior of an infinite number of microscopic degrees of freedom by a small number of macroscopic degrees of freedom. As a result, the collective behavior of users of the social network is defined by several parameters or degrees of freedom: an order parameter η_t , its role is the number of microposts relevant to a certain topic that are sent by SOUs and, unwittingly following their strategies, by ROUs; a conjugate field h_t is information associated with microposts distributed on the network; and a control parameter S_t which is the number of SOUs of the networks. On the other hand, in Twitter's self-organization as the nonequilibrium system, the dissipation of flows of microposts on the network should play a crucial role, which ensures the transition of the network to the stationary state. In the process of self-organization in a critical state of the network, all three degrees of freedom have an equal character, and the description of the process requires a self-consistent view of their evolution. The restriction to three degrees of freedom is also determined by the Ruelle–Takens theorem [62], according to which a nontrivial picture of self-organization is observed if the number of selected degrees of freedom is, at least, three.

Kinetic equations and a detailed physical substantiation of the relations between its parameters are given in our paper [63]. The construction of the three-parameter self-organization scheme was based on the analogy between the mechanisms of functioning of a single-mode laser and the microblogging social network. The study of possible modifications of equations leading to models that are capable of describing critical phenomena on Twitter, in particular the SOC or the SupC states, is outside of the scope of this paper. These equations in dimensionless quantities have the following form:

$$\begin{cases} \dot{\eta}_t = -\eta_t^\varepsilon + h_t + \sqrt{I_\eta} \xi_t, \\ \frac{\tau_h}{\tau_\eta} \dot{h}_t = -h_t + \eta_t^\varepsilon S_t + \sqrt{I_h} \xi_t, \\ \frac{\tau_S}{\tau_\eta} \dot{S}_t = (S_0 - S_t) - \eta_t^\varepsilon h_t + \sqrt{I_S} \xi_t, \end{cases} \quad (9)$$

where I_i is the intensity of fluctuations (or noises) of each of the degrees of freedom $i = \eta, h, S$; τ_i is relaxation times of corresponding quantities; ξ_t is the white noise due to random factors; and S_0 is the number of SOUs of the network at the initial time moment ($t = 0$) of the network evolution. The parameter S_0 determines the degree of external disturbance or pumping of the social network by strategically oriented users, which removes Twitter from the equilibrium state.

Assuming $\varepsilon = 1$, and also neglecting random factors ξ_t , equation (9) represents a well-known system of Lorenz equations, in which dynamic variables describe the self-consistent behavior of the order parameter, the conjugate field, and the control parameter. In such a system, the functions η_t/τ_η , h_t/τ_h , and $(S_t - S_0)/\tau_S$ describe autonomous relaxation of the number of microposts, of conjugate information, and the number of strategically oriented network users to stationary values $\eta_t = 0$, $h_t = 0$, $S_t = S_0$. The Lorenz system takes into account Le Chatelier's principle: since the reason for self-organization is the growth of the control parameter S_t , the values of η_t and h_t should be changed in such a way as to prevent the growth S_t . Finally, the positive feedback between the order parameter η_t and the control parameter S_t , which leads to an increase in the conjugate field h_t , is fundamentally important. This is what causes the self-organization [60]. Despite the fact that the Lorenz system is a rather rough approximation in solving some problems, the system is an adequate model that qualitatively describes the processes of self-organization in systems of various nature, including the kinetics of first- and second-order phase transitions [59].

The feedback intensity indicator ε in equation (9), which also distinguishes it from the Lorenz system, is an indicator of the disturbance of Twitter's ordering on its self-consistent

behavior. From a physical point of view, replacing the order parameter normalized to one ($\eta_t \in (0, 1)$) with a larger value η_t^ε ($\varepsilon < 1$) means that the ordering process affects Twitter's self-consistent behavior more than in the ideal case, when $\varepsilon = 1$. In the case when $\eta_t \in (0, \infty)$, the parameter ε can be determined by introducing the unit step function $\theta(\eta_t)$ using the following replacement:

$$\varepsilon \equiv \varepsilon + \theta(\eta_t - 1), \quad (10)$$

$$\text{where } \theta(\eta_t - 1) = \begin{cases} 0, & \eta_t < 1, \\ 1, & \eta_t \geq 1. \end{cases}$$

Another replacement is the replacement in equation (9) of the order parameter η_t of the following form:

$$\eta_t^\varepsilon \equiv \text{Sign}(\eta_t)|\eta_t|^\varepsilon. \quad (11)$$

The meaning of the transition $\eta_t \rightarrow \text{Sign}(\eta_t)|\eta_t|^\varepsilon$ in the Lorenz system is that the transition of the order parameter to its absolute value avoids the minimum values of the power function η_t^ε with a fractional exponent ε .

Further, if it is not specified separately, the parameters ε and η_t are defined as (10) and (11).

4.2. Self-Organized Criticality of Twitter in Adiabatic Approximation. Equation (9), as well as the system of Lorenz equations, does not have an exact analytical solution. When certain conditions are met, system (9) in an adiabatic approximation can be quite acceptable approximation. The adiabatic self-organization mode corresponds to a phase transition process for which the stationary value of the control parameter does not reduce to the pump parameter (e.g., see the works [59–61]).

In the adiabatic approximation, the characteristic relaxation time of the number of microposts τ_η far exceeds the corresponding relaxation times of the information associated with microposts and the number of strategically oriented users: τ_h and τ_S . This means that the information $h_t \cong h(\eta_t)$ and the number of strategically oriented users $S_t \cong S(\eta_t)$ follow the changes in the number of microposts η_t on Twitter. When the conditions $\tau_\eta \gg \tau_h, \tau_S$ are fulfilled, the principle of subordination makes it possible to neglect the fluctuations of the quantities $h(\eta_t)$ and $S(\eta_t)$ in equation (9), i.e., assume $(\tau_h/\tau_\eta)\dot{h}_t = (\tau_S/\tau_\eta)\dot{S}_t = 0$.

The use of the adiabatic approach to Twitter as an open nonequilibrium system means that, when the value of the social network pumping by strategically oriented users tends to zero ($S_0 \rightarrow 0$), there is a slow decrease in the flow of microposts η_t and a rapid decrease in the associated information h_t as well as in the number of strategically oriented users S_t , who sending microposts.

Using the adiabatic approximation allows to reduce the dimension of the phase space, i.e., transit from the analysis of a three-dimensional dynamic system with additive noise (9) to the analysis of a one-parameter stochastic system with multiplicative noise:

$$\tau_\eta \dot{\eta}_t = f_\eta + \sqrt{I_\eta} \xi_t. \quad (12)$$

In the Langevin equation (12), the drift and diffusion parts are determined by the following values:

$$\begin{aligned} f_\eta &\equiv -\eta_t^\varepsilon + S_0 \eta_t^\varepsilon \mu_\eta, \\ I_\eta &\equiv I_\eta + (I_h + I_S \eta_t^{2\varepsilon}) \mu_\eta^2, \end{aligned} \quad (13)$$

where $\mu_\eta \equiv 1 + \eta_t^{2\varepsilon}$.

4.3. Results and Their Discussion

4.3.1. Self-Organized Critical State of Twitter. Suppose that the social network Twitter is self-organized into a critical state as a result of the agreed actions of SOUs and ROUs. Such a saturated network state by strategically oriented users and information is characterized by the following features: firstly, by the significant intensity of stochastic interactions between strategically oriented users ($I_S \gg I_\eta, I_h$), and secondly, by the significant impact of the streamlining process on Twitter's self-consistent behavior. In this case, equality (10) holds for the feedback intensity indicator ε . In this state, even a negligible external disturbance ($S_0 \cong 0$) is enough to spread avalanches of microposts on the social network.

Therefore, equation (12), describing the being of the social network in the SOC state, will be in the following form:

$$\tau_\eta \dot{\eta}_t = -\eta_t^\varepsilon + \sqrt{I_S} \eta_t^\varepsilon \mu_\eta \xi_t. \quad (14)$$

Suppose that the homogeneous process (14) occurs on the interval $(\eta_{\min}, 1)$ and $\varepsilon < 1$, where η_{\min} is the minimum number of microposts for which power-law PDF is performed. Then, a nonnormalized solution of the corresponding stationary Fokker–Planck equation with reflecting boundaries is given by

$$p_s(\eta) \propto I_S^{-1} \eta^{-2\varepsilon} \mu_\eta^{-2} \exp \left[-I_S^{-1} \int_{\eta_{\min}}^{\eta} \eta'^{-\varepsilon} \mu_{\eta'}^{-2} d\eta' \right]. \quad (15)$$

The integral in PDF (15) has the following form, rather bulky for analysis:

$$\left\{ \frac{\eta^{1-\varepsilon}}{2(\varepsilon-1)\mu_{\eta'}} \left[(3\varepsilon-1)\mu_{\eta'} {}_2F_1 + \eta'^{2\varepsilon} - \varepsilon(3\eta'^{2\varepsilon} + 2) \right] \right\} \Big|_{\eta_{\min}}^{\eta}, \quad (16)$$

where ${}_2F_1(1, (\varepsilon-1/2\varepsilon); (3\varepsilon-1/2\varepsilon); -\eta'^{-2\varepsilon})$ is the hypergeometric function.

The graph of the unnormalized PDF (15) in a log-log scale for $\eta \in (\eta_{\min}, 1)$, $\eta_{\min} = 0.001$ and the values of $\varepsilon \in (0, 1)$ are presented in Figure 1.

Distribution (15) is a power-law PDF of the form (1) with indicator α , corresponding to indicators of feedback intensity ε . Increasing the feedback intensity leads to an increase in the stationary probability $p_s(\eta)$ for all $\eta \in (0.001, 1)$.

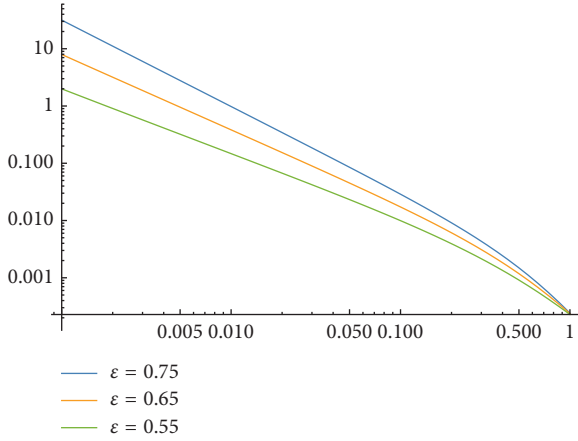


FIGURE 1: Log-log plot of the distribution (15) for $I_S = 1000$, and three different $\varepsilon = 0.55, 0.65, 0.75$.

In order to obtain analytical values for PSD and ACF of a random process (14), it is necessary to obtain an analytical solution $p(\eta_t, t)$ of the corresponding nonstationary Fokker–Planck equation. If it is possible to obtain an exact analytic values for $p(\eta_t, t)$ and, accordingly, an analytical definition of $S(f)$ and $\rho(\tau)$, then it will be difficult to interpret. Therefore, we obtained these dependences as a result of the numerical integration of equation (14). According to the obtained realizations of this random process, the dependences $S(f)$ and $\rho(\tau)$ were determined.

In Figures 2 and 3, the PSD and ACF are presented in a log-log scale for one of the process implementations (14). To obtain implementations of the stochastic processes and to process the results, standard Wolfram Mathematica version 11.2 algorithms were used. First, data were generated using the “ItoProcess” function. Further, based on the data obtained using the “PowerSpectralDensity” functions, PSDs similar to those shown in Figure 2 were built. Using the “CorrelationFunction,” ACFs were found similar to those shown in Figure 3. Also in the figures are shown the following: linear approximations and the estimates of the scaling indicators β and γ which are obtained by averaging over 10,000 realizations of the OLS estimates β and γ of the random process. The straight line shown in Figure 2 is a linear approximation of the PSD with the OLS estimate of the index $\beta = 1.1(0.009)$ that corresponds to a random process with pink noise; straight line in Figure 3 is a linear approximation of ACF with the estimate of the index $\gamma = 0.8(0.010)$ that corresponds to a random process with the long memory. The corresponding p values are shown in brackets.

Consequently, equation (14) is a good approximation for describing the self-organized critical state of Twitter. Indeed, all theoretical indicators of complexity (criticality) ε, β , and γ belong to the spectrum of indicators of complexity (1, 3), (0.5, 1.5), (0, 1).

4.3.2. Subcritical and Supercritical States of Twitter. The SubC state of Twitter is a chaotic state characterized by the

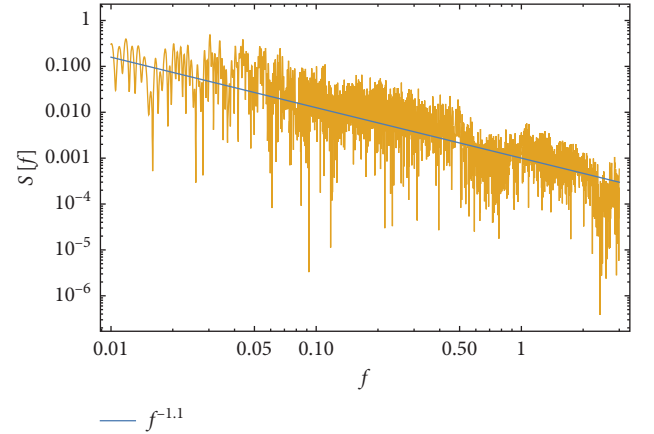


FIGURE 2: Log-log plot of the PSD for $\tau_\eta = 1$, $\varepsilon = 0.75$, and $I_S = 1000$.

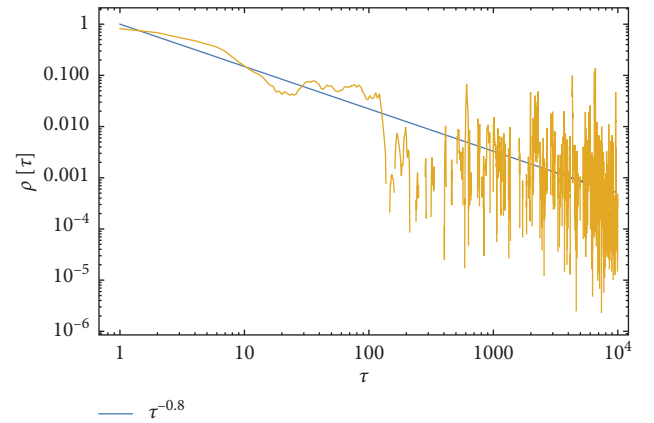


FIGURE 3: Log-log plot of the ACF for $\tau_\eta = 1$, $\varepsilon = 0.75$, and $I_S = 1000$.

presence of a negligible number of avalanches of micro-posts and, therefore, $p_s(\eta)$ is not the power-law PDF. Also SubC state is characterized by resistance to small disturbances. In this state, minor chaotic directed flows of micro-posts are created by all users of the social network, regardless of the size of its pumping by strategically oriented users. The social network functions in the SubC state until S_t reaches a certain critical value S_c . In this state, the streamlining process has almost no effect on the self-consistent behavior of the network, i.e., the feedback intensity indicator $\varepsilon = 1$, and the fluctuation intensity of each of the degrees of freedom is comparable (let us take $I_\eta = I_h = I_S = I$).

Therefore, the SubC state of Twitter is described by the following Langevin equation:

$$\tau_\eta \dot{\eta}_t = -\eta_t + S_0 \eta_t \mu_\eta + \sqrt{I(1 + \mu_\eta^3)} \xi_t, \quad (17)$$

where $\mu_\eta \equiv 1 + \eta_t^2$.

Assuming that the process (17) is on the interval (0, 1), the solution of the corresponding stationary Fokker–Planck equation is a PDF of the following form:

$$p_s(\eta) \propto I^{-1} (1 + \mu_\eta^3)^{-1} \exp \left[I^{-1} \int_0^\eta \frac{S_0 \eta' \mu_{\eta'}^2 - \eta'}{1 + \mu_{\eta'}^3} d\eta' \right]. \quad (18)$$

The integral in the distribution (18) has the following form:

$$\left\{ \frac{1}{12I} \left[2\sqrt{3} (S_0 - 1) \tan^{-1} \left(\frac{2\eta'^2 + 1}{\sqrt{3}} \right) - (S_0 + 1) \ln \frac{(2 + \eta'^2)^2}{\eta'^4 + \eta'^2 + 1} \right] \right\} \Big|_0^\eta. \quad (19)$$

Distribution graph (18) is presented in Figure 4 in a log-log scale.

It is obvious that PDF presented in Figure 4 is not a power-law PDF and, therefore, such a distribution describes the appearance of avalanches of microposts only of relatively small size. In addition, an increase in the network pumping S_0 leads to an increase, although not significant, in the frequency of appearance of relatively large numbers of microposts.

Thus, it is reasonable to assume that a further increase in the number of strategically oriented social network users to a certain critical value S_c , accompanied by a significant increase in the intensity of stochastic interactions between them ($I_S \gg I_\eta, I_h$), will lead the network to self-organization in a critical state.

Twitter in the SubC state is able to generate time series of microposts with relatively small values. Perhaps, these time series correspond to the following tweet identifiers: "End of Term 2016 US Government," "Winter Olympics 2018," "US Government," and "News Outlet."

If $S > S_c$, then chaos changes in order, and instead of insignificant chaotic directed flows of microposts, a dedicated directional flow (avalanche) of microposts appears on the network. This flow becomes significant at the macrolevel. Like the SubC state, the SupC state is resistant to small disturbances (for example, adding only one SOU). In the SupC state, small disturbances cannot tangibly affect the size of the avalanche of microposts.

The distribution of the number of microposts which is characterized by the SupC state of Twitter is presented in Figure 5 in a log-log scale. PDFs are presented (see distribution (15)) for $\varepsilon = 0.75$ and various values of the network pumping parameter.

The distributions shown in this figure correspond to the power-law PDF. Moreover, the weighting of the distribution tails is due to the increased pumping of the network by the strategically oriented users. If Twitter is in the SupC state, then the number of SOUs and, accordingly, the microposts avalanche sizes continue to grow.

5. Discussion

The obtained results are of interest both for identifying the SubC state or the SupC state of Twitter that are stable to small disturbances based on the analysis of the observed time series of microposts and for determining the causes of the social network self-organization in a critical state.

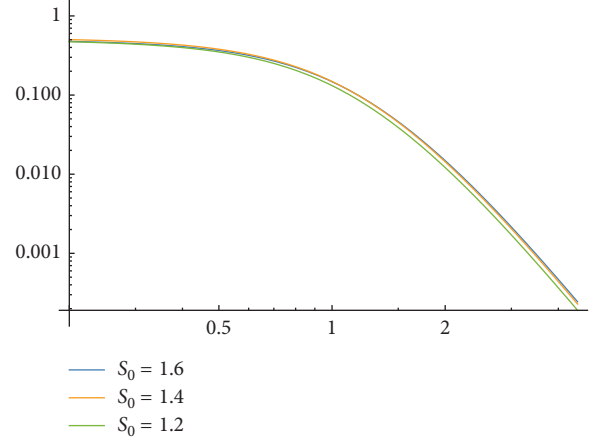


FIGURE 4: Log-log plot of the distribution (18) for $I = 1$ and three different $S_0 = 1.2, 1.4, 1.6$.

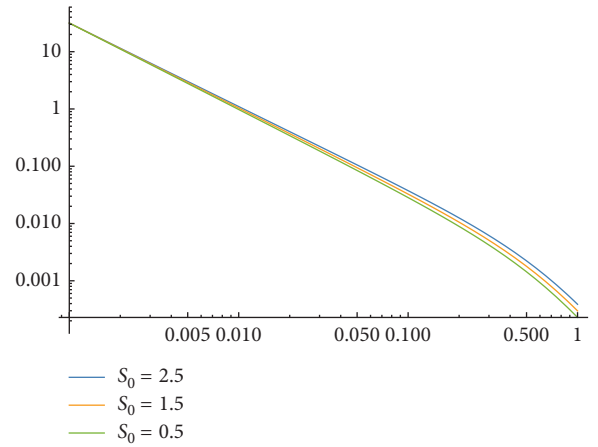


FIGURE 5: Log-log plot of the distribution (15) for $I_s = 1000$, $\varepsilon = 0.75$, and three different $S_0 = 0.5, 1.5, 2.5$.

The presence of a spectrum of criticality indicators $(1, 3), (0.5, 1.5), (0, 1)$ for the observed time series of microposts is a sufficient feature that Twitter is in the SupC state. Such a state appears from time t_c on the network evolution process and continues to exist during the time interval Δt_{SupC} . Starting from time t_c , the network's behavior becomes unpredictable: avalanches of microposts of any size can appear over time $t \geq t_c$.

It is important that the identification of the SupC state of the network does not require a detailed analysis of the interactions between its users at the microlevel. Only an analysis of the time series of microposts for being in the spectrum is sufficient, which does not require significant resource costs. Moreover, estimates of β and γ can be obtained independently, for example, using the DFA method.

Prior to the transition of the network in the SOC state at time t_c and then in the SupC state, it is in the SubC state during the time interval Δt_{SubC} . If the network is in this state, then PDF and ACF for the observed time series of microposts are not scale-invariant (see dependencies (1) and (4), respectively). This state can be characterized by exponential laws for PDF and ACF, and the exponent β of PSD has a

value close to 0. It is important to note, it is possible that a network in this state can arise a critical state over time. Before transition in the SOC state, there will be a slow increase in the size of avalanches of microposts over time until a large splash appears in the time series at $t = +t_c$. But the appearance of the SOC state on the network is not necessary at all: the network can continue to be in the SubC state until it is completely relaxed due to the loss of user interest in the discussed topic.

An approach to monitor the social network state based on the spectrum analysis, for example, can be effective for identifying the origin of protest movements for which Twitter is one of the tools. In addition, the approach can be used to study the activity of users on the network related to political elections. For example, if the social network is in the SubC state and for the corresponding time series of microposts it is possible to find the interval $\Delta t \in \Delta t_{\text{SubC}}$, in which a slow increase in the size of avalanches is observed, then the existence of such Δt is a possible precursor of the appearance of the SOC state and further transition to the SupC state. Another situation is possible. If it is possible to find a relatively small interval $(t_c, t) \in \Delta t_{\text{SubC}}$, then the existence of such an interval is a possible precursor of the unpredictability of the behavior on the social network. Starting from time t , avalanches of microposts of all sizes will appear. Note that all this is nothing more than a discussion of possible applications. To conduct such studies, it is necessary to develop and test algorithms for detecting such integrals, but this is beyond the scope of our study.

The proposed phenomenological social network self-organization equation (9) in the adiabatic approximation (14) describes not only the functioning of Twitter in the SubC, the SOC, and the SupC states, but also the conditions for the transition from one critical state to another. The latter is clearly demonstrated in Table 2.

SubC state of Twitter is a typical social network state. Indeed, the network consists of a large number of users \mathcal{N} ; each of which follows its own strategy, not related to the strategies of other network users. The intensity of fluctuations of each of the degrees of freedom is commensurate ($I_\eta = I_h = I_S$), and the indicator of the intensity of feedback (ε) is equal to 1. The network that is pumping by strategically oriented users ($S_0 > 0$) does not change the network functioning mode qualitatively.

A necessary condition for the network self-organization in a critical state is the appearance of a certain number of users S within it, who follow a certain strategy, i.e., acting in concert, involving random users as their subscribers. This is an instantaneous unstable state of the network that does not require pumping ($S_0 = 0$). In this state, the intensity of stochastic interactions between SOUs increases significantly ($I_S \gg I_\eta, I_h$), and the streamlining process affects Twitter's self-consistent behavior more strongly ($\varepsilon \in (0, 1)$) than if Twitter was in the SubC state.

As a result of pumping of the network by strategically oriented users ($S_0 > 0$), the network moves to the SupC state. In this state, the intensity of stochastic interactions between SOUs is $I_S \gg I_\eta, I_h$ and $\varepsilon \in (0, 1)$.

TABLE 2: Critical states of Twitter.

State	I_i	ε	S_0
SubC	$I_\eta = I_h = I_S$	1	>0
SOC	$I_S \gg I_\eta, I_h$	(0, 1)	0
SupC	$I_S \gg I_\eta, I_h$	(0, 1)	>0

It is fundamentally important that self-organization in a critical state occurs as a result of the agreed action of a relatively small number of users following a single strategy. Random users can not form avalanches of microposts of all sizes on the network.

6. Conclusion

In conclusion, we formulate important questions, the answers to which cannot be gotten in the analysis of the phenomenological model (12) of Twitter self-organization in the adiabatic approximation, and we also indicate the possible ways to find the solution.

When discussing Twitter's self-organization mechanisms in a critical state (see Section 2.1), it was noted that one of the possible mechanisms of emergence of the SOC state is the formation of a hierarchical structure in the network, through which avalanches of microposts of all sizes appear in the network. The following is a brief overview of research on this.

Moriano and co-authors state in their paper [64] that "Global events trigger viral information cascades that easily cross community boundaries and can thus be detected by monitoring intra- and inter-community communications." They showed, when a global event (Boston Marathon bombing) occurs, it spreads virally, crossing community boundaries and producing more intercommunity. Despite the fact that we are talking about information cascades, there is no evidence in the article of the self-organized critical nature of this phenomenon. The need of existence of hierarchical structure (user, his subscribers, subscribers of their subscribers, etc.) for the emergence of self-organized critical states is presented in [65, 66]. Morse and co-authors [67] consider the persistent cascades, i.e., recurring patterns of communication among individuals, and relate them to hierarchical spreading of content, analogously to what we discuss in our study. Liu and co-authors [68] devise an embedding model which exploits multiple relations of hashtag-hashtag, hashtag-tweet, tweet-word, and word-word relations based on the hierarchical heterogeneous network.

Stella and co-authors [69] detect power-law relationships between cascade rate and size on Twitter during a voting event and they show how social bots used by human users were capable of creating avalanches of microposts. They showed, "online social interactions during a massive voting event can be used to build an accurate map of real-world political parties and electoral ranks for Italian elections in 2018." They provided, "evidence that information flow and collective attention are often driven by a special class of highly influential users, who exploit thousands of automated agents, also known as bots, for enhancing their online

influence.” In addition, they showed, “influential users generate deep information cascades in the same extent as news media and other broadcasters, while they uniformly infiltrate across the full range of identified groups.” Obviously, highly influential users, who exploit thousands of automated agents are exactly SOUs. Rizoiu and co-authors state in their paper [70] that “Socialbots is more active on Twitter—starting more retweet cascades and retweeting more—but they are 2.5 times more influential than humans, and more politically engaged.” There are studies in which the role of social bots in the emergence of information cascades is considered (e.g., see the works [71, 72]).

González-Bailón and co-authors [73] studied “recruitment patterns in the Twitter network and find evidence of social influence and complex contagion.” They identified the network position of early participants (i.e., the leaders of the recruitment process) and of the users who acted as seeds of message cascades (i.e., the spreaders of information). They found that early participants cannot be characterized by a typical topological position, but spreaders tend to be more central in the network.

Finally, let us consider who can act as SOUs or ROUs. It should be noted that for the identification of SOUs and/or ROUs, time series analysis of microposts is not sufficient. A more meaningful such as sentimental data analysis is beyond the scope of our study.

In the first class, as we discussed previously, there are SOUs. In the cases of political elections, SOUs could be network political bots or “botnets,” who act in concert and use Twitter as a platform for the formation of the avalanche of microposts. For example, Kollanyi and co-authors [74], who analyzed Twitter dataset on US Presidential Election 2016, found that “political bot activity reached an all-time high for the 2016 campaign.” In the cases of protest movements, SOUs, such as leaders or organizers of protests, can be coordinated users who use Twitter as a platform to encourage others to protest. Wang and Caskey indicated in [75] that “Twitter is a tool primarily used for sharing objective, logistical information, along with opinions, to create a unified community and mobilize individuals to participate in a physical space of protests.” And finally, in the cases of natural disasters, we assume SOUs can be the most active, but noncoordinated Twitter users. For example, these users can use Twitter to spread the information about the current state of the environment in their neighborhood, the remaining water in the nearest groceries, etc.

However, it is more interesting to consider the possible users’ nature in the second class. As our analysis showed, there are only ROUs in these datasets:

- (1) End of Term 2016 US Government Twitter Archive. The original tweets were made by 3000 users who are connected with federal US government agencies. We assume that these users acted not in agreement with each other and posted general content. There was no consistent behavior in their action, such as collusion. Therefore, they were ROUs.
- (2) Winter Olympics 2018. Obviously, a lot of different users used Twitter as the platform to advertise the

content; however, all the users pursued their own interests. For example, each sportsman used Twitter as the advertising platform of his brand. In this case, they were ROUs.

- (3) US Government. The original tweets were made by 3400 users who are connected with federal US government agencies. As it was previously, these tweets had general content and were not unified by a common goal, so these users were ROUs.
- (4) News Outlet. The basic tweets were made by news agencies. However, each agency has its own subject, as well as its own way of presenting news. Moreover, each agency promotes news in different time and, sometimes, supports different sides of conflict, for example. We suppose this could be the most reasonable description why these news agencies were ROUs.
- (5) 115th US Congress. The original tweets were made by 535 congress members and their official representatives. As it was in Winter Olympics 2018 example, each member used Twitter as the platform to share his ideas, but they were not unified by a common goal. In this case, they were ROUs.

Data Availability

Previously reported Tweet Ids data were used to support this study and are available at [<https://doi.org/10.7910/DVN/PDI7IN>, <https://doi.org/10.7910/DVN/5ZVMOR>, <https://doi.org/10.7910/DVN/TQBLWZ>, <https://doi.org/10.7910/DVN/QRKIBW>, <https://doi.org/10.7910/DVN/5CFLLJ>, <https://doi.org/10.7910/DVN/DVLJTO>, <https://doi.org/10.7910/DVN/YMJPFJ>, <https://doi.org/10.7910/DVN/2N3HHD>, <https://doi.org/10.7910/DVN/2FIFLH>, <https://doi.org/10.7910/DVN/AEZPLU>, <https://doi.org/10.7910/DVN/UIVHQR>, and <https://doi.org/10.7910/DVN/PYCLPE>]. These prior studies (and datasets) are cited at relevant places within the text as references [43–54].

Conflicts of Interest

The authors declare that there are no conflicts of interest regarding the publication of this paper.

Acknowledgments

This work was partially funded by the Russian Foundation for Basic Research (grant 16-07-01027).

References

- [1] P. Sen and B. Chakrabarti, *Sociophysics: An Introduction*, Oxford University Press, Oxford, UK, 2013.
- [2] R. Kutner, M. Ausloos, D. Grech, T. Di Matteo, C. Schinckus, and H. E. Stanley, “Econophysics and sociophysics: their milestones & challenges,” *Physica A: Statistical Mechanics and its Applications*, vol. 516, pp. 240–253, 2019.
- [3] M. Newman, “The physics of networks,” *Physics Today*, vol. 61, no. 11, pp. 33–38, 2008.

- [4] S. N. Dorogovtsev, A. V. Goltsev, and J. F. F. Mendes, "Critical phenomena in complex networks," *Reviews of Modern Physics*, vol. 80, no. 4, pp. 1275–1335, 2008.
- [5] P. Fronczak, A. Fronczak, and J. A. Holyst, "Phase transitions in social networks," *The European Physical Journal B*, vol. 59, no. 1, pp. 133–139, 2007.
- [6] B. C. Eu, "Thermodynamics of irreversible processes non-equilibrium statistical mechanics, fundamental theories of physics (an international book series on the fundamental theories of physics: their clarification)," *Development and Application*, vol. 93, pp. 12–54, 1998.
- [7] P. Bak, C. Tang, and K. Wiesenfeld, "Self-organized criticality: an explanation of the $1/f$ noise," *Physical Review Letters*, vol. 59, no. 4, pp. 381–384, 1987.
- [8] P. Bak, C. Tang, and K. Wiesenfeld, "Self-organized criticality," *Physical Review A*, vol. 38, no. 1, pp. 364–374, 1988.
- [9] D. Markovic and C. Gros, "Power laws and self-organized criticality in theory and nature," *Physics Reports*, vol. 536, pp. 41–74, 2015.
- [10] B. Tadic, M. M. Dankulov, and R. Melnik, "Mechanisms of self-organized criticality in social processes of knowledge creation," *Physical Review E*, vol. 96, Article ID 032307, 2017.
- [11] Q. K. Meng, "Self-organized criticality in small-world networks based on the social balance dynamics," *Chinese Physics Letters*, vol. 28, Article ID 118901, 2011.
- [12] P. A. Noel, C. D. Brummitt, and R. M. D'Souza, "Bottom-up model of self-organized criticality on networks," *Physical Review E*, vol. 89, Article ID 012807, 2014.
- [13] A. Mollgaard and J. Mathiesen, "Emergent user behavior on twitter modelled by a stochastic differential equation," *PLoS One*, vol. 10, Article ID e0123876, 2015.
- [14] M. Aguilera, I. Morer, X. Barandiaran et al., "Quantifying political self-organization in social media. Fractal patterns in the Spanish 15M movement on twitter," in *Proceedings of the 12th European Conference on Artificial Life*, pp. 395–402, Detroit, MI, USA, September 2013.
- [15] L. Kirichenko, V. Bulakh, and T. Radivilova, "Fractal time series analysis of social network activities," in *Proceedings of the IEEE 4th International Scientific-Practical Conference Problems of Infocommunications*, pp. 456–459, Kharkiv, Ukraine, 2017.
- [16] T. De Bie, J. Lijffijt, C. Mesnage C et al., "Detecting trends in twitter time series," in *Proceedings of the IEEE 26th International Workshop on Machine Learning for Signal Processing*, pp. 1–6, Salerno, Italy, 2016.
- [17] D. R. Bild, Y. Liu, R. P. Dick et al., "Aggregate characterization of user behavior in Twitter and analysis of the retweet graph," *ACM Transactions on Internet Technology*, vol. 15, no. 4, 2015.
- [18] C. Remy, N. Pervin, F. Toriumi et al., "Information diffusion on twitter: everyone has its chance, but all chances are not equal," in *Proceedings of the IEEE International Conference on Signal-Image Technology and Internet-Based Systems*, Kyoto, Japan, 2013.
- [19] J. P. Gleeson and R. Durrett, "Temporal profiles of avalanches on networks," *Nature Communications*, vol. 8, p. 1227, 2017.
- [20] C. Liu, X.-X. Zhan, Z.-K. Zhang, G.-Q. Sun, and P. M. Hui, "How events determine spreading patterns: information transmission via internal and external influences on social networks," *New Journal of Physics*, vol. 17, no. 11, Article ID 113045, 2015.
- [21] P. Bak, *How Nature Works. The Science of Self-Organized Criticality*, Springer-Verlag, New York, NY, USA, 1996.
- [22] R. Alvarez, D. Garcia, Y. Moreno et al., "Sentiment cascades in the 15M movement," *EPJ Data Science*, vol. 4, no. 6, 2015.
- [23] S. Pramanik, Q. Wang, M. Danisch et al., "Modeling cascade formation in twitter amidst mentions and retweets," *Social Network Analysis and Mining*, vol. 7, pp. 1–41, 2017.
- [24] M. M. Uddin, M. Imran, and H. Sajjad, "Understanding types of users on twitter," in *Proceedings of the 6th ASE International Conference in Social Computing*, Stanford, CA, USA, 2014.
- [25] A. I. Olemskoi, "Hierarchical pattern of superdiffusion," *Journal of Experimental and Theoretical Physics Letters*, vol. 71, no. 7, pp. 285–288, 2000.
- [26] E. Bakshy, A. Arbor, W. A. Mason et al., "Everyone's an influencer: quantifying influence on twitter," in *Proceedings of the WSDM'11 Fourth ACM International Conference on Web Search and Data Mining*, pp. 65–74, Hong Kong, China, 2011.
- [27] E. Himmelboim, M. A. Smith, L. Rainie et al., *Classifying Twitter Topic-Networks Using Social Network Analysis*, Social Media + Society, New York, NY, USA, 2017.
- [28] D. Antoniadou and C. Dovrolis, "Co-evolutionary dynamics in social networks: a case study of Twitter," *Computational Social Networks*, vol. 2, pp. 1–21, 2015.
- [29] J. Portugali, "Self-organization and the city," in *Encyclopedia of Complexity and Systems Science*, R. Meyers, Ed., Springer, New York, NY, USA, 2009.
- [30] J. W. Kantelhardt, "Fractal and multifractal time series," in *Mathematics of Complexity and Dynamical Systems*, R. Meyers, Ed., Springer, New York, NY, USA, 2012.
- [31] A. Clauset, C. R. Shalizi, and M. E. J. Newman, "Power-law distributions in empirical data," *SIAM Review*, vol. 51, no. 4, pp. 661–703, 2009.
- [32] A.-L. Barabási and R. Albert, "Emergence of scaling in random networks," *Science*, vol. 286, no. 5439, pp. 509–512, 1999.
- [33] M. Boguñá, R. Pastor-Satorras, and A. Vespignani, "Cut-offs and finite size effects in scale-free networks," *European Physical Journal B*, vol. 38, pp. 205–209, 2004.
- [34] J. S. Andrade, H. J. Herrmann, R. F. Andrade et al., "Apollonian networks: simultaneously scale-free, small world, euclidean, space filling, and with matching graphs," *Physical Review Letters*, vol. 94, pp. 1870–1871, 2005.
- [35] W. Willinger, D. Alderson, and J. C. Doyle, "Mathematics and the internet: a source of enormous confusion and great potential," *Notices of the AMS*, vol. 56, pp. 586–599, 2009.
- [36] A. Mislove, M. Marcon, K. P. Gummadi et al., "Measurement and analysis of online social networks," in *Proceedings of the 7th ACM SIGCOMM Conference on Internet Measurement*, San Diego, CA, USA, 2007.
- [37] H. Thomas, J. M. Read, L. Danon et al., "Testing the hypothesis of preferential attachment in social network formation," *EPJ Data Science*, vol. 4, p. 13, 2015.
- [38] A. Barabasi, *Network Science*, Cambridge University Press, Cambridge, UK, 2016.
- [39] M. P. H. Stumpf and M. A. Porter, "Critical truths about power laws," *Science*, vol. 335, no. 6069, pp. 665–666, 2012.
- [40] M. O. Jackson and B. W. Rogers, "Meeting strangers and friends of friends: how random are social networks?," *American Economic Review*, vol. 97, no. 3, pp. 890–915, 2007.
- [41] A. D. Broido and A. Clauset, "Scale-free networks are rare," *Nature Communications*, vol. 10, p. 1017, 2019.
- [42] M. Gerlach and E. G. Altmann, "Testing statistical laws in complex systems," *Physical Review Letters*, vol. 122, Article ID 168301, 2019.
- [43] J. Littman, L. Wrubel, and D. Kerchner, "United States presidential election tweet Ids," 2016.
- [44] J. Littman and S. Park, "Women's march tweet Ids," 2017.

- [45] J. Littman, D. Kerchner, and L. Wrubel, "End of term 2016 U.S. government twitter archive," 2017.
- [46] J. Littman, "Hurricanes harvey and irma tweet Ids," 2017.
- [47] J. Littman, "Immigration and travel ban tweet Ids," 2018.
- [48] J. Littman, "Charlottesville tweet Ids," 2018.
- [49] J. Littman, "Winter olympics 2018 tweet Ids," 2018.
- [50] J. Littman, D. Kerchner, and L. Wrubel, "U.S. government tweet Ids," 2017.
- [51] J. Littman, L. Wrubel, D. Kerchner et al., "News outlet tweet Ids," 2017.
- [52] L. Wrubel, J. Littman, and D. Kerchner D, "U.S. congressional election tweet Ids," 2019.
- [53] J. Littman, "115th U.S. congress tweet Ids," 2017.
- [54] J. Littman, "Ireland 8th tweet Ids," 2018.
- [55] H. E. Hurst, "Long term storage capacity of reservoirs," *Transactions of the American Society of Civil Engineers*, vol. 116, pp. 770–799, 1951.
- [56] C.-K. Peng, S. V. Buldyrev, S. Havlin, M. Simons, H. E. Stanley, and A. L. Goldberger, "Mosaic organization of DNA nucleotides," *Physical Review E*, vol. 49, no. 2, pp. 1685–1689, 1994.
- [57] M. Li, "Fractal time series—a tutorial review," *Mathematical Problems in Engineering*, vol. 2010, Article ID 157264, 2010.
- [58] S. V. Buldyrev, A. L. Goldberger, S. Havlin et al., "Long-range correlation properties of coding and noncoding DNA sequences: GenBank analysis," *Physical Review E*, vol. 51, no. 5, pp. 5084–5091, 1995.
- [59] A. I. Olemskoi and A. V. Khomenko, "Three-parameter kinetics of a phase transition," *Journal of Theoretical and Experimental Physics*, vol. 83, pp. 1180–1192, 1996.
- [60] A. I. Olemskoi, "Theory of stochastic systems with singular multiplicative noise," *Physics-Uspeski*, vol. 41, no. 3, pp. 269–301, 1998.
- [61] A. I. Olemskoi, A. V. Khomenko, and D. O. Kharchenko, "Self-organized criticality within fractional Lorenz scheme," *Physica A: Statistical Mechanics and its Applications*, vol. 323, pp. 263–293, 2003.
- [62] D. Ruelle and F. Takens, "On the nature of turbulence," *Communications in Mathematical Physics*, vol. 20, no. 3, pp. 167–192, 1971.
- [63] A. Dmitriev, V. Kornilov, and S. Maltseva, "Complexity of a microblogging social network in the framework of modern nonlinear science," *Complexity*, vol. 2018, Article ID 4732491, 2018.
- [64] P. Moriano, J. Finke, and Y. Ahn, "Community-based event detection in temporal networks," *Scientific Reports*, vol. 9, p. 4358, 2019.
- [65] J. P. Gleeson, J. A. Ward, K. P. O'Sullivan et al., "Competition-induced criticality in a model of meme popularity," *Physical Review Letters*, vol. 112, Article ID 048701, 2014.
- [66] J. P. Gleeson, K. P. O'Sullivan, R. A. Baños, and Y. Moreno, "Effects of network structure, competition and memory time on social spreading phenomena," *Physical Review X*, vol. 6, Article ID 021019, 2016.
- [67] S. Morse, M. C. González, and N. Markuzon, "Role of persistent cascades in diffusion," *Physical Review E*, vol. 99, pp. 12323–12331, 2019.
- [68] J. Liu, Z. He, and Y. Huang, "Hashtag2Vec: learning hashtag representation with relational hierarchical embedding model," in *Proceedings of the Twenty-Seventh International Joint Conference on Artificial Intelligence*, pp. 3456–3462, Stockholm, Sweden, July 2018.
- [69] M. Stella, M. Cristoforetti, and M. De Domenico, "Influence of augmented humans in online interactions during voting events," *PLoS One*, vol. 14, Article ID e0214210, 2019.
- [70] M.-A. Rizoio, T. Graham, R. Zhang et al., "DEBATENIGHT: the role and influence of socialbots on twitter during the first 2016 U.S. Presidential debate," in *Proceedings of the Twelfth International AAAI Conference on Web and Social Media (ICWSM 2018)*, pp. 300–309, Palo Alto, CA, USA, June 2018.
- [71] M. T. Bastos and D. Mercea, "The brexit botnet and user-generated hyperpartisan news," *Social Science Computer Review*, vol. 27, 2017.
- [72] C. Shao, G. L. Ciampaglia, O. Varol et al., "The spread of low-credibility content by social bots," *Nature Communications*, vol. 9, p. 4787, 2018.
- [73] S. González-Bailón, J. Borge-Holthoefer, A. Rivero, and Y. Moreno, "The dynamics of protest recruitment through an online network," *Scientific Reports*, vol. 1, pp. 1–7, 2011.
- [74] B. Kollanyi, P. N. Howard, and S. C. Woolley, *Bots and Automation over Twitter during the U.S. Election, Data Memo*, Project on Computational Propaganda, Oxford, UK, 2016.
- [75] Z. Wang and K. Caskey, "#Occupywallstreet: an analysis of twitter usage during a protest movement," *Social Networking*, vol. 5, no. 4, pp. 101–117, 2016.

Research Article

Modeling a Simulation for Sociotechnical Resilience

Fredy Tantri^{1,2,3} and Sulfikar Amir^{3,4}

¹*Interdisciplinary Graduate Programme, Nanyang Technological University, Singapore*

²*Institute of Catastrophe Risk Management, Nanyang Technological University, Singapore*

³*Future Resilient Systems (FRS) Programme, Singapore-ETH Centre, Singapore*

⁴*School of Social Sciences, Nanyang Technological University, Singapore*

Correspondence should be addressed to Sulfikar Amir; sulfikar@ntu.edu.sg

Received 16 August 2019; Revised 4 November 2019; Accepted 26 November 2019; Published 19 December 2019

Guest Editor: Francisco G. Montoya

Copyright © 2019 Fredy Tantri and Sulfikar Amir. This is an open access article distributed under the Creative Commons Attribution License, which permits unrestricted use, distribution, and reproduction in any medium, provided the original work is properly cited.

This paper proposes a conceptual model to simulate the response of sociotechnical systems to crisis. The model draws on a concept of “sociotechnical resilience” as the theoretical framework, which underscores the hybrid nature of sociotechnical systems. Revolving around the notion of transformability, the concept considers sociotechnical resilience to be constitutive of three fundamental attributes, namely, informational relations, sociomaterial structures, and anticipatory practices. Our model aims to capture the complex interactions within a sociotechnical system during a recovery process by incorporating these core attributes in the operational units embedded in a multilevel directed acyclic graph, information networks, and recovery strategies. Furthermore, the model emphasizes specifically the role of informational configuration during a disruption. We introduce two recovery strategies in our simulation, namely, random recovery and informed recovery. The former represents the unprepared responses to crisis, while the latter incorporates the reporting process to support the command centre in making optimum decisions. The simulation results suggest the importance of system flexibility to allow structural reconfiguration at the organizational level. Our proposed model complements the theoretical principles of sociotechnical resilience while laying a practical foundation of sociotechnical modeling for resilience enhancement in real-world settings.

1. Introduction

Since ecologist Holling propounded the concept of resilience [1], the notion of resilience as a system stability has ramified into various fields. As the world is seeing more turbulences and disruptions caused by ecological and human-made disasters, studies on resilience have burgeoned in various fields such as, to name a few, social systems [2], supply chain [3], enterprise management [4], catastrophe management [5], and coastal engineering [6]. Generally, resilience is defined as the systems’ capability to survive and maintain its function by absorbing or recovering from internal or external changes [7–10]. It is generally distinguished from the traditional concept of safety, which seeks to identify and eliminate negative behaviors within the system resulting in an accident. In contrast, the resilience concept recognizes the coexistence of both the negative and positive behaviors within the system and focuses on improving the probability

of positive outcomes while reducing the probability of negative outcomes [11].

Recently, the concept of resilience has been adopted into the study of sociotechnical systems [12] to analyze resilient capacity of critical urban infrastructures such as power grid, water supply networks, and telecommunication/cyber infrastructures [13, 14]. It is driven by a realization that these critical urban infrastructures are fundamentally sociotechnical systems; they are composed of technical components while being run by human organizations. Conceptually, the sociotechnical framework helps to uncover minutiae interactions between human agents and technical apparatuses. In this area of study, the emphasis is placed on technical aspects [5, 15, 16], as well as on individuals and organizational entities [17, 18]. In advanced urban environments, sociotechnical systems are designed and built as complex adaptive systems that consist of multiple agents organized around a specific hierarchy,

contain feedback loops, and embody emergent properties [19–22]. Due to the complex nature of sociotechnical systems, understanding the behavior of these systems cannot be adequately achieved through a linear formulation because each of the components is interconnected in a nonlinear fashion. In such multiplex interactions, the behavior of sociotechnical systems is influenced by emergent properties that shape the dynamic movement of the system.

Following Hettinger et al., we consider computational modeling and simulation to be an effective method to study sociotechnical behavior [23]. Furthermore, given the hyperdynamic nature of sociotechnical systems, the agent-based model is a suitable method for the simulation purpose because of its flexibility to incorporate complex agent interactions. The merit of this method is that it can support the decision-making process when a structural change in a sociotechnical system is taking place [24]. Today, the use of agent-based methods is largely common in various fields such as air traffic control [25–27], health care [28, 29], energy systems [30, 31], and complex organization [32]. However, the application of agent-based modeling in sociotechnical systems for resilience analysis remains relatively limited. This is likely caused by the availability of social and technical data for model validation, as well as the lack of a solid theoretical framework in the field. While sociotechnical modeling and resilience studies such as power grid networks in South Korea [33], Twitter interactions and epidemic processes [34], as well as supply chains and CO₂ policies [35] are well validated by the technical and organization data, there is still a gap in incorporating the notion of sociotechnical systems as a hybrid entity.

To date, works on sociotechnical modeling continue to grow. We note substantial shortcomings in existing models in which the hybrid nature of sociotechnical systems is not strongly reflected. Some of these models are nearly completely devoid of social elements or at best taking into account marginal social variables [36–39]. It is this gap that we wish to fill in this paper by offering a new approach in developing a sociotechnical model, and at the same time, using this model to create a computational simulation in sociotechnical systems. Since the existing framework of resilience remains fragmented between those emphasizing engineered features and those focusing on social and organizational conditions, we develop our model by emphasizing the hybrid nature of sociotechnical systems as they consist of the social constructs of people and technologies [12]. Thus, the concept of sociotechnical resilience is adopted in our model. This model also incorporates the paradigm of resilience as the complementary attribute of risk management which emphasizes strategies on minimizing loss or increasing the recovery rate [40]. The quantification of the system’s resilience adopts the use of *critical functionality*, a concept that is embodied in operational resilience [41]. This concept will be discussed in detail later in the paper. The following section will introduce the theoretical framework, which we have adopted in our model.

2. Conceptualizing Sociotechnical Resilience

Studies on sociotechnical systems are abundant, and conceptualizations of resilience are plenty. Yet, studies that

combine the two are quite a few. One of them is conducted by Amir and Kant who have proposed the concept of sociotechnical resilience [12]. Recognizing the hybrid nature of sociotechnical systems, sociotechnical resilience is characterized as an inherent capacity built around transformability. In contrast to Walker et al. in defining resilience, adaptability, and transformability in the context of socioecological systems [42], transformability is placed at the core of sociotechnical resilience. Amir and Kant maintain a distinction of transformability in sociotechnical systems from the one in socioecological systems. This distinction is the result of the difference in temporal and spatial scale of the systems of interest. While Walker et al. focus on socioecological systems that centre on social and natural environments, sociotechnical systems are artificial systems where humans and machines interact in a structured configuration such as transportation systems, water supply systems, telecommunication systems, and energy systems. As a result, sociotechnical resilience revolves around the idea that the “building block” of sociotechnical systems are intentional hybrids [43–45], meaning they are both technical as well as social at the same time; both are entangled entities where humans and technologies are social constructs.

Given its unique characterization of sociotechnical resilience, our model adopts this concept and frames the resilience of sociotechnical systems as an integrative capacity to cope with internal failures or external shock. This capacity lies in system agility to transform its configuration from one form to another. The process of transformation is extremely crucial because it facilitates repair and adaptation in the aftermath of crisis and disruption. The aftermath transformations involve technical, organizational, and even institutional reconfiguration following the changing environment after a disruption. Thus, it is transformability, the ability to transform, which constitutes sociotechnical resilience [12]. A distinctive feature of this concept appears from its emphasis on key attributes of sociotechnical networks rather than emphasizing protocols and processes of resilience enhancement as found in mainstream resilience analysis [46–48]. Looking further into the way in which transformability is internally built within a sociotechnical system, there are three key attributes of transformability, namely, informational relations, sociomaterial structures, and anticipatory practices. We found the composition of these attributes to be more suitable for our purpose to develop our sociotechnical modeling of resilience. To grasp the meaning of these attributes and how it can be translated into a computational model, it is instructive to elaborate each of them as follows.

2.1. Informational Relations. Informational relations represent the production and distribution of information that are extremely crucial in crisis response. These aspects can be emphasized as one that “deals with how information flows in the systems to support continued operations.” As information is instrumental in determining how effective and efficient the coordination responds to crisis [49–52], any sociotechnical system cannot afford to have weak

informational relations. In the concept of sociotechnical resilience, informational relations refer to the pathways of information between machines, individual operators and managers, subsystems, and/or organizations. Informational links between various types of elements contain a specific meaning or context, which defines how it is received. The information exchange between machine and human may involve engineering medium and require technical knowledge (e.g., temperature level monitoring in a chemical plant or electrical load monitoring of a power grid by engineers), while information sharing between humans serves to manage interdependencies or coordination purposes [53, 54]. In our sociotechnical model, we treat informational relations as the reporting lines from operational units to command centre or local coordinator to inform the disruption impacts. The information will allow the command centre to decide and perform the optimum system recovery.

2.2. Sociomaterial Structures. The constitutive entanglement of the materials and human organization in sociotechnical systems creates what Amir and Kant called as sociomaterial structures. It is “structures” as they are defined by how each entity is interconnected with one another in a hybrid configuration. The entities in sociotechnical systems belong to social realm such as individuals, groups, and organizations, while at the same time belong to the material realm, thus hybrid in nature. An interesting example is a study by Orlikowski et al. on the use of Blackberry phones in a firm called Plymouth Investments. The communication using Blackberry which has the “push email” capability changed the organization’s communication norms by altering people’s expectations of availability, intensifying interactions, and redefining the working time boundaries [55, 56]. This example of sociomaterial practice shows how a Blackberry, a technological unit that is designed and configured by humans, in turn, changes the organization’s communication culture.

Another aspect that comes along with the hybridity is interpretive flexibility [57]. In the previous example, while Blackberry was intentionally designed to ease email communication, the pressure in the workplace may push people to intentionally use it beyond traditional communication norms. In terms of sociotechnical systems, this aspect determines how flexible the entities are structured or undergo reconfiguration during disruptions in sociotechnical systems. Therefore, in order to improve the resilience of sociotechnical systems, it is important to incorporate the characteristics of hybridity and interpretive flexibility when optimizing correct functioning and minimizing the malfunction probability of the technical dimension. In our proposed model, sociomaterial structures are embodied in agents as the operational units and represented as a network with a specific topology.

2.3. Anticipatory Practices. The last aspects of sociotechnical resilience are anticipatory practices, defined as a set of recovery protocols designed for an organization to rapidly bounce back from crisis or disruption to the normal

operational state. In addition to this definition, the scope of anticipatory practices includes routine activities aiming to anticipate possibilities of future occurrences of events [58, 59]. Since anticipatory practices are highly dependent on the context of a system to function as disaster prevention and management, the conceptual model we designed only incorporates anticipatory practices as recovery strategies during a disruption. In this way, the recovery protocols are reflected as the strategies of the command centre in determining the order of nodes to be repaired.

In this paper, we propose a computational model to simulate sociotechnical resilience, taking into account the three core attributes discussed above. Each of these attributes is translated into the model as a multilevel directed acyclic graph (DAG) of sociotechnical units, reporting lines, and recovery protocols. Furthermore, the simulation is designed to show the performance and resilience of various information flow strategies for a given disruption scenario and physical network configuration. By incorporating information flow in the model, we are aiming to expand the understanding of the complexity of sociotechnical resilience thus helping researchers and practitioners to plan, design, build, and develop organizational and technical aspects in infrastructural systems.

3. Modeling Sociotechnical Resilience

Following the concept of sociotechnical resilience discussed above, our model of sociotechnical resilience is constituted by a graph $G(N, L)$, where N is a set of nodes connected by a set of links L . The graph has α levels of nodes. Each node represents a basic structure of a typical control loop as illustrated by Leveson in which an automated controller is supervised by a human controller [60]. For our purpose, we simplified this control loop into what we called as “operational unit” that serves as the building block of sociotechnical systems in our model. Figure 1 shows our model of *operational unit* which consists of a human operator and machine. Each unit serves a certain amount of demand in its service area, producing output O for the system. The operation of the unit may depend on the service of other units. In that case, a directional link is created from the “dependee” node to the “dependent” node. A link can only be created from the upstream unit (upper level) to the downstream unit (lower level). Creating a link between units at the same level or from a lower to a higher level is not allowed. When a unit is disrupted, all of the downstream units which are connected to the disrupted unit will be disabled. Consequently, units that are disrupted, disabled, or both cannot produce output and service to other units. For simplicity, we only consider one type of system, e.g., power systems that are serving population/households in many cities, or subway systems operating across the city to serve mobility demands of commercial, industrial, or residential areas. Further modification and adjustment of the model will be needed to consider multiple interdependent infrastructures.

The performance or the critical functionality $K(t)$ at time t for our model is defined as the normalized total output of the active nodes A_i in the system (as shown in equation

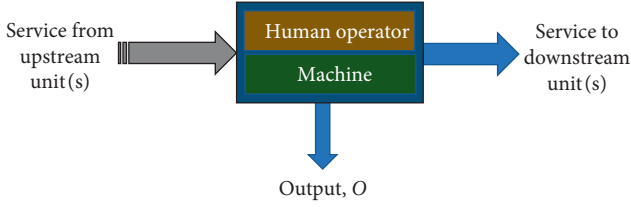


FIGURE 1: Node is modeled as *operational unit* which represents human or organization controlling automated machine. The operation of unit may depend on the service of other upstream units. Each unit serves a certain amount of demand in their service area, producing output O for the system.

(1)). Active nodes are the nodes that are not in disrupted or disabled state. The output of each node is generated randomly between 0.01 and 1. The output becomes 0 when the node is in a disrupted or disabled state and back to its initial value after it is recovered or being active again. The resilience R for each recovery strategy is calculated using equation (1), where T and S are the simulation duration and number of simulations, respectively:

$$K(t) = \frac{\sum_{i \in A_t} O_i}{\sum_{i \in N} O_i}, \quad (1)$$

$$R = \left(\frac{1}{T}\right) \left(\frac{1}{S}\right) \sum_{s=1}^S \sum_{t=1}^T K(t).$$

In this model, we applied two recovery strategies, namely, *random recovery* and *informed recovery*. The former represents the less prepared mode of response during a disruption. For example, when some sections in a subway system are disrupted, the recovery team may be sent to the disruption sites without particular patterns. It is primarily based on received emergency reports without considering the number of passengers in each affected station and trains at that time. This is due to the lack of information and coordination at the organizational level. So, the system responds to crisis in a suboptimum manner. The latter refers to a situation in which the system, before taking action, first considers the impact of each disrupted node to the system performance, thus allowing the command centre to prioritise the most “rewarding” nodes to be repaired. Using the previous example, the command centre of the subway system will take action based on the information of the number of affected passengers sent by all station head and train staff to determine the most critical section to be repaired first. The fundamental distinction between these two strategies lies in the amount of information used to make decisions and take actions in response to disruption.

In the random recovery strategy, each disrupted node is chosen randomly to repair. The time needed to recover one node is T_R . This strategy is illustrated in Figure 2. The second recovery strategy considers the impact of each disrupted node to the system performance before deciding the repair order. The impact of a disrupted node i is calculated by summing the output of the node i and all of the disabled

nodes D_i as the result of its disruption (equation (2)). In other words, the disabled nodes D_i are also the descendants of node i . Subsequently, the information of the disrupted node’s impact is passed to the command centre or local coordinator. It takes T_{info} time step to complete the sending information process.

Since there are multiple ways in which informational links are structured and used, we decided to develop three different simulations of reporting lines configuration. The first is the *direct reporting* mode, where all of the nodes in the system report to the command centre directly. The second configuration is the *hierarchy reporting* mode, where each node reports to its local coordinator. There is one local coordinator for each level. After it receives information from all disrupted nodes of its respective level, the local coordinator will send all of the information it has collected to the command centre, also in T_{info} time step. The third configuration is the *hybrid* mode, which has the same configuration as the hierarchy reporting mode, but a certain percentage of disrupted nodes are reporting directly to command centre. These three configurations of reporting lines are shown in Figure 3. It should be noted that for the local coordinator or command centre, the sending or receiving information process cannot be executed in parallel with another process. Thus, the local coordinator or command centre can only receive information from one unit at one time:

$$I_i = O_i + \sum_{j \in D_i} O_j^t, \quad (2)$$

After the command centre receives all of the information directly from nodes or from local coordinators, it will make an optimum decision to determine an order of the disrupted nodes to be repaired. The decision is based on the projected gain obtained when a disrupted node is repaired. The gain is calculated using equation (3), where t is current time and P_i is the number of disrupted nodes in the upstream levels which provides service to node i directly or indirectly. In this scenario, a disrupted node is counted in P_i if its disruption will cause the node i to be disabled:

$$B_i = (T - t - T_R(P_i + 1))I_i. \quad (3)$$

Figure 4 illustrates the informed recovery strategy using a simple example, where we assume that $T = 100$, $T_{\text{info}} = 1$, $T_R = 10$, and each unit has the same output $O = 1$. In this case, the disrupted nodes are node 2, node 3, and node 6. For the case of the direct reporting mode, the command centre will receive information from all disrupted nodes at $t = 3$ since each unit takes $T_{\text{info}} = 1$ time step to report to the command centre. The information received by the command centre is the impact value of each node. Node 2 has 7 direct and indirect dependent nodes, thus having an impact $I_2 = 1 + 7(1) = 8$, while node 3 and node 6 have impact values of 4 and 1, respectively. And then, the gain for each node is calculated by the command centre. Repairing node 2, 3, and 6 will gain $B_2 = (100 - 3 - 10(0 + 1))8 = 696$, $B_3 = (100 - 3 - 10(0 + 1))4 = 348$, and $B_6 = (100 - 3 - 10(1 + 1))1 = 77$. Therefore, the repair

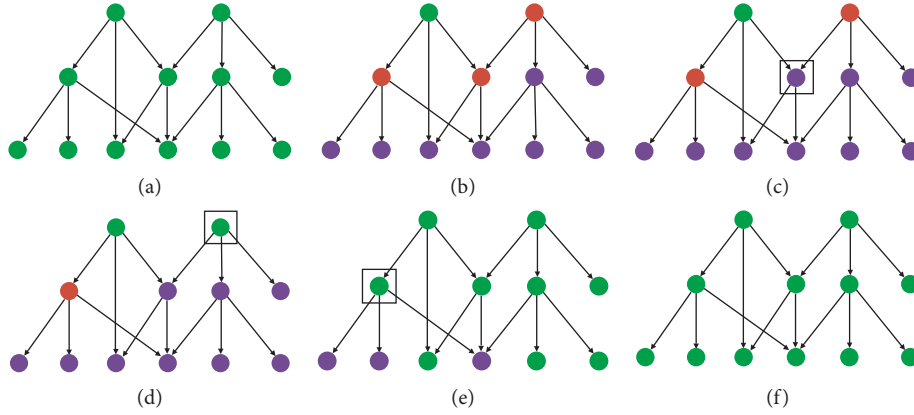


FIGURE 2: Random recovery strategy. (a) Initial configuration of the system. Green node indicates that the node is active and operates normally. (b) Disruption is generated. Red nodes and purple nodes are the disrupted and disabled nodes, respectively. A node will be disabled when at least one of its upstream nodes is disrupted or disabled. (c) A disrupted node which was chosen randomly is recovered. The rectangle indicates the recovered node. In this case, the node is still inactive since one of its upstream nodes is still disrupted. (d) Another disrupted node was chosen and is recovered. Its downstream nodes will be activated in the next time step. (e) Last disrupted node is recovered. (f) All nodes are recovered and activated.

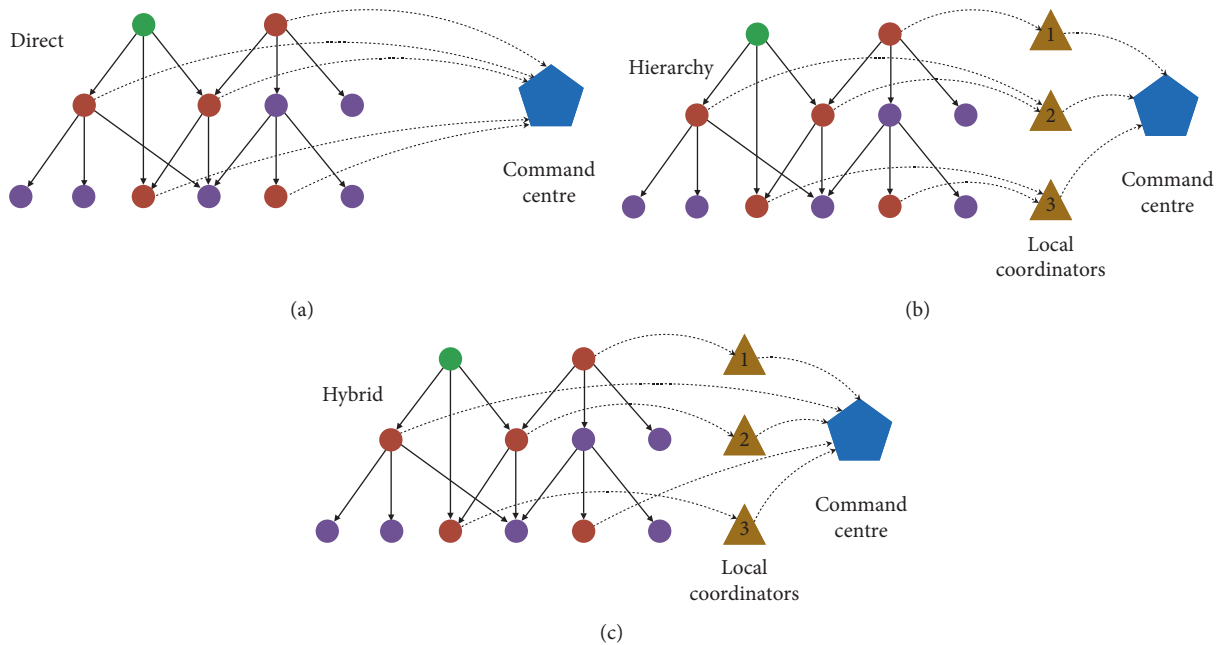


FIGURE 3: (a) *Direct*: all disrupted nodes report to command centre directly. (b) *Hierarchy*: all disrupted nodes report to their respective local coordinator. Each local coordinator will wait until it receives information from all disrupted nodes of its respective level before it reports to command centre. (c) *Hybrid*: mixed of direct and hierarchy reporting mode.

order will be node 2, node 3, and then node 6. Since the time to repair a node is 10 time steps, the system will get fully recovered at $t = 33$.

4. Results and Discussion

In each simulation, we generated a network composed of 300 nodes in four levels ($\alpha = 4$): $N_1 = 9, N_2 = 26, N_3 = 71,$ and $N_4 = 194$. Level 1 is the highest level and level 4 is the lowest level, meaning there will not be any incoming link to any node in level 1 and outgoing link from any node in level 4

since a node cannot provide service to the same or higher-level nodes. In generating the network, each node from level 2 and lower will establish one link randomly with a higher-level node. There is a probability p that the node can have additional links. The links are directional and always flow from the higher-level nodes to the lower-level nodes. For example, a node from level 3 may have a link from a level 1 node and two links from level 2 nodes. In our model, we set the probability $p = 0.02$. Each simulation is started by generating the output value for each node randomly between 0.01 to 1. Afterwards, a disruption event is generated,

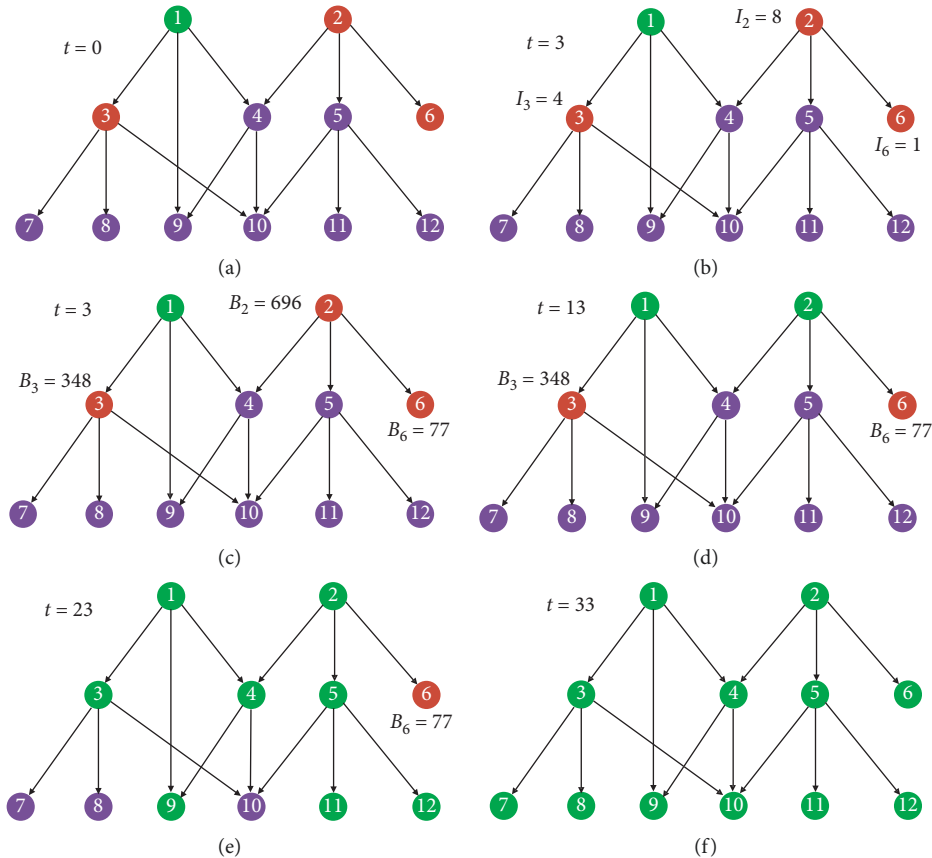


FIGURE 4: An example of informed recovery strategy with direct reporting mode, where $T = 100$, $T_{\text{info}} = 1$, $T_R = 10$, and output of each node is 1. (a) Node 2, 3, and 6 are disrupted. (b) Command centre receives impact information from all disrupted nodes at $t = 3$. (c) The gain of each node is calculated using equation (3). Node 2 has the highest priority and thus chosen to be repaired first. (d) Node 2 is recovered at $t = 13$. Node 3 is the next node to be repaired. (e) Node 3 is recovered. Node 6 is the last disrupted node. (f) Node 6 is repaired, and the system is completely recovered.

causing D percent of nodes in each level to be disrupted which consequently disables all of their dependent nodes. The recovery time T_R and sending information duration T_{info} are set to $0.01TC$ and $0.001TC$, respectively.

We started by simulating the random recovery strategy for initial damage D to 10%, 20%, and 30%. For each disruption level, we averaged the results over 1000 simulations. Figure 5 shows the performance of this strategy. This result shows the impact of initial damage to the system, where a 30% initial damage can cause a drop in system performance to be as low as 0.2. In this strategy, disrupted nodes are recovered in a random order.

The comparison between the performance of random and informed (direct reporting mode) recovery strategy for initial disruption $D = 25\%$ is shown in Figure 6(a). This series of simulations demonstrates that informed recovery strategy is better compared to random strategy since it takes into account the output and impact value of each node before determining the order to repair the disrupted nodes. The process of receiving information is reflected during the early phase of the informed strategy, where the performance does not increase since no disrupted node gets repaired. After that, the performance hikes significantly after it starts repairing nodes by prioritizing the highest gain nodes to be repaired first.

Interestingly, in case of a small initial disruption ($D = 5\%$), as shown in Figure 6(b), the performance between those strategies does not differ significantly. In fact, random strategy may be slightly better off due to the time constraint.

For a large-scale disruption, the high number of disrupted nodes which needs to report to the command centre may cause a bottleneck effect, slowing the decision to start the recovery process. For example, Preece et al. identify the potential of bottleneck effect at the information system of the UK's emergency call centre in case of large-scale disaster [61]. On an individual level, the time pressuring situation, complex, and high information intensity environment can result in cognitive overload due to the mental capacity, which is known as bounded rationality [62, 63].

Regarding the bottleneck issue, the reporting line in the system can be reconfigured to adopt a hierarchical structure. This structure is common in disaster management, which utilizes incident management structure as the command centre to coordinate ambulance, hospitals, police, and fire department [64]. Another example also includes the tiered-structure systems in medical surge capacity management, where the medical response and resource allocation are distributed based on the disaster severity which can be a local, state, interstate, or national level [65]. Our results in

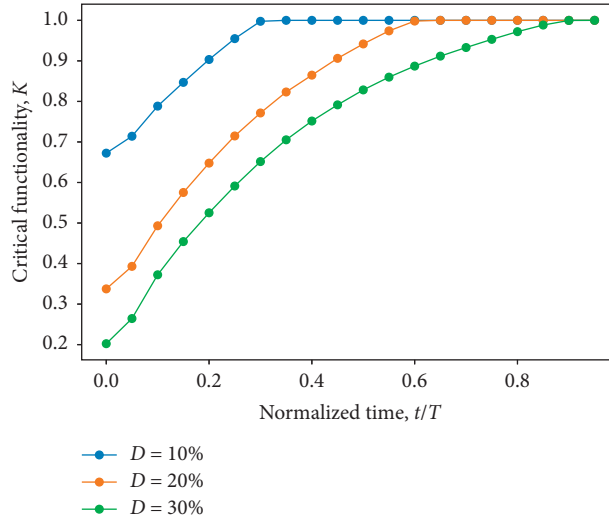


FIGURE 5: Performance of random recovery strategy for disruption percentage of 10%, 20%, and 30%. This result shows the impact of initial damage to the system. Initial damage of 30% can cause the drop of system performance to be as low as 0.2.

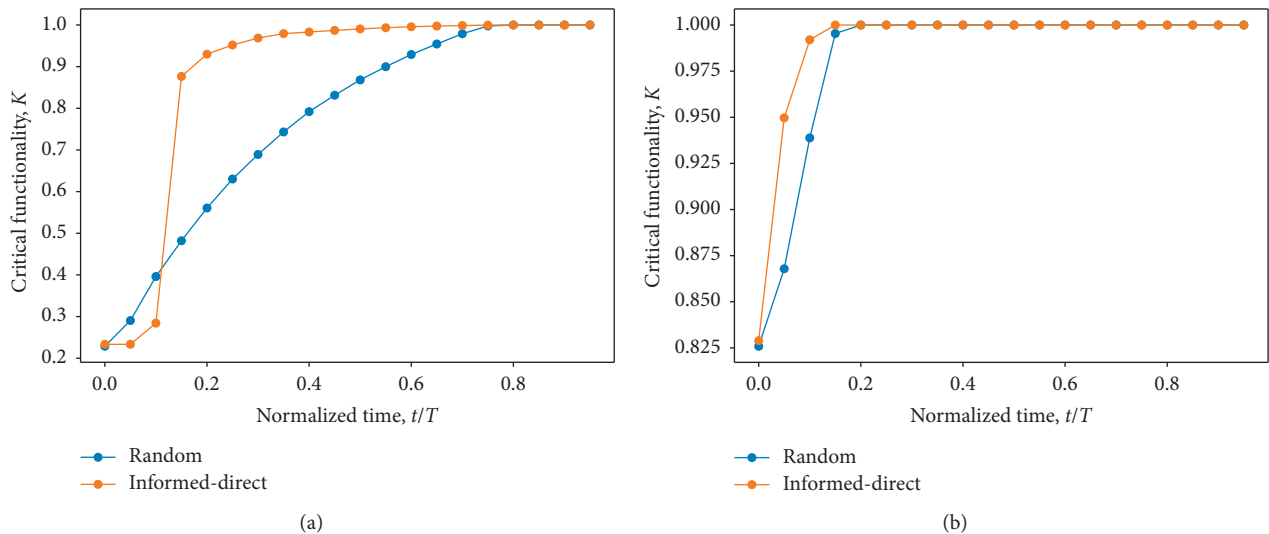


FIGURE 6: Performance comparison between the informed recovery strategy (direct reporting mode) and random recovery strategy for the initial disruption D equals to (a) 25% and (b) 5%. The process of receiving information is reflected during the early phase of the informed strategy in (a). The performance is not increasing during the phase. After that, the performance jumps significantly after it starts repairing nodes by prioritizing the highest gain nodes to be repaired first. In (b), the performance between these two strategies does not differ significantly.

Figure 7 demonstrate the advantage in applying the hierarchical reporting mode compared to random and informed-direct strategies. The gap between the resilience value of the hierarchical and direct reporting mode becomes wider as disruption percentage D increases, indicating a better performance of the hierarchical reporting mode during major disruptions.

While the hierarchical structure is the most practical and widely adopted, we also investigated the hybrid reporting mode. This mode is a mix of direct and hierarchical structures. We can assume that this is the case when the command centre will not only follow the standard rules of the hierarchical structure by waiting for

reports from the local coordinator, but it also proactively seeks information directly by itself. In a specific scenario, this type of information flow can be applied. For example, when a disaster happens in a certain area, the rapid health assessment (RHA) teams are sent to the location to assess the condition and to measure the medical logistics needed for that area. The RHA teams can be provided by the local or national government. These combined resources accelerate the information gathering for the central facility to make the best decisions regarding medical resources allocation to the affected areas. In establishing the reporting lines configuration of the hybrid mode, we used a parameter h as the probability that a disrupted node will

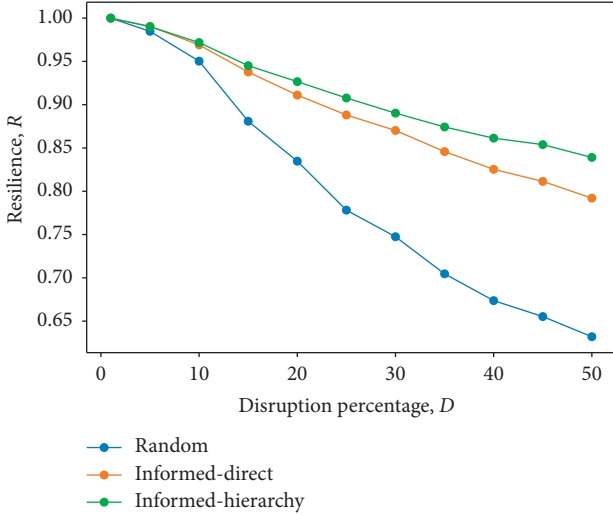


FIGURE 7: Resilience curve of random (blue) and informed recovery strategies (orange = direct mode and green = hierarchy mode). The gap between the resilience value of the hierarchical and direct reporting mode is getting wider along with the increasing of disruption percentage D , indicating the better performance of the hierarchical reporting mode during major disruptions.

report to the local coordinator, not directly to the command centre. Figure 8 shows the mean of the resilience of the informed-hybrid recovery strategy for various levels of probability h . The optimum value of the parameter for this network is 0.65, meaning that the probability of a disrupted node reports to the local coordinator is 65%. Using this value, we compare the resilience curves of all of the recovery strategies (Figure 9) to show how system resilience can be improved by configuring the informational structure.

In practice, our model emphasizes the importance of flexibility in informational relations between entities in a sociotechnical system. Flexibility allows adaptation at an organizational level during a crisis, which can be embodied through different modes of reporting lines configurations. For example, the simulation results can be used to guide stakeholders in designing the system to be able to adapt to the information flow in the system based on various disruption severity, such as using the direct reporting mode for low disruption severity to minimize the cost of manpower, and then change to the hierarchical reporting mode for a rapid and efficient information processing in case of moderate to high disruption severity or directing resources to partially bypass the hierarchical structure for an even faster information collection during large-scale disruptions.

Furthermore, the results of our model and simulations were meant to capture the complex interaction in sociotechnical systems while incorporating the core attributes of sociotechnical resilience. We model the sociomaterial structures as the network of operational (sociotechnical) units representing the human operator and the machine, along with the dependencies of services between those units. Each unit also has output value to represent the demand to

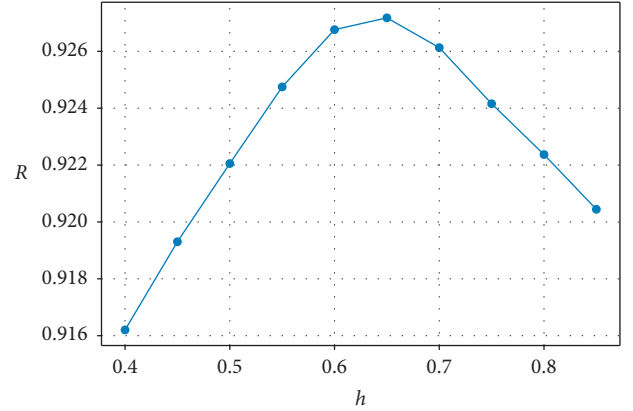


FIGURE 8: Hybrid mode is a mix of direct and hierarchical structures. A parameter h is used as the probability that a node will report to the local coordinator if disrupted. The plot is the mean of the resilience curve as a function of h . The optimum value of the parameter for this network is 0.65, meaning that the probability of a disrupted node reports to the local coordinator is 65%.

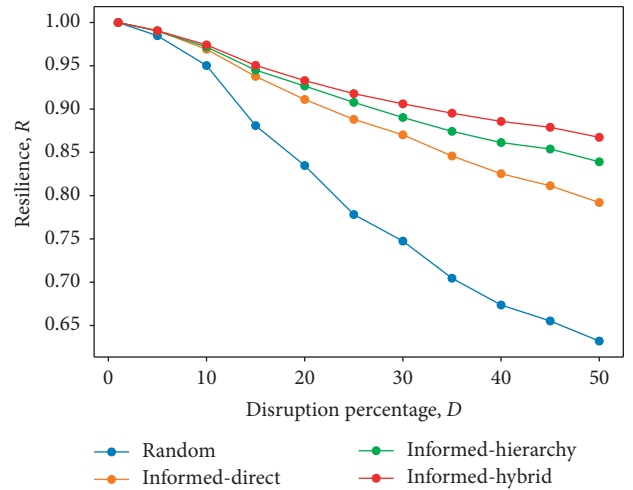


FIGURE 9: Resilience curves of all recovery strategies. These results show how system resilience can be improved by configuring the informational structure.

be served in its respective area. Furthermore, we model informational relations as reporting lines configuration, which allows each unit to report the impact of disruption to the local coordinator or command centre. The decision in a form of recovery order is based on this information of disruption impact. The anticipatory practices are embodied in the recovery strategy employed by the command centre. In this model, we demonstrated how information network plays an impactful effect on the systems' capability to respond to a crisis. While adaptation capability is not implemented in the simulations, our model provides insights into how adaptation can be taken in real-world settings through information network reconfiguration at the organizational level based on the existing sociomaterial structure and the scale of the crisis.

5. Conclusions

Sociotechnical system is not simply an aggregation of social and technical aspects, but it is hybrid in nature. This is the underlying feature of sociotechnical resilience. In this study, a conceptual model has been proposed to lay a stronger foundation to translate the abstract concept of sociotechnical resilience into practical forms. As explained throughout the paper, our research introduced a novel way of modeling sociotechnical resilience as a hybrid phenomenon reflected in network-based interactions which emphasized the role of informational flows in the recovery process of sociotechnical systems. The model allows the adjustment of various configurations of informational relations, rendering it to be useful when stakeholders wish to enhance infrastructure resilience. This is achieved through a computational modeling that informs the design process of a better sociotechnical structure, information-sharing networks, and recovery strategies.

By taking into account the behavior of complex sociotechnical systems, we incorporated the attributes of sociotechnical resilience, namely, informational relations, sociomaterial structures, and anticipatory practices. Our model shows the interplay between these resilience factors through a multilevel directed acyclic graph, reporting lines configurations, and recovery strategies. The practical implication of our model is to guide stakeholders to efficiently and effectively plan their resources to be used in response to a crisis. For example, a direct reporting structure can be applied for a small-scale disruption. Actions can even be taken immediately for a very small disruption as shown in the random recovery scenario. For larger scales of disruption, the reporting lines should be reconfigured to a hierarchical structure to prevent a bottleneck, thus increasing information processing for command centre. The system performance can be further improved in case of large-scale disruption by having flexible procedures, where the command centre utilizes its human resources to proactively receive or seek information on the impact of each disrupted unit.

It should be noted that our model is applicable under three conditions. First, the system has to be hybrid where the operation does not take place in a purely technical realm such as electrical circuit or mechanical devices, but it has to involve organizational interactions in which information and coordination are shared and negotiated. Consequently, the model may have some degrees of unpredictability because it deals with organizational behavior. This is reflected especially in the random recovery scenario. At the same time, as simulated in the informed recovery scenario, we showed that the degree of unpredictability can be minimized through information and coordination that can only be provided by human operators and managers, not only from sensors or automated mechanisms. The second condition is that the system must have dynamic properties such as demands of the population it seeks to serve in its specific operational area. It entails that these properties change from time to time. Lastly, our model is suitable more for systems that are constructed around networks, where the degree of

complexity is high. Having said that, we need to note that our present study did not observe the resilient behavior of sociotechnical networks across different systems. Therefore, further study must address this limitation in order to model large-scale interdependent sociotechnical systems.

Data Availability

The data used to support the findings of this study are available from the corresponding author upon request.

Conflicts of Interest

The authors declare that there are no conflicts of interest regarding the publication of this paper.

Acknowledgments

This work is an outcome of the Future Resilient Systems project at the Singapore-ETH Centre (SEC), which was funded by the National Research Foundation of Singapore (NRF) under its Campus for Research Excellence and Technological Enterprise (CREATE) programme (FI 370074011).

References

- [1] C. S. Holling, "Resilience and stability of ecological systems," *Annual Review of Ecology and Systematics*, vol. 4, no. 1, pp. 1–23, 1973.
- [2] D. J. Davidson, "The applicability of the concept of resilience to social systems: some sources of optimism and nagging doubts," *Society & Natural Resources*, vol. 23, no. 12, pp. 1135–1149, 2010.
- [3] P. Mensah and Y. Merkuriev, "Developing a resilient supply chain," *Procedia—Social and Behavioral Sciences*, vol. 110, pp. 309–319, 2014.
- [4] Y. Sheffi, *The Resilient Enterprise: Overcoming Vulnerability for Competitive Advantage*, MIT Press Books, Cambridge, MA, USA, 2005.
- [5] J. Park, T. P. Seager, P. S. C. Rao, M. Convertino, and I. Linkov, "Integrating risk and resilience approaches to catastrophe management in engineering systems," *Risk Analysis*, vol. 33, no. 3, pp. 356–367, 2013.
- [6] R. J. T. Klein, M. J. Smit, H. Goosen, and C. H. Hulsbergen, "Resilience and vulnerability: coastal dynamics or Dutch dikes?," *The Geographical Journal*, vol. 164, no. 3, pp. 259–268, 1998.
- [7] L. H. Gunderson, "Ecological resilience—in theory and application," *Annual Review of Ecology and Systematics*, vol. 31, no. 1, pp. 425–439, 2000.
- [8] J. Carlson, *Resilience: Theory and Application*, Argonne National Lab. (ANL), Argonne, IL, USA, 2012.
- [9] A. V. Stephenson, *Benchmarking the resilience of organisations*, Ph.D. thesis, University of Canterbury, Christchurch, New Zealand, 2010.
- [10] B. Allenby and J. Fink, "Toward inherently secure and resilient societies," *Science*, vol. 309, no. 5737, pp. 1034–1036, 2005.
- [11] E. Hollnagel, "Resilience engineering and the built environment," *Building Research & Information*, vol. 42, no. 2, pp. 221–228, 2014.
- [12] S. Amir and V. Kant, "Sociotechnical resilience: a preliminary concept," *Risk Analysis*, vol. 38, no. 1, pp. 8–16, 2018.

- [13] A. Boin and A. McConnell, "Preparing for critical infrastructure breakdowns: the limits of crisis management and the need for resilience," *Journal of Contingencies and Crisis Management*, vol. 15, no. 1, pp. 50–59, 2007.
- [14] T. D. O'Rourke, "Critical infrastructure, interdependencies, and resilience," *Bridge-Washington-National Academy of Engineering*, vol. 37, no. 1, p. 22, 2007.
- [15] J. L. Mate and A. Silva, *Requirements Engineering for Socio-technical Systems*, Information Resources Press, Arlington, VA, USA, 2005.
- [16] P. Uday and K. Marais, "Designing resilient systems-of-systems: a survey of metrics, methods, and challenges," *Systems Engineering*, vol. 18, no. 5, pp. 491–510, 2015.
- [17] E. Hollnagel, "Resilience: the challenge of the unstable," in *Resilience Engineering*, pp. 21–30, CRC Press, Boca Raton, FL, USA, 2017.
- [18] P. Carayon, "Human factors of complex sociotechnical systems," *Applied Ergonomics*, vol. 37, no. 4, pp. 525–535, 2006.
- [19] J. S. Lansing, "Complex adaptive systems," *Annual Review of Anthropology*, vol. 32, no. 1, pp. 183–204, 2003.
- [20] N. Goldenfeld and L. P. Kadanoff, "Simple lessons from complexity," *Science*, vol. 284, no. 5411, pp. 87–89, 1999.
- [21] S. M. Rinaldi, J. P. Peerenboom, and T. K. Kelly, "Identifying, understanding, and analyzing critical infrastructure interdependencies," *IEEE Control Systems*, vol. 21, no. 6, pp. 11–25, 2001.
- [22] J. H. Miller and S. E. Page, *Complex Adaptive Systems: An Introduction to Computational Models of Social Life*, Princeton University Press, Princeton, NJ, USA, 2009.
- [23] L. J. Hettinger, A. Kirlik, Y. M. Goh, and P. Buckle, "Modelling and simulation of complex sociotechnical systems: envisioning and analysing work environments," *Ergonomics*, vol. 58, no. 4, pp. 600–614, 2015.
- [24] K. H. Van Dam, *Capturing socio-technical systems with agent-based modelling*, Ph.D. thesis, Delft University of Technology, Delft, The Netherlands, 2009.
- [25] H. A. Blom, S. H. Stroeve, and H. H. de Jong, "Safety risk assessment by monte carlo simulation of complex safety critical operations," in *Developments in Risk-Based Approaches to Safety*, pp. 47–67, Springer, Berlin, Germany, 2006.
- [26] K. Tumer and A. Agogino, "Distributed agent-based air traffic flow management," in *Proceedings of the 6th International Joint Conference on Autonomous Agents and Multiagent Systems, ACM*, p. 255, Honolulu, HI, USA, May 2007.
- [27] A. Sharpanskykh and S. H. Stroeve, "An agent-based approach for structured modeling, analysis and improvement of safety culture," *Computational and Mathematical Organization Theory*, vol. 17, no. 1, pp. 77–117, 2011.
- [28] O. Kazar, Z. Sahnoun, and L. Frecon, "Multi-agents system for medical diagnosis," in *Proceedings of the International Conference on Intelligent System and Knowledge Engineering*, vol. 1, pp. 1265–1270, Xiamen, China, November 2008.
- [29] K. Mustapha and J.-M. Frayret, "Agent-based modeling and simulation software architecture for health care," in *Proceedings of the 2016 6th International Conference on Simulation and Modeling Methodologies, Technologies and Applications (SIMULTECH)*, pp. 1–12, IEEE, Lisbon, Portugal, July 2016.
- [30] M. D. Galus, *Agent-based Modeling and Simulation of Large Scale Electric Mobility in Power Systems*, ETH Zurich, Zürich, Switzerland, 2012.
- [31] C. Cai, P. Jahangiri, A. G. Thomas, H. Zhao, D. C. Aliprantis, and L. Tesfatsion, "Agent-based simulation of distribution systems with high penetration of photovoltaic generation," in *Proceedings of the 2011 IEEE Power and Energy Society General Meeting*, pp. 1–7, IEEE, Detroit, MI, USA, July 2011.
- [32] J. Tasic, F. Tantri, and S. Amir, "Modelling multilevel interdependencies for resilience in complex organisation," *Complexity*, vol. 2019, Article ID 3946356, 23 pages, 2019.
- [33] D. A. Eisenberg, J. Park, and T. P. Seager, "Sociotechnical network analysis for power grid resilience in South Korea," *Complexity*, vol. 2017, Article ID 3597010, 14 pages, 2017.
- [34] A. Vespignani, "Modelling dynamical processes in complex socio-technical systems," *Nature Physics*, vol. 8, no. 1, pp. 32–39, 2012.
- [35] K. H. Van Dam, I. Nikolic, and Z. Lukszo, *Agent-Based Modelling of Socio-Technical Systems*, Springer Science & Business Media, Berlin, Germany, 2012.
- [36] K. Adjetey-Bahun, B. Birregah, E. Châtelet, and J.-L. Planchet, "A model to quantify the resilience of mass railway transportation systems," *Reliability Engineering & System Safety*, vol. 153, pp. 1–14, 2016.
- [37] M. Cavallaro, D. Asprone, V. Latora, G. Manfredi, and V. Nicosia, "Assessment of urban ecosystem resilience through hybrid social-physical complex networks," *Computer-Aided Civil and Infrastructure Engineering*, vol. 29, no. 8, pp. 608–625, 2014.
- [38] R. Guidotti, H. Chmielewski, V. Unnikrishnan, P. Gardoni, T. McAllister, and J. van de Lindt, "Modeling the resilience of critical infrastructure: the role of network dependencies," *Sustainable and Resilient Infrastructure*, vol. 1, no. 3-4, pp. 153–168, 2016.
- [39] Y. Almoghathawi, K. Barker, and L. A. Albert, "Resilience-driven restoration model for interdependent infrastructure networks," *Reliability Engineering & System Safety*, vol. 185, pp. 12–23, 2019.
- [40] I. Linkov, T. Bridges, F. Creutzig et al., "Changing the resilience paradigm," *Nature Climate Change*, vol. 4, no. 6, pp. 407–409, 2014.
- [41] A. A. Ganin, E. Massaro, A. Gutfraind et al., "Operational resilience: concepts, design and analysis," *Scientific Reports*, vol. 6, no. 1, Article ID 19540, 2016.
- [42] B. Walker, C. S. Holling, S. R. Carpenter, and A. Kinzig, "Resilience, adaptability and transformability in social-ecological systems," *Ecology and Society*, vol. 9, no. 2, 2004.
- [43] P. Kroes, M. Franssen, I. van de Poel, and M. Ottens, "Treating socio-technical systems as engineering systems: some conceptual problems," *Systems Research and Behavioral Science*, vol. 23, no. 6, pp. 803–814, 2006.
- [44] P. Vermaas, P. Kroes, I. van de Poel, M. Franssen, and W. Houkes, "A philosophy of technology: from technical artefacts to sociotechnical systems," *Synthesis Lectures on Engineers, Technology and Society*, vol. 6, no. 1, pp. 1–134, 2011.
- [45] P. M. Leonardi, "Materiality, sociomateriality, and socio-technical systems: what do these terms mean? How are they different? Do we need them," *Materiality and Organizing: Social Interaction in a Technological World*, vol. 25, 2012.
- [46] M. Panteli, D. N. Trakas, P. Mancarella, and N. D. Hatziargyriou, "Power systems resilience assessment: hardening and smart operational enhancement strategies," *Proceedings of the IEEE*, vol. 105, no. 7, pp. 1202–1213, 2017.
- [47] M. Memarzadeh and M. Pozzi, "Integrated inspection scheduling and maintenance planning for infrastructure systems," *Computer-Aided Civil and Infrastructure Engineering*, vol. 31, no. 6, pp. 403–415, 2016.

- [48] Z. Li, M. Shahidehpour, F. Aminifar, A. Alabdulwahab, and Y. Al-Turki, "Networked microgrids for enhancing the power system resilience," *Proceedings of the IEEE*, vol. 105, no. 7, pp. 1289–1310, 2017.
- [49] J. Sutton, E. S. Spiro, B. Johnson, S. Fitzhugh, B. Gibson, and C. T. Butts, "Warning tweets: serial transmission of messages during the warning phase of a disaster event," *Information, Communication & Society*, vol. 17, no. 6, pp. 765–787, 2014.
- [50] L. Appleby, *Connecting the Last Mile: The Role of Communications in the Great East Japan Earthquake*, Internews, London, UK, 2013.
- [51] J. D. Fraustino, B. Liu, and Y. Jin, *Social Media Use During Disasters: A Review of the Knowledge Base and Gaps*, National Consortium for the Study of Terrorism and Responses to Terrorism, College Park, MD, USA, 2012.
- [52] J. Tasic and S. Amir, "Informational capital and disaster resilience: the case of Jalin Merapi," *Disaster Prevention and Management: An International Journal*, vol. 25, no. 3, pp. 395–411, 2016.
- [53] B. Bjerger, N. Clark, P. Fisker, and E. Raju, "Technology and information sharing in disaster relief," *PLoS One*, vol. 11, no. 9, Article ID e0161783, 2016.
- [54] T. W. Malone and K. Crowston, "What is coordination theory and how can it help design cooperative work systems?," in *Proceedings of the 1990 ACM Conference on Computer-Supported Cooperative Work, ACM*, pp. 357–370, Los Angeles, CA, USA, October 1990.
- [55] W. J. Orlikowski, "Sociomaterial practices: exploring technology at work," *Organization Studies*, vol. 28, no. 9, pp. 1435–1448, 2007.
- [56] M. Mazmanian, J. Yates, and W. Orlikowski, "Ubiquitous email: individual experiences and organizational consequences of blackberry USE," *Academy of Management Proceedings*, vol. 2006, no. 1, pp. D1–D6, 2006.
- [57] W. E. Bijker, T. P. Hughes, and T. J. Pinch, *The Social Construction of Technological Systems: New Directions in the Sociology and History of Technology*, MIT Press, Cambridge, MA, USA, 1987.
- [58] L. K. Comfort, Y. Sungu, D. Johnson, and M. Dunn, "Complex systems in crisis: anticipation and resilience in dynamic environments," *Journal of Contingencies and Crisis Management*, vol. 9, no. 3, pp. 144–158, 2001.
- [59] R. Poli, "The many aspects of anticipation," *Foresight*, vol. 12, no. 3, pp. 7–17, 2010.
- [60] N. Leveson, "A new accident model for engineering safer systems," *Safety Science*, vol. 42, no. 4, pp. 237–270, 2004.
- [61] G. Preece, D. Shaw, and H. Hayashi, "Using the viable system model (VSM) to structure information processing complexity in disaster response," *European Journal of Operational Research*, vol. 224, no. 1, pp. 209–218, 2013.
- [62] C. E. Lindblom, *The Policy-Making Process*, Prentice-Hall, Upper Saddle River, NJ, USA, 1968.
- [63] H. A. Simon, "Bounded rationality," in *Utility and Probability*, pp. 15–18, Springer, Berlin, Germany, 1990.
- [64] R. W. Perry, "Incident management systems in disaster management," *Disaster Prevention and Management: An International Journal*, vol. 12, no. 5, pp. 405–412, 2003.
- [65] J. A. Barbera, A. G. Macintyre, A. Knebel, and E. Trabert, *Medical Surge Capacity and Capability: A Management System for Integrating Medical and Health Resources During Large-Scale Emergencies*, US Department of Health and Human Services, Washington, DC, USA, 2007.

Research Article

Ship Steering Control Based on Quantum Neural Network

Wei Guan , Haotian Zhou, Zuoqing Su , Xianku Zhang , and Chao Zhao

Navigation College, Dalian Maritime University, Dalian 116026, China

Correspondence should be addressed to Zuoqing Su; suzuoqing@163.com

Received 14 August 2019; Accepted 6 November 2019; Published 17 December 2019

Guest Editor: Raúl Baños

Copyright © 2019 Wei Guan et al. This is an open access article distributed under the Creative Commons Attribution License, which permits unrestricted use, distribution, and reproduction in any medium, provided the original work is properly cited.

During the mission at sea, the ship steering control to yaw motions of the intelligent autonomous surface vessel (IASV) is a very challenging task. In this paper, a quantum neural network (QNN) which takes the advantages of learning capabilities and fast learning rate is proposed to act as the foundation feedback control hierarchy module of the IASV planning and control strategy. The numeric simulations had shown that the QNN steering controller could improve the learning rate performance significantly comparing with the conventional neural networks. Furthermore, the numeric and practical steering control experiment of the IASV BAICHUAN has shown a good control performance similar to the conventional PID steering controller and it confirms the feasibility of the QNN steering controller of IASV planning and control engineering applications in the future.

1. Introduction

In the past decade, the research on intelligent automatic surface ship (IASV) technology in academic and marine industries has continued to grow. These developments have been fuelled by advanced sensing, communication, and computing technology together with the potentially transformative impact on automotive sea transportation and perceived social and economic benefits [1–5]. The ship planning and control strategy for IASV, shown in Figure 1, which based on a module-based hierarchical structure, would be a good navigation strategy. It includes the global routing planning module, behaviour decision-making module, local motion planning module, and feedback control module. These modules are in charge of the different tasks especially the feedback control module is the foundation module as action part of the IASV navigation process. The key function of this module is the IASV steering operation to maintain or change ship course. In this paper, a quantum neural network (QNN) for ship steering control is proposed to address the ship steering control problem based on the IASV planning and control concept.

As a good research foundation of the IASV steering control problem, many effective steering feedback control methods had been surveyed. The ship steering control based

on proportional-integral-derivative (PID) strategy is simple and easy to construct. However, the conventional PID occupies the necessary basic controller role in process control, but it is not the trend of controller design due to the lack of learning and adaption capabilities. In addition, the controller parameters are required adjustments in varying conditions, which are time consuming and may not achieve accurate control performance. To solve the issues and obtain better performance, various advanced control strategies have been proposed for the steering control of the ship in recent years, such as adaptive steering control strategy [6–8], steering control strategy based on fuzzy logic algorithm [9, 10], steering controller based on Backstepping controller design method [11–13], and adaptive backstepping method [14, 15]. The robust control schemes such as the sliding mode control method [16, 17] and H_∞ robust control algorithm [18] are also utilized in the ship steering control to achieve better ship course keeping and changing manoeuver.

Since the 1990s, with the introduction of the artificial neural network into the ship steering controller design, experts and scholars had gradually increased ship steering control research on this issue. Witt et al. proposed a PID steering controller to train a neural network, where the output signal of the PID controller acts as the teacher signal and the simulation results showed that the control

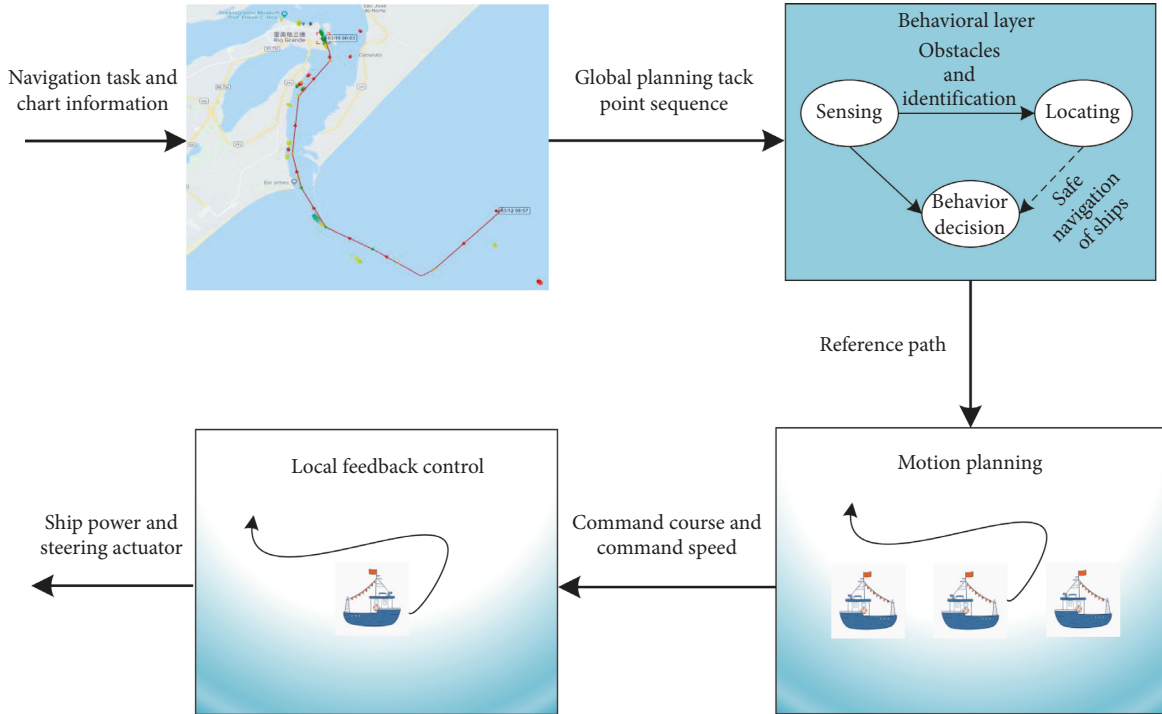


FIGURE 1: IASV planning and control strategy.

effects of the PID controller and the neural network controller have basically the same course control effect [19]. Hearn et al. proposed an online course control neural network to improve the conventional PID steering control effects, but the slow convergence of the ship steering controller based on the neural network is still a big problem to be solved [20].

In order to overcome the shortcomings of the conventional neural network, a ship steering controller based on the QNN is proposed in this paper under the concept of quantum computing [21–23]. The concept of QNN was first proposed by Toth et al. in 1996 [24]. Then, Matsui et al. used a quantum bit and the quantum revolving door to design a QNN for information processing and expression [25]. Another group of Japanese scholars, Kouda et al., summarized their previous research and summed up an emerging model, which is a quantum neuron model based on general quantum logic gates [26]. In 2018, Jeswal and Chakraverty introduced the latest developments of QNN and discussed the application of QNN [22]. And Xie et al. took the general quantum logic gates as the basis function to design a quantum neural computing network, and the simulation results indicated that the QNN is superior to the classical BP neural network and the radial basis function (RBF) neural network computing model in the financial data analysis [27]. Li and Li also pointed out that QNN based on general quantum gate evolution can improve the convergence performance of the conventional BP neural network [28]. Besides, the QNN has been applied to signature verification [29], audio watermarking [30], cardiovascular diseases risk prediction [31], classification recognition of electronic shock fault [32], and English to Hindi machine translator [33] and other fields.

Motivated by the above observations, a QNN steering controller would be applied to the IASV steering to yaw control. Hence, the remainder of the paper is organized as follows. In Section 2, the mathematical model of the IASV steering to yaw motion is given. Section 3 devotes to a systematic procedure for the QNN steering controller design. In Section 4, the numeric comparison simulations for the QNN steering controller and conventional neural networks steering controller were firstly carried out to demonstrate the faster learning convergence of the proposed QNN steering controller. Then, a numeric and practical experiment on smart IASV BAICHUAN has shown the feasibility of the QNN steering controller in practical engineering practice. Finally, Section 5 gives the conclusions of the paper.

2. IASV Mathematical Model

While a mathematical model of the IASV is fully described by coupled nonlinear differential equations, a simple model with predictive capability is usually preferred for the design of a ship-steering autopilot. A three-degree-of-freedom plane motion including surge, sway, and yaw motion is considered satisfactory. However, roll motion cannot be neglected due to couplings and hence a four-degree-of-freedom plane motion including surge, sway, yaw, and roll motion is used to describe the motion of a ship. Consequently, a fourth-order transfer function relating to the yaw rate to rudder deflection is derived based on the linearized equations of motion. Nevertheless, a fourth-order transfer function is further reduced to a second-order Nomoto model and then to a first-order Nomoto model for ease of

controller design. The first-order Nomoto model, from δ to yaw rate r is presented as

$$\frac{r(s)}{\delta(s)} = \frac{K}{(1+Ts)}, \quad (1)$$

where r is the yaw rate, δ is the rudder deflection, T is the time constant of IASV maneuverability, and K is defined as the steering control gain constant of IASV maneuverability. The parameters K and T that describe the ship steering to yaw dynamics can be identified from standard maneuvering tests. Since r is the time derivative of the yaw angle ψ , the transfer function relating to the yaw angle to steering movement can be obtained by adding an integrator ($1/s$) to the first-order Nomoto model of (1), then we can get

$$\frac{\psi(s)}{\delta(s)} = \frac{K}{s(1+Ts)}, \quad (2)$$

and the corresponding differential equation can be expressed as

$$T\ddot{\psi} + \dot{\psi} = K\delta. \quad (3)$$

The model presented in (3) is modified to include a nonlinear steering condition as discussed in [6], wherein the yaw rate $\dot{\psi}$ term is replaced by a nonlinear function $H(\dot{\psi})$. Then, we can get the following equation:

$$T\ddot{\psi} + H(\dot{\psi}) = K\delta, \quad (4)$$

where

$$H(\dot{\psi}) = \alpha_0 + \alpha_1\dot{\psi} + \alpha_2\dot{\psi}^2 + \alpha_3\dot{\psi}^3. \quad (5)$$

Because of the symmetrical structure of ships, the parameters $a_0 = a_2 = 0$ [34] and α_1 is set as +1 for stable ships and -1 for unstable ones, while the value of α_3 , known as the Norbin coefficient [14], can be determined via the ship turning test.

3. QNN Steering Controller Design

In this section, a quantum neural network model was constructed for the ship steering controller design to enhance the convergence performance of the conventional neural network steering controller.

3.1. The Quantum Neuron Model. The structure of the quantum neuron model based on the quantum logic gate is defined as Figure 2, including the input part, phase rotation part, aggregation part, reverse rotation part, and output part. The details of the quantum neural networks working processes are shown as the following steps:

Step 1: let $|x_i\rangle = (\cos t_i, \sin t_i)^T$, and define the qubit phase rotation gate as

$$R(\theta) = \begin{pmatrix} \cos \theta & -\sin \theta \\ \sin \theta & \cos \theta \end{pmatrix}. \quad (6)$$

Then, with the aggregation, we can get

$$\sum_{i=1}^n R(\theta_i) |x_i\rangle = [\cos \theta \quad \sin \theta]^T, \quad (7)$$

where $\theta = \arg\left(\sum_{i=1}^n R(\theta_i) |x_i\rangle\right) = \arg \tan\left(\frac{\sum_{i=1}^n \sin(t_i + \theta_i)}{\sum_{i=1}^n \cos(t_i + \theta_i)}\right)$.

Step 2: the result of equation (7) makes the reverse rotation operation by the controlled-NOT gate as follows:

$$U(\gamma) = \begin{pmatrix} \cos\left(f(\gamma)\frac{\pi}{2} - 2\theta_0\right) & -\sin\left(f(\gamma)\frac{\pi}{2} - 2\theta_0\right) \\ \sin\left(f(\gamma)\frac{\pi}{2} - 2\theta_0\right) & \cos\left(f(\gamma)\frac{\pi}{2} - 2\theta_0\right) \end{pmatrix}, \quad (8)$$

where f is the sigmoid function; then, we can get

$$U(\gamma) \sum_{i=1}^n R(\theta_i) |x_i\rangle = \left[\cos\left(\frac{\pi}{2}f(\gamma) - \theta\right) \quad \sin\left(\frac{\pi}{2}f(\gamma) - \theta\right) \right]^T. \quad (9)$$

Therefore, the relationship between the input and output of the quantum neuron model can be described as

$$y = \sin\left(\frac{\pi}{2}f(\gamma) - \theta\right) = \sin\left(\frac{\pi}{2}f(\gamma) - \arg\left(\sum_{i=1}^n R(\theta_i) |x_i\rangle\right)\right). \quad (10)$$

3.2. QNN Model. Based on the quantum neuron model, a quantum neural network for the ship steering controller design is constructed as shown in Figure 3. The proposed neural network has three layers including an input layer, hidden layer, and output layer. The concept of QNN is applied to the layer that is between the input layer and the hidden layer; there are n quantum neurons in the input layer, m quantum neurons in the hidden layer, and p conventional neurons in the output layer.

Assuming the input variable is $|x_i\rangle$, the output of the hidden layer is h_j , the output of the QNN is y_k , $R(\theta_{ij})$ is the quantum rotation gate between the input layer and the hidden layer to update the qubits, and w_{jk} is the network weight for the hidden layer and the output layer. Taking the qubit-controlled NOT-gate $U(\gamma_j)$ as the transfer function of the hidden layer, then the output of the QNN can be expressed as

$$y_k = g\left(\sum_{j=1}^m w_{jk}h_j\right) = g\left(\sum_{j=1}^m w_{jk} \sin\left(\frac{\pi}{2}f(\gamma_j) - \arg\left(\sum_{i=1}^n R(\theta_{ij}) |x_i\rangle\right)\right)\right), \quad (11)$$

where $i = 1, 2, \dots, n$; $j = 1, 2, \dots, m$; and $k = 1, 2, \dots, p$.

3.3. The Learning Algorithm of QNN. To apply the QNN in practical engineering, the training samples should be transformed into the quantum states. For example, the n -dimensional Euclidean space training sample

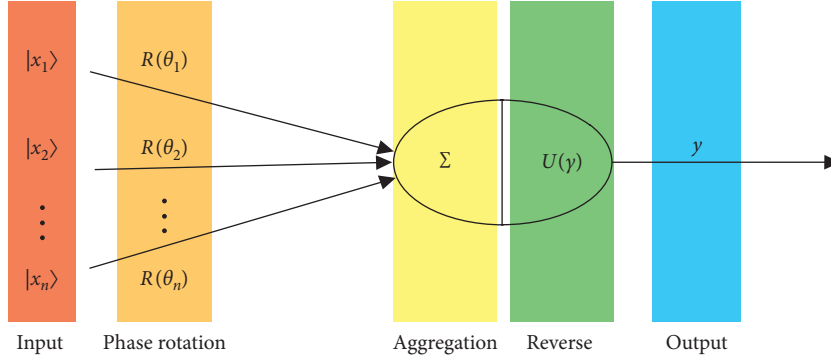


FIGURE 2: The quantum neuron model.

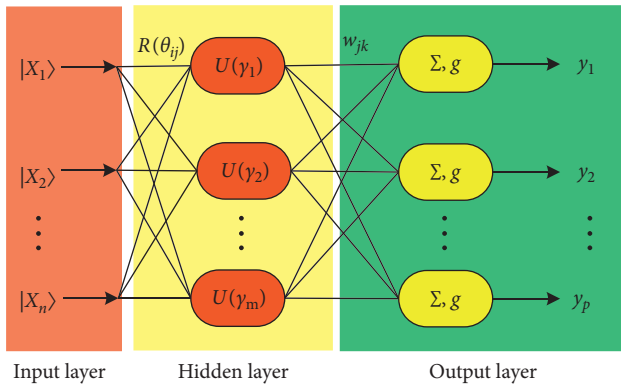


FIGURE 3: The quantum neuron networks model.

$\bar{X} = (\bar{x}_1, \bar{x}_2, \dots, \bar{x}_n)^T$ can be defined as the corresponding quantum state as

$$|X\rangle = (|x_1\rangle, |x_2\rangle, \dots, |x_n\rangle)^T, \quad (12)$$

where

$$\begin{aligned} |x_i\rangle &= \cos\left(\frac{2\pi}{1 + \exp(-\bar{x}_i)}\right)|0\rangle + \sin\left(\frac{2\pi}{1 + \exp(-\bar{x}_i)}\right)|1\rangle \\ &= \left(\cos\left(\frac{2\pi}{1 + \exp(-\bar{x}_i)}\right), \sin\left(\frac{2\pi}{1 + \exp(-\bar{x}_i)}\right)\right)^T. \end{aligned} \quad (13)$$

In the three layers of the QNN model as described in Figure 3, there are 3 groups of parameters, namely, phase rotation parameters θ_{ij} , reverse parameters γ_j , and network weights w_{jk} needed to be updated. Firstly, define the error evaluation function as

$$E = \frac{1}{2} \sum_{k=1}^p (d_k - y_k)^2, \quad (14)$$

where d_k and y_k are the desired outputs and actual outputs of the normalized quantum neural network, respectively. Let $|x_i\rangle = (\cos \varphi_i, \sin \varphi_i)^T$ and $\beta_j = \arctan(\sum_{i=1}^n \sin(\varphi_i + \theta_{ij}) / \sum_{i=1}^n \cos(\varphi_i + \theta_{ij}))$, then equation (11) could be rewritten as

$$y_k = g\left(\sum_{j=1}^m w_{jk} \sin\left(\frac{\pi}{2} f(\gamma_j) - \beta_j\right)\right). \quad (15)$$

Let

$$\begin{cases} S_j = \frac{\sum_{i=1}^n \sin(\varphi_i + \theta_{ij})}{\sum_{i=1}^n \cos(\varphi_i + \theta_{ij})}, \\ S_{j1} = \sum_{i=1}^n \cos(\varphi_i + \theta_{ij}), \\ T_j = \frac{(\cos(\varphi_i + \theta_{ij})S_{j1} + \sin^2(\varphi_i + \theta_{ij}))}{S_{j1}^2}. \end{cases} \quad (16)$$

According to the gradient descent method, we can get

$$\begin{cases} \Delta\theta_{ij} = -\frac{\partial E}{\partial \theta_{ij}} = -\sum_{k=1}^p (d_k - y_k) g' w_{jk} \cos\left(\frac{\pi}{2} f(\gamma_j) - \beta_j\right) \\ \quad \cdot \frac{T_j}{1 + S_j^2}, \\ \Delta\gamma_j = -\frac{\partial E}{\partial \gamma_j} = \frac{\pi}{2} \sum_{k=1}^p (d_k - y_k) g' w_{jk} \cos\left(\frac{\pi}{2} f(\gamma_j) - \beta_j\right) f', \\ \Delta w_{jk} = -\frac{\partial E}{\partial w_{jk}} = (d_k - y_k) g' \sin\left(\frac{\pi}{2} f(\gamma_j) - \beta_j\right). \end{cases} \quad (17)$$

Therefore, the updated rules for phase rotation parameters θ_{ij} , reverse rotation parameters γ_j , and network weights w_{jk} are

$$\begin{cases} \theta_{ij}(t+1) = \theta_{ij}(t) + \eta \Delta\theta_{ij}(t), \\ \gamma_j(t+1) = \gamma_j(t) + \eta \Delta\gamma_j(t), \\ w_{jk}(t+1) = w_{jk}(t) + \eta \Delta w_{jk}(t), \end{cases} \quad (18)$$

where η is the learning rate of the QNN.

3.4. Teacher Controller of QNN. In this paper, the conventional PID steering control controller is acted as the teacher of the QNN controller. The input variable of the PID controller is the heading deviation $\Delta\psi$, and the linear combination of the proportion, integration, and differentiation of the heading deviation $\Delta\psi$ is used as the output value of the PID controller. The command steering angle $\delta(k)$ can be expressed as

$$\delta(k) = k_p \Delta\psi(k) + k_i \sum_{j=0}^k \Delta\psi(j) + k_d [\Delta\psi(k) - \Delta\psi(k-1)], \quad (19)$$

where k_p , k_i , and k_d are the controller proportion parameter, integral parameter, and differential parameter, respectively, and k is the sampling time ($k = 0, 1, 2, \dots$).

3.5. Design of the QNN Steering Controller. In this section, a three layer 2-5-1 QNN model was constructed. The structure of the QNN steering control system is shown in Figure 4. The two inputs of the QNN steering controller are the heading deviation $\Delta\psi(k)$ and yaw rate $r(k)$, respectively, and the output is the command steering angle $\delta_r^{\text{QNN}}(k)$. The difference between the QNN steering controller outputs and PID course keeping controller outputs is defined as the system error. The mean square of the system error (MSE) is defined as the performance evaluation function of the proposed QNN to evaluate the performance of the QNN learning performance and optimized targets. Generally, its value is set as 0.00001. The activation function of the QNN hidden layer and the output layer is defined as hyperbolic tangent sigmoid function (tan-sigmoid) to accelerate the QNN training and convergence performance in the training process. The gradient descent with a quasi-Newton algorithm [35] is offered to the QNN training, and the momentum parameter of the quasi-Newton algorithm is set as 0.8. The initial values of the QNN weights are randomly generated between the intervals $(-1, 1)$, and the learning rate η of QNN is set as 0.1.

4. Simulations and Analysis

In this section, a series of simulations were used to illustrate the fast convergence characteristics and practical engineering effectiveness of the proposed controller. Especially an IASV BAICHUAN is utilized as a practical experiment for validations of the proposed QNN steering controller. Take $K = 0.6$, $T = 1.866$, $a_1 = 1$, and $a_3 = -9.44 \times 10^{-6}$ as the dynamic parameters of the second-order Nomoto ship model equation (4) for IASV BAICHUAN. Set $k_p = 2$, $k_i = 0.00001$, and $k_d = 1.5$ as tuning parameters of the teacher controller equation (19). In the simulations, the initial course of the IASV was set as 000° and the desired course keeping angle was set as 090° . The simulation time was set as 50 s, and the sampling period was set as 0.05 s. From the result of the simulations shown in Figure 5, it can be seen that the PID steering controller, which acted as the teacher of the QNN controller, could track the desired

course after 13s, and the result shows that the PID controller is satisfactory to act as a suitable teacher of the QNN steering controller.

To illustrate the practical effectiveness of the proposed QNN steering control system, as shown in Figure 4, during the QNN steering controller training, the values of phase rotation parameters θ_{ij} , reverse rotation parameters γ_j , and network weights w_{jk} would be updated according to equation (18) by using the training data set extracted from PID controller simulation results in Figure 5.

For comparison, a conventional BP neural network steering controller is also trained using the same training data set extracted from the PID control results in Figure 5. To emphasize the advantages of the faster convergence and fewer learning iterations, the QNN steering controller and BP neural network steering controller were trained 8 times, respectively, and then the epochs in each training time are shown in Figure 6. For the BP neural network, the maximum number of training epoch is 9565 (in the 6th training time), the minimum training epoch is 4325 (in the 2nd training time), and the average number of training epochs for the 8 training times is 7022. Although, for the QNN, the maximum number of training epoch is 4625 (in the 2nd training time), the minimum training epoch is 1526 (in the 4th training time), and the average number of sample training epoch of the 8 training times is 3302. Therefore, it can be concluded that the QNN steering controller is improved significantly in the convergence rate compared with the conventional BP neural network steering controller.

To validate the effectiveness of the trained QNN steering controller, an IASV BAICHUAN QNN steering control simulation was carried out. The weights w_{jk} of the QNN controller were extracted from the 2nd training time and selected as the initial weights of the IASV BAICHUAN QNN steering controller. The values are detailed in Table 1. Then, the simulation result are shown in Figure 7.

It can be seen from Figure 7 that the QNN steering controller could track the desired course at about 13 s. The control result is very similar to the PID controller. It can be concluded that the proposed QNN steering controller has a very strong learning ability and could be widely applied to various fields.

To further confirm the proposed QNN steering controller performance, an IASV BAICHUAN course keeping practical engineering experiment was carried out. The experiment environment is shown in Figure 8. The wind direction of the experiment scene was northwest (310° – 330°), and the wind velocity varied from 0–0.20 m/s. The temperature was about 8°C . The maximum wave height was about 0–0.05 m. The initial course of the IASV is set at 000° , and the desired course keeping angle is set as 090° . The QNN steering controller's initial parameters are also set as Table 1. Also the PID steering control experiment was carried out for comparison. The parameter of the PID steering controller was also set as $k_p = 2$, $k_i = 0.00001$, and $k_d = 1.5$, as mentioned above. The sampling period of the QNN steering controller and PID steering controller are set as 0.05s, respectively. Finally, the experiment results are shown in Figure 9.

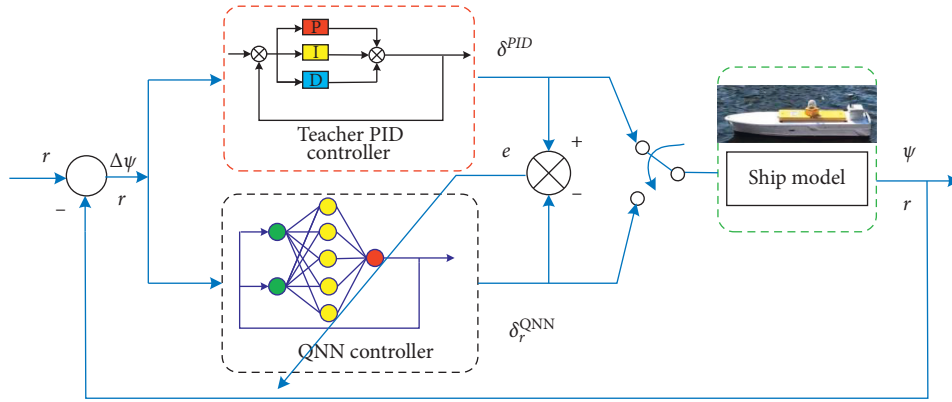


FIGURE 4: IASV QNN-steering autopilot structure.

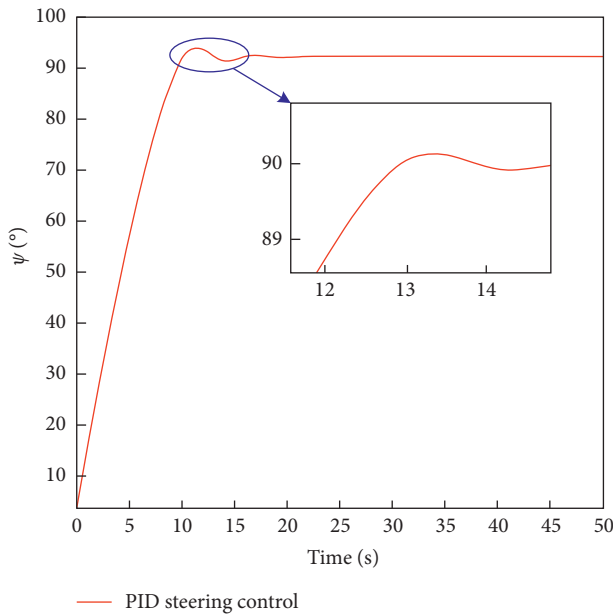


FIGURE 5: The PID steering control results.

The left side of Figure 9 shows the course keeping control effect, and the right side shows the output of the IASV BAICHUAN steering control. It can be seen that the rising time of the QNN steering controller is slightly slower than the PID controller, but both controllers can reach the target course rapidly and both of them can achieve a good course keeping control effect. As it can be seen on the right side of Figure 9, the controller output of the two type steering controller is basically the same and the time to reach the static stabilities are also similar, but the response of the QNN steering controller is also slightly slower (about one second) than the PID steering controller.

To further quantify the controller performance, the controller efficiency function (CEF) is defined as

$$\text{CEF} = \frac{1}{n} \left(\sum_{k=1}^n (\Delta\psi(k))^2 + \sum_{k=1}^n (\Delta\delta(k))^2 \right). \quad (20)$$

Then, we can obtain that the CEF of the QNN steering controller is 0.323 and the CEF of the PID steering controller

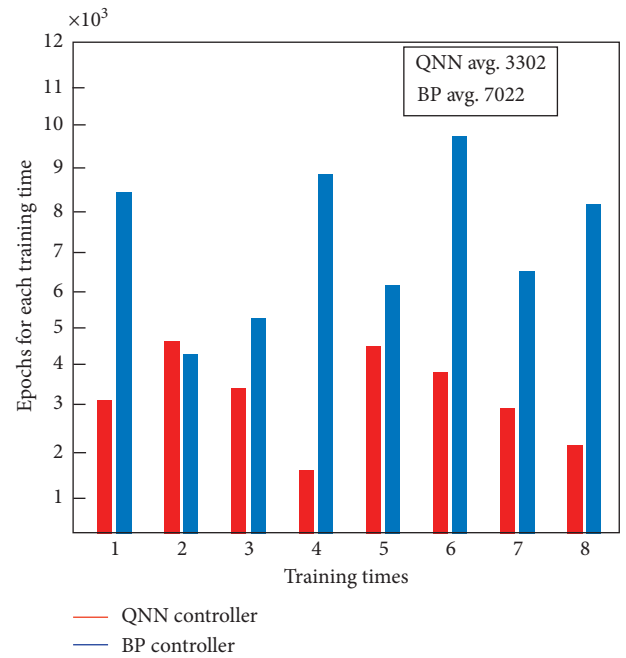


FIGURE 6: The epochs of eight training times.

is 0.299. Hence, it is concluded that the control efficiency of the QNN steering controller can get a similar control effect compared with the PID steering controller for the IASV course keeping.

Remark 1. From the numeric simulation and practical engineering experiment, it can be seen that the proposed QNN steering controller has a slightly delayed response compared with the PID steering controller, although the delayed response phenomenon is not obvious in the numeric simulations. The reason of the delayed response phenomenon might be caused by the larger computation burden of the QNN steering controller. This is a potential disadvantage of the QNN. However, due to the features of strong learning ability and fast convergence performance, the proposed QNN steering controller could be used in learning of other advanced controllers, not only restricted in the PID

TABLE 1: The weights and parameters of the QNN steering controller.

$w_{1,3}$	$w_{1,4}$	$w_{1,5}$	$w_{1,6}$	$w_{1,7}$	$w_{2,3}$	$w_{2,4}$	$w_{2,5}$	$w_{2,6}$	$w_{2,7}$	$w_{3,8}$	$w_{4,8}$	$w_{5,8}$	$w_{6,8}$	$w_{7,8}$	b_1	b_2	b_3	b_4	b_5	b_6
0.0026	-0.165	-0.0012	0.0074	-0.0075	-0.0133	0.1705	-0.0001	0.0230	-0.0233	-0.0190	0.0038	0.0010	0.0271	-0.0275	0.0013	0.0003	-0.0003	0.0026	6.4116	6.4114

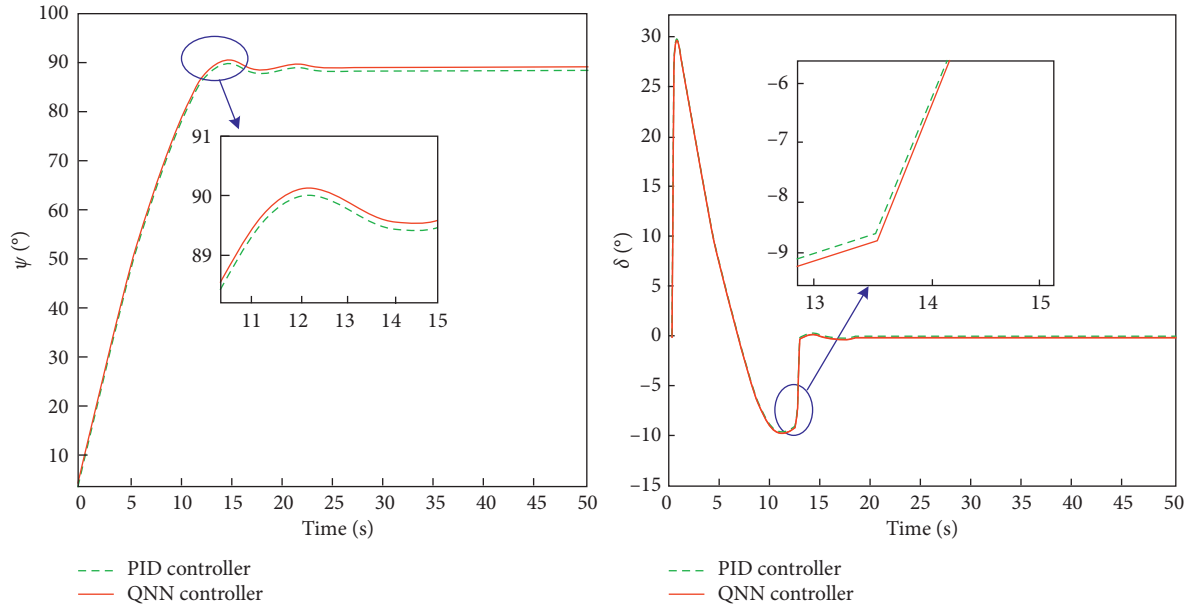


FIGURE 7: The course keeping simulation results for the PID and QNN steering controller.



FIGURE 8: The scene of the experiment.

controller. Therefore, the proposed QNN steering controller might be a universal controller design structure and scheme for the future IASV steering feedback control module.

5. Conclusions

In this paper, a QNN steering controller design method based on the planning and control concept is proposed. Through the numeric simulations of the steering controller based on the conventional BP neural network and QNN, it can be inferred that the QNN steering controller has a faster convergence rate than the conventional BP neural network steering controller. Also, the numeric simulation results show that the QNN steering controller

has a similar course keeping control performance comparing with the training teacher PID steering controller. Furthermore, the practical QNN steering control experiment on an IASV BAICHUAN has shown that the proposed QNN steering controller is feasible to be equipped to a practical IASV for steering to yaw control in the future IASV planning and control engineering. Especially the strong learning characteristics and efficient convergence performance of the QNN steering controller might be the developing trend of the advanced IASV steering controller. However, the QNN steering controller proposed in this paper might be the first step to apply the advanced AI controller to the IASV. Furthermore, the proposed QNN controller structure could apply to other marine control engineering practices.

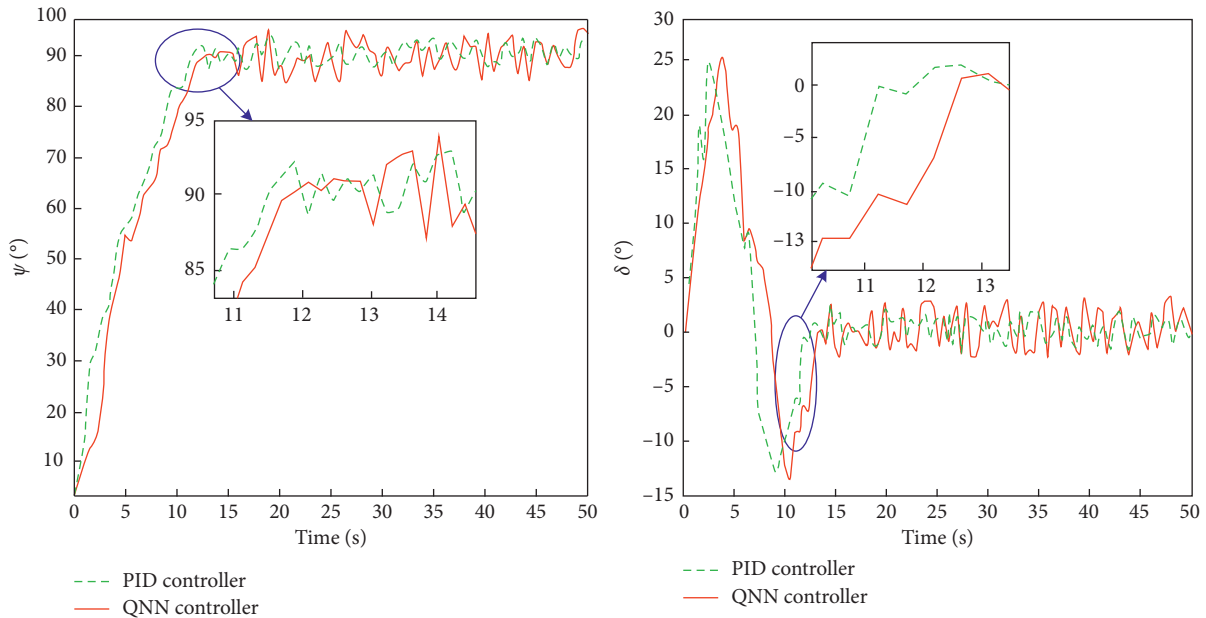


FIGURE 9: The practical course keeping control results of IASV BAICHUAN.

Data Availability

All data generated or analyzed during this study are included in this article.

Conflicts of Interest

The authors declare that there are no conflicts of interest.

Acknowledgments

This work was supported by the National Natural Science Foundation of China (Nos. 51409033 and 51679024) and the Fundamental Research Funds for the Central Universities of China (No. 3132019343).

References

- [1] J. E. Manley, "Unmanned surface vehicles 15 years of development," in *Proceedings of the OCEANS*, pp. 1–4, Quebec City, QC, Canada, September 2008.
- [2] F. Yunsheng, G. Zenglu, Z. Yongsheng, and W. Guofeng, "Design of information network and control system for USV," in *Proceedings of the 2015 54th Annual Conference of the Society of Instrument and Control Engineers of Japan (SICE)*, pp. 1126–1131, Hangzhou, China, July 2015.
- [3] N. H. Tran, H. S. Choi, J. Y. Oh, and S.-K. Jeong, "Design and implementation of dynamic positioning control system for USV," in *AETA 2015. Recent Advances in Electrical Engineering and Related Sciences*, pp. 633–644, Springer, Cham, Switzerland, 2016.
- [4] E. I. Sarda, I. R. Bertaska, A. Qu, and K. D. von Ellenrieder, "Development of a USV station-keeping controller," in *Proceedings of the OCEANS 2015*, pp. 1–10, Genova, Italy, May 2015.
- [5] I. D. Couzin, J. Krause, R. James, G. D. Ruxton, and N. R. Franks, "Collective memory and spatial sorting in animal groups," *Journal of Theoretical Biology*, vol. 218, no. 1, pp. 1–11, 2002.
- [6] J. Van Amerongen, "Adaptive steering of ships—a model reference approach," *Automatica*, vol. 20, no. 1, pp. 3–14, 1984.
- [7] J. Van Amerongen and A. J. Udink Ten Cate, "Model reference adaptive autopilots for ships," *Automatica*, vol. 11, no. 5, pp. 441–449, 1975.
- [8] C. Y. Tzeng and K. F. Lin, "Adaptive ship steering autopilot design with saturating and slew rate limiting actuator," *International Journal of Adaptive Control and Signal Processing*, vol. 14, no. 4, pp. 411–426, 2000.
- [9] G. Rigatos and S. Tzafestas, "Adaptive fuzzy control for the ship steering problem," *Mechatronics*, vol. 16, no. 8, pp. 479–489, 2006.
- [10] Y. Yang and J. Ren, "Adaptive fuzzy robust tracking controller design via small gain approach and its application," *IEEE Transactions on Fuzzy Systems*, vol. 11, no. 6, pp. 783–795, 2003.
- [11] T. I. Fossen and J. P. Strand, "Tutorial on nonlinear backstepping: applications to ship control," *Modeling, Identification and Control: A Norwegian Research Bulletin*, vol. 20, no. 2, pp. 83–135, 1999.
- [12] K. D. Do, Z. P. Jiang, and J. Pan, "Underactuated ship global tracking under relaxed conditions," *IEEE Transactions on Automatic Control*, vol. 47, no. 9, pp. 1529–1536, 2002.
- [13] S. Das, A. Bhatt, and S. E. Talole, "UDE based backstepping design for ship autopilot," in *Proceedings of the 2015 International Conference on Industrial Instrumentation and Control (ICIC)*, pp. 417–422, Pune, India, May 2015.
- [14] J. Du, C. Guo, S. Yu, and Y. Zhao, "Adaptive autopilot design of time-varying uncertain ships with completely unknown control coefficient," *IEEE Journal of Oceanic Engineering*, vol. 32, no. 2, pp. 346–352, 2007.
- [15] J. Li, T. Li, Z. Fan, R. Bu, Q. Li, and J. Hu, "Robust adaptive backstepping design for course-keeping control of ship with parameter uncertainty and input saturation," in *Proceedings of the 2011 International Conference of Soft Computing and*

- Pattern Recognition (SoCPaR)*, pp. 63–67, Dalian, China, October 2011.
- [16] E. W. McGookin, D. J. Murray-Smith, Y. Li, and T. I. Fossen, “Ship steering control system optimisation using genetic algorithms,” *Control Engineering Practice*, vol. 8, no. 4, pp. 429–443, 2000.
- [17] L. Yuan and H.-s. Wu, “Terminal sliding mode fuzzy control based on multiple sliding surfaces for nonlinear ship autopilot systems,” *Journal of Marine Science and Application*, vol. 9, no. 4, pp. 425–430, 2010.
- [18] L. Sheng, Y. Ping, L. Yan-yan, and D. Yan-chun, “Application of H infinite control to ship steering system,” *Journal of Marine Science and Application*, vol. 5, no. 1, pp. 6–11, 2006.
- [19] N. A. J. Witt, R. Sutton, and K. M. Miller, “A track keeping neural network controller for ship guidance,” *IFAC Proceedings Volumes*, vol. 28, no. 2, pp. 385–392, 1995.
- [20] G. E. Hearn, Y. Zhang, and P. Sen, “Alternative designs of neural network based autopilots: a comparative study,” *IFAC Proceedings Volumes*, vol. 30, no. 22, pp. 83–88, 1997.
- [21] R. P. Feynman, “Quantum mechanical computers,” *Foundations of Physics*, vol. 16, no. 6, pp. 507–531, 1986.
- [22] S. K. Jeswal and S. Chakraverty, “Recent developments and applications in quantum neural network: a review,” *Archives of Computational Methods in Engineering*, vol. 26, no. 4, pp. 793–807, 2019.
- [23] S. C. Kak, “On quantum neural computing,” in *Advances in Imaging and Electron Physics*, vol. 94, pp. 259–313, Elsevier, Amsterdam, Netherlands, 1995.
- [24] G. Toth, C. S. Lent, P. D. Tougaw et al., “Quantum cellular neural networks,” *Superlattices and Microstructures*, vol. 20, no. 4, pp. 473–478, 1996.
- [25] N. Matsui, M. Takai, and H. Nishimura, “A network model based on qubitlike neuron corresponding to quantum circuit,” *Electronics and Communications in Japan (Part III: Fundamental Electronic Science)*, vol. 83, no. 10, pp. 67–73, 2000.
- [26] N. Kouda, N. Matsui, H. Nishimura, and F. Peper, “Qubit neural network and its learning efficiency,” *Neural Computing and Applications*, vol. 14, no. 2, pp. 114–121, 2005.
- [27] G. J. Xie, D. Zhou, and H. Q. Fan, “A neural network model based-on quantum gates cell and its applications,” *System Engineering Theory and Practice*, vol. 25, no. 5, pp. 113–117, 2005.
- [28] P. C. Li and S. Y. Li, “Learning algorithm and application of quantum BP neural networks based on universal quantum gates,” *Journal of Systems Engineering and Electronics*, vol. 19, no. 1, pp. 167–174, 2008.
- [29] M. J. Cao, P. C. Li, and H. Xiao, “Application of quantum neural network in PID parameter adjustment,” *Computer Engineering*, vol. 37, no. 12, pp. 182–189, 2011.
- [30] Y. P. Zhang, L. Chen, and H. A. Hao, “New audio watermarking algorithm based on quantum neural network,” *Signal Processing*, vol. 29, no. 6, pp. 684–690, 2013.
- [31] N. Renu, S. Sanjai, and G. Achal, “Cardiovascular risk prediction: a comparative study of Framingham and quantum neural network based approach,” *Patient Preference and Adherence*, vol. 10, pp. 1259–1270, 2016.
- [32] H. Guan, M. Liu, C. Li et al., “Classification recognition model of electric shock fault based on wavelet packet transformation and quantum neural network,” *Transactions of the Chinese Society of Agricultural Engineering*, vol. 34, no. 5, pp. 183–190, 2018.
- [33] R. Narayan, S. Chakraverty, and V. P. Singh, “Quantum neural network based machine translator for English to Hindi,” *Applied Soft Computing*, vol. 38, pp. 1060–1075, 2016.
- [34] W. Guan, W. Cao, J. Sun, and Z. Su, “Steering controller design for smart autonomous surface vessel based on CSF L2 gain robust strategy,” *IEEE Access*, vol. 7, pp. 109982–109989, 2019.
- [35] P. X. Lu, “Research on BP neural network algorithm based on quasi-Newton method,” *Applied Mechanics and Materials*, vol. 686, pp. 388–394, 2014.

Research Article

CC²: Defending Hybrid Worm on Mobile Networks with Two-Dimensional Circulation Control

Hailu Yang ^{1,2}, Deyun Chen ^{1,2}, Guanglu Sun ², Xiaoyu Ding ³ and Yu Xin ⁴

¹Postdoctoral Research Station of Computer Science and Technology, Harbin University of Science and Technology, Harbin 150080, China

²School of Computer Science and Technology, Harbin University of Science and Technology, Harbin 150080, China

³College of Computer Science and Technology, Harbin Engineering University, Harbin 150080, China

⁴Faculty of Electrical Engineering and Computer Science, Ningbo University, Ningbo 315211, China

Correspondence should be addressed to Deyun Chen; chendeyun@hrbust.edu.cn

Received 14 August 2019; Accepted 30 November 2019; Published 14 December 2019

Guest Editor: Raúl Baños

Copyright © 2019 Hailu Yang et al. This is an open access article distributed under the Creative Commons Attribution License, which permits unrestricted use, distribution, and reproduction in any medium, provided the original work is properly cited.

As the hybrid worm can propagate by both personal social interactions and wireless communications, it has been identified as one of the most severe threats to the mobile Internet. This problem is expected to become worse with the boom of social applications and mobile services. In this work, we study the propagation dynamics of hybrid worms and propose a systematic countermeasure. The system maintains a set of community structure which describes the high-speed infection zone of worms and contains worm propagation by distributing the worm signature to the guard nodes selected from the periphery of each community. For those nodes that are geographically close but located in different communities, we evaluate the communication security between them based on the observed infection history and limit communications between insecure ones to avoid the worm spreading across communities. We also design an efficient worm signature forwarding strategy that enables most nodes in the network to reach an immune state before being infected by the worm. Extensive real-trace driven simulations verify the feasibility and effectiveness of the proposed methods.

1. Introduction

With the rapid deployment of mobile Internet technology, smartphone-based social services such as Facebook, Wechat, and LinkedIn have already reached billions of registered users, many of whom choose to incorporate those services into their work and family life. On the positive side, the mobile Internet provides a convenient platform for people to communicate with close friends and interact online. On the negative side, however, it is also a breeding place for the spread of the mobile Internet worm [1].

The propagation of the worm in mobile Internet mainly depends on two dominant patterns [2]. First, the short-range worm infects all Bluetooth or Wi-Fi opened devices within the infection radius, which exhibits a spatial propagation pattern similar to the case of the contact-based disease [3]. Such kinds

of infections rely on peer-to-peer communications between sensors with geographical adjacency, which build a geographic interaction networks (short for GINs). The GINs worm always exploits hardware vulnerabilities of the mobile device to crash them. Defending against this type of infection is a challenge due to the lack of effective centralized regulation. On this account, most of the existing methods utilize a distributed coping scheme that allows users to limit the communications with vulnerable devices to insulate the proximity worm [4, 5]. Second, a long-range worm can replicate itself and infect all smartphones whose identifiers are stored in the infected smartphone's contact list, a delocalized propagation mode based on social relations in the social information networks (short for SINs). The SINs worm is similar to the one observed in Multimedia Messaging Service (MMS), both of which exhibit the characteristics of slow start

and exponential propagation [6]. Recent works mostly utilize a partitioning strategy to insulate the SINs worm in several disjoint “islands” [7–9].

Recent research reveals that as mobile phone functions continue to increase, the worm no longer uses a single model to spread [2]. The hybrid worm uses short-range infections as well as long-range ones. The first variant that utilizes the hybrid propagation mechanism is Commwarrior, which spreads from one phone to another via the Bluetooth interface and MMS. Since the message usually comes from friends or family members, Commwarrior has a high probability of being activated. The most recent malware that exhibits the hybrid propagation feature is WannaCry, devastating ransomware that uses the campus network as the short-range propagation route. Although there has been no case of WannaCry infections on mobile phones yet, people have to be vigilant because of its extremely destructive power. Figure 1 gives a brief description of the propagation dynamics of the hybrid worm. The synergetic infection mechanism visibly increases the infection ability of the worm and brings a considerable challenge to the worm containment task.

To solve this problem, one possible method is to integrate the SINs and the GINs into one single network using the dimensionality reduction method [10]. However, the evolution speed of these two networks is quite different, so the integrating process usually does not make any sense. In this paper, we adopt a divide-and-conquer strategy and propose CC^2 (2-dimensional circulation controller). We first model the propagation dynamics of the hybrid worm in the mobile Internet and analyze the vulnerable spot in the worm propagation chain. Next, two components are designed to reduce infection rates. The first one is the SINs containment unit which aims to solve the secondary forwarding caused by acquaintances based on the fact that the propagation of the worm on social networks mainly depends on the closeness of social relationships. Another one is the GINs feedback unit. Some devices are geographic proximity and offer the chance for the worm to propagate across communities with short-range communications. Based on the security history records, the GINs feedback unit restricts the communication with insecure devices with a certain probability. The outputs of these two units serve as the input parameters of each other, forming a cyclic state.

The rest of the paper is organized as follows: Section 2 introduces related works. Section 3 discusses the propagation dynamics of the hybrid worm. Section 4 gives detailed descriptions of CC^2 . The proposed methods are evaluated in Section 5. In Section 6, we make conclusions and envision further work.

2. Related Works

Although the worm is well understood on the Internet [6, 11], the worm on mobile Internet, however, has received only limited attention. In simple terms, the existing methods fall into two categories. For the short-range worm containment, Su et al. [12] showed that Bluetooth is an essential interface for worm’s propagation. Yan and Eidenbenz [13], Mickens and Noble [14], and Morris-king and Cam [15]

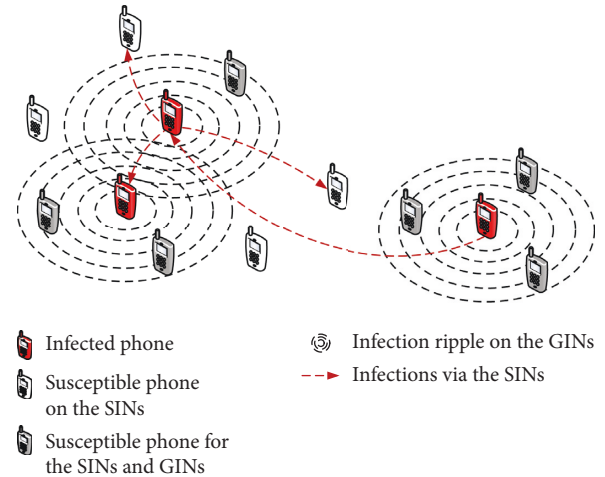


FIGURE 1: The hybrid spreading behavior of the mobile Internet worm.

confirmed this conclusion by analyzing the propagation dynamics of the worm transferred via the Bluetooth interface. Zyba et al. [4] designed a distributed coping scheme to eliminate the adjacent worm by using the worm signature. However, the time complexity of the algorithm is too challenging to solve a vast network. Yang et al. [16] proposed a sensor worm coping scheme based on graph coloring. The basic principle of this method is to increase the diversity of software version in the network. Li et al. [5] proposed a method to evaluate node vulnerability and control the worm by restricting the communication between vulnerable nodes. Miklas et al. [17] exploited social relations to improve the security of the Bluetooth interface and reduced the propagation speed of the worm by refusing connection requests from strangers. Gao and Liu [18] focused on the impacts of human behaviors on worm propagation and proposed a two-layer network model to protect large-scale dynamic mobile networks. The short-range worm relies on the direct connections between hardware interfaces and currently tends to attack wireless sensor networks [19–21] and vehicular networks [22–24].

For the long-range worm containment, Fleizach et al. [25] verified the differences in propagation characteristic between the Internet and the mobile Internet worm and evaluated the propagation effect of the MMS worm on cellular networks. Meng et al. [7] investigated the credibility of the communications in Short Messaging Service (SMS) by analyzing the trajectory data in the mobile networks. Bose et al. [26] utilized a quarantine method to limit the interaction between vulnerable nodes in MMS networks. Zhu et al. [8] considered that the core nodes in social networks should be immunized first, but this method ignores the transmission route of the worm via the Bluetooth interface, so the worm still has an opportunity to quickly forward. Moreover, the algorithm needs the number of clusters k , which is incognizable for social networks in advance. Zhao et al. [27] integrated the centralized and decentralized patch distribution strategy by constructing a new network layer model. Yang and Yang [28] proposed an evaluation

framework for testing patch distribution efficiency. The key to long-range worm containment is to identify the area of high-speed infection. The latest research studies tend to use community detection [9, 29, 30] and social influence analysis [31, 32] to solve this problem.

The above studies have made remarkable progress in the field of SINs and GINs worm containment, respectively. However, hybrid worm containment on the mobile Internet is still an open issue. The contribution of this study is that we formalized the propagation equation of the hybrid worm and proposed a worm containment scheme based on the mesoscopic analysis. Different from the flooding patching strategy, we preferentially distribute patches to the high-impact nodes in the network and establish a link between historical communication records and security predictions through Bayesian inference.

3. Propagation Dynamics of the Hybrid Worm

Susceptible infected recovered (SIR) model is used to measure the propagation dynamics of contagions within a population under contact infections in epidemiological theory [33]. Inspired by [2], we propose the hybrid-SIR model to depict the propagation characteristics of the hybrid worm by changing the propagation criteria of the SIR model.

Let $S(t)$, $I(t)$, and $R(t)$ represent the number of susceptible, infected, and recovered nodes at time t , respectively. $J(t) = I(t) + R(t)$ calculates the number of infected nodes including immune. Let β , γ , and N , respectively, represent the infection rate, the recovery rate, and the total number of nodes, then the differential equations of the SIR model are given by

$$\begin{cases} \frac{dJ(t)}{dt} = \beta J(t)[N - J(t)], \\ J(t) = N - S(t), \\ \frac{dR(t)}{dt} = \gamma I(t). \end{cases} \quad (1)$$

For our hybrid-SIR model, all of the interactions between smartphones derive from the SINs and the GINs. Let $I_{\text{SINs}}(t)$ and $I_{\text{GINs}}(t)$, respectively, represent the number of infections via the SINs and the GINs at time t . $I(t) = I_{\text{SINs}}(t) + I_{\text{GINs}}(t)$ calculates the total number of infected nodes at time t . $S(t)$ denotes the total number of susceptible nodes at time t . Then, we have

$$\begin{aligned} I_{\text{SINs}}(t) + I_{\text{GINs}}(t) + S(t) &= N, \\ \frac{dI(t)}{dt} &= \frac{dI_{\text{SINs}}(t)}{dt} + \frac{dI_{\text{GINs}}(t)}{dt}. \end{aligned} \quad (2)$$

When an infected smartphone intends to propagate the worm through the SINs, it behaves like a traditional SMS virus which sends messages to the one found in the local contact list (reflected in the degree of nodes). Let β_{SINs} denote the probability of the worm being activated, η_{SINs} denote the average degree of nodes in the SINs, the number

of susceptible nodes neighboring a start point equals to $\eta_{\text{SINs}}\beta_{\text{SINs}}$, and the total number of susceptible nodes is thus given by

$$S'(t) = S(t) \frac{\eta_{\text{SINs}}\beta_{\text{SINs}}}{N} I(t). \quad (3)$$

Based on equation (3), the equation that depicts the dynamics of infected nodes in the SINs with time is

$$\frac{dI_{\text{SINs}}(t)}{dt} = \beta_{\text{SINs}}^2 \frac{\eta_{\text{SINs}}S(t)}{N} I^2(t) - \gamma' I(t), \quad (4)$$

where γ' denotes the recovery rate by means of sending patches.

When an infected device tries to propagate the worm through the GINs, it first detects all adjacent neighbors (related to population density) within its propagation range R . We assume that the smartphones are distributed with density ρ , then the average amount of accessible smartphones η_{GINs} equals to $\rho\pi R^2$.

At the new time step, only the infected smartphone that lies on the circumference of the infection ripple has the chance to exchange messages with the susceptible smartphones and therefore have the possibility to infect them, while the smartphones located in the interior of the infection ripple are not contributing to further spatial infections (that part of nodes are immune or still under infection).

Let $F'(t)$ and $F(t)$ represent the number of smartphones lies on and lies within the circumference of the ripple, respectively; the infected dynamics of the periphery nodes with the incremental infected radius $r(t)$ is described as

$$F'(t) = F(t) - \rho\pi(r(t) - R)^2. \quad (5)$$

Here, $r(t) - R$ calculates the radius of the infection ripple at time $t - 1$. We have $F(t) = \rho\pi r^2(t)$ based on the fact that the number of nodes inside the infection ripple is the sum of neighbors of the center node. Thus, equation (5) can be simplified into

$$F'(t) = 2R\sqrt{\rho\pi}\sqrt{F(t)} - \eta_{\text{GINs}}. \quad (6)$$

We assume that the spatial infection ripple of a start node is generated at time r' and achieves the current infection status $F(r' + s')$ after the duration of s' . Then, the incremental infection at time $r' + s'$ is

$$F'(r', s') = \beta_{\text{GINs}} \frac{2\eta_{\text{GINs}} \left(2R\sqrt{\rho\pi}\sqrt{F(r', s')} - \eta_{\text{GINs}} \right)^2}{3N} S(r' + s'). \quad (7)$$

After simplification, we have

$$F'(r', s') = \beta_{\text{GINs}} \frac{2\eta_{\text{GINs}}^2 \left(c\sqrt{F(r', s')} - 1 \right)^2}{3N} S(r' + s'). \quad (8)$$

In equations (7) and (8), $2/3N$ indicates that for each smartphone that lies on the circumference of the ripple (e.g., the node v in Figure 2), approximately two-thirds of its neighbors outside the ripple are susceptible. β_{GINs} denotes

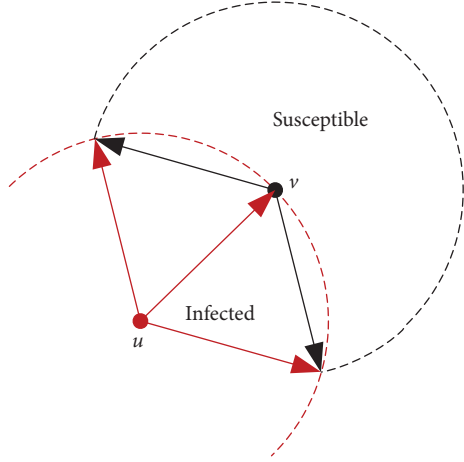


FIGURE 2: Infections outside the ripple.

the probability of a GIN worm being activated in the susceptible device. $c = 2/R(\rho\pi)^{1/2}$ is the proportionality constant [34]. The incremental infection of all infection ripples at time t is thus given by

$$\frac{dI_{\text{GINs}}(t)}{dt} = \int_0^t I'_{\text{SINs}}(s)F'(s, t-s)ds. \quad (9)$$

It means that I_{SINs} dominates the spatial infections of the worm. In other words, there are $I'_{\text{SINs}}(s)$ infected phones emerging at time s and each one approximately contributes $F'(s, t-s)$ incremental infection at time t .

We roughly verified the propagation performance of the worm via the SINs, the GINs, and the hybrid mode based on the proposed model. Two parameter settings are considered: one is $\rho_{\text{GINs}} = 0.75$, $\beta_{\text{SINs}} = \beta_{\text{GINs}} = 0.1$, and $\eta_{\text{GIN}} = \eta_{\text{SIN}} = 6$; the other is $\rho_{\text{GINs}} = 0.85$, $\beta_{\text{SINs}} = \beta_{\text{GINs}} = 0.1$, and $\eta_{\text{GINs}} = \eta_{\text{SINs}} = 10$. Simulation results in Figure 3 indicate that with the increasing number of smartphone's neighbors ($\eta_{\text{GINs}} = \eta_{\text{SINs}} = 10$), the hybrid model greatly enhances the power of worm infection and brings considerable challenges to the worm containment task.

4. Containment Scheme of the Hybrid Worm

In this section, we present the framework of CC^2 (shown in Figure 4) and demonstrate the basic idea of the system. The system consists of five units. On the top, it starts with the Online Community Manager. In social networks, messages from close friends have a higher probability of being received and further opened. Thus, the infection rate β_{SINs} in equation (4) basically equals to one. We cannot expect the recovery rate γ' to be increased, as the mobile operator requires necessarily time to detect worm and code patches. Also, directly modifying η_{SINs} is unrealistic. However, reducing the average degree of nodes is seeking the sparse representation of the network. Online Community Manager maintains a set of community structures [35], in which nodes are closer to each other than anyone else outside the community. In this light, if the nodes are mapped to the

communities, the propagation speed of the worm can be significantly reduced at the mesoscopic level during the exponential growth phase.

node monitor is used to monitor the infection status of nodes, and generate guard nodes lies on the periphery of each community. Once the worm has been found on the network, the system starts generating the worm signature and delivers it to the guard nodes through a data transmitter. If a guard node receives the worm signature before it is infected, it will become immune to the worm. As a result, the worm propagation can be blocked since any malicious message has to go through the guard nodes to reach the adjacent communities.

All the information about the nodes is gathered in the information collector and provides the evidence for the security evaluator. The purpose of security evaluation is to prevent the worm from spreading across communities through location-based infections. For those users with high activity and poor security, we randomly reject the communication with them until their security consciousness is improved. This scheme will reduce η_{GINs} in equation (8) to some extent, while β_{GINs} in the equation is intractable since it describes the density of the population in real space. The output of the security evaluator also guides the community detection process, ensuring security within the community. Section 5 describes more details of CC^2 .

5. System Description

5.1. Online Community Manager. Community detection in this component consists of three steps: security evaluation, label propagation [36], and overlapping community combination. Note that we do not intend to detect ‘‘high-quality’’ partitions (i.e., with higher modularity [37]), but to detect a reasonable structure with higher density and internal forwarding efficiency. We use label propagation (LP) algorithm to simulate the process of nodes receiving neighbor messages. In the algorithm, if a sender satisfies the following conditions, the label he delivers is more likely to be accepted: (1) enough security; (2) with coercive power.

For condition 1, we first analyze the communication security of nodes on the SINs (marked as T_{SINs}) and estimate the probability of secure communication θ with the Bayesian formula as follows:

$$P(\theta | x) = \frac{f(x | \theta)P(\theta)}{\int_{\Theta} f(x | \theta)P(\theta)d\theta}. \quad (10)$$

Let a denote the number of secure communications between node i and its neighbors in n communications (marked as normal in Figure 4), and $b = n - a$ calculates the number of insecure communications in the same situation (marked as infected in Figure 4). Before inference, we assume that the probability of secure communication θ follows uniform distribution $\text{Uni}(0, 1)$, which means $P(\theta) = 1$, $\theta \in (0, 1)$. Estimating communication security is a binomial experiment $\text{Bin}(n, p)$, so the likelihood of a out of n communications being normal is

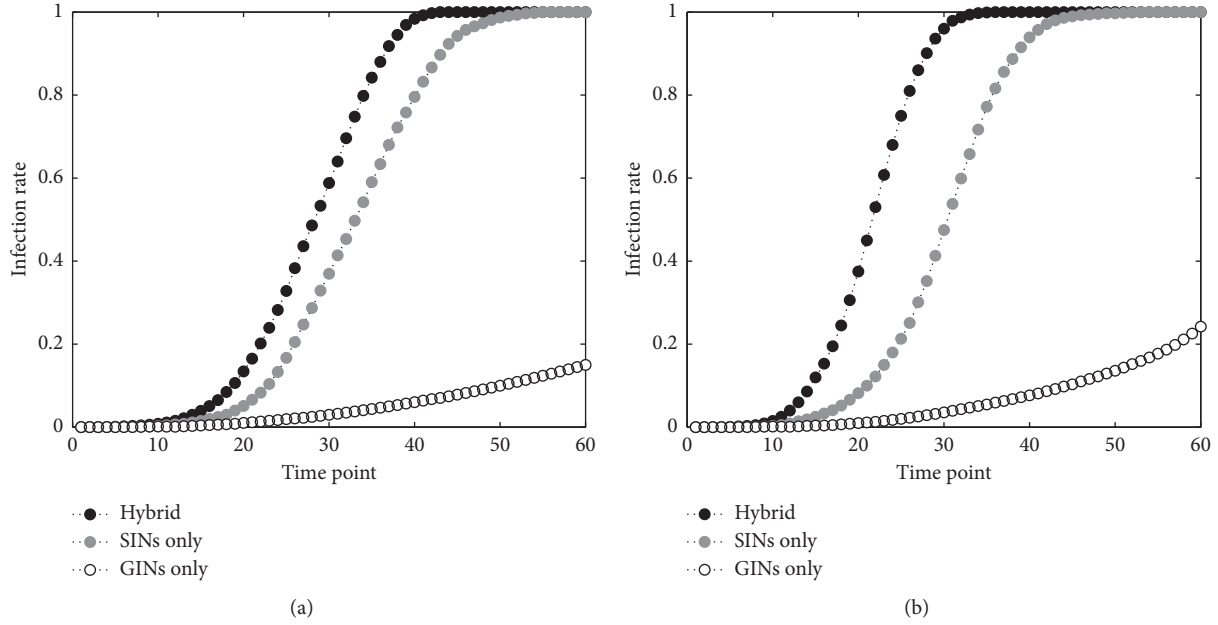


FIGURE 3: Propagation performance of the worm spreading via the SINS, the GINs, and the hybrid mode: (a) GINs = 0.75 and $\eta_{\text{GINs}} = \eta_{\text{SINs}} = 6$ and (b) GINs = 0.85 and $\eta_{\text{GINs}} = \eta_{\text{SINs}} = 10$.

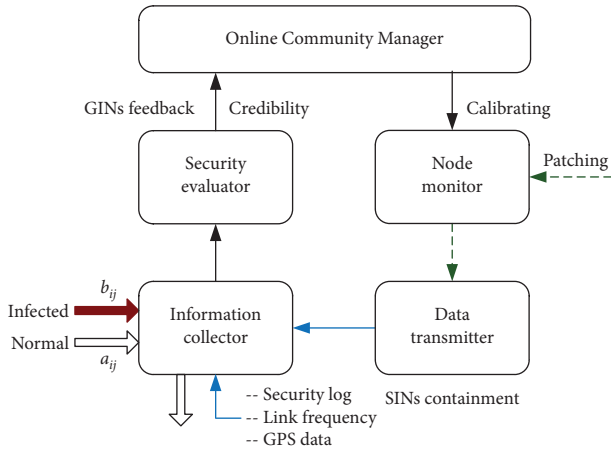


FIGURE 4: System framework of CC².

$$f(x|\theta) = \binom{n}{k} \theta^x (1-\theta)^{n-x}. \quad (11)$$

Substituting (equation (11)) into (equation (10)), we have

$$P(\theta|x) = \frac{\binom{n}{k} \theta^x (1-\theta)^{n-x}}{\int_0^1 \binom{n}{k} \theta^x (1-\theta)^{n-x} d\theta} \quad (12)$$

$$= \frac{\theta^x (1-\theta)^{n-x}}{\int_0^1 \theta^x (1-\theta)^{n-x} d\theta}.$$

Given that for any real number α and β , the beta function satisfies

$$B(\alpha, \beta) = \int_0^1 x^{\alpha-1} (1-x)^{\beta-1} dx. \quad (13)$$

Let $x = a$ and $n-x = b$, respectively, represent the number of normal and infected communications, then we have

$$P(\theta|x) = \frac{\theta^a (1-\theta)^b}{\int_0^1 \theta^{a+1} (1-\theta)^{b+1} d\theta} \quad (14)$$

$$= \frac{\theta^a (1-\theta)^b}{B(a+1, b+1)}.$$

Equation (14) indicates that the communication security of node i follows beta distribution with parameters $a+1$ and $b+1$, and its expectation is

$$E(\Theta) = \frac{a+1}{a+b+2}. \quad (15)$$

According to the law of large numbers, we have $T_{\text{SINs}}(i) = E(\Theta)$. It seems that frequent sending of secure messages is an indication of reliable communication. This conclusion, however, does not consider the security of the adjacent environment. We define the user's security evaluation function as

$$\text{se}(i) = T_{\text{SINs}}(i) \times \exp\left(-\frac{1}{d_i} \sum_{j \in \eta(i)} T_{\text{SINs}}(j)\right). \quad (16)$$

Here, d_i denotes the degree of node i . In equation (16), the multiplier represents the security of the adjacent environment. It can be found that when the adjacent

environment is insecure and the user can still send secure messages with higher probability, the user is considered to be relatively reliable.

Similarly, we can define the likelihood of node i sending insecure messages as $uT_{\text{SINs}}(i) = 1 - T_{\text{SINs}}(i)$. For condition 2, if the malicious message sent by a user does not significantly change the security of the adjacent environment, the coercive power (cp) of the user is weak. We define this condition in equation (17), which measures the probability of a security-conscious user receiving a malicious message:

$$cp(i) = uT_{\text{SINs}}(i) \times \left(1 - \exp\left(\frac{1}{d_i} \sum_{j \in \eta(i)} (se(j) - 1)\right) \right). \quad (17)$$

Based on equations (16) and (17), the transition probability of messages (whether secure or not) sent by node i on the SINs is defined as $\text{soc}(i) = \max\{se(i), cp(i)\}$. Combined with the security evaluation result $\text{geo}(i)$ (equation (27) submitted by the GINs feedback unit, the transition probability of the community label held by node i is defined as

$$L(i) = \frac{\max\{\text{soc}(i), \text{geo}(i)\}}{1 + |\text{soc}(i) - \text{geo}(i)|}. \quad (18)$$

We modify the propagation and acceptance criteria of the LP process and propose a security-based label propagation (SLP) algorithm based on equation (18); the pseudocode is described in Algorithm 1.

The output of Algorithm 1 is a set of overlapping communities, as each node is allowed to have multiple community labels in Step 5. However, this will increase the bandwidth cost of the network, as the more the number of communities, the more the number of guard nodes needs to be monitored. Therefore, we need to execute a merging program to reduce structure redundancy. We define the structure stability of community C as

$$ss(C) = \left(\frac{1}{|C| - 1} \sum_{i \in C} \frac{1}{|C|} |\eta(i)| \right) \times \sum_{i \in C} \frac{1}{|C|} L(i). \quad (19)$$

Equation (19) measures the tradeoff between structure density and security. What we need to evaluate is whether the overlapping part provides significant stability for the entire community. In our method, any two communities $C_A, C_B \in C$ can be merged if $ss(C_A \cap C_B) \geq \min(ss(C_A), ss(C_B))$. Note that the merging program also provides a way to detect dynamic communities. Given a network G , an initial community structure C , and an incremental update ΔG , we have

$$\text{SLP}(G \cup \Delta G) = \text{Merge}(C, \text{SLP}(\Delta G)). \quad (20)$$

Equation (20) indicates that when the network changes, we only need to execute the SLP algorithm on the newly added nodes in the local environment and then run the merging program to avoid repetitive computation of the existing results. Figure 5 shows a three-step example of the SLP process. Each node chooses to join a security sub-structure based on the observed contact history. In the

algorithm, the label in iteration t is always based on its neighboring labels in iteration $t - 1$ to avoid the oscillations of labels [36].

5.2. Data Transmitter. The function of the data transmitter is twofold: (1) construct the forwarding strategy of worm signature and (2) select the guard nodes (the initial delivery node set). When the worm is found in the network, the data transmitter will send the worm signature to the network operations center (NOC) and then distribute it to each network node. Flooding is a possible forwarding strategy. However, this will bring enormous bandwidth costs and influence normal network communications. Besides, the flooding method considers that all the network nodes have the same delivery priority, and the forwarding capability is weak. We propose a new function to calculate the forwarding capability of nodes, which is described as follows:

$$\varphi(i) = \frac{1}{n} \sum_{j=1}^n \left(L(j) \times \exp\left(-\frac{1}{2} h_{ij}^2\right) \right). \quad (21)$$

Here, h_{ij} denotes the hops between node i and node j . Equation (21) shows that the delivery priority of nodes depends on the security and coercive power of its neighbors within 2-hops. The start points of the delivery process include the overlapping nodes and the endpoints of links between communities. This setting will ensure community quarantine [38] as early as possible and prevent worms from spreading across communities. Algorithm 2 describes the pseudocode of the data transmitter.

5.3. Security Evaluator. In the GINs feedback unit, the security evaluator is an essential component which is designed to perform community quarantine procedure and provide security evaluation results for short-range data transmission. Different from social applications, there is not enough evidence to use the Bayesian formula to deduce the communication security of users since short-range interfaces are not used frequently in practice. However, this will not prevent the use of Bayesian thoughts in this component.

Let a'_{ij} and $b'_{ij} = n - a'_{ij}$, respectively, represent the number of normal and infected communications that node i receives from its neighbor j in n rounds. Based on the observed security history, node i will calculate the communication security between neighbor j as

$$cs_{i,j} = \frac{a_{i,j}}{a_{i,j} + b_{i,j}}. \quad (22)$$

When there is no supervision record, the initial value of both $a_{i,j}$ and $b_{i,j}$ equals to one. Equation (22) is unlikely to provide a reliable security calculation directly when the sample is insufficient. To solve this problem, we design an uncertainty computing function $uc_{i,j}$, which is defined as

$$uc_{i,j} = \frac{\min\{a_{i,j}, b_{i,j}\}}{\max^2\{a_{i,j}, b_{i,j}\}}. \quad (23)$$

Require:

Contact history from information collector;

Ensure:Community structure $C = \{C_1, C_2, \dots\}$;

Step 1. Initialize the community label. Each node i in graph G contains a feature vector $\text{vec}_t(i) = \{\{l_1, b_1 \times L(i)\}, \{l_2, b_2 \times L(i)\}, \dots\}$, where l represents the community label, b represents the belonging degree, L represents the transition probability of l , t represents the number of iterations. For example, the feature pair of i is $\text{vec}_0(i) = \{i, 1 \times L(i)\}$ means the initial label of node i is itself and the belonging degree equals to one;

Step 2. Set $t = 1$;**Step 3.** Arrange each $i \in G$ in a random order and assign them to V ;

Step 4. For each $i \in V$, $j \in \eta(i)$, calculate the belonging degree of the adjacent community label l_x as $b_t(l_x) = (1/|l_x|) \sum_{l_x \in \text{vec}_t(j)} (b_x \times L(j))$;

Step 5. For each $i \in V$, if exists $b_y \in \text{vec}_t(i)$ s.t. $b_y < b_t(l_x)$, then replace b_y with b_x , and remain $L(i)$ unchanged. Else stop and jump to **Final**;

Step 6. Set $t = t + 1$ and go to **Step 3**;**Final.**

ALGORITHM 1: Security-based label propagation algorithm.

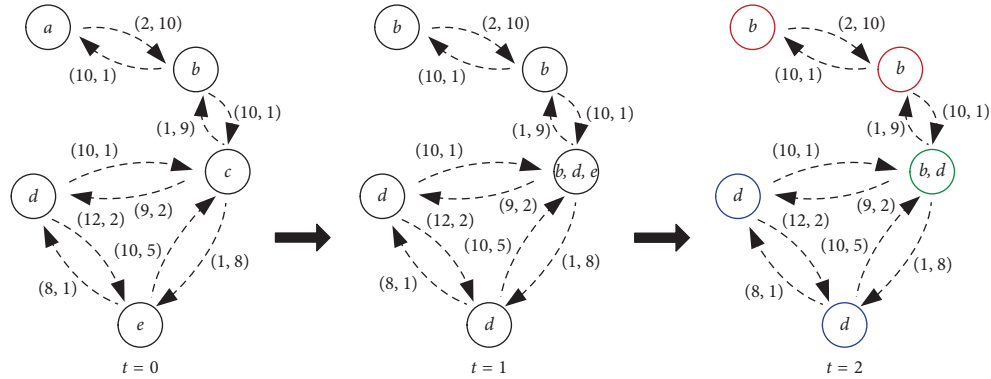


FIGURE 5: A simple simulation of the SLP process. The numbers in parentheses represent the number of normal and infected communications in turn.

In equation (23), when a_i, j or b_i, j dominates, the value of $uc_{i,j}$ declines, which indicates that the security of the next communication will be more predictable. Based on equations (22) and (23), the revised communication security rs_{ij} can be defined as

$$rs_{i,j} = cs_{i,j}(1 - uc_{i,j}). \quad (24)$$

Another parameter that needs to be considered in the security evaluator is the interaction frequency, which is measured in this paper as the regularity of interaction. We present the concept of circulation connections. As shown in the dashed box in Figure 6, the communication interval can be regarded as continuous communication. Let n_{cont} and n_{cycle} , respectively, represent the number of continuous and circulation connections in a sliding window of size ws , then the interaction frequency q_{ij} is thus given by

$$q_{i,j} = \frac{n_{\text{cont}} + n_{\text{cycle}}}{ws}. \quad (25)$$

In the four cases shown in Figure 6, $q_{i,j}$ equals to 0.9, 0.8, 0.2, and 0, respectively. The first two cases show strong

regularity, which probably comes from close friends. While the latter two cases with a low $q_{i,j}$ could be the contact history from acquaintances or strangers. From a statistical point of view, a low communication frequency will not provide sufficient evidence to support the communication security evaluation. For example, when $rs_{ij} = 0.9$ and $q_{ij} = 0.1$, rs_{ij} should be punished appropriately; when $rs_{ij} = 0.1$ and $q_{ij} = 0.1$, rs_{ij} should be gained slightly. We define the communication security of arc (i, j) on the GINs as

$$T_{\text{GINs}}(i, j) = rs_{ij} + \varepsilon(1 - q_{ij}) \times \text{soc}(j). \quad (26)$$

Here, $\varepsilon = \exp(-rs_{ij}) - rs_{ij}$ is used to decide whether the security should be gained or punished and the regulation threshold is approximately equal to 0.5671. When $q_{ij} = 0$, we have $rs_{ij} = 0$. In this case, we use $\text{soc}(j)$ to give a reference value to the GINs security evaluation. Based on equation (26), the security evaluation result of node i in the GINs can be defined as

$$\text{geo}(i) = \frac{1}{|\eta(i)|} \sum_{j \in \eta(i)} T_{\text{GINs}}(j, i). \quad (27)$$

Require:

Graph $G = (V, E)$; community structure $C = (C_1, C_2, \dots)$;

Ensure:

Guard nodes V_G ; signature propagation;

Step 1. Initialize V_G . For each $C_a, C_b \in C$ do $V_G \leftarrow \{i | i \in C_a \cap C_b\}$, $V_G \leftarrow \{i, j | i \in C_a, j \in C_b, (i, j) \in E\}$;

Step 2. For each $i \in V_G$, initialize the worm signature from the NOC in i 's buffer as $\omega(i) = \{\omega_1(i), \omega_2(i), \dots\}$; set initial token τ in i 's buffer;

Step 3. For each $i \in G, j \in \eta(i)$, if exists τ in i 's buffer and j 's buffer is null then duplicate and deliver $\omega(i)$ to node j ; if exists j s.t. $\varphi(j) \geq \varphi(i)$ then duplicate and deliver token τ to node j ;

Step 4. If all nodes have received the worm signature, then stop and jump to **Final**. Else go to **Step 3**;

Final.

ALGORITHM 2: Data transmitter.

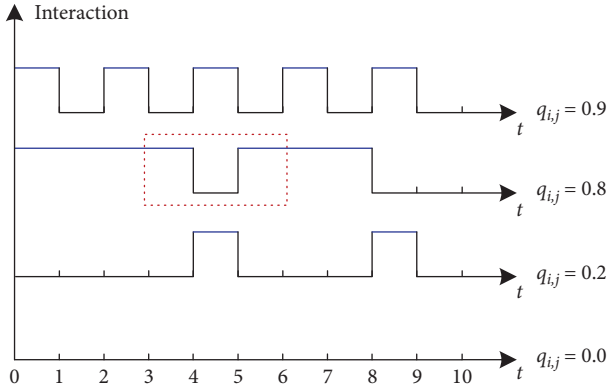


FIGURE 6: Interaction frequency between node i and j in a sliding window of size 10 time units.

Algorithm 3 describes our idea on community quarantine. For node $i \in V, j \in \eta(i)$, if i has not received any worm signature, i will reject j 's messages with a certain probability by using equation (26). Considering channel utilization, we first perform the algorithm on users who are located in different communities but geographically adjacent (i.e., within 30 m [39]). Next, these users will broadcast quarantine notification to other community members to achieve global synchronization.

Here, $uT_{\text{GINs}}(i, j) = 1 - T_{\text{GINs}}(i, j)$. We use counter $\text{cnt}(i, j)$ to record the number of consecutive messages on arc (j, i) and increase the rejection probability P_R with $\text{cnt}(i, j)$ grows.

5.4. Complexity Analysis. The computation complexity of CC^2 mainly consists of three parts: (1) community detection and combination in Online Community Manager; (2) forwarding capability calculation in Algorithm 2; and (3) security evaluation in Algorithm 3.

For the first part, the time complexity of Algorithm 1 is $O(|\text{vec}|(m+n))$ [40], m is the number of edges, n is the number of nodes, and $|\text{vec}|$ is the average number of communities per node. The time complexity of the merging process is $O(d_c|C|)$, where d_c represents the average degree of communities and $|C|$ is the number of communities.

For each community $C_i \in C$, we have

$$|C| < n_{\text{avg}}|C| = \sum_{C_i \in C} |C_i|, \quad (28)$$

where n_{avg} represents the average number of nodes in the community. The SLP algorithm guarantees that each node is at least located in one community, therefore

$$\sum_{C_i \in C} |C_i| = n + \sum_{i < j} |C_i \cap C_j|. \quad (29)$$

It is quite clear that $|C_i \cap C_j| < n$. Let d_{avg} represent the average degree of nodes, then we have

$$\sum_{i < j} |C_i \cap C_j| < nd_{\text{avg}} < m. \quad (30)$$

Based on equations (27)–(30), we have $O(d_c|C|) = O(d_c(m+n))$. Since $d_c < |\text{vec}|$, the time complexity of the first part is $O(|\text{vec}|(m+n))$. For the adaptive procedure (equation (20)), the time complexity of the SLP process and merging process is $O(|\text{vec}|(\Delta G + n) + |C|(\Delta G + n)) = O(|\text{vec}|(\Delta G + n))$, where ΔG represents the incremental update of the network.

For part 2 and part 3, the time complexity is $O(d_{\text{avg}}n) + O(|\text{ws}|d_{\text{avg}}n) = O(|\text{ws}|d_{\text{avg}}n)$, where ws is the size of the sliding window. We use the KMP algorithm to match circulation connections in the window, and the time complexity is $O(\text{ws})$. For the adaptive procedure, the time complexity of part 2 and part 3 is $O(n\Delta G) + O(|\text{ws}|n\Delta G) = O(|\text{ws}|n\Delta G)$.

In CC^2 , all the components are executed sequentially; therefore, the time complexity of the initial phase is $O(|\text{vec}|m + |\text{ws}|d_{\text{avg}}n)$. For the adaptive procedure, the time complexity is $O((|\text{vec}| + |\text{ws}|\Delta G)n)$. Note that in the above analysis, we assume that the system confronts extreme conditions (e.g., we assume that the newly added nodes link to all the existing nodes). In practice, the execution time of CC^2 will be shorter.

6. Experiments and Analyses

In this section, we will present and discuss the experiments of CC^2 on two different kinds of real-world traces including the MIT Reality (consists of students and faculty in the MIT Media Laboratory) (<http://crawdad.org/mit/reality>) and the Hagle Project (conducted for four days during INFOCOM

Require:
 $G = (V, E); C = \{C_1, C_2, \dots\}; T_{\text{GINs}}(i, j);$
Ensure:

Community quarantine;

Step 1. $V_Q \leftarrow \{i, j \mid i, j \in V; \text{vec}(i) \cap \text{vec}(j) = \emptyset; \text{distance}(i, j) < 30 \text{ m}\};$ **Step 2.** For each $i \in V_Q, j \in V$, if $\omega(i) = \emptyset$, i will reject the messages from j (except $\omega(j)$) with probability $P_R(i, j) = uT_{\text{GINs}}(i, j) / (1 - \text{cnt}(i, j) \times uT_{\text{GINs}}(i, j));$ **Step 3.** For each $i \in V_Q$, i broadcasts quarantine notification to node $\{j \mid \text{vec}(i) \cap \text{vec}(j) \neq \emptyset\}$, j will reject messages from other communities with probability P_R ;**Step 4.** For each $i \in V$, if $\omega(i) \neq \emptyset$, then stop and jump to **Final**. Else go to **Step 3**;**Final.**

ALGORITHM 3: Community quarantine.

2006 in Barcelona) (<http://crawdad.org/cambridge/haggle>). In both datasets, Bluetooth contacts, phone call records, and users' locations were provided to construct the GINs and the SINs layer, respectively. Each Bluetooth contact includes the start time, end time, and the IDs of nodes. Each phone call record includes call logs, cell tower IDs, application usage, and phone status (such as charging and idle).

For each round of the simulation, a portion (default 35%) of the dataset was used as the contact history (including normal and infected communications). At the very beginning, we randomly chose 0.05% of the nodes as the seed set of worm sources to initiate the infection. The propagation of the malicious message follows the hybrid propagation model proposed in Section 3. In the model, the recovery rate is $\gamma' = 0.05$ and the probability of a node sending messages to acquaintances (its top 10 neighbors) in the SINs and the GINs is set to 0.2 and 0.05, respectively and to strangers is set to 0.05 and 0.01, respectively. The activation probability of the worm is set to 0.95 (from acquaintances) and 0.05 (from strangers) without running any coping scheme. To avoid flooding broadcast, each infected node attempts to attack its neighbor nodes only once.

6.1. The Analysis on Community Quality. In this section, we test the quality of the community structure generated by the SLP algorithm (Algorithm 1) in terms of the average community size (marked as ACS), the number of detected communities (marked as #Communities), the structure stability of community structure (equation (19) marked as SS), the EQ function, and the execution time. The EQ function proposed by Shen et al. [41] is widely used in evaluating overlapping communities, which is described in the following equation:

$$\text{EQ} = \frac{1}{D} \sum_i \sum_{v \in C_i, w \in C_i} \frac{1}{O_v O_w} \left[A_{vw} - \frac{d_v d_w}{D} \right], \quad (31)$$

where d_v is the degree of node v , $D = \sum_{vw} A_{vw}$ is the total degree of the network nodes, A_{vw} is the element of the adjacency matrix of the network, O_v is the number of communities which the node v belongs to, and C_i is the i -th community in the network. The comparison algorithms include COPRA [40] (based on label propagation), EAGLE

[41] (high-performance overlapping detection algorithm), and A3CS [42] (detecting dynamic community structure). We perform the algorithms mentioned above in Haggles and MIT Reality, respectively, and the experiment results are covered in Tables 1 and 2.

In both datasets, the SLP algorithm makes more numbers of communities (10 and 16, respectively) and smaller size of communities (8 and 6, respectively) than others, which means that the detected communities are more granular. When this feature is applied to Algorithm 2, CC^2 will have more opportunities to find high-impact nodes in the local environment and thereby will increase the performance of worm containment and the efficiency of sending patches. The EQ value of the SLP algorithm (0.439 and 0.441, respectively) is slightly lower than that of COPRA and EAGLE. As we discussed in Section 5, the SLP algorithm is not aiming to find high “modularity” partitions [37], but to find communities with higher security awareness inside. So the structure stability (SS score) of SLP (0.486 and 0.533, respectively) is stronger than the other three algorithms. In terms of the execution time, SLP (1.132 and 1.296, respectively) is slightly slower than COPRA and faster than EAGLE and A3CS, which is in line with the online community monitoring task.

6.2. The Performance of SINs Containment Unit. The test in this section mainly considers three scenarios: (1) turn on and off the GINs feedback unit to demonstrate the performance of the SINs containment unit; (2) replace the SLP algorithm with COPRA, EAGLE, and A3CS to verify the performance of the Online Community Manager in the SINs containment unit; and (3) compare with three community-based coping strategies, including Member [30], I2C [29], and TC-based [9]. We primarily focus on the infected ratio which is reflected in the proportion of nodes infected by the worm.

In Figure 7, the line graph marked as “no coping” depicts the infected ratio of worms with time without any coping scheme, which can be used as the benchmark in comparison. When the GINs feedback unit is turned off, the performance of CC^2 is slightly better than Member and I2C and better than COPRA, EAGLE, and A3CS due to the higher security within the community structure. CC^2 performs significantly when the GINs feedback unit is turned on, primarily because

TABLE 1: The comparison of the four community detection algorithms on Haggle.

Algorithms	#Communities	ACS	EQ	SS	Execution time
COPRA	8	10	0.445	0.450	0.923
EAGLE	5	16	0.472	0.476	1.521
A3CS	6	13	0.423	0.434	1.296
SLP	10	8	0.439	0.486	1.132

TABLE 2: The comparison of the four community detection algorithms on MIT Reality.

Algorithms	#Communities	ACS	EQ	SS	Execution time
COPRA	12	8	0.458	0.502	1.103
EAGLE	8	13	0.477	0.528	1.618
A3CS	11	9	0.436	0.478	1.425
SLP	16	6	0.441	0.533	1.296

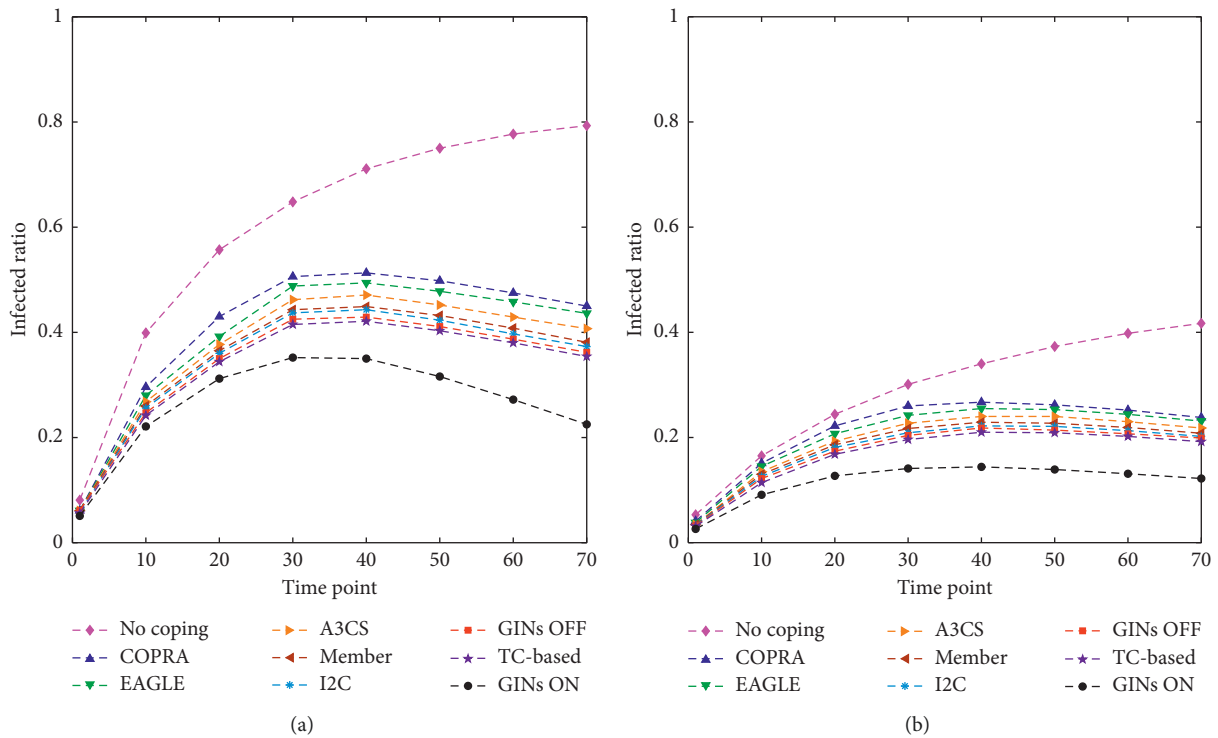


FIGURE 7: Performance comparison of long-range coping schemes on Haggle (a) and MIT Reality (b).

it decreases worm propagation across communities when the user's location is adjacent. When the recovery rate $\gamma' = 5\%$, CC^2 can constrain the further spread of worms around 30 time units and control the final infected ratio at 22.5% (Haggle) and 12.2% (MIT Reality) at 70 time units. We can find that at the mesoscopic level, the smaller the group size, the higher the internal security of the group, and the better the worm containment performance. Besides, the community quarantine strategy significantly improves the effect of worm containment, approximately equal to the difference between GINs ON and GINs OFF.

6.3. The Performance of GINs Feedback Unit. In this section, the SINs containment unit is turned on and off to

demonstrate the performance of the security evaluator in the GINs feedback unit. The comparison methods include (1) a distributed local detection-based scheme [4] (marked as distributed), (2) a proximity signature forwarding-based scheme [4] (marked as proximity), (3) a Bluetooth-based malware coping scheme [21] (marked as hierarchical), (4) a pruning-based proximity malware coping scheme [15] (marked as K -distance), (5) a community-based proximity malware coping scheme [5] (marked as centralized), (6) a social network-based patching scheme [8] (marked as socializing), and (7) TC-based (performs well in the former test). The first four methods primary focus on the GINs worm containment task, while the latter three to contain the propagation of the worm on the SINs. We keep the relevant

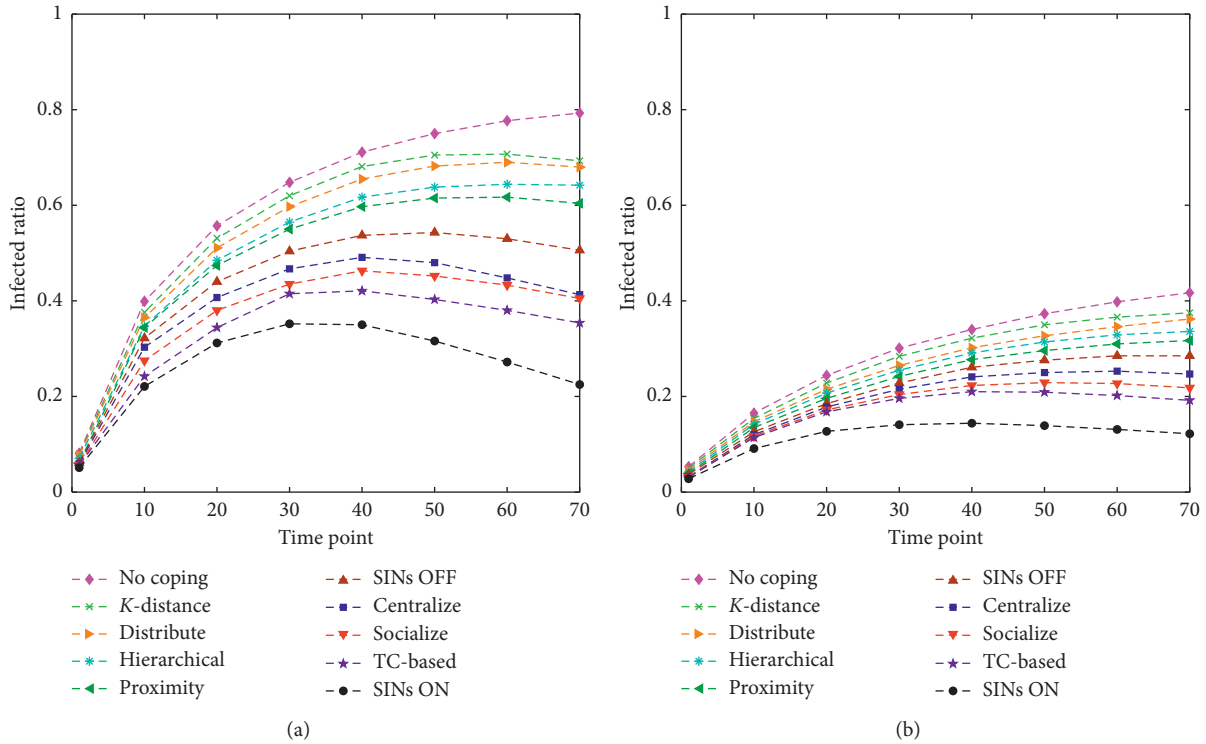


FIGURE 8: Performance comparison of short-range coping schemes on Haggel (a) and MIT Reality (b).

parameters as well as the original literature setting for comparison convenience.

Figure 8 gives the experiment results. In contrast to Figure 7, the performance of SINs OFF is weaker than GINs OFF, which indicates that the high-speed infection of worm relies on the community structure. The comparison with the other seven methods confirms this conclusion, the scheme using social relationships (centralize, socialize, and TC-based) is superior in performance to the scheme using geographic location (distribute, proximity, K -distance, and hierarchical). We also noted that the patching strategy is an effective way to control worms (proximity, centralize, and socialize), and its performance is much higher than that of the structure-based control methods (distribute, K -distance, and hierarchical). On the whole, SINs ON performs better than other methods with an average reduction of 14.4% (Haggel) and 5.9% (MIT Reality) in terms of the infected ratio. Another observation is that although the propagation speed of the GINs worm is slow, ignoring the GINs feedback unit, however, will significantly reduce the containment performance, which is approximately equal to the difference between TC-based and SINs ON.

6.4. The Comparison on Worm Containment Capability.

This section mainly contains three series of experiments. First, we do tests on the percentage of patched nodes, which is defined as the average number of signatures forwarded in the network. Comparing Figures 8 and 9, we can see that CC^2 only needs to deliver 20.9% (Haggel) and 16.7% (MIT Reality) network nodes to control the infected ratio at 22.5%

(Haggel) and 12.2% (MIT Reality). With the same patching ratio, proximity, centralize, socialize, and TC-based can only control the infected ratio around 60.4%, 41.3%, 40.5%, and 35.4% (Haggel) and 31.7%, 24.7%, 21.8%, and 19.2% (MIT Reality), respectively. Distribute does not need to deliver patches, but it also loses the chance to be immune to worms. As a result, the performance of distribute is only slightly better than “no coping” in Figure 8.

In the experiment shown in Figure 9, the start points of the worm signature are automatically generated by Algorithm 2 and grow gradually with time. Next, we manually set the initial immunization ratio (percentage of patched nodes) from 0% to 5% (preferential the guard nodes) and verify the infected ratio at 70 time units. We use a patching threshold μ (initially infected ratio) to decide when to initiate the patching process. The experiments are conducted with $\mu = 5\%$, 10%, 15%, and 20% (beyond 20%, the worm becomes uncontrollable), and the results are described in Figures 10 and 11.

In both cases, CC^2 performs better than the other three containment schemes under the same patching cost. For example, CC^2 is 20.1%, 13.2%, 10.2%, and 7.7% higher than proximity, centralize, socialize, and TC-based on Haggel networks when $\mu = 5\%$. This advantage is even more pronounced when $\mu = 20\%$, with the gap becoming 35.7%, 16.1%, 12.1%, and 10.4%, respectively. We also conclude four observations: (1) the later the worm is discovered (i.e., the higher the threshold μ is), the more difficult it is to control; (2) the control of the worm is proportional to network sparsity; (3) increasing the delivery priority of high-impact nodes can significantly improve worm containment

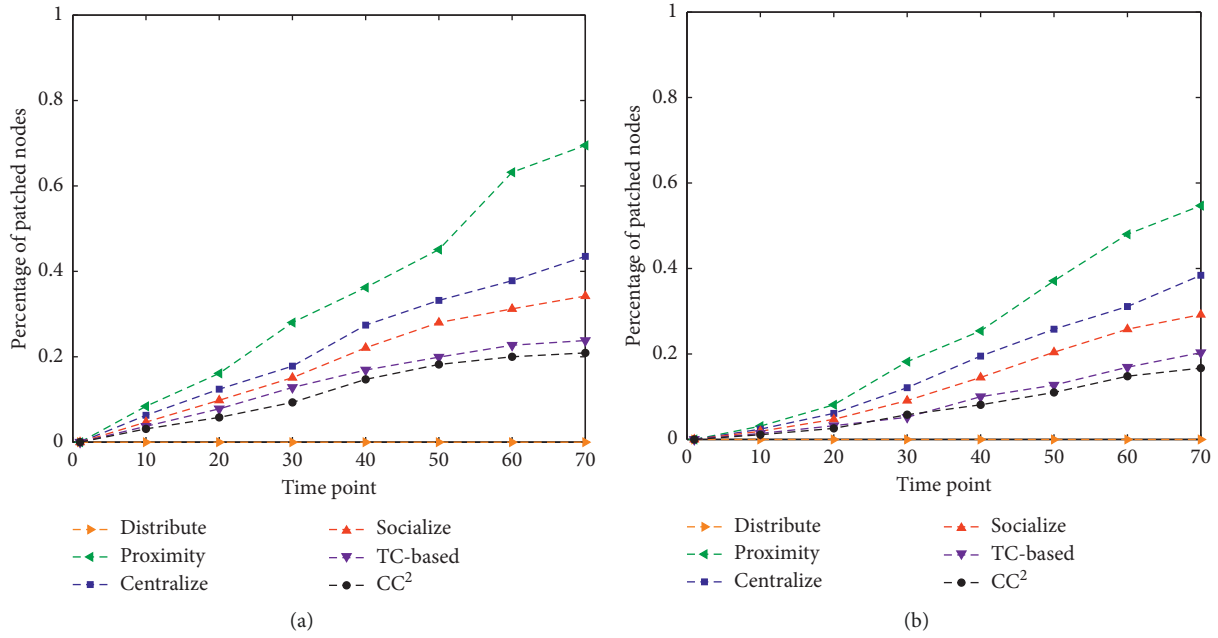


FIGURE 9: Performance comparison of the percentage of patched nodes on Haggel (a) and MIT Reality (b).

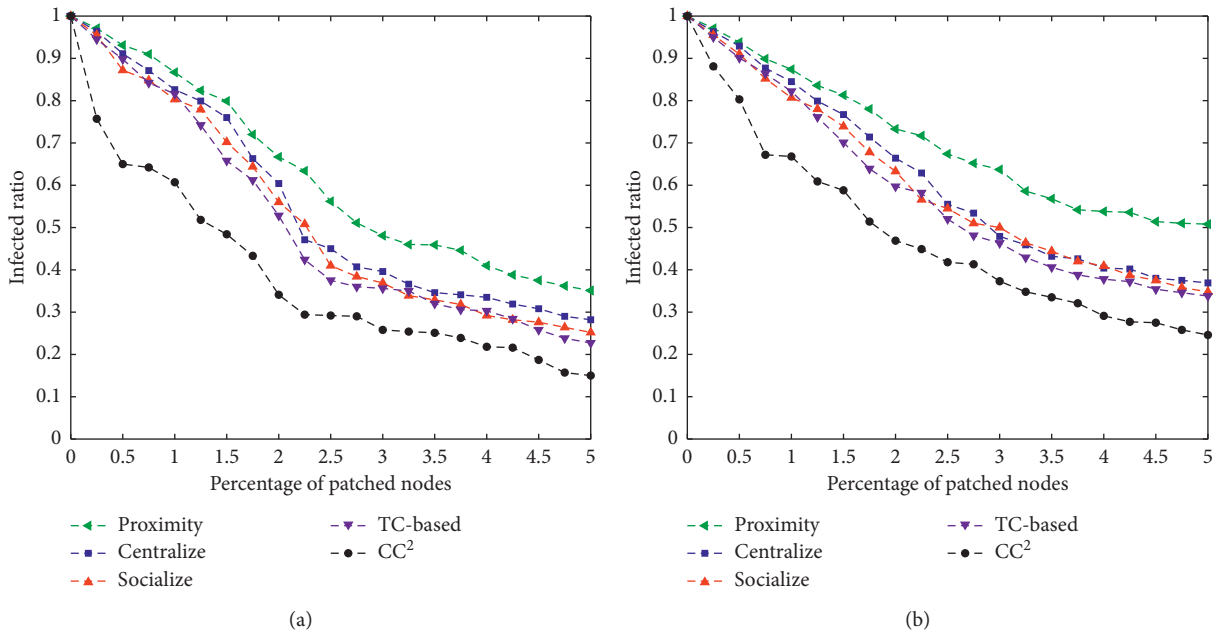


FIGURE 10: Continued.

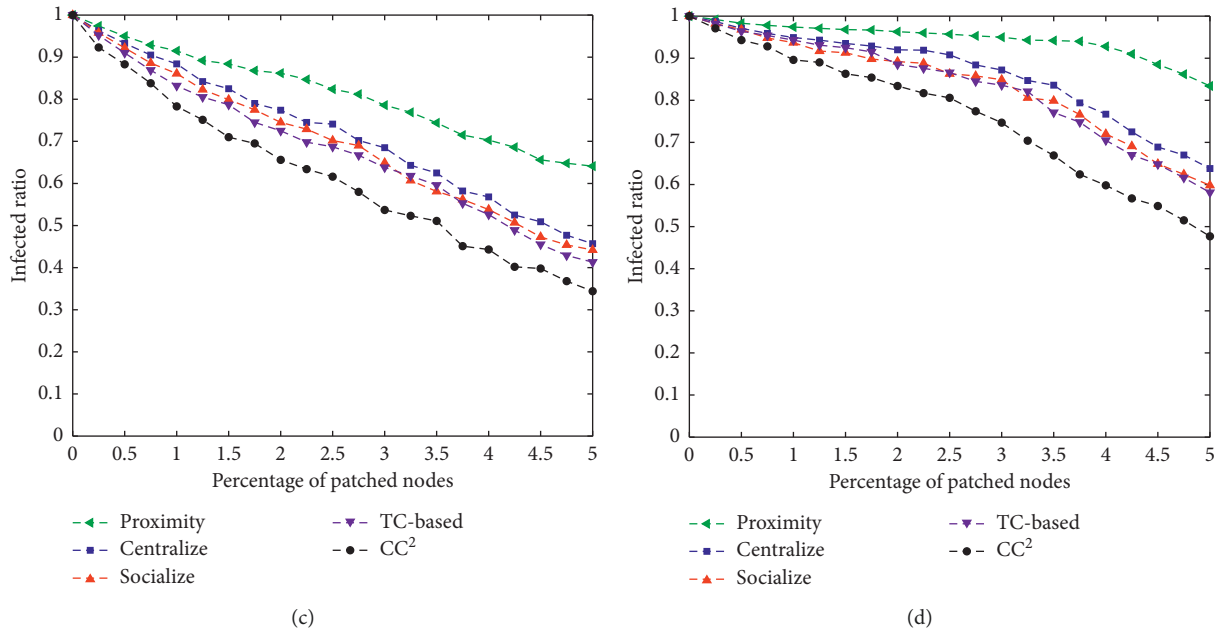


FIGURE 10: Performance comparison of different patching strategy on the Haggle network with an initially infection ratio $\mu = 5\%$ (a), 10% (b), 15% (c), and 20% (d), respectively.

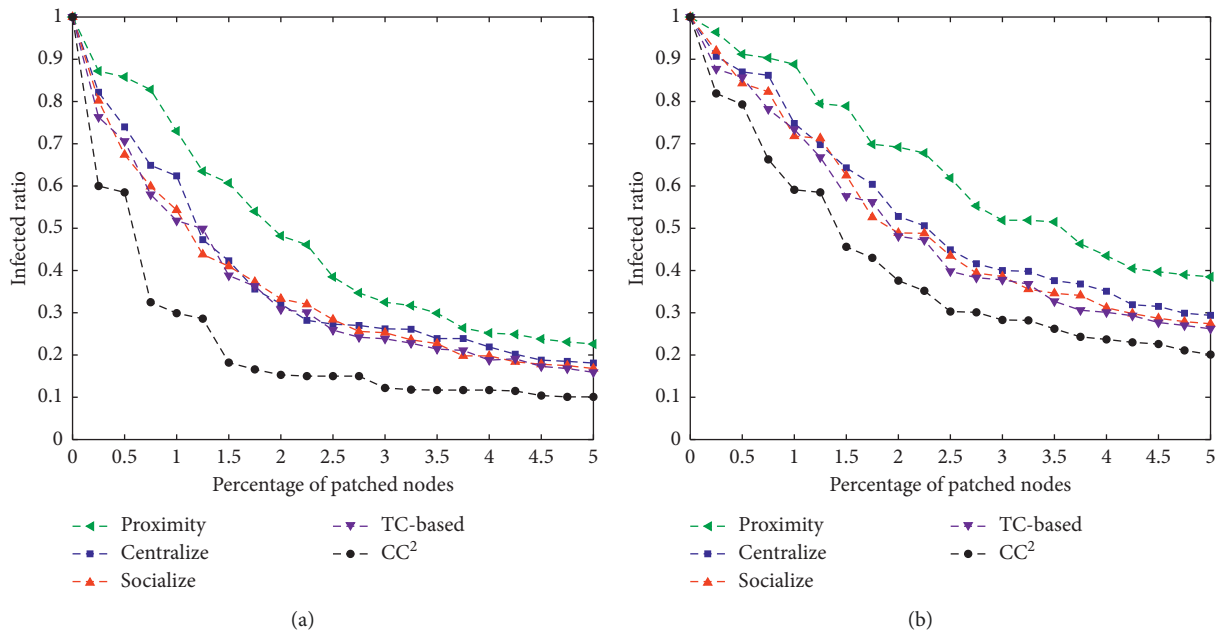


FIGURE 11: Continued.

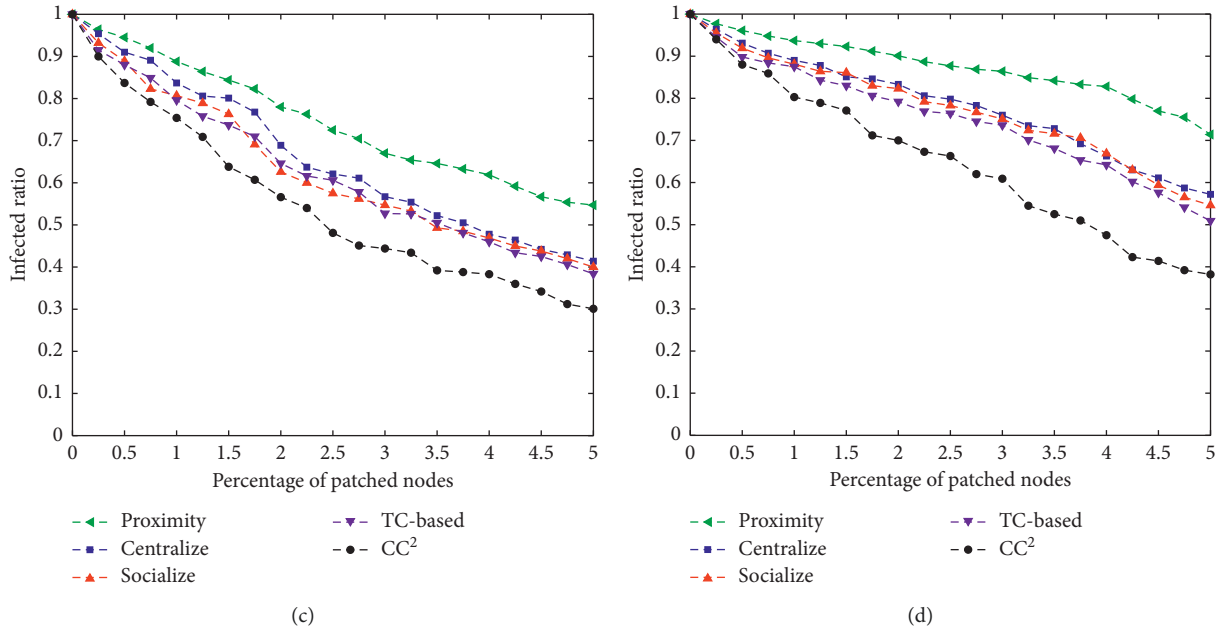


FIGURE 11: Performance comparison of different patching strategy on the MIT Reality network with an initially infected ratio $\mu = 5\%$ (a), 10% (b), 15% (c), and 20% (d), respectively.

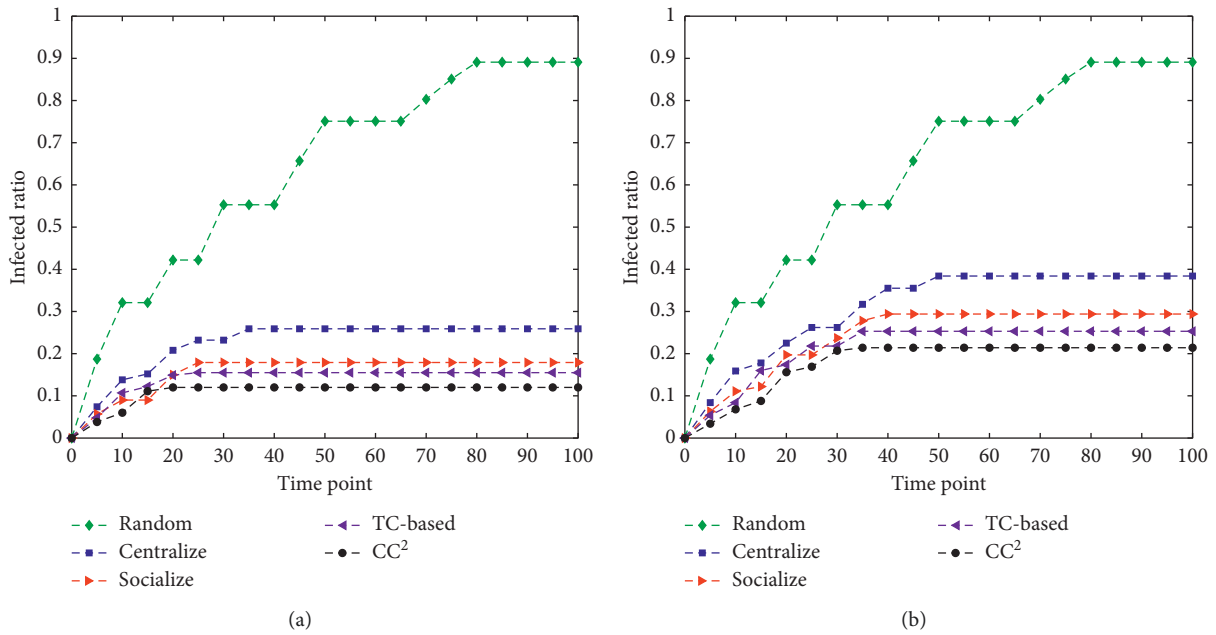


FIGURE 12: Continued.

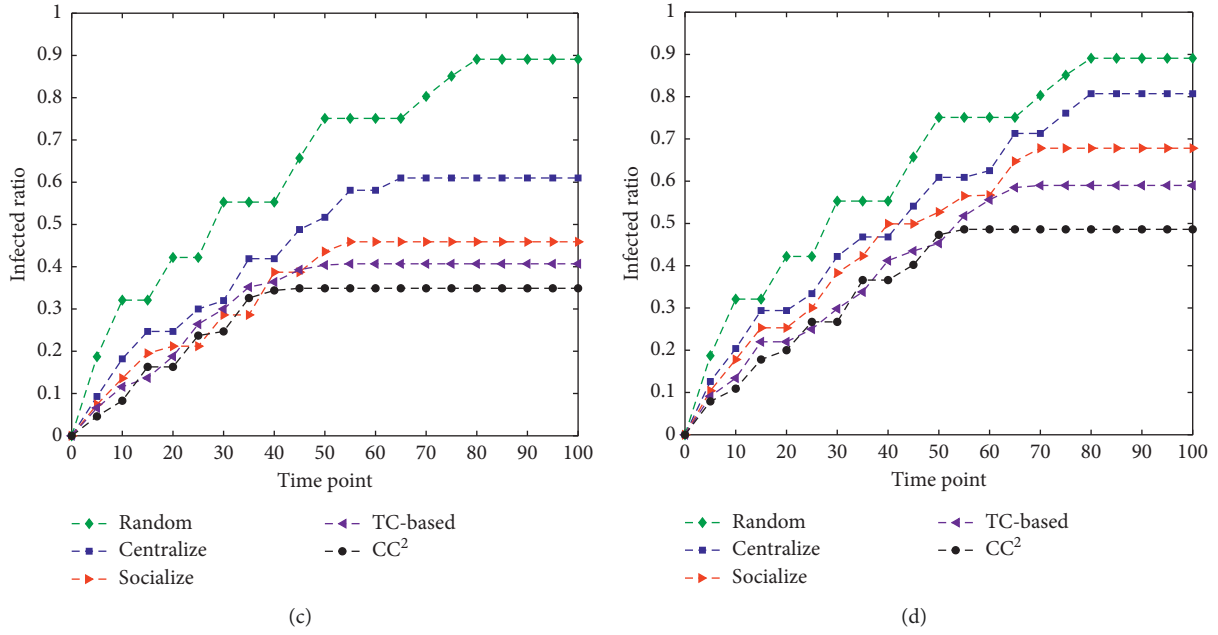


FIGURE 12: Performance comparison of different coping scheme with 5% patching nodes on the Haggie network with initially infected ratio $\mu = 5\%$ (a), 10% (b), 15% (c), and 20% (d), respectively.

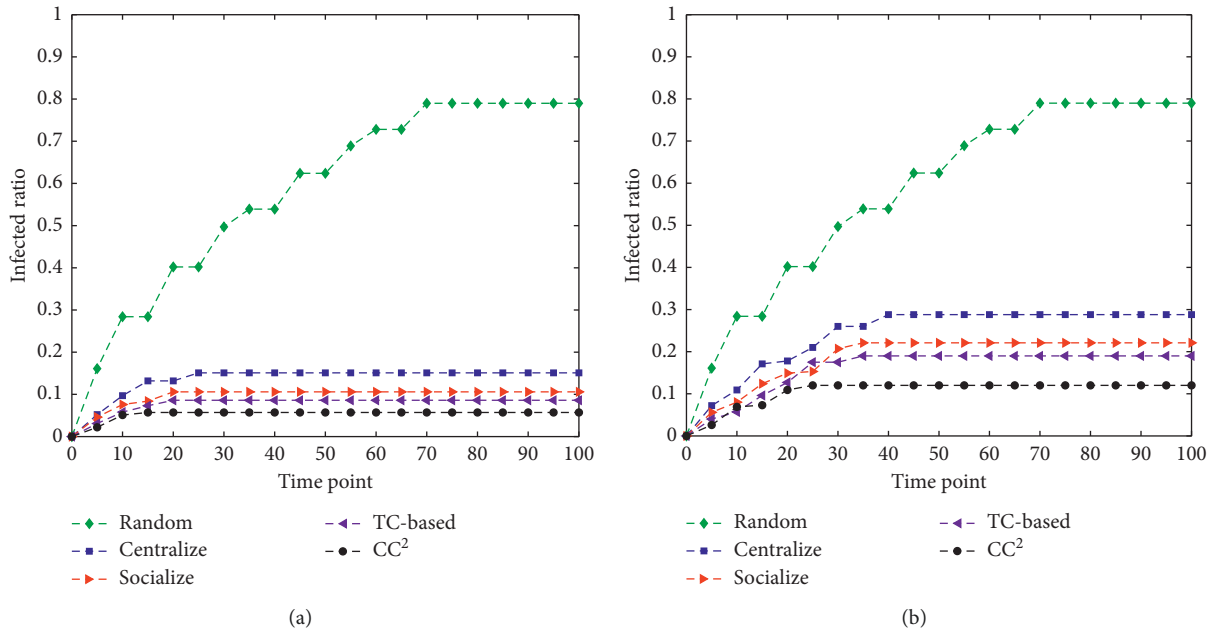


FIGURE 13: Continued.

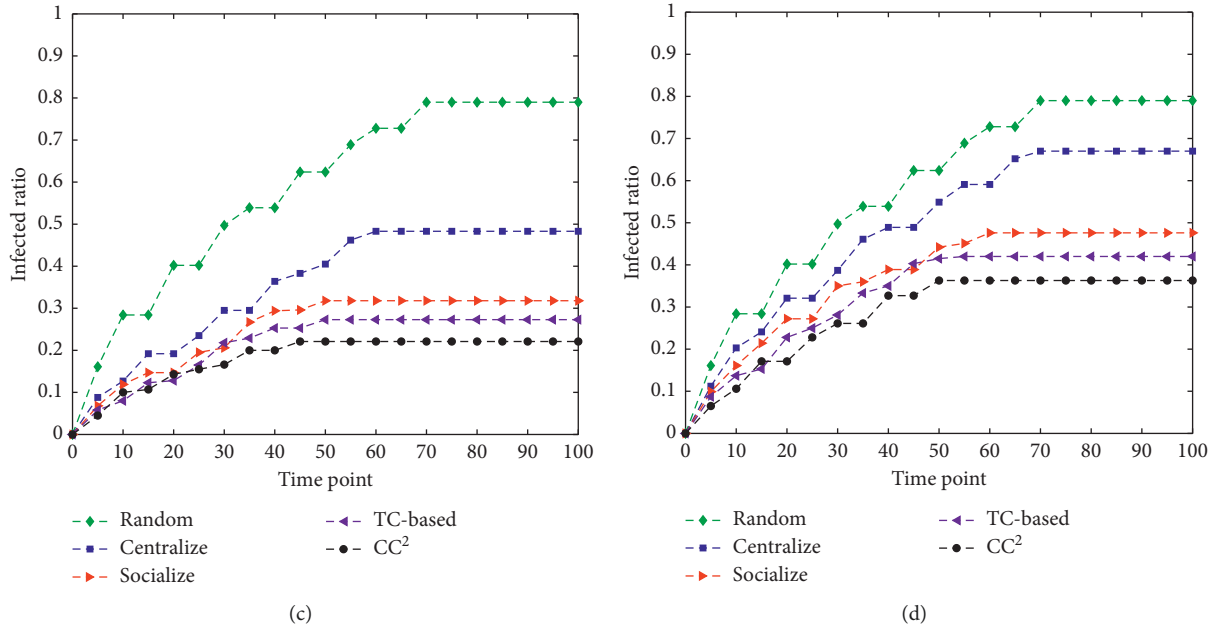


FIGURE 13: Performance comparison of different coping scheme with 5% patched nodes on the MIT Reality network with initially infected ratio $\mu = 5\%$ (a), 10% (b), 15% (c), and 20% (d), respectively.

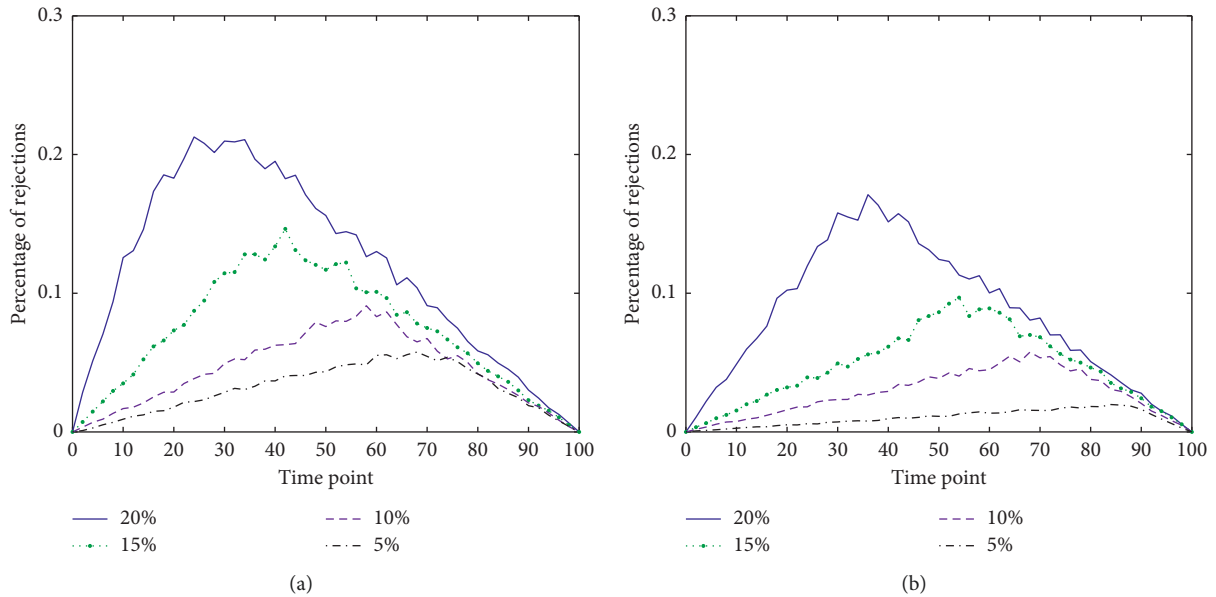


FIGURE 14: Percentage of rejections with initially infected ratio $\mu = 5\%$, 10%, 15%, and 20%: Hagggle (a) and MIT Reality (b).

performance; and (4) when a critical point is reached (such as 2.5% and 1.5% in Figures 10 and 11 when $\mu = 5\%$), further increasing the number of patched nodes will not effectively reduce the infected ratio.

The third experiment in this part verified the infected ratio with time when $\mu = 5\%$, 10%, 15%, and 20%. The comparison methods include (1) random patching (repeated 100 times for consistency), (2) centralize (short-range containment), (3) socialize (long-range containment), and (4) TC-based (community-based coping scheme). To make

the results more explicit, we set the initial percentage of patched nodes to 5% (performs well in the previous simulation), and the results are shown in Figures 12 and 13.

During the experiment, the random patching strategy is not sufficient to control the spread of worms. Even for the MIT Reality dataset with a sparse topology, the infected ratio eventually stabilized at 79.1% (around 70 time units). For the Hagggle dataset, the value rises to 89.1% (around 80 time units). As expected, the later the worm is discovered, the higher the infected ratio. In essence, the worm signature is

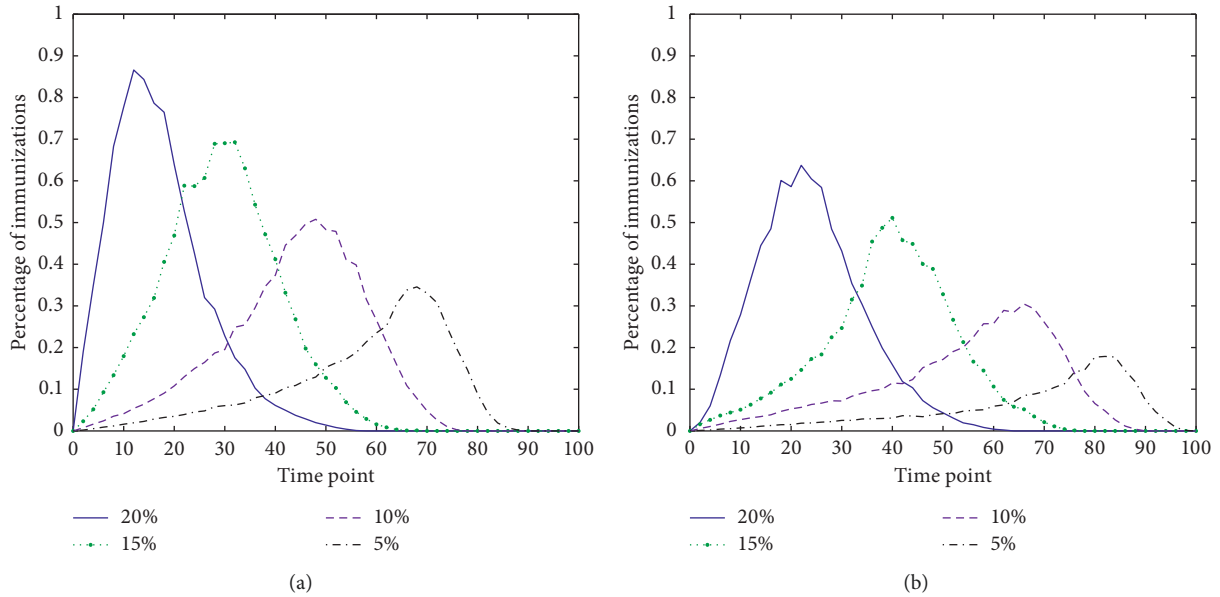


FIGURE 15: Percentage of immunizations with initially infected ratio $\mu = 5\%$, 10% , 15% , and 20% : Haggel (a) and MT Reality (b).

“racing” against the worm. If the worm signature “runs” faster, the containment performance will be better. On both datasets, when $\mu \leq 15\%$, centralize, socialize, TC-based, and CC^2 can control the infected ratio below 50% (around 40 time units). The reason is that the active containment scheme delivers the worm signatures in parallel, while the worm can only randomly move around. When $\mu = 20\%$, only CC^2 can effectively control the further spread of the worm and the network reaches a stable state around 50 time units.

6.5. The Analysis on Rejection and Immunization Number. Finally, we briefly analyze the immunization and rejection strategies of CC^2 . We focus on the percentage of rejections and immunizations with initial infected ratio $\mu = 5\%$, 10% , 15% , and 20% during the iteration. The results are shown in Figures 14 and 15. On average, the number of immunizations is higher than the number of rejections, suggesting that the immunization strategy dominates the worm containment process. This conclusion will be more conspicuous when the link density becomes larger (i.e., the Haggel network). We also noticed that when the number of immunizations and rejections decayed from the peak, the infected ratio is still at a high rate of growth (compared to Figures 12 and 13), which is related to the two-stage propagation pattern of the worm. The first stage is the “strong-link infection” of top ten mutual friends, which makes the number of attacks reach its peak quickly. The second stage is the “weak-link infection” of nontop ten friends. In this mode, the probability of a node being infected is proportional to the degree of the node. Once a high-degree node is infected, it triggers a broader range of secondary infections, which continues to increase the infected ratio. From this perspective, the idea of priority immunization against high-impact nodes is practical and has certain

performance advantages. Besides, the immunization strategy does not affect the normal communication of the network (e.g., the peak is 21.3% and 17.1% when $\mu = 20\%$ in Figure 14), which ensures the channel utilization of the network to a certain extent.

7. Conclusion

This paper models the spreading dynamics of the hybrid worm and propose several designs for worm containment on the mobile Internet. First, we identify the community structure of the network and control the long-range infection by immunizing the guard nodes that lie on the periphery of each community. Second, a worm signature distribution scheme is presented to quickly deliver each signature to all nodes to prevent the worm from spreading out to a larger population. Third, we design a security evaluation method to help users make favorable decisions when exchanging data using short-range transmission interfaces.

Experimental results show that the key to SINs worm containment is to identify high-impact nodes in the network accurately. Besides, although the GINs worm spread slowly, it can significantly improve the propagation performance of hybrid infections. The method has high performance and efficiency in the location-based social networks. Subsequent research will focus on the multilayer network worm containment task to achieve an accurate perception of the real world.

Data Availability

The data used to support the findings of this study are available from the corresponding author upon request. The

data can also be downloaded from the URLs given in Section 6.

Conflicts of Interest

The authors declare that they have no conflicts of interest.

Acknowledgments

This work was sponsored by the National Natural Science Foundation of China (61402126 and 61602133), Nature Science Foundation of Heilongjiang Province of China (F2016024), Heilongjiang Postdoctoral Science Foundation (LBH-Z15095), University Nursing Program for Young Scholars with Creative Talents in Heilongjiang Province (UNPYSCT-2017094), Scientific Research Foundation for the Overseas Returning Person of Heilongjiang Province of China (LC2018030), and National Training Programs of Innovation and Entrepreneurship for Undergraduates (201810214020).

References

- [1] S. Peng, S. Yu, and A. Yang, "Smartphone malware and its propagation modeling: a survey," *IEEE Communications Surveys & Tutorials*, vol. 16, no. 2, pp. 925–941, 2014.
- [2] S.-M. Cheng, W. C. Ao, P.-Y. Chen, and K.-C. Chen, "On modeling malware propagation in generalized social networks," *IEEE Communications Letters*, vol. 15, no. 1, pp. 25–27, 2011.
- [3] P. Kim and C. H. Lee, "Epidemic spreading in complex networks with resilient nodes: applications to fmd," *Complexity*, vol. 2018, Article ID 5024327, 9 pages, 2018.
- [4] G. Zyba, G. M. Voelker, M. Liljenstam, A. Méhes, and P. Johansson, "Defending mobile phones from proximity malware," in *Proceedings of the IEEE INFOCOM 2009—The 28th Conference on Computer Communications*, pp. 1503–1511, IEEE, Rio de Janeiro, Brazil, April 2009.
- [5] F. Li, Y. Yang, and J. Wu, "CPMC: an efficient proximity malware coping scheme in smartphone-based mobile networks," in *Proceedings of the IEEE INFOCOM 2010*, pp. 1–9, IEEE, San Diego, CA, USA, March 2010.
- [6] Y. Wang, S. Wen, Y. Xiang, and W. Zhou, "Modeling the propagation of worms in networks: a survey," *IEEE Communications Surveys & Tutorials*, vol. 16, no. 2, pp. 942–960, 2014.
- [7] X. Meng, P. Zerfos, V. Samanta, S. H. Y. Wong, and S. Lu, "Analysis of the reliability of a nationwide short message service," in *Proceedings of the IEEE INFOCOM 2007—26th IEEE International Conference on Computer Communications*, pp. 1811–1819, IEEE, Barcelona, Spain, May 2007.
- [8] Z. Zhu, G. Cao, S. Zhu, S. Ranjan, and A. Nucci, "A social network based patching scheme for worm containment in cellular networks," in *Proceedings of the IEEE INFOCOM 2009—The 28th Conference on Computer Communications*, pp. 1476–1484, IEEE, Rio de Janeiro, Brazil, April 2009.
- [9] X. Zhang and G. Cao, "Transient community detection and its application to data forwarding in delay tolerant networks," *IEEE/ACM Transactions on Networking*, vol. 25, no. 5, pp. 2829–2843, 2017.
- [10] P.-Y. Chen and A. O. Hero, "Multilayer spectral graph clustering via convex layer aggregation: theory and algorithms," *IEEE Transactions on Signal and Information Processing Over Networks*, vol. 3, no. 3, pp. 553–567, 2017.
- [11] C. C. Zou, D. Towsley, and W. Gong, "Modeling and simulation study of the propagation and defense of internet e-mail worms," *IEEE Transactions on Dependable and Secure Computing*, vol. 4, no. 2, pp. 105–118, 2007.
- [12] J. Su, K. K. W. Chan, A. G. Miklas et al., "A preliminary investigation of worm infections in a bluetooth environment," in *Proceedings of the 4th ACM workshop on Recurring malware*, pp. 9–16, ACM, Alexandria, VA, USA, 2006.
- [13] G. Yan and S. Eidenbenz, "Modeling propagation dynamics of bluetooth worms (extended version)," *IEEE Transactions on Mobile Computing*, vol. 8, no. 3, pp. 353–368, 2009.
- [14] J. W. Mickens and B. D. Noble, "Modeling epidemic spreading in mobile environments," in *Proceedings of the 4th ACM Workshop on Wireless Security*, pp. 77–86, ACM, Cologne, Germany, September 2005.
- [15] J. R. Morris-King and H. Cam, "Controlling proximity-malware infection in diverse tactical mobile networks using K-distance pruning," in *Proceedings of the IEEE MILCOM 2016—2016 IEEE Military Communications Conference*, pp. 503–508, Baltimore, MD, USA, November 2016.
- [16] Y. Yang, S. Zhu, and G. Cao, "Improving sensor network immunity under worm attacks: a software diversity approach," in *Proceedings of the 9th ACM International Symposium on Mobile Ad Hoc Networking and Computing*, pp. 149–158, ACM, Hong Kong, China, May 2008.
- [17] A. G. Miklas, K. K. Gollu, K. K. W. Chan, S. Saroiu, K. P. Gummedi, and E. De Lara, "Exploiting social interactions in mobile systems," in *Proceedings of the 9th International Conference on Ubiquitous Computing*, pp. 409–428, Springer-Verlag, Innsbruck, Austria, 2007.
- [18] C. Gao and J. Liu, "Modeling and restraining mobile virus propagation," *IEEE Transactions on Mobile Computing*, vol. 12, no. 3, pp. 529–541, 2013.
- [19] M. S. Haghghi, S. Wen, Y. Xiang, B. Quinn, and W. Zhou, "On the race of worms and patches: modeling the spread of information in wireless sensor networks," *IEEE Transactions on Information Forensics and Security*, vol. 11, no. 12, pp. 2854–2865, 2016.
- [20] X. Sun, Z. Lu, X. Zhang, M. Salathe, and G. Cao, "Infectious disease containment based on a wireless sensor system," *IEEE Access*, vol. 4, pp. 1558–1569, 2016.
- [21] B. Thompson, J. Morris-King, and R. Harang, "Slowing the spread of bluetooth-based malware in mobile tactical networks," in *Proceedings of the 2016 IEEE Military Communications Conference*, pp. 485–490, Baltimore, MD, USA, November 2016.
- [22] O. Trullols-Cruces, M. Fiore, J. M. Barcelo-Ordinas, and Barcelo-Ordinas, "Worm epidemics in vehicular networks," *IEEE Transactions on Mobile Computing*, vol. 14, no. 10, pp. 2173–2187, 2015.
- [23] Q. Zhang and A. Boukerche, "A novel infrastructure-based worm spreading countermeasure for vehicular networks," *IEEE Transactions on Intelligent Transportation Systems*, vol. 19, no. 7, pp. 2188–2203, 2018.
- [24] A. Boukerche and Q. Zhang, "Countermeasures against worm spreading," *ACM Computing Surveys*, vol. 52, no. 2, pp. 1–25, 2019.
- [25] C. Fleizach, M. Liljenstam, P. Johansson, G. M. Voelker, and A. Mehes, "Can you infect me now?: malware propagation in mobile phone networks," in *Proceedings of the 2007 ACM Workshop on Recurring Malcode*, pp. 61–68, ACM, Alexandria, VA, USA, November 2007.

- [26] A. Bose, X. Hu, K. G. Shin, and T. Park, "Behavioral detection of malware on mobile handsets," in *Proceedings of the 6th International Conference on Mobile Systems, Applications, and Services*, pp. 225–238, ACM, Breckenridge, CO, USA, June 2008.
- [27] D. Zhao, L. Wang, Z. Wang, and G. Xiao, "Virus propagation and patch distribution in multiplex networks: modeling, analysis, and optimal allocation," *IEEE Transactions on Information Forensics and Security*, vol. 14, no. 7, pp. 1755–1767, 2019.
- [28] Lu-X. Yang and X. Yang, "A novel virus-patch dynamic model," *PLoS One*, vol. 10, no. 9, Article ID e0137858, 2015.
- [29] Z. Lu, X. Sun, Y. Wen, G. Cao, and T. L. Porta, "Algorithms and applications for community detection in weighted networks," *IEEE Transactions on Parallel and Distributed Systems*, vol. 26, no. 11, pp. 2916–2926, 2015.
- [30] F. Taghavian, M. Salehi, and M. Teimouri, "A local immunization strategy for networks with overlapping community structure," *Physica A: Statistical Mechanics and Its Applications*, vol. 467, pp. 148–156, 2017.
- [31] S. Peng, M. Wu, G. Wang, and S. Yu, "Containing smartphone worm propagation with an influence maximization algorithm," *Computer Networks*, vol. 74, pp. 103–113, 2014.
- [32] W. Yang, H. Wang, and Y. Yao, "An immunization strategy for social network worms based on network vertex influence," *China Communications*, vol. 12, no. 7, pp. 154–166, 2015.
- [33] D. J. Daley and J. M. Gani, *Epidemic Modelling: An Introduction*, Vol. 15, Cambridge University Press, Cambridge, UK, 2001.
- [34] P. De, Y. Liu, and S. K. Das, "An epidemic theoretic framework for vulnerability analysis of broadcast protocols in wireless sensor networks," *IEEE Transactions on Mobile Computing*, vol. 8, no. 3, pp. 413–425, 2009.
- [35] J. Xie, S. Kelley, and B. K. Szymanski, "Overlapping community detection in networks: the state-of-the-art and comparative study," *ACM Computing Surveys*, vol. 45, no. 4, p. 43, 2013.
- [36] U. N. Raghavan, R. Albert, and S. Kumara, "Near linear time algorithm to detect community structures in large-scale networks," *Physical Review E*, vol. 76, no. 3, p. 036106, 2007.
- [37] M. E. J. Newman, "Modularity and community structure in networks," *Proceedings of the National Academy of Sciences*, vol. 103, no. 23, pp. 8577–8582, 2006.
- [38] N. A. Christakis and J. H. Fowler, "Social network sensors for early detection of contagious outbreaks," *PLoS One*, vol. 5, no. 9, p. e12948, 2010.
- [39] P. Wang, M. C. Gonzalez, C. A. Hidalgo, and A.-L. Barabasi, "Understanding the spreading patterns of mobile phone viruses," *Science*, vol. 324, no. 5930, pp. 1071–1076, 2009.
- [40] S. Gregory, "Finding overlapping communities in networks by label propagation," *New Journal of Physics*, vol. 12, no. 10, p. 103018, 2010.
- [41] H. Shen, X. Cheng, K. Cai, and M.-B. Hu, "Detect overlapping and hierarchical community structure in networks," *Physica A: Statistical Mechanics and Its Applications*, vol. 388, no. 8, pp. 1706–1712, 2009.
- [42] T. N. Dinh, N. P. Nguyen, and M. T. Thai, "An adaptive approximation algorithm for community detection in dynamic scale-free networks," in *Proceedings of the IEEE INFOCOM*, pp. 55–59, IEEE, Turin, Italy, April 2013.

Research Article

An Optimal Composition Strategy for Knowledge Service Component Based on Flexible Tracking Particle Swarm Algorithm

Yan-chao Yin ¹, Fu-zhao Chen,¹ Wei-zhi Liao ², and Cui-yin Liu³

¹Faculty of Mechanical and Electrical Engineering, Kunming University of Science and Technology, Kunming, China

²School of Mechanical and Electrical Engineering, University of Electronic Science and Technology, Chengdu, China

³Yunnan Province Key Laboratory of Computer Technology Applications, Kunming University of Science and Technology, Kunming, China

Correspondence should be addressed to Yan-chao Yin; yinyc@163.com

Received 16 August 2019; Revised 5 November 2019; Accepted 14 November 2019; Published 12 December 2019

Guest Editor: Raúl Baños

Copyright © 2019 Yan-chao Yin et al. This is an open access article distributed under the Creative Commons Attribution License, which permits unrestricted use, distribution, and reproduction in any medium, provided the original work is properly cited.

It is urgent to combine knowledge resources with manufacturing business processes to form a knowledge service in the cloud mode, so as to provide intelligent support for business activities in product development process. The main challenge of knowledge resource service, however, is how to rapidly construct the complex resource service system and respond promptly to the changeable service requirements in the business process, which is similar to the software system modeling using a component in software engineering. This paper is concerned with an optimal composition framework (OCF) of knowledge resource service, including service decomposition, component encapsulation, and optimal composition. Firstly, the typical business processes are decomposed into the dynamic knowledge element (DKE), and all kinds of knowledge resources and service behaviors are encapsulated into the reusable resource service components (RSC). Then, a multicomponent optimal composition mathematical model is presented, which transforms the problem of component composition into a multiobjective optimization problem. On this basis, a heuristic algorithm with the adaptive mutation probability is introduced to composite the multigranularity service component dynamically and robustly. Finally, the case of component composition for maintenance resource service is studied and the simulation results are provided to verify the efficacy of the proposed model and algorithms.

1. Introduction

In the cloud mode, enterprises have a large number of knowledge resources such as standards, specifications, methods, and cases. Therefore, how to reuse the existing knowledge resources and experience quickly and effectively for product innovation and development has become the key to improve the competitiveness of enterprises. Although enterprises have widely implemented and promoted application systems such as the product data management and the enterprise resource management, these systems have not yet been upgraded to the knowledge service, but also limited to the traditional data classification storage and retrieval, lack of interaction with business process activities, resulting in low reuse rate of knowledge. So, it is urgent to integrate knowledge with product business process and package them

into a knowledge service, forming a standardized guidance mechanism, helping users to use knowledge service correctly, and improving product development efficiency.

How to provide resource services according to the characteristics of enterprise knowledge resources in the cloud mode is an urgent problem to be solved [1, 2]. The purpose of knowledge service is to provide recommended solutions to users' knowledge service needs according to product development process and user identity, which often requires multiple knowledge resources to work together, that is, the combination of knowledge services. Specifically, in the process of new product development, on the one hand, they need to actively recommend various knowledge resources related to business activities according to task requirements in the whole manufacturing life cycle and on the other hand, it is necessary to organize various knowledge resources

(including parameters, methods, models, and tools) for a specific function or process in the product development process and provide them to enterprise users in the form of services. This mode of knowledge resource allocation and use on demand urgently needs to combine knowledge with manufacturing business process to form a knowledge service [3]. Consequently, how to combine knowledge resources with manufacturing business processes to form a knowledge service is of great importance for manufacturing industry, which will promote the transformation of industry from “operation mode” to “prediction model” [4, 5]. However, the knowledge service is composed of multiple types of service elements, including service subject, service object, service behavior, knowledge resources, involved organizations and their interaction relationship, which is difficult to respond promptly to the changeable service requirements in business process, that is, on-demand use of knowledge resources requires an effective integration method for resources and business process.

Referring to Figure 1, after analyzing the after-sales maintenance process, it can be divided into five business activities: fault phenomenon analysis, fault cause judgment, fault maintenance guidance, service tool push, and maintenance evaluation. Each service activity organizes knowledge resources such as documents, specifications, patents, cases, methods, empirical parameters, optimization models, and software tools and forms the standardized and curable resources (parameters, models, tools, and methods) into independent functional resource service components through abstraction and encapsulation in these business processes. The knowledge service component encapsulates the intermediate process and only provides the parameter interface, for which a knowledge service activity is a dynamic node of the whole business process, and the output of the previous knowledge service can generally be used as the input of the next knowledge service. When users call the corresponding knowledge services, they only need to combine and optimize different resource service components according to the service requirements to complete the task efficiently.

This paper is concerned with service-oriented encapsulation of knowledge resources and business process, thus transforming knowledge into a resource or product and finally into economic benefits. Following this idea, an optimal composition framework (OCF) including service task decomposition, component encapsulation, and optimal composition was constructed, where the typical business processes of the enterprise are sort out, and knowledge such as tools, methods, and parameters used in typical business activities can be obtained. On this basis, the task of knowledge service is decomposed into a series of subtasks which cannot be subdivided but can be completed by a single knowledge service. For component encapsulation, all kinds of standardized and curable knowledge are encapsulated into different knowledge service components according to their granularity and reuse rate through a business activity. For combinatorial optimization, the candidate set of knowledge services corresponding to each subservice task is searched in the resource pool and an appropriate knowledge service is selected to form the possible combinatorial

knowledge services according to the order of tasks. Finally, according to the given service requirements and constraints, the most satisfactory service combination is selected from all possible combinations.

2. Related Work

Knowledge services are transforming from traditional data classification storage and retrieval to knowledge services in the cloud mode. The construction process mainly includes knowledge resource modeling, knowledge service searching, matching, and combination optimization. In this field, knowledge resource modeling, knowledge service search, and matching have been of great interests during the past decades [6]. In particular, the knowledge resources modeling through multidomain ontology, distributed index, and service encapsulate has been well recognized. In the subsequent studies, knowledge semantic retrieval [7], extended algorithm [8], and word segmentation model [9] are used to propose the knowledge retrieval model that can meet the goal of innovative design, and the prototype system is built [10].

In the cloud mode, combination complexity and uncertainty of the knowledge resources may be unavoidable due to the complex resource types, the various combination, or unmeasured quality evaluation that affects the combination performance. Consequently, how to build and choose the best service composition scheme is of great importance for knowledge service design. To address this issue, some efforts have been advanced to exploit the strategy and algorithm for combination of manufacturing resources and computing resources. In particular, various well-known approaches, for example, process oriented service composition, semantic oriented service composition, and service composition based on service quality optimization, are reviewed and compared in terms of performance. It is shown in [11] that a flexible and light weight workflow framework based on the object modeling system to deploy and execute data-centric workflow in a decentralized manner across multiple distinct cloud resources, avoiding limitations of all data passing through a centralized engine. The author of [12] introduced fundamental guidelines for the automated composition of activities, where the propositions further encompass means to objectively derive these properties based on structure data-flow relation in a PDM. The presented method overcomes the impediments of time consumption and extensive domain knowledge. In [13], ontology of service functional logic and its subtyping rules were constructed to support precise relationship determining among services in cloud computing environment, for which the uncertainty stabilization approached to improve the practical performance of service composition.

It is noted that such composition methods are valid for cloud resource and manufacturing resource without considering service performance and thus a combination strategy with global service composition performance was studied based on the perception of service quality. Following this idea, the author [14] proposed a multiobjective service sharing optimization model considering the attributes of

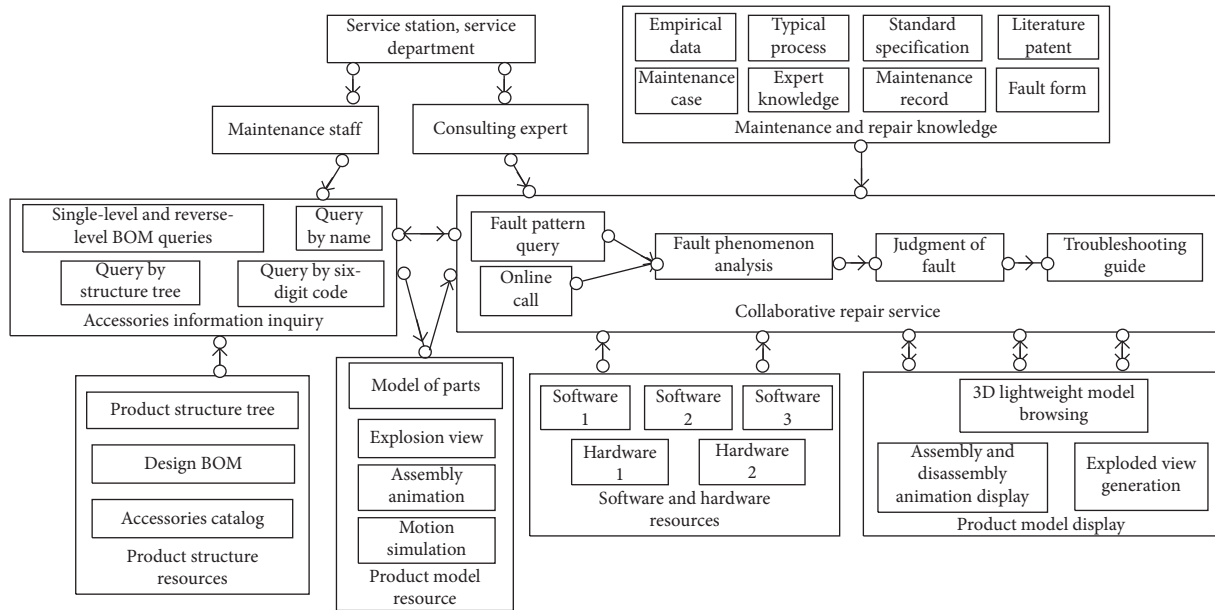


FIGURE 1: The coupling relationship between knowledge resources and business processes.

throughput, latency, and cost, simultaneously, and a particle swarm optimization-based multiobjective algorithm is proposed with deployment strategy to map a particle position to a resource sharing scheme composition. Although it was proved that the service performance converge to a neighborhood of their true values, the complexity, dynamics, and uncertainty of service composition should be conducted. Besides the swarm intelligence optimization algorithm, the deep reinforcement learning [15], and mining strategy of association rules [16] are also exploited to optimize the service composition. In the latest work, some studies optimized service composition on the basis of task requirements to solve the problem of multitask corresponding multiservice selection [17].

On the other hand, it is noted that the vast majority of knowledge service methods assume that knowledge resource and business process are separated or business process oriented knowledge resource retrieval mainly depend on keywords and semantics matching so that repeated retrieval, analysis, and evaluation must be used to acquire accurate knowledge resources. And most of the aforementioned results rarely study how to encapsulate resources and business process as a service and push the corresponding knowledge resources related to business process according to the requirements of tasks. This may result in lower availability of knowledge resource when multiple knowledge resource elements are needed to collaborative service in the process of new product development.

This paper is concerned with service-oriented encapsulation of knowledge resources and business processes, thus transforming knowledge into a resource or product and finally into economic benefits. Consequently, this study is to abstract, encapsulate, optimize, and compose all kinds of knowledge resources and combine them with business processes to form a knowledge service so as to provide intelligent support for product development process.

Following this idea, this paper is organized as follows: the OCF is constructed in Section 2. The problem to be studied and the encapsulation method are proposed in Section 3. Section 4 is devoted to establish the compositional mathematical model and optimization method; simulation results are given in Section 5 and conclusions are made in Section 6.

3. OCF of Knowledge Resource Service

In this paper, we first construct the optimal composition framework (OCF) of knowledge resource service, as shown in Figure 2. The main idea of OCF is all kinds of knowledge resources in business process, such as tools, methods, and parameters, are encapsulated to the reusable service components, and then the knowledge service with specific function are formed by composing such components. Following this idea, the OCF was designed in three parts including service decomposition, component selection, and optimal composition.

Within the task decomposition section, typical business processes of enterprises are sorted out, where knowledge resources such as tools, methods, and parameters used in typical business activities can be obtained. Moreover, the tasks of each stage are different in the business process, which needs knowledge resources in different areas. For example, in the design stage, not only all kinds of documents and design standard resources are needed, but also parametric design templates encapsulated with experience knowledge are needed to improve design efficiency and knowledge reuse. Motivated by this fact, we organize all kinds of knowledge resources through business activity and encapsulate them into a knowledge service, thus business activities completed by a single knowledge service are dynamic node of the whole business process and the output of the former knowledge service is generally the input of the next knowledge service. Consequently, product life cycle

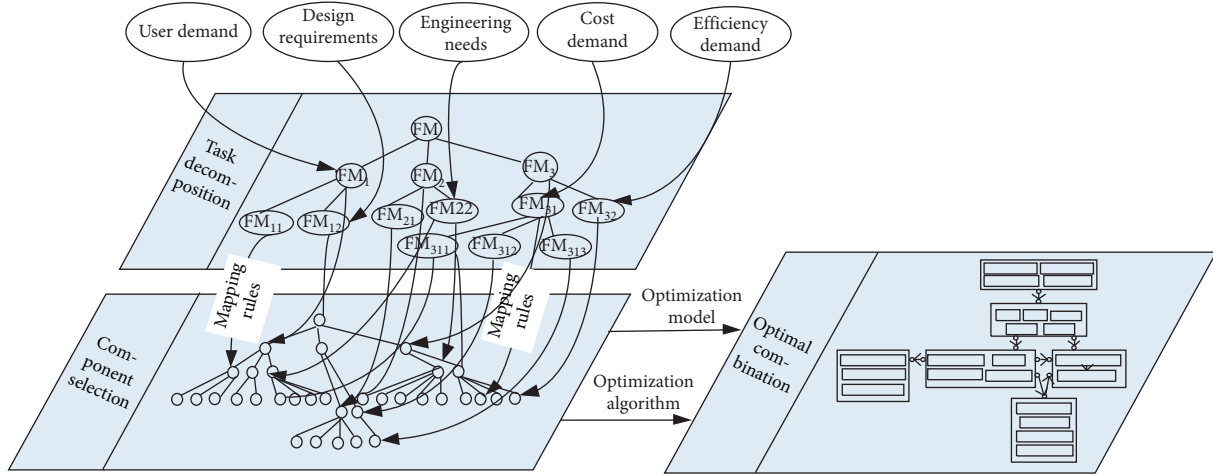


FIGURE 2: Optimal composition framework.

business process can be formed through dynamic integration of knowledge service.

In the component encapsulation section, normative and solidifying knowledge resources (e.g., empirical parameters, tools, and methods) in the process were encapsulated into knowledge service components with independent functions, which encapsulates the intermediate process and provides input and output parameter interface to the outside. When users call the corresponding knowledge service, they only need to input relevant parameter requirements to complete the task efficiently.

Consequently, knowledge service is the smallest unit in business process. Only through dynamic integration can it constitute the whole life cycle business activities. Following this idea, a mathematical model for multicomponent combination optimization was designed in the optimal composition section, which converts the multicomponent combination problem into a multiobjective optimization problem with constraints, where a heuristic algorithm was constructed and utilized to composite the multigranularity service component dynamically and robustly.

4. Encapsulation of Resource Service Component

4.1. Business Processes Decomposition. Aiming at knowledge-intensive business processes in enterprises, the typical solidified resource service activities FM_i are sorted out, as shown in Figure 3, where we use the idea of scenario analysis [18] for reference and regard the business process decomposition as the multilevel attribute subdivision of two dimensions: task unit and business personnel who complete the task, e.g., the task unit dimension, needs to consider such attributes as task basic information, task related knowledge, task relationship in the process, task stability, and the set of personnel performing tasks. And the business personnel dimension needs to consider the attributes of user's basic information, knowledge preference, skill level, function preference, task execution set, etc. It is noted that the dimensions should be divided and refined

according to the characteristics of the business process in the process of the actual business decomposition. In Figure 3, i is the i th dynamic service activity node in the business process and the process knowledge is classified into four aspects of specialty, method, tool, and task. Then, the dynamic knowledge element DKE_{ij} is constructed, where j is the j th resource service unit corresponding to the i th service activity node. In particular, the specialty is to express the category of specialty belonging to knowledge element and the method means how to implement a process application using the rules, reasoning, and description involved in knowledge elements. In addition, the tools are mainly used to describe basic tools such as software and programs involved in knowledge elements and the task is mainly used to express the business stages where knowledge elements can be applied. Thus, the knowledge resources such as tools, methods, and parameters used in the typical business activities can be obtained through decomposing the business process, which will prepare for the subsequent encapsulation of knowledge service components, and $CS_{DKE_{ij}}$ is the number of alternative components corresponding to the j th resource service unit of the i th service activity node.

4.2. Resource Service Component Encapsulation

4.2.1. Assumption and Definition. For the above purpose, the following assumption and definitions are used.

Assumption 1. DKE_{ij} is the minimum service unit of the resource service process, which contains knowledge resources such as standards, specifications, empirical parameters, tools, and methods and can be encapsulated as knowledge service components with independent functions through templates.

Definition 1. f is the dynamic requirement characteristics of users for knowledge resource, where the variability $V(f)$ of f depends on the number of variable requirement attributes and reuse frequentness. That is, the more

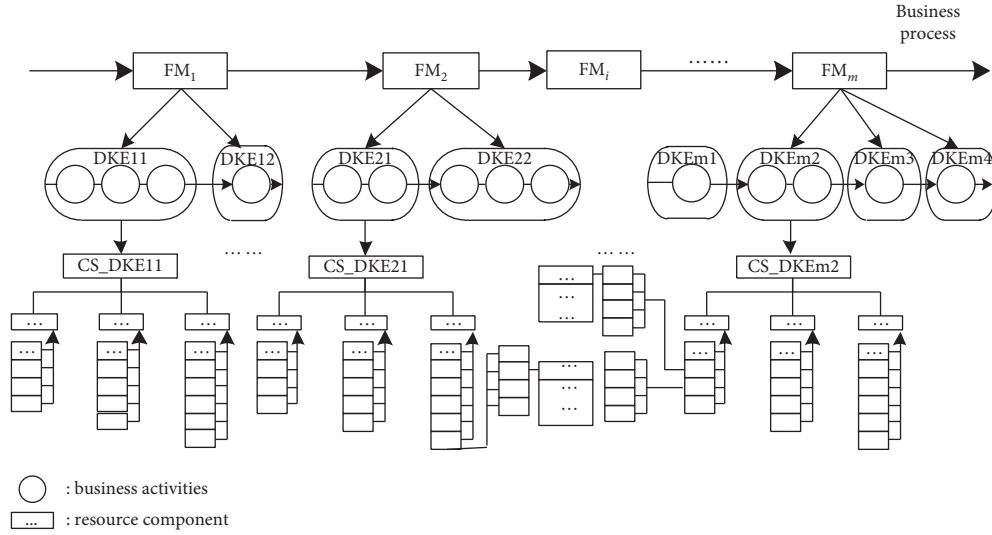


FIGURE 3: Business process decomposition.

frequently knowledge service elements change, the more unstable their performance is and the lower the reuse frequentness is.

Definition 2. Service stable region is a local space of resource service process, where the space is consisted of different DKE_{ij} , and the maximum service stable region is directly mapped to a component. The variation d_f of requirement attributes is restricted by the trust requirement region h_k in the demand library. For this purpose, the stable region sd is considered as $\min sd^{(k)}(d_f) = V(f_k) + p_k d_f + 0.5 d_f Q_k d_f$, where k is the k th stable domain of knowledge service unit, p_k is the changing gradient of service requirements, and Q_k is the requirement trace matrix; thus, the following properties hold:

- ① $\forall f_i \in sd, V(f_i) \leq \delta$, and $\|d_{f_i}\| \leq h_{ki}$
- ② $\forall f_j \notin sd, V(f_j) > V(f_i)$

4.2.2. Component Encapsulation Algorithm. According to the encapsulation algorithm (Algorithm 1), the number of components F_c can be defined as $F_c = \sum_{i=1}^m P_i \sum_{j=1}^{P_i} C_{ij}$, where P_i is the number DKE for the i resource service module and C_{ij} is the component sequence of the j th DKE in the i th resource service module.

5. Optimized Composition for Resource Service Component

5.1. Problem Formulation. In this section, we first address the comprehensive target including performance, cost, and efficiency for composing multiple RSC with user requirements, thus multicomponent composition can be specified as a multiobjective optimization problem. For this purpose, the following mathematic model is considered:

$$\begin{cases}
 \max P_c = \sum_{i=1}^m \sum_{j=1}^{P_i} \sum_{l=1}^{C_{ij}} \gamma_{ijl} \sum_{k=1}^K \lambda_k \mu_{ijl,k}, \\
 \min C_g = \sum_{i=1}^m \sum_{j=1}^{P_i} \sum_{l=1}^{C_{ij}} \gamma_{ijl} C_{Cijl} + \sum_{i=1}^m \sum_{j=1}^{P_i} \sum_{l=1}^{C_{ij}} \gamma_{ijl} C_{Rijl} + \sum_{i=1}^m \sum_{j=1}^{P_i} \sum_{l=1}^{C_{ij}} \gamma_{ijl} C_{Dijl}, \\
 \max E_g = \sum_{i=1}^m \sum_{j=1}^{P_i} \sum_{l=1}^{C_{ij}} \gamma_{ijl} E_{Cijl} + \sum_{i=1}^m \sum_{j=1}^{P_i} \sum_{l=1}^{C_{ij}} \gamma_{ijl} E_{Rijl} + \sum_{i=1}^m \sum_{j=1}^{P_i} \sum_{l=1}^{C_{ij}} \gamma_{ijl} E_{Dijl}, \\
 C_g \leq C_{\max}, \\
 \gamma_{ijl} \in \{0, 1\}, \\
 \sum_{i=1}^m \sum_{j=1}^{P_i} \sum_{l=1}^{C_{ij}} \gamma_{ijl} \leq 1, \\
 \sum_{k=1}^K \lambda_k = 1, \\
 E_l \leq E_{\max},
 \end{cases} \quad (1)$$

where P_c is the comprehensive performance evaluation index of RSC composition, which is evaluated by user satisfaction measurement. The performance includes the ability of composite components to service a business process and the degree of satisfaction to user needs, design needs, and engineering needs. P_c can be expressed as $N = \{N_1, N_2, \dots, N_K\}^T$, $k = 1, 2, \dots, K$, where N_k is the k th performance of composite components and the corresponding weight of each performance is $\lambda_N = (\lambda_1, \lambda_2, \dots, \lambda_K)^T$. In addition, γ_{ijl} corresponds to a binary decision variable, which indicates that the component is selected when it is 1, otherwise it is not selected. $\mu_{ijl,k}$ represents the correlation between the l th component instance of the DKE_j for the FM_i and the k th performance of the RSC, which can be a set of quantified fuzzy comments.

C_g is the total cost of RSC composition evaluated using cost calculation models, which includes customization cost C_c , reuse cost C_R , and development cost C_D , where $C_C =$

Input: the requirement attribute spaces $\Gamma(icbm)$ and resource service spaces $\Psi_i(icbm)$, variability of requirement attributes $V(f)$.
Output: the component sequence $C_{-DKE_{ij}}$ of different DKE_{ij} .
Step 1: set $sd = \Phi$, $CS_{-DKE_{ij}} = \Phi$;
Step 2: $\forall \Psi_i(icbm) \subseteq \Gamma(icbm)$, $\forall f \in \Psi_i(icbm)$;
Step 3: do {
 Searching for the variable threshold δ to meet $\min sd^{(k)}(d_f) = V(f_v) + pd_f + 0.5d_fQd_f \wedge sd \subseteq \Psi_i(icbm)$
 If ($V(f) \leq \delta$)
 {
 Incorporate f and its child attributes $child(f)$ into sd ;
 For ($\forall f_i \in \{f\} \cup child(f)$)
 {
 Set $flag(f_i) = 1$, that is, f_i has been mapped as an independent component or part of a component;
 Go to step 4;
 }
 }
 Else if ($V(f) > \delta$)
 {
 Set $flag(f) = 0$, that is, f_i cannot be directly mapped as a component;
 Go to step 3;
 }
} until (nonexistent such f)
Go to step 5;
Step 4: if ($sd \neq \Phi$)
{
 All the characteristic of sd could be encapsulated into the different granularity components $C_{C_{ij}}$ with the same functionality but different performance.
 Join $C_{C_{ij}}$ into $CS_{-DKE_{ij}}$;
 Set $sd = \Phi$, go to step 3;
}
Else
 Go to step 3;
Step 5: for ($\forall f \in \Gamma(icbm) \wedge flag(f) = 0 \wedge child(f) = \Phi$)
{
 Map f into $C_{C_{ij}}$, and add $C_{C_{ij}}$ into $CS_{-DKE_{ij}}$;
 Set $flag(f_i) = 1$;
}
Step 6: output $CS_{-DKE_{ij}}$;
If ($CS_{-DKE_{ij}} = \Phi$)
{
 Develop again;
}

ALGORITHM 1

$\{C_{C_{111}}, \dots, C_{C_{ijl}}, C_{C_{mP_iC_{ij}}}\}^T$ is the customization cost matrix, $C_R = \{C_{R_{111}}, \dots, C_{R_{ijl}}, C_{R_{mP_iC_{ij}}}\}^T$ is the reuse cost matrix, and $C_D = \{C_{D_{111}}, \dots, C_{D_{ijl}}, C_{D_{mP_iC_{ij}}}\}^T$ is the development cost matrix, $C_{C_{ijl}}$, $C_{R_{ijl}}$, and $C_{D_{ijl}}$ are the customization cost, reuse cost, and development cost of the l th component instance of the DKE_j for the FM_i , respectively.

E_g is the total efficiency of RSC composition evaluated through service platform, which includes customization efficiency, reuse efficiency, and development efficiency, where $E_C = \{C_{C_{111}}, \dots, C_{C_{ijl}}, C_{C_{mP_iC_{ij}}}\}^T$ is the customization efficiency matrix, $E_R = \{C_{R_{111}}, \dots, C_{R_{ijl}}, C_{R_{mP_iC_{ij}}}\}^T$ is the reuse efficiency matrix, and $E_D = \{C_{D_{111}}, \dots,$

$C_{D_{ijl}}, C_{D_{mP_iC_{ij}}}\}^T$ is the development efficiency matrix, $E_{C_{ijl}}$, $E_{R_{ijl}}$, and $E_{D_{ijl}}$ are the customization efficiency, reuse efficiency, and development efficiency of the l th component instance of the DKE_j for the FM_i , respectively.

$C_g \leq C_{\max}$ is the cost constraint, which cannot exceed the specified cost threshold. $\gamma_{ijl} \in \{0, 1\}$ is the decision variable constraints, and its value is only 0 or 1. $\sum_{i=1}^m \sum_{j=1}^{p_i} \sum_{l=1}^{C_{ij}} \gamma_{ijl} \leq 1$ is a single constraint, that is, only one can be selected for component sequences of each DKE . $\sum_{k=1}^K \lambda_k = 1$ is the weight constraint, that is, the sum of weight vectors corresponding to different performances is equal to 1. $E_l \leq E_{\max}$ is the efficiency constraint, and the total efficiency should not be lower than the prescribed minimum efficiency.

5.2. Optimization Algorithm

5.2.1. The FMEA Model of Component Composition. The multicomponent composition presented in this paper is formulated as a large-scale nonlinear multiple objective optimization problem with a considerable number of equality and inequality constraints. Motivated by this fact, the analysis of a fuzzy matter-element [19, 20] is considered, which transformed the multiobjective optimization into a single-objective optimization. That is, the fuzzy matter-element model of the multi component composition in equation (1) can be written as follows:

$$\tilde{C}R_k = \begin{bmatrix} P \\ p_1 \mu(f_1(X)) \\ p_2 \mu(f_2(X)) \\ \dots \\ p_k \mu(f_k(X)) \end{bmatrix}, \quad (2)$$

where $\tilde{C}R_k$ is a component composition matter-element of k dimensions; P is the name of the composition scheme; p_i is the name of the i th subobjective; X_i is the i th composition variable; and $\mu(f_i(X))$ is the excellence of degree for the composition scheme P i th subobjective p_i corresponding to $f_i(X)$, $\mu(f_i(X)) \in [0, 1]$.

If $f_i(X)$ is an ordinary mathematical function expression, one way to compute the excellent dependent degree function $\mu(f_i(X(t))) \in [0, 1]$ is by using the model as follows:

$$\mu(f_i(X)) = \begin{cases} 1, & f_i(X) \leq f_{i \min}, \\ \frac{f_{i \max} - f_i(X)}{f_{i \max} - f_{i \min}}, & f_{i \min} \leq f_i(X) \leq f_{i \max}, \\ 0, & f_i(X) \geq f_{i \max}. \end{cases} \quad (3)$$

It is well known that the weight of respective subobjective may be different for the component composition, so the weight R_λ corresponding to these objectives form a weight set as the following formula:

$$R_\lambda = \begin{bmatrix} p_1 & p_2 & \dots & p_k \\ \lambda_i & \lambda_1 & \lambda_2 & \dots & \lambda_k \end{bmatrix}, \quad (4)$$

where R_λ is a weight compound matter-element of the composition scheme subobjective and $\lambda_i (i = 1, 2, \dots, k)$ is the i th objective weight.

Consequently, the performance of component composition can be evaluated using degree of correlation, and the larger the degree of correlation, the better the composition scheme. The correlation degree function K is designed as follows:

$$K(X(t)) = \sum_{i=1}^k \mu(f_i(X(t)))\lambda_i. \quad (5)$$

Then, it is possible to transform the nonlinear multiple objective optimization problem in equation (1) into the single-objective fuzzy matter-element optimization problem. Consequently, it satisfies

$$\begin{cases} \text{find } X(t) = (x_1(t), x_2(t), \dots, x_m(t))^T \\ \text{max } k(X(t)) \\ \text{s.t. } g_j(X(t)) \leq 0, \quad j = 1, 2, \dots, J. \end{cases} \quad (6)$$

5.2.2. FTPSO Algorithm. One of the major drawbacks of the PSO proposed by Kennedy and Eberhart [21] is the lack of diversity of the swarm, which results in the convergence of the swarm to local optima. Then, the main reasons are that the personal best vector, the global best vector, and their fitness values are all stored in the memory of each particle, and such memory will be not updated until a new vector location with higher fitness was found. That is, it is difficult for particles to detect the change of the latest extremum in a convergence process. Motivated by this fact, we presented a flexible tracking particle swarm optimization (FTPSO), which improves the population's ability to perceive and respond to changes in the external environment. For this purpose, the following rules and definitions are considered.

Rule 1. Each particle detects its individual extreme value before velocity updates to perceive environmental changes.

Rule 2. By comparing with the global optimal fitness and the average fitness of the population, the leading particles and the eliminated particles are judged and different mutation probabilities are given to judge their fitness to the changing environment. Thus, the dynamic update response mode is introduced to update the particles gradually according to their fitness.

Definition 3. In evolutionary process, the particle is regarded as a leading particle with high judgment if the number of times will reach a certain value, where the distance between the individual extreme value ($f_{P_{\text{new}}}$) of the original position of any particle and the global extreme value ($f_{X_{\text{new max}}}$) of the new position for the population is less than the given threshold.

Definition 4. In evolutionary process, the particle is regarded as an eliminated particle if the number of times will reach a certain value, where the individual extreme value ($f_{P_{\text{new}}}$) of the original position of any particle is less than the average extreme value ($\bar{f}_{X_{\text{new}}}$) of the new position for the population.

Consequently, mutation operation is carried out according to the flexible mutation probability given in formula (7). Thus, the historical optimum position of the particle can be initialized by the new position generated by the particle mutation:

$$P_{fm} = \begin{cases} \tau_1 \cdot \frac{|f_{X_{new\ max}} - f_{P_{new}}|}{\varepsilon}, & [|f_{X_{new\ max}} - f_{P_{new}}| \leq \varepsilon]^{iterations} \longrightarrow \text{upto } \alpha, \\ \tau_2 \cdot \frac{|f_{X_{new\ max}} - f_{P_{new}}|}{f_{X_{new\ max}} - \bar{f}_{X_{new}}}, & \bar{f}_{X_{new}} < f_{P_{new}} \leq f_{X_{new\ max}}, \\ \tau_3, & [f_{P_{new}} \leq \bar{f}_{X_{new}}]^{iteration\ times} \longrightarrow \text{upto } \beta, \end{cases} \quad (7)$$

where τ_1, τ_2 , and τ_3 is a constant less than 0.5, which is used to constrain the flexible mutation probability P_{fm} to 0.0–0.5. ε is the given threshold, α and β are the given number of times, respectively. $f_{X_{new\ max}}$ is the new global optimal fitness, $f_{P_{new}}$ is the particle fitness value for mutation according to mutation probability, $\bar{f}_{X_{new}}$ is the average fitness of the population, and p_{fm} is a flexible mutation probability. In addition, the values of ε, α , and β can be adjusted appropriately according to the actual demand, so that the convergence rate of the population can be controlled more flexibly.

According to the adaptability of particles to changes in external environment, the self-renewal ability of particles is gradually improved as follows:

$$P_i(t+1) = \begin{cases} P_i(t)(1 - P_{fm}), & f_{X_{new}} \leq f_{P_{new}}(1 - P_{fm}), \\ X_i(t+1), & f_{X_{new}} > f_{P_{new}}(1 - P_{fm}). \end{cases} \quad (8)$$

According to the above improvement ideas, the FTPSO algorithm based on FMEA can be expressed as follows:

Step 1 (initialize the particle population).

Initialize the population space of the component composition scheme P_i ($i = 1, 2, \dots, m$) by choosing from the composition problem space with k sub-objectives randomly. Within this space, T_{\max} is the maximum generation, t is the number of current iterations, and c_1 and c_2 are the acceleration coefficients. Then, the space of component composition scheme can be represented as the compound matter-element form of $m \times k$:

$$\bar{R}_{mk} = \begin{bmatrix} P_1 & P_2 & \dots & P_m \\ p_1 & \mu(f_{11}(X)) & \mu(f_{21}(X)) & \dots & \mu(f_{m1}(X)) \\ p_2 & \mu(f_{12}(X)) & \mu(f_{22}(X)) & \dots & \mu(f_{m2}(X)) \\ \dots & \dots & \dots & \dots & \dots \\ p_k & \mu(f_{1k}(X)) & \mu(f_{2k}(X)) & \dots & \mu(f_{mk}(X)) \end{bmatrix}, \quad (9)$$

where $\mu(f_{ij}(X))$ ($i = 1, 2, \dots, m; j = 1, 2, \dots, k$) is the j th object optimal membership degree for the i th scheme, P_i is the name of the i th composition scheme, and p_j is the j th composition subobject.

Step 2 (calculating fitness function).

It is well known that fuzzy matter-element correlation function can be served as the fitness function [22]. According to (5), fitness function can be derived as

$$f_i(X) = k_i(X) \cdot \text{pun}(X), \quad i = 1, 2, \dots, m, \quad (10)$$

where $k_i(X)$ is the fuzzy matter-element correlation function and $\text{pun}(X)$ is a penalty function.

Step 3. In the following, $f_{X_{new\ max}}$ and $\bar{f}_{X_{new}}$ can be calculated.

Step 4 (assessment of particle adaptability).

Then, we assess the adaptability of each particle using flexible mutation probability represented in (7), where the $f_{P_{new}}$ will be updated in each iteration.

Step 5. It is now ready to update the P according to formula (8).

Step 6. Finally, to contrast the current fitness value with the population previous optimal, we set g_{best} to the current particle's array value if it is better than g_{best} .

Step 7. Calculate and update particle's velocity and position with each particle.

Step 8. Continue to circulate from the second step until the maximum iteration criterions algebra is satisfied.

6. A Case Study: Maintenance Resources Service

In this section, a resources service case for auto parts are given to validate the optimization model and method proposed in Sections 4 and 5. Firstly, according to the idea of business processes decomposition in Section 4.1, the maintenance process of auto parts are decomposed into five business feature spaces, that is, $\Gamma(\text{icbm}) = \{\Psi_i(\text{icbm}) \mid i = 1, 2, \dots, 5\} = \{\text{maintenance case training, maintenance knowledge reasoning and query, maintenance tool pushing, maintenance process guidance, maintenance collaborative interaction}\}$. Then, the dynamic knowledge element DKE_{ij} is constructed, as shown in Table 1, where the component sequences can be encapsulated using the selection method in Section 4.2, and the components for different sequences are given in Table 2. Moreover, the reuse efficiency and cost of different component sequences can be obtained through the performance analysis.

TABLE 1: Component sequences for $CS_{-DKE_{ij}}$.

Ψ_i (icbm)	Name	DKE _{ij}	$CS_{-DKE_{ij}}$	Included component	Reuse efficiency	Reuse cost
Ψ_1 (icbm)	Maintenance training	Maintenance knowledge training	1	$C_{11} C_{12} C_{13} C_{21} C_{22}$	0.04	23.54
			2	$C_{11} C_{12} C_{14} C_{21} C_{24}$	0.05	27.93
			3	$C_{35} C_{36} C_{37} C_{311}$	0.06	32.46
		Maintenance case training	1	$C_{14} C_{15} C_{16} C_{24} C_{25}$	0.04	24.57
			2	$C_{14} C_{15} C_{16} C_{21} C_{24}$	0.05	28.32
			3	C_{310}	0.07	33.65
Ψ_2 (icbm)	Maintenance knowledge, reasoning, and query	Maintenance knowledge and tool reasoning	1	$C_{17} C_{27} C_{28}$	0.05	23.44
			2	$C_{18} C_{28} C_{29}$	0.06	25.26
			3	$C_{18} C_{211} C_{212}$	0.06	24.53
		Maintenance knowledge and technology query	1	$C_{111} C_{112} C_{213} C_{214}$	0.05	26.21
			2	$C_{111} C_{22} C_{23}$	0.07	31.13
Ψ_3 (icbm)	Maintenance tool pushing	Maintenance tool information pushing	1	$C_{211} C_{222}$	0.05	25.33
			2	$C_{18} C_{19} C_{110} C_{219}$	0.06	26.45
		Maintenance tool information customization	1	$C_{112} C_{213} C_{221} C_{212}$	0.06	19.78
			2	$C_{111} C_{213} C_{214} C_{223}$	0.05	21.34
Ψ_4 (icbm)	Maintenance process guidance	Maintenance knowledge and case query	1	$C_{116} C_{14} C_{16} C_{24} C_{25}$	0.04	27.45
			2	$C_2 C_{111} C_{111}$		
			3	$C_{116} C_{14} C_{15} C_{23} C_{24}$	0.06	28.25
		Maintenance posture and tool pushing	1	$C_{34} C_{36} C_{38} C_{39}$	0.08	34.16
			2	$C_{14} C_{15} C_{16} C_{113}$	0.05	25.67
			3	$C_{21} C_{22} C_{23} C_{28} C_{29}$	0.05	26.23
Ψ_5 (icbm)	Maintenance collaborative interaction	Synergetic annotation	1	$C_{14} C_{15} C_{16} C_{111}$	0.07	32.61
			2	$C_{213} C_{214} C_{225} C_{226}$	0.05	27.18
		Failure consultation	1	C_{31}	0.07	33.24
			2	$C_{15} C_{16} C_{111} C_{213}$	0.05	27.54
			1	$C_{15} C_{16} C_{31} C_{33} C_{38}$	0.07	31.52
			2			

According to the composition algorithm in Section 3, the RSC for maintenance process were composed, and the composition process is presented below:

- (1) The performance requirements of the RSC for maintenance can be expressed using the natural language, that is, $P = \{P_1, P_2, \dots, P_8\} = \{\text{stability, maintainability, security, reliability, scalability, reusability, flexibility, adaptability}\}$, using AHP to determine the weights of these performance for $\lambda_1 = 0.154$, $\lambda_2 = 0.120$, $\lambda_3 = 0.178$, $\lambda_4 = 0.112$, $\lambda_5 = 0.177$, $\lambda_6 = 0.089$, $\lambda_7 = 0.141$, and $\lambda_8 = 0.029$. Moreover, the 5 levels' quantized values are expressed as strong, less strong, medium, weak, and irrelevant and the measured degree of relative value is defined as 9, 7, 5, 3, and 1. As shown in Table 3, the correlation matrix between component instance and composition performance in $CS_{-DKE_{ij}}$ can be constructed according to formula (5).
- (2) In the process of component composition, the weight of each subobjective including composition performance $P_C(X)$, composition efficiency $E_C(X)$, $E_R(X)$, $E_D(X)$, and composition cost $C_C(X)$, $C_R(X)$, $C_D(X)$ may be different, and then weight R_λ corresponding to these objectives form a weight set as follows:

TABLE 2: List of resource service component.

No.	Name
C_{11}	Maintenance of common sense
C_{12}	Assembly scheduled maintenance
C_{13}	Assembly regular inspection
C_{14}	Maintenance records
C_{15}	Fault form
C_{16}	Maintenance case
C_{17}	Product structure tree
C_{18}	BOM table
C_{19}	Inventory information
C_{110}	Supplier information
C_{111}	Three-dimensional model of product
C_{112}	Exploded view
C_{113}	Assembly animation
C_{114}	Motion simulation
C_{115}	The parts catalogue
C_{116}	Process knowledge of products
C_{21}	General maintenance inquiries
C_{22}	Maintaining common sense queries
C_{23}	Fault shape query
C_{24}	Maintenance record query
C_{25}	Maintenance case analysis
C_{26}	Troubleshooting program query
C_{27}	Query by structure tree
C_{28}	Number by name
C_{29}	Single-level BOM check
C_{211}	Single-level countercheck

TABLE 2: Continued.

No.	Name
C ₂₁₂	Multilevel BOM check
C ₂₁₃	Multilevel countercheck
C ₂₁₄	Three-dimensional model browsing
C ₂₂₁	Supply information query
C ₂₂₂	Inventory information query
C ₂₂₃	Confirm order
C ₂₂₄	Generating order
C ₂₂₅	Online call
C ₂₂₆	Synergetic annotation
C ₃₁	Collaborative calling
C ₃₂	Product structure
C ₃₃	Product 3D model browsing
C ₃₄	Vehicle spectrum
C ₃₅	Vehicle configuration
C ₃₆	Maintenance history
C ₃₇	Assembly maintenance
C ₃₈	Troubleshooting
C ₃₉	Diagnosing trouble
C ₃₁₀	Illustrating product
C ₃₁₁	Installation and dismantling tutorials
C ₃₁₂	Training course
C ₄	Staff
C ₅	Organization
C ₆₁	Software resources
C ₆₂	Hardware resources
C ₆₃	Environment of application service
C ₇₁	Training of maintenance

$$R_\lambda = \begin{bmatrix} h_1 & h_2 & h_3 & h_4 & h_5 & h_6 & h_7 \\ \tau_I & 0.192 & 0.121 & 0.165 & 0.093 & 0.154 & 0.142 & 0.133 \end{bmatrix}. \quad (11)$$

- (3) The composition scheme space like as the compound matter-element form of 50×7 was considered as the initial population of particle:

$$R_{50 \times 7} = \begin{bmatrix} P_1 & P_2 & \dots & P_{50} \\ P_C \mu(f_{11}(X)) & \mu(f_{21}(X)) & \dots & \mu(f_{50,1}(X)) \\ E_C \mu(f_{12}(X)) & \mu(f_{22}(X)) & \dots & \mu(f_{50,2}(X)) \\ E_R \mu(f_{13}(X)) & \mu(f_{23}(X)) & \dots & \mu(f_{50,3}(X)) \\ E_D \mu(f_{14}(X)) & \mu(f_{24}(X)) & \dots & \mu(f_{50,4}(X)) \\ C_C \mu(f_{15}(X)) & \mu(f_{25}(X)) & \dots & \mu(f_{50,5}(X)) \\ C_R \mu(f_{16}(X)) & \mu(f_{26}(X)) & \dots & \mu(f_{50,6}(X)) \\ C_D \mu(f_{17}(X)) & \mu(f_{27}(X)) & \dots & \mu(f_{50,7}(X)) \end{bmatrix}. \quad (12)$$

We now calculate the fitness function $f_i(X)$ as follows:

$$f_i(X) = K_i(X) = \sum_{j=1}^7 \nu(f_j(X))\tau_j, \quad i = 1, 2, \dots, 50, j = 1, 2, \dots, 7. \quad (13)$$

In order to find the optimal composition scheme, we simulated the classical experiment after Angeline [23] and Carlisle and Dozier [24], where three kinds of goal movements such as linear, circular, and random were implemented. As to the linear motion, a constant offset for each dimension is added in the update frequency intervals; for circular motion, a circular path with a cycle of 25 updates is added to the offset in each dimension; and as to the random motion, the Gaussian random variable for each dimension is added in the update frequency interval.

Each experiment with different movement goal, step size, and update frequency has been implemented 100 times, where the APSO and FTPSO were performed with same configuration and dynamic environment. Like in Angeline's and Carlisle's experiments, the motion step size was set as 0.1 and 0.5, updating frequency for simulation was 10 iterations and the maximum generation is set to 500.

Additionally, the fundamental parameters for FTPSO are set as follows: $w = 1.1$, $c_1 = c_2 = 2$; the initial inertia weight is 0.9 descending to 0.4 linearly, acceleration coefficients is $c_1 = c_2 = 1.49$, and the threshold value is $\varepsilon = 0.01$ in calculating the mutation probability p_m of FTPSO; the given iteration times are $\alpha = 15$, $\beta = 20$, and other APSO parameters were specified as reference.

Statistical results with different movement pattern are provided in Table 4, where the proposed method in this paper can achieve better performance for different movement pattern. Note that the performance of component sequence composition with FTPSO has many potential advantages in random movement pattern.

Comparison results of APSO and FTPSO were provided in Figures 4–7.

Figures 4–7 provide the simulation results, where the composition performance and tracking process are estimated for each working condition. From these figures, one can observe that the adaptive mutation probability and the response mode of dynamic updating were introduced to improve the adaptability of particles for FTPSO, where the proposed algorithm can track the latest change of system extreme in the process of component composition. Otherwise, the APSO can track the moving solutions in more than one hundred iterations with low accuracy due to lack of an adaptive updating mechanism for particle's *pbest*.

From the aforementioned results, one can conclude that our work specifies the service component composition problem as a multiobjective optimization problem. Thus, the relevance of the composition performance and the component instance can be estimated quantitatively. Moreover, the mathematical model of component composition can be provided using the fuzzy matter-element model, where the service component composition problem can be solved in the form of combination of qualitative and quantitative, and the multiobject composition optimal problems can be transformed into single-object optimal problems. In particular, FTPSO introduces the adaptive mutation probability and the response mode of dynamic updating, where the adaptability of particles were improved in the initial iterations.

Finally, the presented model and algorithm have been applied to the construction of the maintenance service

TABLE 3: Correlation matrix between component instance and composition performance for $CS_{-DKE_{ij}}$.

	N_1	N_2	N_3	N_4	N_5	N_6	N_7	N_8
L_{111}	9	9	5	1	5	7	5	3
L_{112}	5	7	3	3	5	7	5	7
L_{113}	9	9	3	9	7	7	9	7
L_{121}	7	7	3	9	5	5	4	3
L_{122}	7	5	1	7	5	3	5	7
L_{123}	7	5	7	3	5	5	7	9
L_{211}	9	7	7	5	7	9	3	7
L_{212}	5	7	5	1	3	7	5	3
L_{213}	7	3	1	9	9	5	3	5
L_{221}	9	7	5	9	3	3	5	5
L_{222}	7	3	5	3	5	3	5	9
L_{223}	7	5	3	1	5	5	1	5
L_{311}	7	3	9	7	5	3	5	7
L_{312}	5	7	7	9	5	9	7	7
L_{321}	5	3	7	9	7	9	5	5
L_{322}	9	3	5	7	5	7	9	5
L_{411}	3	5	7	1	3	5	7	5
L_{412}	7	5	3	3	7	7	5	5
L_{413}	9	7	7	5	5	3	5	7
L_{421}	7	9	3	1	7	5	3	7
L_{422}	7	9	5	5	3	5	7	7
L_{423}	9	3	1	7	5	1	7	7
L_{511}	7	5	3	7	7	9	9	5
L_{512}	7	7	9	5	3	1	7	5
L_{521}	9	9	5	7	5	9	3	3
L_{522}	7	3	9	7	7	3	9	7

TABLE 4: Comparison of composition program.

Movement pattern\composition program	Composition program	Composite performance	
Linear motion with step size 0.1	APSO	$L_{111}, L_{122}, L_{211}, L_{223}, L_{312}, L_{311}, L_{411}, L_{511}$	2.13
	FTPSO	$L_{112}, L_{121}, L_{212}, L_{222}, L_{312}, L_{322}, L_{412}, L_{422}, L_{511}$	3.85
Linear motion with step size 0.5	APSO	$L_{112}, L_{123}, L_{212}, L_{223}, L_{312}, L_{412}, L_{423}, L_{521}$	2.67
	FTPSO	$L_{111}, L_{122}, L_{213}, L_{223}, L_{311}, L_{423}, L_{512}, L_{522}$	4.12
Circular motion with step size 0.1	APSO	$L_{112}, L_{121}, L_{213}, L_{221}, L_{321}, L_{411}, L_{521}$	2.08
	FTPSO	$L_{111}, L_{123}, L_{212}, L_{222}, L_{323}, L_{422}, L_{512}, L_{522}$	4.73
Random motion with step size 0.5	APSO	$L_{113}, L_{123}, L_{212}, L_{222}, L_{312}, L_{413}, L_{423}, L_{512}, L_{111}, L_{122}, L_{211}, L_{221}, L_{311}, L_{322}, L_{412}, L_{421}, L_{512}, L_{521}$	1.78
	FTPSO		5.41

system for auto parts in Sichuan Truck Manufacture Plant Co., Ltd., where the architecture is divided into 5 layers including service interface layer, web service layer, business logic, data access layer, and building method layer. In addition, the information transformation and data exchange of component composition algorithm were obtained by using XML. Nowadays, the maintenance service system has been

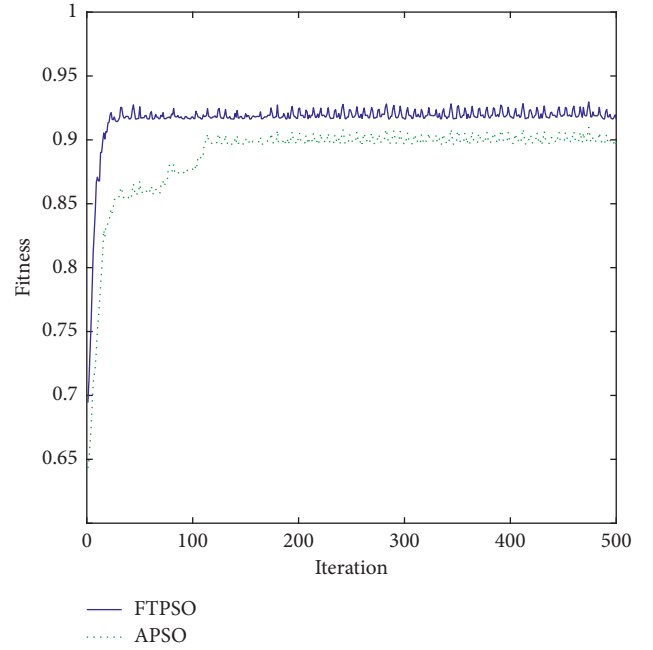


FIGURE 4: Performance comparison with linear motion step size 0.1 and updating frequency 10.

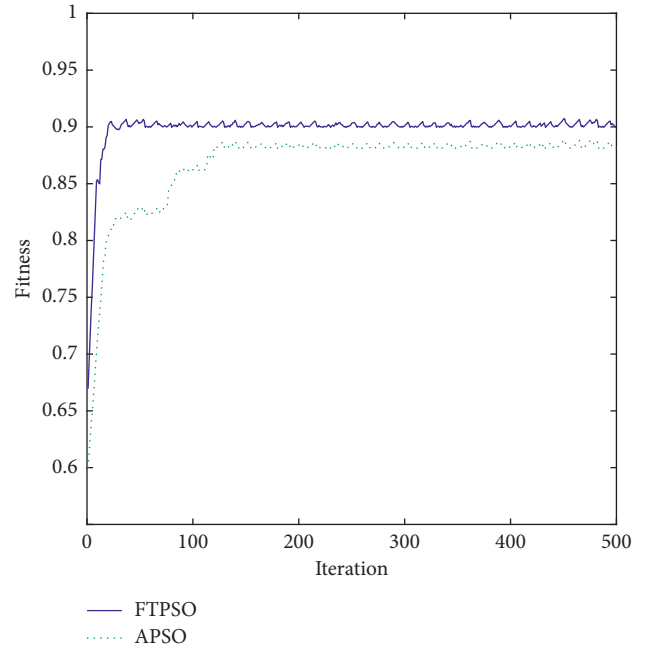


FIGURE 5: Performance comparison with linear motion step size 0.5 and updating frequency 10.

implemented in the process of auto parts' maintenance, where the user first sends the task package of "complete the maintenance of engine rocker shaft" to the platform, and the system will automatically analyze the task and obtain the information related to the task, such as service task description, specialty, undertaker, and other attribute information. Then, the system transforms "complete the

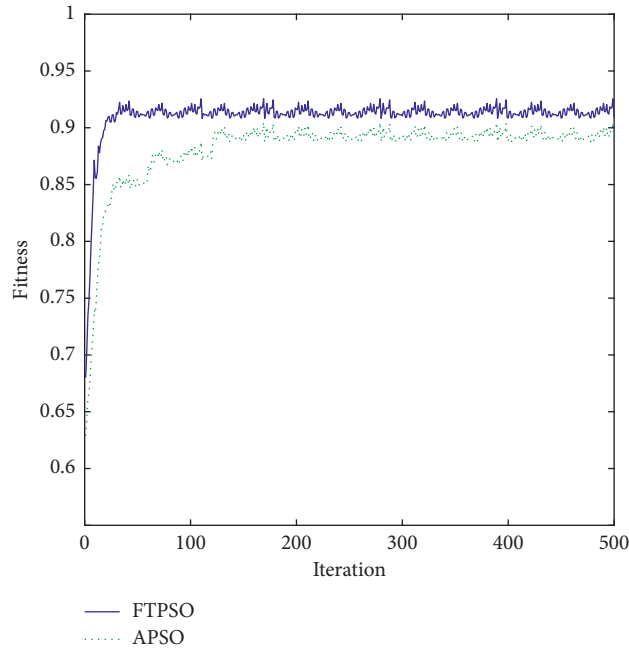


FIGURE 6: Performance comparison with circular motion of 25 updates.

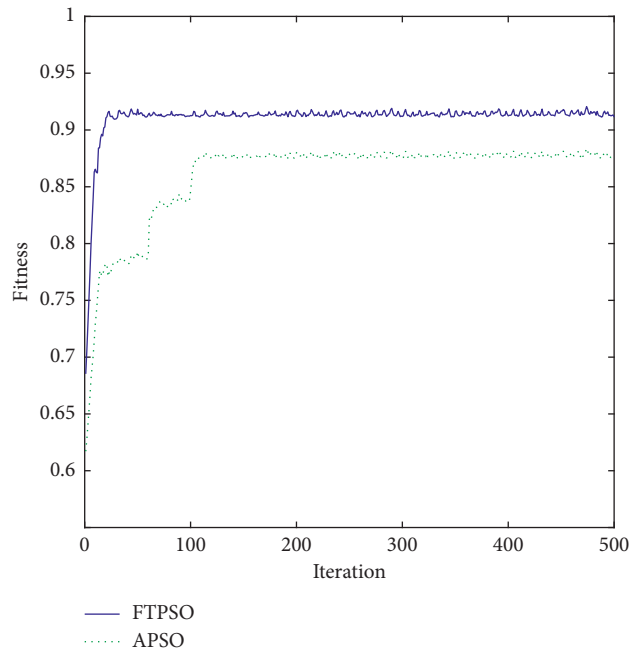


FIGURE 7: Performance comparison with random motion step size 0.5 and updating frequency 10.

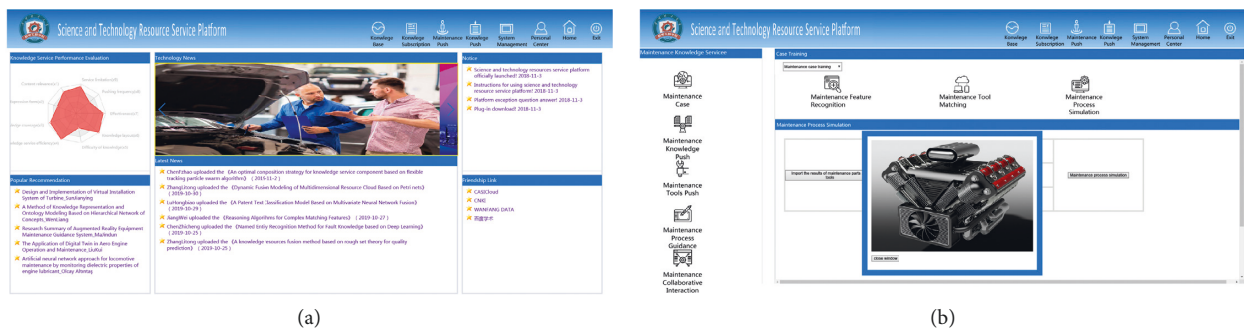


FIGURE 8: Interface of system implementation.

maintenance of engine rocker shaft” into “engine” and “rocker maintenance” semantic terms as the subject words of knowledge service. Users only need to input maintenance parameters step by step according to the guidance of the system, and the system automatically combines service components to generate failure causes, maintenance methods, or cases. The main service interfaces can be seen in Figure 8.

7. Conclusion

This paper addresses a combinatorial optimal strategy for knowledge resource service-oriented business process. Business processes are decomposed into dynamic knowledge elements, and all kinds of knowledge resources through business activity such as standards, specifications, empirical parameters, tools, and methods are encapsulated into knowledge service components with independent functions. In addition, a mathematical model for multicomponent combination optimization is designed, which converts the multicomponent combination problem into a multiobjective optimization problem with constraints. On this basis, we presented a combinatorial heuristic algorithm with the adaptive mutation probability and the response mode of dynamic updating so that the adaptability of particles was improved in the initial iterations to composite the multi-granularity service component dynamically and robustly. Finally, the case of component composition for maintenance resource service is studied and the experimental results show that our model and algorithm improve the efficiency and stability of the resource service system.

Planned future works and improvements include a comprehensive application for knowledge resource service of regional industrial cluster and an extension of the model and algorithm.

Data Availability

The raw/processed data required to reproduce these findings cannot be shared at this time as the data also form part of an ongoing study.

Conflicts of Interest

The authors declare that there are no conflicts of interest regarding the publication of this paper.

Acknowledgments

This paper was supported by the National Key R&D Program of China (2017YFB1400301).

References

- [1] F. Vendrell-Herrero, E. Gomes, O. F. Bustinza, and K. Mellahi, “Uncovering the role of cross-border strategic alliances and expertise decision centralization in enhancing product-service innovation in MMNEs,” *International Business Review*, vol. 27, no. 4, pp. 814–825, 2018.
- [2] A. S. A. Shukor, M. F. Mohammad, R. Mahbub, and F. Halil, “Towards improving integration of supply chain in IBS construction project environment,” *Procedia—Social and Behavioral Sciences*, vol. 222, pp. 36–45, 2016.
- [3] Y. Chao, Z. Yun, and T. Zhong, “Optimization model of cloud manufacturing services resource combination for new product development,” *Computer Integrated Manufacturing Systems*, vol. 18, no. 7, pp. 1368–1378, 2012.
- [4] D. Xue, Y.-L. Yu, G. Chen, and J. Yao, “Formation control of networked multi-agent systems,” *IET Control Theory & Applications*, vol. 4, no. 10, pp. 2168–2176, 2010.
- [5] L. Mu and C. K. Kwong, “A multi-objective optimization model of component selection in enterprise information system integration,” *Computers & Industrial Engineering*, vol. 115, pp. 278–289, 2018.
- [6] J. Lartigau, X. Xu, L. Nie, and D. Zhan, “Cloud manufacturing service composition based on QoS with geo-perspective transportation using an improved Artificial Bee Colony optimisation algorithm,” *International Journal of Production Research*, vol. 53, no. 14, pp. 4380–4404, 2015.
- [7] D. Kyriazis, “Modelling and prediction of resources and services state evolution for efficient runtime adaptations,” *Future Generation Computer Systems*, vol. 94, pp. 1–10, 2019.
- [8] X. Q. Li, H. C. Yang, S. K. Jing et al., “Knowledge service modeling approach for group enterprise cloud manufacturing,” *Computer Integrated Manufacturing Systems*, vol. 18, no. 8, pp. 1869–1880, 2012.
- [9] Y. C. Yin, W. G. Ding, and L. Wu, “Knowledge service method of cloud manufacturing based on uncertain rule reasoning,” *Computer Integrated Manufacturing Systems*, vol. 21, no. 4, pp. 1114–1123, 2015.
- [10] X. F. Xu, J. Hao, Y. R. Deng, and Y. Wang, “Design optimization of resource combination for collaborative logistics network under uncertainty,” *Applied Soft Computing*, vol. 56, pp. 684–691, 2017.
- [11] D.-H. Shin, K.-H. Lee, and T. Suda, “Automated generation of composite web services based on functional semantics,” *Journal of Web Semantics*, vol. 7, pp. 332–343, 2009.
- [12] H. van der Aa, H. A. Reijers, and I. Vanderfeesten, “Designing like a Pro: the automated composition of workflow activities,” *Computers in Industry*, vol. 75, pp. 162–177, 2016.
- [13] C. Huang, X. Wang, and D. Wang, “Type theory based semantic verification for service composition in cloud computing environments,” *Information Sciences*, vol. 469, pp. 101–118, 2018.
- [14] C. Zhang, J. Ning, J. Wu, and B. Zhang, “A multi-objective optimization method for service composition problem with sharing property,” *Swarm and Evolutionary Computation*, vol. 49, pp. 266–276, 2019.
- [15] J.-W. Liu, L.-Q. Hu, Z.-Q. Cai, L.-N. Xing, and T. Xu, “Large-scale and adaptive service composition based on deep reinforcement learning,” *Journal of Visual Communication and Image Representation*, vol. 65, Article ID 102687, 2019.
- [16] C. Jatoth, G. R. Gangadharan, and R. Buyya, “Optimal fitness aware cloud service composition using an adaptive genotypes evolution based genetic algorithm,” *Future Generation Computer Systems*, vol. 94, pp. 185–198, 2019.
- [17] M. Yuan, Z. Zhou, and X. Cai, “Service composition model and method in cloud manufacturing,” *Robotics and Computer Integrated Manufacturing*, vol. 61, pp. 1–13, 2019.
- [18] F. Zhang and L. Li, “Research on knowledge push method for business process based on multidimensional hierarchical context model,” *Journal of Computer-Aided Design & Computer Graphics*, vol. 29, no. 4, pp. 751–758, 2017.
- [19] W. Cai, “Extension theory and its application,” *Chinese Science Bulletin*, vol. 44, no. 17, pp. 1538–1548, 1999.

- [20] Y. W. Zhao and G. X. Zhang, "A new integrated design method based on fuzzy matter-element optimization," *Journal of Materials Processing Technology*, vol. 129, no. 1–3, pp. 612–618, 2002.
- [21] J. Kennedy and R. C. Eberhart, "Particle swarm optimization," in *Proceedings of IEEE International Conference on Neural Networks*, pp. 1942–1948, Perth, Australia, December 1995.
- [22] T. Loukopoulos and I. Ahmad, "Static and adaptive distributed data replication using genetic algorithms," *Journal of Parallel and Distributed Computing*, vol. 64, no. 11, pp. 1270–1285, 2004.
- [23] P. J. Angeline, "Tracking extrema in dynamic environments," in *International Conference on Evolutionary Programming VI*, pp. 335–345, Springer-Verlag, Berlin, Germany, 1997.
- [24] A. Carlisle and G. Dozier, *Tracking Changing Extrema with Adaptive Particle Swarm Optimizer*, World Automation Congress, Orlando, FL, USA, 2002.

Research Article

Computing the Mean-Variance-Sustainability Nondominated Surface by *ev*-MOGA

A. Garcia-Bernabeu ¹, J. V. Salcedo ², A. Hilario ², D. Pla-Santamaria ¹
and Juan M. Herrero²

¹*Campus of Alcoi, Universitat Politècnica de València, 03801 Alcoi, Spain*

²*Institute of Control Systems and Industrial Computing (ai2), Universitat Politècnica de València, 46022 Valencia, Spain*

Correspondence should be addressed to A. Garcia-Bernabeu; angarber@esp.upv.es

Received 9 August 2019; Revised 12 October 2019; Accepted 30 October 2019; Published 11 December 2019

Guest Editor: Raúl Baños

Copyright © 2019 A. Garcia-Bernabeu et al. This is an open access article distributed under the Creative Commons Attribution License, which permits unrestricted use, distribution, and reproduction in any medium, provided the original work is properly cited.

Despite the widespread use of the classical bicriteria Markowitz mean-variance framework, a broad consensus is emerging on the need to include more criteria for complex portfolio selection problems. Sustainable investing, also called socially responsible investment, is becoming a mainstream investment practice. In recent years, some scholars have attempted to include sustainability as a third criterion to better reflect the individual preferences of those ethical or green investors who are willing to combine strong financial performance with social benefits. For this purpose, new computational methods for optimizing this complex multi-objective problem are needed. Multiobjective evolutionary algorithms (MOEAs) have been recently used for portfolio selection, thus extending the mean-variance methodology to obtain a mean-variance-sustainability nondominated surface. In this paper, we apply a recent multiobjective genetic algorithm based on the concept of ϵ -dominance called *ev*-MOGA. This algorithm tries to ensure convergence towards the Pareto set in a smart distributed manner with limited memory resources. It also adjusts the limits of the Pareto front dynamically and prevents solutions belonging to the ends of the front from being lost. Moreover, the individual preferences of socially responsible investors could be visualised using a novel tool, known as level diagrams, which helps investors better understand the range of values attainable and the tradeoff between return, risk, and sustainability.

1. Introduction

Financial markets are a clear example of complexity in action [1–3]. As stated by Brunnermeier and Oehmke [4], complexity is a relevant concept in finance and, in particular, when building an optimization model for portfolio selection. Some authors have been recently concerned about adapting and extending the classical bicriteria Markowitz's mean-variance [5] methodology to integrate additional linear criteria such as dividends, liquidity, or sustainability for a suitable portfolio investor [6–11]. In these pioneering works, the above researchers propose exact optimization techniques to solve complex portfolio selection problems although they cannot deal efficiently with nonlinear objectives.

These works estimate risk, return, and additional criteria using historical data which are inevitably subject to estimation error. According to Nathaphan and Chunhachinda [12], three

groups of studies can be identified dealing with this problem. The first group of contributions is based on historical data and ignores the estimation error, the second group studies estimation risk and proposes a Bayesian resample efficient frontier approach, and finally, the third group focuses on the asset pricing approach by incorporating a factor model such as the Capital Asset Pricing Model or Arbitrage Pricing Theory. One potential way to solve this problem is to use a resampling approach [13, 14].

Within the methodological framework in complex portfolio selection problems, researchers have started to propose advanced computational techniques such as multiobjective evolutionary algorithms (MOEAs) and multiobjective genetic algorithms (MOGAs) to handle two or more conflicting goals subject to several constraints [15]. A literature review of recent contributions of MOEAs and MOGAs for portfolio management is conducted in [16]

where the authors highlight the sharp increase in the number of contributions focused on MOEAs and MOGAs compared with the moderate growth of specific applications for portfolio management, thus revealing that this area of research is still in its early stages. Moreover, this study shows that the majority of scholars applied MOEAs and MOGAs to portfolio selection only in the case of two objectives and only ten percent of the contributions dealt with three objectives. The portfolio expected returns to measure profitability and variance as a risk measure were the most common objectives among authors (see, for example, [17–25]). However, other objectives such as VaR, annual dividends expected shortfall, skewness, or social responsibility have appeared, albeit to a lesser extent [26–29]. Regarding the number of constraints, most models basically make use of two constraints in the problem formulation, namely, cardinality constraints and lower and upper bounds, and transaction round was the most popular.

There are a few academic studies on the application of MOEAs and MOGAs to tackle tricriterion portfolio selection. One of these studies is reference [30], and this has provided a multi-integer multiobjective optimization approach comparing a nondominated sorting genetic algorithm II (NSGA-II), a Pareto envelope-based selection algorithm (PESA), and a strength Pareto evolutionary algorithm II (SPEA2) to find the best possible tradeoffs between profitability, risk, and cardinality of the portfolio. Nonetheless, the purpose of our paper is to propose a MOGAs approach for a tricriterion mean-variance portfolio selection problem as a triobjective optimization problem whose third criterion is sustainability.

In a context of global awareness about climate change and sustainable growth, ethical investing is making inroads into the financial community. In recent years, sustainable investing, which is an approach that considers environmental, social, and governance (ESG) factors in portfolio selection and management, has become a mainstream investment practice. Professional investors, financial institutions, and the research community are working together to propose new quantitative methods to quantify the impact of including sustainability concerns in standard financial analysis. According to the Global Sustainable Investment Review (GSIA [31]), sustainable investments, or socially responsible investments (SRI), have risen to an average of 25% from 2014 to 2016 and have increased to 61% over the previous two-year period. It is remarkable that more than half of total professionally managed assets in Europe use some SRI strategies. For papers that widen the traditional risk-return tradeoff to integrate sustainability criteria in the portfolio selection formulation through different multicriteria decision-making (MCDM) approaches, we can cite a string of contributions such as references [6, 32–38].

This research aims to provide a MOGAs approach to obtain a mean-variance-sustainability nondominated surface. In particular, we apply an elitist multiobjective evolutionary algorithm based on the concept of ϵ -dominance called *ev-MOGA*. This algorithm tries to ensure convergence towards the Pareto set in a smart distributed manner along the Pareto front with limited memory resources. It also

adjusts the limits of the Pareto front dynamically and prevents the solutions belonging to the ends of the front from being lost. Once the Pareto front and the Pareto set have been obtained, the individual preferences of socially responsible investors could be considered using a novel tool known as level diagrams. The level diagram of a Pareto front is a collection of 2D graphical representations synchronized by the y -axis and expressing the x -axis in the units of the objective. This helps the investor better understand the range of values attainable and the tradeoff between the different solutions in physical units. A second important characteristic is that the y -axis synchronizes the different plots and provides a way to show a particular property of each possible portfolio.

Although we rely on historical data to estimate risk and return, our proposal can be applied to the three groups of studies dealing with the estimation error problem described in Nathaphan and Chunchachinda [12].

The paper is organized as follows. In Section 2, we review the problem of tricriterion portfolio selection, including sustainability as a third objective. In Section 3, we formulate the *ev-MOGA* algorithm to analytically derive the mean-variance-sustainability nondominated surface. The use of the level diagrams tool to include particular preferences of the decision maker and represent in 2D the Pareto front and the Pareto set is explained in Section 4 with an illustrative six-stock example. A real-world empirical application is presented in Section 5 using data from Morningstar open-end funds for the period 2009–2019. The paper closes with conclusions and further research proposals.

2. Tricriterion Multiobjective Portfolio Selection from a Sustainable-Financial Perspective

The standard bicriterion portfolio selection problem assumes that investors are only concerned about achieving a certain level of profitability for specific levels of risk. Since the early 1970s, several authors have attempted to include an additional criterion beyond the expected return and variance when constructing a portfolio [39, 40], but it was not until the 2000s that the idea of additional objectives was further boosted from the methodological framework.

In [41], liquidity is introduced as a third criterion into the standard mean-variance portfolio optimization model. By defining several measures of liquidity, the authors constructed a three-dimensional mean-variance-liquidity frontier.

A triobjective optimization problem is proposed in [30] to find the tradeoff between risk, return, and the number of securities in the portfolio. The authors apply and compare three evolutionary multiobjective optimization techniques, namely, the nondominated sorting genetic algorithm II (NSGA-II); the Pareto envelope-based selection algorithm (PESA); and the strength Pareto multiobjective evolutionary algorithm 2 (SPEA2) to find the best tradeoff between risk, return, and cardinality of the portfolio.

In [6], a general framework for computing the non-dominated surface in a tricriterion portfolio selection that extends the Markowitz portfolio selection approach to an additional linear criterion (dividends, liquidity, or sustainability) is addressed. By solving a quad-lin-lin program, they provide an exact method for computing the non-dominated surface that can outperform standard portfolio strategies for multicriteria decision makers. An empirical application where the third criterion is sustainability is developed to illustrate how to compose the nondominated surface.

In [7], sustainability is included as the third criterion to obtain the variance-expected return-sustainability efficient frontier to explain how the sustainable mutual fund industry can increase levels of sustainability. The tricriterion non-dominated surface is computed through the quadratic constrained linear program (QCLP) approach, and from the experimental results, it can be concluded that there was room to expand the sustainability levels without hampering the levels of risk and return.

After reviewing the most significant contributions dealing with tricriterion portfolio selection, we have to take into account that to select portfolios from a purely financial perspective generally requires a two-stage process. The first stage is to define the opportunity set and narrow down the larger pool to a more workable number of securities. The second stage is asset allocation, which is to decide how to distribute the wealth of an investor between the different asset classes. As our scenario consists in making investment decisions from a sustainable-financial perspective, the difference between the way in which assets are managed from purely financial criteria and the way a sustainable portfolio is managed only takes place in the first stage [8]. The stages in this process are as follows.

2.1. First Stage. To define the opportunity set from a sustainable point of view, two types of screening techniques are used [42], thus obtaining an approved list of securities. To this end, one of the earliest methods used by socially responsible investors is negative screening (NS), in which the investors establish a kind of “red line” to rule out companies that do not develop sustainable strategies, and deal in, for example, controversial weapons, tobacco, gambling, pornography, nuclear energy, or animal testing. The other is positive screening (PS), in which investors select companies that set positive examples of environmentally friendly products and socially responsible business practices, for instance, renewable energy and sustainable transport companies.

2.2. Second Stage. The decision maker defines the asset allocation of portfolio from the approved list in the first stage. Thus, the investment decisions are made in terms of profitability and risk, but there is no evidence proving that sustainability is taken into account in the asset allocation stage.

In this second stage, a tricriterion portfolio selection problem including sustainability could be mathematically formulated as follows:

$$\min f_1 = \sum_{i=1}^N \sum_{j=1}^N w_i w_j \sigma_{ij}, \quad (1)$$

$$\max f_2 = \sum_{i=1}^N w_i \mu_i, \quad (2)$$

$$\max f_3 = \sum_{i=1}^N w_i s_i, \quad (3)$$

$$\text{subject to } \sum_{i=1}^N w_i = 1, \quad (4)$$

$$w_{i_{\min}} \leq w_i \leq w_{i_{\max}}, \quad (5)$$

where N is the number of available securities, μ_i is the expected return on security i ($i = 1, 2, \dots, N$), σ_{ij} is the covariance between security i and j . In addition, s_i is the portfolio sustainability score, and w_i is the investment proportion. Constraint (4) is called the budget constraint and implies that 100% of the budget will be invested in the portfolio. Furthermore, a minimum and maximum investment rule is considered in the constraint (5).

The above stated model could be solved by obtaining a Pareto optimal front that represents the best tradeoffs between mean return, variance, and sustainability. When including a third criterion, the nondominated frontier in the two-dimensional space becomes a nondominated surface in a three-dimensional space. In [6], an exact method for computing the nondominated surface in a tricriterion portfolio selection problem was proposed to extend the Markowitz approach to an additional linear criterion. The previous method for computing the non-dominated set when the third criterion was sustainability is applied in [7]. The authors used the CIOS (custom investment objective solver) code to derive the non-dominated surface from quad-lin-lin programs, which is composed of a connected collection of parabolic segments called “platelets”. A quadratic constrained ε -constraint linear program to derive a nondominated surface is proposed in [8] to prove that investors could increase the sustainability levels of their portfolios without undermining risk or return.

Hereafter, we propose a more-integrated second-stage approach to approximate the Pareto front by applying an elitist multiobjective evolutionary algorithm based on the concept of ε -dominance called ev-MOGA [43]. Existing multiobjective techniques for extending mean-variance portfolio selection problems have limited capabilities if the new objectives are nonlinear. The proposed ev-MOGA algorithm adjusts the Pareto front dynamically, ensuring convergence and uniform distribution of solutions with no conditions related to the type of the objective function (quadratic, linear, or nonlinear).

3. Deriving the Nondominated Mean-Variance-Sustainability Surface

Generally speaking, multiobjective programming (MOP) approaches face the simultaneous optimization of multiple objective functions subject to a set of constraints. As no single solution can achieve all the objectives, in most real problems, MOP tries to find the Pareto efficient solution or the Pareto front. Hence, a set of solutions is called Pareto efficient (or nondominated or noninferior), when no other feasible solution can achieve the same or better performance for all the objectives and it is strictly better for at least one criterion.

According to Miettinen [44], the mathematical model of a multiobjective problem with n objectives can be formulated as follows:

$$\min \mathbf{F}(\theta) = \min [F_1(\mathbf{X}), F_2(\mathbf{X}), \dots, F_n(\mathbf{X})], \quad (6)$$

$$\begin{aligned} \text{s.t.} \\ g_q(\mathbf{X}) &\leq 0, & (1 \leq q \leq r), \\ h_k(\mathbf{X}) &= 0, & (1 \leq k \leq m), \\ x_{li} &\leq x_i \leq x_{ui}, & (1 \leq i \leq L), \end{aligned} \quad (7)$$

where $F_j(\mathbf{X})$ $j = 1, \dots, n$ are the n objectives, $g_q(\mathbf{X})$ and $h_k(\mathbf{X})$ are the r inequality and m equality problem constraints, respectively, x_{li} and x_{ui} are the lower and upper constraints which define the solution space, and $\mathbf{X} = (x_1, \dots, x_p)^T$ are the independent variables. Constraint (7) defines a set called searching space D .

The tricriterion multiobjective portfolio model described by equations (1)–(5) can be recast in the form of the MOP, taking $\mathbf{X} = (w_1, \dots, w_n)$ as the portfolio weights and the number of objectives $n = 3$, $p = L = N$, $r = 0$, and $m = 1$. Equations (6) and (7) then become

$$F_1(\mathbf{X}) = f_1 = \sum_{i=1}^N \sum_{j=1}^N w_i w_j \sigma_{ij}, \quad (8)$$

$$F_2(\mathbf{X}) = -f_2 = -\sum_{i=1}^N w_i \mu_i, \quad (9)$$

$$F_3(\mathbf{X}) = -f_3 = -\sum_{i=1}^N w_i s_i, \quad (10)$$

$$h_1(\mathbf{X}) = \sum_{i=1}^N w_i - 1 = 0, \quad (11)$$

$$\begin{aligned} x_{li} &= w_{i_{\min}}, \\ x_{ui} &= w_{i_{\max}}. \end{aligned} \quad (12)$$

According to [16], evolutionary algorithms provide a suitable framework for solving multiobjective problems as they are too complex to be solved using deterministic techniques. Over the last 20 years, MOEAs and MOGAs

have demonstrated their effectiveness in solving MOP problems and approximating their corresponding Pareto optimal front using the concept of dominance [45].

Definition 1 (dominance [43]). Given two feasible solutions, a solution \mathbf{X}^u is said to dominate \mathbf{X}^v , denoted by $\mathbf{X}_u < \mathbf{X}_v$, if and only if

$$\begin{aligned} F_i(\mathbf{X}^u) &\leq F_i(\mathbf{X}^v), & \forall i \in n, \\ F_k(\mathbf{X}^u) &< F_k(\mathbf{X}^v), & \exists k \in n. \end{aligned} \quad (13)$$

Definition 2 (Pareto optimal set and the Pareto front [43]). The Pareto optimal set \mathbf{X}_p , which includes the solutions that are not dominated by any other solutions, is given by

$$\mathbf{X}_p = \{\mathbf{X} \in D \mid \nexists \tilde{\mathbf{X}} \in D : \tilde{\mathbf{X}} < \mathbf{X}\}. \quad (14)$$

The Pareto front $\mathbf{F}(\mathbf{X}_p)$ is the plot of the objective functions whose nondominated vectors are in the Pareto optimal set.

The ev-MOGA [43] is an elitist MOGA based on the concept of ε -dominance [46]. In ev-MOGA, the objective function space is split into a fixed number of boxes forming a grid taking ε as the length of edges. The concept of ε -dominance is based on the idea that a particular solution inside a given box dominates the remaining solutions belonging to this box.

For each dimension $i \in n$, n_box_i cells of ε_i width are created where

$$\begin{aligned} \varepsilon_i &= \frac{(F_i^{\max} - F_i^{\min})}{n_box_i}, \\ F_i^{\max} &= \max_{\mathbf{X} \in \mathbf{X}_p} F_i(\mathbf{X}), \end{aligned} \quad (15)$$

$$F_i^{\min} = \min_{\mathbf{X} \in \mathbf{X}_p} F_i(\mathbf{X}).$$

For a solution \mathbf{X} , $box_i(\mathbf{X})$ is defined by

$$box_i(\mathbf{X}) = \left\lceil \frac{F_i(\mathbf{X}) - F_i^{\min}}{F_i^{\max} - F_i^{\min}} \cdot n_box_i \right\rceil, \quad \forall i \in n, \quad (16)$$

where $\lceil a \rceil$ rounds a to the nearest integer towards infinity.

Remark 1. $box_i(\mathbf{X})$ is always an integer belonging to the set $\{0, 1, 2, \dots, n_box_i\}$.

Definition 3 (ε -dominance [43]). Given $\mathbf{box}(\mathbf{X}) = \{box_1(\mathbf{X}), \dots, box_n(\mathbf{X})\}$, a solution \mathbf{X}^u with value $\mathbf{F}(\mathbf{X}^u)$ ε -dominates the solution \mathbf{X}^v with value $\mathbf{F}(\mathbf{X}^v)$, denoted by $\mathbf{X}^u <_\varepsilon \mathbf{X}^v$, if and only if

$$\begin{aligned} \mathbf{box}(\mathbf{X}^u) &< \mathbf{box}(\mathbf{X}^v) \\ \text{or } (\mathbf{box}(\mathbf{X}^u) &= \mathbf{box}(\mathbf{X}^v), \mathbf{X}^u < \mathbf{X}^v). \end{aligned} \quad (17)$$

This grid preserves the diversity of the Pareto front $\mathbf{F}(\mathbf{X}_p)$ as each box can be occupied by only one solution at the same time and produces a smart distribution since the algorithm

only checks occupied boxes, rather than all boxes. This content management avoids the need to use other clustering techniques to obtain adequate distributions, which leads to a considerable reduction in the computational burden [46].

Definition 4 (ε -Pareto set [43]). A set $\mathbf{X}_{P_\varepsilon}^* \subseteq \mathbf{X}_P$ is ε -Pareto if and only if

$$\begin{aligned} \forall \mathbf{X}^u, \mathbf{X}^v \in \mathbf{X}_{P_\varepsilon}^*, \mathbf{X}^u \neq \mathbf{X}^v, \mathbf{box}(\mathbf{X}^u) \neq \mathbf{box}(\mathbf{X}^v), \\ \mathbf{box}(\mathbf{X}^u) \not\prec_\varepsilon \mathbf{box}(\mathbf{X}^v). \end{aligned} \quad (18)$$

Remark 2. \mathbf{X}_P is unique and normally includes infinite solutions. Hence, a set $\mathbf{X}_{P_\varepsilon}^*$, with a finite number of elements from \mathbf{X}_P , should be obtained. Notice that $\mathbf{X}_{P_\varepsilon}^*$ is not unique.

For the implementation of the ev-MOGA algorithm, three types of populations are defined as follows:

- (1) $P(t)$ (t represents the actual iteration or generation of the algorithm) is the main population, which explores the searching space D (defined by constraints (7)) during the algorithm iterations (t). The main population size is denoted by $Nind_P$.
- (2) $A(t)$ Archive, which stores the solution $\mathbf{X}_{P_\varepsilon}^*$. Its size is denoted by $Nind_A$, which is variable but bounded (see justification below in equation (19)).
- (3) $GA(t)$ is the auxiliary population. Its size is denoted by $Nind_{GA}$, which must be an even number. This population is formed by new individuals obtained by crossover or mutation from individuals belonging to $P(t)$ and $A(t)$. This procedure is explained later in detail.

A uniform distribution of solutions is achieved by only including in the archive population $A(t)$, the ε -dominant solutions allocated in different boxes. If two solutions are shared in the same box, the solution that prevails can be established using different criteria which can be set by the user. For instance, it is possible to choose the closest solution to the centre of the box or the closest to the origin of the searching space D .

The aim of ev-MOGA is to achieve a ε -Pareto set $\mathbf{X}_{P_\varepsilon}^*$ with the greatest possible number of solutions in order to characterize the Pareto front adequately. Although the number of possible solutions will depend on the shape of the front and on n_box_i , it will not exceed the following bound:

$$\begin{aligned} \text{card}(\mathbf{X}_{P_\varepsilon}^*) \leq \frac{\prod_{i=1}^n n_box_i + 1}{n_box_{\max} + 1}, \\ n_box_{\max} = \max_i n_box_i, \end{aligned} \quad (19)$$

where $\text{card}(X)$ is the number of elements of set X . With this bound, it is possible to control the maximum number of solutions that will characterize the Pareto front.

The step-by-step process applying the ev-MOGA algorithm to obtain the nondominated mean-variance-sustainability surface is as follows:

Step 1. Initialize $t = 0$. Create a uniformly distributed initial population of portfolio weights $P(0)$ with $Nind_P$ individuals (portfolios) randomly selected from the searching space D , and create an empty archive population $A_0 = \emptyset$.

Step 2. Conduct the multiobjective evaluation of the main population of portfolios $P(0)$ using equations (8)–(10).

Step 3. Detect the ε -nondominated portfolios (\mathbf{X}_{ND}) from $P(0)$, which are stored in $A(0)$. The Pareto front limits F_i^{\max} and F_i^{\min} are calculated from population $A(0)$.

Step 4. Generate a new auxiliary population $GA(t)$ from the main population $P(t)$ and the archive population $A(t)$ following this procedure:

- (1) Set $j = 0$.
- (2) Two portfolios are randomly selected, \mathbf{X}^P from $P(t)$ and \mathbf{X}^A from $A(t)$.
- (3) A random number $u \in [0, \dots, 1]$ is generated.
- (4) If $u > P_{c/m}$ (probability of crossing/mutation. It has to be prefixed in advance by the user. It usually equals 0.2), \mathbf{X}^P and \mathbf{X}^A are crossed over by means of the extended linear recombination technique, generate two new portfolios for $GA(t)$.
- (5) If $u \leq P_{c/m}$, \mathbf{X}^P and \mathbf{X}^A are mutated using random mutation with Gaussian distribution and then included in $GA(t)$.
- (6) $j = j + 1$.
- (7) If $j < Nind_{GA}/2$, go to (2). Otherwise, the procedure finishes.

Step 5. Evaluate population $GA(t)$ using the multiobjective approach defined by equations (8)–(10).

Step 6. Check which portfolios in $GA(t)$ must be included in $A(t+1)$ on the basis of their location in the objective space. $A(t+1)$ will contain all the portfolios from $A(t)$ that are not ε -dominated by elements of $GA(t)$, and all the portfolios from $GA(t)$ which are not ε -dominated by elements of $A(t)$.

Step 7. Update population $P(t+1)$ with portfolios from $GA(t)$. Every portfolio \mathbf{X}^{GA} from $GA(t)$ is compared with a portfolio \mathbf{X}^P that is randomly selected from the portfolios in $P(t)$. \mathbf{X}^{GA} will replace \mathbf{X}^P in $P(t+1)$ if it ε -dominates \mathbf{X}^P . Otherwise, \mathbf{X}^P will not be replaced.

Step 8. In $t = t + 1$, check if $t < t_{\max}$, then go to Step 4, otherwise stop.

Portfolios from $A(t)$ will belong to $\mathbf{X}_{P_\varepsilon}^*$, the smart and efficient approximation of the Pareto set.

The ev-MOGA algorithm used in this article is a modified version of the algorithm published in Matlab Central [47].

The original ev-MOGA algorithm was unable to cope simultaneously with the weighting constraints stated in equations (11) and (12). Thus, it has been necessary to implement some changes related to the random generation

of a uniformly distributed initial population and the crossover and random mutation of individuals.

Example 1 (six-stock portfolio selection). To show the applicability of the ev-MOGA algorithm to solve a tricriterion multiobjective portfolio selection from a sustainable-financial perspective, we have developed a six-stock example based on equations (8)–(12). In this example, the following vector of expected returns, matrix of covariances, and vector of portfolio sustainability scores have been used:

$$\begin{aligned} \boldsymbol{\mu} &= \begin{pmatrix} 1.8426 \\ 1.4060 \\ 0.8346 \\ 1.5745 \\ 1.4133 \\ -0.4145 \end{pmatrix} \cdot 10^{-2}; \\ \boldsymbol{\sigma} &= \begin{bmatrix} 21.6368 & 3.7021 & -0.9104 & 3.4893 & 3.2989 & 5.1921 \\ 3.7021 & 5.4762 & 0.5264 & -0.0284 & 2.3047 & 1.0302 \\ -0.9104 & 0.5264 & 3.4024 & 0.5005 & 1.0575 & 0.8166 \\ 3.4893 & -0.0284 & 0.5005 & 5.2031 & 0.8882 & 1.9082 \\ 3.2989 & 2.3047 & 1.0575 & 0.8882 & 8.3785 & 1.7110 \\ 5.1921 & 1.0302 & 0.8166 & 1.9082 & 1.7110 & 6.349 \end{bmatrix} \cdot 10^{-3}; \\ \mathbf{s} &= \begin{pmatrix} 45 \\ 58 \\ 55 \\ 46 \\ 52 \\ 60 \end{pmatrix}. \end{aligned} \quad (20)$$

The ev-MOGA algorithm has been executed with the following parameters: $N_{ind_p} = 10^4$, $N_{ind_{GA}} = 8$, $t_{max} = 10^5$, $P_{m/c} = 0.2$, and $n_{box_i} = 1000$ $i = 1, \dots, 6$. After 10^5 iterations, population A has 40414 individuals. Figure 1 shows the ε -Pareto front obtained by applying the ev-MOGA algorithm.

Figure 1 depicts the three-dimensional representation of the approximated ε -Pareto front, thus providing the non-dominated mean-variance-sustainability surface. This ε -Pareto frontier is made up of 40414 uniformly distributed points representing nondominated portfolios for which none of the three objectives can be improved without sacrificing any others. Notice that, the north-west boundary of the plotted surface is the standard Markowitz's mean-variance frontier. For this example, when the risk goes down, the return becomes smaller and the sustainability becomes bigger. Moreover, the points that are performing well in sustainability are plotted in green in the bottom left corner.

4. Representing the Nondominated Mean-Variance-Sustainability Surface with 2D Figures Using Level Diagrams

It is widely recognized that as the number of dimensions increases, it is increasingly difficult to analyse the graphical information provided by the Pareto front. According to

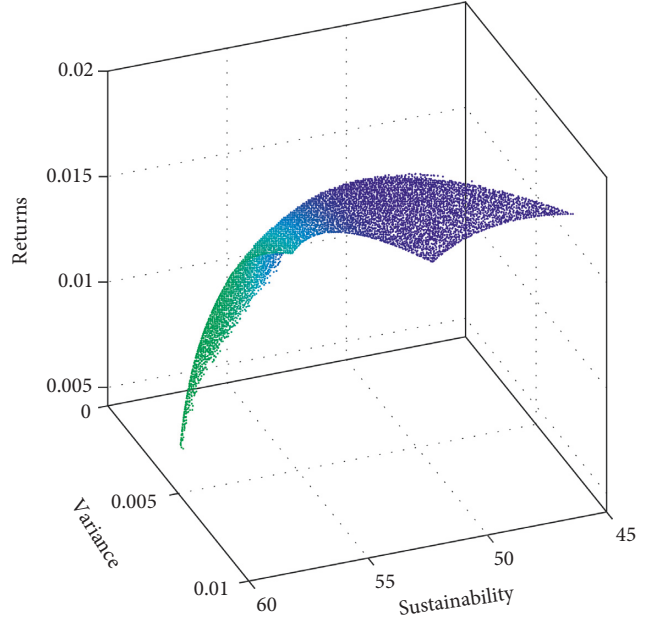


FIGURE 1: 3D ε -Pareto front corresponding to the six-stock example.

Miettinen [44], approximating the Pareto front is an open research field in which a broad array of techniques have been proposed.

In [48], a new visualization tool of n -dimensional Pareto fronts called level diagrams (LDs) is developed. LD is shown to be a useful analysis tool to help decision makers face with large sets of Pareto points obtained from multiobjective optimization problems. With LD, each objective is represented on the X -axis of a separate 2D diagram, and each diagram is synchronized with the others because all share the same Y -axis. To represent the points of the Pareto front in LDs, every objective is normalized with respect to minimum and maximum values by applying a norm, such as, the 1-norm, the Euclidean norm (2-norm), or the infinity norm (∞ -norm) (it is also possible to apply any user-defined function to perform this normalization procedure). In each diagram, the Y -axis corresponds to the sum of the normalized objectives, while the values of a particular objective are represented on the X -axis. There will be as many LDs as objectives. Consequently, LD methodology consists in replacing a n -dimensional Pareto front by n LDs that share the same Y -axis.

For the proposed mean-variance-sustainability problem, the 3D-Pareto front will be replaced with three LDs in two dimensions. In the first LD, the X -axis will be the values of variance (risk), the return values will be represented in the second LD, and the third LD refers to the values of sustainability. LD is available from Matlab Central Reynoso-Meza [49].

Example 2 (six-stock portfolio selection (continued)). According to the previous statement, from Example 1, the 3D-Pareto front of Figure 1 can be represented by three two-dimensional LDs in Figure 2.

In each LD, the Y -axis corresponds to the normalized value of the three objectives using the 2-norm. The green points in the first LD are situated at the lower levels in the X -axis (risk or variance), and they correspond to the zones of the Pareto front nearer to the ideal point which represent the minimum risk. These green points in the LD of risk correspond to the green points in the LD of return and in the LD of sustainability. It is worth noting that all the graphs are synchronized because they share the same Y -axis. This synchronization can be used to check where a particular group of points is located in different LDs.

Imagine that an investor determines a sustainability benchmark hoping to make a positive impact through his/her responsible investing. This sustainability aspiration level can be coloured in purple in the sustainability LD (see the last LD in Figure 3). Furthermore, all the objectives are coordinated and by selecting a given level of sustainability, the decision maker can visualize the corresponding value of risk and return in the remaining LDs and also in the 3D-Pareto front. In this way, the level diagram information on the objective values of returns, variance, and sustainability can be represented in a clearer form than a three-dimensional graph.

LD tool also works with the Pareto set. In this example, the Pareto set is a 6-dimensional set, so it is impossible to represent it using a standard graph. Fortunately, following the same idea used for the Pareto front, it is possible to display this 6-dimensional set with 6 LDs, each one corresponding to each portfolio weight (w_i).

From Example 1, the Pareto set can be equivalently represented by the 6 LDs that are shown in Figure 4. The green points in these new LDs also correspond to the zones of the Pareto set nearer to the ideal point which represents the maximum sustainability. Due to the synchronization of all the graphs, when the decision maker sets a level for one objective in the LDs of the Pareto front, the range of the budget that could be invested in each asset appears in purple in the corresponding LDs of the Pareto set.

Remark 3 (about n -dimensional Pareto sets). Generalising the results of Example 2, it is possible to conclude that a n -dimensional Pareto set can be replaced by n LDs that share the same Y -axis, each one corresponding to each weight (w_i).

Overall, this interactive tool could be interesting for the visualization of the Pareto fronts involving more than three objectives and helping users of a posteriori methods find the best solutions in multiobjective optimization problems.

5. An Application to the European SRI Open-End Funds

In this section, we report the experimental results obtained with the application of ev-MOGA to a real-world empirical study using a data set of institutional SRI open-end funds from Morningstar to explore the variance-expected return-sustainability tradeoff. The data from Morningstar cover an opportunity set that includes 22 institutional SRI open-end funds offered in Spain, and the base currency is

the Euro. For each SRI open-end fund, we have the monthly returns for 120 months for the period 2009–2019. Monthly data for the period were downloaded to compute the expected return vector $\boldsymbol{\mu} = (\mu_1, \dots, \mu_{22})^T$ and the covariance matrix $\boldsymbol{\Sigma} = [\sigma_{ij}]$, $i, j = 1, \dots, 22$.

As for the model sustainability vector $\mathbf{s} = (s_1, \dots, s_{22})^T$, we downloaded the historical portfolio sustainability score that provides reliable information about how well the holdings in a portfolio perform on environmental, social, and governance (ESG) issues. For more information about the sustainability scoring method, see Morningstar [50].

We have applied the ev-MOGA algorithm with these parameters: $N_{ind_p} = 5 \cdot 10^4$, $N_{ind_{GA}} = 20$, $t_{max} = 3 \cdot 10^5$, $P_{m/c} = 0.2$, and $n_box_i = 500$ $i = 1, \dots, 22$.

The set of points belonging to ε -Pareto front in Figure 5 represents the set of nondominated (or efficient) portfolios for which none of the three objectives, risk, return, or sustainability, can be improved without sacrificing any others. In this case, it is shown that improving the level of sustainability in a second stage of the portfolio multi-objective optimization undermines the financial goal in terms of return but improves the risk. In fact, the area of the surface for the highest level of sustainability coloured in green corresponds to low level of returns and low values for risk.

Figure 6 shows the three LDs in two dimensions for return, variance (risk), and sustainability related to the previous 3D ε -Pareto front. If a particular investor sets a level of sustainability using the purple marker, the LD tool immediately offers the corresponding values of risk and return. Moreover, Figure 7 plots the 22 LDs of the Pareto set, thus providing the corresponding portfolio weights.

When analysing Figure 7, we should draw attention to the following groups of SRI open-end funds: (i) a first group including funds 1-2-5-6-15-17-18-20 that does not (or only marginally) contribute to achieving any nondominated point of the ε -Pareto front; (ii) a second group composed of funds 8-11-12-13-19 generating efficient solutions, but not providing the required sustainability benchmark; and (iii) a third group made up of funds 3-4-7-9-10-14-16-21-22 providing efficient solutions in which a high level of sustainability is also ensured.

6. Conclusions

The Markowitz mean-variance approach has been the prevailing model for portfolios for over 60 years and is often viewed as a basic model to represent the complexity of real-world portfolio selection problems, especially when investors are concerned about additional criteria such as sustainability. Therefore, a new ev-MOGA approach has been applied in this paper to approximate the non-dominated mean-variance-sustainability surface by providing a well-distributed Pareto front. We have reviewed the main contributions in the literature addressing the problem of including additional criteria to the classical mean-variance Markowitz portfolio selection approach. Scholars started to use MOGAs for portfolio selection,

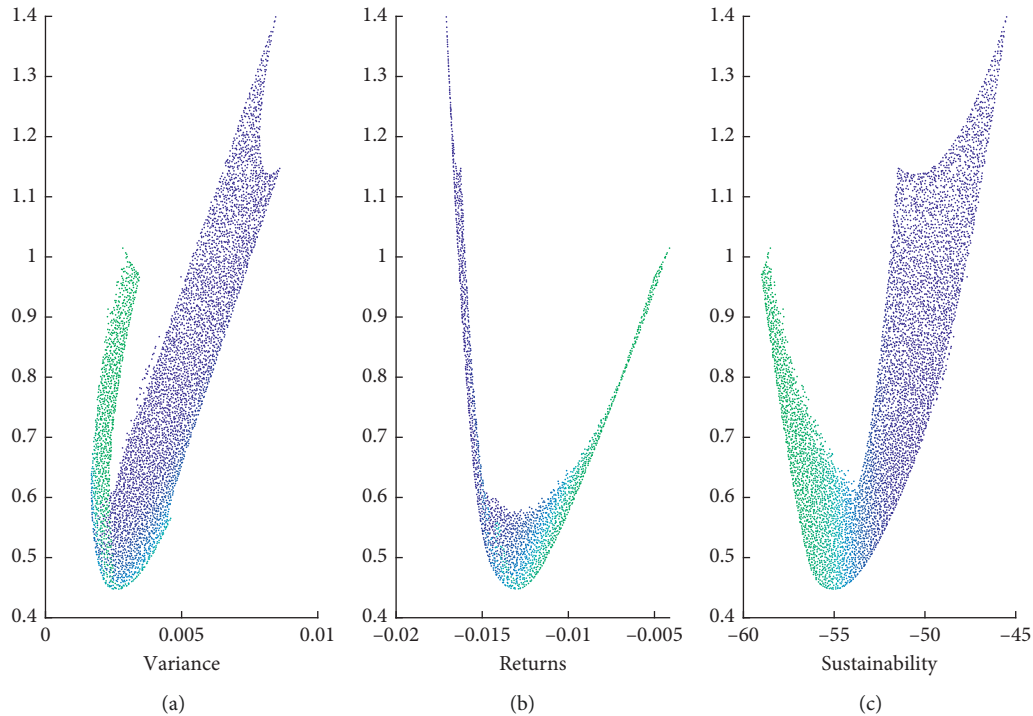


FIGURE 2: 2D-level diagrams corresponding to the Pareto front of the six-stock example.

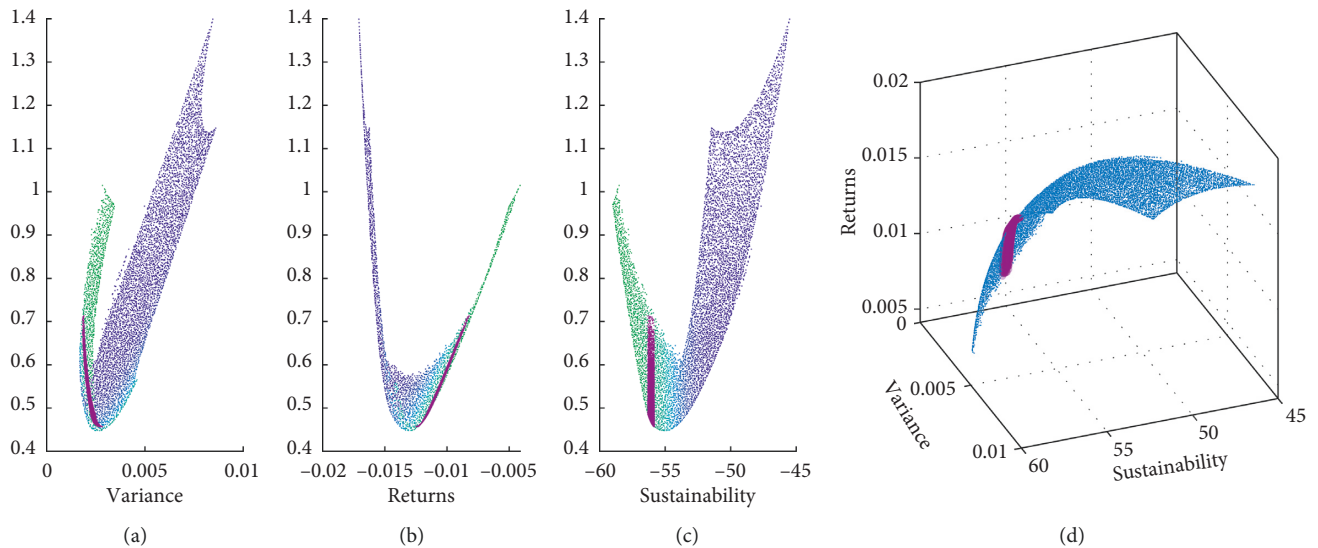


FIGURE 3: 2D LDs and the corresponding 3D-Pareto front of the six-stock example with a coordinated purple set for a sustainability benchmark.

especially to the two-objective case, but few studies have dealt with three or more objectives.

When more dimensions are added to the problem, the complexity increases and graphical analysis tools are needed for the visualization of the Pareto front to facilitate the decision-making process. In our proposal, the level diagrams tool has been used to consider sustainability preferences in the portfolio selection problem to better understand the tradeoffs between risk, return, and sustainability in a 2D graphical representation. To illustrate the methodology, a

retrospective case of portfolio selection in a European stock exchange is developed. By starting with an opportunity set of 22 institutional SRI open-end funds, we derive the non-dominated surface from information of historical returns and sustainability indices.

Our approach has several advantages over previous work on tricriteria portfolio selection because (i) existing multi-objective techniques for extending mean-variance portfolio selection problems have limited capabilities if the new objectives are nonlinear, and our approach could provide a

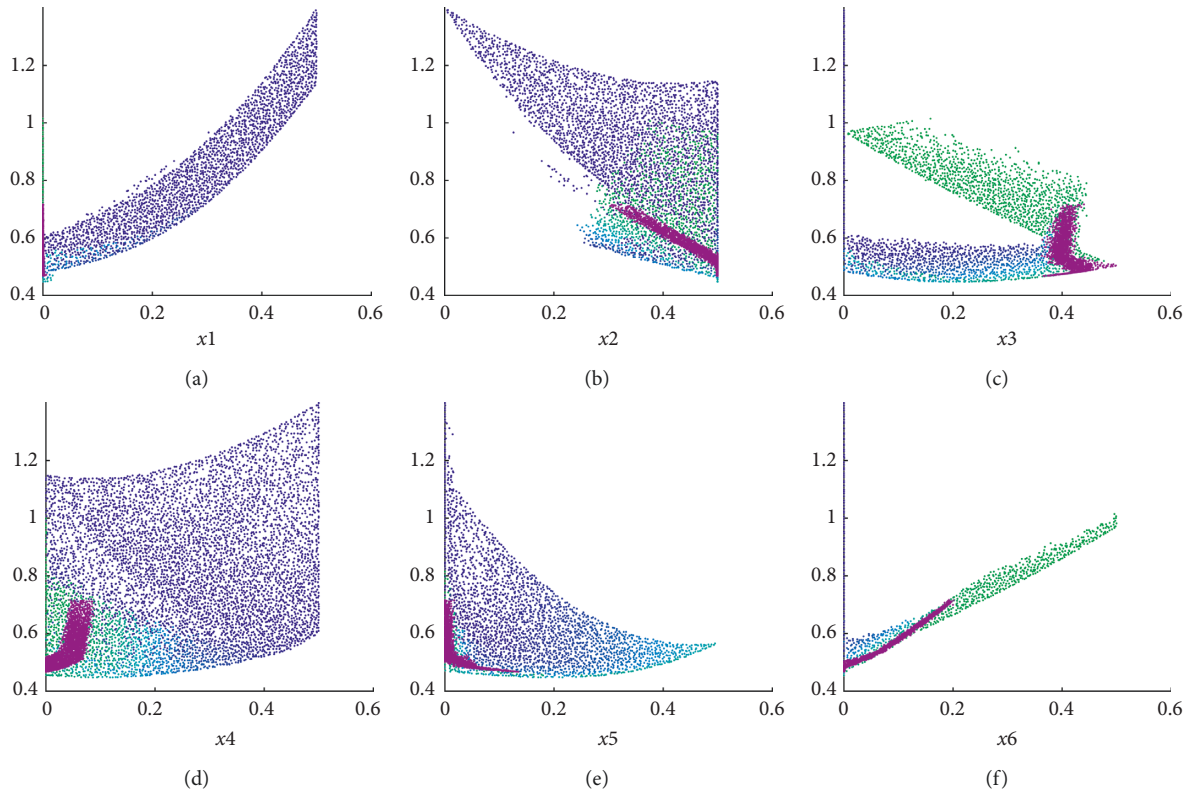


FIGURE 4: 2D LDs corresponding to the Pareto set of the six-stock example.

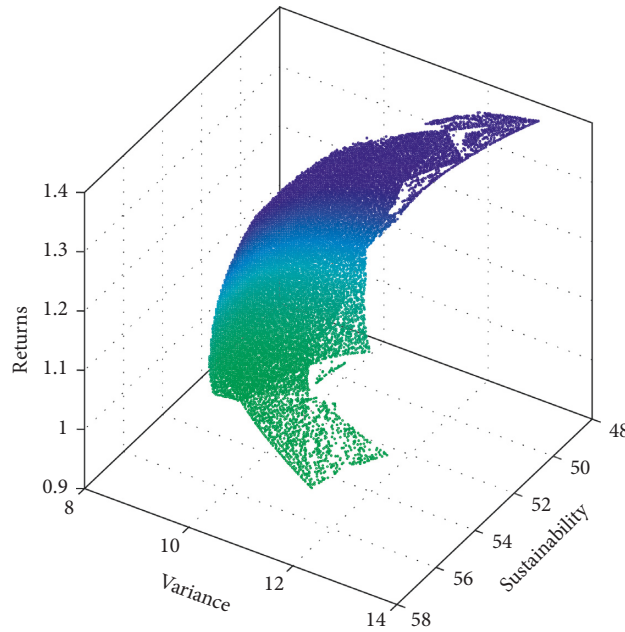


FIGURE 5: 3D ϵ -Pareto front corresponding to the European SRI open-end funds.

general framework for n objectives with no conditions related to the type of the objective function (quadratic, linear, or nonlinear); (ii) the proposed ev-MOGA algorithm adjusts the Pareto front dynamically, ensuring convergence and uniform distribution of solutions; (iii) level diagrams provide a new tool of visualization to better understand the tradeoff between objectives and give a two-dimensional

representation of high-dimensional Pareto fronts and Pareto sets.

Finally, there are several future lines of research for overcoming the limitation of this study. Firstly, to validate the use of our proposed ev-MOGA approach to multi-objective portfolio selection, it would be interesting to conduct a computational comparison of the exact methods

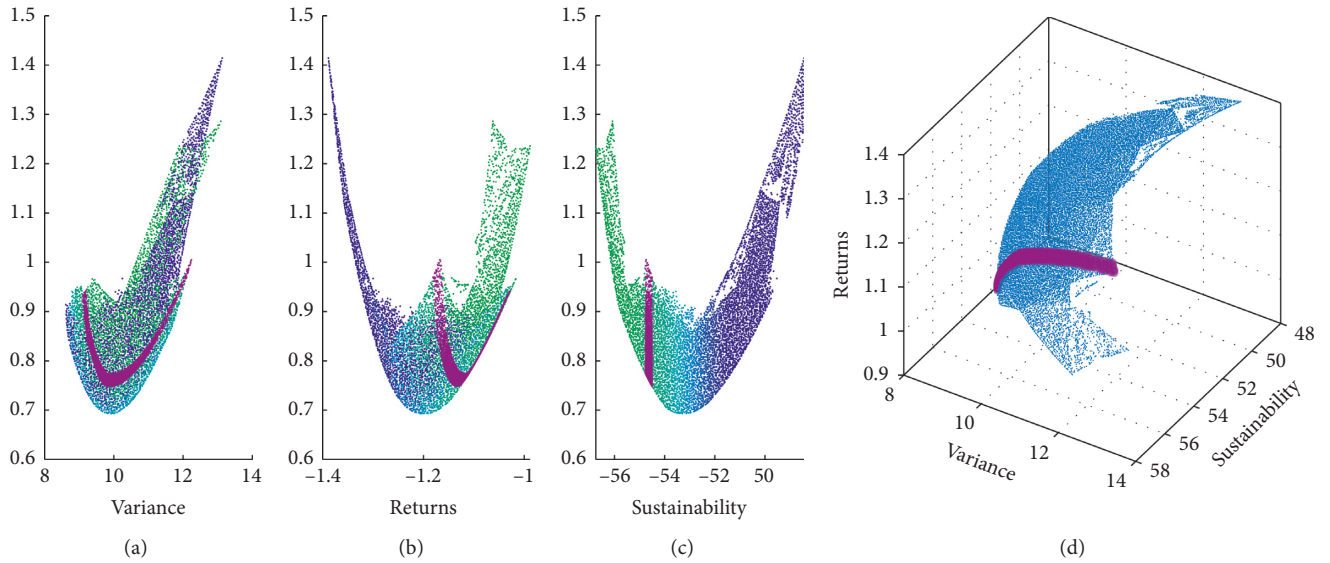


FIGURE 6: 2D LDs corresponding to the Pareto front of the European SRI open-end funds with a coordinated purple set for a sustainability benchmark.

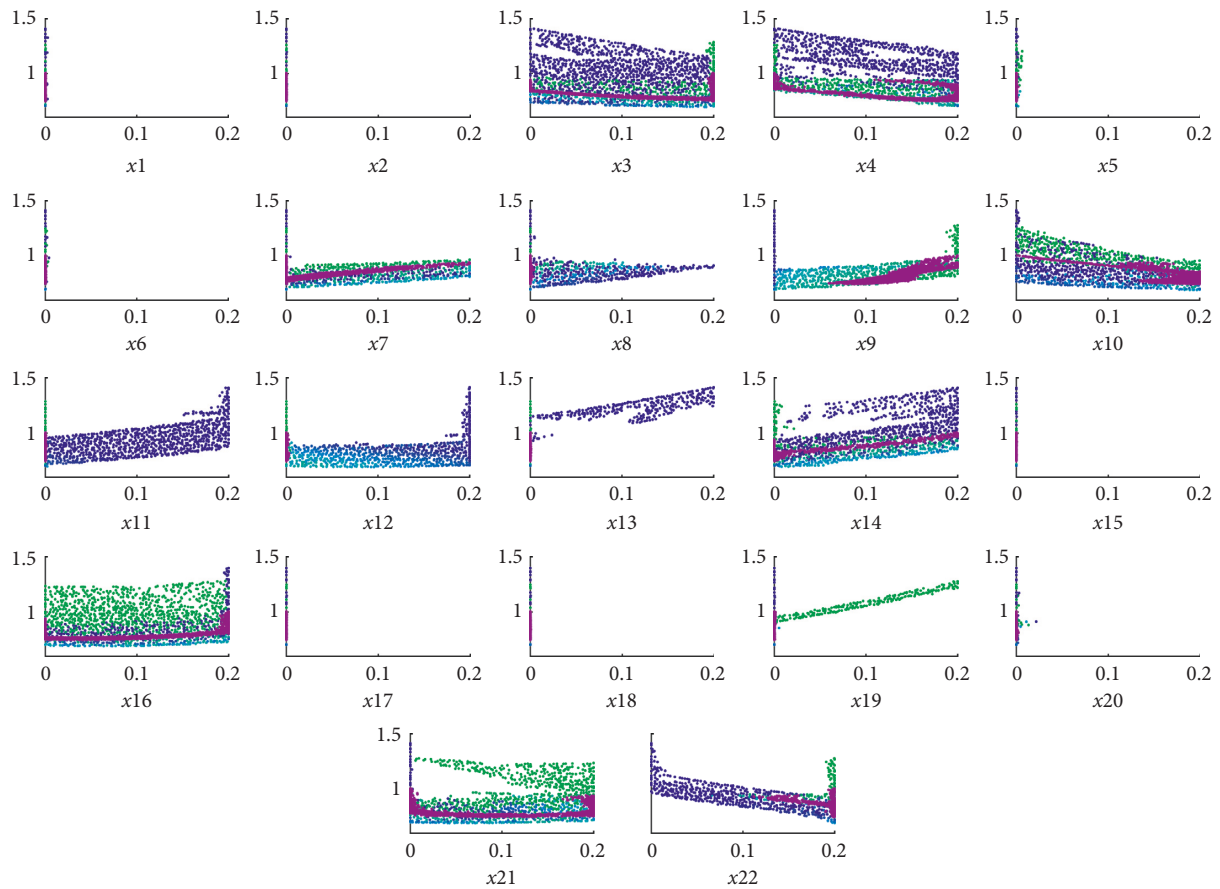


FIGURE 7: 2D LDs corresponding to the Pareto set of the European SRI open-end funds.

previously proposed in the literature, as well as study the advantages and disadvantages of both approaches. Secondly, a future research opportunity would be to extend the proposed model and incorporate other realistic objectives (such

as liquidity, number of securities in the portfolio, or turnover), thus providing a general framework for n objectives. Finally, the impact of estimation errors on mean-variance-sustainability portfolio optimization will be incorporated in

future works to compare the optimal portfolio performance by using resampling approaches and others.

Data Availability

The SRI data from Morningstar of the application used to support the findings of this study are available from the corresponding author upon request.

Conflicts of Interest

The authors declare that they have no conflicts of interest.

Acknowledgments

This work was funded by “Ministerio de Economía y Competitividad” (Spain), research project RTI2018-096904-B-I00, and “Conselleria de Educació, Cultura y Deporte- Generalitat Valenciana” (Spain), research project AICO/2019/055.

References

- [1] N. F. Johnson, P. Jefferies, P. M. Hui et al., *Financial Market Complexity*, OUP Catalogue, Oxford, UK, 2003.
- [2] R. A. Meyers, *Complex Systems in Finance and Econometrics*, Springer Science & Business Media, Berlin, Germany, 2010.
- [3] P. W. Anderson, *The Economy as an Evolving Complex System*, CRC Press, Boca Raton, FL, USA, 2018.
- [4] M. Brunnermeier and M. Oehmke, *Complexity in financial markets*, vol. 8, Princeton University, Princeton, NJ, USA, 2009.
- [5] H. Markowitz, “Portfolio selection,” *The Journal of Finance*, vol. 7, no. 1, pp. 77–91, 1952.
- [6] M. Hirschberger, R. E. Steuer, S. Utz, M. Wimmer, and Y. Qi, “Computing the nondominated surface in tri-criterion portfolio selection,” *Operations Research*, vol. 61, no. 1, pp. 169–183, 2013.
- [7] S. Utz, M. Wimmer, M. Hirschberger, and R. E. Steuer, “Tri-criterion inverse portfolio optimization with application to socially responsible mutual funds,” *European Journal of Operational Research*, vol. 234, no. 2, pp. 491–498, 2014.
- [8] S. Utz, M. Wimmer, and R. E. Steuer, “Tri-criterion modeling for constructing more-sustainable mutual funds,” *European Journal of Operational Research*, vol. 246, no. 1, pp. 331–338, 2015.
- [9] Y. Qi, R. E. Steuer, and M. Wimmer, “An analytical derivation of the efficient surface in portfolio selection with three criteria,” *Annals of Operations Research*, vol. 251, no. 1–2, pp. 161–177, 2017.
- [10] S. M. Gasser, M. Rammerstorfer, and K. Weinmayer, “Markowitz revisited: social portfolio engineering,” *European Journal of Operational Research*, vol. 258, no. 3, pp. 1181–1190, 2017.
- [11] Y. Qi, “On outperforming social-screening-indexing by multiple-objective portfolio selection,” *Annals of Operations Research*, vol. 267, no. 1–2, pp. 493–513, 2018.
- [12] S. Nathaphan and P. Chunhachinda, “Estimation risk modeling in optimal portfolio selection: an empirical study from emerging markets,” *Economics Research International*, vol. 2010, Article ID 340181, 10 pages, 2010.
- [13] R. O. Michaud, “The Markowitz optimization enigma: is “optimized” optimal?,” *Financial Analysts Journal*, vol. 45, no. 1, pp. 31–42, 1989.
- [14] V. DeMiguel, L. Garlappi, and R. Uppal, “Optimal versus naive diversification: how inefficient is the 1/NPortfolio strategy?,” *Review of Financial Studies*, vol. 22, no. 5, pp. 1915–1953, 2009.
- [15] S. Arnone, A. Loraschi, A. Tettamanzi et al., “A genetic approach to portfolio selection,” *Neural Network World*, vol. 3, pp. 597–604, 1993.
- [16] K. Metaxiotis and K. Liagkouras, “Multiobjective evolutionary algorithms for portfolio management: a comprehensive literature review,” *Expert Systems with Applications*, vol. 39, no. 14, pp. 11685–11698, 2012.
- [17] D. Bertsimas and R. Shioda, “Algorithm for cardinality-constrained quadratic optimization,” *Computational Optimization and Applications*, vol. 43, no. 1, pp. 1–22, 2009.
- [18] T.-J. Chang, S.-C. Yang, and K.-J. Chang, “Portfolio optimization problems in different risk measures using genetic algorithm,” *Expert Systems with Applications*, vol. 36, no. 7, pp. 10529–10537, 2009.
- [19] K. Deb, R. E. Steuer, R. Tewari, and R. Tewari, “Bi-objective portfolio optimization using a customized hybrid nsga-ii procedure,” in *Proceedings of the International Conference on Evolutionary Multi-Criterion Optimization*, pp. 358–373, Springer, Ouro Preto, Brazil, April 2011.
- [20] K. P. Anagnostopoulos and G. Mamanis, “The mean–variance cardinality constrained portfolio optimization problem: an experimental evaluation of five multiobjective evolutionary algorithms,” *Expert Systems with Applications*, vol. 38, pp. 14208–14217, 2011.
- [21] M. Woodside-Oriakhi, C. Lucas, and J. E. Beasley, “Heuristic algorithms for the cardinality constrained efficient frontier,” *European Journal of Operational Research*, vol. 213, no. 3, pp. 538–550, 2011.
- [22] B. Chen, Y. Lin, W. Zeng, H. Xu, and D. Zhang, “The mean-variance cardinality constrained portfolio optimization problem using a local search-based multi-objective evolutionary algorithm,” *Applied Intelligence*, vol. 47, no. 2, pp. 505–525, 2017.
- [23] K. Liagkouras, “A new three-dimensional encoding multi-objective evolutionary algorithm with application to the portfolio optimization problem,” *Knowledge-Based Systems*, vol. 163, pp. 186–203, 2019.
- [24] M. Kaucic, M. Moradi, and M. Mirzazadeh, “Portfolio optimization by improved NSGA-II and SPEA 2 based on different risk measures,” *Financial Innovation*, vol. 5, p. 1, 2019.
- [25] Y. L. T. V. Silva, A. B. Herthel, and A. Subramanian, “A multi-objective evolutionary algorithm for a class of mean-variance portfolio selection problems,” *Expert Systems with Applications*, vol. 133, pp. 225–241, 2019.
- [26] K. P. Anagnostopoulos and G. Mamanis, “Multiobjective evolutionary algorithms for complex portfolio optimization problems,” *Computational Management Science*, vol. 8, no. 3, pp. 259–279, 2011.
- [27] M. Gilli, E. Kellezi, and H. Hysi, *A Data-Driven Optimization Heuristic for Downside Risk Minimization*, Swiss Finance Institute, Zürich, Switzerland, 2006.
- [28] M. Ehrgott, K. Klamroth, and C. Schwehm, “An mcdm approach to portfolio optimization,” *European Journal of Operational Research*, vol. 155, no. 3, pp. 752–770, 2004.
- [29] R. E. Steuer, Y. Qi, and M. Hirschberger, “Suitable-portfolio investors, nondominated frontier sensitivity, and the effect of

- multiple objectives on standard portfolio selection,” *Annals of Operations Research*, vol. 152, no. 1, pp. 297–317, 2007.
- [30] K. P. Anagnostopoulos and G. Mamanis, “A portfolio optimization model with three objectives and discrete variables,” *Computers & Operations Research*, vol. 37, no. 7, pp. 1285–1297, 2010.
- [31] GSIA, *Global Sustainable Investment Review 2016*, GSIA, Sydney, Australia, 2016, http://www.gsi-alliance.org/wpcontent/uploads/2015/02/GSIA_Review_download.pdf_1.
- [32] W. Hallerbach, H. Ning, A. Soppe, and J. Spronk, “A framework for managing a portfolio of socially responsible investments,” *European Journal of Operational Research*, vol. 153, no. 2, pp. 517–529, 2004.
- [33] E. Ballester, M. Bravo, B. Pérez-Gladish, M. Arenas-Parra, and D. Plà-Santamaria, “Socially responsible investment: a multicriteria approach to portfolio selection combining ethical and financial objectives,” *European Journal of Operational Research*, vol. 216, no. 2, pp. 487–494, 2012.
- [34] J. M. Cabello, F. Ruiz, B. Pérez-Gladish, and P. Méndez-Rodríguez, “Synthetic indicators of mutual funds’ environmental responsibility: an application of the reference point method,” *European Journal of Operational Research*, vol. 236, no. 1, pp. 313–325, 2014.
- [35] E. Ballester, B. Pérez-Gladish, and A. Garcia-Bernabeu, “Socially responsible investment. A multi-criteria decision making approach,” *International Series in Operations Research & Management Science*, vol. 219, 2015.
- [36] C. Calvo, C. Ivorra, and V. Liern, “Fuzzy portfolio selection with non-financial goals: exploring the efficient frontier,” *Annals of Operations Research*, vol. 245, no. 1-2, pp. 31–46, 2016.
- [37] H. Masri, B. Pérez-Gladish, and C. Zopounidis, *Financial Decision Aid Using Multiple Criteria: Recent Models and Applications*, Springer, Berlin, Germany, 2018.
- [38] A. Bilbao-Terol, M. Jiménez-López, M. Arenas-Parra, and M. V. Rodríguez-Uría, “Fuzzy multi-criteria support for sustainable and social responsible investments: the case of investors with loss aversion,” in *The Mathematics of the Uncertain*, pp. 555–564, Springer, Berlin, Germany, 2018.
- [39] S. M. Lee, *Goal Programming for Decision Analysis*, Auerbach Publishers, Philadelphia, PA, USA, 1972.
- [40] J. Spronk and G. M. Zambruno, “A multiple-criteria approach to portfolio selection,” in *Geld, Banken und Versicherungen, Band 1*, H. Göppel and R. Henn, Eds., pp. 451–459, Athenum, New York, NY, USA, 1981.
- [41] A. Lo, C. Petrov, and M. Wierzbicki, “It’s 11pm—do you know where your liquidity is? the mean- variance-liquidity frontier,” *Journal of Investment Management*, vol. 1, pp. 55–93, 2006.
- [42] M. S. Knoll, “Ethical screening in modern financial markets: the conflicting claims underlying socially responsible investment,” *The Business Lawyer*, vol. 57, pp. 681–726, 2002.
- [43] J. Herrero, *Non-linear Robust Identification Using Evolutionary Algorithms*, Ph.D. thesis, Polytechnic University of Valencia, Valencia, Spain, 2006.
- [44] K. Miettinen, *Nonlinear multiobjective optimization*, vol. 12, Springer Science & Business Media, Berlin, Germany, 2012.
- [45] C. A. C. Coello, “Evolutionary multi-objective optimization and its use in finance,” in *Handbook of Research on Nature Inspired Computing for Economy and Management*, Idea Group Publishing, London, UK, 2006.
- [46] M. Laumanns, L. Thiele, K. Deb, and E. Zitzler, “Combining convergence and diversity in evolutionary multiobjective optimization,” *Evolutionary Computation*, vol. 10, no. 3, pp. 263–282, 2002.
- [47] J. M. Herrero, “Ev-MOGA multiobjective evolutionary algorithm,” 2017, <https://es.mathworks.com/matlabcentral/fileexchange/31080-ev-moga-multiobjective-evolutionary-algorithm>.
- [48] X. Blasco, J. M. Herrero, J. Sanchis, and M. Martínez, “A new graphical visualization of n-dimensional pareto front for decision-making in multiobjective optimization,” *Information Sciences*, vol. 178, no. 20, pp. 3908–3924, 2008.
- [49] G. Reynoso-Meza, “Level diagrams for multiobjective decision making and design concepts comparison,” 2017, <https://es.mathworks.com/matlabcentral/fileexchange/39458-level-diagrams-for-multiobjective-decision-making-and-design-concepts-comparison>.
- [50] Morningstar, “Morningstar sustainability rating,” 2018, https://www.morningstar.com/content/dam/marketing/shared/research/methodology/744156_Morningstar_Sustainability_Rating_for_Funds_Methodology.pdf.

Research Article

Traffic Model and On-Ramp Metering Strategy under Foggy Weather Conditions Using T-S Fuzzy Systems

Changle Sun and Hongyan Gao 

College of Electrical Engineering and Automation, Shandong University of Science and Technology, Qingdao 266590, China

Correspondence should be addressed to Hongyan Gao; gaohongyan0107@163.com

Received 25 June 2019; Revised 15 September 2019; Accepted 19 November 2019; Published 9 December 2019

Guest Editor: Raúl Baños

Copyright © 2019 Changle Sun and Hongyan Gao. This is an open access article distributed under the Creative Commons Attribution License, which permits unrestricted use, distribution, and reproduction in any medium, provided the original work is properly cited.

Foggy weather seriously deteriorates the performance of freeway systems, particularly regarding traffic safety and efficiency. General macroscopic traffic models have difficulty reflecting the characteristics of a freeway under foggy weather conditions. In the present study, a macroscopic traffic model using a correction factor under foggy weather conditions is therefore proposed, which is regulated according to the different levels of visibility and curve radius of the freeway using the Takagi–Sugeno (T-S) model. Based on the proposed traffic model, a local ramp metering strategy with density correction under foggy weather conditions is proposed to improve traffic safety. The proposed local ramp metering strategy regulates the on-ramp flow using the T-S model according to the mainstream density, speed, and visibility. The correction factors are determined based on the parameters of the consequent part in the T-S model, which are optimized using the particle swarm optimization algorithm. The sum of the mean absolute percentage error of the mainstream traffic density and speed is used to evaluate the proposed traffic model. The real-time crash-risk prediction model, which reflects the degree of traffic safety, is used to evaluate the proposed local ramp metering strategy. Simulations using VISSIM and MATLAB show that the proposed traffic model is suitable under foggy weather conditions and that the proposed local ramp metering strategy achieves a better performance in reducing fog-related crashes.

1. Introduction

Foggy weather not only deepens the uncertainty, complexity, and randomness of freeway systems but also brings about a decrease in traffic efficiency and an increase in the number of crashes [1]. Fog-related crashes are mainly related to poor visibility and a large curve radius, which is the radius of a circularly curved section of a freeway [2].

Traffic management strategies for improving traffic safety and efficiency under foggy weather conditions can be divided into two types: advisory strategies and control strategies [3]. Advisory strategies using atmospheric and pavement data combined with the traffic flow and incident data can provide more timely and accurate freeway traffic information for travelers and thereby reduce fog-related crashes [4]. Dynamic traffic information can be automatically conveyed to travelers through dynamic message signs

and freeway advisory announcements provided through a radio station. Control strategies can be divided into two types as well: speed management strategies and traffic flow management strategies. Regarding speed management, automatic visibility warning systems estimate a safe traffic speed for motorists based on the real-time visibility of the freeway as derived from visibility sensors to reduce fog-related crashes [5]. Real-time speed recommendations derived from visibility warning systems can be conveyed using an intelligent transportation system [6, 7]. A visibility warning system is widely used to ensure traffic safety under foggy weather conditions. Using six types of visibility sensors with forward-scatter technology and 25 closed circuit TV cameras, the Alabama Department of Transportation implemented a visibility warning system to reduce fog-related crashes [3]. The Utah Department of Transportation used an Adverse Visibility Information System Evaluation,

which provides real-time speed recommendations for motorists, to reduce fog-related crashes [8, 9]. However, visibility warning systems have significant challenges in terms of cost and the application of appropriate sensor technologies.

In terms of traffic flow management, control strategies are applied to permit or restrict the traffic flow and regulate the freeway capacity. Ramp metering has been recognized as an effective and economic way to regulate mainstream freeway traffic flow at the cost of increasing or decreasing the on-ramp queue length [10]. Existing ramp metering strategies, including fixed-time and real-time ramp metering, have been used well. Based on historical traffic data, fixed-time ramp metering strategies may lead to freeway congestion or underutilization. Real-time ramp metering strategies including local responsive and coordinated ramp metering strategies regulate the mainstream traffic flow based on real-time traffic data. Local ramp metering strategies such as demand capacity, occupancy control, and Asservissement Linéaire d'Entrée Autoroutière (ALINEA) determine the on-ramp flow based on the real-time mainstream traffic conditions. Among them, ALINEA is the most typical type of ramp metering strategy owing to its closed-loop control [11]. Extended algorithms of ALINEA such as downstream-measurement-based adaptive ALINEA (AD-ALINEA), upstream-measurement-based adaptive ALINEA (AU-ALINEA) [12], and proportional-integral extension of ALINEA (PI-ALINEA) [13] have recently been proposed. In addition, intelligent control algorithms such as iterative learning control [14–16], fuzzy logic control (FLC), neural network control [17], and a reinforcement learning control algorithm [18] are used in local ramp metering. Coordinated ramp metering strategies such as METALINE, FLOW, the Zone algorithm, Helper, and SWARM aim at improving the network-wide traffic efficiency of freeways by making full use of all on-ramps. However, the complexity and cost of coordinated ramp metering are much higher than those of local ramp metering [19].

A freeway system is an interconnected nonlinear system that can be represented using a set of linear state equations by applying a fuzzy model. Therefore, FLC appears to be more suitable for ramp metering than an analytic control algorithm. A fuzzy logic controller based on six input variables and three output variables was proposed for ramp metering, which took into account the upstream and downstream traffic states and the length of the on-ramp queue [20]. Experimentally, the fuzzy controller proved its superior performance in reducing congestion and dealing with traffic incidents. In addition, a T-S-type fuzzy controller based on the mainstream density, speed, and queue length applied as inputs and the desired mainstream density applied as the output was proposed [21]. The proposed T-S-type fuzzy controller implements an optimal ramp metering according to the different traffic states using the PSO algorithm. The self-adjusted fuzzy ramp metering strategy based on the correction factor was proposed [21]. The fuzzy control rules of the proposed self-adjusted fuzzy ramp metering strategy are replaced with correction factors. The proposed correction factors simplify the rule definitions of the three-dimensional fuzzy controller. Based on the fuzzy

logic algorithm, many different control strategies such as a genetic-fuzzy algorithm [22] and a genetic-fuzzy algorithm with the optimization algorithm [23] have been proposed. Moreover, a ramp metering strategy based on the fuzzy logic algorithm achieves a good robustness and rapid response to traffic demand [24].

Although studies on local ramp metering under normal weather conditions have been exploited well, few studies have been conducted on local ramp metering under foggy weather conditions. In this study, a macroscopic traffic model based on a model correction factor (c_m) under foggy weather conditions is proposed using the T-S model. The traffic model is regulated using the T-S model according to the different degrees of visibility and the curve radius of the freeway. Freeway traffic data derived from the VISSIM simulator are used for traffic modelling under foggy weather conditions. The sum of the mean absolute percentage error based on the mainstream traffic density and speed is used to evaluate the proposed traffic model. The traffic model parameters are optimized using the PSO algorithm. The proposed traffic model is simulated in MATLAB.

Based on the proposed macroscopic traffic model, a local ramp metering strategy based on a density correction factor (c_d) under foggy weather conditions is proposed. Based on a T-S-type FLC, the proposed local ramp metering strategy regulates the on-ramp flow according to the mainstream density, mainstream speed, and visibility. A real-time crash-risk prediction model reflecting the level of safety of the freeway traffic is used to evaluate the proposed local ramp metering strategy. The parameters of the proposed ramp metering strategy are also optimized using the PSO algorithm, and the proposed local ramp metering strategy is simulated in MATLAB.

2. Macroscopic Traffic Model under Foggy Weather Conditions

2.1. T-S-Type Fuzzy Theory. In this study, the T-S model is adopted for use as a macroscopic traffic model and for local ramp metering under foggy weather conditions. For a T-S-type fuzzy controller, x_m is denoted as the m -th input variable, with $m = 1, \dots, M$, where M is the number of input variables; in addition, $A^i(x_m)$ is denoted as the input fuzzy subset of the input variable x_m corresponding to the i -th fuzzy rule, in which $i = 1, \dots, N$, where N is the number of fuzzy rules. The i -th fuzzy rule is expressed in the IF-THEN form as follows:

$$\begin{array}{l} \text{IF } x_1 \text{ is } A^i(x_1) \text{ AND } x_2 \text{ is } A^i(x_2) \cdots \text{ AND } x_M \text{ is } A^i(x_M) \\ \quad \text{antecedent part} \\ \text{THEN } y^i = p_0^i + p_1^i x_1 + \cdots + p_M^i x_M, \\ \quad \text{consequent part} \end{array} \quad (1)$$

where p_l^i is a constant parameter of the consequent part related to the i -th fuzzy rule, in which $l = 0, 1, \dots, M$, and y^i denotes the output value corresponding to this rule.

In addition, $\mu^i(x_m)$ denotes the membership value of the input variable x_m corresponding to the linguistic variable

$A^i(x_m)$, and μ^i refers to the membership value of the i -th fuzzy rule, which is calculated as follows:

$$\begin{aligned} \mu^i &= \min(\mu^i(x_1), \mu^i(x_2), \dots, \mu^i(x_M)) \\ \text{or } \mu^i &= \mu^i(x_1) * \mu^i(x_2) * \dots * \mu^i(x_M). \end{aligned} \quad (2)$$

The final output of the T-S model is expressed as follows:

$$y = \frac{\sum_i \mu^i y^i}{\sum_i \mu^i}. \quad (3)$$

2.2. Macroscopic Traffic Model with Correction Factor under Foggy Weather Conditions. Considering such factors as the topography and construction costs in the design of a freeway plane alignment, circular curved sections are unavoidable and are applied as a main linear section of a freeway. Owing to the particularity of its linear conditions and the complexity of driving behaviors, such sections have become areas with a high incidence of traffic accidents. The freeway friction coefficient and visibility are reduced under foggy weather conditions, adding to the complexity of driving behaviors on curved sections. The curve radius is the main characteristic of a circular curved section of a freeway, and the crash risk will increase with a decrease in the curve radius. The freeway visibility and curve radius are two of the most critical factors affecting the traffic model applied under foggy weather conditions. METANET [25] is a well-known macroscopic traffic model. However, it has difficulty reflecting freeway characteristics under foggy weather. Therefore, in this study, a traffic model applied under foggy weather conditions that introduces a model correction factor (c_m) into the METANET traffic model is proposed. This model correction factor can reflect the effects of foggy weather on a freeway because the factor is regulated according to the different levels of visibility and the curve radius of the freeway. The model correction factor is directly determined using the T-S model. The proposed traffic model is expressed as follows:

$$\rho_i(k+1) = c_m \cdot \left(\rho_i(k) + \frac{T}{\Delta_i} [q_{i-1}(k) - q_i(k) + u_i(k)] \right), \quad (4)$$

$$q_i(k) = \rho_i(k) \cdot v_i(k) \cdot \lambda_i, \quad (5)$$

$$\begin{aligned} v_i(k+1) &= c_m \cdot \left(v_i(k) + \frac{T}{\tau} [V(\rho_i(k)) - v_i(k)] \right. \\ &\quad + \frac{T}{\Delta_i} v_i(k) [v_{i-1}(k) - v_i(k)] \\ &\quad \left. - \frac{\gamma T}{\tau \Delta_i} \frac{\rho_{i+1}(k) - \rho_i(k)}{\rho_i(k) + \theta} \right), \end{aligned} \quad (6)$$

$$V(\rho_i(k)) = v_f \cdot \left[1 - \left(\frac{\rho_i(k)}{\rho_{\text{jam}}} \right)^\delta \right]^m, \quad (7)$$

where T is the length of the time step; k indicates the time step $t = kT$, where $k = 1, \dots, \lambda_i$ denotes the number of lanes

in the segment i ; $v_i(k)$ and $\rho_i(k)$ are the average speed and average mainstream density in the segment i at the time step kT , respectively; $q_i(k)$ represents the mainstream flow through the segment i entering the next segment during the time step kT ; $u_i(k)$ represents the on-ramp metering flow entering the segment i at the time step kT ; the notations v_f , ρ_{jam} , Δ_i , and $V(\rho_i(k))$ represent the free-flow speed, the jam density, the length of the segment i , and the static speed in the segment i at the time step kT , respectively; m , γ , τ , δ , and θ are global parameters reflecting the freeway characteristics; and c_m denotes the model correction factor. Equations (4)–(7) are for determining the conservation, traffic parameter relationship, dynamic mean speed, and static speed-density relationship, respectively.

2.3. Model Correction Factor Regulation Based on T-S Model.

The visibility and curve radius are the two most important factors affecting freeway traffic under the foggy weather condition. Thus, in this study, the freeway visibility and curve radius are applied as input variables of the T-S model, and the model correction factor is applied as the output variable. The freeway visibility and curve radius can be obtained from a freeway information system. The freeway visibility and curve radius at the time step kT are denoted as $r(k)$ and $b(k)$, respectively. Assume that $A(r)$ and $A(b)$ are the input fuzzy sets of the input variables $r(k)$ and $b(k)$, respectively. Two input fuzzy subsets are defined for each input fuzzy set. The normalized domain of the input fuzzy sets and the input variables is $[-1, 1]$. It is assumed that the actual physical domains of the visibility and radius curve are $[r_1, r_2]$ and $[b_1, b_2]$, respectively. The mean values of r_m and b_m and the scaling factors K_r and K_b are used to transform the physical domains $[r_1, r_2]$ and $[b_1, b_2]$ into the normalized domains $[-1, 1]$ and $[-1, 1]$, respectively, the mathematical formulas of which are as follows:

$$\begin{aligned} r_m &= \frac{r_1 + r_2}{2}, \\ b_m &= \frac{b_1 + b_2}{2}, \\ K_r &= \frac{1}{(r_2 - r_m)}, \\ K_b &= \frac{1}{(b_2 - b_m)}. \end{aligned} \quad (8)$$

Thus, the measured values $r(k)$ and $b(k)$ can be transformed into the normalized domain using the appropriate scaling factors as follows:

$$\begin{aligned} A(r) &= K_r \cdot (r(k) - r_m), \\ A(b) &= K_b \cdot (b(k) - b_m). \end{aligned} \quad (9)$$

The membership function of normalized input fuzzy sets described using a trapezoidal function [26] is as shown in Figure 1.

There are four different combinations of input variables in the fuzzy rules, as summarized in Table 1.

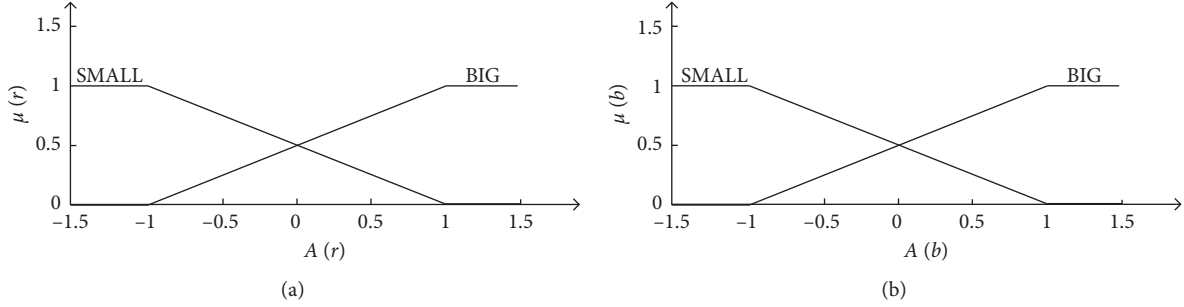


FIGURE 1: Membership functions of (a) visibility and (b) curve radius.

TABLE 1: Combinations of input variables in fuzzy rules.

i	$A(r)$	$A(b)$
1	SMALL	BIG
2	SMALL	SMALL
3	BIG	SMALL
4	BIG	BIG

An example of a fuzzy rule is expressed in the IF-THEN form as follows:

$$\begin{array}{l} \text{IF } r \text{ is BIG AND } b \text{ is SMALL} \\ \text{antecedent part} \\ \text{THEN } c_m^i = \beta_0^i + \beta_1^i r + \beta_2^i b, \\ \text{consequent part} \end{array} \quad (10)$$

where β_j^i , in which $j=0, 1, 2$, is a constant parameter of the consequent part corresponding to the i -th fuzzy rule and c_m^i denotes the output value corresponding to the i -th fuzzy rule.

According to equations (1)–(3), the model correction factor (c_m) is calculated as follows:

$$c_m = \frac{\sum_i \mu^i c_m^i}{\sum_i \mu^i}. \quad (11)$$

The T-S model of the model correction factor contains four fuzzy rules, and each fuzzy rule has three parameters to be regulated. Thus, the T-S model regulates a total of 12 parameters. Including v_f , τ , ρ_{jam} , m , γ , θ , and δ , there are a total of 19 parameters to be regulated in the proposed traffic model. The performance of the T-S model depends on the structure and parameter identification. However, in this study, the performance of the T-S model is merely related to the parameters of the consequent part because the input fuzzy sets are predefined. Therefore, to minimize the performance objective, the problem of traffic modelling under foggy weather conditions is equivalent to seeking the optimal values of the 19 parameters. The PSO algorithm is adopted to optimize these parameters.

2.4. Parameter Regulation Based on PSO. As a swarm intelligence algorithm, PSO is inspired by the search strategy applied in the foraging behaviors of organisms such as flocking bird [27]. The PSO algorithm is based on a population iterative search. For the parameter optimization, each particle denotes a set of candidate solutions. Each

particle includes the position and velocity, which determine its direction and distance of flight, as well as the fitness value calculated using a fitness function. During the particle search process, each particle can update its position in a better direction by tracking the individual and global best positions. If the number of iterations reaches the maximum, the global best position of the particle swarm is the optimal solution. During each iteration, each particle updates its velocity and position by tracking the individual and global best positions as follows [28]:

$$\begin{aligned} v_i^{j+1} &= wv_i^j + c_1r_1(p_i^j - x_i^j) + c_2r_2(p_g^j - x_i^j), \\ x_i^{j+1} &= x_i^j + v_i^{j+1}, \end{aligned} \quad (12)$$

where i refers to the index of the particle, j represents the index of the iteration, v_i^j denotes the velocity of the i -th particle during the j -th iteration, x_i^j denotes the position of the i -th particle during the j -th iteration, p_i^j is the individual best position of the i -th particle during the j -th iteration, p_g^j is the global best position of the particle swarm during the j -th iteration, w is the inertia weight, c_1 and c_2 are learning factors regulating the attraction of the individual and global best positions to the particle, and r_1 and r_2 are random values within the range of zero to 1.

During the application of the PSO algorithm, the fitness function is used to evaluate the effectiveness of the parameter optimization during the k -th iteration. The sum of the mean absolute percentage error of the mainstream traffic density and speed is used for the fitness function. The fitness function is expressed as follows:

$$J = 0.5 \sum_{1 \leq k \leq K} \left\{ \frac{|\rho_o(k) - \rho_i(k)|}{\rho_o(k)} + \frac{|v_o(k) - v_i(k)|}{v_o(k)} \right\}, \quad (13)$$

where k indicates the time step $t = kT$, where $k = 1, 2, \dots, K$ is the total time period; $\rho_o(k)$ and $\rho_i(k)$ are the actual mainstream density and the density derived from the proposed traffic model at the time step kT , respectively; and $v_o(k)$ and $v_i(k)$ are the actual mainstream speed and the speed derived from the proposed traffic model at the time step kT , respectively; in addition, the data on $\rho_o(k)$ and $v_o(k)$ under foggy weather conditions can be obtained from a freeway information system.

The mainstream traffic flow is a product of the mainstream traffic density and speed, and thus, the mainstream flow is indirectly taken into account through the fitness

function. It is known that the speed, density, and flow are considered to be explanatory variables of the freeway traffic model. Therefore, the fitness function, which includes the mainstream speed, density, and flow, represents a comprehensive assessment of the proposed traffic model.

The implementation steps of the PSO algorithm are divided into two parts: initialization and iteration.

2.4.1. Initialization Part

Step 1. Set the particle swarm size as 100, the number of particle dimensions as 19, the maximum number of iterations as 300, both c_1 and c_2 as 2, and the inertia weight w as 0.8.

Step 2. Initialize the position and velocity vectors for each particle randomly while taking into account the particle limits.

Step 3. Input the traffic data on the flow, speed, and density.

Step 4. Randomly set the initial solution of each particle, and initialize the individual and global best positions.

2.4.2. Iteration Part

Step 1. Calculate the fitness value of each particle according to equations (4)–(7) and (12).

Step 2. Determine the individual and global best positions for the i -th particle at the j -th iteration, and if the fitness value is smaller than the previous fitness value, let the individual best position $p_i^j = x_i^j$; otherwise, the individual best position p_i^j remains unchanged. In addition, if the individual best position p_i^j is smaller than the global best position p_g^j , let $p_g^j = p_i^j$; otherwise, the global best position p_g^j remains unchanged.

Step 3. Update the velocity and position of each particle according to equation (11).

Step 4. Repeat the iteration part until the maximum number of iterations is satisfied.

3. Local Ramp Metering under Foggy Weather Conditions

During the past several decades, studies on local ramp metering under normal weather conditions have been well exploited. However, the problem of local ramp metering under foggy weather conditions has been rarely studied. Because of traffic safety, on-ramps are typically closed under foggy weather conditions. The consequence of closing an on-ramp is not only a reduction in the mainstream traffic flow but also a decrease in the traffic efficiency. Therefore, improving the freeway traffic efficiency during foggy weather on the basis of ensuring traffic safety is a popular area of study. Owing to the complexity of foggy weather conditions, the desired density

varies from moment to moment, which cannot be properly solved using PI-ALINEA. Thus, the application of local ramp metering under foggy weather conditions is proposed.

A ramp metering strategy similar to PI-ALINEA is applied in the present paper. PI-ALINEA is expressed as follows:

$$u(k+1) = u(k) - K_P[\rho(k) - \rho(k-1)] + K_R[\rho_d - \rho(k)], \quad (14)$$

where K_P and K_R are the gain factors for the proportional and integral terms, respectively.

The proposed local ramp metering strategy based on the density correction factor (c_d) can regulate the on-ramp flow according to the freeway traffic state. In addition, the density correction factor (c_d) is directly determined using the T-S model. The proposed local ramp metering strategy based on the density correction factor (c_d) can be expressed as follows:

$$u(k+1) = u(k) - K_P[\rho(k) - \rho(k-1)] + K_R[\rho_d - \rho(k)], \quad (15)$$

$$\rho_d = \rho_p \cdot c_d, \quad (16)$$

where K_P and K_R are the gain factors for the proportional and integral terms, respectively; ρ_p is the predefined density value; and c_d represents the density correction factor.

The mainstream traffic density (ρ), speed (v), and visibility (r) of the freeway are three key factors affecting the traffic safety under foggy weather conditions. Thus, this paper sets the mainstream traffic density (ρ), speed (v), and visibility (r) as input variables of the T-S model and the density correction factor (c_d) as the output variable. Assume that $A(\rho)$, $A(v)$, and $A(r)$ are input fuzzy sets of the mainstream density, speed, and visibility, respectively. Two fuzzy subsets are defined for each input fuzzy set. The normalized domains of the input fuzzy sets and input variables are all $[-1, 1]$. Assume that the actual physical domains of the visibility, speed, and visibility are $[\rho_1, \rho_2]$, $[v_1, v_2]$, and $[r_1, r_2]$, respectively. The mean values of ρ_m , v_m , and r_m and the scaling factors K_ρ , K_v , and K_r transform the physical domains $[\rho_1, \rho_2]$, $[v_1, v_2]$, and $[r_1, r_2]$ into the normalized domains $[-1, 1]$, $[-1, 1]$, and $[-1, 1]$, respectively, the mathematical formulas of which are as follows:

$$\begin{aligned} \rho_m &= \frac{\rho_1 + \rho_2}{2}, \\ v_m &= \frac{v_1 + v_2}{2}, \\ r_m &= \frac{r_1 + r_2}{2}, \\ K_\rho &= \frac{1}{\rho_2 - \rho_m}, \\ K_v &= \frac{1}{v_2 - v_m}, \\ K_r &= \frac{1}{r_2 - r_m}. \end{aligned} \quad (17)$$

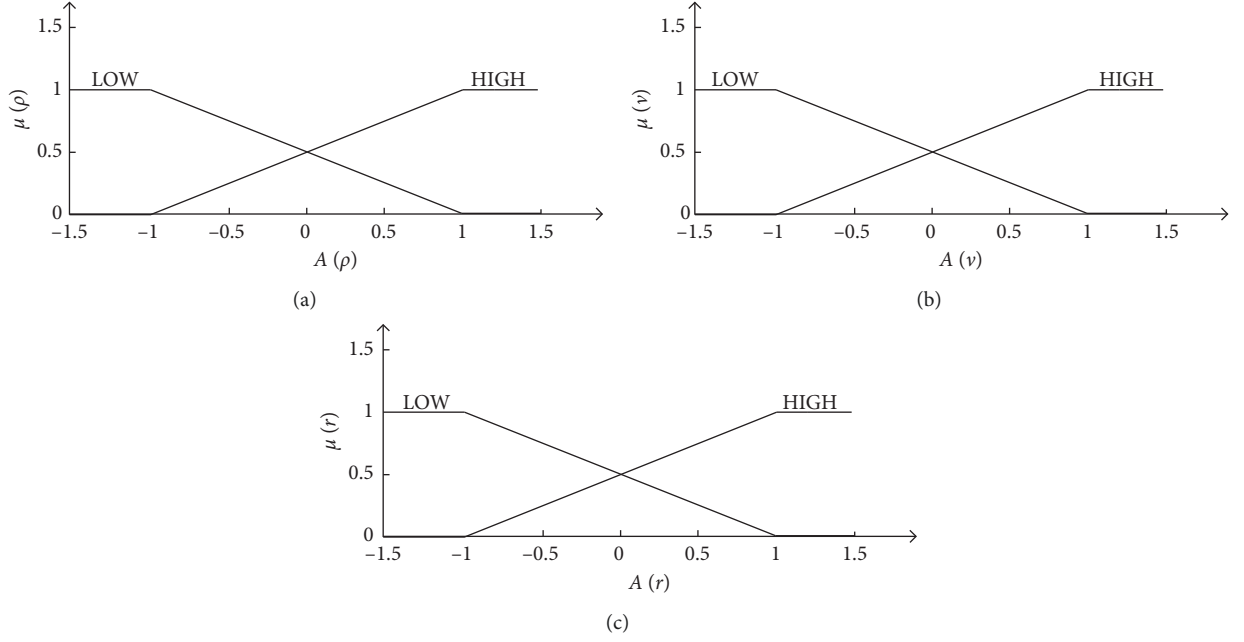


FIGURE 2: Membership functions of (a) mainstream density, (b) mainstream speed, and (c) visibility.

TABLE 2: Combinations of input variables used in fuzzy rules.

i	$A(\rho)$	$A(v)$	$A(r)$
1	HIGH	LOW	HIGH
2	HIGH	LOW	LOW
3	LOW	HIGH	HIGH
4	LOW	HIGH	LOW

Thus, the measured values $r(k)$ and $b(k)$ can be transformed into the normalized domain as follows:

$$\begin{aligned} A(\rho) &= K_\rho \cdot (\rho(k) - \rho_m), \\ A(v) &= K_v \cdot (v(k) - v_m), \\ A(r) &= K_r \cdot (r(k) - r_m). \end{aligned} \quad (18)$$

The membership function of the normalized input fuzzy sets described using a trapezoidal function is shown in Figure 2.

Owing to dynamic characteristics of a traffic flow, when the mainstream traffic density is high, the mainstream traffic speed should be low. Therefore, four different combinations of input variables are applied in the fuzzy rules, as summarized in Table 2.

For example, the i -th fuzzy rule is expressed as follows:

$$\begin{aligned} &\underbrace{\text{IF } \rho \text{ is HIGH AND } v \text{ is LOW AND } r \text{ is HIGH}}_{\text{antecedent part}} \\ &\quad \underbrace{\text{THEN } c_d^i = o_0^i + o_1^i \rho + o_2^i v + o_3^i r}_{\text{consequent part}}, \end{aligned} \quad (19)$$

where o_j^i , in which $j = 0, 1, 2, 3$, is a constant parameter of the consequent part corresponding to the i -th fuzzy rule and c_d^i denotes the output value corresponding to the i -th fuzzy rule.

According to equations (1)–(3), the density correction factor (c_d) can be calculated as follows:

$$c_d = \frac{\sum_i \mu^i c_d^i}{\sum_i \mu^i}. \quad (20)$$

According to equations (15) and (18), the desired density can be calculated as follows:

$$\rho_d = \rho_p \cdot \left(\frac{\sum_i \mu^i c_d^i}{\sum_i \mu^i} \right). \quad (21)$$

The T-S model of the density correction factor contains four fuzzy rules, each of which has four parameters to be regulated. Thus, the T-S model has 16 parameters to regulate in the proposed local ramp metering strategy. The PSO algorithm is used to optimize these 16 parameters.

The principle and implementation steps of the PSO algorithm are described in Section 2.4. The determined difference is the fitness function. Freeway traffic safety during foggy weather conditions is the primary control target. Thus, the real-time crash-risk prediction model, which reflects the traffic safety, is used as the fitness function to evaluate the proposed local ramp metering. The real-time crash-risk prediction model is actually described as a logistic regression function of the freeway traffic variables and regulates the model parameters using the actual freeway traffic incident data. The real-time crash-risk prediction model [29] is calculated as follows:

$$\bar{V}_U(t - \Delta T, t) = \frac{\sum_{\lambda=1}^{\lambda_i} \sum_{n=1}^{N_1} V_U^\lambda(t_n - \Delta t, t_n)}{\lambda_i \cdot N_1}, \quad (22)$$

$$\bar{V}_D(t - \Delta T, t) = \frac{\sum_{\lambda=1}^{\lambda_i} \sum_{n=1}^{N_1} V_D^\lambda(t_n - \Delta t, t_n)}{\lambda_i \cdot N_1}, \quad (23)$$

$$\bar{O}_U(t - \Delta T, t) = \frac{\sum_{\lambda=1}^{\lambda_i} \sum_{n=1}^{N_1} O_D^\lambda(t_n - \Delta t, t_n)}{\lambda_i \cdot N_1}, \quad (24)$$

$$\text{RCRI} = \frac{[\bar{V}_U(t - \Delta T, t) - \bar{V}_D(t - \Delta T, t)] \cdot \bar{O}_U(t - \Delta T, t)}{1 - \bar{O}_U(t - \Delta T, t)}, \quad (25)$$

$$\sigma(O_U) = \sqrt{\frac{\sum_{\lambda=1}^{\lambda_i} \sum_{n=1}^{N_1} [O_U^\lambda(t_n - \Delta t, t_n) - \bar{O}_U(t - \Delta T, t)]^2}{\lambda_i \cdot N_1}}, \quad (26)$$

$$\sigma(O_D) = \sqrt{\frac{\sum_{\lambda=1}^{\lambda_i} \sum_{n=1}^{N_1} [O_D^\lambda(t_n - \Delta t, t_n) - \bar{O}_D(t - \Delta T, t)]^2}{\lambda_i \cdot N_1}}, \quad (27)$$

$$\text{Logit}(P(Y = 1)) = \alpha_1 + \alpha_2 \cdot \text{RCRI} + \alpha_3 \cdot \sigma(O_U) + \alpha_4 \cdot \sigma(O_D), \quad (28)$$

$$P(Y = 1) = \frac{\exp(\alpha_1 + \alpha_2 \cdot \text{RCRI} + \alpha_3 \cdot \sigma(O_U) + \alpha_4 \cdot \sigma(O_D))}{1 + \exp(\alpha_1 + \alpha_2 \cdot \text{RCRI} + \alpha_3 \cdot \sigma(O_U) + \alpha_4 \cdot \sigma(O_D))}, \quad (29)$$

where $\bar{V}_U(t - \Delta T, t)$ and $\bar{V}_D(t - \Delta T, t)$ are the average speed in the upstream and downstream segments during the time period ΔT , respectively; $\bar{O}_U(t - \Delta T, t)$ denotes the average occupancy in the upstream segment during the time period ΔT ; RCRI represents the rear-end collision risk induced by kinematic waves; and $V_U^\lambda(t_n - \Delta t, t_n)$ and $V_D^\lambda(t_n - \Delta t, t_n)$ are the average speed of the λ -th lane in the upstream and downstream segments during the time interval Δt , respectively. In addition, $O_U^\lambda(t_n - \Delta t, t_n)$ is the average occupancy of the λ -th lane in the upstream segment during the time interval Δt ; $\sigma(O_U)$ and $\sigma(O_D)$ are the standard deviation of the occupancy in the upstream and downstream segments during the time period ΔT , respectively; λ_i is the number of lanes in the segment i ; N_1 is the number of time intervals in a single time period ($N_1 = \Delta T / \Delta t$); $P(Y = 1)$ is the probability of a crash; and α_1 , α_2 , α_3 , and α_4 are constant parameters.

In this study, the performance of the T-S model is simply related to the parameters of the consequent part because the input fuzzy sets are predefined. Therefore, the problem of local ramp metering under foggy weather conditions is equivalent to seeking the optimal values of the 16 parameters to minimize the performance objective. The configuration parameters of the PSO algorithm used in the proposed local ramp metering strategy are listed in Table 3.

4. Simulation Experiment and Analysis

4.1. Simulation of Traffic Model under Foggy Weather Conditions

4.1.1. Experimental Setup. The hypothetical freeway stretch is divided into five segments with a length of Δx_i , namely, $\Delta x_1 = 643$ m, $\Delta x_2 = 643$ m, $\Delta x_3 = 643$ m, $\Delta x_4 = 643$ m, and $\Delta x_5 = 643$ m. The hypothetical freeway stretch has two lanes and two on-ramps. The lengths of on-ramps R1 and R2 are

TABLE 3: Combinations of input variables in fuzzy rules.

Parameter	Value
N_2 (swarm size)	100
K	300
w	0.8
c_1	2.0
c_2	2.0

both 400 m. The hypothetical freeway stretch is shown in Figure 3.

Segment 4 is used for traffic modelling under foggy weather conditions. The freeway traffic data under such conditions derived from VISSIM with time intervals of 5 min are used as inputs for the traffic modelling, as shown in Figure 4. The demand (Q_3) of segment 3 from detector 4 and demand (d_2) of on-ramp R2 from detector 8 are shown in Figure 4(a). The units of the segment 3 demand (Q_3) and on-ramp R2 demand (d_2) are both the hourly flow. The average speed (V_3) of segment 3 from detector 4 and the density (ρ_5) of segment 5 from detector 6 are shown in Figures 4(b) and 4(c), respectively. The experiment simulates the freeway traffic from 1:00 am to 23:40 pm with a simulation time step of 10 s.

The higher the fog concentration, the lower the visibility. To analyze the effects of foggy weather on the freeway conditions, the traffic data on the density and speed in segment 4 are sampled from VISSIM under different freeway visibility conditions, as shown in Figure 5. As Figure 5(a) indicates, the desired density of the freeway decreases with the elevated concentration of fog. As shown in Figure 5(b), the speed fluctuation is greater with the increase in fog concentration. Therefore, the freeway traffic safety and efficiency decrease with the elevated concentration of fog. The influence of foggy weather on the traffic model is mainly in terms of density and speed.

The proposed traffic model was simulated using the traffic data under foggy weather conditions as derived from VISSIM. Two cases were simulated with a visibility of $r = 150$ m and a curve radius of $b = 1,500$ m. For case 1, one model correction factor is used for the traffic model under foggy weather conditions. For case 2, two model correction factors are used for the traffic model under such conditions. The parameters used for the proposed traffic model are set as follows: initial speed $v(1) = 97$ km/h and initial density $\rho(1) = 0.735$ veh/km/ln, where the actual physical domains of the visibility and curve radius in the traffic model are [100 m, 200 m] and [500 m, 1,500 m], respectively. According to equation (8), mean values of $r_m = 100$ m and $b_m = 1000$ m and scaling factors of $K_r = 0.02$ and $K_b = 0.002$ are used.

4.1.2. Simulation Results and Analysis. As shown in Figure 6, one model correction factor (c_m) is applied to the main-stream traffic density and velocity. The fitness value is used to evaluate the performance of the proposed traffic model. According to equation (12), the fitness value of the traffic model with one model correction factor (c_m) is 5.96%. As

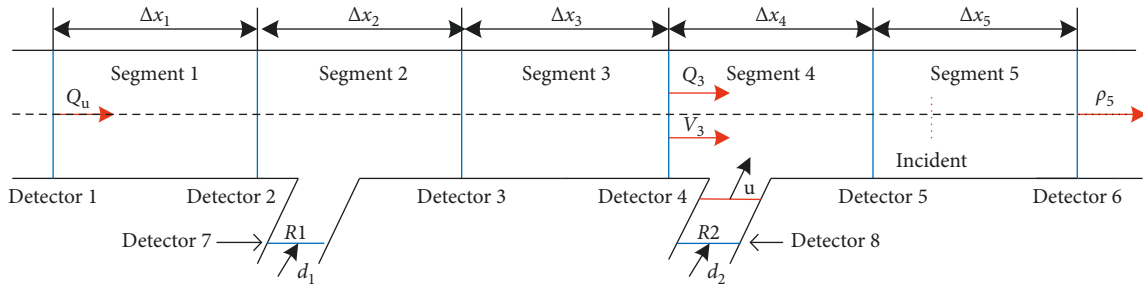


FIGURE 3: Hypothetical freeway stretch.

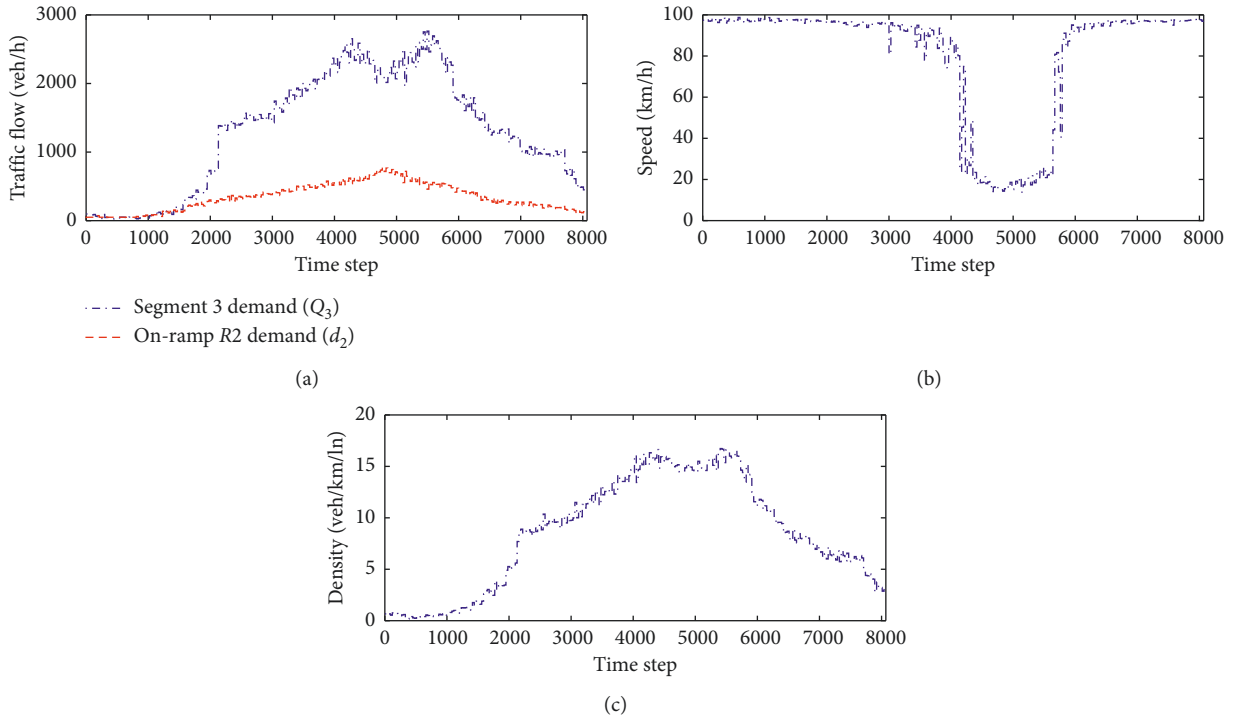


FIGURE 4: (a) Demands of segment 3 and on-ramp R2, (b) average speed of segment 3, and (c) average density of segment 5.

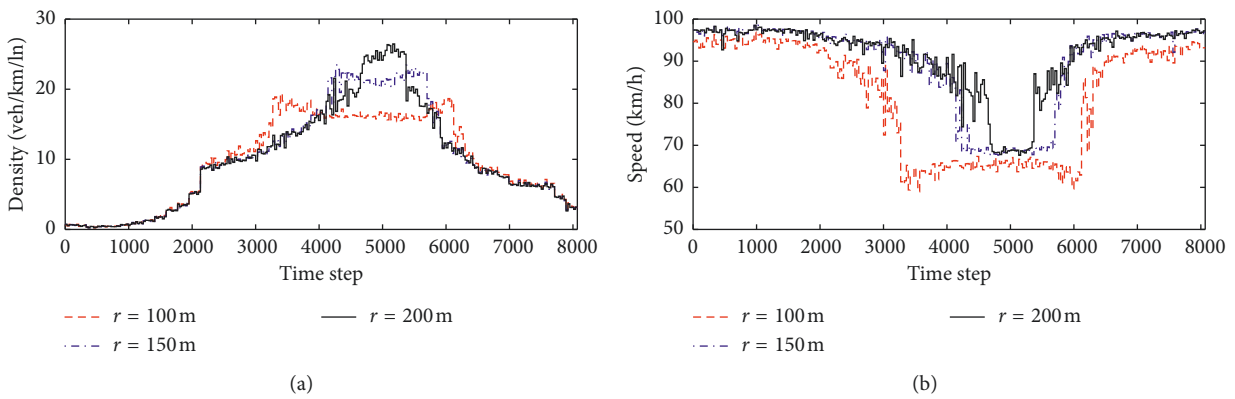


FIGURE 5: (a) Mainstream density and (b) mainstream speed under different foggy weather conditions.

indicated in Figure 7, two model correction factors c_{m1} and c_{m2} are applied to the mainstream traffic density and speed, respectively. The fitness value of the traffic model with two

model correction factors is 6.22%. Clearly, the traffic model with one model correction factor achieves a better performance than that with two factors.

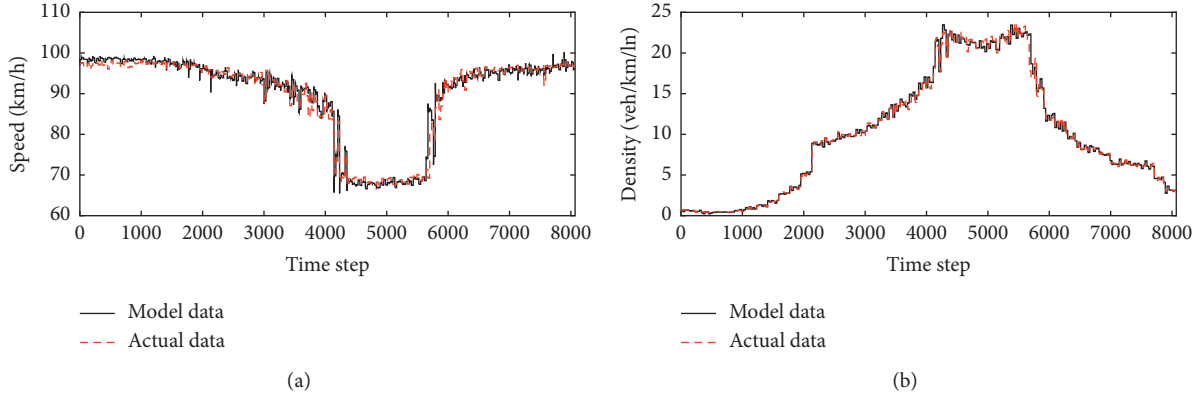


FIGURE 6: (a) Model speed and actual speed and (b) model density and actual density of case 1.

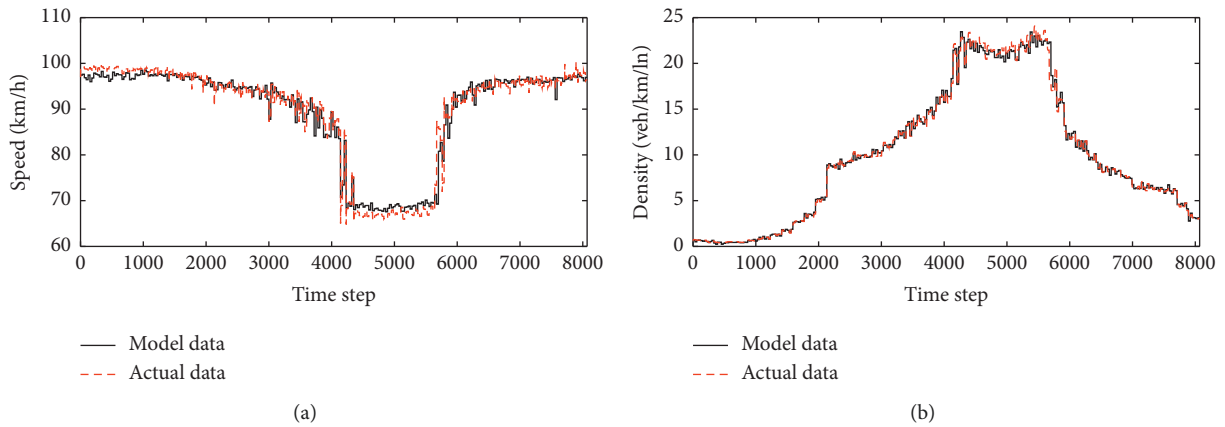


FIGURE 7: (a) Model speed and actual speed and (b) model density and actual density of case 2.

The 19 parameters used in the traffic model with one model correction factor through the PSO algorithm are regulated as follows: $\rho_{jam} = 88.9889$ veh/km/ln, $v_f = 99.1510$ km/h, $\tau = 18$ s, $\gamma = 45.5616$ km²/h, $\theta = 11.0836$ veh/km, $m = 1$, $\delta = 1.1861$, $f_1 = 0.7631$, $f_2 = 0.5976$, $f_3 = 0.2099$, $f_4 = 0.6452$, $f_5 = 0.1955$, $f_6 = 0.3291$, $f_7 = 0.7095$, $f_8 = 0.1745$, $f_9 = 0.3159$, $f_{10} = 0.0034$, $f_{11} = 0.0535$, and $f_{12} = 0.3515$. The model correction factor (c_m) is calculated from parameters f_1 through f_{12} , and the value of 0.99 is obtained.

4.2. Simulation of the Proposed Ramp Metering Strategy under Foggy Weather Conditions

4.2.1. Experimental Setup. Freeway traffic data with time intervals of 10 s, such as for the upstream demand (Q_u) and on-ramp demand (d_1 and d_2), are employed as the input data of the local ramp metering under foggy weather conditions, as shown in Figure 8. The units of upstream demand (Q_u), on-ramp R1 demand (d_1), and on-ramp R2 demand (d_2) are all hourly flow. The simulation time step is 10 s, and the control time step is 30 s. Owing to the low on-ramp flow, a no-control measure is used for on-ramp R1. On-ramp R2 is controlled using PI-ALINEA and the proposed ramp metering strategy. PI-ALINEA is described in equation (13). The simulations are carried out using a visibility of 150 m

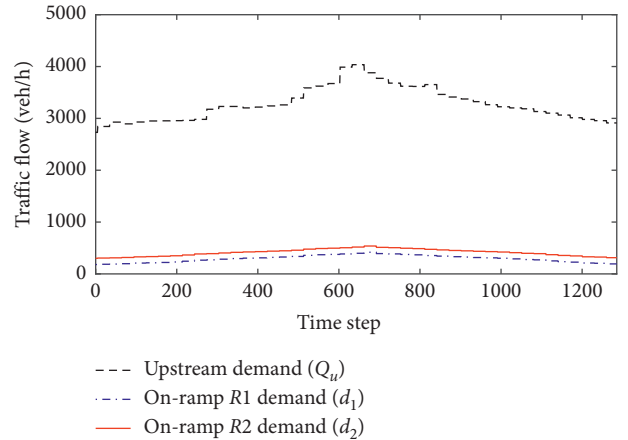


FIGURE 8: Traffic demand of upstream, on-ramp R1, and on-ramp R2.

and a curve radius of 1,200 m. The parameters used for the traffic modelling are set as follows: initial upstream demand $Q_u(1) = 2730$ veh/h, initial on-ramp R1 demand $d_1(1) = 181$ veh/h, initial on-ramp R2 demand $d_2(1) = 301$ veh/h, maximum ramp metering flow $u_{max} = 1000$ veh/h, and minimum ramp metering $u_{min} = 100$ veh/h, and the actual

TABLE 4: Partial traffic data.

$\sigma(O_U)$	$\sigma(O_D)$	RCRI	Y
0.098089	0.088339	-4.50532	1
0.031236	0.032004	-23.0141	1
0.113061	0.013629	-34.9231	1
0.072684	0.014553	-0.28159	0
0.031923	0.045414	-0.68701	0
0.672758	0.080934	-4.76873	0
...

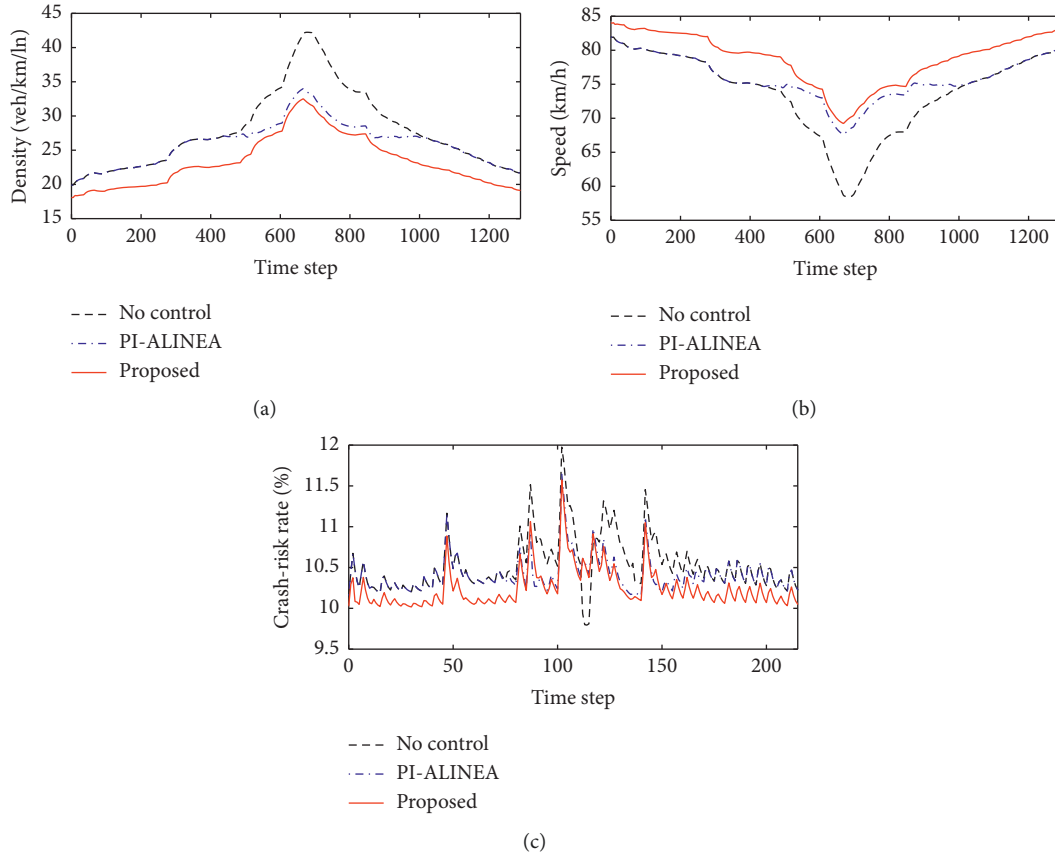


FIGURE 9: (a) Mainstream density, (b) mainstream speed, and (c) real-time crash-risk probability of different local ramp metering strategies.

physical domains of the density, speed, and visibility of the ramp metering are [32 veh/km/ln, 38 veh/km/ln], [80 km/h, 90 km/h], and [100 m, 200 m], respectively. According to equation (16), the mean values are $\rho_m = 35$ veh/km/h, $v_m = 85$ km/h, and $r_m = 150$ m, and the scaling factors are $K_p = 0.2$, $K_v = 0.2$, and $K_r = 0.02$. The parameters in equations (13) and (14) are listed as follows: $K_p = 10$ and $K_R = 40$.

4.2.2. Simulation Results and Analysis. According to equations (20)–(27), a real-time crash-risk prediction model reflecting traffic safety is used to evaluate the proposed local ramp metering. The data on traffic incidents are obtained through a simulation in VISSIM. The location of a traffic incident is shown in Figure 3. The time interval is $\Delta t = 10$ s, the time period is $\Delta T = 60$ s, and $N_1 = \Delta T / \Delta t = 6$ is applied.

The real-time crash-risk probability is calculated during every six simulation time steps. The parameters in equation (27) are obtained through the logistic regression of the traffic incident data as follows: $\alpha_1 = -2.2028$, $\alpha_2 = -0.035$, $\alpha_3 = 10.4302$, and $\alpha_4 = 13.3114$. Partial traffic data used for the parameter fitting are listed in Table 4.

The freeway traffic density and speed under different local ramp metering strategies are shown in Figures 9(a) and 9(b), respectively. Equation (27) shows the real-time collision rate, which is used to evaluate the proposed local ramp metering strategy. The real-time collision rate of different local ramp metering strategies is shown in Figure 9(c).

As shown in Figure 9, within the first 500 time steps and the last 260 time steps during the simulation time, the strategies of no-control and PI-ALINEA have similar control results under the traffic state and real-time crash-risk

TABLE 5: Partial real-time collision rate of different strategies.

No.	PI-ALINEA	Proposed
1	0.101575	0.100297
2	0.104457	0.102950
3	0.106739	0.103447
4	0.104717	0.100847
5	0.103336	0.100757
6	0.102541	0.100483
7	0.104219	0.102161
8	0.105752	0.103796
...

probability. Because the mainstream density of a freeway is always lower than the desired density, the flow of on-ramp $R2$ is not controlled by PI-ALINEA. As the freeway mainstream density gradually exceeds the desired density, PI-ALINEA will reduce the entrance flow of on-ramp $R2$ and slow down the increasing trend of density to maintain the mainstream density around its critical value at the cost of increasing the ramp queue. Correspondingly, the real-time crash-risk probability will decrease during this period.

As indicated in Figure 9, the proposed ramp metering strategy under foggy weather conditions differs from the PI-ALINEA strategy, which has a consistent effect on on-ramp $R2$. At the beginning of the simulation, on-ramp $R2$ is continuously controlled by the proposed ramp metering strategy under the premise of reducing the real-time crash-risk probability. As shown in Figures 9(a) and 9(b), the fluctuations of the mainstream density and speed are smaller than those controlled by PI-ALINEA. As shown in Figure 9(c), the real-time crash-risk probability of the proposed ramp metering strategy is always lower than that controlled by PI-ALINEA during the entire simulation time step.

In order to further analyze the effects of PI-ALINEA and the proposed strategy, the experimental results of PI-ALINEA and the proposed strategy are used for statistical study. Because the real-time collision rate of different strategies characterizes normal distribution, the t -test is used to evaluate statistical significance with MATLAB. The significant difference between these results is characterized by a significance threshold fixed at a p value less than or equal to 0.05. The calculated p value is much less than 0.01; therefore, the proposed strategy is superior to PI-ALINEA in ensuring traffic safety. Partial experimental data used to evaluate statistical significance are listed in Table 5. On the whole, the proposed ramp metering strategy achieves a better performance in ensuring traffic safety and is more suitable for a freeway system under foggy weather conditions.

5. Conclusions

A macroscopic traffic model applied under foggy weather conditions and based on a model correction factor (c_m) was proposed in this paper. The model correction factor (c_m) is regulated online based on different visibility conditions and curve radius of the freeway to better optimize the traffic model under foggy weather conditions. The sum of the mean

absolute percentage error of the mainstream density and speed is used as the fitness function to evaluate the proposed traffic model. A local ramp metering strategy under foggy weather conditions based on the density correction factor (c_d) is proposed when considering the proposed traffic model. The density correction factor (c_d) is regulated online based on the mainstream traffic density, speed, and visibility. A real-time crash-risk prediction model that reflects the level of traffic safety is used to evaluate the performance of the proposed local ramp metering strategy. The simulation results show the effectiveness of the proposed traffic model and ramp metering strategy under foggy weather conditions.

Data Availability

The (Excel) data used to support the findings of this study are included within the supplementary information files.

Conflicts of Interest

The authors declare that there are no conflicts of interest regarding the publication of this paper.

Supplementary Materials

Data 1: data derived from VISSIM by simulating the traffic incident, which are used for parameter regulation in the real-time crash-risk prediction model. These data are complete part corresponding to Table 4 in the manuscript. data 2: data on the real-time collision rate of PI-ALINEA and the proposed strategy, which are used for statistical study. These data are complete part corresponding to Table 5 in the manuscript. (*Supplementary Materials*)

References

- [1] K. C. Dey, A. Mishra, and M. Chowdhury, "Potential of intelligent transportation systems in mitigating adverse weather impacts on road mobility: a review," *IEEE Transactions on Intelligent Transportation Systems*, vol. 16, no. 3, pp. 1107–1119, 2015.
- [2] S. Choi and C. Oh, "Proactive strategy for variable speed limit operations on freeways under foggy weather conditions," *Transportation Research Record: Journal of the Transportation Research Board*, vol. 2551, no. 1, pp. 29–36, 2016.
- [3] P. A. Pisano and L. C. Goodwin, "Research needs for weather-responsive traffic management," *Transportation Research Record: Journal of the Transportation Research Board*, vol. 1867, no. 1, pp. 127–131, 2004.
- [4] T. H. Maze, M. Agarwai, and G. Burchett, "Whether weather matters to traffic demand, traffic safety, and traffic operations and flow," *Transportation Research Record: Journal of the Transportation Research Board*, vol. 1948, no. 1, pp. 170–176, 2006.
- [5] L. Chris, B. Hellinga, and F. Saccomanno, "Evaluation of variable speed limits to improve traffic safety," *Transportation Research Part C: Emerging Technologies*, vol. 14, no. 3, pp. 213–228, 2006.
- [6] B. Ran, P. J. Jin, D. Boyce, T. Z. Qiu, and Y. Cheng, "Perspectives on future transportation research: impact of intelligent transportation system technologies on next

- generation transportation modelling,” *Journal of Intelligent Transportation Systems*, vol. 16, no. 4, pp. 226–242, 2012.
- [7] M. Cools, E. Moons, and G. Wets, “Assessing the impact of weather on traffic intensity,” *Weather, Climate, and Society*, vol. 2, no. 1, pp. 60–68, 2010.
- [8] M. Abdel-Aty, J. Dilmore, and L. Hsia, “Applying variable speed limits and the potential for crash migration,” *Transportation Research Record: Journal of the Transportation Research Board*, vol. 1953, no. 1, pp. 21–30, 2006.
- [9] C. Lee, B. Hellinga, and F. Saccomanno, “Assessing safety benefits of variable speed limits,” *Transportation Research Record: Journal of the Transportation Research Board*, vol. 1897, no. 1, pp. 183–190, 2004.
- [10] M. Papageorgiou and A. Kotsialos, “Freeway ramp metering: an overview,” *IEEE Transactions on Intelligent Transportation Systems*, vol. 3, no. 4, pp. 271–281, 2003.
- [11] M. Papageorgiou, H. Hadj-Salem, and J. M. Blasseville, “ALINEA: a local feedback control law for on-ramp metering,” *Transportation Research Record*, vol. 1320, pp. 58–64, 1991.
- [12] E. Smaragdis, M. Papageorgiou, and E. Kosmatopoulos, “A flow-maximizing adaptive local ramp metering strategy,” *Transportation Research Part B: Methodological*, vol. 38, no. 3, pp. 251–270, 2004.
- [13] Y. Wang, E. B. Kosmatopoulos, M. Papageorgiou, and I. Papamichail, “Local ramp metering in the presence of a distant downstream bottleneck: theoretical analysis and simulation study,” *IEEE Transactions on Intelligent Transportation Systems*, vol. 15, no. 5, pp. 2024–2039, 2014.
- [14] Z. Hou, J.-X. Xu, and J. Yan, “An iterative learning approach for density control of freeway traffic flow via ramp metering,” *Transportation Research Part C: Emerging Technologies*, vol. 16, no. 1, pp. 71–97, 2008.
- [15] R. Chi, M. Li, Z. Hou, X. Liu, and Z. Yu, “Freeway traffic density and on-ramp queue control via ILC approach,” *Mathematical Problems in Engineering*, vol. 2014, Article ID 321934, 8 pages, 2014.
- [16] Z. Hou, J. Yan, J.-X. Xu, and Z. Li, “Modified iterative-learning-control-based ramp metering strategies for freeway traffic control with iteration-dependent factors,” *IEEE Transactions on Intelligent Transportation Systems*, vol. 13, no. 2, pp. 606–618, 2012.
- [17] H. M. Zhang and S. G. Ritchie, “Freeway ramp metering using artificial neural networks,” *Transportation Research Part C: Emerging Technologies*, vol. 5, no. 5, pp. 273–286, 1997.
- [18] C. Lu and J. Huang, “A self-learning system for local ramp metering with queue management,” *Transportation Planning and Technology*, vol. 40, no. 2, pp. 182–198, 2017.
- [19] M. Hasan, M. Jha, and M. Ben-Akiva, “Evaluation of ramp control algorithms using microscopic traffic simulation,” *Transportation Research Part C: Emerging Technologies*, vol. 10, no. 3, pp. 229–256, 2002.
- [20] L. L. Chen, A. D. May, and D. M. Auslander, “Freeway ramp control using fuzzy set theory for inexact reasoning,” *Transportation Research Part A: General*, vol. 24, no. 1, pp. 15–25, 1990.
- [21] J. Xu, X. Zhao, and D. Srinivasan, “On optimal freeway local ramp metering using fuzzy logic control with particle swarm optimisation,” *IET Intelligent Transport Systems*, vol. 7, no. 1, pp. 95–104, 2013.
- [22] A. Ghods, A. Kian, and M. Tabibi, “Adaptive freeway ramp metering and variable speed limit control: a genetic-fuzzy approach,” *IEEE Intelligent Transportation Systems Magazine*, vol. 1, no. 1, pp. 27–36, 2009.
- [23] X. F. Yu, F. Alam, and W. L. Xu, “Genetic-fuzzy logic ramp metering control for ramp metering of motorway,” *International Journal of Computer Applications in Technology*, vol. 50, no. 1/2, p. 30, 2014.
- [24] T.-C. Chiang and W.-J. Wang, “Highway on-ramp control using fuzzy decision making,” *Journal of Vibration and Control*, vol. 17, no. 2, pp. 205–213, 2011.
- [25] H. J. Payne, “FREFLO: a macroscopic simulation model for freeway traffic,” *Transportation Research Record*, vol. 722, pp. 68–77, 1979.
- [26] W. Z. Qiao, W. P. Zhuang, T. H. Heng, and S. S. Shan, “A rule self-regulating fuzzy controller,” *Fuzzy Sets and Systems*, vol. 47, no. 1, pp. 13–21, 1992.
- [27] M. R. Bonyadi and Z. Michalewicz, “Particle swarm optimization for single objective continuous space problems: a review,” *Evolutionary Computation*, vol. 25, no. 1, pp. 1–54, 2017.
- [28] I. C. Trelea, “The particle swarm optimization algorithm: convergence analysis and parameter selection,” *Information Processing Letters*, vol. 85, no. 6, pp. 317–325, 2003.
- [29] Z. Li, S. Ahn, K. Chung, D. R. Ragland, W. Wang, and J. W. Yu, “Surrogate safety measure for evaluating rear-end collision risk related to kinematic waves near freeway recurrent bottlenecks,” *Accident Analysis & Prevention*, vol. 64, pp. 52–61, 2014.

Research Article

Dynamic Game and Coordination Strategy of Multichannel Supply Chain Based on Brand Competition

Junhai Ma ¹, Fang Zhang ^{1,2}, and Binshuo Bao ¹

¹College of Management and Economics, Tianjin University, Tianjin 300072, China

²Department of Mathematics, Tianjin Polytechnic University, Tianjin 300387, China

Correspondence should be addressed to Fang Zhang; zhanfangxs@163.com and Binshuo Bao; baobinshu01024@163.com

Received 10 May 2019; Revised 14 August 2019; Accepted 20 September 2019; Published 5 December 2019

Guest Editor: Raúl Baños

Copyright © 2019 Junhai Ma et al. This is an open access article distributed under the Creative Commons Attribution License, which permits unrestricted use, distribution, and reproduction in any medium, provided the original work is properly cited.

In this paper, two noncooperative dynamic pricing strategies are used in a supply chain. Two dynamic Stackelberg game models have been built involving both a manufacturer and a retailer assumed to be the leader in order. In the two models, the manufacturer sells national-brand (NB) product to an independent retailer or directly to consumers through a direct channel. The retailers sell a store-brand (SB) product when they sell the NB product coming from the manufacturer. Thus, there is competition both in different channels and in products with different brands. To analyze the complexity of the model, parameter bifurcation diagrams and strange attractor diagrams have been therefore plotted. The results show that the game leader has advantages when the market is stable, but it turns disadvantageous if the state falls into unstable as the game follower can quickly adjust the strategy to seize the market. The wholesale price and the direct selling price are high that they incur larger profits if the manufacturer is dominant, but it gets worse when the adjustment speed increases. While in the model where the retailer plays a dominant role, the increase in the adjustment speed is unfavorable to retailer. By controlling the total cost of the direct channel and increasing channel competition strength and brand competition strength, the manufacturers can increase their profits in the game dominated by the retailer. In addition, the stable region within the system will be narrow since the market is sensitive to the channel competition, brand competition, and advertising indifference.

1. Introduction

The e-commerce has already been rapidly developed and widely applied with the spread of the Internet around the world. More and more manufacturing enterprises set up their own network of direct sales channels; thus, their hybrid channels include both traditional distribution channels and e-channels. These network platforms can help the manufacturers to meet the demands of consumers without the hands of retailers.

A considerable amount of study has been done on a dual-channel supply chain. For instance, with the consideration of shortage caused by random yields, Xiao and Shi [1] establish a dual-channel supply chain framework and study the pricing and channel priority strategy. They find it is the decentralization that really counts in determining the channel priority strategy. Kurata et al. [2] analyze the competition in multiple distribution channels. They explore

cross-brand and cross-channel pricing policies and find that brand loyalty building is profitable for both a national-brand and a store-brand. Cai et al. [3] study a dual-channel supply chain game with a price discount. They show that a consistent pricing scheme can reduce the channel conflict by inducing more profit to the retailer. To investigate the optimal decisions for a dual-channel, Soleimani et al. [4] discuss the pricing strategies both in centralized and decentralized scenarios considering production cost disruptions. They figure out the optimal decisions and reveal that if the demand disruption (cost disruption) is enhanced, the optimal prices will also be increased for a given cost disruption (demand disruption). Also by researching a dual-channel model, Batarfi et al. [5] point out dual-channel strategy is better off than the single-channel strategy. Liu and Xiao [6] build a dyadic closed-loop supply chain based on green consumer and corporate social responsibility in which consumers and firms show environmental responsibility

behaviors. The price and collection rate decision and reverse channel strategy are analyzed. Zheng et al. [7] build a dual-channel closed loop supply chain that consists of a manufacturer, a retailer, and a collector. The effect of forward channel competition and power structure is investigated, and a centralized and three decentralized models are analyzed. He et al. [8] construct a dual-channel closed loop supply chain in which manufacturers can distribute new products by independent retailers and sell remanufactured products by a third part enterprise. The channel structure and pricing decisions for the manufacturer and government's subsidy with competing remanufactured products are discussed. Giri and Dey [9] extend a closed-loop supply chain which included one collector, one recycler, and one manufacturer with a backup supplier considering uncertainty of collection of used products. And the performance of the model increases compared to that of the conditional closed loop supply chain.

Many research studies show that if the manufacturers set up a direct channel to sell products, they can improve their profits largely, but this behavior can reduce the profit of the retailer. Hence, retailer will in turn take some measures to reduce the loss. The retailers often sell a store-brand (SB) product while they sell the national-brand (NB) product coming from the manufacturer. SB products and NB products compete in the market. Existing literatures [10–13] show that when retailers provide the SB products, they can not only reduce the dependence to the NB products but also enhance the market competitiveness. A previous research [10] studies the competition between many NB products and a single SB product. Narasimhan and Wilcox [11] calculate the pricing decision and the corresponding changes of the profit of the manufacturers and retailers when they provide the SB product in the market. The article points out that when retailers do not sell their SB products, leading manufacturers can make the retailers' profit down to zero through setting a wholesale price, so the retailer has to minimize losses by selling SB products. The literature [12] points out that selling the SB products can weaken the "double marginal effect." Tyagi [13] indicates that introducing the SB products is good for retailers but is unfavorable for manufacturers.

The aforementioned studies make some research on introducing the SB products but has seldom discussed the two problems in one thesis: multichannel competition and the NB product and the SB product competition. In addition, there has been no literature using dynamic game theory to discuss the aforementioned competition in the supply chain. The multistage dynamic repeated game model combined with system dynamics theory has been studied in some literature recently. Zhang and Ma [14] considered two different pricing policies in a dual-channel supply chain with a fair caring retailer. Many dynamic behaviors, such as the bifurcation, periodic cycles, and strange attractors of the systems, are shown in their papers. In this paper, we consider a dynamic pricing model in which the manufacturer has the option of exploiting the direct channel to compete with the retail channel, whereas the retailer has the option of introducing a SB product to compete with the NB product. In order to improve the competitiveness, the retailer will advertise for the SB product. Two noncooperative Stackelberg

game models have been established: in one the manufacturer acts as the leader and in the other the retailer acts as the leader. We carried out numerical simulations on two models with different conditions and analyzed the complex dynamic behaviors, such as bifurcation and chaos [15–17].

The structure of this paper is arranged in the following order. In Section 2, we introduce the assumptions and notations. Section 3 investigates a Stackelberg model which is led by the manufacturer and reveals numerical simulations for this scenario. In Section 4, we discuss a retailer leading game framework. In Section 5, a comparison of the prices and profits between the two models are exhibited. Finally, some conclusions have been shown.

2. Model Notations and Assumptions

In this paper, we study a multichannel supply chain which includes a manufacturer and a retailer. The manufacturer produces a national-brand (NB) product at a marginal cost c_1 and distributes it through their wholly owned direct channel at a price p_0 as well as an independent retailer channel at a wholesale price w . The retailers will resell the product through their own channel at price p_1 . At the same time, the retailers sell the SB product to the customers at a price p_2 . Different products and different channels compete in the supply chain. We develop two noncooperative Stackelberg game models. The supply chain is shown in Figure 1.

We consider the demand for products in the market as a linear function of the product price because linear demand functions are tractable and widely used in supply chain analysis (Ma and Xie [18]; Dai et al. [19]; and Yao et al. [20]). Assume that consumers are divided into two categories: manufacturer loyalty consumers and retailer loyalty consumers. Consumers loyal to the manufacturer buy products only from the manufacturer. Consumers loyal to the retailer choose products from the retailer. Two types of consumers are both sensitive to price. The demands in our models are as follows:

$$\begin{aligned} D_0 &= a_0 - b_0 p_0 + \eta p_1, \\ D_1 &= a_1 - b_1 p_1 + \eta p_0 + \eta p_2 - \theta \sqrt{A}, \\ D_2 &= a_2 - b_2 p_2 + \eta p_1 + \theta \sqrt{A}. \end{aligned} \quad (1)$$

For the convenience, we assume $\sqrt{A} = B$, and then the demand functions are

$$\begin{aligned} D_0 &= a_0 - b_0 p_0 + \eta p_1, \\ D_1 &= a_1 - b_1 p_1 + \eta p_0 + \eta p_2 - \theta B, \\ D_2 &= a_2 - b_2 p_2 + \eta p_1 + \theta B. \end{aligned} \quad (2)$$

Here, the parameter $\alpha_i (>0)$ ($i = 0, 1, 2$) represents the potential market size. $b_i (>0)$ ($i = 0, 1, 2$) is the price elasticity coefficient. $\gamma (>0)$ is the channel competition coefficient. $\eta (>0)$ is the brand competition coefficient $b_i > \gamma$, η ($i = 0, 1, 2$), i.e., the ownership-price effect is greater than the cross-price effect. In addition, θ is the demand sensitivity to the advertising level of the retailer. The price and demand functions should be satisfied: (i) $c_1 < w < p_1$, (ii) $c_1 < c_0 < p_0$, (iii) $c_2 < p_2$, and (iv) $D_i > 0$ ($i = 0, 1, 2$).

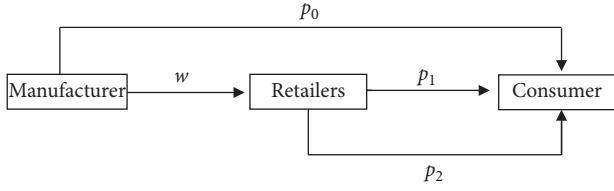


FIGURE 1

3. Manufacturer Stackelberg (MS)

3.1. Model Construction. In this model, the manufacturer is the leader and the retailer is the follower, and they form a Stackelberg game. The manufacturer decides the wholesale price w and the direct selling price p_0 of the NB product. According to the decision-making of the manufacturer, the retailer makes decision of the retail price p_1 of the NB product, the price p_2 of the SB product, and the advertising investment A .

The profit function of the manufacturer is as follows:

$$p_1 = \frac{((-4\eta + \theta^2)(-2a_2 - 2b_2c_2 + 2w\eta + c_2\theta^2 - w\theta^2) - (4b_2 - \theta^2)(-2(a_1 + b_1w + p_0\gamma - c_2\eta) + (-c_2 + w)\theta^2))}{4(4b_1b_2 - 4\eta^2 - b_1\theta^2 - b_2\theta^2 + 2\eta\theta^2)}, \quad (7)$$

$$p_2 = \frac{(-4a_1\eta - 4p_0\gamma\eta + 4c_2\eta^2 + a_1\theta^2 + b_2c_2\theta^2 + p_0\gamma\theta^2 - 3c_2\eta\theta^2 + w\eta\theta^2 + a_2(-4b_1 + \theta^2) - b_1(4b_2c_2 - 2c_2\theta^2 + w\theta^2))}{2(-4b_1b_2 + 4\eta^2 + b_1\theta^2 + b_2\theta^2 - 2\eta\theta^2)}, \quad (8)$$

$$B = \frac{(-b_1b_2c_2 + b_1b_2w - b_2p_0\gamma + a_2(b_1 - \eta) + p_0\gamma\eta + c_2\eta^2 - w\eta^2 + a_1(-b_2 + \eta))\theta}{(4b_1b_2 - 4\eta^2 - b_1\theta^2 - b_2\theta^2 + 2\eta\theta^2)}. \quad (9)$$

Substituting (7)–(9) into (3) and then taking the first-order partial derivatives of π_m with respect to w and p_0 , respectively, we can obtain the following

$$\begin{aligned} \frac{\partial \pi_m^M}{\partial w} = & (4c_0\gamma\eta^2 - 8p_0\gamma\eta^2 - 4c_2\eta^3 + 2b_2c_0\gamma\theta^2 - 2b_2p_0\gamma\theta^2 + a_2\eta\theta^2 - b_2c_2\eta\theta^2 - 3c_0\gamma\eta\theta^2 + 4p_0\gamma\eta\theta^2 - c_1\eta^2\theta^2 \\ & + c_2\eta^2\theta^2 + 2w\eta^2\theta^2 + b_1^2(c_1 - 2w)(4b_2 - \theta^2) + a_1(b_1(4b_2 - \theta^2) + \eta(-4\eta + \theta^2)) \\ & + b_1(8w\eta^2 - a_2\theta^2 + c_0\gamma\theta^2 - 2p_0\gamma\theta^2 - c_2\eta\theta^2 - 4w\eta\theta^2 + 2c_1\eta(-2\eta + \theta^2) + b_2(-4c_0\gamma + 8p_0\gamma + 4c_2\eta + c_2\theta^2))) \\ & \cdot (8b_1b_2 - 8\eta^2 - 2b_1\theta^2 - 2b_2\theta^2 + 4\eta\theta^2)^{-1}, \end{aligned} \quad (10)$$

$$\begin{aligned} \frac{\partial \pi_m^M}{\partial p_0} = & (2b_0(c_0 - 2p_0)(4b_1b_2 - 4\eta^2 - b_1\theta^2 - b_2\theta^2 + 2\eta\theta^2) + a_0(8b_1b_2 - 8\eta^2 - 2b_1\theta^2 - 2b_2\theta^2 + 4\eta\theta^2) \\ & - \gamma(4b_2c_0\gamma - 8b_2p_0\gamma - 4a_2\eta - 4c_1\eta^2 + 8w\eta^2 + a_2\theta^2 - b_2c_2\theta^2 + 2b_2w\theta^2 - c_0\gamma\theta^2 + 2p_0\gamma\theta^2 + c_1\eta\theta^2 + c_2\eta\theta^2 - 4w\eta\theta^2 \\ & + b_1(c_1 - 2w)(4b_2 - \theta^2) + a_1(-4b_2 + \theta^2))) \cdot (8b_1b_2 - 8\eta^2 - 2b_1\theta^2 - 2b_2\theta^2 + 4\eta\theta^2)^{-1}. \end{aligned} \quad (11)$$

$$\pi_R^M = D_0(p_0 - c_0) + D_1(w - c_1). \quad (3)$$

The profit function of the retailer is as follows:

$$\pi_r^M = D_1(p_1 - w) + D_2(p_2 - c_2) - B^2. \quad (4)$$

Taking the first-order partial derivatives of π_r^M with respect to p_1 , p_2 , and B , respectively, and taking the second-order derivatives further, we can get the Hessian matrix:

$$\begin{pmatrix} -2b_1 & 2\eta & -\theta \\ 2\eta & -2b_2 & \theta \\ -\theta & \theta & -2 \end{pmatrix}. \quad (5)$$

Note that $b_1b_2 > \eta^2$ when

$$-4b_1b_2 + 4\eta^2 + b_1\theta^2 + b_2\theta^2 - 2\eta\theta^2 < 0. \quad (6)$$

The retailer's profit function is concave and has a unique maximum solution. The retailer's best response to the wholesale price w and the direct sale price p_0 setting by the manufacturer is given in the following:

Taking the second-order derivatives further, we can get the Hessian matrix:

$$\begin{pmatrix} H_1 & \gamma \\ \gamma & H_2 \end{pmatrix}. \quad (12)$$

See note 4 From (6), we have $\theta^2(b_1 - \eta)^2 - 4b_1(b_1b_2 - \eta^2) < \theta^2(b_1 - \eta)^2 - \theta^2b_1(b_1 + b_2 - 2\eta) < \theta^2(\eta^2 - b_1b_2) < 0$.

So, while satisfying

$$\begin{aligned} & \frac{\theta^2(b_1 - \eta)^2 - 4b_1(b_1b_2 - \eta^2)}{4b_1b_2 - 4\eta^2 - b_1\theta^2 - b_2\theta^2 + 2\eta\theta^2} - \gamma\gamma 2b_0 \\ & + \frac{\gamma^2(-4b_2 + \theta^2)}{4\eta^2 - 4b_1b_2 + b_1\theta^2 + b_2\theta^2 - 2\eta\theta^2} - \gamma\gamma^2 > 0, \end{aligned} \quad (13)$$

the manufacturer's profit function is concave and has a unique maximum solution because the Hessian matrix is negative definite. So, we get the optimal wholesale price w^M and the optimal direct sale price p_0^M by letting (10) and (11) be equal to zero. Furthermore, substituting w^M and p_0^M into (7)–(9), we have the optimal retail price p_1^M and p_2^M and the optimal advertising investment A^M . See the appendix for a list of functions w^M , p_0^M , p_1^M , p_2^M , and B^M .

Now we develop a dynamic Stackelberg game model. In fact, while making price decision, restricted by the

objective conditions such as the decision-making ability, the decision makers cannot get the whole market information and their price decision is also not completely rational. Suppose that the decision in next period can be adjusted with bounded rationality (Ma et al. [17, 21]) and is based on partial estimation of the marginal profits of the current period; that is, if the marginal profits in period t is positive, the manufacturer will raise the price in period $t + 1$. Otherwise, the manufacturer will reduce it. The model can be constructed as follows:

$$\begin{cases} \omega(t+1) = \omega(t) + \alpha_1\omega(t) \frac{\partial \pi_m^M(\omega, p_0)}{\partial \omega(t)}, \\ p_0(t+1) = p_0(t) + \alpha_2p_0(t) \frac{\partial \pi_m^M(\omega, p_0)}{\partial p_0(t)}. \end{cases} \quad (14)$$

System (14) gives the manufacturer's dynamic price decision and the decision variables directly relate to the positive parameter α_i ($i = 1, 2$), which represents the price adjustment speed. $(\partial \pi_m^M(\omega, p_0))/(\partial \omega(t))$ and $(\partial \pi_m^M(\omega, p_0))/(\partial p_0(t))$ are the marginal profits, and they can be obtained by equations (10) and (11). Furthermore, the retailer's price decision can be obtained by $w(t)$ and $p_0(t)$:

$$p_1(t) = \frac{((-4\eta + \theta^2)(-2a_2 - 2b_2c_2 + 2w(t)\eta + c_2\theta^2 - w(t)\theta^2) - (4b_2 - \theta^2)(-2(a_1 + b_1w(t) + p_0(t)\gamma - c_2\eta) + (-c_2 + w(t)\theta^2)))}{(4(4b_1b_2 - 4\eta^2 - b_1\theta^2 - b_2\theta^2 + 2\eta\theta^2))}, \quad (15)$$

$$p_2(t) = \frac{(-4a_1\eta - 4p_0(t)\gamma\eta + 4c_2\eta^2 + a_1\theta^2 + b_2c_2\theta^2 + p_0(t)\gamma\theta^2 - 3c_2\eta\theta^2 + w(t)\eta\theta^2 + a_2(-4b_1 + \theta^2) - b_1(4b_2c_2 - 2c_2\theta^2 + w(t)\theta^2))}{(2(-4b_1b_2 + 4\eta^2 + b_1\theta^2 + b_2\theta^2 - 2\eta\theta^2))}, \quad (16)$$

$$B(t) = \frac{((-b_1b_2c_2 + b_1b_2w(t) - b_2p_0(t)\gamma + a_2(b_1 - \eta) + p_0(t)\gamma\eta + c_2\eta^2 - w(t)\eta^2 + a_1(-b_2 + \eta))\theta)}{(4b_1b_2 - 4\eta^2 - b_1\theta^2 - b_2\theta^2 + 2\eta\theta^2)}. \quad (17)$$

3.2. Model Analysis. We have four equilibrium solutions of system (14), described by

$$\begin{aligned} E_1 &= (0, 0), \\ E_2 &= \left((4c_0\gamma\eta^2 - 4c_2\eta^3 + 2b_2c_0\gamma\theta^2 + a_2\eta\theta^2 - b_2c_2\eta\theta^2 - 3c_0\gamma\eta\theta^2 - c_1\eta^2\theta^2 + c_2\eta^2\theta^2 + b_1^2c_1(4b_2 - \theta^2) \right. \\ & \quad \left. + a_1(b_1(4b_2 - \theta^2) + \eta(-4\eta + \theta^2)) + b_1(-a_2 - c_0\gamma + c_2\eta)\theta^2 + 2c_1\eta(-2\eta + \theta^2) + b_2(-4c_0\gamma + c_2(4\eta + \theta^2))) \right) \\ & \quad \cdot (-2\eta^2\theta^2 + b_1^2(8b_2 - 2\theta^2) + 4b_1\eta(-2\eta + \theta^2))^{-1}, 0), \\ E_3 &= \left(0, (2b_0c_0(4b_1b_2 - 4\eta^2 - b_1\theta^2 - b_2\theta^2 + 2\eta\theta^2) + a_0(8b_1b_2 - 8\eta^2 - 2b_1\theta^2 - 2b_2\theta^2 + 4\eta\theta^2) \right. \\ & \quad \left. + \gamma(4a_1b_2 - 4b_1b_2c_1 - 4b_2c_0\gamma + 4a_2\eta + 4c_1\eta^2 - a_1\theta^2 - a_2\theta^2 + b_1c_1\theta^2 + b_2c_2\theta^2 + c_0\gamma\theta^2 - c_1\eta\theta^2 - c_2\eta\theta^2)) \right) \\ & \quad \cdot (2(\gamma^2(-4b_2 + \theta^2) + b_0(8b_1b_2 - 8\eta^2 - 2b_1\theta^2 - 2b_2\theta^2 + 4\eta\theta^2)))^{-1}), \\ E^M &= (\omega^M, p_0^M). \end{aligned} \quad (18)$$

$E_i (i = 1, 2, 3)$ are boundary equilibrium solutions, while E^M is the only Stackelberg equilibrium solution. Its expression is shown as (A.1) and (A.2) in Appendix. In order to

guarantee the practical significance, we assume that all equilibriums are positive.

The Jacobian matrix of system (14) is given by

$$J = \begin{pmatrix} 1 + \alpha_1 h_1 & \alpha_2 p_0 \gamma \\ \alpha_1 w \gamma & 1 + \alpha_2 h_2 \end{pmatrix},$$

$$h_2 = 2H_1 \omega + \gamma p_0 + \frac{1}{2}(a_1 + b_1 c_1 + \eta c_2 - \gamma c_0) + \frac{\theta^2 ((b_1 b_2 - \eta^2)(c_1 + c_2) + a_2(\eta - b_1) + (a_1 + \gamma c_0)(b_2 - \eta))}{2(4b_1 b_2 - 4\eta^2 - b_1 \theta^2 - b_2 \theta^2 + 2\eta \theta^2)},$$

$$h_2 = \frac{2H_2 p_0 + \gamma \omega + a_0 + b_0 c_0 - \gamma(4c_1(b_1 b_2 - \eta^2) + c_1 \theta^2(\eta - b_1) + c_2 \theta^2(\eta - b_2) + a_2(\theta^2 - 4\eta^2) + (4b_2 - \theta^2)(\gamma c_0 - a_1))}{2(4b_1 b_2 - 4\eta^2 - b_1 \theta^2 - b_2 \theta^2 + 2\eta \theta^2)}.$$

(19)

The stability of equilibrium points will be determined by the nature of the eigenvalues of the Jacobian matrix evaluated at the corresponding equilibrium points. Then, we substitute the value of $E_i (i = 1, 2, 3)$ into (19), and we have the following proposition.

Proposition 1. *All the boundary equilibrium points $E_i (i = 1, 2, 3)$ are unstable under our assumptions and conditions (6) and (13).*

The significance of boundary equilibrium is that all players can predict the emergence of this equilibrium, and it is unprofitable for anyone to deviate from the equilibrium. For enterprises, unstable boundary equilibrium is not conducive to the stability of the overall system. We investigate the stability of E^R by utilizing Jury's stability condition [22]:

$$\begin{aligned} \text{(i)} & 1 + \text{Tr}(J) + \text{Det}(J) > 0, \\ \text{(ii)} & 1 - \text{Tr}(J) + \text{Det}(J) > 0, \\ \text{(iii)} & 1 - \text{Det}(J) > 0, \end{aligned} \quad (20)$$

where $\text{Tr}(J)$ and $\text{Det}(J)$ are the trace and determinant of J , respectively. The condition (20) gives a stable region in the place of the adjustment parameters α_1 and α_2 .

3.3. The Experimental Calculation and Numerical Simulation. In this section, numerical simulations are carried to show the influence of parameters. We will research how the adjust parameters, channel competition coefficient, brand competition coefficient, and advertising coefficient affect the system stability domain, the product prices, and the long-term average profit by Matlab simulation software. Based on the model assumptions and conditions (6) and (13), we choose some parameters as follows: $a_0 = 30$; $a_1 = 55$; $a_2 = 35$; $b_0 = 2.2$; $b_1 = 4.05$; $b_2 = 2.35$; $\gamma = 0.7$; $\eta = 0.6$; $\theta = 0.5$; $c_0 = 7$; $c_1 = 5$; and $c_2 = 7$. We have the equilibrium prices of the system: $\omega^M = 11.406$; $p_0^M = 13.3228$; $p_1^M = 15.0705$; $p_2^M = 13.4116$; and $B^M = 0.6868$. The

manufacturer and retailer's optimal profit of stable domain are $\pi_m^M = 141.49$ and $\pi_r^M = 122.32$.

3.3.1. The Stability Region Diagrams of the System. The stability of the equilibrium E^M and the two-dimensional bifurcation diagrams of the system are presented in Figure 2. We assign different colors to different areas, namely, stable steady area (blue), stable cycles of periods 2 (green), 3 (pink), 4 (red), 5 (dark blue), 6 (brown), 7 (yellow-green), 8 (red pink), chaos (yellow), and divergence (gray). We can see from the figure that when $0 < \alpha_1 < 0.042$, $0 < \alpha_2 < 0.034$ (blue area), the system is stable. The two-dimensional bifurcation diagrams of the system show that they have two paths of the system entering into the chaos. One is that when the parameter (α_1, α_2) located in the region of blue, green, red, and red pink moves to yellow step by step, the system enters into chaos through flip bifurcation. Another case is that the system from 2 cycles enters into chaos through Neimark-Sacker bifurcation if the parameters from the green area directly enter into the yellow area.

3.3.2. The Influence of Parameters γ , η , and θ on the Stable Regions. Figure 3 shows the stable regions of the Stackelberg equilibrium point with different channel competition coefficients (γ), different brand competition coefficients (η), and different advertising coefficients (θ). In Figure 3(a), when $\gamma = 0.7$, $\gamma = 1.1$, and $\gamma = 1.5$, we assign blue, yellow, and green to the stable region, respectively. It shows that the stable region of the system decreases with the increase of γ . That is to say, the fiercer the channel competition, the more unstable the system. In Figure 3(b), when $\eta = 0.6$, $\eta = 1$, and $\eta = 1.4$, the stable region is shown by blue, pink, and gray, respectively. We can see from the figure that the stable region of the system decreases with the increase of the brand competition coefficient η . In Figure 3(c), when $\theta = 0.5$, $\theta = 0.9$, and $\theta = 1.3$, we assign blue, red, and brown to the stable region, respectively. The figure shows that the more sensitive the market is, the less the stability of the system is.

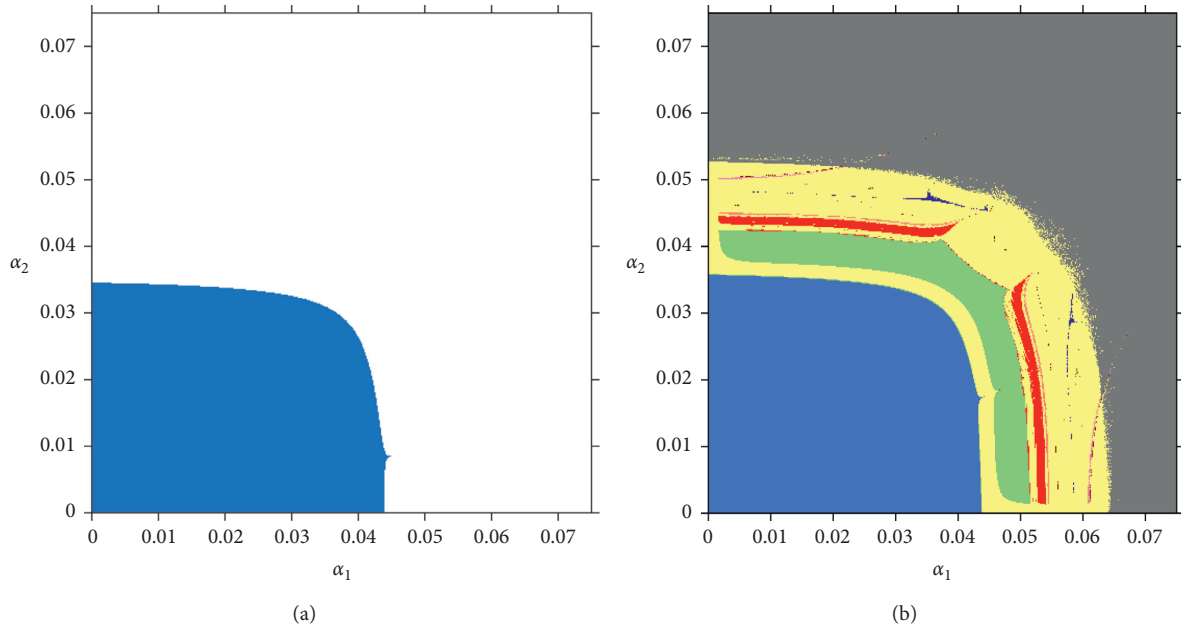


FIGURE 2: The stability region diagrams of the system.

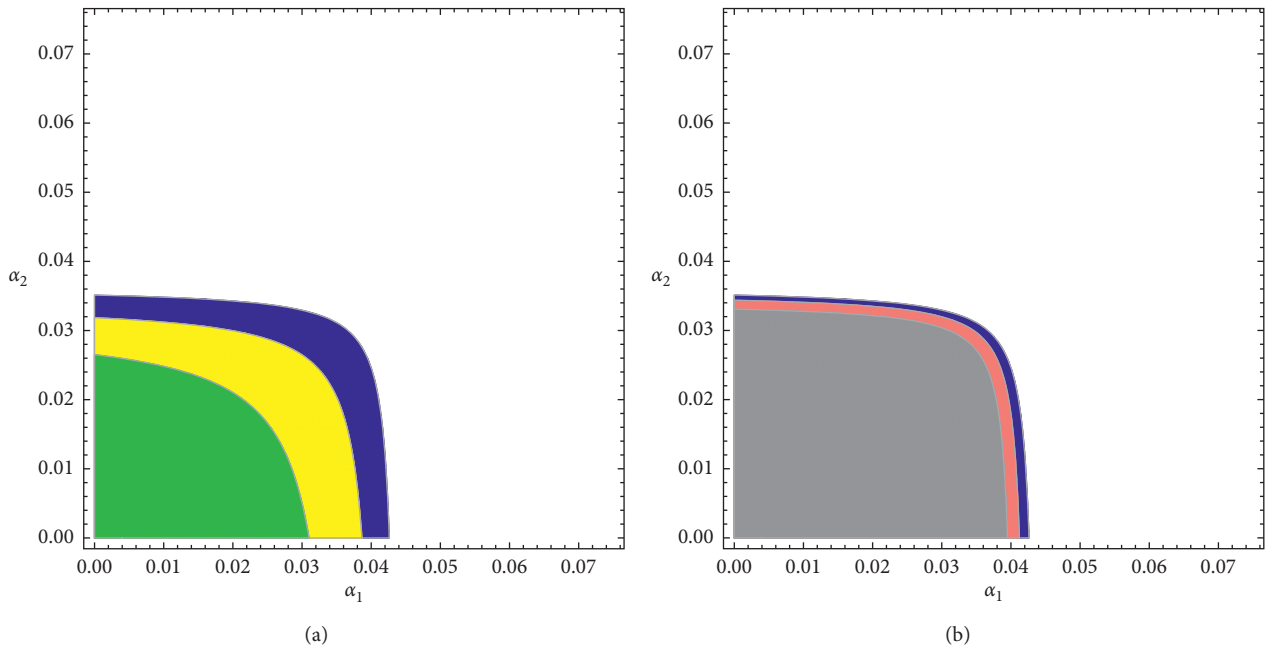


FIGURE 3: Continued.

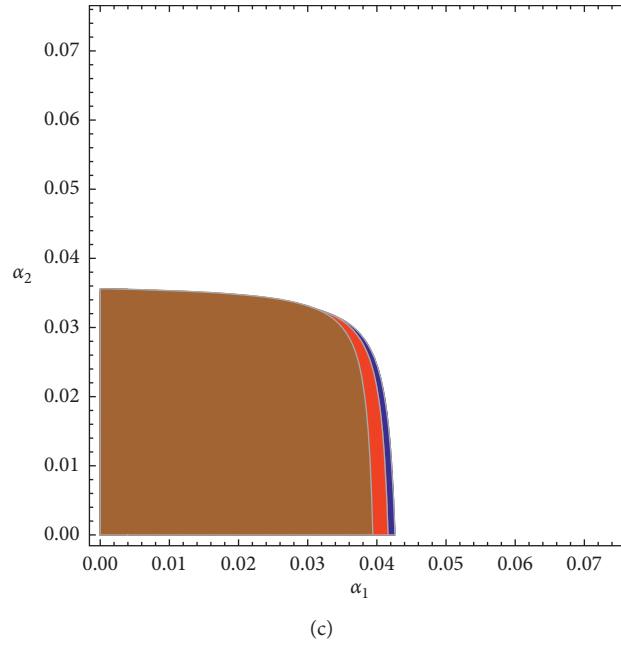


FIGURE 3: The influence of the parameters δ and b_2 on the stable regions.

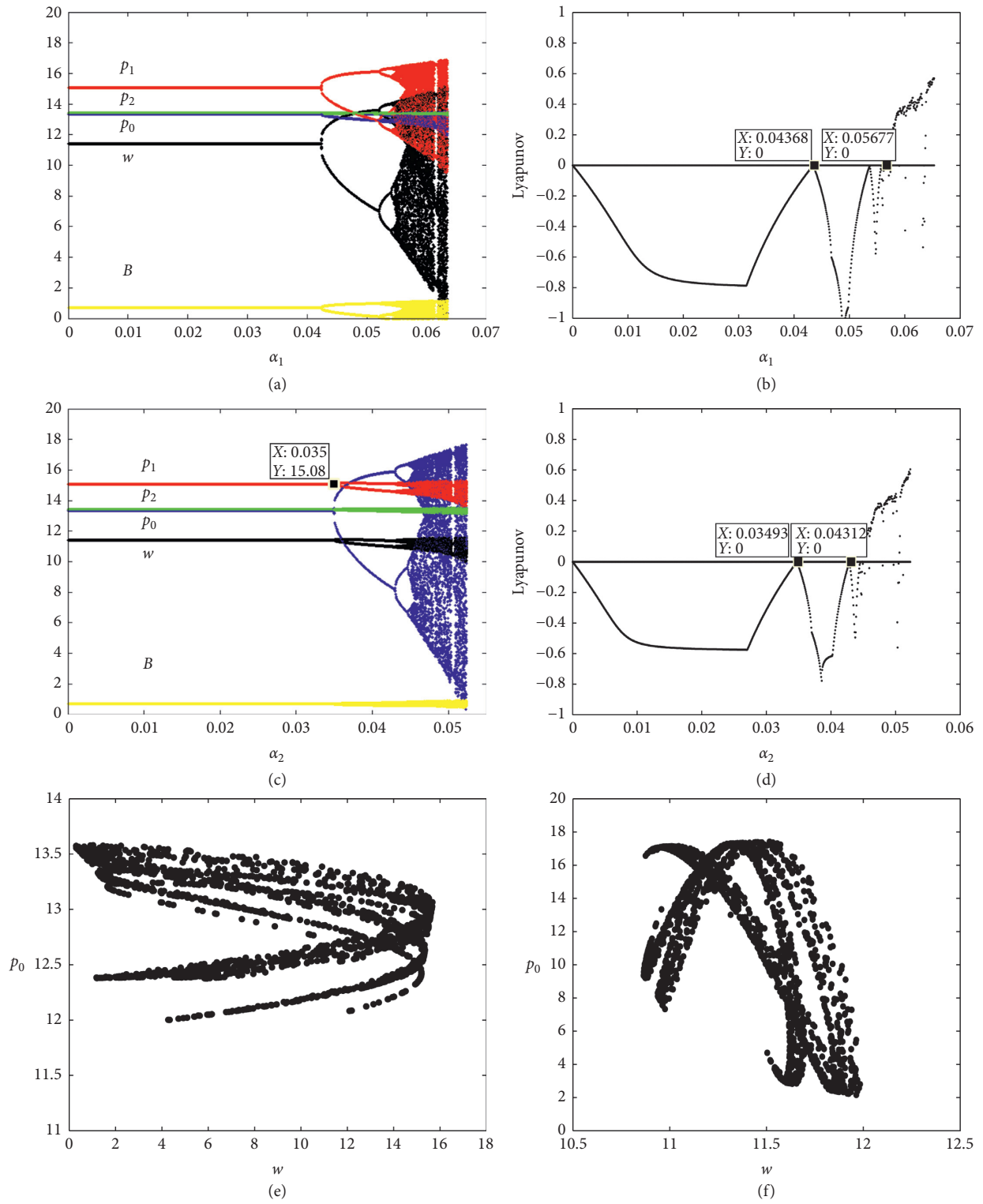
3.3.3. Complex Dynamics Analysis on the System. Figure 4 gives the bifurcation diagrams, the corresponding largest Lyapunov exponent plot of system (14) and chaos attractor. We assign black curve to wholesale price w , blue curve to direct selling price p_0 , red curve to retail price p_1 , green curve to retail price p_2 , and yellow curve to advertising investment B. Figures 4(a) and 4(b) show the bifurcation diagrams of price and the corresponding largest Lyapunov exponent plot of the system with $\alpha_2 = 0.01$ and α_1 varying from 0 to 0.065. We can see that with the change of the α_1 , the system enters the chaos from the stable region through flip bifurcation. When $\alpha_1 = 0.044$, the system appears in the first double period orbit. The system becomes chaotic eventually at $\alpha_1 = 0.057$. Figures 4(c) and 4(d) give the bifurcation diagrams of price and the corresponding largest Lyapunov exponent plot of the system with α_2 at 0, 0.065 and α_1 at 0.01. We can see that the system appears the first bifurcation at $\alpha_2 = 0.035$ and appears the second bifurcation at $\alpha_2 = 0.043$, and then through a series of bifurcation the system enters into the chaos eventually. Figures 4(e) and 4(f) show the chaotic attractor when $\alpha_1 = 0.06$, $\alpha_2 = 0.01$ and $\alpha_1 = 0.01$, $\alpha_2 = 0.05$. Figures 4(g)–4(l) give the case that the system enters into the chaos through Neimark–Sacker bifurcation. It shows that when $\alpha_2 = 0.038$, with the change of α_1 the system enters into chaos from the period-two orbit directly. Figures 4(g) and 4(h) show the bifurcation diagram and the corresponding largest Lyapunov exponent plot of the wholesale price w when $\alpha_2 = 0.08$. Figures 4(i)–4(l) show the process from the limit cycle to the strange attractor of the system (18).

3.3.4. The Influence of Parameters on the Profits. Figure 5 shows the influence of adjustment parameters α_i ($i = 1, 2$) and advertising parameter θ on the profits of the

manufacturer and the retailer. The black curve represents the manufacturer's profits and the blue curve represents the retailer's profits. Figure 5 shows the influence of α_i ($i = 1, 2$) on the long-term average profit of the supply chain. In stable state, the profits of the manufacturer are more than the profits of the retailer. With the increase in adjustment speed, in Figure 5(a), when $\alpha_1 > 0.0441$, the manufacturer's profits begin to decrease but the retailer's profits begin to increase, and the retailer's profits exceed the manufacturer's profits when $\alpha_1 > 0.0441$. Similarly, Figure 5(b) shows that the profits of the manufacturer decrease while the profits of retailer increase when $\alpha_1 > 0.035$. Therefore, we conclude that, in the dynamic Stackelberg game, the higher adjustment speed of the wholesale or the direct price has adverse effect on the leader manufacturer, but it is favorable for the follower retailer. Figures 5(c) and 5(d) show the influence of advertising parameter θ on the long-term average profit in the system's stable region ($\alpha_1 = 0.01$ and $\alpha_2 = 0.01$) (Figure 5(c)) and bifurcation region ($\alpha_1 = 0.01$ and $\alpha_2 = 0.04$) (Figure 5(d)), respectively. As shown, with the increase in θ , both in stable region and unstable region, the profit of the manufacturer decreases and the profit of the retailer increases. Therefore, it is unfavorable for the leader manufacturer but favorable for the follower retailer in this model when market is more sensitive to the advertising investment.

4. Retailer Stackelberg (RS)

4.1. Model Construction. In this case, the retailer plays the dominant role in the supply chain and becomes the leader of the Stackelberg game. The retailer first decides the retail price p_1 of the NB product, the retail price p_2 of the SB product, and the advertising investment B. The manufacturer decides the wholesale price w and direct selling price p_0



(a)
FIGURE 4: Continued.

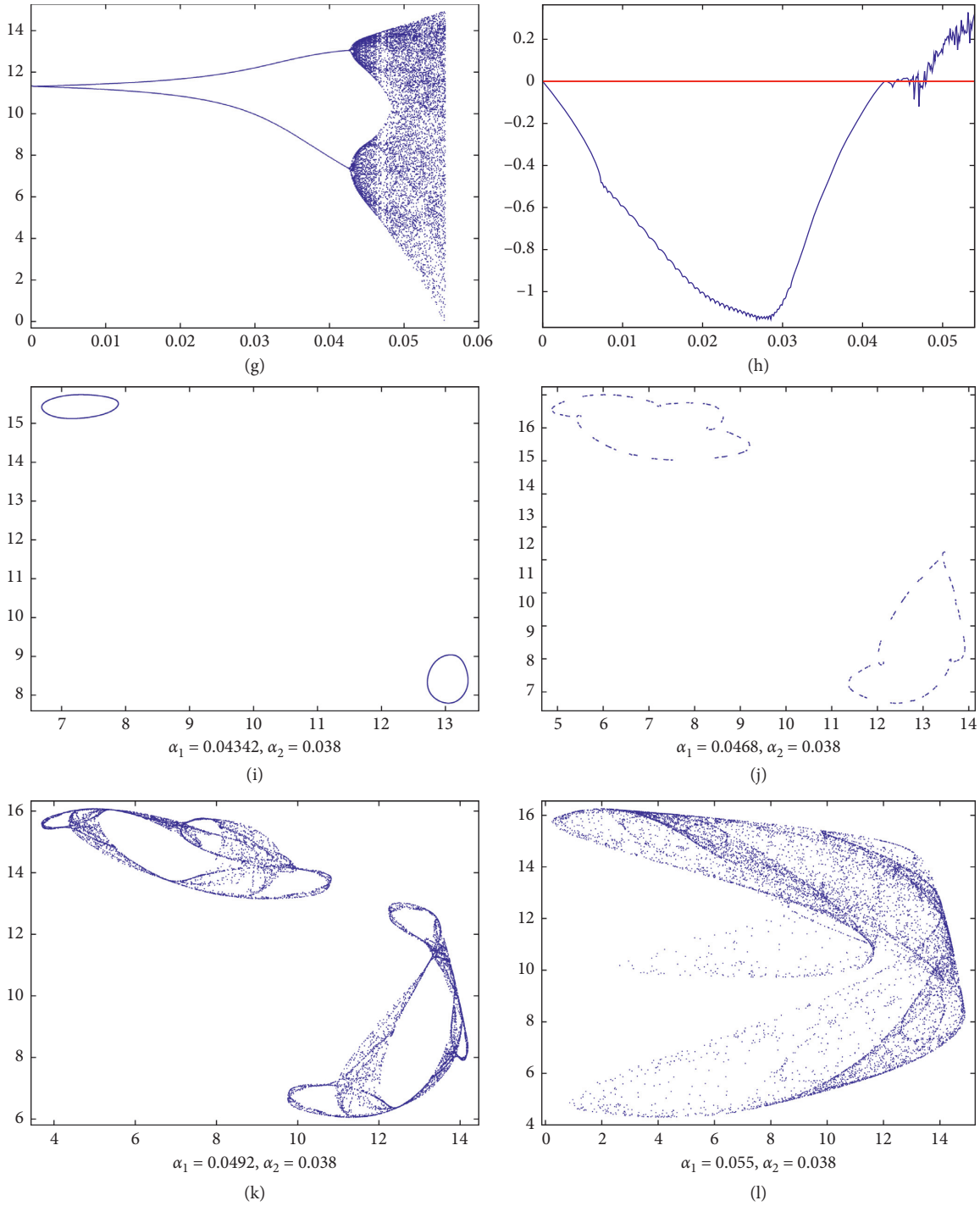


FIGURE 4: Bifurcation diagrams and chaos attractor.

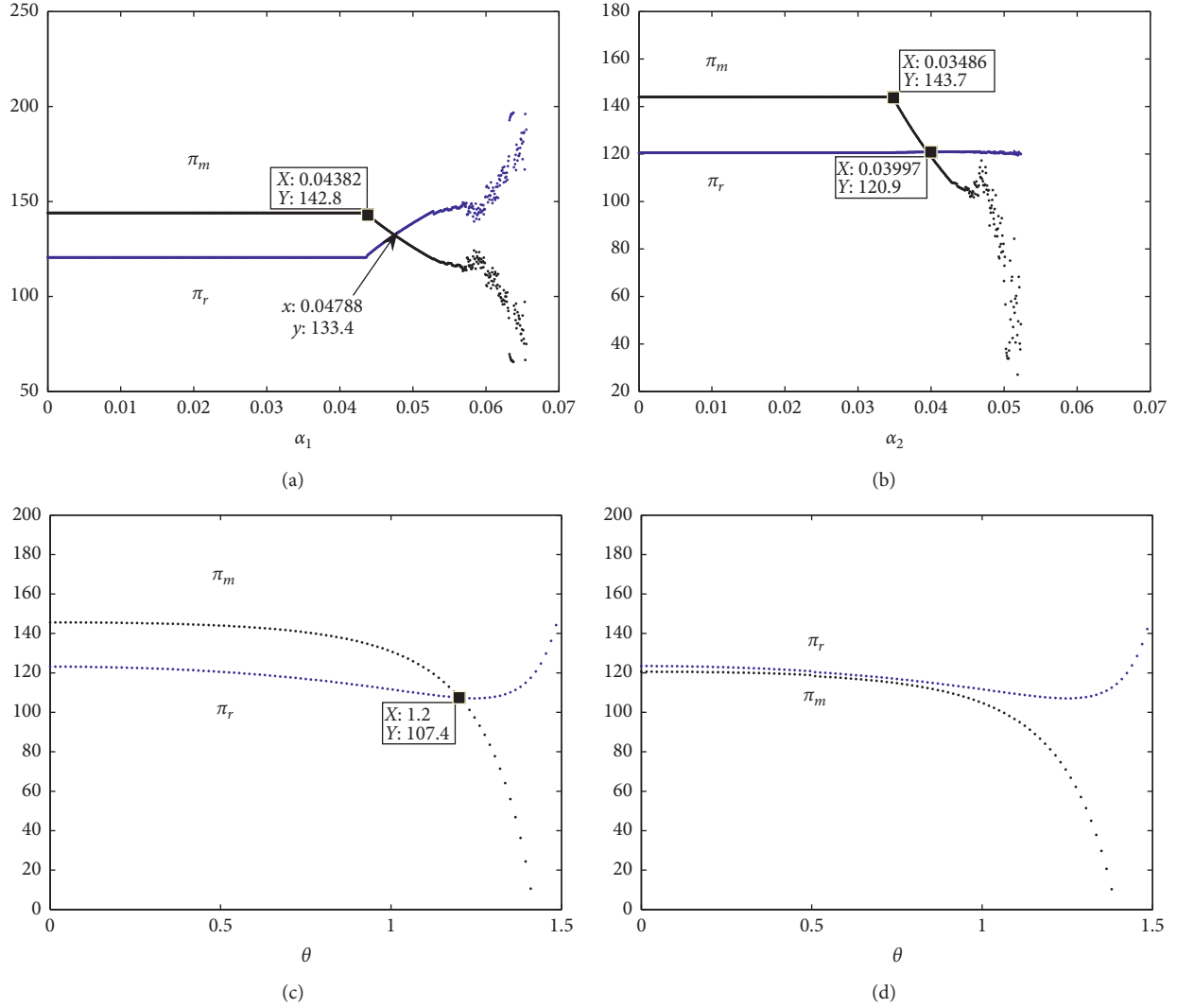


FIGURE 5: The influence of parameters on the profits.

based on the retailer's decision. We assume the unit retail margin is u , and then $p_1 = w + u$. Similar to the model MS, the optimization problem is solved with backward induction.

The profit function of the manufacturer and the retailer are as follows:

$$\pi_m^R = D_0(p_0 - c_0) + D_1(w - c_1), \quad (21)$$

$$\pi_r^R = D_1u + D_2(p_2 - c_2) - B^2. \quad (22)$$

Taking the first-order partial derivatives of π_m^R with respect to w and p_0 , respectively, and taking the second-order derivatives further, we can get the Hessian matrix:

$$\begin{pmatrix} -2b_1 & 2\gamma \\ 2\gamma & -2b_0 \end{pmatrix}. \quad (23)$$

Note that $-2b_1 < 0$ and $4b_0b_1 - 4\gamma^2 > 0$. So, the manufacturer's profit function is concave and has a unique

maximum solution. We can work out the manufacturer's best reaction function by $(\partial\pi_m^R/\partial w) = 0$ and $(\partial\pi_m^R/\partial p_0) = 0$. That is,

$$\begin{aligned} w &= \frac{(a_1b_0 + b_0b_1c_1 - b_0b_1u + a_0\gamma - c_1\gamma^2 + u\gamma^2 + b_0p_2\eta - Bb_0\theta)}{2(b_0b_1 - \gamma^2)} \\ &= c_1 - p_1 + \frac{a_1b_0 + a_0\gamma + b_0p_2\eta - Bb_0\theta}{(b_0b_1 - \gamma^2)}, \end{aligned} \quad (24)$$

$$p_0 = \frac{c_0}{2} + \frac{a_0b_1 + a_1\gamma + \gamma\eta p_2 - \gamma\theta B}{2(b_0b_1 - \gamma^2)}. \quad (25)$$

Substituting (24) and (25) into (22) and then taking the first-order partial derivatives of π_r^R with respect to p_1 , p_2 , and B , respectively, we can obtain the following

$$\frac{\partial \pi_r^R}{\partial p_1} = a_1 + b_1 c_1 + c_0 \gamma - c_1 \eta - 4b_1 p_1 + 2\eta p_2 - B\theta + \frac{(2a_1 b_0 b_1 + 2a_0 b_1 \gamma + 2b_0 b_1 (\eta p_2 - B\theta))}{(b_0 b_1 - \gamma^2)}, \quad (26)$$

$$\frac{\partial \pi_r^R}{\partial p_2} = a_2 + b_2 c_2 - \frac{c_1 \eta}{2} - 2b_2 p_2 + 2\eta p_1 + \theta B + \frac{(b_0^2 b_1 \eta (-\eta p_2 + \theta B) - b_0 b_1 \eta (a_0 \gamma + a_1 b_0))}{(b_0 b_1 - \gamma^2)^2} + \frac{\eta (a_0 \gamma + b_0 b_1 c_1 + 2a_1 b_0 + b_0 c_0 \gamma)}{2(-b_0 b_1 + \gamma^2)} + \frac{2b_0 b_1 \eta p_1 - b_0 \eta^2 p_2 + b_0 \eta \theta B}{b_0 b_1 - \gamma^2}, \quad (27)$$

$$\frac{\partial \pi_r^R}{\partial B} = \frac{1}{2(-b_0 b_1 + \gamma^2)^2} \left(\gamma^3 (-a_0 + (c_1 - 2(c_2 + p_1 - p_2))\gamma) + 2a_1 b_0 (2b_0 b_1 - \gamma^2) + b_0^2 b_1 (2b_1 (c_1 - c_2 - 3p_1 + p_2) + c_0 \gamma + 4p_2 \eta) - b_0 \gamma (-3a_0 b_1 + \gamma (b_1 (3c_1 - 4c_2 - 8p_1 + 4p_2) + c_0 \gamma + 2p_2 \eta)) \right) \theta + B \cdot (-4\gamma^4 - 4b_0^2 b_1 (b_1 + \theta^2) + 2b_0 \gamma^2 (4b_1 + \theta^2)). \quad (28)$$

Taking the second-order derivatives further, we can get the Hessian matrix:

$$\begin{pmatrix} -4b_1 & f_1 & f_2 \\ f_1 & f_3 & f_4 \\ f_2 & f_4 & f_5 \end{pmatrix}, \quad (29)$$

where

$$\begin{aligned} f_1 &= \frac{4b_0 b_1 \eta - 2\gamma^2 \eta}{b_0 b_1 - \gamma^2}, \\ f_2 &= \frac{(-3b_0 b_1 + \gamma^2)\theta}{b_0 b_1 - \gamma^2}, \\ f_3 &= -2b_2 + \frac{b_0 (-2b_0 b_1 + \gamma^2)\eta^2}{(-b_0 b_1 + \gamma^2)^2}, \\ f_4 &= \frac{(\gamma^4 - b_0 \gamma^2 (2b_1 + \eta) + b_0^2 b_1 (b_1 + 2\eta))\theta}{(-b_0 b_1 + \gamma^2)^2}, \\ f_5 &= \frac{-2\gamma^4 - 2b_0^2 b_1 (b_1 + \theta^2) + b_0 \gamma^2 (4b_1 + \theta^2)}{(-b_0 b_1 + \gamma^2)^2}. \end{aligned} \quad (30)$$

While satisfying

$$\frac{8b_0 b_1 (b_1 b_2 - \eta^2) + 4\gamma^2 (-2b_1 b_2 + \eta^2)}{b_0 b_1 - \gamma^2} > 0, \quad (31)$$

$$\frac{1}{(-b_0 b_1 + \gamma^2)^2} \left(2\gamma^4 (-8b_1 b_2 + 4\eta^2 + 2b_1 \theta^2 + b_2 \theta^2 - 2\eta \theta^2) + 2b_0^2 b_1 (\eta^2 \theta^2 + b_1^2 (-8b_2 + 2\theta^2) + b_1 (8\eta^2 + b_2 \theta^2 - 4\eta \theta^2)) + b_0 \gamma^2 (-\eta^2 \theta^2 + 8b_1^2 (4b_2 - \theta^2) - 4b_1 (6\eta^2 + b_2 \theta^2 - 3\eta \theta^2)) \right) < 0, \quad (32)$$

the retailer's profit function is concave and has a unique maximum solution because the Hessian matrix is negative definite. So, we get the optimal retail price p_1^R , p_2^R , and B^R . Furthermore, we also get the optimal wholesale price w^R and direct selling price p_0^R (see Appendix A.16–A.20).

Similar to the MS model, we develop a dynamic Stackelberg game model. Suppose that the decision in next period can be adjusted with bounded rationality and is based on partial estimation of the marginal profits of the current period. The model can be constructed as follows:

$$\begin{cases} p_1(t+1) = p_1(t) + \beta_1 p_1(t) \frac{\partial \pi_r^R(p_1, p_2, B)}{\partial p_1(t)}, \\ p_2(t+1) = p_2(t) + \beta_2 p_2(t) \frac{\partial \pi_r^R(p_1, p_2, B)}{\partial p_2(t)}, \\ B(t+1) = B(t) + \beta_3 B(t) \frac{\partial \pi_r^R(p_1, p_2, B)}{\partial B(t)}. \end{cases} \quad (33)$$

System (45) gives the retailer's dynamic price decision, and the decision variables directly relate to the positive parameter β_i ($i = 1, 2, 3$) which represents the price adjustment speed. $(\partial \pi_r^R(p_1, p_2, B))/(\partial p_1(t))$, $(\partial \pi_r^R(p_1, p_2, B))/(\partial p_2(t))$, and $(\partial \pi_r^R(p_1, p_2, B))/(\partial B(t))$ are the marginal profits, and they can be obtained from (26)–(28). Furthermore, the manufacturer's price decision can be worked out based on $p_1(t)$, $p_2(t)$, and $B(t)$.

$$\begin{aligned} w(t) &= c_1 - p_1(t) + \frac{a_1 b_0 + a_0 \gamma + b_0 \eta p_2(t) - b_0 \theta B(t)}{(b_0 b_1 - \gamma^2)}, \\ p_0(t) &= \frac{c_0}{2} + \frac{a_0 b_1 + a_1 \gamma + \gamma \eta p_2(t) - \gamma \theta B(t)}{2(b_0 b_1 - \gamma^2)}. \end{aligned} \quad (34)$$

4.2. Model Analysis. The eight equilibrium solutions of system (33) (E_1, E_2, \dots, E_8) can be shown as follows (here only giving the nonzero equilibrium solutions):

$$\begin{aligned}
E_7 = & \left\{ \left(4a_1(3b_0^2b_1^2 - 4b_0b_1\gamma^2 + \gamma^4) + \gamma^3(a_0(-8b_1 + \theta^2) + \gamma(4b_1c_1 + 4c_0\gamma - 4c_2\eta - c_1\theta^2 + 2c_2\theta^2)) \right. \right. \\
& + b_0^2b_1(4b_1^2c_1 + (c_0\gamma - 4c_2\eta)\theta^2 + b_1(4c_0\gamma - 4c_2\eta - 2c_1\theta^2 + 6c_2\theta^2)) - b_0\gamma(a_0b_1(-8b_1 + \theta^2) \\
& + \gamma(8b_1^2c_1 + (c_0\gamma - 2c_2\eta)\theta^2 + b_1(8c_0\gamma - 8c_2\eta - 3c_1\theta^2 + 8c_2\theta^2))) \\
& \cdot \left(2(-b_0b_1 + \gamma^2)(8b_1 - \theta^2) \right)^{-1}, 0, \left((a_1(-b_0b_1 + \gamma^2) + \gamma^2(-b_1c_1 + 4b_1c_2 + c_0\gamma - c_2\eta)) \right. \\
& \left. \left. + b_0b_1(b_1c_1 - 4b_1c_2 - c_0\gamma + 3c_2\eta)\theta \right) \cdot \left((b_0b_1 - \gamma^2)(8b_1 - \theta^2) \right)^{-1} \right\}, \\
E^R = & (p_1^R, p_2^R, B^R).
\end{aligned} \tag{35}$$

E_i ($i = 1, 2, \dots, 7$) are boundary equilibrium solutions, while E^R is the only Stackelberg equilibrium solution. Its expression is shown (A.16)–(A.18) in Appendix. In order to guarantee the practical significance, we assume that all equilibriums are positive.

The Jacobian matrix of system (33) is given by

$$\begin{pmatrix} 1 + \beta_1 t_1 & \beta_2 f_1 p_2 & \beta_3 f_2 B \\ \beta_1 f_1 p_1 & 1 + \beta_2 t_2 & \beta_3 f_4 B \\ \beta_1 f_2 p_1 & \beta_2 f_4 p_2 & 1 + \beta_3 t_3 \end{pmatrix}, \tag{36}$$

where

$$\begin{aligned}
t_1 = & a_1 + b_1c_1 - \eta c_2 + \gamma c_0 + 2\eta p_2 - 8b_1p_1 - B\theta \\
& + \frac{2b_1(a_1b_0 + a_0\gamma + b_0\eta p_2 - b_0B\theta)}{b_0b_1 - \gamma^2}, \\
t_2 = & \frac{1}{2(-b_0b_1 + \gamma^2)^2} \left(2a_2(-b_0b_1 + \gamma^2)^2 + \gamma^3(2b_2(c_2 - 4p_2)\gamma \right. \\
& + a_0\eta - c_1\gamma\eta + 4p_1\gamma\eta + 2B\gamma\theta) + b_0^2b_1(-\eta(4a_1 + c_0\gamma \\
& + 8p_2\eta - 4B\theta) + 2b_1(b_2c_2 - 4b_2p_2 - c_1\eta + 4p_1\eta + B\theta)) \\
& + b_0\gamma(\gamma\eta(2a_1 + c_0\gamma + 4p_2\eta - 2B\theta) - b_1(4b_2(c_2 - 4p_2)\gamma \\
& \left. + 3a_0\eta - 3c_1\gamma\eta + 12p_1\gamma\eta + 4B\gamma\theta)) \right), \\
t_3 = & \frac{1}{2(-b_0b_1 + \gamma^2)^2} \left((\gamma^3(-a_0 + (c_1 - 2(c_2 + p_1 - p_2))\gamma) \right. \\
& + 2a_1b_0(2b_0b_1 - \gamma^2) + b_0^2b_1(2b_1(c_1 - c_2 - 3p_1 + p_2) \\
& + c_0\gamma + 4p_2\eta) - b_0\gamma(-3a_0b_1 + \gamma(b_1(3c_1 - 4c_2 - 8p_1 \\
& + 4p_2) + c_0\gamma + 2p_2\eta)))\theta - 4B(2\gamma^4 + 2b_0^2b_1(b_1 + \theta^2) \\
& \left. - b_0\gamma^2(4b_1 + \theta^2)) \right).
\end{aligned} \tag{37}$$

The stability of equilibrium points will be determined by the nature of the eigenvalues of the Jacobian matrix

evaluated at the corresponding equilibrium points. Then, we substitute the value of E_i ($i = 1, 2, \dots, 7$) into (36) and we have the following proposition.

Proposition 2. *All the boundary equilibrium points E_i ($i = 1, 2, \dots, 7$) are unstable under our assumptions and conditions (31) and (32).*

We investigate the stability of E^M by utilizing Jury's stability condition [22]. Assuming the characteristic polynomial for the Jacobian matrix J is

$$f(\lambda) = \lambda^3 + A\lambda^2 + B\lambda + C. \tag{38}$$

Then, the local stability domain can be determined by the following conditions:

$$\begin{aligned}
\text{(i)} : & f(1) = A + B + C + 1 > 0, \\
\text{(ii)} : & f(-1) = A - B + C - 1 < 0, \\
\text{(iii)} : & C^2 - 1 < 0, \\
\text{(iv)} : & (1 - C^2)^2 - (B - AC)^2 > 0.
\end{aligned} \tag{39}$$

4.3. The Experimental Calculation and Analysis. In this section, numerical simulations are carried to show the influence of parameters. We will study how the adjust parameters, advertising coefficients, and cost parameters affect the product prices and the long-term average profit. We first choose some values for some parameters based on actual competition: $a_0 = 30$; $a_1 = 55$; $a_2 = 35$; $b_0 = 2.2$; $b_1 = 4.05$; $b_2 = 2.35$; $\gamma = 0.7$; $\eta = 0.6$; $\theta = 0.5$; $c_0 = 7$; $c_1 = 5$; and $c_2 = 7$ (the values are the same as the model of MS). These parameters should meet the model assumptions and conditions (34) and (A.16). We can calculate the equilibrium prices of the system: $p_1^R = 15.0997$; $p_2^R = 13.4153$; $B^R = 0.6879$; $w^R = 8.7782$; and $p_0^R = 13.3215$. The manufacturer and retailer's optimal profit of stable region are $\pi_m^R = 112.289$ and $\pi_r^R = 150.898$.

4.3.1. The Stability Region and the Bifurcation Diagrams of the System. In Figure 6, the stability of the equilibrium region is presented. We can see that the system is stable when $\beta_1 < 0.008$, $\beta_2 < 0.02$, and $\beta_3 < 1.4$. A high adjustment speed will make the system leave the stable area.

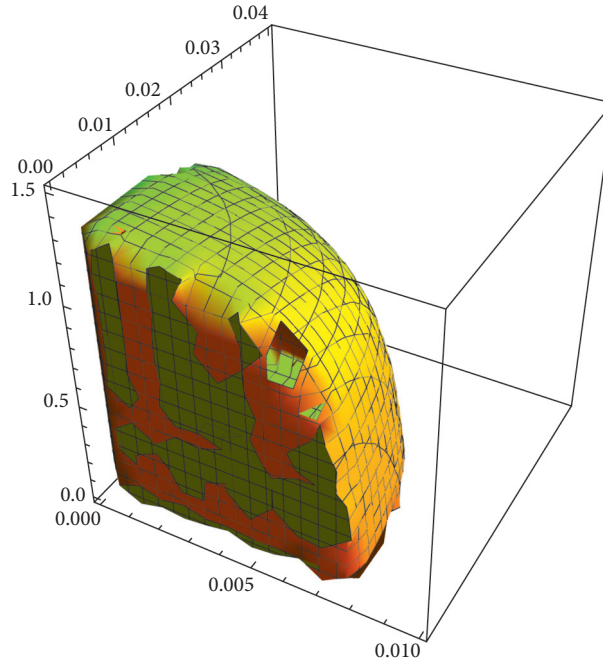


FIGURE 6: The stability region of the system.

Figure 7(a) presents the parameter basin with respect to the parameters (β_1, β_2) ($\beta_3 = 0.1$) and assigns different colors to different periods (see the MS model). From this two-dimensional bifurcation diagram of the system, we can see that the system enters into chaos through period-doubling bifurcation and Neimark–Sacker bifurcation. Figure 7(b) gives the bifurcation diagrams of the retail price p_1 with $\beta_2 = 0.018, \beta_3 = 0.1$, and β_1 at 0, 0.012. Figure 7(c) gives the limit cycle diagram when $\beta_1 = 0.0103, \beta_2 = 0.018$, and $\beta_3 = 0.1$. Figure 7(d) is the corresponding largest Lyapunov exponent plot.

4.3.2. Chaos Attractor and Sensitivity to Initial Values. Figure 8 shows the chaotic attractor and the butterfly effect. Figure 8(a) is the chaotic attractor of system (33) when $\beta_1 = 0.011, \beta_2 = 0.01$, and $\beta_3 = 0.1$. Figures 8(b)–8(d) show the sensitivity to initial values of system (33) when $p_1 = 15.09969, p_2 = 13.4153$, and $B = 0.68792$. In Figure 8(b), blue curve is the retail price p_1 with the initial values $p_1 = 15.09969$, and red curve is the retail price p_1 with the initial values $p_1 = 15.09968$. We can see from the figure that when the retail price p_1 initial value changed 0.00001, the system tends to be significantly different after about 20 cycles iteration. Similarly, Figures 8(c)–8(d) give the case when the retail price p_2 initial value changed 0.0001 and the advertising investment B changed 0.00001. It can be seen that a small change of the initial value will cause quite different results in the end.

4.3.3. The Influence of Parameters on the Profits. Figures 9(a)–9(d) give the influence of β_i ($i = 1, 2, 3$) on the long-term average profit of the manufacturer (black curve) and the retailer (blue curve). As shown, with the increase of the

β_i ($i = 1, 2, 3$), the profit of the manufacturer and the retailer is stable at first, and when the system enters into the bifurcation region, the retailer’s profits begin to decrease. But, the result is opposite for the manufacturer. Therefore, we conclude that in the RS model, the higher adjustment speed of the price is adverse to the leader retailer, but it is favorable to the follower manufacturer.

Figures 9(e)–9(j) show the influence of the cost c_0 , channel competition coefficient γ , and brand competition coefficient η on the long-term average profit in the system stable region ($\beta_1 = 0.001, \beta_2 = 0.01$, and $\beta_3 = 0.1$) and the bifurcation region ($\beta_1 = 0.01, \beta_2 = 0.01$, and $\beta_3 = 0.1$), respectively. From Figures 9(e) and 9(f), we can see that both profits are in the stable region and the bifurcation region separately. So, in the RS model, the manufacturers can improve their profit through controlling the cost of the direct channel. From Figures 9(g) and 9(h), we can see that channel competition coefficient γ has obvious effects on profits. In the stable region, with the increase of γ , both manufacturer’s profit and retailer’s profit are rising; the profit of the manufacturer rise significantly greater than that of the retailer; when $\gamma > 0.005$, the profit of the manufacturer and the profit of the retailer are the same; when $\gamma > 0.005$, the profit of the manufacturer exceed the profit of the retailer. In the bifurcation region with the increase of γ , the manufacturer’s profit is still increasing while the retailer’s profit decreases rapidly. It shows that in the RS model, the manufacturer who sets up a direct sales channel is more advantageous than the retailer when the market is sensitive to channel competition. Figures 9(i) and 9(j) give the influence of the brand competition coefficient η on the profit. We can see from the figure, in the stable region, with the increase of η , both manufacturer’s and retailer’s profit will increase, but when the system enters into the bifurcation

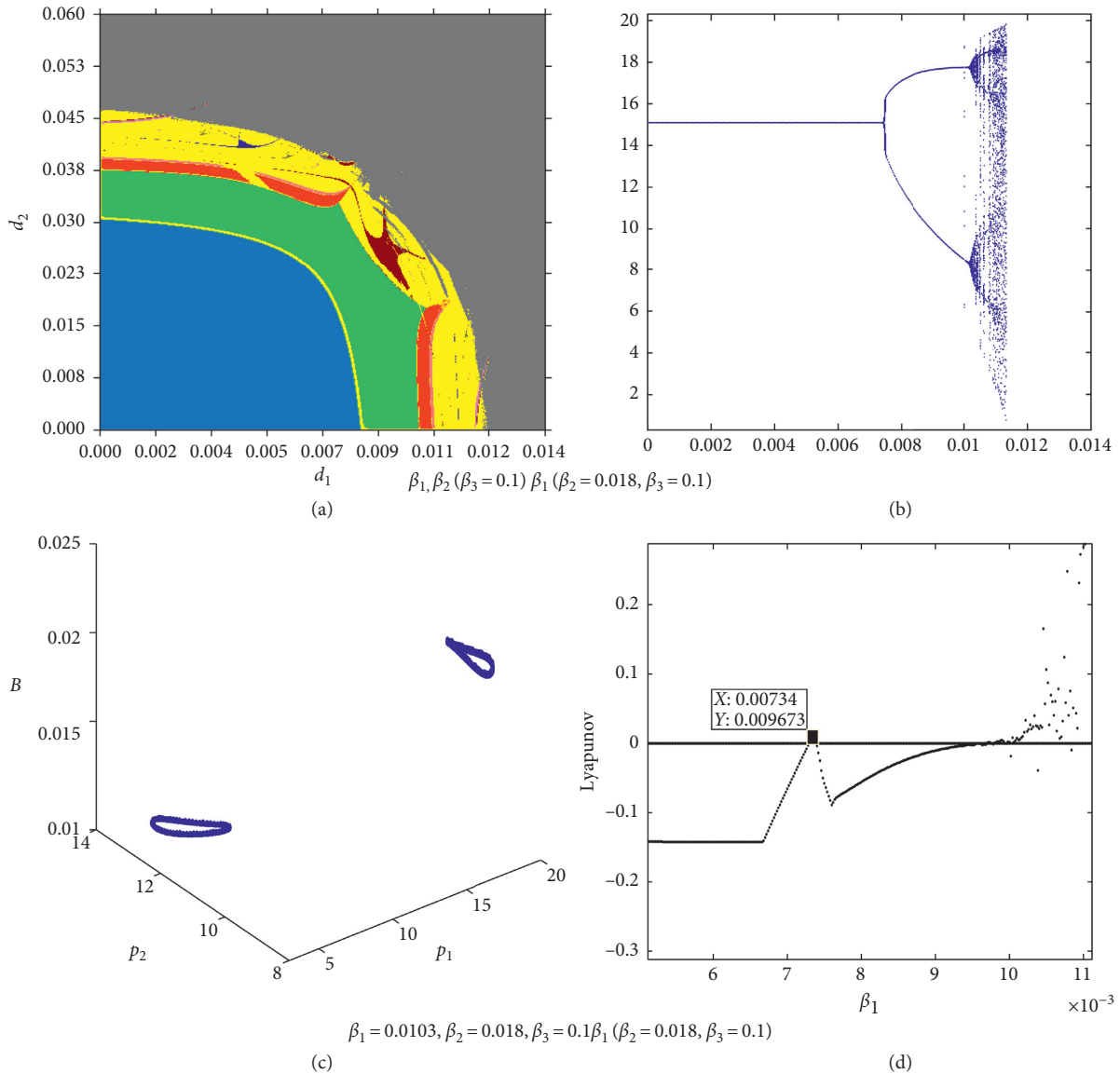


FIGURE 7: Two-dimensional bifurcation diagrams of the system.

region, the manufacturer’s profit is still increasing while the retailer’s profit decreases rapidly. So, in a word, controlling the cost and increasing the channel competitive strength and brand competition strength will make the manufacturer increase its profit in the game dominated by the retailer.

5. Comparison of the Two Models and Analysis

In this section, we compare the prices and profits of the two models in the stable region and in the bifurcation region, respectively. The results are shown in Table 1.

Table 1 shows the prices and the profits of the two models in different regions.

In Table 1, we compare different variables of the two models in the stable region and bifurcation region, respectively. It can be seen from Table 1, in the stable region, the wholesale price and direct selling price is higher in the MS model than that in the RS model. The total profit of the

supply chain in the MS model is also more than that in the RS model. In the RS model, the lower wholesale price makes the retailer gain more profit. In the bifurcation region, with the increase of the competitive level, both in the MS model and the RS model, the retailer has the lower NB product price and SB product price. In addition, we can see that the game leader will have advantages in the stability region, but once enters into the bifurcation region or the chaos region, the game followers will adjust their price to follow the leader’s decision so that they can make a profit.

6. Conclusions

This paper researches two noncooperative dynamic pricing strategies used in a supply chain. We establish dynamic Stackelberg game models in which either the manufacturer or the retailer acts as a leader. In these two models, the manufacturer sells a national-brand (NB) product to an

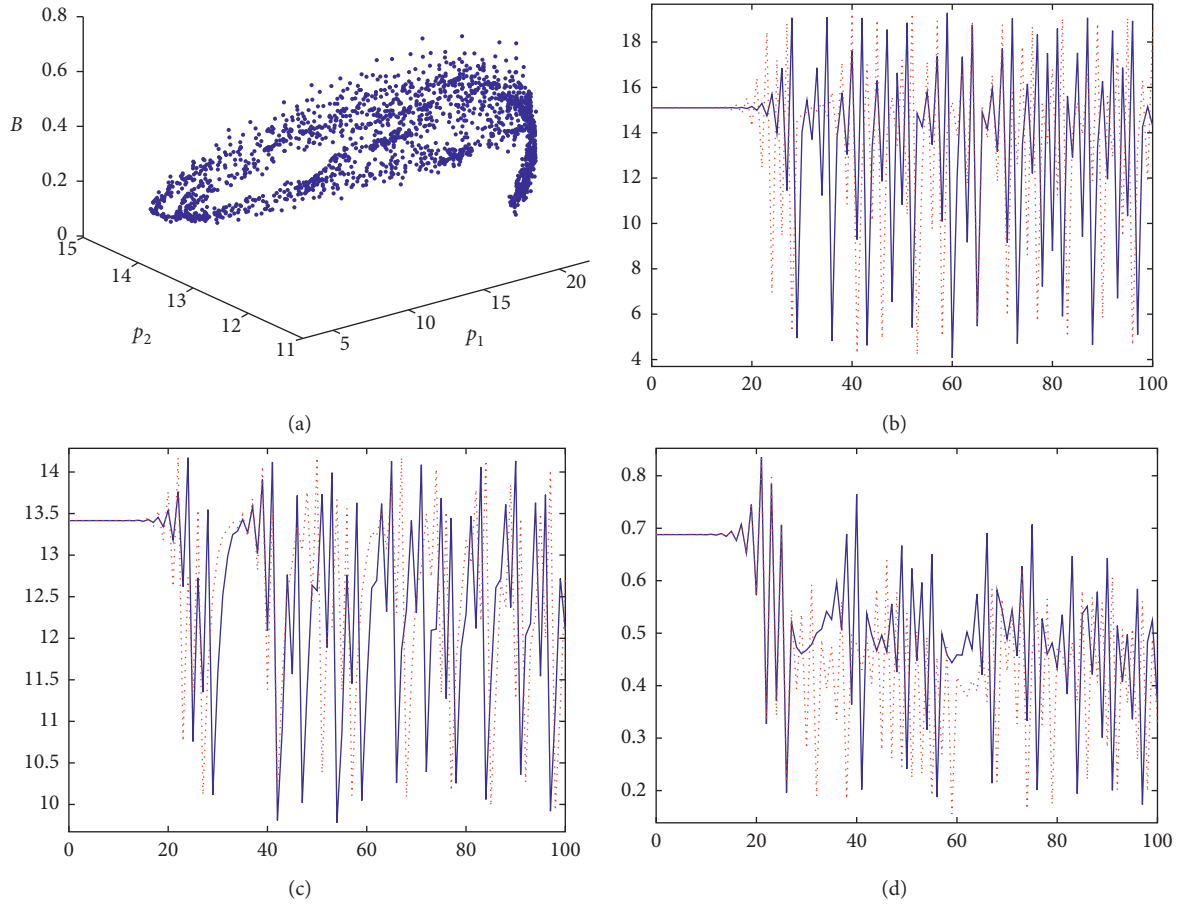
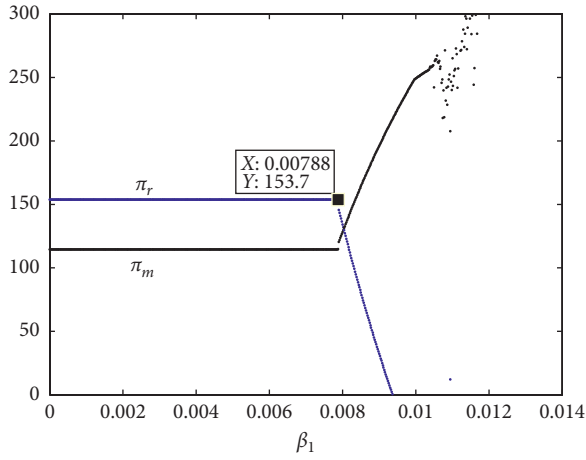


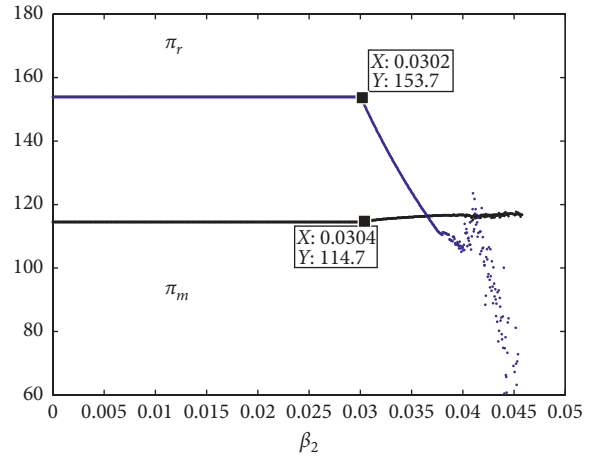
FIGURE 8: Chaos attractor and the sensitivity to initial value.

independent retailer or directly to consumers through a direct channel. The retailers sell a store-brand (SB) product when they sell the NB product coming from the manufacturer. So, there is competition both in different channels and in products with different brands. We consider the two Stackelberg game: either the manufacturer acts as a leader or the retailer acts as a leader. We use dynamic theory to analyze the complexity of the model, such as bifurcation and chaos. The results indicate that in the MS model, with the increase of the adjustment speed, both the wholesale price and the direct selling price are higher which in turn incur larger profits for the manufacturer, but it gets worse when

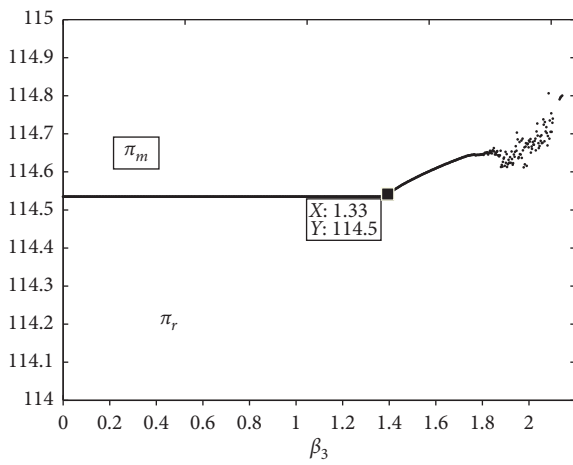
the adjustment speed increases. In the RS model, with the increase of the adjustment speed, the increase of the adjustment speed is unfavorable to the retailer. By controlling the total cost of the direct channel and increasing channel competition strength and brand competitive strength, the manufacturers can increase their profits in the game dominated by the retailer. In addition, the stable region within the system will become smaller when the market is sensitive to the channel competition, brand competition, and advertising indifference. The research will serve as a good guidance for the supply chain managers who wish to achieve the best business results.



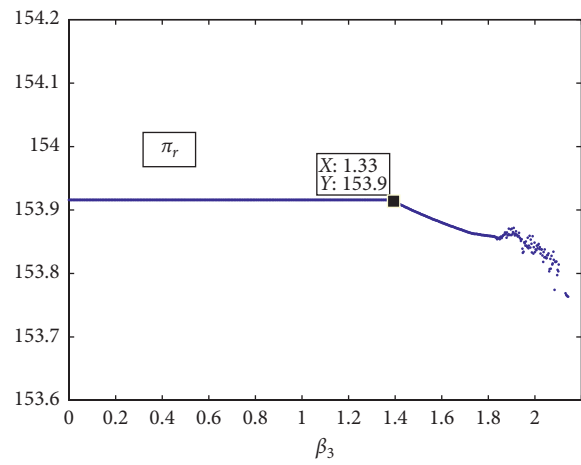
(a)



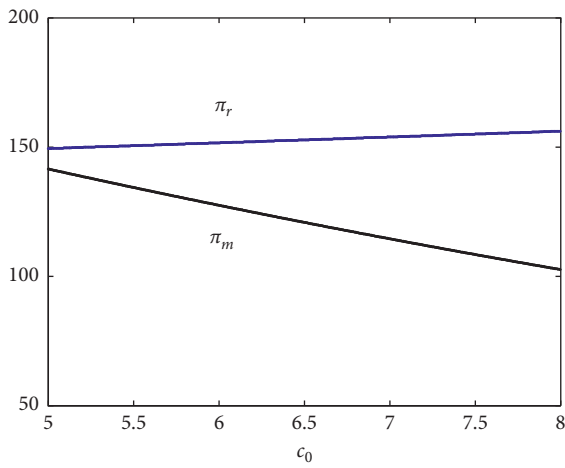
(b)



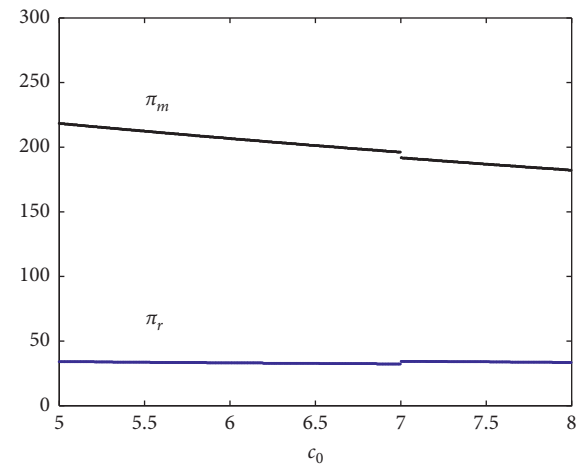
(c)



(d)



(e)



(f)

FIGURE 9: Continued.

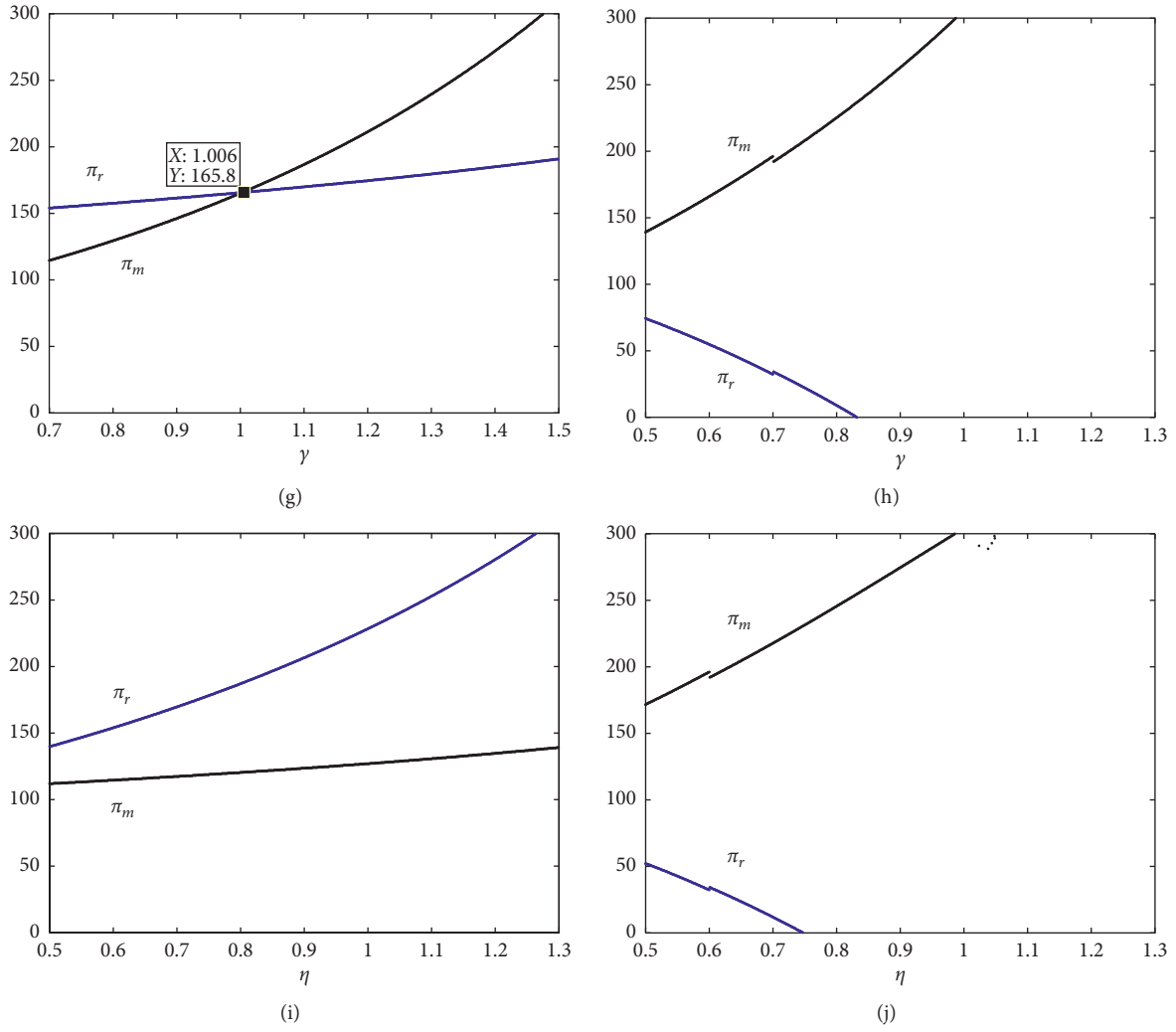


FIGURE 9: The influence of parameters on the profits.

TABLE 1: Units for magnetic properties.

	MS	MS	RS	RS
	$\alpha_1 = 0.01,$ $\alpha_2 = 0.01$	$\alpha_1 = 0.05,$ $\alpha_2 = 0.01$	$\beta_1 = 0.001,$ $\beta_2 = 0.01,$ $\beta_3 = 0.1$	$\beta_1 = 0.009,$ $\beta_2 = 0.01,$ $\beta_3 = 0.1$
w	11.406	10.4333	8.7782	9.7763
p_0	13.3228	13.1668	13.3215	13.3111
p_1	15.0705	14.5760	15.0997	14.0365
p_2	13.4116	13.3964	13.4153	12.7192
B	0.6868	0.5634	0.6879	0.3506
π_m	141.4914	120.1906	112.289	192.2792
π_r	122.3231	143.2053	150.898	31.6133
π	263.8145	263.3959	263.187	223.8925

Appendix

$$\begin{aligned}
w^M = & (2b_0(4b_1b_2 - 4\eta^2 - b_1\theta^2 - b_2\theta^2 + 2\eta\theta^2) (((b_2c_0\gamma + \eta(a_2 - c_0\gamma - c_1\eta)\theta^2 + b_1^2c_1(4b_2 - \theta^2) + c_2\eta(-4\eta^2 - b_2\theta^2 + \eta\theta^2) \\
& + b_1(-a_2 + c_2\eta)\theta^2 + 2c_1\eta(-2\eta + \theta^2) + b_2c_2(4\eta + \theta^2))) + \gamma(2a_0(4\eta^2 + b_2\theta^2 - 2\eta\theta^2 + b_1(-4b_2 + \theta^2))^2 \\
& - \gamma(-16b_2c_2\eta^3 + 16c_1\eta^4 + 4b_2^2c_0\gamma\theta^2 - 4b_2^2c_2\eta\theta^2 - 4b_2c_0\gamma\eta\theta^2 + 8b_2c_2\eta^2\theta^2 - 12c_1\eta^3\theta^2 + b_2^2c_2\theta^4 - b_2c_0\gamma\theta^4 - b_2c_1\eta\theta^4 \\
& - 2b_2c_2\eta\theta^4 + c_0\gamma\eta\theta^4 + 3c_1\eta^2\theta^4 + c_2\eta^2\theta^4 + 2b_1^2c_1(-4b_2 + \theta^2)^2 - b_1(4b_2 - \theta^2)(4a_2\eta - 4b_2c_2\eta + 12c_1\eta^2 + b_2c_1\theta^2 - 5c_1\eta\theta^2) \\
& + a_2(16\eta^3 + 8b_2\eta\theta^2 - 12\eta^2\theta^2 - b_2\theta^4 + \eta\theta^4))) + a_1(-\gamma^2(b_2 - \eta)\theta^2(4b_2 - \theta^2) + 2b_0(b_1^2(-4b_2 + \theta^2)^2 \\
& + \eta(4\eta - \theta^2)(4\eta^2 + b_2\theta^2 - 2\eta\theta^2) + b_1(-4b_2^2\theta^2 + \eta\theta^2(8\eta - 3\theta^2) + b_2(-32\eta^2 + 12\eta\theta^2 + \theta^4)))) \\
& \cdot (2(2b_0(b_1^3(-4b_2 + \theta^2)^2 + \eta^2\theta^2(4\eta^2 + b_2\theta^2 - 2\eta\theta^2) + b_1\eta(16\eta^3 - 16\eta^2\theta^2 - 2b_2\theta^4 + 5\eta\theta^4) + b_1^2(-4b_2^2\theta^2 + 4\eta\theta^2(2\eta - \theta^2) \\
& + b_2(-32\eta^2 + 16\eta\theta^2 + \theta^4)))) - \gamma^2(16\eta^4 - 16\eta^3\theta^2 + b_2^2\theta^4 - 4b_2\eta\theta^4 + 2b_1^2(-4b_2 + \theta^2)^2 + \eta^2(4b_2\theta^2 + 5\theta^4) \\
& + b_1(-8b_2^2\theta^2 + 6\eta\theta^2(2\eta - \theta^2) + b_2(-48\eta^2 + 24\eta\theta^2 + 2\theta^4))))^{-1},
\end{aligned} \tag{A.1}$$

$$\begin{aligned}
p_0^M = & (2a_0(b_1^3(-4b_2 + \theta^2)^2 + \eta^2\theta^2(4\eta^2 + b_2\theta^2 - 2\eta\theta^2) + b_1\eta(16\eta^3 - 16\eta^2\theta^2 - 2b_2\theta^4 + 5\eta\theta^4) + b_1^2(-4b_2^2\theta^2 + 4\eta\theta^2(2\eta - \theta^2) \\
& + b_2(-32\eta^2 + 16\eta\theta^2 + \theta^4))) + 2b_0c_0(b_1^3(-4b_2 + \theta^2)^2 + \eta^2\theta^2(4\eta^2 + b_2\theta^2 - 2\eta\theta^2) + b_1\eta(16\eta^3 - 16\eta^2\theta^2 - 2b_2\theta^4 + 5\eta\theta^4) \\
& + b_1^2(-4b_2^2\theta^2 + 4\eta\theta^2(2\eta - \theta^2) + b_2(-32\eta^2 + 16\eta\theta^2 + \theta^4))) + \gamma(-16c_0\gamma\eta^4 + 16c_2\eta^5 - 8b_2c_0\gamma\eta^2\theta^2 - 8a_2\eta^3\theta^2 + 8b_2c_2\eta^3\theta^2 \\
& + 20c_0\gamma\eta^3\theta^2 - 12c_2\eta^4\theta^2 - 2b_2^2c_0\gamma\theta^4 - \theta^2)((2c_0\gamma + c_1\eta - 2c_2\eta)\theta^2 + a_2(4\eta - 2\theta^2) + b_2(-8c_0\gamma + 4c_2\eta - c_1\theta^2 + 2c_2\theta^2)) \\
& + a_1(2b_1^2(-4b_2 + \theta^2)^2 + \eta(16\eta^3 - 12\eta^2\theta^2 - b_2\theta^4 + 3\eta\theta^4) + b_1(-4b_2^2\theta^2 + \eta\theta^2(12\eta - 5\theta^2) + b_2(-48\eta^2 + 20\eta\theta^2 + \theta^4))) \\
& + b_1(-b_2^2\theta^2(-12c_0\gamma + c_2(8\eta + \theta^2))) + b_2(\theta^2(4a_2\eta + 4c_1\eta^2 + a_2\theta^2 - 2c_1\eta\theta^2) + c_0\gamma(48\eta^2 - 28\eta\theta^2 - 3\theta^4) \\
& + c_2(-32\eta^3 + 4\eta^2\theta^2 + 6\eta\theta^4)) + \eta(a_2(-16\eta^2 + 16\eta\theta^2 - 5\theta^4) + \theta^2(c_0\gamma(-12\eta + 7\theta^2) + \eta(-4c_1\eta + 12c_2\eta + 2c_1\theta^2 - 5c_2\theta^2)))) \\
& \cdot (2(2b_0(b_1^3(-4b_2 + \theta^2)^2 + \eta^2\theta^2(4\eta^2 + b_2\theta^2 - 2\eta\theta^2) + b_1\eta(16\eta^3 - 16\eta^2\theta^2 - 2b_2\theta^4 + 5\eta\theta^4) \\
& + b_1^2(-4b_2^2\theta^2 + 4\eta\theta^2(2\eta - \theta^2) + b_2(-32\eta^2 + 16\eta\theta^2 + \theta^4))) - \gamma^2(16\eta^4 - 16\eta^3\theta^2 + b_2^2\theta^4 - 4b_2\eta\theta^4 + 2b_1^2(-4b_2 + \theta^2)^2 \\
& + \eta^2(4b_2\theta^2 + 5\theta^4) + b_1(-8b_2^2\theta^2 + 6\eta\theta^2(2\eta - \theta^2) + b_2(-48\eta^2 + 24\eta\theta^2 + 2\theta^4))))^{-1},
\end{aligned} \tag{A.2}$$

$$\begin{aligned}
P_1^M = & \left(a_1 \left(-\gamma^2 (4b_2 - \theta^2) (b_1 (4b_2 - \theta^2) + \eta (-2\eta + \theta^2)) + b_0 \left(3b_1^2 (-4b_2 + \theta^2)^2 + b_1 (-64b_2\eta^2 - 8b_2^2\theta^2 + 32b_2\eta\theta^2 + 16\eta^2\theta^2 \right. \right. \right. \\
& + 2b_2\theta^4 - 8\eta\theta^4) + \eta (16\eta^3 - 16\eta^2\theta^2 - 2b_2\theta^4 + 5\eta\theta^4) \left. \left. \left. \right) + \gamma \left(a_0 \left(16\eta^4 - 20\eta^3\theta^2 + 2b_2^2\theta^4 - 7b_2\eta\theta^4 + 2b_1^2 (-4b_2 + \theta^2)^2 \right. \right. \right. \\
& + \eta^2 (8b_2\theta^2 + 7\theta^4) + b_1 (-12b_2^2\theta^2 + \eta\theta^2 (12\eta - 7\theta^2) + b_2 (-48\eta^2 + 28\eta\theta^2 + 3\theta^4)) \left. \left. \left. \right) - \gamma \left(b_1^2 c_1 (-4b_2 + \theta^2)^2 \right. \right. \right. \\
& - qb_1 (4b_2 - \theta^2) (6c_1\eta^2 + c_0\gamma\theta^2 - 3c_1\eta\theta^2 + c_2\eta\theta^2 + a_2 (-4\eta + \theta^2) + b_2 (-4c_0\gamma + (c_1 - c_2)\theta^2)) \\
& + \eta (-2b_2^2c_2\theta^2 - a_2(8\eta^2 - 4\eta\theta^2 + \theta^4) + (2\eta - \theta^2) ((c_0\gamma + c_2\eta)\theta^2 + 2c_1\eta(2\eta - \theta^2)) + b_2(4c_0\gamma(-2\eta + \theta^2) \\
& + \theta^2(2a_2 + 2c_1\eta - c_1\theta^2 + c_2\theta^2))) \left. \left. \left. \right) + b_0 \left(b_1^3 c_1 (-4b_2 + \theta^2)^2 + b_1^2 (4b_2 - \theta^2) (8a_2\eta - 8c_1\eta^2 - 3a_2\theta^2 - c_0\gamma\theta^2 \right. \right. \right. \\
& + 5c_1\eta\theta^2 - 3c_2\eta\theta^2 + b_2(4c_0\gamma + 4c_2\eta - 2c_1\theta^2 + 3c_2\theta^2)) + c_2\eta(16\eta^4 - 16\eta^3\theta^2 + 2b_2^2\theta^4 - 7b_2\eta\theta^4 + \eta^2(12b_2\theta^2 + 5\theta^4)) \\
& + \theta^2 (-2b_2^2c_0\gamma\theta^2 + \eta^2(-12a_2\eta + 4c_0\gamma\eta + 4c_1\eta^2 + 5a_2\theta^2 - 2c_0\gamma\theta^2 - 3c_1\eta\theta^2) + b_2\eta(-2(a_2 - c_1\eta)\theta^2 + c_0\gamma(-8\eta + 5\theta^2))) \\
& + b_1 - 2b_2^2\theta^2(-2c_0\gamma + c_2(6\eta + \theta^2)) + \eta(-4a_2(8\eta^2 - 7\eta\theta^2 + 2\theta^4) + c_1\eta(16\eta^2 - 20\eta\theta^2 + 7\theta^4) + \theta^2(8c_2\eta(2\eta - \theta^2) \\
& + c_0\gamma(4\eta - \theta^2))) \left. \left. \left. \right) + b_2(-c_0\gamma(16\eta^2 - 4\eta\theta^2 + \theta^4) + 2(c_2\eta(-16\eta^2 + 2\eta\theta^2 + 5\theta^4) + \theta^2(2c_1\eta(\eta - \theta^2) + a_2(2\eta + \theta^2)))) \right. \right. \\
& \cdot \left(2 \left(2b_0 \left(b_1^3 (-4b_2 + \theta^2)^2 + \eta^2\theta^2(4\eta^2 + b_2\theta^2 - 2\eta\theta^2) + b_1\eta(16\eta^3 - 16\eta^2\theta^2 - 2b_2\theta^4 + 5\eta\theta^4) \right. \right. \right. \\
& + b_1^2(-4b_2^2\theta^2 + 4\eta\theta^2(2\eta - \theta^2) + b_2(-32\eta^2 + 16\eta\theta^2 + \theta^4)) \left. \left. \left. \right) - \gamma^2 \left(16\eta^4 - 16\eta^3\theta^2 + b_2^2\theta^4 - 4b_2\eta\theta^4 + 2b_1^2(-4b_2 + \theta^2)^2 \right. \right. \right. \\
& + \eta^2(4b_2\theta^2 + 5\theta^4) + b_1(-8b_2^2\theta^2 + 6\eta\theta^2(2\eta - \theta^2) + b_2(-48\eta^2 + 24\eta\theta^2 + 2\theta^4)) \left. \left. \left. \right) \right)^{-1},
\end{aligned} \tag{A.3}$$

$$\begin{aligned}
P_2^M = & \left(a_2 \left(-\gamma^2 (2\eta^2\theta^2 + b_2\theta^4 - 2\eta\theta^4 + 8b_1^2(4b_2 - \theta^2) + b_1(-24\eta^2 - 8b_2\theta^2 + 12\eta\theta^2 + \theta^4)) + b_0(-2b_1\eta\theta^4 + \eta^2\theta^4 + 8b_1^3(4b_2 - \theta^2) \right. \right. \\
& + b_1^2(-32\eta^2 - 8b_2\theta^2 + 16\eta\theta^2 + \theta^4)) \left. \left. \right) - \gamma \left(-8a_1\gamma\eta^3 - 8c_0\gamma^2\eta^3 + 24c_2\gamma\eta^4 - 2a_1b_2\gamma\eta\theta^2 - 2b_2c_0\gamma^2\eta\theta^2 + 8a_1\gamma\eta^2\theta^2 \right. \right. \\
& + 4b_2c_2\gamma\eta^2\theta^2 + 8c_0\gamma^2\eta^2\theta^2 + 2c_1\gamma\eta^3\theta^2 - 24c_2\gamma\eta^3\theta^2 + a_1b_2\gamma\theta^4 + b_2^2c_2\gamma\theta^4 + b_2c_0\gamma^2\theta^4 - a_0b_2\eta\theta^4 - 2a_1\gamma\eta\theta^4 - 5b_2c_2\gamma\eta\theta^4 \\
& - 2c_0\gamma^2\eta\theta^4 + a_0\eta^2\theta^4 - c_1\gamma\eta^2\theta^4 + 8c_2\gamma\eta^2\theta^4 + b_1^2(4b_2 - \theta^2)(8b_2c_2\gamma - 4a_0\eta + (c_1 - 4c_2)\gamma\theta^2) \\
& + b_1(16a_0\eta^3 - 8b_2^2c_2\gamma\theta^2 - 4c_0\gamma^2\eta\theta^2 - 8a_0\eta^2\theta^2 - 4c_1\gamma\eta^2\theta^2 + 20c_2\gamma\eta^2\theta^2 + c_0\gamma^2\theta^4 - a_0\eta\theta^4 + 2c_1\gamma\eta\theta^4 - 11c_2\gamma\eta\theta^4 \\
& - a_1\gamma(4b_2 - \theta^2)(-4\eta + \theta^2) + b_2(4c_0\gamma^2(4\eta - \theta^2) + \theta^2(4a_0\eta - 2c_1\gamma\eta + a_0\theta^2) + c_2\gamma(-56\eta^2 + 32\eta\theta^2 + 3\theta^4)) \left. \left. \right) \right. \\
& + b_0 \left(b_1^3(4b_2 - \theta^2)(8b_2c_2 + (c_1 - 4c_2)\theta^2) + \eta\theta^2(a_1\eta(-4\eta + \theta^2) - c_0\gamma(4\eta^2 + b_2\theta^2 - 2\eta\theta^2) \right. \\
& + \eta(12c_2\eta^2 + 3b_2c_2\theta^2 + c_1\eta\theta^2 - 7c_2\eta\theta^2)) + b_1^2(-8b_2^2c_2\theta^2 - a_1(4b_2 - \theta^2)(-8\eta + \theta^2) \\
& + b_2(-64c_2\eta^2 - 4c_1\eta\theta^2 + 44c_2\eta\theta^2 + 3c_2\theta^4 + 4c_0\gamma(4\eta - \theta^2)) + \theta^2(c_0\gamma(-4\eta + \theta^2) + \eta(-4c_1\eta + 24c_2\eta + 3c_1\theta^2 - 15c_2\theta^2)) \left. \left. \right) \right. \\
& - b_1(2a_1\eta(16\eta^2 + 2b_2\theta^2 - 10\eta\theta^2 + \theta^4) + c_0\gamma(16\eta^3 - 12\eta^2\theta^2 - b_2\theta^4 + 3\eta\theta^4) + \eta(c_1\eta\theta^2(-4\eta + 3\theta^2) \\
& + c_2(-32\eta^3 + 4b_2\eta\theta^2 + 44\eta^2\theta^2 + 6b_2\theta^4 - 18\eta\theta^4))) \left. \left. \left. \right) \cdot \left(2 \left(2b_0 \left(b_1^3 (-4b_2 + \theta^2)^2 + \eta^2\theta^2(4\eta^2 + b_2\theta^2 - 2\eta\theta^2) \right. \right. \right. \right. \\
& + b_1\eta(16\eta^3 - 16\eta^2\theta^2 - 2b_2\theta^4 + 5\eta\theta^4) + b_1^2(-4b_2^2\theta^2 + 4\eta\theta^2(2\eta - \theta^2) + b_2(-32\eta^2 + 16\eta\theta^2 + \theta^4)) \\
& - \gamma^2 \left(16\eta^4 - 16\eta^3\theta^2 + b_2^2\theta^4 - 4b_2\eta\theta^4 + 2b_1^2(-4b_2 + \theta^2)^2 + \eta^2(4b_2\theta^2 + 5\theta^4) + b_1(-8b_2^2\theta^2 + 6\eta\theta^2(2\eta - \theta^2) \right. \\
& \left. \left. \left. \right) + b_2(-48\eta^2 + 24\eta\theta^2 + 2\theta^4)) \right)^{-1},
\end{aligned} \tag{A.4}$$

$$\begin{aligned}
B^M = & \left(\theta(8b_0b_1^3b_2^2c_1 - 16b_0b_1^3b_2^2c_2 - 8b_0b_1^2b_2^2c_0\gamma - 8b_1^2b_2^2c_1\gamma^2 + 16b_1^2b_2^2c_2\gamma^2 + 8b_1b_2^2c_0\gamma^3 + 8b_0b_1^2b_2^2c_2\eta + 8a_0b_1^2b_2\gamma\eta \right. \\
& + 8b_0b_1^2b_2c_0\gamma\eta - 8b_1b_2^2c_2\gamma^2\eta - 8b_1b_2c_0\gamma^3\eta - 16b_0b_1^2b_2c_1\eta^2 + 32b_0b_1^2b_2c_2\eta^2 - 8a_0b_1b_2\gamma\eta^2 + 8b_0b_1b_2c_0\gamma\eta^2 \\
& + 12b_1b_2c_1\gamma^2\eta^2 - 20b_1b_2c_2\gamma^2\eta^2 - 4b_2c_0\gamma^3\eta^2 - 16b_0b_1b_2c_2\eta^3 - 8a_0b_1\gamma\eta^3 - 8b_0b_1c_0\gamma\eta^3 + 8b_2c_2\gamma^2\eta^3 + 4c_0\gamma^3\eta^3 \\
& + 8b_0b_1c_1\eta^4 - 16b_0b_1c_2\eta^4 + 8a_0\gamma\eta^4 - 4c_1\gamma^2\eta^4 + 4c_2\gamma^2\eta^4 + 8b_0c_2\eta^5 - 2b_0b_1^3b_2c_1\theta^2 + 4b_0b_1^3b_2c_2\theta^2 + 2b_0b_1^2b_2^2c_2\theta^2 \\
& - 2a_0b_1b_2^2\gamma\theta^2 + 2b_0b_1^2b_2c_0\gamma\theta^2 + 2b_0b_1b_2^2c_0\gamma\theta^2 + 2b_1^2b_2c_1\gamma^2\theta^2 - 4b_1^2b_2c_2\gamma^2\theta^2 - 2b_1b_2^2c_2\gamma^2\theta^2 - 2b_1b_2c_0\gamma^3\theta^2 - 2b_2^2c_0\gamma^3\theta^2 \\
& + 4b_0b_1^2b_2c_1\eta\theta^2 - 10b_0b_1^2b_2c_2\eta\theta^2 - 2b_0b_1b_2^2c_2\eta\theta^2 - 2a_0b_1^2\gamma\eta\theta^2 - 2b_0b_1^2c_0\gamma\eta\theta^2 - 6b_0b_1b_2c_0\gamma\eta\theta^2 - 3b_1b_2c_1\gamma^2\eta\theta^2 \\
& + 8b_1b_2c_2\gamma^2\eta\theta^2 + b_2^2c_2\gamma^2\eta\theta^2 + 2b_1c_0\gamma^3\eta\theta^2 + 5b_2c_0\gamma^3\eta\theta^2 + 2b_0b_1^2c_1\eta^2\theta^2 - 2b_0b_1b_2c_1\eta^2\theta^2 - 4b_0b_1^2c_2\eta^2\theta^2 + 4b_0b_1b_2c_2\eta^2\theta^2 \\
& + 6a_0b_1\gamma\eta^2\theta^2 + 4a_0b_2\gamma\eta^2\theta^2 + 4b_0b_1c_0\gamma\eta^2\theta^2 - b_1c_1\gamma^2\eta^2\theta^2 + b_2c_1\gamma^2\eta^2\theta^2 + 2b_1c_2\gamma^2\eta^2\theta^2 - 2b_2c_2\gamma^2\eta^2\theta^2 - 3c_0\gamma^3\eta^2\theta^2 \\
& - 4b_0b_1c_1\eta^3\theta^2 + 10b_0b_1c_2\eta^3\theta^2 + 2b_0b_2c_2\eta^3\theta^2 - 6a_0\gamma\eta^3\theta^2 + c_1\gamma^2\eta^3\theta^2 - 3c_2\gamma^2\eta^3\theta^2 + 2b_0c_1\eta^4\theta^2 - 6b_0c_2\eta^4\theta^2 \\
& + a_1(\gamma^2(b_2 - \eta)(8b_1b_2 - 4\eta^2 - 2b_1\theta^2 - 2b_2\theta^2 + 3\eta\theta^2) - 2b_0(b_1^2(b_2 - 2\eta)(4b_2 - \theta^2) + b_1\eta(8\eta^2 + 3b_2\theta^2 - 5\eta\theta^2)) \\
& + \eta^2(-4\eta^2 - 2b_2\theta^2 + 3\eta\theta^2))) + a_2(-2b_0(b_1 - \eta)(\eta^2\theta^2 + b_1^2(-8b_2 + 2\theta^2) + b_1(8\eta^2 + b_2\theta^2 - 4\eta\theta^2)) + \gamma^2(4b_1^2(-4b_2 + \theta^2) \\
& + 2b_1(8b_2\eta + 6\eta^2 + b_2\theta^2 - 5\eta\theta^2) + \eta(-12\eta^2 - 3b_2\theta^2 + 7\eta\theta^2)))) \cdot \left(2\left(2b_0\left(b_1^3(-4b_2 + \theta^2)^2 + \eta^2\theta^2(4\eta^2 + b_2\theta^2 - 2\eta\theta^2) \right. \right. \right. \\
& + b_1\eta(16\eta^3 - 16\eta^2\theta^2 - 2b_2\theta^4 + 5\eta\theta^4 + b_1^2(-4b_2^2\theta^2 + 4\eta\theta^2(2\eta - \theta^2) + b_2(-32\eta^2 + 16\eta\theta^2 + \theta^4)))\gamma^2(16\eta^4 - 16\eta^3\theta^2 \\
& \left. \left. \left. + b_2^2\theta^4 - 4b_2\eta\theta^4 + 2b_1^2(-4b_2 + \theta^2)^2 + \eta^2(4b_2\theta^2 + 5\theta^4) + b_1(-8b_2^2\theta^2 + 6\eta\theta^2(2\eta - \theta^2) + b_2(-48\eta^2 + 24\eta\theta^2 2\theta^4)) \right) \right) \right)^{-1}.
\end{aligned} \tag{A.5}$$

Proof of Proposition 1. We substitute E_1 into (19) and then get two eigenvalues:

$$\begin{aligned}
r_1 = & \left(1 + \left(\alpha_1(4c_0\gamma\eta^2 - 4c_2\eta^3 + 2b_2c_0\gamma\theta^2 + a_2\eta\theta^2 - b_2c_2\eta\theta^2 - 3c_0\gamma\eta\theta^2 - c_1\eta^2\theta^2 + c_2\eta^2\theta^2 + b_1^2c_1(4b_2 - \theta^2) + \alpha_1(b_1(4b_2 - \theta^2) \right. \right. \\
& + \eta(-4\eta + \theta^2)) + b_1(-a_2\theta^2 + c_0\gamma\theta^2 - c_2\eta\theta^2 + 2c_1\eta(-2\eta + \theta^2) + b_2(-4c_0\gamma + 4c_2\eta + c_2\theta^2))) \right) \\
& \cdot (8b_1b_2 - 8\eta^2 - 2b_1\theta^2 - 2b_2\theta^2 + 4\eta\theta^2)^{-1}, \\
r_2 = & \left(1 + \left(\alpha_2(2b_0c_0(4b_1b_2 - 4\eta^2 - b_1\theta^2 - b_2\theta^2 + 2\eta\theta^2) + a_0(8b_1b_2 - 8\eta^2 - 2b_1\theta^2 - 2b_2\theta^2 + 4\eta\theta^2) \right. \right. \\
& - \gamma(4b_2c_0\gamma - 4a_2\eta - 4c_1\eta^2 + a_2\theta^2 - b_2c_2\theta^2 - c_0\gamma\theta^2 + c_1\eta\theta^2 + c_2\eta\theta^2 + b_1c_1(4b_2 - \theta^2) + \alpha_1(-4b_2 + \theta^2))) \right) \\
& \cdot (8b_1b_2 - 8\eta^2 - 2b_1\theta^2 - 2b_2\theta^2 + 4\eta\theta^2)^{-1}.
\end{aligned} \tag{A.6}$$

Comparing the eigenvalue with the wholesale price w in the equilibrium point E_2 and the direct sale price p_0 in the

equilibrium point E_3 and noting the condition (13), we draw the conclusion that $|r_{1,2}| > 1$. So, E_1 is unstable.

For E_2 , we calculate the eigenvalue of its Jacobian matrix to obtain

$$\begin{aligned}
r_1 &= \left(1 - \left(\alpha_1(4c_0\gamma\eta^2 - 4c_2\eta^3 + 2b_2c_0\gamma\theta^2 + a_2\eta\theta^2 - b_2c_2\eta\theta^2 - 3c_0\gamma\eta\theta^2 - c_1\theta^2 + c_2\eta^2\theta^2 + b_1^2c_1(4b_2 - \theta^2) + \alpha_1(b_1(4b_2 - \theta^2) \right. \right. \\
&\quad \left. \left. + \eta(-4\eta + \theta^2)) + b_1(-a_2 - c_0\gamma + c_2\eta)\theta^2 + 2c_1\eta(-2\eta + \theta^2) + b_2(-4c_0\gamma + c_2(4\eta + \theta^2))\right)\right) \\
&\quad \cdot (8b_1b_2 - 8\eta^2 - 2b_1\theta^2 - 2b_2\theta^2 + 4\eta\theta^2)^{-1}, \\
r_2 &= \left(1 + \left(\alpha_2\left(2a_0\left(b_1^3(-4b_2 + \theta^2)^2 + \eta^2\theta^2(4\eta^2 + b_2\theta^2 - 2\eta\theta^2) + b_1\eta(16\eta^3 - 16\eta^2\theta^2 - 2b_2\theta^4 + 5\eta\theta^4) \right. \right. \right. \\
&\quad \left. \left. + b_1^2(-4b_2^2\theta^2 + 4\eta\theta^2(2\eta - \theta^2) + b_2(-32\eta^2 + 16\eta\theta^2 + \theta^4))\right) + 2b_0c_0\left(b_1^3(-4b_2 + \theta^2)^2 + \eta^2\theta^2(4\eta^2 + b_2\theta^2 - 2\eta\theta^2) \right. \right. \\
&\quad \left. \left. + b_1\eta(16\eta^3 - 16\eta^2\theta^2 - 2b_2\theta^4 + 5\eta\theta^4) + b_1^2(-4b_2^2\theta^2 + 4\eta\theta^2(2\eta - \theta^2) + b_2(-32\eta^2 + 16\eta\theta^2 + \theta^4))\right) \right. \\
&\quad \left. + \gamma(16c_0\gamma\eta^4 + 16c_2\eta^5 - 8b_2c_0\gamma\eta^2\theta^2 - 8a_2\eta^3\theta^2 + 8b_2c_2\eta^3\theta^2 + 20c_0\gamma\eta^3\theta^2 - 12c_2\eta^4\theta^2 - 2b_2^2c_0\gamma\theta^4 - a_2b_2\eta\theta^4 + b_2^2c_2\eta\theta^4 \right. \\
&\quad \left. + 7b_2c_0\gamma\eta\theta^4 + 3a_2\eta^2\theta^4 + b_2c_1\eta^2\theta^4 - 4b_2c_2\eta^2\theta^4 - 7c_0\gamma\eta^2\theta^4 - c_1\eta^3\theta^4 + 3c_2\eta^3\theta^4 + b_1^2(4b_2 - \theta^2) \right. \\
&\quad \cdot \left((2c_0\gamma + c_1\eta - 2c_2\eta)\theta^2 + a_2(4\eta - 2\theta^2) + b_2(-8c_0\gamma + 4c_2\eta - c_1\theta^2 + 2c_2\theta^2)\right) + a_1\left(2b_1^2(-4b_2 + \theta^2)^2 \right. \\
&\quad \left. + \eta(16\eta^3 - 12\eta^2\theta^2 - b_2\theta^4 + 3\eta\theta^4) + b_1(-4b_2^2\theta^2 + \eta\theta^2(12\eta - 5\theta^2) + b_2(-48\eta^2 + 20\eta\theta^2 + \theta^4))\right) \\
&\quad \left. + b_1(-b_2^2\theta^2(-12c_0\gamma + c_2(8\eta + \theta^2)) + b_2(\theta^2(4a_2\eta + 4c_1\eta^2 + a_2\theta^2 - 2c_1\eta\theta^2) + c_0\gamma(48\eta^2 - 28\eta\theta^2 - 3\theta^4) \right. \\
&\quad \left. + c_2(-32\eta^3 + 4\eta^2\theta^2 + 6\eta\theta^4)) + \eta(a_2(-16\eta^2 + 16\eta\theta^2 - 5\theta^4) + \theta^2(c_0\gamma(-12\eta + 7\theta^2) \right. \\
&\quad \left. + \eta(-4c_1\eta + 12c_2\eta + 2c_1\theta^2 - 5c_2\theta^2))))\right) \cdot (2(4b_1b_2 - 4\eta^2 - b_1\theta^2 - b_2\theta^2 + 2\eta\theta^2)(-\eta^2\theta^2 + b_1^2(4b_2 - \theta^2) + 2b_1\eta(-2\eta + \theta^2)))^{-1}.
\end{aligned} \tag{A.7}$$

According to the assumption, the wholesale price w in the equilibrium point E_2 is bigger than zero. Comparing w and r_1 , we have $|r_1| < 1$. For r_2 , because $p_0^M > 0$ and based on condition (6), we have $|r_2| > 1$. So, E_2 is unstable.

For E_3 , two eigenvalues of its Jacobian matrix are as follows:

$$\begin{aligned}
r_1 &= \left(1 + \left(\alpha_1(2b_0(4b_1b_2 - 4\eta^2 - b_1\theta^2 - b_2\theta^2 + 2\eta\theta^2)((b_2c_0\gamma + \eta(a_2 - c_0\gamma - c_1\eta))\theta^2 + b_1^2c_1(4b_2 - \theta^2) + c_2\eta(-4\eta^2 - b_2\theta^2 + \eta\theta^2) \right. \right. \\
&\quad \left. \left. + b_1(-a_2 + c_2\eta)\theta^2 + 2c_1\eta(-2\eta + \theta^2) + b_2c_2(4\eta + \theta^2))\right) + \gamma\left(2a_0(4\eta^2 + b_2\theta^2 - 2\eta\theta^2 + b_1(-4b_2 + \theta^2))^2 \right. \\
&\quad \left. - \gamma(-16b_2c_2\eta^3 + 16c_1\eta^4 + 4b_2^2c_0\gamma\theta^2 - 4b_2^2c_2\eta\theta^2 - 4b_2c_0\gamma\eta\theta^2 + 8b_2c_2\eta^2\theta^2 - 12c_1\eta^3\theta^2 + b_2^2c_2\theta^4 - b_2c_0\gamma\theta^4 - b_2c_1\eta\theta^4 \right. \\
&\quad \left. - 2b_2c_2\eta\theta^4 + c_0\gamma\eta\theta^4 + 3c_1\eta^2\theta^4 + c_2\eta^2\theta^4 + 2b_1^2c_1(-4b_2 + \theta^2)^2 - b_1(4b_2 - \theta^2)(4a_2\eta - 4b_2c_2\eta + 12c_1\eta^2 + b_2c_1\theta^2 - 5c_1\eta\theta^2) \right. \\
&\quad \left. + a_2(16\eta^3 + 8b_2\eta\theta^2 - 12\eta^2\theta^2 - b_2\theta^4 + \eta\theta^4)\right) + a_1\left(-\gamma^2(b_2 - \eta)\theta^2(4b_2 - \theta^2) + 2b_0\left(b_1^2(-4b_2 + \theta^2)^2 + \eta(4\eta - \theta^2) \right. \right. \\
&\quad \cdot \left.(4\eta^2 + b_2\theta^2 - 2\eta\theta^2) + b_1(-4b_2^2\theta^2 + \eta\theta^2(8\eta - 3\theta^2) + b_2(-32\eta^2 + 12\eta\theta^2 + \theta^4))\right) \\
&\quad \cdot \left(2(4b_1b_2 - 4\eta^2 - b_1\theta^2 - b_2\theta^2 + 2\eta\theta^2)(\gamma^2(-4b_2 + \theta^2) + b_0(8b_1b_2 - 8\eta^2 - 2b_1\theta^2 - 2b_2\theta^2 + 4\eta\theta^2))\right)^{-1}, \\
r_2 &= \left(1 - \left(\alpha_2(2b_0c_0(4b_1b_2 - 4\eta^2 - b_1\theta^2 - b_2\theta^2 + 2\eta\theta^2) + a_0(8b_1b_2 - 8\eta^2 - 2b_1\theta^2 - 2b_2\theta^2 + 4\eta\theta^2) + \gamma(4a_1b_2 - 4b_1b_2c_1 - 4b_2c_0\gamma \right. \right. \\
&\quad \left. \left. + 4a_2\eta + 4c_1\eta^2 - a_1\theta^2 - a_2\theta^2 + b_1c_1\theta^2 + b_2c_2\theta^2 + c_0\gamma\theta^2 - c_1\eta\theta^2 - c_2\eta\theta^2)\right)\right) \cdot (8b_1b_2 - 8\eta^2 - 2b_1\theta^2 - 2b_2\theta^2 + 4\eta\theta^2)^{-1}.
\end{aligned} \tag{A.8}$$

For r_1 , using condition (10) and $\omega^M > 0$, we have $|r_1| > 1$. We also have $|r_2| < 1$ by comparing the direct sale price p_0 in the equilibrium point E_3 . So, E_3 is unstable too. \square

Proof of Proposition 2. We substitute E_1 into (36) and then get one eigenvalue:

$$r_1 = 1 + \beta_1 \left(\frac{a_1(3b_0b_1 - \gamma^2) + b_0b_1(b_1c_1 + c_0\gamma - c_2\eta) + \gamma(2a_0b_1 - \gamma(b_1c_1 + c_0\gamma - c_2\eta))}{b_0b_1 - \gamma^2} \right). \quad (\text{A.9})$$

Comparing r_1 with p_1 in the E_4 , we draw the conclusion that $|r_1| > 1$. So, E_1 is unstable.

For E_2 , we calculate one eigenvalue of its Jacobian matrix to obtain

$$\begin{aligned} r_1 = & (1 + \beta_1(a_1(2b_2\gamma^4 + 2b_0^2b_1(3b_1b_2 - \eta^2) + b_0\gamma^2(-8b_1b_2 + \eta^2)) + \gamma^3(a_0(-4b_1b_2 + \eta^2) + \gamma(2b_1b_2c_1 + 2b_2c_0\gamma + 2a_2\eta - c_1\eta^2)) \\ & + 2b_0^2b_1(b_1^2b_2c_1 - c_2\eta^3 + b_1(b_2c_0\gamma + 2a_2\eta + b_2c_2\eta - c_1\eta^2)) + b_0\gamma(2a_0b_1(2b_1b_2 - \eta^2) + \gamma(-4b_1^2b_2c_1 + c_2\eta^3 \\ & - b_1(4b_2c_0\gamma + 6a_2\eta + 2b_2c_2\eta - 3c_1\eta^2)))))) \cdot (2b_2b_0b_1 - \gamma^2 + b_0\eta^2(2b_0b_1 - \gamma^2))^{-1}. \end{aligned} \quad (\text{A.10})$$

Comparing r_1 with p_1 in the E_6 , we have that $|r_1| > 1$. So, E_2 is unstable.

For E_3 , one eigenvalue is

$$\begin{aligned} r_1 = & (1 + \beta_1(4a_1(3b_0^2b_1^2 - 4b_0b_1\gamma^2 + \gamma^4) + \gamma^3(a_0(-8b_1 + \theta^2) + \gamma(4b_1c_1 + 4c_0\gamma - 4c_2\eta - c_1\theta^2 + 2c_2\theta^2)) \\ & + b_0^2b_1(4b_1^2c_1 + (c_0\gamma - 4c_2\eta)\theta^2 + b_1(4c_0\gamma - 4c_2\eta - 2c_1\theta^2 + 6c_2\theta^2)) - b_0\gamma(a_0b_1(-8b_1 + \theta^2) + \gamma(8b_1^2c_1 + (c_0\gamma - 2c_2\eta)\theta^2 \\ & + b_1(8c_0\gamma - 8c_2\eta - 3c_1\theta^2 + 8c_2\theta^2)))))) \cdot (4\gamma^4 + 4b_0^2b_1(b_1 + \theta^2) - 2b_0\gamma^2(4b_1 + \theta^2))^{-1}. \end{aligned} \quad (\text{A.11})$$

Comparing r_1 with p_1 in the E_7 , we have that $|r_1| > 1$. So, E_3 is unstable.

For E_4 , we get one eigenvalue as follows:

$$r_2 = \frac{1 + \beta_2(2a_2b_1(b_0b_1 - \gamma^2) + b_0b_1(2b_1b_2c_2 + \eta(2a_1 + c_0\gamma - 2c_2\eta)) + \gamma(b_1(-2b_2c_2\gamma + a_0\eta) - \gamma\eta(a_1 + c_0\gamma - c_2\eta)))}{(2b_1(b_0b_1 - \gamma^2))}. \quad (\text{A.12})$$

Comparing r_2 with p_2 in the E_6 , we have that $|r_2| > 1$. So, E_4 is unstable.

For E_5 , one eigenvalue of its Jacobian matrix is

$$\begin{aligned}
r_1 = & \left(1 + \beta_1 \left(\gamma^3 \left(\gamma \left(8b_1b_2c_1 + 8b_2c_0\gamma + 8a_2\eta - 4c_1\eta^2 - 2a_2\theta^2 - 2b_1c_1\theta^2 - 2b_2c_1\theta^2 + 2b_2c_2\theta^2 + a_1 \left(2\gamma^4 \left(4b_2 - \theta^2 \right) \right. \right. \right. \right. \right. \right. \right. \right. \\
& - 2b_0\gamma^2 \left(4b_1 \left(4b_2 - \theta^2 \right) + \eta \left(-2\eta + \theta^2 \right) \right) + 2b_0^2b_1 \left(3b_1 \left(4b_2 - \theta^2 \right) + 2\eta \left(-2\eta + \theta^2 \right) \right) + b_0^2b_1 \left(\left(2b_2c_0\gamma + 4a_2\eta - c_0\gamma\eta \right) \theta^2 \right. \\
& + b_1^2 \left(8b_2c_1 - 2c_1\theta^2 \right) - 4c_2\eta \left(2\eta^2 + b_2\theta^2 - \eta\theta^2 \right) + 2b_1 \left(8a_2\eta - 4c_1\eta^2 - 3a_2\theta^2 - c_0\gamma\theta^2 + 3c_1\eta\theta^2 - 3c_2\eta\theta^2 \right. \\
& + b_2 \left(4c_0\gamma + 4c_2\eta - 2c_1\theta^2 + 3c_2\theta^2 \right) \left. \right) + b_0\gamma \left(a_0b_1 \left(16b_1b_2 - 8\eta^2 - 4b_1\theta^2 - 2b_2\theta^2 + 5\eta\theta^2 \right) + \gamma \left(\left(-2b_2c_0\gamma - 2a_2\eta + c_0\gamma\eta \right) \theta^2 \right. \right. \\
& + 4b_1^2c_1 \left(-4b_2 + \theta^2 \right) + 2c_2\eta \left(2\eta^2 + b_2\theta^2 - \eta\theta^2 \right) + b_1 \left(-24a_2\eta + 12c_1\eta^2 + 8a_2\theta^2 + 4c_0\gamma\theta^2 - 9c_1\eta\theta^2 + 8c_2\eta\theta^2 \right. \\
& - 2b_2 \left(8c_0\gamma - 3c_1\theta^2 + 4c_2 \left(\eta + \theta^2 \right) \right) \left. \left. \right) \right) \cdot \left(2\gamma^4 \left(4b_2 - \theta^2 \right) + 2b_0^2b_1 \left(4b_1b_2 + 4\eta^2 - b_1\theta^2 + 4b_2\theta^2 - 4\eta\theta^2 \right) \right. \\
& \left. - 4b_0\gamma^2 \left(4b_1b_2 + \eta^2 - b_1\theta^2 + b_2\theta^2 - \eta\theta^2 \right) \right)^{-1}.
\end{aligned} \tag{A.13}$$

Comparing r_1 with p_1 in the E^R , we have that $|r_1| > 1$. So, E_5 is unstable.

For E_6 , we get one eigenvalue as follows:

$$\begin{aligned}
r_3 = & \left(1 + \beta_3 \left(\left(2b_0^2b_1^3b_2c_1 - 4b_0^2b_1^3b_2c_2 - 2b_0^2b_1^2b_2c_0\gamma - 4b_0b_1^2b_2c_1\gamma^2 + 8b_0b_1^2b_2c_2\gamma^2 + 4b_0b_1b_2c_0\gamma^3 + 2b_1b_2c_1\gamma^4 - 4b_1b_2c_2\gamma^4 \right. \right. \right. \\
& - 2b_2c_0\gamma^5 + 2b_0^2b_1^2b_2c_2\eta + 2a_0b_0b_1^2\gamma\eta + 2b_0^2b_1^2c_0\gamma\eta - 2b_0b_1b_2c_2\gamma^2\eta - 2a_0b_1\gamma^3\eta - 4b_0b_1c_0\gamma^3\eta + 2c_0\gamma^5\eta - 2b_0^2b_1^2c_1\eta^2 \\
& + 4b_0^2b_1^2c_2\eta^2 - 2a_0b_0b_1\gamma\eta^2 + 3b_0b_1c_1\gamma^2\eta^2 - 6b_0b_1c_2\gamma^2\eta^2 + a_0\gamma^3\eta^2 - c_1\gamma^4\eta^2 + 2c_2\gamma^4\eta^2 - 2b_0^2b_1c_2\eta^3 + b_0c_2\gamma^2\eta^3 \\
& + 2a_2 \left(b_0b_1 - \gamma^2 \right) \left(2b_0b_1 \left(b_1 - \eta \right) + \gamma^2 \left(-2b_1 + \eta \right) \right) + a_1 \left(2\gamma^4 \left(-b_2 + \eta \right) + b_0\gamma^2 \left(4b_1b_2 - 6b_1\eta + \eta^2 \right) \right. \\
& \left. - 2b_0^2b_1 \left(b_1b_2 - 2b_1\eta + \eta^2 \right) \right) \theta \left. \right) \cdot \left(4 \left(b_0b_1 - \gamma^2 \right) \left(2b_0b_1 \left(b_1b_2 - \eta^2 \right) + \gamma^2 \left(-2b_1b_2 + \eta^2 \right) \right) \right)^{-1}.
\end{aligned} \tag{A.14}$$

Comparing r_3 with B in the E^R , we have that $|r_3| > 1$. So, E_6 is unstable.

For E_7 , there is one eigenvalue of its Jacobian matrix, as follows:

$$\begin{aligned}
r_2 = & \left(1 + \beta_2 \left(2a_2 \left(-b_0b_1 + \gamma^2 \right)^2 \left(8b_1 - \theta^2 \right) + \gamma^3 \left(8a_1\gamma\eta + 8c_0\gamma^2\eta - 8c_2\gamma\eta^2 - 2a_1\gamma\theta^2 - 2b_2c_2\gamma\theta^2 - 2c_0\gamma^2\theta^2 + a_0\eta\theta^2 - c_1\gamma\eta\theta^2 \right. \right. \right. \\
& + 6c_2\gamma\eta\theta^2 + 2b_1 \left(8b_2c_2\gamma - 4a_0\eta + \left(c_1 - 4c_2 \right) \gamma\theta^2 \right) + b_0^2b_1 \left(\eta \left(c_0\gamma - 4c_2\eta \right) \theta^2 + 2b_1^2 \left(8b_2c_2 + \left(c_1 - 4c_2 \right) \theta^2 \right) \right. \\
& + 2b_1 \left(8a_1\eta + 4c_0\gamma\eta - 8c_2\eta^2 - a_1\theta^2 - b_2c_2\theta^2 - c_0\gamma\theta^2 - c_1\eta\theta^2 + 7c_2\eta\theta^2 \right) + b_0\gamma \left(\gamma\eta \left(-c_0\gamma + 2c_2\eta \right) \theta^2 - 4b_1^2 \left(8b_2c_2\gamma - 2a_0\eta \right. \right. \\
& + \left. \left. \left(c_1 - 4c_2 \right) \gamma\theta^2 \right) + b_1 \left(24c_2\gamma\eta^2 + 4b_2c_2\gamma\theta^2 - a_0\eta\theta^2 + 3c_1\gamma\eta\theta^2 - 20c_2\gamma\eta\theta^2 + 4a_1\gamma \left(-6\eta + \theta^2 \right) + 4c_0\gamma^2 \left(-4\eta + \theta^2 \right) \right) \right) \left. \right) \right. \\
& \left. \cdot \left(2 \left(\left(-b_0b_1 + \gamma^2 \right)^2 \left(8b_1 - \theta^2 \right) \right) \right)^{-1}.
\end{aligned} \tag{A.15}$$

Comparing r_2 with p_2 in the E^R , we have that $|r_2| > 1$. So, E_7 is unstable:

$$\begin{aligned}
p_1^R = & \left(\gamma^3 (\gamma (8b_1b_2c_1 + 8b_2c_0\gamma + 8a_2\eta - 4c_1\eta^2 - 2a_2\theta^2 - 2b_1c_1\theta^2 - 2b_2c_1\theta^2 + 2b_2c_2\theta^2 - 2c_0\gamma\theta^2 + 3c_1\eta\theta^2 - 2c_2\eta\theta^2) \right. \\
& + a_0(4\eta^2 + 2b_2\theta^2 - 3\eta\theta^2 + 4b_1(-4b_2 + \theta^2))) + a_1(2\gamma^4(4b_2 - \theta^2) - 2b_0\gamma^2(4b_1(4b_2 - \theta^2) + \eta(-2\eta + \theta^2))) \\
& + 2b_0^2b_1(3b_1(4b_2 - \theta^2) + 2\eta(-2\eta + \theta^2))) + b_0^2b_1((2b_2c_0\gamma + 4a_2\eta - c_0\gamma\eta)\theta^2 + b_1^2(8b_2c_1 - 2c_1\theta^2) - 4c_2\eta(2\eta^2 + b_2\theta^2 - \eta\theta^2) \\
& + 2b_1(8a_2\eta - 4c_1\eta^2 - 3a_2\theta^2 - c_0\gamma\theta^2 + 3c_1\eta\theta^2 - 3c_2\eta\theta^2 + b_2(4c_0\gamma + 4c_2\eta - 2c_1\theta^2 + 3c_2\theta^2))) \\
& + b_0\gamma(a_0b_1(16b_1b_2 - 8\eta^2 - 4b_1\theta^2 - 2b_2\theta^2 + 5\eta\theta^2) + \gamma((-2b_2c_0\gamma - 2a_2\eta + c_0\gamma\eta)\theta^2 + 4b_1^2c_1(-4b_2 + \theta^2) + 2c_2\eta(2\eta^2 \\
& + b_2\theta^2 - \eta\theta^2) + b_1(-24a_2\eta + 12c_1\eta^2 + 8a_2\theta^2 + 4c_0\gamma\theta^2 - 9c_1\eta\theta^2 + 8c_2\eta\theta^2 - 2b_2(8c_0\gamma - 3c_1\theta^2 + 4c_2(\eta + \theta^2)))))) \\
& \cdot (2(2\gamma^4(8b_1b_2 - 4\eta^2 - 2b_1\theta^2 - b_2\theta^2 + 2\eta\theta^2) - 2b_0^2b_1(\eta^2\theta^2 + b_1^2(-8b_2 + 2\theta^2) + b_1(8\eta^2 + b_2\theta^2 - 4\eta\theta^2)) \\
& + b_0\gamma^2(\eta^2\theta^2 + 8b_1^2(-4b_2 + \theta^2) + 4b_1(6\eta^2 + b_2\theta^2 - 3\eta\theta^2))))^{-1}, \tag{A.16}
\end{aligned}$$

$$\begin{aligned}
p_2^R = & \left(2a_2(-b_0b_1 + \gamma^2)^2(8b_1 - \theta^2) + \gamma^3(8a_1\gamma\eta + 8c_0\gamma^2\eta - 8c_2\gamma\eta^2 - 2a_1\gamma\theta^2 - 2b_2c_2\gamma\theta^2 - 2c_0\gamma^2\theta^2 + a_0\eta\theta^2 - c_1\gamma\eta\theta^2 \right. \\
& + 6c_2\gamma\eta\theta^2 + 2b_1(8b_2c_2\gamma - 4a_0\eta + (c_1 - 4c_2)\gamma\theta^2)) + b_0^2b_1(\eta(c_0\gamma - 4c_2\eta)\theta^2 + 2b_1^2(8b_2c_2 + (c_1 - 4c_2)\theta^2) \\
& + 2b_1(8a_1\eta + 4c_0\gamma\eta - 8c_2\eta^2 - a_1\theta^2 - b_2c_2\theta^2 - c_0\gamma\theta^2 - c_1\eta\theta^2 + 7c_2\eta\theta^2)) + b_0\gamma(\gamma\eta(-c_0\gamma + 2c_2\eta)\theta^2 - 4b_1^2(8b_2c_2\gamma - 2a_0\eta \\
& + (c_1 - 4c_2)\gamma\theta^2) + b_1(24c_2\gamma\eta^2 + 4b_2c_2\gamma\theta^2 - a_0\eta\theta^2 + 3c_1\gamma\eta\theta^2 - 20c_2\gamma\eta\theta^2 + 4a_1\gamma(-6\eta + \theta^2) + 4c_0\gamma^2(-4\eta + \theta^2))) \\
& \cdot (2(2\gamma^4(8b_1b_2 - 4\eta^2 - 2b_1\theta^2 - b_2\theta^2 + 2\eta\theta^2) - 2b_0^2b_1(\eta^2\theta^2 + b_1^2(-8b_2 + 2\theta^2) + b_1(8\eta^2 + b_2\theta^2 - 4\eta\theta^2)) \\
& + b_0\gamma^2(\eta^2\theta^2 + 8b_1^2(-4b_2 + \theta^2) + 4b_1(6\eta^2 + b_2\theta^2 - 3\eta\theta^2))))^{-1}, \tag{A.17}
\end{aligned}$$

$$\begin{aligned}
B^R = & \left((2b_0^2b_1^3b_2c_1 - 4b_0^2b_1^3b_2c_2 - 2b_0^2b_1^2b_2c_0\gamma - 4b_0b_1^2b_2c_1\gamma^2 + 8b_0b_1^2b_2c_2\gamma^2 + 4b_0b_1b_2c_0\gamma^3 + 2b_1b_2c_1\gamma^4 - 4b_1b_2c_2\gamma^4 - 2b_2c_0\gamma^5 \right. \\
& + 2b_0^2b_1^2b_2c_2\eta + 2a_0b_0\gamma\eta + 2b_0^2b_1^2c_0\gamma\eta - 2b_0b_1b_2c_2\gamma^2\eta - 2a_0\gamma^3\eta - 4b_0b_1c_0\gamma^3\eta + 2c_0\gamma^5\eta - 2b_0^2b_1^2c_1\eta^2 + 4b_0^2b_1^2c_2\eta^2 \\
& - 2a_0b_0b_1\gamma\eta^2 + 3b_0b_1c_1\gamma^2\eta^2 - 6b_0b_1c_2\gamma^2\eta^2 + a_0\gamma^3\eta^2 - c_1\gamma^4\eta^2 + 2c_2\gamma^4\eta^2 - 2b_0^2b_1c_2\eta^3 + b_0c_2\gamma^2\eta^3 2a_2(b_0b_1 - \gamma^2) \\
& \cdot (2b_0b_1(b_1 - \eta) + \gamma^2(-2b_1 + \eta)) + a_1(2\gamma^4(-b_2 + \eta) + b_0\gamma^2(4b_1b_2 - 6b_1\eta + \eta^2) - 2b_0^2b_1(b_1b_2 - 2b_1\eta + \eta^2)))\theta \\
& \cdot (2\gamma^4(8b_1b_2 - 4\eta^2 - 2b_1\theta^2 - b_2\theta^2 + 2\eta\theta^2) - 2b_0^2b_1(\eta^2\theta^2 + b_1^2(-8b_2 + 2\theta^2) + b_1(8\eta^2 + b_2\theta^2 - 4\eta\theta^2)) \\
& + b_0\gamma^2(\eta^2\theta^2 + 8b_1^2(-4b_2 + \theta^2) + 4b_1(6\eta^2 + b_2\theta^2 - 3\eta\theta^2))))^{-1}, \tag{A.18}
\end{aligned}$$

$$\begin{aligned}
w^R = & \left(2a_1(2b_0\gamma^2\eta^2 + \gamma^4(-4b_2 + \theta^2) + b_0^2b_1(b_1(4b_2 - \theta^2) + \eta(-4\eta + \theta^2))) + \gamma^3(a_0(12\eta^2 + 2b_2\theta^2 - 5\eta\theta^2 + 4b_1(-4b_2 + \theta^2)) \right. \\
& + \gamma(-8a_2\eta - 12c_1\eta^2 + 2a_2\theta^2 + 2c_0\gamma\theta^2 + 5c_1\eta\theta^2 + 2c_2\eta\theta^2 + 6b_1c_1(4b_2 - \theta^2) - 2b_2(4c_0\gamma + (c_1 + c_2)\theta^2))) \\
& + b_0\gamma(-a_0(\eta^2\theta^2 + 4b_1^2(-4b_2 + \theta^2) + b_1(16\eta^2 + 2b_2\theta^2 - 7\eta\theta^2)) + \gamma(12b_1^2c_1(-4b_2 + \theta^2) + \eta^2(4c_2\eta + c_1\theta^2) \\
& + c_0\gamma(-8\eta^2 - 2b_2\theta^2 + 5\eta\theta^2) + b_1(8a_2\eta + 36c_1\eta^2 - 4c_0\gamma\theta^2 - 17c_1\eta\theta^2 + 2b_2(8c_0\gamma - 4c_2\eta + 3c_1\theta^2)))) \\
& + b_0^2(c_0\gamma\eta^2\theta^2 + 6b_1^3c_1(4b_2 - \theta^2) - 2b_1^2((a_2 - c_0\gamma + c_2\eta)\theta^2 + 6c_1\eta(2\eta - \theta^2) + b_2(4c_0\gamma + 2c_1\theta^2 - c_2(4\eta + \theta^2))) \\
& + b_1(c_0\gamma(8\eta^2 + 2b_2\theta^2 - 5\eta\theta^2) - 2\eta((-a_2 + c_1\eta)\theta^2 + c_2(4\eta^2 + b_2\theta^2 - \eta\theta^2)))) \\
& \cdot (2(2\gamma^4(8b_1b_2 - 4\eta^2 - 2b_1\theta^2 - b_2\theta^2 + 2\eta\theta^2) - 2b_0^2b_1(\eta^2\theta^2 + b_1^2(-8b_2 + 2\theta^2) + b_1(8\eta^2 + b_2\theta^2 - 4\eta\theta^2)) \\
& + b_0\gamma^2(\eta^2\theta^2 + 8b_1^2(-4b_2 + \theta^2) + 4b_1(6\eta^2 + b_2\theta^2 - 3\eta\theta^2))))^{-1}, \tag{A.19}
\end{aligned}$$

$$\begin{aligned}
p_0^R = & (-4b_0^2b_1c_0(\eta^2\theta^2 + b_1^2(-8b_2 + 2\theta^2) + b_1(8\eta^2 + b_2\theta^2 - 4\eta\theta^2)) + a_0(-4b_0b_1(\eta^2\theta^2 + b_1^2(-8b_2 + 2\theta^2) + b_1(8\eta^2 + b_2\theta^2 - 4\eta\theta^2))) \\
& + \gamma^2(\eta^2\theta^2 + 8b_1^2(-4b_2 + \theta^2) + 4b_1(6\eta^2 + b_2\theta^2 - b_1^2(-8b_2 + 2\theta^2) + b_1(8\eta^2 + b_2\theta^2 - 4\eta\theta^2))) + \gamma^2(\eta^2\theta^2 + 8b_1^2(-4b_2 + \theta^2) \\
& + 4b_1(6\eta^2 + b_2\theta^2 - 2c_2\eta^2\theta^2 + a_1(2\eta(4\eta - \theta^2) + 8b_1(-4b_2 + \theta^2))) + 2b_1((-4c_0\gamma - (c_1 - 4c_2)\eta)\theta^2 + a_2((-8\eta + 4\theta^2)) \\
& + 2b_2(8c_0\gamma + c_1\theta^2 - 2c_2(2\eta + \theta^2)))) + b_0\gamma(3c_0\gamma\eta^2\theta^2 + 2a_1b_1(16b_1b_2 - 8\eta^2 - 4b_1\theta^2 + 3\eta\theta^2) + 2b_1^2((8c_0\gamma + c_1\eta - 4c_2\eta)\theta^2 \\
& + a_2(8\eta - 4\theta^2) + b_2(-32c_0\gamma + 8c_2\eta - 2c_1\theta^2 + 4c_2\theta^2)) + 2b_1(c_0\gamma(28\eta^2 + 6b_2\theta^2 - 15\eta\theta^2) + \eta((3a_2 + c_1)\eta)\theta^2 \\
& + c_2(-8\eta^2 - 3b_2\theta^2 + 3\eta\theta^2)))))) \cdot (4(2\gamma^4(8b_1b_2 - 4\eta^2 - 2b_1\theta^2 - b_2\theta^2 + 2\eta\theta^2) - 2b_0^2b_1(\eta^2\theta^2 + b_1^2(-8b_2 + 2\theta^2) \\
& + b_1(8\eta^2 + b_2\theta^2 - 4\eta\theta^2))) + b_0\gamma^2(\eta^2\theta^2 + 8b_1^2(-4b_2 + \theta^2) + 4b_1(6\eta^2 + b_2\theta^2 - 3\eta\theta^2))))^{-1}.
\end{aligned}
\tag{A.20}$$

□

Notations

w /unit: Unit wholesale price of the NB product
 p_0 /unit: Unit of direct selling price of the NB product
 p_1 /unit: Unit retail price of the NB product
 p_2 /unit: Unit retail price of the SB product
 c_0 : The marginal cost of production and operation in the direct channel
 c_1 : The marginal production cost of the NB product
 c_2 : The marginal production cost of the SB product
 A : The advertising investment of the retailer
 u : Unit retail margin, $p_1 = w + u$
 D_0 : The demand function of the NB product in direct channel
 D_1 : The demand function of the NB product in retail channel
 D_2 : The demand function of the SB product in retail channel.

Data Availability

The data used to support the findings of this study are available from the corresponding author upon request.

Conflicts of Interest

The authors declare that they have no conflicts of interest.

Acknowledgments

The research was supported by the National Natural Science Foundation of China (no. 61273231 and no. 71571131).

References

- [1] T. Xiao and J. Shi, "Pricing and supply priority in a dual-channel supply chain," *European Journal of Operational Research*, vol. 254, no. 3, pp. 813–823, 2016.
- [2] H. Kurata, D.-Q. Yao, and J. J. Liu, "Pricing policies under direct vs. indirect channel competition and national vs. store brand competition," *European Journal of Operational Research*, vol. 180, no. 1, pp. 262–281, 2007.
- [3] G. Cai, Z. G. Zhang, and M. Zhang, "Game theoretical perspectives on dual-channel supply chain competition with price discounts and pricing schemes," *International Journal of Production Economics*, vol. 117, no. 1, pp. 80–96, 2009.
- [4] F. Soleimani, A. A. Khamseh, and B. Naderi, "Optimal decisions in a dual-channel supply chain under simultaneous demand and production cost disruptions," *Annals of Operations Research*, vol. 243, no. 1-2, pp. 301–321, 2016.
- [5] R. Batarfi, M. Y. Jaber, and S. Zanoni, "Dual-channel supply chain: a strategy to maximize profit," *Applied Mathematical Modelling*, vol. 40, no. 21-22, pp. 9454–9473, 2016.
- [6] Y. Liu and T. Xiao, "Pricing and collection rate decisions and reverse channel choice in a socially responsible supply chain with green consumers," *IEEE Transactions on Engineering Management*, pp. 1–13, 2019.
- [7] B. Zheng, C. Yang, J. Yang, and M. Zhang, "Dual-channel closed loop supply chains: forward channel competition, power structures and coordination," *International Journal of Production Research*, vol. 55, no. 12, pp. 3510–3527, 2017.
- [8] P. He, Y. He, and H. Xu, "Channel structure and pricing in a dual-channel closed-loop supply chain with government subsidy," *International Journal of Production Economics*, vol. 213, pp. 108–123, 2019.
- [9] B. C. Giri and S. K. Dey, "Game theoretic analysis of a closed-loop supply chain with backup supplier under dual channel recycling," *Computers and Industrial Engineering*, vol. 129, pp. 179–191, 2019.
- [10] J. S. Raju, R. Sethuraman, and S. K. Dhar, "The introduction and performance of store brands," *Management Science*, vol. 41, no. 6, pp. 957–978, 1995.
- [11] C. Narasimhan and R. T. Wilcox, "Private labels and the channel relationship: a cross-category Analysis," *The Journal of Business*, vol. 71, no. 4, pp. 573–600, 1998.
- [12] D. E. Mills, "Why retailers sell private labels," *Journal of Economics*, vol. 4, no. 3, pp. 509–528, 1995.
- [13] R. K. Tyagi, "Sequential product positioning under differential costs," *Management Science*, vol. 46, no. 7, pp. 928–940, 2000.
- [14] F. Zhang and J. Ma, "Research on the complex features about a dual-channel supply chain with a fair caring retailer," *Communications in Nonlinear Science and Numerical Simulation*, vol. 30, no. 1–3, pp. 151–167, 2016.
- [15] H. Liu, M. Lei, H. Deng, G. K. Leong, and T. Huang, "A dual channel, quality-based price competition model for the WEEE recycling market with government subsidy," *Omega*, vol. 59, pp. 290–302, 2016.
- [16] Z. Liu, J. Tang, B. Li, and Z. Wang, "Trade-off between remanufacturing and recycling of WEEE and the environmental implication under the Chinese Fund Policy," *Journal of Cleaner Production*, vol. 167, pp. 97–109, 2017.
- [17] W. Zhou, Y. Zheng, and W. Huang, "Competitive advantage of qualified WEEE recyclers through EPR legislation," *European Journal of Operational Research*, vol. 257, no. 2, pp. 641–655, 2017.

- [18] J. Ma and L. Xie, "The comparison and complex analysis on dual-channel supply chain under different channel power structures and uncertain demand," *Nonlinear Dynamics*, vol. 83, no. 3, pp. 1379–1393, 2016.
- [19] Y. Dai, X. Chao, S. C. Fang, and H. L. W. Nuttle, "Pricing in revenue management for multiple firms competing for customers," *International Journal of Production Economics*, vol. 98, no. 1, pp. 1–16, 2005.
- [20] D. Q. Yao, X. Yue, and J. J. Liu, "Vertical cost information sharing in a supply chain with value-adding retailers," *Omega*, vol. 36, no. 5, pp. 838–851, 2008.
- [21] J. Ma, T. Li, and W. Ren, "Research on the complexity of dual-channel supply chain model in competitive retailing service market," *International Journal of Bifurcation and Chaos*, vol. 27, no. 7, Article ID 1750098, 2017.
- [22] J. Ma and H. Ren, "Influence of government regulation on the stability of dual-channel recycling model based on customer expectation," *Nonlinear Dynamics*, vol. 94, no. 3, pp. 1775–1790, 2018.

Research Article

Dynamically Dimensioned Search Grey Wolf Optimizer Based on Positional Interaction Information

Fu Yan ¹, Jianzhong Xu ¹, and Kumchol Yun ^{1,2}

¹School of Economics and Management, Harbin Engineering University, Harbin 150001, China

²Faculty of Mechanics, Kim Il Sung University, Pyongyang 950003, Democratic People's Republic of Korea

Correspondence should be addressed to Jianzhong Xu; xujianzhongxjz@163.com

Received 22 June 2019; Revised 13 September 2019; Accepted 21 October 2019; Published 5 December 2019

Guest Editor: Raúl Baños

Copyright © 2019 Fu Yan et al. This is an open access article distributed under the Creative Commons Attribution License, which permits unrestricted use, distribution, and reproduction in any medium, provided the original work is properly cited.

The grey wolf optimizer (GWO) algorithm is a recently developed, novel, population-based optimization technique that is inspired by the hunting mechanism of grey wolves. The GWO algorithm has some distinct advantages, such as few algorithm parameters, strong global optimization ability, and ease of implementation on a computer. However, the paramount challenge is that there are some cases where the GWO is prone to stagnation in local optima. This drawback of the GWO algorithm may be attributed to an insufficiency in its position-updated equation, which disregards the positional interaction information about the three best grey wolves (i.e., the three leaders). This paper proposes an improved version of the GWO algorithm that is based on a dynamically dimensioned search, spiral walking predation technique, and positional interaction information (referred to as the DGWO). In addition, a nonlinear control parameter strategy, i.e., the control parameter that is nonlinearly increased with an increase in iterations, is designed to balance the exploration and exploitation of the GWO algorithm. The experimental results for 23 general benchmark functions and 3 well-known engineering optimization design applications validate the effectiveness and feasibility of the proposed DGWO algorithm. The comparison results for the 23 benchmark functions show that the proposed DGWO algorithm performs significantly better than the GWO and its improved variant for most benchmarks. The DGWO provides the highest solution precision, strongest robustness, and fastest convergence rate among the compared algorithms in almost all cases.

1. Introduction

The rapid development of artificial intelligence (AI) is primarily attributed to the considerable progress of computational intelligence (CI). CI that is based on complex systems mainly consists of two categories [1], i.e., single-solution-based metaheuristics and population-based metaheuristics. Both single-solution-based algorithms and population-based algorithms employ a variety of mechanisms and are designed to solve extremely challenging problems in different complex systems.

Single-solution-based metaheuristics are usually only suitable for specific complex optimization problems because of their single particle scale and weak coordination capability. A heuristic based on simulated annealing (SA) is designed to solve the machine reassignment problem [2]. The threshold-accepting (TA) metaheuristic method is

applied to solve the job shop scheduling problem of de-hydration plants [3]. The microcanonical annealing (MA) algorithm is proposed for remote sensing image segmentation [4]. The tabu search (TS) metaheuristic is collaborated with a regenerator-reducing procedure to solve the regenerator location problem [5]. The guided local search (GLS) approach is introduced for multiuser detection in ultra-wideband systems [6]. The dynamically dimensioned search (DDS) is introduced for automatic calibration in watershed simulation models [7–11].

Compared with single-solution-based algorithms, the research and applications of population-based algorithms are more extensive because of the following three main advantages [11, 12]: more information can be obtained to guide the trial solutions toward a promising area within the search space by a set of trial solutions; local optimization can be effectively avoided because of the interaction of a set of

trial solutions; and in terms of exploration ability, population-based heuristic algorithms are superior to single-solution-based heuristic algorithms. The genetic algorithm (GA) is used to address the characterization of hyperelastic materials [12, 13]. Particle swarm optimization (PSO) is attributed to improving and evaluating the performance of automated engineering design optimization [13, 14]. Differential evolution (DE) is presented for mobile robots to avoid obstacles [14, 15]. The dragonfly algorithm (DA) has been improved to train multilayer perceptrons [15, 16]. Shuffled complex evolution (SCE) is designed to optimize the load balancing of gateways in wireless sensor networks [16, 17]. The dolphin echolocation algorithm (DEA) is applied to design a steel frame structure [17, 18]. The bat algorithm (BA) is introduced to optimize the placement of a steel plate shear wall [18, 19], and the artificial bee colony (ABC) algorithm is presented to image steganalysis [19, 20]. The grey wolf optimizer (GWO) is adopted for parameter estimation in surface waves [20, 21].

The GWO is one of the most impressive swarm intelligence algorithms and is the only algorithm that is based on leadership hierarchy theory; it was introduced by Mirjalili et al. [22]. The GWO algorithm has three advantages [23, 24]: it has universal applicability to some real-life optimization problems; it is insensitive to derived information in the initial search; and it requires fewer algorithm parameters for adjustment. These features render it a simple, flexible, adaptable, usable, and stable algorithm [24, 25]. Therefore, since the GWO was proposed, researchers have conducted a considerable amount of in-depth research and applications. Regarding the improvements in research on the GWO algorithm, researchers tend to improve the performance of the GWO from four aspects [25]: position-updating mechanisms, new control parameters, encoding scheme of individuals, and population structure and hierarchy. Typical study cases are listed as follows: Mittal et al. [26] used the exponential decay function a to enhance the exploration process in the GWO. However, this algorithm suffers premature convergence. Kishor and Singh [27] proposed a modified version of the GWO by incorporating a simple crossover operator between two randomly selected individuals. However, this technique has low capacity in solving high-dimensional complex problems. A complex-valued encoding strategy was employed by Luo et al. [28] to substitute a typical real-valued strategy that was adopted in the standard GWO and propose a complex-encoded GWO. The main shortcoming of this method is that it suffers premature convergence. Yang et al. [29] used an effective cooperative hunting group and a random scout group strategy to propose a novel grouped grey wolf optimizer. This approach employs a complex mechanism. Xu et al. [30] proposed a chaotic dynamic weight grey wolf optimizer (CDGWO), in which a new position-updated equation, formed by employing a chaotic map and dynamic weight, was built to guide the search process for potential candidate solutions. Gupta and Deep [23] proposed a novel random walk grey wolf optimizer (RW-GWO); in the RW-GWO, the random walk strategy was used for improving the search ability of the GWO. However, it shows low solution

accuracy. In addition, an improved grey wolf optimization (VW-GWO) algorithm based on variable weight strategies and the social hierarchy in the searching positions was presented by Gao and Zhao [31]. However, it employs a complex methodology. In terms of successful applications of the GWO, representative application research can be summarized as flow shop scheduling [32], machine learning [33–36], economic load dispatch [37], robotics and path planning [38, 39], channel estimation in wireless communication systems [40], and other applications detailed in References [24, 25]. Theoretical and practical research has shown the potential of the GWO algorithm in real life. However, numerous studies and experimental results concluded that the optimization performance of the GWO algorithm needs improvement. Specifically, the trial solution diversity would be hampered by the three best wolves that were identified in the accumulative search [12]. Many metaheuristics, such as the GWO, can be easily trapped in the local optima when solving multimodal optimization problems, where multiple global optimum solutions exist [41] and the linear control parameter strategy is not the perfect design for balancing the exploration and exploitation. These drawbacks may lead to an undesirable optimal performance of the algorithm [27, 42]. In addition, existing research on the GWO algorithm does not discuss improvements in the performance of the GWO algorithm by considering the positional interaction information among the three leaders (i.e., the first three best wolves). In the actual hunting process, however, better predation efficiency can be obtained only when positional information is communicated among the three leaders. In this paper, the positional interaction information refers to the information communication among the three leaders in their predation process as reflected by the relative change in position. In addition to not considering the positional interaction information among the three leaders of the grey wolves, existing research does not explore other predation methods, such as spiral walking hunting, which may help hunting and increase the chance of jumping out of the local optima for the GWO algorithm. In summary, the GWO algorithm is a strong algorithm but suffers from the abovementioned shortcomings. Considering the drawbacks of the GWO algorithm, this paper decided to improve upon it.

Based on this analysis, this paper improves the GWO algorithm from the following three aspects: a hunting model is built based on the spiral walking, a position-updated equation is rebuilt based on the positional interaction information among the three leaders of grey wolves, and a nonlinear control parameter is designed to replace the linear control parameter of the standard GWO algorithm. The proposed algorithm is tested on 23 classical benchmark problems, CEC2014 suite, and three well-known engineering optimization problems. The experimental results reveal that the proposed method is robust, efficient, and superior compared to other algorithms.

The remaining sections of the paper are organized as follows: The original GWO algorithm and DDS are briefly overviewed in Section 2. In Section 3, the dynamically dimensioned search grey wolf optimizer, which is based on the

deep search strategy (DGWOD), is proposed. The principle of searching the GWO by the DDS is detailed, and the position-updated equations, which are based on the deep search strategy and the nonlinear control parameter equation, are constructed. Section 4 provides the experimental results and a discussion of a set of well-known test functions. This paper is concluded and future research directions are presented in Section 5.

2. Overview of GWO and DDS

2.1. Standard GWO Algorithm. In this section, four parts of the basic GWO algorithm [22] inspired by the complete process of hunting the grey wolf for preying are described.

2.1.1. Foundation of the Social Hierarchy. In the GWO algorithm, the search is executed by the joint guidance of the first three best grey wolves (i.e., α , β , and δ), and the positions of the ω grey wolves (solutions) are constantly adjusted with the guidance of the first three best grey wolves with an increase in the iteration number.

2.1.2. Encircling Prey. Grey wolves hunt their prey by encircling them, which is considered to be wise behavior. To describe the principle of this predation from the perspective of a mathematical model, Mirjalili et al. [22] constructed the following equation:

$$\vec{D} = |\vec{C} \cdot \vec{X}_p(t) - \vec{X}(t)|, \quad (1)$$

$$\vec{X}(t+1) = \vec{X}_p(t) - \vec{A} \cdot \vec{D}, \quad (2)$$

$$\vec{A} = 2\vec{a} \cdot \vec{r}_1 - \vec{a}, \quad (3)$$

$$\vec{C} = 2 \cdot \vec{r}_2, \quad (4)$$

where t is the current number of iterations, $\vec{X}(t+1)$ is the position vector of the grey wolf at the $(t+1)$ th iteration, the symbol “ \cdot ” indicates dot product, $\vec{X}_p(t)$ is the position vector of the prey at the (t) th iteration, \vec{D} is a vector that is relative to the position of the prey $\vec{X}_p(t)$, \vec{A} and \vec{C} are the coefficient vectors, \vec{a} is a vector whose values are linearly decreased from 2 to 0 over iterations, and \vec{r}_1 and \vec{r}_2 are randomly generated vectors whose values lie between 0 and 1.

2.1.3. Hunting. As described in Section 2.1.2, the action of the grey wolf that encircles its prey provides the leader of the grey wolf group with necessary position information and forces the prey into promising areas. After the leader of the grey wolf group receives the position information about the prey, the next step is to guide omega (ω) wolves to conduct the hunting. To describe the hunting behaviors of grey wolves from the perspective of a mathematical model, we assumed that \vec{X}_α , \vec{X}_β , and \vec{X}_δ represent the positions of the α wolf, β wolf, and δ wolf, respectively. Therefore, the

mathematical models for grey wolf hunting are described as follows:

$$\vec{X}_1 = \vec{X}_\alpha(t) - \vec{A}_1 \cdot \vec{D}_\alpha, \quad (5)$$

$$\vec{X}_2 = \vec{X}_\beta(t) - \vec{A}_2 \cdot \vec{D}_\beta, \quad (6)$$

$$\vec{X}_3 = \vec{X}_\delta(t) - \vec{A}_3 \cdot \vec{D}_\delta, \quad (7)$$

$$\vec{X}(t+1) = \frac{1}{3}(\vec{X}_1 + \vec{X}_2 + \vec{X}_3). \quad (8)$$

\vec{D}_α , \vec{D}_β , and \vec{D}_δ are calculated using equation (1) as follows:

$$\vec{D}_\alpha = |\vec{C}_1 \cdot \vec{X}_\alpha(t) - \vec{X}(t)|, \quad (9)$$

$$\vec{D}_\beta = |\vec{C}_2 \cdot \vec{X}_\beta(t) - \vec{X}(t)|, \quad (10)$$

$$\vec{D}_\delta = |\vec{C}_3 \cdot \vec{X}_\delta(t) - \vec{X}(t)|. \quad (11)$$

2.1.4. Attacking Prey. In the GWO algorithm, the behaviors of grey wolves that attack their prey are controlled by constant changes in the value of the linear control parameter \vec{a} . According to equation (3), the expression of the vector \vec{A} is correlated with the parameter \vec{a} . When the value of \vec{a} linearly decreases from 2 to 0, the value of the vector \vec{A} also decreases. When $|\vec{A}| \leq 1$, the hunting of a grey wolf will occur at any position between its current position and that of its prey. When $|\vec{A}| > 1$, wolves will search the entire solution space to locate the prey (optima). Therefore, $|\vec{A}|$ represents a controlling parameter vector that causes exploration and exploitation. We determine that different values of the control parameter \vec{a} have a different role in the exploration and exploitation of the GWO algorithm. According to Reference [42], a larger \vec{a} is favorable for global exploration, while a smaller \vec{a} facilitates local exploitation. Therefore, the control parameter \vec{a} has an important role in balancing the exploration and exploitation of the GWO algorithm. However, for the standard GWO algorithm, several studies have shown that the value of the control parameter \vec{a} linearly changes and the design of the position-updated equation will cause some drawbacks, such as premature convergence of the algorithm and powerlessness when solving multimodal problems [12, 27, 42].

Based on this description, the pseudocode of the GWO algorithm is shown in Algorithm 1.

2.2. DDS Algorithm. The DDS algorithm is a powerful single-solution-based metaheuristic algorithm, which was employed for calibration problems that arise in watershed simulation models. DDS was developed by Tolson and Shoemaker in 2007 [7] and was proposed for optimization problems that are bound constrained. Thus, achieving excellent optimization results for bounded constrained global

Input: population size N and the maximum number of iterations MaxIter
Output: optimal individual position \vec{X}_α and best fitness values $f(\vec{X}_\alpha)$
(1) Randomly initialize N individuals' position to construct a population
(2) Calculate the fitness value of each individual and find α , β , and δ
(3) **while** $t \leq \text{MaxIter}$ or stopping criteria not met **do**
(4) **for** each individual **do**
(5) Update current individuals' position according to equation (8)
(6) **end**
(7) Update \vec{a} , \vec{A}_i , and \vec{C}_i , $i = 1, 2, 3$
(8) Evaluate the fitness value of each individual
(9) Update α , β , and δ
(10) **end while**

ALGORITHM 1: Pseudocode of the GWO algorithm.

optimization problems is the advantage of the DDS algorithm.

DDS is a point-to-point stochastic-based heuristic global search algorithm with no parameter tuning; global solutions are obtained by scaling within a user-specified maximum number of function evaluations (MaxIter) [43]. Since it is a simple model that is easily programmed and a global search algorithm, many researchers have focused their great attention on it. At the beginning, when the number of iterations is small, the global search of the algorithm is dominant. As the number of iterations approached the maximum, the algorithm evolved into a local search. The key idea for the DDS algorithm to transit from a global search to a local search is to dynamically and probabilistically reducing the number of dimensions to be perturbed in the neighborhood of the current best solution [11, 43]. The operation to dynamically and probabilistically reduce the number of dimensions to be perturbed can be summarized as follows: in each iteration, the j th variable is randomly selected with the probability P_t from m decision variables for inclusion in the neighborhood I_{perturb} . The probability P_t is expressed as

$$P_t = 1 - \frac{\ln(t)}{\ln(\text{MaxIter})}, \quad (12)$$

where t indicates the current iteration and MaxIter represents the maximum number of iterations.

At each iteration t , a new potential solution $\vec{X}^{\text{new}}(t)$ is obtained by perturbing the current best $\vec{X}^{\text{best}}(t)$ in randomly selected dimensions. These perturbation magnitudes are sampled using the standard normal random variable $N(0, 1)$ and reflecting decision variable bounds as [11]

$$\vec{X}_j^{\text{new}}(t) = \begin{cases} \vec{X}_j^{\text{best}}(t) + r \times \vec{\mu}_j \times (\text{ub}_j - \text{lb}_j), & \text{if } j \in I_{\text{perturb}}, \\ \vec{X}_j^{\text{best}}(t), & \text{otherwise,} \end{cases} \quad (13)$$

where $j = 1, 2, \dots, m$; r is a scalar neighborhood size perturbation factor; $\vec{\mu}_j$ is a random vector that is generated for the j th variable to be perturbed; ub_j and lb_j correspond to

the upper bound and lower bound of the j th variable; and $\vec{X}_j^{\text{new}}(t)$ and $\vec{X}_j^{\text{best}}(t)$ denote the j th variable of the trial potential solution and the current best solution, respectively.

To accurately choose the best solution between the current best $\vec{X}^{\text{best}}(t)$ and the trial potential $\vec{X}^{\text{new}}(t)$ for the next iteration, the greedy search method is employed. The current best solution $\vec{X}^{\text{best}}(t)$ will be replaced by the trial solution $\vec{X}^{\text{new}}(t)$ if the objective function value of $\vec{X}^{\text{new}}(t)$ is smaller than that of $\vec{X}^{\text{best}}(t)$, i.e., $f(\vec{X}^{\text{new}}(t)) < f(\vec{X}^{\text{best}}(t))$; otherwise, the current best solution $\vec{X}^{\text{best}}(t)$ is reserved for the next iteration. The pseudocode description of the DDS algorithm is presented in Algorithm 2 [11].

3. Proposed Algorithm

As presented in the previous sections, the GWO algorithm encounters a few drawbacks, such as premature convergence and a low capability to handle the difficulties of a multimodal search landscape [25]. To overcome these weaknesses, the most effective improvement is to increase the diversity of candidate solutions and further improve the balance between exploration and exploitation during the iteration. In terms of increasing the diversity of candidate solutions, inspired by the core idea of the DDS algorithm, this study adopts two improved strategies to increase the performance of the GWO algorithm. One approach is to dynamically and probabilistically reduce the number of dimensions to be perturbed in the neighborhood, which enables candidate solutions to be perturbed between the current solutions and each of the three best solutions. Another method is to use the positional interaction information about the first three best grey wolf individuals (i.e., α , β , and δ) in the process of encircling and preying on the prey to perform a deep search. The position-updated equation of the GWO algorithm, which is based on the dynamically dimensioned perturbation and position interaction information, is proposed, which is referred to as the DGWO. To balance the exploration and exploitation of the GWO algorithm, the introduction of the search mechanism of the DDS algorithm enables the GWO algorithm to gradually transform from a

Input: scalar neighborhood size perturbation factor $r = 0.2$, maximum number of iterations MaxIter , number of variables (dimension) m , and upper bounds ub and lower bounds lb

Output: \vec{X}^{best} and f^{best}

- (1) Initialization
 - $\vec{X}^0 = [x_1^0, x_2^0, \dots, x_m^0]$, $x_i^0 = \text{lb}_j + \text{rand} \cdot (\text{ub}_j - \text{lb}_j)$
 - Set $t = 1$, $\vec{X}^{\text{best}} = \vec{X}^0$, $f^{\text{best}} = f(\vec{X}^{\text{best}})$, $I_{\text{perturb}} = [0, 0, \dots, 0]$
- (2) **while** $t \leq \text{MaxIter}$ **do**
- (3) Compute the probability of perturbing the decision variables P_t using equation (12)
- (4) **for** $j = 1$ to m **do**
- (5) Generate uniform random numbers, $\text{rand}(j)$
- (6) **if** $\text{rand}(j) < P_t$ **then**
- (7) Set $I_{\text{perturb}}(j) = 1$
- (8) **end if**
- (9) **end for**
- (10) Generate a standard normal random vector, $\vec{\mu}$
- (11) **for** $j = 1$ to m **do**
- (12) $\vec{X}_j^{\text{new}} = \vec{X}_j^{\text{best}} + (\text{ub}_j - \text{lb}_j) \cdot I_{\text{perturb}}(j) \cdot r \cdot \vec{\mu}$ //equation (13)
- (13) **end for**
- (14) **for** $j = 1$ to m **do**
- (15) **if** $\vec{X}_j^{\text{new}} < \text{lb}_j$ **then**
- (16) Set $\vec{X}_j^{\text{new}} = \text{lb}_j + (\text{lb}_j - \vec{X}_j^{\text{new}})$
- (17) **if** $\vec{X}_j^{\text{new}} > \text{ub}_j$ **then**
- (18) Set $\vec{X}_j^{\text{new}} = \text{ub}_j - (\vec{X}_j^{\text{new}} - \text{ub}_j)$
- (19) **end if**
- (20) **end for**
- (21) **if** $\vec{X}_j^{\text{new}} > \text{ub}_j$ **then**
- (22) Set $\vec{X}_j^{\text{new}} = \text{ub}_j - (\vec{X}_j^{\text{new}} - \text{ub}_j)$
- (23) **if** $\vec{X}_j^{\text{new}} < \text{lb}_j$ **then**
- (24) Set $\vec{X}_j^{\text{new}} = \text{lb}_j + (\text{lb}_j - \vec{X}_j^{\text{new}})$
- (25) **end if**
- (26) **end if**
- (27) **end for**
- (28) Evaluate $f(\vec{X}^{\text{new}})$
- (29) **if** $f(\vec{X}^{\text{new}}) < f^{\text{best}}$ **then**
- (30) Set $\vec{X}^{\text{best}} = \vec{X}^{\text{new}}$, $f^{\text{best}} = f(\vec{X}^{\text{new}})$
- (31) **end if**
- (32) Set $t = t + 1$
- (33) **end while**

ALGORITHM 2: Pseudocode of the DDS algorithm.

global search to a local search with an increase in the number of iterations. The GWO algorithm has a strong exploration ability in the initial search stage and a strong exploitation ability in the subsequent stage of iteration. The nonlinear control parameter \vec{a}' is proposed to replace the linear control parameter \vec{a} of the standard GWO algorithm. This nonlinear control parameter strategy produces a GWO algorithm with a strong exploitation ability in the early stage of searching and a strong exploration ability in the subsequent stage of searching. Therefore, the introduction of the DDS and the nonlinear control parameter strategy strengthens the balance between exploration and exploitation of the GWO algorithm, and positional interaction information is utilized to conduct in-depth search and ensure the diversity of the candidate solution.

3.1. Two Ways to Hunt Prey Are Freely Switched Using DDS. As described in Section 2.1.3, a grey wolf hunts by direct encirclement. However, though actual observation, we found that, in addition to the previously mentioned hunting strategy, the grey wolf also approaches its prey by spiral walking when hunting. This way of spiral walking around the prey is often considered to be a very effective way to hunt [44]. Although we have determined that a grey wolf hunts by direct encirclement and spiral walking, a reasonable conversion of these two hunting methods has not been performed via research. The traditional method is to randomly convert between those two hunting methods by equal probability [44]. In an actual situation, the conversion probability between these two methods is not equal. A reasonable conversion method is that the grey

wolf can freely switch between these two hunting methods during its predation process. Thus, the grey wolf has the best hunting effect, that is, to ensure that the grey wolf achieves the best prey (global optimum) in the best situation or obtains the relatively better prey (global approximation solution) in poorer conditions. We determined that the DDS method employs the conversion technique that we expected. According to Section 2.2, the core principle of the DDS algorithm is to transit the search from global to local by dynamically and probabilistically reducing the number of dimensions to be perturbed in the neighborhood of the current best solution, which causes the DDS to converge to the desired region to locate the global optimum in the best case or a reasonable local optimum in the worst case. Based on this analysis, the DDS method is introduced in the GWO algorithm to conduct free switching of the hunting behavior between direct encirclement and spiral walking to improve the quality of the solution of the GWO algorithm. The implementation steps are described as follows:

- (i) First, at each iteration t , \vec{D}_α , \vec{D}_β , and \vec{D}_δ are calculated using equations (9)–(11).
- (ii) Second, at each iteration t , $\vec{D}_\alpha^{\text{new}}$, $\vec{D}_\beta^{\text{new}}$, and $\vec{D}_\delta^{\text{new}}$ are computed using the following equations:

$$\vec{d}_\alpha = |\vec{X}_\alpha(t) - \vec{r}_3 \cdot \vec{X}(t)|, \quad (14)$$

$$\vec{d}_\beta = |\vec{X}_\beta(t) - \vec{r}_4 \cdot \vec{X}(t)|, \quad (15)$$

$$\vec{d}_\delta = |\vec{X}_\delta(t) - \vec{r}_5 \cdot \vec{X}(t)|, \quad (16)$$

$$\vec{D}_\alpha^{\text{new}} = \vec{X}(t) + r \cdot \vec{d}_\alpha \cdot \exp(-2\pi \cdot \vec{d}_\alpha) \cdot \cos(\pi \cdot \vec{d}_\alpha), \quad (17)$$

$$\vec{D}_\beta^{\text{new}} = \vec{X}(t) + r \cdot \vec{d}_\beta \cdot \exp(-2\pi \cdot \vec{d}_\beta) \cdot \cos(\pi \cdot \vec{d}_\beta), \quad (18)$$

$$\vec{D}_\delta^{\text{new}} = \vec{X}(t) + r \cdot \vec{d}_\delta \cdot \exp(-2\pi \cdot \vec{d}_\delta) \cdot \cos(\pi \cdot \vec{d}_\delta). \quad (19)$$

- (iii) Finally, using the ideas of the DDS algorithm to transition the search from global to local, \vec{D}_α , \vec{D}_β ,

and \vec{D}_δ are recalculated using the following equations:

$$\vec{D}_{\alpha,j} = \begin{cases} \vec{D}_{\alpha,j}^{\text{new}}, & \text{if } P_t > \text{rand}(j), \\ \vec{D}_{\alpha,j}, & \text{otherwise,} \end{cases} \quad (20)$$

$$\vec{D}_{\beta,j} = \begin{cases} \vec{D}_{\beta,j}^{\text{new}}, & \text{if } P_t > \text{rand}(j), \\ \vec{D}_{\beta,j}, & \text{otherwise,} \end{cases} \quad (21)$$

$$\vec{D}_{\delta,j} = \begin{cases} \vec{D}_{\delta,j}^{\text{new}}, & \text{if } P_t > \text{rand}(j), \\ \vec{D}_{\delta,j}, & \text{otherwise,} \end{cases} \quad (22)$$

where \vec{r}_3 , \vec{r}_4 , and \vec{r}_5 are random vectors between 0 and 1 and r is a scalar neighborhood size perturbation factor, whose value is 0.2 in this paper.

3.2. Position-Updated Equation Based on the Positional Interaction Information. As described in the original literature [22] of the GWO algorithm, the alpha (α) wolf is the supreme leader of the grey wolf pack and is primarily responsible for commanding all wolves to hunt, sleep, and wake. The leader in the second tier is referred to as the beta (β) wolf, which is controlled by α and is responsible for commanding the remaining wolves. The third tier of leadership entails the delta (δ) wolf, who has to submit to α and β but dominates the ω wolf. ω is the common wolf and has the subordinate role of listening to the orders of the first three leaders. This top-down leadership mechanism of the grey wolf pack enables the GWO algorithm to have strong exploration ability. As previously described, the cooperative hunting behavior of the grey wolf group is outstanding. One situation is that the first three best grey wolves (leaders) directly lead the ω wolf to hunt. In another situation, the α wolf commands the β wolf and the δ wolf to hunt and the β wolf commands the δ wolf to hunt. The leadership relationship between these three leaders usually occurs via the relative position changes, that is, positional interaction information. In the standard GWO algorithm, however, only the former case is considered and the latter case is disregarded, which is very important for the hunting of the grey wolf group. Based on this shortcoming of the standard GWO algorithm, we design a position-updated equation that is based on positional interaction information as

$$\vec{X}_{11} = \vec{X}_\alpha(t) - \vec{r}_6 \cdot \vec{A}_1 \cdot \vec{X}_\beta(t), \quad (23)$$

$$\vec{X}_{22} = \vec{X}_\beta(t) - \vec{r}_7 \cdot \vec{A}_2 \cdot \vec{X}_\delta(t), \quad (24)$$

$$\vec{X}_{33} = \vec{X}_\alpha(t) - \vec{r}_8 \cdot \vec{A}_3 \cdot \vec{X}_\delta(t), \quad (25)$$

$$\vec{X}_j(t+1) = \begin{cases} w_1 \cdot \frac{1}{3} \cdot (\vec{X}_{11,j} + \vec{X}_{22,j} + \vec{X}_{33,j}) + w_2 \cdot \frac{1}{3} (\vec{X}_{1,j} + \vec{X}_{2,j} + \vec{X}_{3,j}), & \text{if } P_n > \text{rand}(j), \\ w_2 \cdot \frac{1}{3} \cdot (\vec{X}_{11,j} + \vec{X}_{22,j} + \vec{X}_{33,j}) + w_1 \cdot \frac{1}{3} (\vec{X}_{1,j} + \vec{X}_{2,j} + \vec{X}_{3,j}), & \text{otherwise,} \end{cases} \quad (26)$$

where \vec{X}_{11} , \vec{X}_{22} , and \vec{X}_{33} indicate the positional interaction information about the three leaders; \vec{r}_6 , \vec{r}_7 , and \vec{r}_8 are random vectors between 0 and 1; and w_1 and w_2 are the position weights.

3.3. Nonlinear Control Parameter Design. As previously presented, the DDS algorithm has a strong global search ability (i.e., strong exploration) at the initial search stage and a strong local search ability (i.e., exploitation) in the subsequent search stage. In addition, the exploration and exploitation of the GWO algorithm are primarily controlled by the control parameter \vec{a} . When \vec{a} linearly decreases from 2 to 0, the algorithm exhibits strong exploration and weak exploitation in the initial stage of searching and exhibits strong exploitation and weak exploration in the subsequent stage. Since both the GWO algorithm and DDS algorithm have strong exploration in the initial iteration and strong exploitation in the subsequent iteration, introducing the search mechanism of the DDS algorithm into the GWO algorithm has further aggravated the imbalance between the exploration and the exploitation of the GWO algorithm. Therefore, an imbalance between exploration and exploitation occurs at different search stages of the algorithm. To address this problem, we designed the new nonlinear control parameter \vec{a}' , which nonlinearly increases from -2 to 2 , to substitute the linear control parameter \vec{a} of the standard GWO algorithm. In the initial search phase, because the population has a higher diversity, small \vec{a}' values are needed to enhance the exploitation capability and accelerate convergence. In contrast, in the later stage of the search, since the diversity decreases in the population, larger \vec{a}' values facilitate exploration and can help the search agents to be away from the local optimum. Therefore, the new nonlinear control parameter \vec{a}' can ensure the relative strong exploitation at the initial iteration and a strong exploration in the subsequent iteration of the GWO algorithm. The nonlinear control parameter \vec{a}' is designed as

$$\vec{a}' = 2 - 4 \cdot \exp\left(-\frac{t}{\text{MaxIter}}\right) \cdot \cos\left(\frac{\pi}{2} \cdot \sqrt{\frac{t}{\text{MaxIter}}}\right), \quad (27)$$

where t and MaxIter indicate the current iteration and the maximum iteration number, respectively.

Figure 1 shows the transition between exploration and exploitation that was caused by the adaptive values of the control parameters \vec{a} and \vec{a}' . As shown in Figure 1, with respect to the GWO algorithm, half of the iterations are adapted to exploration ($|\vec{A}| > 1$) and the rest of the iterations are devoted to exploitation ($|\vec{A}| \leq 1$). However, with regard

to the DGWO algorithm, the number of iterations used for exploration and exploitation is 60.2% and 39.8%, respectively.

3.4. Framework and Pseudocode of the DGWO Algorithm. In this paper, the proposed hunt strategy of spiral walking is added to the GWO algorithm to enhance the ability of the predation. This strategy is freely switched between the original encirclement methods using the search mechanism of DDS. This method combines the proposed nonlinear control parameter strategy and the position-updated equation, which considers the positional interaction information, and develops the DGWO algorithm. The pseudocode of the proposed DGWO algorithm is shown in Algorithm 3.

3.5. Time Complexity of DGWO. The time complexities of the DGWO and GWO are summarized as follows:

- (1) In the initialization phase, the DGWO and GWO require $O(N \times m)$ time, where N represents the population size and m represents the dimension of the problem
- (2) Calculation of the control parameters of the DGWO and GWO requires $O(N \times m)$ time
- (3) Update of the agents' position-updated equations of the DGWO and GWO requires $O(N \times m)$ time
- (4) Evaluation of the fitness value of each agent requires $O(N \times m)$ time

Based on the above analysis, for each generation, the total time complexity is $O(N \times m)$, and given a maximum number of iterations, the total time complexity of the DGWO and GWO is $O(N \times m \times \text{MaxIter})$, where MaxIter indicates the maximum number of iterations.

3.6. Analysis and Comparison of the Diversity between GWO and DGWO. From equations (5) to (8), we can know that the grey wolves update their position under the leadership of the three best wolves. However, when the three fittest wolves get into local optimum, the whole search agents will all concentrate in this region, which leads to the decrease in diversity in the population, and the algorithm easily falls into local optimum. Based on this point, the DGWO algorithm is proposed to enhance the diversity of the GWO algorithm. To analyze and compare the diversity between the GWO and the DGWO, we choose the Sphere function as the benchmark test problem to see the difference in diversity between the GWO and the DGWO at different iterations. We set the population size as 30, the dimension of the problem as 2, and the upper and lower boundaries of

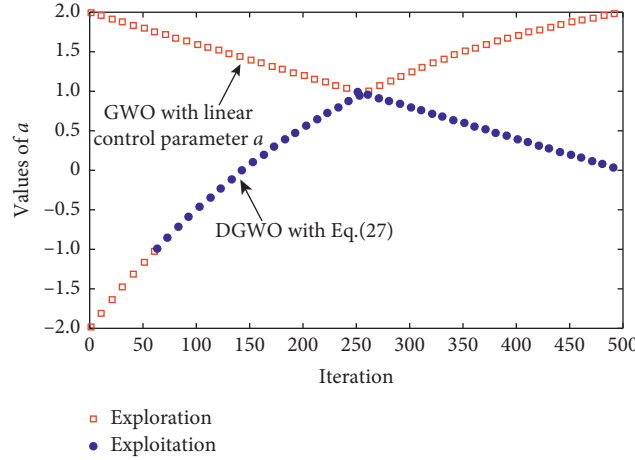


FIGURE 1: Updating the values of control parameters \vec{a} and \vec{a}' over the course of iterations.

Input: population size N , scalar neighborhood size perturbation factor r , maximum number of iterations MaxIter , number of variables m , and upper bounds ub and lower bounds lb

Output: optimal individual position \vec{X}_α and best fitness value $f(\vec{X}_\alpha)$

- (1) Randomly initialize N individuals' position r to construct a population
- (2) Calculate the fitness value of each individual, find α , β , and δ , and set $t = 0$
- (3) **while** $t \leq \text{MaxIter}$ **do**
- (4) Compute the probability (P_n) of perturbing the decision variables using equation (12) and the value of the nonlinear control parameter \vec{a}' using equation (27)
- (5) Generate uniform random numbers $\text{rand}(j) \in [0, 1]$
- (6) **for** $i = 1$ to N **do**
- (7) **for** $j = 1$ to m **do**
- (8) **if** $P_n(t) < \text{rand}(j)$ **then**
- (9) Calculate $\vec{D}_\alpha^{\text{new}}$, $\vec{D}_\beta^{\text{new}}$, and $\vec{D}_\delta^{\text{new}}$ according to equations (14)–(19)
- (10) Calculate \vec{X}_{11} , \vec{X}_{22} , and \vec{X}_{33} using equations (23)–(25)
- (11) Calculate \vec{X}_1 , \vec{X}_2 , and \vec{X}_3 using equations (5)–(7)
- (12) Update current individuals' position according to equation (26)
- (13) **else**
- (14) Calculate \vec{D}_α , \vec{D}_β , and \vec{D}_δ according to equations (9)–(11)
- (15) Calculate \vec{X}_{11} , \vec{X}_{22} , and \vec{X}_{33} using equations (23)–(25)
- (16) Calculate \vec{X}_1 , \vec{X}_2 , and \vec{X}_3 using equations (5)–(7)
- (17) Update current individuals' position according to equation (26)
- (18) **end if**
- (19) **end for**
- (20) **end for**
- (21) Update \vec{a}' , \vec{A}_i , and \vec{C}_i , $i = 1, 2, 3$
- (22) Evaluate the fitness value of each individual
- (23) Update α , β , and δ
- (24) Set $t = t + 1$
- (25) **end while**

ALGORITHM 3: Pseudocode of the proposed DGWO algorithm.

the problem as 10 and -10 , respectively. The diversity distributions of the DGWO and GWO at different iterations are plotted in Figure 2.

From Figure 2(a), when the number of iterations is 2, both the DGWO and GWO have high diversity individuals. However, from Figures 2(b) to 2(d), the DGWO algorithm shows better diversity of solutions than the GWO algorithm. This comparison confirms that the DGWO algorithm has higher diversity of solutions than the standard GWO algorithm.

4. Results and Discussion

4.1. Test Function Selection and Control Parameter Settings. In this section, to validate the performance of the proposed DGWO algorithm, 23 benchmark problems with various complexity and sizes are collected from studies [21, 23, 43]. The characteristics of the selected test functions are summarized in Table 1, where f_{\min} denotes the global optimal value. In this table, the key to test functions, the mathematical expression of

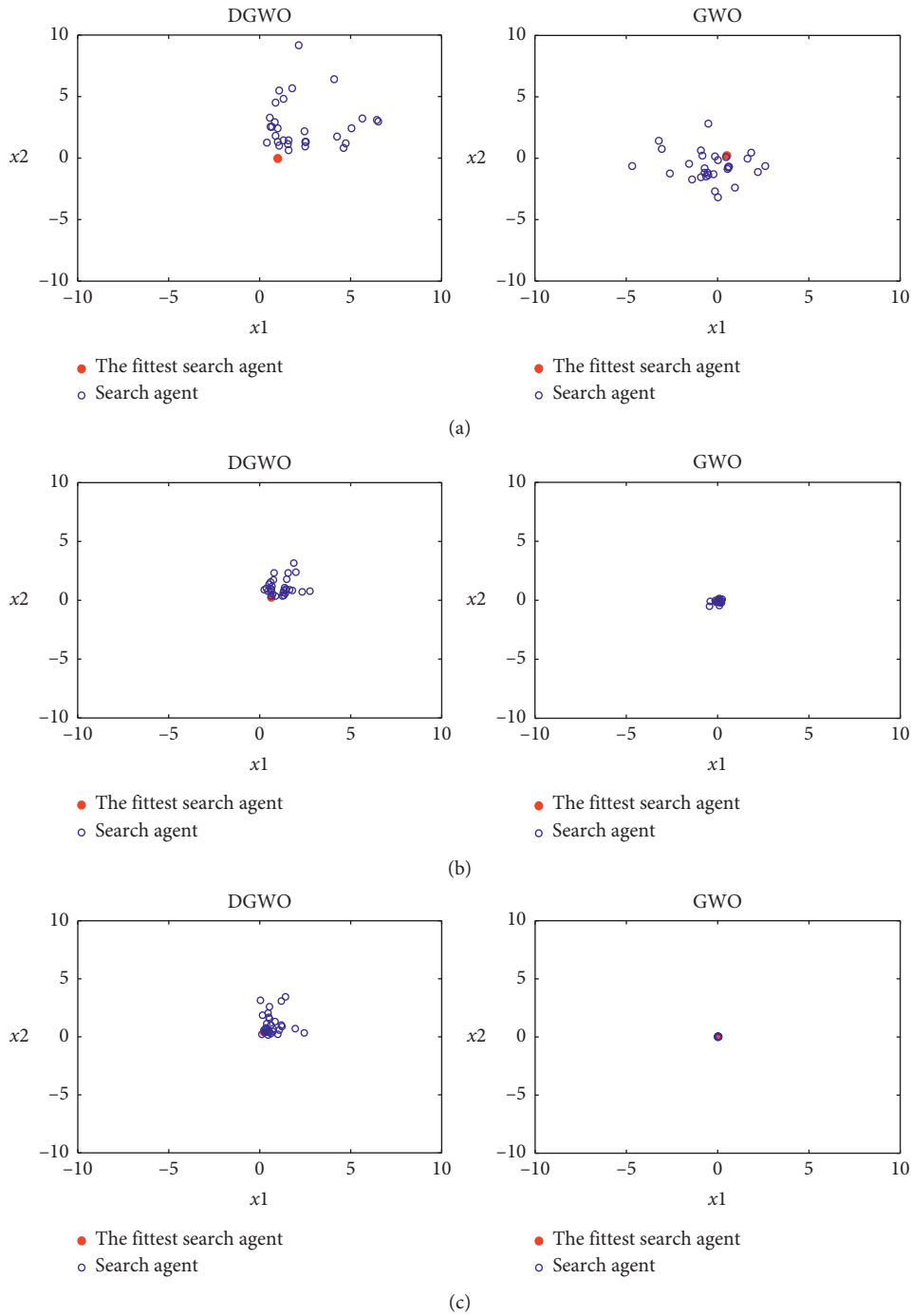


FIGURE 2: Continued.

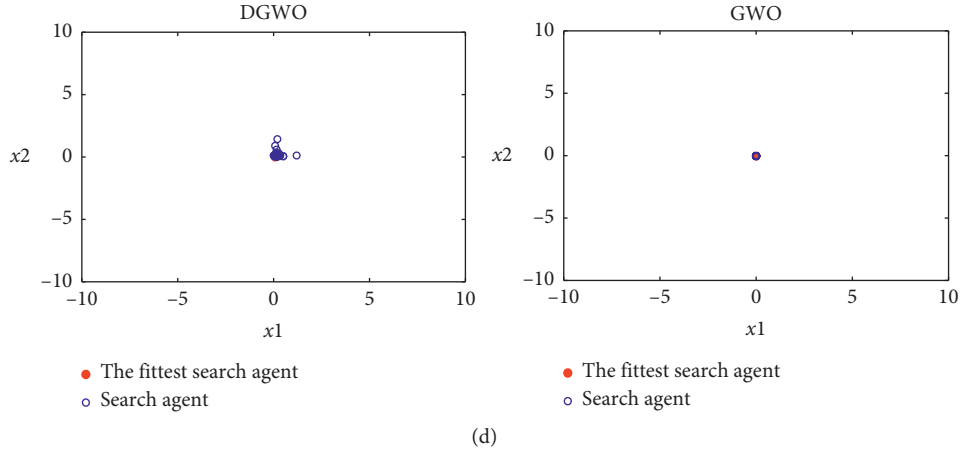


FIGURE 2: Search agents' distribution observed at different iterations in the DGWO and GWO for solving Sphere function ($m=2$). (a) Number of iterations $t=2$. (b) Number of iterations $t=4$. (c) Number of iterations $t=6$. (d) Number of iterations $t=12$.

TABLE 1: Description of 23 classic benchmark functions.

Key	Function	Range	m	C	f_{\min}
f_1	$\sum_{i=1}^n x_i^2$	$[-100, 100]$	10, 30, 50, 100	U	0
f_2	$\sum_{i=1}^n x_i + \prod_{i=1}^n x_i $	$[-10, 10]$	10, 30, 50, 100	U	0
f_3	$\sum_{i=1}^n (\sum_{j=1}^i x_j)^2$	$[-100, 100]$	10, 30, 50, 100	U	0
f_4	$\max_i \{ x_i , 1 \leq i \leq n\}$	$[-100, 100]$	10, 30, 50, 100	U	0
f_5	$\sum_{i=1}^{n-1} [100(x_{i+1} - x_i^2)^2 + (x_i - 1)^2]$	$[-30, 30]$	10, 30, 50, 100	U	0
f_6	$\sum_{i=1}^n ((x_i + 0.5)^2)$	$[-100, 100]$	10, 30, 50, 100	U	0
f_7	$\sum_{i=1}^n i x_i^4 + \text{random}[0, 1)$	$[-128, 128]$	10, 30, 50, 100	U	0
f_8	$\sum_{i=1}^n -x_i \sin(\sqrt{ x_i })$	$[-500, 500]$	10, 30, 50, 100	M	$-418.9829 \times D$
f_9	$\sum_{i=1}^n (x_i^2 - 10 \cos(2\pi x_i) + 10)$	$[-5.12, 5.12]$	10, 30, 50, 100	M	0
f_{10}	$-20 \exp(-0.2 \sqrt{1/n \sum_{i=1}^n x_i^2}) - \exp(1/n \sum_{i=1}^n \cos(2\pi x_i)) + 20 + e$	$[-32, 32]$	10, 30, 50, 100	M	0
f_{11}	$1/4000 \sum_{i=1}^n x_i^2 - \prod_{i=1}^n \cos(x_i/\sqrt{i}) + 1$	$[-600, 600]$	10, 30, 50, 100	M	0
f_{12}	$\pi/n \{10 \sin(\pi y_1) + \sum_{i=1}^{n-1} (y_i - 1)^2 [1 + 10 \sin^2(\pi y_{i+1}) + (y_n - 1)^2]\} + \sum_{i=1}^n u(x_i, 10, 100, 4)$	$[-50, 50]$	10, 30, 50, 100	M	0
f_{13}	$1/10 \{ \sin(2(3\pi x_1) + \sum_{i=1}^n (x_i - 1)^2 [1 + \sin^2(3\pi x_i + 1)] + (x_n - 1)^2 [1 + \sin^2(2\pi x_n + 1)]) + \sum_{i=1}^n u(x_i, 5, 100, 4)$	$[-50, 50]$	10, 30, 50, 100	M	0
f_{14}	$(1/500 + \sum_{j=1}^{25} (1/j + \sum_{i=1}^2 (x_i - a_{ij})^6))^{-1}$	$[-65, 65]$	2	F	1
f_{15}	$\sum_{i=1}^{11} [a_i - (x_i (b_i^2 + b_i x_2)/b_i^2 + b_i x_3 + x_4)]^2$	$[-5, 5]$	4	F	0.0003
f_{16}	$4x_1^2 - 2.1x_1^4 + (1/3)x_1^6 + x_1 x_2 - 4x_2^2 + 4x_2^4$	$[-5, 5]$	2	F	-1.0316
f_{17}	$(x_2 - (5.1/4\pi^2)x_1^2) + (5/\pi)x_1 - 6)^2 + 10(1 - (1/8\pi))\cos x_1 + 10$	$[-5, 5]$	2	F	0.398
f_{18}	$[1 + (x_1 + x_2 + 1)^2 (19 - 14x_1 + 3x_1^2 - 14x_2 + 6x_1 x_2 + 3x_2^2)] \times [30 + (2x_1 - 3x_2)^2 \times (18 - 32x_1 + 12x_1^2 + 48x_2 - 36x_1 x_2 + 27x_2^2)]$	$[-2, 2]$	2	F	3
f_{19}	$-\sum_{i=1}^4 c_i \exp(-\sum_{j=1}^3 a_{ij} (x_j - p_{ij})^2)$	$[1, 3]$	3	F	-3.86
f_{20}	$-\sum_{i=1}^4 c_i \exp(-\sum_{j=1}^6 a_{ij} (x_j - p_{ij})^2)$	$[0, 1]$	6	F	-3.32
f_{21}	$-\sum_{i=1}^5 [(X - a_i)(X - a_i)^T + c_i]^{-1}$	$[0, 10]$	4	F	-10.1532
f_{22}	$-\sum_{i=1}^7 [(X - a_i)(X - a_i)^T + c_i]^{-1}$	$[0, 10]$	4	F	-10.4029
f_{23}	$-\sum_{i=1}^{10} [(X - a_i)(X - a_i)^T + c_i]^{-1}$	$[0, 10]$	4	F	-10.5363

m : dimension; C: category; U: unimodal; M: multimodal; F: fixed-dimension multimodal.

each benchmark test problem, the boundary of variables, the dimensions of the solution, and the category of each function are detailed. These test problems were divided into three categories: unimodal, multimodal, and fixed-dimension multimodal. In Table 1, $f_1 - f_7$ are unimodal problems that are used to benchmark the exploitation of algorithms because they have one global optimum and no local optima. Conversely, functions $f_8 - f_{23}$ are multimodal and fixed-dimension multimodal problems, which are helpful in examining exploration and local optima avoidance of algorithms, since they have a large number of local optima [26, 42].

The same control parameter settings for the GWO and DGWO algorithms are listed in Table 2, where “ m ” represents the dimension of the problem, “ N ” represents the size of the population, “MaxIter” represents the maximum number of iterations, “ w_1 ” and “ w_2 ” represent the position weight values, and “ R ” represents the independent simulation experiment times for each test problem. The proposed DGWO and standard GWO algorithms were coded in MATLAB R2015a. All simulation experiments were performed on a personal computer with Windows 10 64 bit professional OS and 4 GB RAM.

4.2. Impact of Position Weights w_1 and w_2 . As described in Section 3.2, the strategy of the modified position-updated equation (i.e., equation (26)) has an important role in balancing between exploration and exploitation in the evolution process. However, in equation (26), w_1 and w_2 are two crucial position weights for improving the optimization performance of the DGWO. In this section, to further investigate the impact of the position weight coefficients w_1 and w_2 , several independent experiments were designed and conducted. We varied the values of w_1 and w_2 and kept other algorithm’s parameters fixed for all benchmark functions. Values $w_1 = 0.1$, $w_2 = 0.9$, $w_1 = 0.3$, $w_2 = 0.7$, $w_1 = 0.5$, $w_2 = 0.5$, $w_1 = 0.7$, $w_2 = 0.3$, and $w_1 = 0.9$, $w_2 = 0.1$ are selected to conduct experiments using 23 test functions. Among these test functions, the dimension of 13 test problems ($f_1 - f_{13}$) is 30. All experimental results are reported in Table 3. “Mean” and “St. dev.” values are two performance evaluation indexes shown in Table 3.

As shown in Table 3, the comprehensive optimization performance of the DGWO algorithm with position weights $w_1 = 0.1$ and $w_2 = 0.9$ is superior to that of other algorithms. Compared with the DGWO with $w_1 = 0.1$ and $w_2 = 0.9$, the proposed DGWO algorithm with position weights $w_1 = 0.3$ and $w_2 = 0.7$ achieved better and similar results for 9 functions (i.e., $f_4 - f_8$, $f_{12} - f_{14}$, and f_{16}) and 3 functions (i.e., f_{11} , f_{17} , and f_{18}), respectively, and achieved worse results for 11 functions (i.e., $f_1 - f_3$, $f_9 - f_{10}$, f_{15} , and $f_{19} - f_{23}$). Compared with the DGWO with $w_1 = 0.1$ and $w_2 = 0.9$, the DGWO with $w_1 = 0.5$ and $w_2 = 0.5$ obtained better and similar results for 6 problems (i.e., $f_5 - f_7$, $f_{12} - f_{13}$, and f_{16}) and 3 problems (i.e., f_{11} , f_{14} , and f_{18}), respectively, and presented worse optimization results for 14 functions (i.e., $f_1 - f_4$, $f_8 - f_{10}$, f_{15} , f_{17} , and $f_{19} - f_{23}$). Compared with the DGWO with $w_1 = 0.1$ and $w_2 = 0.9$, the DGWO method with $w_1 = 0.7$ and $w_2 = 0.3$ attained better results for 6 functions (i.e., f_5 , $f_{12} - f_{14}$, f_{16} , and f_{20}), obtained

similar results for two functions (i.e., f_{11} and f_{18}), and obtained worse results for 15 functions (i.e., $f_1 - f_4$, $f_6 - f_{10}$, f_{15} , f_{17} , f_{19} , and $f_{21} - f_{23}$). Compared with the DGWO algorithm with $w_1 = 0.1$ and $w_2 = 0.9$, the DGWO with $w_1 = 0.9$ and $w_2 = 0.1$ achieved better optimization performance for 4 functions (f_5 , f_{14} , f_{16} , and f_{20}), achieved similar results for one function (i.e., f_{18}), and achieved worse results for the remaining functions. Based on this analysis, the optimization performance of the DGWO worsens as the position weight value w_1 increases and w_2 decreases. Therefore, considering all w_1 and w_2 values, we concluded that setting the position weight values $w_1 = 0.1$ and $w_2 = 0.9$ for the DGWO algorithm was an ideal choice, and the position weights w_1 and w_2 of the DGWO algorithm were set as 0.1 and 0.9, respectively, in the next experiments.

The convergence curves of the average objective function values of the DGWO with different position weight values w_1 and w_2 for 10 typical benchmark functions are plotted in Figure 3.

4.3. Effectiveness Analysis of the Two Components in DGWO.

In the DGWO algorithm, two main components, namely, the modified position-updated equation and the nonlinear control parameter strategy, are proposed. To validate the effectiveness of these two components in improving the optimization performance of the DGWO, two experiments were conducted for 23 benchmark functions recorded in Table 1. Among those functions, the dimension of $f_1 - f_{13}$ is 30. The algorithm parameters are set the same as in Table 2. In the first experiment, the DGWO employed the modified position-updated equation (i.e., equation (26)), and the linear control parameter \vec{a} that is similar to that in the study of Mirjalili et al. [22] is referred to as the DGWO-1. In the second experiment, the DGWO only used the nonlinear control parameter strategy (i.e., equation (27)), and the position-updated equation (8) is referred to as the DGWO-2. Two statistical criteria, “Mean” and “St. dev.,” and the results of the DGWO-1, DGWO-2, and DGWO are shown in Table 4. Sign-rank sum tests at 0.05 and 0.1 significance levels were performed between the DGWO and each of DGWO-1 and DGWO-2.

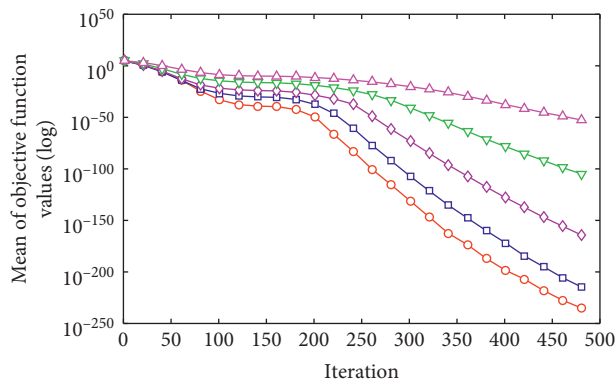
From Table 4, compared to the DGWO, the DGWO-1 achieved better results on 6 functions (i.e., f_4 , f_6 , f_8 , f_{16} , f_{21} , and f_{22}), showed similar or approximate performance on 3 test functions (i.e., f_9 , f_{10} , and f_{11}), and provided slightly poorer results on the rest of the test functions. It should be emphasized that the DGWO-1 could obtain very competitive optimization results compared to the DGWO, and its performance is not significantly inferior to that of the DGWO. We attribute the first experiment results to the fact that the modified position-updated equation has more advantages in balancing between exploration and exploitation and could ensure more potential solution diversity in the evolution process. Therefore, we can conclude that the performance differences between the DGWO and the DGWO-1 were not significant. From the results of the second experiment, it is found that the DGWO surpassed the DGWO-2 on 19 test functions and obtained similar results

TABLE 2: Experimental parameter settings for the GWO and DGWO.

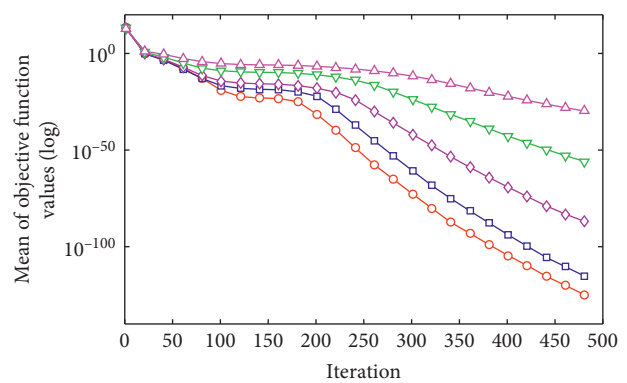
Algorithm	Parameter					
	m	N	MaxIter	w_1	w_2	R
GWO	10, 30, 50, 100	30	500	—	—	30
DGWO	10, 30, 50, 100	30	500	0.1	0.9	30

TABLE 3: Experimental results of the DGWO using different position weight values w_1 and w_2 for 23 functions.

Function	$w_1 = 0.1, w_2 = 0.9$		$w_1 = 0.3, w_2 = 0.7$		$w_1 = 0.5, w_2 = 0.1$		$w_1 = 0.7, w_2 = 0.3$		$w_1 = 0.9, w_2 = 0.1$	
	Mean	St. dev.	Mean	St. dev.	Mean	St. dev.	Mean	St. dev.	Mean	St. dev.
f_1	2.38E-241	0.00E+00	2.70E-220	0.00E+00	8.78E-173	0.00E+00	1.64E-109	8.92E+109	3.62E-56	1.53E-55
f_2	1.39E-127	7.05E-127	2.10E-118	1.06E-117	2.38E-90	1.25E-89	1.05E-58	4.64E-58	3.81E-32	1.29E-31
f_3	9.45E-232	0.00E+00	9.94E-217	0.00E+00	1.71E-168	0.00E+00	2.40E-107	5.95E-105	5.61E-35	2.93E-34
f_4	3.11E-88	1.70E-87	2.69E-89	1.43E-88	7.19E-71	2.55E-70	4.14E-42	1.10E-41	4.80E-04	1.43E-03
f_5	2.85E+01	1.28E-01	2.82E+01	1.63E-01	2.79E+01	2.71E-01	2.64E+01	5.05E-01	2.59E+01	3.03E-01
f_6	9.70E-06	4.71E-06	7.73E-06	3.38E-06	8.52E-06	2.51E-06	2.19E-05	7.35E-06	1.84E-04	5.37E-05
f_7	1.66E-04	1.40E-04	1.26E-04	8.78E-05	1.30E-04	1.03E-04	1.69E-04	1.11E-04	5.48E-04	2.99E-04
f_8	-1.06E+04	2.43E+03	-1.16E+04	1.85E+03	-8.34E+03	2.63E+03	-4.81E+03	9.26E+02	-3.51E+03	4.46E+02
f_9	0.00E+00	0.00E+00	2.78E+00	7.09E+00	2.05E+00	4.23E+00	3.18E+00	1.28E+00	5.22E+00	1.72E+01
f_{10}	8.88E-16	0.00E+00	3.02E-15	1.77E-15	4.44E-15	0.00E+00	4.68E-15	9.01E-16	8.94E-15	2.63E-15
f_{11}	0.00E+00	0.00E+00	0.00E+00	0.00E+00	0.00E+00	0.00E+00	0.00E+00	0.00E+00	2.35E-03	5.60E-03
f_{12}	1.79E-06	2.19E-06	5.43E-07	3.72E-07	6.73E-07	3.03E-07	1.48E-06	4.76E-07	1.22E-05	3.15E-06
f_{13}	2.49E-05	2.75E-05	7.63E-06	7.09E-06	9.13E-06	4.55E-06	2.18E-05	8.46E-06	1.58E-03	4.23E-03
f_{14}	2.94E+00	1.43E+00	2.55E+00	4.04E+00	2.94E+00	4.42E+00	2.17E+00	3.56E+00	2.64E+00	3.29E+00
f_{15}	3.56E-04	2.31E-04	4.70E-04	4.64E-04	5.18E-04	4.92E-04	1.79E-03	5.09E-03	1.24E-03	3.71E-03
f_{16}	-1.0302	5.17E-03	-1.0313	1.00E-03	-1.0316	9.56E-05	-1.0316	1.91E-05	-1.0316	3.03E-06
f_{17}	0.3980	2.11E-04	0.3980	6.02E-05	0.3979	7.36E-05	0.3979	3.39E-05	0.3979	1.16E-05
f_{18}	3	2.41E-04	3	1.07E-03	3	6.36E-04	3	2.71E-04	3	1.24E-04
f_{19}	-3.8590	5.87E-03	-3.8501	1.27E-02	-3.8533	8.33E-03	-3.8577	3.16E-03	-3.8612	1.09E-03
f_{20}	-3.1725	5.27E-02	-3.1402	7.59E-02	-3.1681	6.65E-02	-3.2156	7.58E-02	-3.2394	6.61E-02
f_{21}	-10.0984	1.56E-01	-9.7434	1.12E+00	-8.3562	2.40E+00	-8.9645	2.19E+00	-7.3721	2.90E+00
f_{22}	-10.2969	2.58E-01	-9.8997	1.00E+00	-9.5178	2.01E+00	-10.0489	1.34E+00	-9.7407	1.73E+00
f_{23}	-10.5307	2.94E-02	-10.3556	9.87E-01	-10.1956	1.30E+00	-10.1751	1.37E+00	-10.3090	1.01E+00
-		13		15		16		18		
+		9		6		6		5		
≈		1		2		1		0		

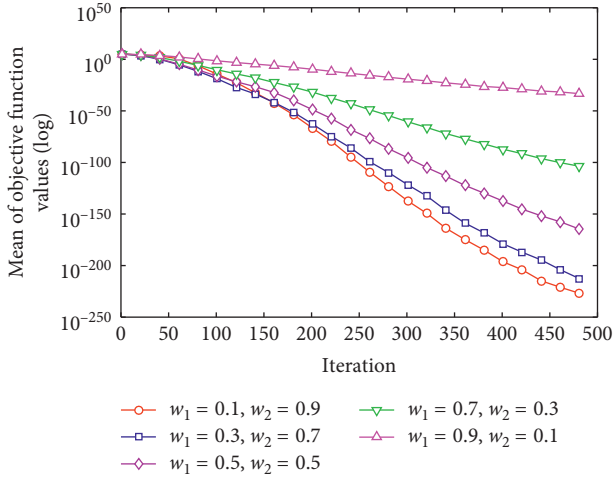


(a)

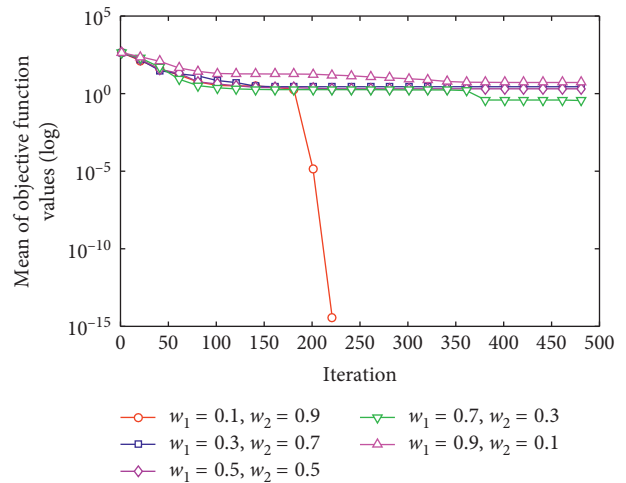


(b)

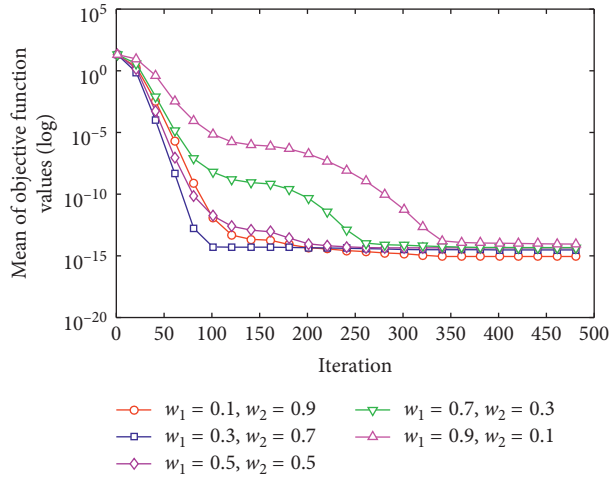
FIGURE 3: Continued.



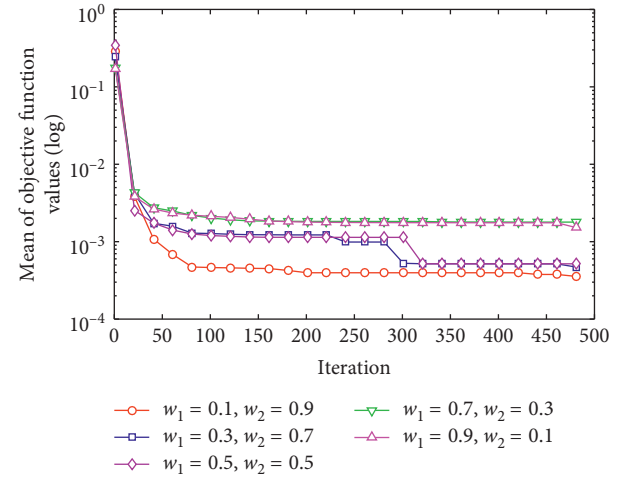
(c)



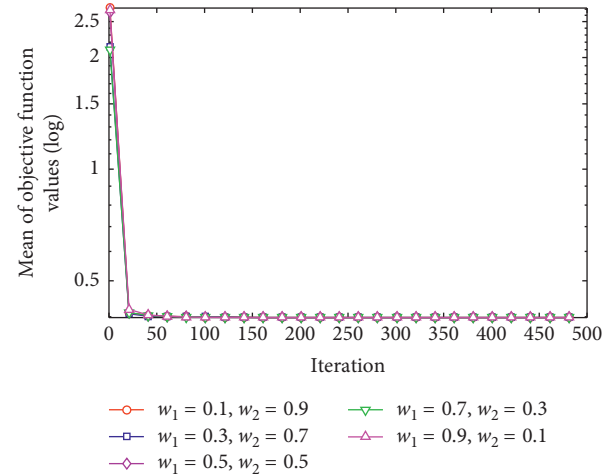
(d)



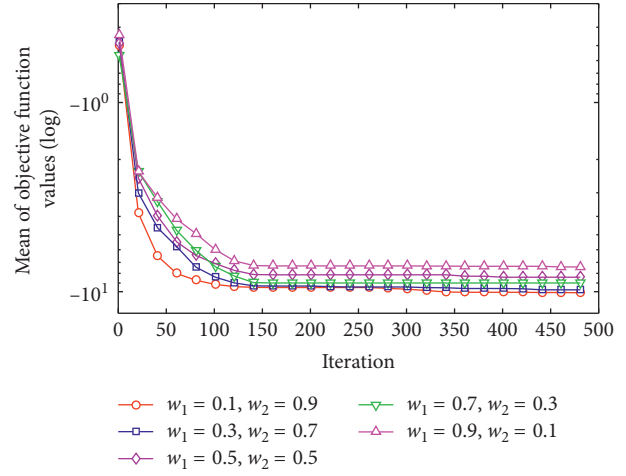
(e)



(f)



(g)



(h)

FIGURE 3: Continued.

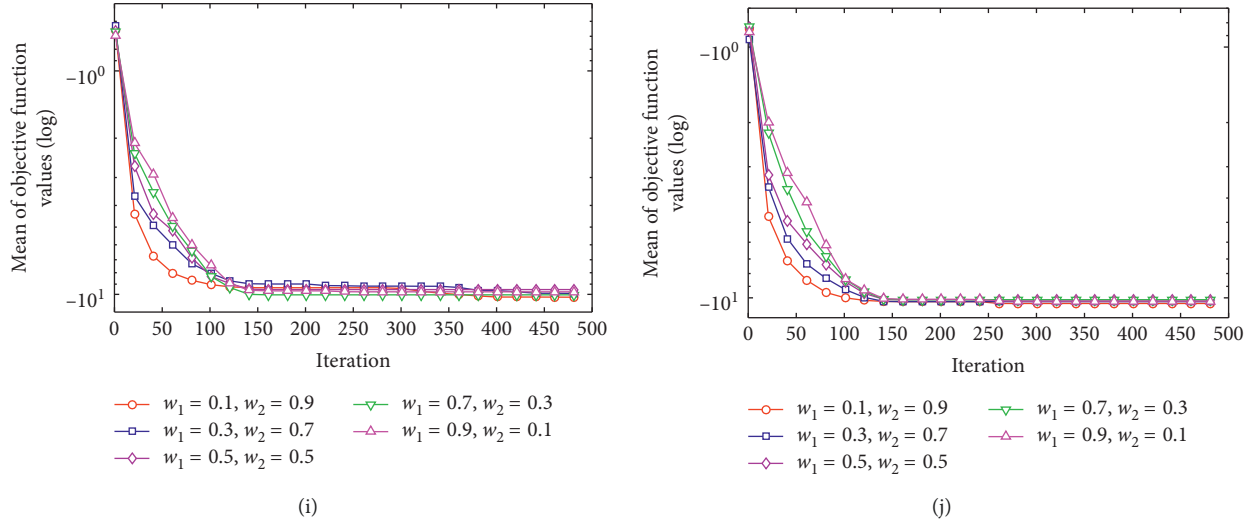


FIGURE 3: Convergence curves of the DGWO with different weights w_1 and w_2 on 10 typical test functions. (a) f_1 . (b) f_2 . (c) f_3 . (d) f_9 . (e) f_{10} . (f) f_{15} . (g) f_{17} . (h) f_{21} . (i) f_{22} . (j) f_{23} .

TABLE 4: Experimental comparison results of the DGWO, DGWO-1, and DGWO-2 on 23 functions ($m = 30$).

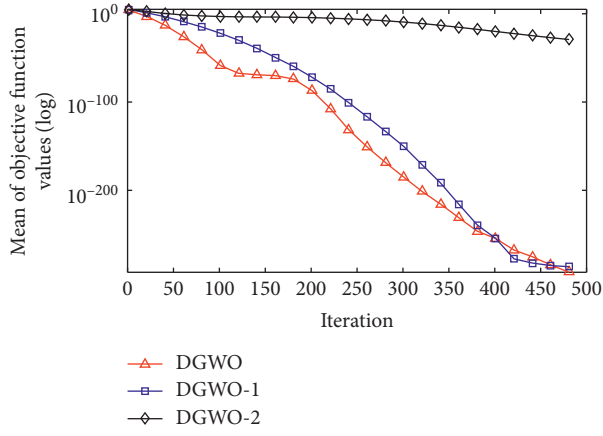
Function	DGWO-1 (Mean \pm St. dev.)	DGWO-2 (Mean \pm St. dev.)	DGWO (Mean \pm St. dev.)
f_1	$1.43E - 237 \pm 0.00E + 00$	$8.73E - 32 \pm 1.16E - 31$	$2.38E - 241 \pm 0.00E + 00$
f_2	$5.60E - 118 \pm 3.06E - 149$	$3.84E - 19 \pm 5.74E - 19$	$1.39E - 127 \pm 7.05E - 127$
f_3	$6.40E - 230 \pm 0.00E + 00$	$2.74E - 04 \pm 1.27E - 03$	$9.45E - 232 \pm 0.00E - 00$
f_4	$1.10E - 110 \pm 5.94E - 110$	$3.34E - 01 \pm 2.48E - 01$	$3.11E - 88 \pm 1.70E - 87$
f_5	$2.85E + 01 \pm 8.56E - 02$	$2.84E + 01 \pm 6.98E - 01$	$2.85E + 01 \pm 1.28E - 01$
f_6	$7.66E - 06 \pm 7.36E - 06$	$2.42E + 00 \pm 7.32E - 01$	$9.70E - 06 \pm 4.71E - 06$
f_7	$1.74E - 04 \pm 1.23E - 04$	$4.35E - 03 \pm 2.11E - 03$	$1.66E - 04 \pm 1.40E - 04$
f_8	$-1.22E + 04 \pm 1.08E + 03$	$-5.97E + 03 \pm 8.42E + 02$	$-1.06E + 04 \pm 2.43E + 03$
f_9	$0.00E + 00 \pm 0.00E + 00$	$2.48E + 01 \pm 1.24E + 01$	$0.00E + 00 \pm 0.00E + 00$
f_{10}	$8.88E - 16 \pm 0.00E + 00$	$1.15E - 14 \pm 3.73E - 15$	$8.88E - 16 \pm 0.00E + 00$
f_{11}	$0.00E + 00 \pm 0.00E + 00$	$7.43E - 03 \pm 1.11E - 02$	$0.00E + 00 \pm 0.00E + 00$
f_{12}	$3.82E - 06 \pm 4.75E - 06$	$2.27E - 01 \pm 1.85E - 01$	$1.79E - 06 \pm 2.19E - 06$
f_{13}	$5.47E - 05 \pm 5.82E - 05$	$1.60E + 00 \pm 4.21E - 01$	$2.49E - 05 \pm 2.75E - 05$
f_{14}	$4.89E + 00 \pm 5.60E + 00$	$6.69E + 00 \pm 5.01E + 00$	$2.94E + 00 \pm 4.43E + 00$
f_{15}	$3.76E - 04 \pm 3.04E - 04$	$5.11E - 03 \pm 8.56E - 03$	$3.56E - 04 \pm 2.31E - 04$
f_{16}	$-1.0316 \pm 1.77E - 05$	$-1.0316 \pm 2.83E - 08$	$-1.0303 \pm 5.17E - 03$
f_{17}	$0.3987 \pm 1.00E - 03$	$0.3979 \pm 6.65E - 07$	$0.3980 \pm 2.11E - 04$
f_{18}	$3.0007 \pm 1.22E - 03$	$3.0001 \pm 8.14E - 05$	$3.0001 \pm 2.41E - 04$
f_{19}	$-3.8566 \pm 5.02E - 03$	$-3.8617 \pm 1.71E - 03$	$-3.8590 \pm 5.87E - 03$
f_{20}	$-3.12163 \pm 6.50E - 02$	$-3.2543 \pm 8.34E - 02$	$-3.1725 \pm 5.27E - 02$
f_{21}	$-10.1433 \pm 1.22E - 02$	$-8.1941 \pm 2.93E + 00$	$-10.0984 \pm 1.56E - 01$
f_{22}	$-10.3958 \pm 6.49E - 03$	$-9.8783 \pm 1.73E + 00$	$-10.2969 \pm 2.58E - 01$
f_{23}	$-10.5221 \pm 2.25E - 02$	$-10.0848 \pm 1.75E + 00$	$-10.5334 \pm 2.94E - 02$
Losses (-)	14	19	
Wins (+)	6	3	
Approximations (\approx)	3	1	
Detected differences (α)	—	0.05	

on function f_{18} . To better understand this phenomenon, we need to know that the nonlinear control parameter strategy was specifically designed for the modified position-updated equation and is not suitable for independent use in the search process. Thus, the performance of the DGWO significantly outperformed that of the DGWO-2.

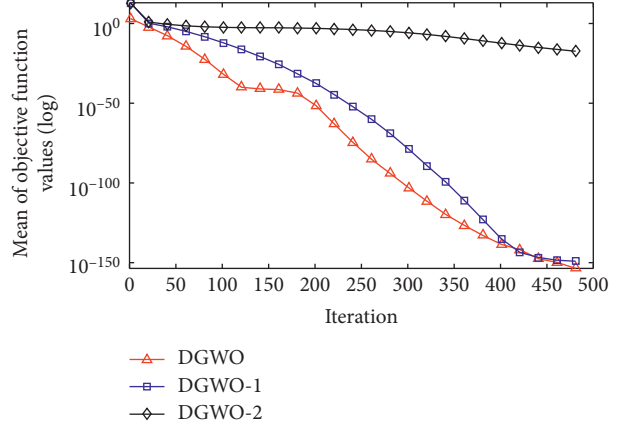
The convergence curves of the average objective function values of the DGWO, DGWO-1, and DGWO-2 on 10 typical

test functions are plotted in Figure 4. From Table 4 and Figure 4, we can conclude that the two components of the DGWO are able to compensate for each other to improve the optimization performance of the GWO.

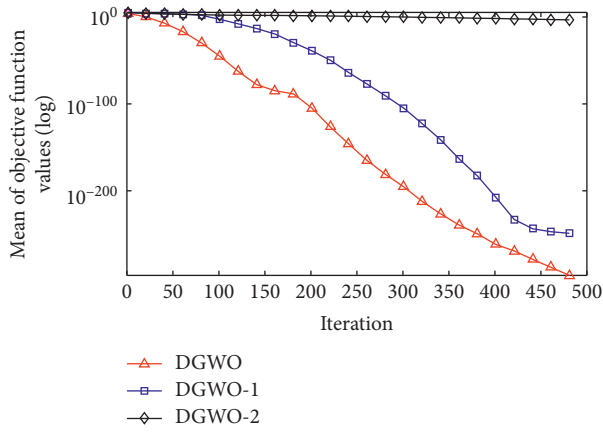
4.4. Performance Comparison with the Standard GWO Algorithm. We independently tested each problem 30 times



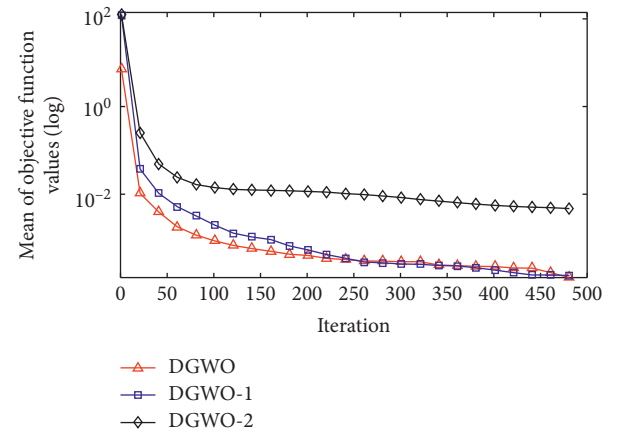
(a)



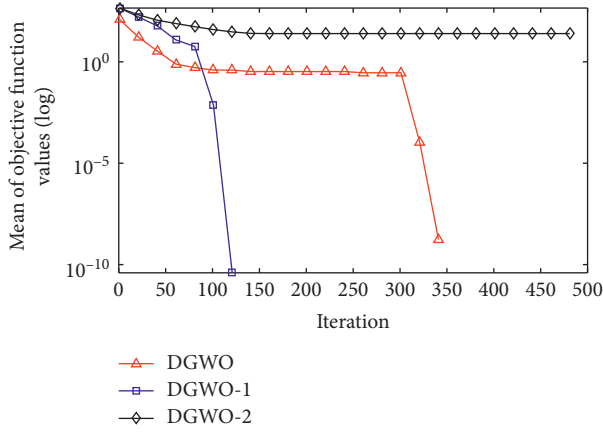
(b)



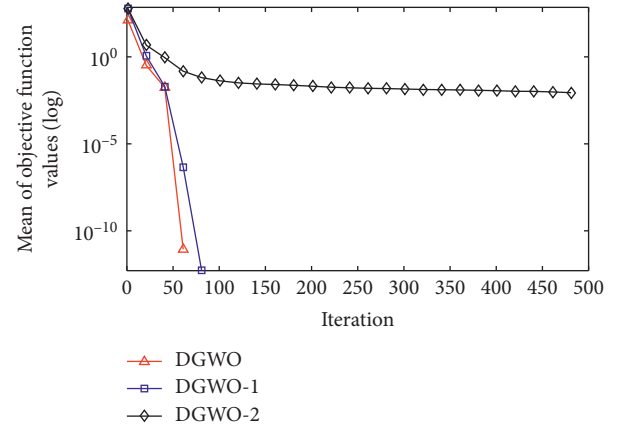
(c)



(d)



(e)



(f)

FIGURE 4: Continued.

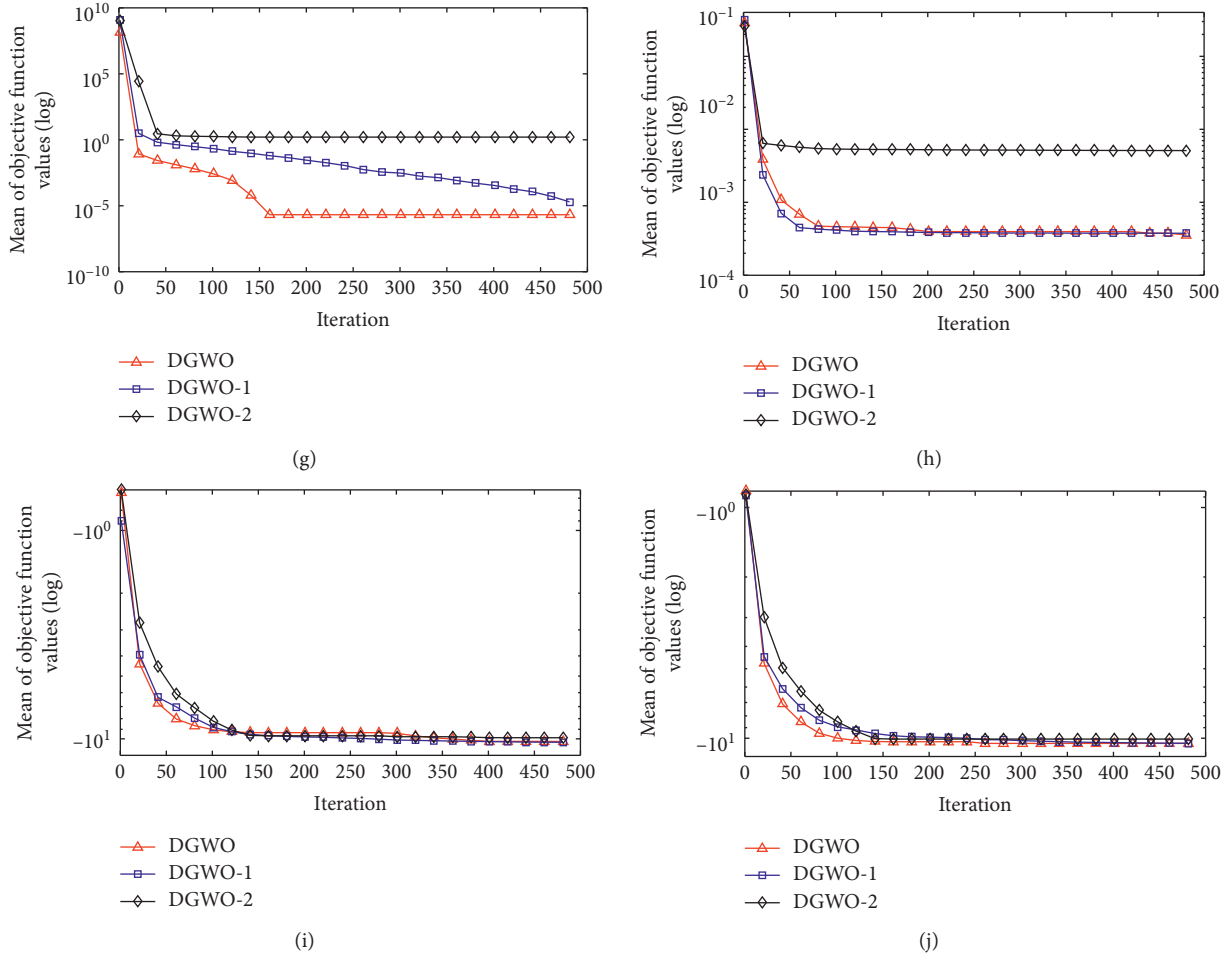


FIGURE 4: Convergence curves of the DGWO, DGWO-1, and DGWO-2 on ten typical test functions. (a) f_1 . (b) f_2 . (c) f_3 . (d) f_7 . (e) f_9 . (f) f_{11} . (g) f_{13} . (h) f_{15} . (i) f_{22} . (j) f_{23} .

to obtain four statistical criteria for comparing the performance of the algorithms; that is, “Best” indicates the best value, “Worst” represents the worst value, “Mean” denotes the average best values, and “St. dev.” indicates the standard deviation value. The simulation experimental results are described in Table 5.

As shown in Table 5, the DGWO has a better optimization performance for the seven unimodal benchmarks, with the exception of f_5 and compared with the standard versions of the GWO, since the DGWO provides the best “Best,” “Worst,” “Mean,” and “St. dev.” values for 6 of 7 unimodal benchmarks. For the six multimodal benchmarks (f_8 – f_{13}) in Table 5, none of the standard versions of the GWO has a better optimization performance than the DGWO algorithm for all test problems using the “Mean” statistical criterion. As observed in Table 5, the DGWO algorithm achieved a better performance than the GWO for 5 fixed-dimension multimodal test functions (i.e., f_{14} , f_{20} – f_{23}) and provided slightly better results than the GWO for functions f_{16} , f_{18} , and f_{19} . For function f_{16} , however, the GWO obtained better results than the DGWO.

The percentage of problems solved by the GWO and DGWO is recorded in Table 6. It should be noted that

when we use a certain algorithm to solve the 13 test functions (i.e., f_1 – f_{13}) and 10 test functions (i.e., f_{14} – f_{23}) listed in Table 1, if the error between the actual value and its theoretical value is 10^{-5} and 10^{-3} , respectively, then this problem can be regarded as having been successfully solved. From Table 6, it can be seen that, for functions f_1 , f_2 , f_{10} , f_{16} , f_{18} , and f_{23} , the DGWO and GWO obtained the same percentage of solving problems. On 13 test problems (i.e., f_3 , f_4 , f_6 – f_9 , f_{11} – f_{15} , and f_{21} – f_{22}), the DGWO has shown a higher percentage than the GWO. However, the GWO has shown a higher percentage than the DGWO for functions f_{17} , f_{19} , and f_{20} .

To obtain an intuitive cognition of the convergence rate of the DGWO and GWO algorithms, Figure 5 shows the convergence curves of the DGWO and GWO for 12 typical test functions with $m = 10, 30, 50,$ and 100 . As shown in Figure 5, the DGWO algorithm achieved a faster convergence than the standard GWO algorithm for all 12 test problems. This finding verifies that the position-updated strategy and the nonlinear control parameter proposed in this paper can achieve faster search and excellent optimization performance of the DGWO algorithm for low- and high-dimensional problems.

TABLE 5: Results obtained by the DGWO and GWO algorithms on 23 test problems.

Key	m	GWO				DGWO			
		Best	Worst	Mean	St. dev.	Best	Worst	Mean	St. dev.
f_1	10	7.89E-61	5.72E-55	3.02E-56	1.07E-55	0.00E-00	7.08E-298	2.36E-299	0.00E-00
	30	1.48E-29	4.31E-27	8.83E-28	1.09E-27	1.63E-287	5.44E-240	2.38E-241	0.00E-00
	50	4.89E-21	1.30E-19	4.62E-20	3.83E-20	2.18E-244	1.88E-203	6.27E-205	0.00E-00
	100	1.97E-13	2.88E-12	1.05E-12	6.38E-13	1.43E-183	1.01E-163	8.19E-169	0.00E-00
f_2	10	7.44E-35	2.11E-32	3.62E-33	4.99E-33	7.09E-190	4.34E-154	1.45E-155	7.92E-155
	30	2.82E-17	2.79E-16	1.22E-16	6.95E-17	3.74E-148	3.86E-126	1.39E-127	7.05E-127
	50	8.15E-13	5.92E-12	2.64E-12	1.31E-12	4.61E-132	5.38E-109	1.80E-110	9.81E-110
	100	1.37E-08	1.43E-07	4.59E-08	2.38E-08	1.26E-102	1.84E-63	1.62E-84	8.48E-84
f_3	10	1.07E-29	9.17E-24	5.56E-25	1.78E-24	0.00E-00	9.71E-299	3.24E-300	0.00E-00
	30	5.46E-11	3.20E-04	2.06E-05	5.95E-05	1.67E-260	2.83E-230	9.45E-232	0.00E-00
	50	2.20E-03	1.69E+00	2.68E-01	3.45E-01	2.45E-209	1.65E-169	6.52E-171	0.00E-00
	100	4.99E+01	1.80E+03	5.60E+02	5.34E+02	7.91E-144	3.02E-18	1.01E-19	5.52E-19
f_4	10	6.43E-20	2.03E-17	2.64E-18	4.31E-18	1.06E-150	3.41E-129	1.25E-130	6.22E-130
	30	9.39E-08	3.48E-06	7.97E-07	7.84E-07	1.30E-106	9.33E-87	3.11E-88	1.70E-87
	50	4.84E-05	1.55E-03	3.28E-04	3.51E-04	9.12E-88	1.21E-76	8.25E-78	2.36E-77
	100	9.62E-02	1.25E+00	5.42E-01	3.25E-01	1.08E-65	9.02E-42	3.01E-43	1.65E-42
f_5	10	5.33E+00	8.04E+00	6.61E+00	5.88E-01	4.09E-01	8.39E+00	3.10E+00	2.31E+00
	30	2.55E+01	2.87E+01	2.69E+01	7.47E+01	2.82E+01	2.87E+01	2.85E+01	1.28E-01
	50	4.59E+01	4.87E-01	4.74E+01	8.18E-01	4.83E+01	4.85E+01	4.84E+01	7.31E-02
	100	9.61E+01	9.85E+01	9.77E+01	7.81E-01	9.80E+01	9.80E+01	9.80E+01	9.99E-03
f_6	10	9.48E-07	2.53E-01	2.47E-02	7.55E-02	2.96E-08	4.66E-06	5.84E-07	8.37E-07
	30	2.50E-01	2.00E+00	7.73E-01	3.91E-01	1.48E-06	1.73E-05	9.70E-06	4.71E-06
	50	1.25E+00	3.70E+00	2.58E+00	6.23E+00	9.62E-06	2.05E-04	5.16E-05	4.87E-05
	100	8.21E+00	1.19E-01	1.01E+01	8.45E-01	8.52E-05	1.12E-03	3.28E-04	2.40E-04
f_7	10	9.10E-05	2.14E-03	7.23E-04	5.93E-04	1.14E-05	3.40E-04	1.24E-04	9.64E-05
	30	8.25E-04	3.97E-03	1.98E-03	9.59E-04	2.88E-05	6.20E-04	1.66E-04	1.40E-04
	50	1.13E-04	8.73E-03	3.17E-03	1.58E-03	8.94E-06	9.17E-04	2.31E-04	2.28E-04
	100	3.02E-03	2.18E-02	8.20E-03	4.02E-03	2.51E-06	1.93E-03	2.62E-04	3.68E-04
f_8	10	-3.38E+03	-2.05E+03	-2.64E+03	3.12E+02	-4.19E+03	-2.33E+03	-3.85E+03	5.85E+02
	30	-7.81E+03	-3.32E+03	-6.02E+03	9.48E+02	-1.26E+04	-5.66E+03	-1.05E+03	2.43E+03
	50	-1.08E+04	-4.16E+03	-9.23E+04	1.22E+03	-2.10E+04	-8.76E+03	-1.59E+04	3.94E+03
	100	-1.99E+04	-5.36E+03	-1.57E+04	3.05E+03	-4.19E+04	-1.56E+04	-2.28E+04	5.58E+03
f_9	10	0.00E-00	7.13E+00	9.06E-01	1.98E+00	0.00E-00	0.00E-00	0.00E-00	0.00E-00
	30	5.68E-14	9.58E+00	2.91E+00	3.16E+00	0.00E-00	0.00E-00	0.00E-00	0.00E-00
	50	1.14E-13	2.86E+01	5.00E+00	5.99E+00	0.00E-00	0.00E-00	0.00E-00	0.00E-00
	100	2.80E-07	3.73E+00	1.12E+00	7.67E+00	0.00E-00	0.00E-00	0.00E-00	0.00E-00
f_{10}	10	4.44E-15	7.99E-15	7.52E-15	1.23E-15	8.88E-16	8.88E-16	8.88E-16	0.00E-00
	30	6.84E-14	1.47E-13	1.07E-13	1.45E-14	8.88E-16	8.88E-16	8.88E-16	0.00E-00
	50	1.44E-11	1.12E-10	3.98E-11	2.59E-11	8.88E-16	8.88E-16	8.88E-16	0.00E-00
	100	4.91E-08	1.96E-07	1.10E-07	4.08E-08	8.88E-16	8.88E-16	8.88E-16	0.00E-00
f_{11}	10	0.00E-00	9.22E-02	1.96E-02	2.00E-02	0.00E-00	0.00E-00	0.00E-00	0.00E-00
	30	0.00E-00	5.14E-02	5.48E-03	1.13E-02	0.00E-00	0.00E-00	0.00E-00	0.00E-00
	50	0.00E-00	3.17E-02	2.59E-03	7.27E-03	0.00E-00	0.00E-00	0.00E-00	0.00E-00
	100	1.34E-13	3.69E-02	7.97E-03	1.27E-02	0.00E-00	0.00E-00	0.00E-00	0.00E-00
f_{12}	10	3.25E-07	2.03E-02	4.91E-03	8.54E-03	1.38E-08	1.58E-06	3.09E-07	3.33E-07
	30	1.96E-02	1.05E-01	4.80E-02	2.31E-02	1.34E-07	8.29E-06	1.79E-06	2.19E-06
	50	4.83E-02	3.93E-01	1.14E-01	6.21E-02	4.71E-07	1.72E-05	3.12E-06	3.31E-06
	100	1.87E-01	4.65E-01	2.93E-01	6.46E-02	4.04E-06	7.82E-05	1.61E-05	1.43E-05
f_{13}	10	2.99E-06	1.01E-01	9.94E-03	3.03E-02	3.31E-08	9.79E-06	2.09E-06	2.46E-06
	30	2.93E-01	1.20E+00	6.78E-01	2.39E-01	5.30E-07	1.09E-04	2.49E-05	2.75E-05
	50	1.34E+00	2.93E+00	2.15E+00	4.24E-01	1.75E-05	4.30E-04	1.12E-04	8.81E-05
	100	6.01E+00	8.03E+00	6.89E+00	4.38E-01	1.86E-04	2.34E-03	9.13E-04	5.72E-04
f_{14}	2	0.9980	1.08E+01	3.2259	3.15E+00	0.9980	1.27E+00	2.9434	4.43E+00
f_{15}	4	0.0003	2.04E-02	0.0090	1.01E-02	0.0003	1.58E-03	0.0003	2.31E-04
f_{16}	2	-1.0316	-1.0316	-1.0316	2.50E-08	-1.0316	-1.0096	-1.0303	5.17E-03
f_{17}	2	0.3979	0.3979	0.3979	1.22E-06	0.3979	0.3990	0.3980	2.11E-04
f_{18}	2	3.0000	3.0001	3.0000	2.58E-05	3.0000	3.0013	3.0001	2.41E-04
f_{19}	3	-3.8628	-3.8549	-3.8613	2.74E-03	-3.8626	-3.8360	-3.8590	5.87E-03
f_{20}	6	-3.3220	-2.8404	-3.2626	1.06E-01	-3.2959	-3.1034	-3.1725	5.27E-02

TABLE 5: Continued.

Key	m	GWO				DGWO			
		Best	Worst	Mean	St. dev.	Best	Worst	Mean	St. dev.
f_{21}	4	-10.1530	-5.0552	-9.4765	1.7505	-10.1532	-9.5340	-10.0984	1.56E-01
f_{22}	4	-10.4027	-5.0877	-10.2240	9.70E-01	-10.4028	-9.4206	-10.2969	2.58E-01
f_{23}	4	-10.5360	-2.4217	-10.2642	1.4812	-10.5364	-10.3753	-10.5334	2.94E-02

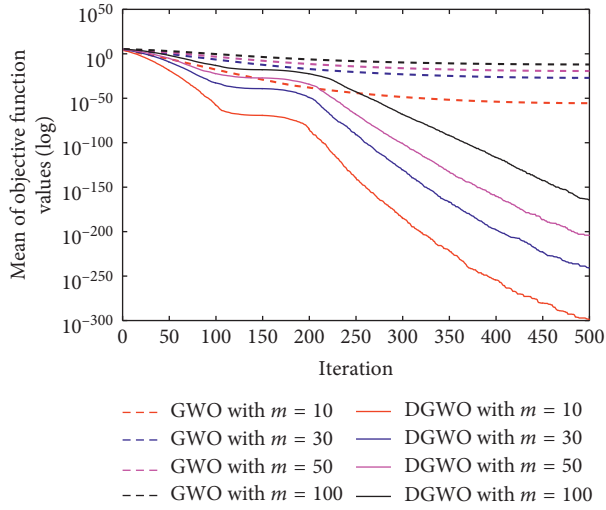
TABLE 6: Percentage of problems solved by the GWO and DGWO.

Function	GWO (%)				DGWO (%)			
	Dimension				Dimension			
	10	30	50	100	10	30	50	100
f_1	100	100	100	100	100	100	100	100
f_2	100	100	100	100	100	100	100	100
f_3	100	96	0	0	100	100	100	100
f_4	100	100	23	0	100	100	100	100
f_5	0	0	0	0	0	0	0	0
f_6	80	0	0	0	100	100	80	6
f_7	3	0	0	0	50	46	26	33
f_8	0	0	0	0	73	46	36	3
f_9	60	36	33	9	100	100	100	100
f_{10}	100	100	100	100	100	100	100	100
f_{11}	26	73	86	70	100	100	100	100
f_{12}	73	0	0	0	100	100	100	100
f_{13}	90	0	0	0	100	96	50	0
f_{14}	40				83			
f_{15}	43				96			
f_{16}	100				100			
f_{17}	100				96			
f_{18}	100				100			
f_{19}	100				90			
f_{20}	66				0			
f_{21}	0				66			
f_{22}	53				80			
f_{23}	96				96			

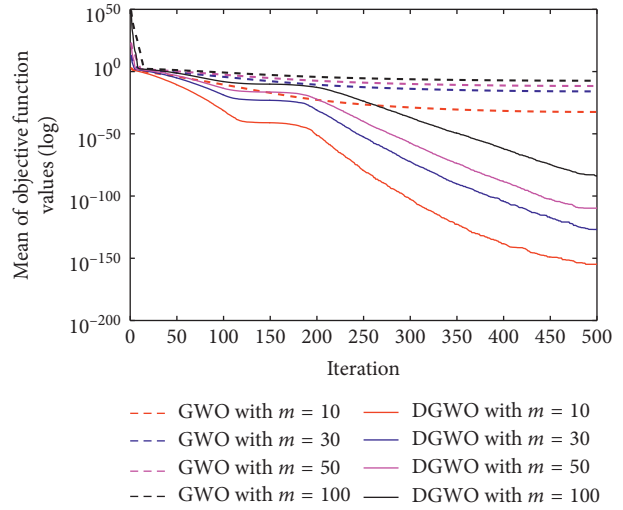
4.5. *Performance Comparison with the Modified GWO Algorithm.* To further compare the optimization performance of the proposed DGWO algorithm with that of other improved GWO variants, i.e., the modified grey wolf optimizer (mGWO) algorithm [26], the grey wolf optimizer, which is based on the Powell local optimization (PGWO) method [45], and the exploration-enhanced grey wolf optimizer (EEGWO) algorithm [42], the parameters of the mGWO, PGWO, and EEGWO algorithms were established as follows: their population size was set to 30, and the maximum number of iterations was 500. The 23 benchmark test functions were selected from Table 1. The dimensions for 13 test functions (f_1 - f_{13}) were set to 10, 30, 50, and 100. Each algorithm was independently run 30 times using each test function for their corresponding dimension. The mean (denoted by “Mean”) and standard deviation (denoted by “St. dev.”) of the fitness value are the two statistical criteria used to evaluate the performance of the algorithm. The simulation results of these four algorithms are recorded in Table 7.

As shown in Table 7, the DGWO obtained the best “Mean” and “St. dev.” for functions $f_1, f_2, f_3, f_8,$ and f_{13} with

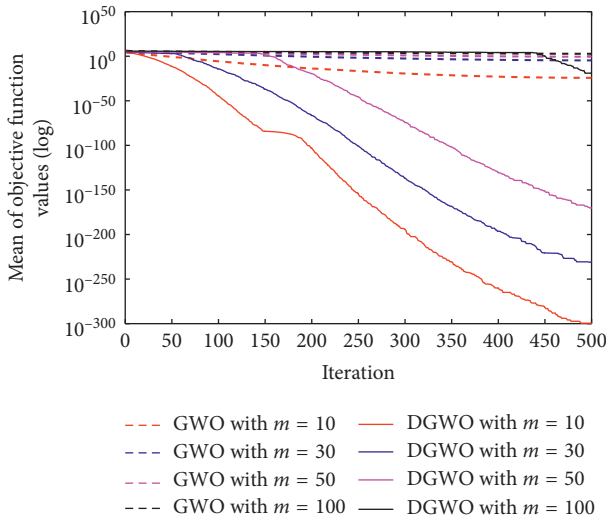
low dimensions ($m=10$ and 30) and high dimensions ($m=50$ and 100) compared with the mGWO, PGWO, and EEGWO. For the test problems f_4 and f_7 with $m=30, 50,$ and 100 , the EEGWO achieved the best results among the four modified GWO algorithms, and the DGWO achieved slightly worse results than the EEGWO but better results than the mGWO and PGWO. For functions $f_9, f_{10},$ and f_{11} , the DGWO and EEGWO achieved the same results and are better than the mGWO and PGWO; note that the DGWO and EEGWO can obtain theoretical optima (0) for functions f_9 and f_{11} . The PGWO obtained the best results on test problems $f_5, f_6,$ and f_{12} with all dimensions ($m=10, 30, 50,$ and 100) and attained the global theoretical optima (0) on problem f_6 . However, the DGWO obtained the second best results for functions $f_5, f_6,$ and f_{12} , which are similar to the results of the PGWO. For functions f_{14} to f_{23} with a fixed number of dimensions, the DGWO achieved the best results for 7 test functions ($f_{14}, f_{15}, f_{17}, f_{19},$ and f_{21} - f_{23}). Compared to the mGWO, the PGWO attained almost the same results for functions f_{16} and f_{20} , which are better than those of the DGWO and EEGWO. On test function f_{18} , the mGWO and PGWO obtained the best fitness values. In addition, the



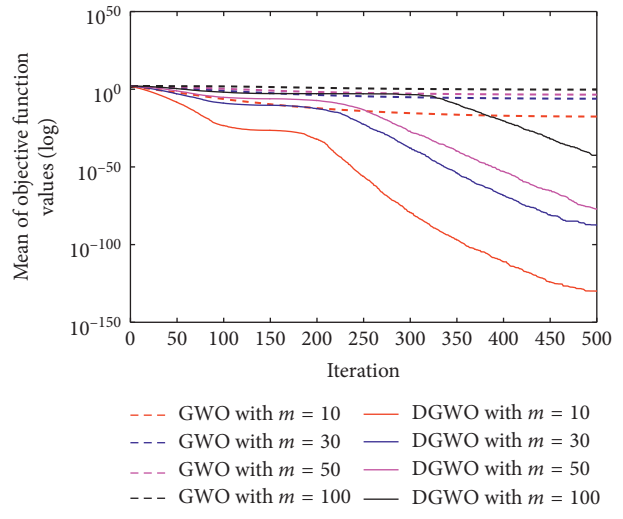
(a)



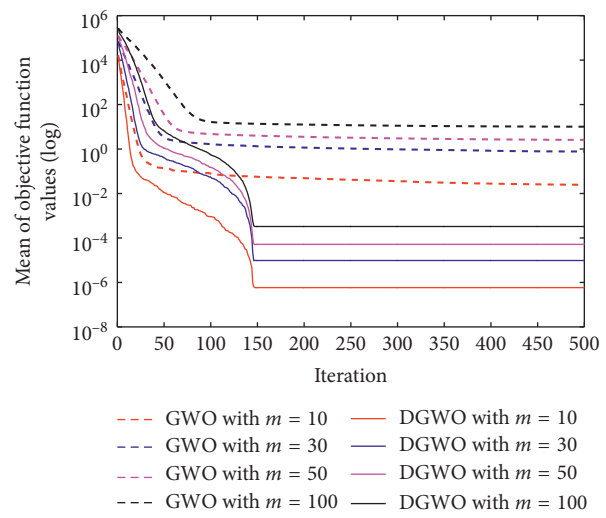
(b)



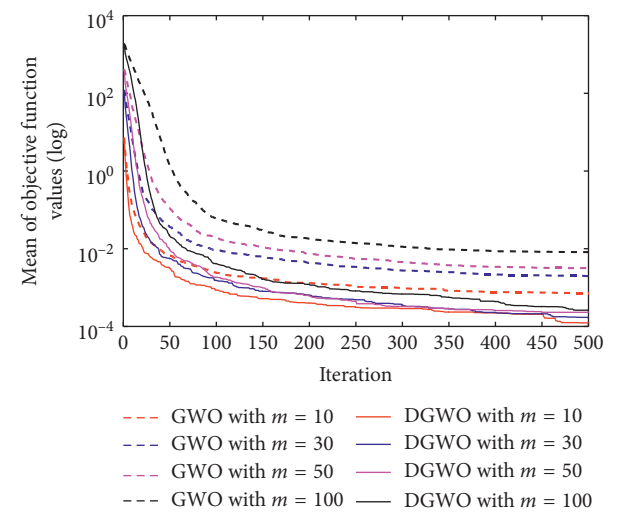
(c)



(d)

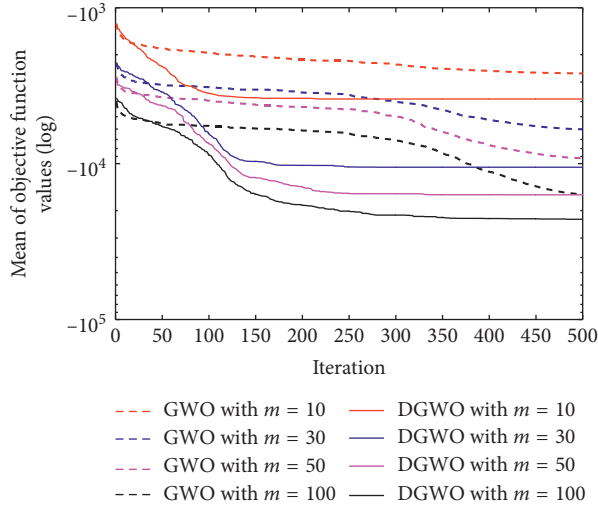


(e)

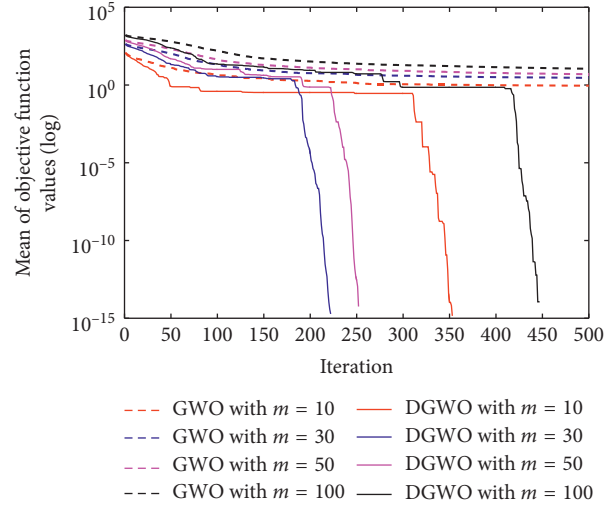


(f)

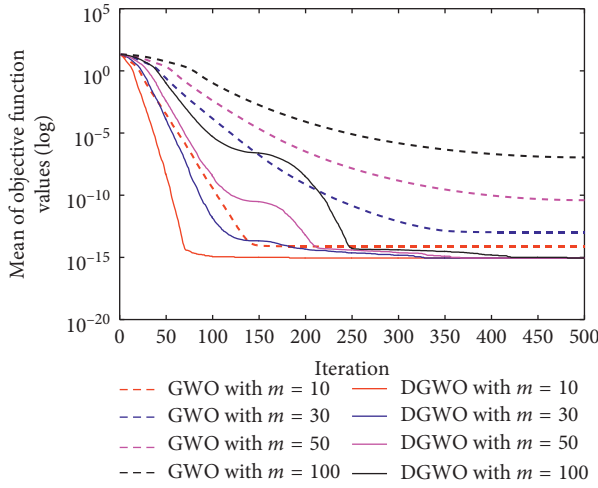
FIGURE 5: Continued.



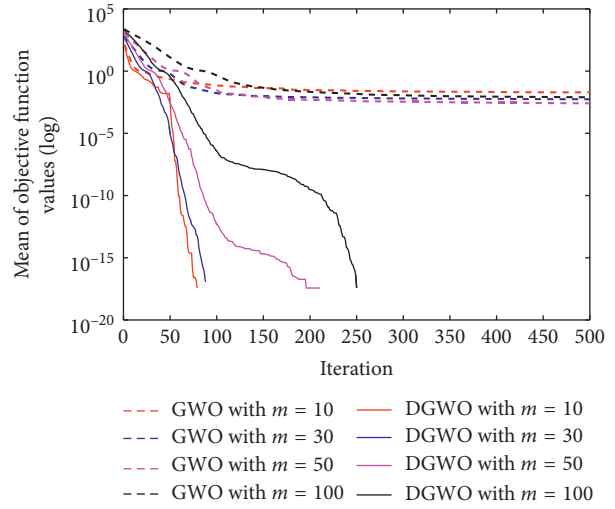
(g)



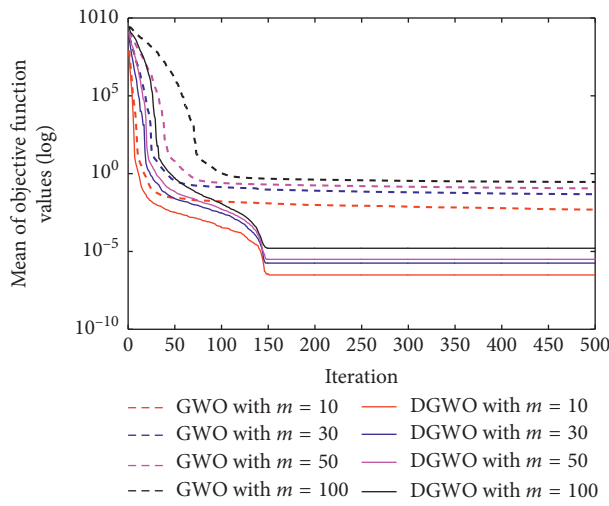
(h)



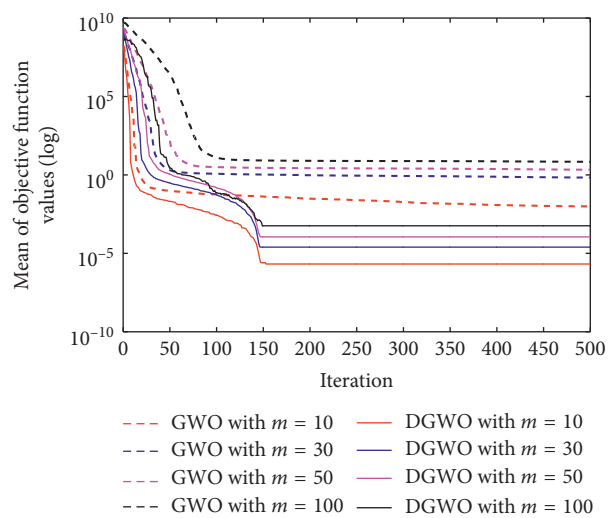
(i)



(j)



(k)



(l)

FIGURE 5: Convergence curves of the GWO and DGWO with $m = 10, 30, 50,$ and 100 on 12 typical test functions. (a) f_1 . (b) f_2 . (c) f_3 . (d) f_4 . (e) f_6 . (f) f_7 . (g) f_8 . (h) f_9 . (i) f_{10} . (j) f_{11} . (k) f_{12} . (l) f_{13} .

TABLE 7: Results obtained by the three GWO variants and DGWO on 23 test problems.

Function	m	mGWO		PGWO		EEGWO		DGWO	
		Mean	St. dev.	Mean	St. dev.	Mean	St. dev.	Mean	St. dev.
f_1	10	1.39E-74	6.61E-74	1.65E-75	3.98E-75	1.81E-245	0.00E-00	2.36E-299	0.00E-00
	30	3.90E-36	8.61E-36	1.01E-53	1.14E-53	3.23E-201	0.00E-00	2.38E-241	0.00E-00
	50	8.64E-26	9.26E-26	1.77E-48	1.78E-48	5.31E-192	0.00E-00	6.27E-205	0.00E-00
	100	2.40E-16	1.40E-16	5.99E-44	4.77E-44	2.87E-182	0.00E-00	8.19E-169	0.00E-00
f_2	10	3.49E-43	7.29E-43	6.20E-41	1.83E-40	1.51E-123	5.46E-123	1.45E-155	7.92E-155
	30	8.16E-22	4.82E-22	2.69E-28	1.53E-28	2.74E-102	2.95E-102	1.39E-127	7.05E-127
	50	6.72E-16	5.42E-16	3.26E-25	7.98E-26	6.15E-97	9.14E-97	1.80E-110	9.81E-110
	100	2.12E-10	9.47E-11	2.09E-22	6.37E-23	7.23E-92	9.38E-92	1.62E-84	8.48E-84
f_3	10	9.97E-33	2.68E-32	1.41E-40	3.29E-40	1.68E-244	0.00E-00	3.24E-300	0.00E-00
	30	1.82E-06	7.68E-06	5.16E-18	2.34E-17	1.62E-201	0.00E-00	9.45E-232	0.00E-00
	50	8.38E-02	2.12E-01	1.04E-08	2.32E-08	1.25E-190	0.00E-00	6.52E-171	0.00E-00
	100	1.16E+03	1.90E+03	1.37E-01	1.32E-01	4.18E-180	0.00E-00	1.01E-19	5.52E-19
f_4	10	1.59E-25	4.70E-25	1.24E-28	3.35E-28	3.31E-123	1.29E-122	1.25E-130	6.22E-130
	30	1.44E-09	2.07E-09	3.11E-21	2.06E-21	3.39E-102	5.25E-102	3.11E-88	1.70E-87
	50	9.12E-06	1.06E-05	6.59E-02	3.61E-01	4.73E-97	8.96E-97	8.25E-78	2.36E-77
	100	1.11E-00	1.00E-00	2.21E+01	1.40E+01	2.96E-92	2.25E-92	3.01E-43	1.65E-42
f_5	10	6.63E-00	6.38E-01	4.62E-01	1.39E-00	8.91E-00	5.51E-02	3.09E-00	2.31E-00
	30	2.68E+01	7.19E-01	1.18E-01	2.73E-00	2.89E+01	2.35E-02	2.85E-01	1.28E-01
	50	4.72E+01	6.63E-01	2.96E+01	7.25E-00	4.89E+01	1.66E-02	4.84E+01	7.32E-02
	100	9.79E+01	4.48E-01	8.67E+01	2.19E+01	9.89E+01	1.79E-02	9.80E+01	9.99E-03
f_6	10	5.57E-06	2.37E-06	0.00E-00	0.00E-00	1.31E-00	2.45E-01	5.84E-07	8.37E-07
	30	5.97E-01	2.94E-01	0.00E-00	0.00E-00	6.11E-00	3.04E-01	9.70E-06	4.71E-06
	50	2.57E-00	6.05E-01	0.00E-00	0.00E-00	1.07E+01	6.03E-01	5.16E-05	4.87E-05
	100	9.53E-00	1.05E-00	0.00E-00	0.00E-00	2.31E+01	5.84E-01	3.28E-04	2.40E-05
f_7	10	4.48E-04	3.02E-04	7.13E-04	5.41E-04	6.13E-05	4.72E-05	1.24E-04	9.64E-05
	30	1.31E-03	7.25E-04	2.05E-03	9.42E-04	7.70E-05	7.05E-05	1.66E-04	1.40E-04
	50	2.19E-03	1.13E-03	3.59E-03	1.68E-03	5.67E-05	6.06E-05	2.31E-04	2.28E-04
	100	4.75E-03	1.88E-03	6.93E-03	2.34E-03	7.88E-05	5.60E-05	2.62E-04	3.68E-04
f_8	10	-2.60E+03	3.16E+02	-2.92E+03	3.05E+02	-1.18E+03	2.35E+02	-3.85E+03	5.86E+02
	30	-5.51+03E	1.47E+03	-7.79E+03	8.40E+02	-2.11E+03	4.82E+02	-1.06E+03	2.43E+03
	50	-8.51E+03	1.47E+03	-1.28E+04	1.38E+03	-2.85E+03	5.25E+02	-1.59E+04	3.94E+03
	100	-1.57E+04	2.45E+03	-2.49E+04	1.74E+03	-4.13E+03	9.09E+02	-2.28E+04	5.58E+03
f_9	10	9.06E-01	3.49E-00	1.00E+01	8.23E-00	0.00E-00	0.00E-00	0.00E-00	0.00E-00
	30	7.58E-15	2.47E-14	1.71E+02	4.31E+01	0.00E-00	0.00E-00	0.00E-00	0.00E-00
	50	3.40E-02	1.86E-01	3.26E+02	5.89E+01	0.00E-00	0.00E-00	0.00E-00	0.00E-00
	100	5.35E-01	1.71E-00	6.95E+02	9.52E+01	0.00E-00	0.00E-00	0.00E-00	0.00E-00
f_{10}	10	4.56E-15	6.49E-16	4.20E-15	9.01E-16	8.88E-16	0.00E-00	8.88E-16	0.00E-00
	30	2.32E-14	4.27E-15	4.56E-15	6.49E-16	8.88E-16	0.00E-00	8.88E-16	0.00E-00
	50	1.45E-13	5.01E-14	4.44E-15	0.00E-00	8.88E-16	0.00E-00	8.88E-16	0.00E-00
	100	1.45E-09	7.57E-10	1.40E+01	8.04E-00	8.88E-16	0.00E-00	8.88E-16	0.00E-00
f_{11}	10	1.31E-02	2.19E-02	6.67E-02	9.37E-02	0.00E-00	0.00E-00	0.00E-00	0.00E-00
	30	2.82E-03	7.94E-03	1.48E-02	3.65E-02	0.00E-00	0.00E-00	0.00E-00	0.00E-00
	50	4.56E-04	2.50E-03	1.19E-02	4.22E-02	0.00E-00	0.00E-00	0.00E-00	0.00E-00
	100	1.32E-03	5.02E-03	0.00E-00	0.00E-00	0.00E-00	0.00E-00	0.00E-00	0.00E-00
f_{12}	10	4.63E-03	9.95E-03	4.91E-32	2.04E-33	5.36E-01	1.73E-01	3.09E-07	3.33E-07
	30	4.89E-02	2.87E-02	1.65E-32	1.70E-33	5.57E-01	2.13E-01	1.79E-06	2.19E-06
	50	9.40E-02	3.20E-02	9.76E-33	6.89E-34	1.03E-00	7.70E-02	3.12E-06	3.31E-06
	100	2.68E-01	5.55E-02	1.04E-03	5.68E-03	1.11E-00	4.21E-02	1.61E-05	1.43E-05
f_{13}	10	1.24E-02	3.23E-02	3.25E-03	1.78E-02	7.83E-01	1.17E-01	2.09E-06	2.46E-06
	30	5.23E-01	2.00E-01	2.33E-02	5.10E-02	2.99E-00	3.12E-02	2.49E-05	2.75E-05
	50	1.79E-00	2.58E-00	7.32E-02	9.48E-02	4.99E-00	1.61E-03	1.12E-04	8.81E-05
	100	6.21E-00	4.17E-01	1.61E-01	2.40E-01	9.99E-00	2.12E-03	9.13E-04	5.72E-04
f_{14}	2	4.3347	3.70E+00	4.3244	4.35E+00	10.2709	2.74E+00	2.9434	4.43E+00
f_{15}	4	0.0032	6.86E-03	0.0005	4.16E-04	0.0049	2.97E-03	0.0003	2.31E-04
f_{16}	2	-1.0316	1.02E-07	-1.0316	1.42E-08	-0.9661	5.57E-02	-1.0303	5.17E-03
f_{17}	2	0.3979	1.18E-06	0.3979	5.87E-12	1.7185	1.23E+00	0.3980	2.11E-04
f_{18}	2	3.0000	5.43E-05	3.0000	4.61E-07	20.0084	2.05E+01	3.0001	2.41E-04
f_{19}	3	-3.8619	2.06E-03	-3.8628	8.57E-08	-3.2895	3.11E-01	-3.8590	5.80E-04
f_{20}	6	-3.2436	7.74E-02	-3.2744	5.92E-02	-1.5884	4.50E-01	-3.1725	5.27E-02

TABLE 7: Continued.

Function	m	mGWO		PGWO		EEGWO		DGWO	
		Mean	St. dev.	Mean	St. dev.	Mean	St. dev.	Mean	St. dev.
f_{21}	4	-8.5891	2.69E+00	-8.9728	2.18E+00	-0.6512	2.36E-01	-10.0984	1.56E-01
f_{22}	4	-10.2238	9.70E-01	-10.0513	1.34E+00	-0.6848	2.16E-01	-10.2969	2.58E-01
f_{23}	4	-10.5334	1.79E-03	-9.9085	1.96E+01	-0.9298	2.72E-01	-10.5334	2.94E-02

EEGWO algorithm exhibits poor optimization performance on functions f_{14} to f_{23} .

From Table 7, we can see that the EEGWO provides very competitive results compared to the DGWO, and it is challenging to determine which algorithm is better. Therefore, it is necessary to conduct an appropriate statistical analysis to see whether the obtained results of the employed algorithms are significant at a given confidence interval. In this paper, the sign test is adopted, which is obtained from references [11, 46]. The statistical results are recorded in Table 8. It should be noted that these statistical analysis results are conducted based on the average results of the 20 independently obtained best results. As seen from Table 8, the DGWO is significantly better than the GWO, mGWO, and PGWO on unimodal and multimodal test functions at a significance level of 0.05 but shows a non-significant performance difference on 10 fixed-dimension multimodal benchmark functions. In addition, when compared to the EEGWO, the DGWO provides a non-significant performance difference on 13 unimodal and multimodal test functions but obtains significantly better results on 10 fixed-dimension multimodal benchmark functions at a significance level of 0.1.

The percentages of problems solved by the mGWO, PGWO, and EEGWO are recorded in Table 9. Compared to the mGWO, the DGWO obtained the same percentage on six functions (i.e., f_1 , f_2 , f_5 , f_{16} , f_{18} , and f_{23}) and a higher percentage on thirteen functions (i.e., f_3 - f_4 , f_6 - f_9 , f_{11} - f_{13} , f_{15} , and f_{21} - f_{22}), while the DGWO showed a lower percentage on three functions (i.e., f_{17} , f_{19} , and f_{20}). Compared to the PGWO, the DGWO provided the same and higher percentage on five functions (i.e., f_1 , f_2 , f_6 , f_{11} , and f_{18}) and eleven functions (i.e., f_3 - f_4 , f_7 - f_{12} , f_{14} - f_{15} , and f_{23}), respectively; on the contrary, the PGWO showed a higher percentage than the DGWO on six functions (i.e., f_5 , f_{17} , f_{19} , and f_{20} - f_{22}). For function f_{13} , the DGWO showed a higher percentage than the PGWO when the dimensions were 10, 30, and 50 but obtained a lower percentage when the dimension was 100. Compared to the EEGWO, the DGWO achieved the same and higher percentage on nine functions (i.e., f_1 - f_5 , f_9 - f_{11} , and f_{20}) and twelve functions (i.e., f_8 , f_{12} - f_{13} , f_{14} - f_{19} , and f_{21} - f_{23}), respectively. For function f_7 , however, the EEGWO obtained a higher percentage than the DGWO.

To investigate the convergence speed of the three modified versions of the GWO mentioned in this paper and the proposed DGWO algorithm for low-dimensional and high-dimensional problems, Figure 6 plots the convergence curves of 10 typical functions (f_1 - f_4 , f_6 - f_7 , f_9 - f_{10} , and f_{12} - f_{13}) with dimensions of 30 and 100. For functions f_1 - f_4 , f_7 , and f_9 , the DGWO and EEGWO achieve the fastest convergence

speed, whereas the EEGWO achieves a faster convergence speed for high-dimensional functions; however, the DGWO attains a better convergence speed for low-dimensional problems. The PGWO has a fast convergence speed for functions f_6 and f_{12} , and the DGWO ranked second. The DGWO exhibits the fastest convergence speed for functions f_{10} and f_{13} , and the EEGWO shows the same convergence speed for function f_{10} . These analysis results verify that the proposed DGWO achieves excellent convergence performance for both low-dimensional problems and high-dimensional problems.

In addition to the abovementioned GWO versions, an interesting GWO variant named ‘‘GWO-EPD’’ [47] has successfully caught our attention because it exhibits some similarities and differences compared with our proposed DGWO algorithm. The GWO-EPD algorithm has some features that are similar to those of the DGWO algorithm, such as dynamically removing some inferior solutions and repositioning them by adopting alpha, beta, and delta wolves. However, the differences between those two algorithms are also easy to distinguish. For example, in the DGWO, some variables of the current best solution are removed and repositioned by using probability that was modeled as equation (12), while in GWO-EPD, half of the worst search agents are eliminated and reinitialized with equal probability. In addition, in the DGWO, the variables are repositioned by employing the modified position-updated equation (see equation (26)); however, in GWO-EPD, the mechanism of EDP is applied in the GWO algorithm to randomly reinitialize its worst search agents. To further verify the scalability of the DGWO, we compared it with GWO-EPD on 13 test functions (i.e., f_1 - f_{13}), and the results are recorded in Table 1, with dimensions from 30 to 100. All of the DGWO parameters were kept the same as those defined in the above section. The parameter values of GWO-EPD were kept the same as in its original papers. In addition, the maximum number of iterations and population size were set as 500 and 30, respectively, and 30 independent runs were executed for each test function. The experimental results are presented in Table 10.

As seen from Table 10, for $m=30$, compared to the GWO-EPD algorithm, the DGWO provided better results on eleven functions (i.e., f_1 - f_4 , f_6 - f_7 , and f_9 - f_{13}). Similarly, for $m=100$, when compared to GWO-EPD, the DGWO also offered better results on eleven functions (i.e., f_1 - f_4 , f_6 - f_7 , and f_9 - f_{13}). However, better results for f_5 and f_8 were obtained by the GWO-EPD algorithm. In summary, the increase in dimensions has little impact on the performance of the DGWO algorithm. Even when suffering from large-scale optimization problems, the DGWO still worked well and obtained promising results.

TABLE 8: Sign test results of the five different GWO algorithms.

DGWO	GWO			mGWO			PGWO			EEGWO								
	$f_{14}-f_{23}$	$f_{14}-f_{23}$	$f_{14}-f_{23}$	$f_{14}-f_{23}$	$f_{14}-f_{23}$	$f_{14}-f_{23}$	$f_{14}-f_{23}$	$f_{14}-f_{23}$	$f_{14}-f_{23}$	$f_{14}-f_{23}$	$f_{14}-f_{23}$	$f_{14}-f_{23}$						
Dimension	10	30	50	100	10	30	50	100	10	30	50	100						
Wins (+)	13	12	12	12	6	11	11	11	5	13	12	12	6	8	8	7	5	10
Approximations (\approx)	0	0	0	0	0	0	0	1	1	0	0	1	0	0	3	3	3	0
Losses (-)	0	1	1	1	4	2	2	1	4	0	1	1	4	2	2	2	3	5
Detected differences (α)	0.05	0.05	0.05	0.05	n	0.05	0.05	0.05	n	0.05	0.05	0.05	0.05	n	n	n	n	0.1

Note: "n" refers to nonsignificant at the significance levels of 0.05 and 0.1.

TABLE 9: Percentage of problems solved by the mGWO, PGWO, and EEGWO.

Function	mGWO (%)				PGWO (%)				EEGWO (%)			
	Dimension				Dimension				Dimension			
	10	30	50	100	10	30	50	100	10	30	50	100
f_1	100	100	100	100	100	100	100	100	100	100	100	100
f_2	100	100	100	100	100	100	100	100	100	100	100	100
f_3	100	100	6	0	100	100	100	0	100	100	100	100
f_4	100	100	100	0	100	100	96	0	100	100	100	100
f_5	0	0	0	0	6	0	0	0	0	0	0	0
f_6	100	0	0	0	100	100	100	100	0	0	0	0
f_7	13	0	0	0	0	0	0	0	83	70	73	70
f_8	0	0	0	0	0	0	0	0	0	0	0	0
f_9	90	96	96	83	6	0	0	0	100	100	100	100
f_{10}	100	100	100	100	100	100	100	10	100	100	100	100
f_{11}	53	86	96	93	33	80	90	100	100	100	100	100
f_{12}	80	0	0	0	100	100	100	96	0	0	0	0
f_{13}	86	0	0	0	96	66	30	13	0	0	0	0
f_{14}	23				43				0			
f_{15}	16				66				0			
f_{16}	100				100				0			
f_{17}	100				100				0			
f_{18}	100				100				0			
f_{19}	100				100				0			
f_{20}	46				60				0			
f_{21}	0				76				0			
f_{22}	26				93				0			
f_{23}	96				90				0			

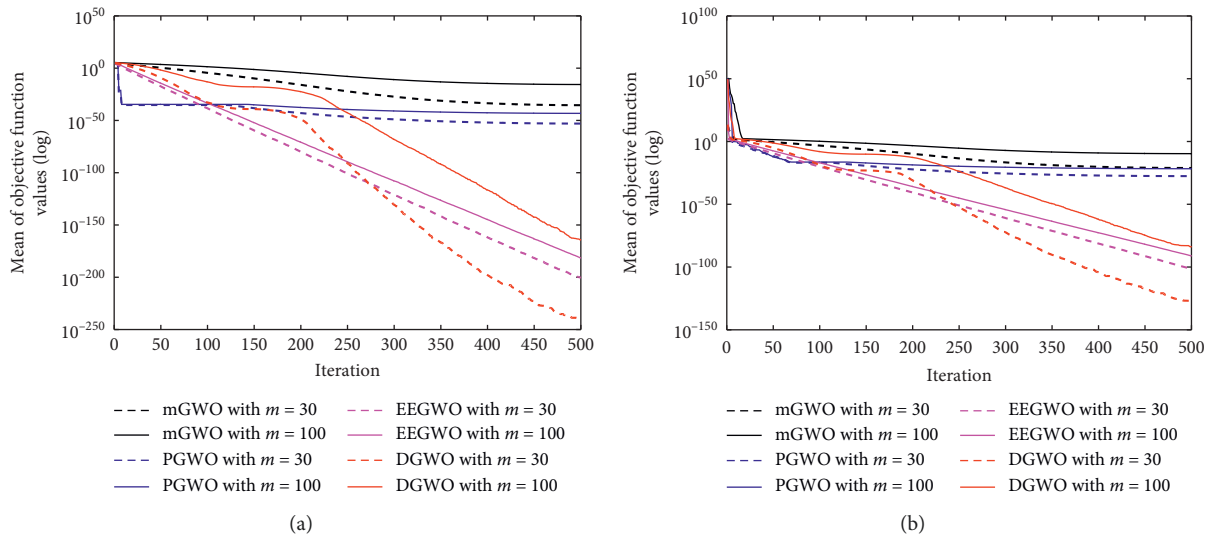


FIGURE 6: Continued.

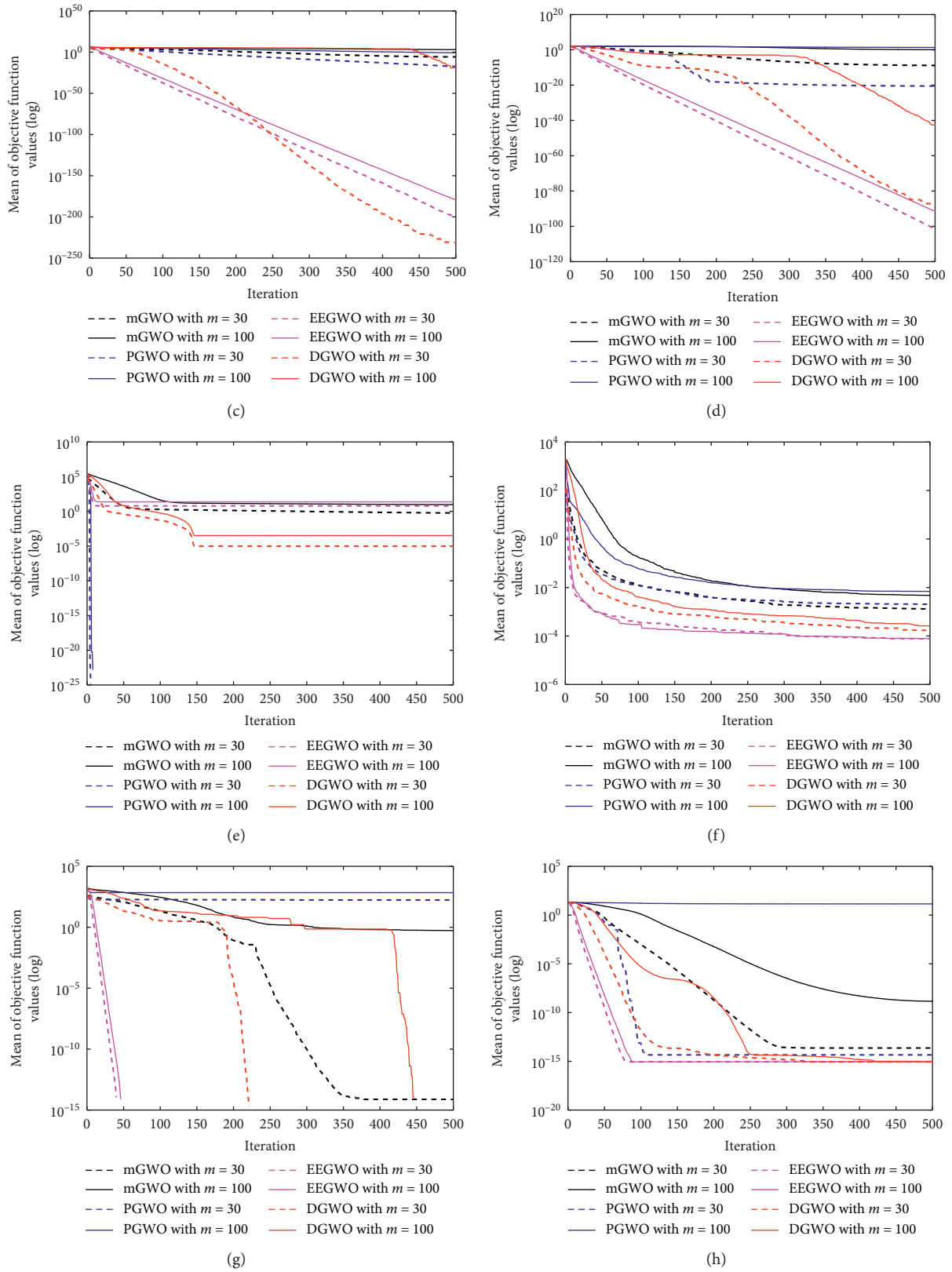


FIGURE 6: Continued.

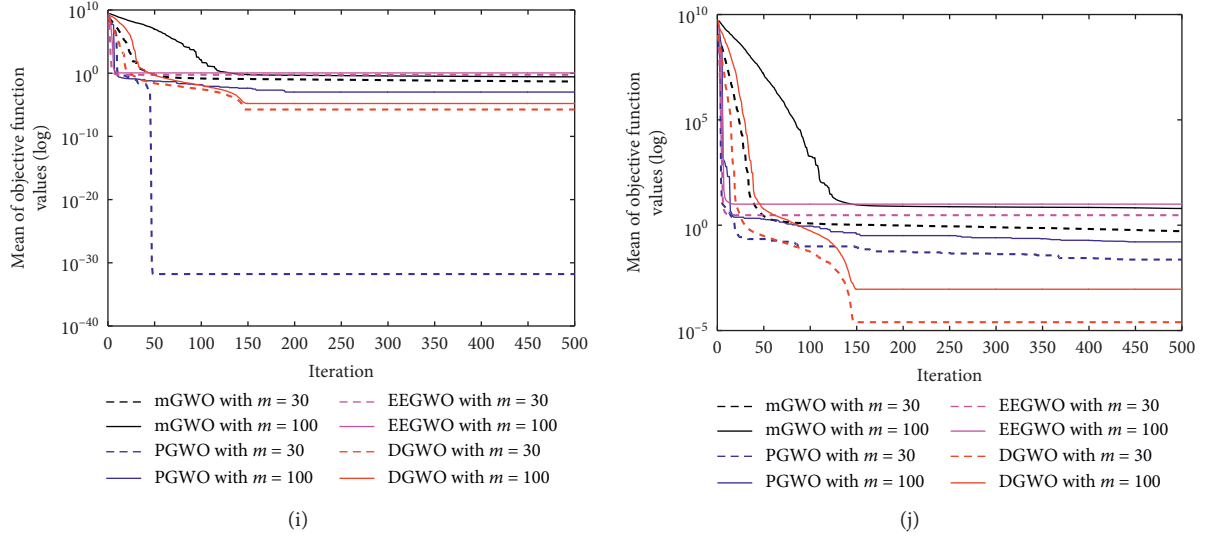


FIGURE 6: Convergence curves of the four different GWO variants with $m = 30$ and 100 on 10 typical test functions. (a) f_1 . (b) f_2 . (c) f_3 . (d) f_4 . (e) f_6 . (f) f_7 . (g) f_9 . (h) f_{10} . (i) f_{12} . (j) f_{13} .

TABLE 10: Mean and St. dev. results of the DGWO and GWO-EPD for thirteen functions ($m = 30$ and 100).

Function	GWO-EPD with $m = 30$ Mean \pm St. dev.	DGWO with $m = 30$ Mean \pm St. dev.	GWO-EPD with $m = 100$ Mean \pm St. dev.	DGWO with $m = 100$ Mean \pm St. dev.
f_1	$6.75E-25 \pm 1.16E-24$	$2.36E-299 \pm 0.00E+00$	$3.64E-01 \pm 5.28E-01$	$8.19E-165 \pm 0.00E+00$
f_2	$4.52E-15 \pm 3.98E-15$	$1.45E-155 \pm 7.92E-155$	$3.00E-02 \pm 3.04E-02$	$1.62E-84 \pm 8.48E-84$
f_3	$2.89E-04 \pm 6.38E-04$	$3.24E-300 \pm 0.00E+00$	$2.50E+00 \pm 1.99E+00$	$1.01E-19 \pm 5.52E-19$
f_4	$5.41E-02 \pm 5.16E-02$	$1.25E-130 \pm 6.22E-130$	$4.87E-02 \pm 4.92E-02$	$3.01E-43 \pm 1.65E-42$
f_5	$2.02E-01 \pm 3.50E-01$	$3.10E+00 \pm 2.85E+00$	$2.10E+01 \pm 4.34E+01$	$9.80E+01 \pm 9.99E-03$
f_6	$2.34E-01 \pm 1.93E-01$	$5.84E-07 \pm 8.37E-07$	$2.24E+02 \pm 1.29E+01$	$3.28E-04 \pm 2.40E-04$
f_7	$3.87E-03 \pm 2.59E-03$	$1.24E-04 \pm 9.64E-05$	$2.31E-02 \pm 2.20E-02$	$2.62E-04 \pm 3.68E-04$
f_8	$-1.26E+04 \pm 1.63E-01$	$-3.85E+03 \pm 5.86E+02$	$-4.19E+05 \pm 1.50E+01$	$-2.28E+04 \pm 5.58E+03$
f_9	$1.57E-08 \pm 8.57E-08$	$0.00E+00 \pm 0.00E+00$	$2.80E-01 \pm 4.20E-01$	$0.00E+00 \pm 0.00E+00$
f_{10}	$2.46E-11 \pm 1.32E-10$	$8.88E-16 \pm 0.00E+00$	$1.33E-02 \pm 1.33E-02$	$8.88E-16 \pm 0.00E+00$
f_{11}	$1.53E-03 \pm 5.05E-03$	$0.00E+00 \pm 0.00E+00$	$3.22E-02 \pm 1.23E-01$	$0.00E+00 \pm 0.00E+00$
f_{12}	$3.45E-02 \pm 1.35E-02$	$3.09E-07 \pm 3.33E-07$	$7.70E-01 \pm 7.58E-02$	$1.61E-05 \pm 1.43E-05$
f_{13}	$3.20E-04 \pm 1.94E-04$	$9.13E-04 \pm 5.72E-04$	$7.07E-02 \pm 2.07E-01$	$9.13E-04 \pm 5.72E-04$

The bold values in GWO-EPD with $m = 30$ are losses (-): 10, wins (+): 2, approximations (=): 1, and detected differences (α): 0.05. The bold values in GWO-EPD with $m = 100$ are losses (-): 11, wins (+): 2, approximations (=): 0, and detected differences (α): 0.05.

4.6. *Performance Comparison with Other State-of-the-Art Algorithms ($m = 30$)*. In this section, we compared the DGWO to seven recently proposed state-of-the-art population-based optimization methods, such as the autonomous particles groups for particle swarm optimization (AGPSO) [48], the improved PSO with time-varying accelerator coefficients (IPSO) [49], the improved PSO algorithm based on asymmetric time-varying acceleration coefficients (MPSO) [50], the time-varying acceleration coefficients particle swarm optimization (TACPSO) [51], the hybrid differential evolution with biogeography-based optimization (DEBBO) [52], the hybrid whale optimization algorithm with simulated annealing (WOA-SA) [53], and the salp swarm algorithm (SSA) [54]. All DGWO parameters were kept the same as those listed in Section 4.1. The parameter settings of the seven algorithms are listed as follows: the population size is 30, the maximum number of iterations is 500, and the other algorithm parameters are the same as in their original papers.

To compare the optimization performance of the seven algorithms, the results are achieved over 30 independent runs. The best (denoted by “Best”), average (denoted by “Mean”), and standard deviation (denoted by “St. dev.”) of the best solution in the last iteration are collected in Table 11. The best obtained results are highlighted in boldface type.

Table 11 shows the results for 23 test functions. As presented in this table, the DGWO had the best results for three of seven unimodal benchmark problems (i.e., f_3 , f_4 , and f_7). For function f_6 , the DGWO performed slightly worse than the SSA and obtained the second best result. For functions f_1 and f_2 , the WOA-SA achieved the global optimal values (0), and the DGWO provided solutions near 0. For the multimodal benchmark functions f_8 – f_{13} , the DGWO presented the best results, with the exception of functions f_{12} and f_{13} . For functions f_8 , f_{12} , and f_{13} , the DEBBO obtained almost the same results as the DGWO. Compared to the WOA-SA, the DGWO obtained similar and worse results for

TABLE 11: Comparison results of the DGWO and other seven algorithms on 23 test functions ($m = 30$).

Test function	AGPSO	IPSO	MPSO	TACPSO	DEBBO	WOA-SA	SSA	DGWO	
f_1	Best	1.04E-03	1.75E-04	9.29E-03	8.09E-04	1.04E-05	0.00E+00	3.49E-08	1.63E-287
	Mean	2.42E-01	1.12E-01	1.00E+03	2.35E-01	3.48E-05	0.00E+00	2.03E-07	2.38E-241
	St. dev.	1.05E+00	4.89E-01	3.05E+03	8.70E-01	1.93E-05	0.00E+00	2.52E-07	0.00E+00
f_2	Best	1.78E-02	3.78E-02	1.00E+01	6.65E-02	2.11E-04	0.00E+00	2.78E-01	3.74E-148
	Mean	5.99E+00	6.04E-00	3.84E+01	8.35E-01	3.63E-04	0.00E+00	2.13E+00	1.39E-127
	St. dev.	7.61E+00	7.69E-00	1.99E+01	1.84E+00	9.71E-05	0.00E+00	1.56E+00	7.05E-127
f_3	Best	2.64E+02	6.23E+02	1.09E+03	1.66E+02	6.45E+03	1.70E-02	3.81E+02	1.67E-260
	Mean	4.26E+03	6.65E+03	1.95E+04	1.09E+03	1.59E+04	5.46E-01	1.59E+03	9.45E-232
	St. dev.	4.97E+03	5.40E+03	9.13E+03	1.47E+03	3.40E+03	3.06E-01	1.02E+03	0.00E+00
f_4	Best	7.93E+00	4.34E+00	7.86E+00	2.78E+00	4.25E+00	2.53E-02	6.69E+00	1.30E-106
	Mean	1.63E+01	1.03E+01	2.00E+01	9.64E+00	6.76E+00	7.82E-01	1.09E+01	3.11E-88
	St. dev.	4.77E+00	3.58E+00	5.87E+00	3.44E+00	1.64E+00	4.02E-01	3.71E+00	1.70E-87
f_5	Best	2.47E+01	7.40E+01	7.83E+01	2.91E+01	2.53E+01	0.00E+00	4.51E+00	2.82E+01
	Mean	3.29E+02	3.45E+03	1.26E+04	3.20E+03	5.09E+01	3.03E+01	1.49E+02	2.85E+01
	St. dev.	7.38E+02	1.64E+04	3.09E+04	1.64E+04	3.13E+01	2.82E+01	3.48E+02	1.28E-01
f_6	Best	1.51E-03	1.64E-04	3.74E-03	4.87E-04	1.09E-05	3.39E-04	3.72E-08	1.48E-06
	Mean	7.83E-02	7.14E-02	3.30E+02	1.73E-01	3.32E-05	8.44E-04	2.09E-07	9.70E-06
	St. dev.	9.30E-02	2.78E-01	1.81E+03	3.42E-01	1.93E-05	3.07E-04	3.00E-07	4.71E-06
f_7	Best	4.63E-02	3.38E-02	3.89E-02	4.32E-02	2.04E-02	1.50E-02	4.64E-02	2.88E-05
	Mean	1.14E-01	7.41E-02	1.25E+00	8.62E-02	4.22E-02	4.93E-02	1.78E-01	1.66E-04
	St. dev.	5.01E-02	3.05E-02	2.89E+00	3.67E-02	1.41E-02	2.39E-02	7.96E-02	1.40E-04
f_8	Best	-7.83E+03	-7.77E+03	-7.44E+03	-7.20E+03	-1.22E+04	-8.86E+03	-6.31E+03	-1.24E+04
	Mean	-9.30E+03	-9.23E+03	-8.85E+03	-8.52E+03	-1.25E+04	-1.03E+04	-7.36E+03	-1.26E+04
	St. dev.	7.09E+02	7.04E+02	7.51E+02	7.72E+02	1.09E+02	8.47E+02	6.76E+02	2.43E+03
f_9	Best	4.38E+01	3.68E+01	7.76E+01	2.81E+01	2.36E+01	0.00E+00	2.09E+01	0.00E+00
	Mean	8.39E+01	9.73E+01	1.34E+02	7.11E+01	3.27E+01	0.00E+00	5.13E+01	0.00E+00
	St. dev.	2.65E+01	2.84E+01	3.37E+01	2.27E+01	5.66E+00	0.00E+00	1.68E+01	0.00E+00
f_{10}	Best	2.26E+00	6.08E-03	6.78E-01	9.33E-01	7.68E-04	8.88E-16	1.16E+00	8.88E-16
	Mean	3.69E+00	2.23E+00	7.37E+00	2.34E+00	1.34E-03	8.88E-16	2.78E+00	8.88E-16
	St. dev.	8.02E-01	9.89E-01	6.23E+00	9.60E-01	5.11E-04	0.00E+00	7.52E-01	0.00E+00
f_{11}	Best	1.00E-02	2.46E-03	1.16E-02	2.84E-03	1.53E-05	0.00E+00	9.26E-04	0.00E+00
	Mean	1.50E-01	9.81E-02	6.31E+00	1.12E-01	1.20E-03	0.00E+00	1.47E-02	0.00E+00
	St. dev.	1.22E-01	1.26E-01	2.29E+01	1.74E-01	2.76E-03	0.00E+00	1.34E-02	0.00E+00
f_{12}	Best	9.88E-01	1.09E-01	5.83E-01	6.81E-04	1.22E-06	2.04E-05	2.81E+00	4.04E-06
	Mean	4.18E-00	1.47E+00	3.59E+00	1.92E+00	9.46E-06	6.36E-05	6.75E+00	1.61E-05
	St. dev.	2.48E-00	1.28E+00	1.77E+00	1.55E+00	9.45E-06	5.37E-05	3.10E+00	1.43E-05
f_{13}	Best	1.30E+00	1.89E-03	2.19E-01	3.10E-02	8.50E-06	1.35E-32	1.92E-01	1.86E-04
	Mean	9.78E+00	4.00E+00	9.39E+00	4.62E+00	4.46E-05	1.35E-32	1.63E+01	9.13E-04
	St. dev.	7.45E+00	6.42E+00	6.58E+00	4.26E+00	2.39E-05	5.57E-48	1.43E+01	5.72E-04
f_{14}	Best	0.9980	0.9980	0.9980	0.9980	0.9980	0.9980	0.9980	0.9980
	Mean	0.9980	0.9980	0.9980	0.9980	1.0900	7.4300	1.3900	2.9400
	St. dev.	1.70E-16	1.60E-16	7.14E-17	2.30E-16	3.03E-01	5.13E+00	8.86E-01	4.43E+00
f_{15}	Best	0.0003	0.0003	0.0003	0.0003	0.0003	0.0003	0.0004	0.0003
	Mean	0.0021	0.0013	0.0043	0.0012	0.0020	0.0032	0.0015	0.0003
	St. dev.	4.98E-03	3.63E-03	7.34E-03	3.64E-03	5.00E-03	1.19E-02	3.57E-03	2.31E-04
f_{16}	Best	-1.0316	-1.0316	-1.0316	-1.0316	-1.0316	-1.0316	-1.0316	-1.0316
	Mean	-1.0316	-1.0316	-1.0316	-1.0316	-1.0316	-1.0316	-1.0316	-1.0316
	St. dev.	6.12E-16	6.05E-16	6.25E-16	5.83E-16	6.65E-16	1.80E-10	4.87E-14	5.17E-03
f_{17}	Best	0.3979	0.3979	3.9789	0.3979	0.3979	0.3979	0.3979	0.3979
	Mean	0.3989	0.3979	3.9789	0.3979	0.3979	0.3979	0.3979	0.3980
	St. dev.	0.00E+00	0.00E+00	0.00E+00	0.00E+00	0.00E+00	5.82E-06	7.11E-14	2.11E-04
f_{18}	Best	3.0000	3.0000	3.0000	3.0000	3.0000	3.0000	3.0000	3.0000
	Mean	3.0000	3.0000	3.0000	3.0000	3.0000	4.8000	3.0000	3.0000
	St. dev.	2.27E-15	2.46E-15	2.48E-15	1.59E-15	1.36E-15	6.85E+01	2.64E-13	2.41E-04
f_{19}	Best	-3.8629	-3.8628	-3.8628	-3.8628	-3.8628	-3.8628	-3.8628	-3.8626
	Mean	-3.8628	-3.8628	-3.8628	-3.8628	-3.8628	-3.8628	-3.8628	-3.8590
	St. dev.	2.61E-15	2.61E-15	2.64E-15	2.63E-15	2.71E-15	4.17E-09	1.23E-10	5.87E-03
f_{20}	Best	-3.3220	-3.3220	-3.3220	-3.3220	-3.3220	-3.3220	-3.3220	-3.2959
	Mean	-3.2643	3.2600	-3.2691	-3.2467	-3.2903	-3.2903	-3.2136	-3.1725
	St. dev.	6.38E-02	6.41E-02	6.78E-02	5.83E-02	5.35E-02	5.35E-02	5.03E-02	5.27E-02

TABLE 11: Continued.

Test function	AGPSO	IPSO	MPSO	TACPSO	DEBBO	WOA-SA	SSA	DGWO
f_{21}	Best	-10.1532	-10.1532	-10.1532	-10.1532	-10.1532	-10.1532	-10.1532
	Mean	-6.1332	-6.6316	-6.3807	-5.8073	-8.3101	-5.2251	-6.8967
	St. dev.	3.06E+00	3.06E+00	3.07E+00	3.27E+00	2.94E+00	9.31E-01	3.42E+00
f_{22}	Best	-10.4029	-10.4029	-10.4029	-10.4029	-10.4029	-5.0877	-10.4029
	Mean	-7.5123	-8.9999	-8.4546	-8.3648	-9.2703	-5.0877	-9.0951
	St. dev.	3.26E+00	2.63E+00	2.88E+00	3.21E+00	2.59E+00	3.18E-07	2.70E+00
f_{23}	Best	-10.5364	-10.5364	-10.5364	-10.5364	-10.5364	-5.1285	-10.5364
	Mean	-9.0557	-9.8342	-9.1913	-8.4994	-10.0064	-5.1285	-8.9619
	St. dev.	2.79E+00	2.15E+00	2.78E+00	3.22E+00	2.00E+00	1.86E-12	2.96E+00

TABLE 12: Percentage of problems solved by the GWO and DGWO.

Function	AGPSO (%)	IPSO (%)	MPSO (%)	TACPSO (%)	DEBBO (%)	WOA-SA (%)	SSA (%)	DGWO (%)
f_1	0	0	0	0	100	100	100	100
f_2	0	0	0	0	0	100	0	100
f_3	0	0	0	0	0	0	0	100
f_4	0	0	0	0	0	0	0	100
f_5	0	0	0	0	0	3	0	0
f_6	0	0	0	0	100	0	100	100
f_7	0	0	0	0	0	0	0	46
f_8	0	0	0	0	60	0	0	46
f_9	0	0	0	0	0	100	0	100
f_{10}	0	0	0	0	0	100	0	100
f_{11}	0	0	0	0	50	100	0	100
f_{12}	0	0	0	0	100	80	0	100
f_{13}	0	0	0	0	96	100	0	96
f_{14}	100	100	100	100	90	20	80	83
f_{15}	10	53	3	70	10	60	0	96
f_{16}	100	100	100	100	100	100	100	100
f_{17}	100	100	100	100	100	100	100	96
f_{18}	100	100	100	100	100	90	100	100
f_{19}	100	100	100	100	100	100	100	90
f_{20}	53	50	60	36	70	70	16	0
f_{21}	33	40	36	30	70	3	50	66
f_{22}	53	76	66	70	80	0	80	80
f_{23}	76	90	80	70	90	0	76	96

three functions (f_9 - f_{11}) and one function (f_{13}), respectively. Table 11 also shows the results for 10 fixed-dimension multimodal benchmark functions (f_{14} - f_{23}). As shown in Table 11, the results of the AGPSO, IPSO, MPSO, and TACPSO are equal for four functions (f_{14} , f_{16} , f_{18} , and f_{20}) and better than those of the DGWO. However, the DGWO achieved the best results of all algorithms for six fixed-dimension unimodal benchmark problems (i.e., f_{15} , f_{17} , f_{19} , and f_{21} - f_{23}). The WOA-SA and SSA obtained similar results for function f_{20} and are better than the other algorithms.

The percentages of problems solved by the seven state-of-the-art algorithms are listed in Table 12. As seen from this table, the AGPSO, IPSO, MPSO, and TACPSO have all failed to solve thirteen test functions (i.e., f_1 - f_{13}) but completely solved all five test functions (i.e., f_{14} and f_{16} - f_{19}). Of the thirteen functions f_1 - f_{13} , nine functions are completely solved by the DGWO, three functions are fully solved by the DEBBO, six functions are fully solved by the WOA-SA, and two functions are fully solved by the SSA. Of the ten functions f_{14} - f_{23} , four functions are completely solved by the DEBBO and SSA, three functions are fully solved by the

WOA-SA, and two functions are fully solved by the DGWO. However, for functions f_{15} and f_{22} - f_{23} , the DGWO has achieved the highest percentage.

Figure 7 plots the convergence curves of the average objective function values of the algorithms for some typical test problems, where f_1 , f_3 , f_4 , and f_7 are unimodal functions, f_9 , f_{10} , and f_{11} are multimodal benchmark functions, and f_{15} , f_{21} , and f_{23} are fixed-dimension multimodal benchmark functions. As observed from these curves, the DGWO has the best convergence rates for all 10 classic benchmark functions. Note that unimodal test problems are suitable for benchmarking the convergence ability of algorithms since they have only one global minimum and do not have local minima in the search space [48]. Since multimodal and fixed-dimension multimodal benchmark functions have more than one local optimal solution, they are suitable for benchmarking the capability of algorithms in avoiding local minima [48]. As indicated by the results, the DGWO performs better than the seven compared algorithms on both the unimodal and multimodal benchmark functions. The DGWO achieves superior results because the candidate

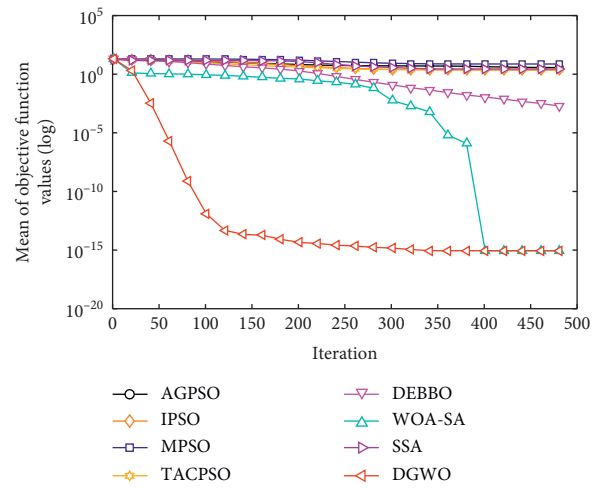
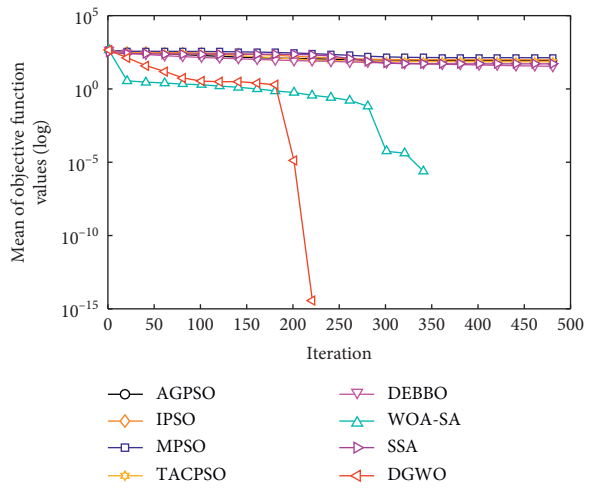
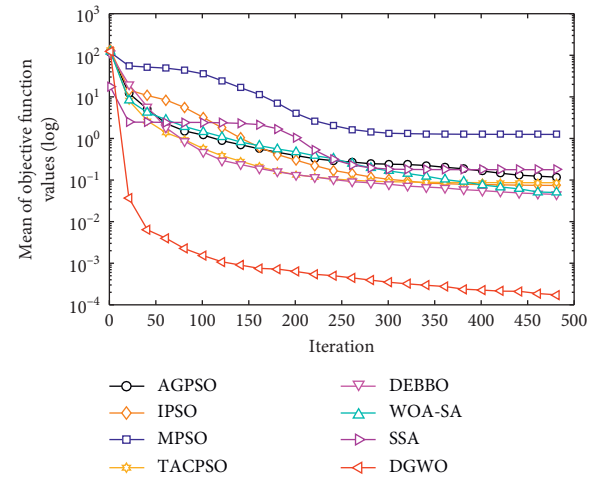
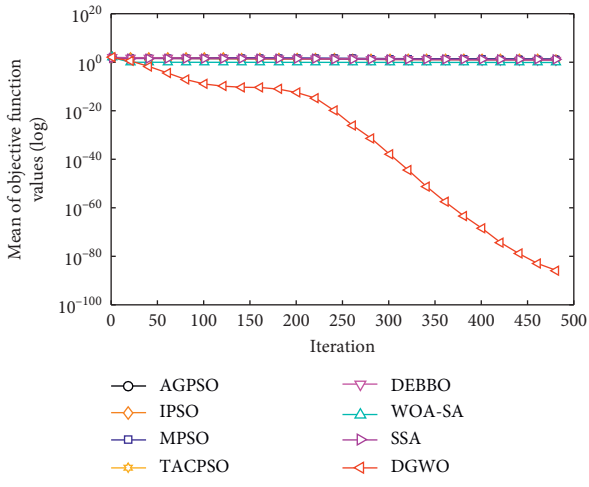
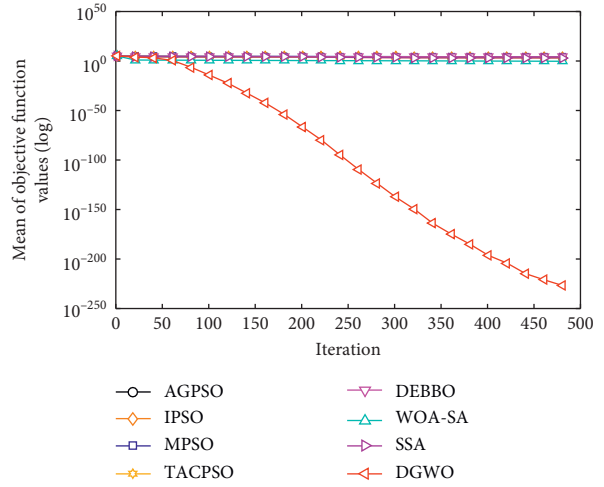
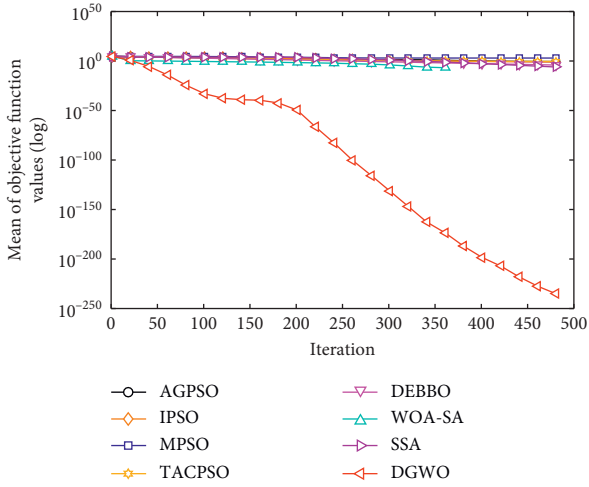


FIGURE 7: Continued.

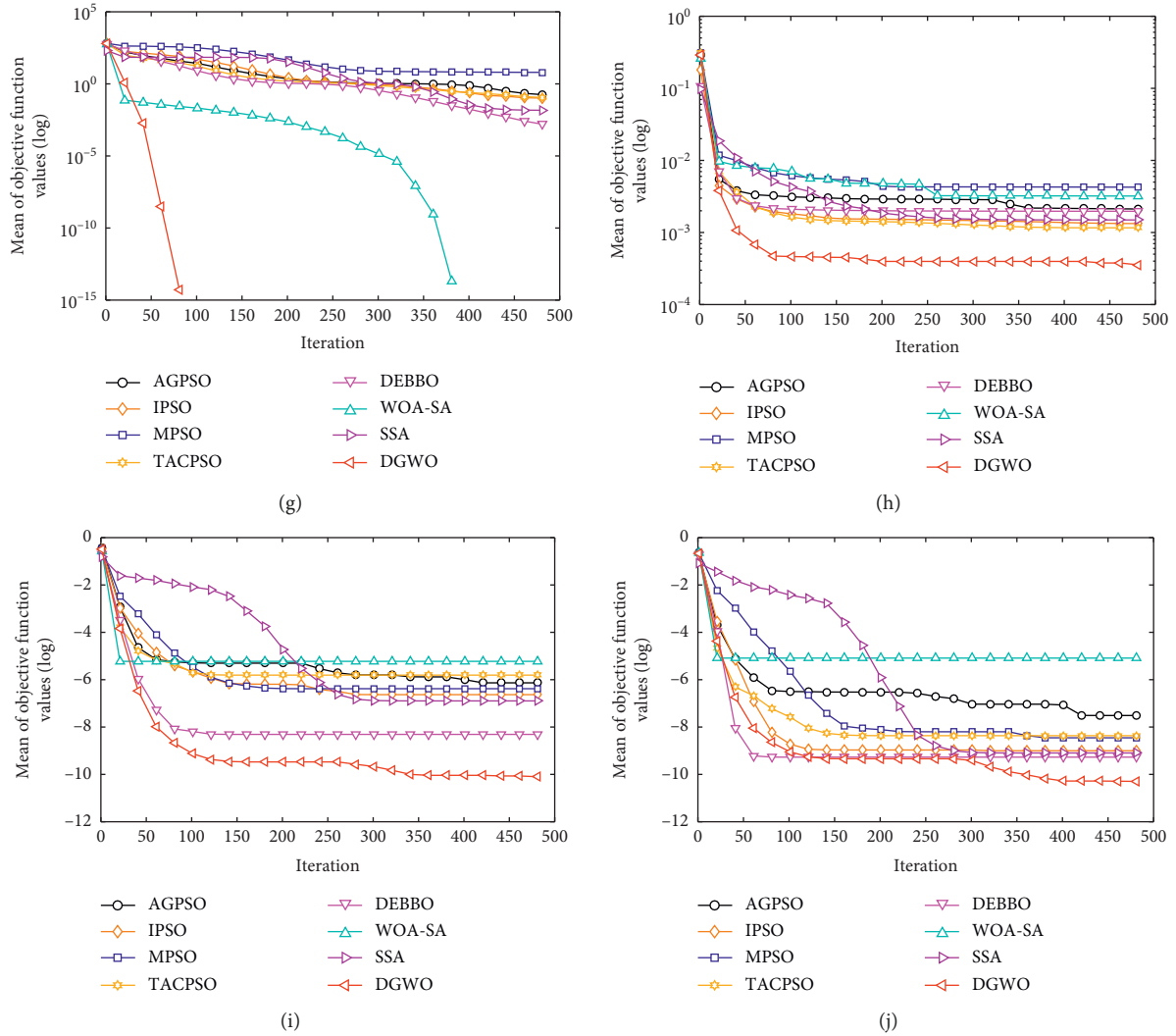


FIGURE 7: Convergence curves of the algorithms on the 10 classic benchmark functions. (a) f_1 . (b) f_3 . (c) f_4 . (d) f_7 . (e) f_9 . (f) f_{10} . (g) f_{11} . (h) f_{15} . (i) f_{21} . (j) f_{23} .

particles have diversity in the population and the balance between exploration and exploitation during the iteration is achieved by the strategies of the modified position-updated equation (i.e., equation (26)) and nonlinear control parameter (i.e., equation (27)).

To further investigate the optimization performance of the DGWO on some standard and complex benchmark problems, we compared it with the TACPSO, IPSO, and GWO on a CEC2014 benchmark test suite with the dimension 30. The parameter settings of the DGWO and other selected algorithms were the same as mentioned above. The maximum number of iterations for the DGWO was 5×10^4 , and for each problem, 20 independent runs were implemented. The experiment results are shown in Table 13.

From Table 13, it can be seen that, of the unimodal test functions (f_1 - f_3), the proposed DGWO achieves the best performance on f_1 and f_2 . Of the 13 multimodal functions (f_4 - f_{16}), the DGWO shows better results on 11 benchmark test functions and similar results on two test functions (i.e., f_{13} and f_{16}). Of the 6 hybrid functions (f_{17} - f_{22}), the DGWO

gives the best results on four functions (f_{17} , f_{19} , f_{21} , and f_{22}), while it becomes the second best algorithm for function f_{18} . Of the 8 composition functions (f_{23} - f_{30}), the proposed DGWO gives the best results on all test functions except for function f_{26} but provides the worst result on function f_{26} .

From the statistical analysis listed in Table 13, the DGWO performs better than the TACPSO at a significance level of 0.05 and better than the IPSO and GWO at a significance level of 0.1.

4.7. Experiment on Real-World Engineering Problems. In this section, several classic real-world engineering optimization problems were selected to validate the practical optimization performance of our proposed algorithm. The DGWO and GWO methods were applied to solve three well-known constrained engineering design problems, including Himmelblau's problem, the gear train design, and the pressure vessel design. It is noted that the penalty function methods were employed to address the constrained optimization

TABLE 13: Comparison between the DGWO and other algorithms on CEC2014 benchmark functions.

Function	TACPSO	IPSO	GWO	DGWO
	Mean \pm St. dev.	Mean \pm St. dev.	Mean \pm St. dev.	Mean \pm St. dev.
f_1	1.30E+08 \pm 9.99E+07	7.75E+07 \pm 2.13E+07	8.59E+07 \pm 6.67E+07	5.79E+07 \pm 2.74E+07
f_2	1.64E+10 \pm 1.10E+10	2.55E+09 \pm 2.69E+09	2.31E+09 \pm 2.32E+09	2.18E+09 \pm 2.02E+09
f_3	5.18E+04 \pm 2.89E+04	8.77E+03 \pm 7.99E+03	3.39E+04 \pm 8.81E+03	3.56E+04 \pm 9.79E+03
f_4	1.98E+03 \pm 1.49E+03	6.64E+02 \pm 8.69E+01	6.55E+02 \pm 1.07E+02	6.63E+02 \pm 1.17E+02
f_5	5.21E+02 \pm 1.91E-01	5.20E+02 \pm 2.83E-01	5.21E+02 \pm 5.65E-02	5.20E+02 \pm 5.74E-02
f_6	6.24E+02 \pm 2.79E+00	6.19E+02 \pm 3.24E+00	6.14E+02 \pm 3.42E+00	6.13E+02 \pm 2.57E+00
f_7	8.79E+02 \pm 7.77E+01	7.26E+02 \pm 1.95E+01	7.17E+02 \pm 1.27E+01	7.10E+02 \pm 1.21E+01
f_8	9.23E+02 \pm 2.23E+01	8.76E+02 \pm 1.62E+01	8.77E+02 \pm 2.04E+01	8.67E+02 \pm 2.37E+01
f_9	1.07E+03 \pm 2.66E+01	1.02E+03 \pm 3.08E+01	9.98E+02 \pm 2.24E+01	9.76E+02 \pm 2.08E+01
f_{10}	4.49E+03 \pm 5.73E+02	3.68E+03 \pm 6.16E+02	3.18E+03 \pm 6.01E+02	3.11E+03 \pm 4.96E+02
f_{11}	5.22E+03 \pm 6.52E+02	4.52E+03 \pm 5.19E+02	3.94E+03 \pm 7.09E+02	3.79E+03 \pm 5.93E+02
f_{12}	1.21E+03 \pm 3.09E-01	1.20E+03 \pm 3.13E-01	1.20E+03 \pm 1.06E+00	1.20E+03 \pm 1.15E+00
f_{13}	1.30E+03 \pm 1.29E+00	1.30E+03 \pm 8.80E-01	1.30E+03 \pm 1.08E-01	1.30E+03 \pm 1.41E-01
f_{14}	1.45E+03 \pm 2.09E+01	1.41E+03 \pm 1.17E+01	1.40E+03 \pm 5.06E+00	1.40E+03 \pm 4.99E+00
f_{15}	4.17E+04 \pm 7.37E+04	1.64E+03 \pm 2.10E+02	1.67E+03 \pm 4.72E+02	1.57E+03 \pm 4.15E+02
f_{16}	1.61E+03 \pm 5.48E-01	1.61E+03 \pm 5.32E-01	1.61E+03 \pm 7.61E-01	1.61E+03 \pm 6.28E-01
f_{17}	4.14E+06 \pm 2.87E+06	5.17E+06 \pm 7.06E+05	2.31E+06 \pm 3.48E+05	2.13E+06 \pm 3.93E+05
f_{18}	9.93E+07 \pm 2.70E+08	6.91E+06 \pm 2.61E+05	9.28E+07 \pm 2.00E+07	2.14E+07 \pm 3.13E+06
f_{19}	2.01E+03 \pm 6.35E+01	1.94E+03 \pm 3.13E+01	1.94E+03 \pm 2.46E+01	1.94E+03 \pm 3.00E+01
f_{20}	1.74E+04 \pm 1.73E+04	5.26E+03 \pm 2.62E+03	2.01E+04 \pm 7.77E+03	1.95E+04 \pm 9.63E+03
f_{21}	7.15E+05 \pm 8.92E+05	1.68E+05 \pm 1.21E+05	7.15E+05 \pm 9.20E+04	1.42E+05 \pm 2.92E+04
f_{22}	2.86E+03 \pm 1.96E+02	2.71E+03 \pm 1.53E+02	2.60E+03 \pm 1.35E+02	2.56E+03 \pm 1.76E+02
f_{23}	2.68E+03 \pm 3.88E+01	2.63E+03 \pm 1.21E+01	2.64E+03 \pm 1.18E+01	2.63E+03 \pm 1.18E+01
f_{24}	2.68E+03 \pm 1.64E+01	2.64E+03 \pm 1.19E+01	2.60E+03 \pm 1.68E-03	2.60E+03 \pm 1.53E-03
f_{25}	2.72E+03 \pm 5.08E+00	2.71E+03 \pm 5.77E+00	2.71E+03 \pm 4.82E+00	2.71E+03 \pm 5.24E+00
f_{26}	2.72E+03 \pm 6.35E+01	2.73E+03 \pm 6.23E+01	2.74E+03 \pm 4.87E+01	2.75E+03 \pm 5.08E+01
f_{27}	3.78E+03 \pm 8.68E+01	3.53E+03 \pm 2.48E+02	3.35E+03 \pm 1.06E+02	3.35E+03 \pm 1.19E+02
f_{28}	4.50E+03 \pm 6.12E+02	4.36E+03 \pm 3.87E+02	4.03E+03 \pm 3.52E+02	3.96E+03 \pm 2.93E+02
f_{29}	1.64E+07 \pm 1.47E+07	2.18E+07 \pm 1.68E+07	6.46E+06 \pm 2.21E+06	1.01E+06 \pm 2.13E+06
f_{30}	1.14E+05 \pm 7.79E+04	6.04E+04 \pm 6.63E+04	4.09E+04 \pm 1.72E+04	4.07E+04 \pm 2.37E+04
Losses (-)	26	19	20	
Wins (+)	2	4	2	
Approximations (\approx)	2	7	8	
Detected differences (α)	0.05	0.1	0.1	

problems [55]. DGWO and GWO parameters for these three real-world engineering optimization applications were provided as follows: the population size was 30, the maximum number of iterations was 1000, and each problem was run independently 30 times.

4.7.1. Himmelblau's Nonlinear Optimization Problem. Himmelblau's problem is a well-known benchmark nonlinear constrained optimization problem that was developed by Himmelblau [56]. This type of optimization is performed to find the decision vector $Y = [y_1, y_2, y_3, y_4, y_5]$. To obtain the minimize function f , the objective function f is modeled as

$$\begin{aligned}
 &\text{minimize } f(Y) = 5.3578547y_3^2 + 0.8356891y_1y_5 \\
 &\quad + 37.293239y_1 - 40792.141 \\
 &\text{s.t. } \quad 0 \leq g_1(Y) \leq 92 \\
 &\quad \quad 90 \leq g_2(Y) \leq 110 \\
 &\quad \quad 20 \leq g_3(Y) \leq 25,
 \end{aligned} \tag{28}$$

where

$$\begin{aligned}
 g_1(Y) &= 85.334407 + 0.0056858y_2y_5 + 0.0006262y_1y_4 \\
 &\quad - 0.0022053y_3y_5, \\
 g_2(Y) &= 80.51249 + 0.0071317y_2y_5 + 0.0029955y_1y_2 \\
 &\quad - 0.0021813y_3^2, \\
 g_3(Y) &= 9.300961 + 0.0047026y_3y_5 + 0.0012547y_1y_3 \\
 &\quad + 0.0019085y_3y_4, \\
 &78 \leq y_1 \leq 102, 33 \leq y_2 \leq 45, 27 \leq y_3, y_4, y_5 \leq 45.
 \end{aligned} \tag{29}$$

Several researchers have employed different algorithms to solve this problem, such as the generalized reduced gradient (GRG) [56], the genetic algorithm (GA) [57], GA solution based on a global reference (GA-G) [58], and GA solution based on a local reference (GA-L) [58]. Table 14 illustrates the results of the best run obtained by the DGWO and the previously mentioned methods. Table 14 reveals that the results achieved by employing the DGWO algorithm are better than those of the previously reported best feasible

TABLE 14: Comparison results of the best Himmelblau's nonlinear optimization problem obtained by different algorithms.

Methods	Design variables					$f(Y)$	Constraints		
	y_1	y_2	y_3	y_4	y_5		$0 \leq g_1 \leq 92$	$90 \leq g_2 \leq 110$	$20 \leq g_3 \leq 25$
GRG [8]	78.62	33.44	31.07	44.18	35.22	-30373.95	90.52	NA	20.13
GA [9]	80.39	35.07	32.05	40.33	33.34	-30005.70	91.66	99.53690	20.03
GA-G [10]	80.61	34.21	31.34	42.05	34.85	-30175.80	92.00	NA	20.00
GA-L [10]	81.49	34.09	31.24	42.20	34.37	-30182.27	90.57	NA	20.12
GWO	78.01	33.00	30.0063	45.00	36.7570	-30662.42	92.00	94.91	20.00
Present study	78.00	33.00	30.0468	45.00	36.71	-30653.30	91.99	94.89	20.01

NA: not available.

solution and that the DGWO could provide very competitive results compared to the GWO.

4.7.2. Gear Train Design Problem. The gear train design problem has four integer variables and was initially introduced by Sandgran [59]. The task of solving this problem is to determine the optimal number of teeth of the gearwheel between 12 and 60 to minimize the gear ratio of the gear train displayed in Figure 8. The optimization model of this problem, with the decision vector $Y = [T_d, T_b, T_a, T_f] = [y_1, y_2, y_3, y_4]$, is formulated as follows:

$$\begin{aligned} \text{minimize } f(Y) &= \left(\frac{1}{6.931} - \frac{y_1 y_2}{y_3 y_4} \right)^2, \\ 12 \leq y_1, y_2, y_3, y_4 &\leq 60, y_i \in \mathbb{Z}^+, \end{aligned} \quad (30)$$

where the gear ratio = $y_1 y_2 / y_3 y_4$.

Table 15 shows the optimization results of the best run of the gear train design problem, which is solved by different algorithms and the proposed DGWO algorithm. The statistical results of these algorithms and the results of the GSA-GA and CS algorithms proposed by Gandomi et al. [60] and Garg [61], which are shown in Table 16 with studies [60, 61], conclude that the result proposed by the DGWO algorithm is superior to the results of the two algorithms, and the worst (Worst), mean (Mean), and standard deviation (St. dev.) are low. The results obtained by the DGWO are slightly better than those by the GWO and are significantly better than those reported by different methods in [59–62].

4.7.3. Pressure Vessel Design Problem. In this problem, a cylindrical pressure vessel is mounted on both ends by hemispherical balls, and its cylinder is formulated by combining two longitudinal welds, as described in Figure 9 [63]. The four decision variables, which include the thickness of the pressure vessel (T_s), thickness of the head (T_h), inner radius of the vessel (R), and length of the cylindrical section of the vessel (L), are selected to be optimized to achieve the minimized total cost of the pressure vessel. Therefore, the formulation for this problem consists of four variables $Y = [T_s, T_h, R, L]$, which are modeled as follows:

$$\begin{aligned} \text{minimize } f(Y) &= 0.6224y_1y_3y_4 + 1.7781y_2y_3^2 \\ &\quad + 3.1661y_1^2y_4 + 19.84y_1^2y_3 \\ \text{s.t. } g_1(Y) &= -y_1 + 0.0193y_3 \leq 0 \\ g_2(Y) &= -y_2 + 0.00954y_3 \leq 0 \\ g_3(Y) &= -\pi y_3^2 y_4 - \frac{4}{3} \pi y_3^3 + 1296000 \leq 0 \\ g_4(Y) &= y_4 - 240 \leq 0 \\ 1 \times 0.0625 \leq y_1, y_2 &\leq 99 \times 0.0625 \quad 10 \leq y_3, y_4 \leq 200. \end{aligned} \quad (31)$$

The results obtained for this problem are computed by the proposed DGWO method and are compared with the results of the best run achieved by other algorithms in Table 17. The practical optimization performance of the DGWO algorithm is superior to that of existing approaches but slightly worse than that of the GWO. The statistical results after 30 independent runs are recorded in Table 18, which further validates the finding that the standard deviation of the proposed DGWO method is less than that of other algorithms except for the result reported in [64] and the worst result is better than that of the compared algorithms. In addition, the DGWO could obtain very close best and average results to the GWO and is better than other compared algorithms.

4.8. Several Insights for Applying the DGWO Algorithm. As discussed above, the optimization performance of the DGWO algorithm has been validated on several classical well-known benchmark functions. As seen from Table 3, the different position weight values w_1 and w_2 play an important role in improving the optimization performance of different types of problems. If the objective problems are a kind of unimodal or multimodal problem (such as f_1 – f_{13}), the values of w_1 and w_2 can be 0.1 and 0.9 or 0.3 and 0.7, respectively, and both of these two strategies can obtain relatively high-quality solutions. If the objective problems are a

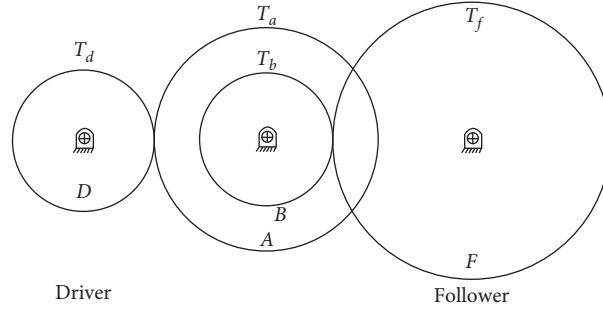


FIGURE 8: Structure of the gear train design problem.

TABLE 15: Comparison results of the best gear train design problem obtained by different algorithms.

Variables	Sandgren [59]	Deb and Goyal [62]	Gandomi et al. [60]	Garg [61]	GWO	Present study
$T_d(y_1)$	18	19	19	19	19	19
$T_b(y_2)$	22	16	16	16	16	16
$T_a(y_3)$	45	49	43	43	43	43
$T_f(y_4)$	60	43	49	49	49	49
Gear ration	0.15	0.14	0.14	0.14	0.14	0.14
$f(Y)$	5.71×10^{-6}	2.70×10^{-12}	2.70×10^{-12}	2.70×10^{-12}	2.70×10^{-12}	2.70×10^{-12}

TABLE 16: Statistical results of different algorithms for the gear train design problem.

Algorithms	Best	Worst	Mean	St. dev.
Gandomi et al. [60]	2.70×10^{-12}	2.36×10^{-9}	1.98×10^{-9}	3.56×10^{-9}
Garg [61]	2.70×10^{-12}	3.30×10^{-9}	1.22×10^{-9}	8.77×10^{-10}
GWO	2.70×10^{-12}	1.36×10^{-9}	6.25×10^{-9}	6.22×10^{-10}
Present study	2.70×10^{-12}	1.36×10^{-9}	5.65×10^{-10}	5.72×10^{-10}

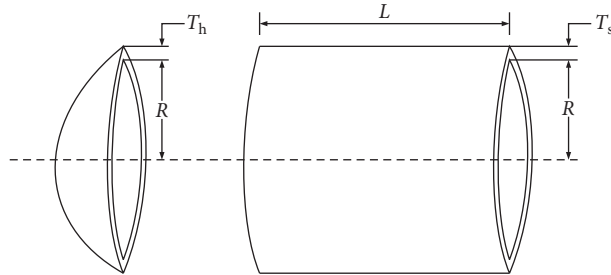


FIGURE 9: Structure of the pressure vessel design problem.

TABLE 17: Comparison results of the best pressure vessel design problem obtained by different algorithms.

Algorithms	Decision variables				Cost $f(Y)$
	y_1	y_2	y_3	y_4	
Sandgren [59]	1.13	0.63	47.70	117.70	8129.10
Kannan and Kramer [63]	1.13	0.63	58.29	43.69	7198.04
Coello [64]	0.81	0.44	40.32	200.00	6288.75
He and Wang [65]	0.81	0.44	42.09	176.75	6061.08
Kaveh and Talatahari [66]	0.81	0.44	42.10	176.57	6059.09
Gandomi et al. [60]	0.81	0.44	42.10	176.64	6059.71
GWO	0.78	0.39	40.36	199.46	5890.18
Present study	0.80	0.40	41.58	183.25	5938.78

kind of fixed-dimension multimodal problem (such as $f_{14}-f_{23}$), $w_1 = 0.1$ and $w_2 = 0.9$ can achieve better results than other position weight values. In addition, from Table 4,

we can observe that the DGWO-1 algorithm, which employed the modified position-updated equation (i.e., equation (26)) and the linear control parameter \vec{a} , can

TABLE 18: Statistical results of different algorithms for the pressure vessel design problem.

Algorithms	Best	Worst	Mean	St. dev.
Sandgren [59]	8129.10	N/A	N/A	N/A
Kannan and Kramer [63]	7198.04	N/A	N/A	N/A
Coello [64]	6288.75	6308.15	6293.84	7.41
He and Wang [65]	6061.08	6363.80	6147.13	86.46
Kaveh and Talatahari [66]	6059.09	6135.33	6075.26	41.68
Gandomi et al. [60]	6059.71	6495.35	6447.74	502.69
GWO	5890.18	6674.46	5938.88	141.64
Present study	5938.78	6113.47	6013.93	85.53

N/A: not available.

provide very competitive results for unimodal and multimodal problems and slightly poorer results on fixed-dimension multimodal problems. Therefore, if the objective problems are unimodal or multimodal problems, the control parameter of the DGWO can adopt both \vec{a} and \vec{a}' ; otherwise, if the objective problems are fixed-dimension multimodal problems, we recommend that the practitioners use the nonlinear control parameter strategy proposed in this paper (i.e., equation (27)).

5. Conclusions

In this paper, an improved version of the GWO (referred to as the DGWO) algorithm is proposed to solve continuous numerical optimization problems. First, the DDS method is introduced into the GWO algorithm to perturb a set of dimensions of the first three best solutions to increase the diversity of a particle and to enhance the exploration ability of the GWO algorithm. This method realizes the predation mode of freely switching between direct encirclement and spiral walking. Second, the position interaction information about the three leaders (i.e., α , β , and δ) in the predation process is further considered, and the position-updated equation that is based on this information is proposed to increase the ability of the GWO algorithm to jump out of the local optimum. Finally, the proposed nonlinear control parameter strategy is designed to enhance the exploitation ability of the GWO algorithm, as well as the convergence precision and convergence rate. Based on the three improvements to the GWO algorithm, the balance between exploration and exploitation, convergence precision, and convergence rate have been enhanced. Twenty-three benchmark test problems, the CEC2014 benchmark suite, and three classic real-world engineering design applications were employed to verify the practical optimization performance of the proposed DGWO technique. First, the experimental results on unimodal functions show the exploitation ability of the DGWO, which helps accelerate the convergence speed and enhance the solution accuracy. Second, the exploration capability of the DGWO was demonstrated by the results on the multimodal functions. Third, the results from fixed-dimension multimodal functions and composite functions show that the DGWO succeeds in jumping out of local optima by balancing the exploration and exploitation. The simulations confirmed that the DGWO could find very competitive optimization

results compared to recent GWO variants and state-of-the-art heuristic algorithms. However, the optimization performance of the DGWO algorithm for Himmelblau's nonlinear engineering design problem is not very competitive but shows excellent results for the gear train design problem and the pressure vessel design problem. Although several experiments have demonstrated that the DGWO is efficient, effective, and robust, it also has several obvious shortcomings, such as the greater number of parameters that need to be adjusted compared with the original GWO algorithm, the poor optimization performance on the complex problems that are included in the CEC2014 suite, and the percentage of problems solved is not 100% guaranteed.

In future works, there are two main aspects that need to be implemented. An interesting research point is to further simplify the spiral walking predation technique and to improve the positional interaction information strategy to propose a variant of the GWO with a simpler algorithm structure and higher optimization performance. In addition, we intend to utilize the proposed DGWO algorithm for solving multiobjective optimization problems and economic load dispatch problems and training neural networks in our future research.

Data Availability

The MATLAB code used to support the findings of this study is available from the corresponding author upon request.

Conflicts of Interest

The authors declare that they have no conflicts of interest.

Acknowledgments

This research was funded in part by the National Natural Science Foundation of China (grant no. 71841054), the Young Innovative Talents Training Program for Universities in Heilongjiang Province (grant no. UNPYSCT-2018151), the Fundamental Research Funds for the Central Universities (grant no. 2572018BM07), the Natural Science Foundation of Heilongjiang Province of China (grant no. LH2019G014), the Postdoctoral Foundation of Heilongjiang Province of China (grant no. LBH-Z18015), and the 2019 Annual Basic Project of the Party's Political Construction Research Center of the Ministry of Industry and Information Technology (grant no. 19GZY411).

References

- [1] I. Boussaïd, J. Lepagnot, and P. Siarry, "A Survey on optimization metaheuristics," *Information Sciences*, vol. 237, pp. 82–117, 2013.
- [2] G. M. Portal, M. Ritt, L. M. Borba, and L. S. Buriol, "Simulated annealing for the machine reassignment problem," *Annals of Operations Research*, vol. 242, no. 1, pp. 93–114, 2016.
- [3] C. D. Tarantilis and C. T. Kiranoudis, "A threshold-accepting metaheuristic method for scheduling the operations of dehydration plants," *Drying Technology*, vol. 20, no. 6, pp. 1143–1160, 2002.
- [4] Z. H. Jia and Y. Liao, "Based on micro canonical annealing and improved FCM algorithm for remote sensing image segmentation," *Laser Journal*, vol. 32, no. 2, pp. 20–21, 2011.
- [5] X. Li, C. Yue, Y. P. Aneja, S. Chen, and Y. Cui, "An iterated tabu search metaheuristic for the regenerator location problem," *Applied Soft Computing*, vol. 70, pp. 182–194, 2018.
- [6] A. Naanaa and S. Belghith, "An efficient guided local search approach for multiuser detection in UWB systems," *Physical Communication*, vol. 26, pp. 141–148, 2018.
- [7] B. A. Tolson and C. A. Shoemaker, "Dynamically dimensioned search algorithm for computationally efficient watershed model calibration," *Water Resources Research*, vol. 43, no. 1, pp. 208–214, 2007.
- [8] S. Kang, S. Lee, and T. Kang, "Development and application of storage-zone decision method for long-term reservoir operation using the dynamically dimensioned search algorithm," *Water Resources Management*, vol. 31, no. 1, pp. 219–232, 2017.
- [9] F.-R. Lin, N.-J. Wu, C.-H. Tu, and T.-K. Tsay, "Automatic calibration of an unsteady river flow model by using dynamically dimensioned search algorithm," *Mathematical Problems in Engineering*, vol. 2017, Article ID 7919324, 19 pages, 2017.
- [10] B. A. Tolson, M. Asadzadeh, H. R. Maier, and A. Zecchin, "Hybrid discrete dynamically dimensioned search (HD-DDS) algorithm for water distribution system design optimization," *Water Resources Research*, vol. 45, no. 12, 2009.
- [11] J. Xu, F. Yan, K. Yun, S. Ronald, F. Li, and J. Guan, "Dynamically dimensioned search embedded with piecewise opposition-based learning for global optimization," *Scientific Programming*, vol. 2019, Article ID 2401818, 20 pages, 2019.
- [12] C. Lu, L. Gao, and J. Yi, "Grey wolf optimizer with cellular topological structure," *Expert Systems With Applications*, vol. 107, pp. 89–114, 2018.
- [13] J. R. Fernández, J. A. López-Campos, A. Segade, and J. A. Vilán, "A genetic algorithm for the characterization of hyperelastic materials," *Applied Mathematics and Computation*, vol. 329, pp. 239–250, 2018.
- [14] F. Vesting and R. E. Bensow, "Particle swarm optimization: an alternative in marine propeller optimization?," *Engineering Optimization*, vol. 50, no. 1, pp. 70–88, 2018.
- [15] E. G. Martinez-Soltero and J. Hernandez-Barragan, "Robot navigation based on differential evolution," *IFAC-PapersOnLine*, vol. 51, no. 13, pp. 350–354, 2018.
- [16] J. Xu and F. Yan, "Hybrid Nelder–Mead algorithm and Dragonfly algorithm for function optimization and the training of a multilayer perceptron," *Arabian Journal for Science and Engineering*, vol. 44, no. 4, pp. 3473–3487, 2019.
- [17] D. R. Edla, A. Lipare, and R. Cheruku, "Shuffled complex evolution approach for load balancing of gateways in wireless sensor networks," *Wireless Personal Communications*, vol. 98, no. 4, pp. 3455–3476, 2018.
- [18] S. Gholizadeh and H. Poorhoseini, "Optimum design of steel frame structures by a modified dolphin echolocation algorithm," *Structural Engineering and Mechanics*, vol. 55, no. 3, pp. 535–554, 2015.
- [19] S. Gholizadeh and A. M. Shahrezaei, "Optimal placement of steel plate shear walls for steel frames by bat algorithm," *The Structural Design of Tall and Special Buildings*, vol. 24, no. 1, pp. 1–18, 2015.
- [20] H. Sajedi, "Image steganalysis using artificial bee colony algorithm," *Journal of Experimental & Theoretical Artificial Intelligence*, vol. 29, no. 5, pp. 949–966, 2017.
- [21] X. Song, L. Tang, S. Zhao et al., "Grey wolf optimizer for parameter estimation in surface waves," *Soil Dynamics and Earthquake Engineering*, vol. 75, pp. 147–157, 2015.
- [22] S. Mirjalili, S. M. Mirjalili, and A. Lewis, "Grey wolf optimizer," *Advances in Engineering Software*, vol. 69, pp. 46–61, 2014.
- [23] S. Gupta and K. Deep, "A novel random walk grey wolf optimizer," *Swarm and Evolutionary Computation*, vol. 44, pp. 101–112, 2019.
- [24] M. A. Al-Betar, M. A. Awadallah, H. Faris, I. Aljarah, and A. I. Hammouri, "Natural selection methods for grey wolf optimizer," *Expert Systems With Applications*, vol. 113, pp. 481–498, 2018.
- [25] H. Faris, I. Aljarah, M. A. Al-Betar, and S. Mirjalili, "Grey wolf optimizer: a review of recent variants and applications," *Neural Computing and Applications*, vol. 30, no. 2, pp. 413–435, 2018.
- [26] N. Mittal, U. Singh, and B. S. Sohi, "Modified grey wolf optimizer for global engineering optimization," *Applied Computational Intelligence and Soft Computing*, vol. 2016, Article ID 7950348, 16 pages, 2016.
- [27] A. Kishor and P. K. Singh, "Empirical study of grey wolf optimizer," Edited by M. Pant, K. Deep, J. Bansal, A. Nagar, and K. Das, Eds., in *Proceedings of Fifth International Conference on Soft Computing for Problem Solving*, vol. 436, pp. 1037–1049, Springer, Singapore, 2015.
- [28] Q. Luo, S. Zhang, Z. Li, and Y. Zhou, "A novel complex-valued encoding grey wolf optimization algorithm," *Algorithms*, vol. 9, no. 1, pp. 1–23, 2015.
- [29] B. Yang, X. Zhang, T. Yu, H. Shu, and Z. Fang, "Grouped grey wolf optimizer for maximum power point tracking of doubly-fed induction generator based wind turbine," *Energy Conversion and Management*, vol. 133, pp. 427–443, 2017.
- [30] J. Xu, F. Yan, O. Grace Ala, L. Su, and F. Li, "Chaotic dynamic weight grey wolf optimizer for numerical function optimization," *Journal of Intelligent & Fuzzy Systems*, vol. 37, no. 2, pp. 2367–2384, 2019.
- [31] Z.-M. Gao and J. Zhao, "An improved grey wolf optimization algorithm with variable weights," *Computational Intelligence & Neuroscience*, vol. 2019, Article ID 2981282, 13 pages, 2019.
- [32] G. M. Komaki and V. Kayvanfar, "Grey wolf optimizer algorithm for the two-stage assembly flow shop scheduling problem with release time," *Journal of Computational Science*, vol. 8, pp. 109–120, 2015.
- [33] E. Emary, H. M. Zawbaa, C. Grosan, and A. E. Hassenian, "Feature subset selection approach by gray-wolf optimization," *Advances in Intelligent Systems and Computing*, vol. 334, pp. 1–13, 2015.
- [34] S. Mirjalili, "How effective is the grey wolf optimizer in training multi-layer perceptrons," *Applied Intelligence*, vol. 43, no. 1, pp. 150–161, 2015.
- [35] S. A. Bessedik, R. Djekidel, and A. Ameer, "Performance of different kernel functions for LS-SVM-GWO to estimate

- flashover voltage of polluted insulators,” *IET Science, Measurement & Technology*, vol. 12, no. 6, pp. 739–745, 2018.
- [36] V. Kumar, J. K. Chhabra, and D. Kumar, “Grey wolf algorithm based clustering technique,” *Journal of Intelligent Systems*, vol. 26, no. 1, pp. 153–168, 2017.
- [37] J. Xu, F. Yan, K. Yun, L. Su, F. Li, and J. Guan, “Noninferior solution grey wolf optimizer with an independent local search mechanism for solving economic load dispatch problems,” *Energies*, vol. 12, no. 12, p. 2274, 2019.
- [38] S. Zhang, Y. Zhou, Z. Li, and W. Pan, “Grey wolf optimizer for unmanned combat aerial vehicle path planning,” *Advances in Engineering Software*, vol. 99, pp. 121–136, 2016.
- [39] P.-W. Tsai, T.-T. Nguyen, and T.-K. Dao, “Robot path planning optimization based on multiobjective grey wolf optimizer,” *Advances in Intelligent Systems and Computing*, vol. 536, pp. 166–173, 2017.
- [40] J. Sujitha and K. Baskaran, “Genetic grey wolf optimizer based channel estimation in wireless communication system,” *Wireless Personal Communications*, vol. 99, no. 2, pp. 965–984, 2018.
- [41] B. Y. Qu, J. J. Liang, Z. Y. Wang, Q. Chen, and P. N. Suganthan, “Novel benchmark functions for continuous multimodal optimization with comparative results,” *Swarm and Evolutionary Computation*, vol. 26, pp. 23–34, 2016.
- [42] W. Long, J. Jiao, X. Liang, and M. Tang, “An exploration-enhanced grey wolf optimizer to solve high-dimensional numerical optimization,” *Engineering Applications of Artificial Intelligence*, vol. 68, pp. 63–80, 2018.
- [43] M. J. F. G. Macêdo, M. F. P. Costa, A. M. A. C. Rocha, and E. W. Karas, “Combining filter method and dynamically dimensioned search for constrained global optimization,” in *Computational Science and Its Applications—ICCSA*, pp. 119–134, 2017.
- [44] S. Mirjalili and A. Lewis, “The whale optimization algorithm,” *Advances in Engineering Software*, vol. 95, pp. 51–67, 2016.
- [45] J. Zhang, “Optimal control problem of converter steelmaking production process based on operation optimization method,” *Discrete Dynamics in Nature and Society*, vol. 2015, Article ID 483674, 13 pages, 2015.
- [46] J. Derrac, S. García, D. Molina, and F. Herrera, “A practical tutorial on the use of nonparametric statistical tests as a methodology for comparing evolutionary and swarm intelligence algorithms,” *Swarm and Evolutionary Computation*, vol. 1, no. 1, pp. 3–18, 2011.
- [47] S. Saremi, S. Z. Mirjalili, and S. M. Mirjalili, “Evolutionary population dynamics and grey wolf optimizer,” *Neural Computing and Applications*, vol. 26, no. 5, pp. 1257–1263, 2015.
- [48] S. Mirjalili, A. Lewis, and A. S. Sadiq, “Autonomous particles groups for particle swarm optimization,” *Arabian Journal for Science and Engineering*, vol. 39, no. 6, pp. 4683–4697, 2014.
- [49] Z. Cui, J. Zeng, and Y. Yin, “An improved PSO with time-varying accelerator coefficients,” in *Proceedings of the Eighth International Conference on Intelligent Systems Design and Applications*, pp. 638–643, Kaohsiung, Taiwan, November 2008.
- [50] G. Q. Bao and K. F. Mao, “Particle swarm optimization algorithm with asymmetric time varying acceleration coefficients,” in *Proceedings of the IEEE International Conference on Robotics and Biomimetics*, pp. 2134–2139, Guilin, China, December 2009.
- [51] T. Ziyu and Z. Dingxue, “A modified particle swarm optimization with an adaptive acceleration coefficients,” in *Proceedings of the Asia-Pacific Conference on Information Processing*, pp. 330–332, Shenzhen, China, July 2009.
- [52] W. Gong, Z. Cai, and C. X. Ling, “DE/BBO: A hybrid differential evolution with biogeography-based optimization for global numerical optimization,” *Soft Computing*, vol. 15, no. 4, pp. 645–665, 2010.
- [53] M. M. Mafarja and S. Mirjalili, “Hybrid whale optimization algorithm with simulated annealing for feature selection,” *Neurocomputing*, vol. 260, pp. 302–312, 2017.
- [54] S. Mirjalili, A. H. Gandomi, S. Z. Mirjalili, S. Saremi, H. Faris, and S. M. Mirjalili, “Salp swarm algorithm: a bio-inspired optimizer for engineering design problems,” *Advances in Engineering Software*, vol. 114, pp. 163–191, 2017.
- [55] A.-q. Xing, “Applications of the penalty function method in constrained optimal control problems,” *Journal of Applied Mathematics and Simulation*, vol. 2, no. 4, pp. 251–265, 1989.
- [56] D. M. Himmelblau, *Applied Nonlinear Programming*, McGraw-Hill, New York, NY, USA, 1972.
- [57] H. Garg, “Solving structural engineering design optimization problems using an artificial bee colony algorithm,” *Journal of Industrial and Management Optimization*, vol. 10, no. 3, pp. 777–794, 2013.
- [58] H. Abdollah, X. Q. Charlene, and H. L. Steven, “Constrained optimization via genetic algorithms,” *Simulation*, vol. 62, no. 4, pp. 242–254, 1994.
- [59] E. Sandgren, “Nonlinear integer and discrete programming in mechanical design optimization,” *Journal of Mechanical Design*, vol. 112, no. 2, pp. 223–229, 1990.
- [60] A. H. Gandomi, X.-S. Yang, and A. H. Alavi, “Cuckoo search algorithm: a metaheuristic approach to solve structural optimization problems,” *Engineering with Computers*, vol. 29, no. 1, pp. 17–35, 2013.
- [61] H. Garg, “A hybrid GSA-GA algorithm for constrained optimization problems,” *Information Sciences*, vol. 478, pp. 499–523, 2019.
- [62] K. Deb and M. Goyal, “A combined genetic adaptive search (GeneAS) for engineering design,” *Computer Science and Informatics*, vol. 26, no. 4, pp. 30–45, 1996.
- [63] B. K. Kannan and S. N. Kramer, “An augmented Lagrange multiplier based method for mixed integer discrete continuous optimization and its applications to mechanical design,” *Journal of Mechanical Design*, vol. 116, no. 2, pp. 318–320, 1994.
- [64] C. A. C. Coello, “Use of a self-adaptive penalty approach for engineering optimization problems,” *Computers in Industry*, vol. 41, no. 2, pp. 113–127, 2000.
- [65] Q. He and L. Wang, “An effective co-evolutionary particle swarm optimization for constrained engineering design problems,” *Engineering Applications of Artificial Intelligence*, vol. 20, no. 1, pp. 89–99, 2007.
- [66] A. Kaveh and S. Talatahari, “Engineering optimization with hybrid particle swarm and ant colony optimization,” *Asian Journal of Civil Engineering*, vol. 10, pp. 611–628, 2009.

Research Article

Simulation Modeling of a Pharmaceutical Tablet Manufacturing Process via Wet Granulation

Zhongsong Wang ¹, Zhen Pan,¹ Dakuo He ^{1,2}, Jiahui Shi,¹ Shouxin Sun,³ and Yue Hou⁴

¹College of Information Science and Engineering, Northeastern University, Shenyang 110004, Liaoning, China

²State Key Laboratory of Synthetical Automation for Process Industries, Northeastern University, Shenyang 110004, China

³H3C Technologies Co., Limited, Beijing 100102, China

⁴College of Life and Health Sciences, Northeastern University, Shenyang 110169, China

Correspondence should be addressed to Dakuo He; hedakuo@ise.neu.edu.cn

Received 14 August 2019; Revised 4 November 2019; Accepted 14 November 2019; Published 30 November 2019

Guest Editor: Raúl Baños

Copyright © 2019 Zhongsong Wang et al. This is an open access article distributed under the Creative Commons Attribution License, which permits unrestricted use, distribution, and reproduction in any medium, provided the original work is properly cited.

The pharmaceutical tablet manufacturing process (PTMP) via wet granulation holds a critical position in pharmaceutical industry. The interest in integrating mechanistic process modeling into the pharmaceutical development has been increased because simulation model is a prerequisite for process design, analysis, control, and optimization. So the simulation modeling for PTMP via wet granulation is very necessary and significant. This study aims at proposing a simulation modeling framework for PTMP via spray fluidized bed granulation (SFBG), which is one of the most widely used wet granulation techniques in pharmaceutical industry. For SFBG, a simulation model that simultaneously involves the influences of operating variables and material attributes on average particle size (APS) is firstly developed, and then a drying model to determine the particle moisture content is introduced to be coupled with the established model predicting APS. For PTMP, considering the important effect of porosity on tablet qualities, a model describing the changes in tablet porosity is developed based on a promoted form of the Heckel equation, and then several recognized models that are all related to porosity are introduced or constructed to calculate important tablet quality indexes. The feasibility and effectiveness of the developed simulation models are validated by performing a computational experimental study to explore the scientific understanding of process and process quality control.

1. Introduction

Oral dosage forms, such as tablets, account for the most popular drug delivery systems for treating patients today [1–3]. So a pharmaceutical tablet manufacturing process (PTMP) holds a critical position in pharmaceutical industry. It is well known that tablet manufacturing via wet granulation is the most common processing route and mainly consists of several consecutive steps, including mixing, wet granulation, drying of wet granules, milling (if necessary), and tableting [4–6]. The spray fluidized bed granulation (SFBG) is one of the most widely used wet granulation techniques in pharmaceutical industry since the mixing, granulation, and drying of the granules can be achieved in a single operation [7].

Simulation model is a prerequisite for the design, analysis, control, and optimization of processes [5], and the pharmaceutical industry is showing increasing interest in integrating mechanistic process modeling into the workflow of pharmaceutical development, which is mainly motivated not only by quality and cost concerns but also by the need to improve understanding of the influence of materials and processes on the final product [8]. First of all, mechanistic simulation models can in fact be used for increasing scientific understanding by summarizing available process knowledge which would help to understand the influence of input variables on the pharmaceutical process and the product quality [4, 8]. Secondly, the models can also be used to explore a design space or develop control strategies during pharmaceutical development, and an advantage of using

models is their solution speed, allowing to compute many different scenarios as opposed to performing expensive experiments [4, 8, 9]. Furthermore, simulation modeling is also an important segment of Quality by Design [9]. Therefore, the simulation modeling for SFBG-based PTMP is of great significance both theoretically and practically.

In the SFBG-based PTMP, although some of the unit operations considered can be run continuously and also growing attention has been paid to continuous manufacturing, they are still operated in a batchwise manner due to the presence of intermediate bulk mixing steps [8]. Additionally, with the introduction and development of Industry 4.0 and intelligent manufacturing, product customization will be an inevitable trend in the future, with applications such as drug customization, which further reinforces the importance of batch processes in the pharmaceutical industry especially in small batch drug customization. Consequently, the simulation modeling for SFBG-based PTMP operated in a batchwise manner is necessary. However, to the authors' knowledge, research studies on simulation modeling for such an integrated process, i.e., PTMP via wet granulation, are very limited and mainly focused on continuous tablet manufacturing [5, 10]. And even few studies have been reported in the simulation modeling for SFBG-based PTMP. Furthermore, SFBG is a complicated process influenced by both the material- and process-related factors, but not much attention has been paid to the modeling considering material attributes except for Hussain's work [11, 12], in which the effects of process parameters and material attributes are modeled in the kernel. However, the limitation of this model is that it contains only one critical operating variable.

The primary aim of the present study is to develop a simulation modeling framework which can link the key operating variables and material attributes with the properties of granules or tablets to predict the granulation and tableting behavior in the SFBG-based PTMP. The contributions and limitation are listed as follows:

- (i) A simulation model for SFBG, which simultaneously involves the influences of operating variables and material attributes on a key quality index, i.e., average particle size (APS), is developed using population balance model (PBM), in which a Hussain's aggregate kernel [11, 12] and a Walzel's model [13, 14] are applied to, respectively, introduce the material attributes and the critical operating variables into modeling framework.
- (ii) A drying model to determine the particle moisture content (another critical particle quality significantly affecting tableting) [15] is introduced to be coupled with the established PBM predicting APS, so that the simulation model for a multiple-input multiple-output SFBG is developed.
- (iii) Considering the important effect of porosity on tablet quality, a model describing the change in tablet porosity is developed based on a promoted form of the Heckel equation, in which several empirical models for state variables such as initial

porosity and punch pressure are constructed according to the widely accepted analysis and conclusions in the field, and then the model parameters are identified using experimental data from the literature. Following the porosity model, several recognized models relating to porosity are introduced or constructed to calculate important tablet quality indexes, such as tensile strength, hardness, disintegration time, and dissolution rate so that the simulation modeling for tableting is achieved.

- (iv) The simulation modeling for a SFBG-based PTMP is developed by integrating the models of SFBG and tableting. And then a computational experimental study is carried out by exploring the scientific understanding of process and process quality control to validate the feasibility and effectiveness of the simulation models. But this work is limited to a simulation study and lacks validation based on actual process data. Therefore, this paper only puts forward a preliminary simulation modeling framework. Once the actual experimental data are available in the future studies, the modeling framework can be identified and validated with the actual process data to make it practical for simulation, which is important for intending to use the models as a tool for the pharmaceutical Quality by Design.

The remainder of this paper is arranged as follows. Section 2 gives the process description of SFBG-based PTMP. In Section 3, the simulation models for SFBG-based PTMP are, respectively, developed. In Section 4, the computational experimental study is performed to verify the feasibility and effectiveness of simulation models, and then the results and discussions are given. Section 5 concludes this paper.

2. Process Description

As shown in Figure 1, a typical PTMP via wet granulation can be subdivided into a number of stages [4, 5]: (1) mixing/blending, in which the active pharmaceutical ingredients (APIs) are mixed with excipients in a certain ratio; (2) wet granulation, in which the particles are consolidated into granules to obtain a desirable size distribution, improve powder flow properties, reduce the dust formation, promote the compressibility, and so on; (3) drying of wet granules, in which the wet granules are dried to the desired moisture content level that is suitable for tableting; (4) milling (if necessary), in which the lumps or oversized granules formed during the wet granulation are broken; (5) tableting, in which the granules are compressed into a solid tablet by mechanical means; and (6) coating (if necessary), in which the tablet is covered with a thin layer of polymer.

2.1. Spray Fluidized Bed Granulation. SFBG is a well-known process that forms particles into larger granules by spraying a binder solution onto fluidized particles with a spray nozzle

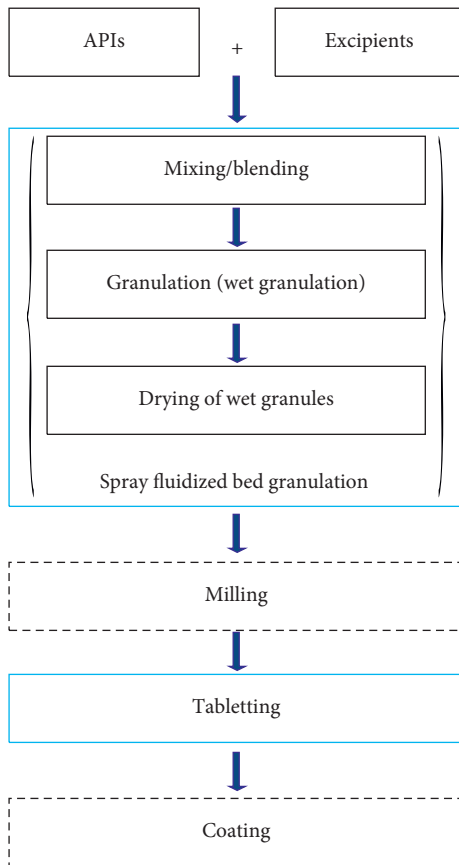


FIGURE 1: Schematic diagram of typical PTMP via wet granulation.

at the top of the fluidized bed. Since the mixing, granulation, and drying of the granules can be achieved in a single operation (Figure 1), which helps avoid transfer losses, enables dust containment, and saves labor costs and time, SFBG is thus widely used in pharmaceutical industry [7, 16, 17].

The overall granulation process in a top-spray fluidized bed granulator shown in Figure 2 is divided into three stages. Initially, in order to sufficiently blend materials, the powder particles circulate within granulator by pumping fluidizing air from a distributor at the bottom of the fluidized bed. Next, liquid binder is atomized into fine droplets by atomizing air and then sprayed onto fluidized bed. The droplets are dispersed over the surface of fluidized particles, which contributes to the agglomeration of surface-wetted particles to form granules. During granulation, the particle size increases due to agglomeration. Lastly, the final granules are dried to a predetermined moisture content level by continuously pumping fluidizing air into the bed.

SFBG is a complicated process influenced by both the material- and process-related factors [17–19]. The material-related factors include wetting properties of solid particles and its solubility, load and micrometric properties of powder, and properties of binding agents, and among them, the important material attributes affecting SFBG consist of primary particle size, particle density, binder viscosity, and

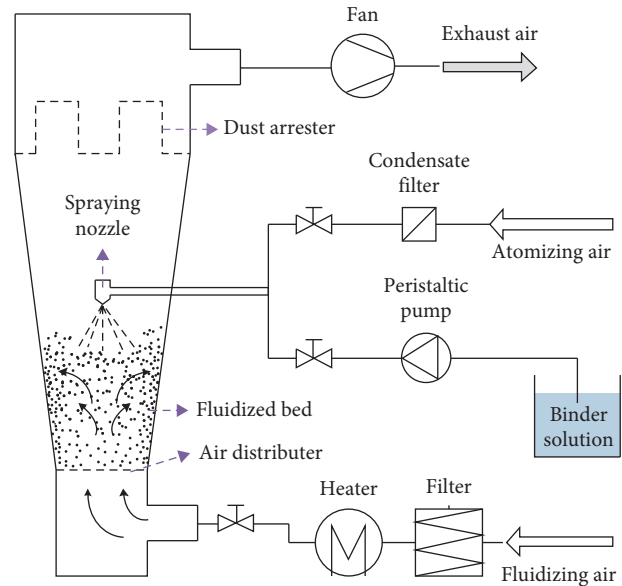


FIGURE 2: Schematic diagram of a top-spray fluidized bed granulator.

so forth [20–23]. Among many process-related factors, such as the geometry of granulator chamber, airflow rate, and inlet air temperature, it has been found that the particle quality changes remarkably due to variations in the operating conditions of binder solution spray, including binder feed rate and atomizing air pressure [17, 19]. Particle quality can be evaluated by many factors, and among them, APS is the key factor to be controlled [17, 18]. Additionally, moisture content is another important particle quality index because of its influences on tableting.

2.2. Tableting Process. Tableting on rotary tablet presses, where the powder material is compressed into tablets in a die between rigid punches, is widely used in pharmaceutical industry [1, 3]. The schematic diagram of a rotary tablet press is shown in Figure 3. The central part of a rotary press is the turret (or die table) which is equipped with a number of tool stations consisting of upper punch-die-lower punch assemblies, and each station passes successively through the following mechanisms as the die table rotates [3]:

- (1) Feed frame, where the powder is introduced into the die
- (2) Precompression and main compression, where the powder is compressed into a tablet
- (3) Ejection cam, where the tablet is ejected from the die

The rotary tablet presses have many adjustable process parameters affecting the tablet properties, and among them, the most important ones during compression include turret speed, rolling reduction, and compression pressure [3]. Additionally, it is reported that the critical quality attributes of tablets can be represented by the properties of tensile strength, hardness, disintegration time, and dissolution rate [24–26].

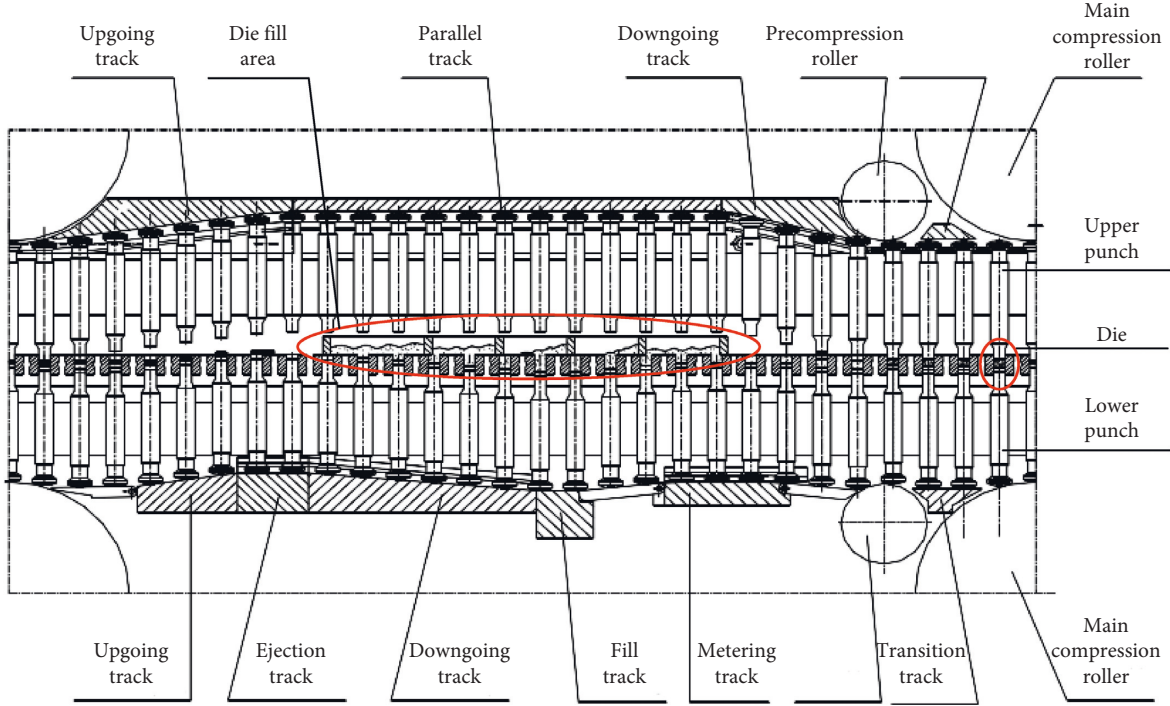


FIGURE 3: Schematic diagram of unfolded view of a rotary tablet press.

3. Simulation Modeling for SFBG-Based PTMP

The process to be modeled is comprised of SFBG and tableting in series, and the models should be connected so that a change in materials or operating conditions can be related to intermediate and final product attributes. Figure 4 gives the framework overview of simulation modeling for SFBG-based PTMP.

3.1. Simulation Modeling for SFBG

3.1.1. The Model Predicting APS. In this subsection, a simulation model which simultaneously links the operating variables, including binder feed rate and atomizing air pressure, and material attributes such as binder viscosity, particle density, and primary particle size with the APS is developed using PBM. Population balance is simply a number balance around each size fraction of particle size distribution based on number conservation law, and it describes the change rate of number of particles entering and leaving that size interval by different occurring phenomena within a granulation system, such as nucleation, aggregation, and breakage [27]. But many studies paid attention to pure agglomeration and ignored other mechanisms when constructing PBM framework [11, 12, 28–31]. Pure agglomeration is not only considered for simplicity but also justified for SFBG because raw materials and operating conditions, in the practical application, are chosen as to avoid other mechanisms [31].

The discrete form of a general one-dimensional and length-based PBM for pure agglomeration is given by [32, 33]

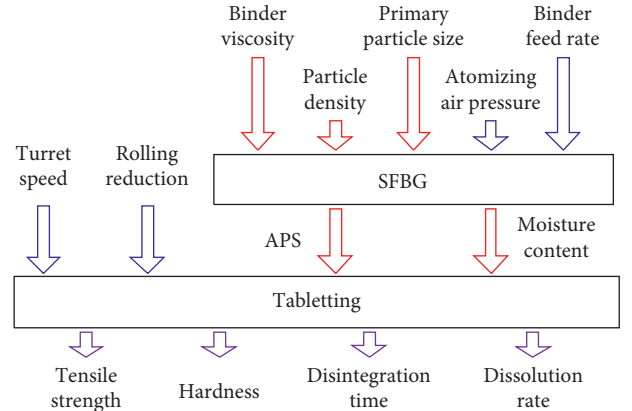


FIGURE 4: The framework overview of simulation modeling for SFBG-based PTMP.

$$\frac{dN_i}{dt} = \sum_{j=1}^{i-2} 2^{j-i+1} \beta_{i-1,j} N_{i-1} N_j + \frac{1}{2} \beta_{i-1,i-1} N_{i-1}^2 - N_i \sum_{j=1}^{i-1} 2^{j-i} \beta_{i,j} N_j - N_i \sum_{j=i}^{n_{\max}} \beta_{i,j} N_j, \quad (1)$$

where N_i is the number of particles within particle size interval (L_i, L_{i+1}) , L_i and L_{i+1} are the lower and upper limits of i -th size interval with a geometric ratio of $L_{i+1}/L_i = \sqrt[3]{2}$ and the particle size in i -th size interval is represented by the left edge L_i , n_{\max} is the number of size intervals, and $\beta_{i,j}$ is the aggregation kernel between particles from i -th and j -th size intervals.

The aggregation model $\beta(t, l, \delta)$ can be generally formulated as [11, 17]

$$\beta(t, l, \delta) = \beta_0(t)\beta^*(l, \delta), \quad (2)$$

where β_0 is the aggregation rate constant which depends on the time, operating conditions, and material attributes except particle size, $\beta^*(l, \delta)$ reflects the influence of particle size on the probability of aggregation between particles with different diameters of l and δ , and $\beta^*(l, \delta)$ is set as a shear form [17]:

$$\beta^*(l, \delta) = (l + \delta)^3, \quad (3)$$

and β_0 is given by [11, 12]

$$\beta_0 = \frac{\psi f_c N_{\text{wet}}}{N_{\text{tot}}^2} \left(\frac{2(N_{\text{tot}} - N_{\text{wet}})}{N_{\text{tot}} - 1} \eta_{\text{wd}} + \frac{N_{\text{wet}} - 1}{N_{\text{tot}} - 1} \eta_{\text{ww}} \right). \quad (4)$$

Here, f_c is the collision frequency per particle which should be given in advance; N_{tot} is the total number of particles in the granulation system; N_{wet} is the number of wet particles; ψ is the success factor concerning the dissipation of kinetic energy according to Stokes criterion [34]; η_{wd} is the probability of collision at wet parts in a wet-dry collision; and η_{ww} is the probability of collision at wet parts in a wet-wet collision.

By substituting (3) and (4) into (1), we have

$$\begin{aligned} \frac{dN_i}{dt} = & \frac{\psi f_c N_{\text{wet}}}{N_{\text{tot}}^2} \left(\frac{2(N_{\text{tot}} - N_{\text{wet}})}{N_{\text{tot}} - 1} \eta_{\text{wd}} + \frac{N_{\text{wet}} - 1}{N_{\text{tot}} - 1} \eta_{\text{ww}} \right) \\ & \times \left(\sum_{j=1}^{i-2} 2^{j-i+1} (L_{i-1} + L_j)^3 N_{i-1} N_j + 4L_{i-1}^3 N_{i-1}^2 \right. \\ & \left. - N_i \sum_{j=1}^{i-1} 2^{j-i} (L_i + L_j)^3 N_j - N_i \sum_{j=i}^{n_{\text{max}}} (L_i + L_j)^3 N_j \right), \end{aligned} \quad (5)$$

where L_i and L_j represent the particle sizes in i -th and j -th size interval, respectively.

Then, N_{tot} and N_{wet} can be modeled as [11, 12]

$$\begin{aligned} \frac{dN_{\text{tot}}}{dt} = & \frac{f_c \psi N_{\text{tot}}}{2} \left(\frac{2(N_{\text{tot}} - N_{\text{wet}})}{N_{\text{tot}} - 1} \eta_{\text{wd}} + \frac{N_{\text{wet}} - 1}{N_{\text{tot}} - 1} \eta_{\text{ww}} \right), \\ \frac{dN_{\text{wet}}}{dt} = & \dot{N}_{\text{drop}} - N_{\text{wet}} \left(\psi f_c \left(\eta_{\text{wd}} - (\eta_{\text{wd}} - \eta_{\text{ww}}) \left(\frac{N_{\text{wet}} - 1}{N_{\text{tot}} - 1} \right) \right) \right. \\ & \left. + \left(1 - \frac{t_{\text{dry}}}{t_g} \right) \frac{N_{\text{wet}}}{\dot{N}_{\text{drop}} t_{\text{dry}}^2} \right), \end{aligned} \quad (6)$$

where \dot{N}_{drop} is the number addition rate of binder droplets and t_{dry} and t_g are the mean drying time of a binder droplet and the granulation time, respectively. Besides, ψ is determined by Stokes criterion [34, 35]:

$$\begin{aligned} \text{St}_{\text{coal}} = & \frac{4\rho_p u_c d_p}{9\mu_b}, \\ \text{St}_{\text{coal}}^{\text{crit}} = & \left(1 + \frac{1}{e} \right) \ln \left(\frac{h}{h_a} \right). \end{aligned} \quad (7)$$

If $\text{St}_{\text{coal}} < \text{St}_{\text{coal}}^{\text{crit}}$, then $\psi = 1$, which reveals that the colliding particles are merged to form one agglomerate. Otherwise, $\psi = 0$. Here, ρ_p and d_p are the particle density and APS during granulation, respectively; μ_b is the binder viscosity. Refer to [12, 36] for the other parameters; they will not be covered here.

The above discussions clearly indicate that the material attributes including binder viscosity, particle density, and primary particle size (primary particle size is a necessary initial condition for solving PBM) are involved in modeling framework. But the current model has only one operating variable, \dot{N}_{drop} . Therefore, by introducing a Walzel's model described in the following equation [13, 14], in which binder feed rate and atomizing air pressure are used to predict binder droplet size, the operating variables of binder feed rate and atomizing air pressure can be introduced into modeling framework.

$$d_{\text{drop}} = \frac{0.35 d_{\text{noz}} (P_{\text{air}} d_{\text{noz}})^{-0.4}}{\left(\sigma \left(1 + (\dot{M}_{\text{liq}} / \dot{M}_{\text{air}}) \right)^2 \right)^{-0.4} \left(1 + \left(2.5 \mu_b / (\sigma \rho_{\text{liq}} d_{\text{noz}})^{0.5} \right) \right)}, \quad (8)$$

where d_{drop} is the diameter of binder droplet, d_{noz} is the diameter of spray nozzle, σ is the surface tension of binder solution, P_{air} is the atomizing air pressure, \dot{M}_{liq} is the binder feed rate, \dot{M}_{air} is the atomizing air flow rate, and ρ_{liq} is the density of binder solution. Then, \dot{N}_{drop} can be expressed as

$$\dot{N}_{\text{drop}} = \frac{\dot{M}_{\text{liq}}}{\rho_{\text{liq}} V_{\text{drop}}} = \frac{6 \dot{M}_{\text{liq}}}{\rho_{\text{liq}} \pi d_{\text{drop}}^3}. \quad (9)$$

Because the above PBM is built based on a discrete calculation method, and in order to facilitate the coupling of this model with the model predicting moisture content, the SFBG is discrete into multiple stages and the schematic diagram of simulation modeling for a segmented SFBG is shown in Figure 5. The PBM is solved by "ode45" in MATLAB to obtain the number of final particles in i -th size interval at m -th stage, $N_{f,i,m}$, where $i = 1, 2, \dots, n_{\text{max}}$, $m = 1, 2, \dots, n_s$. Then, the APS of final granules at m -th stage is calculated by

$$d_{p,m} = \sum_{i=1}^{n_{\text{max}}} V(N_{f,i,m}) d_{\text{gm},i}, \quad (10)$$

where $V(N_{f,i,m})$ is the volume fraction of end particles in i -th size interval at m -th stage and $d_{\text{gm},i}$ is the geometric mean of lower limit and upper limit of i -th size interval. By taking $d_{p,0}$ as the initial APS and solving PBM n_s times according to the sequence shown in Figure 5, the final APS, d_{p,n_s} , can be calculated by (10).

3.1.2. The Model of Moisture Content and Its Coupling with the Model Predicting APS. The focus of this subsection is on the introduction of a drying model that determines the particle moisture content and its coupling with the above-described PBM predicting APS. The basis of their coupling is the commonality in a discrete calculation method, by which the SFBG process is discrete into multiple stages in series.

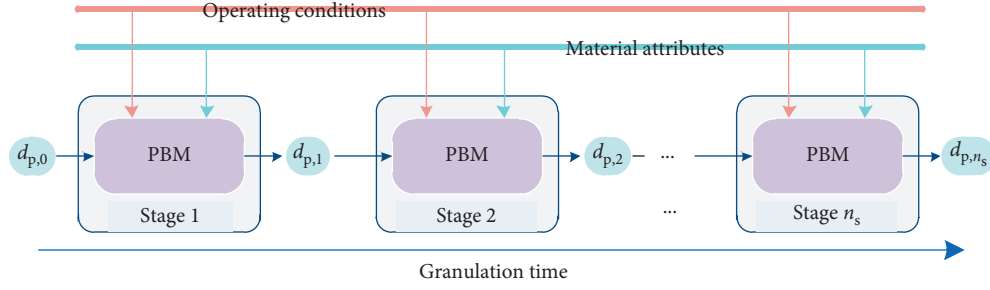


FIGURE 5: Schematic diagram of the simulation modeling for a segmented SFBG.

Next, we first briefly introduce the drying model, and for its detailed derivations, refer to [15].

The following formula can be used to evaluate the mean moisture content,

$$X_{mc} = \frac{M_w}{M_{s,dry}}, \quad (11)$$

of the solid, i.e., water mass M_w per mass of dry solid $M_{s,dry}$.

The drying of droplets can be expressed by the mass balance as follows:

$$\frac{dM_{drop}}{dt} = -\dot{M}_{evap} \approx \frac{\Delta M_{drop}}{\Delta t}, \quad (12)$$

with the kinetics,

$$\dot{M}_{evap} = \rho_g k_{mt} A_{drop} (Y_{sat} - Y_{out}), \quad (13)$$

where Y_{sat} and Y_{out} are the adiabatic saturation moisture content and the steady-state moisture content of the gas phase, respectively, and ρ_g is the gas density. (Y_{sat}) can be calculated by [37]

$$Y_{sat} = 0.622 \frac{p_{sat}}{P_t - p_{sat}}, \quad (14)$$

where P_t is the total pressure of wet air and p_{sat} is the saturation vapour pressure and can be obtained from the Antoine equation which links p_{sat} to the bed temperature T_{bed} . The expression Y_{out} can be calculated by assuming maximum evaporation of liquid (\dot{M}_{liq}) added via the nozzle:

$$Y_{out} = Y_{in} + \frac{\dot{M}_{liq}}{\dot{M}_g} (1 - w_b), \quad (15)$$

where Y_{in} is the inlet moisture content, \dot{M}_{liq} and \dot{M}_g are the mass flows of binder liquid and gas, respectively, and w_b is the solid mass fraction of the binder liquid. The mass transfer coefficient can be computed as

$$k_{mc} = \frac{S_h \delta_{wg}}{d_p}, \quad (16)$$

where S_h is the dimensionless Sherwood number, δ_{wg} is the diffusion coefficient of water in gas, and d_p is the primary particle diameter. The total evaporation of water per time step i is a cumulative measure of all liquid droplets j being present:

$$\Delta M_{w,i} = \sum_{j=1}^{N_{drop}} M_{evap,j} \Delta t_i. \quad (17)$$

The water mass carried by the particles can now be calculated by

$$M_{w,i} = M_{w,i-1} - \Delta M_{w,i}. \quad (18)$$

Then, two models are coupled to form the simulation model of SFBG, as shown in Figure 6.

3.2. Simulation Modeling for Tableting. Porosity is an important concept in the study of tablets because it is related to various quality indexes of tablets. The tablet press model calculates tablet porosity from the tablet reduced density as a function of the pressure [8]. The Heckel equation is a widely studied model to calculate this relationship. A lot of research works by Picker et al. [38–49] have studied the influences of pressure, compression time, and compression distance (rolling reduction) on the porosity through a promoted form of the Heckel equation:

$$-\ln \varepsilon = \ln \frac{1}{1 - \rho_{rel}} = e_t t_c + e_p p_c + e_0, \quad (19)$$

where $\varepsilon = 1 - \rho_{ref}$ is the porosity; ρ_{ref} is the relative density of the tablet (the ratio of tablet density to true density of powder); e_t represents the densification over the compression time; e_p represents the densification over the pressure; and e_0 represents the intersection with y -axis $\ln(1/(1 - \rho_{rel}))$ and it is described as

$$e_0 = \ln \frac{1}{1 - \rho_{ref,0}} + K = \ln \frac{1}{\varepsilon_0} + K, \quad (20)$$

where ε_0 is the initial porosity and K represents the change in porosity due to the rearrangement of particles in the initial state [50].

Picker et al. [38–49] carried out a large number of experiments, by which we give the following models in (21)–(23) to be identified after the analysis of each variable, and then the model parameters are calibrated with the experimental data from literature studies:

$$e_t = a_{11} d_p + a_{12} d_r + \frac{a_{13}}{n_r} + a_{14}, \quad (21)$$

$$e_p = b_{11} d_p + b_{12} d_r + b_{13}, \quad (22)$$

$$K = c_{11} d_p + \frac{c_{12}}{n_r} + c_{13}, \quad (23)$$

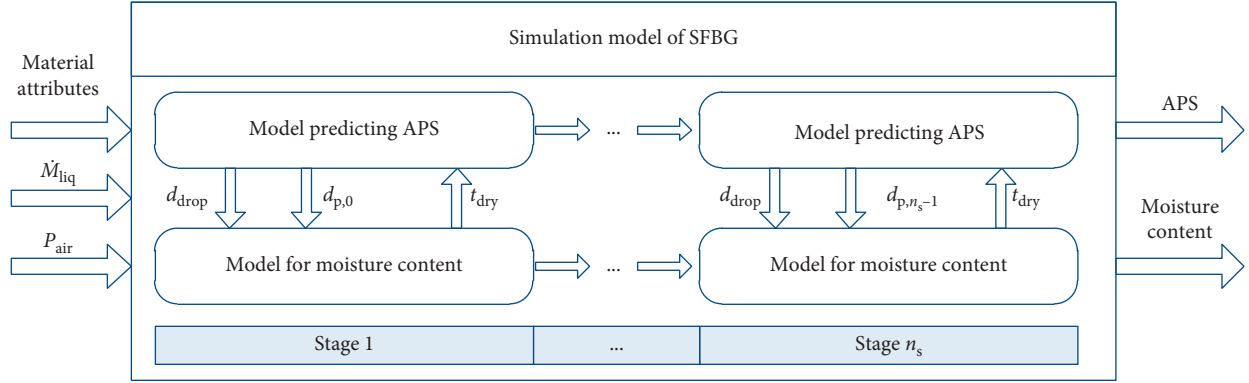


FIGURE 6: The coupling structure of the two models for SFBG.

where d_p is APS, d_r is the rolling reduction, n_r is the turret speed (rpm), and the others are the parameters to be identified.

The initial porosity is related to the APS of particles. Generally speaking, the initial porosity increases as the APS increases due to the gradually increasing space between the particles [50]. But when the particle size increases to a threshold, the initial porosity no longer changes with increasing APS, that is, the initial porosity has a maximum value. By referring to the form of Cooper–Eaton equation [51], we give the following form of initial porosity model:

$$\varepsilon_0 = d_{11} \exp(d_{12}d_p) + d_{13} \exp(d_{14}d_p), \quad (24)$$

where d_{11} , d_{12} , d_{13} , and d_{14} are the coefficients to be identified with the experimental data from literature studies.

The compression time t_c can be divided into process time t_p and dwell time t_d , i.e., $t_c = t_p + t_d$, as shown in Figure 7, in which d_e is the diameter of the upper punch head and also is the punch displacement during the dwell time.

Because the punch follows the turret for circular motion, the punch velocity is given by $v_p = 2\pi R_t n_r$, and then

$$t_p = \frac{h_p}{v_p} = \frac{R_{cr} \sin(\arccos((R_{cr} - d_r)/R_{cr}))}{2\pi R_t n_r}, \quad (25)$$

$$t_d = \frac{d_e}{v_p} = \frac{d_e}{2\pi R_t n_r},$$

where R_t is the radius of turret, t_p and t_d are closely related to the tablet quality, and t_d plays a major role in the tableting.

The powder in the die has both viscous and elastic properties, and the punch pressure p_c is related to this viscoelasticity. The existing viscoelastic model in powder mechanics [52] is quite complicated so that it has theoretical analysis significance but is not applicable in practical applications. Therefore, based on the analysis of the viscoelastic model and the effect of each state variable on the pressure, we try to establish a model for pressure. Firstly, the smaller pressure required during tableting for the greater sized particles can be attributed to a smaller surface area, smaller contact points, and a lower cohesion or frictional force, which requires less pressure to offset [50, 53]. So there is an inverse relationship between pressure and particle size.

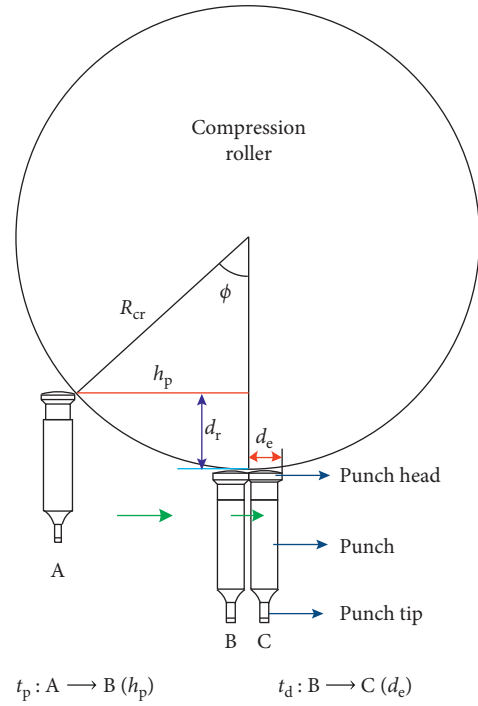


FIGURE 7: Two time periods of tableting.

Secondly, the moisture content represents the viscous properties of the particles to some extent. The smaller pressure required to form a tablet when the particles have a larger moisture content. So there is also an inverse relationship between pressure and moisture content. Thirdly, if the total amount of particles is constant, the smaller the thickness of the tablet, i.e., the greater the degree of compression, the greater the rebound force of the particle column [50]. So the punch pressure is inversely proportional to the remaining particle column height. Additionally, the pressure is also proportional to the compression speed [54]. Therefore, the following empirical equation is used to model the punch pressure:

$$p_c = k_p \frac{(1 - X_{mc})v_c}{d_p(l_0 - d_r)}, \quad (26)$$

with a compression speed model [55]:

$$v_c = \frac{\pi R_t n_t}{15} \sqrt{\frac{d_t}{r}}, \quad (27)$$

where k_p is the pressure coefficient that is related to the viscoelasticity of particles and l_0 is the initial powder column height without compression.

With this, we have constructed the simulation model for the porosity, based on which the following models are introduced to calculate the tablet quality indexes, including tensile strength H_{ts} , hardness H_h , disintegration time D_t , and dissolution rate D_r .

Tensile strength is obtained by solving the following equation [25]:

$$H_{ts} = H_{ts,max} \left(1 - \exp \left(\varepsilon_0 - \varepsilon + \ln \frac{\varepsilon}{\varepsilon_0} \right) \right), \quad (28)$$

where $H_{ts,max}$ is the maximum tensile strength representing the strength of tablets at a theoretical zero porosity, and it is a regressed parameter based on the experimental data from [25].

Hardness is obtained by solving the following equation [24]:

$$H_h = H_{h,max} \left(\varepsilon - \varepsilon_0 - \ln \frac{\varepsilon}{\varepsilon_0} \right), \quad (29)$$

where $H_{h,max}$ holds for the maximal hardness.

For disintegration time, we give the following polynomial model according to the known influence trend of the tablet porosity on the disintegration time [3, 56]:

$$D_t = f_{11} \varepsilon^2 + f_{12} \varepsilon + f_{13}, \quad (30)$$

where f_{11} , f_{12} , and f_{13} are the coefficients to be identified with the experimental data.

Dissolution rate is obtained by solving the following equation [26]:

$$\frac{3}{2} \left(1 - \left(1 - \frac{M_t}{M_\infty} \right)^{2/3} \right) - \frac{M_t}{M_\infty} = \frac{3D_f C_{fs} \varepsilon}{r_0^2 C_0 \tau} t, \quad (31)$$

and refer to [26] for details.

4. Computational Experimental Study: Results and Discussions

In this section, the feasibility and effectiveness of simulation models are tested through a computational experimental study—simulations. The influences of process parameters and material attributes on the intermediate or final quality attributes are firstly studied by implementing simulation experiments, whose results are compared with the widely accepted conclusions in the field. The feasibility and effectiveness will be confirmed by the consistencies of simulation results and recognized analysis or conclusions. On another level, in order to verify the effectiveness of simulation models in process quality control, a validated control method is applied to determine whether the simulated SFBG-based PTMP can be used for designing or testing control algorithms.

TABLE 1: The simulation experiment settings for SFBG.

Property (unit)	Value
$d_{p,0}$ (μm)	[50, 126]
μ_b (Pa·s)	[0.025, 0.15]
ρ_p (kg/m^3)	[300, 1200]
M_{liq} ($10^{-5}\text{kg}/\text{s}$)	[0.5, 3.0]
P_{air} (10^5Pa)	[1.5, 4.5]
T_{bed} ($^\circ\text{C}$)	[30, 60]
M_g (kg/s)	1.6×10^{-5}
ρ_{liq} (kg/m^3)	1014
ρ_g (kg/m^3)	1.225
w_b (%)	6
$M_{s,dry}$ (kg)	0.05
S_h	4
δ_{wg} ($10^{-4}\text{m}^2/\text{s}$)	2.9
n_{max}	12
L_1 (μm)	50
$L_{n_{max}+1}$ (μm)	800
f_c (s^{-1})	1
η_{wd}	0.5
η_{ww}	0.75
σ (mN/m)	43.1
t_g (s)	1200

4.1. Computational Experiments on Model Verification for SFBG. The focus of this section is on the study of influences of critical material attributes and important process parameters on the APS and moisture content. The simulation experimental conditions are shown in Table 1.

The simulation results about the influences of material attributes on APS are shown in Figure 8. Firstly, APS increases with the increase of binder viscosity up to maximum at a critical value, and then, APS decreased with the continuous increase of binder viscosity, which is consistent with the conclusion in [35]. As stated in [35], binders of viscosity less than a critical value will be referred to as “lower viscosity” binders and binders of viscosity larger than this critical value will be referred to as “higher viscosity” binders. With “lower viscosity” binders, the degree of size enlargement increases with increasing binder viscosity because the granule growth occurs by layering and, conversely, the extent of size enlargement decreases with increasing viscosity with “higher viscosity” binders because the growth occurs by coalescence [35, 57]. Secondly, APS increases as the primary particle size increases when keeping operating variables and other material attributes constant, which agrees with the conclusions in [20, 22]. This is attributed to the fact that an increase in the particle initial size leads to an enhancement of the layering mechanism and further results in an increase in final particle size [20, 22]. Thirdly, APS decreases as the particle density increases. The mechanism of particle density affecting particle growth can be reasonably explained from the kinetic energy level of the particle. The increase in particle density directly leads to an increase in the weight of particles, which directly increases the kinetic energy of particle motion. Therefore, in the case where the operating variables and the binder viscosity are constant, the probability that the adhesive layer dissipates the kinetic energy of particles is reduced, and the probability of collision

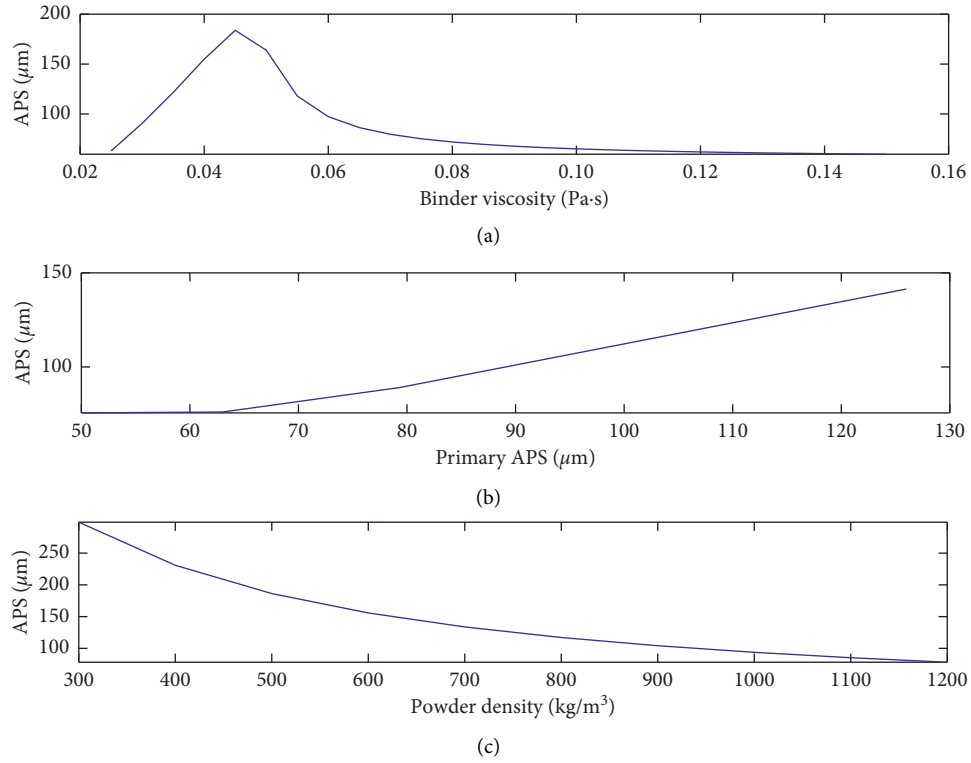


FIGURE 8: The simulation results for SFBG: influences of material attributes.

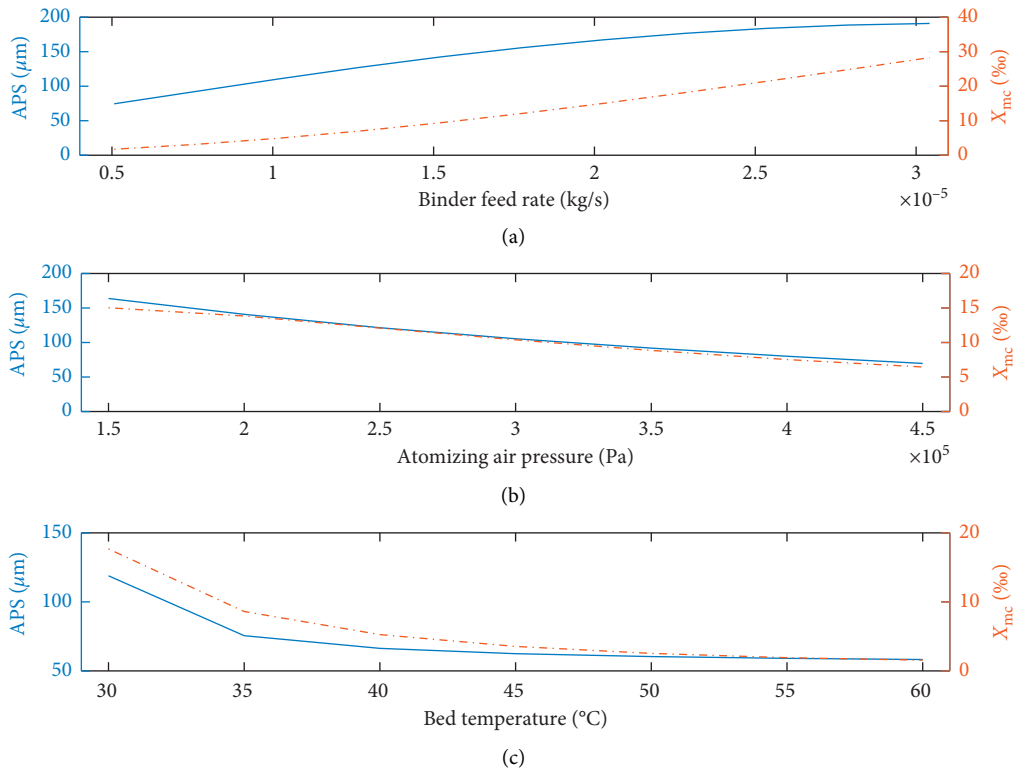


FIGURE 9: The simulation results for SFBG: influences of process parameters.

TABLE 2: The simulation experimental conditions for tableting.

Property (unit)	Value	Parameter	Value	Parameter	Value
n_r (rpm)	[40, 100]	a_{11}	7.19×10^{-4}	d_{11}	0.4500
d_r (mm)	[1, 4]	a_{12}	0.0049	d_{12}	-6.27×10^{-5}
d_p (μm)	[80, 150]	a_{13}	-0.0164	d_{13}	-0.0106
X_{mc} (‰)	[10, 300]	a_{14}	0.0114	d_{14}	-23.44
R_t (mm)	250	b_{11}	-0.0063	f_{11}	167.2125
R_{cr} (mm)	50	b_{12}	-0.0005	f_{12}	-173.4375
d_e (mm)	15	b_{13}	0.0072	f_{13}	44.5875
l_0 (mm)	10	c_{11}	-6.98×10^{-4}		
$H_{ts,max}$ (Mpa)	8.2927	c_{12}	0.0155		
$H_{h,max}$ (N)	250	c_{13}	-0.0128		

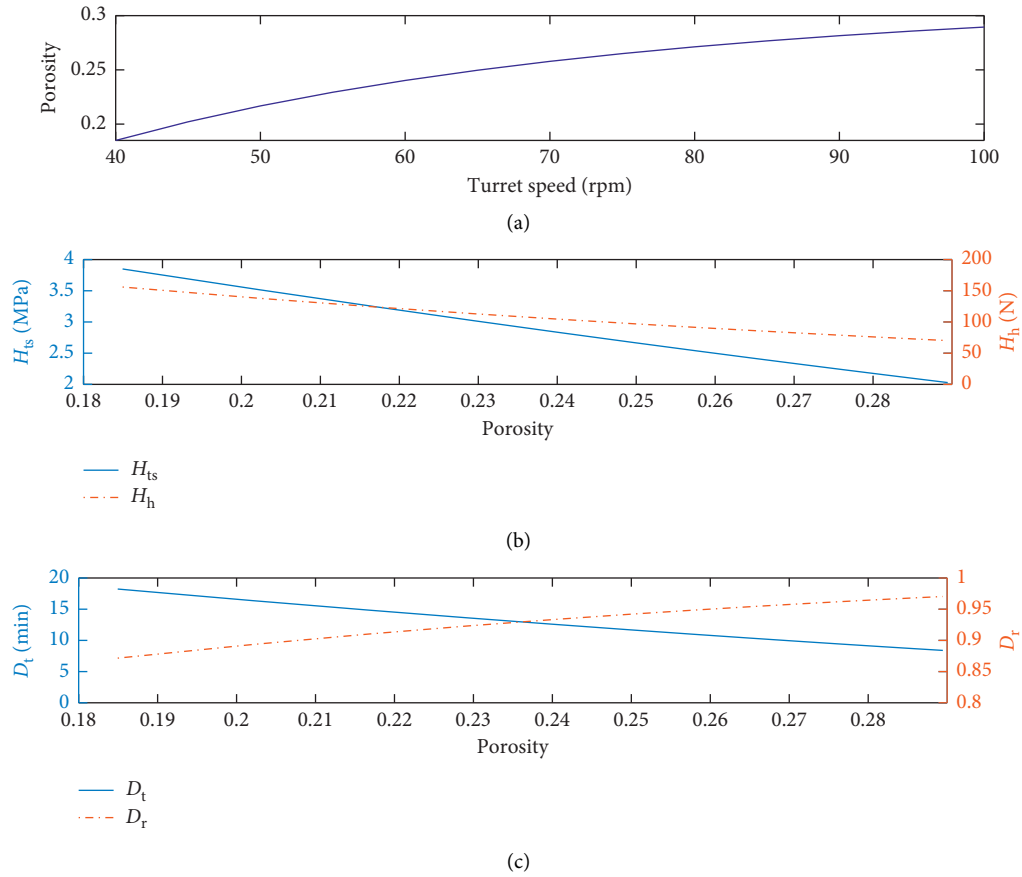


FIGURE 10: The experimental results for tableting: the influences of turret speed.

between particles merged into one larger granule is reduced [11, 12], so that the final APS is reduced.

The simulation results about the influences of process parameters on APS and moisture content are shown in Figure 9. Firstly, the granules with larger APS will be generally produced by increasing the binder feed rate because of the significant enhancement on moisture content, which explains that both moisture content and APS increase with the increase of binder feed rate and agrees with the conclusions in [16, 18, 21, 58]. Secondly, as the atomizing air pressure increased, a smaller value of the liquid droplets size is obtained and the moisture in the droplets is more likely to evaporate, leading to the reduction of moisture content and

final APS, which is consistent with the conclusion in [16, 21]. Thirdly, the bed temperature is found to be dependent on the inlet air temperature and the APS decreases with the increase of bed temperature [21, 59]. In addition, the moisture content decreases as the bed temperature increased because of the faster evaporation rate [58].

4.2. Computational Experiments on Model Verification for Tableting. The input variables of tableting process such as APS, moisture content, turret speed, and rolling reduction first affect the tablet porosity, which in turn affect the tablet quality. Refer to Table 2 and Figures 10–13 for the experimental conditions and results, respectively.

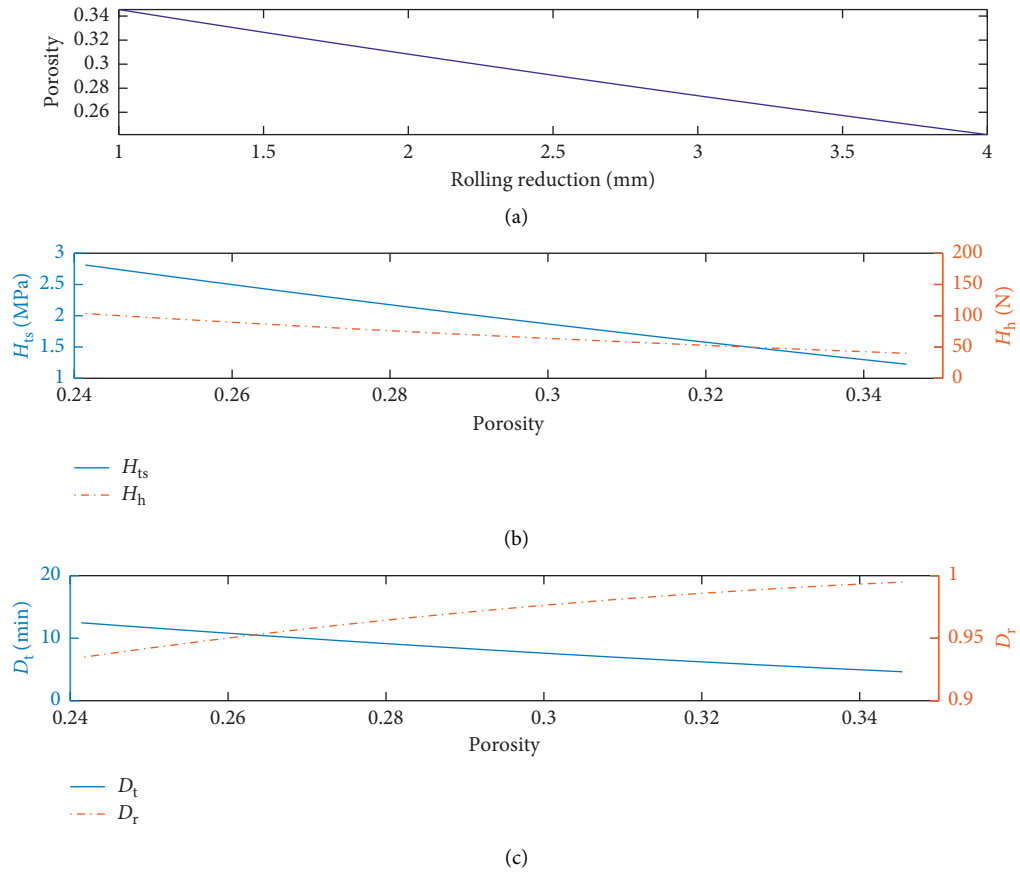


FIGURE 11: The experimental results for tableting: the influences of rolling reduction.

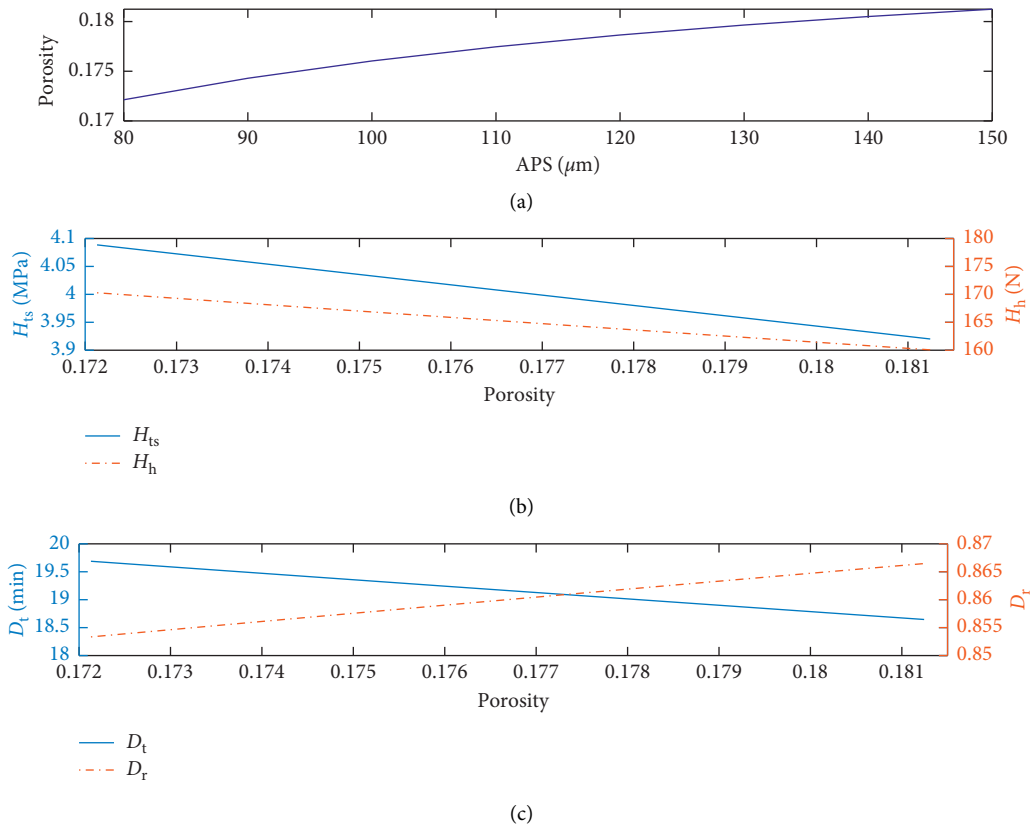


FIGURE 12: The experimental results for tableting: the influences of APS.

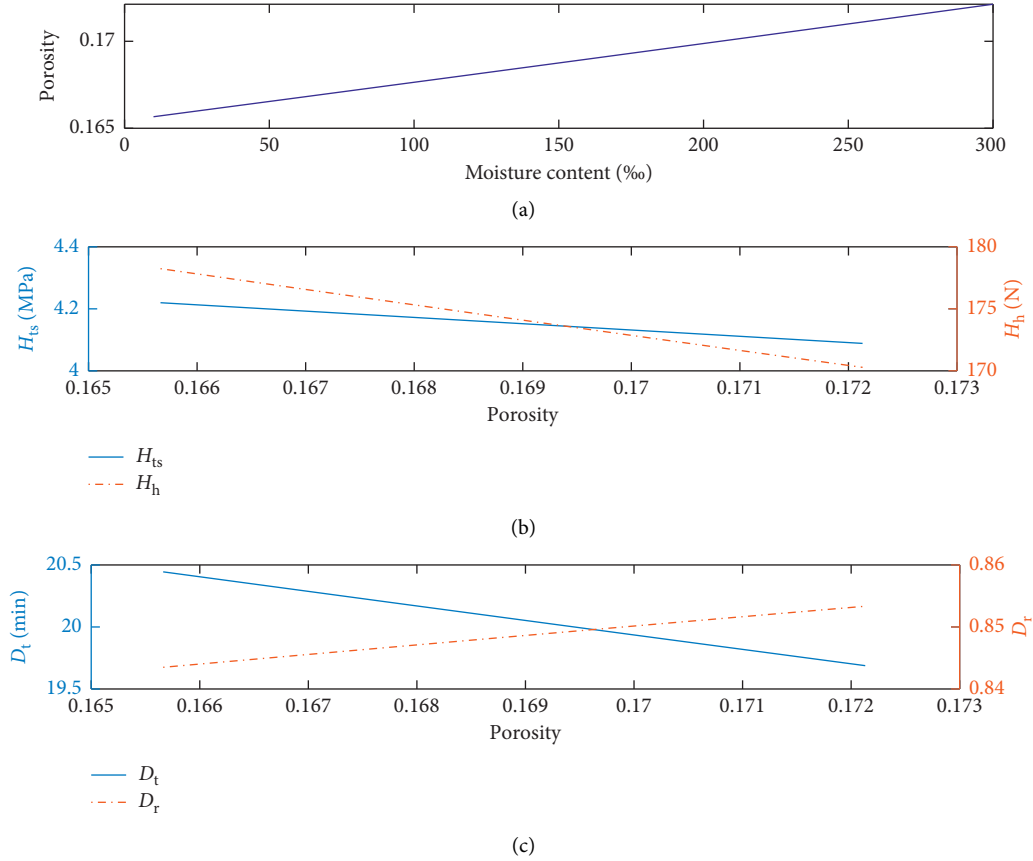


FIGURE 13: The experimental results for tableting: the influences of moisture content.

First we discuss the effects of input variables on porosity. As shown in Figure 10, firstly, as the turret speed increases, the dwell time of the tablet will be reduced [3], and the work on the powder column will also be reduced. The degree of compression of the powder column will decrease accordingly, such as the plastic deformation and the crushing and recombination of the fragments will weaken, and then the effect of forming the new contact points between the particles and the interparticle forces will be reduced [60]. Therefore, the degree of elastic recovery will increase after the tablet is completed [61], and so the porosity will increase with the increase of the turret speed. Secondly, the effect of rolling reduction on porosity is like the human foot stepping into loose dust. When other variables are constant, the greater the rolling reduction, the more the work done on the powder column, the smaller the apparent volume of tablet and the greater the bulk density of tablet, so the smaller the porosity [62], as shown in Figure 11. Thirdly, the smaller pressure required to reduce the same powder column volume for the greater sized particles, which is attributed to a smaller surface area, lesser contact points, and a lower cohesion and frictional force [50]. Moreover, the initial porosity is large when the particles are large due to the relatively looser packing arrangement, and a higher elastic recovery is also observed for larger size particles [50, 53]. Therefore, when other variables are constant such as the same rolling reduction, the smaller pressure, the larger initial

TABLE 3: The simulation conditions for process quality control.

Material attributes	Desired qualities	Algorithm parameters
$d_{p,0}$ (μm)	H_{ts} (MPa)	1.5 γ 0.6 n_p 3
	H_h (N)	48 r 1 κ 0.01
ρ_p (kg/m^3)	D_t (min)	6 q 1 ν 5
	μ_b (Pa·s)	0.0474 η 0.5 b_1 1×10^{-6}
	D_r	0.9 μ 5 b_2 0.03
		\mathbf{Q} $\mathbf{I}_{4 \times 4}$ α 1×10^{-5}
		\mathbf{G}_0 $2 \times \mathbf{I}_{4 \times 4}$ Γ_1 $0.1 \times \mathbf{I}_{4 \times 4}$

porosity, and the higher elastic recovery together result in a large porosity in case of larger APS [8, 56], as shown in Figure 12. Lastly, in general, the moisture in the particles acts as an intrinsic lubricant, contributing to the sliding and plastic flow of the powder, and the humidity of powder can affect its mechanical properties, i.e., the strength and hardness are greatly reduced as humidity increases [60]. Because the mechanism of influence of moisture on porosity is very complicated, we carry out simple analysis based on this theory. Powder particles with high moisture content are softer, and the degree of fragmentation is lower when the particles are combined, i.e., less fragment particles are formed [60]. Therefore, the pores in the original powder are preserved relatively intact, resulting in a larger porosity of the final powder column, as shown in Figure 13.

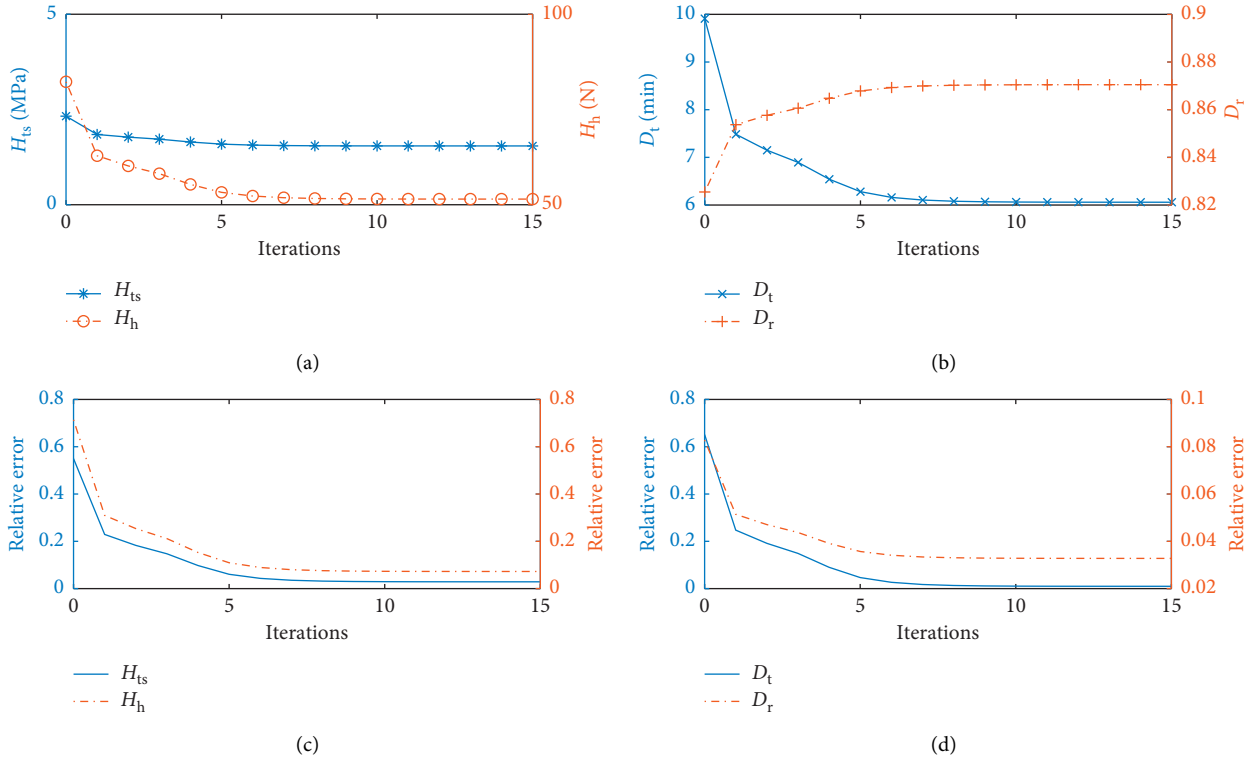


FIGURE 14: The simulation results of tablet quality indexes for process quality control.

Then the influences of porosity on tablet quality indexes are, respectively, analyzed based on the results shown in Figures 10–13 and compared with the widely accepted conclusions to verify the effectiveness of simulation models for tableting.

Firstly, the tensile strength and hardness decrease with increasing porosity, which is agreed with the experimental conclusions in [3, 8, 56, 62]. Tensile strength and hardness reflect the degree of bonding between the particles in the tablet [24]. From the point of view of work, the more the work done on the powder column, the greater the degree of compression (such as more plastic deformation and crushing and recombination of the fragments), the greater the interparticle force is formed, the greater the degree of bonding between the particles, and the greater the tensile strength and hardness [60]. So we analyze the effect of turret speed and rolling reduction on tensile strength and hardness from the perspective of work. When the other variables are kept constant, the turret speed increases, the tablet dwell time becomes shorter, and less work for overcoming the elastic rebound is needed [61]. So the interparticle force is small, resulting in smaller tensile strength and hardness. The rolling reduction is directly applied to the powder column. When the other variables are constant, the amount of work is proportional to the rolling reduction. Therefore, the larger the rolling reduction, the greater the tensile strength and hardness of the formed tablet. APS affects the interaction between particles. Reduction in particle size can give an increase in the number of contact points between particles and an increase in interparticulate frictional and cohesive forces [53]. These factors may explain the increase in tablet tensile strength and hardness with decreasing particle size.

The increase in moisture content leads to an obvious reduction in Young's modulus that determines the rigidity of the powder [60]. When the moisture content is high, the powder particles are soft and then the tensile strength and hardness of the tablets are small.

Secondly, the disintegration time decreases with increasing porosity, which is consistent with the conclusions in [3, 56]; meanwhile, the dissolution rate increases with the increase of porosity, which is consistent with the results in [63]. The disintegration and dissolution of tablets are somewhat similar in mechanism. The tablet comes into contact with the solution to initiate disintegration or dissolution, whose rate is related to the surface area of the solution in contact with the tablets, i.e., large contact surface area leads to rapid disintegration or dissolution. Porosity can reflect the contact surface area to a certain extent: tablets with large porosity generally have large contact surface areas. So the effect of operations or process variables on disintegration time and dissolution rate is analogous to the effect on porosity. Additionally, from the simulation results, it can also be found that the tensile strength and the dissolution rate show an opposite trend, as described in [8].

Lastly, the operating variables and material attributes of SFBG ultimately affect the tablet quality by affecting intermediate particle quality of APS and moisture content, so these simulation analyses are no longer discussed.

4.3. Computational Experiments on Model Verification in the Level of Process Control. In this subsection, using the developed simulation models to simulate the reality of

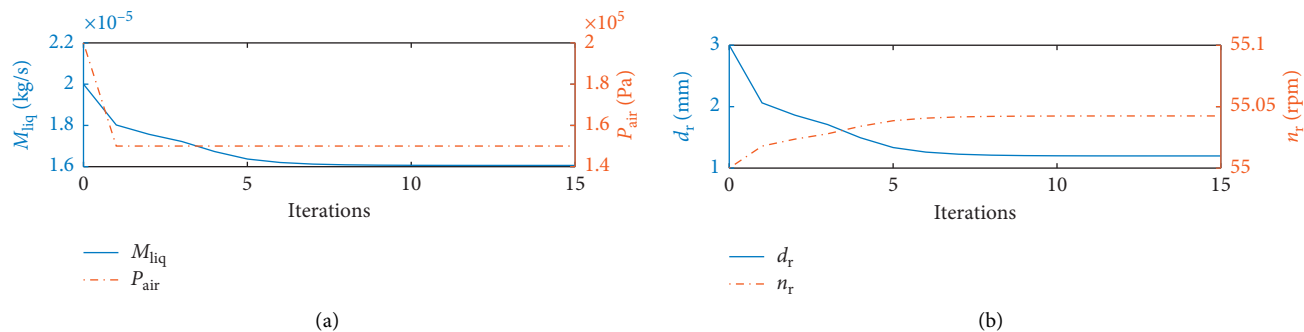


FIGURE 15: The simulation results of process inputs for quality control.

SFBG-based PTMP, process quality control is performed to further validate the feasibility and effectiveness of simulation models in the level of process control. The SFBG-based PTMP can be described by the following repeatable MIMO nonlinear system:

$$\mathbf{y}(k) = f(\mathbf{u}(k), \mathbf{x}), \quad (32)$$

where k denotes the iteration number, $\mathbf{y}(k)$ and $\mathbf{u}(k)$ are the system outputs (tablet quality indexes) and inputs (all operating variables for SFBG-based PTMP) of the k -th iteration, respectively, \mathbf{x} represents the vector of material attributes, and $f(\cdot)$ is an unknown nonlinear function. Given the material attributes \mathbf{x} and a desired output \mathbf{y}_d , the control objective is to find an appropriate control input $\mathbf{u}(k)$ such that the system outputs $\mathbf{y}(k)$ follows the desired one.

A data-driven predictive iterative learning control (DDPILC) method is applied to validate the feasibility of the simulated SFBG-based PTMP in the process quality control. For the specific form of the controller, refer to [64] for details. The simulation conditions are listed in Table 3, and the simulation results are shown in Figures 14 and 15, which indicate that the developed simulation models can be effectively used for the process quality control and further for designing and validating control algorithms.

5. Conclusions

In this work, a simulation modeling framework is developed for a SFBG-based PTMP. Firstly, a simulation model that simultaneously reflects the influences of process operations and material attributes on APS is built using PBM, in which a Hussain's aggregate kernel and a Walzel's model are utilized to, respectively, introduce critical material attributes and important operating variables into modeling framework, and a drying model to determine particle moisture content is then introduced to be coupled with the established PBM predicting APS, so that the simulation model of SFBG is developed. Secondly, because all the tablet quality indexes depend on the porosity, a promoted Heckel equation-based simulation model is developed to describe the changes in porosity with compression time, punch pressure, and initial particle rearrangement, where several empirical models for state variables such as initial porosity and punch pressure are constructed according to the widely accepted analysis and

conclusions in the field. After that, several recognized models that are all related to porosity are introduced or constructed to calculate important tablet quality indexes, including tensile strength, hardness, disintegration time, and dissolution rate. Lastly, the feasibility and effectiveness of simulation models are validated by performing a computational experimental study. On the one hand, the scientific process understanding is explored by analyzing the influences of process inputs on intermediate or final quality indexes and the simulation results are consistent with the widely accepted conclusions in the field. On the other hand, a process control algorithm is introduced to study the quality control of simulated PTMP, and the results show that the developed simulation models can be effectively used for the process quality control and further for designing and validating control algorithms.

Data Availability

The data of model parameters supporting the development of simulation models are from previously reported studies and datasets, which have been cited.

Conflicts of Interest

The authors declare that they have no conflicts of interest.

Acknowledgments

This research work was funded by the National Natural Science Foundation of China under grant nos. 61773105, 61533007, 61873049, 61873053, 61703085, and 61374147 and the Fundamental Research Funds for the Central Universities under grant no. N182008004.

References

- [1] W. Grymonpré, V. Vanhoorne, B. Van Snick et al., "Optimizing feed frame design and tableting process parameters to increase die-filling uniformity on a high-speed rotary tablet press," *International Journal of Pharmaceutics*, vol. 548, no. 1, pp. 54–61, 2018.
- [2] D. Markl, S. Yassin, D. I. Wilson, D. J. Goodwin, A. Anderson, and J. A. Zeitler, "Mathematical modelling of liquid transport in swelling pharmaceutical immediate release tablets,"

- International Journal of Pharmaceutics*, vol. 526, no. 1-2, pp. 1–10, 2017.
- [3] I. C. Sinka, F. Motazedian, A. C. F. Cocks, and K. G. Pitt, “The effect of processing parameters on pharmaceutical tablet properties,” *Powder Technology*, vol. 189, no. 2, pp. 276–284, 2009.
- [4] S. T. F. C. Mortier, T. De Beer, K. V. Gernaey, J. P. Remon, C. Vervae, and I. Nopens, “Mechanistic modelling of fluidized bed drying processes of wet porous granules: a review,” *European Journal of Pharmaceutics and Biopharmaceutics*, vol. 79, no. 2, pp. 205–225, 2011.
- [5] F. Boukouvala, A. Chaudhury, M. Sen et al., “Computer-aided flowsheet simulation of a pharmaceutical tablet manufacturing process incorporating wet granulation,” *Journal of Pharmaceutical Innovation*, vol. 8, no. 1, pp. 11–27, 2013.
- [6] R. Singh, D. Barrasso, A. Chaudhury, M. Sen, M. Ierapetritou, and R. Ramachandran, “Closed-loop feedback control of a continuous pharmaceutical tablet manufacturing process via wet granulation,” *Journal of Pharmaceutical Innovation*, vol. 9, no. 1, pp. 16–37, 2014.
- [7] A. Tamrakar and R. Ramachandran, “CFD-DEM-PBM coupled model development and validation of a 3D top-spray fluidized bed wet granulation process,” *Computers & Chemical Engineering*, vol. 125, pp. 249–270, 2019.
- [8] E. Gavi and G. K. Reynolds, “System model of a tablet manufacturing process,” *Computers & Chemical Engineering*, vol. 71, pp. 130–140, 2014.
- [9] A. J. Rogers, C. Inamdar, and M. G. Ierapetritou, “An integrated approach to simulation of pharmaceutical processes for solid drug manufacture,” *Industrial & Engineering Chemistry Research*, vol. 53, no. 13, pp. 5128–5147, 2014.
- [10] N. Metta, M. Ghijs, E. Schäfer et al., “Dynamic flowsheet model development and sensitivity analysis of a continuous pharmaceutical tablet manufacturing process using the wet granulation route,” *Processes*, vol. 7, no. 4, p. 234, 2019.
- [11] M. Hussain, J. Kumar, M. Peglow, and E. Tsotsas, “Modeling spray fluidized bed aggregation kinetics on the basis of Monte-Carlo simulation results,” *Chemical Engineering Science*, vol. 101, pp. 35–45, 2013.
- [12] M. Hussain, J. Kumar, and E. Tsotsas, “A new framework for population balance modeling of spray fluidized bed agglomeration,” *Particuology*, vol. 19, pp. 141–154, 2015.
- [13] S. Groom, G. Schaldach, M. Ulmer, P. Walzel, and H. Berndt, “Adaptation of a new pneumatic nebulizer for sample introduction in ICP spectrometry,” *Journal of Analytical Atomic Spectrometry*, vol. 20, no. 3, pp. 169–175, 2005.
- [14] P. D. Hede, P. Bach, and A. D. Jensen, “Two-fluid spray atomisation and pneumatic nozzles for fluid bed coating/agglomeration purposes: a review,” *Chemical Engineering Science*, vol. 63, no. 14, pp. 3821–3842, 2008.
- [15] M. Dervede, M. Peglow, and E. Tsotsas, “Stochastic modeling of fluidized bed agglomeration: determination of particle moisture content,” *Drying Technology*, vol. 31, no. 15, pp. 1764–1771, 2013.
- [16] J. Bouffard, M. Kaster, and H. Dumont, “Influence of process variable and physicochemical properties on the granulation mechanism of mannitol in a fluid bed top spray granulator,” *Drug Development and Industrial Pharmacy*, vol. 31, no. 9, pp. 923–933, 2005.
- [17] H. Liu and M. Li, “Population balance modelling and multi-stage optimal control of a pulsed spray fluidized bed granulation,” *International Journal of Pharmaceutics*, vol. 468, no. 1-2, pp. 223–233, 2014.
- [18] T. Närvänen, T. Lipsanen, O. Antikainen, H. Räikkönen, and J. Yliruusi, “Controlling granule size by granulation liquid feed pulsing,” *International Journal of Pharmaceutics*, vol. 357, no. 1-2, pp. 132–138, 2008.
- [19] H. Ehlers, A. Liu, H. Räikkönen et al., “Granule size control and targeting in pulsed spray fluid bed granulation,” *International Journal of Pharmaceutics*, vol. 377, no. 1-2, pp. 9–15, 2009.
- [20] M. Hemati, R. Cherif, K. Saleh, and V. Pont, “Fluidized bed coating and granulation: influence of process-related variables and physicochemical properties on the growth kinetics,” *Powder Technology*, vol. 130, no. 1–3, pp. 18–34, 2003.
- [21] T. Jiménez, C. Turchiuli, and E. Dumoulin, “Particles agglomeration in a conical fluidized bed in relation with air temperature profiles,” *Chemical Engineering Science*, vol. 61, no. 18, pp. 5954–5961, 2006.
- [22] H. Zhai, S. Li, G. Andrews, D. Jones, S. Bell, and G. Walker, “Nucleation and growth in fluidised hot melt granulation,” *Powder Technology*, vol. 189, no. 2, pp. 230–237, 2009.
- [23] J. M.-H. Poon, R. Ramachandran, C. F. W. Sanders et al., “Experimental validation studies on a multi-dimensional and multi-scale population balance model of batch granulation,” *Chemical Engineering Science*, vol. 64, no. 4, pp. 775–786, 2009.
- [24] M. Kuentz and H. Leuenberger, “A new model for the hardness of a compacted particle system, applied to tablets of pharmaceutical polymers,” *Powder Technology*, vol. 111, no. 1-2, pp. 145–153, 2000.
- [25] M. S. Escotet-Espinoza, S. Vadodaria, R. Singh, F. J. Muzzio, and M. G. Ierapetritou, “Modeling the effects of material properties on tablet compaction: a building block for controlling both batch and continuous pharmaceutical manufacturing processes,” *International Journal of Pharmaceutics*, vol. 543, no. 1-2, pp. 274–287, 2018.
- [26] P. Costa and J. M. Sousa Lobo, “Modeling and comparison of dissolution profiles,” *European Journal of Pharmaceutical Sciences*, vol. 13, no. 2, pp. 123–133, 2001.
- [27] H. S. Tan, A. D. Salman, and M. J. Hounslow, “Kinetics of fluidized bed melt granulation-II: modelling the net rate of growth,” *Chemical Engineering Science*, vol. 61, no. 12, pp. 3930–3941, 2006.
- [28] M. Peglow, J. Kumar, S. Heinrich et al., “A generic population balance model for simultaneous agglomeration and drying in fluidized beds,” *Chemical Engineering Science*, vol. 62, no. 1-2, pp. 513–532, 2007.
- [29] L. X. Liu and J. D. Litster, “Population balance modelling of granulation with a physically based coalescence kernel,” *Chemical Engineering Science*, vol. 57, no. 12, pp. 2183–2191, 2002.
- [30] C. Turchiuli, T. Jimenez, and E. Dumoulin, “Identification of thermal zones and population balance modelling of fluidized bed spray granulation,” *Powder Technology*, vol. 208, no. 2, pp. 542–552, 2011.
- [31] M. Hussain, J. Kumar, M. Peglow, and E. Tsotsas, “On two-compartment population balance modeling of spray fluidized bed agglomeration,” *Computers & Chemical Engineering*, vol. 61, pp. 185–202, 2014.
- [32] H. S. Tan, M. J. V. Goldschmidt, R. Boerefijn, M. J. Hounslow, D. Salman, and J. A. M. Kuipers, “Population balance modelling of fluidized bed melt granulation: an overview,” *Chemical Engineering Research and Design*, vol. 83, no. 7, pp. 871–880, 2005.
- [33] M. J. Hounslow, R. L. Ryall, and V. R. Marshall, “A discretized population balance for nucleation, growth, and aggregation,” *AIChE Journal*, vol. 34, no. 11, pp. 1821–1832, 1988.

- [34] B. J. Ennis, G. Tardos, and R. Pfeffer, "A microlevel-based characterization of granulation phenomena," *Powder Technology*, vol. 65, no. 1–3, pp. 257–272, 1991.
- [35] P. J. T. Mills, J. P. K. Seville, P. C. Knight, and M. J. Adams, "The effect of binder viscosity on particle agglomeration in a low shear mixer/agglomerator," *Powder Technology*, vol. 113, no. 1–2, pp. 140–147, 2000.
- [36] K. Terrazas-Velarde, M. Peglow, and E. Tsotsas, "Kinetics of fluidized bed spray agglomeration for compact and porous particles," *Chemical Engineering Science*, vol. 66, no. 9, pp. 1866–1878, 2011.
- [37] M. Zeller and U. Busweiler, *M8 Humidifying and Drying of Air*, VDI Heat Atlas, Springer, Berlin, Germany, 2010.
- [38] K. M. Picker, "A new theoretical model to characterize the densification behavior of tableting materials," *European Journal of Pharmaceutics and Biopharmaceutics*, vol. 49, no. 3, pp. 267–273, 2000.
- [39] K. Picker, "Three-dimensional modeling to determine properties of tableting materials on rotary machines using a rotary tableting machine simulator," *European Journal of Pharmaceutics and Biopharmaceutics*, vol. 50, no. 2, pp. 293–300, 2000.
- [40] K. M. Picker and F. Bikane, "An evaluation of three-dimensional modeling of compaction cycles by analyzing the densification behavior of binary and ternary mixtures," *Pharmaceutical Development and Technology*, vol. 6, no. 3, pp. 333–342, 2001.
- [41] K. M. Picker, "The 3-D model: comparison of parameters obtained from and by simulating different tableting machines," *AAPS PharmSciTech*, vol. 4, no. 3, pp. 55–61, 2003.
- [42] K. M. Picker, "The 3-D model: does time plasticity represent the influence of tableting speed?," *AAPS PharmSciTech*, vol. 4, no. 4, pp. 523–530, 2003.
- [43] K. M. Picker, "'Soft tableting': a new concept to tablet pressure sensitive materials," *Pharmaceutical Development and Technology*, vol. 9, no. 1, pp. 107–121, 2004.
- [44] K. M. Picker, "The 3D model: explaining densification and deformation mechanisms by using 3D parameter plots," *Drug Development and Industrial Pharmacy*, vol. 30, no. 4, pp. 413–425, 2004.
- [45] K. Hauschild and K. M. Picker-Freyer, "Evaluation of tableting and tablet properties of kolidon SR: the influence of moisture and mixtures with theophylline monohydrate," *Pharmaceutical Development and Technology*, vol. 11, no. 1, pp. 125–140, 2006.
- [46] K. M. Picker-Freyer, "The 3-D model: experimental testing of the parameters d , e , and ω and validation of the analysis," *Journal of Pharmaceutical Sciences*, vol. 96, no. 5, pp. 1408–1417, 2007.
- [47] O. Odeku, W. Schmid, and K. Picker-Freyer, "Material and tablet properties of pregelatinized (thermally modified) Dioscorea starches," *European Journal of Pharmaceutics and Biopharmaceutics*, vol. 70, no. 1, pp. 357–371, 2008.
- [48] S. Hein, K. M. Picker-Freyer, and J. Langridge, "Simulation of roller compaction with subsequent tableting and characterization of lactose and microcrystalline cellulose," *Pharmaceutical Development and Technology*, vol. 13, no. 6, pp. 523–532, 2008.
- [49] L. Salbu, K. M. Picker-Freyer, W. Schmid, A. Bauer-Brandl, and I. Tho, "Use of 3-D modelling in early development phase of pectin tablets," *Journal of Excipients and Food Chemicals*, vol. 3, no. 1, 2012.
- [50] S. Patel, A. M. Kaushal, and A. K. Bansal, "Effect of particle size and compression force on compaction behavior and derived mathematical parameters of compressibility," *Pharmaceutical Research*, vol. 24, no. 1, pp. 111–124, 2007.
- [51] A. R. Cooper Jr. and L. E. Eaton, "Compaction behavior of several ceramic powders," *Journal of the American Ceramic Society*, vol. 45, no. 3, pp. 97–101, 1962.
- [52] E. G. Rippie and D. W. Danielson, "Viscoelastic stress/strain behavior of pharmaceutical tablets: analysis during unloading and postcompression periods," *Journal of Pharmaceutical Sciences*, vol. 70, no. 5, pp. 476–482, 1981.
- [53] A. Nokhodchi, M. H. Rubinstein, and J. L. Ford, "The effect of particle size and viscosity grade on the compaction properties of hydroxypropylmethylcellulose 2208," *International Journal of Pharmaceutics*, vol. 126, no. 1–2, pp. 189–197, 1995.
- [54] H. Larhrib, J. I. Wells, and M. H. Rubinstein, "Compressing polyethylene glycols: the effect of compression pressure and speed," *International Journal of Pharmaceutics*, vol. 147, no. 2, pp. 199–205, 1997.
- [55] Y. H. Tian, "Technical innovation and cost reduction effect of sub-high speed tablet press with 55 punches," *Electromechanical Information*, vol. 11, pp. 31–35, 2009, in Chinese.
- [56] M. Kidokoro, Y. Haramiishi, S. Sagasaki, T. Shimizu, and Y. Yamamoto, "Application of fluidized hot-melt granulation (FHMG) for the preparation of granules for tableting; properties of granules and tablets prepared by FHMG," *Drug Development and Industrial Pharmacy*, vol. 28, no. 1, pp. 67–76, 2002.
- [57] P. Thapa, J. Tripathi, and S. H. Jeong, "Recent trends and future perspective of pharmaceutical wet granulation for better process understanding and product development," *Powder Technology*, vol. 344, pp. 864–882, 2019.
- [58] X. Hu, J. Cunningham, and D. Winstead, "Understanding and predicting bed humidity in fluidized bed granulation," *Journal of Pharmaceutical Sciences*, vol. 97, no. 4, pp. 1564–1577, 2008.
- [59] B. Rambali, L. Baert, and D. L. Massart, "Using experimental design to optimize the process parameters in fluidized bed granulation on a semi-full scale," *International Journal of Pharmaceutics*, vol. 220, no. 1–2, pp. 149–160, 2001.
- [60] G. Alderborn and C. Nystrom, *Pharmaceutical Powder Compaction Technology*, Marcel Dekker Inc., New York, NY, USA, 1996.
- [61] R. Blanchard, "The case for extended dwell flat tooling: increasing dwell time can improve tablet production," *Pharmaceutical Technology*, vol. 42, p. 26, 2018.
- [62] C. Sun and D. J. W. Grant, "Effects of initial particle size on the tableting properties of l-lysine monohydrochloride dihydrate powder," *International Journal of Pharmaceutics*, vol. 215, no. 1–2, pp. 221–228, 2001.
- [63] G. Frenning, F. Fichtner, and G. Alderborn, "A new method for characterizing the release of drugs from single agglomerates," *Chemical Engineering Science*, vol. 60, no. 14, pp. 3909–3918, 2005.
- [64] Q. Yu and Z. Hou, "Data-driven predictive iterative learning control for a class of multiple-input and multiple-output nonlinear systems," *Transactions of the Institute of Measurement and Control*, vol. 38, no. 3, pp. 266–281, 2016.

Research Article

A Novel Model with GA Evolving FWNN for Effluent Quality and Biogas Production Forecast in a Full-Scale Anaerobic Wastewater Treatment Process

Zehua Huang,^{1,2,3,4} Renren Wu,² XiaoHui Yi,¹ Hongbin Liu,³ Jiannan Cai,⁵ Guoqiang Niu,¹ Mingzhi Huang ,¹ and Guangguo Ying¹

¹SCNU Environmental Research Institute, Guangdong Provincial Key Laboratory of Chemical Pollution and Environmental Safety & MOE Key Laboratory of Theoretical Chemistry of Environment, School of Environment, South China Normal University, Guangzhou 510006, China

²South China Institute of Environmental Science, Ministry of Environmental Protection, Guangzhou 510650, China

³Jiangsu Co-Innovation Center of Efficient Processing and Utilization of Forest Resources, Nanjing Forestry University, Nanjing 210037, China

⁴College of Chemical Engineering, Huaqiao University, Xiamen 361021, Fujian, China

⁵Zhongshan Environmental Monitoring Station, Zhongshan 528400, China

Correspondence should be addressed to Mingzhi Huang; h mz2002xa@163.com

Received 24 May 2019; Revised 5 August 2019; Accepted 29 August 2019; Published 26 November 2019

Guest Editor: Raúl Baños

Copyright © 2019 Zehua Huang et al. This is an open access article distributed under the Creative Commons Attribution License, which permits unrestricted use, distribution, and reproduction in any medium, provided the original work is properly cited.

The anaerobic treatment process is a complicated multivariable system that is nonlinear and time varying. Moreover, biogas production rates are an important indicator for reflecting operational performance of the anaerobic treatment system. In this work, a novel model fuzzy wavelet neural network based on the genetic algorithm (GA-FWNN) that combines the advantages of the genetic algorithm, fuzzy logic, neural network, and wavelet transform was established for prediction of effluent quality and biogas production rates in a full-scale anaerobic wastewater treatment process. Moreover, the dataset was preprocessed via a self-adapted fuzzy c-means clustering before training the network and a hybrid algorithm for acquiring the optimal parameters of the multiscale GA-FWNN for improving the network precision. The analysis results indicate that the FWNN with the optimal algorithm had a high speed of convergence and good quality of prediction, and the FWNN model was more advantageous than the traditional intelligent coupling models (NN, WNN, and FNN) in prediction accuracy and robustness. The determination coefficients R^2 of the FWNN models for predicting both the effluent quality and biogas production rates were over 0.95. The proposed model can be used for analyzing both biogas (methane) production rates and effluent quality over the operational time period, which plays an important role in saving energy and eliminating pollutant discharge in the wastewater treatment system.

1. Introduction

Because of the economic advantages and low generation of excess sludge, the anaerobic biological treatment process is an efficient process for treating high-concentration organic wastewater, such as paper-mill wastewater, where the complex organic contaminants can be converted into clean energy (methane gas) in the anaerobic treatment process [1–3]. However, the anaerobic treatment process is a complicated multivariable system and is influenced by

various influent characteristics and operating conditions, which is difficult to be solved within a short time [4, 5]. Therefore, biogas (methane) production rates are also influenced by various influent characteristics and operating conditions [6].

Because of the nonlinearity, uncertainty, and posteriority of the anaerobic treatment process, it is difficult to operate and control that process. To increase the steadiness and reliability of the anaerobic treatment process, modeling is a significant method, which can be used in controlling,

operation, and optimization of the anaerobic treatment process at a reasonable cost [7]. In recent years, numerous studies have been carried out and various modeling methods have been developed to control and simulate the anaerobic treatment process [8–11]. However, because of the superficial understanding of the mechanisms associated with the anaerobic treatment process, it is difficult to analyze and estimate more underlying phenomena in anaerobic digestion using conventional mathematical models. Therefore, to eliminate the complicity, difficulty, and applicability, more practical, secure, and simple models are needed to be investigated [4, 12].

Because artificial intelligence has logic thought, fast disposal capability, and nonlinear characteristics, it may carry on the free precision to any continual nonlinear function approaching. The commonly used artificial intelligence methods are the neural network (NN), fuzzy logic (FL), wavelet transform (WT), genetic algorithm (GA), and metaheuristic algorithms [13, 14]. Hence, the model based on artificial intelligence can achieve precise simulation results in the wastewater treatment process.

In recent years, a variety of models based on the NN for estimating the performance of the anaerobic treatment process have been conducted by many researchers [15]. A backpropagation neural network (BPNN) model integrating the additional momentum method with the adaptive learning rate method was developed to estimate the operational status of the upflow anaerobic sludge bed (UASB) [16]. The results indicated that the model can predict and optimize the control parameters and propose strategies of the reactor. In addition, another BPNN model based on the Levenberg–Marquardt algorithm was designed by Sridevi et al. [17], which can be used to successfully predict the biodegradation and biohydrogen production in a hybrid UASB reactor treating the distillery wastewater. Above all, the model based on the NN can efficiently simulate and predict the nonlinear characteristic of the anaerobic wastewater treatment system. However, the NN has some defects, such as converging slowly and immersing in local vibration frequently [18, 19].

Therefore, there are many neural network coupling algorithms, such as the wavelet neural network (WNN) and fuzzy neural network (FNN), to be proposed to solve the problems faced by the ordinary NN [20–22]. The FNN based on fuzzy logic (FL) and NN can realize FL by the NN. In the meantime, the coupled algorithm can capture fuzzy rules effectively and realize fuzzy reasoning by using the NN structure. So if the FNN is applied in the wastewater treatment system, it will more effectively simulate the wastewater treatment system.

Many research studies about modeling the anaerobic wastewater treatment process using the hybrid FNN have been carried out in recent years [23–25]. Erdirencelebi and Yalpir integrated FL and NN to develop a hybrid FNN model for simulating the anaerobic wastewater treatment process [2]. The results illustrated the developed hybrid FNN model could be used for forecasting the effluent quality accurately in a UASB system. In order to monitor degradation of the penicillin-G wastewater in an anaerobic hybrid reactor, a hybrid FNN model was established by Mullai et al. [26] using

the adaptive network-based fuzzy inference system (ANFIS). The simulation results exhibited that the developed hybrid model was effective and the correlation coefficient (R^2) of the model for chemical oxygen demand (COD) values was high. Therefore, clarification of the place of the present subject in the scheme of the FNN methodology can be considered a particular field of investigation to evaluate real-time effluent quality and biogas (methane) production rates that are necessary to control the anaerobic process and to establish fault diagnosis. Nevertheless, the FNN also has drawbacks, which are no time-frequency localization characteristics and may easily cause the low convergence rate and accuracy. This is exactly the advantage of the wavelet transform (WT). Hanbay et al. [27] have successfully used wavelet packet decomposition and NN for prediction of the anaerobic wastewater treatment plant. Furthermore, on the basis of kernel principal component analysis and WNN, a soft sensor system could realize real-time detection of redox potential, dissolved oxygen, pH, and COD in the wastewater treatment process [28].

Hence, a new system with the fuzzy wavelet neural network (FWNN) was established by integrating advantages of various intelligent techniques. This network could effectively increase the detection rate and reliability of the model by improving the discernment, generalization, and approximation capacities [3, 29, 30]. Such an integrated intelligent system can overcome the shortcomings mentioned above. Therefore, the hybrid FWNN offers a more efficient method for modeling, simulation, control, and operation optimization of the complex process system, such as the wastewater treatment process.

The performance of the anaerobic treatment process is very complicated and makes remarkable changes based on various influent characteristics and operating conditions, such as organic loading rates (OLRs), pH, hydraulic retention time (HRT), and toxic organic compounds. Various potential advantages based on such an artificial intelligence-based model for real-time evaluation of effluent quality and biogas production rates would be fully demonstrated, such as withstanding various shock loads caused by substantial influent fluctuations, optimizing operational parameters of the process for controlling operational cost, providing an online evaluation and estimation of emissions on an energetic basis, and building a continuous early-warning strategy without requiring a complicated model structure. However, studies on modeling biodegradation and biogas (methane) production rates in a full-scale mesospheric internal circulation (IC) anaerobic reactor treating paper-mill wastewater using the FWNN are very limited.

Based on the relationship between the effluent COD and the biogas flow rate under various operating parameters such as influent COD (COD_{inf}), HRT, OLR, pH in the reactor (pH), and alkalinity in the reactor (ALK), an FWNN model is developed to predict and estimate the effluent quality and biogas production rates based on the existing historical data. The key objective of this study was to develop a novel hybrid genetic algorithm evolving FWNN model for simulating the functioning problem of a full-scale internal circulation (IC) anaerobic wastewater treatment plant. The proposed hybrid model may be used for analyzing the biogas

production rate and effluent quality over the operational time period, which plays an important role in saving energy and eliminating pollutant discharge in the wastewater treatment system.

2. Materials and Methods

2.1. Reactor System. A full-scale IC anaerobic treatment plant system was selected for a demonstration site. This treatment system used in the study is located in Guangdong, China. As shown in Figure 1, the wastewater treatment process including four IC reactors was operated to treat approximately $3 \times 10^4 \text{ m}^3$ paper-mill wastewater streams per day. Each IC reactor has a diameter of 9 m and a volume of 1100 m^3 . The treatment system is equipped with online flow, pH, DO, ORP, temperature, COD, and gas flow meter (HACH®) sensors. The signals delivered from above parameters were also used to control peristaltic pumps, stirrers, and air blower. The model used data from the full-scale sequential system that were collected over a period of 150 days. Other chemical indexes were determined according to standard methods [31, 32].

2.2. Genetic Algorithm Evolving Fuzzy Wavelet Neural Network (FWNN)

2.2.1. Identification of Model Parameters. The identification of model parameters is one of the key demands on modeling the anaerobic wastewater treatment processes. The most appropriate choice of model components, which can exactly display the running state of the anaerobic treatment process, can help improve the management efficiency and reduce functioning costs of the system [6].

OLR is used to measure the biological conversion ability. This parameter is a vital factor, which can significantly influence microbial ecology and performance characteristics of anaerobic treatment systems.

HRT is an important variable in the anaerobic treatment system. It is used to measure the amount of time the wastewater remains in the system. Retention time of the feed in the system is too short, to complete the entire treatment process, and biogas production will not be restrained.

pH is a chief parameter, which significantly affects the performance characteristics of anaerobic treatment systems. pH has a substantial effect on methanogenic bacteria.

ALK is reflected in the solution, to neutralize acids towards the equivalence point of carbonate or bicarbonate in the anaerobic treatment system. In order to control pH in the anaerobic treatment system, it must ensure there is enough ALK, which is effective in preventing the dramatic changes of pH.

COD is used to measure the organic compounds in wastewater. This parameter refers to substrate utilization proficiency and microbial metabolic activity in the anaerobic treatment systems.

Biogas production rate is usually used to refer to the processing efficiency of the anaerobic treatment system. In the anaerobic treatment system, the most significant operation is to control the effluent superiority and maximize the rate of biogas production by breaking pollutants.

Therefore, influent COD (COD_{inf}), HRT, OLR, pH in the reactor (pH), and alkalinity in the reactor (ALK) were selected as the input parameters of the proposed FWNN model. Biogas production rates and effluent COD (COD_{eff}) were selected as the output parameters of the proposed FWNN model.

2.2.2. Structure of the Proposed FWNN. The architecture of the FWNN for modeling the anaerobic treatment system is illustrated in Figure 2. For the FWNN, the wavelet was used for the neuron's activation functions on the basis of the five-layer NN, and fuzzy inference can be realized [33, 34]. The FWNN includes five layers as follows.

The first layer consists of all input factors that act as the input layer. The layer data of input factors $x_1; x_2; \dots; x_n$ are the input mode. In this layer, there are five input parameters that are COD_{inf} , HRT, OLR, pH, and ALK, so $n = 5$.

The second layer is the fuzzy layer. The fuzzy layer set theory was employed to processing of linguistic variables, and the selected membership function was the Gaussian function. The input characteristic variables were translated into fuzzy variables in this layer, which can be defined as follows:

$$F_j(x_i) = \exp \left\{ \frac{(x_i - c_{ij})^2}{2\sigma_{ij}^2} \right\}, \quad j = 1, 2, \dots, n, i = 1, 2, \dots, m, \quad (1)$$

where c_{ij} and σ_{ij} are the center and width parameters of the membership functions, respectively, and i and j are the number of input parameters and linguistic variables in the FWNN, respectively.

A self-adapted fuzzy c-means clustering has been used in this work. It has been used to address the fuzzy factors, and 18 sets of fuzzy control rules have been established by analyzing the actual database of knowledge. The third layer is the fuzzy rule layer. This layer consists of numeral hidden units representing fuzzy logic rules and numeral fuzzy partitions. The fuzzy rule base is generated from the given input and output data, and the logical inference can be realized, which can be given as follows:

$$\mu_j(x) = \prod_{j=1}^n F_j(x_i), \quad i = 1, 2, \dots, n, \quad (2)$$

where n is the number of fuzzy rules.

The fourth layer is the wavelet network. In this layer, a wavelet network is designed using wavelet functions as the activation function of its nerve cells, based on the good local performance of wavelet transformation. The WNNs are used for the consequence of the FWNN. The output of WNNs with the j th wavelet neuron can be given as follows:

$$\begin{cases} w_o_j = w_j \psi_j(z), \\ \psi_j(z) = \sum_{i=1}^m \frac{1}{\sqrt{|a_{ij}|}} (1 - z_{ij}^2) e^{-\left(\frac{z_{ij}^2}{2}\right)}, \end{cases} \quad (3)$$

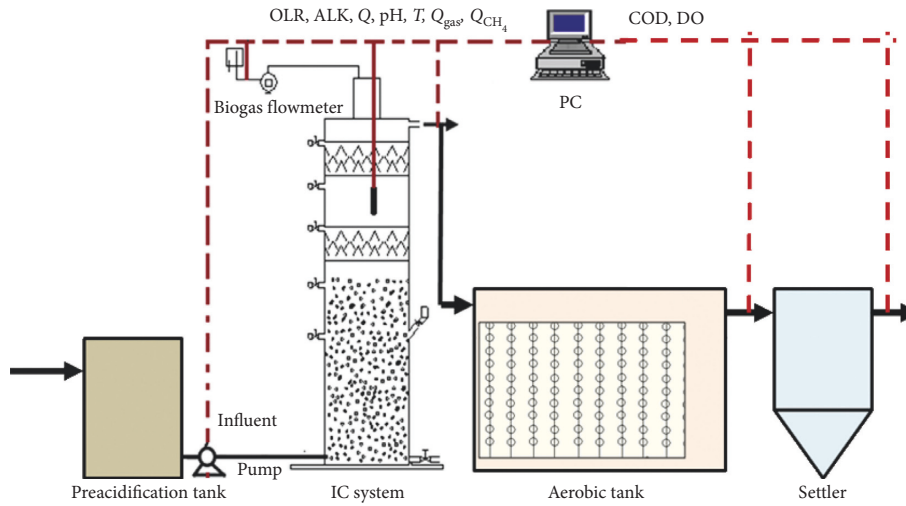
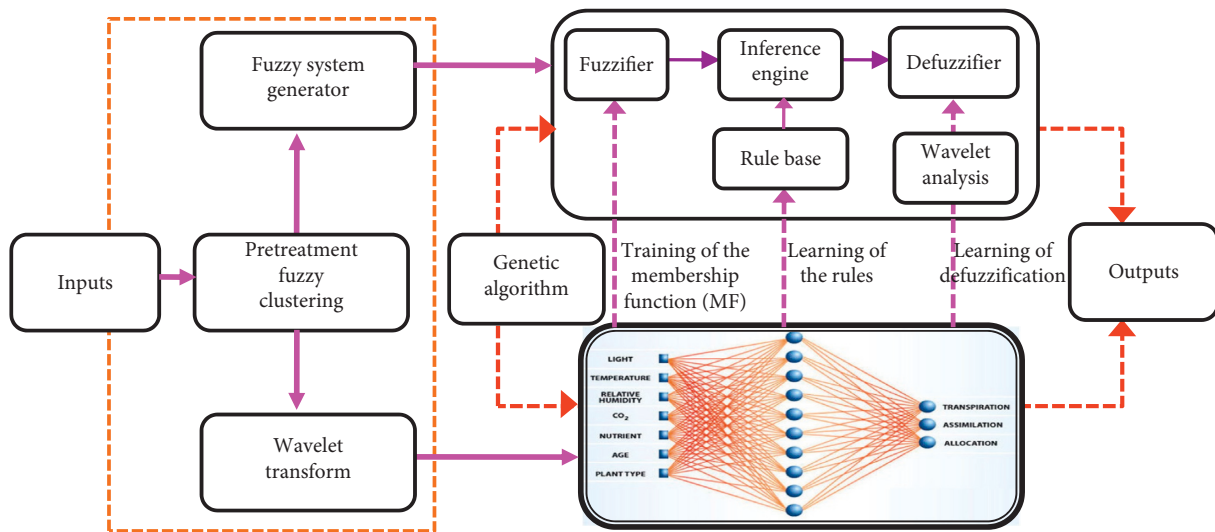


FIGURE 1: Schematic diagram of the full-scale anaerobic process.



Corresponding FWNN schematic architecture

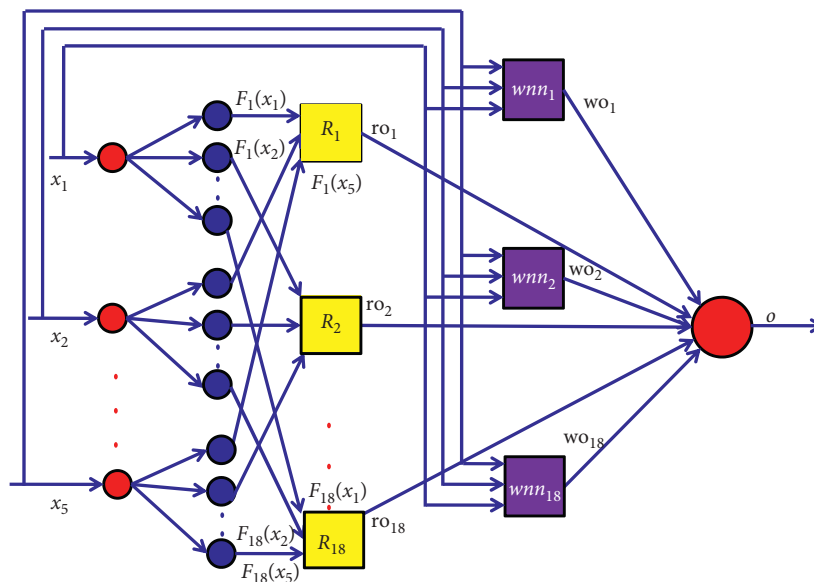


FIGURE 2: Schematic structure of FWNN models.

where $z_{ij} = (x_i - b_{ij})/a_{ij}$, a_{ij} is the dilation of the WNNs, b_{ij} is the translation of the WNNs, and w_j is the weight of the WNNs.

The fifth layer is the output layer. The total output of the FWNN (y) in this layer is defined as follows:

$$y_k = \frac{\sum_{j=1}^n \mu_j(x) \text{wo}_j}{\sum_{j=1}^n \mu_j(x)}. \quad (4)$$

In this proposed design, to monitor the anaerobic treatment system's operational status, effluent COD and production rates of biogas (methane) were chosen as the network outputs.

2.2.3. Training Algorithm to Optimize the Proposed FWNN.

A hybrid learning algorithm was applied to train and optimize the network parameters to further improve the prediction capabilities of the network. It has integrated genetic algorithm (GA) into gradient descent algorithm (GDA) to enhance the efficiency and robustness of the network.

GA is a kind of well-rounded global optimization method that owns the features with strong robustness and broad applicability [35]. Since the GDA easily falls into the optimum local and is sensitive to the initial values, the initial values of the network's parameters are first determined by a real-coded GA, and then the GDA is used to train the network, thereby greatly accelerating its convergence. In this work, the formulation of the objective function can be defined as follows:

$$E = \frac{1}{2} \sum_{k=1}^n (y_{dk} - y_k)^2, \quad (5)$$

where y_{dk} is the desired value, y_k is the output value of the FWNN, and n is the sample number. The output of the FWNN according to the s -th chromosome with $y_k(L)$ can be defined as follows:

$$y^s(L) = \frac{\sum_{j=1}^n \mu_j^s(x_i(L)) \cdot \text{wo}_j^s}{\sum_{j=1}^n \mu_j^s(x_i(L))} = \frac{\sum_{j=1}^n \text{wo}_j^s \cdot \left[\prod_i \exp \left\{ - \left(\frac{(x_i(L) - c_{ij}^s)^2}{(\sigma_{ij}^s)^2} \right) \right\} \right]}{\sum_{j=1}^n \left[\prod_i \exp \left\{ - \left(\frac{(x_i(L) - c_{ij}^s)^2}{(\sigma_{ij}^s)^2} \right) \right\} \right]}, \quad (6)$$

in which

$$\text{wo}_j^s = w_j^s \cdot \sum_{i=1}^m |a_{ij}^s|^{-(1/2)} \left(1 - \left(\frac{(x_i(L) - b_{ij}^s)}{a_{ij}^s} \right)^2 \right) \cdot \exp \left(-0.5 \left(\frac{(x_i(L) - b_{ij}^s)}{a_{ij}^s} \right)^2 \right). \quad (7)$$

GA is an artificial intelligence method, which simulates natural evolution using the three main operations: selection, crossover, and mutation, to produce better fitness for individuals. The goal of the GA for the selection operation is to

give population members (or solutions) more reproductive opportunities with better fitness values. Crossover and mutation operations produce new individuals in combining the information contained in two parents, and they can ensure that the new initial chromosomes are always feasible. The selection of the tournament is used to get the new generation. For the next generation, the member with the better fitness is selected.

Hence, the chromosome can be operated according to the following real-coded set:

$$Xn^s = [c_{ij}^s \ \sigma_{ij}^s \ a_{ij}^s \ b_{ij}^s \ w_j^s], \quad (8)$$

where

$$\begin{aligned} c_{ij}^s &= [c_{11}^s \cdots c_{m1}^s \cdots c_{1n}^s \cdots c_{mn}^s], \\ \sigma_{ij}^s &= [\sigma_{11}^s \cdots \sigma_{m1}^s \cdots \sigma_{1n}^s \cdots \sigma_{mn}^s], \\ a_{ij}^s &= [a_{11}^s \cdots a_{m1}^s \cdots a_{1n}^s \cdots a_{mn}^s], \\ b_{ij}^s &= [b_{11}^s \cdots b_{m1}^s \cdots b_{1n}^s \cdots b_{mn}^s], \\ w_j^s &= [w_1^s \cdots w_n^s]. \end{aligned} \quad (9)$$

Thus, the optimal initial variables of the FWNN would be finally obtained with the three genetic operations of selection, crossover, and mutation. The initial population size N_{pop} is 100 in this design, the crossover rate P_c is 0.7, and the mutation interval P_m is 0.01.

2.2.4. Parameter Updation through Gradient Descent Algorithm.

As the parameters of the network were initialized by the GA, the parameters of the FWNN and model were verified and revised by the GDA [36]. Finally, all the parameters of the developed FWNN were made up of the center and width parameters of Gaussian functions, and the dilation, translation, and weight parameters of WNNs were simultaneously optimized according to the following:

$$E = \frac{1}{2} [(y_d(t) - y(t))^2], \quad (10)$$

where y_d is the desired value and y is the output value of the FWNN. Accordingly, the parameter values of the FWNN can be given as follows:

$$\begin{aligned} w_j(t+1) &= w_j(t) + \eta \frac{\partial E}{\partial w_j} + \xi(w_j(t) - w_j(t-1)), \\ a_{ij}(t+1) &= a_{ij}(t) + \eta \frac{\partial E}{\partial a_{ij}} + \xi(a_{ij}(t) - a_{ij}(t-1)), \\ b_{ij}(t+1) &= b_{ij}(t) + \eta \frac{\partial E}{\partial b_{ij}} + \xi(b_{ij}(t) - b_{ij}(t-1)), \\ \sigma_{ij}(t+1) &= \sigma_{ij}(t) + \eta \frac{\partial E}{\partial \sigma_{ij}} + \xi(\sigma_{ij}(t) - \sigma_{ij}(t-1)), \\ c_{ij}(t+1) &= c_{ij}(t) + \eta \frac{\partial E}{\partial c_{ij}} + \xi(c_{ij}(t) - c_{ij}(t-1)), \end{aligned} \quad (11)$$

where η and ξ are the learning rate and the FWNN developed momentum factor, respectively.

2.3. Self-Adapted Fuzzy c-Means Clustering. In this work, according to the characteristics of the anaerobic treatment system, a self-adapted fuzzy c-means (FCM) clustering algorithm was proposed to deal with the fuzzy factors and thus determine the number of the FWNN's fuzzy rules. Objects are strictly divided into clusters based on the fuzzy clustering method, and the best class number is obtained by the valid analysis of clustering [37]. The calculating equations are designed as follows:

$$B(K) = \frac{\sum_{i=1}^K \sum_{j=1}^n u_{ij}^m \|v_i - \bar{x}\|^2 / (K-1)}{\sum_{i=1}^K \sum_{j=1}^n u_{ij}^m \|v_i - \bar{x}\|^2 / (n-K)}$$

$$\bar{x} = \frac{1}{n} \sum_{i=1}^K \sum_{j=1}^n u_{ij}^m x_j$$

$$J_m(U, V) = \sum_{i=1}^K \sum_{j=1}^n u_{ij}^m d_{ij}^2$$

$$\sum_{i=1}^K u_{ij} = 1, \quad 1 \leq j \leq n,$$
(12)

where $B(K)$ represents the sum of weighted Euclidean distances, $J_m(U, V)$ is the objective function representing the minimum square sum of weighted Euclidean distances, K is the number of clusters, n is the number of objects, x_j is the observed value, and m is the weighted exponent.

d_{ij} represent the Euclidean distance and can be designed as follows:

$$d_{ij} = \|x_j - v_i\|. \quad (13)$$

u_{ij} are the membership function values and can be represented as follows:

$$u_{ij}^{(k)} = \frac{1}{\sum_{r=1}^c (d_{ij}^{(k)} / d_{rj}^{(k)})^{2/(m-1)}}. \quad (14)$$

v_i are the cluster centers, and the formula for their specific calculation is as follows:

$$v_i^{(k+1)} = \frac{\sum_{j=1}^n (u_{ij}^{(k)})^m x_j}{\sum_{j=1}^n (u_{ij}^{(k)})^m}. \quad (15)$$

3. Results and Discussion

3.1. Data Collection and Preprocessing. In order to evaluate the hybrid FWNN model for the anaerobic wastewater process, 150 datasets were collected, the network was trained with 120 datasets, and 30 sets were proved. Standardization, which eliminates data redundancies and effectively organizes the data, has been used to improve the FWNN's performance. In this work, all datasets were converted to the range between 0 and 1 through scaling.

3.2. FWNN Development. Using all these data, the effluent COD and biogas (methane) production rates were predicted using an FWNN model. In addition, the datasets were analyzed using a self-adapted fuzzy c-means clustering, and the optimal clustering number with 18 sets was identified. The structure model shown in Figure 2 was determined based on the analysis of technology and experimental data as well as the forecast target. It included three models of the FWNN (FWNNCOD, FWNNQ, and FWNNCH₄) for COD, Q_{gas}, and CH₄ prediction, respectively. For each model, there was a separate rule basis, but the models' input parameters were the same.

A hybrid learning algorithm was applied after initializing the model structure and parameter to train and optimize network parameters. Because the GDA easily falls into local optimum and is sensitive to the initial values, the initial values of parameters of the network were firstly determined by a real-coded GA, and then the GDA was used to train the network, thereby greatly accelerating its convergence.

3.3. Simulation of FWNN Model. Three FWNN-based models were simulated and verified by the experimental data using the MATLAB program. The initial population size N_{pop} , crossover rate P_c , interval of mutation P_m , maximum number of generations, learning rate η , and momentum factor ξ are 100, 0.7, 0.01, 200, 0.02, and 0.5, respectively. Figure 3 sketches the training process of the developed FWNN (taking FWNNCOD for example). From Figure 3, it can be easily understood that this network has virtues of good memory, fast convergence ability, and strongly stable capability. Consequently, the new parameters of FWNN models were obtained by repeated training and studying through the hybrid learning algorithm, as shown in Tables 1 and 2.

Figure 4(a) shows the predictive values of the FWNN models according to the testing datasets. As shown in Figure 4(a), it is easily found that the predicted values are in good conformity with those observed values. In this work, in order to assess the performance of models, various indicators were used to analyze and estimate the developed FWNN models, such as the determination coefficient (R^2), correlation coefficient (R), root mean square error (RMSE), mean square error (MSE), and mean absolute percentage error (MAPE). As shown in Table 3, the performance indicators of the proposed FWNN models were acquired by comparing the predicted results with real values.

Table 3 clearly shows that using the FWNN, the MAPE values of 2.9083%, 3.3563%, and 4.0660% for COD, Q_{gas}, and CH₄ could be achieved. R^2 values were 0.9647, 0.9681, and 0.9501, respectively, for COD, Q_{gas}, and CH₄. R values of COD, Q_{gas}, and CH₄ were 0.9822, 0.9839, and 0.9747, respectively. The RMSE values of 28.7439, 199.2556, and 155.0499 for COD, Q_{gas}, and CH₄ could also be achieved. Simulations on the proposed model showed that this proposed model not only could accomplish parameter calibration rapidly and find out the optimal solutions of parameters accurately but also could improve the converging rate and the stability of the models. The results

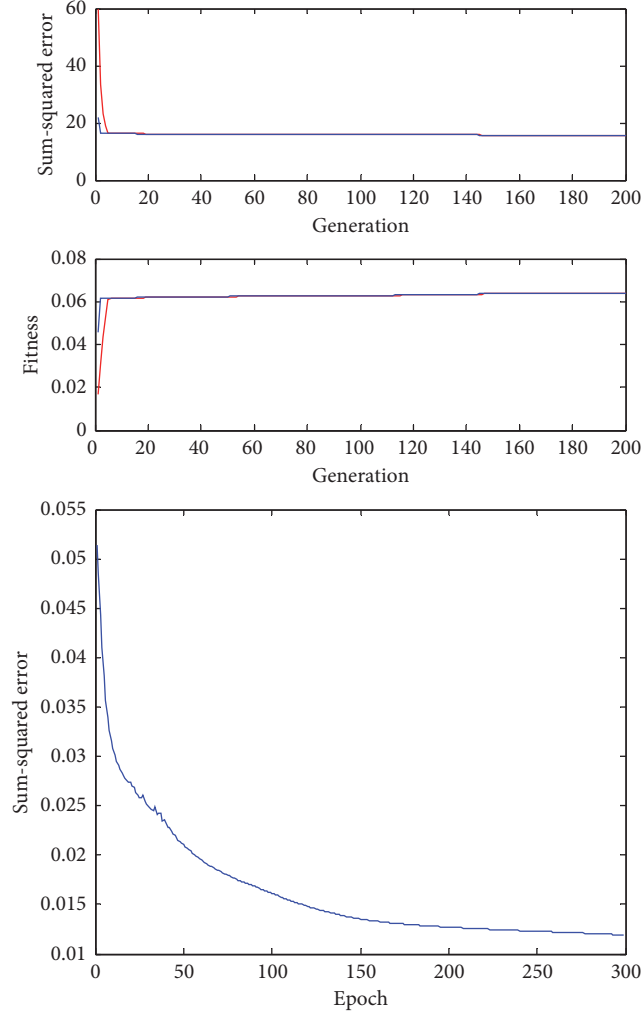


FIGURE 3: Training performance of the FWNN based on hybrid GA-GDA algorithms.

TABLE 1: Parameters of the FNNCOD.

Rules	COD (t)		HRT (t)		OLR (t)		pH (t)		ALK (t)	
	c	σ	c	σ	c	σ	c	σ	c	σ
1	0.0136	0.1607	0.5268	-0.7421	-0.3635	-0.5529	-0.3051	-0.9233	0.4253	0.1944
2	-0.7069	0.7358	-0.3188	-0.3580	0.3703	-0.2483	-0.3542	1.1877	-0.7381	0.6980
3	-0.7367	-0.6604	1.3965	0.2865	-0.6298	0.9426	-0.0589	1.0751	-0.5281	0.3233
4	-0.1518	1.7925	-0.5607	-1.2634	0.4315	9.6476	0.0743	0.0939	-0.5717	0.1826
5	-1.2089	0.2705	0.0115	-1.0385	0.6881	-1.9966	0.0109	30.2334	0.3907	-0.1104
6	0.6641	-0.2334	-0.4112	0.6708	0.0439	0.8663	-0.3301	-0.2831	0.4050	-0.5511
7	0.0064	0.9719	-0.7012	-4.8530	0.9405	-0.6621	0.7832	-0.0767	0.4281	0.7108
8	0.3419	0.1058	0.8441	1.1613	1.1604	-74.1843	-0.1981	0.8107	0.5553	0.4536
9	-0.5602	0.5057	1.1063	-26.4556	0.0843	-7.2215	-0.8100	-6.8183	-1.7993	0.3474
10	0.4907	-0.5534	-0.0703	-0.4569	-0.2704	0.9582	-0.3745	0.5942	-3.0162	1525.6060
11	-0.6621	-0.4266	0.5657	1.0340	0.1292	-0.1692	-0.2571	-2.6569	-0.4486	-8.9554
12	0.2888	-0.3405	-0.0953	-0.3502	0.5470	-83.4372	-0.6050	2.0040	0.3772	-13.0426
13	-0.2228	1.3588	0.3659	0.7005	-0.1630	-0.4162	0.4636	-0.6097	-1.0012	1.0308
14	-0.4807	-0.4252	-0.0355	-0.6217	0.1970	0.6718	0.0845	-0.5032	-0.1502	0.9260
15	-0.8972	-0.8169	0.1483	-1.4908	-0.1679	0.9453	0.4577	-0.8348	-0.1577	-0.7370
16	0.2736	-0.3070	0.3224	-0.5635	0.3254	7.5609	0.1766	0.6113	0.5786	-3.1036
17	-0.4311	3.5123	0.4850	-0.9749	0.3135	-0.6053	-1.1362	1.8104	-0.4111	-0.4197
18	0.1273	0.6391	-0.2829	4.1239	0.1948	0.6960	0.5902	0.2422	0.0614	0.0985

TABLE 2: Wavelet layer parameters of the FWNNCOD.

Rules	w	COD (t)		HRT (t)		OLR (t)		pH (t)		ALK (t)	
		a	b	a	b	a	b	a	b	a	b
1	1.5886	-0.1273	-1.1428	1.6123	0.7959	2.1101	1.6534	1.7961	1.8034	-0.0412	-1.4770
2	-1.4397	-1.0635	0.3172	0.3292	1.8075	1.8048	1.9308	-0.5009	-3.3946	-0.1592	-1.6507
3	-3.2344	8.8674	8.2901	8.6132	8.6776	0.0000	-0.6094	0.4513	-3.3283	-0.0012	-1.2749
4	-2.8787	9.4875	8.8757	9.3742	9.3019	9.4737	8.7495	-0.5562	-3.8668	0.3150	-2.7147
5	-0.1198	-0.2082	-1.9909	-0.5800	-2.8096	-0.1405	-1.7493	-0.3507	-2.4843	-0.0722	-4.1235
6	0.5239	-1.1138	-0.4318	-2.4781	-36.4693	0.2082	-0.3899	-0.0686	-1.7075	-0.1363	-2.8063
7	-2.0347	-0.0948	-1.5617	-0.1529	-1.9035	-0.2736	-2.4728	6.3255	6.7699	-0.1353	-1.7480
8	0.1759	0.1584	-1.1703	1.0586	0.1860	-0.8765	-1.1716	-0.2192	-2.1848	0.4971	0.2769
9	-1.4778	5.4539	4.8521	-0.1985	-2.1011	5.4583	4.7566	-0.5334	-3.6407	-0.2719	-4.3257
10	-0.7646	-0.0413	1.3235	-1.3483	-3.2882	0.0383	3.1448	1.4188	0.8019	-1.3864	-1.4296
11	-2.4920	6.0096	5.4610	0.2843	-2.6436	0.2806	-2.5572	0.3079	-2.6510	5.5745	5.5132
12	-0.6872	-0.2137	-2.5483	0.0607	-2.2885	0.0257	-1.1678	0.3778	-2.3892	-0.4407	-1.8772
13	0.6707	1.4191	0.8041	-0.1416	-1.7496	0.0004	-1.3015	-0.1572	-2.8354	0.1461	2.4996
14	-2.5713	8.8880	8.2832	-0.0014	-2.1207	8.9002	8.1486	-0.3254	-5.0826	8.7261	8.5458
15	-1.2637	-0.9244	-12.2623	1.1685	0.0916	1.8175	0.6263	-0.4936	-3.2684	-0.3105	-2.5201
16	0.9024	-1.6801	-6.3276	0.9363	0.5837	1.7794	1.7951	-0.1902	-1.2803	0.9617	0.0144
17	0.0526	-0.5795	0.7473	-1.0763	-1.2789	-6.9178	-96.1241	0.7802	2.6923	0.7286	2.7465
18	-0.0466	-0.5801	-1.5784	-0.3502	-2.5046	-0.3109	-1.3356	0.9269	2.3812	1.0120	0.8650

showed a good concordance with the experimental values predicted. As shown in Table 3, for the three FWNN models, the predictive performance of the proposed FWNN models on effluent quality and production rates for biogas was satisfactory with a very high determination coefficient (R^2), which were all over 0.95. In other words, a high R^2 showed that only 3.53%, 3.19%, and 4.91% of the total variations for COD, Q_{gas} , and CH_4 were not explained by the proposed FWNN models. In addition, a high R for the three FWNN models illustrates that there was a good concordance of the predicted values with the experimental ones. Accordingly, based on the other small evaluation indicators (MAPE, RMSE, and MSE), it also shows that the predicted model developed had high predictive accuracy and satisfied robustness and fitness, making the system highly adaptable.

3.4. Comparisons with FNN, WNN, and NN. The developed FWNN models were compared with FNN, WNN, and NN models to demonstrate the correctness, efficiency, and benefits of the hybrid network. Based on the comparison of results, as shown in Table 3, it can be seen that FWNN models have lower RMSE (or MSE) and MAPE values and higher R^2 and R values. Taking COD_{eff} for example, when predicting, R , R^2 , MAPE, RMSE, and MSE values were 0.9822, 0.9647, 2.9083%, 28.7439, and 826.2142 using the FWNN, respectively. However, when using the FNN, WNN, and NN models, R values were 0.9645, 0.9351, and 0.8222, respectively; R^2 values were 0.9302, 0.7697, and 0.6760, respectively; MAPE values were 4.077%, 4.4575%, and 8.3163%, respectively; RMSE values were 41.1297, 55.8223, and 88.2468, respectively; and MSE values were $1.6917 E + 3$, $3.1161 E + 3$, and $7.7875 E + 3$, respectively.

Table 3 shows that FWNN models have higher estimation accuracy and better robustness than FNN, WNN, and NN models, showing that FWNN models are more accurate than FNN, WNN, and NN models for predicting

effluent quality and biogas (methane) production rates. The results of this study suggest that the FWNN model was highly capable of extracting the dynamic IC system changes. Considering the nonlinearity, complexity, and randomness of the anaerobic treatment process, such a good predictive performance of FWNN models was particularly important for modeling the wastewater treatment process. The FWNN is a good choice for modeling the IC anaerobic treatment process. The simulated models based on the FWNN model can be effectively applied to a full-scale IC anaerobic reactor to cope with influent variations. The results show that anaerobic wastewater treatment can be better described with the FWNN than the FNN, WNN, and NN. Maintaining environmental standards, FWNN models can effectively achieve the IC anaerobic system's environmental and economic goals in real time. In the future, in order to optimize the anaerobic treatment system, a control system will be developed to monitor and control the system based on the FWNN model.

3.5. Multidimensional Graphs of Affecting Factors and Regulating Strategies of IC. Using the partitioning connection weights (PCW) method, the importance of the influencing factors could generally be analyzed. In this work, four-dimensional graphs with two outputs were used for analyzing the importance of input parameters to outputs.

3.5.1. Influence of pH and OLR on COD Removal Rate and CH_4 Production Rate. Figure 5(a) shows the influence of pH and OLR on the COD removal rate and the CH_4 production rate. From Figure 5(a), when pH and OLR values varied from 6.8 to 7.4 and from 5 to 15 kg COD/ $\text{m}^3\cdot\text{d}$, the rate of COD removal and the rate of production of CH_4 increased, respectively. The treatment system was particularly sensitive to changes in pH when the OLR was high. However, when the OLR was above 15 kg COD/ $\text{m}^3\cdot\text{d}$, changes in pH values

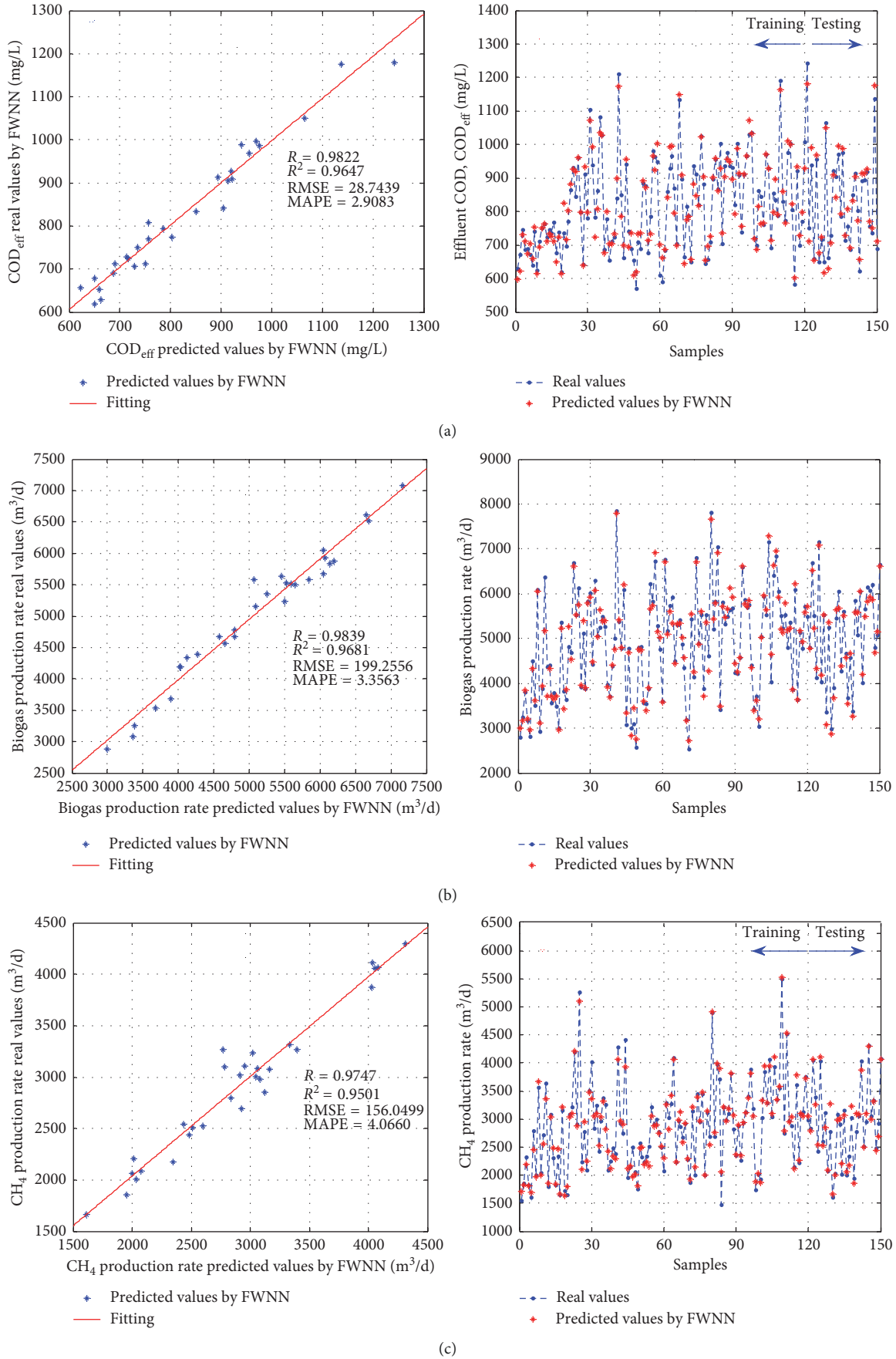


FIGURE 4: FWNN performance of the estimation of effluent concentrations and biogas (methane) production rate.

TABLE 3: Performances of the FWNN, FNN, WNN, and NN in modeling the IC anaerobic system.

Model	COD _{eff}				CH ₄ production rate				Biogas production rate			
	FWNN	FNN	WNN	NN	FWNN	FNN	WNN	NN	FWNN	FNN	WNN	NN
<i>R</i>	0.9822	0.9645	0.9351	0.8222	0.9747	0.9068	0.8895	0.7885	0.9839	0.9405	0.9282	0.8027
<i>R</i> ²	0.9647	0.9302	0.7697	0.6760	0.9501	0.8223	0.8399	0.6217	0.9681	0.8846	0.8789	0.6446
MAPE	2.9083	4.0770	4.4575	8.3163	4.0660	7.3867	7.5853	12.8657	3.3563	5.9532	5.1695	11.8740
RMSE	28.7439	41.1297	55.8223	88.2468	156.0499	298.0273	329.7642	730.9969	199.2556	366.6599	407.6466	681.9047
MSE	826.2142	1.6917E + 3	3.1161E + 3	7.7875E + 3	2.4352E + 4	8.882E + 4	1.0874E + 5	5.3436E + 5	3.9703E + 4	1.3665E + 5	1.6618E + 5	4.6499E + 5

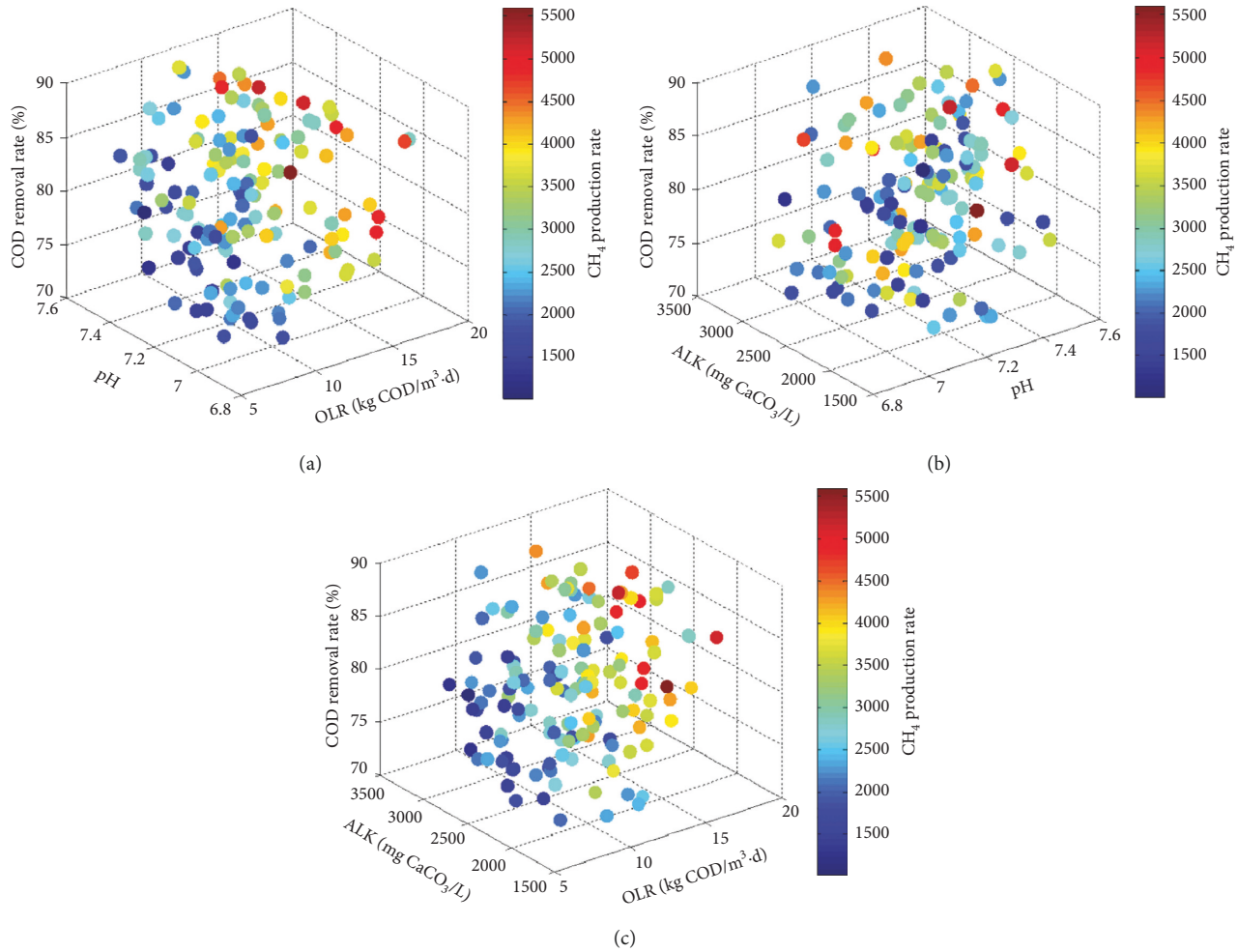


FIGURE 5: Impact of the parameters (a) pH and OLR, (b) ALK and pH, and (c) ALK and OLR on COD removal and CH₄ production rates.

rarely affected the performance of the treatment system. When the OLR exceeded 15 kg COD/m³·d or pH was above 7.5, there was a negative effect on the rate of COD removal and the rate of production of CH₄, and the negative effect on the rate of COD removal and the rate of production of CH₄ caused by the increased OLR was lower than that caused by low pH. Hence, when the OLR of the treatment system was enhanced by shortening HRT or increasing the influent COD, it was conducive to the stability of the treatment system through adding alkali to improve pH values.

3.5.2. Influence of pH and ALK on COD Removal Rate and CH₄ Production Rate. Figure 5(b) shows the influence of pH and influent COD on the COD removal rate and CH₄ production rate. Whatever pH was in the system, when ALK was low, it is not good for the rate of COD removal and the rate of production of CH₄. The treatment system also became immovable at low pH. When the ALK exceeded 2500 mg/L and the pH in the treatment system exceeded 7.5, the rate of COD removal and the production of CH₄ increased. Therefore, when the influent concentration of COD was high, pH and ALK values were kept higher than 7.5 and 2500 mg/L, respectively.

3.5.3. Influence of OLR and ALK on COD Removal Rate and CH₄ Production Rate. Figure 5(c) shows the influence of OLR and ALK on the treatment system. When the OLR was lower than 15 kg COD/m³·d, the treatment system was rarely affected by ALK, and the CH₄ production rate was low. When ALK was higher than 2500 mg/L, especially when it increased from 3000 mg/L to 3500 mg/L, the CH₄ production rate decreased dramatically with the changes of ALK. The COD removal rate was low when the OLR was over 18 kg COD/m³·d. If the OLR continuously remained higher, the worsening trend in the treatment system would have occurred. If the OLR remained constant, the COD removal rate rules were obtained with the change of ALK. Moreover, it was shown that the optimal influent OLR was about 15 kg COD/m³·d when the treatment system ran in the operating conditions with a pH of 7.5 and alkalinity of 3000 mg/L.

4. Conclusion

The proposed research was to establish an artificial intelligence-based model for modeling a full-scale anaerobic wastewater treatment system. Combining the benefits of the NN, FL, and WT, the FWNN could be used successfully to

predict effluent quality and the rate of production of biogas according to the strong nonlinear ship between its inputs and outputs. The FWNN model showed higher estimation accuracy and better robustness compared to FNN, WNN, and NN models and achieved better performance in predicting effluent quality and production rates of biogas with high determination coefficients R^2 over 0.95. Meanwhile, the FWNN model can be used for analyzing the importance of the affecting factors. The proposed hybrid approach will provide a very impactful and cost-effective tool for modeling the anaerobic process that helps engineers monitor operational parameters to improve the performance of anaerobic treatment.

Data Availability

The data used to support the findings of this study have not been made available because the authors are asked to sign a confidentiality agreement with the Chinese government which provides the basis of the data.

Conflicts of Interest

The authors declare that there are no conflicts of interest regarding the publication of this paper.

Authors' Contributions

Zehua Huang, Renren Wu, and Xiaohui Yi contributed equally to this work and shared the first authorship. Zehua Huang and Renren Wu conducted the experiments and wrote the main manuscript text, Xiaohui Yi contributed in the manuscript preparation and modification (revise process), Hongbin Liu prepared figures 1–3, Jiannan Cai prepared figures 4–5, and Guoqiang Niu prepared tables 1–3. Mingzhi Huang designed this research and supervised analyses including data interpretation and discussion and manuscript preparation as a principal investigator (PI). Guangguo Ying was involved in experimental design and supervised manuscript preparation.

Acknowledgments

This research was supported by the National Natural Science Foundation of China (nos. 41977300 and 41907297), Guangdong Provincial Natural Science Foundation (no. 2016A030306033), Science and Technology Program of Guangzhou (no. 907224176081) and Guangdong Foundation for Program of Science and Technology Research (no. 2017B030314057).

References

- [1] C. Zhang, D. Tian, X. Yi et al., "Occurrence, distribution and seasonal variation of five neonicotinoid insecticides in surface water and sediment of the Pearl Rivers, South China," *Chemosphere*, vol. 217, pp. 437–446, 2019.
- [2] D. Erdirencelebi and S. Yalpir, "Adaptive network fuzzy inference system modeling for the input selection and prediction of anaerobic digestion effluent quality," *Applied Mathematical Modelling*, vol. 35, no. 8, pp. 3821–3832, 2011.
- [3] X. Yi, C. Zhang, H. Liu et al., "Occurrence and distribution of neonicotinoid insecticides in surface water and sediment of the Guangzhou section of the Pearl River, South China," *Environmental Pollution*, vol. 251, pp. 892–900, 2019.
- [4] M. Cakmakci, "Adaptive neuro-fuzzy modelling of anaerobic digestion of primary sedimentation sludge," *Bioprocess and Biosystems Engineering*, vol. 30, no. 5, pp. 349–357, 2007.
- [5] C. W. Chan and G. H. Huang, "Artificial intelligence for management and control of pollution minimization and mitigation processes," *Engineering Applications of Artificial Intelligence*, vol. 16, no. 2, pp. 75–90, 2003.
- [6] F. I. Turkdoganaydinol and K. Yetilmesoy, "A fuzzy-logic-based model to predict biogas and methane production rates in a pilot-scale mesophilic UASB reactor treating molasses wastewater," *Journal of Hazardous Materials*, vol. 182, pp. 460–471, 2010.
- [7] M. Huang, W. Han, J. Wan, Y. Ma, and X. Chen, "Multi-objective optimisation for design and operation of anaerobic digestion using GA-ANN and NSGA-II," *Journal of Chemical Technology & Biotechnology*, vol. 91, no. 1, pp. 226–233, 2016.
- [8] J. Biswas, R. Chowdhury, and P. Bhattacharya, "Mathematical modeling for the prediction of biogas generation characteristics of an anaerobic digester based on food/vegetable residues," *Biomass and Bioenergy*, vol. 31, no. 1, pp. 80–86, 2007.
- [9] Y. Chen, J. He, Y. Mu et al., "Mathematical modeling of upflow anaerobic sludge blanket (UASB) reactors: simultaneous accounting for hydrodynamics and bio-dynamics," *Chemical Engineering Science*, vol. 137, pp. 677–684, 2015.
- [10] Z. Cetecioglu, "Aerobic inhibition assessment for anaerobic treatment effluent of antibiotic production wastewater," *Environmental Science and Pollution Research*, vol. 21, no. 4, pp. 2856–2864, 2014.
- [11] X. Zhang, Z. Wang, Z. Wu et al., "Membrane fouling in an anaerobic dynamic membrane bioreactor (AnDMBR) for municipal wastewater treatment: characteristics of membrane foulants and bulk sludge," *Process Biochemistry*, vol. 46, no. 8, pp. 1538–1544, 2011.
- [12] J. Eason and S. Cremaschi, "Adaptive sequential sampling for surrogate model generation with artificial neural networks," *Computers & Chemical Engineering*, vol. 68, pp. 220–232, 2014.
- [13] S. Hosseini and A. Al Khaled, "A survey on the imperialist competitive algorithm metaheuristic: implementation in engineering domain and directions for future research," *Applied Soft Computing*, vol. 24, pp. 1078–1094, 2014.
- [14] A. A. Khaled and S. Hosseini, "Fuzzy adaptive imperialist competitive algorithm for global optimization," *Neural Computing and Applications*, vol. 26, no. 4, pp. 813–825, 2015.
- [15] M. Huang, Y. Ma, J. Wan et al., "A hybrid genetic—neural algorithm for modeling the biodegradation process of DnBP in AAO system," *Bioresource Technology*, vol. 102, no. 19, pp. 8907–8913, 2011.
- [16] Y. Shi, X.-T. Zhao, Y.-M. Zhang, and N.-Q. Ren, "Back propagation neural network (BPNN) prediction model and control strategies of methanogen phase reactor treating traditional Chinese medicine wastewater (TCMW)," *Journal of Biotechnology*, vol. 144, no. 1, pp. 70–74, 2009.
- [17] K. Sridevi, E. Sivaraman, and P. Mullai, "Back propagation neural network modelling of biodegradation and fermentative biohydrogen production using distillery wastewater in a hybrid upflow anaerobic sludge blanket reactor," *Bioresource Technology*, vol. 165, pp. 233–240, 2014.
- [18] T. Ferenci and L. Kovács, "Predicting body fat percentage from anthropometric and laboratory measurements using

- artificial neural networks,” *Applied Soft Computing*, vol. 67, pp. 834–839, 2018.
- [19] G. Sorrosal, E. Irigoyen, C. E. Borges, C. Martin, A. M. Macarulla, and A. Alonso-Vicario, “Artificial neural network modelling of the bioethanol-to-olefins process on a HZSM-5 catalyst treated with alkali,” *Applied Soft Computing*, vol. 58, pp. 648–656, 2017.
- [20] M. Z. Huang, J. Q. Wan, Y. W. Ma, Y. Wang, W. J. Li, and X. F. Sun, “Control rules of aeration in a submerged biofilm wastewater treatment process using fuzzy neural networks,” *Expert Systems with Applications*, vol. 36, pp. 10428–10437, 2009.
- [21] M. Sedighi, K. Keyvanloo, and J. Towfighi, “Modeling of thermal cracking of heavy liquid hydrocarbon: application of kinetic modeling, artificial neural network, and neuro-fuzzy models,” *Industrial & Engineering Chemistry Research*, vol. 50, no. 3, pp. 1536–1547, 2011.
- [22] J. Wan, M. Huang, Y. Ma et al., “Prediction of effluent quality of a paper mill wastewater treatment using an adaptive network-based fuzzy inference system,” *Applied Soft Computing*, vol. 11, no. 3, pp. 3238–3246, 2011.
- [23] J. Cai, P. Zheng, M. Qaisar, and T. Luo, “Prediction and quantifying parameter importance in simultaneous anaerobic sulfide and nitrate removal process using artificial neural network,” *Environmental Science and Pollution Research*, vol. 22, no. 11, pp. 8272–8279, 2015.
- [24] A. Perendeci, S. Arslan, A. Tanyolaç, and S. S. Çelebi, “Effects of phase vector and history extension on prediction power of adaptive-network based fuzzy inference system (ANFIS) model for a real scale anaerobic wastewater treatment plant operating under unsteady state,” *Bioresource Technology*, vol. 100, no. 20, pp. 4579–4587, 2009.
- [25] J. Ruan, X. Chen, M. Huang, and T. Zhang, “Application of fuzzy neural networks for modeling of biodegradation and biogas production in a full-scale internal circulation anaerobic reactor,” *Journal of Environmental Science and Health, Part A*, vol. 52, no. 1, pp. 7–14, 2017.
- [26] P. Mullai, S. Arulselvi, H.-H. Ngo, and P. L. Sabarathinam, “Experiments and ANFIS modelling for the biodegradation of penicillin-G wastewater using anaerobic hybrid reactor,” *Bioresource Technology*, vol. 102, no. 9, pp. 5492–5497, 2011.
- [27] D. Hanbay, I. Turkoglu, and Y. Demir, “Prediction of wastewater treatment plant performance based on wavelet packet decomposition and neural networks,” *Expert Systems with Applications*, vol. 34, no. 2, pp. 1038–1043, 2008.
- [28] W. C. Wang, K. Li, Z. X. Chen, and Q. Z. Niu, “Soft measurement technique of sewage treatment parameters based on wavelet neural networks,” *Applied Mechanics Materials*, vol. 556–562, pp. 3168–3171, 2015.
- [29] H. Loussifi, K. Nouri, and N. Benhadj Braiek, “A new efficient hybrid intelligent method for nonlinear dynamical systems identification: the wavelet kernel fuzzy neural network,” *Communications in Nonlinear Science and Numerical Simulation*, vol. 32, pp. 10–30, 2016.
- [30] M. Huang, D. Tian, H. Liu et al., “A hybrid fuzzy wavelet neural network model with self-adapted fuzzy c-means clustering and genetic algorithm for water quality prediction in rivers,” *Complexity*, vol. 2018, pp. 1–11, 2018.
- [31] W. E. Federation, *American Public Health Association. Standard Methods for the Examination of Water and Wastewater*, American Public Health Association (APHA), Washington, DC, USA, 2005.
- [32] Z. Zhang, C. Zhang, Z. Huang et al., “Residue levels and spatial distribution of phthalate acid esters in water and sediment from urban lakes of Guangzhou, China,” *Journal of Environmental Science and Health, Part A*, vol. 54, no. 2, pp. 127–135, 2019.
- [33] H. Wang and Y. Cao, “Predicting power consumption of GPUs with fuzzy wavelet neural networks,” *Parallel Computing*, vol. 44, pp. 18–36, 2015.
- [34] M. Z. Huang, T. Zhang, J. J. Ruan, and X. H. Chen, “A new efficient hybrid intelligent model for biodegradation process of DMP with fuzzy wavelet neural networks,” *Sci. Rep.*, vol. 7, p. 41239, 2017.
- [35] M. Huang, J. Wan, Y. Ma et al., “A GA-based neural fuzzy system for modeling a paper mill wastewater treatment process,” *Industrial & Engineering Chemistry Research*, vol. 50, no. 23, pp. 13500–13507, 2011.
- [36] Z. Liu, Q. Wu, Y. Zhang, Y. Wang, and C. L. P. Chen, “Adaptive fuzzy wavelet neural network filter for hand tremor canceling in microsurgery,” *Applied Soft Computing*, vol. 11, no. 8, pp. 5315–5329, 2011.
- [37] J. Ruan, C. Zhang, Y. Li et al., “Improving the efficiency of dissolved oxygen control using an on-line control system based on a genetic algorithm evolving FWNN software sensor,” *Journal of Environmental Management*, vol. 187, pp. 550–559, 2017.

Research Article

Path Optimization of Mobile Sink Node in Wireless Sensor Network Water Monitoring System

Fan Chao, Zhiqin He, Aiping Pang , Hongbo Zhou, and Junjie Ge

School of Electrical Engineering, Guizhou University, Guiyang 550025, China

Correspondence should be addressed to Aiping Pang; 417524788@qq.com

Received 13 August 2019; Revised 11 October 2019; Accepted 6 November 2019; Published 25 November 2019

Guest Editor: Raúl Baños

Copyright © 2019 Fan Chao et al. This is an open access article distributed under the Creative Commons Attribution License, which permits unrestricted use, distribution, and reproduction in any medium, provided the original work is properly cited.

In the water area monitoring of the traditional wireless sensor networks (WSNs), the monitoring data are mostly transmitted to the base station through multihop. However, there are many problems in multihop transmission in traditional wireless sensor networks, such as energy hole, uneven energy consumption, unreliable data transmission, and so on. Based on the high maneuverability of unmanned aerial vehicles (UAVs), a mobile data collection scheme is proposed, which uses UAV as a mobile sink node in WSN water monitoring and transmits data wirelessly to collect monitoring node data efficiently and flexibly. In order to further reduce the energy consumption of UAV, the terminal nodes are grouped according to the dynamic clustering algorithm and the nodes with high residual energy in the cluster are selected as cluster head nodes. Then, according to the characteristics of sensor nodes with a certain range of wireless signal coverage, the angular bisection method is introduced on the basis of the traditional ant colony algorithm to plan the path of UAV, which further shortens the length of the mobile path. Finally, the effectiveness and correctness of the method are proved by simulation and experimental tests.

1. Introduction

The wireless sensor network, composed of a large number of static or mobile sensors in a self-organizing and multihop manner, is widely used in military, medical health, smart homes, building monitoring, environmental monitoring, and other fields [1]. In the water area detection of traditional wireless sensor networks, a terminal node transmits data to a sink node by multihop [2]. However, multihop transmission tends to cause an energy hole. In other words, the nodes around the sink node, undertaking too many data forwarding tasks and thus consuming a lot of energy or even exhausting the energy, will damage the connectivity of the entire wireless network. At the same time, the multihop transmission also produces additional communication overhead due to collision caused by frequent communication and data transmission between nodes.

In order to solve the above problems, a wireless sensor network with mobile nodes was born. The sink nodes are

carried on by mobile terminals to collect data, which not only avoids energy hole and uneven energy consumption, prolongs the life cycle of the whole network, but also improves the flexibility of data collection and the reliability of data transmission [3–14]. In reference [2], the data acquisition strategy of the mobile sink node is studied, which improves the efficiency of the work, but the specific acquisition path is not planned and studied. In reference [3], the ant colony algorithm is optimized to plan the path of mobile sink nodes, which solves the problem that the global search ability of traditional ant colony algorithm is weak and easy to fall into the local optimal solution, but it fails to make use of the wireless signal coverage characteristics of nodes in WSN. Reference [4], taking into consideration the characteristics of wide deployment range and irregular position of the mobile terminal in the farmland information acquisition system, proposes an energy-efficient data collection scheme. According to factors such as node energy and location, the node cluster head can be selected optimally, but this scheme cannot be applied to the scene with high real-time

requirements. In reference [5], a maximum-minimum energy consumption probability model is proposed to optimize the path between network neutron nodes and sink nodes, but the energy limitation of the mobile sink itself is not taken into account. On the basis of introducing a mobile data collector, an algorithm of maximizing cache mechanism is proposed in reference [6] to avoid the overflow of cluster head due to insufficient cache space and prolong the life cycle of the network, but the energy consumption of mobile data collector is also not taken into account. A mobile data collection strategy combined with DSDV routing protocol is proposed in [7], which improves the reliability of data transmission and extends the network life cycle, however, the level of timeliness and adaptability is not high. In reference [8], the mobile data transmitter (MDT) is used as the mobile sink node, and a heuristic discrete firefly algorithm is proposed, which can be used to collect the data optimally from the sensor node. In reference [9], in order to solve the problem of energy hole in traditional wireless sensor networks, a new path planning scheme is proposed in this paper. It forms a generating tree to connect all sensors, and then selects each convergence point according to the number and distance of hops in the tree and the amount of forwarding data from other sensors, and proposes an enhancement algorithm to further reduce the path distance. This paper presents a new optimization method for the path of the mobile node, which is simple in principle and has high practicability and can provide some reference for such problems.

This paper mainly considers the self-moving energy consumption in the mobile data collection of the mobile sink node from the actual environment. UAV is applied to wireless sensor networks as a mobile sink node and puts forward a new path optimization algorithm to optimize its moving path and reduce the total energy consumption. According to the dynamic clustering algorithm, the network is divided into clusters, and the cluster head nodes are selected according to the energy level. The cluster head nodes of each cluster become the residence point of UAV. UAV traverses each cluster head node from the base station, collects the data, and returns to the base station. Its energy consumption is mainly composed of two parts: the first part is mobile energy consumption; the second part is consumption due to data collection. Compared with the energy consumption of receiving data, the mobile energy consumption of UAV is an important part of its total energy consumption. Therefore, how to plan the moving path of UAV and reduce its moving length as much as possible has become an important part of the problem of mobile data collection. This paper takes into account the path planning of mobile sink nodes in WSN and the wireless signal coverage characteristics of nodes, further reduces the line distance of mobile sink nodes, improves the efficiency of data extraction, and increases the endurance ability of mobile sink nodes.

The remainder of this paper is as follows: In the second part, we present the model of the problem and analyze it. In the third part, the optimization scheme is put forward, and the simulation and experiment are carried out to prove the

effectiveness and reliability of the scheme. In the fourth part, the summary of the proposed work is made.

2. Problem Modeling and Formulation

2.1. Problem Modeling. In the water area monitoring system of the wireless sensor network, the sensor monitoring node collects the data to send to each cluster head node, and then the UAV collects the data of each cluster head node [15–17]. The overall network model is shown in Figure 1.

Combined with the given network model, before putting forward the model of the UAV path planning problem, the following assumptions are made for the problem, which is convenient for analysis and calculation.

- (1) The altitude of the monitoring nodes will be different in the area where the monitoring nodes are arranged. In order to simplify the problem without losing its generality, it is assumed that the monitoring nodes are all in the same plane.
- (2) The wireless signal coverage area of the mobile sink node and the monitoring node is circular, and the specific range is determined by the radius of the stable transmission data of the hardware wireless communication module. Each monitoring node and the mobile sink node are respectively the centers of the circle. At the same time, the monitoring node and the mobile sink node are abstracted into the points in the area.

Based on the above assumptions, considering the coverage of the mobile sink node and the monitoring node, the schematic diagram of the mobile sink node line can be analyzed, as shown in Figure 2.

In Figure 2, z_0 is the original position of the mobile sink node, $\{x_1, x_2, x_3, x_4\}$ is the location of each monitoring node. If there are overlapping areas between the two nodes, the middle point between the selected quantity nodes is taken as the extraction point on the line, if not, the edge of the coverage area is selected as the stop point, expressed as $\{a_1, a_2, a_3\}$, and it is called the middle selection point. $\{y_1, y_2, y_3, y_4\}$ is the point with considering the wireless signal coverage. So the line $z_0 - x_1 - x_2 - x_3 - x_4$ is the traditional traveling salesman problem routes [8–14], represented as TS; the line of the middle selection point is represented as MS, $y_1 - y_2 - y_3 - y_4$ is the line of best stop point with considering the coverage of wireless signal, represented as SS. As we can see from Figure 2, the line SS line is shorter than the other two.

2.2. Problem Formulation. The problem model is analyzed and explained in detail below.

The conventional travel quotient line TS is a better line without regard to the coverage of the wireless signal. For line MS, the radius of wireless signal coverage is usually smaller than the interval distance of node arrangement, and the final line is not as good as line SS even when there is an intersection area. Therefore, the line planning of the mobile sink node considering the coverage of the wireless

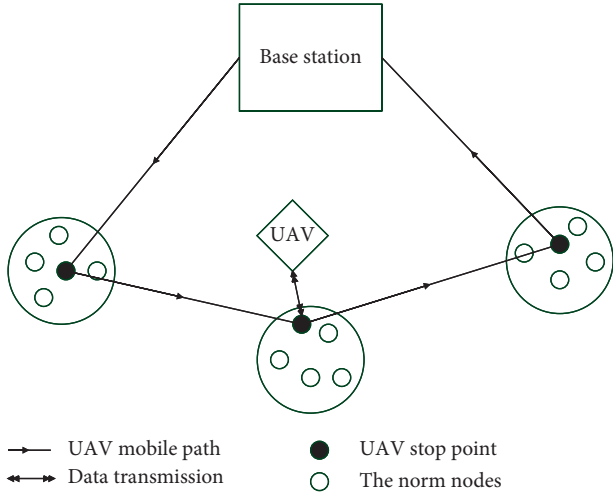


FIGURE 1: Overall structure diagram of the system.

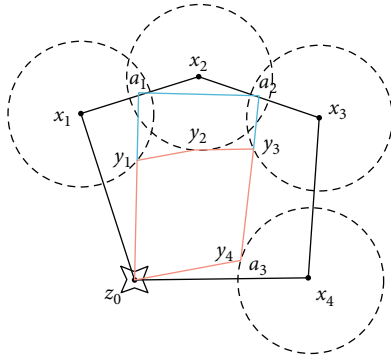


FIGURE 2: Schematic diagram of the problem model.

signal is transformed into the solution of the SS line. At the same time, in the SS line, the position of the best stop point can be found by a strategy, and the final SS line section is composed of the initial position of the mobile sink node and each satisfactory solution point. The shortest line planning is mainly to determine the location of each best stop point and the access order between them by joint programming to construct the optimization expression [18–24].

In the shortest route planning problem of the flight path of the mobile sink node, there are directly connected road sections between the origin point and the best stop point of the mobile sink node and the best stop point without considering the obstacle. Therefore, the initial position point and the best stop point of the moving sink node form a directed graph, which is expressed as follows: $G = (V, E)$, in which $V = \{x_0, y_0, y_1, \dots, y_n\}$, E is the set of lines in figure G , and the S matrix is used to indicate whether the line segment in E is selected as the optimal line section; if $S_{ij} = 1$, the line (y_i, y_j) is selected, if $S_{ij} = 0$, it means (y_i, y_j) is not selected for the optimal line section.

Through the above definition and explanation of the symbol, the flight path planning problem of the mobile sink node considering the wireless signal coverage area will be expressed as follows:

$$\begin{aligned}
 \text{SS} : \text{Min } \Gamma(Y, S) &= \sum_{i=0}^n \sum_{j=0}^n S_{ij} \|y_i - y_j\|, \\
 \|x_i - y_i\| &\leq r, \quad i = 1, 2, \dots, n, \\
 \sum_{i=0}^n S_{ij} &= 1, \quad j = 1, 2, \dots, n, \\
 \sum_{j=0}^n S_{ij} &= 1, \quad i = 1, 2, \dots, n, \\
 S_{ij} &\in \{0, 1\}.
 \end{aligned} \tag{1}$$

In the above model, Γ is the objective function. The parameter is the position Y of the best stop point and the road selection matrix S . At the same time, the model is explained as follows:

- (1) The expression 1 is the objective function of the model, indicating the length of the travel path of the mobile aggregation node. At the same time, in the formula, S_{ij} indicates whether the line segment is a segment in the travel path of the mobile aggregation node. The distance between the best stop point i and the best stop point j is expressed as $\|y_i - y_j\|$.
- (2) The expression 2 is a constraint condition of the mobile aggregation node and the best stop point and indicates that the mobile aggregation node needs to be satisfied with the path corresponding to the effective communication range of each sensor monitoring node and the mobile aggregation node, and the range is a circle centered on x_i and the effective communication radius is r .
- (3) Expressions 3 and 4 represent the access constraints of each satisfactory solution point. On the flight line of the mobile sink node, there is only one line that leaves and enters each satisfactory solution point.
- (4) Expression 5 represents the selected matrix of the road section, with 1 for selection and 0 for unchecked.

3. Path Optimization Algorithm

In view of the above analysis, it can be seen that the main problem of the shortest path planning of mobile sink nodes is the need to determine the location of best stop points in the wireless signal coverage range of each node and their access order (that is, the order in which the data of each monitoring node is extracted). In this paper, the problem is divided into three steps: one is to cluster the nodes through the dynamic clustering algorithm and select the cluster head nodes, the other is to determine the access order of each cluster head node, and the third is to determine the location of each optimal stop point.

3.1. Prioritization Scheme

3.1.1. Improved K-Means Clustering Algorithm. In order to divide the nodes in the network into clusters evenly and

balance the energy consumption of the network and the cluster heads of each cluster, we use the dynamic clustering algorithm to cluster the nodes in the monitoring area.

In the practical application, the K -means algorithm is simple and practical and has higher efficiency with respect to the clustering algorithm such as neighbor clustering and fuzzy clustering. The K -means algorithm is based on minimizing the clustering function [25], and the clustering function is defined as

$$J_j = \sum_{i=1}^{N_j} \|X_i - Z_j\|^2, \quad X_i \in S_j, \quad (2)$$

where S_j is the J cluster set, Z_j is a clustering center, and N_j is the number of samples contained in the J cluster set and the selection of the cluster center should minimize J_j , so $\partial J_j / \partial Z_j = 0$, so

$$\begin{aligned} \frac{\partial}{\partial Z_j} \sum_{i=1}^{N_j} \|X_i - Z_j\|^2 &= 0, \\ Z_j &= \frac{1}{N_j} \sum_{i=1}^{N_j} X_i. \end{aligned} \quad (3)$$

The algorithm flow is as follows:

- (1) Optional K initial clustering centers: $Z_1(1), Z_2(1), \dots, Z_k(1)$
- (2) According to the principle of minimum distance (Euclidean distance), the remaining samples are assigned to one of the K clustering centers
- (3) To get $Z_j(k+1), j=1, 2, \dots, k$
- (4) If $Z_j(k+1) \neq Z_j(k)$, then go back to (2) reclassify the samples and repeat the iterative calculation until $Z_j(k+1) = Z_j(k)$, the algorithm converges, results are calculated and retained

However, the final clustering results of the K -means algorithm will be affected by the location and number of the initial clustering center, and it is easy to converge to the local optimal rather than the global optimum. Therefore, we use the binary K -means algorithm, which can overcome the convergence of the K -means clustering algorithm to the local optimal. The basic idea is that first, all points are treated as a cluster, clustering is performed ($K=2$), and then the cluster that can minimize the sum of error squares (SES) is selected to be divided ($K=2$), until the number of clusters is equal to the number specified by us [26–29]. The region is divided into K clusters by the dynamic clustering algorithm; then, with energy as the competitive weight, the node with the highest energy in each cluster is selected as the cluster head node.

3.1.2. Determine the Order of Access to Nodes. In the research and discussion of analyzing the data extraction order of each monitoring node, it can be classified as a travel dealer problem [30, 31], because the coverage area of

the wireless signal is not considered at this time. At the same time, for the following research, the access order of the monitoring node is found; that is to say, the access sequence of the best stop point corresponding to the monitoring node is found.

Through the analysis, it can be seen that the path planning of the UAV is the traversal optimal path problem in the discrete area [32]. Therefore, when determining the order of extracting the data from each monitoring node, the ant colony algorithm [33] is used to realize the optimal path planning of the mobile sink node, and the line here is presented as the connection of each sensor monitoring node, and the access order of the node is also determined.

In the above analysis, the ant colony algorithm is used to plan the flight path, and the access sequence of node data extraction is determined, as shown in Figure 3. Therefore, when solving the shortest line planning of the mobile sink node considering the coverage of wireless signal, the preliminary line planning and access sequence are obtained according to the ant colony algorithm, and then the access order of best stop points is determined. In this paper, according to the constraint that the access node is 1, a monitoring node will correspond to the best stop point, so the access order of the monitoring node is determined; that is, the access order of the best stop point is obtained. At this point, we can classify it as a simplified NP problem [34]. In the next step, a suitable and feasible method is needed to solve the position of the best stop point.

3.1.3. Determination of Best Stop Points. The position of the best stop point needs not only qualitative analysis but also a quantitative solution. Since the wireless signal coverage area of the sensor monitoring node and the mobile sink node is circular and the center of the circle is its own position, According to the preliminary planning of the flight line in the previous section, a preliminary schematic diagram containing the coverage of the wireless signal can be obtained, as shown in Figure 4:

Combined with the problem model diagram and the requirement for the quantitative solution of best stop points, an angular bisection method is proposed to solve the specific position of satisfactory solution points. The specific implementation methods are as follows:

Starting from the preliminary path line diagram planned by the ant colony algorithm, L is used to represent the distance sum of the initially planned path, and there is

$$L = l_0 + l_1 + l_2 + \dots + l_n, \quad (4)$$

where l_0 is the section of the road (x_0, x_1) , l_1 is the section of the road (x_1, x_2) , l_2 is the section of the road (x_2, x_3) , and l_n is the section of the road (x_n, x_0)

Bisect the angle (the inferior angle) which is formed by two paths across the center of a node. And extend to the intersection of the boundary of the wireless signal coverage area, at which point of intersection is identified as the best stop point, and the intuitive effect is shown in Figure 5:

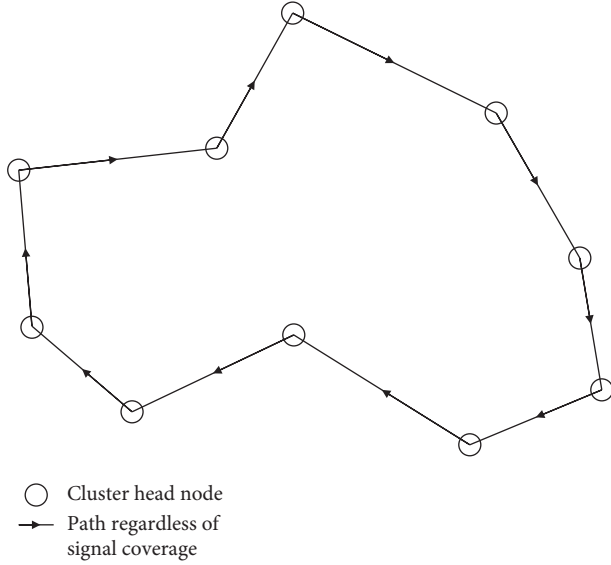


FIGURE 3: An example of path planning with ant colony algorithm regardless of signal range.

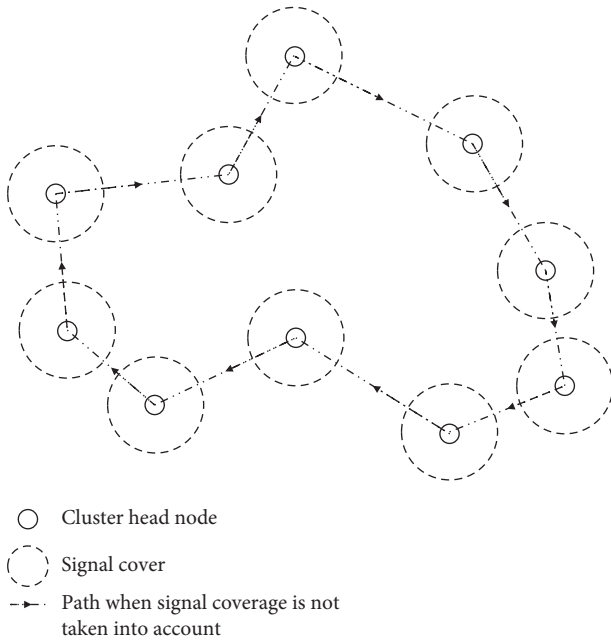


FIGURE 4: An example of considering node wireless signal coverage.

And then cross point x_0 to make the angular bisection of clip $2\varphi_0$ between l_0 and l_n , the extension line of the angular bisector intersects the communication boundary of point x_0 at point y_0 , in the same manner, cross point x_1 to make the angular bisection of angle $2\varphi_1$ between l_0 and l_1 , the

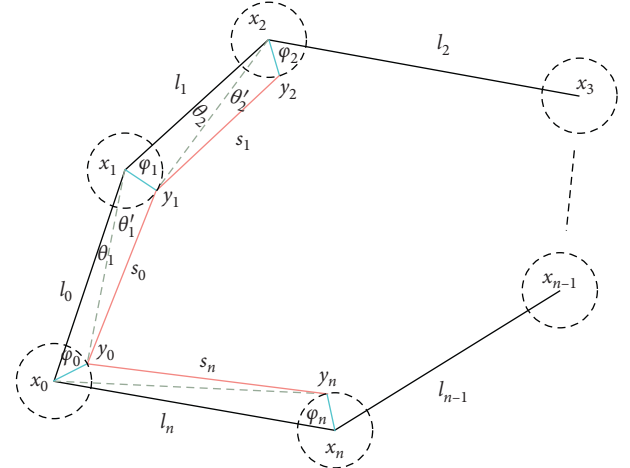


FIGURE 5: Angular bisection line to solve best stop point diagram.

extension line of the angular bisector intersects the communication boundary of point x_1 at point y_1 and connects points y_0 and x_1 and points y_0 and point y_1 . At this point, the first optimized line segment with best stop point connection can be reached, that is, the path of the final planning for the mobile sink node after considering the wireless signal coverage area. s_0 is the line segment connecting points y_0 and y_1 , and $\varphi_1 = \theta_1 + \theta_1'$. As shown in Figure 5, at this point, the length of s_0 can be expressed:

$$s_0 = \sqrt{d_0^2 + r^2 - 2rd_0 \cos \theta_1'}$$

$$d_0^2 = l_0^2 + r^2 - 2rl_0 \cos \varphi_0, \quad (5)$$

$$\cos \theta_1 = \frac{l_0^2 + d_0^2 - r^2}{2l_0d_0}.$$

The simultaneous formula can be obtained:

$$\cos \theta_1 = \frac{l_0 - r \cos \varphi_0}{d_0}. \quad (6)$$

Because $\varphi_1 = \theta_1 + \theta_1'$,

$$\theta_1' = \varphi_1 - \arccos \frac{l_0 - r \cos \varphi_0}{d_0},$$

$$\cos \theta_1' = \frac{l_0 - r \cos \varphi_0}{d_0} \cos \varphi_1 + \sin \varphi_1 \sqrt{1 - \left(\frac{l_0 - r \cos \varphi_0}{d_0} \right)^2}. \quad (7)$$

So we can figure out the length of S_0 :

$$s_0 = \sqrt{d_0^2 + r^2 - 2rd_0 \left(\frac{l_0 - r \cos \varphi_0}{d_0} \cos \varphi_1 + \sin \varphi_1 \sqrt{1 - \left(\frac{l_0 - r \cos \varphi_0}{d_0} \right)^2} \right)}. \quad (8)$$

In the same way, there is

$$\begin{aligned}
 s_1 &= \sqrt{d_1^2 + r^2 - 2rd_1 \cos \theta'_2} \\
 d_1^2 &= l_1^2 + r^2 - 2rl_1 \cos \varphi_1, \\
 \cos \theta_2 &= \frac{l_1^2 + d_1^2 - r^2}{2l_1 d_1}, \\
 s_1 &= \sqrt{d_1^2 + r^2 - 2rd_1 \left(\frac{l_1 - r \cos \varphi_1}{d_1} \cos \varphi_2 + \sin \varphi_2 \sqrt{1 - \left(\frac{l_1 - r \cos \varphi_1}{d_1} \right)^2} \right)}.
 \end{aligned} \tag{9}$$

of which $\varphi_2 = \theta_2 + \theta'_2$.

In the end, there are

$$\begin{aligned}
 s_{n-1} &= \sqrt{d_{n-1}^2 + r^2 - 2rd_{n-1} \left(\frac{l_{n-1} - r \cos \varphi_{n-1}}{d_{n-1}} \cos \varphi_n + \sin \varphi_n \sqrt{1 - \left(\frac{l_{n-1} - r \cos \varphi_{n-1}}{d_{n-1}} \right)^2} \right)}, \\
 s_n &= \sqrt{d_n^2 + r^2 - 2rd_n \left(\frac{l_n - r \cos \varphi_n}{d_n} \cos \varphi_0 + \sin \varphi_0 \sqrt{1 - \left(\frac{l_n - r \cos \varphi_n}{d_n} \right)^2} \right)}.
 \end{aligned} \tag{10}$$

After the last best stop node is obtained, it is necessary to return to the position of the original node. Therefore, for any line segment connected by best stops points, it can be obtained by making angular bisection of the angle formed by each line segment after the preliminary path diagram planned by the ant colony algorithm, and the length of each line segment can be obtained. This section mainly focuses on the flight path of UAV when extracting monitoring node data. Firstly, through the analysis of the traditional path planning algorithm, then according to the actual situation, the path system model diagram with wireless signal coverage area is constructed, and the reasonable system model and objective function are established. Then the solution is put forward, the angular bisection method is introduced to quantitatively calculate the position of the optimal stop point, and the rationality and feasibility of the method are proved by formula derivation.

3.2. Simulation of Path Optimization Results. In this part, we simulate and analyze the above optimization scheme. The main parameters and their values of the simulation are given in Table 1.

First, we randomly deploy 100 monitoring nodes in the monitoring area, as shown in Figure 6. Then, the improved K -means dynamic clustering algorithm is used to cluster the 100 nodes, and the nodes with the largest remaining energy in the

cluster are used as cluster head nodes. The clustering results and cluster head selection results are shown in Figure 7.

After determining the cluster head node, then the ant colony algorithm is used to plan the path of the ten cluster head nodes according to the position of the ten cluster head nodes, as shown in Figure 8 and the average path distance and final collection of the iteration are optimized for the given ten nodes by the algorithm at this time. The shortest path of convergence is shown in Figure 9.

According to the analysis in the previous section, after considering the coverage of the wireless signal of the node, the preliminary lines of the ten cluster head nodes are obtained, as shown in Figure 10.

The path optimization of the ten cluster head nodes is carried out again after the introduction of the angle bisection method. The optimization results are shown in Figures 11 and 12.

Through the comparison of the simulation results of Figures 9 and 12, it can be seen that the shortest distance of the path is 695.3 m without considering the wireless signal coverage, and the final distance of the path replanned by the angular bisection method is 602.1 m without considering the wireless signal coverage area. Then, we simulated the path optimization of different clustering results and obtained the results in Table 2 and Figure 13.

From the above results, we can see that it is feasible to use the angular bisection method to optimize the path according

TABLE 1: Simulation parameter.

Parameter name	Parameter values
Number of nodes (N)	100
Clustering quantity (K)	10
Cluster head proportion (P)	0.1
Heuristic factor (α)	1
Expectation heuristic factor (β)	5
Information intensity (Q)	500
Pheromone volatile factor (η)	0.5
Number of ant colonies (m)	18
Communication radius (r)	15 m

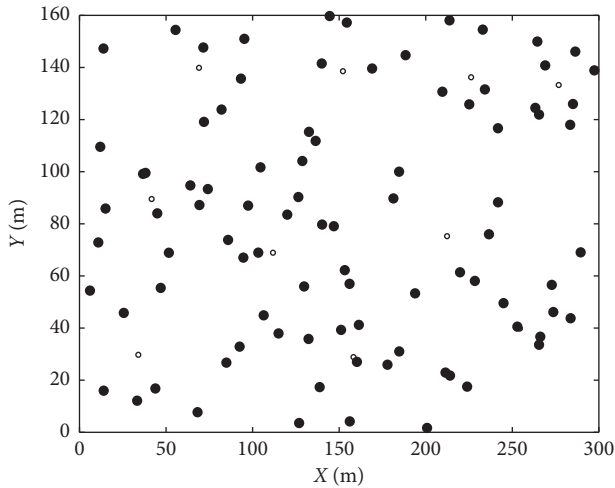


FIGURE 6: Node distribution.

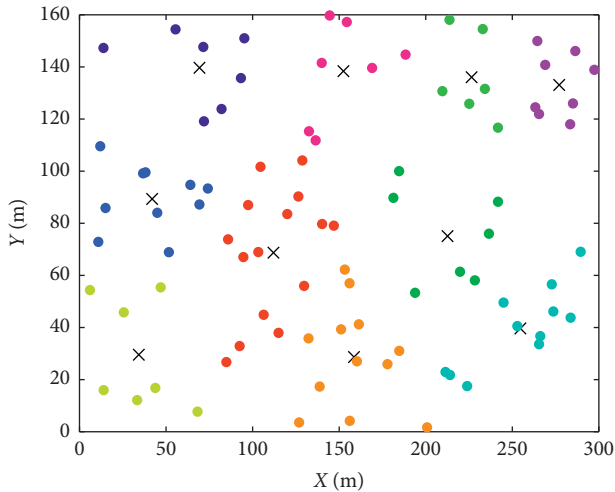


FIGURE 7: Selection of cluster and cluster head.

to the characteristics of wireless signal coverage (where the position of the ten nodes is set in the simulation, and the radius of the wireless signal coverage area r is 15 m when the path is planned by the angular bisection method, the value of r is measured by the wireless communication module, and the size of r is measured by the hardware of the wireless module).

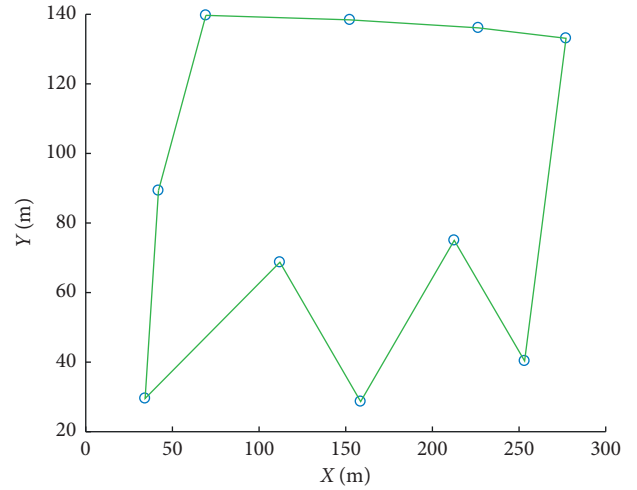


FIGURE 8: Path that does not initially consider wireless signal coverage.

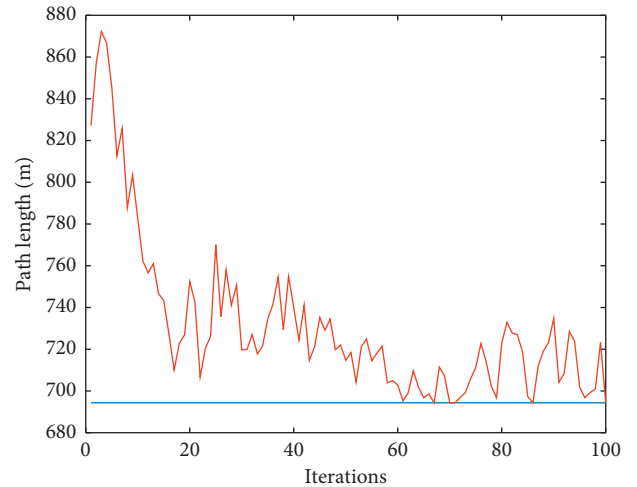


FIGURE 9: Average distance and shortest distance.

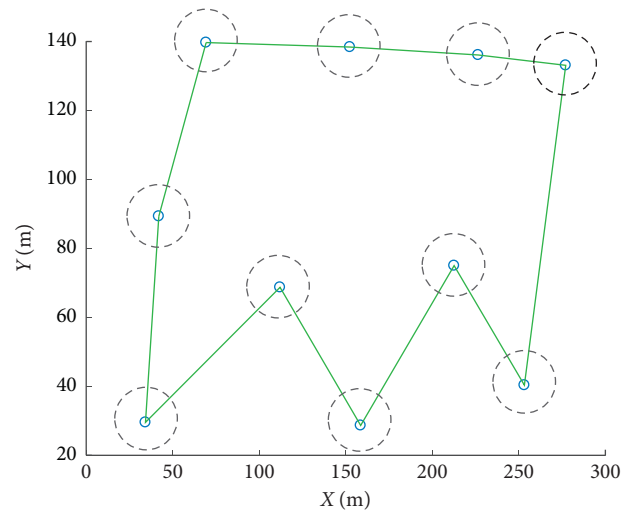


FIGURE 10: Cluster head node wireless signal coverage.

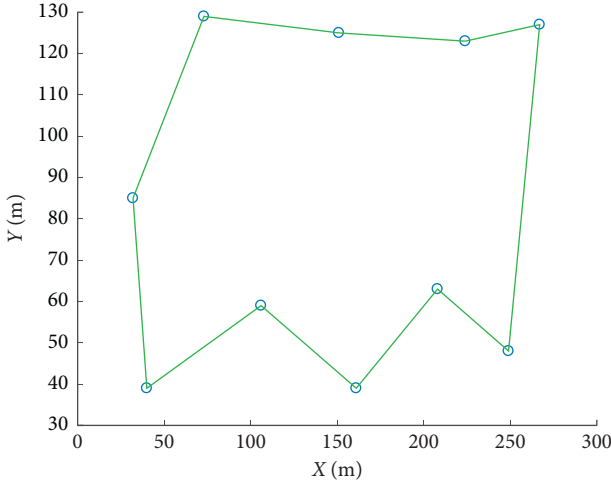


FIGURE 11: Optimal diagram of angular bisection path.

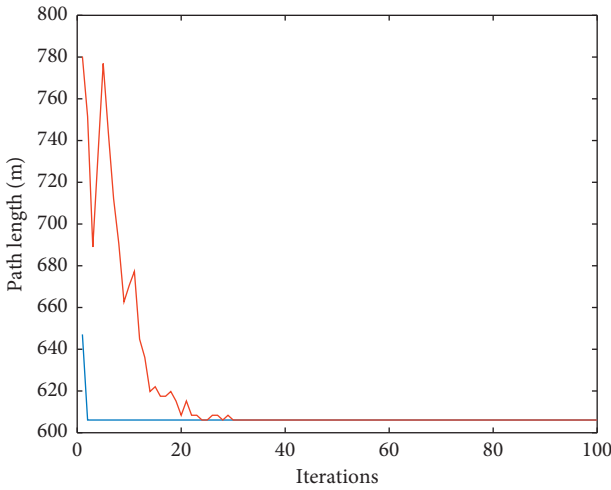


FIGURE 12: Average distance and shortest distance after optimization.

TABLE 2: Comparison of path simulation results at $r = 15$ m.

Number of cluster heads ($r = 15$ m)	Traditional distance (m)	Optimized distance (m)	Optimization degree (%)
10	684.2	581.6	15
10	736.7	617.6	16
10	767.4	636.9	17

3.3. *Verification of Experimental Results.* According to the simulation results, the actual test of the scheme is carried out to verify the reliability of data collection. The workflow of data collection is shown in Figure 14.

Due to the limited experimental conditions, we select the representative temperature and PH value as a monitoring index. The detection range of the DS18B20 temperature sensor with waterproof type is 55–125. The detection accuracy is 0.5. We used the E-201-C PH composite electrode, and its detection range is 0–14. The physical diagram is shown in Figure 15.

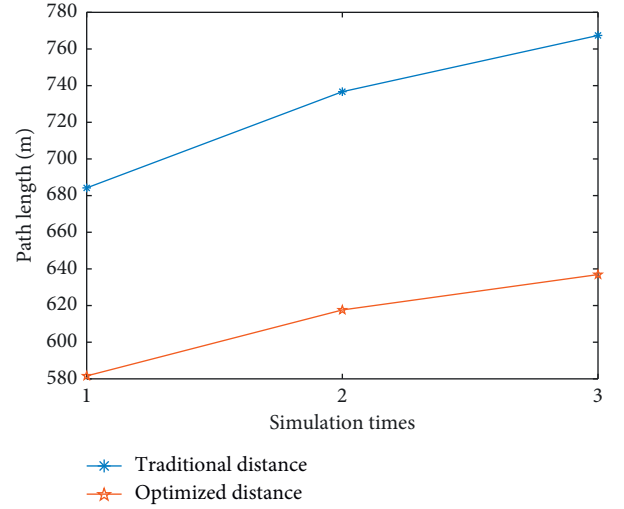


FIGURE 13: Comparison of path length before and after optimization.

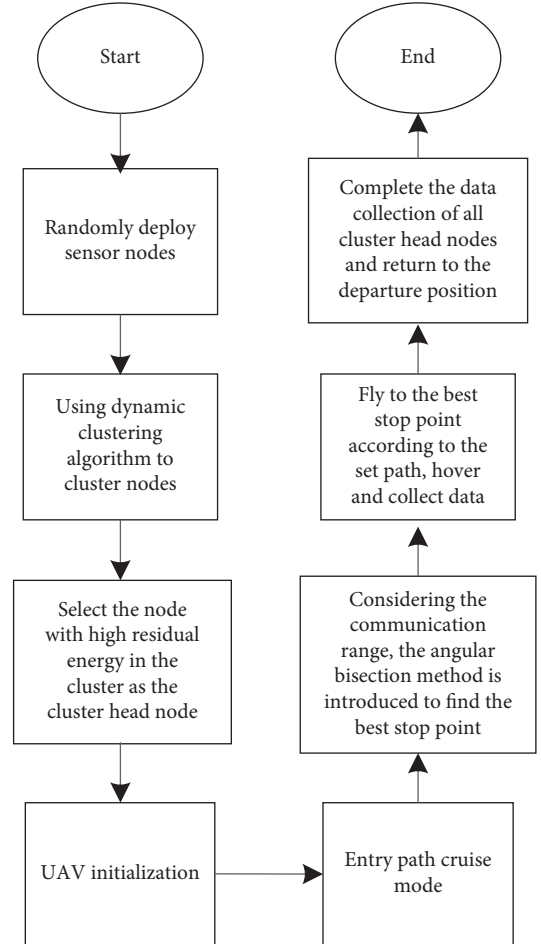


FIGURE 14: Data collection flowchart.

The whole test process is carried out in the visual environment on the edge of the water area, and the test distance is widened continuously during the test process. Through the test of the reception of 1000 packets, the test

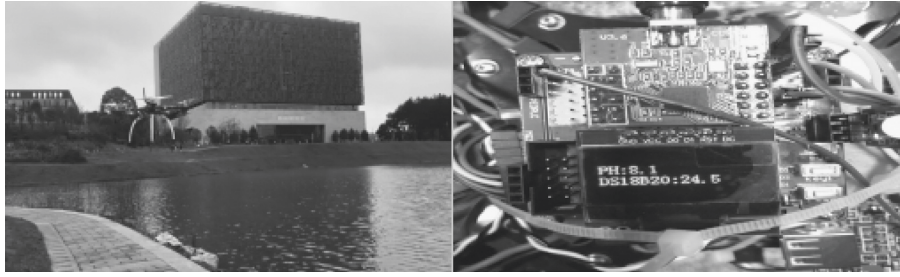


FIGURE 15: Physical image of UAV test.

TABLE 3: Test results of communication quality.

Distance (m)	Number of packets sent	Number of packets lost	Packet loss rate
10	1000	0	0
15	1000	0	0
20	1000	1	0.001
25	1000	23	0.022
30	1000	101	0.121
35	1000	382	0.394
40	1000	1000	1

TABLE 4: Comparison of the experimental and actual measured values of the system.

Acquisition time	Average measurement value °C/pH	Actual value °C/pH	Fractional error (%)
14:00	24.5/8.1	24.7/8.2	0.81/1.22
14:30	24.5/8.1	24.7/8.2	0.81/1.22
15:00	24.5/8.2	24.7/8.2	0.81/1.22
15:30	24.5/8.1	24.6/8.2	0.47/1.22
16:00	24.5/8.1	24.7/8.2	0.81/1.22
16:30	24.1/7.9	24.3/8.0	0.82/1.25
17:00	23.9/7.9	24.2/8.0	1.24/1.25

results are shown in Table 3. It can be seen from the table that, with the increase of test distance, the packet loss rate and packet error rate will also increase, and the transmission quality cannot be guaranteed after more than 30 m and basically cannot be transmitted after 40 m, so the distance should be controlled within 20 m when deploying the node, which can meet the requirements of data transmission.

Data are collected every 30 minutes of the system, and statistical analysis of the experimental data is carried out to obtain the experimental value and the actual measurement value of the system (Table 4). The results show that the temperature error is between 0.81% and 1.24%, and the error range is reasonable. Therefore, the system can collect the data of the water area monitoring more accurately.

4. Conclusion

In this paper, a new mobile data collection scheme for WSN water monitoring is proposed, which combines UAV with WSN. According to the characteristics of the water monitoring network, the path planning problem of the mobile sink node in WSN is discussed. In view of the wireless signal coverage of nodes in WSN, the nodes are divided into

clusters and the cluster head nodes are selected as the residence points of mobile sink nodes according to the remaining energy. Then, on the basis of the ant colony algorithm, the angular bisection method is added to find the best stop point in the coverage area, and the new path is replanned. The derivation and simulation results show that the optimal stop point position and the new path can be obtained, and the distance of the new path is shorter than that planned by the traditional algorithm. Finally, experiments are carried out to further verify the reliability of the proposed path planning scheme for collecting data.

Data Availability

The data used to support the findings of this study are included within the article. If other data or programs used to support the findings of this study are needed, you can obtain them from the corresponding author.

Conflicts of Interest

The authors declare that they have no conflicts of interest.

Acknowledgments

This work was supported partly by the National Natural Science Foundation of China (51867005)(61861007), Guizhou Province Science and Technology Innovation Talent Team Project ([2018] 5615), and the Science and Technology Foundation of Guizhou Province ([2018]5781).

References

- [1] T. Xiao, C. Guanghua, and D. Qinghua, "Design of aquatic culture environmental monitoring system based on WSN," *Computer Measurement and Control*, vol. 26, no. 10, pp. 9–13, 2018.
- [2] L. Yifeng and F. Haihong, "Water quality monitoring system based on wireless sensor," *Electronic Technology and Software Engineering*, vol. 24, pp. 59–60, 2018.
- [3] K. Yinghui, L. Peiyu, C. Zhixiong, and Q. Qiong, "Design of a gateway for adaptive wireless sensor network monitoring system," *Computer Measurement and Control*, vol. 23, no. 9, pp. 3178–3181, 2015.
- [4] X. Jia, F. Xin, Y. Fugui, W. Chuanping, and W. Ruzhuan, "Data collection method for mobile Sink wireless sensor networks with maximum minimum energy consumption probability," *Journal of Electronic Science*, vol. 43, no. 12, pp. 2470–2475, 2015.

- [5] L. Mingzhou, S. Mingxia, S. Yuwen, X. Yingjun, L. Longshen, and L. Xiangze, "Field wireless sensor network mobile terminal data collection scheme," *Journal of Agricultural Engineering*, vol. 27, no. 8, pp. 242–246, 2011.
- [6] L. Chuan, H. Ren, and Y. Cong, "Research on motion strategy of mobile data collector in WSN," *Computer Engineering*, vol. 45, no. 1, pp. 84–90, 2019.
- [7] G. Pinfan, L. Chuan, W. Yangchun, L. Shuri, and X. Wei, "WSN energy saving strategy with mobile data collector," *Radio Communication Technology*, vol. 45, no. 2, pp. 150–155, 2019.
- [8] G. Yogarajan and T. Revathi, "Nature inspired discrete firefly algorithm for optimal mobile data gathering in wireless sensor networks," *Wireless Networks*, vol. 24, no. 8, pp. 2993–3007, 2018.
- [9] Y.-C. Wang and K.-C. Chen, "Efficient path planning for a mobile sink to reliably gather data from sensors with diverse sensing rates and limited buffers," *IEEE Transactions on Mobile Computing*, vol. 18, no. 7, pp. 1527–1540, 2019.
- [10] J. Wang, Y. Gao, W. Liu, A. K. Sangaiah, and H.-J. Kim, "An intelligent data gathering schema with data fusion supported for mobile sink in wireless sensor networks," *International Journal of Distributed Sensor Networks*, vol. 15, no. 3, Article ID 155014771983958, 2019.
- [11] J. Wang, Y. Gao, X. Yin, F. Li, and H.-J. Kim, "An enhanced PEGASIS algorithm with mobile sink support for wireless sensor networks," *Wireless Communications and Mobile Computing*, vol. 2018, Article ID 9472075, 9 pages, 2018.
- [12] J. Wang, J. Cao, R. S. Sherratt, and J. H. Park, "An improved ant colony optimization-based approach with mobile sink for wireless sensor networks," *The Journal of Supercomputing*, vol. 74, no. 12, pp. 6633–6645, 2018.
- [13] L. I. Hai-Po and D. U. Qing-Wei, "Energy efficient coverage control algorithm for wireless sensor networks," *Journal of Chinese Computer Systems*, vol. 32, no. 2, pp. 233–236, 2011.
- [14] J. Wang, Y. Gao, W. Liu, W. Wu, and S.-J. Lim, "An asynchronous clustering and mobile data gathering schema based on timer mechanism in wireless sensor networks," *Computers, Materials & Continua*, vol. 58, no. 3, pp. 711–725, 2019.
- [15] C. Xingang, Z. Tang, and M. Jun, "Design of on-line monitoring system for temperature of vacuum circuit breaker based on ZigBee wireless networking," *Instrumentation Technology & Sensors*, vol. 8, pp. 39–42, 2018.
- [16] G. Xuezhong, Z. Lili, and C. Fan, "Ground monitoring system of UAV based on STM32," *Chemical Automation and Instruments*, vol. 44, no. 3, pp. 277–278, 2017.
- [17] Y. Song, Z. Shaowei, S. Peizhuang, and G. Jun, "UAV farming monitoring system based on STM32 and OV5640," *Internet of Things Technology*, vol. 8, no. 7, pp. 22–25, 2018.
- [18] W. Haizhen, L. Z. Zheng, and T. Yanping, "Cc2530 single chip microcomputer multi-point temperature acquisition experimental design," *Laboratory Research and Exploration*, vol. 37, no. 12, pp. 98–101, 2018.
- [19] L. Zhonghua, "New progress in the research and application of ant colony algorithm," *Computer Engineering and Science*, vol. 41, no. 1, pp. 173–184, 2019.
- [20] X. Liu, B. Zhang, and F. Du, "Integrating relative coordinates with simulated annealing to solve a traveling salesman problem," in *Proceedings of the 2014 Seventh International Joint Conference on Computational Sciences and Optimization*, July 2014.
- [21] L. Xiaoming, "Enhancement of directional graphs—an example of appropriate problem-oriented teaching," *Computer Education*, vol. 2, pp. 1–4, 2019.
- [22] S. M. Hosseinirada, M. Ali Mohammadib, S. K. Basua, and A. A. Pouyanb, "LEACH routing algorithm optimization through imperialist approach," *International Journal of Engineering*, vol. 27, no. 1, 2014.
- [23] F. H. L. Z. Shu, "Delay-based cross-layer QoS scheme for video streaming in wireless Ad-Hoc networks," *China communication*, vol. 15, no. 9, pp. 215–234, 2018.
- [24] C. Yourong, L. Siyi, and L. Banteng, "Mobile sensing path selection algorithm for mobile wireless sensing networks," *Journal of Sensing Technology*, vol. 32, no. 1, pp. 117–126, 2019.
- [25] W. Jianren, M. J. Xin, and D. J. Ganglong, "Improved K-means clustering k-value selection algorithm," *Computer Engineering and Application*, vol. 55, no. 8, pp. 27–33, 2019.
- [26] C. Jianxin, C. Yuanyuan, Z. Yun, and D. Yuelin, "Adaptive data acquisition strategy for mobile sink nodes," *Computational Science*, vol. 39, no. 11, pp. 45–50, 2012.
- [27] F. Shumin, W. Haiyue, and W. Dixin, "Research on multi-objective shortest path solution algorithm based on ideal point method," *Road Traffic Technology*, vol. 33, no. 3, pp. 97–101, 2016.
- [28] T. Jiqiang, *Line Planning of Mobile Sink Nodes in Wireless Sensor Networks*, Chongqing University, Chongqing, China, 2016.
- [29] L. Xin and W. Yajuan, "Trajectory design of WSN mobile sink node based on Hilbert space filling curve," *Modern Electronic Technology*, vol. 39, no. 23, pp. 17–21, 2016.
- [30] M. Cunjin, D. Qingzhi, and H. Bingqian, "Mobile node path planning algorithm based on WSN," *Information Technology*, vol. 11, pp. 117–120, 2018.
- [31] Y. Yingying, C. Yan, and L. Taoying, "Improved genetic algorithm for traveling salesman problem," *Control and Decision-Making*, vol. 29, no. 8, pp. 1483–1488, 2014.
- [32] H. Fu Shuyun, T. Shoufeng, and T. Ziyuan, "A review of path planning methods for autonomous mobile robots," *Software Guide*, vol. 17, no. 10, pp. 1–5, 2018.
- [33] M. Jinke and W. Zhi, "Path planning of counting robot based on improved ant colony algorithm," *Computer Technology and Development*, vol. 7, pp. 1–4, 2019.
- [34] W. Xiaochu, *Research on Flight Control System of Four-Rotor UAV*, Dalian University of Technology, Dalian, China, 2018.

Research Article

Research on Dynamic Game Model and Application of China's Imported Soybean Price in the Context of China-US Economic and Trade Friction

Yi Wang ¹, Hui Wang,¹ and Shubing Guo ²

¹Shandong University of Finance and Economics, School of Mathematics and Quantitative Economics, Jinan 250014, China

²College of Management and Economics, Tianjin University, Tianjin 300072, China

Correspondence should be addressed to Yi Wang; ywangsd2015@126.com and Shubing Guo; sbguo20160831@126.com

Received 1 June 2019; Accepted 9 September 2019; Published 12 November 2019

Guest Editor: Francisco G. Montoya

Copyright © 2019 Yi Wang et al. This is an open access article distributed under the Creative Commons Attribution License, which permits unrestricted use, distribution, and reproduction in any medium, provided the original work is properly cited.

China's soybean price fluctuates due to the current economic and trade frictions between China and the United States. Brazil and the United States are regarded as two oligarchs in China's soybean import market. A dynamic price game model is established, and price elasticity parameters are estimated by using statistical data and Rotterdam model. The stability of Nash equilibrium point is discussed through bifurcation diagram, maximum Lyapunov exponent, evolutionary trajectory, and time series diagram. The influence of price adjustment speed on equilibrium price is analyzed. The numerical simulation of price adjustment speed is carried out, which is compared with the actual situation of imported soybean price before and after the trade friction. The results show that the model constructed in this paper can reflect the changing trend of price and demand and predict the short-term import soybean prices of Brazil and the United States. The forecast accuracy of price fluctuation is high. The results provide model and theoretical reference for price game under trade disputes and provide methodological reference for forecasting the price of imported goods.

1. Introduction

Soybean is an important food crop in China. With the rapid development of economy and society, China's demand for soybeans is increasing year by year. Due to the limitation of domestic planting area and huge demand for soybeans, China's soybean production is far from self-sufficient, and imported soybeans have become the main source of demand for soybeans in China. Today, China is the world's largest soybean importer, accounting for 62.6% of global soybean exports. Brazil, the United States, and Argentina are the main sources of China's soybean imports, accounting for more than 95% of China's total soybean imports. Brazil and the United States account for more than 70% of China's soybean imports, and in recent years, their share has even exceeded 80%. Brazil and the United States become the two oligarchy source countries of China's soybean import market.

Since July 6, 2018, China has imposed a 25% tariff on US soybeans. China's demand for US soybeans has declined, and as a buyer of soybeans, China has turned its attention to other countries. However, some Brazilian soybean farmers raised their prices by as much as 8% in a month. Argentina suffered from drought and soybean production plummeted. China's soybean production is insufficient, and the huge demand for soybeans for domestic life and production makes the price of imported soybeans fluctuate. Therefore, it is of great practical significance to study and compare the changes of soybean price before and after the trade friction.

The application of game theory and complexity theory to product market has always been a hot topic for international scholars. A lot of research is to analyze the complexity of market hypothesis as oligopoly market. Limited rationality and incomplete information are embodied in parameters that cannot be fixed in the model. Once the parameters of describing the economic system change across the linear

stable region, they may change qualitatively, resulting in seemingly complex multiperiodic and nonperiodic motions. In the aspect of complexity analysis of oligopoly model, Agiza et al. [1–4] studied the dynamic behavior of the limited rational yield adjustment model and found stable period, quasi-periodic bifurcation, and chaos phenomena. Considering the influence of incomplete information, bounded rationality, and other factors on enterprises, they give the equilibrium output solution of the dynamic model. Bischi and Lamantia [5] proposed a Cournot duopoly monopoly game. Considering the interdependence between enterprises under given demand function, cost reduction simulation technology spillover is introduced.

In order to study whether oligarchy types affect Nash equilibrium, Tramontana [6] studied the duopoly competition of bounded rationality and naive type. On the premise of equal elastic demand function, they analyzed the evolution of Neimark–Sacker bifurcation and Flip bifurcation to chaos, respectively, and proved that the type of oligarch did not affect Nash equilibrium, but affected its stability, as well as the chaotic state entered after instability. Bonatti et al. [7] considered that, in a signaling oligopoly, market prices are impacted by unobservable demand. In a long enough time range, the game converges to the static result of complete information.

For the Cournot or duopoly models, Nagurney and Wolf [8] developed a game theory model of a service-oriented Internet in which profit-maximizing service providers provide substitutable services and compete with the quantities of services in a Cournot–Nash manner. Matouk et al. [9] established a nonlinear Quadropoly game based on Cournot model with fully heterogeneous players. Wang et al. [10] developed an integrated duopoly model for coordinating R&D, product positioning, and pricing strategy. Taking the product substitutability into account, Nie [11] considered the horizontal mergers under Cournot with Bertrand competition. Saglam [12] provided a welfare ranking for the equilibria of the supply function and quantity competitions in a differentiated product duopoly with demand uncertainty. A dynamic Cournot game characterized by players with bounded rationality is modeled by two nonlinear difference equations in [13]. Wang and Ma [14] considered a Cournot–Bertrand mixed duopoly model with different expectations, where the market has linear demand and the firms have fixed marginal cost functions. In this article, we will apply a Cournot model to the trade friction problem, study the nature of the model through modeling and dynamics analysis, and explain the trade friction phenomenon.

For game model and dynamics analysis, a lot of work has been done in research of the supply chains. Guo and Ma [15] applied the theory of nonlinear dynamic system to the cooperative advertising model in supply chain, modeled the decision-making mechanism of enterprises as a dynamic adjustment process, and analyzed the influence of key parameters on the stability of forward Nash equilibrium. Apart from bounded rationality, oligarchy types are characterized by diversification. Ma and Wang [16] discussed a dual-channel supply chain composed of one manufacturer and one retailer. For more research about supply chains, see [17–21].

For the study of dynamic games, evolutionary games are also very popular. Li et al. [22] presented a model of changing the intensity of interaction based on the individual behavior to study the iterated prisoner’s dilemma game in social networks. In [23], results illuminated the conditions under which the steady coexistence of competing strategies is possible. These findings revealed that the evolutionary fate of the coexisting strategies can be calculated analytically and provided novel hints for the resolution of cooperative dilemmas in a competitive context. For more research about evolutionary game theory, see [24, 25].

For the research about the application of game theory in economics and management, see [26–31]. Ma and Guo [26] considered dynamic game with estimation and two-stage consideration. The results have an important theoretical and practical significance to the game models with two-stage consideration. Ma and Wu [27] applied heterogeneous Triopoly game with multiproduct to related markets. In [28], macroeconomic model with time delays is discussed. Recently, in [29], Ma et al. established a cold chain dynamic game model including a milk manufacturer and two downstream oligopoly supermarkets under the wholesale price contract in the real world. Mu et al. [30] proposed a real estate game model with nonlinear demand function. And an analysis of the game’s local stability was carried out. It was shown that the stability of Nash equilibrium point is lost through period-doubling bifurcation as some parameters are varied. The authors discussed a nonlinear four oligopolies price game with heterogeneous players using two different special demand costs in [31]. Based on the theory of complex discrete dynamical system, the stability and the existing equilibrium point are investigated.

However, these models focus on abstract and parameter discussion, but not on the reality of models. In this paper, we will not only model and perform dynamic analysis but also estimate the parameters in the model through statistical and quantitative methods. Furthermore, we will try to predict future prices by the game model.

On the methods of calculation and analysis, Wang et al. [32] took needs as the starting point, used the trade-off model between accuracy and information quantity as the optimization criterion to construct the confidence interval, derived the theoretical formula of the optimal confidence interval, and proposed a practical and efficient algorithm based on entropy theory and complexity theory. The accurate positioning of market oligarchs directly affects the accuracy and practical value of stability analysis of game models.

On the game model of agricultural products, with the innovation of industrial model, based on evolutionary game theory, Su et al. [33, 34] established the income matrix and replication dynamic equation of the tripartite game and discussed and analyzed the effectiveness, stability, and key factors of the new industrial model of agricultural supermarket docking. They used multivariate test to identify the nonlinearity, fractal, and chaos of the data. It is found that there is some confusion in the wholesale price data of agricultural products in China.

At present, there are few studies on dynamic analysis of agricultural product price game model by Chinese scholars.

In this paper, the soybean import market in China is assumed to be a duopoly market, and a bounded rational duopoly dynamic price game model is established. Using game theory and chaotic dynamics theory, the import price of soybean from Brazil and the United States was analyzed dynamically.

This paper studies the stability of equilibrium point, discusses the impact of price adjustment speed of oligarchy countries on the stable region, simulates the price evolution law by using data statistics, and predicts the future soybean import price and its trend. The innovation of this paper is to use Rotterdam model and statistical data to estimate the actual elasticity coefficient and specific price adjustment speed value, to realize the abstract dynamic model, and to get the actual equilibrium price. It provides theoretical basis and price forecasting methods for predicting the trend of soybean import price under trade disputes and formulating soybean import strategy [33–39].

2. Price Game Model

China's soybean imports mainly come from the United States, Brazil, and Argentina, the three largest soybean producers in the world. According to the statistics of soybean imports from China's Customs and the Ministry of Agriculture and Rural Areas, Table 1 lists the proportion of soybean imports from the United States and Brazil in China from 2006 to 2017. Since 2011, soybeans from the United States and Brazil have accounted for more than 80% of the country's soybean imports. In this section, Brazil and the United States are regarded as the two oligarchs in China's soybean import market. Based on duopoly game model, a dynamically adjusted duopoly game model is established.

2.1. Model Assumptions. In order to get a reasonable conclusion, this paper simplifies the complex game process and makes the following assumptions in line with the laws of economy and trade.

Hypothesis 1. Brazil and the United States as two oligarchs for China's soybean imports, in order to make a more intuitive dynamic analysis of the game model, it is assumed that the imported soybeans from Brazil and the United States are of the same kind, and the price of soybeans is the average import price after paying taxes.

Hypothesis 2. According to the statistics of Wind Financial Terminal, the import costs of soybeans from South America and the United States are mainly inland freight, sea freight, port miscellaneous and insurance costs. In a year, sometimes the cost will be very close, and sometimes there will be a 100 yuan/ton gap, accounting for about 2.5% of the import price per ton. Therefore, this paper ignores the difference of arrival cost between Brazilian and American soybean imports. Assuming that the import costs of Brazilian and American soybeans are the same, the symbol w is used.

TABLE 1: China's share of soybean imports from Brazil and the United States in 2006–2017.

Time	Brazil (%)	America (%)	The sum (%)
2006	41.19	34.95	76.14
2007	34.34	37.75	72.09
2008	31.13	41.22	72.35
2009	37.59	51.25	88.84
2010	33.93	43.06	76.99
2011	39.18	42.47	81.65
2012	40.92	44.48	85.4
2013	50.17	35.12	85.29
2014	44.82	42.06	86.88
2015	49.09	34.76	83.85
2016	45.68	40.42	86.1
2017	54.41	34.19	88.6

Hypothesis 3. Under the bounded rationality, the game of soybean sales between the two countries is set as a duopoly game model. The two sides of the game take price adjustment as a game strategy to maximize their own interests. They make decisions independently at discrete periodic points $t = 0, 1, 2, \dots$

Hypothesis 4. Assume that the demand function $q_i (i = 1, 2)$ is

$$\begin{aligned} q_1 &= a_1 - b_1 p_1 + c_1 p_2, \\ q_2 &= a_2 - b_2 p_2 + c_2 p_1, \end{aligned} \quad (1)$$

where p_1 indicates the price of soybeans imported from Brazil by China, p_2 indicates the price of soybeans imported from the United States, q_1 indicates China's demand for Brazilian soybeans, q_2 indicates China's demand for American soybeans, a_1 indicates China's demand preference for Brazilian soybeans, and a_2 indicates China's demand preference for American soybeans. $-b_1$ shows the effect of the rising price of imported Brazilian soybean on the demand of imported Brazilian soybean in China. It is the marginal demand of imported Brazilian soybean. $-b_2$ shows the effect of the rising price of imported American soybean on the demand of imported American soybean in China. It is the marginal demand of imported American soybean. The symbol c_1 is used to represent the impact of the rising price of imported US soybeans on China's demand for imported Brazilian soybeans, c_2 is used to indicate the impact of the rising price of imported Brazilian soybeans on China's demand for imported US soybeans.

Hypothesis 5. As the number of soybeans imported by China from Brazil and the United States is increasing year by year, before the trade friction, China had a positive demand preference for soybeans imported from Brazil and the United States. After the outbreak of the trade friction, China's demand preference for imported soybeans from Brazil remained positive, while other countries except Brazil could not fill the gap of imported soybeans from the United States in the short term. Therefore, in the short run, China

still has a positive demand preference for imported soybeans from the United States. So we assume $a_1 > 0, a_2 > 0$.

Hypothesis 6. In the commodity market, people's demand for a certain commodity is affected by the commodity's own price and the price of similar substitutes. The rise of the product's own price will lead to the decrease in the demand for the product, and the rise of the price of similar substitutes will increase people's consumption of the commodity. So we assume $b_1 > 0, b_2 > 0, c_1 > 0, c_2 > 0$.

Hypothesis 7. Assuming that the participants in the competition are bounded rationality, the two oligarchs constantly adjust their price strategies to carry out long-term repeated dynamic game. Suppose that the decision-making of the $t + 1$ period is adjusted on the basis of the marginal income of the t period and the repeated game model which satisfies the dynamic adjustment [13]. Suppose that the price of oligopoly i ($i = 1, 2$) in $t + 1$ is

$$p_i(t+1) = p_i(t) + g_i \times p_i(t) \times \frac{\partial \pi_i(t)}{\partial p_i(t)}, \quad (2)$$

$g_i \geq 0$ denotes the rate of price adjustment of manufacturer i ($i = 1, 2$).

2.2. Dynamic Adjustment of the Repeated Game Model. Under the assumption in the previous section, the profit function π_i ($i = 1, 2$) of two soybean manufacturers can be expressed as follows:

$$\begin{aligned} \pi_1 &= q_1(p_1 - w) = (a_1 - b_1 p_1 + c_1 p_2)(p_1 - w), \\ \pi_2 &= q_2(p_2 - w) = (a_2 - b_2 p_2 + c_2 p_1)(p_2 - w). \end{aligned} \quad (3)$$

Marginal profit is

$$\begin{aligned} \frac{\partial \pi_1}{\partial p_1} &= a_1 - 2b_1 p_1 + c_1 p_2 + b_1 w, \\ \frac{\partial \pi_2}{\partial p_2} &= a_2 - 2b_2 p_2 + c_2 p_1 + b_2 w. \end{aligned} \quad (4)$$

If the marginal profit is equal to 0, the Cournot–Nash equilibrium price is

$$\begin{aligned} p_1 &= \frac{a_1 b_2 - a_2 b_1 + 2b_1 b_2 p_2 + b_2 c_1 p_2}{b_1 (2b_2 + c_2)}, \\ p_2 &= \frac{-2a_2 b_1 - a_1 c_2 + 4b_1 b_2 p_2 - c_1 c_2 p_2}{b_1 (2b_2 + c_2)}. \end{aligned} \quad (5)$$

By introducing (3) into (2), the dynamic model of two oligopoly games is obtained:

$$\begin{aligned} p_1(t+1) &= p_1(t) + g_1 \times p_1(t) \times (a_1 - 2b_1 p_1(t) + c_1 p_2(t) + b_1 w), \\ p_2(t+1) &= p_2(t) + g_2 \times p_2(t) \times (a_2 - 2b_2 p_2(t) + c_2 p_1(t) + b_2 w). \end{aligned} \quad (6)$$

It can be seen from (6) that oligarchs will adjust their decision-making according to the current marginal profits in

order to pursue profits. If margins are positive, they will raise prices in the next period and, vice versa, lower prices.

2.3. Parameter Estimation. In this section, based on the actual data obtained, the parameters in model (6) will be estimated by statistical methods, and more practical concrete model will be obtained. Since only the annual soybean demand samples from 2006 to 2017 can be obtained at present, this paper uses Rotterdam model suitable for small sample data to study China's soybean import demand. In order to make the study more accurate, the United States, Brazil, and Argentina, which account for more than 95% of total imports, are brought into the Rotterdam model.

2.3.1. Rotterdam Model. The Rotterdam model was first proposed by Barten (1964) and Theil [35]. This model can reasonably estimate the expenditure elasticity and price elasticity of demand under the condition of unsatisfactory sample size. It is widely used in the research of agricultural import demand. The form of this model is as follows:

$$\omega_i d \log q_i = r_i + \alpha_i d \log Q + \sum_{i,j=1}^n \beta_{ij} d \log p_i, \quad (7)$$

for $i, j = 1, 2, 3$, where ω_i represents the proportion of China's imports of soybeans from country i to the total imports of soybeans, q_i represents China's soybean imports from countries i , p_i represents the import price of soybeans from country i , $d \log q_i$ represents the incremental ratio of imported soybeans, $d \log p_i$ represents the increase ratio of import prices, r_i represents the change of consumption demand of imported soybean caused by nonprice factors in the model, α_i is the Chinese marginal expenditure share on imported soybeans, and β_{ij} represents the compensation price coefficient. When the model is applied, ω_i is usually approximated to $(\omega_i + \omega_{i-1})/2$, $d \log q_i$ is usually approximated to $(\omega_i + \omega_{i-1})/2$, $d \log p_i$ is usually approximated to $\log(p_i/p_{i-1})$, and $d \log Q$ is usually approximated to $\sum_{i=1}^n \omega_i d \log q_i$.

At the same time, the Rotterdam model needs to satisfy the following restrictions: (1) adding-up $\sum_{i=1}^n \alpha_i = 1$, $\sum_{i=1}^n \beta_{ij} = 0$; (2) homogeneity $\sum_{j=1}^n \beta_{ij} = 0$; (3) symmetry $\beta_{ij} = \beta_{ji}$.

2.3.2. Model Fitting. This paper collects the statistical data of China's soybean import trade from 2006 to 2017, mainly from China Customs, Ministry of Agriculture and Rural Areas, and Wind Financial Terminal. Some data are converted and sorted out. The integrated data are applied to this study. In order to make the dynamic analysis image more intuitive, the price dimension is selected as yuan/half kilogram. In the latter analysis, the price dimension will be converted into yuan/kg.

Firstly, the relevant data collected are converted into Rotterdam model by units, and α_i, β_{ij} ($i, j = 1, 2, 3$) is fitted; then Slutsky price elasticity is used to derive price elasticity and cross-price elasticity [36].

Slutsky price elasticity is the price elasticity after eliminating the income effect, that is, the change of demand caused by the change of commodity price and the change of real

income. We can get self-price elasticity by $\eta_{ii} = \beta_{ii}/\omega_i$ and get cross-price elasticity by $\eta_{ij} = \beta_{ij}/\omega_i$. Through model fitting, the constant term r_i , the marginal expenditure share of imported soybean α_i , and the compensation price coefficient β_{ij} can be obtained as shown in Table 2. The price elasticity coefficient is calculated from the proportion of imports ω_i and the compensation price coefficient β_{ij} . According to the Cournot model, Table 3 lists the price elasticity calculated from the parameters in Table 2. We remark that the data in parentheses are the t -statistics of the corresponding parameter estimators; the symbols *, **, and *** represent the levels of significance at 10%, 5%, and 1%, respectively.

As can be seen from Table 3, the self-price elasticity coefficients of soybeans in Argentina, Brazil, and the United States are -3.2 , -1.5 , and -1.6 , respectively. The price elasticities are negative, the cross-price elasticities between the main source countries are greater than 0, and the demand variations caused by nonprice factors described by the constant term are also greater than 0. They are in line with the actual economic significance.

Letting $-b_1 = -1.5$, $-b_2 = -1.6$, $c_1 = 1$, and $c_2 = 1.2$, the import quantities of soybeans from Brazil and the United States are weighted and the import demand parameters of Brazil and the United States are obtained as $a_1 = 2.3$ and $a_2 = 2.1$. According to the statistics, the cost w after unit conversion fluctuates is approximately equal to 0.26. Therefore, we get a concrete duopoly dynamic game model of soybean price:

$$\begin{aligned} p_1(t+1) &= p_1(t) + g_1 \times p_1(t) \times (2.69 - 3p_1(t) + p_2(t)), \\ p_2(t+1) &= p_2(t) + g_2 \times p_2(t) \times (2.516 - 3.2p_2(t) + 1.2p_1(t)). \end{aligned} \quad (8)$$

3. Equilibrium Point and Stability Analysis of Model

In this section, by solving the equilibrium points of system (6), the stability of each equilibrium point is analyzed, and the condition that Nash equilibrium points satisfy the local stability is obtained. The stability of the equilibrium point is further verified by the estimated values of the economic parameters in this section, which provides a reference range of g_i ($i = 1, 2$) for the dynamic analysis of the game model in the future.

When $p_i(t+1) = p_i(t)$ ($i = 1, 2$), the four equilibrium points of the discrete system (6) are obtained as follows:

$$\begin{aligned} E_1 &(0, 0), \\ E_2 &\left(0, \frac{a_2 + b_2 w}{2b_2}\right), \\ E_3 &\left(\frac{a_1 + b_1 w}{2b_1}, 0\right), \\ E_4 &\left(\frac{b_2(2a_1 + c_1 w + 2b_1 w) + a_2 c_1}{4b_1 b_2 - c_1 c_2}, \frac{2b_1(b_2 w + a_2) + c_2(b_1 w + a_1)}{4b_1 b_2 - c_1 c_2}\right). \end{aligned} \quad (9)$$

According to $a_1 > 0$, $a_2 > 0$, $b_1 > 0$, $b_2 > 0$, $c_1 > 0$, $c_2 > 0$, and $w > 0$, these four equilibrium points are all nonnegative

TABLE 2: Estimation results of model parameters.

Country	r_i	α_i	β_{ij}		
			Argentina	Brazil	America
Argentina	0.06 (2.81)	0.30* (0.435)	-0.49 (-0.011)	0.31** (2.98)	0.19 (1.2)
Brazil	0.35*** (4.40)	0.44*** (4.40)		-0.61* (-1.10)	0.38** (3.82)
America	0.74** (5.43)	0.26*** (5.43)			-0.64*** (-5.07)

TABLE 3: The price elasticity of China's demand for imported soybeans from different countries.

Country	Price elasticity		
	Argentina	Brazil	America
Argentina	-3.2	2.0	1.21
Brazil	0.7	-1.5	1.0
America	0.5	1.2	-1.6

equilibrium solutions, and E_1, E_2 , and E_3 are bounded equilibrium points and E_4 is a Nash equilibrium point. Next, we study the local stability of these four points.

Theorem 1. *The bounded equilibrium points E_1, E_2 , and E_3 are unstable points.*

Proof. As we all know, (6) can be regarded as a dynamic system, and its Jacobian matrix is

$$J = \begin{bmatrix} \frac{\partial p_1(t+1)}{\partial p_1(t)} & \frac{\partial p_1(t+1)}{\partial p_2(t)} \\ \frac{\partial p_2(t+1)}{\partial p_1(t)} & \frac{\partial p_2(t+1)}{\partial p_2(t)} \end{bmatrix}, \quad (10)$$

where

$$\begin{cases} \frac{\partial p_1(t+1)}{\partial p_1(t)} = 1 + g_1(a_1 - 2b_1 p_1 + c_1 p_2 + b_1 w) - 2b_1 g_1 p_1, \\ \frac{\partial p_1(t+1)}{\partial p_2(t)} = g_1 p_1 c_1, \\ \frac{\partial p_2(t+1)}{\partial p_1(t)} = g_2 p_2 c_2, \\ \frac{\partial p_2(t+1)}{\partial p_2(t)} = 1 + g_2(a_2 - 2b_2 p_2 + c_2 p_1 + b_2 w) - 2b_2 g_2 p_2. \end{cases} \quad (11)$$

At equilibrium point $E_1(0, 0)$, the Jacobian matrix is

$$J_1 = \begin{bmatrix} 1 + g_1(a_1 + b_1 w) & 0 \\ 0 & 1 + g_2(a_2 + b_2 w) \end{bmatrix}. \quad (12)$$

Two eigenvalues are $\lambda_1 = 1 + g_1(a_1 + b_1w)$ and $\lambda_2 = 1 + g_2(a_2 + b_2w)$. Since $a_i > 0$, $b_i > 0$ ($i = 1, 2$), $\lambda_1 > 1, \lambda_2 > 1$. So E_1 is unstable.

At equilibrium point $E_2(0, (a_2 + b_2w/2b_2))$, the Jacobian matrix is

$$J_2 = \begin{bmatrix} 1 + g_1 \left(a_1 + c_1 \frac{a_2 + b_2w}{2b_2} + b_1w \right) & 0 \\ \frac{g_2 c_2 (a_2 + b_2w)}{2b_2} & 1 - g_2 (a_2 + b_2w) \end{bmatrix}. \quad (13)$$

Two eigenvalues are $\lambda_1 = 1 - g_2(a_2 + b_2w)$ and $\lambda_2 = 1 + g_1(a_1 + c_1(a_2 + b_2w/2b_2) + b_1w)$. The feature vectors are $\gamma_1 = (0, 1)$ and

$$\gamma_2 = \left(\frac{b_2 g_1 (2a_1 + 2b_1w + c_1w) + b_2 g_2 (2a_2 + 2b_2w) + a_2 c_1 g_1}{c_2 g_2 (a_2 + b_2w)} \right). \quad (14)$$

When $g_2 < (2/a_2 + b_2w)$, E_2 is a saddle point and is stable along the tangent of γ_1 . When $g_2 > (2/a_2 + b_2w)$, E_2 is unstable. Since E_2 and E_3 have symmetrical structure, E_3 is also an unstable point. So E_1, E_2 , and E_3 are unstable. This is the end of the proof.

Remark 1. (the economic parameters obtained in Section 2.4). $a_1 = 2.3, a_2 = 2.1, b_1 = 1.5, b_2 = 1.6, c_1 = 1, c_2 = 1.2$, and $w = 0.26$ are put into the proof of theorem 1. Then we obtained the three marginal equilibrium points $E_1(0, 0)$, $E_2(0, (629/800))$, and $E_3((269/300), 0)$, respectively. The value of the three equilibrium points represents the corresponding value of the price of imported soybeans from the United States and Brazil in the context of the trade friction at that time.

Remark 2. The point $E_1(0, 0)$ means that the price of imported soybeans from the United States and Brazil is 0, which means that there are no Brazilian and American soybeans sold in the commodity market, and China does not import soybeans from Brazil and the United States. If China

were not importing soybeans from Brazil and the United States, there would be no imported soybeans from either country in circulation, and the equilibrium of zero prices would remain. However, the reality is that China still imports soybeans from Brazil and the United States from the past to the trade friction, so this balance does not exist in the reality.

Remark 3. The points $E_2(0, (629/800))$ and $E_3((269/300), 0)$ mean that the price of at least one imported soybean from the United States and Brazil is 0. Moreover, if the soybean price of either party becomes 0, it will cause a rapid and substantial increase in the demand of the corresponding party, and the equilibrium will be broken quickly in a very short time, which is extremely unstable. According to the expression form before substituting into the parameter value, no matter what the value of price elasticity coefficient and price adjustment speed is, the equilibrium is unstable and cannot exist for a long time. From this point of view, the three equilibrium points E_1, E_2 , and E_3 obtained by solving the discrete system (8) will not happen in the real economic situation. Even if it happens in a very small probability, the equilibrium will be spontaneously broken in a very short time under the action of the market. In such cases, there is no need for policy intervention to move towards generalization.

Next, we study the stability of point

$$E_4 \left(\frac{b_2(2a_1 + c_1w + 2b_1w) + a_2c_1}{4b_1b_2 - c_1c_2}, \frac{2b_1(b_2w + a_2) + c_2(b_1w + a_1)}{4b_1b_2 - c_1c_2} \right). \quad (15)$$

Theorem 2. If g_1, g_2 satisfy

$$\begin{cases} 1 + j_1 + j_4 + j_1j_4 - j_2j_3 > 0, \\ 1 - j_1 - j_4 + j_1j_4 - j_2j_3 > 0, \\ |j_1j_4 - j_2j_3| < 1, \end{cases} \quad (16)$$

then E_4 is stable, where

$$\begin{aligned} j_1 &= 1 + g_1 \left(\frac{a_1(1 - c_2) + c_1c_2(2a_1 + 2b_1w) - 2b_1b_2(4a_1 + c_1w + 4b_1w) - b_1c_2w}{4b_1b_2 - c_1c_2} + b_1w \right), \\ j_2 &= g_1c_1 \frac{2b_1b_2(2a_1 + c_1w + 2b_1w) - c_1c_2(a_1 + b_1w) + c_2(b_1w + a_1) + 2a_2b_1c_1}{2b_1(4b_1b_2 - c_1c_2)}, \\ j_3 &= g_2c_2 \frac{2b_1(b_2w + a_2) + c_2(b_1w + a_1)}{4b_1b_2 - c_1c_2}, \\ j_4 &= 1 + g_2 \left(\frac{2b_1b_2(6a_2 - 4b_2w + 2c_2w + 2a_1c_2 + c_1c_2w) - c_1c_2(a_2 + a_1 + b_1w)}{4b_1b_2 - c_1c_2} + \frac{c_2(4a_1b_2 + 3b_1w + a_1) - 2a_2b_1c_1}{4b_1b_2 - c_1c_2} + b_2w \right). \end{aligned} \quad (17)$$

Proof. The Jacobian matrix of E_4 is

$$J_4 = \begin{bmatrix} j_1 & j_2 \\ j_3 & j_4 \end{bmatrix}. \quad (18)$$

The characteristic equation is

$$f(\lambda) = \lambda^2 - A\lambda + B = 0, \quad (19)$$

where

$$A = \text{tr}(J_4) = j_1 + j_4,$$

$$B = \det(J_4) = j_1j_4 - j_2j_3,$$

$$\begin{aligned} \text{tr}(J_4)^2 - 4\det(J_4) &= (j_1 + j_4)^2 - 4(j_1j_4 - j_2j_3) \\ &= (j_1 - j_4)^2 + 4j_2j_3 \\ &= \frac{F_1}{F_2} + (j_1 - j_4)^2, \end{aligned} \quad (20)$$

$$F_1 = 2g_1g_2c_1c_2F_{11}F_{12},$$

$$F_2 = b_1(4b_1b_2 - c_1c_2)^2,$$

$$\begin{aligned} F_{11} &= 2b_1b_2(2a_1 + c_1w + 2b_1w) + 2a_2b_1c_1 \\ &\quad + c_2(b_1w + a_1)(1 - c_1), \end{aligned}$$

$$F_{12} = 2b_1(b_2w + a_2) + c_2(b_1w + a_1).$$

Since the values of parameters in economics are greater than 0, we can obtain $\text{tr}(J_4)^2 - 4\det(J_4) \geq 0$. Thus, the Nash equilibrium point E_4 has real eigenvalues.

According to Jury condition [37], if E_4 is stable, it is necessary to satisfy

$$\begin{cases} 1 + \text{tr}(J_4) + \det(J_4) > 0, \\ 1 - \text{tr}(J_4) + \det(J_4) > 0, \\ |\det(J_4)| < 1. \end{cases} \quad (21)$$

When

$$\begin{cases} 1 + j_1 + j_4 + j_1j_4 - j_2j_3 > 0, \\ 1 - j_1 - j_4 + j_1j_4 - j_2j_3 > 0, \\ |j_1j_4 - j_2j_3| < 1, \end{cases} \quad (22)$$

hold, E_4 is locally stable. By solving the inequality, the range of each parameter is obtained as follows:

$$\begin{aligned} a_1 &> 1.17, \\ a_2 &> 0.35, \\ b_1 &> 1.22, \\ b_2 &> 0.25, \\ c_1 &> 0.7, \\ c_2 &> 0.29, \\ w &> 0.1. \end{aligned} \quad (23)$$

This completes the proof. \square

We introduce the economic parameters $a_1 = 2.3, a_2 = 2.1, b_1 = 1.5, b_2 = 1.6$, and $c_1 = 1$ to the proofs of Theorem 2. Then equilibrium point $E_4((927/700), (898/700))$ is obtained. For E_4 , all the values of $a_1, a_2, b_1, b_2, c_1, c_2$ are within the range of (23). By using the values of estimated parameters, we can compute and get the Jacobian matrix:

$$J_4 = \begin{bmatrix} 1 - 5.249g_1 & 1.3243g_1 \\ 1.5394g_2 & 1 + 11.5186g_2 \end{bmatrix}. \quad (24)$$

The characteristic equation is $f(\lambda) = \lambda^2 - A\lambda + B = 0$, where

$$A = \text{tr}(J_4) = 2 - 5.249g_1 + 11.5186g_2, \quad (25)$$

$$B = \det(J_4) = 1 + 11.5186g_2 - 5.249g_1 - 62.5g_1g_2.$$

Since $\text{tr}(J_4)^2 - 4\det(J_4) = (5.249g_1 + 11.5186g_2)^2 + 8.15451g_1g_2, g_1 \geq 0, g_2 \geq 0$, and $\text{tr}(J_4)^2 - 4\det(J_4) \geq 0$, we can attain that $E_4((927/700), (898/700))$ has real eigenvalues.

According to the Jury condition,

$$\begin{cases} 4 - 10.498g_1 + 23.0372g_2 - 62.5g_1g_2 > 0, \\ 11.5186g_2 - 5.249g_1 - 62.5g_1g_2 < 0, \\ 11.5186g_2 - 5.249g_1 - 62.5g_1g_2 > -2, \end{cases} \quad (26)$$

hold. The inequalities define the stable region of Nash equilibrium.

Remark 4. In the proof of Theorem 2, we calculate the stable level of E_4 under the condition of the value range of g_1 and g_2 , that is, the analysis of local stability of E_4 . That means that when the speed of price adjustment is controlled within a certain range, the price of imported American soybeans and Brazilian soybeans reaches the Nash equilibrium in the competition of product market. There is no fluctuation and the price of soybean market is stable. And when g_1 and g_2 go beyond a certain range, E_4 is no longer Nash equilibrium. Both prices adjust too fast, leading to a certain degree of fluctuations in the price of imported American soybeans and Brazilian soybeans. The equilibrium reached in the competition between the two will be broken, and the market price fluctuates, which is likely to have a certain impact on consumers' life and the healthy development of the product market. As for the reality, after the start of the trade friction, the imposition of high soybean tariffs will lead to the rapid rise of the price of imported soybeans in the United States, which will accelerate the speed of price adjustment in the model to some extent, and thus affect the equilibrium of soybean market.

In order to maintain the smooth operation of Chinese soybean market, China must take corresponding policies and measures according to the situation. When the speed of price adjustment increases slightly and the threat to soybean market equilibrium is relatively small, China should accelerate agricultural supply-side structural reform, appropriately increase soybean planting subsidies, encourage soybean planting, and increase research and development input. In this way, we can improve the quality and quantity

of domestic soybeans in the future, reduce Chinese continuous dependence on imported soybeans, and increase domestic soybean supply. At the same time, we should increase the investment in soybean planting abroad, so as to effectively improve the enthusiasm of soybean planting in other countries, diversify the import market, and optimize the import choice. When the speed of price adjustment is greatly accelerated, which is a great threat to soybean market equilibrium, China can quickly turn the import channels to South America and southeast Asian countries in a short time and, at the same time, reduce the soybean import tariffs to these countries in the short term to make up for the US soybean import source gap. It is also possible to seek substitutes with similar nutrition and taste to soy products, reduce the price of substitutes, strengthen media publicity and popularization of nutrition knowledge, and stimulate people's enthusiasm for the consumption of substitutes.

4. Simulation Analysis

How does one know whether the equilibrium is affected according to the change of price adjustment speed, so as to know what kind of measures should be taken? Next, we will conduct simulation analysis on the speed of price adjustment and price change to make a more intuitive analysis.

In this section, the numerical dynamic evolution simulation of model (8) is carried out to observe the law of price evolution. The estimated values $a_1, a_2, b_1, b_2, c_1, c_2$ will remain relatively stable for a short time in the future. Therefore, after the trade friction, China's tax increase on imported soybeans from the United States is reflected in the rapid rise in the customs value of imported soybeans at a certain stage. Then the price fluctuates near the high level after rising, which is mainly reflected in the change of price adjustment speed g in model (8). In this section, we study the effect of the change of the rate of price adjustment g on the equilibrium price.

4.1. The Effect of Price Adjustment Speed on Equilibrium Price. From (2), we can reduce that

$$g_i = \frac{p_i(t+1) - p_i(t)}{p_i(t)} \left(\frac{\partial \pi_i}{\partial p_i(t)} \right)^{-1}. \quad (27)$$

According to the relevant data of imported Brazilian and American soybeans from 2006 to 2017 provided by Wind Financial Terminal, the price adjustment speeds of imported soybeans $g_i (i = 1, 2)$ from Brazil and the United States are calculated on the basis of (27). The values of $p_i (i = 1, 2)$ are taken as the average monthly prices of each year. The corresponding economic parameters obtained by Rotterdam model are introduced into $(\partial \pi_i / \partial p_i(t)) (i = 1, 2)$. According to the analysis based on accurate monthly data statistics, before the trade friction began, the adjustment speeds of imported soybean prices g_1, g_2 of Brazil and the United States changed slowly, fluctuating around 0.03 in the stable stage. Therefore, in this section, 0.03 is selected as the control value of speed adjustment.

Fixing the adjustment speed of imported US soybean price g_2 , we can observe the changes of imported soybean prices of the two countries with the adjustment speed of imported Brazilian soybean price g_1 . Assuming that the adjustment speed of imported US soybean price is $g_2 = 0.03$, with the change of the rate of price adjustment of imported Brazilian soybeans, the trajectories of p_1 and p_2 are shown in Figure 1.

Fixing the adjustment speed of imported Brazilian soybean price g_1 , we can observe the changes of imported soybean prices of the two countries with the adjustment speed of imported American soybean price g_2 . Assuming that the adjustment speed of imported Brazilian soybean price is $g_1 = 0.03$, with the change of the US import soybean price adjustment speed g_2 , the tracks of p_1 and p_2 are shown in Figure 2.

As can be seen from Figures 1 and 2, with the increase of the speed of price adjustment $g_i (i = 1, 2)$, soybean prices remain stable at the beginning, and oligarchs' profits are maximized. Neither side can make more profits by changing prices to reach Nash equilibrium $(p_1, p_2) = (1.324, 1.283)$. However, too fast speed of price adjustment will break the state of stable equilibrium, and the system will enter the counter-periodic bifurcation. Faster price adjustment even leads to chaos in the system, resulting in disorder in the imported soybean market. Figure 3 shows the maximum Lyapunov exponents with p_1 and p_2 changing, respectively.

In the max Lyapunov exponent graph, when the max Lyapunov exponent equals 0, the system bifurcates, and when the max Lyapunov exponent is greater than 0, the system enters chaos. The bifurcation and chaos in Figures 1 and 2 coincide with the change of largest Lyapunov exponent in Figure 3; that is, the system goes from stable state to double bifurcation and finally goes to chaos.

In both cases, there is little difference in the point of bifurcation between the two oligarchs. But when the price adjustment speed of imported soybeans from the United States is fixed and the price adjustment speed of imported soybeans from Brazil is gradually changing, the bifurcation range of equilibrium price of imported soybeans from the US increases and the range of chaotic price enlarges. Similarly, when the price adjustment speed of Brazilian soybean imports is fixed and the price adjustment speed of American soybean imports gradually changes, the equilibrium price bifurcation of Brazil soybean imports increases and the range of chaotic price enlarges. It can be seen that when one oligarch country's price adjustment speed is fixed and the other party's price adjustment speed is changed, the price of the fixed party will fluctuate greatly, while the changing party will be less affected.

4.2. Time Series Evolution Analysis of Price. The time series of game price reflects the change of equilibrium price over time. When $g_1 = 0.03$ and $g_2 = 0.03$, the system is in a stable state, at which time the stable Nash equilibrium price evolves over time as shown in Figure 4.

At this point, the evolutionary orbit of (p_1, p_2) converges to a fixed point, which is the Nash equilibrium price obtained previously, as shown in Figure 5.

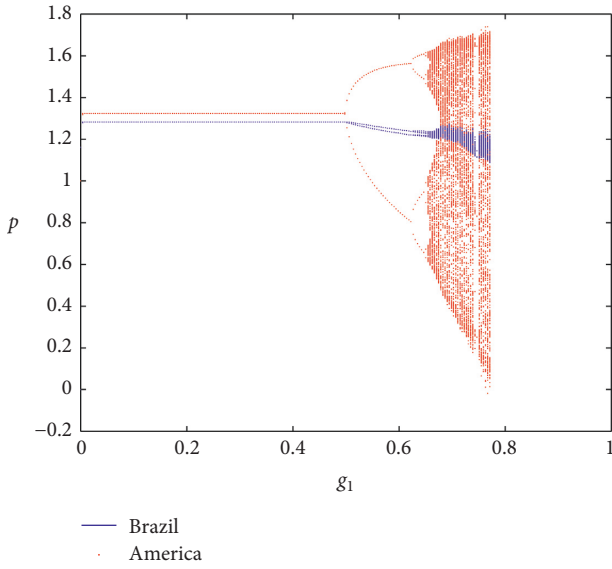


FIGURE 1: The trajectories of p_1 and p_2 diagram.

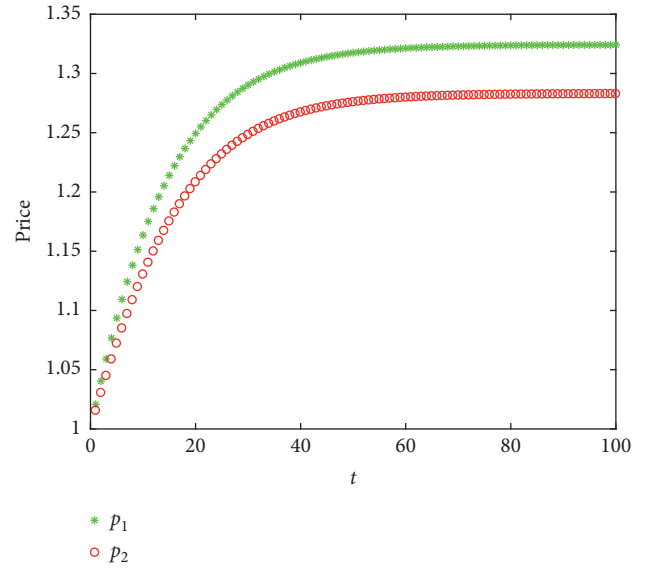


FIGURE 4: The stable Nash equilibrium price evolves over time diagram.

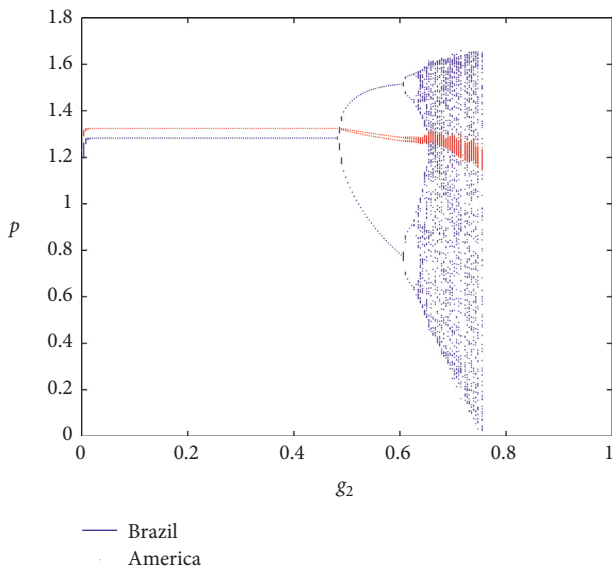


FIGURE 2: The tracks of p_1 and p_2 diagram.

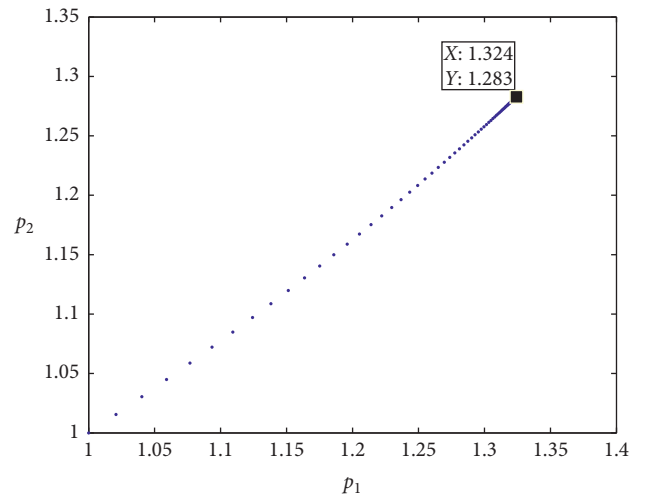


FIGURE 5: The Nash equilibrium price p_1 and p_2 diagram.

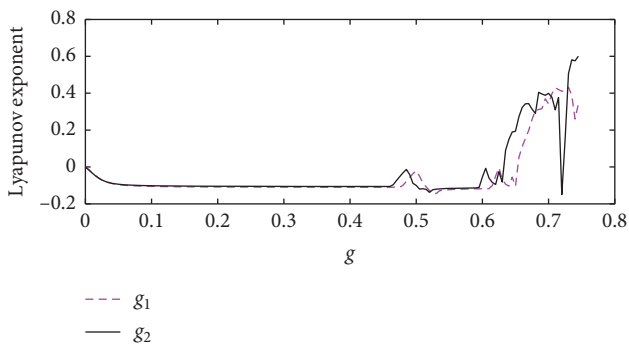


FIGURE 3: The maximum Lyapunov exponents with p_1 and p_2 diagram.

From the time point of data collected, it is found that after China imposed tariffs on US soybeans, the price of US imported soybeans increased significantly in a short period of time, while the price of Brazilian imported soybeans changed slightly. According to (27), $g_1 = 0.03$ and $g_2 = 0.54$. The maximum Lyapunov index changes from less than 0 to equal 0 and then to less than 0. The system goes from stable state to bifurcation state. Time series graphs of game price $p_i (i = 1, 2)$ under the current price adjustment speed are drawn in Figure 6.

At this time, there are two price trends in both countries. At this point, the evolution trajectory of the bounded rational duopoly game is shown in Figure 7. The change trajectories finally converge to two points (1.294, 1.486) and (1.306, 0.9361). It is confirmed that the system of Figure 2 has entered the double bifurcation state.

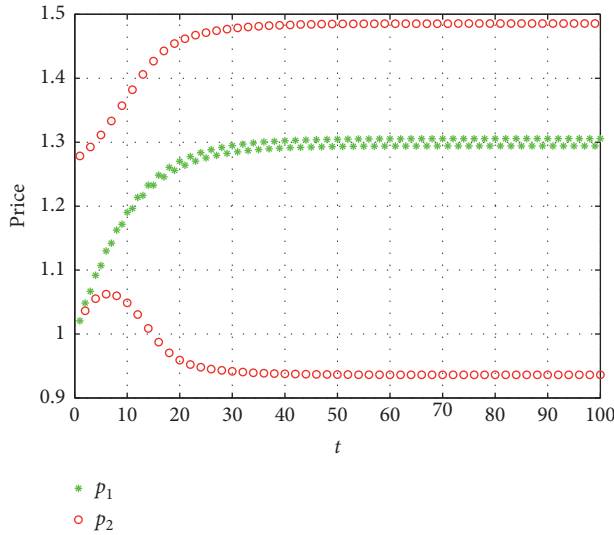


FIGURE 6: The current price adjustment speed diagram.

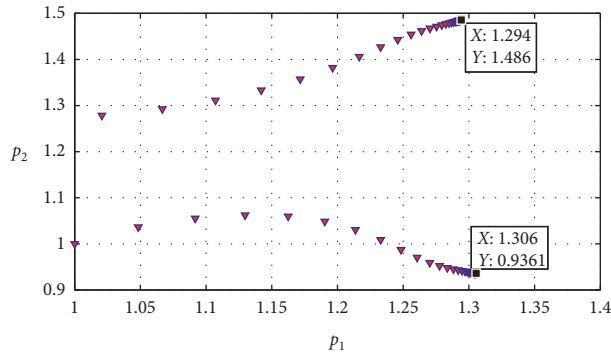


FIGURE 7: Time series graph of game prices with $g_1 = 0.03$ and $g_2 = 0.54$.

From the analysis in this section, when the price adjustment speeds of both players are controlled at a low level, the equilibrium price will remain stable in the region over time without interference from other external factors. If the speed of price adjustment is accelerated and beyond the stable region, the price of imported soybean will fluctuate greatly with the cycle, and the equilibrium price will change accordingly. Before the trade friction, the tariff preferential policy was implemented, and the change of soybean import price in the two oligarchs tended to be smooth. The emergence of tariff increases has led to rapid price changes, accelerated price adjustment, and consequently changed equilibrium prices, which confirms the above conclusions.

5. Conclusion and Discussion

Based on the classical game model, this paper constructs the bounded rational duopoly game models of the United States and Brazil. The demand elasticity is solved by Rotterdam model, and the elastic parameters in the game model are obtained. Then the elastic parameters are put into the model, the theorems are obtained and verified, and the corresponding economic analysis and policy recommendations

are made. Through the simulation, we made some intuitive explanations about the meaning of economics. In this section, the model is used to predict the future soybean price.

5.1. Price Forecast. The above analysis shows that the price adjustment speed is an important parameter in the model (8). Estimating the price adjustment speed from the statistical data can predict the future soybean price.

From Figure 7, we can see that the equilibrium price tends to two points after the price adjustment speed changes, $(p_1, p_2) = (1.294, 1.486)$ and $(1.306, 0.9361)$. In reality, the price of imported soybeans in the United States has risen. Obviously $(p_1, p_2) = (1.306, 0.9361)$ is not in line with the actual situation. So we only discuss the case that $(p_1, p_2) = (1.294, 1.486)$.

At the point $(1.294, 1.486)$, the price of imported soybeans from Brazil dropped slightly by 2.26%, while the price of imported soybeans from the United States rose by 15.82%. Before the trade friction, China imposed tariff preferential policies on Brazil and the United States, and only 3% tariff was levied on imported soybeans. As the two oligarchs in China's soybean import market, Brazil and the United States have constantly adjusted their price strategies to maximize profits, but the fluctuation of prices has slowed down. From the end of 2017 to the beginning of 2018, the average customs value of imported soybeans in Brazil and the United States remained 3.4yuan/kg and 3.2yuan/kg, respectively. Referring to Wind Financial Terminal data, through (26) data statistics, it is concluded that the price adjustment speed in this stage is $g_1 = 0.03$ and $g_2 = 0.03$. They are brought into the model (8) and the equilibrium prices of the model are 2.648 yuan/kg and 2.566 yuan/kg (dimensional conversion has been overdone), respectively. Both prices are slightly lower than the real price.

The China-US trade friction broke out in April 2018. As of June 2018, the customs value of imported soybeans from the United States rose rapidly to an average of 13.72 yuan per kilogram in a short period of time, while that of imported soybeans from Brazil dropped to an average of 3.28 yuan per kilogram. Referring to the detailed data statistics, we can get the price adjustment speed $g_1 = 0.03$ and $g_2 = 0.54$ at this time. In model (8), the equilibrium prices of Brazil and the United States are 2.588 yuan/kg and 2.972 yuan/kg, respectively, which are still slightly lower than the real prices. The price prediction errors are shown in Table 4.

In addition, our model has good prediction accuracy for price fluctuations. In reality, Brazil's soybean import price decreased by 3.5% while the US soybean import price increased by 16.25%. In our model (8), the import price of Brazil decreased by 2.26%. The import price of the United States increased by 15.82%. The relative errors of model are 35.98% and 2.65%, respectively. The prediction for price fluctuations is shown in Table 5.

5.2. Evaluation of the Model. In the actual import trade, the change of soybean imports from Brazil and the United States to any extent can be quantified by (26) the price adjustment speed value and then brought into the model (8) to obtain

TABLE 4: Price prediction errors.

g_i	$g_1 = 0.03, g_2 = 0.03$			$g_1 = 0.03, g_2 = 0.54$		
p_i	Model	Real	Relative error (%)	Model	Real	Relative error (%)
Brazil	1.324	1.7	22.4	1.294	1.64	21.1
America	1.283	1.6	20	1.486	1.86	20.11

TABLE 5: Prediction for price fluctuations.

p_i	Model (%)	Real (%)	Relative errors (%)
Brazil	-2.26	-3.53	35.98
America	15.82	16.25	2.65

the game equilibrium price under this situation. From the above analysis, we can see that the price obtained by the model is about 20% lower than the real price, and the price before and after the model is very close to the real price before and after the rise and fall; the difference of the US price is less than 3%. It can be seen that the model used to simulate and predict the rise and fall of imported soybean prices in Brazil and the United States in a short period of time is ideal. When prices fluctuate dramatically, we can get a more accurate range of price changes.

There may be two reasons for the underestimation of the price predicted by the model. On the one hand, this paper only collects and uses the annual data from 2006 to 2017. The sample size is small, which results in the deviation of economic parameter estimation, and then affects the prediction of equilibrium price in the game model. On the other hand, the import cost will fluctuate due to RMB exchange rate, sea freight, weather, and other factors. In the future, the transportation mode of the two countries may be improved, and the cost will also change. Next, we can refer to the relevant import literature, establish cost function, and systematically consider the factors affecting the cost. According to the latest data, after the trade friction, Brazil and the United States fluctuated smoothly on the basis of fluctuating prices, further concretizing the model, and bringing the latest large-scale sample data into the Rotterdam model to obtain more economic parameters in line with the present stage and in the future. It can not only predict the increase of imported soybean price before and after the trade friction but also make the model more accurate in predicting the imported soybean price in the short time after the trade friction.

China imposed a 25% tariff on soybeans from the United States, which caused the import price of soybeans to rise rapidly in a short period of time. The import price of soybeans from the United States increased substantially but had little impact on the import price of soybeans from Brazil. This conclusion is the same as that obtained in Section 4.1. If soybean importers want to maintain stable market demand, they should take price reduction actions to maintain volatile import demand and avoid large losses. Otherwise, China will turn its demand for US soybeans to other countries.

The reason why the duopoly game model of Brazil and the United States was used before and after the trade friction is that after the outbreak of the trade friction, because of the

soybean growth cycle and the past soybean planting inertia of other countries, as well as the impact of natural disasters in some countries this year, other countries cannot quickly meet the huge demand of soybean import in China in the short term of six months to one year. In order to maintain domestic supply stability, the United States is still a major oligopolistic supplier except Brazil in the short term, and the duopoly game model is still applicable to the United States and Brazil in the short term.

5.3. Requirement Analysis. In demand forecasting, the equilibrium prices corresponding to $g_1 = 0.03$ and $g_2 = 0.03$ are $p_1 = 1.324$ and $p_2 = 1.283$, and the equilibrium prices corresponding to $g_1 = 0.03$ and $g_2 = 0.54$ are $p_1 = 1.294$ and $p_2 = 1.486$. The equilibrium price under the above two conditions and the economic parameter values $a_1 = 2.3, a_2 = 2.1, b_1 = 1.5, b_2 = 1.6, c_1 = 1$, and $c_2 = 1.2$ obtained by Rotterdam model above are brought into the demand function (1). The comparative analysis shows that the demand for imported Brazilian soybeans increases by 15.53%, while the demand for imported American soybeans decreases by 22.05%. This means that China-US trade frictions have led to a decrease in China's demand for imported soybeans from the United States and an increase in Brazil's demand for imported soybeans. According to the daily import data of soybean collected by Wind Financial Terminal, since January 2018, there are a lot of incomplete data, which cannot get the precise change range of import volume. However, we can roughly compare the increase and decrease of soybean imports in the postwar period of 2018 with the same period in previous years. The demand for imported Brazilian soybeans increased compared with the same period in previous years, and the demand for imported American soybeans decreased significantly compared with the same period in previous years, which is consistent with the predicted trend of the demand model in this paper.

Demand will affect prices to a certain extent. In the current state of high tension in Sino-US trade relations, a substantial reduction in the import of US soybeans in the short term will help China to take the initiative in the late China-US trade negotiations. However, China has a large demand for soybeans. In the short run, the demand for soybeans from the United States will be transferred to other countries, which will theoretically lead to the rise of imported soybean prices from other countries. In Section 5.1, the price change of Brazilian imported soybeans predicted by the model is consistent with the actual trend of Brazilian imported soybean price change, showing a downward trend. The difference may be due to the decrease of China's demand for imported soybeans from the United States, which to a certain extent leads to competition among soybean

producers other than the United States. South America, Southeast Asia, and other countries have lowered prices in order to obtain opportunities to export to China.

5.4. Suggestions. From a long-term point of view, without affecting domestic consumption demand and industrial development, we need to take certain measures to reduce the import scale substantially. As far as China is concerned, there is great potential for soybean cultivation in China. China should speed up the structural reform of agricultural supply side, properly increase the subsidy for soybean cultivation, encourage soybean cultivation, increase R&D investment, improve the quality and quantity of domestic soybean, reduce the dependence on imported soybean, and increase domestic soybean supply. As far as China's foreign strategy is concerned, the economic and trade frictions between China and the United States continue to increase China's imports of soybeans to South America and the "along the way" countries and further reduce the dependence on us soybeans. Since July 1, China has reduced the tariff rates on soybean imports from 3% to zero in India, Korea, Bangladesh, Laos, and Sri Lanka. Through the tariff reduction and exemption policy, developing and tapping the soybean planting potential of other countries in the world, increasing investment in soybean planting abroad, improving the enthusiasm of soybean planting in other countries, realizing diversification of import market, and optimizing import choice are very important for filling the vacancy of imported soybean in the United States and maintaining the stability of soybean market in China.

Data Availability

The data used to support the findings of this study are available from the corresponding author upon request. The questionnaire data were acquired mainly through e-mail and paper filling out.

Conflicts of Interest

The authors declare no conflicts of interest.

Authors' Contributions

Yi Wang selected the topic and Hui Wang drafted the manuscript. All the authors edited the paper. All authors have read and approved the final manuscript.

Acknowledgments

This work was supported by the National Natural Science Foundation of China (no. 11601270). This work was also supported by the Philosophy and Social Science Program of Jinan (no. JNSK18B17).

References

- [1] H. N. Agiza, A. S. Hegazi, and A. A. Elsadany, "The dynamics of Bowley's model with bounded rationality," *Chaos, Solitons & Fractals*, vol. 12, no. 9, pp. 1705–1717, 2001.
- [2] H. N. Agiza and A. A. Elsadany, "Nonlinear dynamics in the Cournot duopoly game with heterogeneous players," *Physica A: Statistical Mechanics and Its Applications*, vol. 320, no. 1, pp. 512–524, 2003.
- [3] H. N. Agiza and A. A. Elsadany, "Chaotic dynamics in nonlinear duopoly game with heterogeneous players," *Applied Mathematics and Computation*, vol. 149, no. 3, pp. 843–860, 2004.
- [4] A. A. Elsadany, "Dynamics of a delayed duopoly game with bounded rationality," *Mathematical and Computer Modelling*, vol. 52, no. 9–10, pp. 1479–1489, 2010.
- [5] G.-I. Bischi and F. Lamantia, "Nonlinear duopoly games with positive cost externalities due to spillover effects," *Chaos, Solitons & Fractals*, vol. 13, no. 4, pp. 701–721, 2002.
- [6] F. Tramontana, "Heterogeneous duopoly with isoelastic demand function," *Economic Modelling*, vol. 27, no. 1, pp. 350–357, 2010.
- [7] A. Bonatti, G. Cisternas, and J. Toikka, "Dynamic oligopoly with incomplete information," *The Review of Economic Studies*, vol. 84, no. 2, pp. 503–546, 2016.
- [8] A. Nagurny and T. Wolf, "A Cournot-Nash-Bertrand game theory model of a service-oriented Internet with price and quality competition among network transport providers," *Computational Management Science*, vol. 11, no. 4, pp. 475–502, 2014.
- [9] A. E. Matouk, A. A. Elsadany, and B. Xin, "Neimark-Sacker bifurcation analysis and complex nonlinear dynamics in a heterogeneous quadropoly game with an isoelastic demand function," *Nonlinear Dynamics*, vol. 89, no. 4, pp. 2533–2552, 2017.
- [10] X. Wang, Y. Xie, H. S. Jagpal, and S. Yenyurt, "Coordinating R&D, product positioning, and pricing strategy: a duopoly model," *Customer Needs and Solutions*, vol. 3, no. 2, pp. 104–114, 2016.
- [11] P.-y. Nie, "Comparing horizontal mergers under Cournot with bertrand competitions," *Australian Economic Papers*, vol. 57, no. 1, pp. 55–80, 2018.
- [12] I. Saglam, "Ranking supply function and Cournot equilibria in a differentiated product duopoly with demand uncertainty," *Games*, vol. 9, no. 3, p. 60, 2018.
- [13] H. N. Agiza, A. S. Hegazi, and A. A. Elsadany, "Complex dynamics and synchronization of a duopoly game with bounded rationality," *Mathematics and Computers in Simulation*, vol. 58, no. 2, pp. 133–146, 2002.
- [14] H. Wang and J. Ma, "Complexity analysis of a Cournot-Bertrand duopoly game with different expectations," *Nonlinear Dynamics*, vol. 78, no. 4, pp. 2759–2768, 2014.
- [15] Z. Guo and J. Ma, "Dynamics and implications on a cooperative advertising model in the supply chain," *Communications in Nonlinear Science and Numerical Simulation*, vol. 64, pp. 198–212, 2018.
- [16] J. Ma and H. Wang, "Complexity analysis of dynamic non-cooperative game models for closed-loop supply chain with product recovery," *Applied Mathematical Modelling*, vol. 38, no. 12, pp. 5562–5572, 2014.
- [17] J. Ma and L. Xie, "The comparison and complex analysis on dual-channel supply chain under different channel power structures and uncertain demand," *Nonlinear Dynamics*, vol. 83, no. 3, pp. 1379–1393, 2016.
- [18] J. Zhang and J. Chen, "Externality of contracts on supply chains with two suppliers and a common retailer," *Journal of Industrial and Management Optimization*, vol. 6, no. 4, pp. 795–810, 2010.
- [19] J. Ma and L. Sun, "Complexity analysis about nonlinear mixed oligopolies game based on production cooperation," *IEEE*

- Transactions on Control Systems Technology*, vol. 26, no. 4, pp. 1532–1539, 2018.
- [20] J. Ma and H. Ren, “Influence of government regulation on the stability of dual-channel recycling model based on customer expectation,” *Nonlinear Dynamics*, vol. 94, no. 3, pp. 1775–1790, 2018.
- [21] D. Li and A. Nagurney, “Supply chain performance assessment and supplier and component importance identification in a general competitive multitiered supply chain network model,” *Journal of Global Optimization*, vol. 67, no. 1–2, pp. 223–250, 2017.
- [22] J. Li, C. Zhang, Q. Sun, Z. Chen, and J. Zhang, “Changing the intensity of interaction based on individual behavior in the iterated prisoner’s dilemma game,” *IEEE Transactions on Evolutionary Computation*, vol. 21, no. 4, pp. 506–517, 2017.
- [23] J. Zhang and Z. Chen, “Contact-based model for strategy updating and evolution of cooperation,” *Physica D: Nonlinear Phenomena*, vol. 323–324, pp. 27–34, 2016.
- [24] J. Zhang, Z. Xu, and Z. Chen, “Effects of strategy switching and network topology on decision-making in multi-agent systems,” *International Journal of Systems Science*, vol. 49, no. 9, pp. 1934–1949, 2018.
- [25] J. Zhang, Y. Zhu, Q. Li, and Z. Chen, “Promoting cooperation by setting a ceiling payoff for defectors under three-strategy public good games,” *International Journal of Systems Science*, vol. 49, no. 10, pp. 2267–2286, 2018.
- [26] J. Ma and Z. Guo, “The parameter basin and complex of dynamic game with estimation and two-stage consideration,” *Applied Mathematics and Computation*, vol. 248, pp. 131–142, 2014.
- [27] J. Ma and F. Wu, “The application and complexity analysis about a high-dimension discrete dynamical system based on heterogeneous triopoly game with multi-product,” *Nonlinear Dynamics*, vol. 77, no. 3, pp. 781–792, 2014.
- [28] J. Ma and H. Tu, “Analysis of the stability and Hopf bifurcation of money supply delay in complex macroeconomic models,” *Nonlinear Dynamics*, vol. 76, no. 1, pp. 497–508, 2014.
- [29] J. Ma, T. Xu, Y. Hong, and X. Zhan, “Impact research on a nonlinear cold chain evolutionary game under three various contracts,” *International Journal of Bifurcation and Chaos*, vol. 29, no. 5, Article ID 1950058, 2019.
- [30] L. Mu, P. Liu, Y. Li, and J. Zhang, “Complexity of a real estate game model with a nonlinear demand function,” *International Journal of Bifurcation and Chaos*, vol. 21, no. 11, pp. 3171–3179, 2011.
- [31] F. Liu and Y. Li, “Complex nonlinear dynamic system of oligopolies price game with heterogeneous players under noise,” *International Journal of Bifurcation and Chaos*, vol. 26, no. 11, Article ID 1650183, 2016.
- [32] Y. Wang, X. Su, and S. Guo, “The optimal confidence intervals for agricultural products’ price forecasts based on hierarchical historical errors,” *Entropy*, vol. 18, no. 12, p. 439, 2016.
- [33] X. Su, H. Liu, and S. Hou, “The trilateral evolutionary game of agri-food quality in farmer-supermarket direct purchase: a simulation approach,” *Complexity*, vol. 2018, no. 2, p. 11, 2018.
- [34] X. Su, Y. Wang, S. Duan, and J. Ma, “Detecting chaos from agricultural product price time series,” *Entropy*, vol. 16, no. 12, pp. 6415–6433, 2014.
- [35] H. Theil, “The information approach to demand analysis,” *Econometrica*, vol. 33, no. 1, pp. 67–87, 1965.
- [36] J. M. Alston and J. A. Chalfant, “The silence of the lambdas: a test of the almost ideal and Rotterdam models,” *American Journal of Agricultural Economics*, vol. 75, no. 2, pp. 304–313, 1993.
- [37] T. Puu, *Attractors, Bifurcations, and Chaos: Nonlinear Phenomena in Economics*, Springer-Verlag, Berlin, Germany, 2003.
- [38] J.-h. Ma and Y.-s. Chen, “Study for the bifurcation topological structure and the global complicated character of a kind of nonlinear finance system(I),” *Applied Mathematics and Mechanics*, vol. 22, no. 11, pp. 1240–1251, 2001.
- [39] J.-h. Ma and Y.-s. Chen, “Study for the bifurcation topological structure and the global complicated character of a kind of nonlinear finance system(II),” *Applied Mathematics and Mechanics*, vol. 22, no. 12, pp. 1375–1382, 2001.

Research Article

Study on the User Density Identification via Improved Whale Optimization Algorithm in Device-to-Device Communication

Yao Zhang ¹, Zhongliang Deng,¹ and Aihua Hu^{1,2}

¹Beijing University of Posts and Communication, Beijing 100876, China

²Hebei University of Economic and Business, Shijiazhuang 050061, China

Correspondence should be addressed to Yao Zhang; yao0@bupt.edu.cn

Received 7 May 2019; Revised 23 July 2019; Accepted 13 September 2019; Published 3 November 2019

Guest Editor: Raúl Baños

Copyright © 2019 Yao Zhang et al. This is an open access article distributed under the Creative Commons Attribution License, which permits unrestricted use, distribution, and reproduction in any medium, provided the original work is properly cited.

The present study proposes a new algorithm for device-to-device (D2D) user density identification in a 5G network based on resource allocation. The method initially established a multiobjective optimization function that calculates system throughput and quality of service (QoS) of D2D users. The optimal resource allocation result of the multiobjective function is obtained via the improved whale optimization algorithm (IWOA). System throughput after resource allocation exhibits a linear relationship with the number of users. Therefore, the D2D user density areas are accurately identified via the throughput value. The simulation result reveals that the accuracy of D2D user density identification reaches 95%.

1. Introduction

With the popularization and performance improvement of smartphones, it is important for a 5G network to satisfy individuals' demands for ultrahigh traffic density and connection density. Conversely, it is necessary to consider the effect of different resource allocation strategies under different scenarios and traffic loads [1]. The resource allocation method of device-to-device (D2D) technology in D2D and cellular hybrid networks improves system throughput and decreases transmission delay, and D2D technology allows adjacent users to directly communicate. The transmitting power of the node is low and can eliminate self-interference and solve the resource allocation problem in crowd-gathering scenarios [2], and throughput after resource allocation effectively reflects regional D2D user density. Thus, the performance of the resource allocation algorithm directly determines the accuracy of the D2D user density.

Currently, the main achievements of extant studies on D2D resource allocation technology are as follows. The study [3] considers a communication scenario, and each D2D technology can reuse a cellular resource. The study proposes a method to solve the optimal power allocation scheme via

establishing an optimal objective function. The study [4] examines a scenario in which a pair of D2D multiplexers reuses a cellular downlink resource. Additionally, the study proposes a resource allocation method based on user interrupt probability and connection probability to maximize system throughput. The study [5] proposes a new resource allocation method based on the interference control mechanism of DT maximum/minimum power standard, and this decreases the interference of hybrid cellular networks. The study [6] proposes a method that guarantees the quality of service (QoS) although the method does not improve the throughput. The study [7] proposes the resource allocation method under a 28 GHz bandwidth, and this improves system throughput via limiting the interference value although it does not significantly decrease interference. The study [8] proposes an adaptive power control method based on the cellular user interference threshold that maximizes energy efficiency under the condition of satisfying the minimum QoS of D2D users. In [9], the resource allocation problem in the underlying cellular network of D2D communication was defined as a game of alliance formation, and the power allocation was optimized by the whale optimization algorithm (WOA). This method maximizes the throughput of the D2D system and guarantees the

minimum rate per user. But it does not show any difference between the WOA and traditional optimization algorithms.

In summary, the aforementioned methods including those in [3–5] are unable to guarantee the QoS of D2D users, and thus, this constitutes a simple choice for cellular users based on distance. The aforementioned methods including those in [6–9] guarantee the QoS of D2D users although most of them do not limit the interference value and improve system throughput. Therefore, the result of the resource allocation technology does not reflect real D2D user density areas.

For the aforementioned problem, this study presents a new resource allocation method in the 5G network. The method initially establishes a multiobjective optimization function that contains system throughput and QoS of D2D users. Furthermore, the multiobjective optimization function is solved via the improved whale optimization algorithm (IWOA), and the result corresponds to an optimal resource allocation method. The method guarantees an approximate linear relationship between the system throughput and the number of users. Therefore, D2D user density areas are accurately identified by the throughput value after performing the optimal resource allocation method.

This study consists of four main sections: Section 2 describes the 5G communication scenario and existing problems. Section 3 describes resource allocation based on the IWOA. Section 4 presents simulated results. Experimental results indicate that the proposed algorithm obtains a high-accuracy result for D2D user density identification.

2. Scenario Description

In this study, we assume that there are D2D users and cellular users in a scenario. Furthermore, there is disturbance between the D2D users and the cellular users. To satisfy the users' QoS, each cellular resource can be multiplexed by only one D2D pair, and each D2D pair can multiplex the multilink resource of cellular users. The D2D users can share spectrum resources of cellular users. The D2D users can communicate with each other through the cellular mode, D2D special mode, and D2D multiplexing mode. The D2D users can be grouped into the same group by distance [10]. Figure 1 shows the D2D and cellular hybrid network system.

In this scenario, the path loss model can be defined as follows [11]:

$$PL(d) = \mu + 10\alpha \log_{10}(d) + \varepsilon, \quad (1)$$

where ε denotes the response lognormal shadow, α denotes the path loss index, μ denotes the path loss coefficient, and d denotes the communication distance. Normally, the path loss model can be divided into the line-of-sight (LOS) model PL_{LOS} and the non-line-of-sight (NLOS) model PL_{NLOS} , and equation (1) can be represented as

$$PL_{D2D} = p_1 \times PL_{LOS} + (1 - p_1) \times PL_{NLOS}. \quad (2)$$

Based on the Shannon equation, the throughput of the CU and DU is [12]

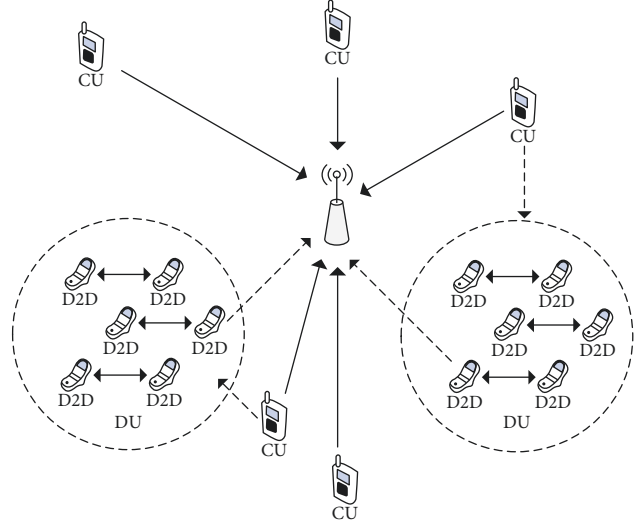


FIGURE 1: D2D and cellular hybrid network system (CU = cellular user and DU = D2D user).

$$R_j^{DU} = B \log_2(1 + r_j^{DU}), \quad (3)$$

$$R_i^{CU} = B \log_2(1 + r_i^{CU}), \quad (4)$$

where r_j^{DU} denotes the signal-to-interference-plus-noise ratio (SINR) of D2D users, $j \in \{1, \dots, M\}$, in which M denotes the number of D2D users; r_i^{CU} denotes the SINR of cellular users, $i \in \{1, \dots, N\}$, in which N denotes the number of cellular users; and B denotes the channel resource bandwidth.

r_j^{DU} and r_i^{CU} can be defined as

$$r_j^{DU} = \frac{P_j^{DU} G_{j,j}}{\sum_{i=1}^N x_{i,j} P_i^{CU} G_{i,j} + \sum_{i=1}^N \sum_{i=1}^M x_{i,j} P_j^{DU} G_{j,j} + \delta_\xi^2}, \quad (5)$$

$$r_i^{CU} = \frac{P_i^{CU} G_{i,B}}{\sum_{j=1}^M x_{i,j} P_j^{DU} G_{j,B} + \delta_\xi^2}, \quad (6)$$

where $G_{j,j}$ denotes the channel gain between CU_i and DU_j , $G_{i,B}$ denotes the channel gain between CU_i and the base station, $G_{j,B}$ denotes the channel gain between DU_j and the base station, δ_ξ^2 denotes the white Gaussian noise, P_i^{CU} denotes the transmitting power of CU_i , and P_j^{DU} denotes the transmitting power of DU_j . When $x_{i,j} = 0$, DU_j does not multiplex the resource of CU_i . Equation (5) can be rewritten as $r_j^{DU} = P_j^{DU} G_{j,j} / \delta_\xi^2$. When $x_{i,j} = 1$, DU_j multiplexes the resource of CU_i .

Based on equation (3), the maximum system throughput of D2D users can be defined as

$$R = \max_x \left\{ \sum_{j \in M} R_j^{DU} \right\}. \quad (7)$$

To identify the D2D user density, it is necessary to find the resource allocation method to obtain the optimal system throughput, which has a linear relationship with the

number of D2D users. As shown in Figure 2, when the number of D2D users is dense, the throughput of D2D users is larger.

Conversely, to guarantee the QoS of D2D users, the function of satisfaction is used [12–14]:

$$U_j^{\text{DU}} = \frac{\log(1 + b_j^{\text{DU}})}{\log(1 + b_j^{\text{DU,max}})}, \quad (8)$$

where b_j^{DU} denotes the allocated resources of DU_j and $b_j^{\text{DU,max}}$ denotes the maximum value of b_j^{DU} . When $b_j^{\text{DU}} = b_j^{\text{DU,max}}$, U_j^{DU} can achieve the maximum value, which means the customer's satisfaction of users reaches the maximum value; namely, the system QoS achieves the optimal value.

3. D2D User Density Identification Based on IWOA

Normally, when the number of D2D users is low, given the linear relationship between the number of D2D users and the throughput, it is possible to identify the area of D2D user density in a 5G network via the throughput estimation in each region. However, for many traditional resource allocation algorithms (e.g., cheat-proof pricing method [15], heuristic method [16], and GA-based method [17]), with the increasing D2D users, the relationship between the number of D2D users and the throughput estimated becomes nonlinear. Thus, the identification of the D2D user density region is more difficult.

In Figure 3, the points correspond to the actual collected data between the number of D2D users and the throughput and the line denotes the fitting curve of the collected data. With increases in D2D users, the interference of D2D communication with cellular communication increases, and interference between D2D communications also increases. The increase of system throughput tends to be gentle. Therefore, it is difficult to accurately estimate the number of D2D users via the traditional method. To solve this problem, an optimal resource allocation algorithm based on the IWOA is proposed.

Firstly, a multiobjective optimization function is established and contains the system throughput and QoS of D2D users. Subsequently, an improved whale optimization algorithm (IWOA) is provided to search for the optimal value of the objective function. Finally, the system throughput will increase linearly with the increasing number of D2D users. The basic principles of the improved algorithm are described as follows.

3.1. Multiobjective Optimization Function. Based on equations (3), (5), and (7) the maximum system throughput of D2D users' objective optimization function is given as follows:

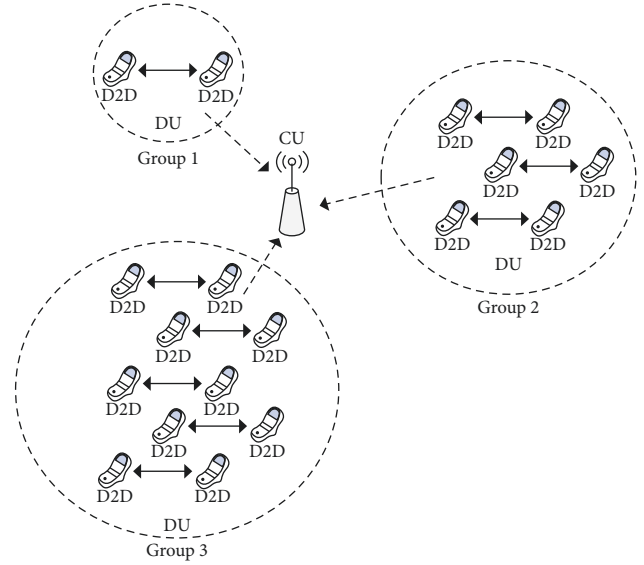


FIGURE 2: D2D user density in different regions.

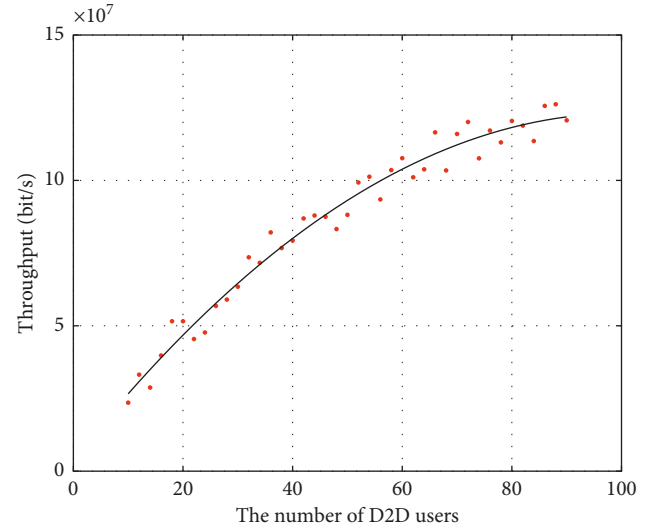


FIGURE 3: Distribution of the number of D2D users and throughput.

$$f_{\text{obj1}} = \max_x \left\{ \sum_{j \in M} R_j^{\text{DU}} \right\} = \max_x \left\{ \sum_{j \in M} B \log_2(1 + r_j^{\text{DU}}) \right\}, \quad (9)$$

$$\text{s.t. } r_i^{\text{CU}} \geq \text{SINR}_{i,\text{min}}^{\text{CU}}, \quad (10)$$

$$r_i^{\text{DU}} \geq \text{SINR}_{i,\text{min}}^{\text{DU}}, \quad (11)$$

$$0 \leq P_j^{\text{DU}} \leq P_{j,\text{max}}^{\text{DU}}, \quad j = 1, \dots, M, \quad (12)$$

$$0 \leq P_i^{\text{CU}} \leq P_{i,\text{max}}^{\text{CU}}, \quad i = 1, \dots, N, \quad (13)$$

$$\sum_{i=1}^M x_{i,j} \leq 1, \quad (14)$$

$$\sum_{j=1}^N x_{i,j} \leq K. \quad (15)$$

Equation (9) denotes the objective function, equation (10) denotes the minimum SINR threshold of CU_i , equation (11) denotes the minimum SINR threshold of DU_j , equation (12) denotes the transmitting power limitation of DU_j , equation (13) denotes the transmitting power limitation of CU_i , equation (14) means that each D2D user can only share resources with a cellular user, and equation (15) shows that the resource of each cellular user can be multiplexed via the K D2D users.

To guarantee the QoS of D2D users, the QoS objective optimization function is given as follows:

$$f_{\text{obj}2} = \max_x \left\{ \frac{\log(1 + b_j^{\text{DU}})}{\log(1 + b_j^{\text{DU,max}})} \right\}, \quad (16)$$

$$\text{s.t. } b_j^{\text{DU}} \geq 0, \quad (17)$$

$$\sum_{j \in M} b_j^{\text{DU}} \leq B^{\text{DU}}. \quad (18)$$

Equation (16) denotes the objective function, equation (17) denotes the minimum value of the allocated resources DU_j , and equation (18) denotes the total resources.

Therefore, the multiobjective optimization function is defined as follows:

$$f_{\text{obj}} = \max_x \{ \alpha f_{\text{obj}1} + (1 - \alpha) f_{\text{obj}2} \}. \quad (19)$$

The constraint condition of equation (19) denotes equations (10)–(15), (17), and (18). Specifically, α denotes a constant number within (0, 1). If the optimization objective focuses on optimizing the system throughput, then $\alpha > 0.5$. If the optimization objective focuses on optimizing the QoS of D2D users, then $\alpha < 0.5$.

3.2. Resource Allocation Mechanism Based on IWOA. Evidently, the optimization problem of equation (19) corresponds to a nonlinear optimization problem, which belongs to the NP-hard problem. It is difficult to directly obtain the global optimal solution. For the problem, the IWOA is proposed in this study, and the IWOA corresponds to an improved form of the whale optimization algorithm (WOA) [17–21].

The IWOA is a bionic intelligent optimization algorithm that imitates the feeding behavior of humpback whales. Specifically, the IWOA includes the following three stages: the walking and foraging stage, the encircling and contracting stage, and the spiral predation stage.

- (a) In the walking and foraging stage, humpback whales can recognize the location of the prey via the location

of a random individual whale. The behavior is represented by the following equations:

$$\begin{aligned} \vec{D} &= \left| \vec{C} \cdot \vec{X}_{\text{rand}} - \vec{X}_t \right|, \\ \vec{X}_{t+1} &= \vec{X}_{\text{rand}} - \vec{A} \times \vec{D}, \end{aligned} \quad (20)$$

where \vec{A} and \vec{C} denote coefficient vectors, \vec{D} denotes the distance vector from an agent to target food, \vec{X}_{rand} denotes the random position vector of the best solution, \vec{X}_t denotes the current position vector, and \vec{X}_{t+1} denotes the next position vector.

The vectors \vec{A} and \vec{C} are defined as follows:

$$\vec{A} = 2\vec{a} \cdot \vec{r} - \vec{a}, \quad (21)$$

$$\vec{C} = 2 \cdot \vec{r}, \quad (22)$$

where \vec{r} denotes a random vector in [0,1], and \vec{a} linearly decreases from 2 to 0 in the WOA. When $|A| \geq 1$, the whales are in the walking and foraging stage, and when $|A| < 1$, the whales go to the next stage.

In this study, the new resource allocation mechanism should satisfy the D2D user's throughput and QoS, and the QoS of cellular users must also be guaranteed. Therefore, the whale population vector variable \vec{X}_t is defined as follows:

$$\vec{X}_t = [P_j^{\text{DU}}, r_j^{\text{DU}}, b_j^{\text{DU}}, P_i^{\text{CU}}, r_i^{\text{CU}}, b_i^{\text{CU}}, x_{i,j}]. \quad (23)$$

As shown in equation (21), the variables that should be optimized include the following: transmission power variables P_j^{DU} and P_i^{CU} , SINR variables r_j^{DU} and r_i^{CU} , allocated resources b_j^{DU} and b_i^{CU} , and the multiplex variable $x_{i,j}$.

- (b) In the encircling and contracting stage, when the whales search for food, the other whales approach the optimal whale position and surround their food. The mathematical model is given as follows:

$$\begin{aligned} \vec{D} &= \left| \vec{C} \cdot \vec{X}_t^* - \vec{X}_t \right|, \\ \vec{X}_{t+1} &= \vec{X}_t^* - \vec{A} \cdot \vec{D}, \end{aligned} \quad (24)$$

where \vec{X}_t^* denotes a random position vector selected from the current population.

- (c) In the spiral predation stage, the whales usually move in a spiral direction towards the optimum position of the whale and create bubble nets to surround the prey for predation. The mathematical model of whale spiral migration for predation is given as follows:

$$\vec{X}_{t+1} = \vec{D}^i \cdot e^{b \cdot \vec{l}} \cdot \cos(2\pi \vec{l}) + \vec{X}_t^*, \quad (25)$$

where $\vec{D}^i = |\vec{X}_t^* - \vec{X}_t|$ denotes the distance of the whale to the best solution obtained, b denotes a

constant to define the shape of the logarithmic spiral, and l denotes a random number in $(-1, 1)$.

Additionally, we then define a random variable p to distinguish the contraction-bounding stage from the spiral predator, and the mathematical model is given as follows:

$$\vec{X}_{t+1} = \begin{cases} \vec{X}_* - \vec{A} \cdot \vec{D}, & p < 0.5, \\ \vec{D} \cdot e^{b\vec{l}} \cdot \cos(2\pi\vec{l}) + \vec{X}_t^*, & p \geq 0.5. \end{cases} \quad (26)$$

However, the WOA exhibits the disadvantage of inadequate global search capability in the early stage and slow convergence speed in the later stage [19]. To solve the issues, the IWOA is proposed, and the difference between the IWOA and the WOA is in the spiral predation stage. The equation of spiral walking in the IWOA is defined as follows:

$$\vec{X}_{t+1} = w \times \vec{D}^l \cdot e^{b\vec{l}} \cdot \cos(2\pi\vec{l}) + \vec{X}_t^*, \quad (27)$$

where w denotes the updated weight and is given as follows:

$$\begin{aligned} w &= w_{\min} + (w_{\max} - w_{\min})\beta, \\ \beta &= \cos\{\arctan[\text{std}(f_{\text{obj}})]\}, \end{aligned} \quad (28)$$

where β denotes the humpback whale aggregation factor, w_{\min} denotes the minimum weight value, w_{\max} denotes the maximum weight value, and $\text{std}(f_{\text{obj}})$ denotes the variance of the fitness value. In the initial stage of iteration, $\text{std}(f_{\text{obj}})$ is big, the value of $\arctan[\text{std}(f_{\text{obj}})]$ is close to $\pi/2$, and the value of β is close to 0. At the end of the iteration, $\text{std}(f_{\text{obj}})$ is small, the value of $\arctan[\text{std}(f_{\text{obj}})]$ is close to 0, and the value of β is close to 1. Therefore, with the continuous iteration, w will increase from w_{\min} to w_{\max} gradually. The optimal objective function f_{obj} is given in equation (19).

In the initial iteration stage of the IWOA, β and w are higher, and this accelerates the convergence of the algorithm. In the late iteration stage of the IWOA, β and w are low, and this improves the accuracy of optimization.

Based on the aforementioned principle of the IWOA, the IWOA can be considered a global optimizer. It solves the NP-hard problem and obtains the global optimal solution of equation (19).

3.3. D2D User Density Identification. After optimization by the IWOA, the optimal parameters after resource allocation are achieved as follows:

$$X_{\text{optimal}} = [\hat{P}_j^{\text{DU}}, \hat{r}_j^{\text{DU}}, \hat{b}_j^{\text{DU}}, \hat{P}_i^{\text{CU}}, \hat{r}_i^{\text{CU}}, \hat{b}_i^{\text{CU}}, \hat{x}_{i,j}]. \quad (29)$$

We assume that the number of regions in a large region corresponds to S , and the optimal throughput of D2D users in each region by the IWOA is expressed as follows:

$$\text{TPS} = [\text{TPS}_1, \text{TPS}_2, \dots, \text{TPS}_S]. \quad (30)$$

Furthermore, we assume the number of D2D users in each region is

$$N_p = [N_{p1}, N_{p2}, \dots, N_{ps}]. \quad (31)$$

The proposed method in this study considers the QoS of D2D users that decreases the interference of D2D communication with cellular communication and interference between D2D communications. Therefore, the data distribution between the number of individuals and the throughput in different regions is shown in Figure 4.

As shown in Figure 4, the relationship between the number of D2D users and the system throughput in different regions by data fitting is defined as follows:

$$N_p = k_0 \times \text{TPS} + k_1, \quad (32)$$

where k_0 and k_1 denote the function fitting value, and N_p and TPS satisfy a linear relationship. Although k_0 and k_1 are unknown, the D2D user density areas can be identified by the throughput value after the optimal resource allocation method provided that they satisfy the linear relationship.

In summary, the flow chart of the proposed method in this study is shown in Figure 5.

3.4. Algorithmic Complexity Analysis. The optimization algorithm proposed in this study consists of initializing the whale population, calculating the fitness function, and updating the whale location. When the whale population corresponds to N and the dimension of the optimization problem corresponds to D (D denotes the number of variables in equation (23)), the complexity of the proposed algorithm is analyzed as follows: the complexity of the initial whale population corresponds to $O(ND)$, and the complexity of fitness calculation corresponds to $O(N \log N)$. In the whale-position-updating process, the computational complexity corresponds to $O(ND)$. Therefore, in each iteration, the complexity of the algorithm corresponds to $O(N \log N + 2ND)$.

4. Simulation and Analysis of the Proposed Method

The proposed algorithm is validated in a 5G network scenario of a large region, and many cells exist in the scenario. The D2D users and cellular users are randomly distributed in the cells. The proposed algorithm is simulated through MATLAB to identify D2D user density.

4.1. Parameters of the Simulation Experiment. The simulation parameters are shown in Table 1. The system performance of the algorithm proposed in this study is simulated and analyzed via MATLAB.

4.2. Simulation and Experimental Analysis. The simulation scenario and D2D user scatter map are shown in Figure 6.

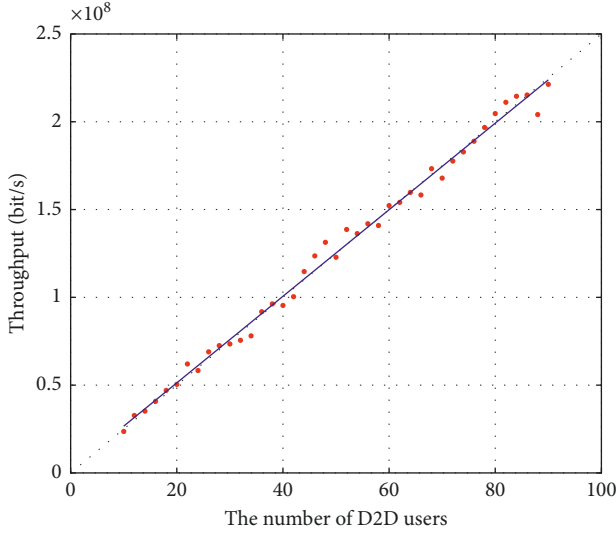


FIGURE 4: Data distribution between the number of individuals and the throughput.

In Figure 6, “+” denotes the D2D sender, “*” denotes the D2D receiver, and “o” denotes the cellular user. Figure 6 shows areas with different D2D user densities. Table 2 lists the system throughput and user satisfaction of different algorithms including the random distribution, heuristic distribution [16], and geometric programming resource allocation [22].

As shown in the simulation results in Table 2, increases in D2D users linearly increase the throughput from the proposed algorithm. When the number of D2D users exceeds 40, the throughput of other algorithms increases slowly. Therefore, it is difficult to identify the density from the throughput indicators. Conversely, the QoS of the proposed algorithm also exceeds that of the other three algorithms.

To compare the advantages of the algorithm more clearly, we change the number of D2D user pairs from 10 to 80. Then, the system throughput performance comparison is shown in Figure 7.

The system QoS performance comparison is shown in Figure 8.

As shown in Figure 7, increases in D2D users also increase the complete system throughput. Furthermore, the growth of the proposed algorithm exceeds that of the other three reference algorithms. The number of D2D users and throughput satisfy a linear relationship. This is because the proposed algorithm selects the optimal D2D users for cellular users to multiplex. However, the interference of D2D communication with cellular communication increases, and the interference between the D2D communications also increases through the other three algorithms. Therefore, the performance of the proposed algorithm exceeds that of the other reference algorithms.

Based on the simulation result in Figure 6, the linear relationship between the number of D2D users and the system throughput satisfies the following expression:

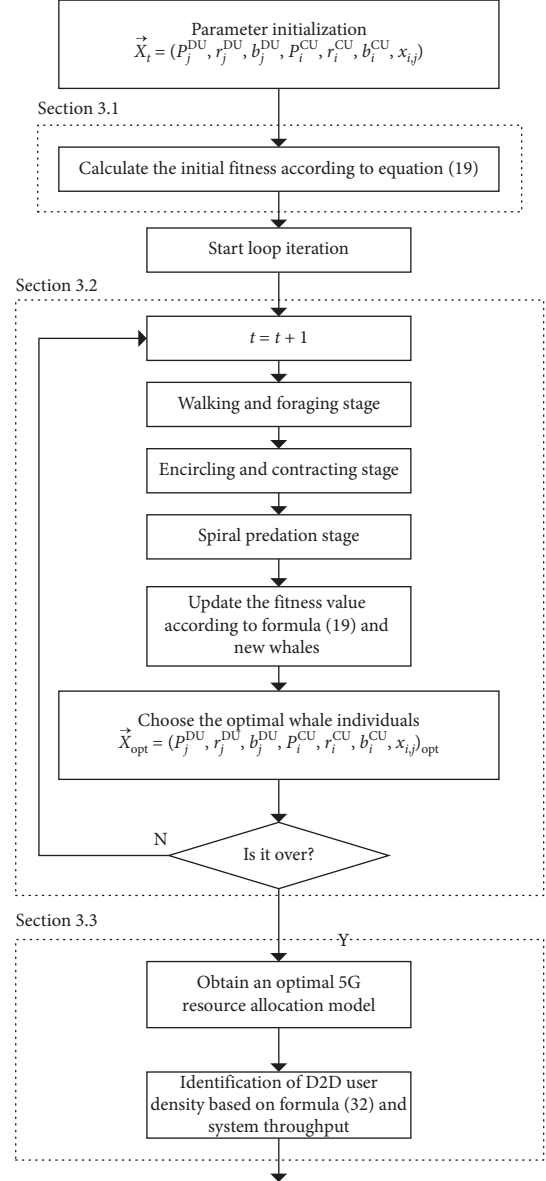


FIGURE 5: Data progression.

TABLE 1: Simulation parameters.

No.	Performance index	Value
1	Cell radius, R	400 m
2	Number of D2D user pairs, M	10:10:80
3	Number of cellular users, N	10
4	Maximum power of the DU, $P_{j,\max}^{\text{DU}}$	15 dBm
5	Maximum power of the CU, $P_{j,\max}^{\text{CU}}$	24 dBm
6	Minimum distance of D2D users, d_{\min}	10 m
7	Maximum distance of D2D users, d_{\max}	50 m
8	SINR threshold of the CU, $\text{SINR}_{i,\min}^{\text{CU}}$	2
9	SINR threshold of the DU, $\text{SINR}_{i,\min}^{\text{DU}}$	2
10	Total resources of the cell, B^{DU}	100
11	Noise power density, N_0	-174 dBm/Hz
12	Subchannel bandwidth, B_W	180 kHz
13	Path loss model of the DU	$148 + 40\log_{10}(d)$
14	Path loss model of the CU	$128.1 + 36.7\log_{10}(d)$

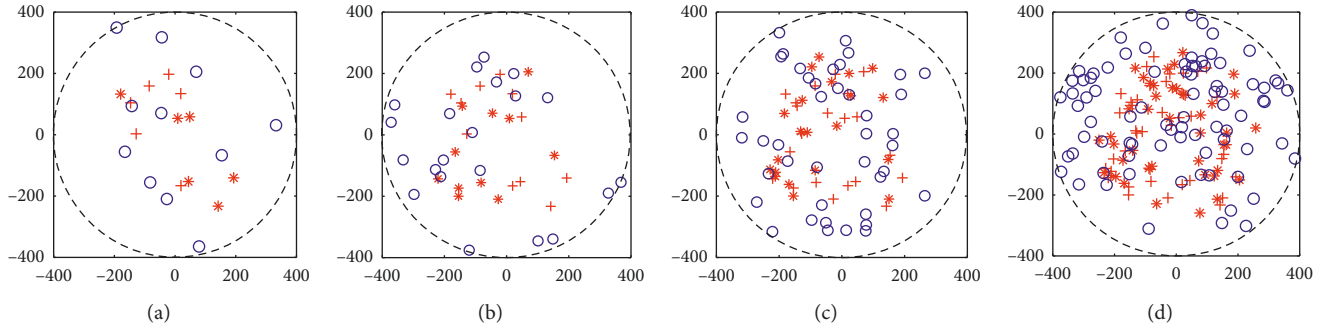


FIGURE 6: Distribution of D2D users in different areas. (a) Area 1, $N=10$. (b) Area 2, $N=20$. (c) Area 3, $N=40$. (d) Area 4, $N=80$.

TABLE 2: System throughput and user satisfaction of different algorithms.

Algorithm	Area no.	Throughput (Mbps)	QoS (%)
The proposed algorithm	1	18.30	84.30
	2	35.57	83.28
	3	71.59	84.70
	4	140.62	73.65
Random distribution	1	17.67	82.30
	2	34.48	81.28
	3	65.70	78.65
	4	88.69	65.21
Heuristic distribution	1	18.67	83.22
	2	34.87	82.19
	3	67.76	81.70
	4	97.79	72.65
Geometric programming resource allocation	1	18.98	86.22
	2	35.62	81.56
	3	70.31	80.53
	4	120.76	73.21

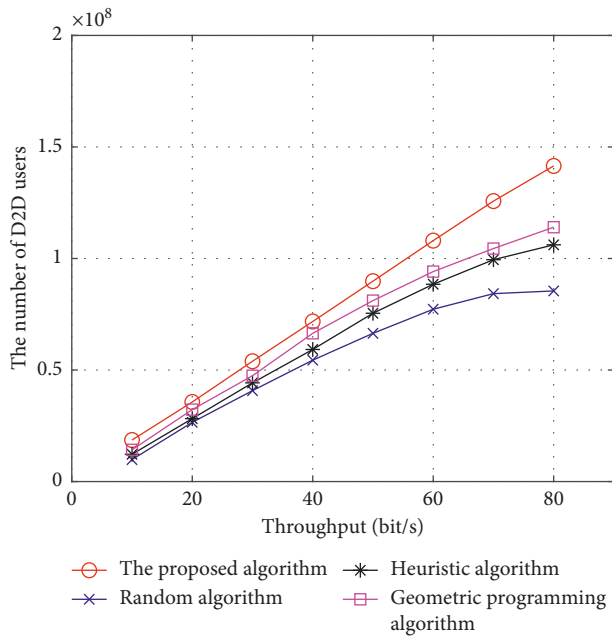


FIGURE 7: Throughput comparison.

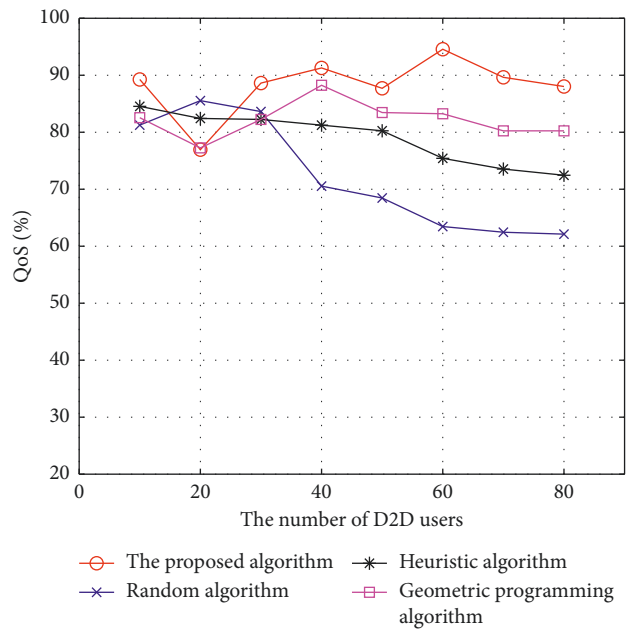


FIGURE 8: QoS comparison.

TABLE 3: Accuracy of the proposed algorithm.

Throughput	Estimated D2D number	Real D2D number	Accuracy (%)
88.36	44	45	98.65
168.74	88	89	99.86
264.50	124	132	94.45
351.74	168	170	99.61
434.93	230	230	99.91
486.57	278	284	97.90
610.45	310	320	97.02
708.85	372	370	99.44

TABLE 4: Accuracy of different algorithms.

Algorithm	Estimated D2D number	Real D2D number	Accuracy (%)
Proposed algorithm	230	230	99.91
	278	284	97.90
	310	320	97.02
	372	370	99.44
Random distribution	205	230	89.13
	254	284	89.44
	275	320	85.94
	332	370	89.73
Heuristic distribution	224	230	97.39
	268	284	94.37
	293	320	91.56
	355	370	95.95
Geometric programming resource allocation	225	230	97.83
	273	284	96.13
	305	320	95.13
	362	370	97.84

$$N_p = 0.5635 \times \text{TPS} - 0.4331. \quad (33)$$

As shown in Figure 8, with increases in D2D users, the QoS of the proposed algorithm is maintained at approximately 80%. The QoS of the other three reference algorithms decreases. It is worth noting that there is a drop in the QoS at 20 D2D users for the proposed algorithm. This is because the number of simulation cycles is fewer, which may cause some drops at some points.

Finally, we analyze the D2D user density based on the conclusion of equation (33), and the accuracy of the proposed algorithm is listed in Table 3.

Table 4 lists the accuracy of different algorithms including the random distribution, heuristic distribution [16], and geometric programming resource allocation [22].

The simulation results show that D2D user density in different areas is accurately calculated by the algorithm proposed in this study.

5. Conclusion

In this study, a new resource allocation method is proposed for the problem of D2D user density identification in a 5G network. The method initially establishes an optimization function that contains the system throughput and QoS of D2D users. Additionally, the optimization function is solved via the IWOA. The method obtains a linear relationship

between the system throughput and the number of users. Therefore, the D2D density is accurately identified by the system throughput. The experimental results indicate that the proposed algorithm obtains high-accuracy results for D2D user density identification. In the future work, we will research a more general model, which is suitable for various 5G communication scenarios. On the contrary, we may introduce some deep learning ideas to improve the algorithm to improve the accuracy.

Data Availability

The data used to support the findings of this study are available from the corresponding author upon request.

Conflicts of Interest

The authors declare that there are no conflicts of interest regarding the publication of this paper.

Acknowledgments

This work was supported in part by the National Key Research and Development Program of China under Grant No. 2018YFC1504403-03 and by the Research and Practice Project of Higher Education Teaching Reform in Hebei Province under No. 2017GJJG091.

References

- [1] A. Gupta and R. K. Jha, *A Survey of 5G Network: Architecture and Emerging Technologies*, IEEE Access, Piscataway, NJ, USA, 2015.
- [2] S. Ali, N. Rajatheva, and M. Latva-aho, "Full duplex device-to-device communication in cellular networks," in *Proceedings of the 2014 European Conference on Networks and Communications (EuCNC)*, pp. 1–5, Bologna, Italy, June 2014.
- [3] W. Cheng, X. Zhang, and H. Zhang, "Optimal power allocation for full-duplex D2D communications over wireless cellular networks," in *Proceedings of the 2014 IEEE Global Communications Conference (GLOBECOM)*, Austin, TX, USA, December 2014.
- [4] H. Bagheri, F. A. M. Bonomi, and M. Katz, "Spectral efficiency and throughput enhancement by full-duplex D2D communication in mobile clouds," in *Proceedings of the 21st European Wireless Conference*, Budapest, Hungary, May 2015.
- [5] J. Sun, T. Zhang, X. Liang, Z. Zhang, and Y. Chen, "Uplink resource allocation in interference limited area for D2D-based underlying cellular networks," in *Proceedings of the 2016 IEEE 83rd Vehicular Technology Conference (VTC Spring)*, pp. 1–6, Nanjing, China, May 2016.
- [6] W. O. Oduola, X. Li, L. Qian, and Z. Han, "Power control for device-to-device communications as an underlay to cellular system," in *Proceedings of the 2014 IEEE International Conference on Communications (ICC)*, pp. 5257–5262, Sydney, Australia, June 2014.
- [7] Z. Guizani and N. Hamdi, "Spectrum resource management and interference mitigation for D2D communications with awareness of BER constraint in mm wave 5G underlay network," in *Proceedings of the IEEE Symposium on Computers and Communications*, pp. 855–860, Messina, Italy, June 2016.
- [8] S. A. R. Naqvi, S. A. Hassan, H. Pervaiz, Q. Ni, and L. Musavian, "Self-adaptive power control mechanism in D2D enabled hybrid cellular network with mm wave small cells: an optimization approach," in *Proceedings of the 2016 IEEE Globecom Workshops (GC Workshops)*, pp. 1–6, Washington, DC, USA, December 2016.
- [9] Y. Sun, F. Wang, and Z. Liu, "Coalition formation game for resource allocation in D2D uplink underlying cellular networks," *IEEE Communications Letters*, vol. 23, no. 5, pp. 888–891, 2019.
- [10] S. Ali, A. Ghazanfari, N. Rajatheva, and M. Latva-aho, "Effect of residual of self-interference in performance of full-duplex D2D communication," in *Proceedings of the 1st International Conference on 5G for Ubiquitous Connectivity*, pp. 46–51, Akaslompolo, Finland, November 2014.
- [11] S. Bulusu, N. B. Mehta, and S. Kalyanasundaram, "Rate adaptation, scheduling, and mode selection in D2D systems with partial channel knowledge," *IEEE Transactions on Wireless Communications*, vol. 17, no. 2, pp. 1053–1065, 2018.
- [12] M. N. Tehrani, M. Uysal, and H. Yanikomeroglu, "Device-to-device communication in 5G cellular networks: challenges, solutions, and future directions," *IEEE Communications Magazine*, vol. 52, no. 5, pp. 86–92, 2014.
- [13] S. Lin and H. Tian, "Clustering based interference management for QoS guarantees in OFDMA femtocell," in *Proceedings of the IEEE Wireless Communications and Networking Conference (WCNC)*, pp. 649–654, Shanghai, China, April 2013.
- [14] T. O. Olwal, K. Djouani, and A. M. Kurien, "A survey of resource management towards 5G radio access networks," *IEEE Communications Surveys & Tutorials*, vol. 18, no. 3, pp. 1565–1686, 2016.
- [15] F. Shen and E. Jorswieck, "Universal non-linear cheat-proof pricing framework for wireless multiple access channels," *IEEE Transactions on Wireless Communications*, vol. 13, no. 3, pp. 1436–1448, 2014.
- [16] A. Kammoun, N. Tabbane, G. Diaz, A. Dandoush, and N. Achir, "End-to-end efficient heuristic algorithm for 5G network slicing," in *Proceedings of the International Conference on Advanced Information Networking and Applications (AINA)*, pp. 386–392, Krakow, Poland, May 2018.
- [17] K. Nakamura, T. Tashiro, K. Yamamoto, and K. Ohno, "Transmit power control and channel assignment for femto cells in HetNet systems using genetic algorithm," in *Proceedings of the 2015 IEEE 26th Annual International Symposium on Personal, Indoor, and Mobile Radio Communications (PIMRC)*, pp. 1669–1674, Hong Kong, China, September 2015.
- [18] S. Mirjalili and A. Lewis, "The whale optimization algorithm," *Advances in Engineering Software*, vol. 95, pp. 51–67, 2016.
- [19] M. F. Horng, T. K. Dao, C. S. Shieh, and T. T. Nguyen, "Advances in intelligent information hiding and multimedia signal processing," *Intelligent Information Hiding and Multimedia Signal Processing*, vol. 82, pp. 371–380, 2018.
- [20] I. N. Trivedi, J. Pradeep, J. Narottam, K. Arvind, and L. Dilip, "Novel adaptive whale optimization algorithm for global optimization," *Indian Journal of Science and Technology*, vol. 9, no. 38, pp. 1–6, 2016.
- [21] R. H. Bhesdadiya, S. A. Parmar, and I. N. Trivedi, "Optimal active and reactive power dispatch problem solution using whale optimization algorithm," *Indian Journal of Science and Technology*, vol. 9, no. S1, pp. 1–6, 2016.
- [22] S. Fu, H. Wen, and B. Wu, "Power-fractionizing mechanism: achieving joint user scheduling and power allocation via geometric programming," *IEEE Transactions on Vehicular Technology*, vol. 67, no. 3, pp. 2025–2034, 2018.

Research Article

The Evolution of Collective Strategies in SMEs' Innovation: A Tripartite Game Analysis and Application

Lixia Liu ¹, Yuanshi Huang¹ and Xueli Zhan ^{2,3}

¹School of Economics, Tianjin University of Commerce, Tianjin 300134, China

²College of Management and Economics, Tianjin University, Tianjin 300072, China

³School of Economics, Beijing Wuzi University, Beijing 101149, China

Correspondence should be addressed to Lixia Liu; liulixia77@163.com and Xueli Zhan; xuelz20163205@126.com

Received 27 June 2019; Revised 12 September 2019; Accepted 26 September 2019; Published 30 October 2019

Guest Editor: Raúl Baños

Copyright © 2019 Lixia Liu et al. This is an open access article distributed under the Creative Commons Attribution License, which permits unrestricted use, distribution, and reproduction in any medium, provided the original work is properly cited.

Financing difficulty is recognized as the main bottleneck in the technology innovation process of small- and medium-sized enterprises (SMEs). The governments generally provide financial support for SMEs' innovation activities. Numerous research studies have been conducted on the role of the government in enterprises' innovation, while there is no consistent conclusion on whether government subsidies can improve stakeholder collaboration and effectively ease financing constraints of SMEs' innovation. Due to information asymmetry and the bounded rationality, the dynamic game among the government, external investors, and SMEs has the characteristics of complexity. This paper aims to explore the collective strategies of the major stakeholders in SMEs' innovation and investigate the effect of antecedents on innovation activities. We establish a trilateral evolutionary game model on the relationship among the government, external investors, and SMEs. The simulation results show that the evolutionary system converges quickly to the equilibrium; when the government subsidies decrease, the external investors' appraisal costs decrease and the investment amount and return rates of external investors increase. Furthermore, under the condition of government subsidies, external investors will not change their investment strategies even if the external investors' recognition costs have exceeded their return on SMEs' investment. The findings can provide good reference for the government to solve the financing problem of SMEs' innovation.

1. Introduction

Technology innovation is widely believed to be the main driving force for economic growth [1]. The enterprises may require a substantial capital investment, since technology innovation is a long-term and sustainable process. However, due to the high risk and information asymmetry, external investors are reluctant to invest in technology innovation [2, 3]. Therefore, insufficient funds have been bothering the innovation enterprises and hindering their ability to innovate [4].

Small- and medium-sized enterprises (SMEs), the largest innovation group in China, play an irreplaceable role in promoting economic growth, enabling innovation, increasing taxes, creating employment, and improving people's livelihood. According to China's Ministry of Industry

and Information Technology (MIIT), SMEs increase more than 50% of tax revenue, create more than 60% of GDP, complete more than 70% of invention patents, and provide more than 80% of urban jobs, accounting for more than 99% of the total number of enterprises. The financing channels for SMEs compared to large enterprises are relatively narrow, and SMEs have more serious difficulty in raising money [5–7]. The research on SMEs' innovation financing is of great significance both in theory and in practice.

Government subsidies have become the common measures adopted by many countries to support enterprises' innovation. The widely accepted reason for the government to subsidize R&D activities is the existence of market failures, which create a gap between private benefits and social benefits derived from R&D activities [8]. The positive spillover effect of R&D activities will lead to lower R&D

investment of enterprises than the optimal level. Although a large number of studies have confirmed the value of government subsidies, to our knowledge, few scholars pay attention to the impact of government subsidies on the SMEs' innovation [9]. No one tries to examine the interrelationship between the government, SMEs, and external investors in innovation activities.

In this paper, we seek to contribute to the literature on SMEs' innovation in four ways. First, we focus purely on SMEs and hope this research can help to understand how public instruments affect these enterprises. We also consider the effects of government subsidies on the investment decisions of external investors to SMEs' innovation. So far, there is little empirical evidence on the effectiveness of public tools on SMEs' innovation [10–14]. In our paper, we examine the effects of government subsidies on the strategy choices of SMEs and external investors.

Second, this paper mainly focuses on the cooperation mechanism among the government, SMEs, and external investors in the decision-making process of SMEs' innovation. Prior studies only consider the relationship between the government and subsidized enterprises, or between the government and external investors. Moreover, the academics have made considerable effort to understand and evaluate the effect of government subsidies on enterprises' R&D investment but paid less attention to the effect of government subsidies on enterprises' innovation willingness and the use of R&D investment. And there is no consistent conclusion on whether government subsidies can actually alleviate the financing constraints of enterprises and bring significant increase in innovation output [4, 15]. To solve this problem, it is necessary to sort out the decision-making behavior, disclose the conflicts of interest among groups of stakeholders, and find a practical solution. The cooperation strategy among the government, external investors, and SMEs has attracted virtually no scrutiny. Our paper seeks to fill this gap by examining the interaction mechanism of the three parties.

The third contribution of this paper is to try to construct a tripartite evolutionary game model of the relationship among the government, SMEs, and external investors. We regard the government, SMEs, and external investors as the players with bounded rationality, who will constantly adjust their strategies in SMEs' innovation process. In recent years, the application of game theory in the field of enterprise innovation has been increasing, but the application of evolutionary game theory is rare [16–18]. This study can provide new ideas for the scholars in this field.

Lastly, we attempt to explore the interaction mechanism and the antecedents influencing the strategy selections. Using Matlab software, the effects of government subsidies, external investors' appraisal costs, external investors' return rate, and external investors' investment amount on the players are simulated. This paper will enable us to determine the conditions and ranges under which the relevant factors work. The results of this study can provide a theoretical guidance for solving the financing problem of SMEs' innovation.

The remainder of this paper is organized as follows. Section 2 provides a brief view of the extant literature. Section 3 establishes a trilateral evolutionary game theory model of the interaction among the government, investors, and SMEs. Section 4 discusses the replicator dynamic equation and the equilibrium points. Section 5 describes the results of evolutionary game simulation. Section 5 presents the conclusion and some policy suggestions.

2. Literature Review

2.1. Effects of Government Subsidies on Enterprises' Innovation. Research on the effect of government subsidies on enterprises innovation has been a hot issue in the academic community. There is a great deal of research on the relationship of government subsidies and enterprises' innovation investment. Theoretically, government subsidies on the one hand can directly increase enterprises' R&D funds and on the other hand can enhance the confidence of the enterprises' innovation and promote the increase of corporate R&D investment [19–21]. Busom [22], Lee and Hwang [23], Hud and Hussinger [24], Radas et al. [9], and Hottenrott and Lopes-Bento [11] considered that government subsidies are positively correlated with enterprises' R&D investment. However, Wallsten [14] and Marino et al. [25] believed that government subsidies had a substitution effect on enterprise R&D investment, i. e., government subsidies will reduce enterprise R&D investment. Marino et al. empirically showed that there was a significant substitution between private and public funds to R&D, especially for medium-high levels of government subsidies [25].

In the past few years, the effect of government subsidies on the external investors funding the enterprises' innovation has attracted significant scholarly attention. Asymmetric information may be the reason for the external investors not willing to fund R&D due to its inherent risk, even if the innovation enterprises promised high expected returns [2]. The government agency identifies and evaluates the R&D projects and then decides whether to subsidize innovation enterprises. Enterprises funded by the government are often those with relatively high innovation ability and relatively low risk. Therefore, government subsidies could provide a certification effect about enterprises quality and improve enterprises' access to external finance [13, 26–28].

In recent years, some scholars investigated the effect of government subsidies on enterprises' innovation output, and most of them believed that government subsidies had a significant role in promoting innovation output [19, 29, 30]. Bérubé and Pierre found that the R&D subsidy program implemented in northern Italy had a significant impact on the amount of patents, but the increment was markedly greater in the case of smaller firms [29]. Some scholars also paid attention to the effect of government R&D subsidies on enterprises' innovation efficiency [31, 32]. Jin et al. found that government subsidies had a negative influence on innovation efficiency of China's high-tech industries [32].

2.2. Application of Game Theory in Enterprises' Innovation. Game theory has proven to be an effective method for analyzing the firms' innovation strategies [33–39]. Existing studies usually assume that all participants are rational and static, which is inconsistent with the facts. Enterprises' innovation is a dynamic process. The participants in enterprises' innovation, such as enterprises, governments, scientific research institutions, and banks, cannot be completely rational. It is often unreasonable to apply general game theory to analyze innovation decision-making problems.

Since 1980s, evolutionary game has quickly grown into an active area of research in social economy, which is based on the theories of biological evolutionism, nonlinear dynamics, and game theory. Evolutionary game is an increasingly popular approach among the research of enterprises' innovation. Ying et al. proposed an evolutionary game model and analyzed the effects of cluster informal contracts on innovation cooperation among cluster enterprises [40]. Yang et al. established an evolutionary game model among the government, enterprises, universities, and research institutes and explored the mechanism of intellectual property cooperation [41]. Shen used evolutionary game to examine the enterprise decision-making behavior in the process of open innovation from the perspective of endogenous knowledge spillovers [42]. Lin et al. set up an evolutionary game model of human innovation behaviors and discussed the impact of the heterogeneous structure on the evolution of innovation behaviors based on the scale-free network [43–48].

Today, the financing mechanisms to support SMEs' innovation have been a subject of great interest and a major challenge to policy makers as SMEs are considered as the key element to promote economic growth and stability. Following the above research trends, we specifically study the investment decision-making behavior of the government, external investors, and SMEs in the process of SMEs' innovation and discuss how to maximize the benefits of the government, SMEs, and external investors. To the best of our knowledge, this problem is not solved in the existing literature. Different from previous research, we construct a trilateral evolutionary game model among the government, SMEs, and external investors and formulate the replicator dynamic equations to analyze the evolutionarily stable strategies (ESSs) of multiple stakeholders. Finally, the theoretical results are verified by simulation and experiments. Our paper not only provides a different perspective for the existing literature to analyze the effects of public subsidies but also provides ideas for how to optimize public subsidies.

3. Tripartite Evolutionary Game Model in SMEs' Innovation

The government, external investors, and SMEs are three critical stakeholders in the process of SMEs' innovation investment. The government represents the public interest and mainly guides SMEs to carry out innovation activities through innovation policies. It acts as the promoter and direct beneficiary of SMEs' innovation. External investors who pursue profit maximization mainly refer to financial

institutions and often decide whether to invest in innovation projects after rigorous evaluations. SMEs are regarded as the main driving forces for innovation. Accounting irregularity, lacking collateral for banks, and information asymmetry are common issues inherent to SMEs. SMEs have to choose between adopting an innovation and maintaining the status quo when making business decisions. Although innovation is an important way for SMEs' growth, all have increased the demand for talent, increased financial burdens and costs, and created uncertainties that could only make SMEs more reluctant to innovate. It can be seen that in the process of SMEs' innovation, the government, external investors, and SMEs will make behavioral choices in their own interests. The government has the responsibility for supporting access to finance for SMEs' innovation. Only by finding an equilibrium mechanism under incomplete information can the three parties form a virtuous circle system in innovation game and fundamentally solve the financing problem of SMEs' innovation. Therefore, this paper makes the following assumptions:

- (1) The government, external investors, and SMEs are the main stakeholders in the process of SMEs' innovation investment. The three parties interact with each other in the decision-making process and finally reach the evolutionary equilibrium.
- (2) The government, external investors, and SMEs all have bounded rationality and incomplete information.
- (3) Due to information asymmetry, the government is the dominant force in the decision-making process, and the external investors are its subordinates. Under the conditions of the government subsidizing SMEs' innovation, external investors can invest directly in SMEs without spending costs.

We assume that the strategies of the government are {Subsidize, Not subsidize}. The optional strategies of external investors are {Invest, Not invest}, while the strategies of SEMs are {Innovate, Not innovate}. Suppose the probability that the government chooses the "Subsidize" strategy is x ($x \in [0, 1]$) and the probability that the government chooses the "Not subsidize" strategy is $1 - x$. Suppose the probability that the external investors adopt the "Invest" strategy is y ($y \in [0, 1]$) and the probability that the external investors adopt the "Not invest" strategy is $1 - y$. The probability of selecting the "Innovate" strategy for SMEs is assumed to be z ($z \in [0, 1]$), and the probability of selecting the "Not innovate" strategy is $1 - z$.

S represents the amount of government subsidies for SMEs' innovation. V_1 and V_2 , respectively, represent the social benefit obtained by the government, when SMEs adopt "Innovate" and "Not innovate" strategies. Under the condition of selecting "Subsidize" strategy for the government, when the external investors adopt the "Invest" strategy, there will be some social benefit increase for the government, compared to the case where the external investors adopt the "Not invest" strategy. This benefit increase is denoted as ΔV_{11} . Similarly, under the condition of selecting the "Not subsidize" strategy for the government, ΔV_{12} represents the social benefit increase that

the government can obtain, when the external investors adopt the “Invest” strategy instead of the “Not invest” strategy.

P represents the investment amount of choosing “Invest” strategy for external investors. If the average annual return rate obtained by external investors through innovation investment is i , their annual return is $P * i$. It is assumed that due to the existence of the certification effect, when the government adopts the “Subsidize” strategy, the external investors can choose to invest directly without spending money to identify the same enterprise. When the government adopts the “Not subsidize” strategy, the appraisal costs of the external investors for SMEs are C_1 .

Q_1 and Q_2 , respectively, represent the benefits obtained by the SMEs, when they adopt “Innovate” and “Not innovate” strategies. ΔQ represents the benefit increase that the SMEs can obtain, when the external investors adopt the “Invest” strategy instead of the “Not invest” strategy. According to the actual situation in emerging economies, we suppose that $V_1 \geq V_2$ and $Q_1 \geq Q_2$. The corresponding parameters are described in Table 1.

Based on the above analysis, we can establish the payoff matrix among the government, investors, and SMEs, as shown in Table 2.

4. Game Model Solution and Analysis

4.1. Replicator Dynamic Equation. Let U_x and U_{1-x} represent, respectively, the expected earnings of “Subsidize” and “Not subsidize” for the government. According to the payoff matrix, the fitness of the government with two different strategies can be calculated as follows:

$$\begin{aligned} U_x &= V_2 - S + yz\Delta V_{11} + z(V_1 - V_2), \\ U_{1-x} &= V_2 + yz\Delta V_{12} + z(V_1 - V_2). \end{aligned} \quad (1)$$

The average expected earnings of the government can be calculated as

$$\bar{U}_A = xU_x + (1-x)U_{1-x}. \quad (2)$$

The replicator dynamic equation for the government can be achieved as follows:

$$A(x) = \frac{dx}{dt} = x(U_x - \bar{U}_A) = x(1-x)[-S + yz(\Delta V_{11} - \Delta V_{12})]. \quad (3)$$

Let U_y and U_{1-y} represent, respectively, the expected earnings of “Invest” and “Not invest” for external investors. According to the payoff matrix, the fitness of the external investors with two different strategies can be calculated as follows:

$$\begin{aligned} U_y &= -P - C_1 + xC_1 + zP(i+1), \\ U_{1-y} &= 0. \end{aligned} \quad (4)$$

The average expected earnings of external investors can be calculated as

$$\bar{U}_B = yU_y + (1-y)U_{1-y}. \quad (5)$$

TABLE 1: Parameter description.

Parameters	Descriptions
x	The probability that the government subsidizes SMEs' innovation
y	The probability that the external investors invest SMEs' innovation
z	The probability that SMEs implement technological innovation
V_1	The social benefit of SMEs with general production management
V_2	The social benefit of SMEs with technological innovation
ΔV_{11}	The social benefit increase of SMEs' innovation when the government adopts the “Subsidize” strategy and external investors adopt the “Invest” strategy
ΔV_{12}	The social benefit increase of SMEs' innovation when the government adopts the “Not subsidize” strategy and the external investors adopt the “Invest” strategy
S	The amount of government subsidies for SMEs' innovation
P	The investment amount of the external investors in SMEs' innovation
i	The investment return rate of the external investors in SMEs' innovation
C_1	Investors' appraisal costs for SMEs
Q_1	The benefits of SMEs when they adopt the “Innovate” strategy
Q_2	The benefits of SMEs when they adopt the “Not innovate” strategy
ΔQ	The increase in benefits of SMEs' innovation when the external investors adopt the “Invest” strategy

TABLE 2: The payoff matrix among the government, investors, and SMEs.

Government	External investors	
	Innovate (z)	Not innovate ($1-z$)
Subsidize (x)	$V_1 - S + \Delta V_{11}$	$V_2 - S$
Invest (y)	$P * i$	$-P$
	$Q_1 + \Delta Q + S$	$Q_2 + S + P$
Not invest ($1-y$)	$V_1 - S$	$V_2 - S$
	0	0
	$Q_1 + S$	$Q_2 + S$
Not subsidize ($1-x$)		
Invest (y)	$V_1 + \Delta V_{12}$	V_2
	$P * i - C_1$	$-P - C_1$
	$Q_1 + \Delta Q$	$Q_2 + P$
Not invest ($1-y$)	V_1	V_2
	0	0
	Q_1	Q_2

The replicator dynamic equation for external investors can be achieved as follows:

$$\begin{aligned} B(y) = \frac{dy}{dt} &= y(U_y - \bar{U}_B) = y(1-y)[-P - C_1 + xC_1 \\ &\quad + zP(i+1)]. \end{aligned} \quad (6)$$

Let U_z and U_{1-z} represent, respectively, the expected earnings of “Innovate” and “Not innovate” for SMEs. According to the payoff matrix, the fitness of SMEs with two different strategies can be calculated as follows:

$$\begin{aligned} U_z &= Q_1 + xS + y\Delta Q_1, \\ U_{1-z} &= Q_2 + xS + yP. \end{aligned} \quad (7)$$

The average expected earnings of SMEs can be calculated as

$$\bar{U}_C = zU_z + (1-z)U_{1-z}. \quad (8)$$

The replicator dynamic equation for SMEs can be achieved as follows:

$$C(z) = \frac{dz}{dt} = z(U_z - \bar{U}_C) = z(1-z)[(Q_1 - Q_2) + y(\Delta Q - P)]. \quad (9)$$

Therefore, the replicator dynamic equation of the SMEs’ innovation system can be obtained from combining equations (3), (6), and (9):

$$\begin{cases} A(x) = x(1-x)[-S + yz(\Delta V_{11} - \Delta V_{12})], \\ B(y) = y(1-y)[-P - C_1 + xC_1 + zP(i+1)], \\ C(z) = z(1-z)[(Q_1 - Q_2) + y(\Delta Q - P)]. \end{cases} \quad (10)$$

4.2. Replicator Dynamic Analysis of Each Stakeholder. As for the government, it can be inferred from equation (3) that

- (1) When $y = y^* = S/z(\Delta V_{11} - \Delta V_{12})$, $A(x) = 0$, all game strategies are at a stable state (see Figure 1(a)).
- (2) When $y \neq S/z(\Delta V_{11} - \Delta V_{12})$, $x = 0$ and $x = 1$ are two stable points of $A(x) = 0$. The stability strategies of the government need to be further analyzed. The derivative of equation (3) can be calculated as

$$A'(x) = \frac{\partial A(x)}{\partial x} = (1-2x)[-S + yz(\Delta V_{11} - \Delta V_{12})]. \quad (11)$$

Then, we discuss two circumstances according to equations (3) and (11):

- ① When $S > (\Delta V_{11} - \Delta V_{12})$, under the constraints of $0 < x < 1$, $0 < y < 1$, and $0 < z < 1$, we can prove $-S + yz(\Delta V_{11} - \Delta V_{12}) < 0$. Therefore, $\partial A(x)/\partial x(x=0) < 0$ and $\partial A(x)/\partial x(x=1) > 0$. Thus, $x=0$ is the ESS, as shown in Figure 1(b).
- ② If $S < (\Delta V_{11} - \Delta V_{12})$, then
 - (i) When $y > y^*$, $\partial A(x)/\partial x(x=0) > 0$ and $\partial A(x)/\partial x(x=1) < 0$. Therefore, $x=1$ is the ESS, as shown in Figure 1(b).
 - (ii) When $y < y^*$, $\partial A(x)/\partial x(x=0) < 0$ and $\partial A(x)/\partial x(x=1) > 0$. Therefore, $x=0$ is the ESS, as shown in Figure 1(b).

As for external investors, it can be inferred from equation (6) that

- (1) When $x = x^* = P + C_1 - zP(i+1)/C_1$, $B(y) = 0$, all game strategies are at a stable state (see Figure 2(a)).
- (2) When $x \neq P + C_1 - zP(i+1)/C_1$, $y = 0$ and $y = 1$ are two stable points of $B(y) = 0$. The stability strategies of the government need to be further analyzed. The derivative of equation (6) can be calculated as

$$B'(y) = \frac{\partial B(y)}{\partial y} = (1-2y)[-P - C_1 + xC_1 + zP(i+1)]. \quad (12)$$

Then, we discuss two circumstances according to equations (6) and (12):

- ① When $P + C_1 > xC_1 + zP(i+1)$, under the constraints of $0 < x < 1$, $0 < y < 1$, and $0 < z < 1$, we can prove $-P - C_1 + xC_1 + zP(i+1) < 0$. Therefore, $\partial B(y)/\partial y(y=0) < 0$ and $\partial B(y)/\partial y(y=1) > 0$. Thus, $y=0$ is the ESS, as shown in Figure 2(b).
- ② If $P + C_1 < xC_1 + zP(i+1)$, then
 - (i) When $x > x^*$, $\partial B(y)/\partial y(y=0) > 0$ and $\partial B(y)/\partial y(y=1) < 0$. Therefore, $y=1$ is the ESS, as shown in Figure 2(b).
 - (ii) When $x < x^*$, $\partial B(y)/\partial y(y=0) < 0$ and $\partial B(y)/\partial y(y=1) > 0$. Therefore, $y=0$ is the ESS, as shown in Figure 2(b).

As for SMEs, it can be inferred from equation (9) that

- (1) When $y = y^* = (Q_1 - Q_2)/(P - \Delta Q)$, $C(z) = 0$, all game strategies are at a stable state (see Figure 3(a)).
- (2) When $y \neq (Q_1 - Q_2)/(P - \Delta Q)$, $z = 0$ and $z = 1$ are two stable points of $C(z) = 0$. The stability strategies of the government need to be further analyzed. The derivative of equation (9) can be calculated as

$$C'(z) = \frac{\partial C(z)}{\partial z} = (1-2z)[(Q_1 - Q_2) + y(\Delta Q - P)]. \quad (13)$$

Then, we discuss two circumstances according to equations (9) and (13):

- ① When $Q_2 - Q_1 > y(\Delta Q - P)$, under the constraints of $0 < x < 1$, $0 < y < 1$, and $0 < z < 1$, we can prove $(Q_1 - Q_2) + y(\Delta Q - P) < 0$. Therefore, $\partial C(z)/\partial z(z=0) < 0$ and $\partial C(z)/\partial z(z=1) > 0$. Thus, $y=0$ is the ESS, as shown in Figure 3(b).
- ② If $Q_2 - Q_1 < y(\Delta Q - P)$, then
 - (i) When $y > y^*$, $\partial C(z)/\partial z(z=0) > 0$ and $\partial C(z)/\partial z(z=1) < 0$. Therefore, $z=1$ is the ESS, as shown in Figure 3(b).

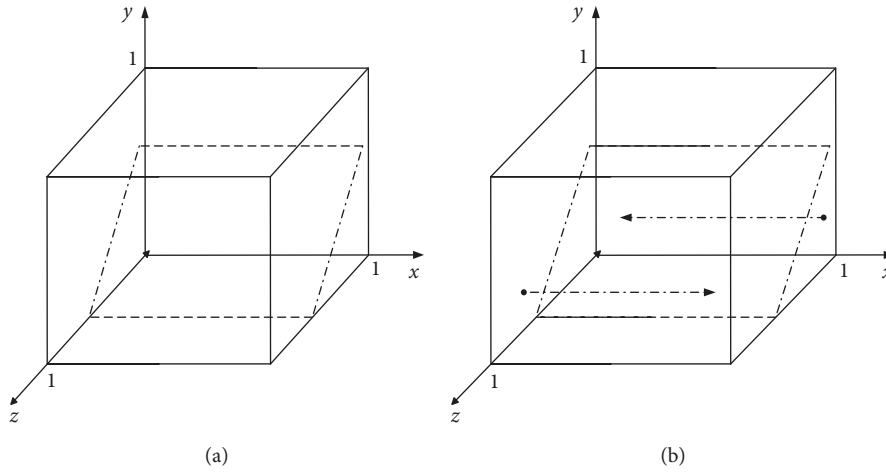


FIGURE 1: Replicator dynamic phase diagram of the government. (a) $y = y^*$. (b) $y > y^*$, $x \rightarrow 1$; $y < y^*$, $x \rightarrow 0$.

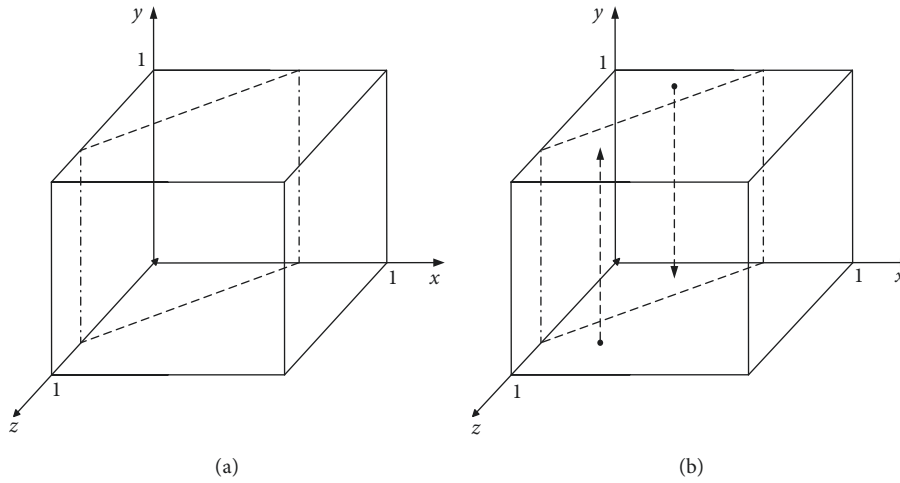


FIGURE 2: Replicator dynamic phase diagram of external investors. (a) $z = z^*$. (b) $z > z^*$, $y \rightarrow 1$; $z < z^*$, $y \rightarrow 0$.

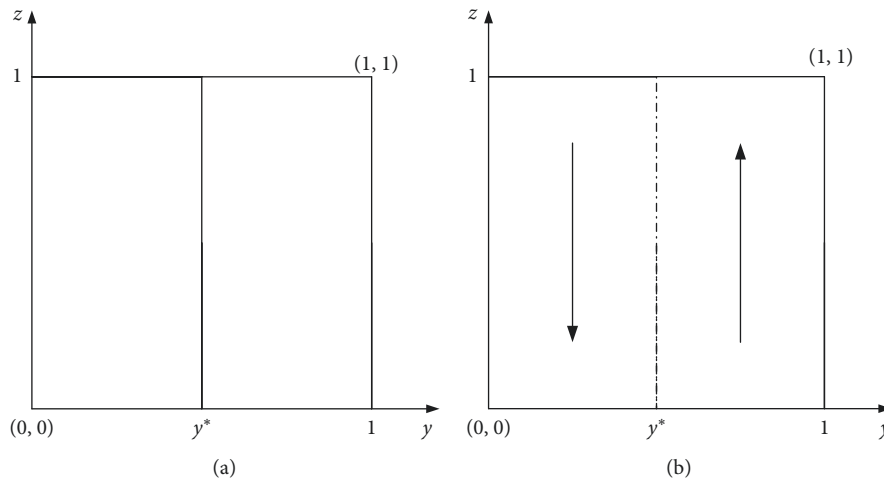


FIGURE 3: Replicator dynamic phase diagram of SMEs. (a) $y = y^*$. (b) $y > y^*$, $z \rightarrow 1$; $y < y^*$, $z \rightarrow 0$.

- (ii) When $y < y^*$, $\partial C(z)/\partial z(z=0) < 0$ and $\partial C(z)/\partial z(z=1) > 0$. Therefore, $z=0$ is the ESS, as shown in Figure 3(b).

4.3. Stability Analysis of the Dynamic Systems. According to the replicator dynamic analysis of three stakeholders mentioned above, the strategy choice of SMEs is only related to external investors, but the strategy choice of the government and external investors depends on the decision-making behavior of the other two groups. Therefore, the evolutionary stability strategy can be analyzed by stepwise analysis. First, taking x as a constant, we analyze the evolution

strategy of external investors and the enterprise. Then, taking z as a constant, we discuss the evolution strategy of the government and investors.

Under the condition that x is regarded as constant, let the replicator dynamic equation be $B(y) = C(z) = 0$, we can get equilibrium points $(0, 0)$, $(0, 1)$, $(1, 0)$, $(1, 1)$. When $y^* = (Q_1 - Q_2)/(P - \Delta Q)$, $z^* = (P + C_1 - xC_1)/(P(i + 1))$, and $y^* \in [0, 1]$, $z^* \in [0, 1]$, we can get equilibrium points (y^*, z^*) . According to the research of Friedman, the stability of the equilibrium points can be judged from the Jacobin matrix [44]. The Jacobin matrix of replicator dynamic equation is as follows:

$$J_1 = \begin{bmatrix} \frac{\partial F_y}{\partial y} & \frac{\partial F_y}{\partial z} \\ \frac{\partial F_z}{\partial y} & \frac{\partial F_z}{\partial z} \end{bmatrix} = \begin{bmatrix} (1-2y)[xC_1 + zP(i+1) - P - C_1] & P(i+1)y(1-y) \\ (\Delta Q - P)z(1-z) & (1-2z)[y(\Delta Q - P) + (Q_1 - Q_2)] \end{bmatrix}. \quad (14)$$

The determinants $\det(J_1)$ and trace $\text{tr}(J_1)$ of the matrix J_1 are as follows:

$$\begin{aligned} \det(J_1) &= (1-2y)[xC_1 + zP(i+1) - P - C_1] \\ &\quad \cdot (1-2z)[y(\Delta Q - P) + (Q_1 - Q_2)], \\ \text{tr}(J_1) &= (1-2y)[xC_1 + zP(i+1) - P - C_1] \\ &\quad + (1-2z)[y(\Delta Q - P) + (Q_1 - Q_2)]. \end{aligned} \quad (15)$$

If the equilibrium point satisfies the conditions of $\det(J_1) > 0$ and $\text{tr}(J_1) < 0$, it is an ESS. According to the stability analysis method, we analyze the local stability of five equilibrium points. To facilitate the observation of the calculation results, we set $v_1 = xC_1 - P - C_1$, $v_2 = xC_1 + P - C_1$, $v_3 = Q_1 - Q_2$, and $v_4 = \Delta Q - P + Q_1 - Q_2$. Under the constraint of $0 < x < 1$, we can prove $v_1 < 0$. Based on the hypothesis of $Q_1 > Q_2$, we can deduce $v_3 > 0$. The results of stability analysis between external investors and SMEs are shown in Table 3 and Figure 4. According to the criteria, the equilibrium points $(0, 0)$, (y^*, z^*) are saddle points. When

$v_4 < 0$, the equilibrium point $(1, 0)$ is a saddle point; otherwise, when $v_4 > 0$, the equilibrium point $(1, 0)$ is an unstable point, and the equilibrium points $(0, 1)$, $(1, 1)$ are an ESS. The results indicate that in the case of external investors participating in SMEs' innovation, when the earnings obtained by SMEs adopting the "Innovate" strategy are greater than the earnings obtained by SMEs adopting the "Not innovate" strategy, i.e., $Q_1 + \Delta Q > Q_2 + P$, the equilibrium point $(1, 1)$ is an ESS. The decisions of external investors will be greatly influenced by the probability of government subsidies. When the probability of government subsidies is high, external investors tend to choose the "Invest" strategy.

Under the condition that z is regarded as constant, let the replicator dynamic equation be $A(x) = B(y) = 0$, and we can get equilibrium points $(0, 0)$, $(0, 1)$, $(1, 0)$, $(1, 1)$. When $x^* = P + C_1 - zP(i + 1)/C_1$, $y^* = S/z(\Delta V_{11} - \Delta V_{12})$, and $x^* \in [0, 1]$, $y^* \in [0, 1]$, we can get equilibrium points (x^*, y^*) . The Jacobin matrix of replicator dynamic equation is as follows:

$$J_2 = \begin{bmatrix} \frac{\partial F_x}{\partial x} & \frac{\partial F_x}{\partial y} \\ \frac{\partial F_y}{\partial x} & \frac{\partial F_y}{\partial y} \end{bmatrix} = \begin{bmatrix} (1-2x)[yz(\Delta V_{11} - \Delta V_{12}) - S] & x(1-x)z(\Delta V_{11} - \Delta V_{12}) \\ C_1y(1-y) & (1-2y)[xC_1 + zP(i+1) - P - C_1] \end{bmatrix}. \quad (16)$$

TABLE 3: Local stability analysis between external investors and SMEs.

y, z	$\det(J_1)$	$\text{tr}(J_1)$	State	Stability condition
(0, 0)	-	N	Saddle point	Saddle point in any condition
(0, 1)	+	-	ESS	$v_2 < 0$
(1, 0)	-	N	Saddle point	$v_4 < 0$
(1, 1)	+	+	Unstable point	$v_4 > 0$
(1, 1)	+	-	ESS	$v_2 > 0, v_4 > 0$
(y^*, z^*)	0	0	Saddle point	Saddle point in any condition

“+” denotes greater than 0; “-” denotes less than 0; N denotes uncertainty.

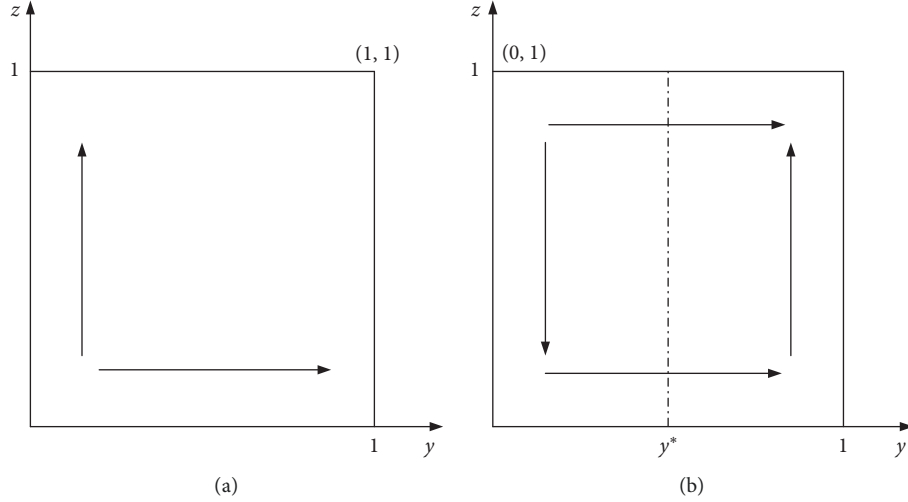


FIGURE 4: Dynamic evaluation diagram of strategies between external investors and SMEs. (a) $v_2 < 0$. (b) $v_2 > 0, v_4 > 0$.

The determinants $\det(J_2)$ and trace $\text{tr}(J_2)$ of the matrix J_2 are as follows:

$$\begin{aligned}
 \det(J_2) &= (1 - 2x)[yz(\Delta V_{11} - \Delta V_{12}) - S] \\
 &\quad \cdot (1 - 2y)[xC_1 + zP(i + 1) - P - C_1], \\
 \text{tr}(J_2) &= (1 - 2x)[yz(\Delta V_{11} - \Delta V_{12}) - S] \\
 &\quad + (1 - 2y)[xC_1 + zP(i + 1) - P - C_1].
 \end{aligned} \tag{17}$$

We analyze the local stability of five equilibrium points. To facilitate the observation of the calculation results, we set $v_5 = -S_1$, $v_6 = z(\Delta V_{11} - \Delta V_{12}) - S$, $v_7 = zP(i + 1) - P - C_1$, and $v_8 = zP(i + 1) - P$. Based on the hypothesis of $S > 0$, we can deduce $v_5 < 0$. The results of stability analysis between the government and external investors are shown in Table 4 and Figure 5. According to the criteria, when $v_7 < 0$, the equilibrium point (0, 0) is an ESS. When $v_6 < 0$ and $v_7 > 0$, (0, 1) is an ESS. When $v_8 > 0$, the equilibrium point (1, 0) is an unstable point, and when $v_8 < 0$, the equilibrium point (1, 0) is a saddle point. When $v_6 > 0$ and $v_8 > 0$, (1, 1) is an ESS. The equilibrium points (x^*, y^*) are saddle points. The results indicate that the decisions of the government and external investors will be greatly influenced by the probability of SMEs' innovation. When the probability of enterprise innovation is high, the government tends to choose the “Subsidize” strategy and the external investors tend to choose the “Invest” strategy. Otherwise, when the probability of enterprise innovation is low, the government tends

to choose the “Not subsidize” strategy and the investors tend to choose the “Not invest” strategy.

As discussed in Tables 3 and 4, the evolutionary stable strategy in trilateral evolutionary game needs to be subjected to the local stable conditions in both stages. Therefore, we can obtain 3 stable strategy combinations (0, 0, 1), (0, 1, 1), and (1, 1, 1). When $P * i < C_1$, (0, 0, 1) is an ESS. When $Q_1 + \Delta Q > Q_2 + P$, $(\Delta V_{11} - \Delta V_{12}) < S$, and $P * i > C_1$, (0, 1, 1) is an ESS. When $Q_1 + \Delta Q > Q_2 + P$, $(\Delta V_{11} - \Delta V_{12}) > S$, and $i > 0$, (1, 1, 1) is an ESS. According to the analysis results, when the return on investment of external investors is greater than 0 ($i > 0$), external investors will invest in enterprises' innovation, regardless of whether the government supports it. In fact, due to the high risks of SMEs' innovation, the external investors are often afraid or reluctant to invest. This paper is dedicated to promoting SMEs' innovation and establishing an ideal model of government support, external investor participation, and SMEs' innovation. That is to say, the trilateral evolutionary game evolved into the ideal strategy selection state of government subsidizing, investor investing, and enterprise innovating ($x = 1, y = 1, z = 1$). Based on the above analysis, when $Q_1 + \Delta Q > Q_2 + P$, that is, under the condition that external investors invest in SMEs' innovation, the gains of SMEs choosing the “Innovate” strategy are greater than those of SMEs choosing the “Not innovation” strategy, and all SMEs will choose “Innovate” strategy ($z \rightarrow 1$). When $\Delta V_{11} - S > \Delta V_{12}$, that is, under the condition that external investors invest in SMEs' innovation,

TABLE 4: Local stability analysis between the government and SMEs.

x, y	$\det(J_2)$	$\text{tr}(J_2)$	State	Stability condition
(0, 0)	+	-	ESS	$v_7 < 0$
(0, 1)	+	-	ESS	$v_6 < 0, v_7 > 0$
(1, 0)	+	+	Unstable point	$v_8 > 0$
(1, 1)	-	N	Saddle point	$v_8 < 0$
(1, 1)	+	-	ESS	$v_6 > 0, v_8 > 0$
(x^*, y^*)	0	0	Saddle point	Saddle point in any condition

“+” denotes greater than 0; “-” denotes less than 0; N denotes uncertainty.

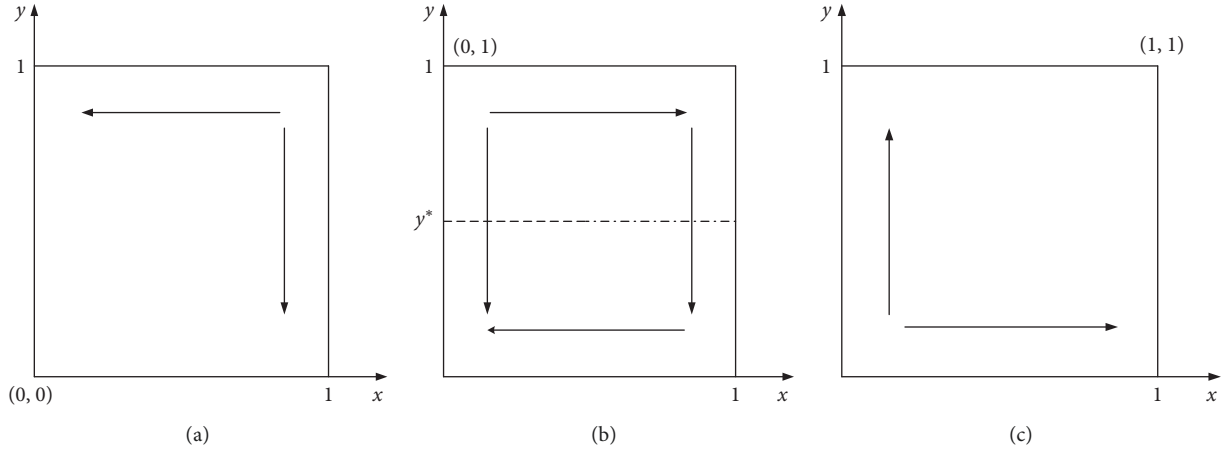


FIGURE 5: Dynamic evaluation diagram of strategies between the government and external investors. (a) $v_7 < 0$. (b) $v_6 < 0, v_7 > 0$. (c) $v_6 > 0, v_8 > 0$.

the social benefit increases of the government choosing “Subsidize” strategy are greater than those of the government choosing “Not subsidize” strategy, and all governments will choose “Subsidize” strategy ($x \rightarrow 1$). When the investment return rate of investors in SMEs’ innovation is greater than 0, all external investors will choose “Invest” strategy ($y \rightarrow 1$).

5. Simulation Analysis

Numerical simulations of the trilateral game model are performed using Matlab software. In order to promote the model to achieve the “ideal state” {Subsidize, Invest, Innovate} and reach the ESS point ($x=1, y=1, z=1$), the parameters need to satisfy the evolution conditions: $Q_1 + \Delta Q > Q_2 + P$, $(\Delta V_{11} - \Delta V_{12}) > S$, and $i > 1$. We set $V_1 = 100$, $V_2 = 50$, $\Delta V_{11} = 40$, $\Delta V_{12} = 20$, $S = 5$, $Q_1 = 50$, $Q_2 = 30$, $\Delta Q = 5$, $P = 10$, $i = 0.15$, and $C_1 = 0.3$. The time is set to $t = 20$.

5.1. Phase 1: Effect of Initial Strategy Selection Differences on Evolution Results. The strategy selection results of participants are shown in Figure 6 when the initial values of the strategy combination (x, y, z) are set as $P_0 = (0.2, 0.4, 0.5)$. From the figure, we can see that the strategy ratios of participants increase with time. Ultimately, the government chooses the “Subsidize” strategy, the investors choose the “Invest” strategy, and the firms choose the “Innovate”

strategy, thus reaching the ESS point $P_1 = 1, 1, 1$. The evolution results are shown in Figure 7 when the initial values of the strategy combination (x, y, z) are set as $P_0 = (0.4, 0.6, 0.8)$. From the two-dimensional and three-dimensional simulation diagrams, we can see that the change of initial strategy ratio does not affect the results of system evolution. It can be seen from the comparison between Figures 6 and 7 that the higher the initial probability of participants is, the faster the evolutionary system converges to the ideal state.

5.2. Phase 2: Effect of the Antecedents on the Strategy Selection.

The model involves government subsidies, external investors’ appraisal costs, external investors’ return rate, and the investment amount of external investors, which may have a significant effect on the strategy choices of the three players. We examine the above four antecedents on the evolutionary results.

5.2.1. Government Subsidies. In order to examine the effect of government subsidies, we set the parameter S at the interval $[5, 25]$, while fixing the value of the other parameters. The simulation results shown in Figure 8 suggest that the “Subsidize” strategy ratio of the government decreases when the government subsidy increases from 5 to 20. When the amount of government subsidies exceeds 20, the governments will change their strategy from “Subsidize” to “Not

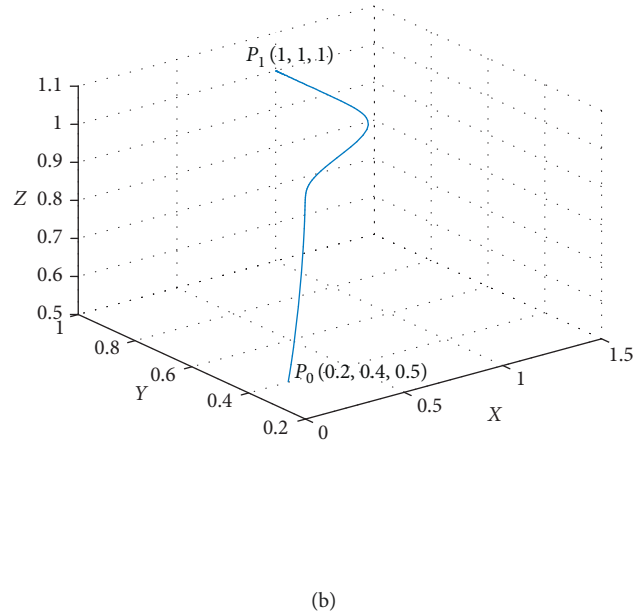
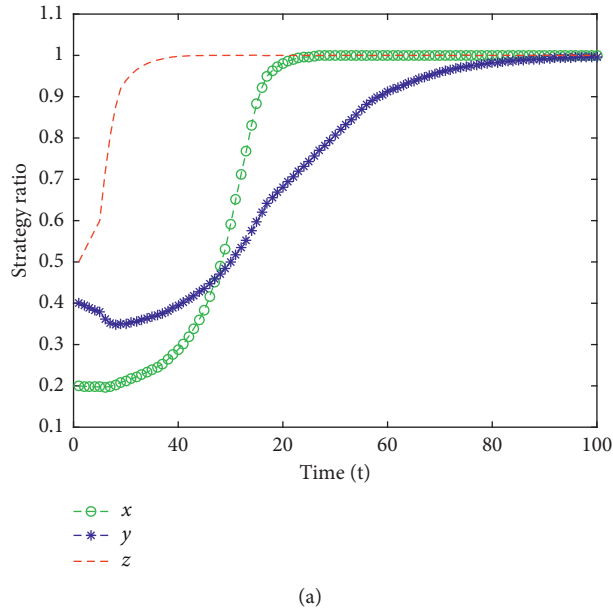


FIGURE 6: The dynamic evolution of the tripartite game model when $x = 0.2$, $y = 0.4$, and $z = 0.5$. (a) Time evolutions of x , y , and z . (b) Time evolution of (x, y, z) .

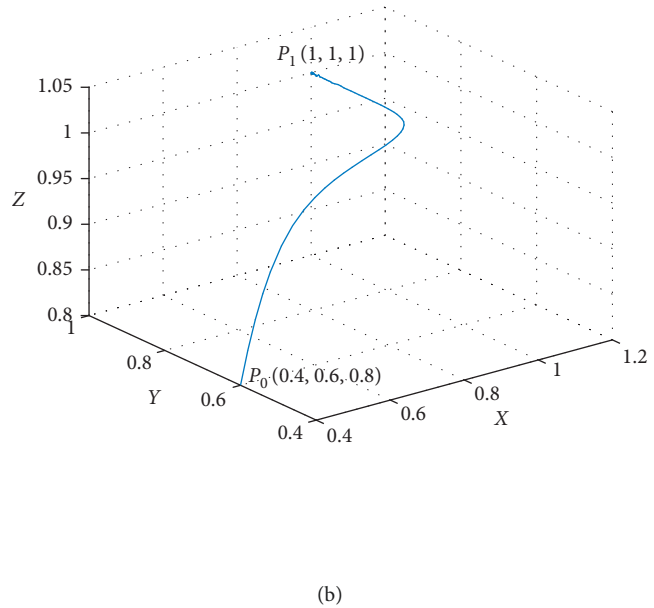
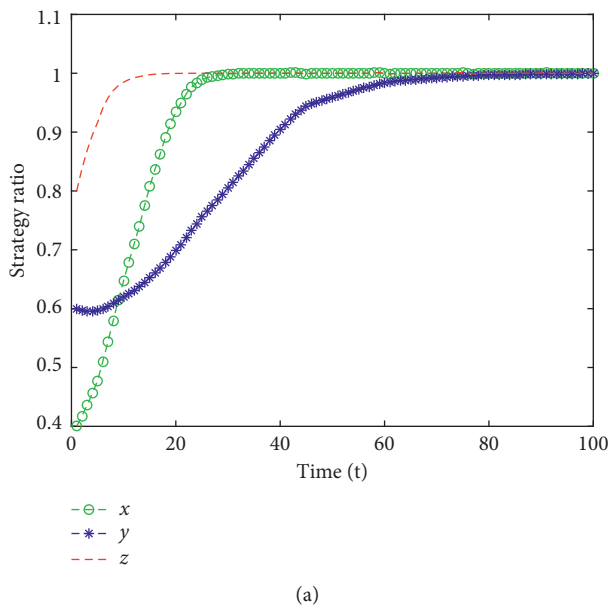


FIGURE 7: The dynamic evolution of the tripartite game model when $x = 0.4$, $y = 0.6$, and $z = 0.8$. (a) Time evolutions of x , y , and z . (b) Time evolution of (x, y, z) .

subsidize.” This result coincides with the explanation that market failure is the fundamental reason for the government to subsidize innovation activities, which creates a gap between private interests and social interests. The government can obtain more social benefits through supporting firms’ innovation. When the amount of government subsidies is greater than the social benefits obtained by the government, the government will select the “Not subsidize” strategy. But if it is profitable, the external investors will still choose the “Invest” strategy.

5.2.2. *External Investors’ Return Rate.* In order to examine the effect of the external investors’ return rate, we set the parameter i at the interval $[0.05, 1]$, while fixing the other parameters. The simulation results shown in Figure 9 indicate that the “Invest” strategy ratio of external investors increases when the investment return rate increases from 0.05 to 1. The objective of external investors is to maximize their benefits. Therefore, the higher the benefits are, the more external investors will invest in SMEs’ innovation.

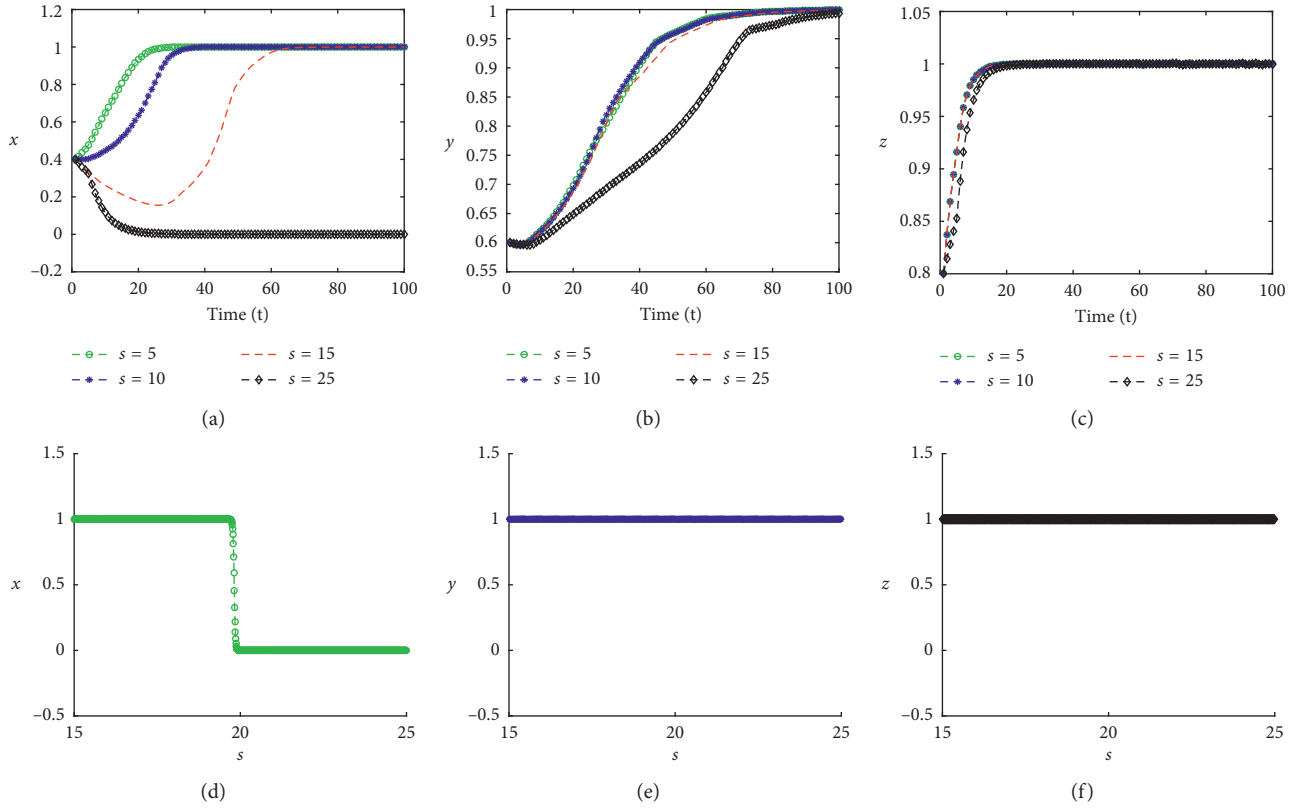


FIGURE 8: The effect of government subsidies on the evolutionary strategies.

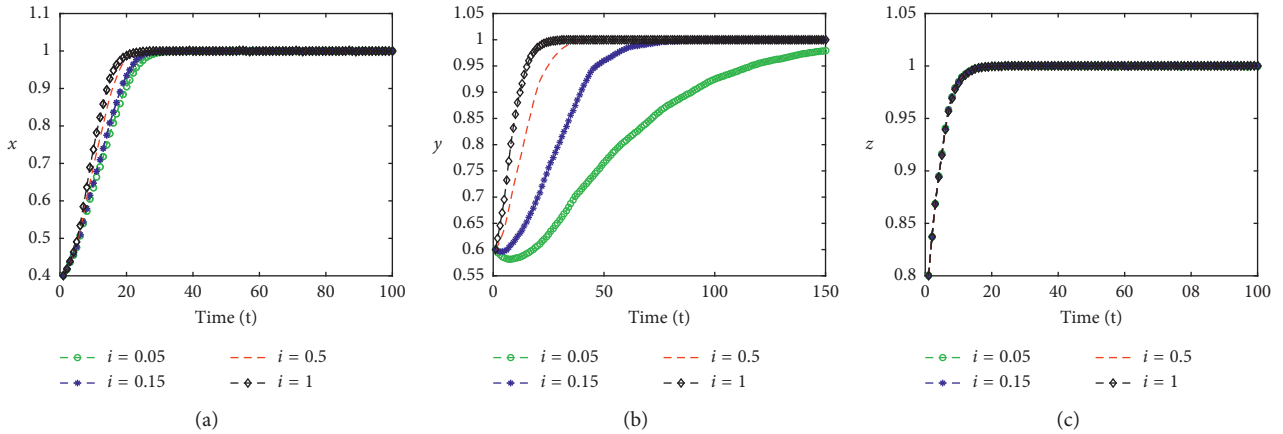


FIGURE 9: The effect of external investors' return rate on the evolutionary strategies.

5.2.3. *External Investors' Appraisal Costs.* In order to examine the effect of external investors' appraisal costs, we set the parameter C_1 at the interval $[0.3, 5]$, while keeping all other parameters constant. The simulation results shown in Figure 10 indicate that the increase of external investors' appraisal costs can lead the government and external investors to change their strategy. When the external investors' appraisal costs are less than or equal to the return of external investors' innovation investment, the government and external investors will choose "Subsidize" and "Invest" strategies, respectively. When the external investors' appraisal costs exceed 1.5, although it is greater than the investment

return, the external investors will also invest in SMEs' innovation directly as the government chooses the "Subsidize" strategy. This result coincides with the explanation that government subsidies have signaling effects, which can enhance external investors' confidence in innovation enterprises and save external investors' identification costs [13]. However, when the external investors' appraisal costs exceed 9, the government and external investors will choose the "Not subsidize" and "Not invest" strategies, respectively. The results imply that the higher the cost of identification for external investors is, the greater the risk of innovation enterprises become. When the investors'

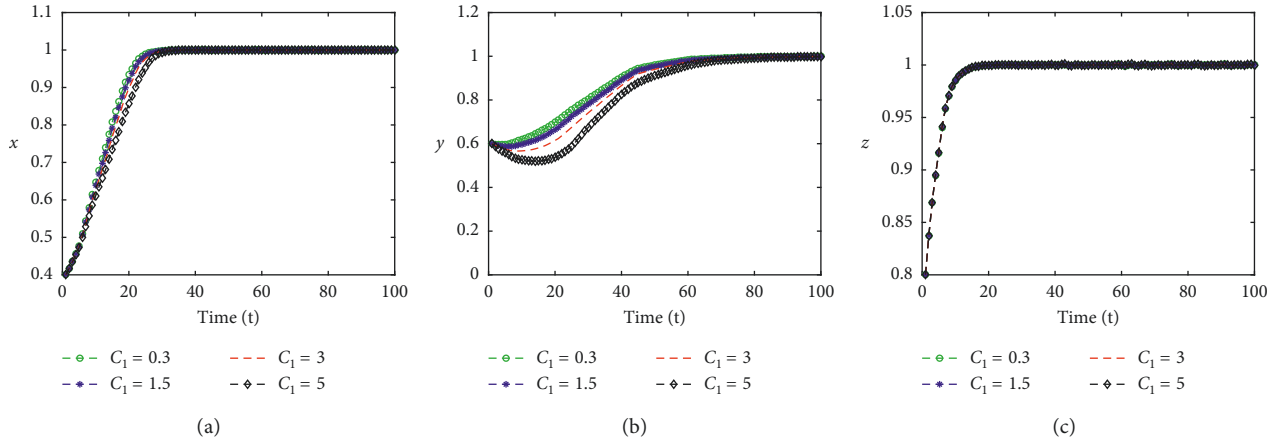


FIGURE 10: The effect of external investors’ appraisal costs on the evolutionary strategies.

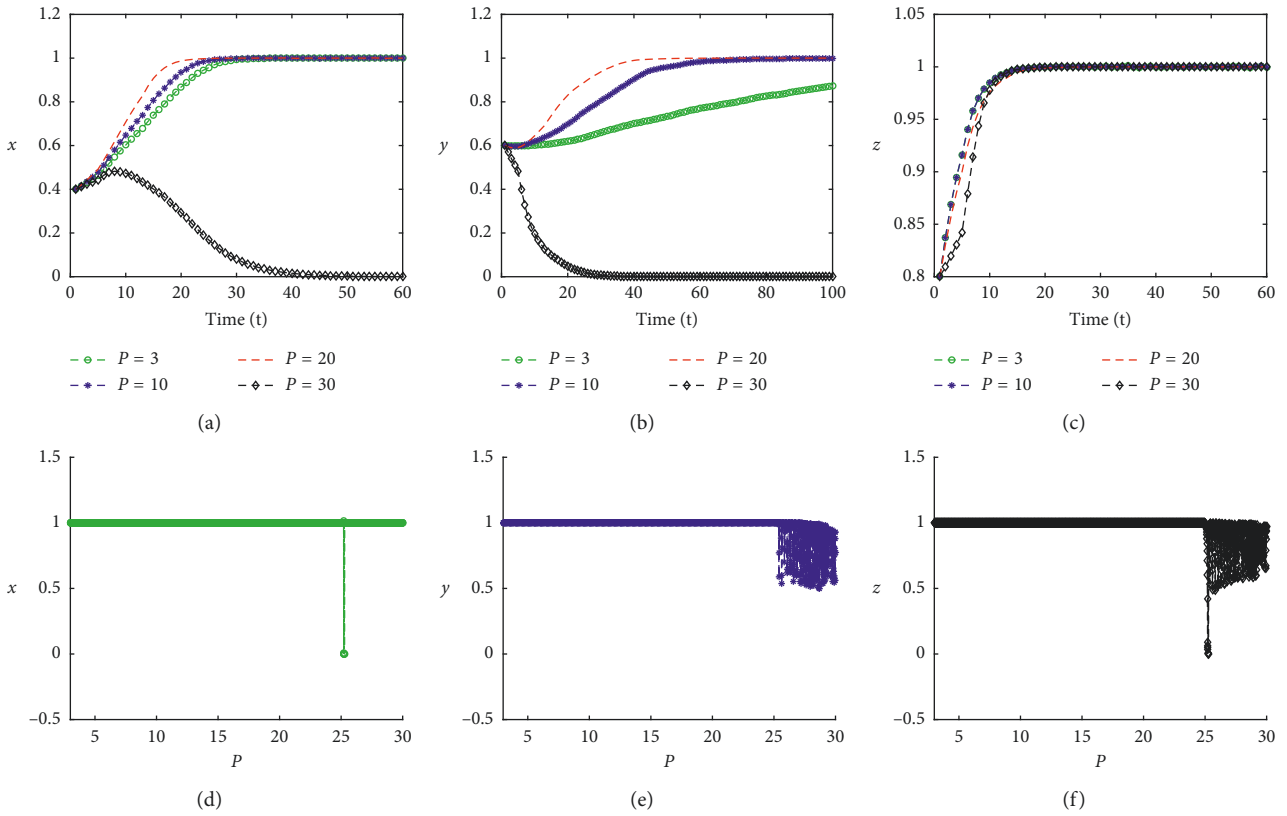


FIGURE 11: The effect of external investors’ investment amount on the evolutionary strategies.

appraisal costs are too large, the willingness of the government to subsidize and external investors to invest will decline.

5.2.4. Investment Amount of External Investors. In order to examine the effect of the external investors’ investment amount, we set the parameter P at the interval $[3, 30]$, while keeping all other parameters constant. The simulation results shown in Figure 11 indicate that the increase of external investors’ investment amount can lead the government and

external investors to change their strategies. When the investors’ investment amounts increase from 3 to 25, the government and external investors choose “Subsidize” and “Invest” strategies, respectively. When the external investors’ investment amount exceeds 25, the government will still choose the “Subsidize” strategy in the long run, while the external investors and SMEs are in a difficult state of choice and cannot reach a balance in the long run. The results imply that when the amount of government subsidies remains unchanged, the higher the amount of external investor’s investment is, the more the government tends to choose the

“Subsidize” strategy, and the more the SMEs tend to choose the “Innovate” strategy. However, when the investors’ investment amount is too high and the return of SMEs choosing “Not innovate” strategy is higher than that of SMEs choosing “Innovate” strategy, the external investor will choose not to invest and the government will choose not to subsidize in short time. However, in long time, external investors and SMEs will fall into a dilemma and cannot reach equilibrium.

6. Conclusions and Suggestions

Various aspects of SMEs’ innovation financing have been investigated concerning the reasons for financing difficulties, how to obtain external financing, and government support policies. However, studies on the behavior of the multiple stakeholders in SMEs’ innovation investment are limited. This paper fills gaps in existing theory by focusing on the collective strategies in SMEs’ innovation investment. The tripartite evolutionary game model, including the government, external investors, and SMEs, is built to study how to choose strategies for the participants under limited relational conditions. We also analyze the antecedents on the strategy selection of the participants. Based on the game analysis and simulation, we can draw the following conclusions: (1) When the social benefits of the government by “Subsidize” strategy are more than those by “Not subsidize” strategy, the investors’ return rate in SMEs’ innovation is greater than 1, and when the SMEs’ gains by “Innovate” strategy are more than those by “Not innovate” strategy, the ESS of the system is {Subsidize, Invest, Innovate}. (2) The game ESS changes into {Not subsidize, Invest, Innovate} when the social benefits of the government by “Subsidize” strategy are less than those by “Not subsidize” strategy. (3) The evolutionary system converges to desirable equilibrium stability faster, when government subsidies and external investors’ appraisal costs decrease, and the investment amount and return rates of external investors increase.

The financing difficulty of SMEs’ innovation is partly caused by the high risk characteristics of SMEs’ innovation and information asymmetry between SMEs and external investors. For the broad masses of SMEs, insufficient funds prevent them from conducting normal production operations and innovation activities. It is very necessary for the government to provide innovation subsidies for SMEs. Government subsidies directly increase enterprises’ R&D funds and turn SMEs’ innovation ideas into reality. However, government subsidies mainly come from financial allocations, which are limited by the state and local government fiscal revenue. Therefore, it is difficult to fully compensate for the financing gap faced by innovating SMEs. Building up effective cooperation among SMEs, governments, and external investors is an inevitable path to promote SMEs’ innovation and sustainable development.

Severe asymmetric information makes external investors afraid to participate in SMEs’ innovation, so SMEs cannot obtain sufficient R&D funds and achieve satisfactory innovation returns. The government is required to implement a set of measures to ensure transparency and fairness in the

process of supporting SMEs’ innovation. In this paper, the simulation results of the trilateral game provide evidence that government subsidies have a signal transmission effect. The SMEs subsidized by the government can obtain evidence of good enterprises’ qualifications. The external investors can invest in the SMEs subsidized by the government without having to spend on identifying costs. Therefore, on the one hand, the government should design a scientific and reasonable evaluation system and conduct rigorous screening procedures to select potential innovation SMEs. On the other hand, the government should timely publicize the information of the subsidized SMEs so that the external investors can receive the relevant information. The evolution paths of game strategies for the external investors and SMEs show that the higher the probability of SMEs choosing “Innovate” strategy, the higher the probability of the external investors choosing “Invest” strategy. Thus, the government should strictly supervise the subsidized SMEs to ensure that the public funds are used in innovation instead of other activities. Only in this way will more external investors be attracted to participate in SMEs’ innovation and the equilibrium of {Subsidize, Invest, Innovate} be finally reached. This study has important theoretical and practical significance for solving the problem of SMEs’ innovation financing difficulties. Yet, this study unavoidably has some limitations due to preset research objective and limited time. Future research should further analyze the role of the government, such as the effect of regulatory intensity, subsidy models, and subsidy levels, on the stakeholder behaviors.

Data Availability

The data used to support the findings of this study are available from the corresponding author upon request.

Conflicts of Interest

The authors declare no conflicts of interest regarding the publication of this paper.

Acknowledgments

This study was supported by the Tianjin Planning Leading Group Office of Philosophy and Social Sciences under grant no. TJYY17-017.

References

- [1] N. Rosenberg, *Innovation and Economic Growth*, Centre for Economic Performance, London, UK, 1996.
- [2] B. H. Hall, “The financing of research and development,” *Oxford Review of Economic Policy*, vol. 18, no. 1, pp. 35–51, 2002.
- [3] J. R. Brown, G. Martinsson, and B. C. Petersen, “Do financing constraints matter for R&D?,” *European Economic Review*, vol. 56, no. 8, pp. 1512–1529, 2012.
- [4] T. H. Clausen, “Do subsidies have positive impacts on R&D and innovation activities at the firm level?,” *Structural Change and Economic Dynamics*, vol. 20, no. 4, pp. 239–253, 2009.

- [5] R. E. Carpenter and B. C. Petersen, "Is the growth of small firms constrained by internal finance?," *Review of Economics and Statistics*, vol. 84, no. 2, pp. 298–309, 2002.
- [6] D. Czarnitzki, "Research and development in small and medium-sized enterprises: the role of financial constraints and public funding," *Scottish Journal of Political Economy*, vol. 53, no. 3, pp. 335–357, 2006.
- [7] M. S. Freel, "Are small innovators credit rationed?," *Small Business Economics*, vol. 28, no. 1, pp. 23–35, 2007.
- [8] T. J. Klette, J. Møen, and Z. Griliches, "Do subsidies to commercial R&D reduce market failures? microeconomic evaluation studies," *Research Policy*, vol. 29, no. 4–5, pp. 471–495, 1999.
- [9] S. Radas, I.-D. Anić, A. Tafro, and V. Wagner, "The effects of public support schemes on small and medium enterprises," *Technovation*, vol. 38, pp. 15–30, 2015.
- [10] L. Herrera and R. B. I. Edna, "Distribution and effect of R&D subsidies: a comparative analysis according to firm size," *Intangible Capital*, vol. 6, no. 2, pp. 272–299, 2010.
- [11] H. Hottenrott and C. Lopes-Bento, "(International) R&D collaboration and SMEs: the effectiveness of targeted public R&D support schemes," *Research Policy*, vol. 43, no. 6, pp. 1055–1066, 2014.
- [12] H. Jung, J. Hwang, and B.-K. Kim, "Does R&D investment increase SME survival during a recession?," *Technological Forecasting and Social Change*, vol. 137, pp. 190–198, 2018.
- [13] M. Miguel and D. M. Wouter, "Do R&D subsidies affect SMEs' access to external financing?," *Research Policy*, vol. 41, no. 3, pp. 580–591, 2012.
- [14] S. J. Wallsten, "The effects of government-industry R&D programs on private R&D: the case of the small business innovation research program," *The RAND Journal of Economics*, vol. 31, no. 1, pp. 82–100, 2000.
- [15] X. Dai and L. Cheng, "The effect of public subsidies on corporate R&D investment: an application of the generalized propensity score," *Technological Forecasting and Social Change*, vol. 90, pp. 410–419, 2015.
- [16] J. Ma and Z. Guo, "The parameter basin and complex of dynamic game with estimation and two-stage consideration," *Applied Mathematics and Computation*, vol. 248, pp. 131–142, 2014.
- [17] J. Ma and W. Ren, "Complexity and hopf bifurcation analysis on a kind of fractional-order IS-LM macroeconomic system," *International Journal of Bifurcation & Chaos*, vol. 26, no. 11, article 1650181, 2016.
- [18] R. Dai, J. Zhang, and S. Zhang, "Standard setting with considerations of energy efficiency evolution and market competition," *Complexity*, vol. 2019, p. 21, 2019.
- [19] R. Bronzini and P. Piselli, "The impact of R&D subsidies on firm innovation," *Research Policy*, vol. 45, no. 2, pp. 442–457, 2016.
- [20] O. A. Carboni, "The effect of public support on investment and R&D: an empirical evaluation on European manufacturing firms," *Technological Forecasting and Social Change*, vol. 117, pp. 282–295, 2017.
- [21] J. Ma and H. Ren, "Influence of government regulation on the stability of dual-channel recycling model based on customer expectation," *Nonlinear Dynamics*, vol. 94, no. 3, pp. 1775–1790, 2018.
- [22] I. Busom, "An empirical evaluation of the effects of R&D subsidies," *Economics of Innovation and New Technology*, vol. 9, no. 2, pp. 111–148, 2000.
- [23] M. H. Lee and I. J. Hwang, "Determinants of corporate R&D investment: an empirical study comparing korea's IT Industry with its non-IT Industry," *ETRI Journal*, vol. 25, no. 4, pp. 258–265, 2013.
- [24] M. Hud and K. Hussinger, "The impact of R&D subsidies during the crisis," *Research Policy*, vol. 44, no. 10, pp. 1844–1855, 2015.
- [25] M. Marino, S. Lhuillery, P. Parrotta, and D. Sala, "Additionality or crowding-out? An overall evaluation of public R&D subsidy on private R&D expenditure," *Research Policy*, vol. 45, no. 9, pp. 1715–1730, 2016.
- [26] J. Lerner, "The government as venture capitalist: the long-run impact of the SBIR program," *The Journal of Business*, vol. 72, no. 3, pp. 285–318, 1999.
- [27] R. Kleer, "Government R&D subsidies as a signal for private investors," *Research Policy*, vol. 39, no. 10, pp. 1361–1374, 2010.
- [28] A. Wu, "The signal effect of Government R&D Subsidies in China: does ownership matter?," *Technological Forecasting and Social Change*, vol. 117, pp. 339–345, 2017.
- [29] C. Bérubé and P. Mohnen, "Are firms that receive R&D subsidies more innovative?," *Canadian Journal of Economics/Revue Canadienne D'économique*, vol. 42, no. 1, pp. 206–225, 2009.
- [30] K. Szczygielski, W. Grabowski, M. T. Pamukcu, and V. S. Tandogan, "Does government support for private innovation matter? Firm-level evidence from two catching-up countries," *Research Policy*, vol. 46, no. 1, pp. 219–237, 2017.
- [31] D. J. Justo and S. Cristina, "Influence of R&D subsidies on efficiency: the case of Spanish manufacturing firms," *Cuadernos de Economía y Dirección de la Empresa*, vol. 14, no. 3, pp. 185–193, 2011.
- [32] H. Jin, B. Feng, Y. Wu, and L. Wang, "Do government grants promote innovation efficiency in China's high-tech industries?," *Technovation*, vol. 57, pp. 4–13, 2016.
- [33] M. R. Baye and H. C. Hoppe, "The strategic equivalence of rent-seeking, innovation, and patent-race games," *Games and Economic Behavior*, vol. 44, no. 2, pp. 217–226, 2003.
- [34] R. Casadesus-Masanell and F. Zhu, "Business model innovation and competitive imitation: the case of sponsor-based business models," *Strategic Management Journal*, vol. 34, no. 4, pp. 464–482, 2013.
- [35] J. Ma and H. Wang, "Complexity analysis of dynamic non-cooperative game models for closed-loop supply chain with product recovery," *Applied Mathematical Modelling*, vol. 38, no. 12, pp. 5562–5572, 2014.
- [36] O. Slivko and B. Theilen, "Innovation or imitation? The effect of spillovers and competitive pressure on firms' R&D strategy choice," *Journal of Economics*, vol. 112, no. 3, pp. 253–282, 2014.
- [37] J. Ma and L. Xie, "The comparison and complex analysis on dual-channel supply chain under different channel power structures and uncertain demand," *Nonlinear Dynamics*, vol. 83, no. 3, pp. 1379–1393, 2016.
- [38] J. Ma and L. Sun, "Complexity analysis about nonlinear mixed oligopolies game based on production cooperation," *IEEE Transactions on Control Systems Technology*, vol. 99, pp. 1–8, 2017.
- [39] B. D. Leibowicz, "Welfare improvement windows for innovation policy," *Research Policy*, vol. 47, no. 2, pp. 390–398, 2018.
- [40] H. Ying, G. Chen, and E. Poh, "Effects of informal contracts on innovative cooperation among enterprises in industrial clusters: an evolutionary game analysis," *Discrete Dynamics in Nature and Society*, vol. 2018, p. 10, 2018.

- [41] Z. Yang, Y. Shi, and Y. Li, "Analysis of intellectual property cooperation behavior and its simulation under two types of scenarios using evolutionary game theory," *Computers & Industrial Engineering*, vol. 125, pp. 739–750, 2018.
- [42] B. Shen, "The influence of endogenous knowledge spillovers on open innovation cooperation modes selection," *Wireless Personal Communications*, vol. 102, no. 4, pp. 2701–2713, 2018.
- [43] Y. Lin, X. Han, B. Chen, J. Zhou, and B. Wang, "Evolution of innovative behaviors on scale-free networks," *Frontiers of Physics*, vol. 4, pp. 275–283, 2018.
- [44] J. W. Weibull, *Evolutionary Game Theory*, MIT press, Cambridge, MA, USA, 1997.
- [45] J. Ma, T. Xu, Y. Hong, and X. Zhan, "Impact research on a nonlinear cold chain evolutionary game under three various contracts," *International Journal of Bifurcation and Chaos*, vol. 29, no. 5, p. 1950058, 2019.
- [46] X. Su, H. Liu, and S. Hou, "The trilateral evolutionary game of agri-food quality in farmer-supermarket direct purchase: a simulation approach," *Complexity*, vol. 2018, no. 2, pp. 1–11, 2018.
- [47] X. Su, Y. Wang, S. Duan, S. Duan, and J. Ma, "Detecting chaos from agricultural product price time series," *Entropy*, vol. 16, no. 12, pp. 6415–6433, 2014.
- [48] J. Ma and H. Tu, "Analysis of the stability and Hopf bifurcation of money supply delay in complex macroeconomic models," *Nonlinear Dynamics*, vol. 76, no. 1, pp. 497–508, 2014.

Research Article

A New Decision Method for Public Opinion Crisis with the Intervention of Risk Perception of the Public

Zhiying Wang ^{1,2}, Xiaodi Liu ³, and Shitao Zhang³

¹School of Management Science and Engineering, Anhui University of Technology, Ma'anshan, Anhui 243032, China

²Center for Corporate Governance and Operation, Anhui University of Technology, Ma'anshan, Anhui 243032, China

³School of Mathematics and Physics, Anhui University of Technology, Ma'anshan, Anhui 243032, China

Correspondence should be addressed to Zhiying Wang; zywang87@163.com

Received 9 May 2019; Revised 4 July 2019; Accepted 14 July 2019; Published 31 July 2019

Guest Editor: Raúl Baños

Copyright © 2019 Zhiying Wang et al. This is an open access article distributed under the Creative Commons Attribution License, which permits unrestricted use, distribution, and reproduction in any medium, provided the original work is properly cited.

Decision-making for selecting response plans problem (SRPP) has been widely concerning to scholars. However, most of the existing studies on this problem are focused on public emergencies, and little attention has been paid to the decision-makers' urgent need for solving the SRPP in response to public opinion crisis (POC) that may lead to panic buying of materials derived from public emergencies. POC has obvious characteristics of group behaviors that directly resulted from panics and psychological appeals of the public. Therefore, for solving the SRPP in POC, it is necessary to consider the deep-seated cause that result in panics and psychological appeals of the public, i.e., risk perception of the public (RPP). Firstly, the multicase study is employed to describe the SRPP of POC, and thus eight typical cases are chosen to analyze POC and its relevant response measures. Then, the RPP is described with prospect theory through considering the behavioral characteristics and critical sense of the public, the response measures of decision-makers, and the importance and ambiguity of POC. Further, considering the behavioral characteristics of decision-makers and the impact of alternative response plans on the evolution of POC scenarios, a new decision method for solving the SRPP with the intervention of the RPP is proposed by using cumulative prospect theory and a manner of comparing alternatives for each other. Finally, an example is given to illustrate the potential application and effectiveness of the proposed method.

1. Introduction

In recent years, with the frequent outbreaks of public emergencies (e.g., the “9.11” terrorist attack, hurricane Sandy in the U.S.; the SARS, Wenchuan earthquake, milk products pollution and H1N1 flu in China; the nuclear leakage in Japan; the earthquake in Haiti), relevant emergency management activities have increasingly become the focus of attention of the international community, governments and scholars [1–3]. It is against this background that the International Federation of Red Cross and Red Crescent Societies (IFRC) clearly defines the types of public emergencies, including hurricanes, tornadoes, typhoons, floods, droughts, earthquakes, volcanoes, epidemics, famines, food safety, man-made disasters, population migration, and technological disasters [4]. Public emergencies can not only endanger the human society directly but also cause a series of secondary or derivative events because of their chain reaction. Thus,

this kind of indirect harm cannot be ignored. POC is often one of them and refers to the crisis resulted from the spread of emotions, views, and attitudes of the public [5]. With the rapid development of Internet-based new media and we-media technology, the formation of POC becomes faster and broader, which can alter social psychology and affect social stability in a short period of time. For example, during China's SARS in 2003, the POC about “epidemic of infectious pneumonia” triggered a rush to buy rice vinegar, isatis root, and medical products. During Japan's nuclear leakage accident in 2011, the POC on “seawater pollution” and “iodine can resist nuclear radiation” caused a rush for iodized salt in China, iodine tablets in the United States, and seaweed in South Korea. In the early stage of POC, if decision-makers can select and initiate the targeted response plan in time with certain standards and methods, it will be helpful to avoid unnecessary losses; thus this study is of great significance.

A large number of cases show that POC usually occurs because of public opinion on public emergencies themselves and decision-makers' response measures (such as the above-mentioned China's SARS in 2003 and Japan's nuclear leakage in 2011) after outbreaks of public emergencies. Therefore, similar to public emergencies, POC has gradually become an important research direction in academia, focusing on evolution process modeling [6, 7], evolution path exploration [8], opinion leader identification [9], and influencing factors analysis [10, 11]. Accordingly, as an important means for decision-makers to deal with social risks or public crises, the selection or evaluation methods of alternative response plans have attracted much attention of scholars [12–22]. Amaief and Lu [12] proposed an ontology-based case-based reasoning (OS-CBR) method, which provides a feasible strategy for the evaluation and start-up of decision support systems in emergency situations by constructing a case retrieval process. Wex et al. [13] analyzed the effect of the distribution efficiency of rescue materials on reducing the harm of natural disasters. Then, by weighting the materials according to their importance, a decision support model was designed to minimize the total distribution time, and the starting strategy of the material distribution plan was given. Hämäläinen et al. [14] proposed a risk analysis method based on multi-attribute utility theory for screening the optimal response plan in emergency activities of nuclear accidents. Geldermann et al. [15] proposed a multicriteria decision support method for solving the optimal selection of multiple feasible alternatives in nuclear or radiological accidents. For decision-making of multicriteria and multiperson in unconventional emergencies, Yu and Lai [16] proposed a distance-based group decision making method (GDM). To quickly and effectively relieve the victims of disasters, Chang et al. [17] proposed a greedy search and multiobjective genetic algorithm (GSMOGA) to adjust the allocation of available resources and generate a feasible emergency logistics scheduling scheme. For solving the multicriteria decision-making problem in fuzzy environment, Fu [18] proposed a fuzzy optimization method and applied it to the scheme selection of reservoir flood control. Yang and Xu [19] established an engineering model of the interaction between decision-makers and emergencies by means of sequential games, which was used to generate the optimal relief scheme for emergencies. Liu et al. [20] proposed a fault tree analysis-(FTA-) based evaluation method of response schemes and applied it to the response of H1N1 infectious diseases. Aiming at the interruption risk of supply chain caused by natural disasters, Nejad et al. [21] suggested a mixed integer programming model to study the emergency preparedness of suppliers in the process of improving emergency response capability of the supply chain. He and Zhuang [22] pointed out that the hazard is determined by both preparation and rescue, and thus they studied the allocation of emergency preparedness and rescue costs by constructing a two-stage dynamic programming model. In addition, some scholars believe that considering the behavioral characteristics of decision-makers in the selection of alternatives is helpful to improve the reliability of decision-making [23–26]. Liu et al. [23], Fan et al. [24], and Li et al. [25] considered the behavioral

characteristics (loss aversion, reference dependence, diminishing sensitivity, etc.) of decision-makers and the impact of the alternatives on hazards of emergency scenarios and applied prospect theory to study the selection of alternatives. Wang and Li [26] put forward a set description method of behavioral decision-making in emergencies and then studied the selection of alternatives with cumulative prospect theory by considering the evaluation of scenario attributes and the intervention of alternatives on both scenario hazards and scenario evolution.

To sum up, the existing studies have made significant contributions to the identification of the evolution law of public emergencies and POC and the selection of alternative response plans. However, it is worth mentioning that most of the abovementioned achievements on the decision method for selecting the optimal response plan from alternatives are based on public emergencies; little attention has been paid to decision-makers' urgent need for decision methods in response to POC that may lead to panic buying of materials (e.g., during the POC on "seawater pollution" and "iodine can resist nuclear radiation" triggered by Japan's nuclear leakage in 2011, the Chinese Government adopted a response plan that combines measures such as holding press conferences, punishing lawbreakers, and increasing the supply of related materials). Different from public emergencies, POC generally has clear promoters and media channels, and its evolution process (including appearance, development, climax, decline, and disappearance [27]) is essentially the change process of behavioral relationships between the public (disseminator, recipient, etc.). From the perspective of cognitive psychology, the deep-seated cause for the formation of this change process is the change of RPP [28]. In fact, the change of RPP is synchronized with the change of POC to some extent, because the level of RPP directly determines the intensity of POC, and the intensity of POC directly reflects the level of RPP. So far, the description of RPP has been widely concerned by scholars, and the related studies are mainly based on sociocultural paradigm and psychometric paradigm [29–33], but there is no quantitative model of RPP in the context of POC. Prospect theory and its improved version (e.g., cumulative prospect theory) [34, 35] have attracted much attention in recent years because of their ability to describe some human decision-making behaviors in risk or uncertainty situations (loss aversion, reference dependency, diminishing sensitivity, etc.) [36–38]. In the field of emergency management, prospect theory has been applied to the public level [39, 40] in addition to the decision-makers level [23–26] described above. Campos-Vazquez and Cuilty [39] used prospect theory to measure the impact of student emotions on the risk and loss aversion parameters when manipulated by drug violence and youth unemployment in Mexico City. Wang et al [40] used prospect theory to describe the RPP on the arrival time of emergency materials in the study of optimal scheduling problem of emergency materials under emergencies. Different from these previous studies, this paper will use prospect theory to describe the perceived value of the public on the supply of materials and then deduce the change and formula of RPP after analyzing the behavioral characteristics and critical sense of

the public, the response measures of decision-makers, and the importance and ambiguity of POC. On this basis, considering the behavioral characteristics of decision-makers and the impact of alternative response plans on the evolution of POC scenarios, this paper proposes a new decision method for solving the SRPP in response to POC from the perspective of the intervention of RPP by using cumulative prospect theory and a manner of comparing alternatives for each other.

The rest of this paper is arranged as follows. Section 2 describes the selecting response plans problem (SRPP) in POC in detail with the multicase study, based on which some influencing factors of RPP are analyzed, and a formula of RPP is derived. Then, Section 3 proposes a new decision method for solving the SRPP in POC from the perspective of the intervention of RPP. Further, in Section 4, an example is given to illustrate the potential application and effectiveness of the proposed method. Finally, Section 5 summarizes and highlights the contributions of this paper.

2. The Description of SRPP and RPP in POC

The multicase study has become a universal method for construction and testing of theories because it can guarantee the reliability and make up for some shortcomings in data collection, and relevant research objects are usually extracted from sampling [41]. Therefore, for ensuring the universality of the rest of this paper, the multicase study will be used to describe the SRPP in POC, and then a formula of RPP will be proposed. Note that the different types of mass incidents may be induced by POC in different cases, which can lead to differences in the emphasis of the preparation of alternative response plans. Therefore, it is advisable to take the common mass incident of panic buying of materials as the supporting background of this study. For obeying the principle of triangulation [42], this paper adopts the method of data collection on official websites (e.g., the People's Daily Online and Xinhua Online) and expert discussion and chooses eight typical cases, i.e., SARS, explosion of Jilin petrochemical enterprise, Wenchuan earthquake, milk products pollution and H1N1 flu in China, earthquake in Haiti, nuclear leakage in Japan, and hurricane Sandy in the United States. The criteria we follow for choosing these cases include (1) these cases have triggered POC and panic buying of materials, and which have serious social hazards; (2) these cases are characterized by group and publicity, and thus are highly representative; (3) the evolution process of these cases is easy to review, which helps to ensure the completeness of collected key details; (4) these cases come from different parts of the world and China, helping to ensure the universality of this study. On this basis, the POC resulted from these cases can be taken as the research object of this paper.

2.1. Description of SRPP in POC. Through analyzing the POC and the relevant response measures (i.e., the specific content of response plans carried out) of the decision-makers (relevant government departments, enterprises and institutions, etc.) derived from the above eight typical cases,

respectively, the results can be sorted out as shown in Table 1.

Through comparing the above cases, we can find that on the one hand the POC in public emergencies usually has the following hazards. First, it aggravates panics and psychological appeals of the public and increases the difficulty of emergency management of leading public emergencies. Second, mass incidents of materials snapping-up are easily induced when panic reaches a certain height and psychological appeals is not satisfied sufficiently. Therefore, it is necessary and urgent to deal with POC by taking the intervention of panics and psychological appeals of the public as a breakthrough point, and to be more important, panics and psychological appeals of the public are actually the reflection of RPP (refers to the level of perception of the public for their lives and safety threatened [43]). On the other hand, after the appearance of POC in above cases, decision-makers (central and local government departments, enterprises, institutions, etc.) have adopted relevant response plans in different degrees. However, as described in the literature review, little attention has been paid to the decision-makers' urgent need for decision methods in response to POC that may lead to panic buying of materials in the existing studies.

In fact, the RPP has an obvious psychological quality, i.e., which is the public's cognitive and psychological response to threats to some valuable things [44], including both risk assessment and safety education management for disasters [45]. According to this essential meaning of RPP and the accounting method of social welfare for disaster risk management in [46], optimizing behaviors of RPP is consistent with the goal of improving social welfare that decision-makers pay attention to when selecting the optimal response plan. For this reason, the following two problems should be taken into account when a certain scenario of POC that may lead to panic buying of materials appears. One is how to determine a decision method for the SRPP in POC that may lead to panic buying of materials from the perspective of intervention of RPP in time. The other one is how to solve this SRPP and obtain the optimal response plan from alternatives with the determined method. These two problems are significant for decision-makers to face in practice and are key scientific problems worthy of our in-depth study. In view of this, this paper studies how to propose a new decision method and apply it to solve the SRPP in POC that may lead to panic buying of materials (i.e., determine the optimal response plan from alternatives) from the perspective of the intervention of RPP with the consideration of behavioral characteristics (loss aversion, reference dependence, diminishing sensitivity, etc.) of decision-makers. To sum up, the description of the SRPP in POC and its solution with the proposed method in this paper are given by referring to the drawing ideas in [47], as shown in Figure 1.

2.2. Description of RPP in POC. According to the cases studied above, the supply of materials that the public may snap-purchase is also an important decision for decision-makers besides appeasing sentiments of the public and

TABLE 1: The POC and its response measures.

Source of POC	Introduction of POC	Hazard of POC	Response measures
China's SARS in 2003	Diffusion of views and attitudes on "epidemic of infectious pneumonia"	On December 15th 2002, the same symptoms appeared in medical staff who had treated patients in Guangdong Province of China, and the POC ensued. In late January 2003, which triggered a rush to buy masks, rice vinegar and isatis root.	The Guangdong provincial government adopted measures to crack down on price hikes, issue the statement of the epidemic, remove derelict managers and increase the supply of related materials.
China's explosion of Jilin petrochemical enterprise in 2005	Diffusion of emotions on "water pollution" and "water stoppage rumors"	On November 13th 2005, an explosion occurred in the Jilin petrochemical enterprise of PetroChina. On November 21, the POC was ensued and led to residents of Harbin to snap up purified water, mineral water and packaged fresh milk.	China's State Environmental Protection Administration publicized the public concerns about water pollution. Harbin municipal government issued a four-day ban on water supplies due to overhaul of water pipelines.
China's Wenchuan earthquake in 2008	Diffusion of the panic on "huge casualties and economic losses"	On May 12th 2008, an 8.0 earthquake broke out in Wenchuan, Sichuan, China. Due to the damage caused by the earthquake is great, the POC ensued and led to a rush to buy tents, food and drinking water in many parts of Sichuan.	National and local seismological bureau of China held press conferences several times to publish information on the disaster, to clarify rumors, to answer doubts and placate emotions of the public.
China's milk products pollution in 2008	Diffusion of emotions on "trust crisis of milk products made in mainland China"	On September 8th 2008, 14 infants were found to have kidney stones. Since then, similar cases have occurred one after another because of milk products pollution. Thus, the POC ensued and resulted in the mainland people rushing to Hong Kong and Taiwan to buy milk products.	The AQSIQ repeatedly announced the progress of investigation the incident, and abolished the national inspection exemption system for food industries. Local authorities in China urged related enterprises to recall tainted products.
China's H1N1 flu in 2009	Diffusion of the fear and panic on "infectious epidemic"	On May 10th 2009, the first suspected case of influenza A (H1N1) was detected in Sichuan, China, triggering the POC that led to protective drugs at local drugstores out of stock.	Central government of China took measures such as investigation, immigration control and strengthening material reserves. Chengdu municipal government held press conferences to clarify the related information.
Haiti earthquake in 2010	Diffusion of panic on "casualties and food shortages"	On January 2th 2010, a 7.3 earthquake broke out in the Caribbean island of Haiti. The tremendous harm triggered the POC and led to the panic buying and robbery of food.	The government of Haiti publicized information on the disaster and appeased the public sentiment. WFP and international community distribute food such as high-energy biscuits to the disaster areas.
Japan's nuclear leakage accident in 2011	Diffusion of views on "seawater pollution" and "iodine can resist nuclear radiation"	On March 11th 2011, a 9.0 earthquake broke out in Japan and triggered a nuclear leakage accident. Since then, the POC ensued and triggered mass grabbing of salt in China.	Local government in China answered doubts of the public and clarified rumors in time, and the Chinese NDRC issued timely announcements to punishing those who fabricate rumors.
United States' hurricane Sandy in 2012	Diffusion of emotions on "hurricane attacks, water and power supply cut-off"	On October 29th 2012, hurricane Sandy made landfall in the eastern United States. In previous days, the POC spread rapidly and triggered the panic buying of mineral water, batteries and flashlights.	The New York government warned vendors to prohibit price hikes, and appealed to the public to keep abreast of the news from the city government and be prepared for evacuation.

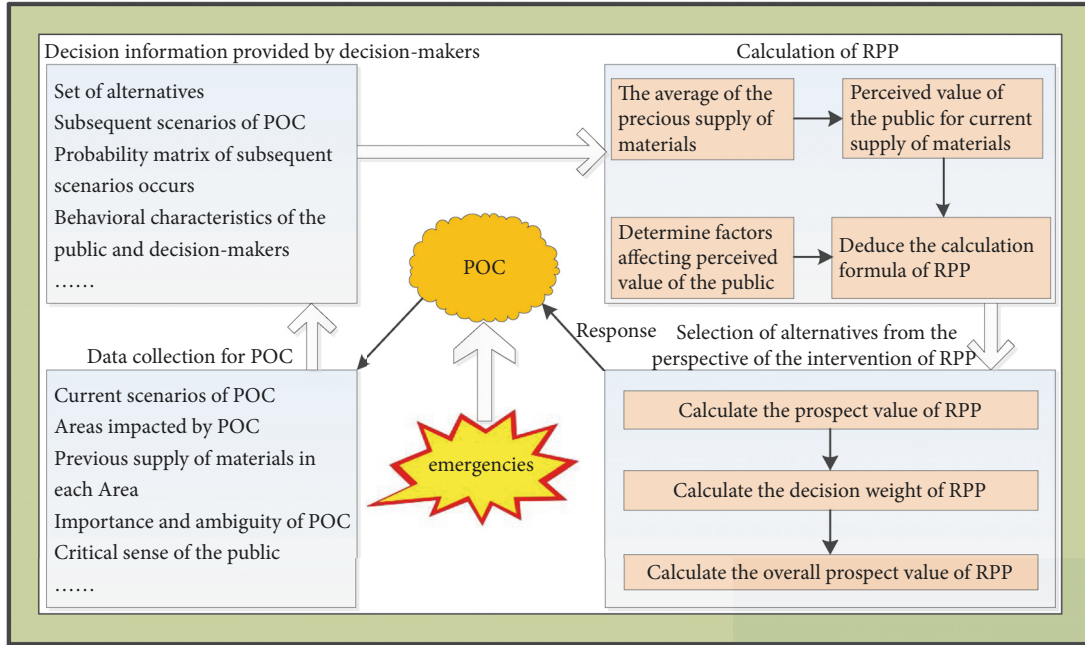


FIGURE 1: The description of the SRPP in POC and its solution with the proposed method.

cracking down on illegal behaviors. In fact, the actual supply of materials greatly affects the level of RPP. Specifically, according to the theory of memory manipulation proposed by Sarafidis [48], memory has the effects of proximity, imitation and similarity, and the public will observe the supply of materials at present in the POC-impacted regions (e.g., state, province, city, district, county, community) they concern by referring to that in the past. That is, if the public observe the supply of materials at present is not as good as that in the past, then the RPP increases; otherwise, the RPP does not change. In addition, the application of prospect theory in the decision-making of the public [39, 40] shows that the public usually has the behavioral characteristics of loss aversion and diminishing sensitivity. Under the background of this study, these two kinds of behavioral characteristics can be explained as follows: if the public observe that the current supply of materials is not as good as that of before, they feel “loss”; otherwise, they feel “gain”. Meanwhile, the public generally consider the utility produced from “loss” is larger than that produced from the equivalent “gain”, and their sensitivity to “loss” or “gain” is gradually diminishing [49].

Based on the above considerations, it is assumed that the total number of POC-impacted regions the public concern is A , hence the region $a \in \{1, 2, \dots, A\}$. The total amount of the past period of time that the public observe for supply of materials is T , hence the past period of time $t \in \{1, 2, \dots, T\}$. Accordingly, the supply of materials in region a during the past period of time t is \hat{d}_{at} . Considering the difficulty in obtaining accurate data and the bounded rationality of the public [50, 51], \hat{d}_{at} is set to be a fuzzy number [52] and its expected value is d_{at} . Therefore, the average D_{AT} of the past

supply of materials in the regions that the public observe is as follows:

$$D_{AT} = \frac{1}{AT} \sum_{a=1}^A \sum_{t=1}^T d_{at} \quad (1)$$

On this basis, if it is assumed that $d_{a(T+1)}$ represents the supply of materials in region a during the current time period, then the average $D_{A(T+1)}$ of supply of materials in the regions the public observe during the current time period can similarly be obtained, namely:

$$D_{A(T+1)} = \frac{1}{A} \sum_{a=1}^A d_{a(T+1)} \quad (2)$$

Considering the above analysis for behavioral characteristics of the public such as reference dependence, loss aversion, and diminishing sensitivity, this paper uses the value function of the prospect theory [34, 35] to obtain the perceived value $v(D_{A(T+1)})$ of the public for $D_{A(T+1)}$, that is,

$$v(D_{A(T+1)}) = \begin{cases} (D_{A(T+1)} - D_{AT})^{\alpha_1}, & D_{A(T+1)} - D_{AT} \geq 0; \\ -\lambda_1 [-(D_{A(T+1)} - D_{AT})]^{\beta_1}, & D_{A(T+1)} - D_{AT} < 0. \end{cases} \quad (3)$$

where $D_{A(T+1)} - D_{AT} \geq 0$ and $D_{A(T+1)} - D_{AT} < 0$ denote the “gain” and “loss” of the public respectively when D_{AT} is taken

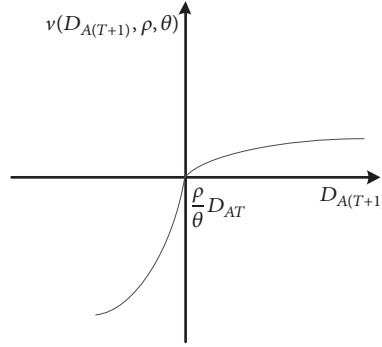


FIGURE 2: Curve of perceived value of the public.

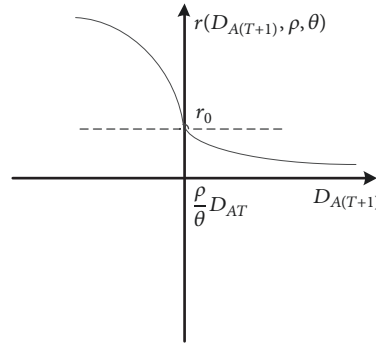


FIGURE 3: Curve of risk perception of the public.

as the reference point. Correspondingly, α_1 and β_1 denote the convexity of the perceived value function on the “gain” and “loss” side, respectively, and they depict the diminishing sensitivity of the perceived value of the public. λ_1 ($\lambda_1 > 1$) describes the loss aversion of the public, that is, for the same amount of the “gain” and “loss”, and the public is more sensitive to the latter.

Allport and Postman pointed out that the importance and ambiguity of events would affect the appearance of rumors and proposed a famous rumor formula, namely, $R = I \times A$ [53, 54]. Then Chorus considered that critical sense of the public was also an important factor affecting the rumor production and improved the rumor formula to $R = (I \times A)/C$ [55]. Since rumors can be regarded as a product of the evolution of POC, the importance and ambiguity of POC and critical sense of the public also affect the perceived value of the public, in addition to the above-mentioned behavioral characteristics of the public and the supply of materials of decision-makers. On the one hand, the loss aversion of the public usually makes the importance and ambiguity of POC affect their judgment on the current and past situations and easily causes them to deliberately amplify the psychological reference point. On the other hand, [55] points out that the critical sense includes three aspects, namely, knowledge level, wisdom and insight, and moral values, so that the stronger the critical sense of the public is, the greater the cognitive accuracy of the psychological reference point is. Thus, the importance and ambiguity parameter ρ ($\rho \geq 1$) of POC and the critical sense parameter θ ($\theta \geq 1$) of

the public are introduced, and formula (3) is improved as follows:

$$v(D_{A(T+1)}, \rho, \theta) = \begin{cases} \left(D_{A(T+1)} - \frac{\rho}{\theta} D_{AT}\right)^{\alpha_1}, & D_{A(T+1)} - \frac{\rho}{\theta} D_{AT} \geq 0; \\ -\lambda_1 \left[-\left(D_{A(T+1)} - \frac{\rho}{\theta} D_{AT}\right)\right]^{\beta_1}, & D_{A(T+1)} - \frac{\rho}{\theta} D_{AT} < 0. \end{cases} \quad (4)$$

where $v(D_{A(T+1)}, \rho, \theta)$ denotes the perceived value of the public to $D_{A(T+1)}$ on the premise that the importance and ambiguity of POC is ρ and the critical sense of the public is θ .

As can be seen from this, $v(D_{A(T+1)}, \rho, \theta)$ has a graphical representation as shown in Figure 2. In addition, if $r(D_{A(T+1)}, \rho, \theta)$ is defined as the RPP for $D_{A(T+1)}$ on the premise that the importance and ambiguity of POC is ρ and the critical sense of the public is θ ; then the function curve of $r(D_{A(T+1)}, \rho, \theta)$ can be obtained by analyzing the function curve of $v(D_{A(T+1)}, \rho, \theta)$, as shown in Figure 3.

In Figure 2, if $D_{A(T+1)} = (\rho/\theta)D_{AT}$, then $v(D_{A(T+1)}, \rho, \theta) = 0$, which denotes that the public believe the supply of materials in the regions at present is roughly equal to that in the past, thus their attitude of hesitation appears and their risk perception to be constant, that is $r(D_{A(T+1)}, \rho, \theta) = r_0$, as shown in Figure 3. In Figure 2, if $D_{A(T+1)} > (\rho/\theta)D_{AT}$, then $v(D_{A(T+1)}, \rho, \theta) > 0$, and the growth rate of $v(D_{A(T+1)}, \rho, \theta)$ decreases with $D_{A(T+1)}$ increases. Which indicates that the public believe the supply of materials in the regions at present is better than that in the past, hence they do not believe the POC and their risk perception decreases,

that is, $r(D_{A(T+1)}, \rho, \theta) < r_0$, as shown in Figure 3. In Figure 2, if $D_{A(T+1)} < (\rho/\theta)D_{AT}$, then $v(D_{A(T+1)}, \rho, \theta) < 0$, $v(D_{A(T+1)}, \rho, \theta)$ rapidly decreases and its decreasing rate declines with the decreasing $D_{A(T+1)}$, which indicates that the public believe the supply of materials in the regions at present is not as good as that in the past; hence they believe the POC to some extent and their risk perception increases, that is $r(D_{A(T+1)}, \rho, \theta) > r_0$, as shown in Figure 3.

Furthermore, comparing the function curve of $v(D_{A(T+1)}, \rho, \theta)$ with that of $r(D_{A(T+1)}, \rho, \theta)$, we conclude that the curve of $r(D_{A(T+1)}, \rho, \theta)$ can be approximately obtained by transforming the curve of $v(D_{A(T+1)}, \rho, \theta)$ symmetrically along $D_{A(T+1)}$ -axis and then moving up r_0 along $v(D_{A(T+1)}, \rho, \theta)$ -axis. Therefore, the formula of $r(D_{A(T+1)}, \rho, \theta)$ can be obtained according to formula (4), that is,

$$r(D_{A(T+1)}, \rho, \theta) = \begin{cases} r_0 - \left(D_{A(T+1)} - \frac{\rho}{\theta}D_{AT}\right)^{\alpha_1}, & D_{A(T+1)} - \frac{\rho}{\theta}D_{AT} \geq 0; \\ r_0 + \lambda_1 \left[-\left(D_{A(T+1)} - \frac{\rho}{\theta}D_{AT}\right)\right]^{\beta_1}, & D_{A(T+1)} - \frac{\rho}{\theta}D_{AT} < 0. \end{cases} \quad (5)$$

3. The Proposed Method for Solving the SRPP in POC

As described in formula (5), the behavioral characteristics and critical sense of the public, the response measures (i.e., the supply of materials) of decision-makers, and the importance and ambiguity of POC jointly determine the RPP. For this reason, it is necessary to consider the effect of alternative response plans on these four factors when solving the SRPP in POC from the perspective of the intervention of RPP. Among them, the behavioral characteristics (reference dependence, loss aversion, diminishing sensitivity, etc.) and critical sense are inherent in the public; hence they can be assumed to be unaffected by alternative response plans in a short period of time. The effect of alternatives on the response measures of decision-makers can be reflected in the different response measures in different alternatives. The effect of alternatives on the importance and ambiguity of POC can be reflected by introducing different scenarios of POC and considering the importance of each scenario is different and the evolution of scenarios affected by alternatives.

3.1. Symbol Definition. For conducting the research on a new decision method for solving the SRPP in POC from the perspective of the intervention of RPP, we first define the following symbols.

$S = \{S_1, S_2, \dots, S_n\}$ denotes a set of current scenarios that may appear during the evolution of POC. The identification of the current scenario is considered as a part of the response of decision-makers in order to be consistent with the observation of the public for response measures in the current scenario described above.

$E^k = \{E_1^k, E_2^k, \dots, E_l^k\}$ denotes a set of subsequent scenarios may be evolved by the current scenario S_k of POC.

$R = \{R_1, R_2, \dots, R_m\}$ denotes a set of alternative response plans.

$D_{A(T+1)}^R = \{D_{A(T+1)}^{R_1}, D_{A(T+1)}^{R_2}, \dots, D_{A(T+1)}^{R_m}\}$ indicates a set of the average of current supply of materials in the regions the public concern under carrying out alternatives, where $D_{A(T+1)}^{R_i}$ represents the average under carrying out the alternative plan R_i .

$\hat{\rho} = \{\hat{\rho}_1, \hat{\rho}_2, \dots, \hat{\rho}_g\}$ denotes a set of indicators used to evaluate the importance and ambiguity of POC.

$\hat{\rho}^k = \{\hat{\rho}_1^k, \hat{\rho}_2^k, \dots, \hat{\rho}_g^k\}$ denotes a set of values of the set $\hat{\rho}$ in the current scenario S_k , and the total value is $\bar{\rho}^k = \sum_{h=1}^g \hat{\rho}_h^k$.

$P = [P(E_j^k | R_i)]_{m \times l} = [p_{ij}^k]_{m \times l}$ denotes a probability matrix of the new scenario E_j^k appears, that is, $P(E_j^k | R_i)$ (abbreviated as p_{ij}^k) indicates the probability that the current scenario S_k evolves into the new scenario E_j^k after carrying out the alternative plan R_i .

$\hat{\rho}^{kij} = \{\hat{\rho}_1^{kij}, \hat{\rho}_2^{kij}, \dots, \hat{\rho}_g^{kij}\}$ denotes a set of values of the set $\hat{\rho}$ when the current scenario S_k evolves into the new scenario E_j^k after carrying out the alternative plan R_i , where $\hat{\rho}_h^{kij} = \hat{\rho}_h^{kij} | (E_j^k | R_i)$ is the value of the h-th indicator, and the total value is $\bar{\rho}^{kij} = \sum_{h=1}^g \hat{\rho}_h^{kij}$.

$\bar{\theta} = \{\bar{\theta}_1, \bar{\theta}_2, \dots, \bar{\theta}_A\}$ denotes a set of the critical sense parameter of the public in the POC-impacted regions, where $\bar{\theta}_a$ indicates the critical sense of the public in the region a .

$i \in \{1, 2, \dots, m\}$, $j \in \{1, 2, \dots, l\}$, $k \in \{1, 2, \dots, n\}$, $h \in \{1, 2, \dots, g\}$, $a \in \{1, 2, \dots, A\}$.

3.2. The Proposed Method. In fact, limited to the subjective and objective conditions such as asymmetric information, time pressure and limited rationality of decision-makers, the solution of the SRPP will be inevitably affected by behavioral characteristics (e.g., reference dependence, loss aversion, and diminishing decrease [34, 37]) of decision-makers when a scenario of POC appears. However, different from the application of prospect theory to describe behavioral characteristics of the public above, decision-makers need to take into account the perception probability of the effect of alternative response plans on RPP in POC-impacted regions when solving the SRPP. Therefore, the cumulative prospect theory [35] is introduced to describe the behaviors of decision-makers and to present a new decision method for solving the SRPP in POC. In brief, the specific decision process of this method is as follows.

Step 1. Calculate the prospect value of RPP in each POC-impacted region.

According to the above symbol definition and formula (5), when the current scenario S_k evolves into the new scenario E_j^k after carrying out the alternative plan R_i , the RPP $r_a(D_{A(T+1)}^{R_i}, \bar{\rho}^{kij}, \bar{\theta}_a)$ in POC-impacted region a can be described as follows:

$$r_a \left(D_{A(T+1)}^{R_i}, \bar{p}^{kij}, \bar{\theta}_a \right) = \begin{cases} r_0 - \left(D_{A(T+1)}^{R_i} - \frac{\bar{p}^{kij}}{\bar{\theta}_a} D_{AT} \right)^{\alpha_1}, & D_{A(T+1)}^{R_i} - \frac{\bar{p}^{kij}}{\bar{\theta}_a} D_{AT} \geq 0; \\ r_0 + \lambda_1 \left[- \left(D_{A(T+1)}^{R_i} - \frac{\bar{p}^{kij}}{\bar{\theta}_a} D_{AT} \right) \right]^{\beta_1}, & D_{A(T+1)}^{R_i} - \frac{\bar{p}^{kij}}{\bar{\theta}_a} D_{AT} < 0. \end{cases} \quad (6)$$

According to the description of SRPP in Section 2.1, the intervention effect of RPP is the basic criterion we follow to judge which alternative plan is the best in alternatives. Therefore, it is necessary to calculate the prospect value of RPP after carrying out an alternative plan. In addition, it is necessary

to take the manner of comparing alternatives for each other to avoid the deviation probably caused by setting up the reference point artificially when considering the behavioral characteristics of reference dependence of decision-makers. On such basis, the following formula can be obtained.

$$V(r_a | R_{i_1}) = \frac{1}{n(m-1)} \cdot \sum_{k=1}^n \sum_{i_2=1, i_2 \neq i_1}^m \sum_{j_1=1}^l \sum_{j_2=1}^l \left\{ d \left[r_a \left(D_{A(T+1)}^{R_{i_1}}, \bar{p}^{k i_1 j_1}, \bar{\theta}_a \right), r_a \left(D_{A(T+1)}^{R_{i_2}}, \bar{p}^{k i_2 j_2}, \bar{\theta}_a \right) \right] P(S_k) P(E_{j_1}^k | R_{i_1}) P(E_{j_2}^k | R_{i_2}) \right\} \quad (7)$$

Where $V(r_a | R_{i_1})$ denotes the prospect value of RPP r_a in the region a after carrying out the alternative plan R_{i_1} . $P(S_k)$ denotes the probability that the current scenario of POC is S_k . $1/n$ ensures that there is only one current scenario; $1/(m-1)$

guarantees that the average of prospect values of RPP can be obtained after comparing R_{i_1} with others. $d(\cdot, \cdot)$ denotes the value function of cumulative prospect theory and satisfies the following formula:

$$d \left[r_a \left(D_{A(T+1)}^{R_{i_1}}, \bar{p}^{k i_1 j_1}, \bar{\theta}_a \right), r_a \left(D_{A(T+1)}^{R_{i_2}}, \bar{p}^{k i_2 j_2}, \bar{\theta}_a \right) \right] = \begin{cases} -\lambda_2 \left[r_a \left(D_{A(T+1)}^{R_{i_1}}, \bar{p}^{k i_1 j_1}, \bar{\theta}_a \right) - r_a \left(D_{A(T+1)}^{R_{i_2}}, \bar{p}^{k i_2 j_2}, \bar{\theta}_a \right) \right]^{\beta_2}, & r_a \left(D_{A(T+1)}^{R_{i_1}}, \bar{p}^{k i_1 j_1}, \bar{\theta}_a \right) - r_a \left(D_{A(T+1)}^{R_{i_2}}, \bar{p}^{k i_2 j_2}, \bar{\theta}_a \right) \geq 0; \\ \left\{ - \left[r_a \left(D_{A(T+1)}^{R_{i_1}}, \bar{p}^{k i_1 j_1}, \bar{\theta}_a \right) - r_a \left(D_{A(T+1)}^{R_{i_2}}, \bar{p}^{k i_2 j_2}, \bar{\theta}_a \right) \right] \right\}^{\alpha_2}, & r_a \left(D_{A(T+1)}^{R_{i_1}}, \bar{p}^{k i_1 j_1}, \bar{\theta}_a \right) - r_a \left(D_{A(T+1)}^{R_{i_2}}, \bar{p}^{k i_2 j_2}, \bar{\theta}_a \right) < 0. \end{cases} \quad (8)$$

where $r_a \left(D_{A(T+1)}^{R_{i_1}}, \bar{p}^{k i_1 j_1}, \bar{\theta}_a \right) - r_a \left(D_{A(T+1)}^{R_{i_2}}, \bar{p}^{k i_2 j_2}, \bar{\theta}_a \right) \geq 0$ and $r_a \left(D_{A(T+1)}^{R_{i_1}}, \bar{p}^{k i_1 j_1}, \bar{\theta}_a \right) - r_a \left(D_{A(T+1)}^{R_{i_2}}, \bar{p}^{k i_2 j_2}, \bar{\theta}_a \right) < 0$ denote the ‘‘loss’’ and ‘‘gain’’ of decision-makers, respectively, when the reference point of RPP $r_a \left(D_{A(T+1)}^{R_{i_1}}, \bar{p}^{k i_1 j_1}, \bar{\theta}_a \right)$ is $r_a \left(D_{A(T+1)}^{R_{i_2}}, \bar{p}^{k i_2 j_2}, \bar{\theta}_a \right)$ in the region a . Correspondingly, α_2 and β_2 denote the convexity of the value function on ‘‘gain’’ and ‘‘loss’’ side, respectively, and both of them depict the behavioral characteristics of diminishing sensitivity of decision-makers. λ_2 ($\lambda_2 > 1$) describes the behavioral characteristics of loss aversion of decision-makers.

From formulae (1), (6), (7), and (8), it can be seen that the calculation of $V(r_a | R_{i_1})$ involves the expected value d_{at} of the fuzzy number \hat{d}_{at} . Thus, it is necessary to further explore the relationship between \hat{d}_{at} and d_{at} . Without loss of generality, let \hat{d}_{at} be a triangular fuzzy number [56] denoted as $(\hat{d}_{at}^1, \hat{d}_{at}^2, \hat{d}_{at}^3)$ (where \hat{d}_{at}^1 , \hat{d}_{at}^2 , and \hat{d}_{at}^3 are the minimum, the most possible value and the maximum, respectively). On such basis, the following formula can be obtained according to [57]:

$$d_{at} = \frac{(1-\mu)\hat{d}_{at}^1 + \hat{d}_{at}^2 + \mu\hat{d}_{at}^3}{2} \quad (9)$$

where $0 \leq \mu \leq 1$ depicts the risk attitude of the public and $0.5 < \mu < 1$, $\mu = 0.5$, and $0 < \mu < 0.5$ denote the risk pursuit, neutrality, and aversion, respectively. The public have the behavioral characteristics of loss aversion when analyzing the RPP above; that is, the public often show a risk aversion attitude in the face of deterministic and risky gains and often show a risk pursuit in the face of deterministic and risky losses according to the prospect theory. Without loss of generality, let the compromise principle be used; thus $\mu = 0.5$, $d_{at} = (\hat{d}_{at}^1 + 2\hat{d}_{at}^2 + \hat{d}_{at}^3)/4$, which is the third indicator of Yager [58].

Step 2. Calculate the decision weight of RPP in each POC-impacted region.

To avoid the perceived deviation of decision-makers for risk probability, the cumulative probability function in cumulative prospect theory is introduced to describe the decision weight of RPP. To do this, the $V(r_a | R_{i_1})$, $i_1 \in \{1, 2, \dots, m\}$ obtained by formula (7) is ranked, namely,

$V(r_a|R_{(1)}) \leq V(r_a|R_{(2)}) \leq \dots \leq V(r_a|R_{(e)}) \leq 0 \leq V(r_a|R_{(e+1)}) \leq \dots \leq V(r_a|R_{(m-1)}) \leq V(r_a|R_{(m)})$, where $V(r_a|R_{(b)})$, $b \in \{1, 2, \dots, m\}$ indicates that the prospect value of RPP in the region a is ranked at b . Thus, if $b \leq e$, then $V(r_a|R_{(b)}) \leq 0$; otherwise, $V(r_a|R_{(b)}) \geq 0$. Based on this, it is assumed that $P(r_a|R_{(b)})$ denotes the probability that RPP r_a has the current prospect value caused by the alternative plan $R_{(b)}$. From the formula (7), it can be seen that the $P(r_a|R_{(b)})$ is essentially the sum of the multiplication between the probability $P(E_j^k|R_{(b)})$ that S_k evolves into E_j^k after carrying out the alternative plan $R_{(b)}$ and the probability P_a^j that RPP takes the current value, that is $P(r_a|R_{(b)}) = \sum_{k=1}^n \sum_{j=1}^l P(S_k)P(E_j^k|R_{(b)})P_a^j$.

According to the decision weight function in cumulative prospect theory, the perceived probabilities of decision-makers that the RPP r_a in the region a takes the current prospect value $V(r_a|R_{(b)})$ caused by the alternative plan $R_{(b)}$ can be expressed as below:

$$\begin{aligned} \pi^+(r_a|R_{(m)}) &= w^+[P(r_a|R_{(m)})] \\ \pi^-(r_a|R_{(1)}) &= w^-[P(r_a|R_{(1)})] \\ \pi^+(r_a|R_{(b)}) &= w^+\left[\sum_{i=b}^m P(r_a|R_{(i)})\right] \\ &\quad - w^+\left[\sum_{i=b+1}^m P(r_a|R_{(i)})\right], \\ &\quad b \in \{e+1, e+2, \dots, m-1\} \\ \pi^-(r_a|R_{(b)}) &= w^-\left[\sum_{i=1}^b P(r_a|R_{(i)})\right] \\ &\quad - w^-\left[\sum_{i=1}^{b-1} P(r_a|R_{(i)})\right], \\ &\quad b \in \{2, 3, \dots, e\} \end{aligned} \quad (10)$$

where $\pi^+(\cdot)$ and $\pi^-(\cdot)$ denote the perceived probability of decision-makers corresponding to $V(r_a|R_{(b)}) \geq 0$, $b \in \{e+1, e+2, \dots, m\}$ and $V(r_a|R_{(b)}) \leq 0$, $b \in \{1, 2, \dots, e\}$, respectively. $w^+(\cdot)$ and $w^-(\cdot)$ are the following nonlinear functions.

$$\begin{aligned} w^+(p) &= \frac{p^\gamma}{[p^\gamma + (1-p)^\gamma]^{1/\gamma}} \\ w^-(p) &= \frac{p^\delta}{[p^\delta + (1-p)^\delta]^{1/\delta}} \end{aligned} \quad (11)$$

where p denotes the probability. γ and δ are parameters that used to describe the curve degree of $w^+(\cdot)$ and $w^-(\cdot)$, respectively.

Step 3. Calculate the overall prospect value of RPP in each POC-impacted region.

To be convenient for us to compare and discuss the calculated results, it is necessary to ensure that different prospect values of RPP in different regions have the same upper and lower bounds. To do this, $V(r_a|R_{(b)})$ is standardized in the following manner.

$$\bar{V}(r_a|R_{(b)}) = \frac{V(r_a|R_{(b)}) - V_{\min}(r_a|R_{(i)})}{V_{\max}(r_a|R_{(i)}) - V_{\min}(r_a|R_{(i)})}, \quad (12)$$

$$i \in \{1, 2, \dots, m\}$$

where $\bar{V}(r_a|R_{(b)})$ is the standardized result of $V(r_a|R_{(b)})$, obviously $\bar{V}(r_a|R_{(b)}) \in [0, 1]$; $V_{\max}(r_a|R_{(i)}) = \max\{V(r_a|R_{(1)}), V(r_a|R_{(2)}), \dots, V(r_a|R_{(m)})\}$; $V_{\min}(r_a|R_{(i)}) = \min\{V(r_a|R_{(1)}), V(r_a|R_{(2)}), \dots, V(r_a|R_{(m)})\}$. Meanwhile, the positive correlation between $\bar{V}(r_a|R_{(b)})$ and $V(r_a|R_{(b)})$ can be found.

Further, the standardized results of $V(r_a|R_{(b)}) \geq 0$, $b \in \{e+1, e+2, \dots, m\}$ and $V(r_a|R_{(b)}) \leq 0$, $b \in \{1, 2, \dots, e\}$ are denoted as $\bar{V}^+(r_a|R_{(b)})$ and $\bar{V}^-(r_a|R_{(b)})$, respectively. Both $\bar{V}^+(r_a|R_{(b)})$ and $\bar{V}^-(r_a|R_{(b)})$ can be obtained by formula (12), obviously, $\bar{V}^+(r_a|R_{(b)}) \in [0, 1]$, $\bar{V}^-(r_a|R_{(b)}) \in [0, 1]$.

To sum up, it can be seen that $\bar{V}^+(r_a|R_{(b)})$ and $\bar{V}^-(r_a|R_{(b)})$ correspond to the perceived probabilities $\pi^+(r_a|R_{(b)})$ and $\pi^-(r_a|R_{(b)})$ of decision-makers, respectively. Thus, the following formula (13) can be derived by considering the prospect value of RPP in all POC-impacted regions:

$$\begin{aligned} OV(R_{(b)}) &= \sum_{a=1}^A \left[\gamma \pi^+(r_a|R_{(b)}) \bar{V}^+(r_a|R_{(b)}) \right. \\ &\quad \left. + (1-\gamma) \pi^-(r_a|R_{(b)}) \bar{V}^-(r_a|R_{(b)}) \right] \end{aligned} \quad (13)$$

Where $OV(R_{(b)})$ denotes the overall prospect value of RPP in all POC-impacted regions after carrying out the alternative plan $R_{(b)}$. γ is an 0-1 integer variable and satisfies:

$$\gamma = \begin{cases} 0, & b \in \{1, 2, \dots, e\}; \\ 1, & b \in \{e+1, e+2, \dots, m\}. \end{cases} \quad (14)$$

As mentioned above, for determining the optimal response plan from alternatives when a certain scenario of POC appears, decision-makers should focus on the intervention effect of the alternatives on RPP. Meanwhile, combined with the proposed method for solving the SRPP in POC, we can see that the intervention effect of an alternative plan on RPP is reflected in the overall prospect value of RPP in all POC-impacted regions after carrying out this alternative. Therefore, the principle of determining the optimal response plan is which alternative plan can maximize the value of formula (13); in other words, the larger the $OV(R_{(b)})$ is, the better the alternative plan $R_{(b)}$ is. On this basis, the ranking of the alternatives can be obtained. In particular, if alternatives R_{i_1} and R_{i_2} ($i_1 \neq i_2$) satisfy $OV(R_{i_1}) = OV(R_{i_2})$, then which is better can be determined further by comparing their expected cost, difficulty in manipulation, and start-up timeliness, etc.. Eventually, based on the ranking of

TABLE 2: The supply of materials during the past period of time the public observe.

	region 1	region 2	region 3	region 4	region 5
$\widehat{d}_{at}, \forall t \in \{1, \dots, 30\}$	(4,6,8)	(1,3,9)	(3,4,9)	(5,6,11)	(2,3,4)
$d_{at}, \forall t \in \{1, \dots, 30\}$	6	4	5	7	3
D_{AT}			5		

TABLE 3: The importance and ambiguity of POC.

\overline{p}^{ij}	E_1^1	E_2^1	E_3^1
R_1	3	5	7
R_2	2	3	5
R_3	1	2	3

the alternatives, decision-makers can determine the optimal response plan in time according to their empirical data (e.g., the need for related material, financial and human resources) learned from the previous emergency drill.

4. An Example

Major epidemics of infectious diseases have occurred frequently in recent years, and they often lead to the POC and the snap-up of related protective drugs, such as SARS in 2003 and H1N1 flu in 2009 described above. Therefore, a theoretical example of the SRPP in POC in a country under the background of this kind of major epidemics of infectious diseases is given to illustrate the potential application and effectiveness of the proposed method. Symptomatic incidents often occur in the early stages of outbreaks of major epidemics of infectious diseases, such as suspected viral infectors appear and they have a long-term fever. Since this concerns the safety of the public, some panic and rumors have been promptly triggered, which might as well be recorded as the current scenario S_1 faced by decision-makers, i.e., $S = \{S_1\}$ and $P(S_1) = 1$. After estimating the situation of the POC, decision-makers have determined the following three alternatives based on emergency preparedness regulations.

R_1 : Establish a response team to monitor the development of the POC, and notify the relevant enterprises to prepare for the response.

R_2 : Launch guidance strategies for the POC based on the response preparation, and require enterprises to ensure the supply of materials the public may snap up.

R_3 : On the basis of the POC guidance, inform the progress of dealing with the epidemic event in a timely manner and order enterprises to increase the supply of relevant materials.

After carrying out the alternative plan $R_i, i \in \{1, 2, 3\}$, the current scenario S_1 will evolve into one of the following new scenarios:

E_1^1 : Panics of the public are effectively alleviated, rumors are reasonably controlled and the POC is declined or disappeared.

E_2^1 : The spreading scope of the POC is only concentrated in a small part of the country, and most parts of the country are not impacted.

E_3^1 : The POC has an impact on all parts of the country, leading to the spread of serious rumors and panics.

In the current scenario S_1 , we set up the total number of regions the public concern $A = 5$, and $a \in \{1, 2, 3, 4, 5\}$. A day is denoted as the unit of the past period of time t the public observe, and $T = 30, t \in \{1, 2, \dots, 30\}$. The supply of materials \widehat{d}_{at} and its expected value d_{at} calculated by formula (9) are shown in Table 2. Meanwhile, we can obtain $D_{AT} = 5$ by formula (1). The spreading scope $\widehat{\rho}_1$ is set as the evaluation indicator for the importance and ambiguity of POC, and its value ranges from 1 to 7, where 1 and 7 denote the minimum and maximum respectively, thereby $\widehat{\rho} = \{\widehat{\rho}_1\}$. Thus, the values of \overline{p}^{ij} can be obtained, as shown in Table 3. Under carrying out different alternative plans, the current supply of materials $d_{a(T+1)}^{R_i}$ in the region a is shown in Table 4; hence we can obtain $D_{A(T+1)}^{R_1} = 4, D_{A(T+1)}^{R_2} = 6, D_{A(T+1)}^{R_3} = 10$ by formula (2). Assuming that the values of critical sense $\overline{\theta}_a$ of the public range from 1 to 7, where 1 and 7 indicate the lowest and highest respectively, here we assume $\overline{\theta}_a = a, a \in \{1, 2, 3, 4, 5\}$. Considering the completeness of alternative plans and the severity of new scenarios, we can obtain the probability of new scenarios appear by analyzing the related historical data with neural network, Bayesian reasoning, evidence reasoning, etc.; here the data given in [26] is used, as shown in Table 5. For other parameters, it may be appropriate to set up as $\alpha_1 = \alpha_2 = \beta_1 = \beta_2 = 0.88, \lambda_1 = \lambda_2 = 2.25, \gamma = 0.61, \delta = 0.69$ [34, 35]. Based on this, the value of RPP in each region can be obtained by using formula (6) and setting up $r_0 = 10$, as shown in Table 6. In summary, the decision steps for solving the SRPP in the POC with the proposed method are as follows.

Step 1. $V(r_a|R_i)$ and $\overline{V}(r_a|R_i), a = 1, 2, 3, 4, 5; i_1 = 1, 2, 3$ are first obtained with formulae (7), (8), and (12), as shown in Table 7 and Table 8, respectively.

Step 2. The prospect values $V(r_a|R_i), i_1 = 1, 2, 3$ of RPP in different regions are ranked, respectively, and $V(r_a|R_1) < V(r_a|R_2) < 0 < V(r_a|R_3), a = 1, 2, 3, 4, 5$ can be obtained, which is recorded as $V(r_a|R_{(1)}) < V(r_a|R_{(2)}) < 0 < V(r_a|R_{(3)}), a = 1, 2, 3, 4, 5$. Based on this, if we set up the probability that the RPP takes the current value in the region a as $P_a^j = 0.5, a = 1, 2, 3, 4, 5, j = 1, 2, 3$ when S_1 evolves into E_j^1 after carrying out the alternative plan $R_{(b)}$, then the value of $P(r_a|R_{(b)})$ can be obtained in conjunction with Table 5, that is, $P(r_a|R_{(b)}) = \sum_{j=1}^3 P(S_1)P(E_j^1|R_{(b)})P_a^j = 0.5, a = 1, 2, 3, 4, 5, b = 1, 2, 3$. Further, substituting $P(r_a|R_{(b)}) = 0.5$ into formulae (10) and (11), we can obtain $\pi^-(r_a|R_{(1)}) = 0.454, \pi^-(r_a|R_{(2)}) = 0.546, \pi^+(r_a|R_{(3)}) = 0.421, a = 1, 2, 3, 4, 5$.

TABLE 4: The supply of materials in the current period of time the public observe.

$d_{a(T+1)}^{R_i}$	region 1	region 2	region 3	region 4	region 5
R_1	4	5	3	6	2
R_2	5	8	6	7	4
R_3	7	9	10	13	11

TABLE 5: The relationship between alternative plans and new scenarios.

$P(E_j^1 R_i)$	E_1^1	E_2^1	E_3^1
R_1	0.1	0.3	0.6
R_2	0.2	0.25	0.55
R_3	0.3	0.2	0.5

Step 3. As shown in Table 8, $\bar{V}(r_1 | R_{(2)}) = 0.541$, $\bar{V}(r_2 | R_{(2)}) = 0.568$, $\bar{V}(r_3 | R_{(2)}) = 0.610$, and $\bar{V}(r_4 | R_{(2)}) = 0.643$, $\bar{V}(r_a | R_{(1)}) = 0$, $\bar{V}^+(r_a | R_{(3)}) = 1$, $a = 1, 2, 3, 4, 5$. Based on this, the overall prospect value of RPP in all POC-impacted regions after carrying out the alternative plan $R_{(b)}$, $b \in \{1, 2, 3\}$ can be obtained by formulae (13) and (14), namely, $OV(R_{(1)}) = 0$, $OV(R_{(2)}) = 1.636$, $OV(R_{(3)}) = 2.105$. Therefore, according to the principle of determining the optimal response plan, we can obtain $R_{(3)} > R_{(2)} > R_{(1)}$ (where “>” denotes “better than”), i.e., $R_3 > R_2 > R_1$.

In fact, the calculation results are also consistent with the actual situation of emergency decision-making for POC in the context of such a major epidemic of infectious diseases. For example, during the response to the POC caused by SARS in 2003, it is precisely because the characteristics of SARS virus are not clear and the evolution trend of POC is difficult to be identified effectively in the early stage of SARS outbreaks that some rumors and panics failed to draw sufficient attention from decision-makers, i.e., which accords with R_1 or R_2 . As a result, the POC evolves at an amazing speed and lead to large regions of panic buying of materials (thermometers, masks, rice vinegar, isatis root, etc.). Until the Department of Health of Guangdong Province of China and the CPC Central Committee and State Council one after another issued a variety of strong response measures, i.e., which accords with R_3 , the evolution of the POC is finally subsided and controlled.

5. Conclusions

The multicase study is first employed to describe the SRPP in POC that may lead to panic buying of materials derived from public emergencies, and thus eight typical cases are chosen to analyze the POC and its relevant response measures. Then, the SRPP is defined in detail, that is, how to determine the optimal response plan from the alternatives from the perspective of the intervention of RPP with the consideration of behavioral characteristics of decision-makers. To do this, the RPP is described with prospect theory through considering the behavioral characteristics and critical sense

of the public, the response measures of decision-makers, and the importance and ambiguity of POC. Further, considering the behavioral characteristics of decision-makers and the impact of alternative plans on the evolution of scenarios of POC, a new decision method for solving the SRPP with the intervention of the RPP is proposed by using cumulative prospect theory and a manner of comparing alternative response plans for each other. The proposed method shows that the different overall prospect values of the RPP after carrying out different alternative plans can be compared to obtain the ranking of alternatives. Finally, an example of the SRPP in POC in the context of major epidemics of infectious diseases is given to illustrate the potential application and effectiveness of the proposed method.

This study can not only enrich the methodology of selecting optimal response plan but also provide some theoretical support for how to restrict the outbreak of secondary incidents in POC such as the panic buying of materials. To sum up, the specific contributions of this study are threefold. First, the RPP is described with prospect theory through considering the behavioral characteristics and critical sense of the public, the response measures of decision-makers, and the importance and ambiguity of POC. Second, a new decision method for solving the SRPP in POC that may lead to panic buying of materials is proposed from the perspective of the intervention of alternatives on RPP. Third, a manner of comparing the alternatives for each other is taken to avoid the deviation probably caused by setting up the reference point artificially, and the impact of the alternatives on the evolution of POC scenarios is considered in the proposed method. The above contributions overcome the shortages that the existing studies neglect the decision-makers' urgent need for decision methods in response to POC that may lead to panic buying of materials in practice.

For the future research, there are two directions to be attached great importance to. One is that the SRPP with time constraint probably needs to be solved further, and thus the proposed method in this paper needs to be extended. The reason is that the response time is probably an important factor affecting the accuracy of the decision-making when determining the optimal plan in response to POC. This direction is motivated by the response to natural disasters and environmental emergencies. For example, Wex et al. [13] point out that response plans should be determined within 30 minutes after the outbreak of natural disasters. In addition, according to “the emergency plan for environmental emergencies in Beijing of China” (the revised edition in 2015), the emergency management office in Beijing stipulates that the municipal environmental protection bureau and the district government must submit the general and detailed situation within 10 minutes and 2 hours respectively after

TABLE 6: The relationship between alternative plans and RPP.

$\{r_a\}$	E_1^1	E_2^1	E_3^1
R_1	{28.561, 16.776, 12.250, 9.705, 9.000}	{42.790, 24.794, 18.177, 14.593, 12.250}	{56.194, 32.227, 23.509, 18.865, 15.916}
R_2	{9.621, 9.000, 7.629, 6.989, 6.613}	{25.557, 13.215, 9.000, 7.959, 7.371}	{40.025, 21.683, 14.742, 10.664, 9.000}
R_3	{5.878, 4.111, 3.539, 3.255, 3.086}	{10.000, 5.878, 4.691, 4.111, 3.767}	{19.274, 7.760, 5.878, 4.984, 4.458}

TABLE 7: The prospect value of RPP.

$V(r_a R_{i_1})$	r_1	r_2	r_3	r_4	r_5
R_1	-39.953	-26.594	-20.357	-16.735	-14.043
R_2	-8.674	-4.924	-2.835	-1.741	-1.577
R_3	17.888	11.582	8.380	6.591	5.615

TABLE 8: The standardization for the prospect value of RPP.

$\bar{V}(r_a R_{i_1})$	r_1	r_2	r_3	r_4	r_5
R_1	0	0	0	0	0
R_2	0.541	0.568	0.610	0.643	0.634
R_3	1	1	1	1	1

environmental emergencies happen. The other is that the SRPP with dynamic alternative response plans need to be studied further due to the content and the quantity of alternatives are probably dynamic or can be updated with the evolution of POC.

Data Availability

The data used to support the findings of this study are included within this paper. It is also available from the corresponding author upon request.

Additional Points

Highlights. The RPP is described with prospect theory through considering the behavioral characteristics and critical sense of the public, the response measures of decision-makers, and the importance and ambiguity of POC.

A new decision method for solving the SRPP in POC that may lead to panic buying of materials is proposed from the perspective of the intervention of alternatives on RPP.

A manner of comparing the alternatives for each other is taken to avoid the deviation probably caused by setting up the reference point artificially, and the impact of the alternatives on the evolution of POC scenarios is considered in the proposed method.

Conflicts of Interest

The authors declare that there are no conflicts of interest regarding the publication of this paper.

Acknowledgments

This work was jointly supported by the National Natural Science Foundation of China (Project nos. 71704001 and

71601002), the Natural Science Foundation in Anhui Province (Project nos. 1808085QG224 and 1708085MG168), the Humanities and Social Science Key Project of Anhui Provincial Education Department (Project no. SK2019A0075), the Planning Funds of Philosophy and Social Science in Anhui Province (Project nos. AHSKY2018D13 and AHSKQ2016D19), and the Humanities and Social Sciences Foundation of Ministry of Education of China (Project no. 18YJC630249).

References

- [1] S. Gupta, M. K. Starr, R. Z. Farahani, and N. Matinrad, "Disaster management from a POM perspective: mapping a new domain," *Production and Operations Management*, vol. 25, no. 10, pp. 1611–1637, 2016.
- [2] İ. Akgün, F. Gümüşbuğa, and B. Tansel, "Risk based facility location by using fault tree analysis in disaster management," *Omega*, vol. 52, pp. 168–179, 2015.
- [3] N. Argyris and S. French, "Nuclear emergency decision support: A behavioural OR perspective," *European Journal of Operational Research*, vol. 262, no. 1, pp. 180–193, 2017.
- [4] N. P. Rachaniotis, T. K. Dasaklis, and C. P. Pappis, "A deterministic resource scheduling model in epidemic control: a case study," *European Journal of Operational Research*, vol. 216, no. 1, pp. 225–231, 2012.
- [5] K. Kim, Y. M. Baek, and N. Kim, "Online news diffusion dynamics and public opinion formation: A case study of the controversy over judges' personal opinion expression on SNS in Korea," *Social Science Journal*, vol. 52, no. 2, pp. 205–216, 2015.
- [6] K. Fan and W. Pedrycz, "Emergence and spread of extremist opinions," *Physica A: Statistical Mechanics and its Applications*, vol. 436, pp. 87–97, 2015.
- [7] M. Xie, Z. Jia, Y. Chen, and Q. Deng, "Simulating the spreading of two competing public opinion information on complex network," *Applied Mathematics*, vol. 3, no. 9, pp. 1074–1078, 2012.

- [8] X. Du, Y. Ye, R. Y. Lau, and Y. Li, "OpinionRings: Inferring and visualizing the opinion tendency of socially connected users," *Decision Support Systems*, vol. 75, pp. 11–24, 2015.
- [9] N. Ma and Y. Liu, "SuperedgeRank algorithm and its application in identifying opinion leader of online public opinion supernetwork," *Expert Systems with Applications*, vol. 41, no. 4, pp. 1357–1368, 2014.
- [10] F. Battiston, A. Cairoli, V. Nicosia, A. Baule, and V. Latora, "Interplay between consensus and coherence in a model of interacting opinions," *Physica D: Nonlinear Phenomena*, vol. 323–324, pp. 12–19, 2016.
- [11] D. Centola, "The spread of behavior in an online social network experiment," *Science*, vol. 329, no. 5996, pp. 1194–1197, 2010.
- [12] K. Amailef and J. Lu, "Ontology-supported case-based reasoning approach for intelligent m-Government emergency response services," *Decision Support Systems*, vol. 55, no. 1, pp. 79–97, 2013.
- [13] F. Wex, G. Schryen, S. Feuerriegel, and D. Neumann, "Emergency response in natural disaster management: allocation and scheduling of rescue units," *European Journal of Operational Research*, vol. 235, no. 3, pp. 697–708, 2014.
- [14] R. P. Hämäläinen, M. R. K. Lindstedt, and K. Sinkko, "Multi-attribute risk analysis in nuclear emergency management," *Risk Analysis*, vol. 20, no. 4, pp. 455–467, 2000.
- [15] J. Geldermann, V. Bertsch, M. Treitz, S. French, K. N. Papamichail, and R. P. Hämäläinen, "Multi-criteria decision support and evaluation of strategies for nuclear remediation management," *Omega*, vol. 37, no. 1, pp. 238–251, 2009.
- [16] L. Yu and K. K. Lai, "A distance-based group decision-making methodology for multi-person multi-criteria emergency decision support," *Decision Support Systems*, vol. 51, no. 2, pp. 307–315, 2011.
- [17] F.-S. Chang, J.-S. Wu, C.-N. Lee, and H.-C. Shen, "Greedy-search-based multi-objective genetic algorithm for emergency logistics scheduling," *Expert Systems with Applications*, vol. 41, no. 6, pp. 2947–2956, 2014.
- [18] G. Fu, "A fuzzy optimization method for multicriteria decision making: an application to reservoir flood control operation," *Expert Systems with Applications*, vol. 34, no. 1, pp. 145–149, 2008.
- [19] J. Yang and C. Xu, "Emergency decision engineering model based on sequential games," *Systems Engineering Procedia*, vol. 5, pp. 276–282, 2012.
- [20] Y. Liu, Z.-P. Fan, Y. Yuan, and H. Li, "A FTA-based method for risk decision-making in emergency response," *Computers & Operations Research*, vol. 42, pp. 49–57, 2014.
- [21] A. Ebrahim Nejad, I. Niroomand, and O. Kuzgunkaya, "Responsive contingency planning in supply risk management by considering congestion effects," *OMEGA*, vol. 48, pp. 19–35, 2014.
- [22] F. He and J. Zhuang, "Balancing pre-disaster preparedness and post-disaster relief," *European Journal of Operational Research*, vol. 252, no. 1, pp. 246–256, 2016.
- [23] Y. Liu, Z.-P. Fan, and Y. Zhang, "Risk decision analysis in emergency response: a method based on cumulative prospect theory," *Computers & Operations Research*, vol. 42, pp. 75–82, 2014.
- [24] Z. Fan, Y. Liu, and R. Shen, "Risk decision analysis method for emergency response based on prospect theory," *Systems Engineering — Theory & Practice*, vol. 32, no. 5, pp. 977–984, 2012.
- [25] S. Li, N. Yang, and Y. Zhang, "Risk decision analysis method for emergency plan selection," *Control and Decision*, vol. 28, no. 12, pp. 1859–1863, 2013.
- [26] Z.-Y. Wang and Y.-J. Li, "Intervention mechanism of behavioral decision-making on emergency and its starting strategy of contingency plan," *Systems Engineering — Theory & Practice*, vol. 35, no. 7, pp. 1863–1870, 2015.
- [27] Z. Wang and Y. Li, "Structural description and interaction law of public opinion propagation and emergency decision-making," *Systems Engineering — Theory & Practice*, vol. 35, no. 8, pp. 2064–2073, 2015.
- [28] M. Frondel, M. Simora, and S. Sommer, "Risk perception of climate change: empirical evidence for germany," *Ecological Economics*, vol. 137, pp. 173–183, 2017.
- [29] G. Wachinger, O. Renn, C. Begg, and C. Kuhlicke, "The risk perception paradox-implications for governance and communication of natural hazards," *Risk Analysis*, vol. 33, no. 6, pp. 1049–1065, 2013.
- [30] L. N. Rickard, "Perception of risk and the attribution of responsibility for accidents," *Risk Analysis*, vol. 34, no. 3, pp. 514–528, 2014.
- [31] T. M. Lee, E. M. Markowitz, P. D. Howe, C.-Y. Ko, and A. A. Leiserowitz, "Predictors of public climate change awareness and risk perception around the world," *Nature Climate Change*, vol. 5, no. 11, pp. 1014–1020, 2015.
- [32] Y. Su, F. Zhao, and L. Tan, "Whether a large disaster could change public concern and risk perception: a case study of the 7/21 extraordinary rainstorm disaster in Beijing in 2012," *Natural Hazards*, vol. 78, no. 1, pp. 555–567, 2015.
- [33] R. A. Ferrer, W. M. Klein, A. Persoskie, A. Avishai-Yitshak, and P. Sheeran, "The tripartite model of risk perception (TRIRISK): distinguishing deliberative, affective, and experiential components of perceived risk," *Annals of Behavioral Medicine*, vol. 50, no. 5, pp. 653–663, 2016.
- [34] D. Kahneman and A. Tversky, "Prospect theory: an analysis of decision under risk," *Econometrica*, vol. 47, no. 2, pp. 263–291, 1979.
- [35] A. Tversky and D. Kahneman, "Advances in prospect theory: cumulative representation of uncertainty," *Journal of Risk and Uncertainty*, vol. 5, no. 4, pp. 297–323, 1992.
- [36] H. Bleichrodt, U. Schmidt, and H. Zank, "Additive utility in prospect theory," *Management Science*, vol. 55, no. 5, pp. 863–873, 2009.
- [37] M. Nagarajan and S. Shechter, "Prospect theory and the newsvendor problem," *Management Science*, vol. 60, no. 4, pp. 1057–1062, 2014.
- [38] X. Long and J. Nasiry, "Prospect theory explains newsvendor behavior: the role of reference points," *Management Science*, vol. 61, no. 12, pp. 3009–3012, 2015.
- [39] R. M. Campos-Vazquez and E. Cuijly, "The role of emotions on risk aversion: A Prospect Theory experiment," *Journal of Behavioral and Experimental Economics*, vol. 50, pp. 1–9, 2014.
- [40] X. Wang, C. Ma, and J. Ruan, "Emergency supplies optimal scheduling considering the public's psychological risk perception," *Systems Engineering — Theory & Practice*, vol. 33, no. 7, pp. 1735–1742, 2013.
- [41] C. Durugbo, "Competitive product-service systems: lessons from a multicase study," *International Journal of Production Research*, vol. 51, no. 19, pp. 5671–5682, 2013.
- [42] K. M. Eisenhardt and M. E. Graebner, "Theory building from cases: opportunities and challenges," *Academy of Management Journal (AMJ)*, vol. 50, no. 1, pp. 25–32, 2007.

- [43] Z. S. Byrne, K. J. Dvorak, J. M. Peters, I. Ray, A. Howe, and D. Sanchez, "From the user's perspective: Perceptions of risk relative to benefit associated with using the Internet," *Computers in Human Behavior*, vol. 59, pp. 456–468, 2016.
- [44] M. Setbon, J. Raude, C. Fischler, and A. Flahault, "Risk perception of the "mad cow disease" in France: Determinants and consequences," *Risk Analysis*, vol. 25, no. 4, pp. 813–826, 2005.
- [45] B. Rohrmann, "A socio-psychological model for analyzing risk communication processes," *The Australasian Journal of Disaster and Trauma Studies*, vol. 2000, no. 2, pp. 30–50, 2000.
- [46] J. Kind, W. J. Wouter Botzen, and J. C. J. H. Aerts, "Accounting for risk aversion, income distribution and social welfare in cost-benefit analysis for flood risk management," *Wiley Interdisciplinary Reviews: Climate Change*, vol. 8, no. 2, pp. 1–20, 2017.
- [47] X. Liu, Z. Wang, and S. Zhang, "A new methodology for hesitant fuzzy emergency decision making with unknown weight information," *Complexity*, vol. 2018, Article ID 5145348, 12 pages, 2018.
- [48] Y. Sarafidis, "What have you done for me lately? Release of information and strategic manipulation of memories," *Economic Journal*, vol. 117, no. 518, pp. 307–326, 2007.
- [49] M. Abdellaoui, H. Bleichrodt, and C. Paraschiv, "Loss aversion under prospect theory: a parameter-free measurement," *Management Science*, vol. 53, no. 10, pp. 1659–1674, 2007.
- [50] J. K. Roehrich, J. Grosvold, and S. U. Hojmoose, "Reputational risks and sustainable supply chain management: Decision making under bounded rationality," *International Journal of Operations and Production Management*, vol. 34, no. 5, pp. 695–719, 2014.
- [51] N. J. Foss and L. Weber, "Moving Opportunism to the Back Seat: Bounded Rationality, Costly Conflict, and Hierarchical Forms," *Academy of Management Review (AMR)*, vol. 41, no. 1, pp. 61–79, 2016.
- [52] S. Chandra and A. Aggarwal, "On solving matrix games with pay-offs of triangular fuzzy numbers: Certain observations and generalizations," *European Journal of Operational Research*, vol. 246, no. 2, pp. 575–581, 2015.
- [53] G. W. Allport and L. Postman, *The Psychology of Rumor*, Henry Holt, Oxford, UK, 1947.
- [54] M. Sääksjärvi, T. Gill, and E. J. Hultink, "How rumors and preannouncements foster curiosity toward products," *European Journal of Innovation Management*, vol. 20, no. 3, pp. 350–371, 2017.
- [55] A. Chorus, "The basic law of rumor," *The Journal of Abnormal and Social Psychology*, vol. 48, no. 2, pp. 313–314, 1953.
- [56] S. Elizabeth and L. Sujatha, "Project scheduling method using triangular intuitionistic fuzzy numbers and triangular fuzzy numbers," *Applied Mathematical Sciences*, vol. 9, no. 1–4, pp. 185–198, 2015.
- [57] T.-S. Liou and M. J. Wang, "Ranking fuzzy numbers with integral value," *Computers in Human Behavior*, vol. 50, no. 3, pp. 247–255, 1992.
- [58] R. R. Yager, "A procedure for ordering fuzzy subsets of the unit interval," *Information Sciences*, vol. 24, no. 2, pp. 143–161, 1981.